

Slow Wave Resonator Based Tunable Multi-Band Multi-Mode Injection- Locked Oscillators

Dr.-Ing. Ajay K. Poddar

Research Report
Ulrich-L.-Rohde Chair for RF and Microwave Techniques
Brandenburg University of Technology Cottbus-Senftenberg
2013

Research Report by Dr.-Ing. Ajay K. Poddar.

This work is an extended version of Dr. Poddar's thesis submitted to the faculty of mechanical, electrical and industrial engineering of the Brandenburgische Technische Universität Cottbus-Senftenberg for the continuation of "Dr.-Ing. Habil" degree.

Copyright by the author.

Author Contact Data:

Dr.-Ing. Ajay K. Poddar.
River Drive
Elmwood Park, NJ 07407, USA
Email: poddar_ajay@yahoo.com
Phone: (001)-201-791-9605

Summary

In modern information technology, increasingly powerful electronic circuits are required for the targeted generation of complex signals with well-defined amplitudes and phases. In circuits of this type, oscillators frequently form the central element because of its phase noise and stability, which essentially determines the achievable precision in the signal generation. Further requirements are derived from the electronic definability of the signal properties and the operational behavior of the oscillators. Conventional oscillator circuit models autonomous circuits, mainly consist of a passive frequency-selective or phase-selective network and an active amplifier element, which together produce an oscillatory circuit via a suitable feedback. At first glance, the circuit topology seems to be quite simple and can often be explained quite visibly. However, when it comes to describing in particular the very important phase noise dynamics and stability of oscillators, it very soon becomes apparent that highly complex structures are involved. A fundamental difficulty in the theoretical description arises due to the non-linear behavior of oscillators, the understanding of which is crucial for a reliable description of jitter and oscillator phase noise. The resonant condition of oscillators arises due to the fact that the noise in the oscillator circuit is always present in the system for $T > 0$ degree Kelvin, which is amplified in a frequency-selective manner to the extent that a stable oscillation arises at most at a fixed frequency because of non-linear limitation of the amplification. The frequency selectivity arises due to the frequency selectivity or phase selectivity of the mainly passive feedback path. The non-linear limitation of the amplification in the oscillator normally results in a very reliable control of the amplitude noise of the output oscillation. It is well understood that any particular oscillator's phase noise could be improved by increasing the generated signal amplitude or increasing the quality factor of the resonant network. Increasing the signal level is limited by the utilized supply voltage or the break down limits of transistors and cannot be increased further to improve the phase noise. Accordingly, the remaining phase noise, which can normally be minimized via resonating circuits with pronounced phase selectivity and therefore a high quality factor resonator, is of great importance for oscillators. Traditional high Q-factor resonators (ceramic resonator, surface acoustic wave, bulk acoustic wave, dielectric resonator, YIG resonator, Whispering gallery mode resonator, Optoelectronic resonator, etc.) are usually 3-dimensional structures and bulky for both handheld and test-measurement equipments and does not offer integration using current foundry technology. The 4th generation wireless communication market is pushing the need for miniaturization to its limits. Printed coupled transmission line resonator is a promising alternative due to its ease of integration and compatibility with planar fabrication processes but limited by its large physical size and low quality factor, making it a challenging choice to design low phase-noise oscillators. This problem is more prominent in integrated circuits (ICs) where high degrees of thin conductor losses reduce the quality factor by orders of magnitude compared to hybrid circuit technologies.

This thesis describes the design and investigation of a variation of printed resonators using Möbius slow-wave structures for the applications in oscillator circuits. A novel Möbius slow-wave mode-coupled structure offers additional degrees of freedom (higher Q-factor and multi-band characteristics) as compared to conventional transmission line printed resonators. A design study has been carried out to optimize the phase noise performance by using the novel resonant structures (mode-coupled, slow-wave, Möbius strips, evanescent mode, negative index metamaterial) in conjunction with mode coupling, and injection locking for improving the overall performances, beyond the limits imposed by conventional limitations. The thesis also covers a broad spectrum of research on DRO and OEO ranging from practical aspects of circuit implementation and measurement through to sophisticated design and the modeling of complex circuits and resonator structures. This thesis is research work carried out from 2004-2014, organized in 11 chapters, theoretical and experimental

results documented by a range of specific measurement results and substantiated by over 150 publications in scientific conferences and over dozen patents approved, which are listed below:

1. *Metamaterial Resonator Based Oscillators*, US Patent applications No. 61976185, April 2014
2. *BALUN*, US Patent applications No. 61976199, April 2014
3. *Integrated production of self injection locked self phase loop locked Opto-electronic Oscillators*, US Patent application no. 13/760767 (Feb 06, 2013).
4. *User-definable, low cost, low phase hit and spectrally pure tunable oscillator*, European Patent No. 1 783 893 - January, 9, 2013
5. *Self Injection Locked Phase Locked Looped Optoelectronic Oscillator*, US Patent application No. 61/746, 919 (Dec 28, 2012).
6. *Wideband Voltage Controlled Oscillator Employing Evanescent Mode*, Japanese Patent No. 5102019 - October 5, 2012
7. *Passive Reflection Mixer*, CA. Patent No. 2524751 - March 1, 2010
8. *Tunable Oscillator*, CA. Patent No. 2533623 - March 1, 2010
9. *Tunable Frequency, Low Phase Noise and Low Thermal Drift Oscillator*, CA. Patent No. 2534370 - February 9, 2010
10. *Low Noise And Low Phase Hits Tunable Oscillator*, US Patent No: 7,636,021 - December 22, 2009
11. *Visually Inspectable Surface Mount Device Pad*, US Patent No: 7,612,296 - November 3, 2009
12. *User-Definable Low Cost, Low Noise, and Phase Hits Insensitive (Multi-Octave-Band Tunable Oscillator)*, US Patent No: 7,605,670 - October 20, 2009
13. *User-Definable Low Cost, Low Phase Hits and Spectrally Pure Tunable Oscillator*, US Patent No: 7,586,381 - September 8, 2009
14. *User-Definable Low Cost, Low Noise, and Phase Hits Insensitive Multi-Octave-Band Tunable Oscillator*, CA. Patent No. 2568244 - September 24, 2009
15. *Passive Reflection Mixer*, U.S. Patent No. 7,580,693 - August 25, 2009
16. *Integrated Low Noise Microwave Wideband Push-Push VCO*, CA. Patent No- 2548311, Aug 2009
17. *User Definable Thermal Drift Voltage Oscillator*, CA. Patent No. 2548317 - August 5, 2009
18. *Low Noise, Hybrid Tuned Wideband Voltage Controlled Oscillator*, US. Patent 7365612, April 2008
19. *Multi-Octave Band Tunable Coupled - Resonator Oscillator*, US Patent No. 7292,113, NoV. 2007
20. *User-Definable Thermal Drift Voltage Controlled Oscillator*, US Patent No. 7265,642, Sept. 2007
21. *Low Thermal Drift, Tunable Frequency VCO*, US Patent No. 7262670 Aug. 2007
22. *Tunable Frequency, Low Phase Noise and Low Thermal Drift Osc.* US Patent 7196591 March 2007
23. *Wideband Voltage Controlled Oscillator Employing Evanescent Mode Coupled-Resonators* U.S. Patent No. 7,180,381 - February 20, 2007
24. *Oscillator Circuit Configuration*, U.S Patent No. 7,102,453 - September 5, 2006
25. *Integrated Low Noise Microwave Wideband Push-Push VCO* U.S. Patent No. 7088189, Aug. 2006

Preface, Appreciation, and Acknowledgement

This work is the result of my research in the area of microwave oscillators and my desire to replace the expensive resonators (ceramic resonator, SAW resonators, Dielectric Resonators, YIG resonators) with new class of printed slow-wave mode-coupled resonator that minimizes microphonics and yet optimizes phase noise, output power, harmonics, and size. The novel injection-mode-locking approach is validated in 100 MHz Crystal oscillator, X-band DRO, X-band Opto-electronic oscillator (OEO), and X-band printed resonator oscillator solution for applications in current and later generation communication systems. This work is a continuation of my Dr.-Ing dissertation in TU-Berlin, Germany. The related research work was only possible based on many measurements and tests performed at Synergy Microwave Corporation. I am thankful for the support of Anisha Apte for doing the required proofreading of the manuscript.

Slow Wave Resonator Based Tunable Multi-Band Multi-Mode Injection-Locked Oscillators

Submitted in February 2013 to the Technischen Universität Cottbus-Senftenberg

The possibility to use this research topic for habilitation made available by Prof. Dr.-Ing. habil Ulrich L. Rohde (BTU-Germany) who made himself available for many discussions on this novel technology. Prof. Dr.-Ing. habil Wolfgang Heinrich (TUB-Germany), Prof. Dr.-Ing. Matthias Rudolph (BTU-Germany), Prof. Ignaz Eisele (UniBW-Germany), Prof. Dr.-Ing. Thomas Eibert (TUM-Germany), Prof. Dr.-Ing. Gerhard Lappus, Prof. Tatsuo Itoh (UCLA-USA), Prof. Afshin Daryoush (DU-USA), Prof. Shiban Koul (IITD-India), Prof. Takashi Ohira (TUT-Japan), Prof. Dr.-Ing. Frank Küppers (TUD-Germany) and Prof. Hans Hartnagel (TUD-Germany) were always available for technical discussions and useful recommendations.

My acknowledgements would not be complete without expressing gratitude towards Mother Nature, our creator and redeemer.

Table of Contents

	Page
Summary	
1. Introduction	7
1.1 Abstract	7
1.2 Motivation	7
1.3 Problem Statement	8
1.4 Definition of the Task and Oscillator Figure of Merit (FOM)	9
1.5 Overview of the Thesis	13
1.6 Publications and Patent Applications arising from this research work	16
1.7 References	16
2. General Comments on Oscillators	18
2.1 Theory of Operation	18
2.2 Specifications of Tunable Oscillators	25
2.2.1 Frequency Range and Tuning Characteristics	25
2.2.2 Tuning Linearity	25
2.2.3 Tuning Sensitivity, Tuning Performance	25
2.2.4 Tuning Speed	25
2.2.5 Post-Tuning Drift	25
2.2.6 Phase Noise	26
2.2.7 Output Power	28
2.2.8 Harmonic Suppression	28
2.2.9 Output Power as a Function of Temperature	28
2.2.10 Spurious Response	28
2.2.11 Frequency Pushing	29
2.2.12 Sensitivity to Load Changes	29
2.2.13 Power Consumption	30
2.3 History of Microwave Oscillators	30
2.4 Resonator Choice	34
2.4.1 LC Resonator	34
2.4.2 Transmission Line Resonator	35
2.4.3 Integrated Resonator	36
2.5 Large Signal S-Parameter Analysis	40
2.5.1 Definition	40
2.5.2 Large Signal S-Parameter Measurements	42
2.6 Passive and Active Inductor Based Resonator Network	54
2.6.1 Passive Inductor	54
2.6.2 Active Inductor	56
2.7 Selection Criteria and Performance Comparison	58
2.8 Tunable Active Inductor Oscillator	59
2.9 RF MEMS Technology	60
2.9.1 RF MEMS Components	61
2.9.2 Tunable Inductor Using RF MEMS Technology	63
2.10 Active Capacitor	63

2.10.1	Diplexer using Active Capacitor Circuit	66
2.10.2	Oscillator using Active Capacitor Circuit	69
2.10.3	Tunable Oscillator using Active Capacitor Circuit	71
2.11	Conclusion	72
2.12	References	72
3	Noise Analysis of the Oscillators	76
3.1	Oscillator Noise	76
3.1.1	Source of Noise	76
3.1.2	Oscillator Noise model Comments	78
3.2	Leeson's Phase Noise Model	83
3.2.1	Leeson's Phase Noise Model (Linear Time Invariant Approach)	84
3.2.2	Lee and Hajimiri's Noise Model (Linear Time Variant Model)	94
3.2.3	Kaertner and Demir's Noise Model (Nonlinear Time Variant)	102
3.2.4	Multiple Threshold Crossing Noise Model	104
3.2.5	Conclusion on Phase Noise Models	105
3.3	References	106
4	Phase Noise Measurement Techniques and Limitations	112
4.1	Introduction	112
4.2	Noise in Circuits and Semiconductors	112
4.2.1	Johnson Noise	113
4.2.2	Planck's Radiation Noise	113
4.2.3	Schottky/Shot Noise	114
4.2.4	Flicker Noise	114
4.2.5	Transit Time and Recombination Noise	114
4.2.6	Avalanche Noise	114
4.3	Phase Noise Measurement Techniques	115
4.3.1	Direct Spectrum Technique	115
4.3.2	Frequency Discriminator Method	117
4.3.2.1	Heterodyne (Digital) Discriminator Method	120
4.3.3	Phase Detector Technique	121
4.3.3.1	Reference Source/PLL Method	122
4.3.4	Residual Method	125
4.3.5	Two-Channel Cross-Correlation Technique	126
4.3.6	Conventional Phase Noise Measurement System	130
4.4	Prediction and Validation of Oscillator PN Measured on Different Equipments	133
4.4.1	Verification of 100MHz Crystal Oscillator Using CAD simulation tool	134
4.4.2	Verification of 100MHz Crystal Oscillator (LNXO100) using Analytical Model	137
4.4.3	Verification of 100 MHz Crystal Oscillator using PN Measurement Equipments	139
4.4.3.1	Experimental Verification of 100 MHz Crystal Oscillator using Agilent E5052B	139
4.4.3.2	Experimental Verification of 100 MHz Crystal Oscillator using R&S FSUP 26)	141
4.4.3.3	Experimental Verification of 100 MHz Crystal Oscillator using Anapico (APPH6000-IS)	142
4.4.3.4	Experimental Verification of 100 MHz Crystal Oscillator using Holzworth (HA7402A)	143

4.4.3.5	Experimental Verification of 100 MHz Crystal Oscillator using Noise XT (DCNTS)	144
4.5	Phase Noise Measurement Evaluation and Uncertainties	145
4.6	Uncertainties in Phase Noise Measurement:	150
4.6.1	Measurement	151
4.7	Factors Influence Phase Noise Measurement	153
4.8	Conclusion	155
4.9	References	155
5	Resonator Dynamics and Applications in Oscillators	159
5.1	Microwave Resonators	159
5.2	Linear Passive 1-Port	159
5.3	Resonator Networks	160
5.4	Resonator Q-Factor	164
5.4.1	Definition of Q Factor for Passive Resonant Circuit	165
5.4.1.1	Fractional 3-dB Bandwidth	165
5.4.1.2	Phase to Frequency Slope	165
5.4.1.3	Stored-to-Dissipated Energy Ratio	166
5.4.2	Definition of Q Factor for Active Resonant Circuit: Sensitive for Oscillation	167
5.4.2.1	Active NISO Circuit Q-Factor (Noise Spectrum Basis)	169
5.4.2.2	Active NISO Circuit Q-Factor (Reflection Coefficient Basis)	170
5.4.2.3	Active NISO Circuit Q-Factor (Energy Basis)	170
5.4.2.4	Active SISO Circuit Q-Factor (Source-Push and Load-Pull Basis)	173
5.4.2.5	Active SIBO Circuit Q-Factor (Injection Locking Basis)	177
5.5	Resonator Design Criteria for Low Phase Noise Oscillator Applications	179
5.5.1	Passive Lumped LC Resonator	180
5.5.2	Planar Transmission Line	181
5.5.2.1	Effective Dielectric Constant and Characteristic Impedance of a Microstrip	182
5.5.2.2	Planar Transmission Line Bends	184
5.5.3	Planar Transmission Line Resonator	185
5.5.3.1	Microstrip Resonator	185
5.5.3.2	Folded Open Loop Microstrip Resonator	185
5.5.3.3	Folded Hair-Pin Resonator	188
5.5.3.4	Ring Resonator	191
5.5.3.5	Annular Ring Resonator Model	192
5.5.3.6	Ring Resonator Modes	193
5.5.4	Active Resonator	194
5.5.4.1	Active Resonator Topology	196
5.6	Conclusion	198
5.7	References	199
6	Printed Coupled Slow-Wave Resonator Oscillators	202
6.1	Introduction	202
6.1.1	Lossless Transmission Line	203
6.1.2	Capacitive Loaded Transmission Lines (CTL)	204
6.2	Slow Wave Resonator (SWR)	205
6.2.1	Slow Wave Evanescent Mode (SWEM) Propagation	208

6.2.2	SWEM Resonator Modes and Noise Dynamics	208
6.3	Slow Wave Resonator Oscillator	209
6.3.1	Slow Wave Resonator Coupling Characteristics and Q-factor	209
6.3.2	Loaded Open Loop Printed Resonator Coupling and Mode Characteristics	218
6.4	Tunable Low Phase Noise Oscillator Circuits	221
6.4.1	Examples: Slow Wave Resonator Based Tunable Oscillator Circuits	223
6.4.1.1	Tunable (2000-3200 MHz) Oscillator Circuits [US Patent No. 7,365,612 B2]	223
6.4.1.2	Hybrid Tuned Wideband Circuit (1600-3600 MHz) with Coarse and Fine Tuning	228
6.4.1.3	Power Efficient Wideband Oscillator (SWRO) Circuits (2000-3000 MHz)	231
6.4.1.4	User-Defined Ultra Low Phase Noise Oscillator Circuits [US Patent No. 7,586,381]	233
6.4.1.5	Multi-Octave Band Oscillator Circuit [US Patent No. 7,605,670]	237
6.4.1.6	High Frequency Push-Push VCO Topology [US Patent No. 7,292,113]	245
6.4.1.7	Multi-Octave Band Push-Push VCO Topology [US Patent No. 7,292,113]	252
6.4.1.8	Substrate Integrated Waveguide (SIW) Resonator Based Oscillators	256
6.4.1.9	Opto-Electronic Oscillator (OEO) using Metamaterial Resonator	273
6.5	Conclusion	277
6.6	References	277
7	Printed Coupled Möbius Resonator Oscillators	284
7.1	Introduction	284
7.2	Planar Möbius strip Resonator	284
7.3	MCPR Oscillator: Inexpensive Alternative of DRO	288
7.3.1	Synthesized Frequency Sources using Möbius coupled resonator VCOs	292
7.4	Möbius Coupled Resonator: Applications	294
7.4.1	Möbius Resonator Strips for RTRD Applications	294
7.4.2	Möbius Coupled Resonator Strips: Discussion	300
7.5	Conclusion	300
7.6	References	301
8	Printed Coupled Metamaterial Resonator Based Frequency Sources	302
8.1	Metamaterial	302
8.2	The Electromagnetic Wave Propagation Dynamics of Metamaterial	305
8.2.1	Backward Wave Propagation Dynamics in Left-Handed Material	309
8.2.2	Evanescence Wave Propagation Dynamics	310
8.2.3	Phase Velocity, Group Velocity, Energy Density	313
8.2.3.1	Phase Velocity	313
8.2.3.2	Group Velocity	313
8.2.3.3	Energy Density	314
8.3	Realization of NRIM Components	314
8.3.1	Split Ring Resonator (SRR) s NRIM	316
8.3.2	Coupled Wire Sets NRIM	316
8.3.3	Dielectric Material Resonator NRIM	316
8.4	Metamaterial NRIM Model	317
8.4.1	Resonator Model	317
8.4.2	Transmission Line Model (TLM)	317
8.5	Physical Realization of Metamaterial Component for Oscillator Circuits	319

8.6	CSRR (Complementary Split Ring Resonator) for Oscillator Circuit Applications	323
8.7	Slow Wave Metamaterial Resonator (SWMR)	325
8.8	Examples: Tunable Oscillators Using SWMR	327
8.8.1	Tunable 2-4 GHz Oscillator using SWMR	330
8.8.2	Multi-band Oscillators using Printed Slow Wave Metamaterial Resonator	331
8.8.3	MCSWMR (Mode Coupled Slow Wave Metamaterial Resonator) VCO	336
8.8.4	Examples: Compact Size MCSWMR VCOs	338
8.8.4.1	Example: 3.385 GHz Evanescent Mode Metamaterial Resonator Oscillator	342
8.8.4.2	Example: 7 GHz Evanescent Mode Phase-Injection Mode Coupled Oscillator	345
8.8.4.3	Example: Tunable EMPIMC Oscillator	347
8.9	High Performance Frequency Synthesizer Using MCSWMR VCO	349
8.10	Conclusion	360
8.11	References	363
9	High Performance X-band Oscillators	373
9.1	Introduction	373
9.2	DRO Circuit Topology	373
9.3	Dielectric Resonator (DR)	375
9.4	Design Methodology of Parallel Feedback 10GHz DRO Circuit	377
9.5	Compact Surface Mounted Device (SMD) 10GHz DRO Circuit	391
9.6	Conclusion	397
9.7	References	397
10	High Performance Opto-Electronic Oscillators (OEOs)	400
10.1	Introduction	400
10.2	Opto-Electronic Oscillator (OEO) System	401
10.3	OEO circuit Theory	402
10.3.1	Dual-Injection-Locked (DIL) OEO	404
10.3.2	Coupled OEO	407
10.3.3	Whispering Gallery Mode (WGM) Based OEO	409
10.3.4	Optimum Fiber Delay Length (Novel Approach)	410
10.3.5	Forced Frequency Stabilization Techniques/Phase Noise Reduction Techniques	411
10.3.5.1	Injection Locking (IL)	411
10.3.5.2	Self-Injection Locking (SIL) using Electrical Feedback	412
10.3.5.3	Self-Injection Locking (SIL) using Optical Feedback	413
10.3.5.4	Phase Locking (PL)	416
10.3.5.5	Self-Phase Locked (SPL) Oscillator using Fiber Optic Delay	417
10.3.5.6	Self-Phase Locking (SPL) with Multiple Delays	419
10.3.5.7	Multi-Loop OEO Circuits	421
10.3.5.8	Electrical Mode-Locking	422
10.3.5.9	Optical Mode-Locking	424
10.3.5.10	ILPLL OEO using self-PLL and Optimum Parameter Selection	427
10.3.6	Optical Filtering	430
10.3.6.1	Optical Filtering using Fabry-Perot Etalon	430
10.3.6.2	Optical Filtering using Transversal Filter	433
10.3.6.3	Novel OEO using optical “Nested Loop” RF Filter	434

10.3.7	Dispersion of Photonic Band Gap (PBG) Fibers	439
10.3.7.1	Dispersion of Solid Core Photonic Band Fibers	439
10.3.7.2	Dispersion of Hollow Core Photonic Band Gap Fibers	442
10.3.8	Raman Amplification in Photonic Crystal Fibers	443
10.3.9	New Methods in OEO FOR Temperature Compensation	446
10.3.10	Composite Fiber with Raman Amplifier	447
10.4	Novel Design Concepts of Passively Temperature Compensated OEOs	449
10.4.1	Evolution of state-of-the-art SILPIL OEO Circuits for Ultra Low Phase Noise	449
10.4.1.1	Basic OEO Circuit	449
10.4.1.2	OEO Circuit with Self-IL (Injection Locked)	449
10.4.1.3	OEO Circuit with Self-PL (Phase Locked)	450
10.4.1.4	OEO Circuit with SIL-PLL (Self Injection Locked Phase Locked Loop)	450
10.4.1.5	OEO Circuit with SIL-PLL-Mode Locking of Optical Modes	451
10.4.2	Key Features Added as a Result of Novel Design Approach for the Validation	451
10.4.3	Realization of Low Phase Noise and Passive Temperature Stable OEO Circuits	452
10.5	Analytical Modeling and CAD Simulation	454
10.6	Integrated OEO Solution	461
10.6.1	Mach Zehnder Modulator (MZM)	463
10.6.1.1	Electro Optic Polymer (EO Polymer)	463
10.6.1.2	Integrated Tunable OEO Circuits	466
10.7	Design Challenges, Pros and Cons: Monolithic OEO Circuits	470
10.8	Conclusion	472
10.9	References	473
11	Conclusion	477
11.1	Summary of Work	477
11.2	Futuristic Work	479
12	Abbreviations and Symbols	480

Appendices

A	Noise Analysis of the N-Coupled Oscillator	A1-A8
B	Active Resonator using Gain Feedback loop	B1-B8
C	Oscillators Based on Passive and Active Resonator	C1-C15
D	Multi-Mode Resonator Oscillators Topology	D1-D16
E	Noise Analysis of the N-Coupled Oscillator	E1-E9
F	Active Resonator using Gain Feedback loop	F1-F21
G	Oscillators Based on Passive and Active Resonator	G1-C19
H	Multi-Mode Resonator Oscillators Topology	H1-H8
I	Multi-Mode Resonator Oscillators Topology	I1-I8

Chapter 1

Introduction

1.1 Abstract

The current generation radio communication market has been experiencing tremendous growth and will continue to do so in the next decade. Future radio communication units will require higher speed for faster data transmit rate, higher operating frequency to accommodate more channels and users, more functionality, light weight, lower power consumption, and low cost. Oscillators are vital components of any radio frequency (RF) communications system. They are necessary for the operation of phase-locked loops commonly used in frequency synthesizers and clock recovery circuits, and are present in digital electronic systems, which require a reference clock signal in order to synchronize operations. Phase noise is of major concern in oscillators, as it affects adjacent channel interference and bit-error-rate, ultimately limiting the overall performance of communication systems. In general, an oscillator's phase-noise determines the overall communication system's capability and places inflexible requirements on the performance of other transceiver modules.

The oscillator theory is complex and mystifying. It is still an open issue despite significant gains in practical experience and modern CAD tools for design. To this end, the oscillator noise theory, on how the resonant circuit builds the transient and stable resonance condition, resonator structure, active device noise mechanism, optimum drive level and conduction angle, the nature of signals generated, and the effect of flicker noise are often considered as research topics. Rohde [1] has formulated a unified noise equation for predicting the phase noise within reasonable degree of accuracy for a given resonator Q-factor and circuit operating condition. However, improving the resonator Q-factor is a challenging task under the given constraints of planar and integrable solutions in miniaturized size and cost. The design of a low noise octave-band VCOs is challenging and difficult because maintaining uniform Q of the resonator/tuning network for wideband is a complex phenomenon. It is a major challenge to find ways to realize low phase noise with low Q-factor components at a higher operating frequency that supports multi-octave-band tunability. This thesis describes the design and investigation of a variation of printed resonators using Möbius slow-wave structures for the applications in tunable low phase noise oscillator circuits, including design basis of optical fiber delay resonator based Optoelectronic Oscillators. A novel Möbius slow-wave mode-coupled structure offers additional degrees of freedom (higher quality factor, multi-band characteristics, compact size, and phase-hits insensitivity) as compared to conventional transmission line printed resonators.

1.2 Motivation

The need for miniaturization of signal sources for application in modern communication systems has presented new challenges to the design of high quality factor compact resonators. The miniaturization of electronic components has received a lot of attention in the last decades due to the rapid development of the telecommunication industry. Traditional high Q-factor resonators (ceramic resonator, dielectric resonator, YIG resonator, Whisper gallery mode resonator, Optoelectronic resonator, etc.) are usually too heavy and bulky for the both

handheld and test-measurement equipments and does not offer integration using current foundry technology. The 4th generation wireless communication market is pushing the need for miniaturization to its limits. Printed coupled transmission line resonator is a promising alternative due to its ease of integration and compatibility with planar fabrication processes but is limited by its large physical size and low quality factor, making it a challenging choice to design low phase-noise oscillators. This problem is more prominent in integrated circuits (ICs) where high degrees of thin conductor losses reduce the quality factor by orders of magnitude compared to hybrid circuit technologies.

Different techniques have been developed to achieve miniaturization of printed resonators, such as negative index resonator network, Möbius coupled resonator network, and slow wave mode-coupling methods using capacitively loaded transmission lines (CLTL) [2]. The CLTL concept has been explored to reduce the size of printed coupled resonator circuits for low cost high performance signal source solutions [3]. The research work done is towards developing mode-coupled slow-wave metamaterial resonator (MCSWMR) topology for multi-band multi-mode resonance condition for switchable band modern radio architecture. In multi-band multi-mode radio architectures, a number of local oscillator (LO) frequencies are required in order to process the information in various frequency bands. Since oscillators consume a substantial part of the IC chip area, and battery power the design approach of slow-wave resonator based tunable multi-band multi-mode injection-locked oscillator offers concurrent multiple frequencies with the user having an option of choosing a frequency or combination of them that eliminate the need of lossy switches for switching the frequency band, thereby improves the throughput. Various techniques, such as switching between VCOs for separate bands, utilizing inter-modal multiple frequency, using switched resonators for band selection have been proposed in past for the realization of multi-octave-band oscillators. But these result in large size of the circuit, current hungry, narrow band, and poor phase noise performances. Switched inductors or capacitor banks suffer from the resistive and capacitive parasitics associated with the switches [4].

1.3 Problem Statement

The definition of problem undertaken in this research work is to investigate the complex resonant structures (mode-coupled, slow-wave, Möbius strips, evanescent mode, negative index metamaterial), including active and high-order resonant circuits, capable of overcoming the limited quality-factor of current planar hybrid and IC fabrication technologies. The research described here explores a different novel topology for both narrowband (<5% tuning) and wideband oscillators (>50% tuning), including the optimization of the performance for low phase-noise signal source applications. The proposed methods can be applied and suited for miniaturized low phase-noise voltage controlled-oscillator solutions at microwave and mm-wave frequencies using hybrid or integrated circuit fabrication technologies.

Furthermore, this work examines systems of coupled oscillators using N-push/push-push configuration in conjunction with slow-wave planar resonator networks, and points out the realization of integrated SiGeHBT/GaAsHBT based MMIC solutions at higher frequencies (2-40 GHz). For millimeter wave application, the active devices are often pushed near to their physical limits of operation, resulting in degraded noise performance of the integrated oscillator/VCOs circuit. The N-push/push-push oscillator basically enhances the even mode harmonics and

suppresses the odd mode output, doubling the frequencies, so higher oscillating frequencies can be obtained beyond the limitation caused by the cut-off frequency of the available three terminal active devices and the tuning diodes. The monolithic VCO implementations suffer from poor phase noise performance partly due to the low quality factor Q of the resonator networks. A design study has been carried out to optimize the phase noise performance by incorporating the N-push/push-push approach to compensate for the low Q-factor in the integrated VCO implementation.

1.4 Definition of the Task and Oscillator Figure of Merit (FOM)

Tunable oscillators are considered as most important RF module, used in portables and test & measurement equipments (spectrum analyzers, frequency sweepers, network analyzers, etc.). The demand of broadband oscillators is increasing in modern communication systems for enabling 4G features. Frequency domain test and measurement systems pose design challenges for wideband VCOs design due to the constraint of size, cost, power-consumption, and phase noise performance. The phase noise performance of the oscillator is very critical, and it is the governing figure of merit for overall system performances. The challenge is to build an ultra low phase noise signal source; but the difficulties related with measurement of low phase noise oscillators using modern phase noise measurement equipments are paramount. Chapters 3 & 4 are dedicated for oscillator phase noise dynamics and phase noise measurement related issues with concluding remarks about the noise model and measurement techniques.

The monolithic VCO implementations suffer from poor phase noise performance partly due to the low quality factor Q of the printed resonator at high frequencies. It is a common-practice to design oscillators using single resonators. However, in this case, the achievable oscillator Q is determined and limited by the resonator technology used. In particular, planar resonators suffer from excessive conductor and substrate losses limiting their achievable quality-factor. Therefore, conventional low phase-noise oscillator design techniques rely on reducing the losses in single resonators by manipulating their circuit designs and layouts. A design study has been carried out to optimize the phase noise performance by incorporating the resonant structures (mode-coupled, slow-wave, Möbius strips, evanescent mode, negative index metamaterial) for high performance signal source applications.

It will be investigated as to how the Q-factor of resonator can be improved, and identifying the effects that limit the tuning range, which leads to the development of the several electromagnetic coupling scheme towards improving the phase noise performance. The objective is to realize low cost, tiny and high performance signal sources using novel planar resonator oscillator for the applications of current and later generation communication systems. Several design examples are discussed in Chapters 5-11 for the validation of the new approaches based on the following tasks listed as follows:

- general closed form expression for quality factor of active and passive resonators
- exploring architecture of high quality factor slow-wave planar resonator
- exploring architecture of Möbius strips planar resonator for low phase noise
- exploring architecture of metamaterial resonator for multi-band operation
- exploring architecture multi-mode multi-band VCOs operation

This dissertation deals with the design, fabrication, and testing of various wideband VCOs using slow-wave multi-coupled resonators based oscillators. A miniaturized printed coupled transmission line resonator using slow wave structure is developed and the methodology for obtaining high quality factor resonator is discussed. The new resonator structure is characterized for various oscillator topology using metamaterial resonators.

The tunable oscillators considered in this work are based on the commercially available discrete Si and SiGe HBTs using abrupt and hyper abrupt varactor diodes for wideband tuning. The manufacturers S-parameters data available for the transistor is valid for small-signal cases but oscillator circuits are large signal circuit operations. As most designers do not have elaborate and expensive equipment for device parameter extraction, the large signals S-parameters are generated using a synthesis-based approach. The high performance oscillators proposed in this thesis offers significant improvement in figure of merit (FOM) for a given phase noise, tuning range, and power consumption. A spot phase noise number is difficult to compare, unless it is compared at the same frequency offset from the carrier and the same carrier frequency for a given tuning range and output power. Comparing oscillators operating at different frequencies, tuning range, and output power levels, a figure of merit (FOM) with a single number has long been desired. In order to make a fair comparison of performances of VCOs (voltage-controlled oscillators) at different operating frequencies are given by *FOM* (figure-of-merit) in $(\frac{dBc}{Hz})$ and PFTN (power-frequency tuning-normalized) in dB, defined as [5]

$$FOM|_{f_{offset}} = \left[\xi(f_{offset}) - 20 \log_{10} \left(\frac{f_0}{f_{offset}} \right) + 10 \log_{10} \left(\frac{P_{DC}}{1mW} \right) \right] \quad (\frac{dBc}{Hz}) \quad (1.1)$$

$$PFTN = - \left[\xi(f_{offset}) - 20 \log_{10} \left(\frac{\Delta f}{f_{offset}} \right) - 10 \log_{10} \left(\frac{P_{DC}}{kT} \right) \right] \quad (dB) \quad (1.2)$$

where f_0 is the oscillation frequency, $\xi(f_{offset})$ is the phase-noise at the offset frequency f_{offset} , k is the Boltzmann constant, $\Delta f = f_{max} - f_{min}$ is tuning range, T is temperature in Kelvin, and P_{DC} is the total consumed DC power in milli-watts. From [5], larger values of $|FOM| \left(\frac{dBc}{Hz} \right)$ and $PFTN$ (dB) values relates to superior oscillators. From (1.1) and (1.2), the FOM for integrated phase noise in dBc from 1 kHz to 1 MHz can be given by $FOM|_{Integrated (1kHz-1MHz)}$

$$FOM|_{Integrated (1kHz-1MHz)} = 10 \log(P^2(\emptyset)) + 10 \log \left(\frac{P_{RF}}{P_{DC}} \right) - 20 \log \left(\frac{2\Delta f}{f_{max} + f_{min}} \right) \quad (1.3)$$

where

$$\Delta f = f_{max} - f_{min}$$

f_{max} = maximum oscillation frequency

f_{min} = minimum oscillation frequency

$P^2(\emptyset)$ = integrated phase noise from 1 kHz to 1 MHz

P_{RF} = signal output power averaged over frequency

P_{DC} = DC power consumption of the oscillator

The novel Möbius coupled slow wave resonator based X-band oscillator proposed in the thesis (Chapter-10) allows for the design of oscillator with state-of-the-art phase-noise

performance, close to the phase-noise of the expensive high Q-factor DROs (shown in Table 1.1), while providing compact and planar structures compatible with hybrid and integrated circuit fabrication technologies. Table 1.1 shows the state-of-the-art oscillators using different fabrication technologies for comparative analysis. Table 1.2 shows the printed resonator based oscillators for comparative analysis. Table 1.3 shows the comparative analysis for tunable voltage controlled oscillator circuits based on *FOM* (figure-of-merit) in $(\frac{dBc}{Hz})$ and PFTN (power-frequency tuning-normalized) parameters. As shown in Tables 1.1, 1.2, and 1.3, this work shows superior FOM and PFTN performance of tunable voltage controlled oscillators (VCOs) compared to published result to date for a given class and topology [6]-[31].

Table 1.1 Comparison of High Q resonator based oscillator circuits performance and this work							
Reference	Oscillator	Technology	f_o GHz	P_o dBm	DC-RF Efficiency	$L(f)$ $(\frac{dBc}{Hz})$ @1MHz	<i>FOM</i> $(\frac{dBc}{Hz})$
ref [6]	DRO	Non Planar	23.8	3.3	3.4%	-146	-215.6
ref [7]	DRO	Non Planar	6.7	14	3.1%	-155	-202.5
ref [8]	DRO	Non Planar	8	14.5	2%	-162	-208.6
ref [13]	DRO	Non Planar	25.9	6.5	3.4%	-122	-188.9
This work Ch-4: Fig. 4-23	OCXO	Non Planar	0.1	15	11.2%	-183.4 @ 100kHz	-218.9
This work Ch-9: Fig. 9-21	DRO	Non Planar	10	11	2.58%	-162	-215.1
This work Ch-9: Fig. 9-28	DRO	Planar Hybrid	10.24	10	8.3%	-160	-218.4
This work Ch-10: Fig. 10-71	OEO	Non Planar	10	10	1%	-170	-220

Table 1.2: Comparison of Planar resonator oscillator circuits performance and this work							
Reference	Resonator	Technology	f_o GHz	P_o dBm	DC-RF Efficiency	$L(f)$ $(\frac{dBc}{Hz})$ @ 1MHz	<i>FOM</i> $(\frac{dBc}{Hz})$
ref [9]	Microstrip ring	Planar	12	5.3	48.7%	-116.2	-189.3
ref [10]	Microstrip hair-pin	Planar	9	9	4.5%	-129	-185.6
ref [11]	IC- FBAR	Quasi-Integrated	2.4	-2.5	1.9%	-144	-195.7
Ref [12]	Ring	CMOS Integrated	10	-15	1%	-110	-185.2
This work Ch-5: Fig. 5-36	Active Resonator	Planar	3.2	5	2.1%	-162	-210.3
This work Ch -6: Fig. 6-22c	Slow Wave Resonator (SWR)	Planar	0.622	5	3.16%	-170	-205.8

This work Ch -6: Fig. 6-22c	Slow Wave Resonator (SWR)	Planar	2.488	4.2	2.63%	-155	-202.9
This work Ch -6: Fig. 6-22c	Slow Wave Resonator (SWR)	Planar	4.2	3.3	2.14%	-150	-202.4
This work Ch -7: Fig. 7-8	Hybrid Coupled Resonator	Planar	10	2.88	1.2%	-138	-195.9
This work Ch -7: Fig. 7-8	Möbius Coupled Resonator	Planar	10	3.3	1.3%	-145	-202.9
This work Ch -7: Fig. 7-8	Mode-Locked Möbius Coupled Resonator	Planar	10	4.5	1.7%	-147	-204.9
This work Ch -8: Fig. 8-27	Mode-Coupled Slow-Wave Metamaterial Resonator	Planar	10.21	5.83	1.276%	-147	-202.4

Table 1.3: Comparison of tunable oscillator circuits performance published and this work

Reference	Technology	f_o (GHz)	P_{DC} (mW)	P_o (dBm)	Tuning Range	$L(f)$ ($\frac{dBc}{Hz}$)@ 1MHz	FOM ($\frac{dBc}{Hz}$)	PFTN (dB)
ref [14]	CMOS (0.18-μm)	25.1	11	-4.2	3.01 GHz (12%)	-99.94	-177.5	-14.7
ref [15]	CMOS (0.18-μm)	20.9	40.32	-6.83	2.17 GHz (10.4%)	-111.67	-181.5	-11.5
ref [16]	CMOS (0.18-μm)	19.9	39	-3	0.51 GHz (2.6%)	-111	-181.06	-24.6
ref [17]	CMOS (0.18-μm)	20.7	10.8	-21.12	1.8 GHz (8.7%)	-108.67	-181.06	-24.6
ref [18]	CMOS (0.18-μm)	40	6		1.12 GHz (2.8%)	-109	-193.26	-14.44
Ref [19]	CMOS (0.13-μm)	28	12		1.87 GHz (6.7%)	-113	-191.151	-6.304
ref [20]	CMOS (90-nm)	20.9	6.3		0.647 GHz (3.1%)	-117.2	-195.61	-8.540
ref [21]	CMOS (0.18-μm)	18.95	3.3		0.678 GHz (3.58%)	-110.82	-191.187	-11.712
ref [22]	CMOS (0.18-μm)	21.37	3.5		1.089 GHz (5.1%)	-109.8	-190.955	-8.8704
ref [23]	CMOS (0.12μm SOI)	44	7.5		4.312 GHz (9.8%)	-101	-185.118	-9.034
ref [24]	CMOS (65-nm)	38.4	80		6.873 GHz (17.9%)	-97.5	-170.156	-18.764
ref [25]	RTD/HBT	17.65	1.42	-9.0	0.37 GHz (2.1%)	-112	-195	-12.13

ref [26]	SiGe HBT	41	280		10.78 GHz (26.3%)	-110	-177.784	-7.794
ref [27]	SiGe BiCMOS	22.1	11.1	-11.3	4.552 GHz (20.6%)	-109	-181.435	-2.265
This Work Ch-6: Fig. 6-19c	Si- Bipolar	2.615	240	3	1390 MHz (53.1%)	-150	-194.4	15.08
This Work Ch-6: Fig. 6-20b	Si- Bipolar	2.6	400	4	2000 MHz (76.9%)	-135	-177.2	1.02
This Work Ch-6: Fig. 6-21c	Si- Bipolar	2.5	150	-3	1000 MHz (40%)	-156	-202.1	20.26
This Work Ch-6: Fig. 6-26a	Si- Bipolar	1.341	200	3	1543MHz (115%)	-148	-187.6	16.02
This Work Ch-6: Fig. 6-26b	Si- Bipolar	1.5	200	-3	2041 MHz (136%)	-157	-197.5	26.20
This Work Ch-6: Fig. 6-28e	SiGe HBT	7.92	300	-3	4644 MHz (58.5%)	-118	-171.2	-7.41
This Work Ch-8: Fig. 8-21b	SiGe HBT SWMR	3	120	3	2000 MHz (66.6%)	-142	-190.75	13.25

1.5 Overview of the Thesis

This thesis is organized in 12 chapters. The scientific chapters are structured in such a way that graduate students and engineers can easily follow the state-of-the art oscillator technology and phase noise measurement scheme for the validation of the approach and techniques discussed.

Chapter 1 – briefly discusses a short introductory abstract, motivation, problem statement, defines the task and oscillator figure of merit (FOM) in order to make a fair comparison of performances of different oscillator topologies operating at different frequencies and DC bias condition, and provides an overview of the contents of this thesis.

Chapter 2 – summarizes important principles of oscillator theory and describes oscillator topologies and important properties of oscillators such as selection of resonator networks and performance matrices (frequency range and tuning characteristics, tuning linearity, tuning sensitivity, tuning speed, post-tuning drift, phase noise, output power, harmonic-suppression, spurious response, pushing and pulling). For the device characterization, large signal S-parameter measurements are carried out for bipolar and field effect transistors. In addition to this, the selection criteria and performance comparison of new technology using active inductor, active capacitor and MEMS based resonator is being discussed for giving brief insights about the emerging Silicon-based MMIC technology and application in oscillators.

Chapter 3 - devoted to the principles of oscillator noise and presents different noise models. To supplement this, different methods for the measurement and simulation of oscillator noise are then presented and evaluated in Chapter 4.

Chapter 4 - describes the phase noise measurement techniques and limitations, prediction and validation of oscillator phase noise measured on commercially available different PN

equipments ((Agilent E5052B, R&S FSUP, Holzworth, Noise XT-DCNTS, and Anapico APPH6000-IS), phase noise measurement evaluation in Faraday Cage, CAD simulation and phase noise measurement of 100 MHz OCXO circuits. The selection of 100 MHz OCXO is done based on on-going demand of ultra low phase noise reference frequency sources, validated during IEEE sponsored 2012 IMS Symposium in Canada, and 2013 IMS Symposium in Seattle, USA for giving brief insights about the uncertainty in phase noise measurement.

Chapter 5 – The different procedures for the implementation of phase-selective feedback networks in microwave oscillators are introduced. Passive and active microwave resonators are considered, provides an overview of definitions of microwave resonators, resonator quality factor, figure-of-merit, resonator design criteria, and oscillator design methodology using active resonator for low phase-noise applications, oscillator topology using passive and active printed resonator and a method for miniaturization of oscillator circuit using active resonator network, Active resonators are analyzed and a design procedure is presented to optimize their performance for low-noise applications. The fundamental options for the implementation of microwave resonators and the normal procedures for their characterization are set out and evaluated in the light of the thesis research work.

Chapter 6- describes printed transmission line resonator networks, resonant properties of capacitively loaded transmission line resonator, and slow wave resonator dynamics, and the discussion focuses on how the phase speed on the line structures can be reduced via capacitive load. The key element of this chapter is the use of evanescently coupled resonance modes, wherein an increased phase selectivity of the resonance modes can be achieved using slow wave resonator (SWR) through the coupling of different modes. Different coupling models are investigated and implemented oscillators with different resonator concepts are presented and compared. The new oscillator structure using slow wave resonator (SWR) shows significant advantages in terms of size, power consumption and frequency tunability, prototype examples are validated and built over million for radio applications. The state-of-the-art technology is disclosed in public domain and also protected with US copyrights and patented.

Chapter 7 – deals with printed planar resonators according to the Möbius principle, characterizes the Q and coupling coefficient of the newly developed Möbius resonator structure, presents a range of oscillator implementations with excellent properties for this purpose. Furthermore, use of Möbius strips for microwave sensors and RFID (real time signal retention device) applications is discussed.

Chapter 8 –deals with a microwave-engineering subject that has been highly newsworthy for a number of years and investigates the extent to which Metamaterials can be appropriately used to implement microwave resonators with advantageous properties. The chapter begins with an introduction to the fundamental properties of Metamaterials, wherein negative-index Metamaterials in particular are considered for high Q-factor resonator applications, different resonator concepts are then proposed, explores the principle behind evanescent mode propagation and explains how it can be applied to store the evanescent mode energy for improving the group delay, investigated in details and used within microwave oscillators. Most of these resonators are singly or multiply coupled resonators, which could also be considered without touching on the concept of Metamaterials, but, as a result of developments in the

implementation of Metamaterials, resonator concepts of this type have since been subjected to closer examination. A brief description of metamaterial component is discussed for the realization of slow wave characteristics in tunable oscillator circuits. As the thesis is focused on slow-wave planar resonators, a common type namely the multiple-coupled slow wave resonator is explored and used. The complex oscillator circuits are subsequently shown and characterized with measurement and simulation results. Very impressive results from specific microwave oscillator implementations in building high performance frequency synthesizer are presented.

Chapter 9 - high-performance oscillators for the X-band are presented which are essentially based on dielectric resonators. The design methodology and implementations of low noise 10 GHz DRO (Dielectric Resonator Oscillators) circuit is described for RADAR applications. Furthermore, inexpensive surface mounted DRO Circuit is fabricated that offers integrable and cost-effective alternative of connectorized version of large size DRO circuits. The choice of DRO is done to prove that Möbius Coupled DRO improves the tuning range without degradation of phase noise performances.

Chapter 10 – deals with Opto-electronic oscillator (OEO) concepts which are based on the phase selectivity of long lines in the form of very low-attenuation optical fibers. The concepts presented are then employed in the present thesis primarily in combination with the previously introduced printed multi-mode microwave resonators. Furthermore, this Chapter discusses elaborately on OEO Circuit Theory, different OEO (Opto-Electronic Oscillator) topologies, Novel Design Concepts of Passively Temperature Compensated OEOs, Self Injection Locking (SIL) using Electrical Feedback, Self Injection Locking (SIL) using Optical Feedback, Dual-Injection-Locked (DIL) OEO, Optical Mode-Locking, Self Phase Locked (SPL) Oscillator using Fiber Optic Delay, Self Phase Locking (SPL) with Multiple Delays, Optimum Fiber Delay Length (Novel Approach), Whispering Gallery Mode (WGM) Based OEO, Raman Amplification in Photonic Crystal Fibers, new methods in OEO using Composite Fiber of SMF-28 and HC-PCF to Achieve Passive Temperature Compensation, Composite Fiber with Raman Amplifier, Modification in ILPLL Oscillator using novel concept of OEO self-ILPLL and Optimum Parameter Selection, Key features added as result of novel design approach, Phase Noise Reduction Techniques in OEO Circuit, Coupled OEO, Integrated 10 GHz OEO Solution, Design Challenges: Monolithic OEO Circuits.

Chapter 11 - concludes the thesis with a summary of the work presented herein and suggests future works (IC fabrication at microwave and millimeter-wave frequencies based on patented techniques) for the benefit of research scientists and engineers.

Chapter 12- Abbreviation and Symbols listed for the abbreviations used throughout the thesis.

Appendices- Appendix-A describes, “Noise Analysis of the N-Coupled Oscillator”, Appendix-B discusses, “Active Resonator using Gain Feedback loop”, Appendix-C describes, “Planar Resonator Oscillators”, Appendix-D explores the, “Multi-Mode Resonator Oscillators”, Appendix-E describes about the, “Radio over Fiber (RoF) Link Characterization”, Appendix-F investigates the, “Forced Oscillations Using Self-Injection Locking”, Appendix-G describes about the, “Forced Oscillations Using Self-Phase Locking”, Appendix-H describes “Forced Oscillations

Using Self-Injection Locking and Phase Locked Loop (SILPLL)”, Appendix-I describes the design methodology and implementation of the, “Phase Noise Performance of OEO Circuit Using Optical Transversal Filters”.

1.6 Publications and Patent Applications arising from this research work

This thesis covers a broad spectrum of research ranging from practical aspects of circuit implementation and measurement through to sophisticated design and the modeling of complex circuits and resonator structures. The results are documented by a range of specific measurement result and backed up by over hundred publications in scientific conferences and several dozen patent applications. The scientific chapters are mainly structured in such a way that certain principles providing an introduction to the subject are presented in very concise form, and in most cases, the relationship between the oscillator circuits and the previously introduced principles is not explained in detail and must be deduced by the reader himself. Based on of this research work, over 200-technical papers have been published in IEEE journals, conferences, workshops, and over two dozen patent applications filed.

1.7 References

- [1] U. L. Rohde, “A New Efficient Method of Designing Low Noise Microwave Oscillators,” Dr.-Ing. Dissertation, Faculty IV, EEC, TU- Berlin, Germany, Feb. 2004.
- [2] A. K. Poddar, U.L. Rohde, D. Sundarrajhan”, A Novel Möbius-Coupled Printed Resonator Based Signal Sources”, 2013 IEEE MTT-S Digest, pp. 1-3, June 2013
- [3] A. K. Poddar and U. L. Rohde, “Slow-Wave Evanescent-Mode Coupled Resonator Oscillator”, 2012 IEEE FCS, pp. 01-07, May 2012.
- [4] U. L. Rohde and A. K. Poddar, “Oscillators Cover Multiple Bands”, Microwaves & RF, pp.122-126, May 2013.
- [5] D. Ham and A. Hajimiri, “Concepts and Methods in Optimization of Integrated LC VCOs”, IEEE Journal of Solid-State Circuits, Vol. 36, No. 6, pp. 896-909, June 2001
- [6] P. Vryonides, S. Nikolaou, and H. Haralambous, “24 GHz low phase noise HBT dielectric resonator oscillator,” *IEEE 11th annual WMTC*, pp. 1-4, April 2010.
- [7] Perez et al, “Extremely low noise InGaP/GaAs HBT oscillator at C-band,” *IEE Electronics Letters*, vol. 34, no. 8, pp. 813-814, April 1998.
- [8] Hittite Microwave Corporation, “HMC-C200 Dielectric resonator oscillator module”, Datasheet, http://www.hittite.com/content/documents/data_sheet/hmcc200.pdf.
- [9] L.-H. Hsieh, and K. Chang, “High-efficiency piezoelectric-transducer tuned feedback microstrip ring-resonator oscillators operating at high resonant frequencies”, *IEEE Trans. Microwave Theory Tech.*, vol. -51, no. 4, pp. 1141-1145, April 2003
- [10] L. Dussopt, D. Guillois, and G. M. Rebeiz, “A low phase noise silicon 9 GHz VCO and 18 GHz push-push oscillator”, *IEEE MTT-S Dig.*, vol. 2, pp. 695-698, June 2002.
- [11] Ostman et al, “Novel VCO architecture using series above-IC FBAR and parallel LC resonance,” *IEEE JSSC*, vol. 41, no. 10, pp. 2248-2256, October 2006.
- [12] D. Ham, and W. Andress, “A circular standing wave oscillator,” *IEEE Solid-State Circuits Conference*, February 2004.
- [13] I. Hilborn, A. P. Freundorfer, J. Show, M. G. Keller,” Design of a Single Chip GaAs MESFET Dielectric Resonator Oscillator at 26 GHz”, IEEE CCECE, pp. 671-674, 2007

- [14] D. Ozis, N. M. Neihart, and D. J. Allstot, "Differential VCO and passive frequency doubler in 0.18 mm CMOS for 24 GHz applications," in *IEEE RF IC Symp. Dig.*, 2006
- [15] S. Ko, J.-G. Kim, T. Song, E. Yoom, and S. Hong, "20 GHz integrated CMOS frequency sources with a quadrature VCO using transformers," in *IEEE RF IC Symp. Dig.*, 2004
- [16] H. H. Hsieh and L. H. Lu, "A Low-Phase-Noise K-Band CMOS VCO," in *IEEE Microwave & Wireless Components Lett.*, Vol. 16, No. 10, pp.552-554, Oct. 2006.
- [17] C. m. Yang, H. L. Kao, Y. C. Chang, and M. T. Chen," A Low phase noise 20 GHz Voltage control oscillator using 0.18 μ m CMOS Technology", IEEE 13TH International Symposium on Design and Diagnostics of Electronic Circuits and Systems (DDECS), pp. 185-188, 2010.
- [18] Chien "40 GHz wide-locking-range regenerative frequency divider and low-phase-noise balanced VCO in 0.18 m CMOS," in *IEEE JSSCs Conf. Tech. Dig.*, pp. 544–545, Feb. 2007
- [19] Y. Wachi, T. Nagasaku, and H. Kondoh, "A 28 GHz low-phase-noise CMOS VCO using an amplitude redistribution technique," in *IEEE SSC Conf. Tech. Dig.*, pp. 482–483, Feb. 2008.
- [20] H.-Y. Chang and Y. -T. Chiu, "K-band CMOS differential and quadrature voltage-controlled oscillators for low-phase-noise and low-power applications," *IEEE Trans. on Microwave Theory Tech.*, vol. 60, no. 1, pp. 46–59, Jan. 2012.
- [21] T. -P. Wang, "A-band low-power Colpitts VCO with voltage-to-current positive-feedback network in 0.18 m CMOS," *IEEE MWCL*, vol. 21, no. 4, pp. 218–220, Apr. 2011.
- [22] S.-L. Liu, K. -H. Chen, T. Chang, and A. Chin, "A low-power-band CMOS VCO with four-coil transformer feedback," *IEEE MWCL*, vol. 20, no. 8, pp. 459–461, Aug. 2010.
- [23] J. Kim *et al.*, "A 44 GHz differentially tuned VCO with 4 GHz tuning range in 0.12 m SOI CMOS," in *IEEE International Solid-State Circuits Conf. Dig.*, pp. 416–417, Feb. 2005.
- [24] O. Richard, A. Siligaris, F. Badets, C. Dehos, C. Dufis, P. Busson, P. Vincent, D. Belot, and P. Urard, "A 17.5-to-20.94GHz and 35-to-41.88 GHz PLL in 65 nm CMOS for wireless HD applications," in *IEEE Int. Solid-State Circuits Conf. Dig.*, pp. 252–253, Feb. 2010.
- [25] S. Choi, Y. Jeong, and K. Yang, "Low DC-Power Ku-Band Differential VCO Based on an RTD/HBT MMIC Technology", *IEEE MWCL*, Vol. 15, No. 11, pp. 742-744, Nov 2005
- [26] H. Li, H.-M. Rein, R. Kreienkamp, and W. Klein, "47 GHz VCO with low phase noise fabricated in a SiGe bipolar production technology," *IEEE Microw. Wireless Component Letter*, vol. 12, no. 3, pp. 79–81, March 2002.
- [27] T. Nakamura, T. Masuda, N. Shiramizu, A. Nakamura, and K. Washio," A 11.1-V Regulator-Stabilized 21.4-GHz VCO and a 11.5% Frequency-Range Dynamic Divider for K-Band Wireless Communication", *IEEE Trans. on MTT*, Vol. 60, No. 9, pp. 2823-2832, Sept. 2012.
- [28] M. Hossain, A. Kravetsm U. Pursche, C. Meliani, W. Heinrich, "A Low voltage 24 GHz VCO in 130nm CMOS for localization purpose in sensor networks", 7TH German Microwave Conference (GeMiC), pp. 1-4, 2012.
- [29] S. Kuhn, W. Heinrich, "GaN large-signal oscillator design using Auxiliary Generator measurements", German Microwave Conference (GeMiC) 2010, pp. 110-113.
- [30] A. K. Poddar, U. L. Rohde, "The Pursuit for Low Cost and Low Phase Noise Synthesized Signal Sources: Theory & Optimization", IEEE UFFC Symposia, May 19-22, 2014
- [31] A. K. Poddar, U. L. Rohde, "Evanescence-Mode Phase-Injection Mode-Coupled (EMPIMC) Metamaterial Resonator Based Tunable Signal Sources", IEEE Wamicon, June 06, 2014

Chapter 2

General Comments on Oscillators

2.1 Theory of Operation

An oscillator is an autonomous circuit consisting of a frequency selective positive feedback network [1]. The noise present in the active device or power supply turn-on transient leads to the initial oscillation build-up [2]. As a basic requirement for producing a self-sustained, near-sinusoidal oscillation, an oscillator must have a pair of complex-conjugate poles on the imaginary axis i.e. in the right half of an s-plane with $\alpha > 0$ [3].

$$P(p_1, p_2) = \alpha \pm j\beta \quad (2.1)$$

While this requirement does not guarantee an oscillation with a well-defined steady state (squeaking), it is nevertheless a necessary condition for any oscillator. When subjected to an excitation due to the power supply turn-on transient or noise associated with the oscillator circuit, the right half plane RHS-poles in the equation above produce a sinusoidal signal with an exponentially growing envelope given as

$$v(t) = V_0 \exp(\alpha t) \cos(\beta t) \quad (2.2)$$

$$v(t)|_{t=0} \rightarrow V_0 \quad (2.3)$$

V_0 is determined by the initial conditions and the growth of the signal amplitude $v(t)$ is eventually limited by the associated nonlinearities of the oscillator circuit.

Oscillators are fundamentally a feedback amplifier with a resonator in the feedback path and if enough gain exists for given oscillation conditions, noise will be amplified sufficiently enough to eventually stabilize the gain via non-linearity effects and create an output signal that consists of narrow band noise. This narrow-band profile of the noise characteristics in the oscillator is the prime issue of the oscillator design. The two methods used for analyzing and understanding noise issues for oscillators are the feedback model approach and the negative resistance model. Using either the feedback model approach or the negative resistance model, one can perform the analysis of the oscillator. Depending on the oscillator topology and characteristics, one approach is preferred over the other. The condition of oscillation build-up and steady state oscillation will be discussed using both approaches. The application of either the feedback model or the negative-resistance model is sufficient for analyzing the linear behavior of the oscillator circuit, and it must be unstable about its bias point or, equivalently, have poles in the RHP if an oscillation buildup is to take place. The feedback model is shown in Figure 2-1, where

an oscillator circuit is decomposed into a frequency-dependent forward loop gain block $H_1(j\omega)$ and a frequency-dependent feedback network $H_2(j\omega)$, both of which are typically multi-port networks. If the circuit is unstable about its operating point (poles in the right half of the s-plane), it can produce an expanding transient when subject to an initial excitation. As the signal becomes large, the active device in the circuit behaves nonlinearly and limits the growth of the signal. When oscillation starts up, the signal level at the input of the amplifier (forward loop gain block) is very small, and the amplitude dependence of the forward amplifier gain can be initially neglected until it reaches saturation.

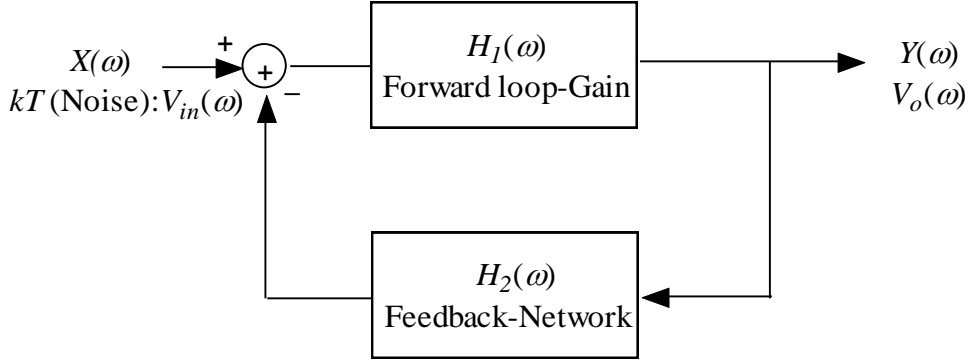


Figure 2-1: Block diagram of basic feedback model-oscillator [4]

The closed loop transfer function (T.F) and output voltage $V_o(\omega)$ are given by [4]

$$[TF(j\omega)]_{closed-loop} = \frac{[Y(j\omega)]_{output}}{[X(j\omega)]_{input}} = \frac{V_o(\omega)}{V_{in}(\omega)} = \frac{H_1(j\omega)}{1+H_1(j\omega)H_2(j\omega)} \quad (2.4)$$

$$[Y(j\omega)]_{output} = V_o(\omega) = \left[\frac{H_1(j\omega)}{1+H_1(j\omega)H_2(j\omega)} \right] V_{in}(\omega) \quad (2.5)$$

For an oscillator, the output voltage V_o is nonzero even if the input signal $V_i = 0$. This is only possible if the forward loop gain is infinite (which is not practical), or if the denominator $1 + H_1(j\omega)H_2(j\omega) = 0$ at some frequency ω_o ; that is the loop gain is equal to unity for some values of the complex frequency $s=j\omega$. This leads to the well-known condition for oscillation (the *Nyquist criterion*), where at some frequency ω_o , $H_1(j\omega_0)H_2(j\omega_0) = -1$ and can be mathematically expressed as

$$|H_1(j\omega_0)H_2(j\omega_0)| = 1 \quad (2.6)$$

and

$$\text{Arg}|H_1(j\omega_0)H_2(j\omega_0)| = (2n + 1)\pi, \text{where } n = 0, 1, 2, \dots \quad (2.7)$$

When the above *criterion* is met, the two conjugate poles of the overall transfer function are located on the imaginary axis of s-plane, and any departure from that position will lead to an increase or a decrease of the oscillation amplitude of the oscillator output signal in time domain, which is shown in Figure 2-2.

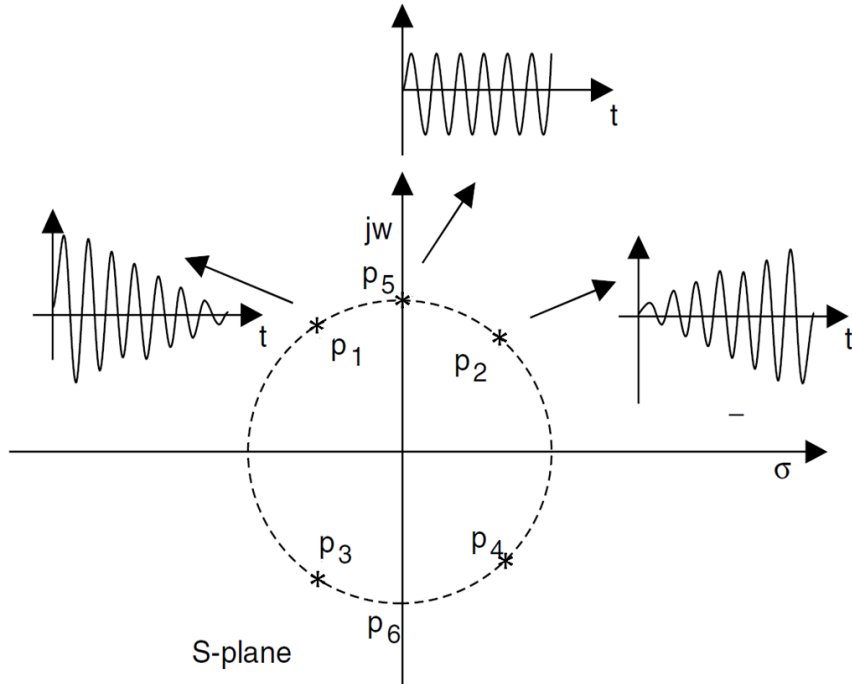


Figure 2-2: Frequency domain root locus and the corresponding time domain response [4]

In practice, the equilibrium point cannot be reached instantaneously without violating some physical laws. As an example, high Q oscillators take longer than low Q types for full amplitude. The oscillator output sine wave cannot start at full amplitude instantaneously after the power supply is turned on. The design of the circuit must be such that at start-up condition, the poles are located in the right half plane, but not too far from the Y-axis. However, the component tolerances and the nonlinearities of the amplifier will play a role. This oscillation is achievable with a small signal loop gain greater than unity, and as the output signal builds up, at least one parameter of the loop gain must change its value in such a way that the two complex conjugate poles migrate in the direction of the Y-axis and that the parameter must then reach that axis for the desired steady state amplitude value at a given oscillator frequency.

Figure 2-3 shows the general schematic diagram of a one-port negative resistance model. The oscillator circuit is separated into a one-port active circuit, which is a nonlinear time variant (NLTV) and a one-port frequency determining circuit, which is a linear time invariant (LTIV) system. The frequency determining circuit, or resonator, sets the oscillation frequency, and it is signal-amplitude independent. The function of the active-circuit is to produce a small-signal negative resistance at the operating point of the oscillator and couple it with the frequency-determining circuit while defining the oscillation frequency. Assuming that the steady state current at the active circuit is almost sinusoidal, the input impedance $Z_d(A, f)$ can be expressed in terms of a negative resistance and reactance as

$$Z_d(A, f) = R_d(A, f) + jX_d(A, f) \quad (2.8)$$

where A is the amplitude of the steady state current and f is the resonance frequency. $R_d(A, f)$ and $X_d(A, f)$ are the real and imaginary parts of the active circuit and depend on the amplitude and frequency. Since the frequency determining circuit is amplitude-independent, it can be represented as

$$Z_r(f) = R_r(f) + jX_r(f) \quad (2.9)$$

where $Z_r(f)$ is the input impedance of the frequency determining circuit, $R_r(f)$ and $X_r(f)$ are the loss resistance and reactance associated with the resonator/frequency determining circuit.

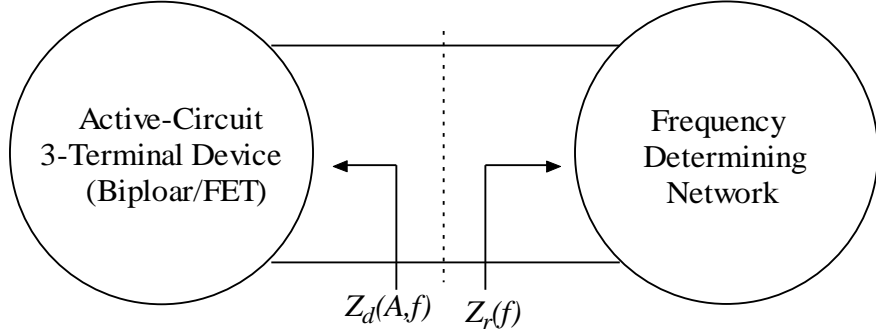


Figure 2-3: Shows the 1-port negative resistance model for the realization of resonant condition using impedance function (compensating the loss resistance associated with the frequency determining network) [4]

To support the oscillator build-up, $R_d(A, f) < 0$ is required so the total loss associated with the frequency determining circuit can be compensated. Oscillation will start build-up if the product of the input reflection coefficient $\gamma_r(f_0)$, looking into the frequency determining circuit and the input reflection coefficient $\gamma_d(A_0, f_0)$ of the active part of the oscillator circuit is unity at $A = A_0$ and $f = f_0$. The steady state oscillation condition can be expressed as

$$\gamma_d(A, f) \gamma_r(f)|_{f=f_0} \Rightarrow \gamma_d(A_0, f_0) \gamma_r(f_0) = 1 \quad (2.10)$$

Figure 2-4 shows the input reflection coefficient $\gamma_d(A_0, f_0)$ and $\gamma_r(f_0)$, which can be represented in terms of the input impedance and the characteristic impedance Z_0 as

$$\gamma_d(A_0, f_0) = \frac{Z_d(A_0, f_0) - Z_0}{Z_d(A_0, f_0) + Z_0} \quad (2.11)$$

$$\gamma_r(f_0) = \frac{Z_r(f_0) - Z_0}{Z_r(f_0) + Z_0} \quad (2.12)$$

$$\gamma_d(A_0, f_0) \gamma_r(f_0) = 1 \Rightarrow \left[\frac{Z_d(A_0, f_0) - Z_0}{Z_d(A_0, f_0) + Z_0} \right] \left[\frac{Z_r(f_0) - Z_0}{Z_r(f_0) + Z_0} \right] = 1 \quad (2.13)$$

$$[Z_d(A_0, f_0) - Z_0][Z_r(f_0) - Z_0] - [Z_d(A_0, f_0) + Z_0][Z_r(f_0) + Z_0] = 0 \quad (2.14)$$

$$\Rightarrow Z_d(A_0, f_0) + Z_r(f_0) = 0 \quad (2.15)$$

The characteristic equation $Z_d(A_0, f_0) + Z_r(f_0) = 0$ can be written as

$$R_d(A_0, f_0) + R_r(f_0) = 0 \quad (2.16)$$

$$\text{and } X_d(A_0, f_0) + X_r(f_0) = 0 \quad (2.17)$$

This means that the one-port circuit is unstable for the frequency range ($f_1 < f < f_2$), where. $R_d(A, f)|_{(f_1 < f < f_2)} < 0 \Rightarrow R_d(A, f)|_{(f_1 < f < f_2)} > R_r(f)$

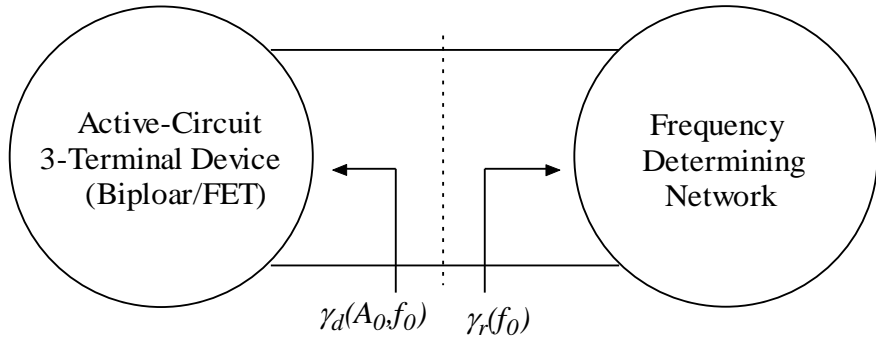


Figure 2-4: Shows the oscillator model for the realization of resonant condition using reflection coefficient (γ), ($\gamma_d(A_0, f_0)$ is input reflection coefficient for active circuit which depends on the signal amplitude A_0 and operating frequency f_0 ; $\gamma_r(f_0)$ is reflection coefficient for resonator and depends mainly on the oscillating frequency f_0) [4]

At the start-up oscillation, when the signal amplitude is very small, the amplitude dependence of the $R_d(A, f)$ is negligible and the oscillation build-up conditions can be given as [7, Ch-6]

$$[R_d(f) + R_r(f)] \Rightarrow R_d(f_x) + R_r(f_x) \leq 0 \quad (2.18)$$

$$\text{And } [X_d(f) + X_r(f)]_{f=f_x} \Rightarrow X_d(f_x) + X_r(f_x) \leq 0 \quad (2.19)$$

where f_x denotes the resonance frequency at which the total reactive component equals zero. The conditions above are necessary, but are not sufficient conditions for oscillation build-up, particularly in a case when multiple frequencies exist to support the above- shown

conditions. To guarantee the oscillation build-up, the following condition at the given frequency needs to be met [1]:

$$\frac{\partial y}{\partial f} [X_d(f) + X_r(f)]_{f=f_x} > 0 \quad (2.20)$$

$$R_d(f_x) + R_r(f_x) < 0 \quad (2.21)$$

$$X_d(f_x) + X_r(f_x) = 0 \quad (2.22)$$

Alternatively, for a parallel admittance topology,

$$Y_d(f_x) + Y_r(f_x) = 0 \quad (2.23)$$

$$G_d(f_x) + G_r(f_x) < 0 \quad (2.24)$$

$$B_d(f_x) + B_r(f_x) = 0 \quad (2.25)$$

$$\frac{\partial}{\partial f} [B_d(f) + B_r(f)]_{f=f_x} > 0 \quad (2.26)$$

Figure 2-5 shows the start-up and steady-state oscillation conditions.

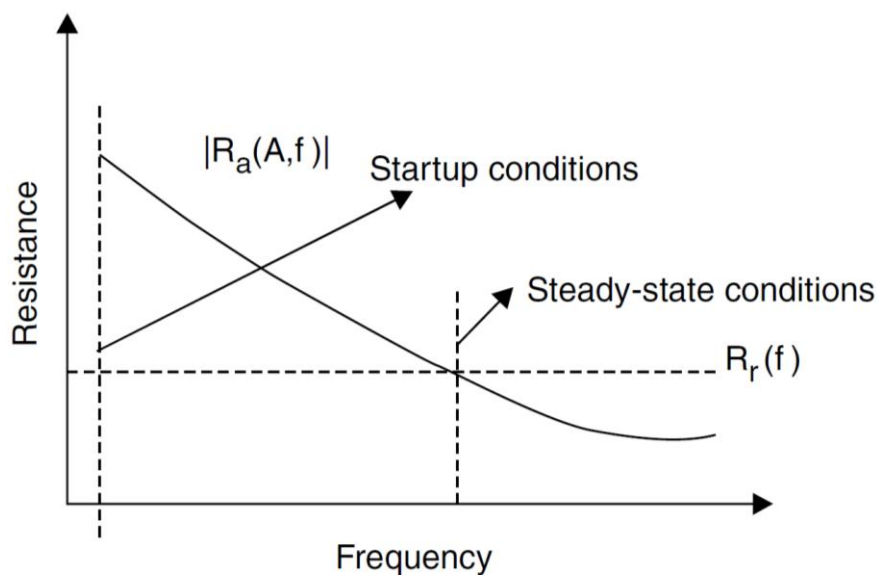


Figure 2-5: Plot of start and steady state oscillation conditions [3]

As discussed earlier, if the closed-loop voltage gain has a pair of complex conjugate poles in the right half of the s-plane, close to the imaginary axis, then due to an ever-present noise voltage generated in the circuit or power-on transient, a growing, near-sinusoidal voltage appears. As the oscillation amplitude grows, the amplitude-limiting capabilities, due to the change in the transconductance from a small signal [g_m] to the large signal [$g_m(t)=G_m$] of the amplifier, produce a change in the location of the poles. The changes are such that the complex-conjugate poles move towards the imaginary axis and at some value of the oscillation amplitude; the poles reach to the imaginary axis giving steady-state oscillation as [2]:

$$|G(j\omega)H(j\omega_0)| = 1 \quad (2.27)$$

In the case of the negative resistance model, the oscillation will continue to build as long as $R_d(A, f)|_{f_1 < f < f_2} < 0 \Rightarrow |R_d(A, f)|_{f_1 < f < f_2} > |R_r(f)|$.

The frequency of oscillation determined by $R_d(A_0, f_0) + R_r(f_0) = 0$, and $X_d(A_0, f_0) + X_r(f_0) = 0$ might not be stable because $Z_d(A, f)$ is frequency and amplitude-dependent. To guarantee stable oscillation, the following condition is to be satisfied as [1]

$$\frac{\partial}{\partial A} [R_d(A)|_{A=A_0}] \times \frac{\partial}{\partial f} [X_r(f)|_{f=f_0}] - \frac{\partial}{\partial A} [X_d(A)|_{A=A_0}] \times \frac{\partial}{\partial f} [R_r(f)|_{f=f_0}] > 0 \quad (2.28)$$

$$\frac{\partial}{\partial A} [R_d(A)|_{A=A_0}] \times \frac{\partial}{\partial f} [X_r(f)|_{f=f_0}] > \frac{\partial}{\partial A} [X_d(A)|_{A=A_0}] \times \frac{\partial}{\partial f} [R_r(f)|_{f=f_0}] \quad (2.29)$$

In the case of an LC resonant circuit, $R_r(f)$ is constant and the equation above can be simplified to

$$\frac{\partial}{\partial A} [R_d(A)|_{A=A_0}] \times \frac{\partial}{\partial f} [X_r(f)|_{f=f_0}] > 0 \quad (2.30)$$

Alternatively, for a paralleled tuned circuit, the steady-state oscillation condition is given as $Y_d(f_0) + Y_r(f_0) = 0$ (where Y_d and Y_r are respective admittances of active circuitry and resonator networks) [5]

$$G_d(f_0) + G_r(f_0) = 0 \quad (2.31)$$

$$B_d(f_0) + B_r(f_0) = 0 \quad (2.32)$$

$$\frac{\partial}{\partial A} \left[G_d(A) \Big|_{A=A_0} \right] \times \frac{\partial}{\partial f} \left[B_r(f) \Big|_{f=f_0} \right] > 0 \quad (2.33)$$

2.2 Specifications of Tunable Oscillators

Today, oscillators are used in test and measurement equipment and communication equipment]. The largest group of users is for the use of two-way radios and “handies” (cell phones). For these applications, oscillators have to meet a variety of specifications, which affect the quality of the operational system. The properties of an oscillator can be described in a set of parameters [6]. The following is a list of the important and relevant parameters, as they need to be discussed with oscillators.

2.2.1 Frequency Range and Tuning Characteristics

The output frequency of Voltage Controlled Oscillators (VCOs) can vary over a wide range. The frequency range is determined by the architecture of the oscillator. A standard tunable oscillator has a frequency range typically less than 2:1; multi-octave-band slow-wave resonator (SWR) oscillator can have 4:1 tuning range (Figure 2-6). This specification shows the relationship, depicted as a graph, between the VCO operating frequency and the tuning voltage applied. Ideally, the correspondence between operating frequency and tuning voltage is linear.

2.2.2 Tuning Linearity

For stable oscillator, a linear deviation of frequency versus tuning voltage is desirable. It is also important to make sure that there are no breaks in tuning range, for example, that the oscillator does not stop operating with a tuning voltage of 0V.

2.2.3 Tuning Sensitivity, Tuning Performance

This datum, typically expressed in megahertz per volt (MHz/V), characterizes how much the frequency of a VCO changes per unit of tuning voltage change.

2.2.4 Tuning Speed

This characteristic is defined as the time necessary for the VCO to reach 90% of its final frequency upon the application of a tuning voltage step. Tuning speed depends on the internal components between the input pin and the tuning diode, including, among other things, the capacitance present at the input port. The input port's parasitic elements, as well as the tuning diode, determine the VCOs maximum possible modulation bandwidth.

2.2.5 Post-tuning Drift

After a voltage step is applied to the tuning diode input, the oscillator frequency may continue to change until it settles to a final value. The post-tuning drift is one of the parameters that limit the bandwidth of the VCO input and the tuning speed.

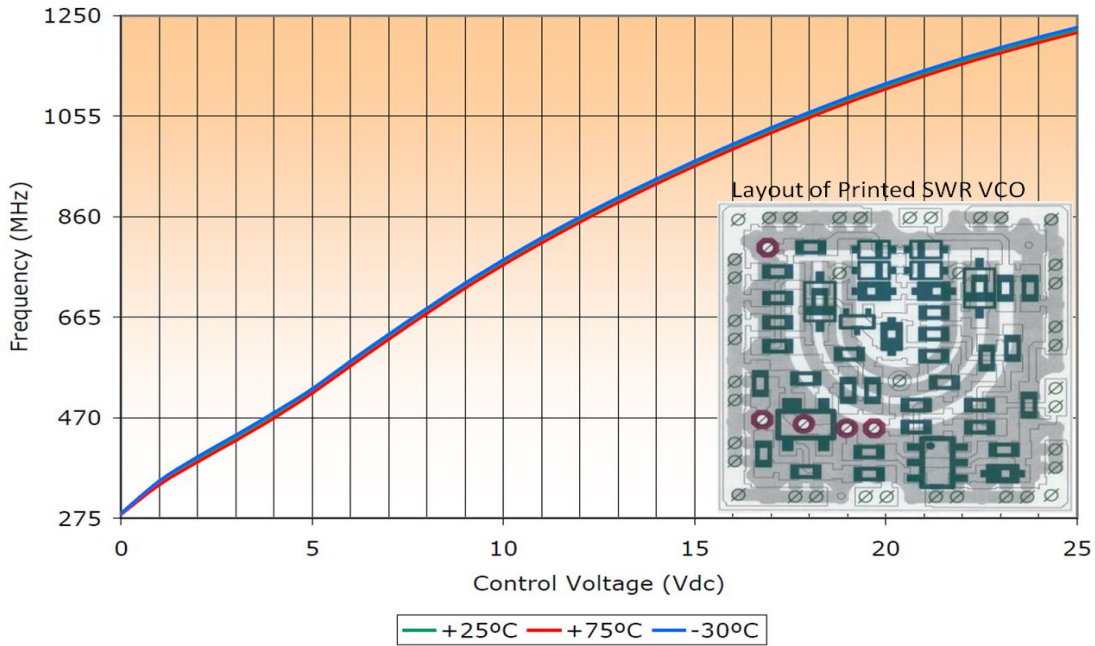


Figure 2-6: Plot of tuning range (300-1200 MHz) of SWR VCO (0.75X0.75X0.18 inches)

2.2.6 Phase Noise

An important feature is the stability of the oscillator (low phase noise) and its freedom from spurious signals and noise. While the oscillator is almost always used as a voltage-controlled oscillator (VCO) in a frequency synthesizer system, its free-running noise performance outside the loop is still extremely important and solely determined by the oscillator.

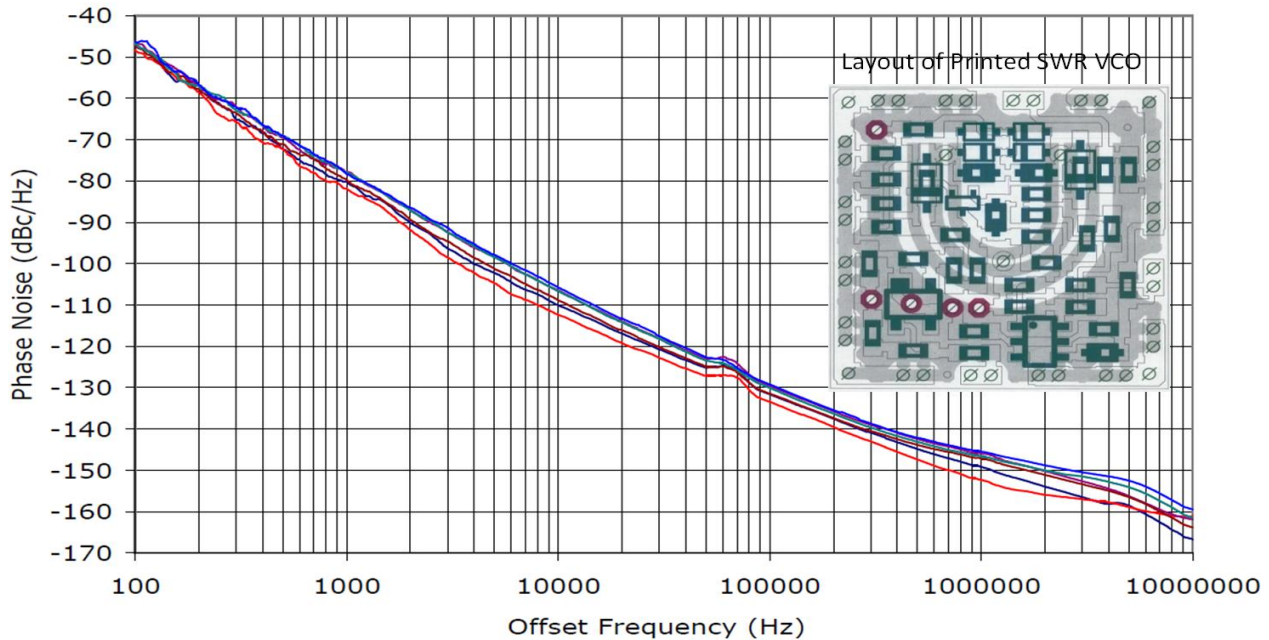


Figure 2-7: Measured phase noise of SWR VCO (300-1200 MHz) (0.75X0.75X0.18 inches)

Unfortunately, oscillators do not generate perfect signals. The various noise sources in and outside of the active device (transistor) modulate the VCO, resulting in energy or spectral distribution on both sides of the carrier due to modulation and frequency conversion. AM and FM noise is expressed as the ratio of noise power in a 1 Hz bandwidth divided by the output power. It is measured at frequency offset of the carrier. Figure 2-7 shows a typical measured phase noise plot of a VCO (300-1200 MHz) using printed slow-wave coupled resonator (SWR) in compact size (0.75X0.75X0.18 inches). The x-axis is the frequency offset from the carrier on a logarithmic scale. The y-axis is the phase noise in dBc/Hz.

The stability or phase noise of an oscillator can be determined in the time or frequency domain. Phase noise is a short-term phenomenon and has various components. Figure 2-8 (a) shows the typical illustration of the stability and phase noise in the time and frequency domain. The major noise contributors are thermal noise, Schottky noise and the flicker noise from the active device. Flicker noise depends on the transistor type and its biasing. The noise contribution from the resonator is mainly thermal noise. The minimum phase noise is at far offsets from the carrier, the best number being $-P_{out}(dBm) + kT_o (-174dBm) + NF$ (large-signal noise figure of the oscillator transistor in dB); all per 1Hz bandwidth.

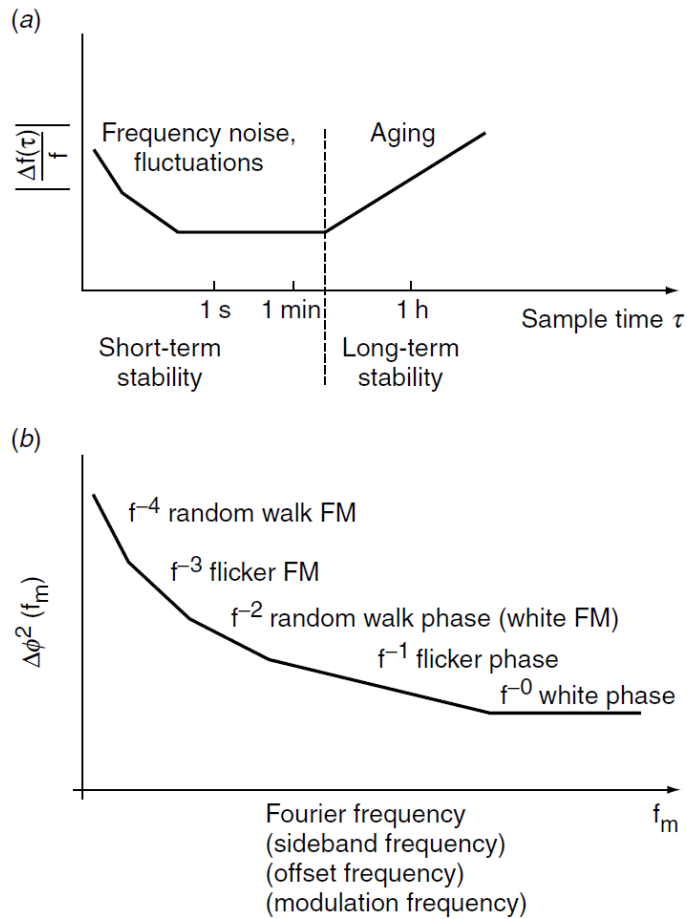


Figure 2-8 typical characterization of the noise sideband in the time and frequency domain and its contributions: (a) time domain and (b) frequency domain. Note that two different effects are considered, such as aging in (a) and phase noise in (b) [2].

2.2.7 Output Power

The output power is measured at the designated output port of the oscillator circuit. Practical designs require one or more isolation stages between the oscillator and the output. The VCO output power can vary as much as ± 2 dB over the tuning range. A typical output level ranges from 0 to +10 dBm.

2.2.8 Harmonic Suppression

The oscillator/VCO has a typical harmonic suppression of better than 15 dB. For high performance applications, a low pass filter at the output will reduce the harmonic contents to a desired level. Figure 2-9 shows a typical second harmonic suppression plot of a 300-1200 MHz) using printed slow-wave coupled resonator (SWCR) in compact size (0.75X0.75X0.18 inches).

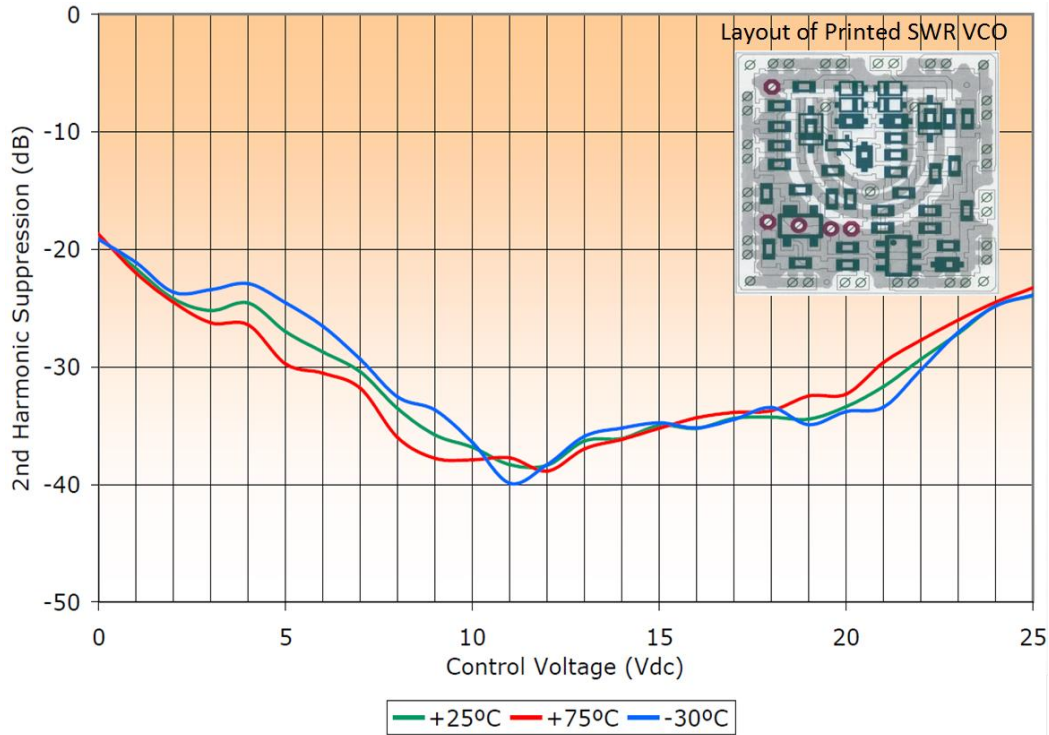


Figure 2-9: Measured harmonics at the output of a slow-wave coupled resonator (SWCR) VCO

2.2.9 Output Power as a Function of Temperature

All active circuits vary in performance as a function of temperature. The output power of an oscillator over a temperature range varies for broadband SWR VCO (300-1200 MHz) as shown in Figure 2-10. Therefore tracking filter with buffer amplifier is needed to enable less than a specified value variation, such as 1 dB over multi-octave-band tuning ranges.

2.2.10 Spurious Response

Spurious outputs are signals found around the carrier of an oscillator, which are not harmonically related. A good, clean oscillator needs to have a spurious-free range of 90 dB, but these requirements make it expensive. Oscillators typically have no spurious frequencies besides possibly 60 Hz and 120 Hz pick-up. The digital electronics in a synthesizer generates

many signals, and when modulated on the VCO, are responsible for these unwanted output products.

2.2.11 Frequency Pushing

Frequency pushing characterizes the degree to which an oscillator's frequency is affected by its supply voltage. For example, a sudden current surge caused by activating a transceiver's RF power amplifier may produce a spike on the VCOs DC power supply and a consequent frequency jump. Frequency pushing is specified in frequency/voltage form and is tested by varying the VCOs DC supply voltage (typically $\pm 1\text{V}$) with its tuning voltage held constant. Frequency pushing must be minimized, especially in cases where power stages are close to the VCO unit and short pulses may affect the output frequency. Poor isolation can make phase locking impossible.

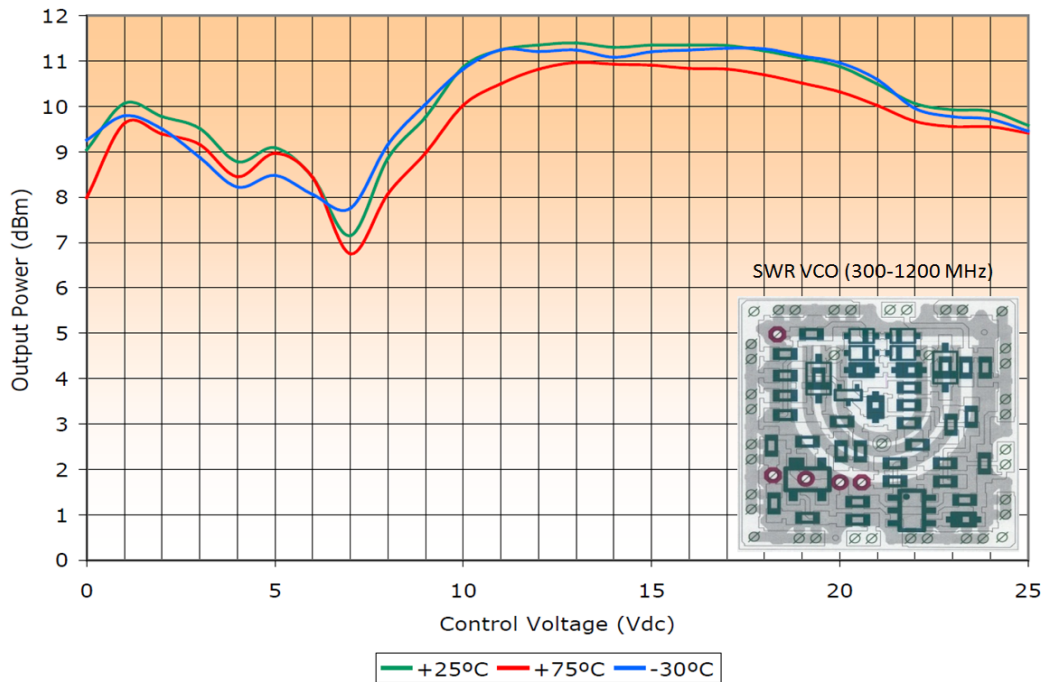


Figure 2-10: Measured output power as a function of temperature of SWR VCO (300-1200 MHz)

2.2.12 Sensitivity to Load Changes

To keep manufacturing costs down, many wireless applications use a VCO alone, without the buffering action of a high reverse-isolation amplifier stage. In such applications, frequency pulling, the change of frequency resulting from partially reactive loads is an important oscillator characteristic. Pulling is commonly specified in terms of the frequency shift that occurs when the oscillator is connected to a load that exhibits a non-unity VSWR (such as 1.75, usually referenced to 50Ω), compared to the frequency that results with unity-VSWR load (usually 50Ω).

2.2.13 Power Consumption

This characteristic conveys the DC power, usually specified in milliwatts and sometimes qualified by operating voltage, required by the oscillator to function properly.

2.3 History of Microwave Oscillators

Early microwave oscillators were built around electron tubes and great efforts were made to obtain gain and power at high frequencies [8]-[12]. Starting from simple glass triodes (lighthouse tubes) and coaxial ceramic triodes, a large number of circuits designed to obtain reasonable performance were built. After using the Lecher lines (quarter-wave length U-shaped parallel wires, shorted at the end, with a few centimeters spacing), the next step was the use of coaxial systems, which became mechanically very difficult and expensive. At higher frequencies, cavities dominated the application and many publications dealt with the various resonant modes. For special applications such as microwave ovens and radar applications, magnetrons and reflex klystrons were developed. Today, the good understanding of the planar structures, such as microstrip, stripline, and coplanar waveguide have been instrumental in extending the practical frequency range up to 100 GHz and higher [13]-[20].

Early transistors followed the same trend. Siemens at one time produced a coaxial microwave transistor, Model TV44 and Motorola offered similar devices. Today, microwave transistors, when packaged, are also in microstrip form or are sold as bare die, which can be connected via bond wires to the circuit. These bond wires exhibit parasitic effects and can be utilized as part of the actual circuit. The highest form of integration is RFICs, either in gallium arsenide (GaAs) or in silicon germanium (SiGe) technology. The SiGe circuits are typically more broadband because of lower impedances and GaAs FETs are fairly high impedance at the input. From an application point of view, in oscillators, SiGe seems to be winning. From a practical design, both transistor types can be considered a black box with a set of *S* parameters, which are bias and frequency dependent [2].

We will see that the transistor operates in large-signal condition, and historically, people have used FETs to demonstrate that there is little change in parameters from small to large-signal operation. Bipolar transistors have much more pronounced changes. Early pioneers have invented a variety of oscillator circuits, which are named after them. The following picture, Figure 2-11, shows a set of schematics, applicable for both bipolar and field-effect transistors [7]. The ones using magnetic coupling are not useful for microwave applications. For Frequencies above 400 MHz resonators are built around helical resonators, ceramic resonators (CR), dielectric resonators (DR), or resonant transmission lines (microstrip or coplanar waveguides) to name a few. Constraints on high-Q resonators used in high performance VCO circuits are particularly demanding, and a MMIC integrable solution has been the dream for decades [13]. In general, a high Q resonator element is required in order to achieve low phase noise characteristics in a VCO, but the realization of planar high-Q resonators is difficult due to the higher loss characteristics of the resonator at high frequency.

The DR (Dielectric resonator) offers high Q factor, and is well known for high spectral purity signal sources at radio and microwave frequencies [14]-[19]. However, a VCO employing a DR has a narrow tuning range, is sensitive to vibration, costly, and not suited for current fabrication process in MMIC technology.

One cost-effective and alternative way to eliminate the DR is to use a printed resonator, which is appropriate for current semiconductor manufacturing processes. However, phase noise characteristics of a VCO using a printed resonator is inferior to that of the VCO using a DR (DR Q factor is much higher than the printed resonator) [28]-[34]. Planar resonators, such as ring, hairpin, spiral, and coupled resonators, are implemented easily in practical MMIC fabrication process at the cost of large size and low Q in comparison to the commercially available DR [35]-[40]. Figure 2-12 shows the typical DR for giving brief insights about the possible resonant condition for given parameters (L , a , ϵ_r), where L is the length of DR, a , is the radius, and ϵ_r is the relative permittivity. Figure 2-13a shows the typical high performance DRO circuit using the DR in Push-Push configuration. It offers low phase noise but limited in tuning and poor sub-harmonic rejection [16]-[18]. As depicted in Figure 2-13 (b), the exact placement of the DR disc between the two parallel microstripline is critical and slight variation may lead to higher harmonics and poor phase noise performance.

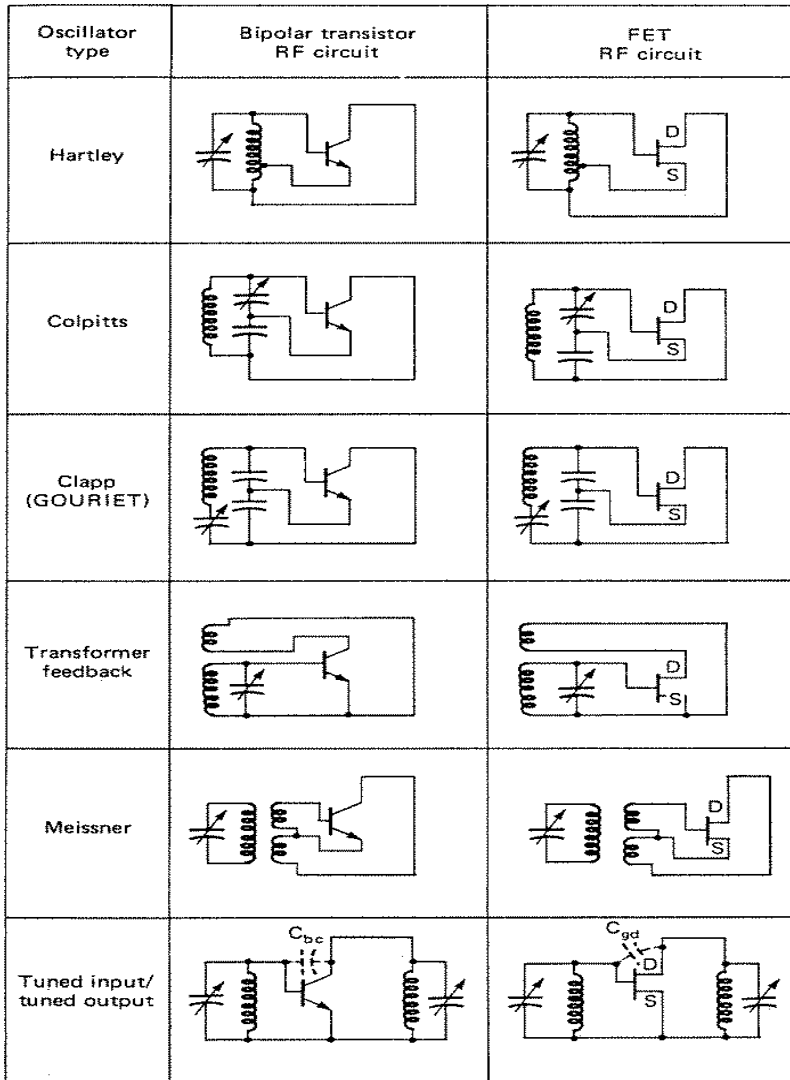


Figure 2-11: Six different configurations which can be built either around bipolar transistors or FETs. Some of the modern microwave oscillators are built around the Colpitts and Clapp oscillator circuits [7].

In addition to this, DR resonant frequencies may differ from the measured result due to the slight variation in temperature that causes problems in integration and mass production. The above problems limit the utility of DRs and the frequency drift is not a straightforward function of the temperature changes (due to different thermal expansion coefficients for the cavity and the dielectric puck). To overcome the above problems and reduce the thermal sensitivity of the DRO, temperature compensation and frequency locking using a PLL (phase locked loop) circuit are needed. However, it is still not a cost-effective solution or suitable for integration [30].

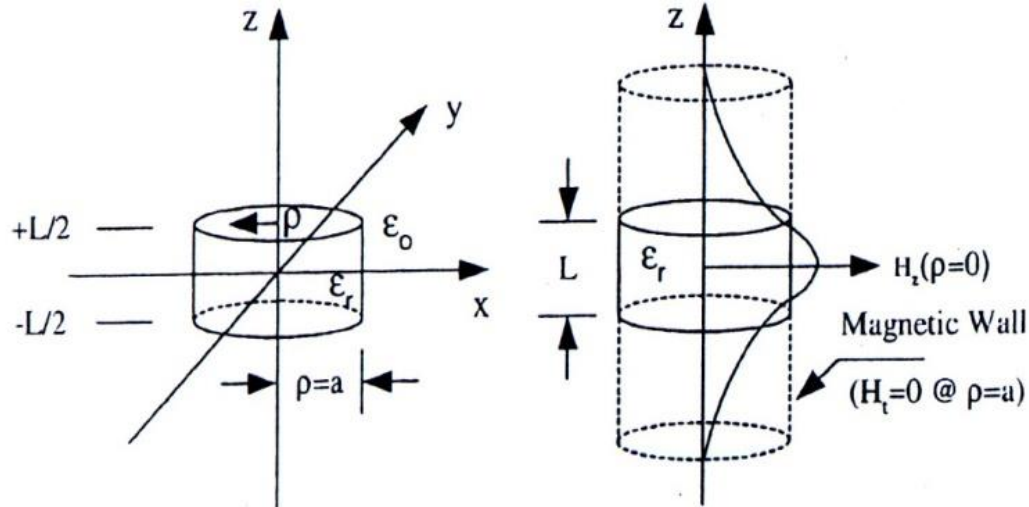


Figure 2-12: A typical DR TE01 δ mode and Hz field distribution [21]

Standard integrated circuits are planar circuits, so only those resonators having a planar structure are suitable in a MMIC/RFIC environment. But integrable planar resonators lack sufficient Q (quality factor) and therefore are a limiting factor of the VCO's phase noise performance. The reason for the poor phase noise performance is due to the slow rate of phase change, and associated group delay characteristics of the resonator over the desired tuning range.

Recent publications explore the possibility of replacing the DR with techniques to improve the Q factor of the planar resonators for VCO applications, which have advantages for low cost, low phase hits, wide tuning range, and suited for on-chip realization [19]-[22].

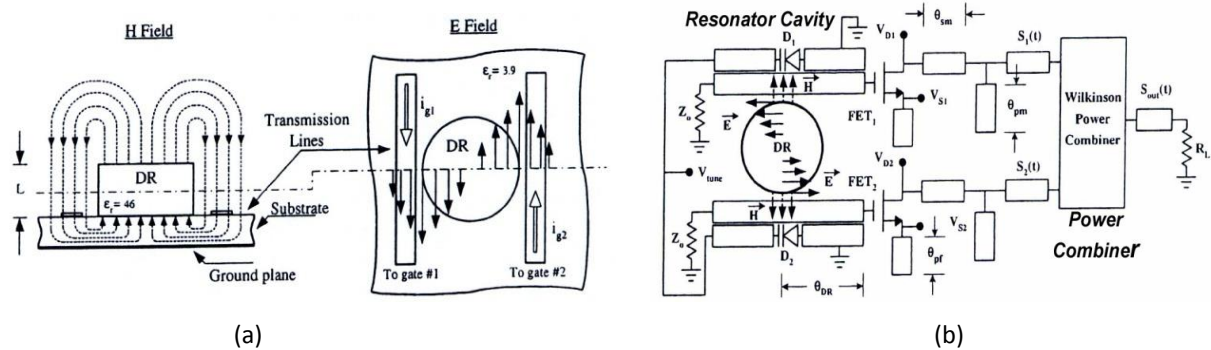


Figure 2-13: (a) DR microstrip coupling EM field distribution, (b) Tunable 12 GHz Push-Push DRO circuit [21]

The low temperature co-fired ceramic (LTCC) resonator (Figure 2-14) is a possible alternative. It exhibits high-Q factor, and is amenable for integration in MMIC process, but is very difficult to integrate in a compact system configuration [14]. Printed helical resonators at microwave frequencies exhibit high Q factor for a given size, and are a strong contender for low phase noise VCO applications. Figure 2-15 depicts a typical 3-D layout of the inductively coupled helical resonator with two $\frac{3}{4}$ turn loops connected together using a via-hole [37].

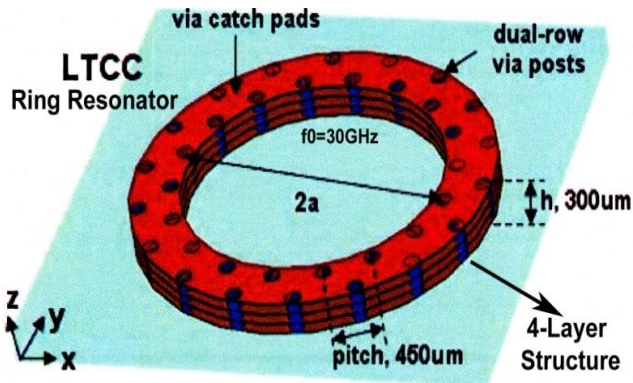


Figure 2-14: Layout of LTCC resonators (resonators are embedded in multilayer LTCC blocks for implementing integrated system in package) [38]

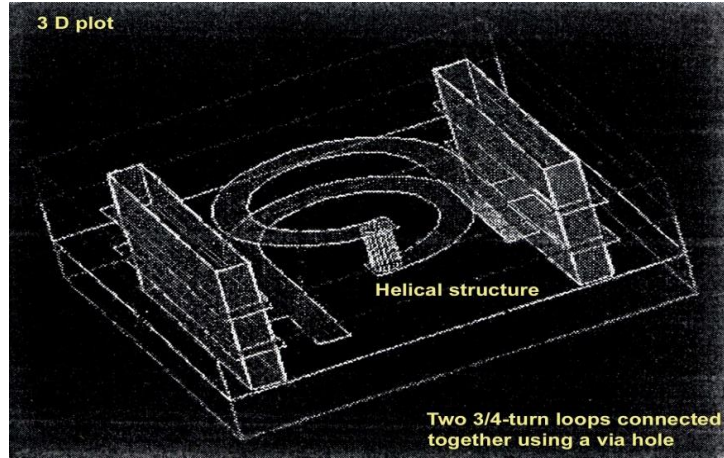


Figure 2-15: 3-D layout of inductively coupled helical resonator [36]

Edward [36], proposed a novel high-Q compact multilayer integrable printed helical resonator that offers optimum Q_L/Q_0 ratio (loaded quality factor/unloaded quality factor) for minimum phase noise for a given VCO topology. Figure 2-16 illustrates the integrable planar helical resonator coupled to coplanar waveguide (CPW) line for high performance VCO applications [6]. The drawbacks of the reported [37]-[38] high-Q helical resonators are limited tuning capability for a given phase noise, size, and cost requirement. For low cost, broadband tunability, and integrable solutions, a new approach is discussed, which is based on the tunable active inductor where total dimensions of the resonator are unaltered while exhibiting wider

tuning and improved Q factor. The solution is reconfigurable and reduction in the number of manufacturing process steps.

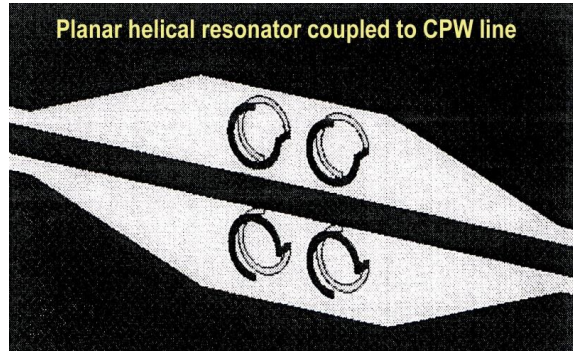


Figure 2-16: Typical planar helical resonator coupled to CPW line [37]

2.4 Resonator Choice

Extensive research work is being done in the area of resonator networks such as passive and active resonator for the applications as the frequency selective element in voltage controlled oscillator applications.

2.4.1 LC Resonator

Figure 2-17 shows the circuit diagram of a simple resonator. The coupling to the port is accomplished by a very small capacitor. The lumped resonator consists of a lossy 2pF capacitor and a lossy 1.76nH inductor with a 0.2pF parasitic capacitor. The capacitor has a lead inductor of 0.2nH and 0.2 Ω losses. Likewise, the inductor has the same value loss resistor. To measure the operating quality factor Q (definition of quality factor is discussed in Ch-5), the simplified method is to connect the tuned network as shown in Figure 2-17 to a network analyzer, which determines S_{11} . For passive network, the quality factor Q is calculated by dividing the center frequency by the 3 dB bandwidth of S_{11} . Alternatively, the quality factor Q is defined as the ratio of stored energy to the dissipated energy. If there is no energy loss or resonator loss is 100% compensated, resulting Q is infinite, therefore new definition of quality factor is needed for analyzing active resonator networks (see Ch-5, section 5.4).

To determine the operating quality factor Q of the circuit as shown in Figure 2-17, let us calculate the Q of the individual branches representing the resonator. The equivalent quality factor Q of the circuit can be calculated by combining the two individual Q values (Q_1 and Q_2) using the equation [2]:

$$Q = \frac{Q_1 \times Q_2}{Q_1 + Q_2} \quad (2.34)$$

$Q_1 = 2 \times \pi \times 2.4 \text{ GHz} \times 1.76\text{nH}/0.2\Omega = 133$, $Q_2 = 165$, $Q = 73$. The reason for the low Q is due to the 0.2Ω loss resistor. It should be possible to reduce this by more than a factor of two.

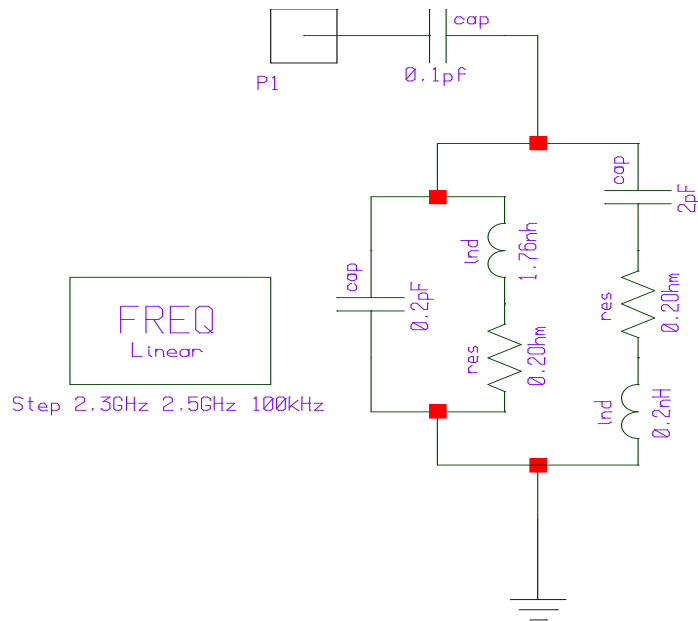


Figure 2-17: A typical circuit diagram of a parallel tuned circuit with lossy components and parasitics loosely coupled to the input [3]

2.4.2 Transmission Line Resonator

The same parallel-tuned circuit shown in Figure 2-17 can be generated by using a printed transmission line instead of the lumped inductor and maintain the same capacitance. This is shown in Figure 2-18. Since the transmission line has losses due to the material, they need to be considered. It is not practical to calculate these by hand, but rather use a CAD program (Ansys-Nexxim, ADS 2013, AWR, and CST) which does this accurately.

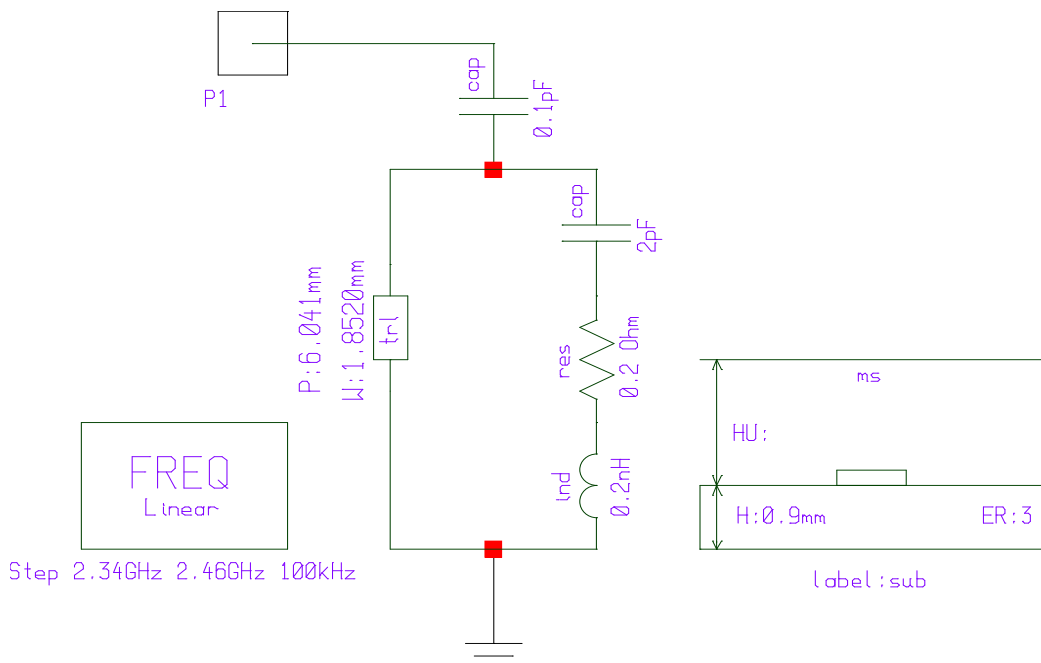


Figure 2-18: Shows a typical 2.4 GHz resonator using both lumped and distributed components [7]

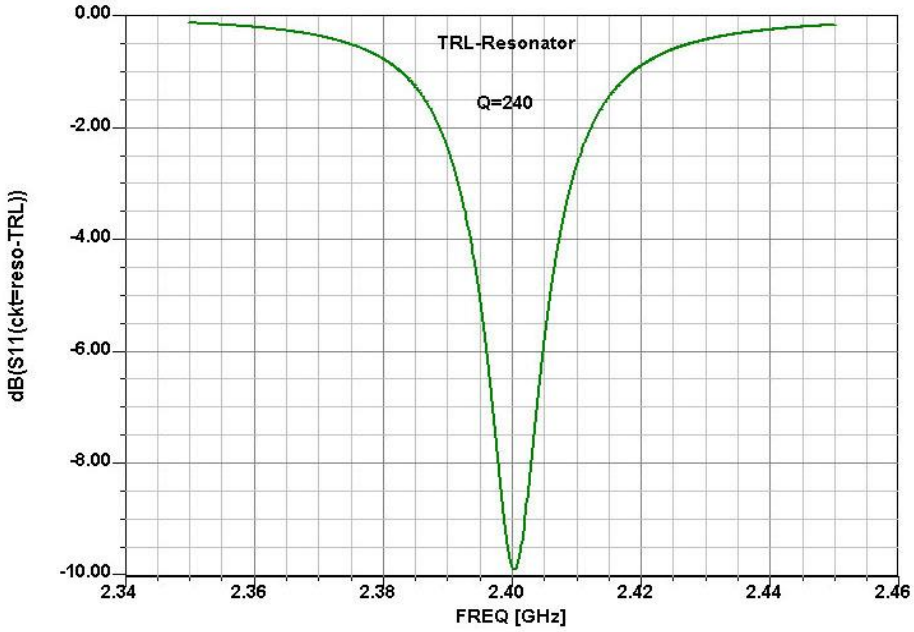


Figure 2-19: A typical CAD simulated reflection coefficient S_{11} to determine the operating Q. Since this material has fairly high losses, an operating Q of only 240 was achieved [3].

These references describe how to get the Q factor from S_{11} measurements. The Q can be determined from the 3dB bandwidth $\left(\frac{\Delta f}{f_0}\right)$ shown in Figure 2-19 and was determined to be 240. This is also valid if the Y or Z parameters are used. This is a typical value for a microstrip resonator. Values up to 300 are possible if the appropriate layout and material is used [1].

2.4.3 Integrated Resonator

The circuit of Figure 2-17 can be generated not only using printed circuit board material, but also in GaAs or silicon. Figure 2-20 shows the schematic of a parallel tuned circuit using a rectangular inductor and an inter-digital capacitor. The ground connections are achieved through vias. At 2.4 GHz, the number of turns and size of the inductor would be significant. The same applies to the capacitor. This arrangement should be reserved for much higher frequencies, above 5 GHz. The inductor losses, both in GaAs and silicon, are substantial and this case is only shown for completeness [7]. For optimum performance, wherever possible an external resonator should be used.

Referring to integrated resonators, a high Q resonator consisting of two coupled inductors has been developed. Figure 2-21 shows a three-dimensional array where the two coupled resonators are easily identifiable. One side of the resonator is connected to ground through a via. The 3-D layout can be reduced to a two-dimensional layout as shown in Figure 2-22, which gives further details about the resonator.

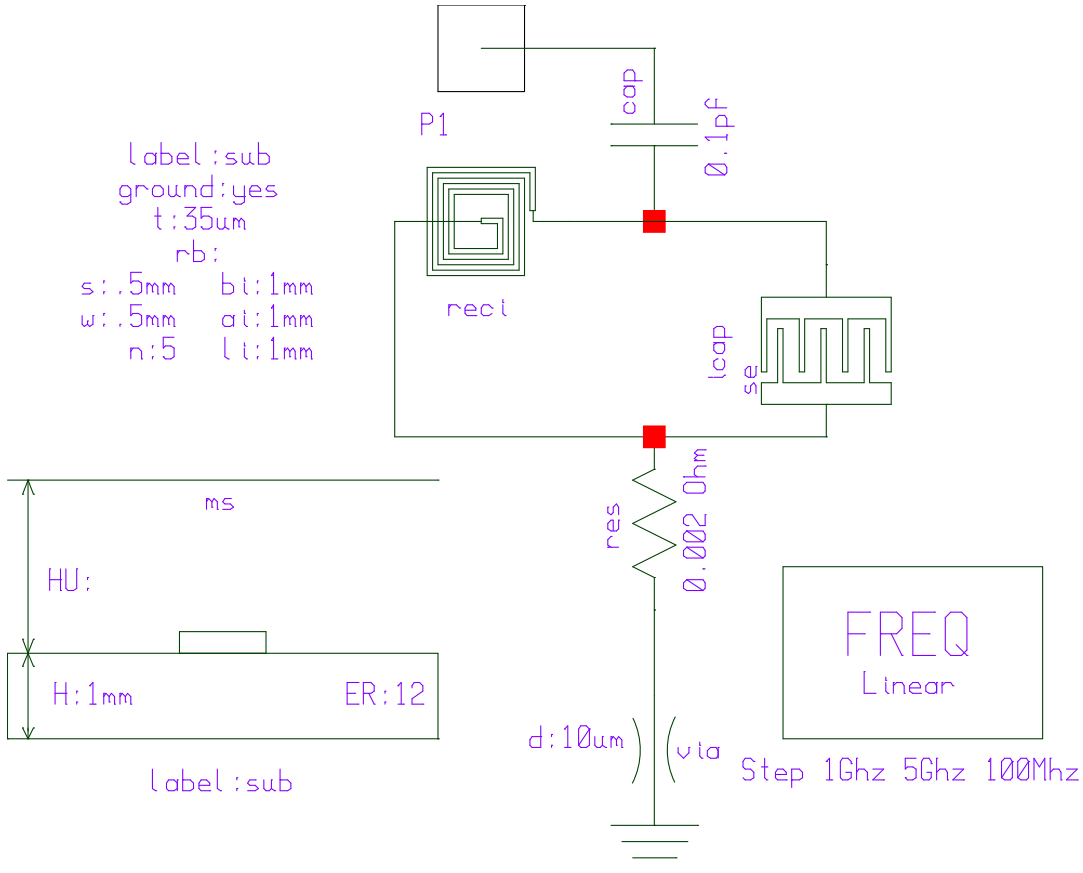


Figure 2-20: Parallel tuned circuit using a rectangular inductor (spiral could also be used) and an interdigital capacitor. If implemented on GaAs or silicon, it exhibits low Q [7].

The resonator analysis was done using Ansoft Designer (now known as Ansys NEXXIM), specifically the 2.5-D simulator. A more conventional resonator analysis can be performed, using the S-parameters obtained from the structure. Figure 2-23 shows the electrical equivalent circuit of the coupled microstrip line resonator [4, 7].



Figure 2-21: A typical 3-D view of the coupled resonator (U.S. patent Nos. 7,088,189 B2 and 7,292,113 B2) [4].

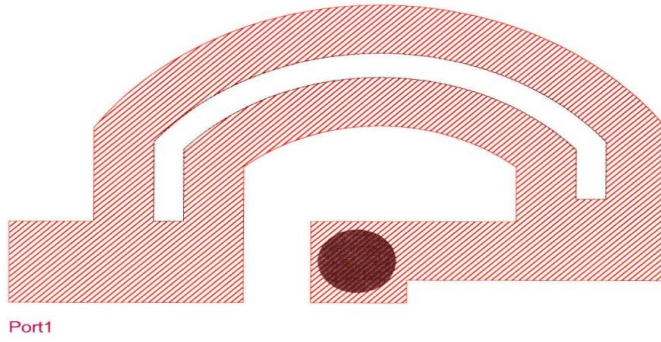


Figure. 2-22: 2-D view of the coupled microstrip resonator (U.S. patent Nos. 7,088,189 B2 and 7,292,113 B2) [4]

Finally, the S_{11} resonant curve is analyzed. The curve seen in Figure 2-24 shows a coupled micro-stripline resonator response, and the resulting Q is determined to be 560. These structures and application covered by U.S. patents 7,088,189 B2 and 7,292,113 B2 [4, 7]. This type of resonator, as shown in Figure 2-21, plays a major role in the design of ultra wide-band oscillators. Figure 2-25 shows the typical circuit layout of a coupled resonator oscillator as it is built on a multi-layer printed circuit board. It is a 1.1-4.5 GHz multi-octave, low-noise oscillator, and this was achieved in our patented approach, US copyright registration No.VAU 603984 [3, 4, and 7]. Besides the coupled resonator, which determines the resonant frequency, there is an additional resonator used for noise filtering. Figure 2-26 shows the measured phase noise plot for this oscillator circuit. Oscillators operate under large-signal conditions.

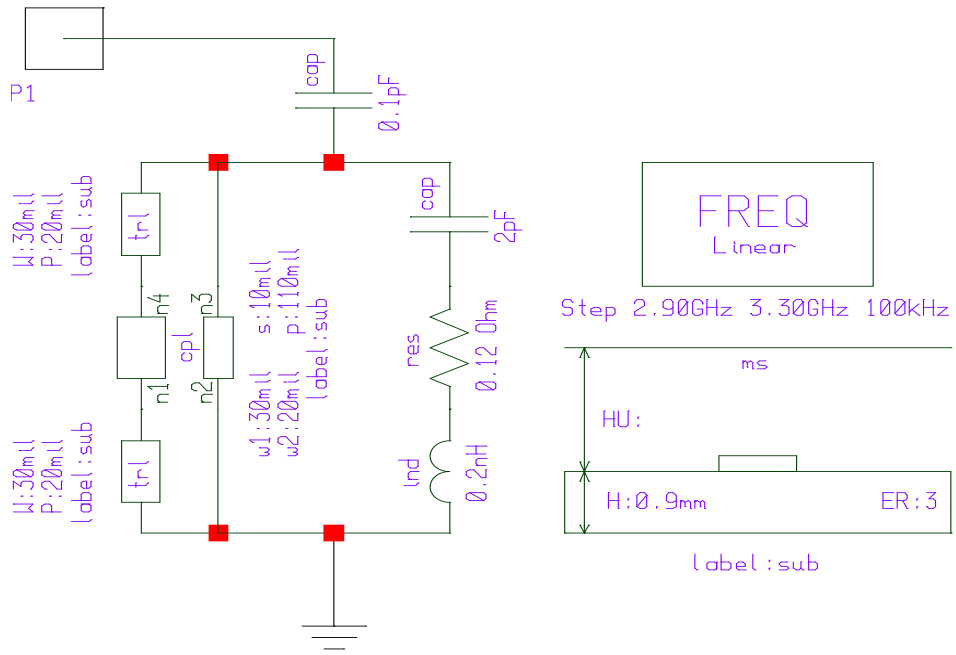


Figure 2-23: Electrical equivalent of the coupled microstrip line resonator [7]

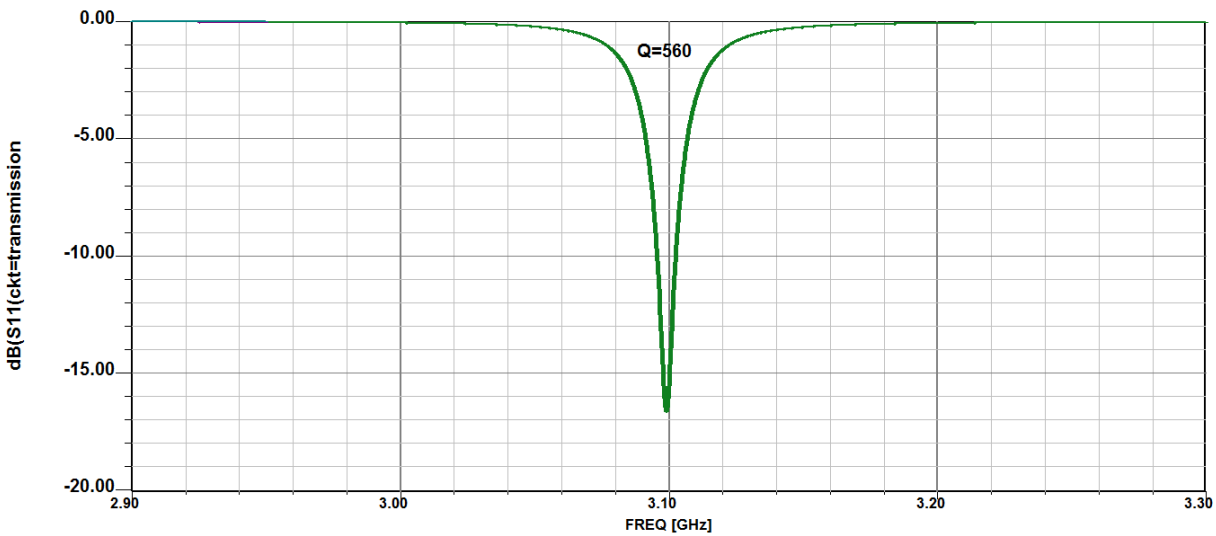


Figure. 2-24: Frequency response of the coupled microstrip line resonator.

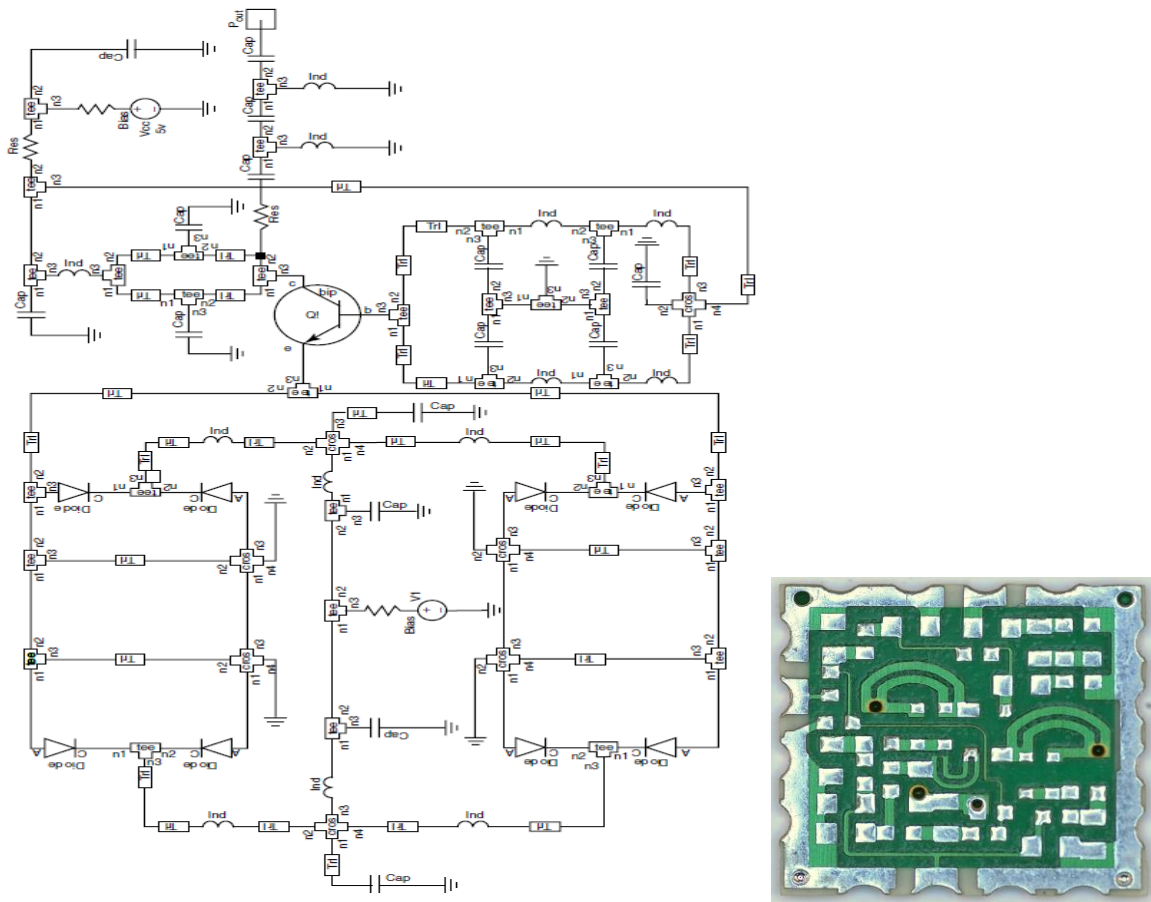


Figure 2-25: An example of a 1.1-4.5 GHz VCO with coupled resonators on a 0.5×0.5 inch 2 PCB (U.S. patent Nos. 7,088,189 B2 and 7,292,113 B2) [4, 7]

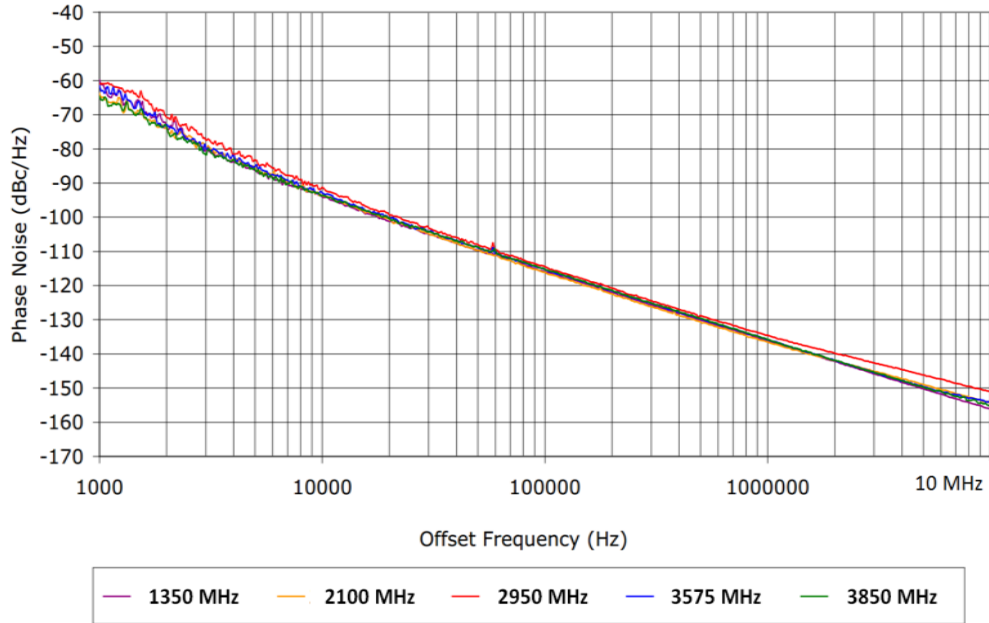


Figure 2-26: Measured phase noise plots of the oscillator layout shown in Figure 2-25

The circuit operates at 5V, 18 mA, and delivers output power better than 3dBm over operating frequency range (1350MHz-3850 MHz). Over few million pieces produced on pick & place machine and commercialized for the applications in Radio and test & measurement equipments, the design layout is stable over temperature and vibration. Under large-signal conditions, the RF currents and voltages are of the same magnitude as the DC values. The most accurate result will be obtained by switching from linear to nonlinear analysis.

2.5 Large Signal S-Parameter Analysis

The description of linear, active or passive 2-ports can be explained in various forms. In the early days Z-parameters were commonly used which then were replaced by the Y-parameters. Z-parameters are open-ended measurements and Y-parameters are short circuit measurements relative to the output or input depending on the parameter. In reality, however, the open circuit condition does not work at high frequencies because it becomes capacitive and results in erroneous measurements. The short-circuit measurements also suffer from non-ideal conditions as most “shorts” become inductive. Most RF and microwave circuits, because of the availability of 50Ω coaxial cables, are now using 50Ω impedances. Component manufacturers are able to produce 50Ω termination resistors, which maintain their 50Ω real impedance up to tens of GHz (40 GHz). The 50Ω system has become a defacto standard. While the Z- and Y-parameter measurements were based on voltage and currents at the input and output, the S-parameters refer to forward and reflected power [2]-[5].

2.5.1 Definition

For low frequency applications, one can safely assume that the connecting cable from the source to the device under test or the device under test to the load plays no significant role [7]. The wavelength of the signal at the input and output is very large compared to the physical length of the cable. At higher frequencies, such as microwave frequencies, this is no longer

true. Therefore, a measuring principle was founded that would look at the incoming and the outgoing power waves at the input and the output port. The following is a mathematical explanation of the S -parameters, which can be described by [2]-[7]

$$b_1 = S_{11}a_1 + S_{12}a_2 \quad (2-35)$$

$$b_2 = S_{21}a_1 + S_{22}a_2 \quad (2-36)$$

or, in matrix form,

$$\begin{bmatrix} b_1 \\ b_2 \end{bmatrix} = \begin{bmatrix} S_{11} & S_{12} \\ S_{21} & S_{22} \end{bmatrix} \begin{bmatrix} a_1 \\ a_2 \end{bmatrix} \quad (2-37)$$

Where, referring to Figure 2-27:

a_1 = (incoming signal wave at Port 1)

b_1 = (outgoing signal wave at Port 1)

a_2 = (incoming signal wave at Port 2)

b_2 = (outgoing signal wave at Port 2)

E_1, E_2 = electrical stimuli at Port 1, Port 2

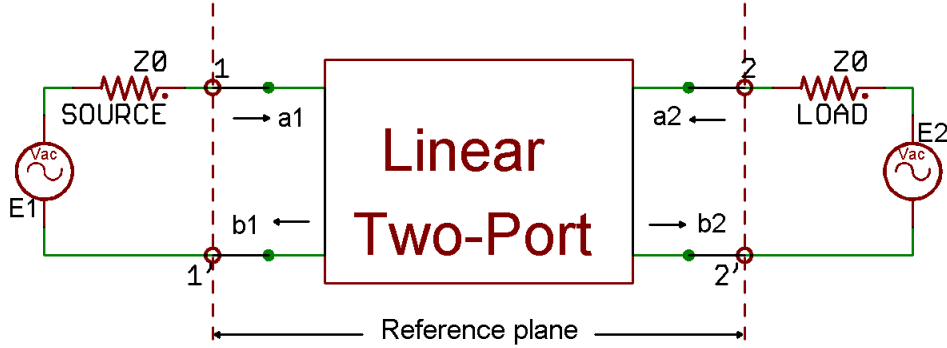


Figure 2-27: Two-port S -parameter definition [2]

From Figure 2-27 and defining linear equations, for $E_2 = 0$, then $a_2 = 0$, following parameters can be derived [2, pp. 205-206]:

$$|S_{11}| = \left| \frac{b_1}{a_1} \right| = \left[\frac{\text{Reflected Voltage}}{\text{Incident Voltage}} \right] = \text{Input Reflection Coefficient} \quad (2-38)$$

$$|S_{21}| = \left| \frac{b_2}{a_1} \right| = \left[\frac{\text{Outgoing Output Power}}{\text{Available Input Power}} \right]^{1/2} = [\text{Forward Transducer Gain}]^{1/2} \quad (2-39)$$

$$\text{Forward Transducer Gain} = G_{TF} = |S_{21}|^2 \quad (2-40)$$

$$Z_i = Z_o \quad (2-41)$$

Similarly at Port 2 for $E_1=0$, then $a_1=0$, and [2, pp. 205-206]:

$$|S_{22}| = \left[\frac{b_2}{a_2} \right] = \text{Output Reflection Coefficient} \quad (2-42)$$

$$|S_{12}| = \left[\frac{b_1}{a_2} \right] [Reverse Transducer Gain]^{1/2} \quad (2-43)$$

$$\text{Reverse Transducer Gain} = G_{TR} = |S_{12}|^2 \quad (2-44)$$

Since many measurement systems display S-parameter magnitudes in decibels, the following relationships are particularly useful:

$$|S_{11}|_{dB} = 10\log|S_{11}|^2 = 20\log|S_{11}| \quad (2-45)$$

$$|S_{22}|_{dB} = 10\log|S_{22}|^2 = 20\log|S_{22}| \quad (2-46)$$

$$|S_{21}|_{dB} = 10\log|S_{21}|^2 = 20\log|S_{21}| = 10\log|G_{TF}| = |G_{TF}|_{dB} \quad (2-47)$$

$$|S_{12}|_{dB} = 10\log|S_{12}|^2 = 20\log|S_{12}| = 10\log|G_{TR}| = |G_{TR}|_{dB} \quad (2-48)$$

2.5.2 Large Signal S-Parameter Measurements

Assume S_{11} and S_{21} are functions only of incident power at port 1 and S_{22} and S_{12} are functions only of incident power at port 2. Note: the plus (+) sign indicates the forward voltage wave and the minus (-) sign would be the reflected voltage wave [3].

$$S_{11} = S_{11}(|V_1^+|), \quad S_{12} = S_{12}(|V_2^+|) \quad (2-49)$$

$$S_{21} = S_{21}(|V_1^+|), \quad S_{22} = S_{22}(|V_2^+|) \quad (2-50)$$

The relationship between the traveling waves now becomes

$$V_1^- = S_{11}(V_1^+)V_1^+ + S_{12}(V_2^+)V_2^+ \quad (2-51)$$

$$V_2^- = S_{21}(V_1^+)V_1^+ + S_{22}(V_2^+)V_2^+ \quad (2-52)$$

Measurement is possible if V_1^+ is set to zero,

$$S_{12}(V_2^+) = \frac{V_1^-}{V_2^+} \quad (2-53)$$

Check the assumption by simultaneous application of V_1^+ and V_2^+

$$\begin{bmatrix} V_1^- \\ V_2^- \end{bmatrix} = \begin{bmatrix} F_1(V_1^+, V_2^+) \\ F_2(V_1^+, V_2^+) \end{bmatrix} \quad (2-54)$$

If harmonics are neglected, a general decomposition is [3]

$$\begin{bmatrix} V_1^-(V_1^+, V_2^+) \\ V_2^-(V_1^+, V_2^+) \end{bmatrix} = \begin{bmatrix} S_{11}(V_1^+, V_2^+) & S_{12}(V_1^+, V_2^+) \\ S_{21}(V_1^+, V_2^+) & S_{22}(V_1^+, V_2^+) \end{bmatrix} \begin{bmatrix} V_1^+ \\ V_2^+ \end{bmatrix} \quad (2-55)$$

If the signal from the signal generator is increased in power, it essentially has no impact on passive devices until a level of several hundred watts is reached where intermodulation distortion products can be created due to dissimilar alloys. However, active devices, depending on the DC bias point, can only tolerate relatively low RF levels to remain in the linear region.

In the case of the oscillator, there is a large RF signal, that is, a large voltage and current, imposed on the DC voltage/current. Assuming an RF output power from 0dBm to 10dBm, and assuming 10-15 dB gain in the transistor, the RF power level driving the emitter/source or base/gate terminal is somewhere in the vicinity of -15dBm.

An RF drive of -15dBm will change the input and output impedance of the transistor, even if the transistor operates at large DC currents. It is important to note that the input and output impedances of field-effect transistors are much less RF voltage-dependent or power-dependent than the bipolar transistor. The generation of “large-signal *S*-parameters” for bipolar transistors is, therefore, much more important than for FETs.

Figure 2-28 shows the test fixture, which was used to measure, the large-signal *S*-parameters for the device under test (DUT). The test fixture was calibrated to provide 50Ω to the transistor leads. The test set-up shown in Figure 2-29 consists of a DC power supply and a network analyzer for combined *S*-parameter measurements. The R&S ZVR network analyzer, as shown in Figure 2-29, was chosen because its output power can be varied between -60dBm and +10dBm. This feature is necessary to perform these measurements.

The picture shown in Figure 2-28 demonstrates the experimental setup for large signal *S*-parameter measurement. The experimental set up is very simple, but unfortunately, very expensive. Currents and voltages follow Kirchhoff's law in a linear system. A linear system implies that there is a linear relationship between currents and voltages. All transistors, when driven at larger levels show nonlinear characteristics.

The FET shows a square law characteristic, while the bipolar transistor has an exponential transfer characteristic. The definition of *S*-parameters in large-signal environment is ambiguous compared to small-signal *S*-parameters. When driving an active device with an increasingly higher level, the output current consists of a DC current and RF currents: the fundamental frequency and its harmonics. When increasing the drive level, the harmonic content rapidly increases. S_{12} , mostly defined by the feedback capacitance, now reflects harmonics back to the input. If these measurements are done in a 50Ω system, which has no reactive components, then we have an ideal system for termination.

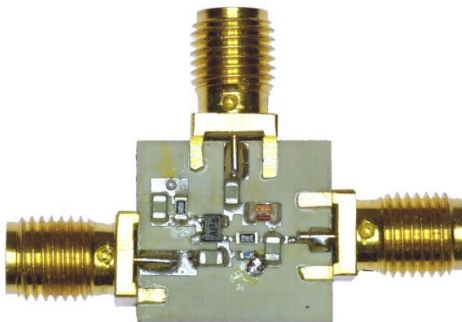


Figure 2-28: Test fixture to measure large signal S -parameters. A proper de-embedding has been done (DC Operating condition, 2V, 20mA) [7]

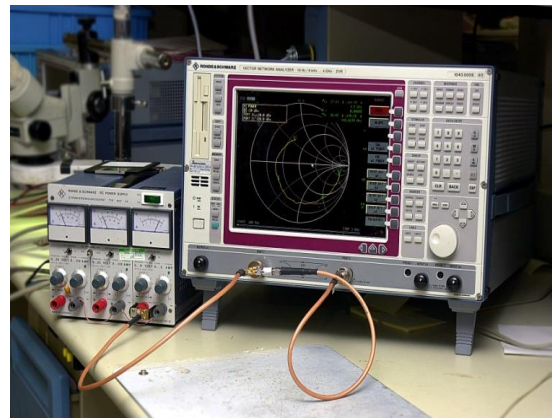


Figure 2-29: Rohde & Schwarz 3 GHz network analyzer to measure the large-signal S -parameters at different drive levels (DC Operating condition, 2V, 20mA) [7].

In practical applications, however, the output is a tuned circuit or matching network, which is frequency selective. Depending on the type of circuit, it typically presents either a short circuit or an open circuit for the harmonic. For example, say the matching network has a resonant condition at the fundamental and second harmonic frequency or at the fundamental and third harmonic frequency (quarter wave resonator). Then a high voltage occurs at the third harmonic, which affects the input impedance, and therefore, S_{11} (Miller effect).

This indicates that S -parameters measured under large-signal conditions in an ideal 50Ω system may not correctly predict device behavior when used in a non- 50Ω environment.

A method called “load pull”, which includes fundamental harmonics, has been developed to deal with this issue [5]. In the case of an oscillator, however, there is only one high-Q resonator, which suppresses the harmonics of the fundamental frequency (short circuit). In this limited case, the S -parameters, measured in a 50Ω system are useful. The following tables show two sets of measurements generated from the Infineon transistor BFP520 under different drive levels.

Since the oscillator will be in quasi-large-signal operation, we will need the large-signal S -parameters as a starting condition for the large-signal design (output power, harmonics, and others). The S -parameters generated from this will be converted into Y -parameters, defined under large-signal conditions and then used for calculating the large-signal behavior. We will use the symbol Y^+ to designate large-signal Y -parameters. In general, the Y parameters computed from the S -parameters with the following equations [7]

$$Y_{11} = \frac{((1-S_{11})*(1+S_{22})+S_{12}*S_{21})}{\Delta} \quad (2-56)$$

$$Y_{22} = \frac{((1+S_{11})*(1-S_{22})+S_{12}*S_{21})}{\Delta} \quad (2-57)$$

$$Y_{12} = -2 * \frac{S_{12}}{\Delta} \quad (2-58)$$

$$Y_{21} = -2 * \frac{S_{21}}{\Delta} \quad (2-59)$$

Where, $\Delta = ((1 + S_{11}) * (1 + S_{22})) + (S_{12} * S_{21})$

Tables 2-1 and 2-2 show the large-signal S-parameters for -20dBm and -10dBm . However, in some cases the analysis starts at small-signal conditions.

The following four plots, Figures 2-30, 2-31, 2-32, 2-33, show S_{11} , S_{12} , S_{21} , and S_{22} measured from 50 MHz to 3000 MHz with driving levels from -20dBm to 5dBm .

The DC operating conditions were 2V and 20mA as shown in Figure 2-29.

Table 2-1: Frequency Dependent S-Parameters [7]

(S-Parameters at -20 dBm)

Freq (Hz)	$S_{11}(\text{Mag})$	$S_{11}(\text{Ang})$	$S_{12}(\text{Mag})$	$S_{12}(\text{Ang})$	$S_{21}(\text{Mag})$	$S_{21}(\text{Ang})$	$S_{22}(\text{Mag})$	$S_{22}(\text{Ang})$
1.0E+08	0.78	-17.15	29.57	-160.6	0.01	69.66	0.96	-7.63
1.5E+08	0.74	-19.95	30.87	-175.17	0.01	73.05	0.94	10.27
2.0E+08	0.71	-23.01	30.87	174.87	0.01	73.61	0.92	12.8
2.5E+08	0.69	-26.34	30.43	167.17	0.01	73.11	0.9	-15.25
3.0E+08	0.66	-29.8	29.8	160.76	0.01	72.13	0.87	-17.61
3.5E+08	0.64	-33.28	29.08	155.2	0.01	70.91	0.85	-19.92
4.0E+08	0.61	-36.73	28.3	150.22	0.01	69.59	0.83	-22.16
4.5E+08	0.59	-40.1	27.5	145.68	0.02	68.24	0.81	-24.33
5.0E+08	0.56	-43.36	26.68	141.5	0.02	66.91	0.78	-26.44
5.5E+08	0.53	-46.47	25.85	137.62	0.02	65.66	0.76	-28.44
6.0E+08	0.51	-49.42	25.02	134	0.02	64.51	0.73	-30.33
6.5E+08	0.48	-52.19	24.18	130.62	0.02	63.5	0.7	-32.07
7.0E+08	0.46	-54.78	23.35	127.46	0.02	62.63	0.68	-33.64
7.5E+08	0.44	-57.2	22.54	124.52	0.02	61.9	0.65	-35.04
8.0E+08	0.42	-59.44	21.74	121.76	0.02	61.3	0.63	-36.26
8.5E+08	0.39	-61.53	20.98	119.19	0.02	60.82	0.6	-37.31
9.0E+08	0.38	-63.48	20.24	116.77	0.03	60.43	0.58	-38.2
9.5E+08	0.36	-65.29	19.53	114.51	0.03	60.13	0.56	-38.95
1.0E+09	0.34	-66.99	18.85	112.38	0.03	59.88	0.54	-39.57
1.5E+09	0.22	-80.06	13.7	96.21	0.04	58.66	0.41	-41.5
2.0E+09	0.14	-91.02	10.61	85.03	0.04	57.04	0.33	-40.51
2.5E+09	0.09	-105.04	8.64	76	0.05	54.51	0.29	-39.1
3.0E+09	0.06	-129.69	7.27	68.07	0.06	51.33	0.25	-37.7

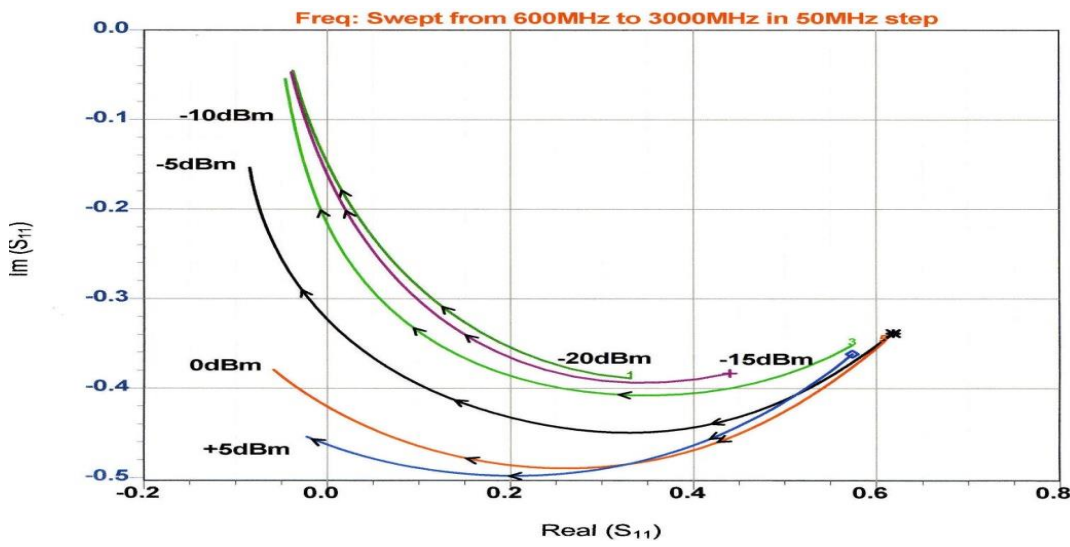


Figure 2-30: Measured large-signal S_{11} of the Infineon BFP520 [7]

Table 2-2 Frequency Dependent S-Parameters [7]
(S-Parameters at -10 dBm)

Freq (Hz)	$S_{11}(\text{Mag})$	$S_{11}(\text{Ang})$	$S_{12}(\text{Mag})$	$S_{12}(\text{Ang})$	$S_{21}(\text{Mag})$	$S_{21}(\text{Ang})$	$S_{22}(\text{Mag})$	$S_{22}(\text{Ang})$
1.00E+08	0.81	-12.8	14.53	179.18	0.02	39.17	0.55	-20.62
1.50E+08	0.79	-14.26	14.51	170.01	0.02	51.38	0.6	-24.42
2.00E+08	0.77	-16.05	14.46	163.78	0.02	57.11	0.65	-27.11
2.50E+08	0.76	-17.94	14.4	158.86	0.03	60.47	0.67	-28.33
3.00E+08	0.74	-19.85	14.31	154.78	0.03	62.9	0.69	-28.28
3.50E+08	0.73	-21.74	14.21	151.32	0.03	64.83	0.7	-27.33
4.00E+08	0.72	-23.62	14.1	148.32	0.03	66.46	0.71	-25.99
4.50E+08	0.71	-25.51	13.99	145.65	0.03	67.72	0.73	-24.6
5.00E+08	0.7	-27.42	13.88	143.19	0.03	68.57	0.74	-23.39
5.50E+08	0.68	-29.37	13.76	140.87	0.03	68.99	0.76	-22.5
6.00E+08	0.67	-31.38	13.65	138.62	0.04	68.98	0.77	-21.93
6.50E+08	0.66	-33.45	13.54	136.4	0.04	68.59	0.77	-21.68
7.00E+08	0.64	-35.56	13.42	134.2	0.04	67.95	0.78	-21.68
7.50E+08	0.63	-37.71	13.31	132	0.04	67.2	0.78	-21.89
8.00E+08	0.61	-39.88	13.19	129.83	0.04	66.31	0.77	-22.25
8.50E+08	0.59	-42.06	13.07	127.7	0.04	65.37	0.77	-22.62
9.00E+08	0.58	-44.23	12.95	125.6	0.04	64.48	0.76	-23.26
9.50E+08	0.56	-46.4	12.82	123.57	0.04	63.69	0.76	-24.04
1.00E+09	0.54	-48.55	12.69	121.6	0.04	62.82	0.75	-24.71
1.50E+09	0.37	-70.76	11.35	104.37	0.05	52.76	0.67	-33.77
2.00E+09	0.21	-91.19	9.99	88.64	0.05	46.68	0.48	-43.79
2.50E+09	0.12	-107.2	8.43	77.36	0.06	49.37	0.33	-43.13
3.00E+09	0.07	-130.38	7.18	68.7	0.06	48.69	0.27	-40.46

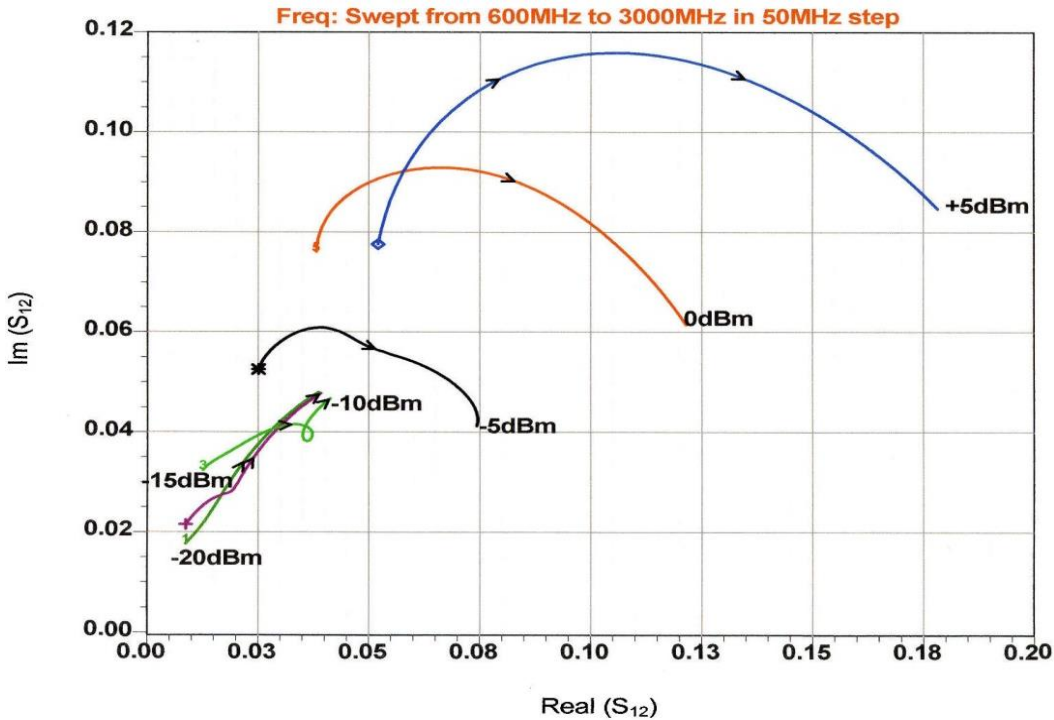


Figure 2-31: Measured large-signal S_{12} of the Infineon BFP520 [7].

When using a SPICE type simulator, or a harmonic balance simulator, then one must use the non-linear model parameters as shown in Figure 2-35. Modern foundries supply relevant data for GaAs and for BiCMOS devices.

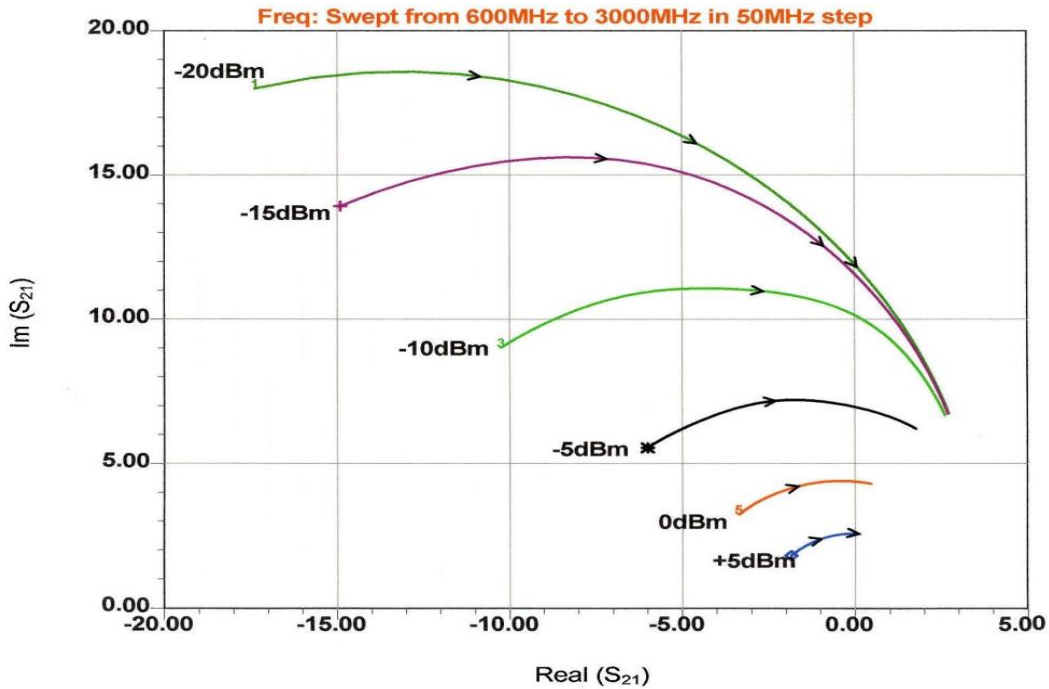


Figure 2-32: Measured large-signal S_{21} of the Infineon BFP520 [7].

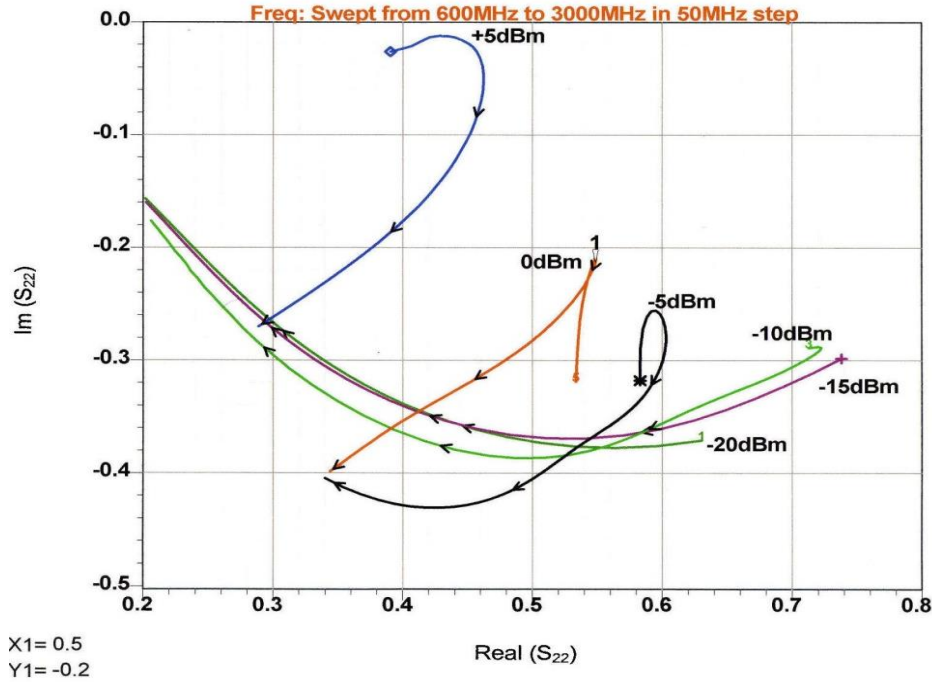


Figure 2-33: Measured large-signal S_{22} of the Infineon BFP520 [7].

The choice of which model to use is not always simple: for bipolar transistors, here the advanced Gummel Poon model [43]-[44] is preferred similar to Figure 2-34. A modification to the base-emitter diffusion capacitance is preferred. Recent publications address this issue in greater detail. For GaAs devices the modified Materka model gives very good results.

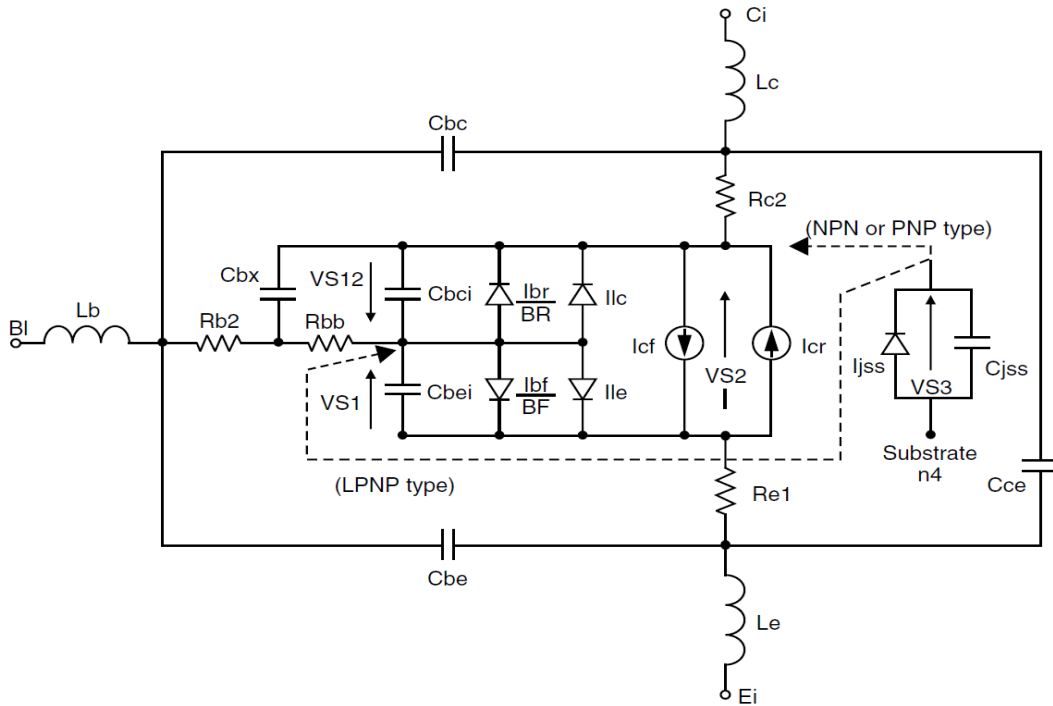


Figure 2-34: A modern equivalent circuit of a bipolar transistor [7, 54]

Transistor Chip Data:

IS	=	15	aA	BF	=	235	-	NF	=	1	-
VAF	=	25	V	IKF	=	0.4	A	ISE	=	25	fA
NE	=	2	-	BR	=	1.5	-	NR	=	1	-
VAR	=	2	V	IKR	=	0.01	A	ISC	=	20	fA
NC	=	2	-	RB	=	11	Ω	IRB	=	-	A
RBM	=	7.5	Ω	RE	=	0.6		RC	=	7.6	Ω
CJE	=	235	fF	VJE	=	0.958	V	MJE	=	0.335	-
TF	=	1.7	ps	XTF	=	10	-	VTF	=	5	V
ITF	=	0.7	A	PTF	=	50	deg	CJC	=	93	fF
VJC	=	0.661	V	MJC	=	0.236	-	XCJC	=	1	-
TR	=	50	ns	CJS	=	0	fF	VJS	=	0.75	V
MJS	=	0.333	-	XTB	=	-0.25	-	EG	=	1.11	eV
XTI	=	0.035	0	FC	=	0.5	-	TNOM	=	298	K

Package Equivalent Circuit:

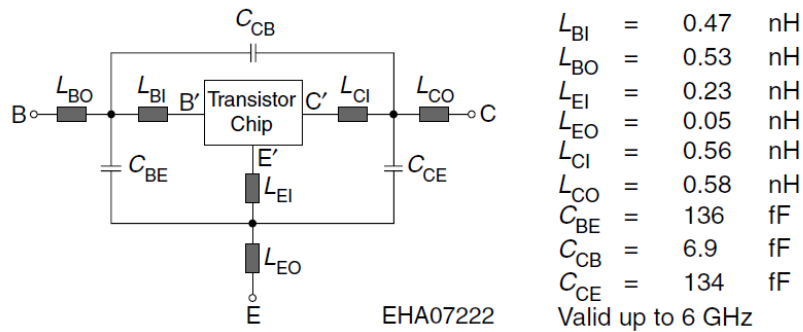
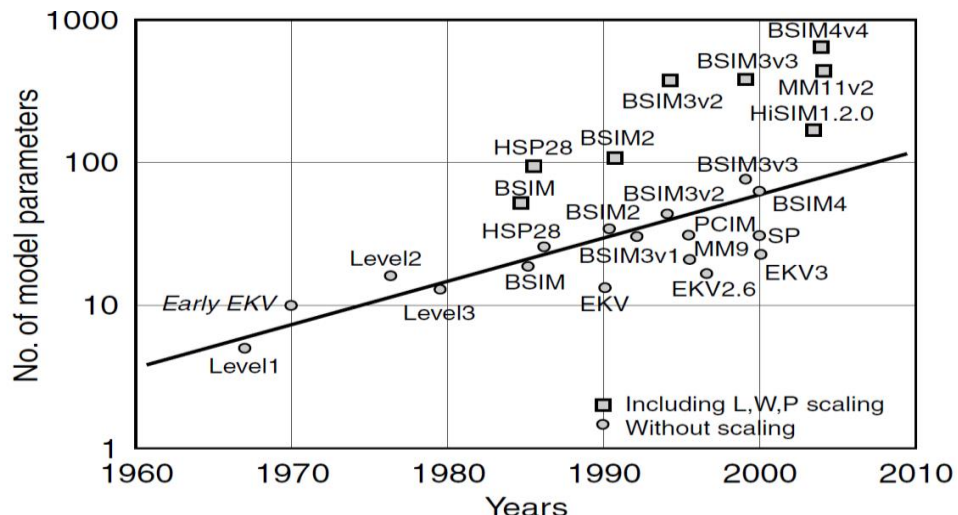


Figure 2-35: SPICE parameters and package equivalent circuit of the Infineon transistor BFP520 [7, 54].



- Number of DC model parameters vs. the year of the introduction of the model
Most recent versions of the EKV, HiSIM, MM11 and SP models are included
- Significant growth of the parameter number that includes geometry (W/L) scaling

Figure 2-36: A survey of MOS model development [5]

Modeling a JFET using the Materka model also yields very accurate RF results. For oscillator circuits a well-documented MOS level-3 models and the EKV3 model can provide accurate simulation. For RF applications, the final optimum model is still undefined [3].

Figure 2-36 shows the developments in MOS models and the large number of model parameters used in modern models. The accompanied parameter extraction to measure the model parameters is similarly complex.

Recently JFETs have found many applications in the higher microwave frequencies and hence their large-signal measurement seems important and useful. The large-signal measurement has been done for the comparative analysis and tabulated in Table 2-3 below for Vishay-Siliconix U310 device [4]. Figure 2-37 shows the test fixture for the measurement of the large-signal S-parameters for the device under test (DUT). The test fixture was calibrated to provide 50Ω to the transistor leads. The test set-up consists of a DC power supply and a network analyzer for combined S-parameter measurements.

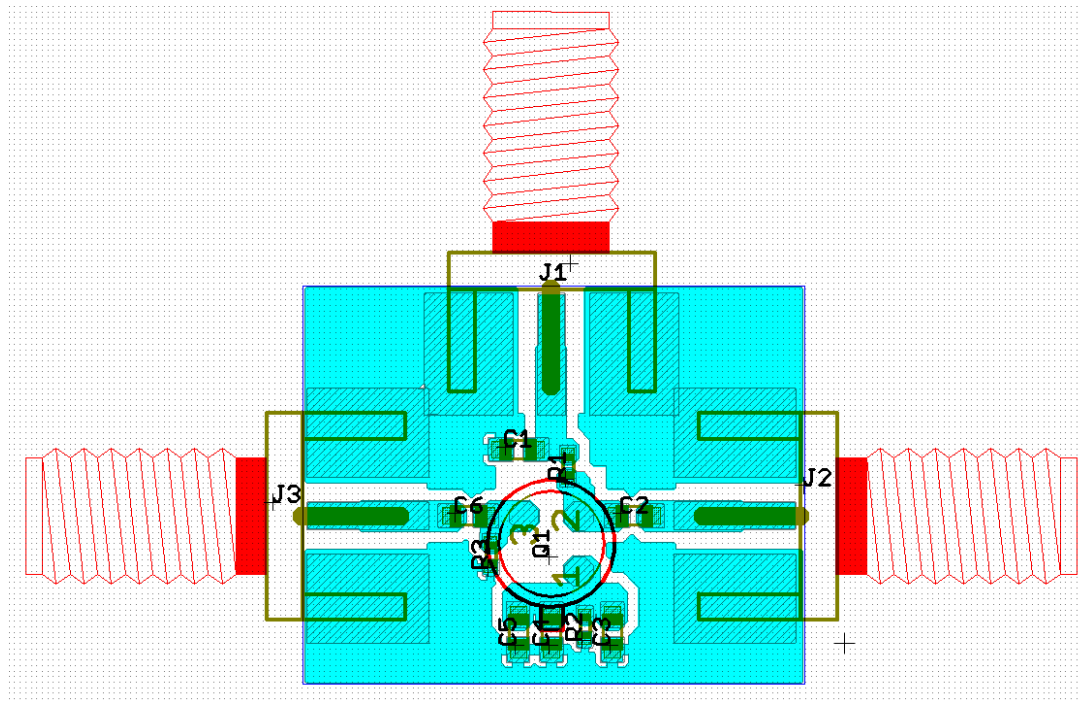


Figure 2-37: Test Fixture to measure large signal S-parameters (A proper de-embedding has been done) [5]

The following four plots, Figures 2-38, 2-39, 2-40, 2-41, show S_{11} , S_{12} , S_{21} , and S_{22} measured from 1 MHz to 250 MHz with driving levels from -20dBm to 14dBm . The DC operating conditions were $V_d = 11.08\text{V}$ and $I_{dss} = 29.9\text{mA}$. Using bipolar and JFET models, the basic topology of frequency selective RF components such as active inductor for the application of oscillator circuits has been developed. The flicker corner frequency for JFET is very small and lends itself for the oscillator application [4]-[5].

Table 2-3 Frequency Dependent S-Parameters [5]
(S-Parameters at “+14 dBm”)

Freq (Hz)	S ₁₁ (Mag)	S ₁₁ (Ang)	S ₁₂ (Mag)	S ₁₂ (Ang)	S ₂₁ (Mag)	S ₂₁ (Ang)	S ₂₂ (Mag)	S ₂₂ (Ang)
1.00E+06	0.98345	-0.6073	0.74017	89.3810	0.00107	44.775	0.6269	-0.0649
2.25E+06	0.95209	-0.7645	0.86255	88.8784	0.00232	45.111	0.6280	0.1060
3.49E+06	0.96476	-1.1922	0.84378	88.6739	0.00367	45.013	0.6260	0.3203
4.74E+06	0.95307	-1.9398	0.81611	88.2794	0.00499	44.972	0.6275	0.6962
5.98E+06	0.93467	-2.6662	0.80225	87.9766	0.00632	45.142	0.6464	1.7483
7.23E+06	0.92762	-3.0482	0.79989	85.5399	0.00791	43.0187	0.70588	-3.3434
8.47E+06	0.89881	-3.8119	0.75921	85.2842	0.00882	43.5229	0.62900	-1.8441
9.72E+06	0.89923	-3.8251	0.73575	85.4880	0.01008	43.8067	0.62435	-1.0041
1.10E+07	0.871265	-4.3860	0.74061	84.9388	0.01137	43.9555	0.62619	-0.4083
1.22E+07	0.884173	-3.9785	0.72533	85.4212	0.01275	43.9893	0.63400	0.29481
1.47E+07	0.880928	-4.1217	0.77674	85.0598	0.01656	43.6024	0.74762	0.07063
1.59E+07	0.882721	-4.2752	0.77538	82.7885	0.01769	41.3358	0.72471	-4.3161
1.97E+07	0.886499	-5.1844	0.74990	81.9078	0.02064	40.8239	0.64484	-4.2865
2.09E+07	0.893321	-5.4519	0.75055	81.6994	0.02184	40.7588	0.64001	-4.1749
3.09E+07	0.882245	-9.4792	0.75864	78.5515	0.03133	39.6213	0.62872	-4.4518
4.08E+07	0.794566	-14.058	0.77894	74.8303	0.04116	38.4796	0.62595	-5.4101
5.08E+07	0.808368	-15.156	0.77562	72.9086	0.05139	37.1143	0.62392	-6.4615
6.08E+07	0.778217	-17.871	0.78890	70.4619	0.06128	35.6020	0.62098	-7.6297
7.07E+07	0.762356	-20.385	0.79244	68.2558	0.07102	34.0935	0.61712	-8.8125
8.07E+07	0.728494	-23.219	0.73504	65.6099	0.08018	32.6745	0.61335	-9.9117
9.06E+07	0.703721	-26.369	0.74215	63.2074	0.08934	31.0434	0.61201	-11.293
1.09E+08	0.652596	-30.981	0.71722	59.2158	0.10492	28.4931	0.60218	-13.437
1.21E+08	0.650091	-32.487	0.71241	57.3856	0.11439	26.9777	0.59779	-14.723
1.30E+08	0.640495	-34.903	0.70960	55.8557	0.12275	25.6739	0.59396	-15.893
1.40E+08	0.635605	-37.384	0.70058	54.2899	0.13108	24.3462	0.59106	-17.032
1.50E+08	0.620072	-40.849	0.69715	52.5803	0.13916	22.9388	0.58622	-18.259
1.60E+08	0.641753	-41.499	0.69645	51.234	0.14736	21.5274	0.58175	-19.346
1.70E+08	0.631621	-44.451	0.69553	49.5893	0.15490	20.1560	0.57491	-20.571
1.80E+08	0.627020	-46.237	0.70098	47.9745	0.16249	18.7355	0.56769	-21.802
1.90E+08	0.616582	-48.279	0.70207	46.3876	0.16929	17.2796	0.55932	-23.090
2.00E+08	0.605802	-50.108	0.69457	44.6884	0.17568	15.8869	0.55198	-24.326
2.10E+08	0.599408	-52.070	0.68750	43.0633	0.18173	14.5259	0.54547	-25.508
2.20E+08	0.589052	-54.780	0.67268	41.2872	0.18759	13.2617	0.53992	-26.605
2.30E+08	0.586526	-56.768	0.66456	39.5673	0.19300	11.9831	0.53487	-27.569
2.40E+08	0.597129	-57.403	0.68821	38.0363	0.19764	10.5722	0.52805	-28.485
2.50E+08	0.579749	-61.132	0.66301	36.3394	0.20239	9.37015	0.52125	-29.407

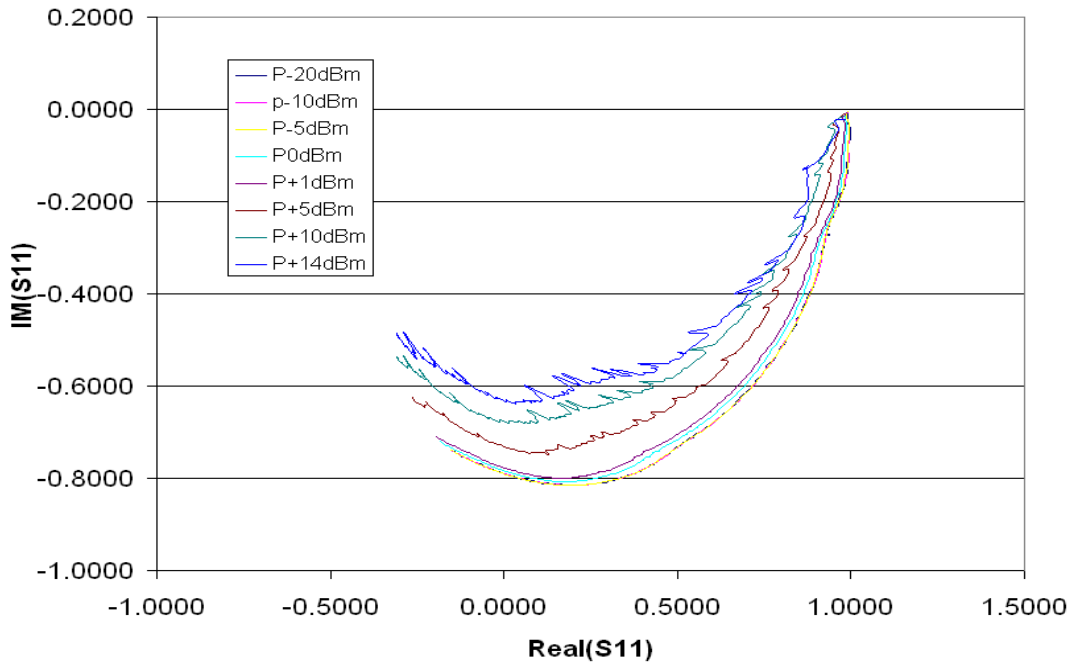


Figure 2-38: Measured large-signal S_{11} of the Vishay-Siliconix U310. Frequency swept from 1MHz to 250MHz [5].

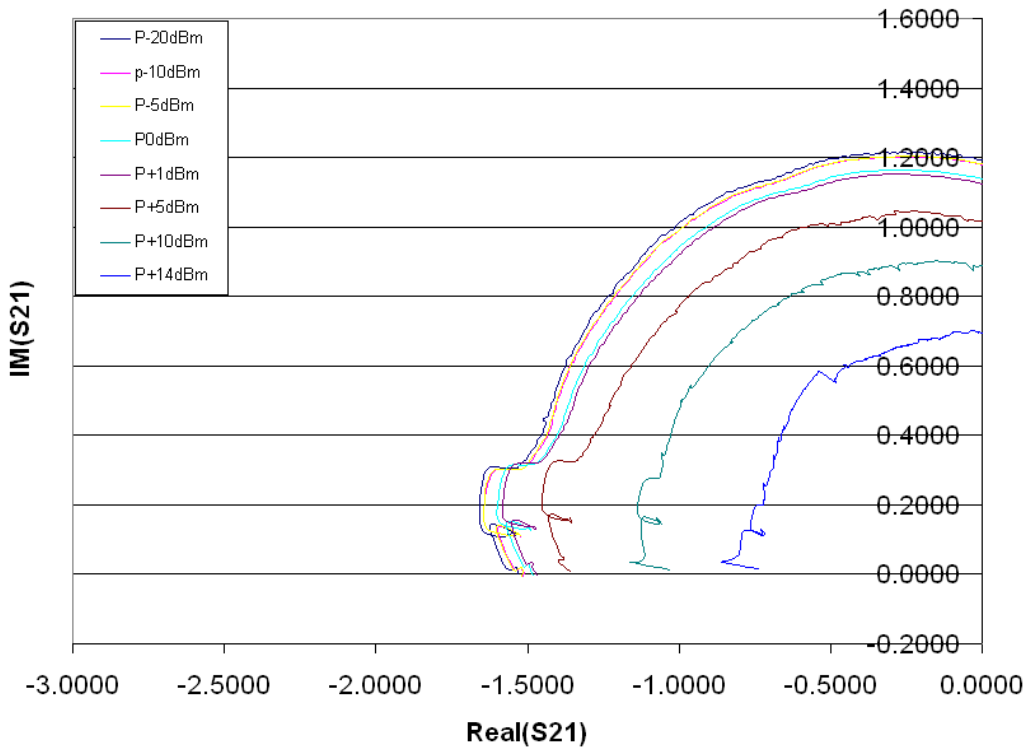


Figure 2-39: Measured large-signal S_{21} of the Vishay-Siliconix U310. Frequency swept from 1MHz to 250MHz [5].

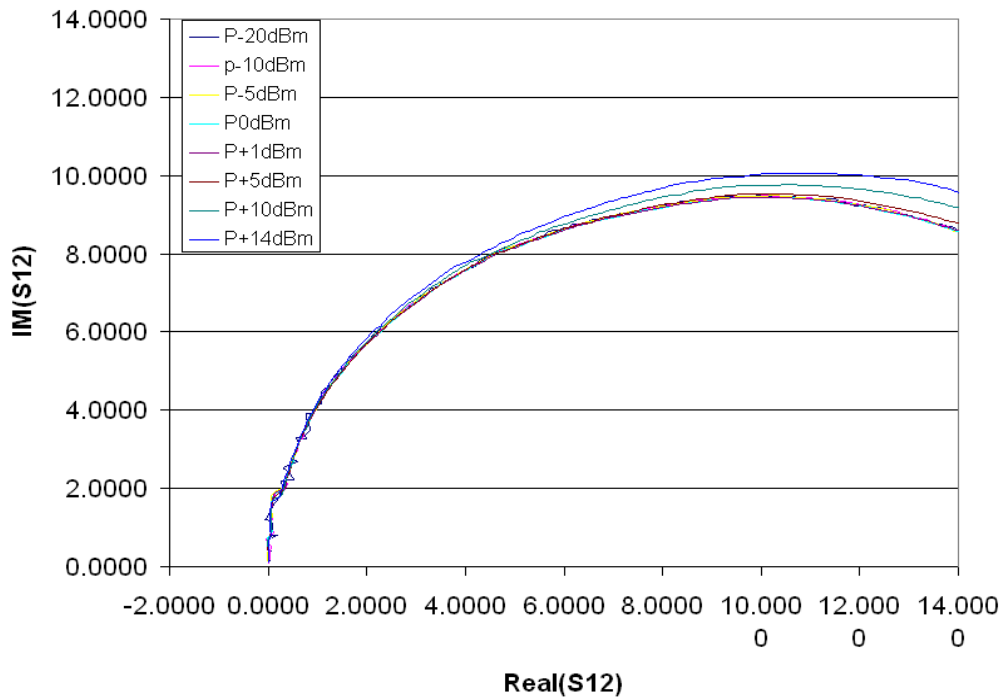


Figure 2-40: Measured large-signal S_{12} of the Vishay-Siliconix U310. Frequency swept from 1MHz to 250MHz [5].

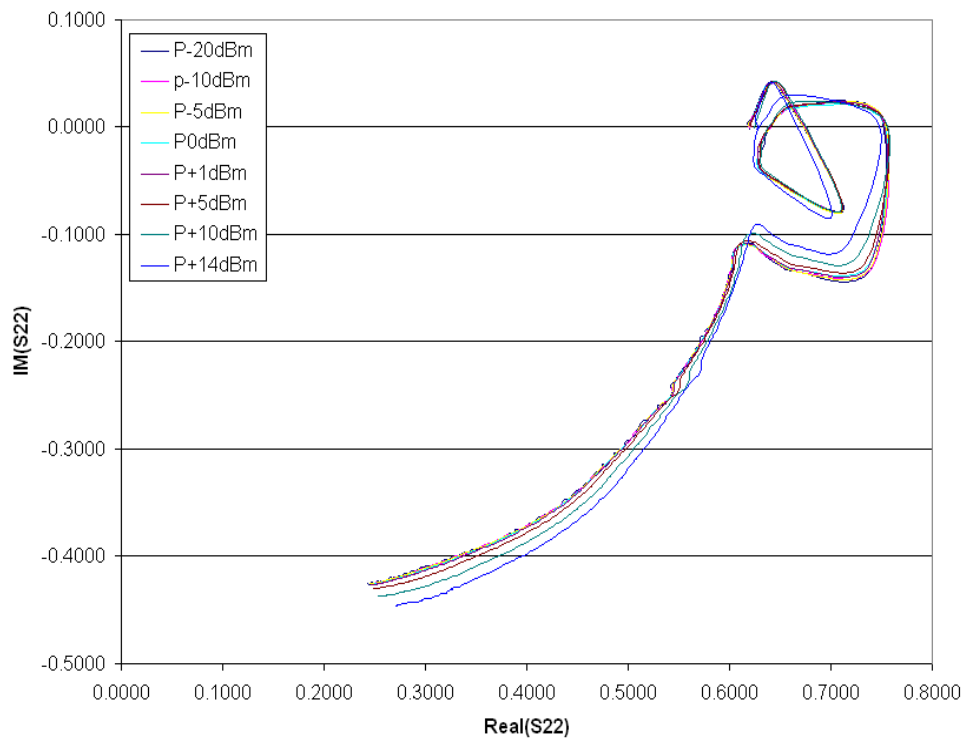


Figure 2-41: Measured large-signal S_{22} of the Vishay-Siliconix U310. Frequency swept from 1MHz to 250MHz [5].

2.6 Passive and Active Inductor Based Resonator Network

Extensive work is being done in the area of passive RF components such as inductor for applications as the frequency selective element in voltage-controlled oscillators. Inductors are essential elements for resonators, filtering and impedance matching purposes within a multitude of circuit solutions for RFICs/MMICs applications. Largely, inductor dictates their cost and performance. Passive integrated spiral inductors occupy large die area and increase costs. The magnetic coupling among inductors on a device initiates cross talk and deteriorates the overall circuit performance. It is also difficult to realize a broadband spiral inductor, especially with high inductance, because of stray capacitances. This motivates the need for alternative solutions such as the active inductor topology, which offers smaller die-area, high Q factor and easier floor planning.

The current trend moves towards multi-standard terminals and the application of active inductors paves the way for inductor-less reconfigurable radio-frequency circuit solutions. Voltage dependent variable capacitors (varactors) show high Q-factor but are limited in tuning range due to the influence of package parasitics, especially at higher operating frequencies. Tunable inductors offer the advantage of a wide tuning range in a small chip area and enable this technology as a cost-effective alternative for applications in filters, phase shifters, couplers, power dividers, and tunable oscillators.

2.6.1 Passive Inductor

Generally, passive inductors occupy large expensive die area. When fabricated on low-resistivity substrates, much of the electromagnetic energy leaks into the substrate resulting in low Q-factors. On the other hand, since the only noise generation mechanism is the loss due to the series resistance and leakage, passive inductors perform better than active inductors in terms of noise and linearity. Figure 2-42 shows a typical die photograph, inductance and quality factor of a 2.5 turn passive spiral inductor using a standard CMOS process [4]. Even though the maximum Q-factors are between 4 and 7 at 4-7 GHz, the Q-factor at 2GHz are as low as 3 because of the thin aluminum metallization and the conductive substrate. Figure 2-43 shows the schematic and layout of a 2GHz GaAs FET oscillator using passive spiral inductors [6, pp. 243]. Figures 2-44 and 2-45 show the load line and phase noise plots for the passive spiral inductor oscillator (shown in Figure 2-43). As shown in Figure 2-43, the two inductors (L_1 and L_2) in the circuit layout determine most of the surface die area, and are therefore not a cost-effective solution.

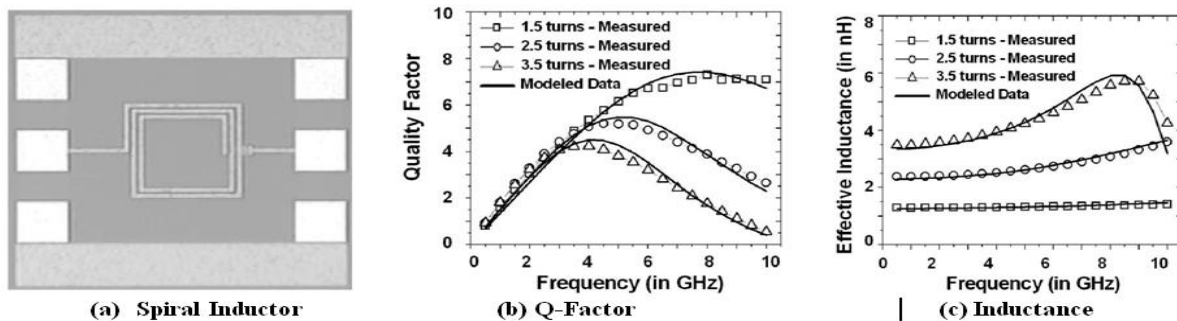


Figure 2-42: A typical 2.5 turn spiral inductor: (a) Die photograph, (b) Plot of Q-factor and (c) Plot of inductance value with frequency [8]

The idea is to explore the possibility to replace the large spiral inductor with an active device requiring only a fraction of its size. It is also necessary to find a solution that gives equal if not better noise and dynamic range at microwave frequencies, as compared with spiral inductor.

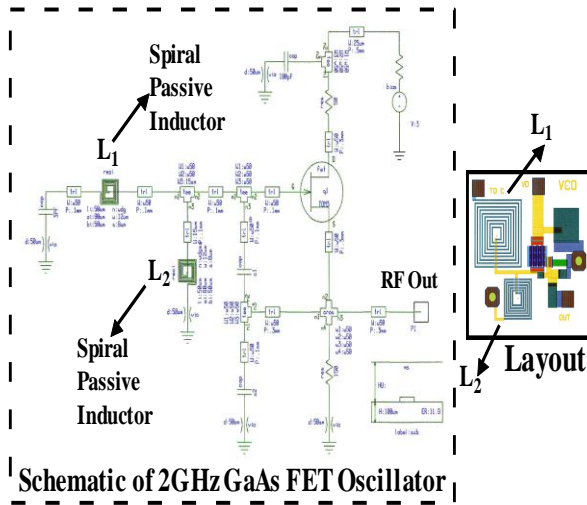


Figure 2-43: Schematic and layout of a 2 GHz GaAs FET Oscillator [5, 7]

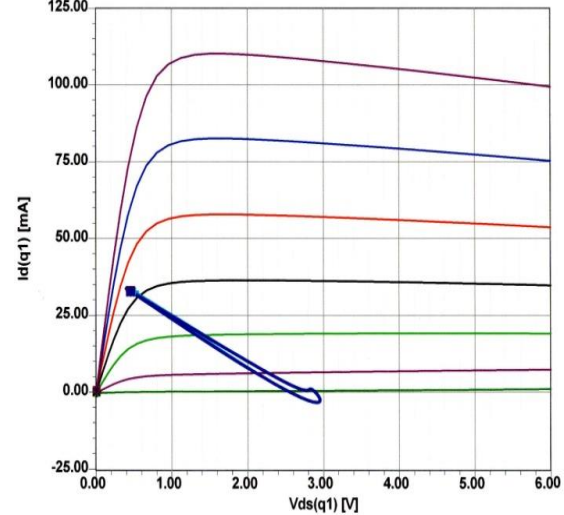
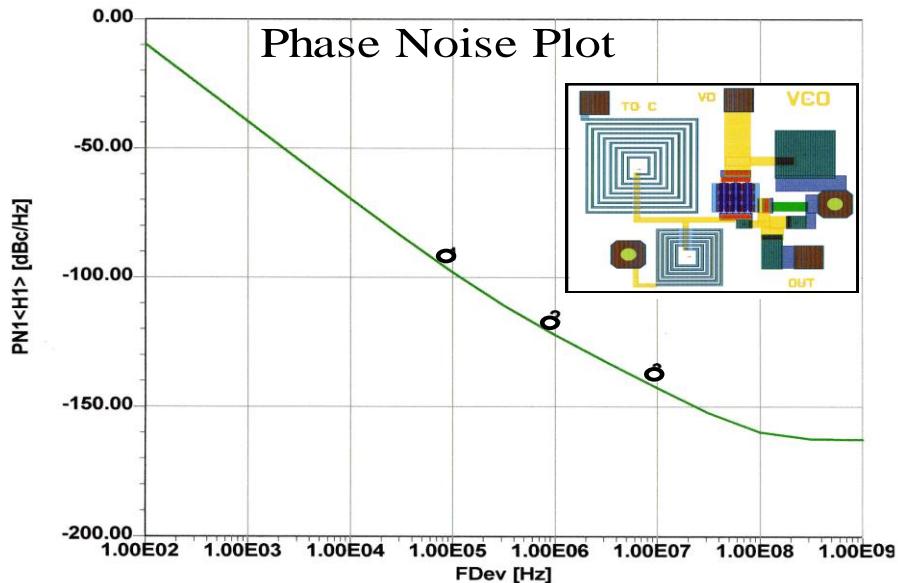


Figure 2-44: DC-IV and load line of the GaAs FET in the oscillator



The measured values are -100 dBc/Hz at 100 kHz and -120 dBc/Hz at 1 MHz offset within 2-3 dB deviation compared to simulation

Figure 2-45: CAD simulated phase noise plot of oscillator shown in Figure 2-42 [5, 7]

2.6.2 Active Inductor

Active inductors are implemented based on the well-known gyrator-C architecture consisting of two transistors in feedback generating inductive impedance [5, 8]. In general, the grounded active inductor topology is commonly used to implement high Q tunable active inductors (TAIs). To enhance the inductance and Q of this active inductor, the introduction of a tunable feedback resistance R_f is incorporated as shown in Figure 2-46 [8].

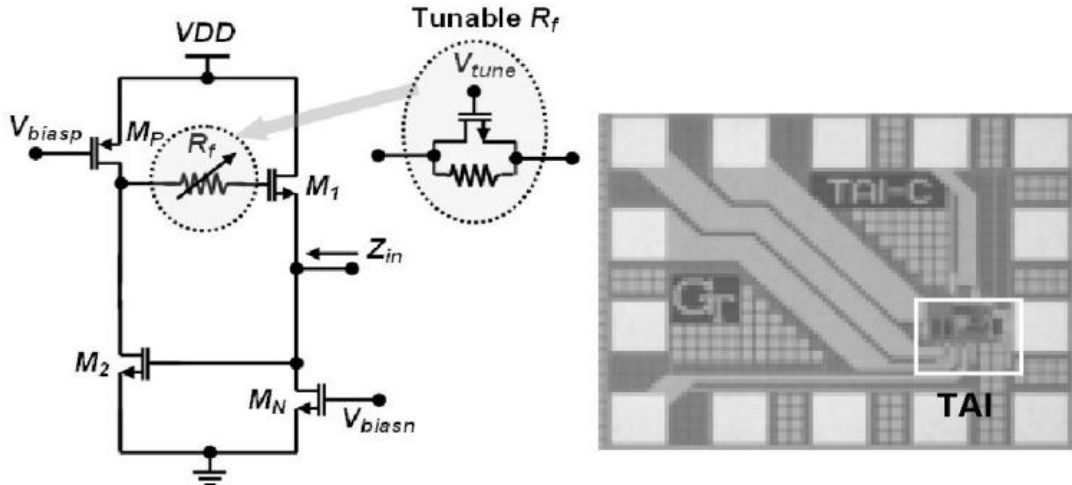


Figure 2-46: Active inductor circuit and its die photograph [8]

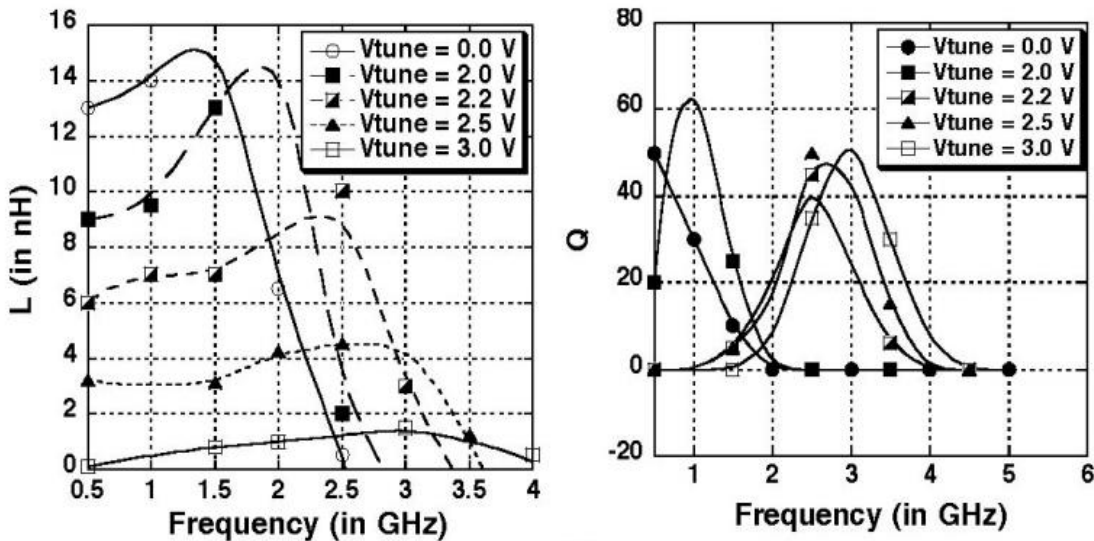


Figure 2-47: Plot of inductance and Q-factor [8]

The tunable feedback resistance increases the effective inductance, L_{eff} , and decreases the equivalent series resistance simultaneously, which enhances its quality factor [8]. The tunability has also been improved as all the three parameters namely L_{eff} , Q and the frequency, f_Q , associated with the maximum Q can be tuned independently.

Detailed analysis of the grounded TAI suggests a direct trade-off between the achievable range of tunable inductance, quality-factor and the output noise that calls for an optimization guideline. From the gyrator-C architecture and the noise analysis, the dependence of L_{eff} , Q, and the output noise on the design parameters is given as [8]

$$L_{eff} \propto \frac{R_f}{g_{m1}g_{m2}} \quad (2-60)$$

$$f_Q \propto \frac{1}{\sqrt{R_f}} \quad (2-61)$$

$$v_n \propto R_f \times g_{m1} \times g_{m2} \quad (2-62)$$

where g_{m1} and g_{m2} are the small-signal transconductance of the transistors M1 and M2 shown in Figure 2-47. Since g_{m1} and g_{m2} are related to each other from the expression for the effective inductance, the dependence on g_{m1} can be eliminated. To analyze the effects of the remaining two design variables on the performance, the simulated effective inductance and the, output noise voltage are plotted vs. the two variables for a fixed frequency of 2 GHz and a fixed $g_{m1} = 20\text{mS}$, as illustrated in Figure 2-48.

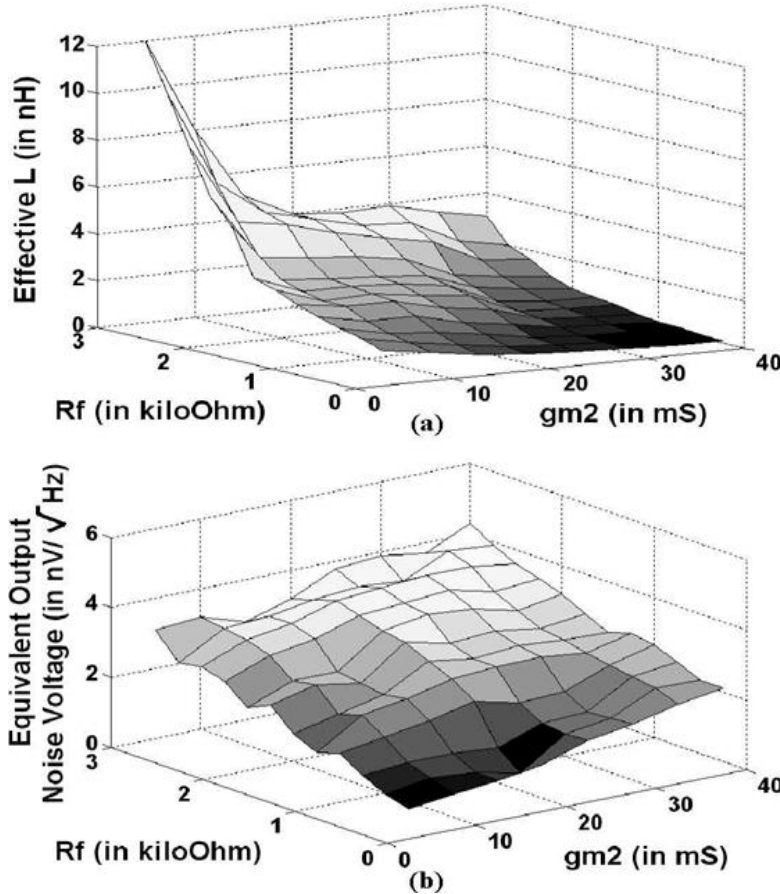


Figure 2-48: CAD simulated plot: (a) effective inductance (b) output noise voltage versus g_{m2} and fixed $g_{m1}=20\text{mS}$ [8]

It is observed that the effective inductance and the output noise voltage shown in Figure 2-48 follow similar trends as in Equation (2-60) and Equation (2-61). The degradation of noise with increasing feedback resistance is prominent from Figure 2-48(b). Higher feedback resistance also decreases the frequency of maximum Q, i.e., the frequency of operation. On the other hand, the range of tunable inductance increases with the range of the tunable feedback resistance. This leads to a direct trade-off between tunable inductance and the frequency of operation on one hand, and low-noise performance on the other. Thus, to achieve wide tunability and high frequency operation for a low output noise, the design parameters need to be optimized based on the 3D-plots of all the performance criteria under consideration.

The optimized active inductor has been fabricated using $0.18\mu\text{m}$ CMOS technology. The TAI achieved an inductance tuning range of $0.1\text{-}15\text{nH}$ with $Q > 50$ for frequencies between $0.5\text{-}4\text{GHz}$, as shown in Figure 2-46. The active inductor consumes around 7.2mW from a 1.8V supply and occupies a very small area of $100 \times 50 \mu\text{m}^2$.

Noise is a major drawback of active inductors. An approximate equivalent output noise voltage due to the thermal and flicker noise sources as shown in Figure 2-49 can be evaluated. It can be observed that the total noise increases with an increase in the feedback resistance and with decrease in the device size. However, both the resistance and the sizing of devices have a significant effect on the inductance and the frequency of operation that leads to the trade-off between the inductance and the operating frequency on one side and the output noise on the other.

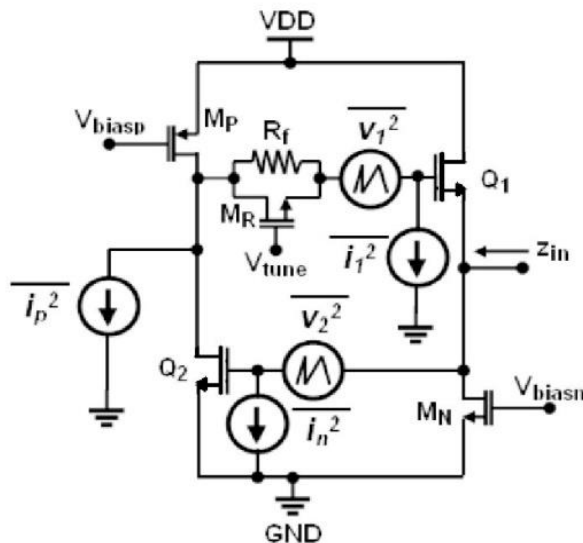


Figure 2-49: Active inductor circuit with its equivalent noise sources [8]

2.7 Selection Criteria and Performance Comparison

The performance comparison criterion (Q-factor, Die-Area, Power Consumption, Linearity, Noise, EMI and Floor Planning) establishes important design guidelines for selection of inductors per particular applications. Table 2-4 describes the comparative analysis of the passive and active inductor for RF and microwave applications. Thus, in spite of the drawbacks

such as noise and linearity, active inductors have a significant advantage over passive inductors in terms of die area, quality factor, and issues regarding EMI and floor planning. Additionally, the potential of extensive tunability of active inductors could be harnessed for multi-standard and wideband applications.

2.8 Tunable Active Inductor Oscillator

The conventional VCO circuit uses a negative-resistance generating network to compensate the loss associated with the passive resonators. For low cost MMIC solution active inductor [51]-[53] is incorporated to replace the negative resistance generating active circuit of the conventional VCO, thereby the active inductor solution features broadband tuning characteristics without tuning diodes.

Figure 2-50 shows the differential PMOS and NMOS cross-coupled VCO with a 400 MHz tuning range (around 3-3.4GHz) using a 1.5nH passive spiral inductor that occupies an area of $900\mu\text{m} \times 800\mu\text{m}$. The VCO core consumes 10mA current from a 2.7V supply and the measured phase noise is -104.3dBc/Hz at 1MHz offset frequency. For comparison, Figure 2-51 shows the single-ended 500MHz tunable inductor Colpitts oscillator with 80% tuning range implemented in $0.18\mu\text{m}$ Si CMOS technology. The output power varies from -29 to -20.8dBm with the power consumption of 13.8mW from a 1.8V supply and occupies an area of $300 \times 300\mu\text{m}^2$. The measured phase noise is typically -80dBc/Hz at 1MHz offset, which is inferior in comparison to commercially available passive inductor oscillator for similar power consumption.

Thus, in spite of the higher phase-noise, the active inductor VCO achieves a much higher tuning range, consumes considerably lower power and occupies $1/8^{\text{th}}$ of the die area. The phase-noise performance could be improved by the use of a differential active inductor in the resonator or a differential VCO topology using injection and mode locking techniques.

Table 2-4: Comparative analysis of the passive and active inductor for RF & MW applications

Performance parameter	Passive Inductor	Active Inductor
Q-factor	Low Q-factor (Q-factor can be relatively improved by incorporating shielding or differential inductors topology but at added cost and large die-area)	High Q-factor (Active inductor offers higher Q than the passive spiral inductor, including the Q and the frequency of maximum Q are independently tunable.)
Tunability	Fixed/Limited	Large tuning range
Die-Area	Large die-area	Small die-area
Power Consumption	Zero	Significant (Active inductor consumes power for generating inductance with negative loss resistance, resulting in high Q factor that offsets the power)

		consumption due to reduction in losses)
Linearity	Good Linearity	Poor Linearity (Active inductor circuit is driven under large-signal condition, causing a shift in operating point, distortion, and impedance fluctuations)
Noise	Superior Noise Performance	Poor Noise Performance (The operating frequency and inductance values of the active inductor depend on device size and feedback resistance R_f but at the cost of the noise and dynamic range, therefore, they trade each other)
EMI	Significant EMI problems (Electromagnetic fields associated with the large metallic structure of the spiral inductors causing EMI)	EMI insensitive
Floor-Planning	Poor (The large unused area in the neighborhood of the inductors due to large die-area makes difficult floor-planning)	Not required

2.9 RF MEMS Technology

Cost-effective, power-efficient and compact RF modules such as tunable VCOs, filters, and mixers are critical components in reconfigurable receiver architectures. RF MEMS are expected to address reconfigurable and concurrent solutions by exploiting RF MEMS technology.

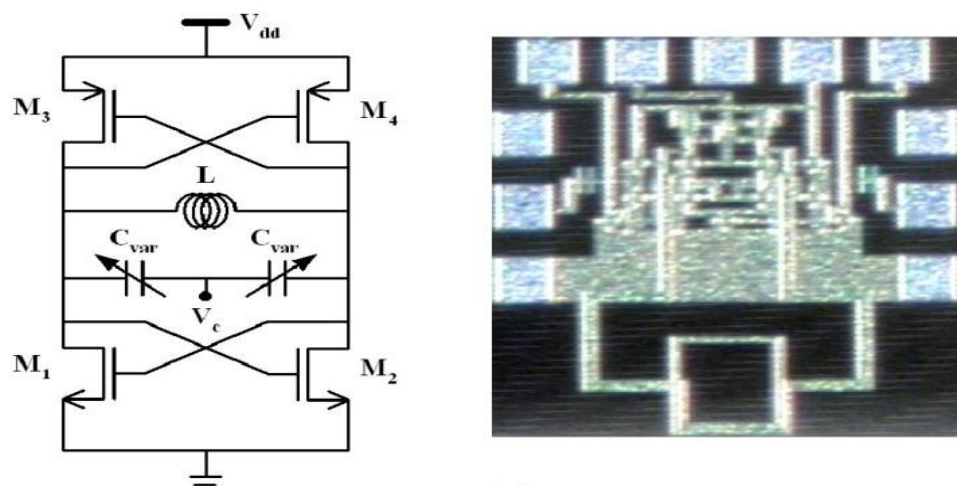


Figure 2-50: Schematic and die of differential spiral inductor VCO [8]

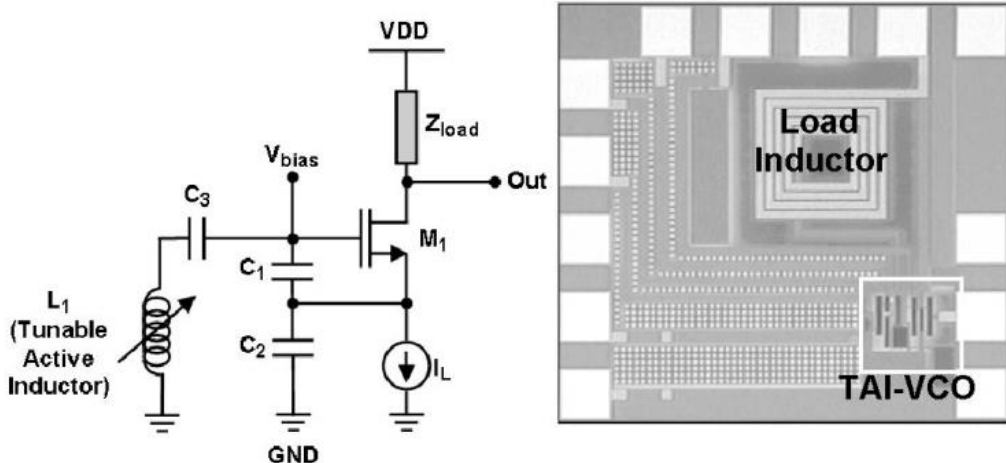


Figure 2-51: Schematic and die of the active inductor VCO [8]

2.9.1 RF MEMS Components

Figure 2-52 shows a typical RF MEMS enhanced dual-loop wideband receiver, which dynamically reconfigures the desired operating frequency from 100MHz to 10GHz [40]-[41]. As shown in Figure 2-52, an array of MEMS mixer-filters, down-convert the received signal from the GHz frequency band to a unique intermediate frequency (IF) in MHz range, set by the resonant conditions of the MEMS device.

Figure 2-53 shows a typical die photograph of an RF MEMS filter that comprises a 0.09mm² 6nH symmetrical spiral inductor surrounded by four 0.13mm² MEMS capacitors in Jazz Semiconductor's SiGe60 four-metal BiCMOS process. Figure 2-54 shows the plot of the measured insertion loss of the RF MEMS filter, which is typically 7dB for a reconfiguration of 490MHz between 1.87GHz (f_{low}) to 2.36GHz (f_{high}).

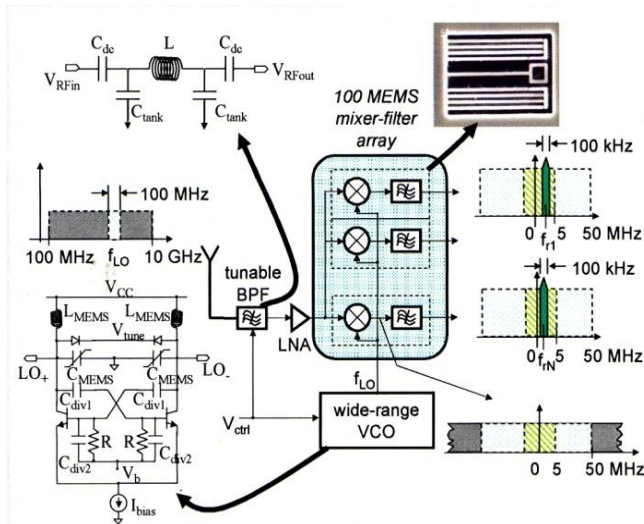


Figure 2-52: RF MEMS enhanced dual-loop wideband receiver [40]

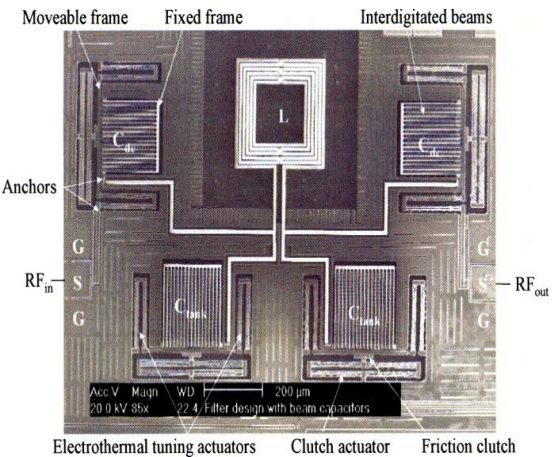


Figure 2-53: RF MEMS filter in the Jazz Semiconductor SiGe60 4-metal BiCMOS process (C_{dc} and C_{tank} switch from 550ff to 250ff and 800ff to 300ff, respectively [40])

Figure 2-55 shows a typical differential cross-coupled oscillator using SiGe BJTs to compensate the losses in a LC tank consisting of a 6.2nH symmetrical MEMS inductor and MEMS capacitors. The capacitors switch between 0.18pF and 1pF. Implementation is in the Jazz Semiconductor SiGe60 4-metal BiCMOS process with total die area 0.87 mm² [5, 42].

Figure 2-56 shows the measured phase noise plot, which is typically lower than -122dBc/Hz at 1MHz offset from the carrier frequency of 2.8GHz. The DC operating point is 2.5V with a core current 1.1mA. The resulting figure of merit is 187dB. Figure 2-57 shows a CAD simulated and measured plot of Q-factor of a RF MEMS mixer filter in the Jazz Semiconductor SiGe60 4-metal BiCMOS process.

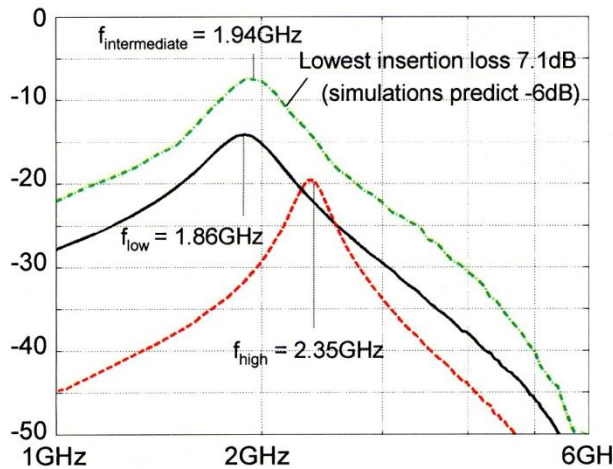


Figure 2-54: The Measured plot of insertion loss of RF MEMS filter [40]

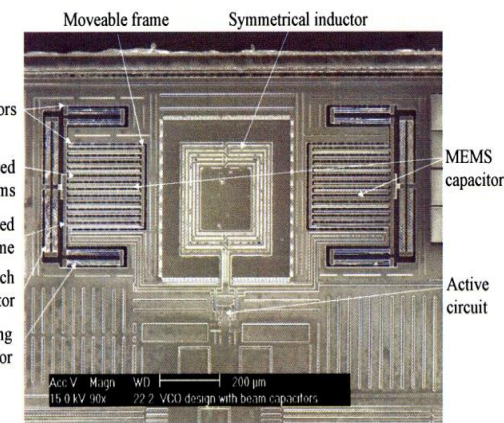


Figure 2-55: RF MEMS VCO in the Jazz Semiconductor SiGe60 4-metal BiCMOS process [40]

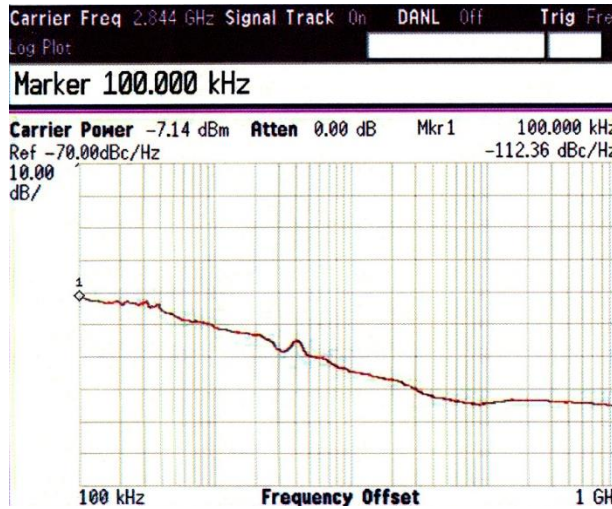


Figure 2-56: Measured phase noise of an RF MEMS VCO in the Jazz Semiconductor SiGe60 4-metal BiCMOS process [40]

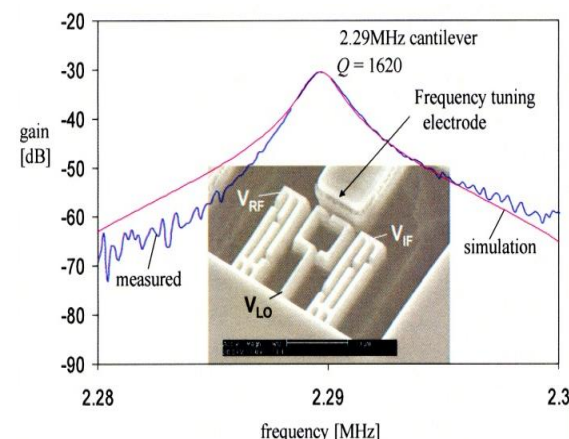


Figure 2-57: CAD simulated and measured Q of an RF MEMS mixer filter in the Jazz Semiconductor SiGe60 4-metal BiCMOS process [40]

2.9.2 Tunable Inductor Using RF MEMS Technology

Figure 2-58 shows the tunable inductor using RF MEMS technology in which tunability is achieved by incorporating thermal actuators that control the spacing between the main and secondary inductor. For planar inductors parasitic capacitance and low resistivity are the main sources of losses [42]. By lifting the inductor off the substrate the losses can be minimized for improved quality factor. Figure 2-58(b) shows two inductors (inner inductor and outer inductor) that are connected in parallel. The inner inductor is raised off the substrate due to residual stress between the metal and the poly silicon layer. The outer inductor is attached to a beam, which is connected to an array of thermal actuators. When the array is actuated, the beam buckle lifts up the outer inductor. The control of the angle separating the two inductors allows tuning the mutual component of the total inductance. The OFF and ON states of the actuator correspond respectively to the maximum and the minimum inductance value.

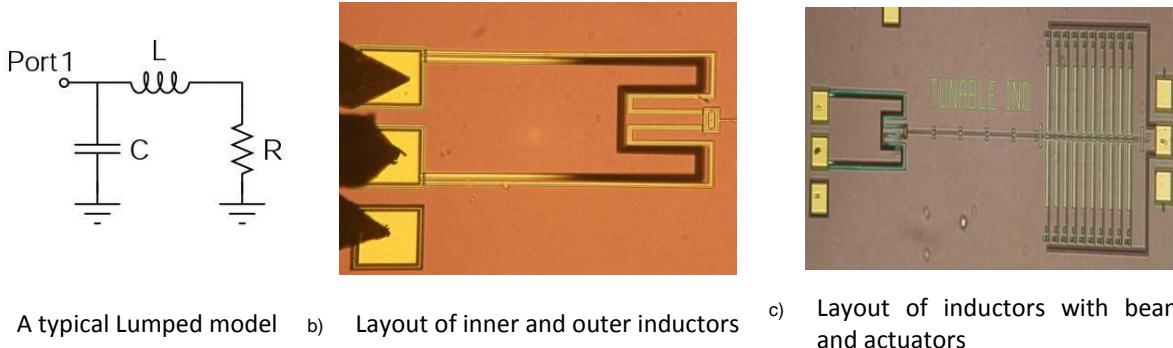


Figure 2-58: (a) Lumped equivalent model of the MEMS tunable inductor, (b) A photograph showing the two inductors with the beam and the actuator, and (c) A photograph showing the inner and the outer inductors [42].

The resulting typical values for the off state are $L_{off} = 1.185\text{nH}$, $R_{off} = 11.5\Omega$, $C_{off} = 0.238\text{pF}$ and for the ON state are $L_{on} = 1.045\text{nH}$, $R_{on} = 14.9\Omega$, $C_{on} = 0.224\text{pF}$. Notice that the resistance value is too high and the yield and realization is warranted. Low-cost packaging still remains a challenge.

The MEMS tunable inductor offers a cost-effective integrable solution for applications in tunable oscillators but at the cost of large series resistance and limited tuning range [5]. In addition to this, negative mutual inductance associated with the MEMS structure can further restrict the operating frequency and tuning range, therefore they are not suitable for high frequency, low phase-noise signal-source applications.

2.10 Active Capacitor

Figure 2-59 shows the active capacitance circuit using BJT in common-emitter configuration where the frequency response can be controlled by adjusting feedback element (R, L, and C) [46].

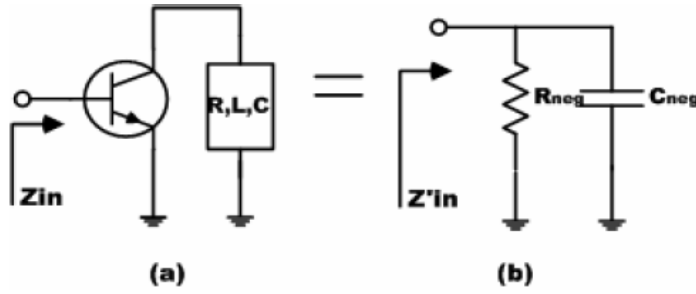


Figure 2-59: Block diagram of the proposed circuit (a) and its equivalent circuit (b) [48].

As shown in Figure 2-60, the input impedance of the circuit can be described by [48]

$$Z_{in} = r_{bb} + r_{be} \parallel Z_{in1} \quad (2.63)$$

Where,

$$Z_{in1} = \frac{Z_1(Z_2 + Z_3)}{Z_1 + Z_2 Z_d + g_m (Z_1 \times Z_3)}$$

$$Z_1 = \frac{1}{j\omega C_{be}}, Z_2 = \frac{1}{j\omega C_{bc}}, Z_3 = \frac{1}{(j\omega C_{ce}) + \frac{1}{Z_d} + \frac{1}{r_0}} \text{ and } Z_d = R_d + j \left(\omega L_d - \left(\frac{1}{\omega C_d} \right) \right) \quad (2.64)$$

Since r_{bb} , C_{ce} and r_0 do not dominate over the negative resistance and equivalent capacitance, the input admittance can be approximated as

$$Y_{in} = \frac{1}{Z_{in}} = \frac{1}{Z_{in1}} = \frac{1}{R_{neg}} + j\omega C_{neg} \quad (2.65)$$

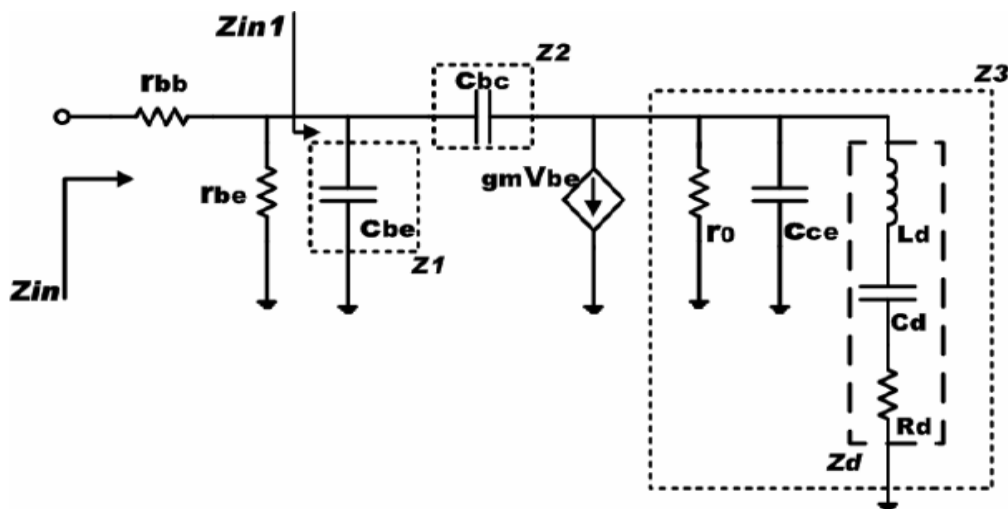


Figure 2-60: For high frequency, small signal equivalent circuit [48]

From Equation (2.65), the equivalent value of the negative resistance and capacitance given by [48]

$$\frac{1}{R_{neg}} = Re[Y_{in}] = g_m + \frac{1}{r_{be}} + \frac{C_d(-(C_{bc}+C_d)g_m+C_{bc}C_d(g_mL_d+C_{bc}R_d)\omega^2)}{k} \quad (2.66)$$

$$C_{neg} = Im[Y_{in}] = \omega \left[C_{bc} + \frac{C_{bc}C_d(C_{bc}+C_d)}{k} + \frac{C_{bc}C_d(C_dg_mR_d-C_{bc}C_dL_d\omega^2)}{k} \right] \quad (2.67)$$

Where,

$$k = (C_{bc} + C_d)^2 + C_{bc}C_d(-2(C_{bc} + C_d)L_d + C_{bc}C_dR_d^2)\omega^2 + C_{bc}^2C_d^2L_d^2\omega^4 \quad (2.68)$$

From Equation (2.66), the frequency range in which the circuit exhibits the negative loss resistance evaluated as [48]

$$f_{low}^{high} = \frac{1}{2\pi} \left(\frac{2C_{bc}L_d + 2C_dL_d - C_{bc}C_dR_d^2}{2C_{bc}C_dL_d^2} \pm \frac{R_d\sqrt{C_{bc}C_d}\sqrt{C_{bc}C_dR_d^2 - 4(C_{bc} + C_d)L_d}}{2C_{bc}C_dL_d^2} \right)^{1/2} \quad (2.69)$$

The frequency, which shows the maximum and minimum negative resistance, given by [5]

$$f_{min}^{max} = \frac{1}{2\pi} \left(\frac{g_m}{g_mL_d + C_{bc}R_d} \left(\frac{1}{C_{bc}} + \frac{1}{C_d} \right) \pm \frac{\sqrt{R_d^2(C_{bc}^2 + C_d^2)[C_{bc}^2 + C_dg_m^2L_d + C_{bc}(C_d + C_dg_mR_d)]}}{C_{bc}C_dL_d(g_mL_d + C_{bc}R_d)} \right)^{1/2} \quad (2.70)$$

The dynamics of the negative resistance network can be stabilized by properly optimizing the behavior estimated by Equation (2.66) – Equation (2.70).

Figure 2-61 shows the comparative plots of CAD simulated and measured impedance data of an active capacitance network for the given feedback parameters: L=23nH, C=10pF and R=46 Ω [4, 46].

As shown in Figure 2-61, the measured active capacitance circuit behaves as a parallel network, consisting of frequency dependent equivalent capacitance and negative resistance, thereby, typically suitable for narrow band applications.

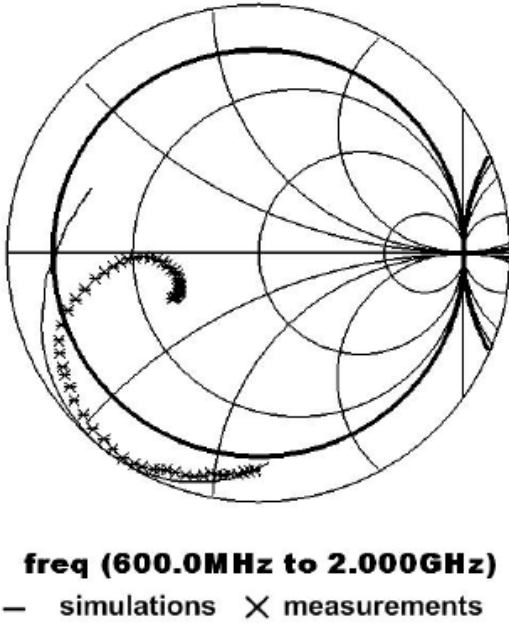


Figure 2-61: Simulated and measured input impedance of an active capacitance circuit using BJT [48].

2.10.1 Diplexer using Active Capacitor Circuit

Figure 2-62 shows the typical example of active duplexer using the active capacitance network of Figure 2-61 (implemented by Infineon SiGe HBTs, BFP 620F).

As illustrated in Figure 2-62, an active duplexer consists of two active BPFs at the cellular Rx/Tx bands. The active duplexer is designed at the Rx band (824~849 MHz) and the Tx band (869~894 MHz), and fabricated using lumped components with the design parameters given in Table 2-5 [48]. Figure 2-63 shows the typical layout of the active duplexer circuit. The DC bias condition is 1V at 5mA.

Figure 2-64 shows the CAD simulated results for the Rx and Tx active BPFs. The duplexer insertion loss is typically less than 1dB and a return loss of 13dB [48].

Table 2-5 Design Parameters [48]

Active duplexer circuit	Feedback element	Matching network
Rx BPF	$R_d' = 5\Omega$ $L_d' = 15nH$ $C_d' = 6pF$	$C \parallel L = 2.4pF \parallel 13nH$ (optimized)
Tx BPF	$R_d = 5\Omega$ $L_d = 13.5nH$ $C_d = 6pF$	$C \parallel L = 3pF \parallel 13nH$ (optimized)

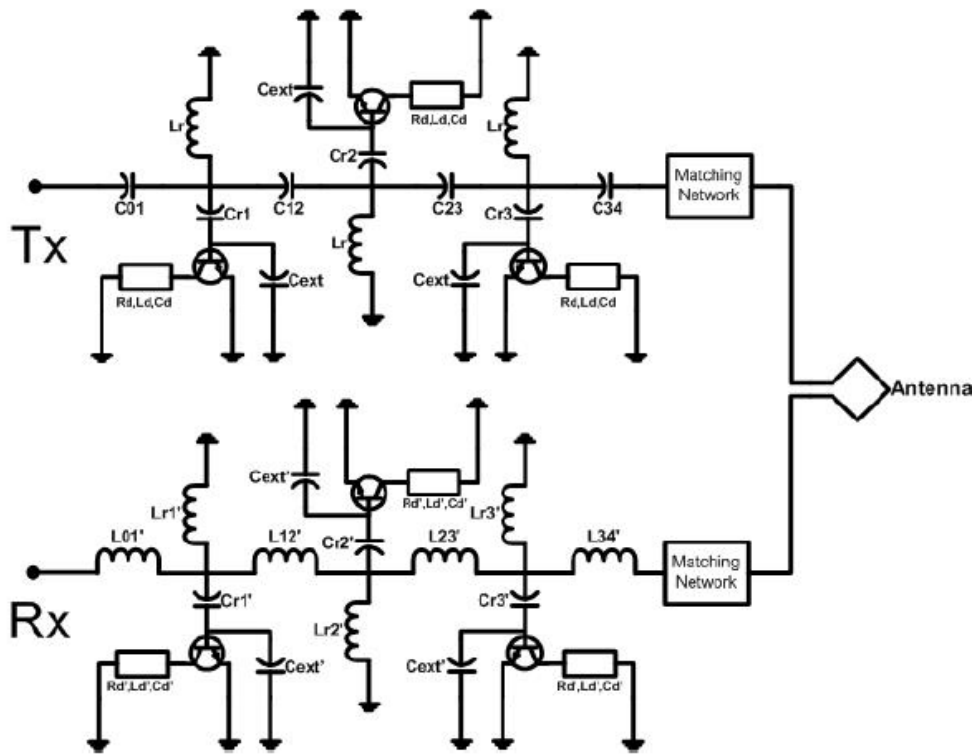


Figure 2-62: Schematic diagram of an active duplexer [48].

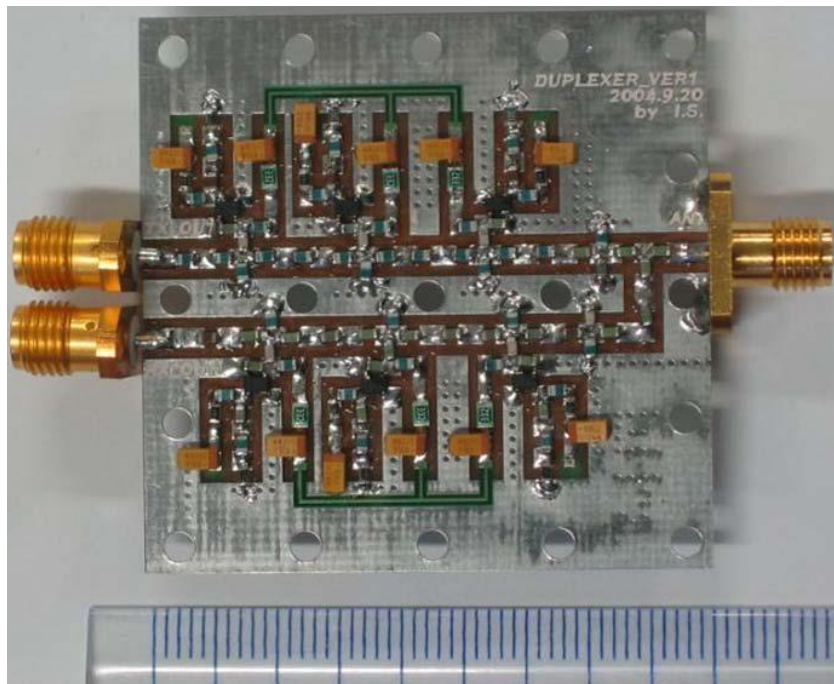
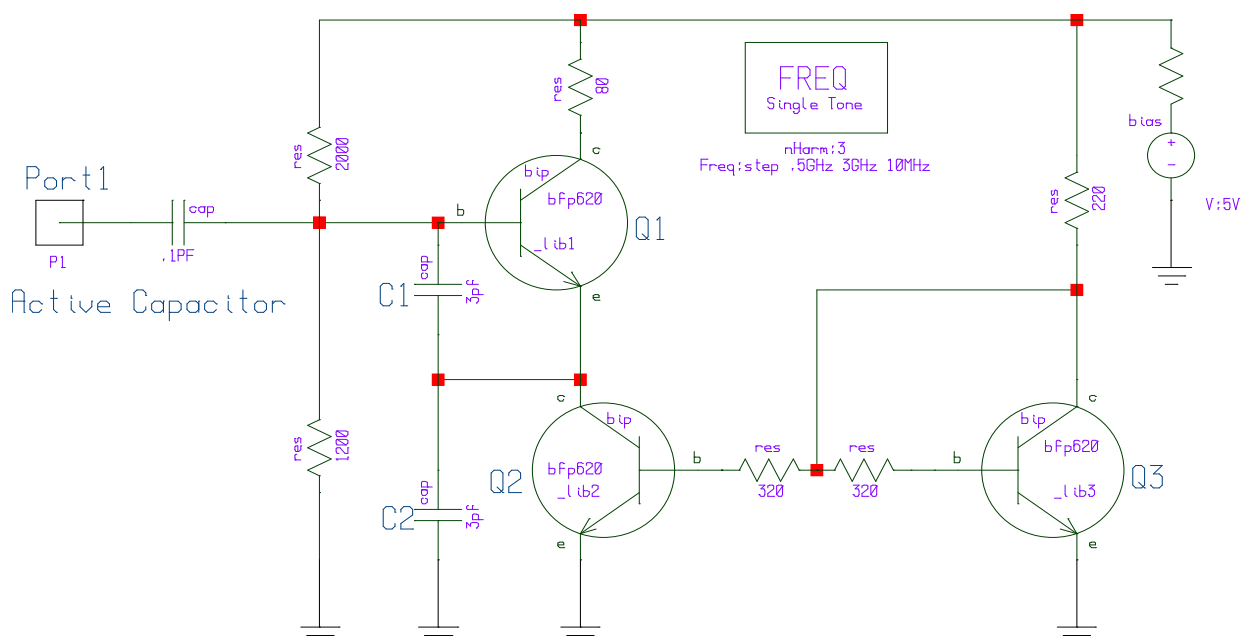
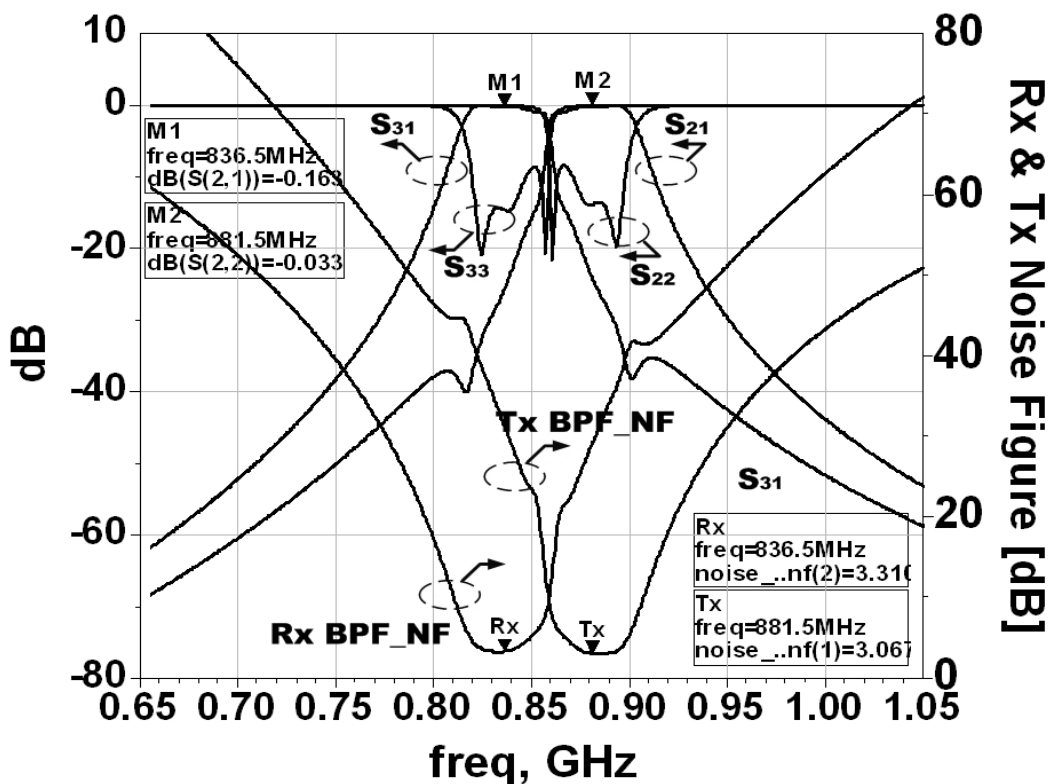


Figure 2-63: Photograph of the fabricated active duplexer [48].



2.10.2 Oscillator using Active Capacitor Circuit

Figure 2-65 shows the typical Clapp-Gouriet oscillator using the active capacitance in a high-performance oscillator circuit [5].

Transistors Q1 exhibits a negative resistance at its base terminal for a given frequency range and Q2 acts as a current source. The negative impedance at the input terminal is generated by capacitive feedback. The circuit can be loaded for stable RF output at the collector terminal of Q1 (Figure 2-67). From Figure 2-65, the input impedance is given by

$$Z_{in} \approx -\frac{g_m}{\omega^2 C_1 C_2} + \frac{1}{j\omega \left(\frac{C_1 C_2}{C_1 + C_2} \right)} \quad (2.71)$$

Figures 2-66 and 2-67 show simulated plots of the negative loss resistance and capacitive impedance at Port 1 for a given operating frequency of 500 MHz to 3GHz. Care must be taken while optimizing the feedback capacitor C1. The base to emitter capacitance of transistor Q1 may dominate C1 and must be taken into account.

Figure 2-68 shows a 2000 MHz oscillator schematic using the active capacitance network of Figure 2-65 for the validation of the active capacitance in a high performance oscillator.

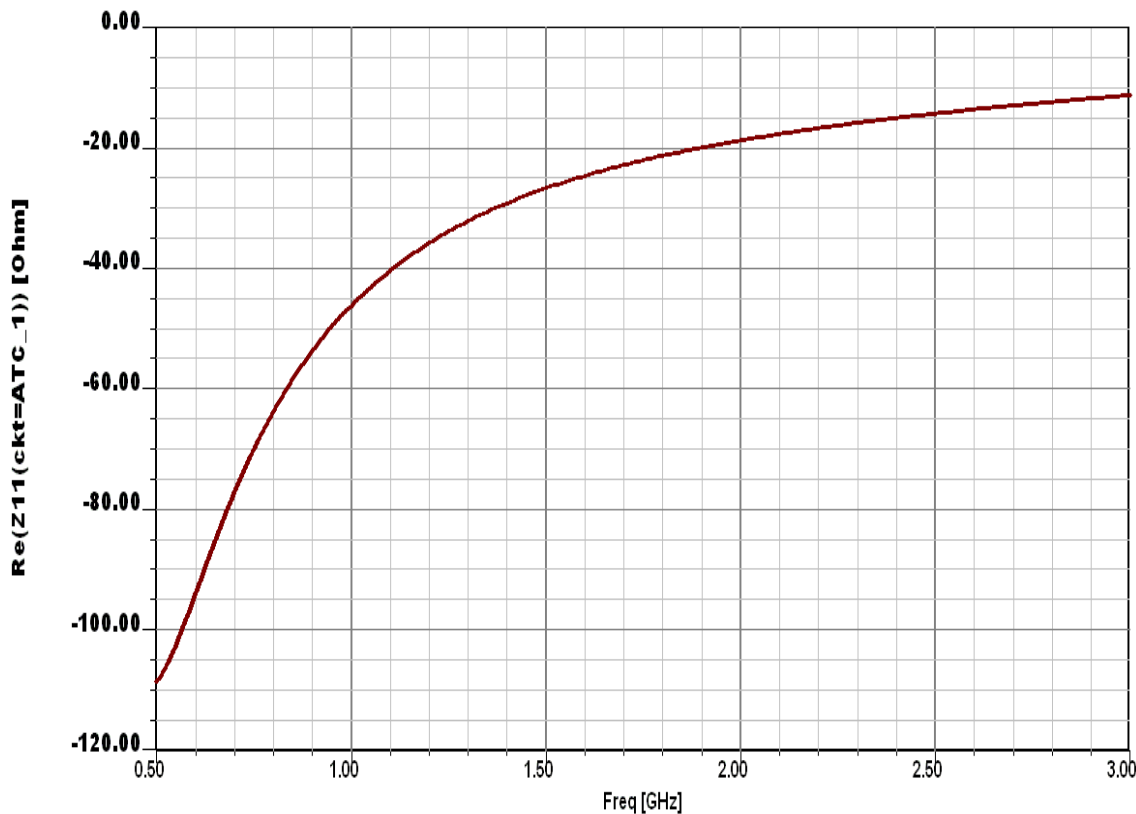


Figure 2-66: Simulated plot of $\text{Re}[Z_{11}]$, shows the negative input resistance at Port 1

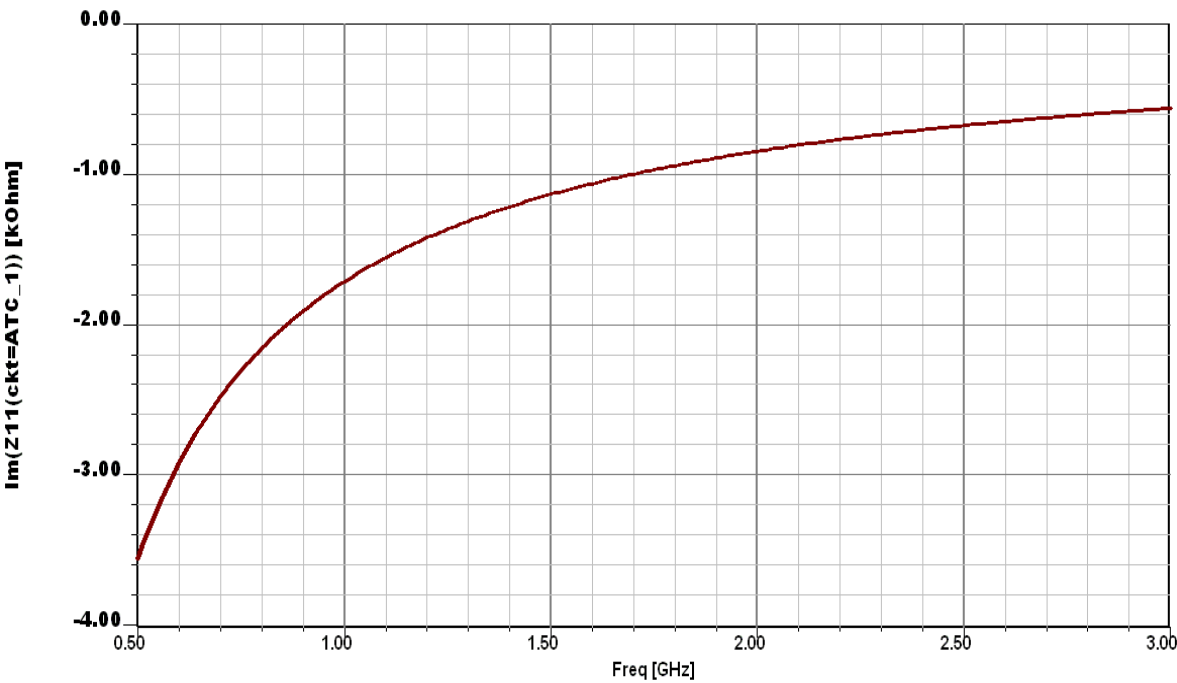


Figure 2-67: Simulated plot of $\text{Im}[Z_{11}]$, shows the capacitive characteristics at Port 1

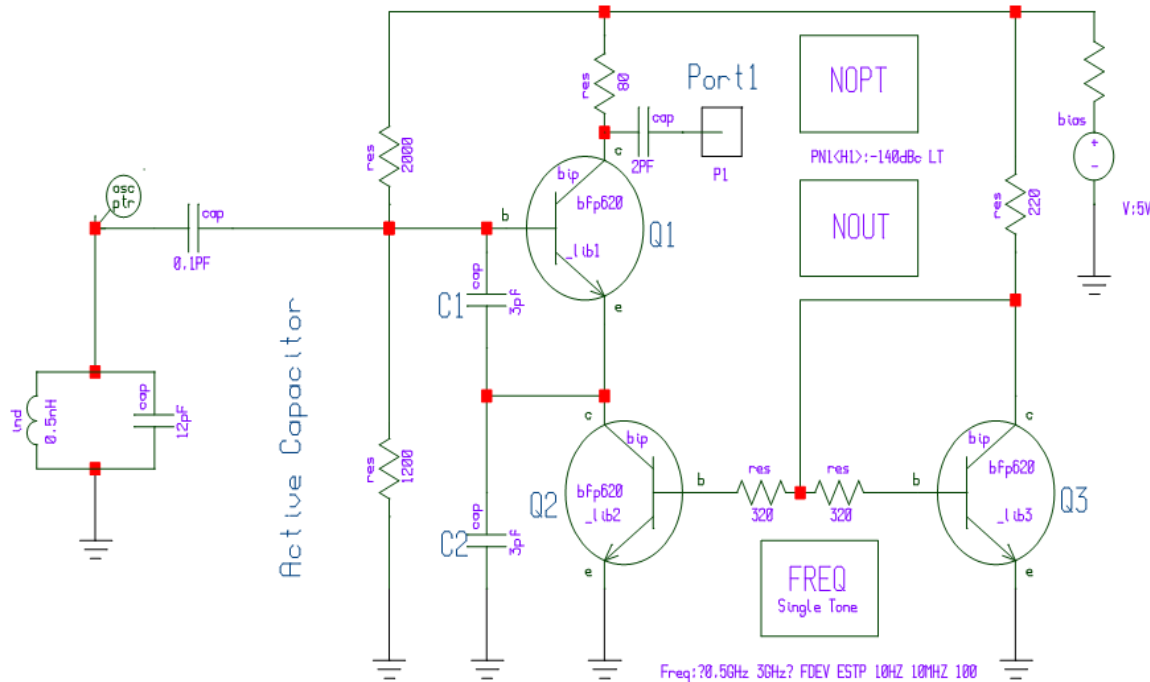


Figure 2-68: 2000 MHz oscillator schematic using an active capacitance network

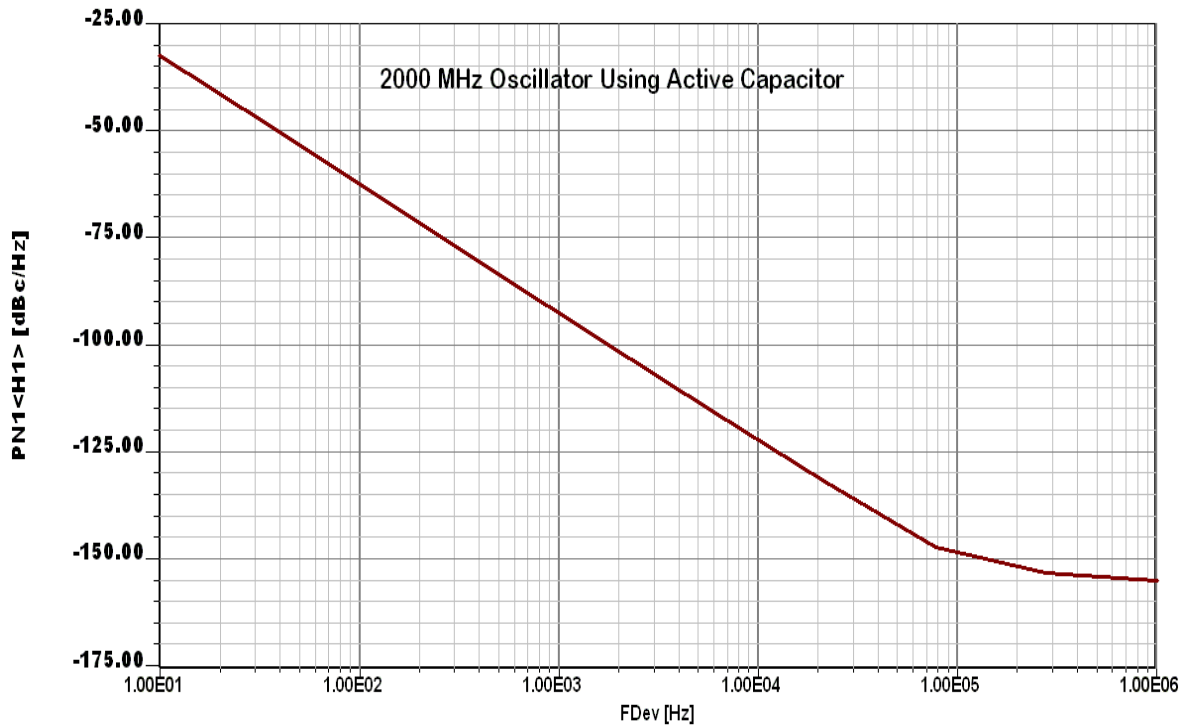


Figure 2-69: The CAD simulated phase noise performance of the 2000 MHz oscillator (Figure 2-67)

As shown in Figure 2-69, the CAD simulated phase noise performance @ 10 kHz offset is better than -122dBc/Hz, indicating a cost-effective and promising topology for application in modern wireless communication systems.

Although, the oscillator circuit shown in Figure 2-67 is a cost-effective alternative of SAW and ceramic resonator frequency references, the lack of tunability is restrictive. Frequency lock to a reference using PLL is still needed to counteract the effect of frequency drift caused by component tolerances, extreme operating temperature, package parasitics, and aging.

2.10.3 Tunable Oscillator using Active Capacitor Circuit

Figure 2-70 shows the typical tunable active capacitance network using a varactor diode for the realization of tunable oscillator circuits [46, 48].

Figure 2-71 shows a broadband oscillator circuit using an active tunable capacitor network. The main drawback of this topology is the limited tuning and stability over the desired operating frequency and temperature, which stems from the active capacitor that comprises the resonator network.

To overcome the limited tunability characteristics, the concept of the tunable active inductor oscillator has been reported throughout the short history of electronics [5].

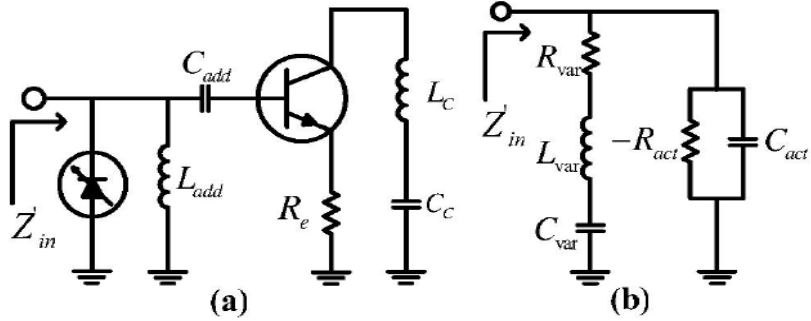


Figure 2-70: (a) A tunable capacitance circuit using a varactor and (b) its equivalent circuit [46]

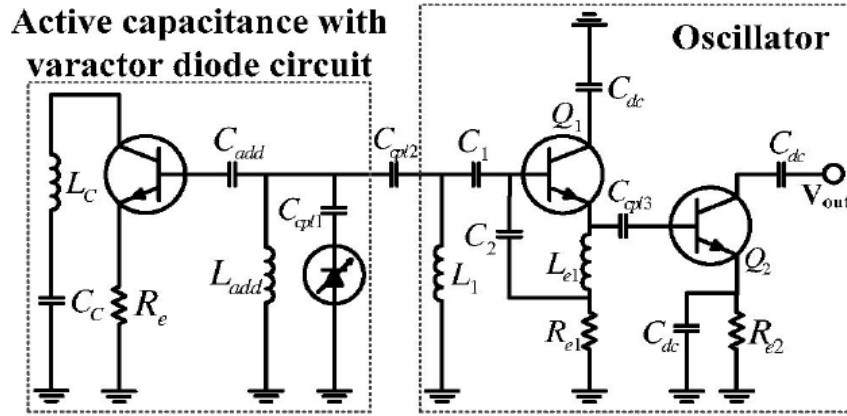


Figure 2-71: A narrow band oscillator with an active capacitance circuit and varactor diode circuit (excluding the bias circuit) [46].

2.11 Conclusion

In this chapter, brief oscillator theory is discussed, including the selection of resonator networks, and performance matrices (frequency range and tuning characteristics, tuning linearity, tuning sensitivity, tuning speed, post-tuning drift, phase noise, output power, harmonic suppression, spurious response, pushing and pulling). The selection criteria and performance comparison of new technology using active inductor, active capacitor and MEMS based resonator is being discussed for giving brief insights about the emerging Silicon-based MMIC technology and application in oscillators. The challenging task is to develop correct lumped and distributed model for passive and active device including the study of package parasitics and electromagnetic coupling for RF & microwave system applications [70]-[75].

2.12 References:

- [1] Byeong-Ha Park, "A Low-Voltage, Low Power, CMOS 900 MHz Frequency Synthesizer," Ph.D. Dissertation, Georgia Institute of Technology, December 1997
- [2] U. L. Rohde, D. P. Newkirk, "RF/Microwave Circuit Design for Wireless Applications", John Wiley & Sons, pp. 205, ISBN 0-471-29818-2, 2000.

- [3] U. L. Rohde, "A New and Efficient Method of Designing Low Noise Oscillators," Dr.-Ing. Dissertation, Technical University of Berlin, Faculty IV, EEC (Electrical Engineering and Computer Sciences), 12 February 2004.
- [4] A. K. Poddar, "A Novel Approach for Designing Integrated Ultra Low Noise Microwave Wideband Voltage Controlled Oscillator", Dr.-Ing. Dissertation, Technical University of Berlin, Faculty IV, EEC (Electrical Engineering and Computer Sciences), 14 December, 2004
- [5] U. L. Rohde, "A Novel Approach for Generating Active Inductors for Microwave Oscillators," Dr.-Ing. Habil, Dissertation, Technical University of Berlin, 2011.
- [6] G.R. Basawapatna, R. B. Stancliff, "A Unified Approach to the Design of Wide- Band Microwave Solid-State Oscillators," IEEE Trans. MTT, Vol. 27, pp. 379-385, May 1979.
- [7] U. L. Rohde, A. K. Poddar, and G. Boeck, *Modern Microwave Oscillators for Wireless Applications: Theory and Optimization*, John Wiley & Sons Inc., ISBN 0-471-72341-8, 2005.
- [8] R. Mukhopadhyay, S. W. Yoon, Y. Park, C.-H. Lee, S. Nuttinck, and J. Laskar, "Investigation of Inductors for Digital Si-CMOS Technologies", pp. 3750-3753, ISCAS 2006.
- [9] S-Li Eun, C. Sik Cho, J. W. Lee and J Kim, " A low power VCO using inductor for low phase noise and wide tuning range", Proceeding of the 39th European Microwave Conference, pp. 1255-1258, Rome, Italy, 2009.
- [10] S. Mons, M.A. Perez, R. Quere, J. Obregon, "A Unified Approach for the Linear and Nonlinear Stability Analysis of Microwave Circuits Using Commercially Available Tools," IEEE MTT-S Symp. Digest, Vol .3, pp. 993-996, 1999.
- [11] Alper Demir, Amit Mehota, and Jaijeet Roychowdhury, "Phase Noise in Oscillators: A Unifying Theory and Numerical Methods for Characterization," IEEE Transactions on Circuits and Systems, Vol. 47, pp.655-674, May 2000.
- [12] A. Grebennikov, "Microwave Transistor Oscillators: An Analytic Approach to Simplify Computer-Aided Design," Microwave Journal, pp 292-299, May 1999.
- [13] U. L. Rohde and A. K. Poddar, "Miniaturized VCOs Arm Configurable Synthesizers", IEEE IMS 2009, pp. 1281-1284, June 7-12, 2009,
- [14] U. L. Rohde and A. K. Poddar, "Hybrid Coupled Planar Resonators Arm Miniaturized Synthesizers", 2009 European Frequency & Time Forum & IEEE Int'l Frequency Control Symposium (EFTF-IFCS 2009), Besançon, France, pp. 949-955, April 20-24 2009.
- [15] U. L. Rohde and A. K. Poddar, "Mode-Coupled VCO Replaces Expensive DRO (Dielectric Resonator Oscillator) 2008 IEEE Int'l FCS, pp. 296-304, 18-21, Hawaii, USA, May 2008.
- [16] U. L. Rohde and A. K. Poddar, "Mode-Coupled Stubs-Tuned Planar Resonator Offers Promising And Integrable Alternatives Of DRO(Dielectric Resonator Oscillator)", IEEE Sarnoff Symposium, pp. 1-7, Princeton, NJ, USA, April 28-30, 2008.
- [17] U. L. Rohde and A. K. Poddar, "STPCR Offers Integrable Alternatives of DRO", Microwave Symposium Digest, 2008 IEEE MTT-S, pp. 233-236, Atlanta, USA, June 15-20, 2008.
- [18] U. L. Rohde and A. K. Poddar, "Injection-Tuned Coupled Oscillators" IEEE Radio Wireless Symposium 2008, pp. 367-370, 22-24, Orlando, FL, USA, January 2008.
- [19] U. L. Rohde and A. K. Poddar, "Reconfigurable Concurrent Oscillator (RCO)" IEEE Radio Wireless Symposium 2008, pp. 371-374, 22-24 Orlando, FL, USA, January 2008.
- [20] A. P. S Khanna, " Review of Dielectric Resonator Oscillator Topology", IEEE, Int, Frequency Control Symposium, pp. 478-486, 1987.

- [21] J-Francois Gravel and J. S. Wight, "On the Conception and Analysis of a 12-GHz Push-Push Phase Locked DRO" IEEE Trans. on MTT, Vol. 54, No. 1, pp. 153-159, Jan. 2006.
- [22] U. L. Rohde and A. K. Poddar, "Noise Minimization Techniques for RF & MW Signal Sources (Oscillators/VCOs)", Microwave J., page 136, Sept. 2007.
- [23] J Choi and A. Mortazawi, " A New X-Band Low Phase-Noise Multiple-Device Oscillator Based on the Extended-Resonance Technique", IEEE Trans. on MTTT, Vol. 55, No. 8, pp. 1642-1648, Aug. 2007.
- [24] C. Florian, P. Andrew, G. Vannini, and F. Filicori, " Design of Low Phase Noise Dielectric Resonator Oscillators with GaInP HBT devices exploiting a Non-Linear Noise Model", 2007 IEEE MTT-S In. Microwave Symposium Dige., pp. 1525-1528, June 2007.
- [25] K. Hosoya, S. Tanaka, Y. Amamiya, T. Niwa, and H. Shimawaki, and K. Honjo, " A low phase-noise 38-GHz HBT MMIC oscillator utilizing a $(\lambda/4 \pm \delta)$ open stubs resonator," APMC, pp. 64-67, Singapore, 1999.
- [26] J. Choi, M-Hung Chen, and A. Mortazawi, " An X-band Low Phase Noise Oscillator Employing a Four-Pole Elliptic-Response Microstrip Bandpass Filter" IEEE-MTT-S, Digest, pp. 1529-1532, 2007.
- [27] A. P. S. (Paul) Khanna, "Microwave Oscillators: The State of The Thechnology", Microwave Journal, pp. 22-42, April 2006.
- [28] J. Everard and K. Theodoropoulos, " Ultra-Low Phase Noise Ceramic Based Dielectric Resonator Oscillators," IEEE International FCS, pp. 869-874, Florida, USA, June 4-7 2006.
- [29] V. Walkar and I. C. Hunter, Design of triple mode TE₀₁ resonator transmission filters, IEEE MWC Lett., vol. 12, pp. 215-217, June 2002.
- [30] U. L. Rohde, A. K. Poddar, and R. Rebel," Integrated Low Noise Microwave Wideband Push-Push VCO", US Patent No. 7,088189, August 8, 2006
- [31] U. L. Rohde and A. K. Poddar, "Low Cost Signal Source for Multi-Band Multi-Mode Wireless Systems", 6th international conference on antenna theory and techniques, pp. 167-169, Sept 2007.
- [32] J S. Kim, W. Wu, J. Lin, A. Verma, S. Jang, F. Ren, S. Pearton, and J. Gillespie, " A High-Efficiency GaN/AlGaN HEMT Oscillator Operating at L-Bnad" Proc. of APMC 2006, pp.631-634, Yokohama, Japan, Dec. 12-15, 2006.
- [33] S. Romisch and R. Lutwak, " Low-Power, 4.6-GHz, Stable Oscillator for CSAC," IEEE International Frequency Control Symposium, pp. 448-451, Florida, USA, June 4-7 2006.
- [34] S. Hamano, K. Kawakami, and T. Takagi. " A Low Phase Noise 19 GHz-bnad VCO using Two Different Frequency Resonators", IEEE-MTT-S, Digest, pp. 2189-2192, 2003.
- [35] W.-M. Lance Kuo, J. D. Cressler, Yi-Jan Emery Chen, and A. J. Joseph, " An Inductorless Ka-band SiGe HBT ring oscillator", IEEE MWCL, Vol. 15, no., 10, pp. 682-684, Oct. 2005.
- [36] J. K. A. Everard and C. D. Broomfield, " High Q Printed Helical Resonators for Oscillators and Filters". IEEE Trans., on Ultrasonics, Ferroelectrics, and Frequency Control, Vol., 54, No. 9, PP. 1741-1750, September 2007.
- [37] C.-G. Hwang and N.-H. Myung, " An Oscillator Incorporating a Planar Helical Resonator for Phase Noise Reduction and Harmonic Supression", JKES, Vol. 6, No.3, pp. 160-164, Sept 2006.

- [38] D. Y. Jung, K. C. Eun, and C. S. Park, "A system-on-Package Structure LTCC Resonator for a Low Phase Noise and Power Efficient Millimeter-Wave Oscillation", IEEE Radio Wireless Symposium 2008, pp. 391-394, 22-24, Orlando, FL, USA, January 2008.
- [39] S.-G. Park, J.-H. Kim, and S.-W. Kim, K.-S. Seo, W.-B. Kim, and J.-In Song, "A Ka-band MMIC Oscillator utilizing a labyrinthine PBG resonator", IEEE Microwave Wireless Component Letter, Vol., 15, no., 11, pp. 727-729, November 2005.
- [40] G. K. Fedder and T. Mukherjee, "Tunable RF AND Analog Circuit using on-chip passive MEMS components" IEEE International Solid-State Circuits Conference", ISSCC Digest of Technical Papers, pp. 390-391, Feb. 2005
- [41] D. Ramchandran et al, "MEMS-Enabled Reconfigurable VCO and RF Filter," RFIC Symp., pp. 251-254, June 2004.
- [42] I. C-El-Abidine, M. Okonewski and J. G. McRory, " A tunable RF MEMS inductor", Proceedings of the International Conference on MEMS, NANO and Smart Systems (ICMENS'03), pp.636-638, 2004.
- [43] H. K. Gummel and R. C. Poon," An integral charge control model of bipolar transistor, "Bell Syst. Tech. J., vol. 49, pp. 827-852, May-June 1970.
- [44] Gettreu, Modeling the Bipolar Transistor, Tektronix, 1976.
- [45] Jae-Ryong Lee, Young-Hoon Chun, Sang-Won Yun, "A novel bandpass filter using active capacitance," 2003 IEEE MTT-S Dig., vol. 3, pp. 1747-1750, June 2003.
- [46] S.-June Cho, Y.-Ho Cho, H.-Il Black, S.-Won Yun, "Analysis of an Active Capacitance Circuit and its Application to VCO", IEEE MTT-S Dig. Pp.1797-1800, June 2006.
- [47] E. Sonmez, A. Trasser, K.-B Schad, P. Abele, H. Schumacher, " High Power Ultra Compact VCO with Active Reactance Concepts at 24 GHz", 31st EuMC, pp. 1-4, Sept 2001.
- [48] Il-Soo Kim, Young-Hoon Chun, Sang-won Yun, "Analysis of a novel active capacitance circuit using BJT and its application to RF bandpass Filters," 2005 IEEE MTT-S Int. Microwave Symp. Dig., pp. 2207-2210, June 2005.
- [49] H-Hung Hsieh, Yu-Te Liao, and L-Hung Lu, "A Compact Quadrature Hybrid MMIC Using CMOS Active Inductors", IEEE Trans. on MTT, Vol. 55, No. 6, June 2007.
- [50] I. Z-El-Abidine, M. Okoniewski and J. G. McRoy, "A new Class of Tunable RF MEMS Inductors", Proc. Of the international conference on MEMS, NANO and smart systems, pp. 1-2 ICMENS, 2003.
- [51] S. Mou, K. Ma, K. S. Yeo, N. Mahalingam, and B. K. Thangarasu, "A compact size low power and wide tuning range vco using dual-tuning LC tanks," *Progress In Electromagnetics Research C*, Vol. 25, 81-91, 2012.
- [52] R. Mukhopadhyay, Y. Park, S. W. Yoon, C.-H. Lee, S. Nuttinck, J.D. Cressler, and J. Laskar, "Active-inductor-based low-power broadband harmonic VCO in SiGe technology for wideband and multi-standard applications", IEEE MTT-S Digest, pp. 1349-1352, 2005.
- [53] S. Del Re, G. Leuzzi and V. Stornelli, "A New Approach to the Design of High Dynamic Range Tunable Active Inductors", Integrated Nonlinear Microwave and Millimeter-Wave Circuits, pp. 25-28, 2008.
- [54] Infineon Datasheet: <http://www.infineon.com>

Chapter 3

Noise Analysis of the Oscillators

3.1 Oscillator Noise

Noise is associated with all the components of the oscillator circuit; however, the major contribution of the noise in an oscillator is from the active device, which introduces AM (amplitude modulation) noise and PM (phase modulation) noise [1]. The conventional wisdom is to ignore AM component of the noise because the gain limiting properties of the active device operating under saturation, allows very little variation in the output amplitude in comparison to PM noise component, which directly affects the frequency stability of the oscillator and creates noise sidebands [2]. But in reality, many oscillator topologies create significant AM noise, therefore effective noise contribution is the combination of $1/f$ spectrum with the $1/f^2$ effect in all phase modulation, makes the low-frequency noise much greater, and that's where the information in most modulated signals reside [2]-[4].

3.1.1 Sources of Noise

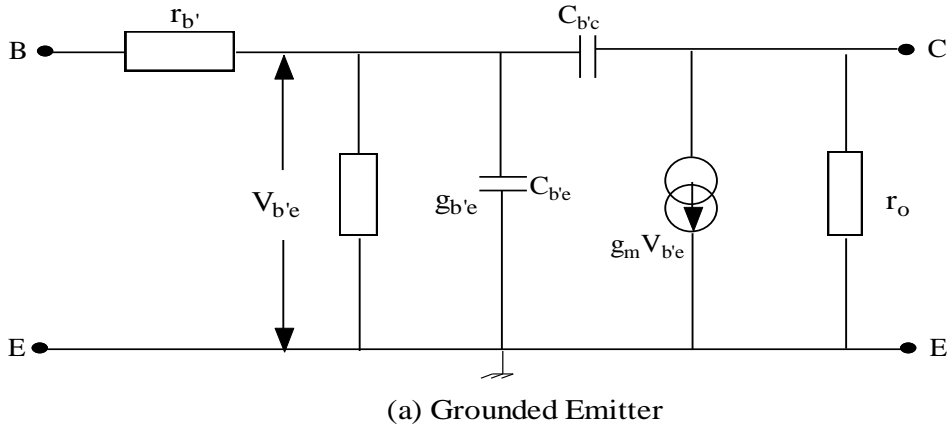
There are mainly two types of noise sources in bipolar oscillator circuit: broadband noise sources due to thermal and shot noise effects and the low-frequency noise source due to $1/f$ (flicker noise effects) characteristics. In FET oscillator, high-field diffusion noise is dominant source of noise generation.

The current flow in a transistor is not a continuous process but is made up of the diffusive flow of large number of discrete carriers and the motions of these carriers are random and explains the noise phenomenon up to certain degree, however many of them are unknown. In conventional terms, the thermal fluctuation in the minority carrier flow and generation-recombination processes in the semiconductor device generates thermal noise, shot noise, partition-noise, burst noise and $1/f$ noise [4]. But in reality, this is not the case, the source of $1/f$ noise is still a subject of research, physicists are still arguing about what causes it.

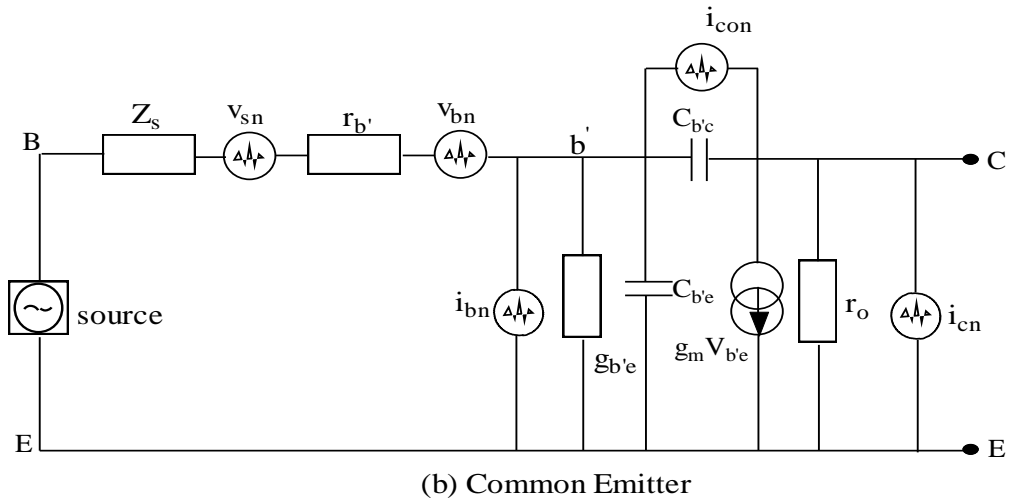
Figure 3-1(a) shows the equivalent schematic of the bipolar transistor in a grounded emitter configuration, and the high frequency noise of a silicon bipolar transistor in common emitter configuration can be modeled by using the three noise sources as shown in equivalent schematic (hybrid- π) in Figure 3-1(b). The emitter junction in this case is conductive and this generates shot noise on the emitter. The emitter current is divided into a base (I_b) and a collector current (I_c) and both these currents generate shot noise. There is the collector reverse current (I_{c0b}), which also generates shot noise. The emitter, base and collector are made of semiconductor material and have finite value of resistance associated with them, which generates thermal noise. The value of the base resistor is relatively high in comparison to resistance associated with emitter and collector, so the noise contribution of these resistors can be neglected.

For noise analysis three sources are introduced in a noiseless transistor and these noise generators are due to fluctuation in DC bias current (i_{bn}), DC collector current (i_{cn}) and thermal noise of the base resistance (v_{bn}). In Silicon transistor the collector reverse current (I_{c0b}) is very

small and noise (i_{con}) generated due to this can be neglected.



(a) Grounded Emitter



(b) Common Emitter

Figure 3-1: (a) π - configuration of the GE-bipolar transistor and (b) π - configuration of CE-bipolar transistor with noise sources [4]

For the evaluation of the noise performances, the signal-driving source should also be taken into consideration because its internal conductance generates noise and its susceptance affects the noise figure through noise tuning.

The mean square values of the noise generator in a narrow frequency interval Δf is given by [4]

$$\overline{i_{bn}^2} = 2qI_b\Delta f \quad (3.1)$$

$$\overline{i_{cn}^2} = 2qI_c\Delta f \quad (3.2)$$

$$\overline{i_{con}^2} = 2qI_{con}\Delta f \quad (3.3)$$

$$\overline{v_{bn}^2} = 4kT r_b \Delta f \quad (3.4)$$

$$\overline{v_{sn}^2} = 4kTR_s \Delta f \quad (3.5)$$

I_b , I_c and I_{cob} are average DC current over Δf noise bandwidth.

The noise power spectral densities due to noise sources is given as [4]

$$S(i_{cn}) = \frac{\overline{i_{cn}^2}}{\Delta f} = 2qI_c = 2KTg_m \quad (3.6)$$

$$S(i_{bn}) = \frac{\overline{i_{bn}^2}}{\Delta f} = 2qI_b = \frac{2KTg_m}{\beta} \quad (3.7)$$

$$S(v_{bn}) = \frac{\overline{v_{bn}^2}}{\Delta f} = 4KTr_b \quad (3.8)$$

$$S(v_{sn}) = \frac{\overline{v_{sn}^2}}{\Delta f} = 4KTR_s \quad (3.9)$$

r_b and R_s are base and source resistance and Z_s is the complex source impedance.

3.1.2 Oscillator Noise Model Comments

The phenomenon of phase noise generation in oscillators/VCOs has been the focus of important research efforts, and it is still an open issue despite significant gains in practical experience and modern CAD tools for design. In the design of VCOs, minimizing the phase noise is usually an important task and these objectives have been accomplished using empirical rules or numerical optimizations, and to this end, are often held as trade secrets by many manufacturers [5]-[12]. The ability to achieve optimum phase noise performance is paramount in most RF design and the continued improvement of phase noise in oscillators is required for the efficient use of frequency spectrum.

The degree to which an oscillator generates constant frequency throughout a specified period is defined as the frequency stability of the oscillator and the cause of the frequency instability is due to the presence of noise in the oscillator circuit that effectively modulates the signal, causing a change in frequency spectrum commonly known as phase noise. Phase noise and timing jitter are both measures of uncertainty in the output of an oscillator. Phase noise defines the frequency domain uncertainty of an oscillator, whereas timing jitter is a measure of oscillator uncertainty in the time domain [13]-[19]. But in reality, phase noise and time jitter correlate each other and tells same thing. The main distinction is just that "jitter" is applied primarily to digital sources [20]-[33]. The Equation for ideal sinusoidal oscillator in time domain is given by

$$V_{out}(t) = A \cos(2\pi f_0 t + \varphi) \quad (3.10)$$

where A , f_0 and φ are the amplitude, frequency and fixed phase of the oscillator.

The Equation of the real oscillator in time domain is given by

$$V_{out}(t) = A(t) \cos[\omega_0 t + \varphi(t)] = [A + \alpha(t)] \cos[2\pi f_0 t + \varphi(t)] \quad (3.11)$$

where $A(t)$, $\varphi(t)$, and f_0 are the time variable amplitude fluctuation, time variable phase fluctuation, frequency respectively.

Because of the fluctuations, the spectrum of a practical oscillator is broadened near the carrier frequency. In practice, amplitude noise (AM noise) is smaller than phase-noise (PN) due to the amplitude-restoring mechanism in LC oscillators, this is illustrated by the limit cycle of an ideal LC oscillator as shown in Figure 3-2 [34]-[37].

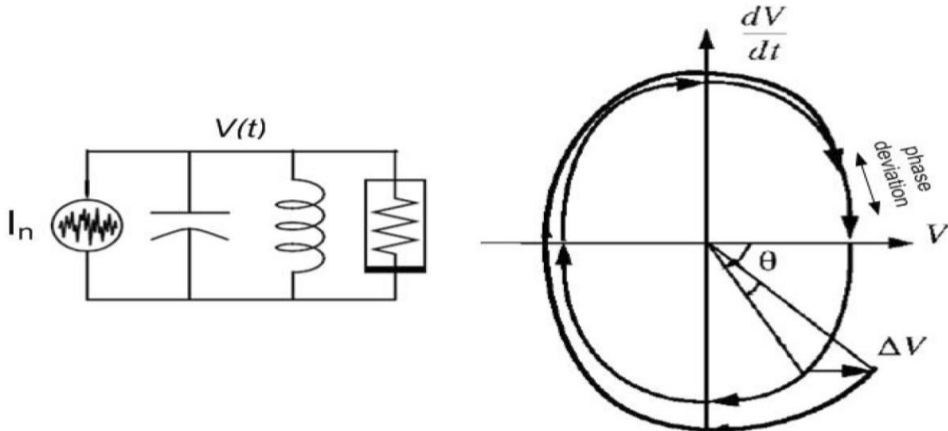


Fig. 3-2 A typical limit cycle of an ideal LC oscillator (The current noise perturbs the oscillator's voltage by ΔV and the perturbed signal restores its stable amplitude whereas its phase is free to drift, causing strong random phase variations) [34].

As shown in Figure 3-2, the current noise perturbs the signal and causes its phasor to deviate from the stable trajectory, producing both amplitude and phase-noise. The amplitude deviation is resisted by the stable limit cycle, whereas the phase is free to drift. Therefore, oscillators almost exclusively generate phase-noise near the carrier [38]-[42]

Figures 3-3 (a), (b), and (c) illustrate the frequency spectrum and time jitter of ideal and real oscillators, and the typical oscillator phase noise plot. From Equations (3.10) and (3.11), the fluctuation introduced by $A(t)$ and $\varphi(t)$ are functions of time and lead to sidebands around the center frequency f_0 . In the frequency domain, the spectrum of the oscillator consists of Dirac-impulses at $\pm f_0$. The SSB phase-noise $E(f)$ is usually expressed in the frequency domain and described in units of dBc/Hz, representing the noise power relative to the carrier contained in a 1 Hz bandwidth centered at a certain frequency offset from the carrier [43]-[46].

In the order of increasing complexity, noise models are grouped into one of the three categories as: (i) linear time invariant (LTIV) model, (ii) linear time variant model (LTV), and (iii) nonlinear time variant model (NLTV) [47]-[68]. The first noise model is proposed by Leeson [1], based on LTIV (Linear-time-invariant) properties of the oscillator, such as resonator Q, feedback gain, output power, and noise figure; a second model is proposed by Lee and Hajimiri [35], based on time-varying properties of the oscillator RF current waveform (LTV); and a third is proposed by Kaertner, Demir, and Ngova using a perturbation model based on numerical techniques (NLTV) [38, 39, 46, 47].

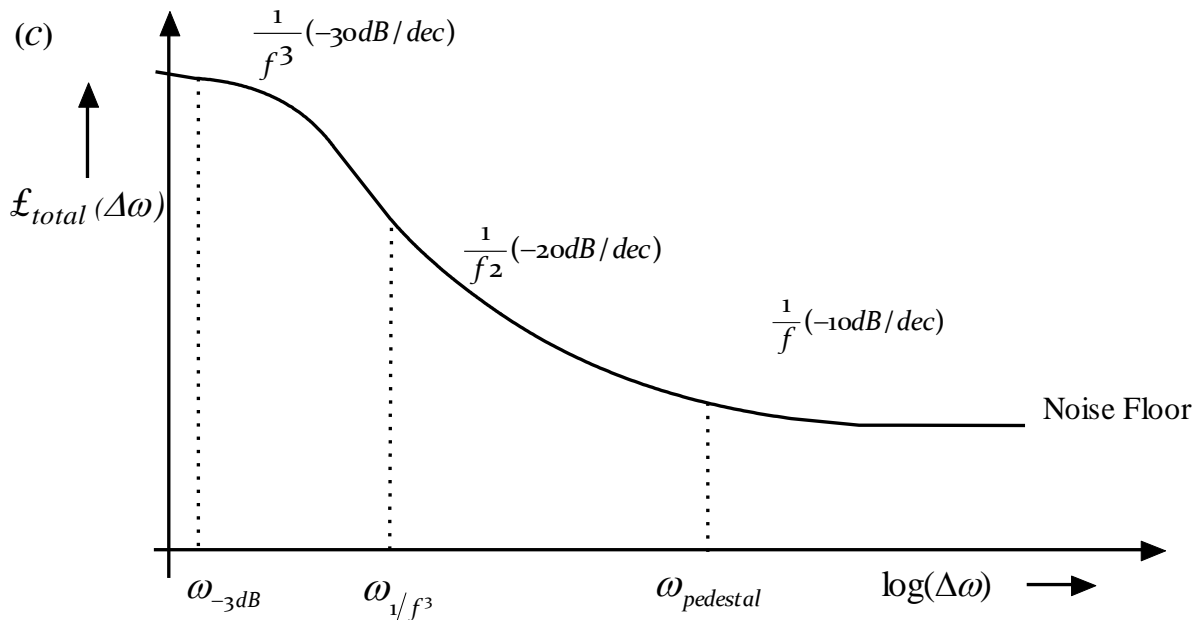
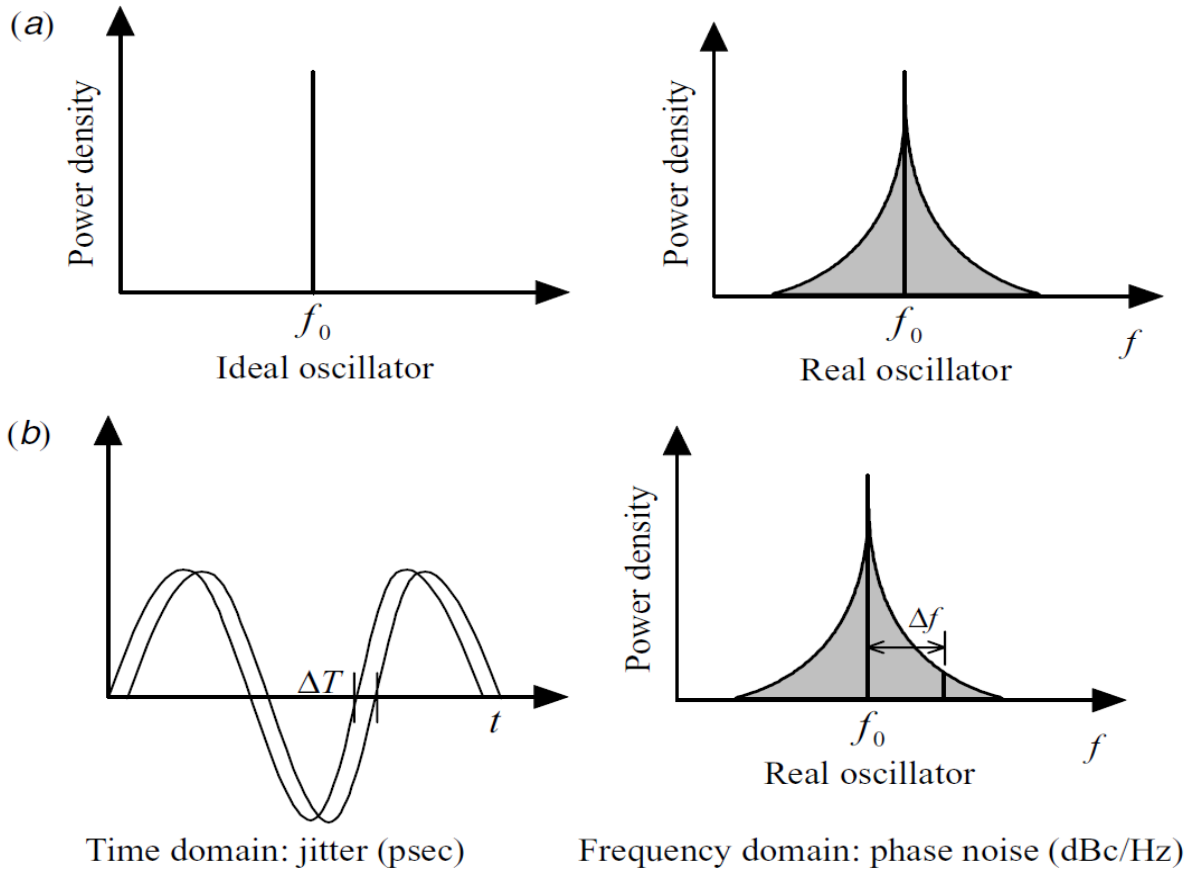


Fig 3-3: (a) Frequency spectrum of ideal and real oscillators and (b) Jitter in time domain relates to phase noise in the frequency domain, and (c) a typical phase noise plot of real oscillator [4].

Nallatamby et al. [6] revisited the Lesson's noise model, providing a detailed and enlightening analysis, demonstrating its applicability to several oscillator circuits. The theories proposed by Hajimiri and Lee, and from Kaertner and Demir are based on time-domain approaches for harmonic oscillator circuits (like LC resonator) [40]-[48]. The approach from Hajimiri and Lee can be seen as a particular case of the theory of Kaertner [46] and Demir [38, 42, 47], as it can be shown in the analytical comparison between time and frequency-domain techniques for phase noise analysis, carried out by Suárez et al. [7]. The Impulse Sensitivity Function (ISF) proposed by Hajimiri [45] and Lee can be employed to optimize the phase noise performances of a given oscillator and ISF can be obtained from Harmonic Balance (HB) as shown by Ver Hoeye et al. [8]. More insight and improvements of phase noise analysis that can be implemented [49]-[66] using commercially available HB tools that can be found in the paper Rizzoli [9], and Sancho et al. [9]-[10].

It is important to distinguish noise dynamics in resonator-based oscillators (harmonic oscillators) with a sharply contrasting oscillator type, time/waveform based oscillator (like relaxation, ring, and multivibrator) [67]-[68]. Generically this comprises a single reactance, usually a capacitor, a regenerative memory element such as a flip-flop or Schmitt trigger, and a means of charging and discharging the capacitor (as shown in Figure 3-4) [69].

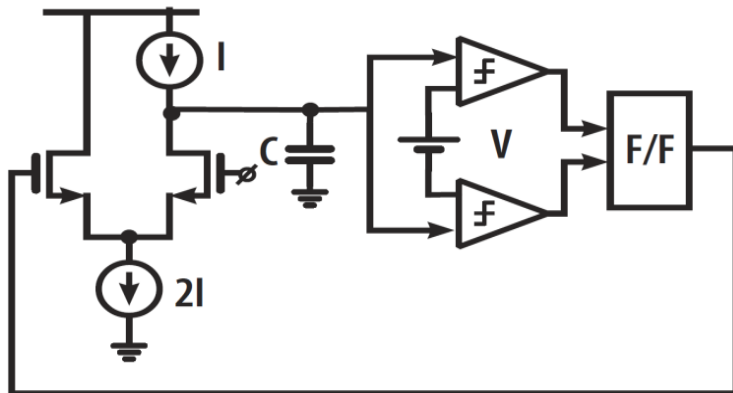


Figure 3-4: A typical simplified relaxation oscillator circuit [69]

Typically, harmonic oscillators can be characterized by equivalence to two energy storage reactive elements (inductor and capacitor), exchanging electrical and magnetic energy at resonance in order to give a periodic output signal. The actual LC resonant element can be high quality factor SAW (surface acoustic wave) resonator or Quartz Crystal resonator or Dielectric Resonator, YIG resonator or printed transmission line or lumped inductor-capacitor resonator. The time/waveform based RC oscillator circuits (like relaxation, ring, and multivibrator) use one energy storage reactive element typically “capacitor” for determining oscillation frequency. The single reactance is not frequency selective like the resonator, and the regenerative element makes this into a discrete-time feedback loop [69].

The basis of noise dynamics is fluctuation-dissipation theorem of thermodynamics in conjunction with probability viewpoints using the concept of Brownian motion (Wiener process), which dictates a lower limit for phase noise in *RC* oscillators. Specifically, the phase noise due to the distinct characteristics of threshold crossing in *RC* oscillators can be expressed

as functions of temperature, power dissipation, frequency of oscillation and the offset frequency [50]-[54].

In the family of inductor less oscillator, ring oscillator is most useful for current and later generation communication systems. As shown in Figure 3-5, the ring oscillator derives its frequency from the cumulative delay in the stages making up the ring. It follows by symmetry that if all the stages are identical, then as the sine wave traverses each stage of the ring, its amplitude remains unchanged, and it experiences a phase lag of 45° [69]. For simplification in analysis, one can assume that only one of the delay stages in the ring generates noise, and the other stages are noiseless so that at frequencies f_c , the ring oscillator can be characterized as a single noisy differential pair with negative feedback from the output to the input through an ideal delay line, t_d (as shown in Figure 3-5). Therefore, the unity gain delay line models the other three noiseless stages because its gain is one (at resonant frequency), and the effective delay of the entire ring is given by $t_d = 1/(2f_c)$ [69].

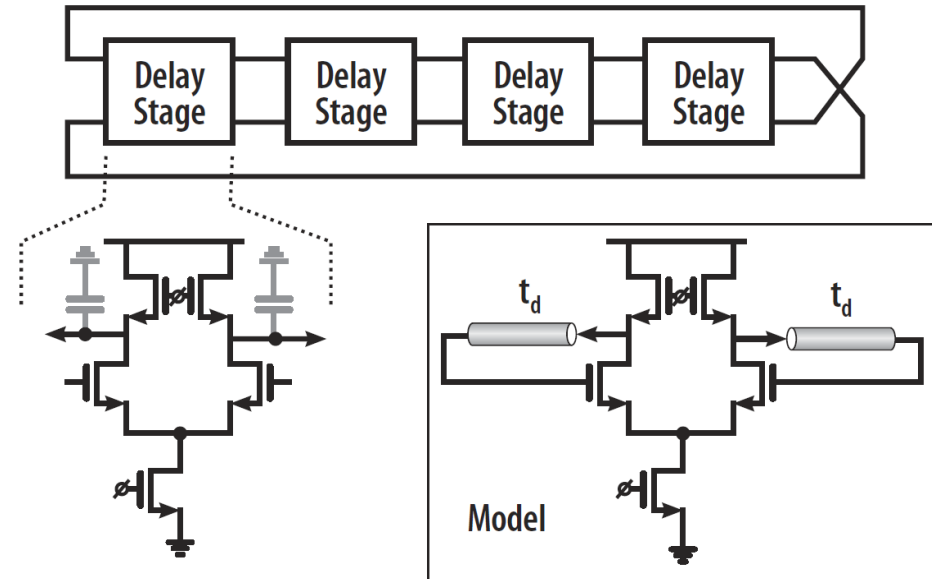


Figure 3-5: A typical simplified Ring Oscillator circuit using CMOS device and equivalent model to calculate the additive noise transfer function [69].

To have a better insight of the noise effects in the oscillator design, it is necessary to understand oscillator topologies and how the noise arises in active (transistors) and passive devices. The designer has very limited control over the noise sources in a transistor, only being able to control the device selection and the operating bias point. However, using knowledge about how noise affects oscillator waveforms, the designer is able to substantially improve phase-noise performance of the oscillator circuits by the optimization of the key parameters (large signal noise factor, output waveform symmetry, circuit topology, drive-level, and noise filtering techniques) [4]-[11].

3.2 Leeson's Phase Noise Model

Phase noise is usually characterized in terms of the single sideband noise spectral density. It has units of decibels below the carrier per hertz (dBc/Hz) and is defined as [4]

$$L_{\text{total}}\{\Delta\omega\} = 10 \cdot \log \left[\frac{P_{\text{sideband}}(\omega_0 + \Delta\omega, 1\text{Hz})}{P_{\text{carrier}}} \right]$$

where, $P_{\text{sideband}}(\omega_0 + \Delta\omega, 1\text{Hz})$ represents the single sideband power at a frequency offset of $\Delta\omega$ from the carrier with a measurement bandwidth of 1Hz [1].

Leeson's phase noise equation is given by [1]

$$\xi(f_m) = 10 \log \left[\left(1 + \frac{f_0^2}{(2f_m Q_L)^2 (1 - \frac{Q_L}{Q_0})^2} \right) \left(1 + \frac{f_c}{f_m} \right) \frac{FkT}{2P_o} \right] \quad (3.12)$$

$\xi(f_m)$ = ratio of sideband power in a 1Hz bandwidth at f_m to total power in dB

f_m = frequency offset from the carrier

f_0 = center frequency

f_c = flicker frequency

Q_L = loaded Q of the tuned circuit

Q_0 = unloaded Q of the tuned circuit

F = noise factor

$kT = 4.1 \times 10^{-21}$ at 300 K (room temperature)

P_o = average power at oscillator output

It is important to understand that the Leeson model is based on linear time invariant characteristics (LTIV) and is the best case since it assumes the tuned circuit filters out all the harmonics. Assuming the phase-noise as a small perturbation, Leeson linearizes the oscillator circuit around the steady-state point in order to obtain a closed-form formula for phase-noise. In all practical cases, it is hard to predict what the operating Q and noise figure will be. The predictive power of the Leeson model is limited due to the following, which is not known prior to measurement: the output power, the noise figure under large signal conditions, and the loaded Q [18].

This classic paper [1] is good design guide with the basic understanding that the "noise factor" as shown in Equation (3.12) is not what we understand; but a measure of the upconverted 1/f noise. Since Leeson's model does not try to account for this, it cannot possibly provide useful noise predictions. The drawback of this approach is the fact that the up-conversion of the low frequency flicker noise components to around carrier phase-noise, which is a necessary input to the equation; the RF output power, the loaded Q , and the noise factor of the amplifier under large signal condition, are not known. In addition to this Equation (3.12) predicts an infinite phase-noise power as $f \rightarrow 0$.

3.2.1 Leeson's Phase Noise Model (Linear Time Invariant Approach)

Since an oscillator can be viewed as an amplifier with feedback as shown in Figure 2-1 (Chapter 2), it is helpful to examine the phase noise added to an amplifier that has a noise factor F . With F defined as [4]

$$F = \frac{(S/N)_{\text{in}}}{(S/N)_{\text{out}}} = \frac{N_{\text{out}}}{N_{\text{in}} G} = \frac{N_{\text{out}}}{GkTB} \quad (3.13)$$

$$N_{\text{out}} = FGkTB \quad (3.14)$$

$$N_{\text{in}} = kTB \quad (3.15)$$

$$\Delta\theta_{1\text{peak}} = \frac{V_{\text{nRMS1}}}{V_{\text{savRMS}}} = \sqrt{\frac{FkT}{P_{\text{sav}}}} \quad (3.16)$$

$$\Delta\theta_{\text{RMS}} = \frac{1}{\sqrt{2}} \sqrt{\frac{FkT}{P_{\text{sav}}}} \quad (3.17)$$

where N_{in} is the total input noise power to a noise-free amplifier, F is the noise factor, T is temperature in Kelvin, k is the Boltzmann constant ($kT = 4.1 \times 10^{-21}$ at 300 K), P_{sav} is average output power.

Figure 3-6 shows the typical representation of noise power versus frequency of a transistor amplifier with an input signal applied. The input phase noise in a 1 Hz bandwidth at any frequency $f_0 + f_m$ from the carrier produces a phase deviation as shown in Figure 3-7.

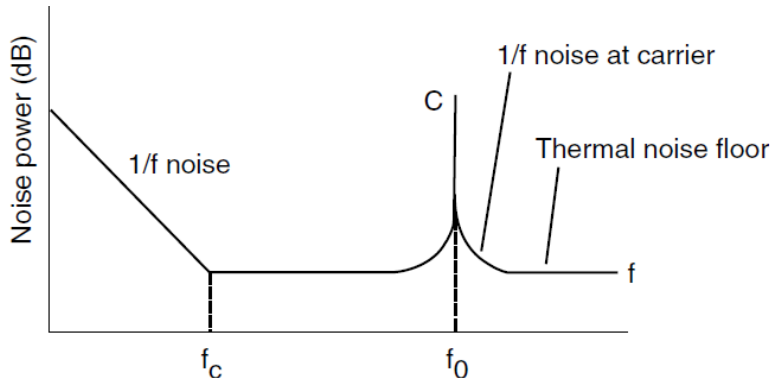


Figure 3-6: Noise power vs frequency of a transistor amplifier with an input signal applied [4, pp. 124]

Since a correlated random phase noise relation exists at $f_0 - f_m$, the total phase deviation becomes

$$\Delta\theta_{\text{RMStotal}} = \sqrt{FkT / P_{\text{sav}}} \quad (\text{SSB}) \quad (3.18)$$

The spectral density of phase noise becomes

$$S_\theta(f_m) = \Delta\theta_{\text{RMS}}^2 = FkTB / P_{\text{sav}} \quad (3.19)$$

where $B = 1$ for a 1 Hz bandwidth. Using

$$kTB = -174 \text{ dBm} \quad (B = 1 \text{ Hz}, T = 300\text{K}) \quad (3.20)$$

allows a calculation of the spectral density of phase noise that is far away from the carrier (that is, at large values of f_m). This noise is the theoretical noise floor of the amplifier. For example, an amplifier with +10 dBm power at the input and a noise figure of 6 dB gives

$$S_\theta(f_m > f_c) = -174 \text{ dBm} + 6 \text{ dB} - 10 \text{ dBm} = -178 \text{ dBm} \quad (3.21)$$

Only if P_{out} is > 0 dBm can we expect L (signal-to-noise ratio) to be greater than -174 dBc/Hz (1 Hz bandwidth.) For a modulation frequency close to the carrier, $S_\theta(f_m)$ shows a flicker or $1/f$ component, which is empirically described by the corner frequency f_c . The phase noise can be modeled by a noise-free amplifier and a phase modulator at the input as shown in Figure 3-8.

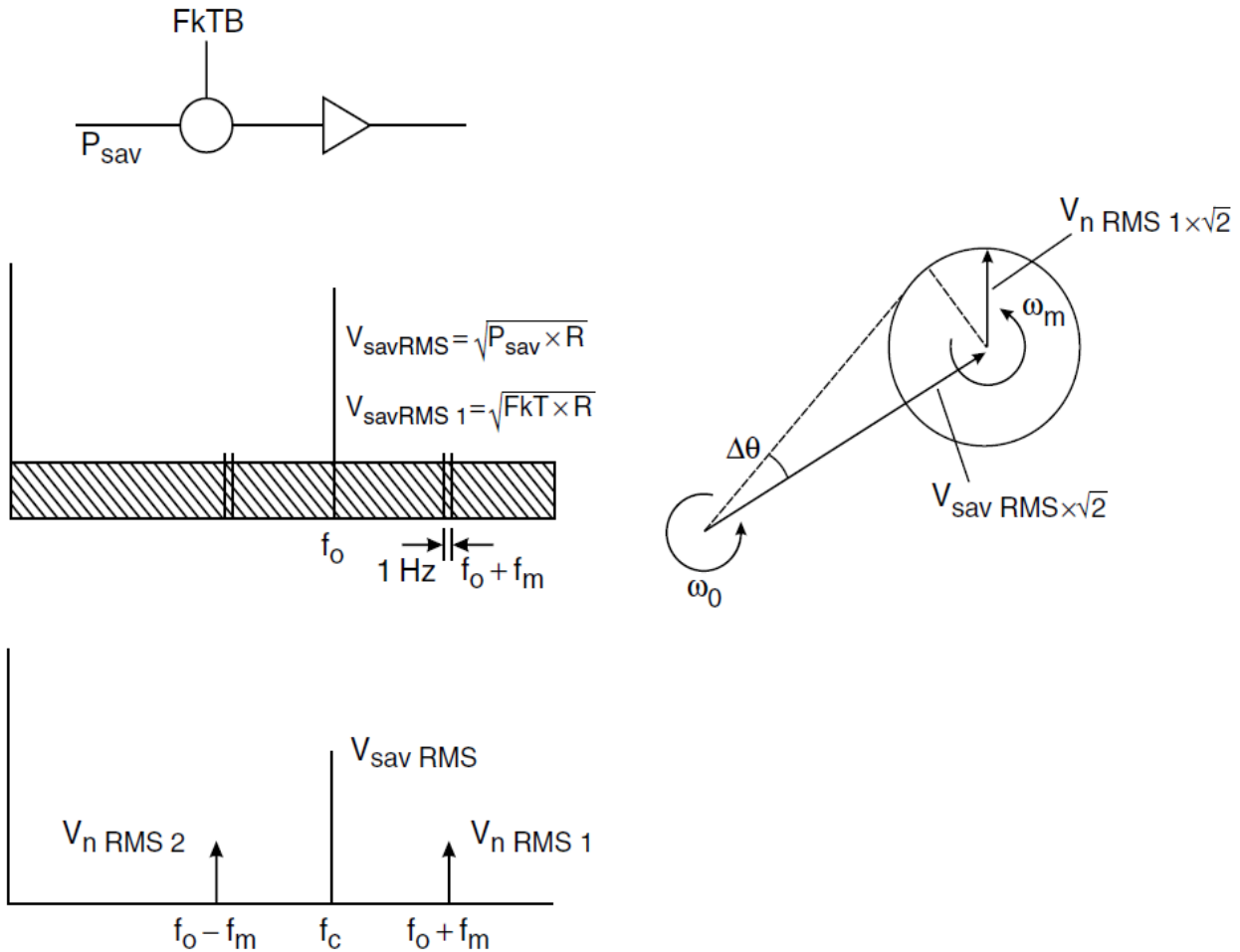


Figure 3-7: Phase noise added to the carrier (the input phase noise in a 1 Hz bandwidth at any frequency $f_0 + f_m$ from the carrier produces a phase deviation) [4, pp. 125].

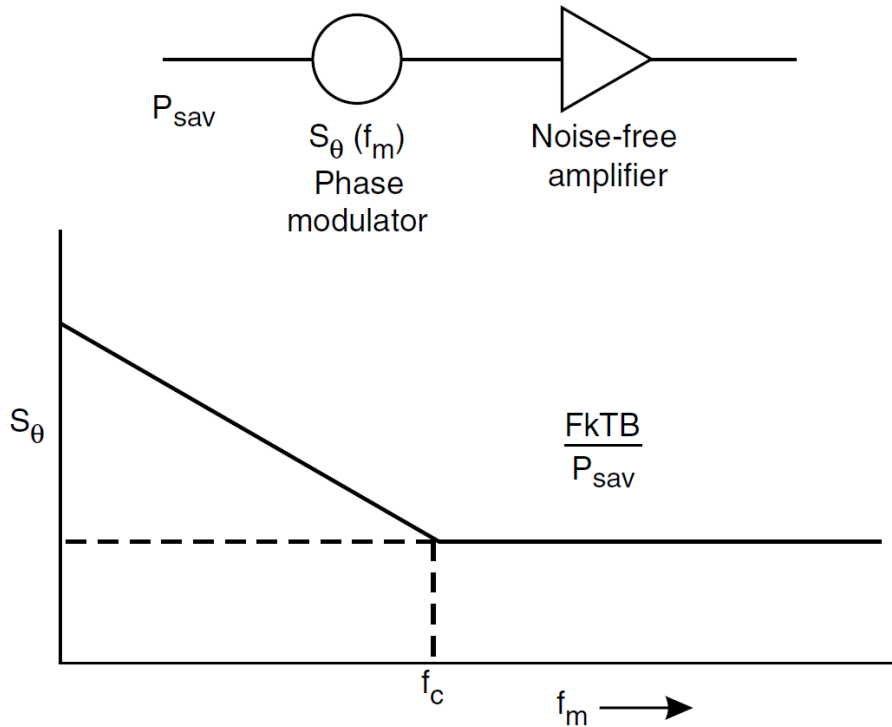


Figure 3-8 Phase noise modeled by a noise free amplifier and phase modulator [Ref. 4, pp. 126, Fig. 7-3]

The purity of the signal is degraded by the flicker noise at frequencies close to the carrier. The phase noise can be described by

$$S_\theta(f_m) = \frac{FkTB}{P_{\text{sav}}} \left(1 + \frac{f_c}{f_m} \right) \quad (B = 1) \quad (3.22)$$

No AM-to-PM conversion is considered in this equation. The oscillator may be modeled as an amplifier with feedback as shown in Figure 3-23.

The phase noise at the input of the amplifier is affected by the bandwidth of the resonator in the oscillator circuit in the following way.

The tank circuit or bandpass resonator has a low pass transfer function

$$H(\omega_m) = \frac{1}{1 + j(2Q_L\omega_m/\omega_0)} \quad \text{where } \omega_0/2Q_L = 2\pi B/2 \quad (3.23)$$

where $\omega_0/2Q_L = 2\pi B/2$, is the half bandwidth of the resonator, Q_L is the loaded quality factor. These equations describe the amplitude response of the bandpass resonator; the phase noise is transferred un-attenuated through the resonator up to the half bandwidth [4].

Leeson's phase-noise formula was derived for an oscillator using a single resonator with the transfer function given in (3.10); thus one might question its validity for oscillators using more complex resonant structures such as slow-wave-resonator (SWR) with different $H(\omega_m)$.

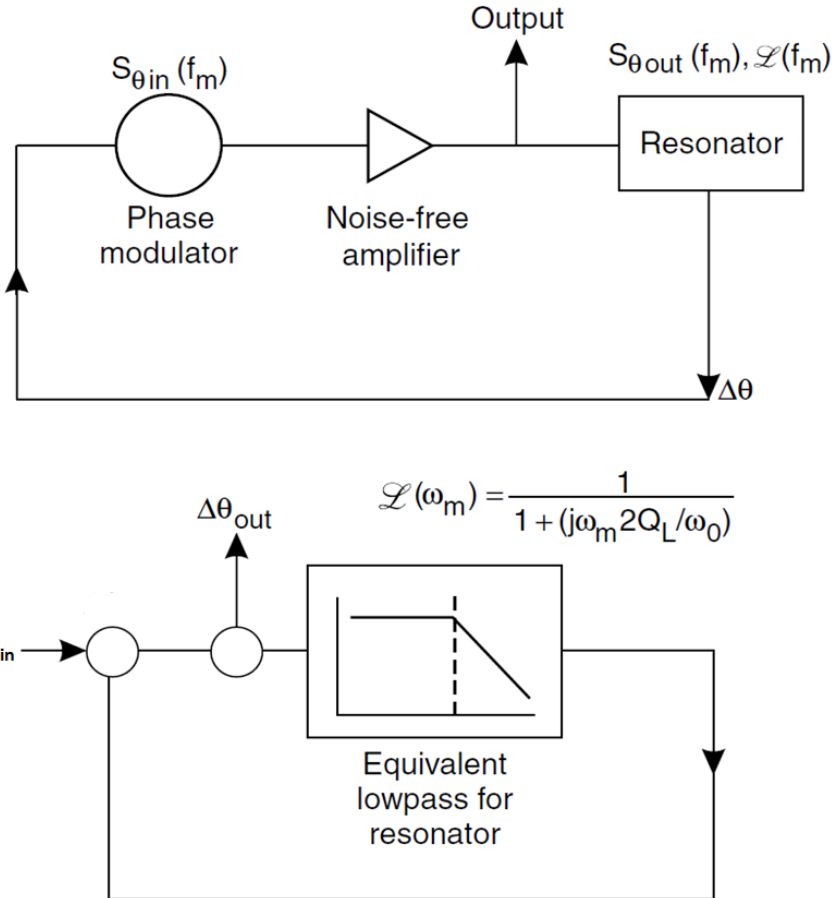


Figure 3-9: Equivalent feedback models of oscillator phase noise [4, pp. 126, Fig. 7-4]

In fact, by replacing $H(\omega_m)$ in (3.23) with its Taylor series expansion around the resonant frequency, one can easily show that the Lesson's phase-noise formula remains valid and can be applied to oscillators with complex resonators, provided that the loaded quality-factor is defined as [39]-[41]

$$Q_L = \frac{\omega_0}{2} \sqrt{\left(\frac{\Delta A(\omega)}{\Delta \omega} \right)^2 + \left(\frac{\Delta \theta(\omega)}{\Delta \omega} \right)^2} \quad (3.24)$$

where $A(\omega)$ and $\vartheta(\omega)$ are the amplitude and phase of the resonator's transfer function $H(\omega_m)$.

The closed loop response of the phase feedback loop as shown in Figure 3-9 is given by

$$\Delta \theta_{\text{out}}(f_m) = \left(1 + \frac{\omega_0}{j2Q_L \omega_m} \right) \Delta \theta_{\text{in}}(f_m) \quad (3.25)$$

The power transfer becomes the phase spectral density

$$S_{\theta \text{ out}}(f_m) = \left[1 + \frac{1}{f_m^2} \left(\frac{f_0}{2Q_L} \right)^2 \right] S_{\theta \text{ in}}(f_m) \quad (3.26)$$

where $S_{\theta \text{ in}}$ was given by Equation (3.9).

Finally, $\mathcal{L}(f_m)$, which is the single sideband phase noise $\frac{1}{2}[S_{\theta_{\text{out}}}(f_m)]$ [4, pp. 127]

$$\mathcal{L}(f_m) = \frac{1}{2} \left[1 + \frac{1}{f_m^2} \left(\frac{f}{2Q_L} \right)^2 \right] S_{\theta_{\text{in}}}(f_m) \quad (3.27)$$

This equation describes the phase noise at the output of the amplifier (flicker corner frequency and AM-to-PM conversion are not considered). The phase perturbation $S_{\theta_{\text{in}}}$ at the input of the amplifier is enhanced by the positive phase feedback within the half bandwidth of the resonator, $f_0/2Q_L$. Depending on the relation between f_c and $f_0/2Q_L$, there are two cases of interest, as shown in Figure 3-10.

For the low Q case, the spectral phase noise is unaffected by the Q of the resonator, but the $\mathcal{L}(f_m)$ spectral density will show a $1/f^3$ and $1/f^2$ dependence close to the carrier. For the high Q case, a region of $1/f^3$ and $1/f$ should be observed near the carrier. Substituting Equation (3.22) in (3.27) gives an overall noise of [4, pp.128]:

$$\mathcal{L}(f_m) = \frac{1}{2} \left[1 + \frac{1}{f_m^2} \left(\frac{f}{2Q_L} \right)^2 \frac{FkT}{P_{\text{av}}} \left(1 + \frac{f_c}{f_m} \right) \right] = \frac{FkT}{2P_{\text{av}}} \left[\frac{1}{f_m^3} \frac{f^2 f_c}{4Q_L^2} + \frac{1}{f_m^2} \left(\frac{f}{2Q_L} \right)^2 + \left(1 + \frac{f_c}{f_m} \right) \right] \text{dBc/Hz} \quad (3.28)$$

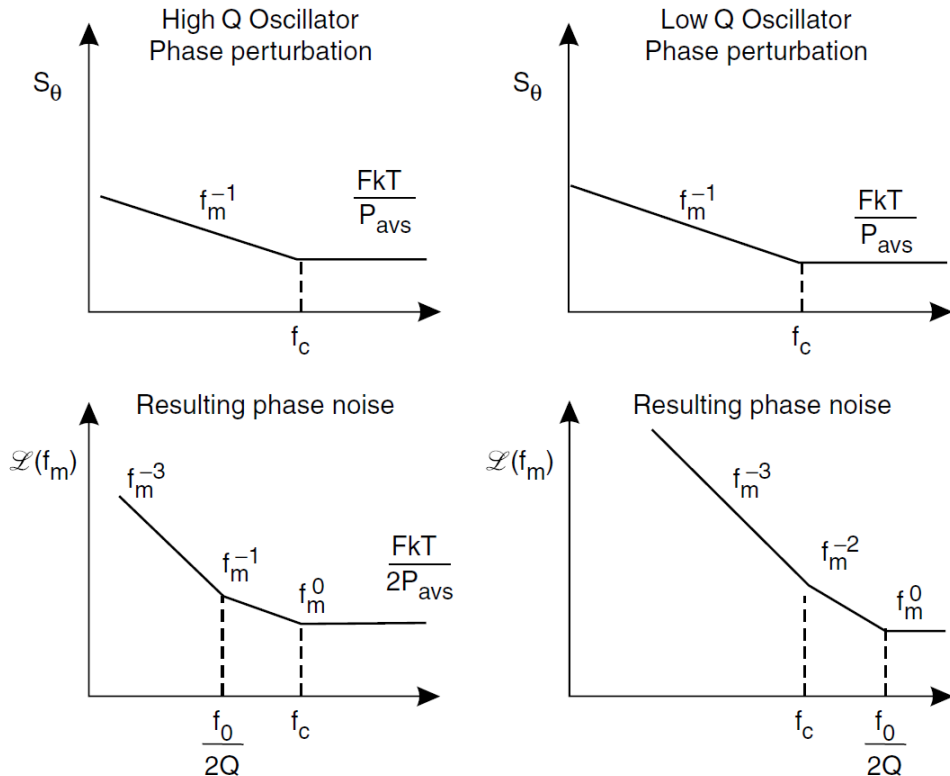


Figure 3-10: A typical representation of oscillator phase noise plots for high and low Q -factor resonator oscillator [4, pp. 128]]

Examining Equation (3.27) gives the four major causes of oscillator noise: the up-converted $1/f$ noise or flicker FM noise, the thermal FM noise, the flicker phase noise, and the thermal noise floor, respectively.

Q_L (loaded Q) can be expressed as

$$Q_L = \frac{\omega_o W_e}{P_{\text{diss, total}}} = \frac{\omega_o W_e}{P_{\text{in}} + P_{\text{res}} + P_{\text{sig}}} = \frac{\text{reactive power}}{\text{total dissipated power}} \quad (3.29)$$

where W_e is the reactive energy stored in L and C ,

$$W_e = \frac{1}{2} CV^2 \quad (3.30)$$

$$P_{\text{res}} = \frac{\omega_o W_e}{Q_{\text{unl}}} \quad (3.31)$$

More comments on the Leeson formula are found in [36]-[39]. The practical oscillator will experience a frequency shift when the supply voltage, is changed. This is due to the voltage and current dependent junction capacitances of the transistor. To calculate this effect, we can assume that the fixed tuning capacitor of the oscillator is a semiconductor junction, which is reverse biased. This capacitor becomes a tuning diode [4].

$$\mathcal{L}(f)_m = \frac{1}{2} \left[1 + \frac{\omega_0^2}{4\omega_m^2} \left(\frac{P_{\text{in}}}{\omega_0 W_e} + \frac{1}{Q_{\text{unl}}} + \frac{P_{\text{sig}}}{\omega_0 W_E} \right)^2 \right] \left(1 + \frac{\omega_c}{\omega_m} \right) \frac{FkT_0}{P_{\text{sav}}} \quad (3.32)$$

This tuning diode itself generates a noise voltage and modulates its capacitance by a slight amount, and therefore modulates the frequency of the oscillator by minute amounts. The following calculates the phase noise generated from this mechanism, which needs to be added to the phase noise calculated above.

It is possible to define an equivalent noise R_{aeq} that, inserted in Nyquist's equation,

$$V_n = \sqrt{4kT_o R_{aeq} \Delta f} \quad (3.33)$$

where $kT_o = 4.2 \times 10^{-21}$ at $T_0=300$ Kelvin, R is the equivalent noise resistor, Δf is the bandwidth, determines an open noise voltage across the tuning diode. Practical values of R_{aeq} for carefully selected tuning diodes are approximately 100Ω , or higher. If we now determine the voltage, $V_n = \sqrt{4 \times 4.2 \times 10^{-21} \times 100}$, the resulting voltage value is $1.265 \times 10^{-9} \text{ V} \sqrt{\text{Hz}}$.

This noise voltage generated from the tuning diode is now multiplied with the VCO gain, resulting in the rms frequency deviation:

$$(\Delta f_{rms}) = K_o \times (1.265 \times 10^{-9} \text{ V}) \text{ in } 1 \text{ Hz bandwidth} \quad (3.34)$$

In order to translate this into the equivalent peak phase deviation,

$$\theta_d = \frac{K_o \sqrt{2}}{f_m} (1.265 \times 10^{-9} \text{ rad}) \text{ in } 1 \text{ Hz bandwidth} \quad (3.35)$$

or for a typical oscillator gain of 10 (MHz/V),

$$\theta_d = \frac{0.00179}{f_m} (\text{ rad in } 1 \text{ Hz bandwidth}) \quad (3.36)$$

For $f_m = 25$ kHz (typical spacing for adjacent channel measurements for FM mobile radios), the $\theta_d = 7.17 \times 10^{-8}$. This can be converted into the SSB signal-to-noise ratio

$$L(f_m) = 20 \log_{10} \frac{\theta_c}{2} = -149 \text{ dBc/Hz} \quad (3.37)$$

Figure 3-11 shows a plot with an oscillator sensitivity of 10 kHz/V, 10 MHz/V, and 100 MHz/V. The center frequency is 2.4 GHz [4]. The lowest curve is the contribution of the Leeson equation. The second curve shows the beginning of the noise contribution from the diode, and the third curve shows that at this tuning sensitivity, the noise from the tuning diode by itself dominates as it modulates the VCO. This is valid regardless of the Q. This effect is called modulation noise (AM-to-PM conversion), while the Leeson equation deals with the conversion noise. Rohde modified the Leeson phase noise Equation (3.12) with the tuning diode contribution, following Equation allows us to calculate the oscillator phase noise as [4, 98]

$$L(f_m) = 10 \log \left\{ \left[1 + \frac{f_0^2}{(2f_m Q_L)^2} \right] \left[1 + \frac{f_c}{f_m} \right] \frac{FkT}{2P_{sav}} + \frac{2kTRK_0^2}{f_m^2} \right\} \quad (3.38)$$

where

$L(f_m)$ = ratio of sideband power in a 1 Hz bandwidth at f_m to total power in dB

f_m = frequency offset

f_0 = center frequency

f_c = flicker frequency

Q_L = loaded Q of the tuned circuit

F = noise factor

$kT = 4.1 \times 10^{-21}$ at $300 K_0$ (room temperature)

P_{sav} = average power at oscillator output

R = equivalent noise resistance of tuning diode (typically 50Ω - $10 \text{ k}\Omega$)

K_o = oscillator voltage gain

The limitation of this equation is that the loaded Q in most cases has to be estimated and the same applies to the noise factor. The microwave harmonic-balance simulator, which is based on the noise modulation theory (published by Rizzoli), automatically calculates the loaded Q and the resulting noise figure as well as the output power [40].

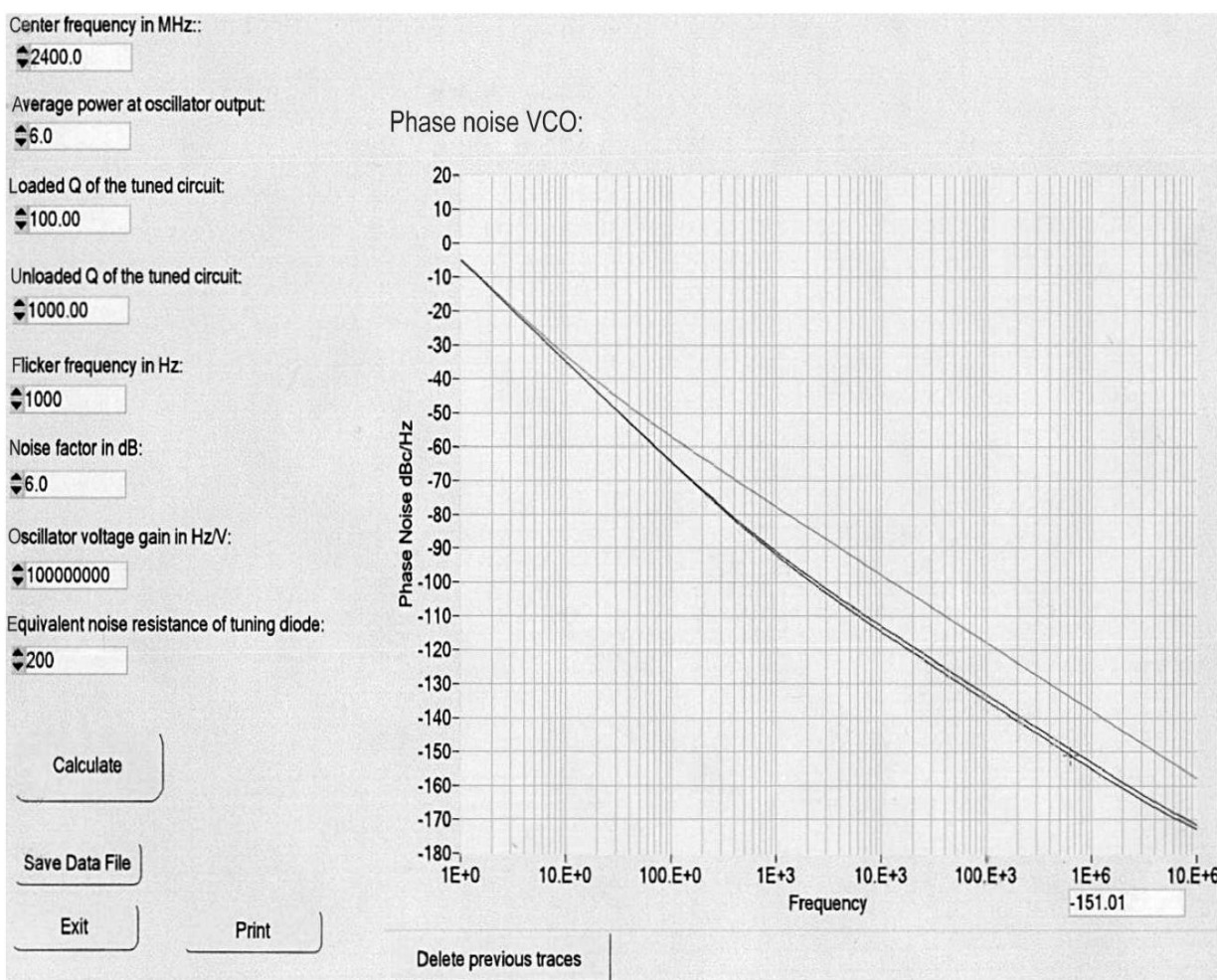


Figure 3-11 Simulated phase noise following Equation (3.24) [4]

When adding an isolating amplifier, the noise of an *LC* oscillator system is determined by

$$\begin{aligned}
 S_\phi(f_m) = & \left[a_R F_0^4 + a_E (F_0 / (2Q_L))^2 \right] / f_m^3 \\
 & + \left[(2GFKT / P_0) (F_0 / (2Q_L))^2 \right] / f_m^2 \\
 & + (2a_R Q_L F_0^3) / f_m^2 \\
 & + a_E / f_m + 2GFKT / P_0
 \end{aligned} \tag{3.39}$$

where

G = compressed power gain of the loop amplifier

F = noise factor of the loop amplifier

k = Boltzmann's constant

T = temperature in Kelvin

P_0 = carrier power level (in watts) at the output of the loop amplifier

F_0 = carrier frequency in Hz

f_m = carrier offset frequency in Hz

$Q_L = (\pi F_0 \tau_g)$ = loaded Q of the resonator in the feedback loop

a_R and a_E = flicker noise constants for the resonator and loop amplifier

From (3.38), resonator Q factor is an important parameter for low phase noise oscillator applications. Care must be taken to maximize the dynamic loaded Q -factor for improved phase noise performances. If the loaded Q is infinite at oscillator steady state condition that leads to "0Hz" noise bandwidth for the negative resistance oscillator circuit. Moreover, if this is the case then this oscillator would take infinite time to build the output transient waveform and reach at the stable state condition [42]. For practical condition, there is a net resistance at turn-on, and the start-up transient depends on the behavior of the nonlinearity associated with the oscillator circuits and the slope parameter of resonator establishes the noise spectrum [42].

Although Leeson's phase-noise model provides a valuable insight into the oscillator design from engineering perspectives, it cannot explain some of the important phase noise phenomena [38]. This is due to simplifying assumptions made about the linearity and time-invariant behavior of the system. When comparing the measured results of oscillators with the assumptions made in Leeson's Equation (3.28), one frequently obtains a *de facto* noise figure in the vicinity of 20 to 30 dB and an operating Q that is different than the assumed loaded Q , therefore must be determined from measurement; diminishing the predictive power of the Leeson's phase noise model [4].

Leeson's model observes the asymptotic behavior of phase-noise at close-to carrier offsets, asserting that phase-noise goes to infinity with $1/f^3$ rate [1]. This is obviously wrong as it implies an infinite output power for oscillator. For noisy oscillators it could also suggest that $L(f) > 0$ dBc/Hz, this singularity arises from linearity assumption for oscillator operation around steady-state point [38]-[43]. In fact, the linear model breaks down at close-to-carrier frequencies where the phase-noise power is strong [39].

Considering a nonlinear model for the oscillator in absence of flicker noise, these singularities can be resolved by expressing the phase noise in the form of a Lorentzian function [42]

$$L(\Delta f_m) \propto \frac{a^2}{a^2 + (\Delta f_m)^2} \quad (3.40)$$

where a is a fitting parameter.

Although Equation (3.40) models the spectrum and avoids any singularity at $\Delta f_m=0$ while maintaining the same asymptotic behavior as illustrated in Figure 3-12, this is only an after-the-fact approach, but not a predictive one [41]-[43].

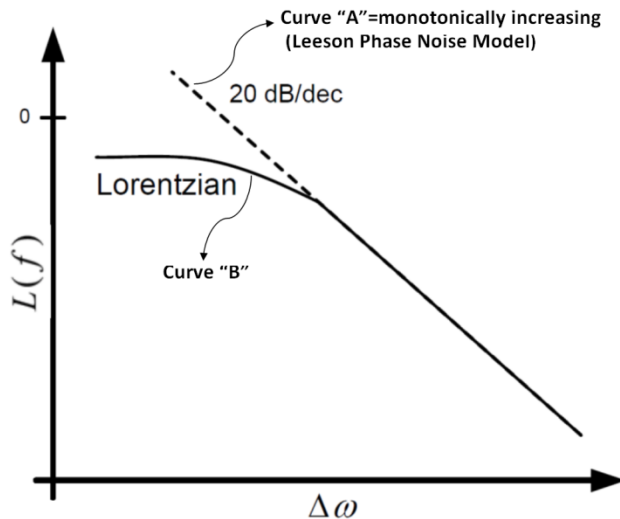


Fig. 3-12 Close-In phase-noise behavior due to white noise sources. Leeson's model predicts phase-noise monotonically increases by approaching the carrier whereas in reality it takes the form of a Lorentzian shape [42]

From Equation (3.40), the total power of phase-noise from minus infinity to plus infinity is 1, this means that phase-noise does not change the total power of the oscillator; it merely broadens its spectral peak. Attempting to match the Leeson calculated curve "A" (Figure 3-12) considering the Equation (3.40), the measured curve requires totally different values than those assumed due to up-conversion and down-conversion of noise components from harmonically related frequencies to around carrier frequency as depicted in Figure 3-13 [37]-[39].

The influence of low frequency noise component in stable frequency sources is paramount and determining factor for phase hits due to time-jitter noise dynamics. Particularly, the effect of low-frequency flicker noise components on close-in phase-noise is not well defined in Leeson's model. The model asserts that the phase-noise $1/f^3$ corner frequency is exactly equal to the amplifier's flicker-noise corner frequency (f_c), but measurements do not clearly show such equality [38]. This is because Leeson models the oscillator as a time-invariant system, whereas oscillators are in general cyclostationary (cyclostationary process: Signal having statistical properties that vary cyclically with time) time-varying systems due to the presence of the periodic large-signal oscillation. This issue has been addressed by several authors [33]-[48]. Lee and Hajimiri [36] has shown that the oscillator's phase-noise $1/f^3$ corner frequency can be

significantly lower than the device's flicker corner frequency, provided that the oscillation signals at the output of the oscillator circuits are odd-symmetric.

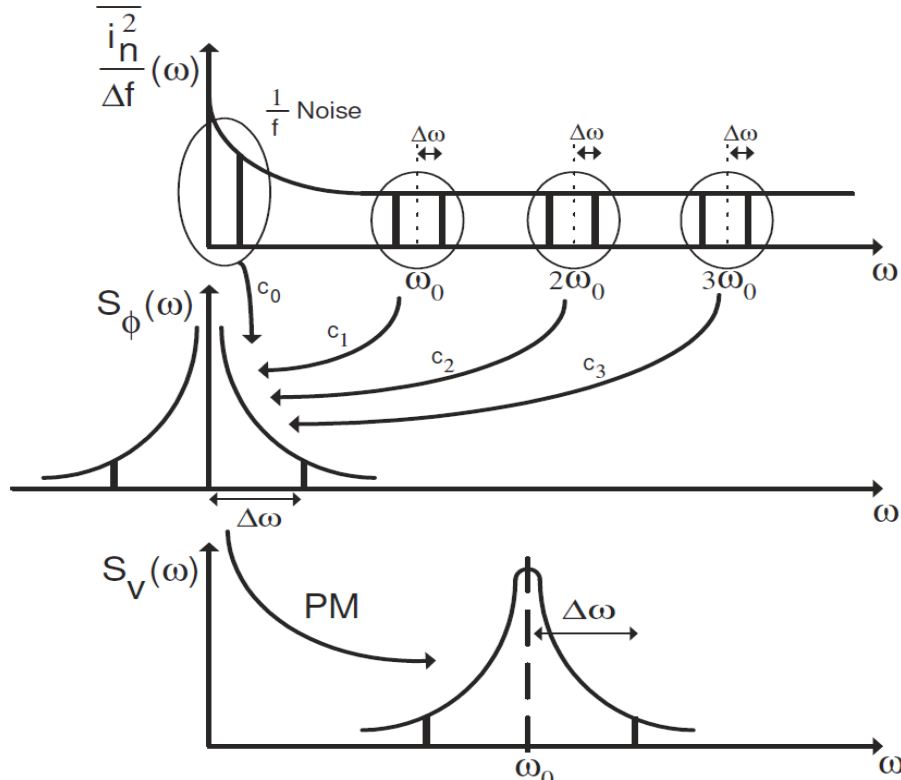


Fig. 3.13 Conversion process from noise ($S_n(\omega)$) to phase-noise ($L(\omega)$). Noise components from harmonically related frequencies are up/down-converted to around carrier phase noise, Leeson's model fails to address this phenomenon [36].

The basic concept of the Leeson equation gives a quick approximate valuation of the phase noise performance for oscillator circuits, including the trend for the minimization of noise if following unknown terms are assumed and inserted properly; the computed results will agree within a reasonable degree of the accuracy but not the error free prediction. The information that is not known prior to the measurement is [4]:

- a) the output power,
- b) the noise figure under large-signal conditions, and
- c) the loaded (operational) noise figure
- d) flicker up conversion dynamics
- e) singularity at close to carrier

In conclusion, Leeson's model assumes linear approach but oscillators are inherently nonlinear, it is expected that such a linear phase noise model would predict the phase noise of an oscillator with a significant error.

3.2.2 Lee and Hajimiri's Noise Model (Linear Time Variant Model)

To overcome the limitation of linear time invariant phase noise model (Leeson's phase noise model), Lee and Hajimiri proposed linear time varying [LTV] phase noise model to predict the noise properties of the oscillator output waveform [36, 43, 44, 45]. There were many LTV

models around and before Lee and Hajimiri, explaining the phase noise dynamics of autonomous circuits (oscillators) for a given nonlinearity associated with the circuits in large signal conditions. Lee and Hajimiri's noise model is based on the linear time varying [LTV] properties of the oscillator current waveform, and the phase noise analysis is given based on the effect of noise impulse on a periodic signal.

Figure 3-14 shows the noise signal in response of the injected impulse current at two different times, peak and zero crossing. As illustrated in Figure 3-14, if an impulse is injected into the tuned circuit at the peak of the signal, it will cause maximum amplitude modulation and no phase modulation whereas; if an impulse is injected at the zero crossing of the signal, there will be no amplitude modulation but maximum phase modulation.

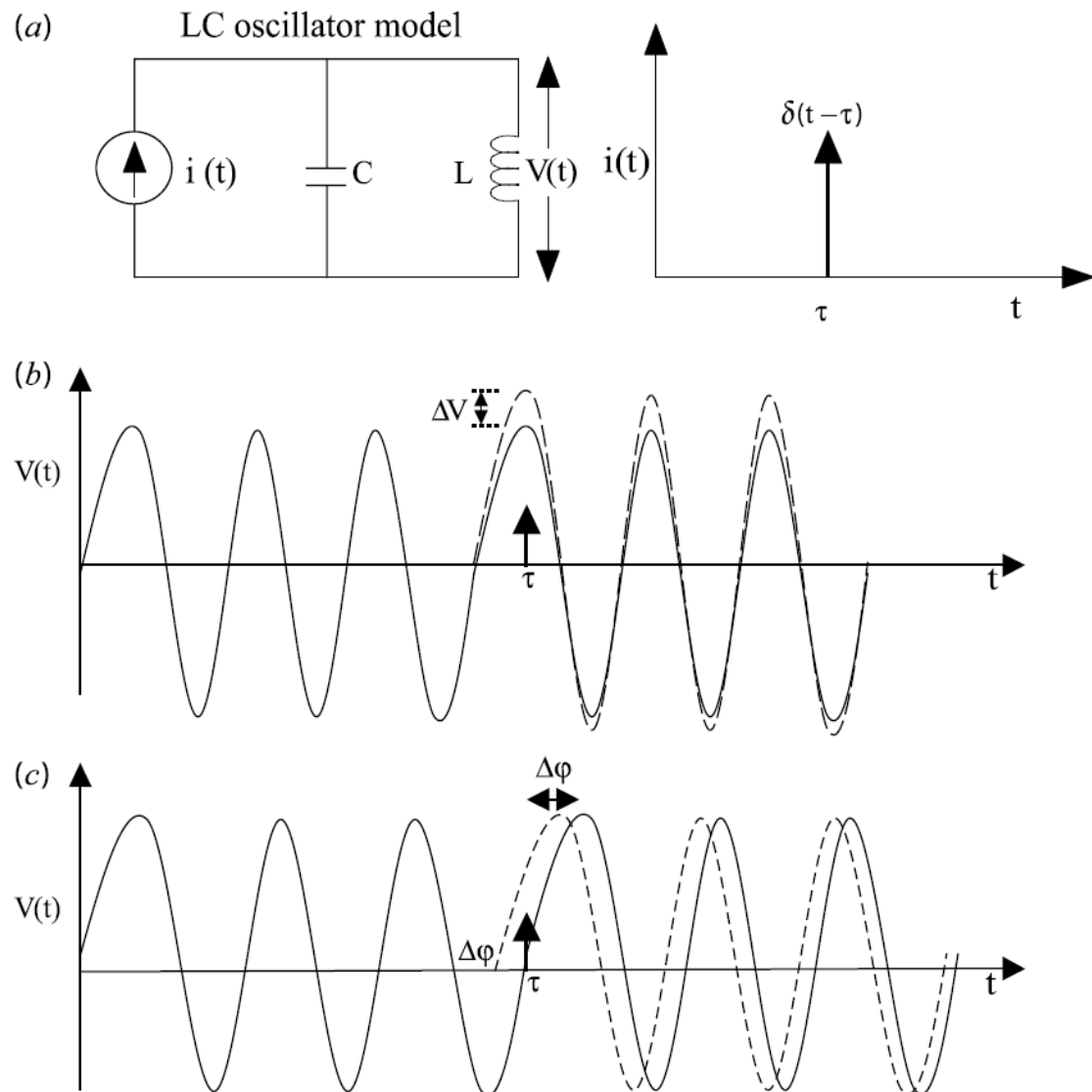


Figure 3-14: a) A typical LC oscillator excited by current pulse b) Impulse injected at peak of the oscillation signal and c) Impulse injected at zero crossing of the oscillation signal [4].

If noise impulses are injected between zero crossing and the peak, there will be components of both phase and amplitude modulation. Variations in amplitude are generally ignored because they are limited by the gain control mechanism of the oscillator. Therefore, according to this theory, to obtain the minimal phase noise, special techniques have to be adopted so that any noise impulse should coincide in time with the peaks of the output voltage signal rather than at the zero crossing or in between of zero-crossing and peak [18].

Lee and Hajimiri introduced an impulse sensitivity function (ISF) based on injected impulse, which is different for each topology of the oscillator [43]-[45]. It has its largest value when the most phase modulation occurs but has the smallest value when only amplitude modulations occur. This model is a kind of impulse response function that defines the phase noise versus device noise transfer function, in a manner similar to an impulse-response function in a linear circuit. The calculation of the ISF is tedious and depends upon the topology of the oscillator. Based on this theory, phase noise equation is expressed as [36]

$$f(f_m) = \begin{cases} 10\log\left[\frac{C_0^2}{q_{\max}^2} * \frac{i_n^2 / \Delta f}{8f_m^2} * \frac{\omega_{1/f}}{f_m}\right] & \frac{1}{f^3} \rightarrow \text{region} \\ 10\log\left[10\log\left[\frac{\Gamma_{rms}^2}{q_{\max}^2} * \frac{i_n^2 / \Delta f}{4f_m^2}\right]\right] & \frac{1}{f^2} \rightarrow \text{region} \end{cases} \quad (3.41)$$

where

$i_n^2 / \Delta f$ = Noise power spectral density

Δf = Noise bandwidth

$\Gamma_{rms}^2 = \frac{1}{\pi} \int_0^{2\pi} |\Gamma(x)|^2 dx = \sum_{n=0}^{\infty} C_n^2$ = Root mean square (RMS) value of $\Gamma(x)$

$\Gamma(x) = \frac{C_0}{2} + \sum_{n=1}^{\infty} C_n \cos(nx + \theta_n)$ = Impulse Sensitivity function (ISF)

C_n = Fourier series coefficient

C_0 = 0th order of the ISF (Fourier series coefficient)

θ_n = Phase of the nth harmonic

f_m = Offset frequency from the carrier

$\omega_{1/f}$ = Flicker corner frequency of the device

q_{\max} = Maximum charge stored across the capacitor in the resonator.

At first glance, it appears that LTV model overcomes the shortcomings of LTIV model presented by Leeson [1]. However, careful assessment of Lee and Hajimiri LTV model reveals that there are difficulties with its application to phase noise prediction. This follows since, apart from the ISF, the phase noise does not directly describe the effect of circuit parameters e.g. capacitance, inductances, resistance, transistor parameters, etc.). In order to obtain a quantitative phase noise solution for a circuit, the ISF is to be calculated by computer

simulation on the oscillator circuit. Since analytical solutions for the ISF in terms of circuit parameters are mostly non-existent, it can only be done numerically. As a result, insight into how the physics of the oscillator circuit parameters can be manipulated to yield improved phase noise performance is lost.

Equation (3.41) is a generalization of Leeson's model if it is evaluated at the hand of underlying assumptions (as shown in Figure 3-12 and Figure 3-13), but it is a step closer to the numerical computer simulation with the penalty of analytical insight bound to physical parameters. While Leeson's model retained the loaded quality factor of the resonator (a physical parameter), Lee and Hajimiri model gives up as many of the physical circuit parameters as possible (unifying the effect of such parameter into a single ISF). This results in loosing valuable insight that its retention could have brought to the approach for minimization of phase noise dependence on such parameters [7].

Various other conclusions are drawn that amount to manipulation of the ISF, but such conclusions are removed from what can be implemented through oscillator circuit design. Nevertheless LTV model does yield some insights that Leeson's model lack, first it reveals that if the active element in an oscillator were able to instantaneously restore the energy transferred to the resonator at precisely the right moment in the oscillation cycle, then it would in principle limit the phase noise to a minimum, which is validated by the examination of the Colpitts oscillator circuit [36]. Second, the phase noise can be reduced by increasing the maximum charge displacement q_{\max} in Equation (3.41), this can in some case be physically accomplished by increasing the output power level of the oscillation signal - although this insight is more specific; it is something already known from LTIV based Leeson's model. Third, any phase noise present around integer multiples of the oscillation frequency is frequency translated to appear as phase noise sidebands around the oscillation signal.

In conclusion, LTI based noise model gives good results once all the data is known, but does not lead to exact design rules. The Equation (3.41) using LTV theory though providing a good tool for explaining the phase noise spectrum in oscillators especially the $1/f^3$ region, suffers from a following shortcomings [38]:

- a) It assumes that oscillators are inherently linear time variant, but does not give a concrete reason for this
- b) It is based on the parameter impulse sensitivity function (ISF), which is very difficult to determine
- c) It does not provide insight into the factors affecting performance in oscillator design

As described above, the implication of Lee and Hajimiri's theory is that the designer does not have much control in terms of the oscillator circuit component parameters over the timing of the noise impulse injected into the oscillator circuit.

The noise analysis based on the signal drive level and the conduction angle of the time-varying properties of the oscillator current waveform can overcome partly the drawback associated with Lee and Hajimiri's Noise Model [33].

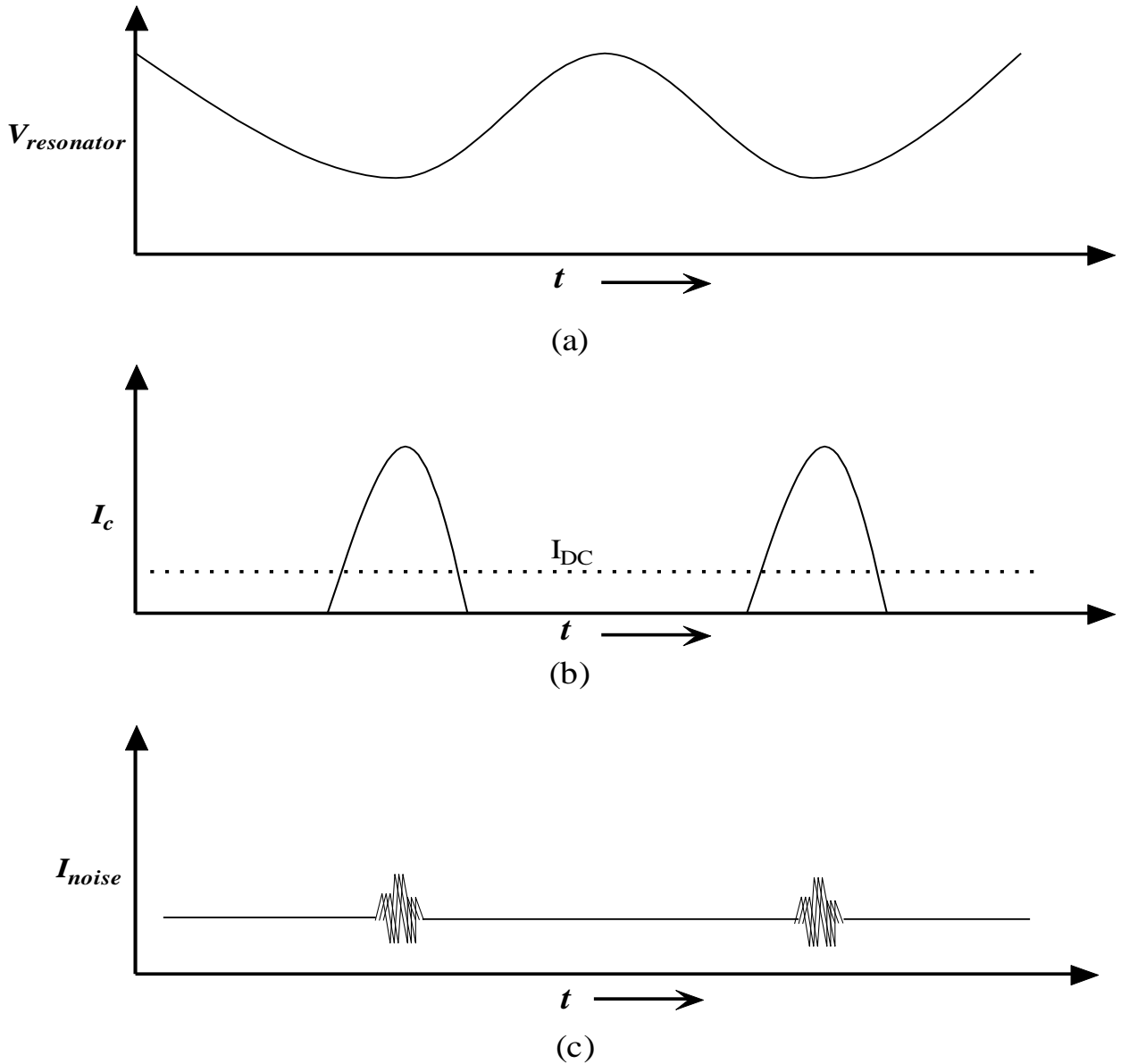


Figure 3-15: The plots show (a) voltage across resonator, (b) oscillator output RF current, and (c) noise current [4].

As shown in Figure 3-15, the drive-voltage ($v_{resonator}$) produces an output current i_c consisting of a series of current pulses, its shape and conduction angle depends upon the strength of the signal drive level [98]. Figure 3-15 (c) shows the typical noise current i_{noise} relative to the RF current i_c as depicted in Figure 3-15 (b) for a LC-Colpitts oscillator in presence of resonator signal voltage $v_{resonator}$ (shown in Fig. 3-15 (a)). The natural operation of the oscillator will cause the current pulses to be centered on the negative peaks of the resonator tank voltages and the associated noise components depend on the conduction angle (width of the RF current pulse). From Rohde's noise model [98], the conduction angle φ ($\varphi \propto 1/C_2$) is inversely proportional to the feedback capacitor C_2 , and directly proportional to the drive-level x ($x \propto C_2$).

The following example given in the Figure 3-16 illustrates the typical circuit diagram of the 100 MHz LC Colpitts oscillator for giving insight into the relationship between the drive level, the current pulse, and the phase noise [4]. As shown in Figure 3-15, the majority of noise current exists only during collector current pulses and the oscillator output current will be negligible or zero during the time between output current pulses, and therefore, aside from thermal noise, the noise sources, which depend on current such as shot, partition, and 1/f, exist only during the conducting angle of output current pulses. If the signal drive level is increased, the oscillator output current pulse will be narrower, and consequently, noise pulse during conduction angle becomes narrower, and thereby, has less PM noise contribution than the wider pulse.

Table 3-1 shows the drive level for different values of C_2 for a 100 MHz oscillator. The collector current of the circuit shown in the Figure 3-16 plotted in Figure 3-17 using CAD simulator (Ansys: Ansoft Designer 8), becomes narrower as the drive level x increases, and the corresponding base voltage V_{base} swing increases as illustrated in Figure 3-18 [18].

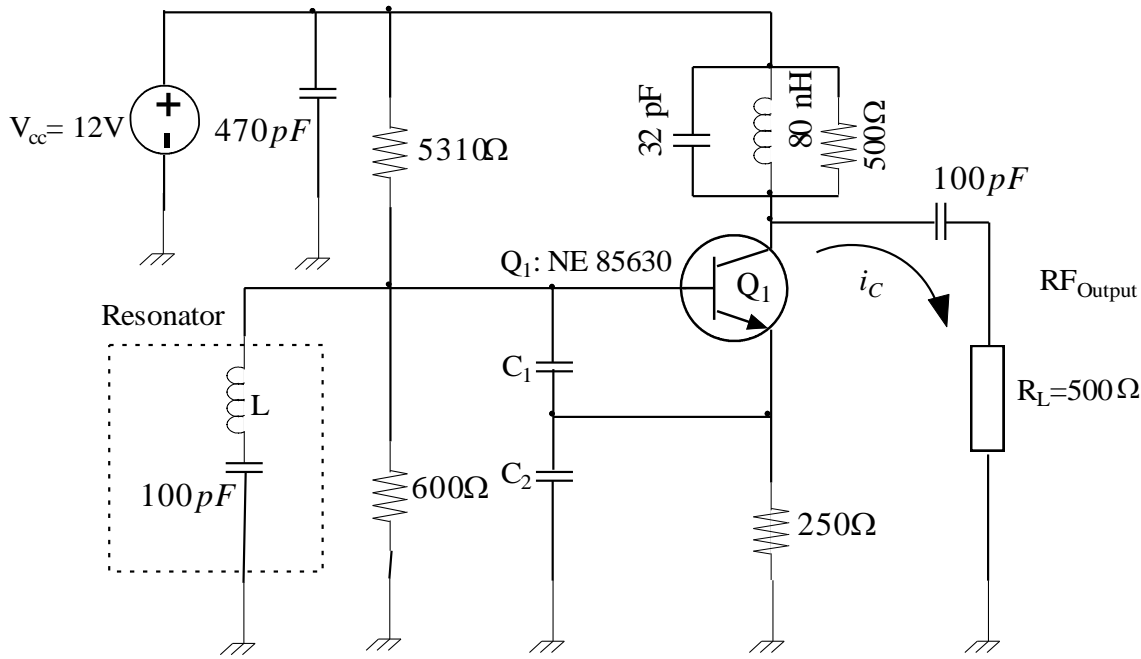


Figure 3-16: Schematic of 100 MHz LC Colpitts oscillator [18]

Table 3-1: Drive level for different values of C_2 for a 100MHz Oscillator

$x = \frac{qV_{base}}{kT}$	C_1	C_2	L	Phase Noise @10 kHz offset	Frequency
3	500pF	50pF	80nH	-98dBc/Hz	100MHz
10	500pF	100pF	55nH	-113dBc/Hz	100MHz
15	500pF	150pF	47nH	-125dBc/Hz	100MHz
20	500pF	200pF	42nH	-125dBc/Hz	100MHz

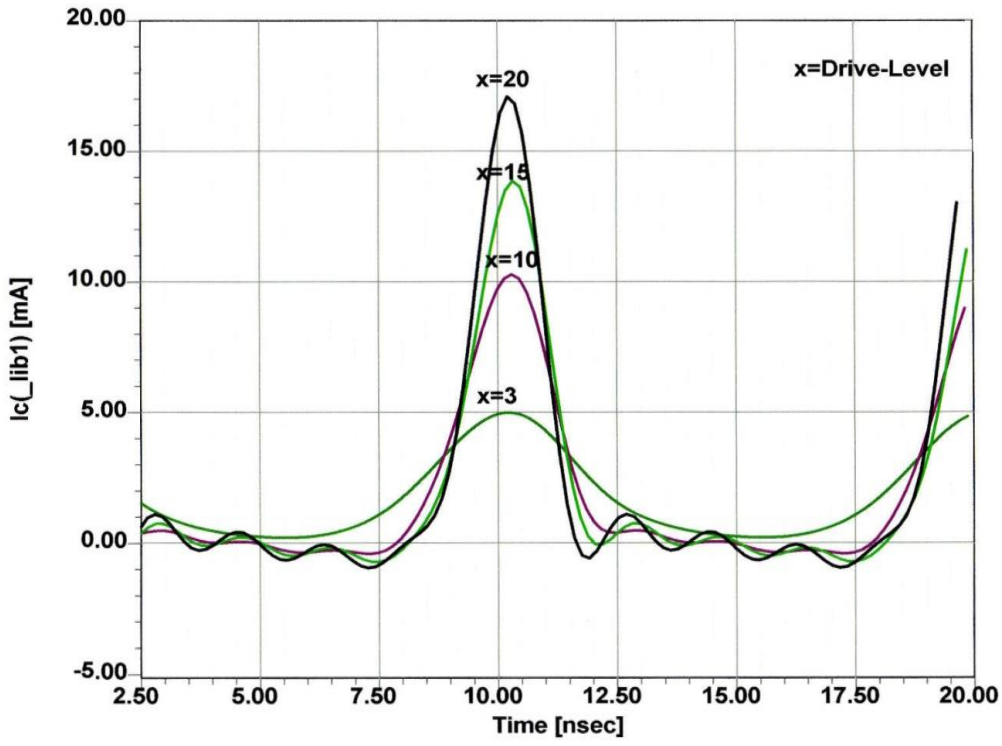


Figure 3-17: RF current as a function of the normalized drive level x for the oscillator circuit (as shown in the Figure 3-16) [18]

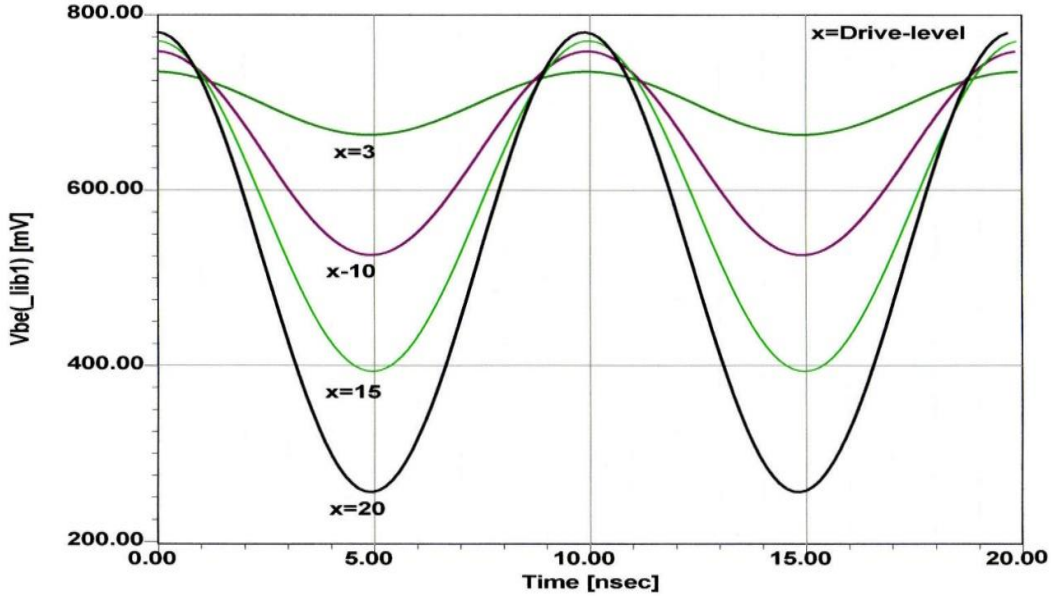


Figure 3-18: RF voltage V_{be} across the base emitter as a function of the normalized drive level x .

The improvement in the phase noise, with respect to the drive level, is shown in Figure 3-19, and it is limited by the strong harmonic content due to the large signal drive level.

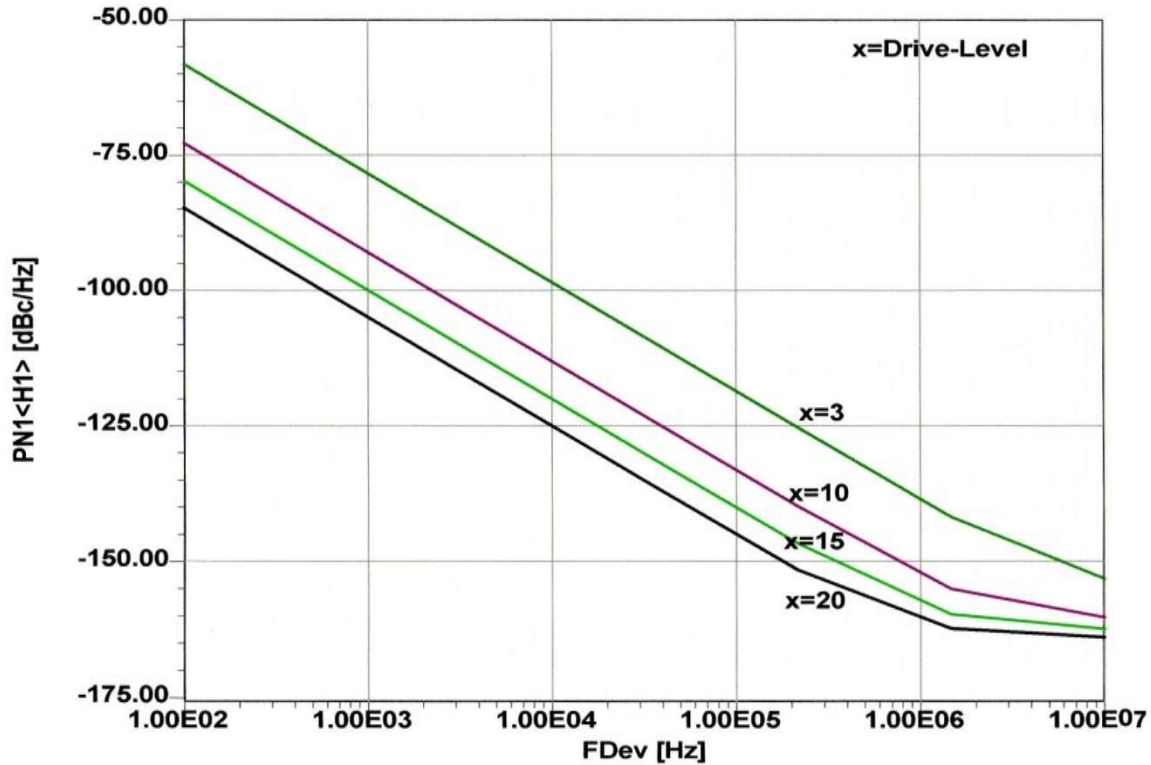


Figure 3-19: Phase noise as a function of the normalized drive level x for the circuit shown in Figure 3-18.

Introducing the signal drive level concept in conjunction with oscillator output current conduction angle, the phase noise Equations (3.28) can be expressed as [4, pp. 180]

$$\xi(\omega) = 10 \log \left\{ 4kTR + \left[\frac{4qI_c g_m^2 + \frac{4K_f I_b^{AF}}{\omega} g_m^2}{\omega_0^2 C_1 (\omega_0^2 (\beta^+)^2 C_2 + g_m^2 \frac{C_2^2}{C_1})} \right] \left[\frac{\omega_0^2}{4\omega^2 V_{cc}^2} \right] \left[\frac{Q_o^2}{Q_L^2} + \frac{[C_1 + C_2]^2}{C_1^2 C_2^2 \omega_0^4 L^2 Q_L^2} \right] \right\} \quad (3.42)$$

where

$$\beta^+ = \left[\frac{Y_{21}^+}{Y_{11}^+} \right] \left[\frac{C_1}{C_2} \right]^p$$

$$g_m = \left[Y_{21}^+ \right] \left[\frac{C_1}{C_2} \right]^q ; \text{ values of } p \text{ and } q \text{ depends upon the drive level (x)}$$

Y_{21}^+ , Y_{11}^+ = large signal [Y] parameter of the active device

K_f = flicker noise coefficient

AF = flicker noise exponent

$\xi(\omega)$ = ratio of sideband power in a 1Hz BW at ω to total power in dB

ω = frequency offset from the carrier

ω_0	= center frequency
Q_L	= loaded Q of the tuned circuit
Q_U	= unloaded Q of the tuned circuit
kT	= 4.1×10^{-21} at 300 K (room temperature)
R	= equivalent loss resistance of the tuned resonator circuit
I_c	= RF collector current
I_b	= RF base current
V_{cc}	= RF collector voltage
C_1, C_2	= feedback capacitor as shown in the Figure 3-16.

Equation (3.42) gives clear insight and apriori estimation of the phase noise in terms of the operating condition and circuit parameters (validation examples and numerical results are described in Ref. 4, pp. 181-199). However, all three noise models discussed above linear and quasi-linear free-running oscillator circuit, do not explain in detail about the chaotic condition witnessed in presence of strong linearity of autonomous circuits. Therefore, suggesting the need for noise analysis for nonlinear time variant noise model for oscillator circuits [47]-[62].

3.2.3 Kaertner, Demir, Ngova's Noise Model (Nonlinear Time Variant)

Even though the LTV method is able to explain how the device noise around the oscillator's harmonics affects the phase noise, it is a matter of fact that the oscillator behavior is nonlinear by nature. Therefore, it can be expected that the results obtained from Linear Time Variant (LTV) noise model will not take into account, the associated nonlinearity in the oscillator circuits, hence cannot offer unified solution. For simplification in analysis, some approximations employed in the LTV method, turn out to be false assumption [48] even though it provides design flow for noise dynamics. To overcome the limitation of LTV noise model, there have been several attempts to analyze the phase noise using nonlinear time variant (NLTV) techniques, perhaps the most acknowledged of these is presented by Kaertner and Demir in [38, 39, 46, and 47].

Kaertner and Demir pointed out the flaws of LTIV and LTV models that both the total integrated power and the noise power density at the carrier are infinite-a physical impossibility. To overcome these discrepancies, nonlinear time variant (NLTV) phase noise model was proposed from the fundamental differential equation description for a general oscillator by taking noise perturbation signals into account [39]. The proposed NLTV phase noise model is based on orbital asymptotic stability theory using white and modulated-white noise sources with power spectrum falling $1/f^k$ for any $k \in N$, it is proved that such white and modulated-white noise sources led to a phase deviation, $\phi(t)$, which is characterized as a stochastic process with characteristic function, $F(\omega, t)$, described by a mean, $\mu(t)$, and a variance, $\sigma(t)$. Stability theory addresses the following questions: will a nearby orbit indefinitely stay close to a given orbit? Will it converge to the given orbit? In the former case, the orbit is called stable and in the latter case, asymptotically stable, or attracting. Figure 3-20 illustrates the stability planes for asymptotically stable, marginally stable, and unstable conditions.

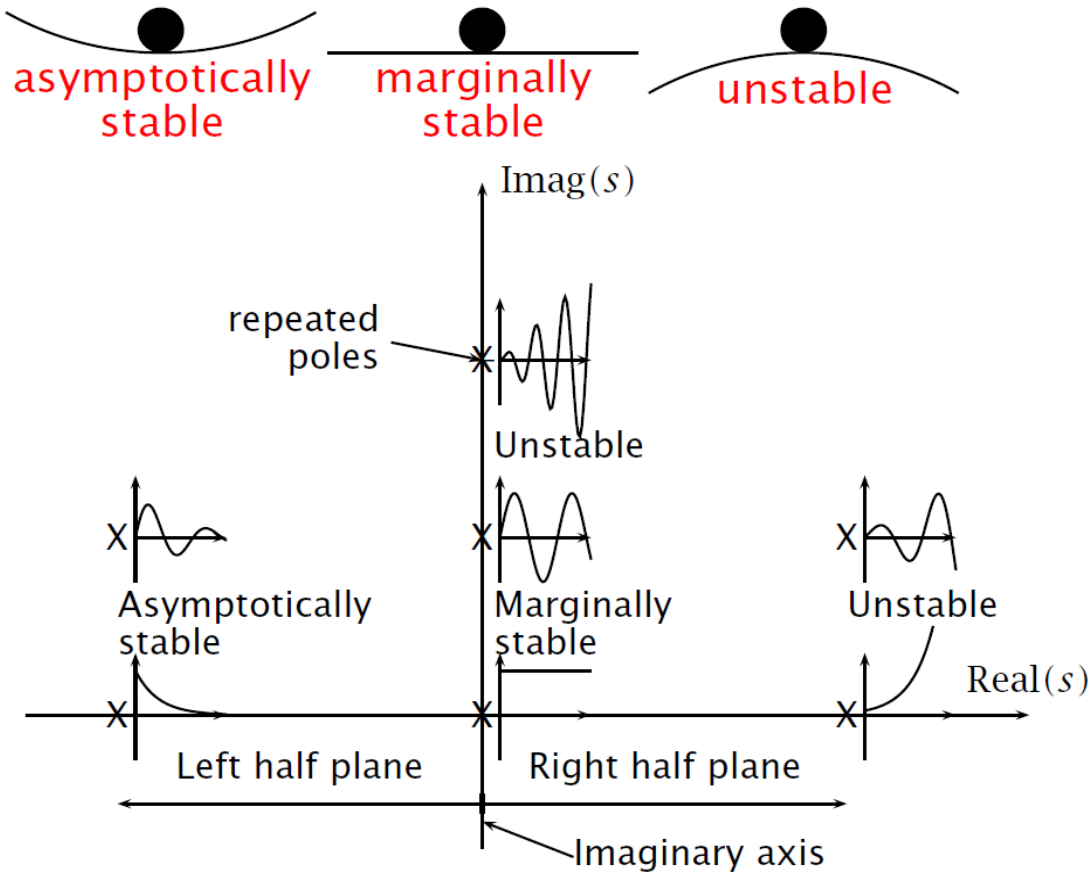


Figure 3-20: shows the stability plane for asymptotically stable, marginally stable, and unstable condition [39]

For such white noise and modulated white noise sources, the phase noise power spectrum is analytically derived for angular frequency ω_o of carrier signal as:

$$S(\omega) = \sum_{k=-\infty}^{\infty} X_k X_k^* \frac{4\omega_o^2 k^2 p}{\omega_o k^4 p^2 + 4(\omega + k\omega_o)^2} \quad (3.43)$$

Where X_k is Fourier coefficient of the asymptotically (as shown in Figure 3-20) orbitally stable periodic solution. This implies that n -dimensional stable limit cycle solution based on standard nonlinear analysis technique of linearizing around a nonlinear stable limit cycle solution, implies that $x_s(t)$ is simply the unperturbed oscillation signal to the oscillation $x_s(t)$, as:

$$x_s(t) = \sum_{k=-\infty}^{\infty} X_k e^{jk\omega_o t} \quad (3.44)$$

$p = \frac{d}{dt} [\sigma^2(t)]$, which physically translates to the rate of change of the squared variance, σ , to the Gaussian solution of the characteristic function, $F(\omega, t)$, of the phase deviation $\phi(t)$.

The Equation (3.43) is so general that it does not even need to be an electrical system and valid for any physically realizable system (electrical, mechanical, biological, etc.) that exhibits stable oscillatory behavior. The NLTV phase noise model proposed by Kaertner and Demir using differential equations for describing the frequency and amplitude response of oscillators

through perturbation techniques is unequalled in its generality, accuracy and efficient computational complexity, but the physics of the circuit is completely lost by a pure statistical characterization of the system [37]-[49].

The solution of Equation (3.43) is derived by computer but poorly suited to analytical computation by hand on paper (It is just like anything else that is useful, correct, and accurate in the world of nonlinearity). Initial guess of Equation (3.43) is the $1/f^2$ phase noise reduction with frequency and so qualitatively reveals nothing more than what can be learned from linear phase noise models [50]-[61].

The noise model is based on differential equations describing the amplitude and phase deviations of the oscillator in terms of Taylor series expansions, assuming that the underlying device noise can be completely described stochastically [63]-[82]. The stochastic differential equations so obtained are solved to obtain the final expression of phase noise. Since flicker noise is difficult to characterize in time domain, Kaertner and Demir obtain approximate series solutions. The time domain phase noise algorithm for Equation (3.43) becomes numerically unstable when the concerned oscillator employs a high Q resonator (Crystal resonator, $Q \geq 10^6$).

Similarly, the frequency domain phase noise algorithm for Equation (3.43) depends on the numerical method of harmonic balance using CAD simulator (AWR, Agilent ADS 2013, Ansys-Ansoft Designer 8) - a method which is similarly known to be problematic (convergence and accuracy) when applied to oscillators with high Q resonators [83]-[92]. The phase noise models depend on complex parameters, have no circuit focus, and require special tools and efficient algorithms to evaluate the model parameters.

The main drawbacks of this model is noise analysis, mainly takes into account white noise sources, hence only phase noise with a $1/f^2$ characteristic, and it is therefore not straightforward to use their result in practical design and also numerical characterization of phase noise, breaks down when extremely low phase noise Crystal oscillators are considered. It mainly attempts to establish a foundation theory for the description of phase noise in nonlinear systems, which has been lacking earlier [93]-[98].

Ngova et.al proposed phase noise model based on envelope transient simulation technique for arbitrary circuit topology [96]. The frequency conversion and modulation effects taking place in a free running oscillator because of noise perturbation are intimately linked within a single equation however phase noise model is not free from convergence problems for high Q resonator based oscillator circuits.

3.2.4 Multiple Threshold Crossing Noise Model

The noise model (LTIV, LTV and NLTV) discussed in section (3.2.1)-(3.2.3) explains the noise dynamics of LC resonator based “Harmonic Oscillators”. The LTIV, LTV and NLTV model (all are frequency based) are good for resonant based (like LC resonator, Crystal resonator, Surface Acoustic Wave resonator, Dielectric resonator, printed transmission line resonator) but not suitable for RC relaxation and ring oscillator circuits. In particular, relaxation oscillator has noise jump/spikes (chaos/bifurcation) due to regeneration during transition, which cannot be easily modeled by frequency-based method. The poor phase noise performance of time/waveform

based oscillator (like relaxation, ring, and multivibrator) limits the figure of merit (FOM) in RF systems as compared to harmonic oscillator (LC tank oscillator).

There is a need to improve the phase noise performance of single energy storage reactive element (capacitor) oscillator such as RC oscillator (like relaxation and ring oscillators) for taking the advantage of integrated solution using existing MMIC technologies. The noise model based on threshold crossing is ideal for time/waveform based oscillator (relaxation and ring) [93]-[96].

3.2.5 Conclusion on Phase Noise Models

Table 3-2 describes the relative strength and weakness of the three-phase noise models discussed above for the characterization of oscillator circuits [97]-[101]. All the three models as discussed above and shown in Table 3-2 for harmonic oscillators, one can argue the superiority of any of the three models based on accuracy, reliability, simulation time, and convergence for a given oscillator circuit topology. The noise model for non-harmonic oscillator circuits (proposed by A. Abidi, A. Hajimiri, B. Razavi, R. Navid, T. Lee, R. Duton, and B. Leung) such as relaxation and ring oscillator circuits, Leung highlighted the inadequacy of traditional first passage time (FPT) model and the need for the last passage time (LPT) model in representing the threshold crossing behavior of time/waveform based oscillator [68]-[84].

The noise model discusses the timing jitter based on the LPT model. Leung's noise model is based on multiple thresholds crossing concept, which considers the impact caused by both noise and slew rate changing as transistors change between triode/saturation. It also develops a link between the last passage and FPT model and indicates when the difference between the two models becomes significant. Using multiple thresholds crossing concept, a new and more accurate way of handling such a regional change is formulated and developed [99]-[101].

For a typical ring oscillator with an arbitrary voltage swing, core transistors in delay cells move between saturation and triode region, resulting timing jitter accumulated within a particular region. Leung's LPT model for the threshold crossing offers more accurate description than the conventional FPT model when the noise/ramp ratio is not small.

Table 3-2: Describes the relative strength and weakness of the 3-noise models [97]-[101]

Model	Leeson	Lee and Hajimiri	Kaertner and Demir
Assumptions	LTIV	LTV	NLTIV
Perturbing noise Source	white noise (KTB)	Cyclostationary $1/f^k$ for any $k \in N$	Modulated $1/f^k$ for any $k \in N$
Accuracy	Reasonable	Good	Exact
Simplicity	Simple	Moderate	Involved
Computer dependence	Independent (Calculation by hand)	Computer to evaluate ISF	Computer dependent (no closed form solutions)
Predicts close-in phase noise	No	Yes	Yes
Retained circuit parameters	Loaded Q-factor (Q_L), output power (P_s)	q_{\max}	None

Comparing the noise models discussed for harmonic (LC resonator type) and non-harmonic oscillator circuits (RC oscillator type), it is up to the designers to choose noise models for analyzing the autonomous circuits because none of the models allow closed form solution for phase noise - a unified solution needed for any typical oscillator circuit for an optimum figure of merit (FOM) is being discussed in this manuscript of Chapter 1, Equation (1.1)-(1.3) [101].

3.3 References

- [1] D. B. Leeson, "A Simple Model of Feedback Oscillator Noise Spectrum," IEEE, Proc. pp. 329-332, 1966.
- [2] U. L. Rohde, A. K. Poddar, and R. Rebel," Integrated Low Noise Microwave Wideband Push-Push VCO", US Patent No. 7,088189, Aug 2006.
- [3] K. Hosoya, S. Tanaka, Y. Amamiya, T. Niwa, and H. Shimawaki, and K. Honjo, "A low phase-noise 38-GHz HBT MMIC oscillator utilizing a $(\lambda/4 \pm \delta)$ open stubs resonator," APMC, pp. 64-67, Singapore, 1999.
- [4] U. L. Rohde, A. K. Poddar, and G. Boeck, Modern Microwave Oscillators for Wireless Applications: Theory and Optimization, John Wiley & Sons Inc., 2005.
- [5] A, P. S. (Paul) Khanna, "Microwave Oscillators: The State of The Technology", Microwave Journal, Vol 4., pp. 22-42, April 2006.
- [6] J.C. Nallatamby, M. Prigent, M. Camiade, and J. Obregon, "Phase noise in oscillators – Leeson formula revisited". IEEE Transactions on Microwave Theory and Techniques, Vol. 51, No. 4, pp. 1386-1394, April 2003.
- [7] A. Suárez, S. Sancho, S. Ver Hoeye, and J. Portilla, "Analytical comparison between time- and frequency-domain techniques for phase-noise analysis". IEEE Transactions on Microwave Theory and Techniques, Vol. 50, No. 10, pp. 2353-2361, October 2002.
- [8] S. Ver Hoeye, A. Suárez, and J. Portilla, "Techniques for oscillator nonlinear optimization and phase-noise analysis using commercial Harmonic-Balance software", IEEE MTT-S Digest, pp. 95-98, 2000.
- [9] V. Rizzoli, F. Mastri, and D. Masotti, "General noise analysis of nonlinear microwave circuits by the piecewise Harmonic Balance technique". IEEE Transactions on Microwave Theory and Techniques, Vol. 42, No. 5, pp. 807-819, May 1994.
- [10] S. Sancho, A. Suárez, J. Dominguez, and F. Ramirez, "Analysis of near-carrier phase-noise spectrum in free-running oscillators in the presence of White and colored noise sources". IEEE Transactions on Microwave Theory and Techniques, Vol. 58, No. 3, March 2010, pp. 587-601.
- [11] Jia-Sheng Hong and M. J. Lancaster, "Aperture-Coupled Microstrip Open-Loop Resonators and Their Applications to the Design of Novel Microstrip Bandpass Filters", "IEEE Tran. MTT, Vol. 47, No. 9, pp. 1848-1855, September 1999.
- [12] Jia-Sheng Hong and M. J. Lancaster, "Coupling of Microstrip Square Open-Loop Resonators for Cross-Coupled Planar Microwave", "IEEE Transaction on MTT, Vol. 44, No. 12, pp. 2099-2109, December 1996.

- [13] Sheng Sun and Lei Zhu, "Guided-Wave Characteristics of Periodically Non uniform Coupled Microstrip Lines-Even and Odd Modes" "IEEE Transaction on MTT, Vol. 53, No. 4, pp. 1221-1227, April 2005.
- [14] U. L. Rohde and A. K. Poddar, "Tunable Frequency, Low Phase Noise and Low Thermal Drift Oscillator", US Patent No.7196591, March 01, 2007.
- [15] U. L. Rohde and A. K. Poddar, "Wideband voltage controlled oscillators employing evanescent mode coupled resonators," US Patent No. 71803812, Feb 2007.
- [16] U.L. Rohde, "A New Efficient Method of Designing Low Noise Microwave Oscillators," Dr.-Ing. Dissertation, TU-Berlin, Germany, Faculty IV, EEC (Electrical Engineering and Computer Sciences), 12 February 2004.
- [17] U. L. Rohde, A. K. Poddar, Juergen Schoepf, Reimund Rebel, and Parimal Patel, "Low Noise Low Cost Wideband N-Push VCO," IEEE, IMS Symposium, USA, MTT-S 2005,.
- [18] A. K. Poddar, "A Novel Approach for Designing Integrated Ultra Low Noise Microwave Wideband Voltage-Controlled Oscillators", Dr.-Ing. Dissertation, TU- Berlin, Germany, Faculty IV, EEC (Electrical Engineering and Computer Sciences), 14 December 2004.
- [19] U. L. Rohde, A. K. Poddar, and R. Rebel, "Ultra Low Noise Low Cost Octave-Band Hybrid-Tuned VCO," 18th IEEE CCECE05, Canada, 2005.
- [20] U. L. Rohde and A. K. Poddar, "Ultra Low Noise Low Cost Multi Octave Band VCO", IEEE Sarnoff Symposium, Princeton, USA, April 2005.
- [21] A. K. Poddar and K. N. Pandey, "Microwave Switch Using MEMS-Technology", 8th IEEE International Symposium on High Performance Electron Device for Microwave and Optoelectronic Applications, November 2000.
- [22] U. L. Rohde and A. K. Poddar, "Configurable Ultra Low Ultra Wideband Power Efficient VCOs", 11th European Wireless, Conference, Cyprus, 10-13 April 2005.
- [23] U. L. Rohde, K. J. Schoepf and A. K. Poddar, "Low-Noise VCOs Conquer Wide Bands", Microwave & RF, pp. 98-106, June 2004.
- [24] U. L. Rohde and A. K. Poddar, "Configurable Adaptive Ultra Low Noise Wideband VCOs," Proc. IEEE Int. Conf. Ultra-Wideband, Switzerland, pp 452-457, Switzerland, September 5-8, 2005.
- [25] U. L. Rohde and A. K. Poddar, "Reconfigurable Wideband VCOs," IEEE, PIMRC2005, Germany, September 11-14, 2005.
- [26] U. L. Rohde and A. K. Poddar, "Ultrawideband (UWB) RF Signal Source," IEEE, ISWCS2005, Italy, September 5-7, 2005.
- [27] To-Po Wang, Zuo-Min Tsai, Kuo-Jung Sun, and Huei Wang, "Phase-Noise Reduction of X-Band Push-Push Oscillator with Second-Harmonic Self-Injection Techniques", IEEE Trans. MTTT, vol. 55, No. 1, pp. 66-77, Jan 2007.
- [28] K. Hoffmann and Z. Skvor," Active resonator", EUROCON 2001 proceeding, IEEE, Vol.1; pp. 164-166, Bratislava, 2001.
- [29] A. K. Poddar and U. L. Rohde, "Techniques Minimize the Phase Noise in Crystal Oscillators", 2012 IEEE FCS, pp. 01-07, May 2012.
- [30] A. K. Poddar, "Expert Tips, Tricks and Techniques", Microwave Journal, pp.22, July 2012
- [31] A. K. Poddar and U. L. Rohde, "Latest Technology, Technological Challenges, and Market Trends for Frequency Generating and Timing Devices", IEEE Microwave Magazine, pp.120-134, October 2012.

- [32] Dorin Calbaza, Chandra Gupta, Ulrich L. Rohde, and Ajay K. Poddar, "Harmonics Induced Uncertainty in Phase Noise Measurements", 2012 IEEE MTT-S Digest, pp. 1-3, June 2012.
- [33] U. L. Rohde and A. K. Poddar, "Noise Minimization Techniques for Voltage Controlled Crystal Oscillator (VCXO) Circuits", IEEE Radio Wireless Symposium, SAN Diego, CA, USA, Jan 18-22, 2009.
- [34] W.P. Robins, "Phase Noise in Signal Sources" London: IEEE Telecommunications Series 9, 1982.
- [35] T. H. Lee, A. Hajimiri, "Oscillator phase-noise: a tutorial," IEEE J. Solid-State Circuits, vol. 35, no. 3, pp. 326-336, March 2000.
- [36] A. Hajimiri and T. H. Lee, "A general theory of phase noise in electrical oscillators," IEEE J. Solid-State Circuits, vol. 33, no. 2, pp. 179-194, Feb. 1998.
- [37] D.B. Sullivan, "Characterization of Clocks and Oscillators" National Bureau of Standards Tech. Note, TN-1337, Feb 28, 1990.
- [38] A. Demir, A. Mehrotra, and J. Roychowdhury, "Phase noise in oscillators: a unifying theory and numerical methods for characterization," IEEE Trans. Circuits Syst. I, vol. 47, no. 5, pp. 655 – 674, May 2000.
- [39] M. Nick, " New Q-Enhanced Planar Resonators for Low Phase-Noise Radio Frequency Oscillators", PhD Dissertation, Electrical Engineering, University of Michigan, 2011
- [40] M. Odyniec, Editor, RF and Microwave Oscillator Design, Chapter 5: Modern Harmonic-Balance Techniques for Oscillator Analysis and Optimization, by V. Rizzoli, A. Neri, A. Costanzo, F. Mastri, Artech House, 2002.
- [41] B. Razavi, "A study of phase-noise in CMOS oscillators," IEEE J. Solid-State Circuits, vol. 31, no. 3, pp. 331-343, March 1996.
- [42] A. Demir, A. Mehrotra, and J. Roychowdhury, "Phase noise and timing jitter in oscillators" IEEE Custom Integrated Circuits Conference Proceeding, pp. 45-48, May 1998.
- [43] Hajimiri A and Lee T.H., Design Issues in CMOS Differential LC Oscillators.. IEEE Journal of Solid-State Circuits, 34(5), May 1999.
- [44] Hajimiri A and Lee T.H. The, "Design Of Low Noise Oscillators", Kluwer Academic Publishers, 1999.
- [45] A. Hajimiri, S. Limotyrakis, and T. H. Lee, "Jitter and Phase Noise in Ring Oscillators," IEEE Journal of Solid-State Circuits, vol. 34, no. 6, pp. 790-04, Jun. 1999.
- [46] Kaertner F X. Analysis of White and $f-\alpha$ Noise in Oscillators. International Journal of Circuit Theory and Application, Vol. 18, pp-485-519, October 1990.
- [47] Demir A., "Phase Noise And Timing Jitter in Oscillators With Colored-Noise Sources", IEEE Transactions on circuits and systems-1, 49(12):1782.1791, Dec 2002.
- [48] G.J. Coram. A simple 2-d oscillator to determine the correct decomposition of perturbations into amplitude and phase noise. Circuits and Systems I: Fundamental Theory and Applications, IEEE Transactions on, 48(7):896 –898, Jul 2001.
- [49] Agilent Phase Noise Measurement Solution, (www.home.agilent.com/application), 2012
- [50] W. F. Walls, "Cross-correlation phase noise measurements", IEEE Frequency Control Symposium, 46th Proceedings of the 1992 IEEE, pp. 257-261, May 1992.
- [51] A. L. Lance, W. D. Seal, F. G. Mendoza and N. W. Hudson, "Automating Phase Noise Measurements in the Frequency Domain," *Proceedings of the 31st Annual Symposium on Frequency Control*, 1977

- [52] W. F. Walls, "Cross-Correlation Phase Noise Measurements", IEEE FCS, pp. 257-261, 1992
- [53] W. F. Walls, "Practical problems involving phase noise measurements, 33th annual precise time interval (PTTI) meeting, pp. 407-416, 2001
- [54] F.L. Walls et al. Extending the Range and Accuracy of Phase Noise Measurements, Proceedings of the 42nd Annual Symposium on Frequency Control, 1988.
- [55] Noise XT, DCNTS manual, http://www.noisext.com/pdf/noisext_DCNTS.pdf, (2013)
- [56] Agilent E5052A Signal Source Analyzer 10 MHz to 7, 26.5, or 110 GHz – Datasheet”, Agilent document 5989-0903EN, p. 12, May 2007
- [57] Frequency Extension for Phase Noise Measurements with FSUP26/50 and Option B60 (Cross-Correlation)”, Rhode & Schwarz Application Note 1EF56, p. 3, Jan 2007
- [58] M. Jankovic, “Phase noise in microwave oscillators and amplifiers” , PhD thesis, Faculty of graduate School of the University of Colorado, Department of Electrical, Computer and Energy Engineering, 2010
- [59] Hewlett Packard, *RF and Microwave phase Noise Measurement Seminar*] Available at: http://www.hparecords.com/seminar_notes/HP_PN_seminar.pdf, April 2010
- [60] Stephan R. Kurz, *WJ Tech note – Mixers as Phase Detectors* Available at: http://www.triquint.com/prodserv/tech_info/docs/WJ_classics/Mixers_phase_detectors.pdf, May 2011.
- [61] Agilent Technologies, “Phase Noise Characterization of Microwave Oscillators – Phase Detector Method”, Product Note 11729B-1, Available at: <http://tycho.usno.navy.mil/ptti/ptti2001/paper42.pdf>, May 2010
- [62] Aeroflex, Application Note #2 – PN9000 automated Phase Noise Measurement System Available at: <http://www.datasheetarchive.com/datasheet-pdf/010/DSA00173368.html>, April 2010
- [63] Hewlett Packard.). *HP 3048A Phase Noise Measurement System Reference Manual* [online]. Available: <http://cp.literature.agilent.com/litweb/pdf/03048-90002.pdf>, (1989, Sept 01
- [64] E. Rubiola and F. Vernotte.. *The cross-spectrum experimental method* [online]. Available: <http://arxiv.org/>, document arXiv:1003.0113v1 [physics.ins-det], Feb 2010
- [65] Hewlett Packard. *HP 3048A Phase Noise Measurement System Operating Manual* [online]. Available: <http://cp.literature.agilent.com/litweb/pdf/03048-61004.pdf>, June 1990.
- [66] *HP 11848A Phase Noise Interface Service Manual*, 1st ed., Hewlett-Packard Company, Spokane., Washington, 1987.
- [67] M. Sampietro, L. Fasoli, and G. Ferrari, “Spectrum analyzer with noise reduction by cross-correlation technique on two channels,” *Rev. Sci. Instrum.*, vol. 70, no. 5, May 1999.
- [68] Abidi, A. A., and R. G. Meyer, "Noise in relaxation oscillators," *IEEE Journal of Solid-State Circuits*, vol. SC-18, no. 6, pp. 794-802, Dec. 1983.
- [69] Stuck, B. W., "Switching-time jitter statistics for bipolar transistor threshold crossing detectors," M. S. thesis, Massachusetts Institute of Technology, 1969.
- [70] A. Abidi, “How phase noise appears in oscillators”, http://www.rfdh.com/ez/system/db/pds_tn/upload/271/phase_noise.pdf, Nov 1997
- [71] R. Navid, T. H. Lee, and R. W. Dutton, “Minimum Achievable Phase Noise of RC Oscillators”, *IEEE JSSC*, VOL. 40, NO. 3, pp. 630-637, March 2005

- [72] L. DeVito, J. Newton, R. Croughwell, J. Bulzacchelli, and F. Benkley, "A 52 MHz and 155 MHz clock-recovery PLL," in *IEEE ISSCC Dig. Tech. Papers*, pp. 142–143, Feb. 1991.
- [73] I. A. Young, J. K. Greason, and K. L. Wong, "APLL clock generator with 5 to 110 MHz of lock range for microprocessors," *IEEE J. Solid-State Circuits*, vol. 27, no. 11, pp. 1599–1607, Nov. 1992.
- [74] A. Hajimiri, S. Limotyrakis, and T. H. Lee, "Jitter and phase noise in ring oscillators," *IEEE J. Solid-State Circuits*, vol. 34, no. 6, pp. 790–804, Jun. 1999.
- [75] R. Navid, T. H. Lee, and R. W. Dutton, "Lumped, inductorless oscillators: How far can they go?" In *Proc., IEEE Custom Integrated Circuits Conf.*, pp. 543–546, Sep. 2003.
- [76] A. A. Abidi and R. G. Meyer, "Noise in relaxation oscillators," *IEEE J. Solid-State Circuits*, vol. 18, no. 12, pp. 794–802, Dec. 1988.
- [77] B. Oksendal, *Stochastic Differential Equations*. Berlin, Heidelberg, Germany: Springer-Verlag, 1998.
- [78] R. L. Stratonovich, *Topics in the Theory of Random Noise*. New York: Gordon and Breach, Translated from Russian by R. A. Silverman, 1963.
- [79] R. Navid, T. H. Lee, and R. W. Dutton, "An analytical formulation of phase noise of signals with Gaussian distribution jitter," *IEEE Trans. Circuits Syst. II*, Vol. 52, Issue 3, pp 149-153, March 2005
- [80] B. Razavi, "A study of phase noise in CMOS oscillators," *IEEE J. Solid-State Circuits*, vol. 31, no. 3, pp. 331–343, Mar. 1996.
- [81] J. G. Sneep and C. J. M. Verhoeven, "A new low-noise 100-MHz balanced relaxation oscillator," *IEEE J. Solid-State Circuits*, vol. 25, no. 6, pp. 692–698, Jun. 1990.
- [82] F. Herzel, M. Pierschel, P. Weger, and M. Tiebout, "Phase noise in a differential CMOS voltage-controlled oscillator for RF applications," *IEEE Trans. Circuits and Syst. II*, vol. CAS2-47, no. 1, pp. 11–15, Jan. 2000.
- [83] Y. P. Tsividis, *Operation and Modeling of MOS Transistors*. New York: McGraw-Hill, 1999.
- [84] J. G. Maneatis and M. A. Horowitz, "Precise delay generation using coupled oscillators," *IEEE J. Solid-State Circuits*, vol. 28, no. 12, pp. 1273–1282, Dec. 1993.
- [85] H. Chang, X. Cao, U. K. Mishra, and R. A. York, "Phase noise in coupled oscillators: Theory and experiment," *IEEE Trans. Microwave Theory Tech.*, vol. MTT-45, no. 5, pp. 604–615, May 1997.
- [86] R. Navid and R. W. Dutton, "The physical phenomena responsible for excess noise in short-channel MOS devices," in *Int. Conf. Simulation of Semiconductor Processes and Devices (SISPAD) Dig. Tech. Papers*, pp. 75–78, Sep. 2002.
- [87] B. H. Leung, "A Novel Model on Phase Noise of Ring Oscillator Based on Last Passage Time", *IEEE Trans. on CS-I*, Vol. 51, No. 3, pp. 471-482, March 2004
- [88] B. Leung, "A Switching Based Phase Noise Model for CMOS Ring Oscillators Based on Multiple Thresholds Crossing", *IEEE Transactions on Circuits and Systems I*, Vol. 57, Issue 11, pp 2858-2869, Nov 2010
- [89] B. Leung, D. Mcleish, "Phase Noise of a Class of Ring Oscillators having Unsaturated Outputs with Focus on Cycle to Cycle Correlation", *IEEE Transactions on Circuits and Systems I*, vol. 56, no. 8. pp.1689-1707, August, 2009

- [90] N. Lam, B. Leung, "Dynamic Quadrant Swapping Scheme Implemented in a Post Conversion Block for I, Q, Mismatch Reduction in a DQPSK Receiver", IEEE Journal of SSC, Vol. 45, Issue 2, pp 322-337, Feb 2012
- [91] B. Leung, "Comparison of Phase Noise Models on a Class of Ring Oscillators Using Low Voltage Swing Fully Differential Delay Cells", Analog Integrated Circuits and Signal Processing, vol. 61, issue 2pp. 129-147, November, 2009
- [92] Z. Shu, K. Lee, B. Leung, "A 2.4 GHz ring oscillator based CMOS frequency synthesizer with a fractional divider dual PLL architecture", IEEE Journal of Solid State Circuits, vol 39, pp. 452-463, March 2004
- [93] B. Leung, "A Novel Model on Phase Noise in Ring Oscillator Based on Last Passage Time", IEEE Transactions on Circuits and Systems I, vol. 51, pp. 471-482, March 2004
- [94] B. Leung, D. Mcleish, "Investigation of phase noise of ring oscillators with time varying current and noise sources by time scaling thermal noise", IEEE Transactions on Circuits and Systems I, vol. 51, pp. 1926-1939, October 2004
- [95] M. Haidi and B. Leung, "PLL based frequency discriminator using the loop filter as an estimator", IEEE Transactions on Circuits and Systems II, pp.721-727 , November, 2002
- [96] A. A. Abidi, "Phase Noise and Jitter in CMOS Ring oscillators," *IEEE J. Solid-State Circuits*, vol. 41, No.8, pp. 1803-1816, Aug 2006.
- [97] M. M. Driscoll, "Modeling Phase Noise in Multifunction Subassemblies", IEEE Transactions on Ultrasonics, Ferroelectrics, and Frequency Control, vol. 59, no. 3, pp. 373-381, March 2012
- [98] U.L. Rohde, "A New Efficient Method of Designing Low Noise Microwave Oscillators," Dr.-Ing. Dissertation, Faculty IV, EEC (Electrical Engineering and Computer Sciences), TU-Berlin, Germany, February 2004.
- [99] Ajay Poddar, Ulrich Rohde, Anisha Apte, " How Low Can They Go, Oscillator Phase noise model, Theoretical, Experimental Validation, and Phase Noise Measurements", IEEE Microwave Magazine , Vol. 14, No. 6, pp. 50-72, September/October 2013.
- [100] Ulrich Rohde, Ajay Poddar, Anisha Apte, "Getting Its Measure", IEEE Microwave Magazine, Vol. 14, No. 6, pp. 73-86, September/October 2013.
- [101] U. L. Rohde, A. K. Poddar, Anisha Apte, "Phase noise measurement and its limitations", Microwave journal, April 2013.

Chapter 4

Phase Noise Measurement Techniques and Limitations

4.1 Introduction

Accurate measurement of phase noise is one of the most difficult measurements tasks in the field of electrical engineering [1]-[5]. The biggest challenge is the huge dynamic range required in phase noise measurements [6]-[11]. There are several methods to measure phase noise and the right method should be chosen to make the necessary measurements [12]. To properly select among the various methods, it is necessary to know and appreciate the weaknesses and strengths of each of the different techniques, because none of these methods is perfect for every situation [8]. This chapter focuses on key phase noise measurement techniques for oscillators and reviews their advantages and disadvantages.

In general, measuring phase noise is more difficult than measuring amplitude or frequency related properties [13]. Different signal sources, whether it is an oscillator alone or a synthesizer, have widely varying phase noise performances [14]-[23]. Higher noise sources do not work well with phase noise measurement equipments that are optimized to measure very low noise levels. An ability to measure the phase noise performance of ultra-low phase noise oscillators drives the specifications of the best performing phase noise analyzers [15].

Phase noise is usually expressed in units of dBc/Hz at some specific offset frequency f , from the carrier, the value of the noise level relative to the carrier level calculated in 1Hz bandwidth. Most often only single sideband (SSB) noise is considered. Some measurement set-ups measure both noise sidebands and a conversion factor is required to report SSB noise. The pioneer in Phase Noise measurement unquestionably was Hewlett Packard [1, 8, 32, and 34].

Once adequate for advanced designs, a noise floor dictated by SSB thermal noise (Johnson Noise at kT) of -174 dBm for zero dBm output power is not enough anymore for some special requirements and also marketing of these reference frequency sources [36]. The noise correlation technique allows us to look below kT level (< -174 dBm). However, the usefulness of the noise contribution below kT is debatable in the perspective of overall system performance [37]. To achieve a very low measurement noise floor, many modern phase noise measurement instruments use the correlation principle, with all its pros and cons as described in the subsequent sections [38]-[48]. The modern test equipments using the cross-correlation methods are at least 20 times faster [49]-[58].

4.2 Noise in Circuits and Semiconductors

In general, phase noise describes how the frequency of an oscillator varies in short time scale. The level of phase noise is deterministically related to the carrier frequency, increasing by 6dB for every doubling in frequency. The long-term frequency stability is called frequency drift, and it must be considered during the measurement process. The output frequency of an oscillator takes finite time to stabilize after the oscillator has been started and this drift can be up to few MHz. The output frequency also usually drifts noticeably during the measurements, especially in the case of free running oscillators. This drift is a real problem, because during the

measurements the system must be able to lock to the carrier or carrier must be stable enough, therefore without the carrier tracking mechanism measurement process is difficult exercise. Therefore, understanding the frequency drift caused due to noise contributions from the active and passive devices, is important.

Any type of amplifier in the test signal chain will also serve as a source of noise. While the main purpose of the amplifier is to increase the power level of a weak carrier signal, it also adds its own noise to the signal and boosts any input noise. The net result is that the amplifier, thermal noise, and flicker noise continue to give any phase-noise plot a characteristic shape and, more significantly, reduce the theoretical lower limit of sensitivity for any phase-noise measurement. These effects appear in the phase-noise characteristics of any high-performance signal generator.

4.2.1 Johnson noise

- The Johnson noise (thermal noise) is due to the movement of molecules in solid devices called Brown's molecular movements.
- This noise voltage is expressed as $v_n^2 = 4kT_0RB$ (emf) (volt²) (4.1)
- The power of thermal noise can thus be written as

$$\text{Noise Power} = \frac{v_n^2}{4R} = kT_0B \quad (W) \quad (4.2a)$$

- It is most common to do noise evaluations using a noise power density, in Watts per Hz. We get this by setting B=1Hz. Then we get:

$$\text{For } B = 1\text{Hz, Noise Power} = kT_0$$

$$T = 290K \text{ and } k - \text{Boltzmann's constant} = 1.38 \times 10^{-23} \text{ J/K}$$

$$\text{by Thevinin, Noise Power} = 1.38 \times 10^{-23} \times 290 = 4 \times 10^{-21} \text{ W} \quad (4.2b)$$

- Noise floor below the carrier for zero dBm output is given by

$$L(\omega) = 10 \log \left(\frac{v_n^2/R}{1mW} \right) = -173.97 \text{ dBm or about } -174 \text{ dBm} \quad (4.2c)$$

In order to reduce this noise, the only option is to lower the temperature, since noise power is directly proportional to temperature.

- The Johnson noise sets the theoretical noise floor.

4.2.2 Planck's Radiation Noise

- The available noise power does not depend on the value of resistor but it is a function of temperature T. The noise temperature can thus be used as a quantity to describe the noise behavior of a general lossy one-port network.
- For high frequencies and/or low temperature, a quantum mechanical correction factor has to be incorporated for the validation of equation. This correction term results from Planck's radiation law, which applies to blackbody radiation.

$$P_{av} = kT \cdot \Delta f \quad (4.3a)$$

- $P_{av} = (kT\Delta f) \times p(f, T)$, with $p(f, T) = \left[\frac{hf}{kT} / \left(e^{\frac{hf}{kT}} - 1 \right) \right]$ (4.3b)
- where $h = 6.626 \times 10^{-34}$ Joule – sec (Planck's Constant)

4.2.3 Schottky/Shot noise

- The Schottky noise occurs in conducting PN junctions (semiconductor devices) where electrons are freely moving. The root mean square (RMS) noise current is given by

$$i_n^2 = 2qI_{dc} \quad (4.4a)$$

$$P = i_n^2 [Z] \quad (4.4b)$$

- Where, q is the charge of the electron, P is the noise power, and I_{dc} is the dc bias current, $[Z]$ is the termination load (can be complex load, comprised of real and reactive load).
- Since this noise process is totally different from other noise processes, this noise is independent from all others.

4.2.4 Flicker noise

- The electrical properties of surfaces or boundary layers are influenced energetically by states, which are subject to statistical fluctuations and therefore, lead to the flicker noise or $1/f$ noise for the current flow.
- $1/f$ - noise is observable at low frequencies and generally decreases with increasing frequency f according to the $1/f$ - law until it will be covered by frequency independent mechanism, like thermal noise or shot noise.

Example: The noise for a conducting diode is bias dependent and is expressed in terms of AF and KF. $\langle i_{Dn}^2 \rangle_{AC} = 2qI_{dc}B + KF \frac{I_{DC}^{AF}}{f} B$

The AF term is a dimensionless quantity and a bias dependent curve fitting parameter. This term has a value generally within the range of 1 to 3 and a typical value of 2.

The KF value ranges from $1E^{-12}$ to $1E^{-6}$, and defines the flicker corner frequency.

4.2.5 Transit time and Recombination Noise

- When the transit time of the carriers crossing the potential barrier is comparable to the periodic signal, some carriers diffuse back and this causes noise. This is really seen in the collector area of NPN transistor.
- The electron and hole movements are responsible for this noise. The physics for this noise has not been fully established.

4.2.6 Avalanche Noise

- When a reverse bias is applied to semiconductor junction, the normally small depletion region expands rapidly.
- The free holes and electrons then collide with the atoms in depletion region, thus ionizing them and produce spiked current called the avalanche current.

- The spectral density of avalanche noise is mostly flat. At higher frequencies the junction capacitor with lead inductance acts as a low-pass filter.
- Zener diodes are used as voltage reference sources and the avalanche noise needs to be reduced by big bypass capacitors!

4.3 Phase Noise Measurement Techniques

The usual goal for measuring phase noise in an R&D environment is to achieve the lowest measurement noise floor possible. As we shall see, this is not necessarily the best choice, depending on the signal source being measured. In a production environment, the objective is fast throughput for product phase noise performance testing. Again, this is best achieved by using a method that is appropriate for the source being measured.

There are some very capable general-purpose phase noise measurement instruments available on the market, including the Agilent-E5052B, Rohde & Schwarz-FSUP, Holzworth-HA7402A, Noise XT-DCNTS, Anapico-APPH6000-IS, and OE Wave-PHENOM™. With the growing demand for improved dynamic range and lower noise floor, equipment companies are introducing general purpose phase noise analysis software driven tools for extracting far out (offset frequency $> 1\text{MHz}$) noise below the kT floor even though claims of -195 dBc/Hz or lower lack the practical utility.

Modern phase noise test equipment addresses these issues, but one must understand the limitations of measurement techniques so that a suitable method can be chosen. The Direct Spectrum Method, PLL method, delay line discriminator method, and cross-correlation method are frequently used to measure the oscillator phase noise. The first one is the simplest and has the biggest limitation. The last one requires the most complex measurement system but useful and can measure oscillator phase noise performance better than that of its reference oscillator.

Here we present the following primary phase noise measurement techniques, listed in the order of increasing precision:

- Direct Spectrum Technique
- Frequency discriminator method
 - Heterodyne (digital) discriminator method
- Phase detector techniques
 - (Reference source/PLL method)
- Residual Method
- Two-channel cross-correlation technique

4.3.1 Direct Spectrum Technique

This is the simplest technique for making phase noise measurements. Using this technique, measurements are valid as long as the analyzer's phase noise is significantly lower than that of the measured device (DUT). Figure 4-1 shows the basic block diagram of a Direct Spectrum Measurement Technique. As shown in Figure 4-1, the signal from the device under test (DUT) is input into a spectrum/signal analyzer tuned to the DUT frequency, directly measuring the

power spectral density of the oscillator in terms of $E(f_m)$. Because the spectral density is measured with the carrier present, this method is limited by the spectrum/signal analyzer's dynamic range. Though this method may not be useful for measuring very close-in phase noise to a drifting carrier, it is convenient for qualitative quick evaluation on sources with relatively high noise. For practical application, the measurement is valid if Spectrum/Signal analyzer internal SSB phase noise at the offset of interest is lower than the noise of the DUT. It is therefore essential to know the internal phase noise of the analyzer we are using.

Because the spectrum/signal analyzer measures total noise power without differentiating amplitude noise from phase noise, the amplitude noise of the DUT must be significantly below its phase noise (typically 10 dB will suffice). This can be assured by first passing the DUT signal through a limiter. The presence of amplitude noise is suggested if the sidebands of the signal are not symmetrical. It is very important to adjust the noise measurement from the spectrum analyzer.

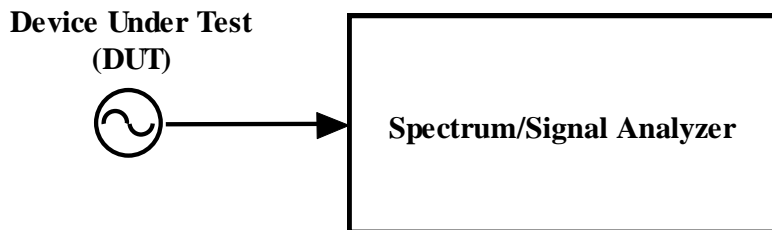


Figure 4-1: Direct Spectrum Measurement Technique

All spectrum analyzers pass signals through a logarithmic amplifier (logamp) before detection and averaging. This distorts the noise waveform, essentially clipping it somewhat from the logarithmic transfer function. A 2.5dB error on the low side results from this average-of-log process. The details of this measurement techniques can be found in Agilent application note AN1303, "Spectrum and Signal Analyzer Measurements and Noise" for more details [1].

Advantages:

- Simple, frequency based measurement
- Fast measurement, for relatively noisy sources
- Relatively low cost
- Suitable for measurements of oscillators that drift slightly (less than the resolution filter bandwidth) during measurement.

Drawbacks:

- Not suitable for measuring oscillators with ultra low phase noise performance, because the noise floor of the instrument is comparatively high.
- Not suitable for measuring the phase noise within 1kHz carrier frequency, mostly because spectrum analyzers have their own noise properties that can degrade the measurement results.
- Limited measurement dynamic range

- One of the major drawbacks of the Direct Spectrum technique is its dynamic range limitation due to the presence of the carrier power. All of the following measurement techniques eliminate this limitation by separating the sideband noise from the carrier power, using a variety of techniques.

4.3.2 Frequency Discriminator Method

In the frequency discriminator method, the frequency fluctuations of the source are translated to low frequency voltage fluctuations, which can then be measured by a baseband analyzer. There are several common implementations of frequency discriminators including cavity resonators, RF bridges and a delay line.

Delay Line Frequency Discriminator:

The delay-line measurement system is often chosen for the flexibility in measuring a free-running oscillator between 1 GHz and 10 GHz. The delay-line technique has sufficient sensitivity to measure most microwave oscillators with loaded Q-factors of several hundred and does not require a second reference oscillator.

The expression of delay can be calculated as

$$t_{\text{delay}} = \sqrt{\epsilon_r} \left(\frac{l_{\text{cable}}}{c} \right) \quad (4.5)$$

Where ϵ_r is the relative dielectric constant in a coaxial cable.

The primary advantage of this method is that it can be used to measure noisy sources but on the other hand, it does not work with low noise sources, because the noise performance of this method is the limiting factor. Delay-line discriminators are limited by the loss of the delay-line due to the power requirements for the mixer. Using lower power than required will lead to degraded performance of the system. The noise floor depends on the length of the cable (delay), the longer the delay the lower the noise floor, but it will also mean higher losses and lower offset frequency. The highest usable offset frequency depends mostly on the length of the delay. There is a null at $f=1/t_{\text{delay}}$ offset frequency, and the recommendation is to use offset frequencies up to $f=1/(4t_{\text{delay}})$. With a 500ns delay, the usable offset frequency range is from 0 to 500 kHz.

As shown in Figure 4-2, the signal power from the DUT is split into two channels. The signal in one path is delayed relative to the signal in the other path. The delay line converts the frequency fluctuation to phase fluctuation. The mixer requires phase quadrature at its two inputs at the carrier frequency, which is achieved by either adjusting the delay line (not likely) or using a small phase shifter in the through-path. As shown in Figure 4-2, the mixer (acting as phase detector) converts the phase difference between the delayed and undelayed paths into a DC voltage related by the phase discriminator constant K_ϕ . The output of this frequency discriminator is then read on the baseband spectrum analyzer as frequency noise. This frequency noise is converted to phase noise using the well-known relationship between FM and PM, and reported as phase noise measurement.

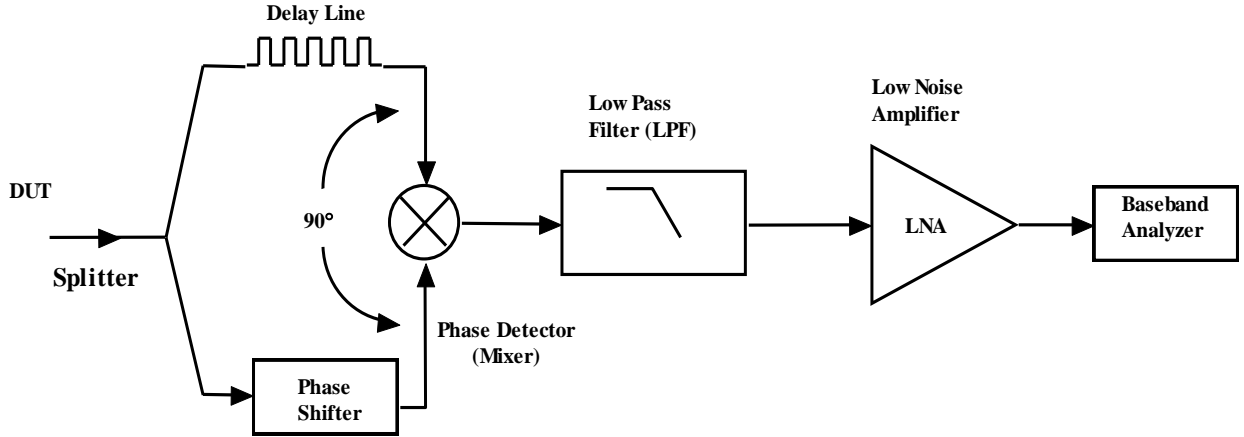


Figure 4-2: Shows the basic block diagram of frequency discriminator method (Courtesy: Agilent Company)

The frequency fluctuations of the oscillator in terms of offset frequency f_m are related to the phase detector constant K_ϕ and the delay τ_d by [31]:

$$\Delta V(f_m) = [K_\phi 2\pi \tau_d] \Delta f(f_m) = K_d \Delta f(f_m) \quad (4.6)$$

Since frequency is the time rate change of phase we have:

$$S_\phi(f_m) = \frac{S_{\Delta f}(f_m)}{f_m^2} = \frac{\Delta f^2(f_m)}{f_m^2} \quad (4.7)$$

The voltage output is measured as a double sideband voltage spectral density $S_v(f_m)$.

From (4.6) and (4.7), phase noise $S_\phi(f_m)$ is related to the measured $S_v(f_m)$ by:

$$S_\phi(f_m) = \frac{\Delta V^2(f_m)}{K_d^2 f_m^2} = \frac{S_v(f_m)}{K_d^2 f_m^2} \quad (4.8)$$

The single sideband phase noise is given by

$$\mathcal{L}_\phi(f_m) = \frac{S_v(f_m)}{2K_d^2 f_m^2} \quad (4.9a)$$

$$\mathcal{L}_\phi(f_m) [dBc/Hz] = S_v(f_m) - 3 - 20 \log(K_d) - 20 \log(f_m) \quad (4.9b)$$

With a single calibration of the mixer as a phase detector, K_ϕ and known delay τ_d , the phase noise of an oscillator can be measured using FFT (baseband) analyzer. The phase discriminator constant K_ϕ is in V/rad and is determined by measuring the DC output voltage change of a mixer while in quadrature (nominally 0V DC) for a known phase change in one branch of discriminator. The value of K_d is dependent upon the RF input power of the mixer that in turn is directly proportional to the noise floor shown in Figure 4-3 [31].

Using Z-parameters the sensitivity of the delay line discriminator can be determined first by introducing the Q-factor defined with respect to the phase of the open-loop transfer function $\phi(\omega)$ at the resonance of parallel RLC circuit [31]-[33]:

$$\phi(j\omega) = \tan^{-1} \frac{\text{Imag}(Z(j\omega))}{\text{Real}(Z(j\omega))} \quad (4.10)$$

$$Q = \frac{1}{R} \sqrt{\frac{L}{C}} = \frac{\omega \delta \phi}{2\delta\omega} \quad (4.11)$$

A typical coaxial delay-line exhibits a linear phase relation with frequency across the usable bandwidth of the transmission line.

The linear phase relationship in a coaxial line to the derivative of the phase change in a resonator results in an effective Q, Q_E for a transmission line with time delay τ_d :

$$Q_E = \pi f_0 \tau_d \quad (4.12)$$

From (4.12), the effective Q-factor increases linearly with both delay line length and frequency of operation. Using Q_E as the Q-factor in the Leeson's equation and using an approximate mixer noise floor of -175 dBc.

The Flicker corner is set at 10 kHz, typical for silicon (Si) diode mixer. The measurement phase noise floor is calculated:

$$\mathcal{L}_\phi(f_m) = 10 \log \left[\left(1 + \frac{1}{(2\pi\tau_d f_m)^2} \right) \left(1 + \frac{f_c}{f_m} \right) \right] + N_{mixer\ floor} \quad (4.13)$$

A plot of (4.13) is shown in Figure 4-3.

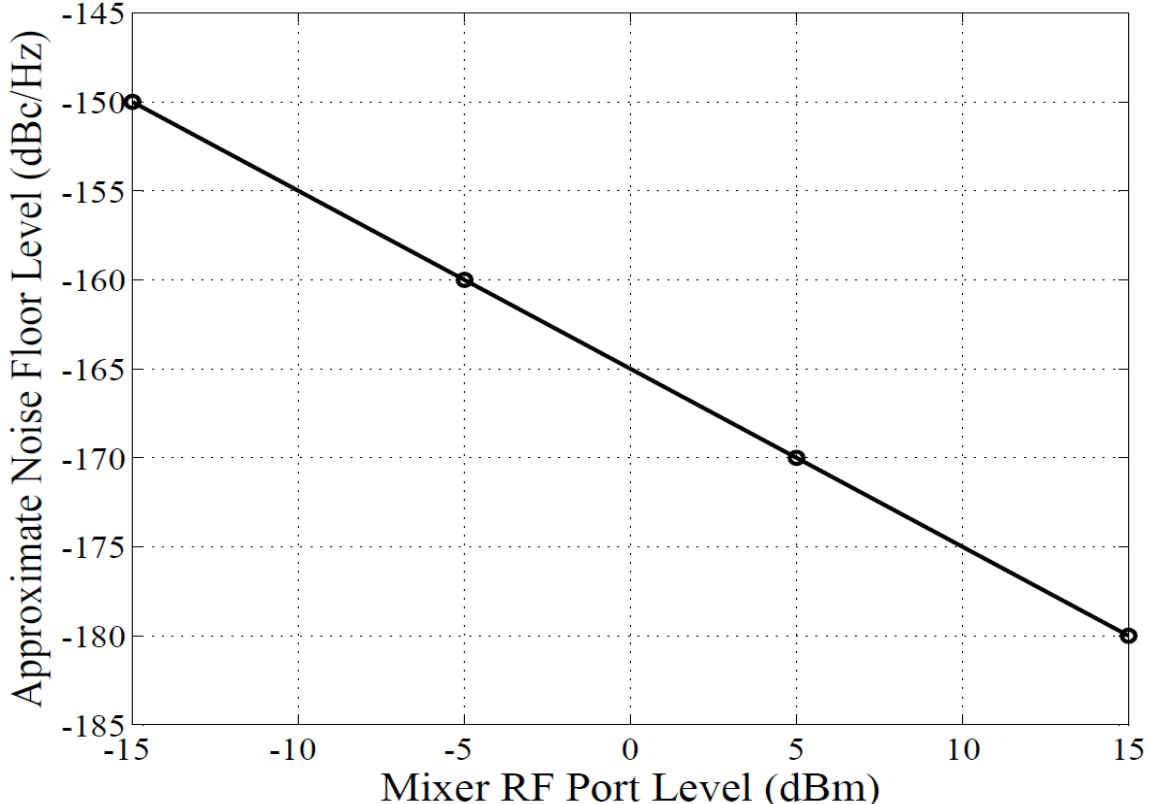


Figure 4-3: The ideal phase detector sensitivity in terms of RF power (assuming LO power is great than RF) and phase detector constant $K\phi$. The noise floor sensitivity is 1:1 to mixer power input [31]

Advantages:

- Better Sensitivity than Direct Spectrum Methods
- Good for free running sources such as LC oscillators or cavity oscillators
- Appropriate when the DUT is a relatively noisy source with high-level, low rate phase noise or high close-in spurious sideband

Drawbacks:

- Significantly less sensitivity than phase detector methods
- A longer delay line will improve the sensitivity but the insertion loss of the delay line may exceed the source power available and cancel any further improvement.
- In addition, longer delay lines limit the maximum offset frequency that can be measured. This method is best used for free running sources such as LC oscillators or cavity oscillators, although the frequency discriminator method degrades the measurement sensitivity, particularly at close to the carrier frequency.

4.3.2.1 Heterodyne (Digital) Discriminator method

As shown in Figure 4-4, the heterodyne (digital) discriminator method is a modified version of the analog delay line discriminator method and can measure the relatively large phase noise of unstable signal sources and oscillators.

Unlike the analog discriminator method, here the input signal is down-converted to a fixed intermediate frequency f_{if} using a separate local oscillator. The local oscillator is frequency locked to the input signal. Working at a fixed frequency, the frequency discriminator does not need re-connection of various analog delay lines at any frequency. This method allows wider phase noise measurement ranges as compared to the PLL method. This option is available in latest commercial phase noise measurement equipments (Agilent E5052B, R&S FSUP).

Advantages:

- Offers easy and accurate AM noise measurements (by setting the delay time to zero) with the same setup and RF port connection as the phase noise measurement
- Frequency demodulation can be implemented digitally

Drawbacks:

- Dynamic range of Phase Noise measurement is further limited by the additional scaling amplifier and ADCs.

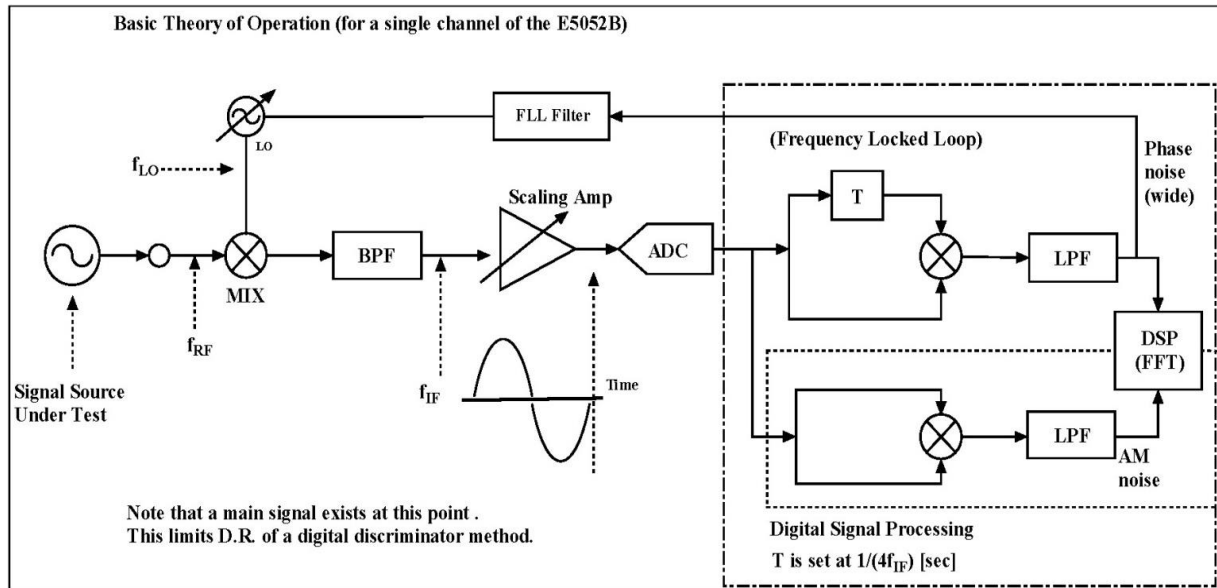


Figure 4-4: Basic block diagram of heterodyne (digital) discriminator method (Courtesy: Agilent) [9]

4.3.3 Phase Detector Technique

Figure 4-5 shows the basic concept for the phase detector technique. The phase detector method measures voltage fluctuations directly proportional to the combined phase fluctuations of the two input sources. To separate phase noise from amplitude noise, a phase detector (PD) is required. The (PD) converts the phase difference of the two input signals into a voltage at the output of the detector. When the phase difference between the two input signals is set to 90° (e.g. at quadrature), the nominal output voltage is zero volts and sensitivity to AM noise is minimized. Any phase fluctuation from quadrature results in voltage fluctuation at the output. This method has a very low noise floor and therefore has a very good measurement dynamic range.

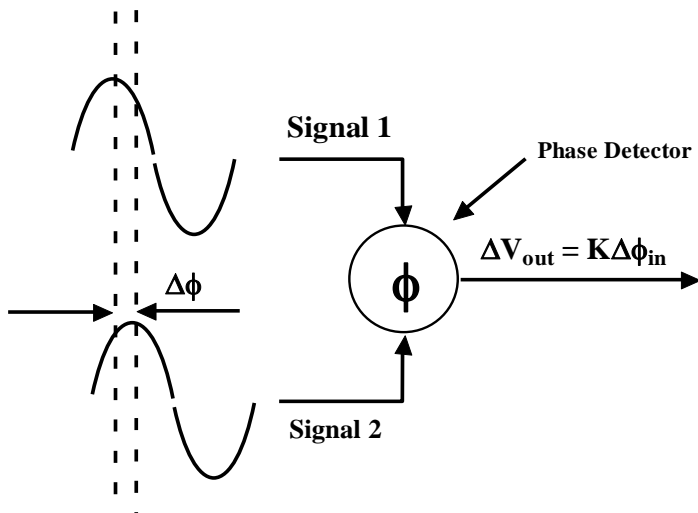


Figure 4-5: Basic concept of Phase detector techniques [1]

4.3.3.1 Reference Source/PLL Method

Figure 4-6 shows the basic block diagram of the phase detector method using reference source/PLL techniques. The basis of this method is to use a phase lock loop (PLL) in conjunction with a double balanced mixer (DBM) used for the phase detector. The PLL compares the phases of two input signals and generates a third signal which is used to steer one of the input signals into phase quadrature with the other. When the phase of the input signals are aligned, the loop is said to be locked and the nominal output from the phase detector is zero. This voltage varies a little due to phase noise on the input signals. The noise present at the output of the mixer includes phase noise of both signals. If the noise from the reference oscillator is more than 20 dB lower than the noise from DUT, the main contributor for phase noise is the DUT.

As shown in Figure 4-6, two sources, one from the DUT and the other from the reference source, provide inputs to the mixer. Again the reference source is controlled such that it follows the DUT at the same carrier frequency (f_c) and in phase quadrature (90° out of phase) to null out the carrier power. The mixer sum frequency ($2f_c$) is filtered out by the low pass filter (LPF), and the mixer difference frequency is 0 Hz (dc) with an average voltage output of 0 V when locked. The DC voltage fluctuations are directly proportional to the combined phase noise of the two sources. The noise signal is amplified using a low noise amplifier (LNA) and measured using a spectrum analyzer.

The advantage of this method is broadband measurement capability for both fixed frequency and tunable oscillators. With only a few different double balanced mixers and suitable reference oscillators, noise on signals from 1MHz to several tens of GHz can be measured. If the DUT is a tunable oscillator, the reference oscillator will then be a free running one and the DUT would be controlled with the PLL, and need a suitable PLL amplifier after the low pass filer (LPF). The limitation of this method is that it is difficult to determine the contribution of noise, i.e. which part of the noise comes from the reference and which from the DUT. Nevertheless, this problem is true for most measurement systems.

Usually, if the phase noise levels of the two signals are not that far from each other, a correction factor ($P_{correction}$) from 0 to 3dB is subtracted from the measured result, where the highest number is used when the noise levels are equal [24]. The expression of the correction factor is given by [32]

$$P_{correction} = 10 \log_{10} \left(1 + 10^{-\frac{\Delta P}{10}} \right) \quad (4.14)$$

Where ΔP is the difference between the noises of the reference and the DUT in dB, Table 4-1 shows the correction factors for different noise level differences.

Table 4-1: Correction factor if the phase noise of the reference oscillator is near the phase noise of DUT

$\Delta P/\text{Db}$	0	2	4	6	8	10	15	20
$P_{\text{Correction}/\text{dB}}$	3	2.12	1.46	0.97	0.64	0.4	0.14	0.04

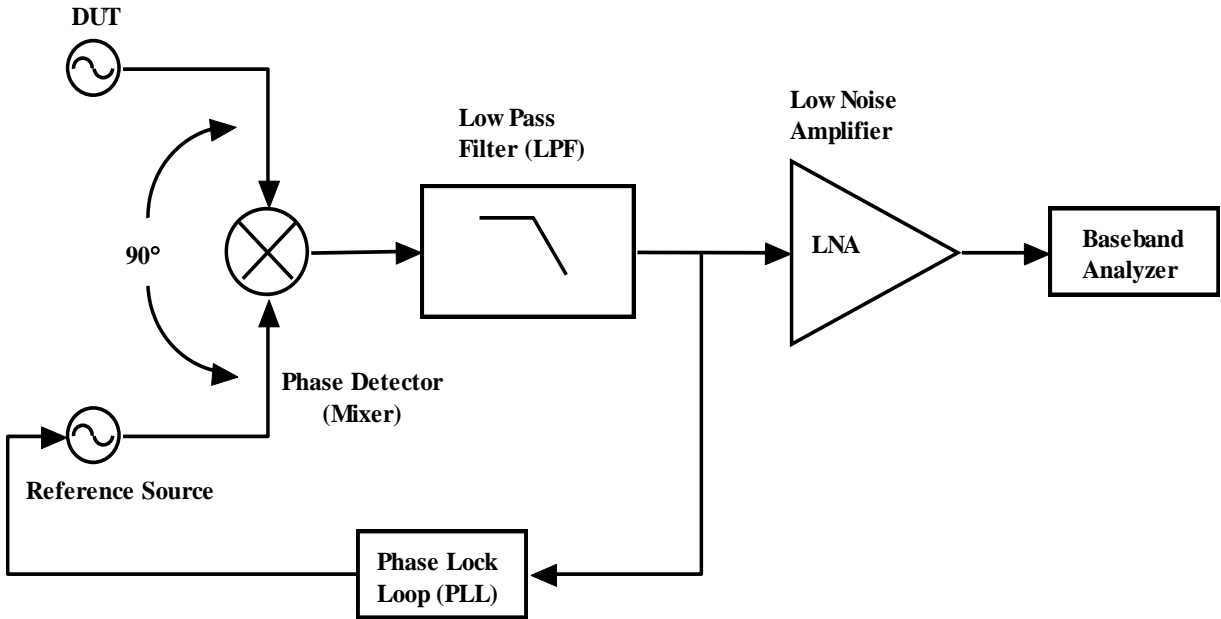


Figure 4-6: Shows the basic block diagram Phase Detector Method using reference source/PLL techniques). Small fluctuations from nominal voltages are equivalent to phase variations. The phase lock loop keeps two signals in quadrature, which cancels carriers and converts phase noise to fluctuating DC voltage (Courtesy of Agilent Technologies) [1]

This method exhibits promising noise floor but the performance is dependent on DBM and reference source characteristics. The selection of a mixer as a phase detector is critical to the overall system performance.

The noise floor sensitivity is related to the mixer input levels; therefore high power level mixers are preferred. However, care must be taken to match mixer drive to available source power.

Choice of DBM as Phase Detector:

Figure 4-7 exhibits typical DBM phase detector response curve, where V_{IF} varies as the cosine of the phase difference $\Delta\phi$ between LO and RF signals [31].

As shown in Figure 4-7, phase detector response (V_{IF}) is reasonably linear in the region $\Delta\phi$ where phase detector sensitivity $\left(\frac{\partial V_{IF}}{\partial \phi}\right)$ is maximum, represented by

$$\Delta\phi = (\phi_{LO} - \phi_{RF}) = \left(\frac{\pi}{2} + \delta\phi\right) \quad (4.15)$$

The phase detector output $V_{IF}(t)$ is given by [5]

$$V_{IF}(t) = \pm V \cos[(\omega_R - \omega_L)t + \Delta\phi(t) + \pi] \quad (4.16)$$

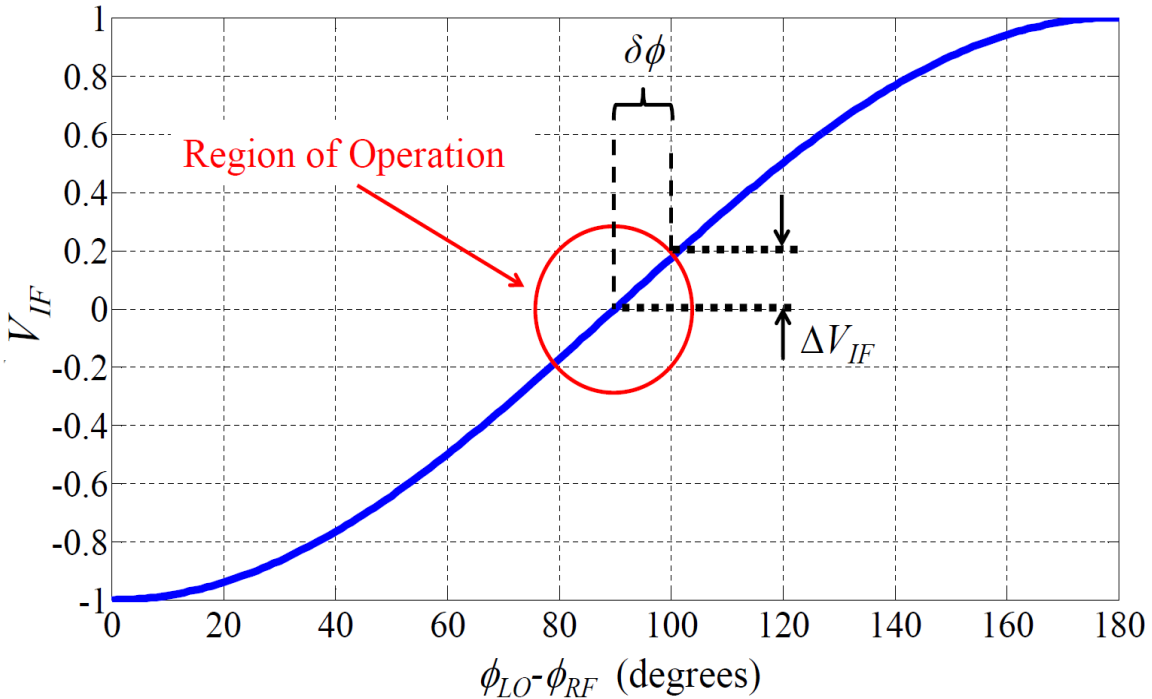


Figure 4-7: Shows the response of DBM as a phase detector varies as $\cos(\Delta\phi + \pi)$, (V_{IF}) is reasonably linear in the region ($\Delta\phi = \frac{\pi}{2} + \delta\phi$) [31]

For mixer's two input signals are at the same frequency, $\omega_R = \omega_L$ and 90° out of phase, $V_{IF}(t)$ is

$$\Delta V_{IF}(t) = \pm V \sin \delta\phi(t) \quad (4.17)$$

where V is the peak amplitude (at $\Delta\phi = 0$ or π), $\Delta V_{IF}(t)$ is the instantaneous voltage fluctuations around DC, and $\delta\phi(t)$ is the instantaneous phase fluctuation.

For $\delta\phi(t) \ll 1 \text{ rad}$, $\sin(\delta\phi(t)) \approx \delta\phi(t)$, which describes a linear response region, the phase detector sensitivity varies linearly with maximum output voltage as

$$\Delta V_{IF}(t) = V \delta\phi = K_\phi \delta\phi \quad (4.18)$$

where, K_ϕ is the phase detector gain constant (volts/radian), equal to the slope of the mixer sine wave output at the zero crossing.

Choice of Reference Sources:

The other critical component of the phase detector method is the reference source. As discussed in the Direct Spectrum technique section, a spectrum analyzer measures the sum of noise from both sources. Therefore, the reference source must have lower phase noise than device under test, DUT. For practical purposes 10 dB margin is sufficient to ensure correct measurements within reasonable degree of accuracy. When a reference source with lower

phase noise is unavailable then it is appropriate to use a source with comparable phase noise to the DUT. In this case, each source contributes equally to the total noise and 3-dB subtracted from the measured value.

Advantages:

- Excellent sensitivity for measuring low phase noise levels
- Wide signal frequency range
- Wide offset frequency range (0.01Hz to 100 MHz)
- Rejects AM noise
- Frequency tracks slowly drifting sources.

Drawbacks:

- Requires a very clean reference source that is electronically tunable,
- Measurement frequency bandwidth matched to the tuning range of the reference sources.
- Locking PLL bandwidth is very narrow, < 10% of the minimum offset frequency used in the measurement.
- Narrow PLL bandwidth cannot track a noisy source.
- Expensive and complex

In conclusion, the phase detector method has excellent system sensitivity, but on the other hand its complexity (PLL and two oscillators are required) must be handled with care.

4.3.4 Residual method

The methods shown thus far can be used to measure only oscillators. There are some methods for measuring 2-port devices, and the residual method is one of them. It can be used for example to measure amplifiers, mixers, cables, and filters.

As shown in Figure 4-8, the output of a reference source is split with a power splitter. One branch is connected through the DUT to the mixer and the other branch through a phase shifter to the mixer. The phase shifter is adjusted until the phases are in quadrature, and the output of the mixer is measured with a spectrum analyzer. Because the noise from the reference source is coherent at the mixer input and the signals are in quadrature, it will be subject to some degree of cancellation.

The degree of cancellation improves as the signal path delay in the two arms of the bridge is minimized. The remaining phase noise at the mixer output is thus added by the DUT. When the DUT is relatively broadband (i.e. low delay) device having equal input and output frequencies, the need for a second device in the other bridge arm is eliminated. When the device is either narrowband, or is one with unequal input and output frequencies (a mixer frequency multiplier or divider etc.) identical devices must be used in both arms of the phase bridge.

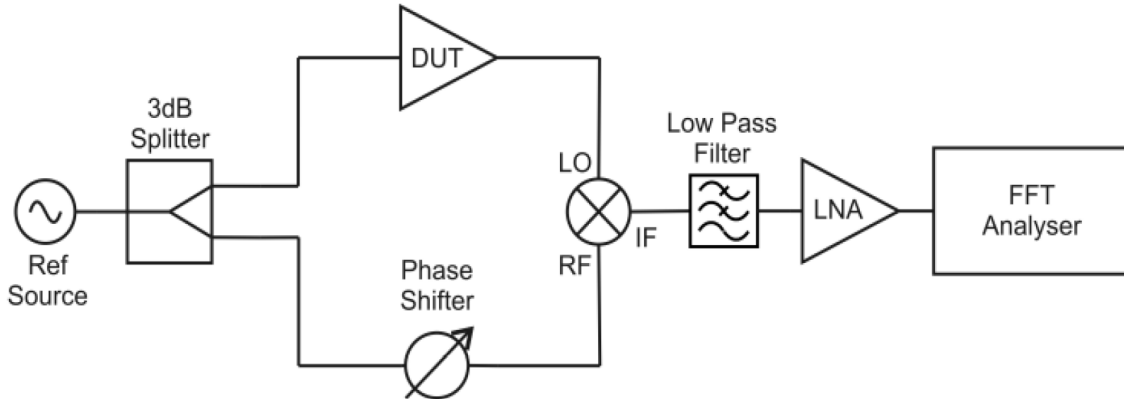


Figure 4-8: Residual method set-up (Simplified single channel residual phase noise measurement system)

The noise floor of a system utilizing this single channel measurement technique is highly dependent on and limited by the noise floors of the mixer, filters and low noise amplifier. This type of system can have a residual phase noise floor in the region of -180dBc/Hz at high offset frequencies [2].

In residual noise measurement system, the noise of the common source might be insufficiently canceled due to improperly high delay-time differences between the two branches. It is therefore vitally important to match the delay times very closely.

A Residual Phase Noise Measurement System

Figure 4-9 shows a system that automatically measures the residual phase noise of the 8662A synthesizer [4]. It is a residual test, since both instruments use one common 10MHz referenced oscillator. Quadrature setting is conveniently controlled by first offsetting the tuning of one synthesizer by a small amount, usually 0.1Hz. The beat signal is then probed with a digital voltmeter and when the beat signal voltage is sufficiently close to zero, matching the synthesizer tuning commands to stop the phase slide between the synthesizers.

4.3.5 Two-Channel Cross-Correlation Technique

Figure 4-10 shows the diagram of the 2-channel cross-correlation technique from Agilent [1]; built around a similar measurement set-up as the PLL method except that there are three oscillators and the measurement involves performing cross-correlation operations among the outputs from each channel. It can be seen that there are two reference oscillators, one power splitter, two mixer/amplifier/PLL circuits and a cross-correlation FFT analyzer. The cross-correlation technique is used to minimize the noise contribution from mixer, filter and LNA from the measurement results. This works because the noise from the DUT is common between both paths, but the noise contributed from each internal reference oscillator is independent. Thus over time, the noise contributions from the independent sources will show a zero cross-correlation. However, the noise from the DUT will correlate, and ultimately dominate the output measurement (as desired).

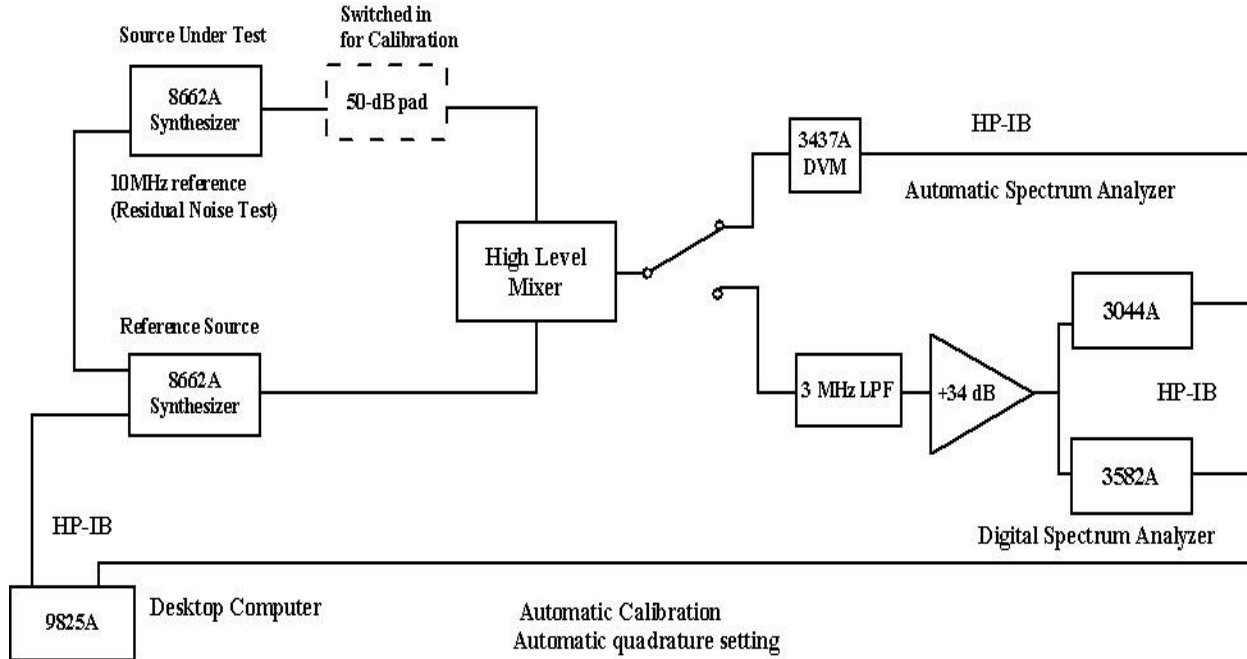


Figure 4-9: Automatic system to measure residual phase noise of two 8662A synthesizers (Courtesy of Hewlett-Packard Company) [32]

The noise from the first reference feeds into the first phase noise detector and ends up on channel 1 of the cross-correlation FFT analyzer. The noise from the second reference passes through in the second phase noise detector and appears on channel 2 of the cross-correlation FFT analyzer. The output of the DUT is connected through a high isolation inductive power splitter to two mixer circuits where it is mixed with the signal from these two reference oscillators. The outputs of the mixer circuits are used for PLL circuits to lock the internal references in phase quadrature to the DUT input signal, as in the PLL method. The mixer output signals are then amplified, the DC is filtered away and finally the signals are fed to two channels of the FFT analyzer to perform a cross-correlation measurement between the two output signals.

The noise from output of each mixer can be modeled using two noisy signals [36]-[39]

$$x(t) = a(t) + c(t) \overleftrightarrow{FFT} X(f) = A(f) + C(f) \quad (4.19)$$

$$y(t) = b(t) + c(t) \overleftrightarrow{FFT} Y(f) = B(f) + C(f) \quad (4.20)$$

Where $a(t)$ and $b(t)$ are uncorrelated equipment noise present in each channel and $c(t)$ represents the correlated DUT noise. The cross-spectrum of these two signals after averaging over M samples is described by

$$\overline{S_{XY}} = \frac{1}{M} \sum_{m=1}^{m=M} [X_m \times Y_m^*] \quad (4.21)$$

Where 'm' represents the sample index and (*) implies the conjugate function.

From (4.19), (4.20) and (4.21) into (4.22) and (4.23),

$$\overline{S_{XY}} = \frac{1}{M} \sum_{m=1}^{M} [(A_m + C_m) \times (B_m + C_m)^*] \quad (4.22)$$

$$\overline{S_{XY}} = \frac{1}{M} \sum_{m=1}^{M} [(A_m B_m^*) + (A_m C_m^*) + (C_m B_m^*) + (C_m C_m^*)] \quad (4.23)$$

Considering that there is no correlation between the noisy signals $a(t)$, $b(t)$ or $c(t)$ then as the number of averages increases the uncorrelated terms in the cross spectrum (AB , AC and CB) will tend toward zero. The only remaining term CC represents the power spectral density of the correlated DUT noise. When the analyzer is set to average, the common noise is kept, and the noise not common to both channels is attenuated and averaged away.

From (4.23) the DUT noise through each channel is coherent and is therefore not affected by the cross-correlation, whereas, the internal noises generated by each channel are incoherent and diminish through the cross-correlation operation at the rate of \sqrt{M} (M =number of correlations)

$$[Noise]_{meas} = [Noise]_{DUT} + \left(\frac{[Noise]_{channel\#1} + [Noise]_{channel\#2}}{\sqrt{M}} \right) \quad (4.24)$$

Where $[Noise]_{meas}$ is the total measured noise at the display; $[Noise]_{DUT}$ the DUT noise; $[Noise]_{channel\#1}$ and $[Noise]_{channel\#2}$ are the internal noise from channels 1 and 2, respectively; and M the number of correlations.

From (4.24), the 2-channel cross-correlation technique achieves superior phase noise measurement capability but the measurement speed suffers when increasing the number of correlations. This method offers 15 to 20 dB improved phase noise measurement sensitivity when compared to the Reference source/PLL method described above, so it can be used to measure oscillators with ultra-low phase noise. It is even possible to measure oscillators with better noise performance than the reference oscillators, because phase noises from the reference oscillators are suppressed considerably [37].

The improved dynamic range and noise floor of the cross-correlation phase noise measurement technique comes at price. Usually many samples are needed in order to average out the uncorrelated noise. The measuring yardstick of the confidence interval of a phase noise detector is expressed by [26]:

$$S_\theta^s(f) = S_\theta^m(f) \left(1 \pm \frac{1}{\sqrt{n}} \right) = \mp 10\% \text{ (for } n = 100) \rightarrow \text{For single-channel} \quad (4.25)$$

$$S_\theta^x(f) = S_\theta^m(f) \left(1 \pm \frac{2S_\theta^s}{\sqrt{n}} \right) = \mp 10\% \text{ (for } n = 20,000) \rightarrow \text{For dual-channel} \quad (4.26)$$

Where

x = cross –correlation

m = measured (noise)

s = single channel

n = number of samples

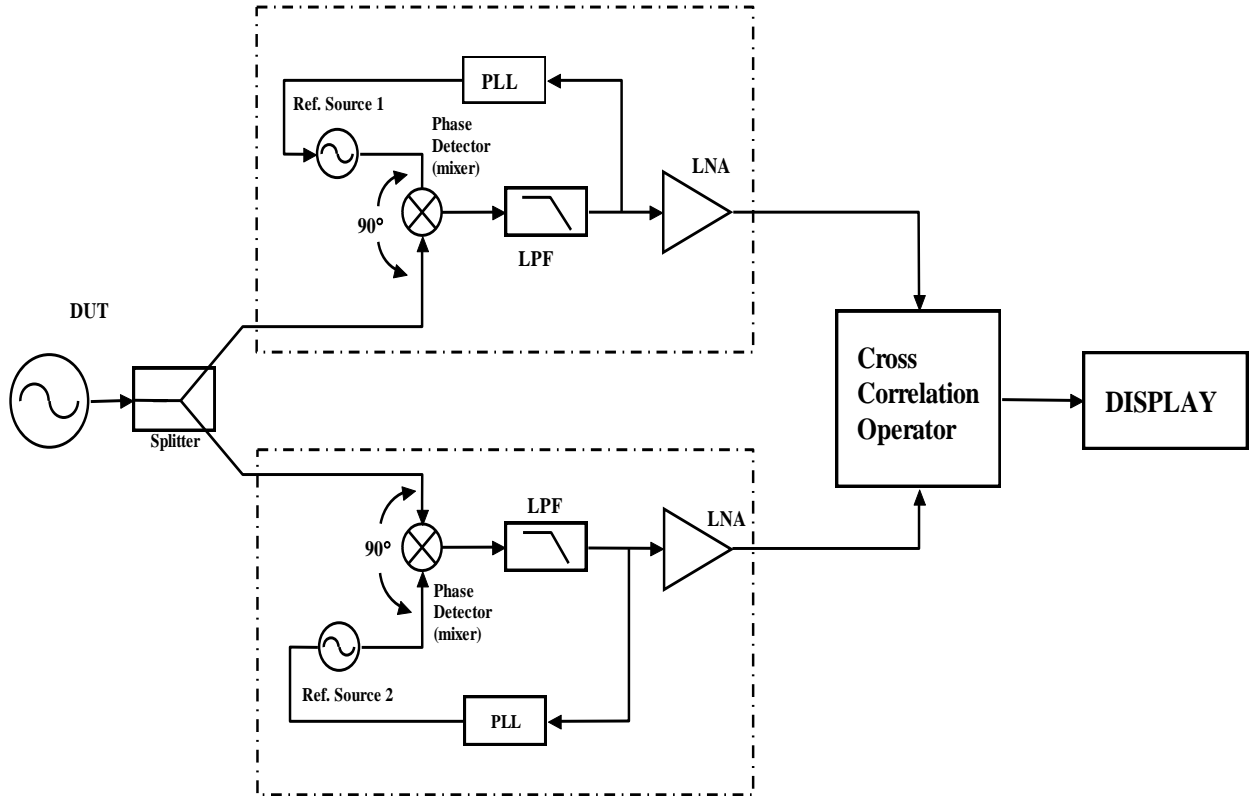


Figure 4-10: Shows the basic block diagram of 2-channel cross-correlation technique (Courtesy: Agilent) [34]

Equation (4.25) shows that for a single channel the confidence interval is $\pm 10\%$ for 100 samples. Equation (4.26) shows that to obtain the same confidence interval for a phase noise measurement 10 dB below the single channel noise floor 20,000 samples are required. Indeed, the dual channel or cross-correlation method of phase noise results in a lower floor than the standard single channel method but there is a cost of measurement speed [49]. From (4.25) and (4.26), more averages are required to achieve the same level of confidence in a measurement for dual-channel cross-correlation method. The advantage of lower noise floor using the cross-correlation method provides a level of characterization of extremely low noise Crystal oscillators, which was not possible using the single channel method. The practical value of the noise floor is [50]:

$$[L(f)_{SSB}] = -177 + N_a - P_i \quad (4.27)$$

Where N_a is the noise figure and P_i is the power available.

Today, the cross-correlation process is the only technique that allows close to thermal noise floor measurements below -177dBc/Hz at far offset from the carrier, and with 20dB of DUT output power can provide a noise floor better than -195 dBc/Hz provided the DUT output buffer stage is low noise amplifier and can handle the 20dBm power. However, this improvement of 20 dB is based on 100,000 correlations, which results in a long measurement time [51]-[58].

Advantages:

- Best sensitivity for measuring low phase noise levels
- Wide signal frequency range
- Wide offset frequency range (0.01 Hz to 100 MHz)
- Frequency tracks slowly drifting sources
- Rejects AM noise

Drawbacks:

- Complexity: Requires two very clean reference sources that are electronically tunable
- Long measurement times when very low noise is being measured
- Measurement frequency bandwidth matched to the tuning range of the reference sources
- Phase Inversion and collapse of the cross-spectral function (condition when the detection of the desired signal using cross-spectral techniques collapses partially or entirely in the presence of second uncorrelated interfering signal).

4.3.6 Conventional Phase Noise Measurement System (Hewlett-Packard)

This section is based on published Hewlett-Packard material [1], described here to give brief insights about the working principle of the early, very low phase noise measurement equipment (during the 1980s) and subsequently the development of modern automated test systems [4].

The most sensitive method to measure the spectral density of phase noise $S_{\Delta\theta}(f_m)$ requires two sources – one or both of them may be the device(s) under test – and a double balanced mixer used as a phase detector. The RF and LO input to the mixer must be in phase quadrature, indicated by 0 Vdc at the mixer IF port. Good phase quadrature assures maximum phase sensitivity K_θ and minimum AM sensitivity. With a linearly operating mixer, K_θ equals the peak voltage of the sinusoidal beat signal produced when both sources are frequency offset (Figure 4-11). When both signals are set in quadrature, the voltage ΔV at the IF port is proportional to the fluctuating phase difference between the two signals.

$$\Delta\theta_{rms} = \frac{1}{K_\theta V_{rms}} \quad (4.28)$$

$$S_{\Delta\theta}(f_m) = \frac{(\Delta V_{rms})^2(1Hz)}{V_B^2_{peak}} \frac{1}{2} \frac{(\Delta V_{rms})^2(1Hz)}{V_B^2_{rms}} \quad (4.29)$$

$$\mathcal{L}(f_m) = \frac{1}{2} S_{\Delta\theta}(f_m) = \frac{1}{4} \frac{(\Delta V_{rms})^2(1Hz)}{V_B^2_{rms}} \quad (4.30)$$

where K_θ is phase detector constant and V_B peak for sinusoidal beat signal

Calibrations required of the wave analyzer or spectrum analyzer can be read from the equations above. For a plot of $\mathcal{L}(f_m)$ the 0-dB reference level is to be set 6 dB above the level of the beat signal. The -6-dB offset has to be corrected by + 1.0 dB for a wave analyzer and by +2.5 dB for a spectrum analyzer with log amplifier followed by an averaging detector. In addition, noise bandwidth corrections likely have to be applied to normalize to 1Hz bandwidth.

Since the phase noise of both sources is summed together in this system, the phase noise performance of one of them needs to be known for definite data on the other source. Frequently, it is sufficient to know that the actual phase noise of the dominant source cannot deviate from the measured data by more than 3 dB. If three unknown sources are available, three measurements with three different source combinations yield sufficient data to calculate accurately each individual performance.

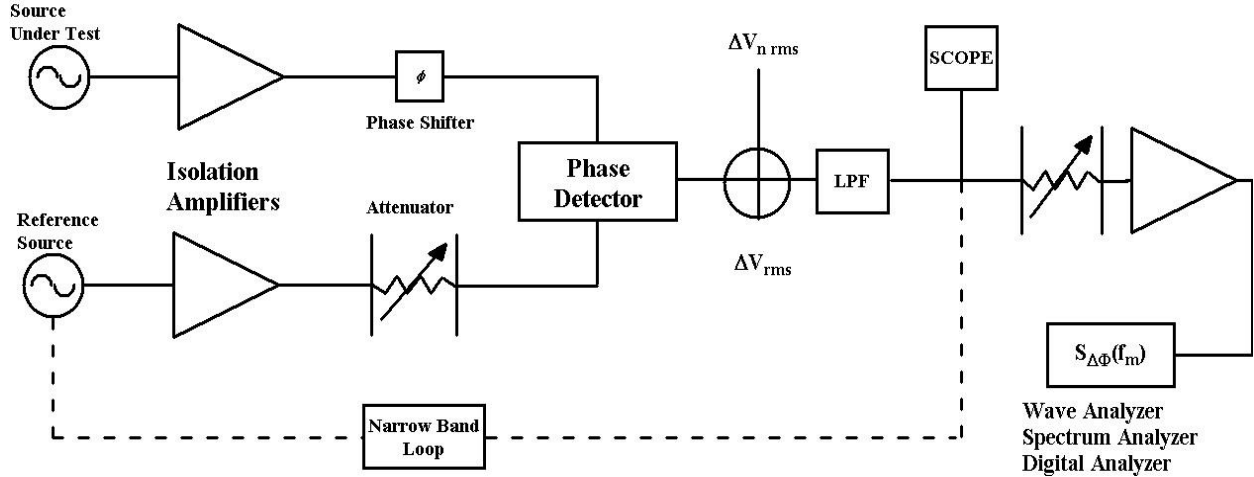


Figure 4-11: Phase Noise system with two sources maintaining phase quadrature

Figure 4-11 indicates a narrowband phase-locked loop that maintains phase quadrature for sources that are not sufficiently phase stable over the period of the measurement. The two isolation amplifiers are to prevent injection locking of the sources to each other. The noise floor of the system is established by the equivalent noise voltage ΔV_n at the mixer output. It represents mixer noise as well as the equivalent noise voltage of the following amplifier:

$$\mathcal{L}_{\text{system}}(f_m) = \frac{1}{4} \frac{(\Delta V_{n \text{ rms}})^2 (1\text{Hz})}{V_B^2 \text{ rms}} \quad (4.31)$$

Wideband noise floors close to -180 dBc can be achieved with a high-level mixer and a low-noise amplifier. The noise floor increases with f_m^{-1} due to the flicker characteristic of ΔV_n . System noise floors of -166dBc/Hz at 1 kHz have been realized.

To get this excellent performance, the phase detector/PLL method is complex and requires significant calibration. In measuring low-phase-noise sources, a number of potential problems have to be understood to avoid erroneous data. These include:

- When two sources are phase locked to maintain phase quadrature, it has to be ensured that the lock bandwidth is significantly lower than the lowest Fourier frequency f_m of interest, unless the test set takes into account (as many do) the loop suppression response
- Even with no apparent phase feedback, two sources can be phase locked through injection locking, resulting in suppressed close-in phase noise and causing a measurement error. This can normally be avoided with the use of high isolation buffer amplifiers or frequency multipliers.

- AM noise of the RF signal can come through if the quadrature setting is not maintained accurately.
- Deviation from the quadrature setting also lowers the effective phase detector constant.
- Nonlinear operation of the mixer results in a calibration error.
- Need for low harmonic content: A non-sinusoidal RF signal causes K_θ to deviate from V_{Bpeak}
- The amplifier or spectrum analyzer input can be saturated during calibration or by high spurious signals such as line frequency multiples.
- Closely spaced spurious signals such as multiples of 60 Hz may give the appearance of continuous phase noise when insufficient resolution bandwidth and averaging are used on the spectrum analyzer.
- Impedance interfaces must remain unchanged when transitioning from calibration to measurement.
- Noise from power supplies for devices under test can be a dominant contributor of error in the measured phase noise.
- Peripheral instrumentation such as an oscilloscope, analyzer, counter, or DVM can inject noise.
- Microphonic effects may excite significant phase noise in devices.

Despite all these hazards, automatic test systems now exist and operate successfully [8]. Oscillator manufacturers and users who frequently need to evaluate the performance of ultra low phase noise oscillators, at some point, recognize that their phase noise test systems could be primarily improved in the following aspects:

- Accuracy
- Speed of test
- Large dynamic range and lower noise floor
- Reliability and repeatability of test data
- Range, ease of use and data retrieval
- Cost (though high performance test systems will never be cheap!)

General Discussion:

Characterizing the phase noise of a system or component is not necessarily very easy. Many different approaches are possible, but the key is to find the best approach for the measurement requirements at hand. Practically, it is advisable to use the cross-correlation approach for the best sources so that keeping them locked is easy during measurement cycle. In principle, each reference is locked to track the DUT, therefore PLL bandwidth needs to be monitored for reliable and accurate measurement. Usually, corrections for PLL bandwidth works to some degree, but corrections beyond certain limit have more errors, leading to inaccurate phase noise measurement of the DUT. One of the weaknesses, with the cross-correlation method is that, many measurements must be made and the average calculated between them. Thus, the

measurement takes longer, and the DUT must be kept locked for a longer time. Usually, 1-sweep takes approximately 10 seconds, and the required amount of sweep is 2^m where $m > 2$ but for a noisy source this may not be easy. Hence, this method is most suitable for measuring low noise oscillators having a small frequency drift. A survey of some of the more common topologies along with some possible trouble spots helps one to review and keep in mind the advantages and limitations of each approach. Figure 4-12 Shows phase noise plots and noise floor for 3-phase noise measurement techniques (Delay line, PLL and cross-correlation).

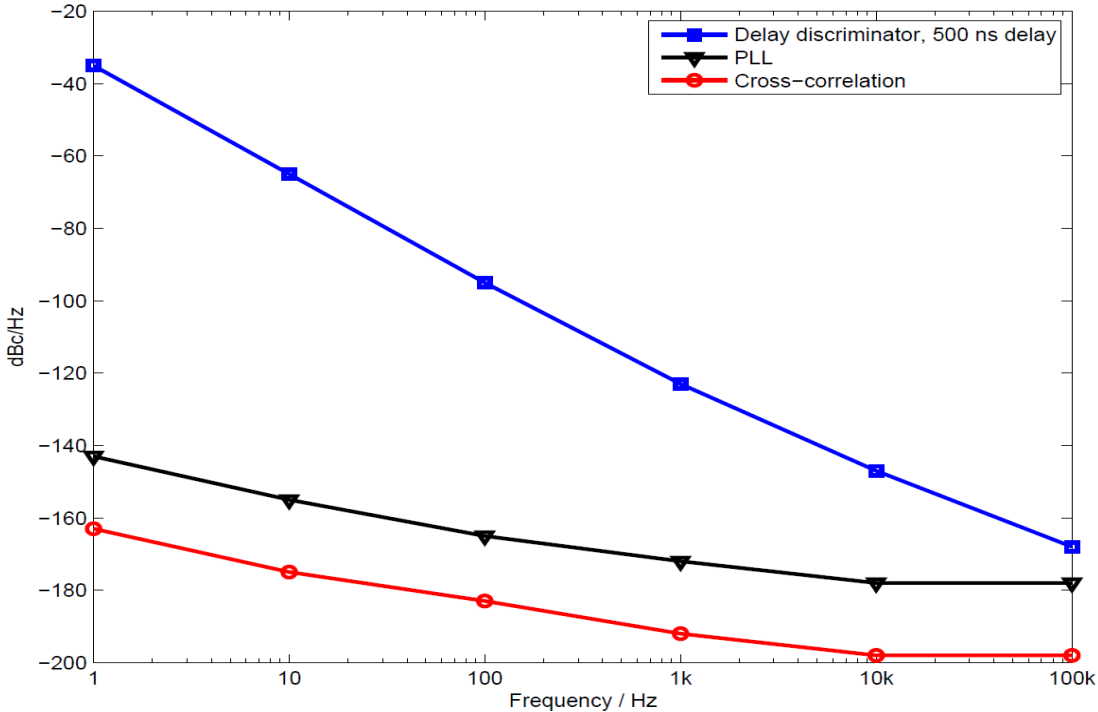


Figure 4-12: Shows phase noise plots and noise floor for 3-techniques (PLL, Delay line, and cross-correlation) [31]

4.4 Prediction and Validation of Oscillator Phase Noise Measured on Different Equipments

The phase noise equation for a Colpitts based oscillator circuit can be expressed as [3]

$$\xi(\omega) = 10 \log \left\{ 4kTR + \left[\frac{4qI_c g_m^2 + \frac{4K_f I_b^{AF}}{\omega} g_m^2}{\omega_0^2 C_1^2 (\omega_0^2 (\beta^+)^2 C_2^2 + g_m^2 \frac{C_2^2}{C_1^2})} \right] \left[\frac{\omega_0^2}{4\omega^2 V_{cc}^2} \right] \left[\frac{Q_o^2}{Q_L^2} + \frac{[C_1 + C_2]^2}{C_1^2 C_2^2 \omega_0^4 L^2 Q_L^2} \right] \right\} \quad (4.32)$$

where

$$\beta^+ = \left[\frac{Y_{21}^+}{Y_{11}^+} \right] \left[\frac{C_1}{C_2} \right]^p \quad g_m = \left[Y_{21}^+ \right] \left[\frac{C_1}{C_2} \right]^q ; \text{ Values of } p \text{ and } q \text{ depends upon the drive level}$$

Y_{21}^+, Y_{11}^+ = large signal [Y] parameter of the active device

- K_f = flicker noise coefficient
 AF = flicker noise exponent
 $F(\omega)$ = ratio of sideband power in a 1Hz BW at ω to total power in dB
 ω = frequency offset from the carrier
 ω_0 = center frequency
 Q_L = loaded Q of the tuned circuit
 Q_o = unloaded Q of the tuned circuit
 kT = 4.1×10^{-21} at 300 K (room temperature)
 R = equivalent loss resistance of the tuned resonator circuit
 I_c = RF collector current
 I_b = RF base current
 V_{cc} = RF collector voltage
 C_1, C_2 = feedback capacitor as shown in Figure (4.13)

4.4.1 Verification of 100 MHz Crystal Oscillator using CAD simulation Tool (Ansoft Designer from Ansys)

Figures 4-13, 4-14, 4-15, 4-16 and 4-17 show the typical simplified Colpitts 100 MHz Crystal oscillator circuit, grounded base buffer circuit, noise Figure plots, phase noise plots, and output power.

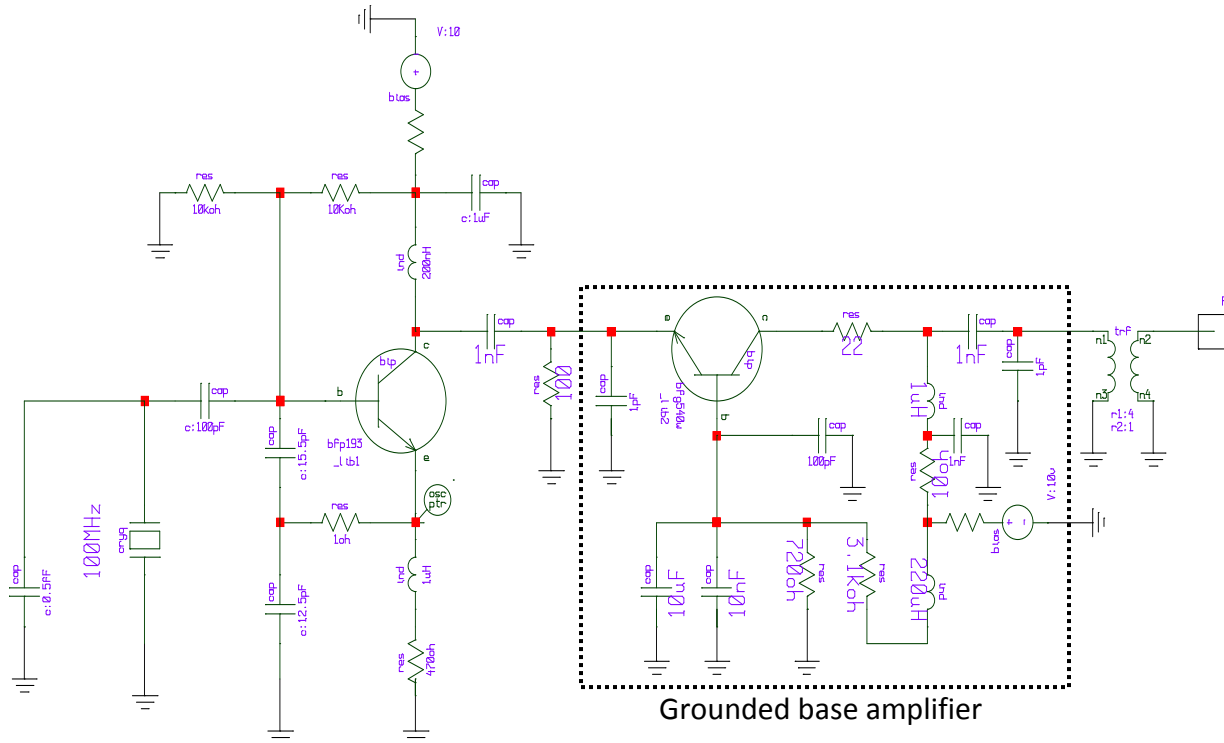


Figure 4-13: 100 MHz Crystal Oscillators with the Grounded-Base low noise Amplifier

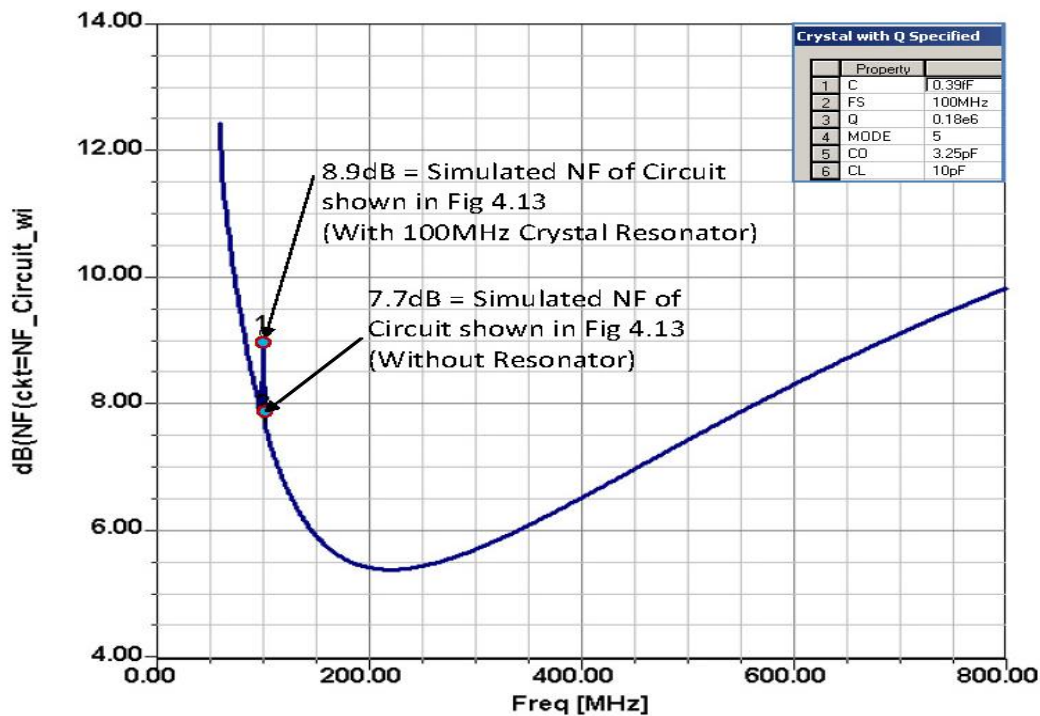


Figure 4-14: Simulated plot showing NF of 100 MHz Oscillator shown in Fig 4-13

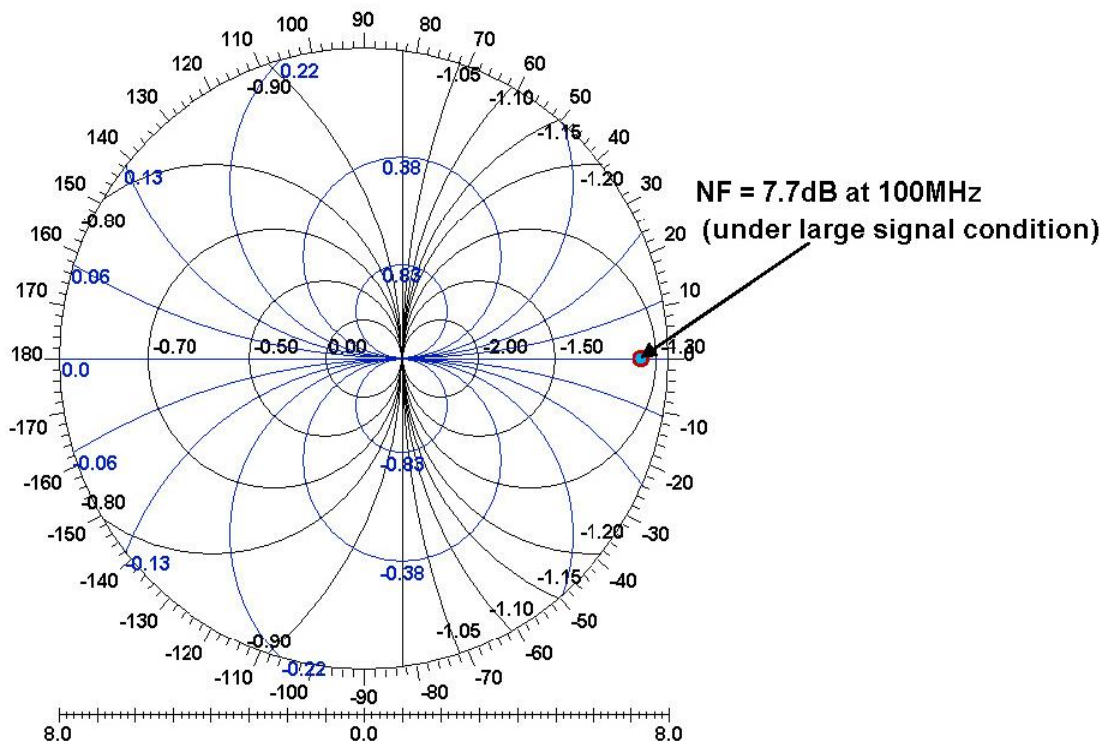


Figure 4-15: CAD simulated Polar Plot of Noise of the Oscillator Circuit shown in Figure 4-13

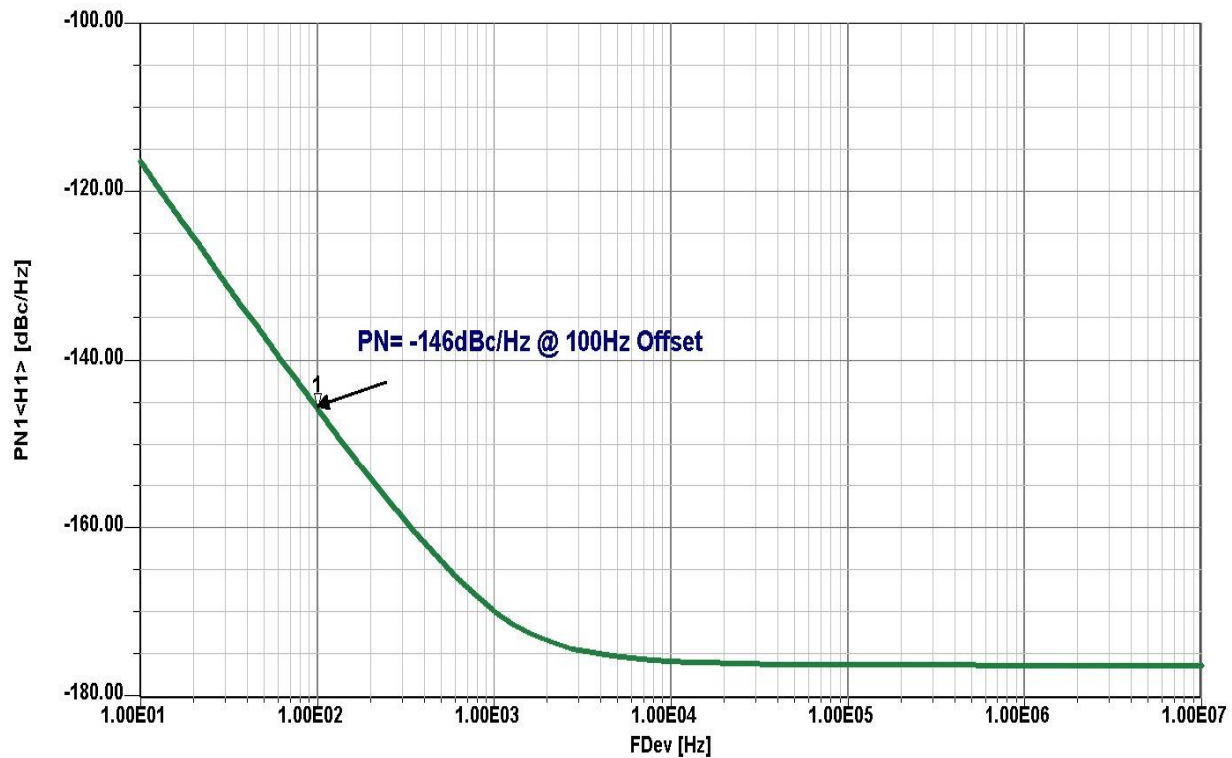


Figure 4-16: CAD simulated Phase Noise Plot of 100MHz Crystal Oscillator with Buffer Stage

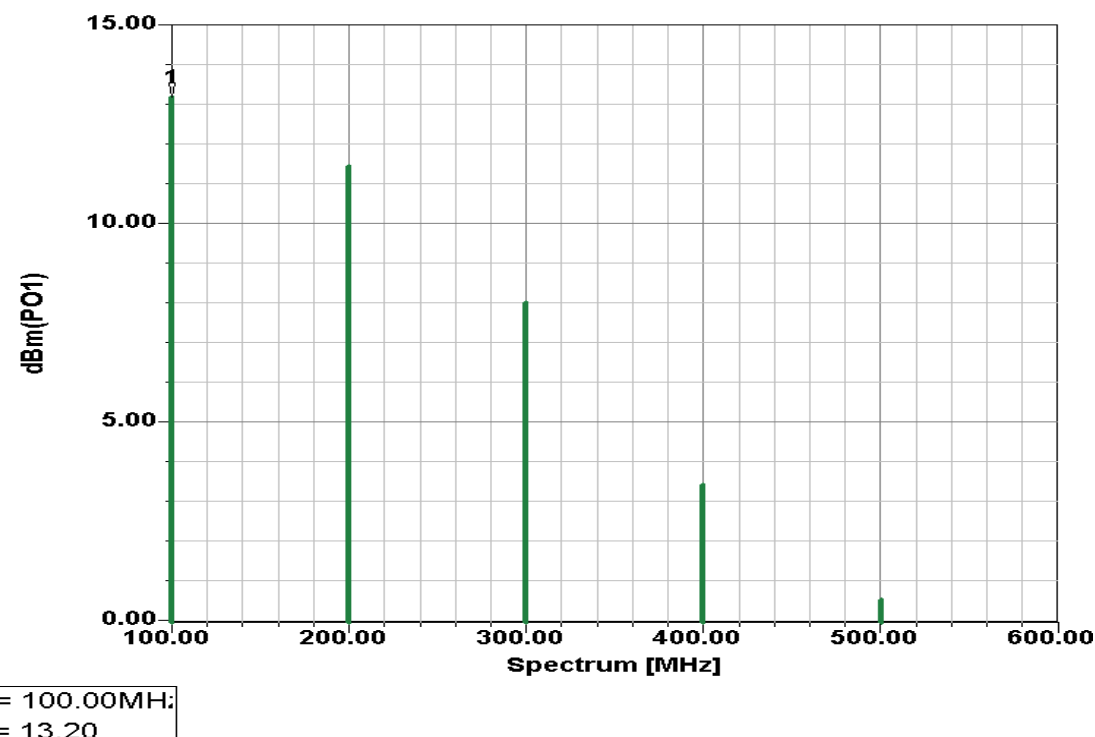


Figure 4-17: Simulated Power Output Plot of 100MHz Crystal Oscillator with Buffer Stage

The basic equation needed to predict the phase noise using CAD simulation for the circuit shown in Figures 4-13 and 4-14 is found in [3]

$$\xi(f_m) = 10 \log \left\{ 1 + \frac{f_0^2}{[2f_m Q_0 m(1-m)]^2} \left[\left(1 + \frac{f_c}{f_m} \right) \frac{FkT}{2P_0} + \frac{2kTRK_0^2}{f_m^2} \right] \right\} \quad (4.33)$$

where $\xi(f_m)$, f_m , f_0 , f_c , Q_L , Q_0 , F , k , T , P_0 , R , K_0 and m are the ratio of the sideband power in a 1Hz bandwidth at f_m to total power in dB, offset frequency, flicker corner frequency, loaded Q , unloaded Q , noise factor, Boltzmann's constant, temperature in degree Kelvin, average output power, equivalent noise resistance of tuning diode, voltage gain and ratio of the loaded Q -factor (Q_o) and unloaded Q -factor (Q_L).

In the past this was done with the Leeson formula, which contains several estimates, those being output power (P_o), flicker corner frequency (f_c), oscillator noise factor (F), and the operating (or loaded) Q . Now, one can assume that the small signal linear estimation of noise factor (F) can give wrong estimation of phase noise when oscillator operates under large signal condition.

The approximate formulae (considering quasi-nonlinear analysis) of the noise factor under the large signal condition can be given by the following equation [3, pp. 135].

$$F \cong 1 + \frac{Y_{21}^+ C_2 C_c}{(C_1 + C_2) C_1} \left[r_b + \frac{1}{2r_e} \left(r_b + \frac{(C_1 + C_2) C_1}{Y_{21}^+ C_2 C_c} \right)^2 \left(\frac{1}{\beta^+} + \frac{f^2}{f_T^2} \right) + \frac{r_e}{2} \right] \quad (4.34)$$

where Y_{21}^+ = large signal [Y] parameter of the active device.

Table 4-2: shows the calculated Noise Figure and Phase Noise for 100MHz Crystal Oscillator using (4.32), (4.33) and (4.34) for unloaded $Q_o = 180000$, and time average loaded Q ($Q < Q_o/4$) under large signal drive level condition is 25000.

Table 4-2: Calculated Noise Figure and Phase Noise for 100MHz Crystal Oscillator

Oscillator Frequency	Simulated Large Signal Noise Figure	Calculated Phase Noise at 100Hz offset
100 MHz	7.7 dB	-146 dBc/Hz

4.4.2 Verification of 100 MHz Crystal Oscillator (LN XO 100) using Analytical Model

The theoretical calculated parameters of 100MHz crystal oscillator circuit is given below [ref. 3, pp.181], after defining all the values, the phase noise can be predicted for comparative analysis.

Theoretical calculated parameters of 100MHz crystal oscillator circuit

C1:= 15.6pF	C2:= 12.5pF	kT:= $4.143 \cdot 10^{-21} \cdot J$	R:= $0.2 \cdot \Omega$
qcharge:= $1.602 \cdot 10^{-19} \cdot \text{coul}$	Ic:= $8.2 \cdot \text{mA}$		Ib = $220 \cdot \mu\text{A}$
y11:= $(0.000884 - 0.0000158j) \cdot \text{mho}$			
y21:= $(0.0105 - 0.00084j) \cdot \text{mho}$			
L:= $6.4949 \cdot 10^{-3} \cdot \text{henry}$	af:= 2	kf:= $1 \cdot 10^{-10}$	$y := \frac{C1}{C2}$
Vcc:= 10V	i:= 0..7	p:= 1.45	q:= 1.05
Q:= 25000	Q0:= 180000	nfdB:= 4.747	PoutdB:= 13
fc:= 100MHz	wc:= $2\pi \cdot fc$	gm:= $ y21 \cdot y^q$	
fo_i:= $10^i \cdot \text{Hz}$	wo_i:= $2\pi \cdot fo_i$	B1i:= $(wo_i)^2 \cdot L^2 \cdot Vcc^2$	
kconstant:= $\frac{KT \cdot R}{wc^2 \cdot C2^2}$	k0_i:= $\frac{kconstant}{B1_i}$	b:= $\frac{ y21 \cdot y^p}{ y11 }$	
$k1constant_i := qcharge \cdot Ic \cdot gm^2 + \frac{kf \cdot Ib^{af} \cdot gm^2}{wo_i}$			
$k1_i := \frac{k1constant_i}{wc^2 \cdot B1_i}$	k3_i:= $wc^2 \cdot gm^2$	$k2_i := wc^4 \cdot b^2$	$k_i := \frac{k3_i}{k2_i \cdot C2^2}$
$t2_i := k0_i \frac{(1+y)^2}{y^2}$	$t1_i := \left[\left(\frac{b^2}{gm^3} \right)^2 \cdot \frac{k_i^3 \cdot k1_i \cdot (wc)^2}{y^2 + k_i} \right] \cdot \frac{(1+y)^2}{y^2}$		$1_i := t1_i + t2_i$
$m_i := 10 \cdot \log \left[1_i \cdot (kg^{-2} \cdot m^{-4} \cdot s^5 \cdot A^2) \cdot \frac{Q0^2}{Q^2} \right]$			
$L_i := \text{if}[m_i < (-177 + Pout(dBm) - nfdB)), (-177 + PoutdB - nfdB)), m_i]$			
m_i	f_{o_i}	L_i	
-88.581	$1 \cdot s^{-1}$	-88.581	
-118.515	$10 \cdot s^{-1}$	-118.515	
-147.901	$100 \cdot s^{-1}$	-147.901	
-174.251	$1 \cdot 10^3 \cdot s^{-1}$	-174.251	
-195.999	$1 \cdot 10^4 \cdot s^{-1}$	-185.253	
-216.22	$1 \cdot 10^5 \cdot s^{-1}$	-185.253	
-236.243	$1 \cdot 10^6 \cdot s^{-1}$	-185.253	
-256.245	$1 \cdot 10^7 \cdot s^{-1}$	-185.253	

Figure 4-18 shows the theoretical phase noise model expressed in (4.23)

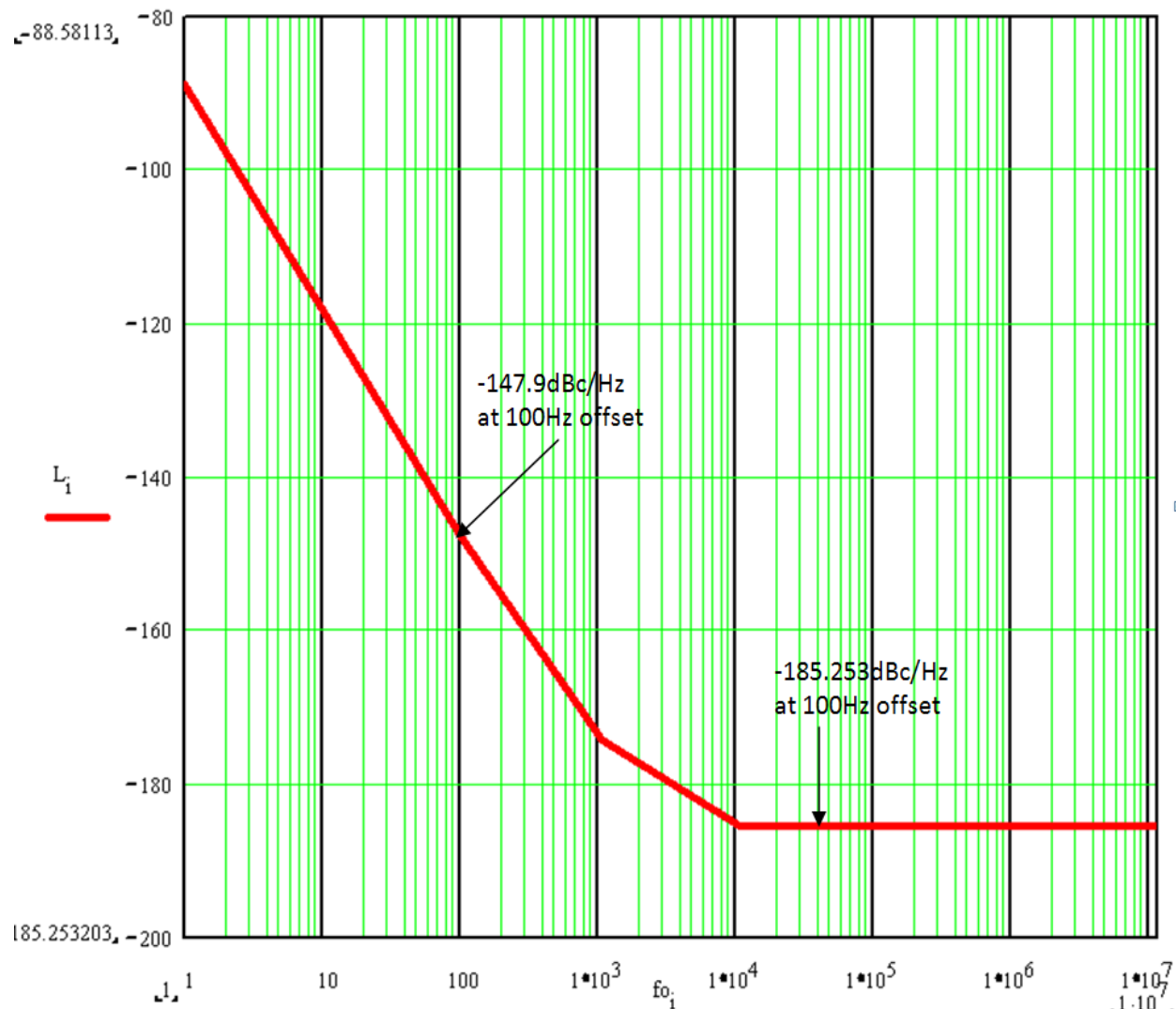


Figure 4-19: Theoretically calculated Phase Noise Plot for 100MHz Crystal Oscillator (LN XO 100)

4.4.3 Verification of 100 MHz Crystal Oscillator using Phase Noise Measurement Equipments

For validation of the theoretical model described in section (4.4.2), 100 MHz Crystal oscillator was built and tested on different Phase Noise Measurement Equipments (Agilent E5052B, R&S FSUP, Holzworth, Noise XT, and Anapico APPH6000-IS) available on the market.

4.4.3.1 Experimental Verification of 100 MHz Crystal Oscillator using Agilent E5052B

The feature of cross-correlation techniques in Agilent E5052B satisfies the established criteria without additional references, nor calibration of the device under test (DUT) on exact frequency.

Figures 4-20 and 4-21 show the picture of Agilent E5052B equipment and measured phase noise plot of 100 MHz crystal oscillator circuit for the purpose of the verification of measurement uncertainty.

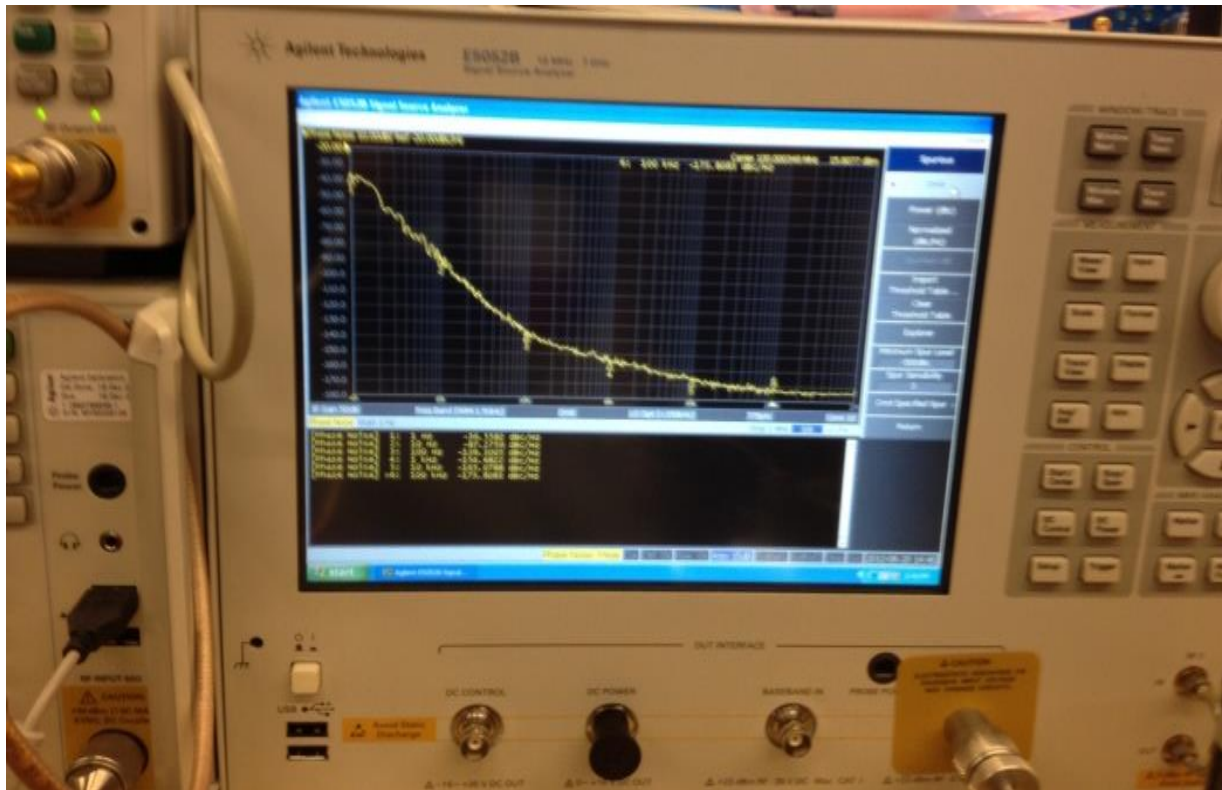


Figure 4-20 shows the picture of E5052B (Courtesy: Agilent) with the phase noise plot of 100 MHz crystal oscillator circuit for the purpose of the verification of measurement uncertainty (IMS show 2012, Montreal, Canada)

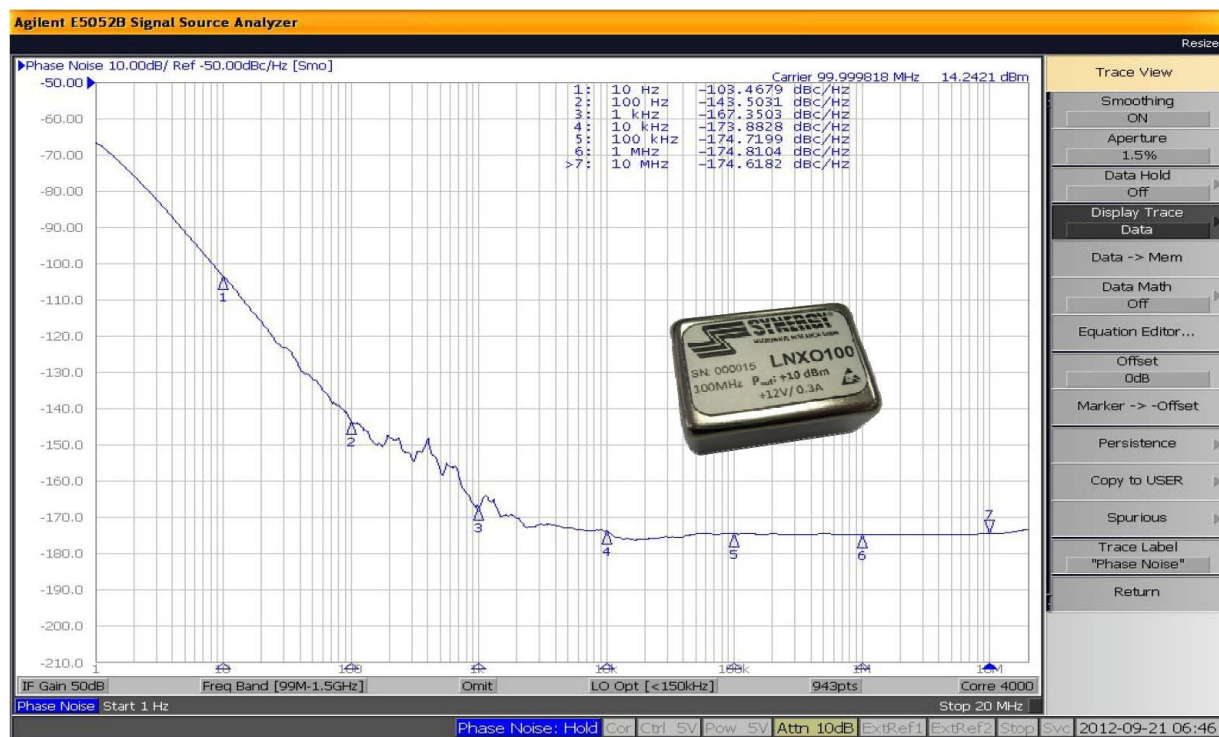


Figure 4-21: 100MHz Crystal Oscillator Measured on Agilent E5052B (Corr_4000) [measurement performed in IMS show 2012, Montreal, Canada]

The measured phase noise at 100 Hz offset is -143 dBc/Hz for LNXO 100 (100MHz carrier frequency), this shows the capability of close-in measurement. The main concern is the dynamic range and noise floor of the equipment measured at large offsets from the carrier, the far offset noise floor is -174 dBc/Hz at offsets greater than 100 KHz.

The theoretical expectations were closer to -191 dBc/Hz at 10 KHz offsets and beyond for 14 dBm output power. The other problem is that the mixer and the post amplifier can easily get into compression, which raises the noise floor.

4.4.3.2 Experimental Verification of 100 MHz Crystal Oscillator using R&S (FSUP 26)

The feature of cross-correlation techniques in R&S (FSUP 26) satisfies the established criteria, and requires neither additional references, nor calibration of the device under test (DUT) on exact frequency.

Figures 4-22 and 4-23 show the picture of R&S (FSUP 26) equipment and measured phase noise plot of 100 MHz crystal oscillator for the purpose of the verification of measurement uncertainty. The measured phase noise at 100 Hz offset is -140 dBc/Hz for LNXO 100 (100MHz carrier frequency), and the far offset noise floor is -174 dBc/Hz at offsets greater than 100 KHz.

The theoretical expectations were closer to -191dBc/Hz at 100 KHz offsets and beyond for 14 dBm output power.

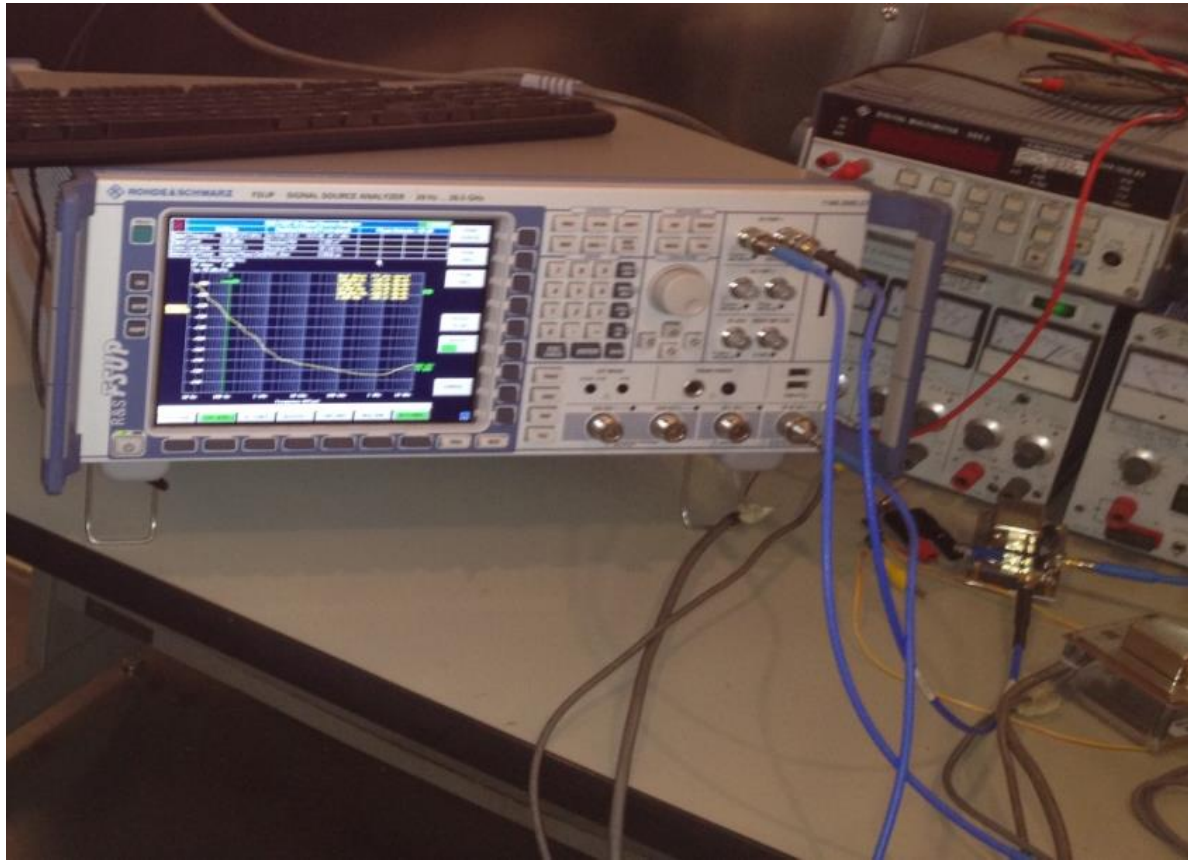


Figure 4-22 shows the picture of R&S FSUP 26 (Courtesy: R&S) while taking measurement

Design Validation: Low Noise Crystal Oscillator (LNXO)

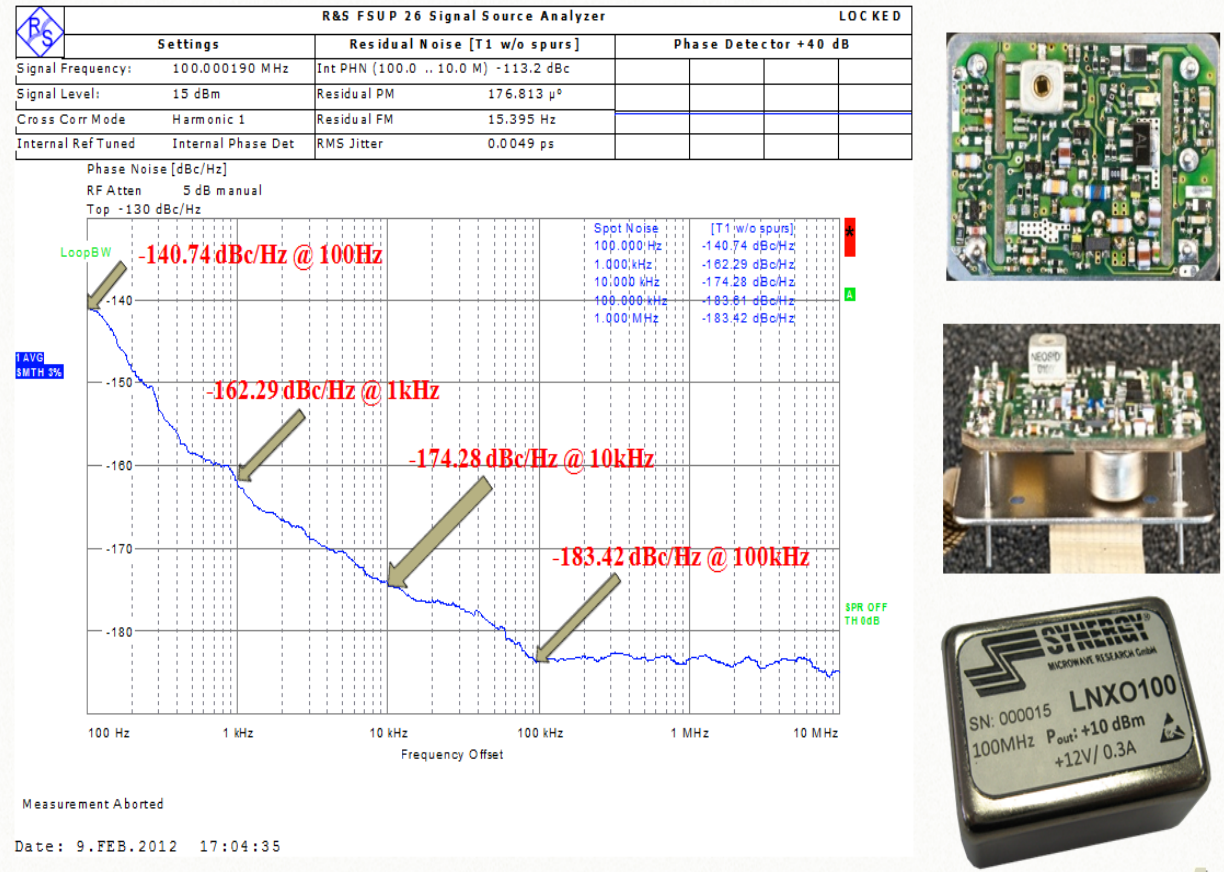


Figure 4-23: 100MHz Crystal Oscillator Measured on R&S FSUP

4.4.3.3 Experimental Verification of 100 MHz Crystal Oscillator using Anapico (APPH6000-IS)

The feature of cross-correlation techniques in APPH 6000 (Anapico) satisfies the established criteria, but require 2-additional references at exact frequency. Figures 4-24 shows the measured phase noise plot of 100 MHz crystal oscillator for the purpose of the verification of measurement uncertainty.

The measured phase noise at 100 Hz offset is -146dBc/Hz for LNXO 100 (100MHz carrier frequency), this shows the capability of close-in measurement. The instrument's specification calls for -184dBc/Hz floor at offsets greater than 100 KHz. The theoretical expectations were closer to -191dBc/Hz at 100 KHz offsets and beyond for 14dBm output power. The main concern is the additional references at exact frequency of DUT.

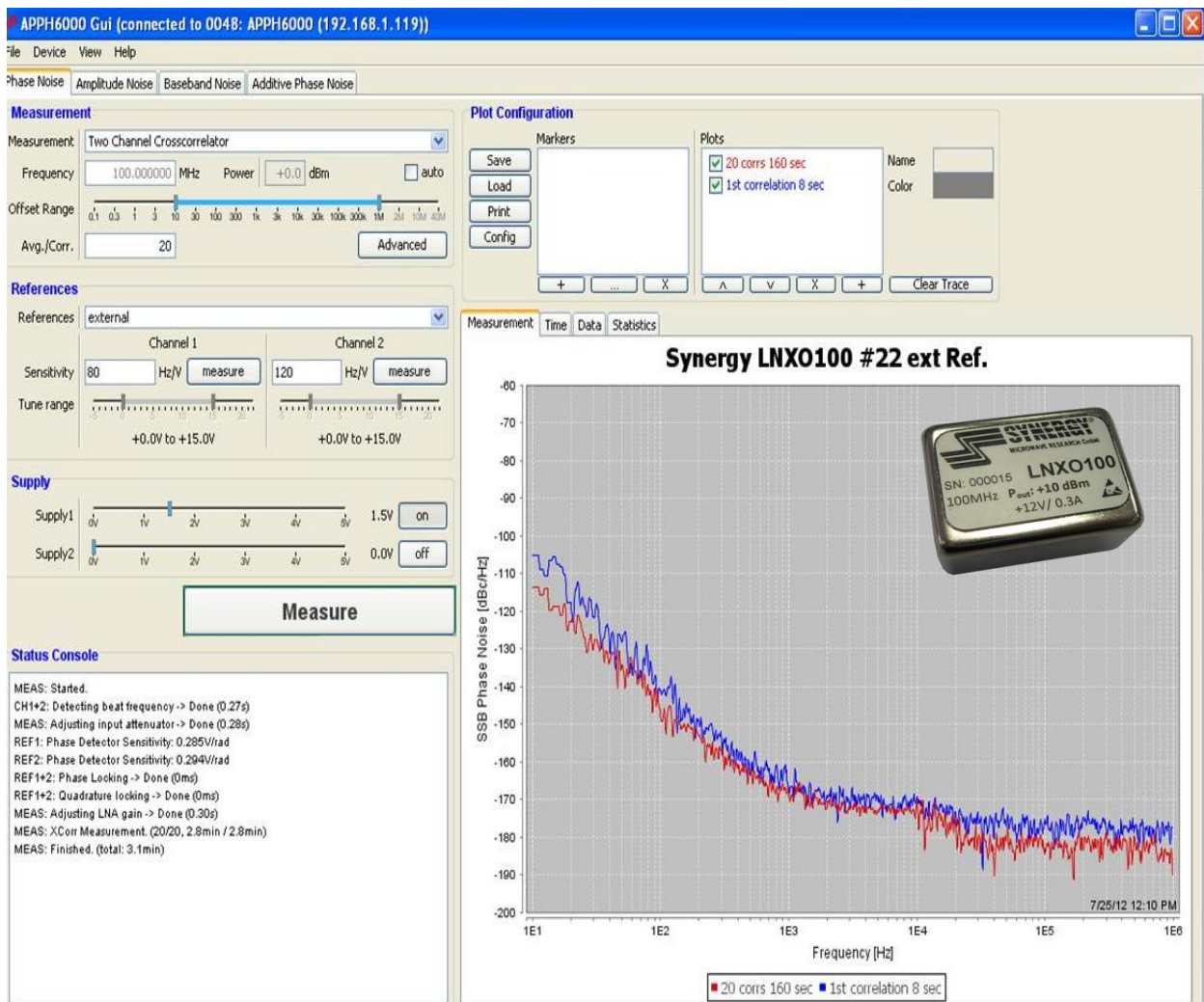


Figure 4-24 shows the picture of phase noise plots and equipment setting (Courtesy: Anapico APPH6000-IS) 100MHz Crystal Oscillator Measured on Anapico phase noise engine

4.4.3.4 Experimental Verification of 100 MHz Crystal Oscillator using Holzworth (HA7402A)

The feature of cross-correlation techniques in Holzworth satisfies the established criteria; require 2-additional references at exact frequency. Figure 4-25 shows the picture of Holzworth phase noise measurement equipment, including the measured phase noise plot of 100 MHz crystal oscillator for the purpose of the verification of measurement uncertainty.

The measured phase noise at 100 Hz offset is -147dBc/Hz for LNXO 100 (100MHz carrier frequency), this shows the capability of close-in measurement. The instrument's specification calls (conservatively) for -178dBc/Hz floor at offsets greater than 100 KHz. The theoretical expectations were closer to -191dBc/Hz at 100 KHz offsets and beyond for 14dBm output power. The main concern is the additional references at exact frequency of DUT.

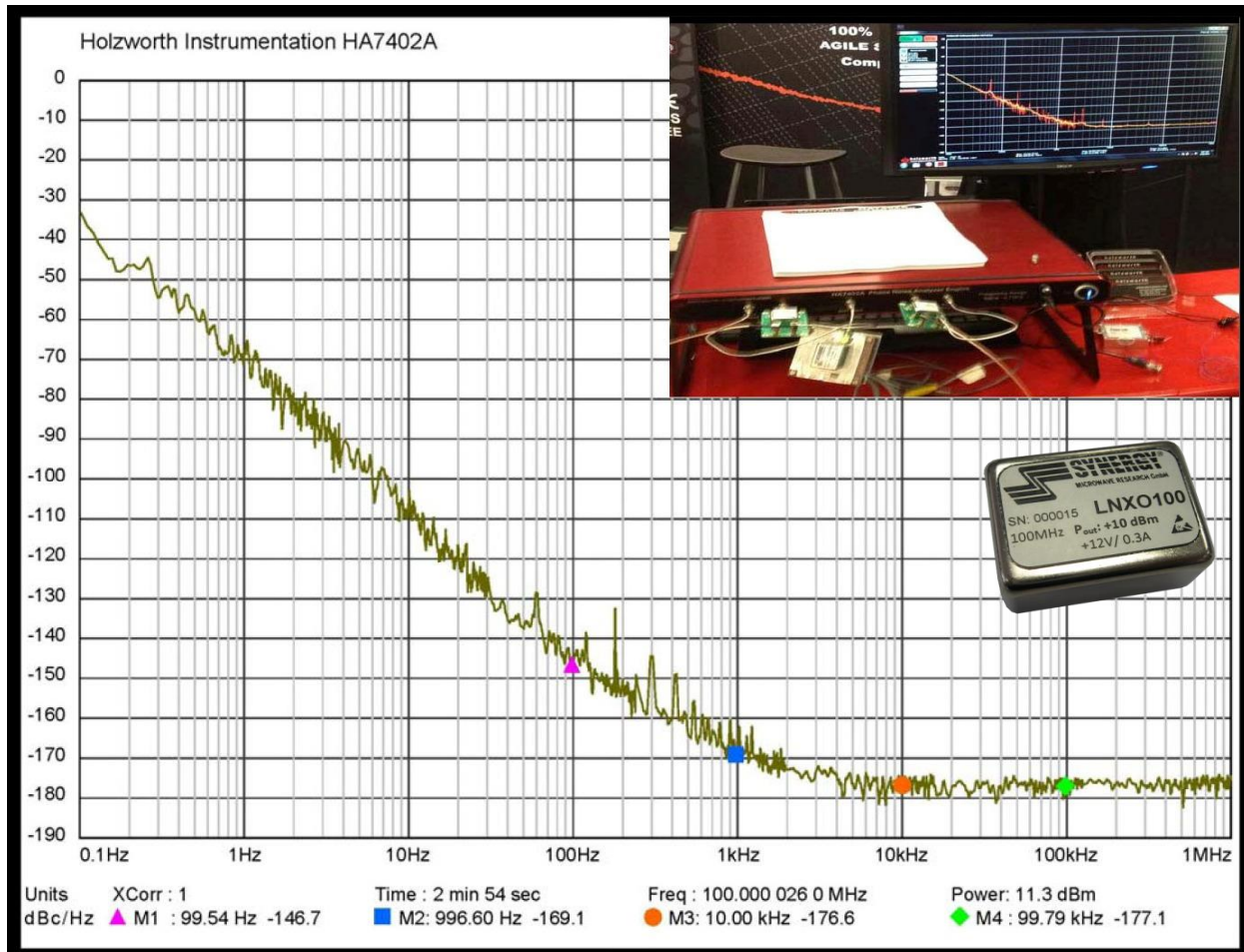


Figure 4-25 shows the picture of phase noise plots and equipment setting (Courtesy: Holzworth) 100MHz Crystal Oscillator Measured on Holzworth Phase Noise Engine [measurement performed in IMS show 2012, Montreal, Canada]

4.4.3.5 Experimental Verification of 100 MHz Crystal Oscillator using Noise XT (DCNTS)

The feature of cross-correlation techniques in Noise XT satisfies the established criteria; require 2-additional references at exact frequency. Figures 4-26 shows the picture of Noise XT (DCNTS) phase noise measurement equipment, including the measured phase noise plot of 100 MHz crystal oscillator for the purpose of the verification of measurement uncertainty.

The measured phase noise at 100 Hz offset is -140dBc/Hz for LNXO 100 (100MHz carrier frequency), this shows the capability of close-in measurement. The instrument's specification calls for -190 dBc/Hz floor at offsets greater than 1 MHz. The theoretical expectations of -191dBc/Hz noise floor closely met with this equipment for 14dBm output power. The main concern is the close-in phase noise, which is 7dB inferior as compared to Holzworth for identical correlations. As shown in Figure 4-26, Noise XT Dual Core Noise Test Set (DCNTS) [28] requires two references with similar performance as the DUT (the better the reference performance – the faster the test), the references must have voltage control (ability to change frequency with the change of the voltage on the control terminal), and be calibrated on the frequency of DUT.

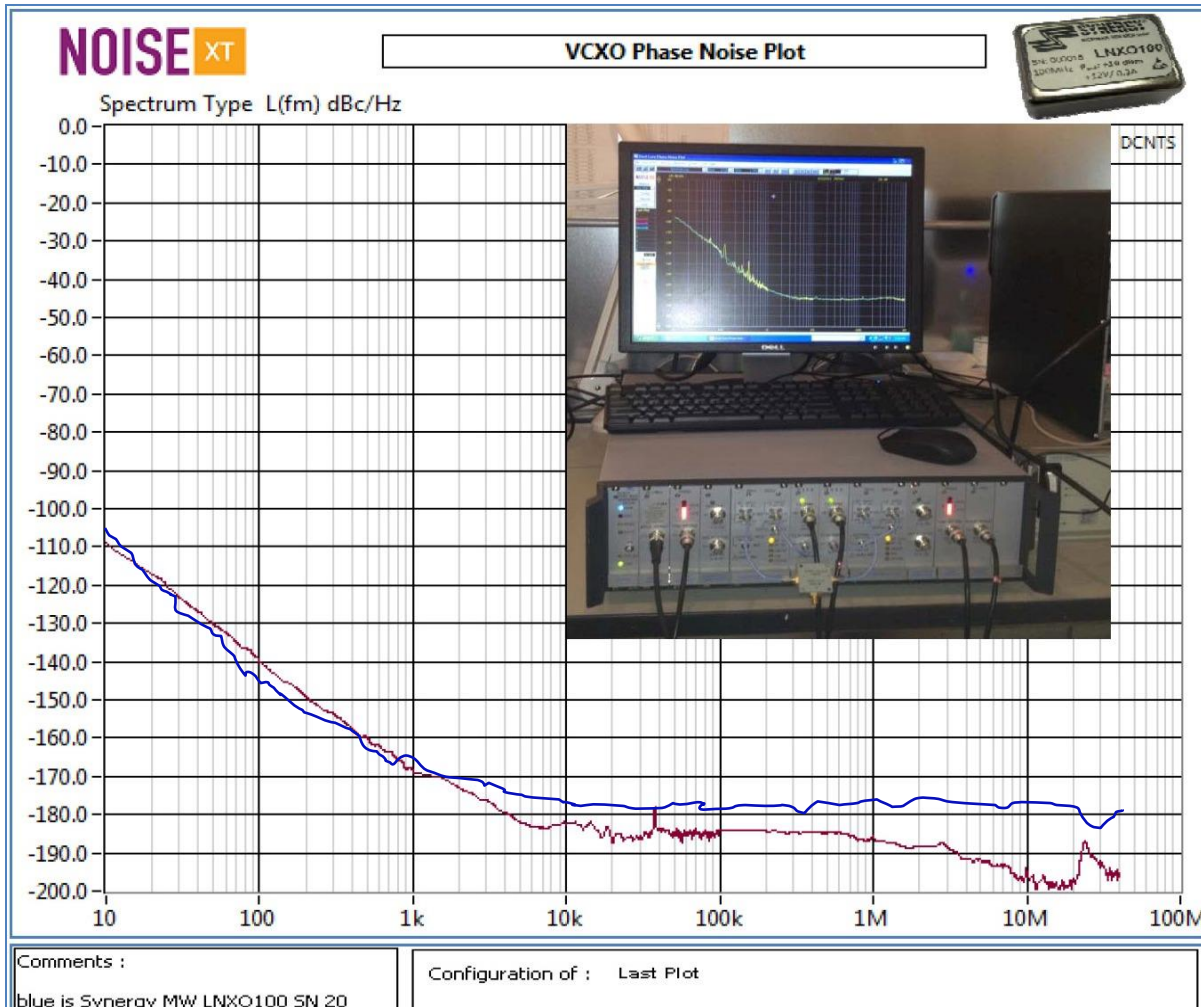


Figure 4-26: Phase noise measurement using cross-correlation techniques using Noise XT DCNTS Engine

4.5 Phase Noise Measurement Evaluation and Uncertainties:

The rigorous measurements are conducted on 100 MHz Crystal oscillator using different Phase Noise Measurement Equipments (Agilent E5052B, R&S FSUP, Holzworth, Noise XT, and Anapico APPH6000-IS) commercially available on the market. Table 4-3 describes the theoretical and measured phase noise on different test equipment for comparative analysis of the measured data under similar test condition. The consequence is this set of equations gives the best possible phase noise. If the equipment in use, after many correlations gives out a better number, either it violates the laws of physics and if it gives a worse number, then the correlations settings needs to corrected or the dynamic range of the equipment is insufficient. This measurement is exhaustive, but it was necessary to explain how things fall in place.

At 20dBm output, the output amplifier certainly has a higher noise figure, as it is driven with more power and there is no improvement possible. Phase Inversion may lead to collapse of the cross-spectral function, failure to truly measure noise occurs when a special phase condition exists between the signals being offered to the cross-spectrum function [49]-[55]. This may be

favorable condition to see optimistic but wrong phase noise measurement due to the established anti-phase condition of second uncorrelated interfering signal. Therefore, the detection of the desired signal using cross-spectral techniques collapses partially or entirely in the presence of the second uncorrelated interfering signal. Cross-spectral analysis is a mathematical tool for extracting the power spectral density of a correlated signal from two time series in the presence of uncorrelated interfering signals [55]. The cross-spectrum of two signals $x(t)$ and $y(t)$ is defined as the Fourier transform of the cross-covariance function of x and y .

For example, $x(t) = a(t) + c(t) + d(t)$; $y(t) = a(t) + c(t) - d(t)$, where $c(t)$ to be the desired signal, $a(t)$ and $b(t)$ are the uncorrelated interfering signals, $d(t)$ is anti-correlated (phase inverted) in x and y then it leads to an unexpected negative hump (exhibits unexpected very low phase noise) in phase noise plot due to cancellation dynamics. This implies that at any frequency f where the average magnitude of signal $C(f)$ is equal to that of signal $D(f)$, the magnitude of the cross-spectrum collapses to zero [56].

Any contribution of the desired signal $c(t)$, or the interferer $d(t)$, to the cross spectral density is eliminated. This occurs even though signals $c(t)$ and $d(t)$ are completely uncorrelated. If $C(f)$ and $D(f)$ have the same shape or slope versus frequency, entire octaves or decades of spectrum can be suppressed and be grossly under-reported. If the PSD (power spectral density) of C and D are not exactly equal, a partial cancelation still occurs. These condition is demonstrated on 100 MHz OCXO measured on different equipments, some of the measurements showing -198 dBc/Hz @ 20 MHz offset for 100 MHz OCXO (Figure 4-26, red plot) can be uncertain for exactly these reasons.

The cross correlation technique allows us to look below kT (k is Boltzmann constant and T is temperature in degree Kelvin), however the usefulness of noise contributions below kT is a matter of discussion among scientific community because not understanding when and how this effect occurs can lead to dramatic underreporting of the desired signal [56]-[58].

Following is a set of measured results of 100MHz Crystal Oscillators with different test equipments shown in Table 4-3 for giving good understanding about the discrepancy in phase noise measurement performed on different commercially available equipments in the market.

Table 4-3: Theoretical and measured phase noise on different test equipments available in market [46]-[47]

100 MHz OCXO O/P=14dBm, NF=7dB	Theoretical Model [1]	Agilent E5052B	R & S FSUP 26	Anapico APPH6000- IS	Holzworth HA7402-A	Noise XT DCNTS
PN @ 100 Hz offset	-147 dBc/Hz	-143 dBc/Hz	-143 dBc/Hz	-141 dBc/Hz	-147 dBc/Hz	-140 dBc/Hz
PN @ 1 kHz offset	-175 dBc/Hz	-167 dBc/Hz	-163 dBc/Hz	-170 dBc/Hz	-170 dBc/Hz	-170 dBc/Hz
PN @ 10kHz offset	-185 dBc/Hz	-173 dBc/Hz	-174 dBc/Hz	-172 dBc/Hz	-178 dBc/Hz	-181 dBc/Hz
PN @ 100KHz offset	-185 dBc/Hz	-174 dBc/Hz	-183 dBc/Hz	-181 dBc/Hz	-179 dBc/Hz	-183 dBc/Hz
PN @ 1 MHz offset	-185 dBc/Hz	-174 dBc/Hz	-184 dBc/Hz	-182 dBc/Hz	-179 dBc/Hz	-186 dBc/Hz
PN @ 10MHz offset	-185 dBc/Hz	-174 dBc/Hz	-185 dBc/Hz	-188 dBc/Hz	-178 dBc/Hz	-196 dBc/Hz

Phase Noise Measurement Issues

There are important measurement issues that, if not well understood, can lead to erroneous results and interpretations [45]. They involve measurement bandwidth masking of, and accurate distinction between, true discrete spurious signals and narrowband noise peaks (typically encountered under vibration). Although the phase noise data displayed by phase noise equipment is usually normalized to 1Hz measurement bandwidth, most automated phase noise measurement equipments actually measure the phase noise in measurement bandwidths that increase with increasing carrier offset frequency. This is done for two reasons: (1) it results in shorter, overall measurement time, and (2) at high carrier offset frequency (i.e., > 100 kHz), many measurement systems employ analog spectrum analyzers that are not capable of 1Hz resolution. Noise measured in a 1 kHz bandwidth, for example, is 30dB higher than that displayed in a 1Hz bandwidth. That means that low-level discrete spurious signals (and narrowband noise peaks typically encountered under vibration as a result of high Q mechanical resonances) may not be detected. The second problem involves the software employed by the noise measurement system vendor used to discriminate between random noise and discrete spurious signals. Usually, when a reasonably sharp increase in noise level is detected, the system software assumes that the increase marks the presence of a “zero bandwidth” discrete signal.

It therefore (when displaying the phase noise on a 1Hz bandwidth basis) applies a bandwidth correction factor to the random noise, but does not make a correction to what was interpreted as a discrete signal. This results in an erroneous plot if/when the detected “discrete” is really a narrowband noise peak. Figures 4-27 and Figure 4-28 attempt to depict the various situations that can result from these issues as described above. Figure 4-29 shows the picture of Faraday Cage, demonstrating the phase noise measurement setup using different equipments (Agilent E5052B, R&S FSUP, Holzworth HA7402-A, Noise XT DCNTS, Anapico APPH6000-IS) for the validation purpose. OEWaves-PHENOM™ and Agilent E5500 claim for improved dynamic ranges and capable of measuring noise floor below kT but these equipments were not made available for the validation in our Faraday Cage. The effort is in progress to validate the phase noise measurement using PHENOM™ and E5500 for broader acceptance of the fact and myth linked with variation in measurement phase noise data below the kT.

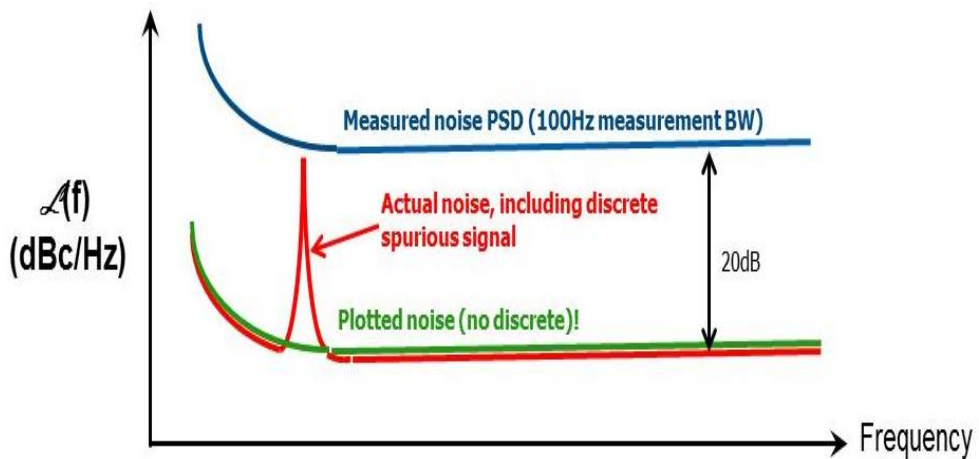


Figure 4-27: Undetected Discrete Spurious Signal [45]

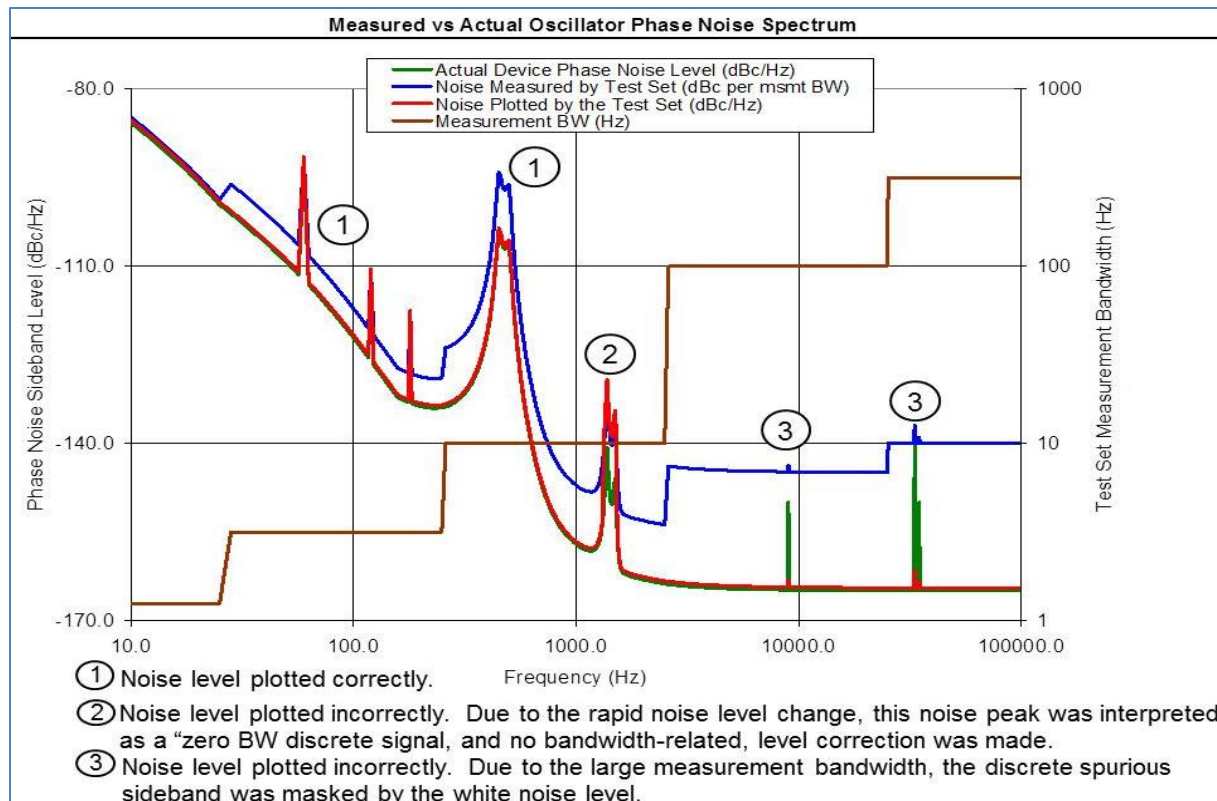


Figure 4-28: Correct and Erroneous Display of Phase Noise Data [45]

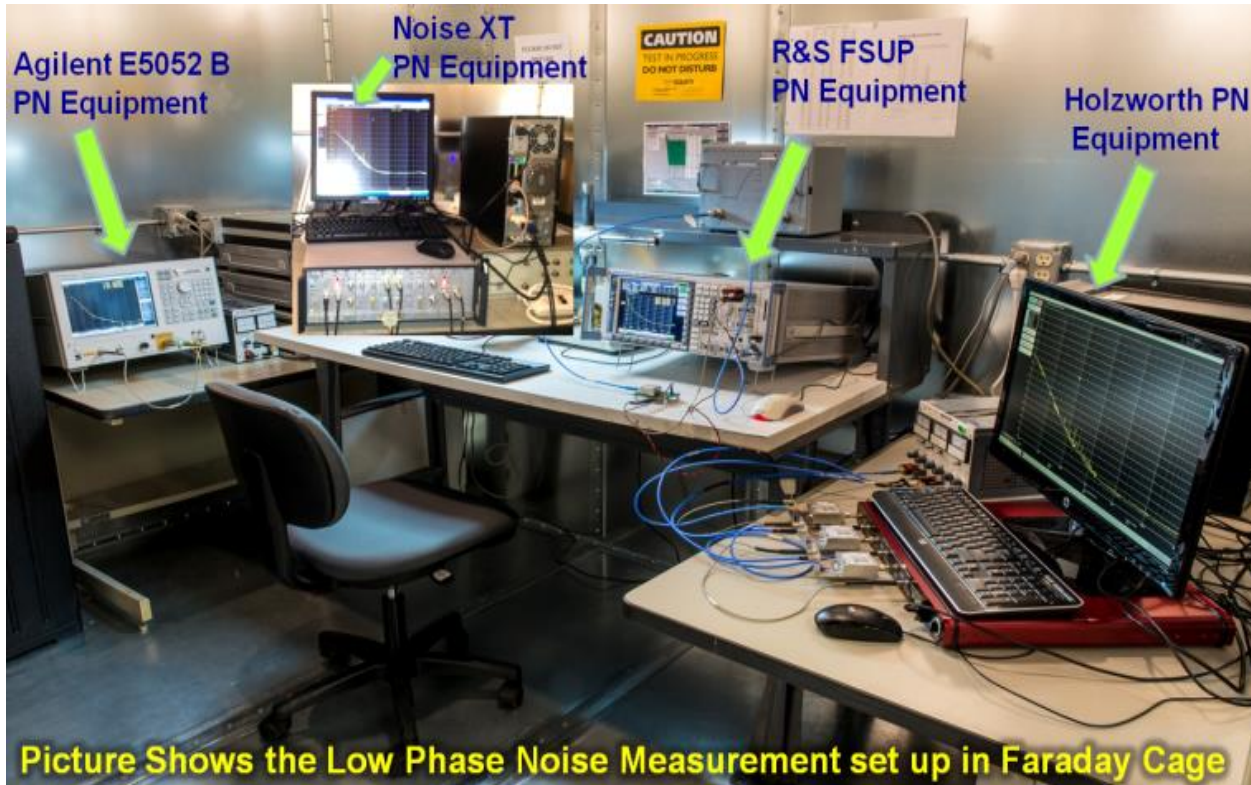


Figure 4-29 – Picture shows Low Phase Noise Measurement Setup in Faraday Cage

Applying the Cross-Correlation

The old systems have an FFT analyzer for close-in calculations and are slower in speed. Modern equipments use noise-correlation method. The reason why the cross-correlation method became popular is that most oscillators have an output between zero to 15dBm and what is even more important is that only one signal source is required. The method with a delay line (Fig. 4-30 and Fig. 4-31), in reality required a variable delay line to provide correct phase noise numbers as a function of offset, shown in ref. [3, pp. 148-153, Fig 7.25 and 7.26].

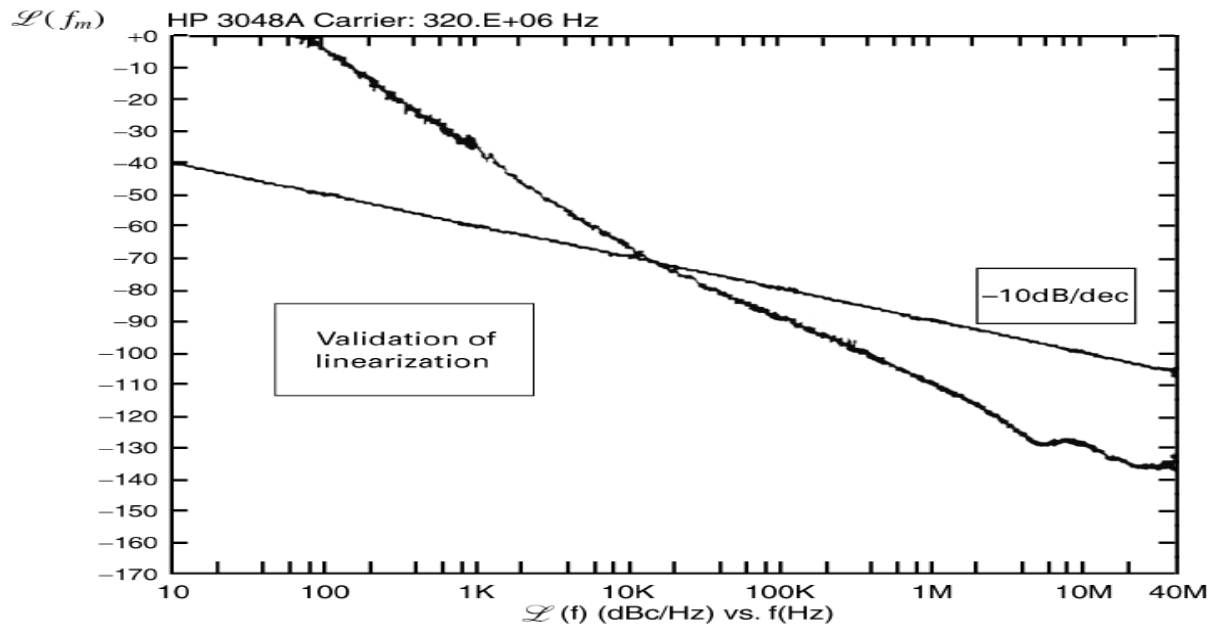


Figure 4-30: Display of a typical phase noise measurement using the delay line principle. This method is applicable only where $x \approx \sin(x)$. The measured values above the solid line violate this relationship and therefore are not valid

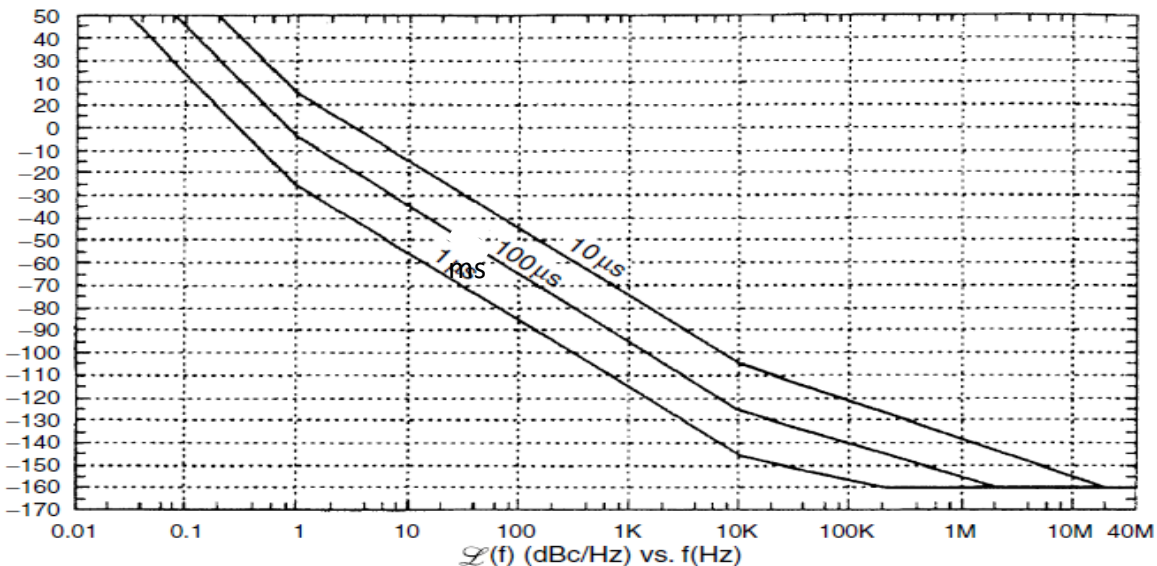


Figure 4-31: Dynamic range as a function of cable delay. A delay line of 1ms is ideal for microwave frequencies.

Advantages of the noise correlation technique:

- Increased speed
- Requires less input power
- Single source set-up
- Can be extended from low frequency 1MHz to 100GHz - depends on the internal synthesizer

Drawbacks of the noise-correlation technique:

- Different manufacturers have different isolation, so the available dynamic range is difficult to predict
- These systems have a “sweet-spot”, both R&S and Agilent start with an attenuator, not to overload the two channels; 1dB difference in input level can result in quite different measured numbers. These “sweet-spots” are different for each machine.
- The harmonic contents of the oscillator can cause an erroneous measurement [8], that’s why a switchable-low-pass filter like the R&S Switchable VHF-UHF Low-pass Filter Type PTU-BN49130 or its equivalent should be used.
- Frequencies below 200MHz, systems such as Anapico or Holzworth using 2 crystal oscillators instead of a synthesizer must be used. There is no synthesizer good enough for this measurement. Example: Synergy LNXO100 Crystal Oscillator measures about -142dBc/Hz, 100Hz after carrier, limited by the synthesizer of the FSUP and -147dBc/Hz with the Holzworth system. Agilent results are similar to the R&S FSUP, just faster.
- At frequencies like 1MHz off the carrier, these systems gave different results. The R&S FSUP, taking advantage of the “sweet-spot”, measures -183dBc, Agilent indicates -175dBc/Hz and Holzworth measures -179dBc/Hz.

We have not researched the “sweet-spots” for Agilent and Holzworth, but we have seen publications for both Agilent and Holzworth showing -190dBc/Hz far-off the carrier. These were selected crystal oscillators from either Wenzel or Pascall [46]-[47].

Another problem is the physical length of the crystal oscillator connection cable to the measurement system. If the length provides something like “quarter-wave-resonance”, incorrect measurements are possible. The list of disadvantages is quite long and there is a certain ambiguity whether or not to trust these measurements or can they be repeated.

4.6 Uncertainties in Phase Noise Measurement

The uncertainties in phase noise measurement due to following:

- Harmonics
- Output Load Mismatch
- Output Phase Mismatch
- Cable Length (Delay)
- Equipment Dynamic Range

RF signals in VCOs, PLLs and synthesizers are characterized by signal power, harmonic content and phase noise; these parameters have to be accurately measured in order to guarantee the system performance. Phase noise measurement methods that use mixers to down-convert the signal to baseband are subject to uncertainty in presence of harmonics.

- Signal Source Analyzer topology
- The conversion characteristic of mixers
- Harmonic Measurement Set-Up
- Effects of fundamental and 3rd harmonic down-conversion on PN measurements
- Harmonic Injection Locking Mechanism
- Harmonic-Injection Locked VCO

4.6.1 Measurement: This work is to perform analysis of harmonics, phase, and delay and load variations during ultra low phase noise measurement.

- Commercially available signal source analyzers (SSA) (Figure 4-32) use a phase detector method to measure the phase noise [29] and [30].
- The signal produced by the DUT is mixed with a reference generated by the instrument's internal oscillator and the result is filtered and sampled by an ADC.
- The ADC samples are analyzed and the information is used to extract the phase noise information and to synchronize the internal oscillator.
- Considering practical mixer and oscillator designs used inside the instrument; the harmonics produced by the DUT will also mix with the local oscillator's signal and will produce low frequency components.
- These low frequency components added to the fundamental components are sampled by the ADC resulting in measurement errors.

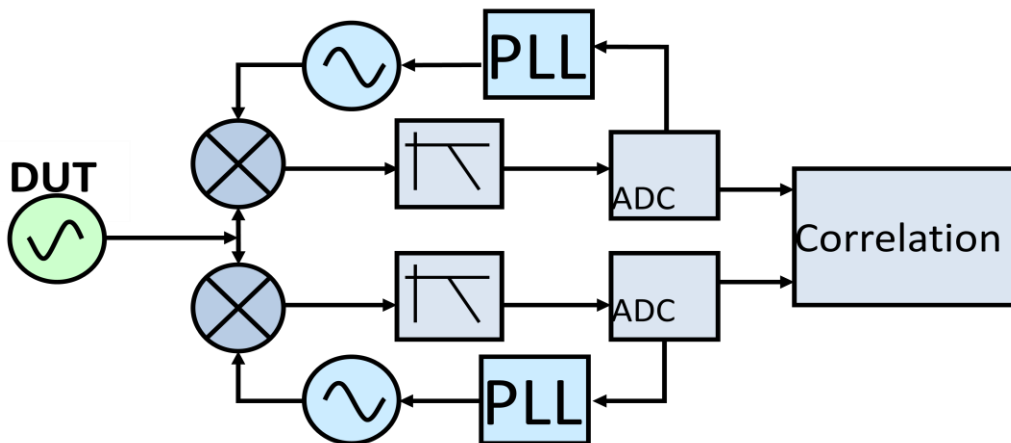


Figure 4-32: A typical Signal source analyzer

- The phase detection measurement uses a mixer to down-convert the DUT signal.
- The phase noise is extracted from the ADC's samples
- A PLL locks the internal oscillators to the DUT frequency.
- Correlation between the 2 channels reduces the noise floor of the instrument.
- Because mixers are used, DUT harmonics will influence the measurements.

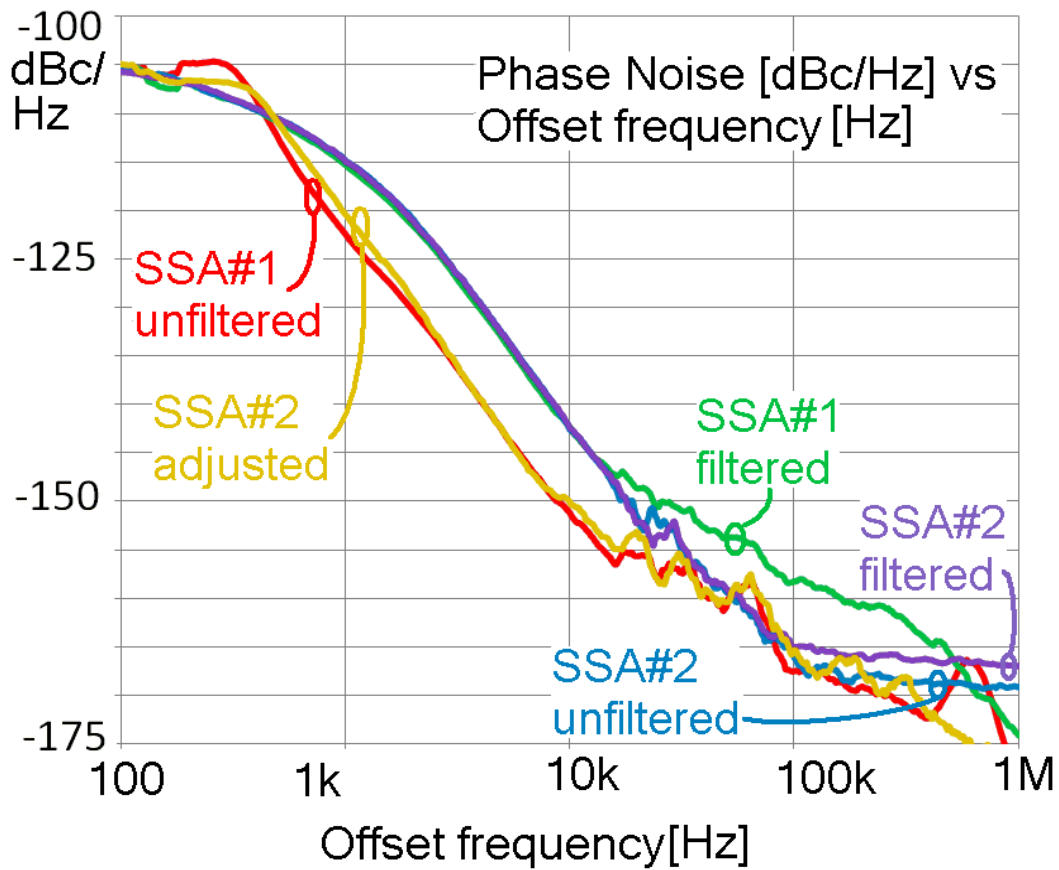


Figure 4-33: Phase noise measurement of 1GHz SAW Oscillator (SSA#1: -151.9dBc/Hz @ 10 kHz for 1GHz carrier frequency, SSA#2: -142.3dBc/Hz @ 10 kHz) HFSO 100

SSA#2 was adjusted (harmonically tuned injection locked source): -152dBc/Hz @ 10 kHz (HFSO 100). The filtered signal on both instruments reported as -142.34 and -142.41dBc.

The phase noise between 100Hz and 10 kHz offset show little variation (less than 1dB) when measured on SSA #1 (filtered), SSA #2 (filtered) or SSA#2 (unfiltered) (Figure 4-33).

Conclusion:

- Phase noise measurement methods that use mixers to down-convert the signal to baseband are subject to uncertainty in presence of harmonics.
- If the mixed signals have harmonics, the mechanism that converts the harmonics to baseband will degrade the measurement accuracy.
- We have demonstrated how the harmonics can alter the accuracy of the phase noise measurements based on the mixer characteristics in the test equipment.
- Based on our observations we recommend that phase noise measurements should be performed on clean signals, harmonics level should be kept below -20dBc.
- In the case where harmonic levels are high we recommend that low pass filters be used to suppress the third harmonic to the levels below 20 dBc to get reliable and repeatable phase noise measurements.
- We developed harmonics-injection mechanism to improve the phase noise of SAW, Crystal and Dielectric Resonator Oscillator, including high performance frequency synthesizers.

Testing phase noise of ultra low noise HPXOs and HFSOs (www.synergymwave.com) requires the cross-correlation technique. Special care must be taken for reduction of RF interference, especially while testing 100MHz OCXO in the vicinity of strong interference caused due to noisy neighborhood. The choice of conducting the measurement in Faraday cage is welcome approach to minimize the error due to EMI.

4.7 Factors Influence Phase Noise Measurement

It is especially pertinent to production environment, where measurement time and accuracy of each measurement becomes critical. Several test methods and test instruments were investigated.

There's no "one size fits all" solution, but for each frequency range the optimum solutions were propose based on (1) Accuracy, (2) Repeatability, (3) Speed of Test, (4) Operating Range, (5) Cost and (6) Ease of data retrieval. The phase noise of -120dBc/Hz at 1Hz offset from the carrier and better than -190dBc/Hz at far offset from the carrier (10 MHz offset) is a challenge using existing test equipment and methods and also the measured data should be reliable and repeatable.

As shown in Figure 4-29, phase noise measurement of 100 MHz OCXO using Agilent E5052B, Rohde & Schwarz FSUP 26, Holzworth, Noise XT, Anapico, was conducted, for understanding the capability and limitations of the equipments for a given test condition.

A survey of some of the more common topologies along with some possible trouble spots helps one to review and keep in mind the advantages and limitations of each approach.

Table 4-4 describes the quick summary that addresses phase noise measurement related problems and possible remedy [2].

Table 4-4: Phase noise measurement related problems and possible remedy [2]

Sr. No	PN measurement related issue	Possible remedy
1	Reference noise compromise measurement	Obtain lower noise reference or use cross-correlation and two-independent references
2	System noise compromise measurement	Use higher drive levels and /or higher drive level mixer
3	Broadband okay, but I/f region too high	Look at a better reference or use carrier suppression or replace mixer
4	System overall noise floor is too high	Change over to a cross-correlation topology.
5	Calibration has errors due to mixer/amplifier gain variations with offset frequency	Use an AM/PM calibration standard to measure the system at each offset frequency
6	Residual detection of AM noise from Ref or DUT compromises measurement	See if a mixer with better balance will solve the problem or try to inject AM on the signal and adjust the phase balance (dc offset in the PLL loop) to minimize AM detection or switch to carrier suppression
7	Injection locking is occurring.	Improve the isolation between the sources and the mixer either by using an attenuator or an isolation amplifier. One may also need to look at power supplies or shielding.
8	PLL bandwidth compensating for the phase noise close to the carrier.	Reduce the PLL gain or switch to the delay line discriminator approach or measure the amount of attenuation and compensate. This can be done using an AM/PM calibration standard.
9	PLL doesn't seem to be locking.	Do you have the right tuning voltage for your PLL output matched to the tuning range of your source? Does the source tune far enough to match the frequency of the other source? An external bias to the tune might be necessary to get the source close to the desired operating frequency.
10	PLL still doesn't seem to work	Frequency-divide the sources to a much lower frequency. Since the phase excursion also is divided, much less PLL gain is required and, hence, the PM bias is much less.
11	The final plot has large excursions between the peaks and valleys.	If you don't have a fairly fine line through the noise sections of the plot, the number of averages needs to be increased. See Table 1 for details.
12	Line harmonics are too high or causing excess measurement noise.	Make sure all of the equipment is on the same side of the ac line. Look at using line filters, conditioners, or batteries. Consider using an inside/outside dc block. Move the measurement system away from high ac current sources and transformers.
13	Dynamic range limitation	It is possible to insert a notch filter between the test object and the analyzing receiver (or spectrum analyzer). This way the carrier can be suppressed while the sideband noise is not much affected.

4.8 Conclusion

The task was for conducting rigorous phase noise measurement using most of the equipment that claims to be measuring below the KT noise floor using cross-correlation techniques. It has been noticed that the simultaneous presence of correlated and anti-correlated signals can lead to gross underestimation of the total signal in cross-spectral analysis. Keeping in view of these circumstances, the danger of downfall of cross-correlation techniques used by many equipment companies is high and must be evaluated and used very carefully. The evaluation and analysis described in this thesis was time consuming exercise and for doing so state-of-the art low noise OCXOs and VCSO (voltage controlled SAW oscillators) were developed that measure typically -147 dBc/Hz @ 100 Hz offset for 100 MHz OCXO and -153 dBc/Hz @ 10kHz offset for 1GHz SAW oscillators and exhibit noise floor -178dBc/Hz at far offset on most of the Phase noise measurement equipment. The challenging exercise was to measure better than -200 dBc/Hz at 1MHz offset from the carrier for output power of 20dBm and the measured data should be reliable and repeatable.

There are many possibilities in which design engineers can be tricked into false readings or frustrated with the process of trying to achieve a good measurement. Characterizing the phase noise of a system or component is not necessarily very easy. Many different approaches are possible, but the key is to find the best approach for the measurement requirements at hand.

4.9 References

- [1] Agilent Phase Noise Measurement Solution (www.home.agilent.com/agilent/application), 2012
- [2] W. F. Walls, "Practical problems involving phase noise measurements, 33th annual precise time interval (PTTI) meeting, pp 407-416, Nov 2001.
- [3] U.L. Rohde, A.K. Poddar, and G. Boeck, "The Design of Modern Microwave Oscillators for Wireless Applications: Theory and Optimization", Wiley, New York, 2005
- [4] U. L. Rohde, "Microwave and Wireless Synthesizers, Theory and Design", Wiley, New York, 1997
- [5] U. L. Rohde, Matthias Rudolph, "RF/Microwave Circuit Design for Wireless Applications", Wiley, New York, 2013
- [6] U. L. Rohde, "Crystal oscillator provides low noise", Electronic Design, 1975
- [7] George D. Vendelin and Anthony M. Pavio, U. L. Rohde, "Microwave circuit design using linear and nonlinear techniques", Wiley, New York, 2005
- [8] A. L. Lance, W. D. Seal, F. G. Mendoza and N. W. Hudson, "Automating Phase Noise Measurements in the Frequency Domain," *Proceedings of the 31st Annual Symposium on Frequency Control*, 1977
- [9] Agilent Phase Noise Selection Guide, June 2011
- [10] Dorin Calbaza, Chandra Gupta, Ulrich L. Rohde, and Ajay K. Poddar, "Harmonics Induced Uncertainty in Phase Noise Measurements", 2012 IEEE MTT-S Digest, pp. 1-3, June 2012.

- [11] U. L. Rohde, Hans Hartnagel, "The Dangers of Simple use of Microwave Software" http://www.mes.tudarmstadt.de/media/mikroelektronische_systeme/pdf_3/ewme2010/proceedings/sessionvii/rohde_paper.pdf, 2010
- [12] "Sideband Noise in Oscillators", <http://www.sm5bsz.com/osc/osc-design.htm>, 2009
- [13] Jeff Cartwright, "Choosing an AT or SC cut for OCXOs", http://www.conwin.com/pdfs/at_or_sc_for_ocxo.pdf, 2008
- [14] Benjamin Parzen, "Design of Crystal and Other Harmonic Oscillators", John Wiley & Sons, 1983
- [15] U. L. Rohde and A. K. Poddar, "Crystal Oscillators", Wiley Encyclopedia of Electrical and Electronics Engineering", pp.1-38, October 19, 2012.
- [16] U. L. Rohde and A. K. Poddar, "Crystal Oscillator Design", Wiley Encyclopedia of Electrical and Electronics Engineering, pp. 1–47, October 2012
- [17] U. L. Rohde and A. K. Poddar, "Latest Technology, Technological Challenges, and Market Trends for Frequency Generating and Timing Devices", IEEE Microwave Magazine, pp.120-134, October 2012.
- [18] U. L. Rohde and A. K. Poddar, "Techniques Minimize the Phase Noise in Crystal Oscillators", 2012 IEEE FCS, pp. 01-07, May 2012.
- [19] M. M. Driscoll, "Low Frequency Noise Quartz Crystal Oscillators", Instrumentation and Measurement, IEEE Trans. Vol 24, pp 21-26, Nov 2007,
- [20] M. M. Driscoll, "Low Noise Crystal Controlled Oscillator", US Patent No. US4797639A, Jan 10, 1989
- [21] M. M. Driscoll, "Reduction of quartz crystal oscillator flicker-of-frequency and white phase noise (floor) levels and acceleration sensitivity via use of multiple resonators", IEEE Trans. UFFCC, Vol. 40, pp 427-430, Aug 2002.
- [22] <http://www.mentby.com/bruce-griffiths/notes-on-the-driscoll-vhf-overtone-crystal-oscillator.html>, Dec 28, 2009
- [23] U. L. Rohde, A. K. Poddar, "Technique to minimize phase noise in crystal oscillator", Microwave Journal, pp132-150, May 2013
- [24] O. Rajala, "Oscillator Phase Noise Measurements using the Phase Lock Method", MS thesis, Department of Electronics, Tampere University of Technology, June 2010.
- [25] W. F. Walls, "Cross-Correlation Phase Noise Measurements", IEEE FCS, pp. 257-261, 1992
- [26] J. Breitbarth, "Cross Correlation in phase noise analysis", Microwave Journal, pp 78-85, Feb 2011.
- [27] F. L. Walls et al. Extending the Range and Accuracy of Phase Noise Measurements, Proceedings of the 42nd Annual Symposium on Frequency Control, 1988.
- [28] Noise XT, DCNTS manual, [\(2013\)](http://www.noisext.com/pdf/noisext_DCNTS.pdf)
- [29] Agilent E5052A Signal Source Analyzer 10 MHz to 7, 26.5, or 110 GHz – Datasheet", Agilent document 5989-0903EN, p. 12, May 2007
- [30] Frequency Extension for Phase Noise Measurements with FSUP26/50 and Option B60 (Cross-Correlation)", Rhode & Schwarz Application Note 1EF56, p. 3 Jan 2007.
- [31] M. Jankovic, "Phase noise in microwave oscillators and amplifiers", PhD thesis, Faculty of graduate School of the University of Colorado, Department of Electrical, Computer and Energy Engineering, 2010

- [32] Hewlett Packard, *RF and Microwave phase Noise Measurement Seminar*, Available at: http://www.hparecords.com/seminar_notes/HP_PN_seminar.pdf, June 1985.
- [33] Stephan R. Kurz, *WJ Tech note – Mixers as Phase Detectors*, Available at: http://www.triquint.com/prodserv/tech_info/docs/WJ_classics/Mixers_phase_detectors.pdf, [WWW][Cited 2010-05-11]
- [34] Agilent Technologies, *Phase Noise Characterization of Microwave Oscillators – Phase Detector Method – Product Note 11729B-1* Available at: <http://tycho.usno.navy.mil/ptti/ptti2001/paper42.pdf>, May 2010
- [35] Aeroflex, Application Note #2 – PN9000 automated Phase Noise Measurement System Available at: <http://www.datasheetarchive.com/datasheet-pdf/010/DSA00173368.html>, April 2010.
- [36] Hewlett Packard. *HP 3048A Phase Noise Measurement System Reference Manual* [online]. Available: <http://cp.literature.agilent.com/litweb/pdf/03048-90002.pdf>, (1989, Sept 01).
- [37] E. Rubiola and F. Vernotte. *The cross-spectrum experimental method* [online]. Available: <http://arxiv.org/>, document arXiv:1003.0113v1 [physics.ins-det], (2010, Feb 27)
- [38] Hewlett Packard *HP 3048A Phase Noise Measurement System Operating Manual* [online]. Available: <http://cp.literature.agilent.com/litweb/pdf/03048-61004.pdf>, (1990, Jun 01)
- [39] *HP 11848A Phase Noise Interface Service Manual*, 1st ed., Hewlett-Packard Company Spokane, Washington 1987.
- [40] M. Sampietro, L. Fasoli, and G. Ferrari, “Spectrum analyzer with noise reduction by cross-correlation technique on two channels,” *Rev. Sci. Instrum.*, vol. 70, no. 5, May 1999.
- [41] Samuel J. Bale, David Adamson, Brett Wakley, Jeremy Everard, “ Cross Correlation Residual Phase Noise Measurements using Two HP3048A Systems and a PC Based Dual Channel FFT Spectrum Analyzer”, 24th European Frequency and Time Forum, pp 1-8, (April 13-16, 2010)
- [42] Jeremy Everard, Min Xu, Simon Bale, “Simplified Phase Noise Model for Negative-Resistance Oscillators and a Comparison With Feedback Oscillator Models”, *IEEE Transactions on Ultrasonics, Ferroelectrics, and Frequency Control*, Vol. 59, No. 3, March 2012
- [43] Jeremy Everard, Min Xu, “Simplified Phase Noise Model for Negative-Resistance Oscillators”, *IEEE Frequency Control Symposium*, 2009 Joint with the 22nd European Frequency and Time forum, pp. 338-343, April 2009
- [44] Time Domain Oscillator Stability Measurement Allan variance, application note, Rohde & Schwarz, pp. 1-16, <http://www.crya.unam.mx/radiolab/recursos/Allan/RS.pdf>, 2009.
- [45] M. M. Driscoll, “Modeling Phase Noise in Multifunction Subassemblies”, *IEEE Transactions on Ultrasonics, Ferroelectrics, and Frequency Control*, vol. 59, no. 3, pp. 373-381, March 2012
- [46] Ajay Poddar, Ulrich Rohde, Anisha Apte, “ How Low Can They Go, Oscillator Phase noise model, Theoretical, Experimental Validation, and Phase Noise Measurements”, *IEEE Microwave Magazine* , Vol. 14, No. 6, pp. 50-72, September/October 2013.
- [47] Ulrich Rohde, Ajay Poddar, Anisha Apte, “Getting Its Measure”, *IEEE Microwave Magazine*, Vol. 14, No. 6, pp. 73-86, September/October 2013.

- [48] U. L. Rohde, A. K. Poddar, Anisha Apte, "Phase noise measurement and its limitations", *Microwave journal*, April 2013.
- [49] E. N. Ivanov and F. L. Walls, "Effect of anomalously low voltage noise in measurement systems with cross-correlation signal processing," in *Conference on Precision Electromagnetic Measurements. Conference Digest. CPEM 2000 (Cat. No.00CH37031)*, Sydney, NSW, Australia, pp. 447–448.
- [50] E. N. Ivanov and F. L. Walls, "Interpreting anomalously low voltage noise in two-channel measurement systems," *IEEE Trans. Ultrason., Ferroelect., Freq. Contr.*, vol. 49, no. 1, pp. 11–19, Jan. 2002.
- [51] E. Rubiola and F. Vernotte, "The cross-spectrum experimental method," arXiv e-print 1003.0113, Mar. 2010.
- [52] E. Rubiola, *Phase Noise and Frequency Stability in Oscillators*. Cambridge University Press, 2010.
- [53] G. Cibiel, M. Regis, E. Tournier, and O. Llopis, "AM noise impact on low level phase noise measurements," *IEEE Transactions on Ultrasonics, Ferroelectrics and Frequency Control*, vol. 49, no. 6, pp. 784–788, 2002.
- [54] E. Rubiola and R. Boudot, "The effect of AM noise on correlation phase-noise measurements," *IEEE Transactions on Ultrasonics, Ferroelectrics and Frequency Control*, vol. 54, no. 5, pp. 926–932, May 2007.
- [55] E. Rubiola, "Primary calibration of AM and PM noise measurements," arXiv e-print 0901.1073, Jan. 2009
- [56] C. W. Nelson, A. Hati, and D. A. Howe, "Collapse of the Cross-spectral Function", IEEE Frequency Control Symposium, FCS proceedings 2014, pp.590-591, Taipei May 2014
- [57] C.W. Nelson, A. Hati, and D.A. Howe, "A Collapse of the Cross spectral Function in Phase Noise Metrology," *Electronics Letters.*, vol. 49, no. 25, pp. 1640-1641, Dec. 2013
- [58] C. W. Nelson, A. Hati, and D. A. Howe, "A collapse of the cross spectral function in phase noise metrology," *Rev. Sci. Instrum.*, vol. 85, pp. 024705-7, Feb. 2014

Chapter 5

Resonator Dynamics and Application in oscillators

5.1 Microwave Resonators

A resonator is an element that is capable of storing both frequency-dependent electric and magnetic energy [1]. At microwave frequencies, resonators can take various shapes and forms. The shape of microwave structure affects the field distribution and hence the stored electric and magnetic energies. Potentially, any microwave structure should be capable of constructing a resonator whose resonant frequency is determined by the structure's physical characteristics and dimensions [2]-[6]. A simple example is a series or parallel combination of inductor (L) and capacitor (C), where the magnetic energy is stored in the inductance L and the electric energy is stored in the capacitance C [7]. The resonant frequency of a resonator is the frequency at which the energy stored in electric field equals the energy stored in the magnetic field. As components, resonators allow a selective transmission or blocking of signals and serve as a 1-port or 2-port frequency-determining elements for oscillator application [8].

5.2 Linear Passive 1-Port

A circuit network with a single port is nomenclatured as a 1-port network. Figure 5-1 illustrates the typical schematic and equivalent representation of a 1-port network where signal at the port can be described by the complex amplitudes \underline{a} and \underline{b} of the incident and reflected or by the voltage \bar{V} and \bar{I} waves. If the relation between \bar{V} and \bar{I} or \underline{a} and \underline{b} is linear, the 1-port network is defined linear 1-port, and the complex power P flowing into the 1-port can be given in terms of active and reactive power as [7]

$$P = \frac{1}{2} \bar{V} \times \bar{I}^* = P = \frac{1}{2} Z |\bar{I}|^2 = \frac{1}{2} Y^* |\bar{V}|^2 = P_{active} + j P_{reactive} \quad (5.1)$$

For the source-free 1-port network complex power P can be described by

$$P = P_{active} + 2j\omega(W_m - W_e) \quad (5.2)$$

where W_m and W_e are the average stored magnetic and electrical energy.

From (5.1) and (5.2) complex impedance Z and admittance Y can be characterized as

$$Z = \frac{P_{active} + 2j\omega(W_m - W_e)}{\frac{1}{2}|\bar{I}|^2} \Rightarrow X = \frac{4\omega(W_m - W_e)}{|\bar{I}|^2} \quad (5.3)$$

$$Y = \frac{P_{active} + 2j\omega(W_e - W_m)}{\frac{1}{2}|\bar{V}|^2} \Rightarrow B = \frac{4\omega(W_e - W_m)}{|\bar{V}|^2} \quad (5.4)$$

where X and B are the reactance and susceptance.

From (5.3) and (5.4)

$$\frac{dX}{d\omega} |\bar{I}|^2 = \frac{dB}{d\omega} |\bar{V}|^2 = 4(W_m - W_e) \quad (5.5)$$

$$W_e = \frac{1}{8} \left(\frac{dX}{d\omega} - \frac{X}{\omega} \right) |\bar{I}|^2 = \frac{1}{8} \left(\frac{dB}{d\omega} + \frac{B}{\omega} \right) |\bar{V}|^2, \quad W_m = \frac{1}{8} \left(\frac{dX}{d\omega} + \frac{X}{\omega} \right) |\bar{I}|^2 = \frac{1}{8} \left(\frac{dB}{d\omega} - \frac{B}{\omega} \right) |\bar{V}|^2 \quad (5.6)$$

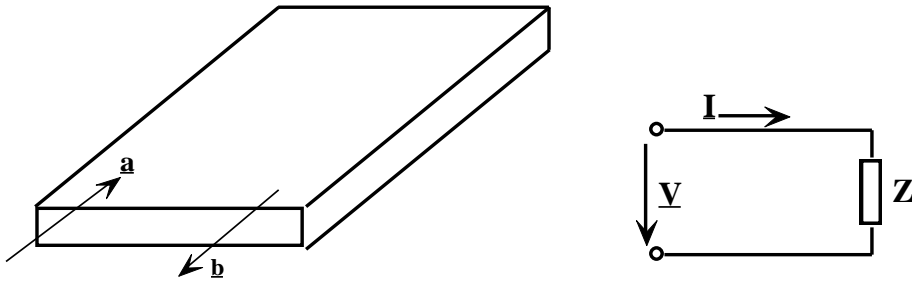


Figure 5-1: 1-port: A typical schematic drawing, and (b) equivalent representation of 1-port network

For passive lossless 1-port network, $P_{\text{active}} = 0$, the port is also called as reactive 1-port network, and complex power P is given by

$$P = 2j\omega(W_m - W_e) \quad (5.7)$$

Since W_m and W_e are positive values for passive lossless 1-port network, Foster [9] established the frequency dependence of a reactance as

$$\frac{dX}{d\omega} > \left| \frac{X}{\omega} \right| \text{ and } \frac{dB}{d\omega} > \left| \frac{B}{\omega} \right| \quad (5.8)$$

From (5.8), the instantaneous values of W_m and W_e oscillate with double the resonance frequency of oscillation, and transformed their stored energy from W_m to W_e and vice versa within a quarter of the period of oscillation. However, for $W_m \neq W_e$ a periodical energy exchange can also occur with an external circuitry (active device that generates gain or negative resistance for stable oscillation) driving the resonator tank circuit. In this case, the reactive power is flowing through the port.

5.3 Resonator Networks

The resonator is the core component of the filter and oscillator circuits. The selection of a resonator for oscillator or filter application involves several tradeoffs: insertion loss, Q-factor, size, cost, power-handling requirements etc. The main design considerations of resonators are the resonator size, unloaded Q, spurious performance, and power handling capability. The unloaded Q represents the inherent losses in the resonator. The higher the losses are the lower is the Q value. It is therefore desirable to use resonators with high Q values since this reduces the insertion loss of the tuned resonator and improves its selectivity performance. Microwave

resonator networks are grouped into three categories: lumped-element LC resonators, planar resonators (distributed printed transmission line resonators), and three-dimensional (3D) cavity-type resonators. Figures 5-2 and 5-3 show the typical comparison between these resonators. Typically, lumped-element resonators are employed in low-frequency applications. Figure 5-4 (a) shows a lumped-element resonator constructed by using a coil inductor and a chip capacitor. The lumped-element resonator can be printed on a dielectric substrate in the form of a spiral inductor and an inter-digital capacitor as shown in Figure 5-4 (b).

As shown in Figure 5-4 (a), lumped element resonators are large but can be made small at microwave frequencies and offer a wide spurious free window; however, they have a relatively low Q value. A typical Q value for lumped LC resonators is between 10 and 50 at 1GHz.

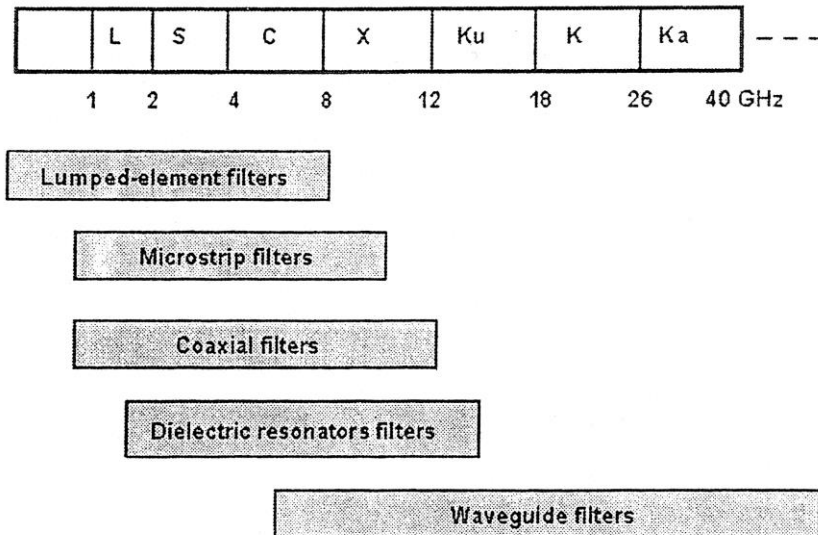


Figure 5-2: Application of the various resonator configurations [8]

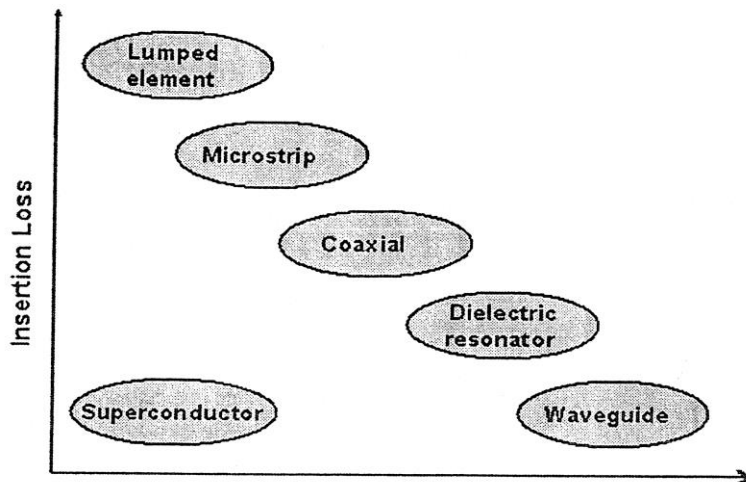


Figure 5-3: A typical relative size and insertion loss of various resonators [8]

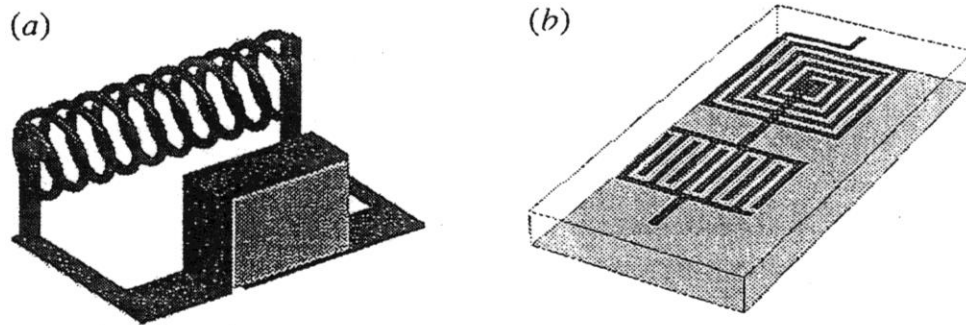


Figure 5-4: Lumped-element resonators realized by (a) coil inductor and chip capacitor, (b) Spiral inductor and inter-digital capacitor [8]

Planar resonators can take the form of a length of a microstrip transmission line, terminated in a short circuit or open circuit, or it can take the form of meander line, folded line, ring resonator, patch resonator or any other configuration [8]-[11]. Any printed structure effectively acts as a resonator whose resonant frequency is determined by the resonator's dimensions, substrate dielectric constant and substrate height, which can be used for covering both narrowband and broadband tuning characteristics of frequency source applications for current and later generation communication systems [12]. Figure 5-5 shows typical planar resonators, usually employed in wideband, compact, and low-cost signal source and filter applications. The typical Q value for planar resonators is in the range of 50-300 at 1GHz [13]-[17]. The state-of-the-art planar resonator circuit using superconductor techniques can exhibit typical Q values ranging from 20,000 to 50,000 at 1 GHz but not a cost-effective alternative because resonator circuitry needs to be cooled down to very low temperatures, below 90 degree Kelvin [18].

In contrast to lumped LC resonators, which have only one resonant frequency, printed transmission line resonators can support an infinite number of electromagnetic field configurations or resonant modes. The spurious performance of a resonator is determined by how close the neighboring resonant modes are to the operating mode. The neighboring resonant modes act as spurious modes interfering with the fundamental resonant mode's performances. It is therefore desirable to increase the spurious free window of the resonator in order to improve the filter out-of-band rejection performance.

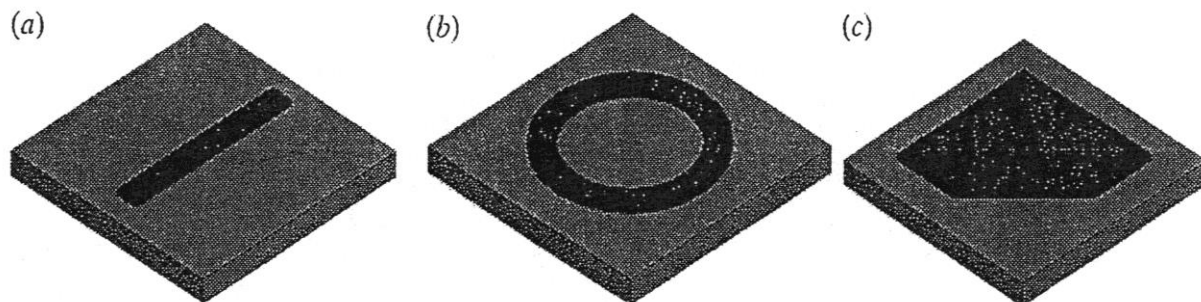


Figure 5-5: Examples of microstrip resonator configurations: (a) half-wavelength resonator, (b) Spiral inductor and interdigital capacitor

The resonant modes in planar resonators exist in the form of a single mode representing one electric resonator or in the form of degenerate modes (i.e., modes having the same resonance frequency with different field distributions) [8]. These degenerate modes allow the realization of two electric resonators (dual-mode resonators) or three electric resonators (triple-mode resonators) within the same physical resonator. Example of dual-modes is TE_{11} modes, which exists in circular waveguide cavities [10]-[13]; HE_{11} modes, which exist in dielectric resonators [14]-[15]; or TM_{11} , which exist in circular or square patch microstrip resonators [16]. Cubic waveguide cavities and cubic dielectric resonators can support triples modes [17]. The key advantage of operating in dual-mode or triple mode configuration is size reduction. However, these modes do have an impact on the unloaded Q, spurious performance, and power handling capability of the cavity resonator. A summary of the features of each mode of operation is given in Table 5.1. Figure 5-6 shows the typical 3-D cavity resonators such as coaxial, waveguide, and dielectric resonators, offer a Q value ranging from 3000 to 30,000 at 1GHz, but not amenable for integration in RFIC/MMIC technology [19]-[20]. In addition to this, 3-D resonators are bulky in size; however, they offer very high Q values; in addition, they are capable of handling high RF power levels.

Table 5.1: Comparison between various modes of operation

Parameter	Single-Mode	Dual-Mode	Triple-Mode
Size	Large	Medium	Small
Spurious Response	Good	Fair	Fair
Unloaded Q	High	Medium	Medium
Power handling capability	Low	Medium	High
Design complexity	Low	Medium	High

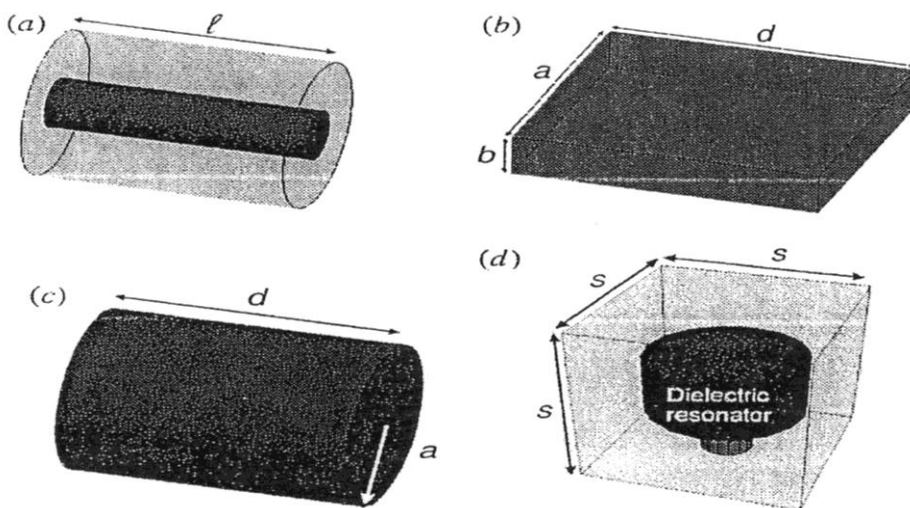


Figure 5-6: Examples of 3-D cavity resonators (a) coaxial resonator (b) rectangular waveguide resonator (c) circular waveguide resonator (d) dielectric resonator

5.4 Resonator Q-factor

Energy dumping in electromagnetic resonance gives the definition of Q-factor for passive networks, and is 2π times the ratio of the reactively stored energy to the energy dissipated in a unit cycle [16].

$$Q_{loaded} = 2\pi \left[\frac{\text{average reactive energy stored}}{\text{energy dissipated in unit cycle}} \right] = \omega_o \left[\frac{W_T}{P_T} \right] \Rightarrow \frac{1}{Q_{loaded}} = \left[\frac{1}{Q_{unloaded}} + \frac{1}{Q_{external}} \right] \quad (5.9a)$$

$$Q_{loaded} = Q_{unloaded} \quad (\text{loosely-coupled resonator}) \quad (5.9b)$$

$$Q_{loaded} = Q_{external} \quad (\text{tightly-coupled resonator}) \quad (5.9c)$$

where

$$Q_{unloaded} = \omega_o \left[\frac{W_T}{P_i} \right] \quad (5.9d)$$

$$Q_{external} = \omega_o \left[\frac{W_T}{P_e} \right] \quad (5.9e)$$

$$P_T = P_i + P_e \quad (5.9f)$$

Where ω_o is the resonant frequency, W_T is average stored energy, and P_T is the total power loss in watts, P_i and P_e are the dissipated energies due to the resonator's internal losses and the external loadings, respectively.

From (5.9b) and (5.9c), the loaded Q-factor is equal to unloaded Q-factor ($Q_{loaded} = Q_{unloaded}$) for loosely coupled resonator, the internal losses are more dominant as compared to external loss; conversely, in a tightly coupled resonator, the external loading is much more dominant, thus $Q_{loaded} = Q_{external}$ [17]-[20]. This definition (Eq.5.9a-Eq.5.9e) is valid for circuit involving passive and active devices or energy sources until the open-loop gain approaches to unity. In positive feedback filters and multipliers or active inductors, frequency selectivity can be as sharp as desired by increasing the open-loop gain and this exceeds the limit, oscillation takes place in the circuit. In such a state, the above definition of Q factor is no longer valid because it runs into infinity. Therefore, unified definition of Q is necessary to evaluate the performance of active circuits even during the transient state of regenerative circuit (oscillators).

The quality factor (Q-factor) is the most important parameter of a resonant circuit for low phase noise oscillator (signal sources) application. The Q-factor is a versatile index of resonator and oscillator performance but its definition is not unified. Ohira [21] did rigorous analysis of the characterization of a Q-factor for general RF components and circuits. Two common definitions of Q-factor are discussed for the understanding about the dynamics of this parameter on autonomous circuit (oscillators). The first definition is based on field theory, which relates the Q-factor to frequency-selectivity, energy-storage and dissipation in resonance for stable passive circuit, whereas the second one relates to resonance for unstable active circuits (oscillators, regenerative circuits). The energy-based definition is ambiguous when a resonator has no energy storage elements, as in the case of ring or distributed oscillators. The two common definitions of Q factor (a) for passive resonant circuit and (b) for active resonant circuit (described in section 5.4.1 and 5.4.2) are explained in a step by step process by Ohira et.al [21]-[28].

(a) Definition of Q Factor for Passive Resonant Circuit

- (i) Fractional 3-dB bandwidth
- (ii) Phase-to-frequency slope
- (iii) Stored-to-dissipated energy ratio

(b) Definition of Q Factor for Active Resonant Circuit

- (i) Noise spectrum Basis
- (ii) Source-Pull/Push Basis
- (iii) Injection locking Basis

5.4.1 Definition of Q Factor for Passive Resonant Circuit

- (i) Fractional 3-dB bandwidth
- (ii) Phase-to-frequency slope
- (iii) Stored-to-dissipated energy ratio

5.4.1.1 Fractional 3-dB bandwidth

Figure 5-7 shows the typical 1-port resonator and impedance versus frequency response function for the evaluation of fractional 3-dB bandwidth and quality factor, which is based on frequency selectivity of resonator, and filter networks.

Steps for Q-factor:

1. Get $|Z(\omega)|^2$ in frequency domain
2. Find ω_0 by solving $\frac{d}{d\omega}|Z(\omega_0)|^2 = 0$
3. Find ω_1 and ω_2 by solving $|Z(\omega_1)|^2 = |Z(\omega_2)|^2 = \frac{1}{2}|Z(\omega_0)|^2$
4. Q factor from the definition of frequency selectivity: $Q = \frac{\omega_0}{\omega_2 - \omega_1} = \frac{f_0}{f_2 - f_1}$

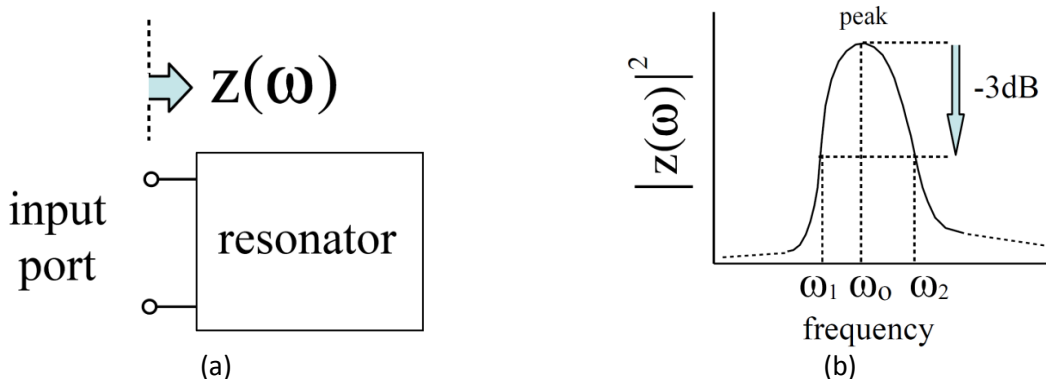


Figure 5-7: Examples of 1-port resonators (a) schematic of 1-port resonator (b) impedance versus frequency response [21]

5.4.1.2 Phase-to-Frequency Slope

An alternative definition of Q-factor is based on resonator's transfer function in the frequency domain. The transfer function is a complex function which governs the relationship between the input and output as

$$H(j\omega) = A(\omega)\exp[j\phi(\omega)] \quad (5.10)$$

where $A(\omega)$ and $\phi(\omega)$ are the amplitude and phase response of the resonator. The Q-factor in terms of the transfer function is given by [34]

$$Q = \frac{\omega_0}{2} \left| \sqrt{\left(\frac{\partial A(\omega)}{\partial \omega} \right)^2 + \left(\frac{\partial \phi(\omega)}{\partial \omega} \right)^2} \right|_{\omega=\omega_0} \quad (5.11)$$

$$Q \approx \frac{\omega_0}{2} \left| \frac{\partial \phi(\omega)}{\partial \omega} \right|_{\omega=\omega_0} \quad \text{for} \quad \left| \frac{\partial A(\omega)}{\partial \omega} \right|_{\omega=\omega_0} \rightarrow 0 \quad (5.12)$$

From (5.12), the approximation $\left(\left| \frac{\partial A(\omega)}{\partial \omega} \right|_{\omega_0} = 0 \right)$ is because variation in phase is more predominant as compared to amplitude variation in well-designed oscillator circuits. From (5.12), the shift in frequency ($\Delta\omega$) from ω_0 can cause large rate of change in phase if the Q-factor is high, therefore forcing the frequency to return to ω_0 .

Figure 5-8 shows the typical 1-port resonator and phase response function for the evaluation of rate of change of phase and quality factor.

Steps for Q-factor (neglects amplitude slope):

1. Get $\phi(\omega)$ in frequency domain $\phi(\omega) = \angle[Z(\omega)]$

$$\phi'(\omega) = \frac{d}{d\omega} \angle[Z(\omega)]$$

2. Find ω_0 by solving

$$\phi(\omega_0) = 0$$

3. Calculate Q factor from

$$Q = \frac{\omega_0}{2} \left| \frac{\partial \phi(\omega)}{\partial \omega} \right|_{\omega=\omega_0} = \frac{\omega_0}{2} |\phi'(\omega_0)|$$

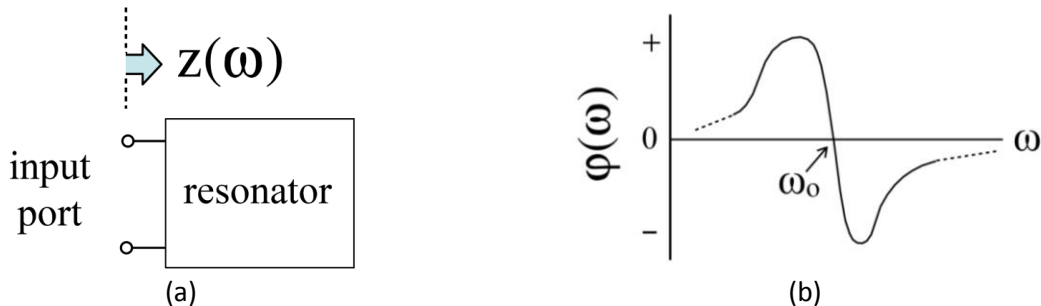


Figure 5-8: Examples of 1-port resonators (a) schematic of 1-port resonator (b) phase versus frequency response [22]

5.4.1.3 Stored-to-Dissipated Energy Ratio

Electromagnetic field inside ideal resonator network stores energy at the resonant frequency, where equal storage of electrical and magnetic energies occurs. However, in reality, part of the stored energy is dissipated due to losses across the loads, thereby reducing the resonator's frequency selectivity [23].

Figure 5-9 shows the typical 1-port resonator for the evaluation of stored energy rate and quality factor.

Steps for Q-factor

1. Estimate input power and stored energy in each component

$$P(\omega) = \frac{1}{2} \operatorname{Re}\{v_{ex} i_{ex}^*\}, \quad W_e(\omega) = \frac{1}{4} \sum_k^{cap} C_k |v_k|^2, \quad W_m(\omega) = \frac{1}{4} \sum_k^{ind} L_k |i_k|^2$$

2. Find ω_0 by solving $W_e(\omega_0) = W_m(\omega_0)$

3. Calculate Q factor from $Q = \omega_0 \frac{W_e(\omega_0) + W_m(\omega_0)}{P(\omega_0)}$

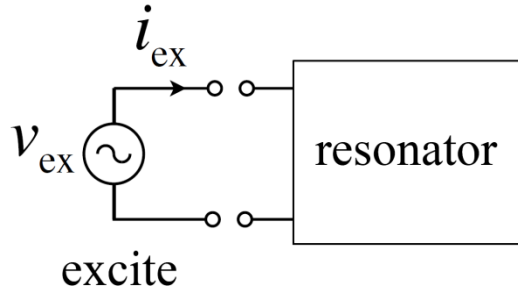


Figure 5-9: Schematic of 1-port resonator (for the estimation of stored energy in each resonating component) [24]

The above method for the evaluation of the Q-factor valid for massive resonator, this definition is no longer valid when the 1-port circuit is unstable and oscillates (example: regenerative active circuits) [25]. Therefore, new definition of Q-factor for active circuit is required for both analysis and synthesis of the oscillator circuits.

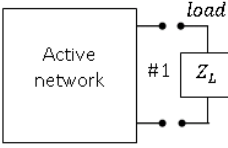
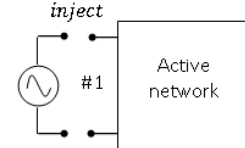
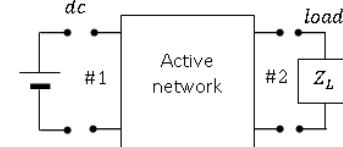
5.4.2 Definition of Q Factor for Active Resonant Circuit: Sensitive for Oscillation

Table 5.2 describes the formulation of oscillation-stability condition for active network under various conditions.

- (i) Noise spectrum Basis
- (ii) Source-Pull/Push Basis
- (iii) Injection locking Basis

Table 5.2: Types of Unstable Active Network [26]

Unstable Active Network (closed-loop gain>= 1) Sensitive to Oscillations ($\omega=\omega_0$)		
Type	Scheme	condition of oscillation-stability
NINO (No Input- No Output)	Active network	Power and energy equilibrium condition stability criterion $W_e(\omega_0) = W_m(\omega_0) \rightarrow \Delta W = 0$

NISO (No Input-Signal Output)		Sideband noise load pulling
SINO (Signal Input-No Output)		Injection locking
SISO (Signal Input-Signal Output)		Source pushing

NINO (No Input-No Output) active network obeys the power and energy balance equilibrium condition. Thus, elements for NINO active network confine to inside and transact energy for equilibrium condition, the complex power $\Psi(\alpha, \omega)$ can be defined as [27]

$$\underbrace{\Psi(\alpha, \omega)}_{\text{complex power}} = \frac{1}{2} [v_1(\omega)i_1^*(\omega) + v_2(\omega)i_2^*(\omega) + v_3(\omega)i_3^*(\omega) + \dots + v_K(\omega)i_K^*(\omega)] \\ = P_a - P_r + 2j\omega W_e - 2j\omega W_m = \Delta P + 2j\omega \Delta W \quad (5.13)$$

From (5.13), the equilibrium state for oscillation condition of zero port (NINO) active circuit can be formulated by [28]-[29]

$$\underbrace{[\Psi(\alpha, \omega)]}_{\text{complex power}}_{\alpha=\alpha_0, \omega=\omega_0} = 0 \rightarrow \text{Equilibrium state for oscillation condition} \quad (5.14)$$

From (5.14), once equilibrium point is reached ($\alpha = \alpha_0, \omega = \omega_0$), the important thing is whether the zero port active circuit (NINO) remains at steady-state at that point ($\alpha = \alpha_0, \omega = \omega_0$) against the small perturbation ($\alpha = \alpha_0 + \delta\alpha, \omega = \omega_0 + \delta\omega$), while maintaining the complex power balance [$\Psi(\alpha = \alpha_0 + \delta\alpha, \omega_0 + \delta\omega) = 0$], i.e.

$$\frac{\partial \Psi(\alpha, \omega)}{\partial \alpha} \delta\alpha + \frac{\partial \Psi(\alpha, \omega)}{\partial \omega} \delta\omega = 0 \Rightarrow \delta\omega = \left(\frac{d\phi}{dt} - j + \frac{d\alpha}{dt} \right) \quad (5.15)$$

From (5.15), the instantaneous frequency deviation ($\delta\omega$) depends not only on phase change in time but also as logarithmic amplitude change for imaginary part, can be described by [24]

$$\frac{\partial \Psi(\alpha, \omega)}{\partial \alpha} \delta\alpha + \left(\frac{d\phi}{dt} - j + \frac{d\alpha}{dt} \right) \frac{\partial \Psi(\alpha, \omega)}{\partial \omega} = 0 \quad (5.16a)$$

$$Imag \left[\frac{\partial \Psi(\alpha, \omega)}{\partial \alpha} \left(\frac{\partial \Psi(\alpha, \omega)}{\partial \omega} \right)^{-1} \right] = \frac{1}{\delta\alpha} \frac{d\alpha}{dt} \quad (5.16b)$$

$$\text{stability criterion } \delta\alpha \frac{d\alpha}{dt} < 0 \text{ at } (\alpha_0, \omega_0)$$

$$\underbrace{Im \left\{ \frac{\partial \psi}{\partial \omega} \frac{\partial \psi^*}{\partial \alpha} \right\}_{\substack{\alpha=\alpha_0 \\ \omega=\omega_0}}}_{\text{discriminant}} > 0 \text{ Or } \underbrace{\begin{vmatrix} \frac{\partial \Delta P}{\partial \alpha} & \frac{\partial \Delta P}{\partial \omega} \\ \frac{\partial \Delta U}{\partial \alpha} & \frac{\partial \Delta U}{\partial \omega} \end{vmatrix}_{\substack{\alpha=\alpha_0 \\ \omega=\omega_0}}}_{\text{Jacobian discriminant}} > 0 \quad (5.17)$$

5.4.2.1 Active NISO Circuit Q-Factor (Noise Spectrum Basis)

Fig. 5-10 shows the typical 1-port oscillator circuit model, as depicted both active and passive components are embedded in a black box, and represented by the $Z(\omega)$ without the load (R).

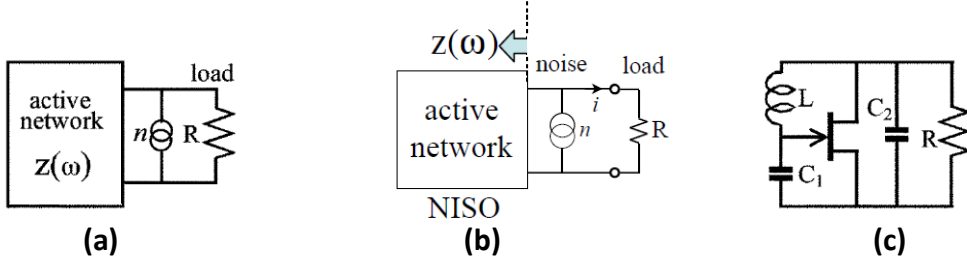


Figure 5-10: Shows the typical 1-port oscillator: (a) General model (b) Equivalent noise model of NISO, and (c) a Colpitts example representing NISO model

Assuming the noise current source in parallel, this yields single sideband (SSB) power on the spectrum. The power observed when the noise source is solely connected to load R is given by

$$P_n = \left[\frac{R}{2} \right] |n|^2 \quad (5.18)$$

The output sideband noise power $P_{SSB}(\omega)$ can be described by [28]

$$P_{SSB}(\omega) = \left[\frac{R}{2} \right] \left| \frac{z(\omega)n}{R+z(\omega)} \right|^2 = P_n \left| \frac{z(\omega)}{R+z(\omega)} \right|^2 \quad (5.19)$$

$$[z(\omega) + R]_{\omega \rightarrow \omega_0} = 0 \text{ (at equilibrium state the resonance frequency } \omega = \omega_0) \quad (5.20)$$

Frequency deviation ($\omega = \omega_o + \delta\omega$) expands output impedance $z(\omega)$ as

$$z(\omega) = z(\omega_o) + \frac{dz(\omega_o)}{d\omega_o} \delta\omega + \dots \quad (\text{Taylor expansion}) \quad (5.21)$$

$$|z(\omega)|^2 = \left| z(\omega_o) + \frac{dz(\omega_o)}{d\omega_o} \delta\omega \right|^2 \approx |z(\omega_o)|^2 \quad (5.22)$$

From (5.19)-(5.22)

$$P_{SSB}(\omega) = P_n \left| \frac{z(\omega)}{z(\omega)-z(\omega_o)} \right|^2 = P_n \left| \frac{z(\omega_o) + \frac{dz(\omega_o)}{d\omega_o} \delta\omega}{\frac{dz(\omega_o)}{d\omega_o} \delta\omega} \right|^2 = P_n \left| 1 + \frac{z(\omega_o)}{\frac{dz(\omega_o)}{d\omega_o} \delta\omega} \right|^2 \approx P_n \left| \frac{z(\omega_o)}{z'(\omega_o) \delta\omega} \right|^2 \quad (5.23)$$

From [34]

$$P_{SSB}(\omega) = \left[\frac{\omega_o}{2Q\delta\omega} \right]^2 [P_n] \Rightarrow Q = \frac{\omega_o}{2} \left| \frac{z'(\omega_o)}{z(\omega_o)} \right| \quad (5.24)$$

From (5.24)

$$\left\{ \begin{array}{l} Q(pz) = \frac{\omega_o}{2} \left| \frac{pz'(\omega_o)}{pz(\omega_o)} \right| = \frac{\omega_o}{2} \left| \frac{z'(\omega_o)}{z(\omega_o)} \right| = Q(z) \rightarrow \text{Scaling operation} \\ Q(z^{-1}) = Q(y) = \frac{\omega_o}{2} \left| \frac{y'(\omega_o)}{y(\omega_o)} \right| = \frac{\omega_o}{2} \left| \frac{z'(\omega_o)}{z(\omega_o)} \right| = Q(z) \rightarrow \text{Inverse operation} \\ Q(z^*) = \frac{\omega_o}{2} \left| \frac{z'(\omega_o)^*}{z(\omega_o)^*} \right| = \frac{\omega_o}{2} \left| \frac{z'(\omega_o)}{z(\omega_o)} \right| = Q(z) \rightarrow \text{Conjugate operation} \end{array} \right\} \quad (5.25)$$

$P_{SSB}(\omega)$ expressed in (5.25) represent the Q-factor of oscillator that includes both active and passive devices embedded in the 1-port black box shown in Figure 5-10. In other words, the above formula is valid for any active network, regardless of oscillator topology that is comprised of types of active devices for providing closed loop gain ≥ 1 and compensating the loss of resonator. From (5.25), Q is invariant against the three operations (scaling, inverse, and conjugate) [29].

5.4.2.2 Active NISO Circuit Q-Factor (Reflection coefficient $\Gamma(\omega)$ Basis)

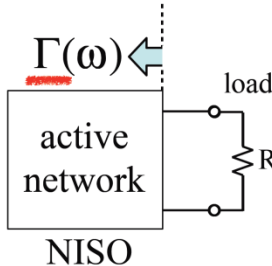


Figure 5-11: Shows the typical 1-port oscillator

From (5.25)

$$Q = \frac{\omega_o}{2} \left| \frac{z'(\omega_o)}{z(\omega_o)} \right|, \quad z'(\omega) = \left[\frac{dz(\omega)}{d\omega} \right] \quad (5.26)$$

The expression for reflection coefficient $\Gamma(\omega)$ for 1-port network shown in Figure 5-11 can be given by [21]

$$\Gamma(\omega) = \left| \frac{z(\omega) - z_o}{z(\omega) + z_o} \right| \Rightarrow \Gamma'(\omega) = \left| \left\{ \frac{[z(\omega) - z_o] z'(\omega) - [z(\omega) + z_o] z'(\omega)}{[z(\omega) + z_o]^2} \right\} \right|, \quad \Gamma'(\omega) = \left[\frac{d\Gamma(\omega)}{d\omega} \right] \quad (5.27)$$

From (5.26) and (5.27)

$$Q = \omega_o \left| \frac{\Gamma'(\omega)}{1 - \Gamma^2(\omega_o)} \right| \quad (5.28)$$

5.4.2.3 Active NISO Circuit Q-Factor (Energy Basis)

Fig 5-12 represents the general model of circuits without port for understanding the energy equilibrium dynamics, even though this kind of configuration does not have practical usefulness. Considering such a system when oscillation takes place Fig. 5-12(a) can be

illustrated as zero-port closed-circuit network Fig. 5-12(b) for the analysis of equilibrium and stability criterion.

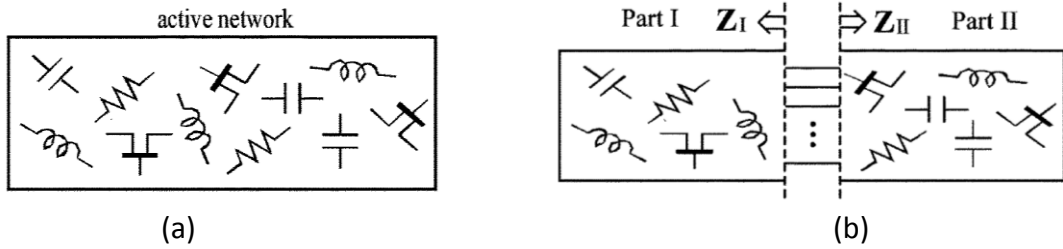


Figure 5-12: A typical Zero-port oscillator: (a) General model, and (b) Separated into two parts [26]

The total complex power of the circuit represented in Figure 5-13 can be described as

$$\psi(\omega) = \frac{1}{2} (+v_1 i_1^* + v_2 i_2^* + v_3 i_3^* \dots + v_k i_k^*) \quad (5.29)$$

$$\psi(\omega) = \Delta P + j2\omega\Delta E \quad (5.30)$$

$$\Delta P = P_a - P_r \quad (5.31)$$

$$\Delta E = E_e - E_m \quad (5.32)$$

where v_k and i_k are sinusoidal voltage and current, respectively, at the k^{th} branch in the system. Asterisk indicates a complex conjugate.

Active devices generate RF power P_a , and this power is dissipated in resistive elements P_r . Some portion of the energy is reactively stored in inductive (E_m) and capacitive (E_e) elements. $\Delta P = 0$, $\Delta E = 0$ (Energy interaction must be completed within the system, since there is no transaction between inside and outside in circuit shown in Figure 5-12). Therefore, both real and imaginary parts of $\psi(\omega)$ must vanish, which implies need for balance in both power and energy.

For circuit designers who are familiar with impedance parameters rather than with terms of energy, it is worthwhile to translate the above criterion into impedance domain. To carry this out, the zero-port oscillator is divided into two pieces as shown in Fig. 5-12(b) As illustrated in Figure 5-12, Parts I and II are interconnected in multiplex, and therefore they are each regarded as a multi-port network with impedance matrix $[Z_I]$ or $[Z_{II}]$ respectively.

From Kirchhoff's law:

$$v = z_I i = -z_{II} i, \quad Z = Z_I + Z_{II} \Rightarrow |Z| = 0 \text{ at resonance for multi-connected active circuits} \quad (5.33)$$

From (5.29)

$$\psi(\omega) = \frac{1}{2} (v_I^T i^* - v_{II}^T i^*) = \frac{1}{2} i^T (Z_I^T + Z_{II}^T) i^* = \frac{1}{2} i^T Z^T i^* = \frac{1}{2} i^T (|Z| \tilde{Z}^{-1})^T i^* = \frac{1}{2} |Z| i^T \tilde{Z}^{-T} i^* \quad (5.34)$$

where superscripts T and $-T$ stand for transposition and inverse transposition, and tilde \sim designates co-factor matrix. Note that term $v_I^T i^*$ for part II has negative polarity due to opposite direction of currents.

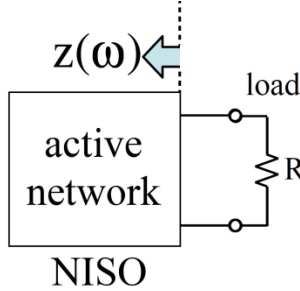


Figure 5-13: Shows the typical 1-port oscillator [21]

Loaded one-port oscillator with R can be considered as a subset of zero-port if the load R in circuit as shown in Figure 5-13 is embedded in $Z(\omega)$ so that resulting impedance is $Z = [Z(\omega) + R]$. From (5.34)

$$\psi(\omega) = \frac{1}{2}|Z|i^T \tilde{Z}^{-T} i^* = \frac{1}{2}\{Z(\omega) + R\}|i|^2 = -\frac{Z(\omega)}{2}|i|^2 - P_{out}(\omega) \quad (5.35)$$

where $P_{out}(\omega)$ is power output to the load. At the equilibrium, oscillation condition forces $\Psi(\omega_0) = 0$. However, its frequency slope remains finite as $z(\omega_0)\Psi'(\omega_0) = -z'(\omega_0)P_{out}(\omega_0)$. From (5.29)-(5.35), the expression of Q is given by [29]-[32]

$$Q = \frac{\omega_0}{2} \left| \frac{\psi'(\omega_0)}{P_{out}(\omega_0)} \right| = \frac{\omega_0}{P_{out}} \sqrt{\frac{1}{4} \left(\frac{\partial \Delta P}{\partial \omega} \right)^2 + \left(\frac{\omega_0 \partial \Delta W}{\partial \omega} \right)^2} \quad (5.36)$$

Considering that the power dissipation takes place only in the load and neglect frequency slope of the active devices, i.e., $P_{out} = P_r$ and $\frac{\partial P_a}{\partial \omega} = 0$, (5.36) can be written as

$$Q = \frac{\omega_0}{P_r} \sqrt{\frac{1}{4} \left(\frac{\partial P_r}{\partial \omega} \right)^2 + \left(\frac{\omega_0 \partial \Delta W}{\partial \omega} \right)^2} \quad (5.37)$$

Equation (5.57) agrees with Equation (8) in [10] and Equation (2) in [11]. Assuming $\left| \frac{\partial P_r}{\partial \omega} \right| \ll \left| \frac{\omega_0 \partial \Delta U}{\partial \omega} \right|$, Q-factor can be given by [30]

$$Q \cong \frac{\omega_0^2}{P_r} \left| \frac{\partial W_e}{\partial \omega} - \frac{\partial W_m}{\partial \omega} \right| \quad (5.38)$$

This agrees with [3, eq. (31)]. If we further additionally assume special relation $(2\omega_0 - \omega)U_m = \omega U_e$ or $\omega U_m = (2\omega_0 - \omega)U_e$ at $\omega = \omega_0$. The Q equation ultimately reduces to

$$Q = \omega_0 \frac{(W_e + W_m)}{P_r} \quad (5.39)$$

Equation (5.39) concurs with the energy-dumping phenomena of Q-factor.

5.4.2.4 Active SISO Circuit Q-Factor (Source-Push and Load-Pull Basis)

Figure 5-14 shows the typical 2-port oscillator model (SISO) for the derivation of Q-factor taking into account the DC source pushing and RF load pulling effect. For high performance oscillator circuit, Q-factor plays important role to make the circuit insensitive of pushing and pulling [32].

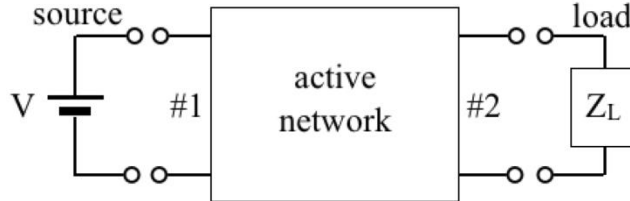


Figure 5-14: A typical 2-port oscillator model

The steady-state oscillation condition for oscillator circuit shown in Figure (5-14) can be expressed as

$$Z_{out}(\omega, V) + Z_L(\omega) = 0 \quad (5.40)$$

$$[R_{out}(\omega, V) + R_L(\omega)] + j[X_{out}(\omega, V) + X_L(\omega)] = 0 \quad (5.41)$$

From (5.41) $R_{out}(\omega, V)$ must exhibit a negative resistance while oscillation exists because R_L is passive load and intrinsically positive resistance. The source pushing on oscillation frequency can be formulated by perturbation techniques:

$$\omega \rightarrow \omega_o + \Delta\omega \quad \text{and} \quad V \rightarrow V_o + \Delta V \quad (5.42)$$

where $|\Delta\omega| \ll \omega_o$ and $|\Delta V| \ll V_o$

With the help of Taylor series expansion, Equation (5.42) can be expanded as [31]

$$Z_{out}(\omega_o, V_o) + Z_{out}^\omega(\omega_o, V_o)\Delta\omega + Z_{out}^V(\omega_o, V_o)\Delta V + \dots + Z_L(\omega_o) = 0 \quad (5.43)$$

Where

$$Z_{out}^\omega(\omega, V) = \frac{\partial Z_{out}(\omega, V)}{\partial \omega}, \quad Z_{out}^V(\omega, V) = \frac{\partial Z_{out}(\omega, V)}{\partial V} \quad (5.44)$$

Neglecting higher order partial differential term,

$$Z_{out}(\omega_o, V_o) + Z_L(\omega_o) = 0 \quad (5.45)$$

$$Z_{out}^\omega(\omega_o, V_o)\Delta\omega + Z_{out}^V(\omega_o, V_o)\Delta V = 0 \quad (5.46)$$

$$\Delta\omega = \left| \frac{Z_{out}^V(\omega_o, V_o)}{Z_{out}^\omega(\omega_o, V_o)} \right| \Delta V \quad (5.47)$$

Normalizing the frequency deviation ($\Delta\omega$) and voltage deviation (ΔV) on both sides of Equation (5.48) by their original values (ω_o, V_o):

$$\frac{\Delta\omega}{\omega_o V_o} = \frac{1}{\omega_o V_o} \left| \frac{Z_{out}^V(\omega_o, V_o)}{Z_{out}^\omega(\omega_o, V_o)} \right| \Delta V \quad (5.48)$$

$$\left| \frac{\Delta\omega}{\omega_o} \right| = \frac{V_o}{\omega_o} \left| \frac{Z_{out}^V(\omega_o, V_o)}{Z_{out}^\omega(\omega_o, V_o)} \right| \left| \frac{\Delta V}{V_o} \right| = \frac{1}{Q} \left| \frac{\Delta V}{V_o} \right| \quad (5.49)$$

$$\left| \frac{\Delta\omega}{\omega_o} \right|_{SSB} = \frac{1}{Q} \left| \frac{\Delta V}{V_o} \right| \quad (5.50)$$

$$\left| \frac{2\Delta\omega}{\omega_o} \right|_{DSB} = \frac{1}{Q} \left| \frac{\Delta V}{V_o} \right| \quad (5.51)$$

On the left-hand side of (5.51) frequency deviation is doubled to measure double sideband (upper and lower sideband frequency from the carrier). The coefficient shown in (5.51) can be expressed as $1/Q$ because the frequency deviation ($\Delta\omega$) must be inversely proportional to a certain figure of merit for sustained oscillation condition. From (5.47) and (5.51), the constant Q can be defined as a dimension free positive scalar quantity [32]

$$Q_{source-pull} = \frac{\omega_o}{2V_o} \left| \frac{Z_{out}^\omega(\omega, V)}{Z_{out}^V(\omega, V)} \right|_{(\omega=\omega_o, V=V_o)} \quad (5.52)$$

From the duality and superposition theorem,

$$Q_{source-pull} = \frac{\omega_o}{2V_o} \left| \frac{Y_{out}^V(\omega, V)}{Y_{out}^\omega(\omega, V)} \right|_{(\omega=\omega_o, V=V_o)} \quad (5.53)$$

Equation (5.52) and (5.53) is nomenclature as a source-pull Q-factor of oscillator circuit.

Similarly, load-pull Q-factor can be formulated to estimate the frequency stability due to load variation.

From (5.40), the condition for stable oscillation for constant voltage V can be expressed as

$$Z_{out}(\omega, g_m) + Z_L(\omega) = 0 \quad (5.54)$$

$$[R_{out}(\omega, g_m) + R_L(\omega)] + jX_{out}(\omega, g_m) + X_L(\omega) = 0 \quad (5.55)$$

From (5.55), $R_{out}(\omega, g_m)$ must exhibit a negative resistance while oscillation exists because R_L is passive load with intrinsically positive resistance. The load-pulling on oscillation frequency can be formulated by perturbation of frequency and transconductance of the active device [32]. For stable oscillation, transconductance of the active device must be adjusting to maintain the gain-to-loss equilibrium condition due to the variation in the load impedance $Z_L(\omega)$. These phenomena can be defined as [33]

$$Z_L(\omega) \rightarrow Z_{Lo}(\omega) + \Delta Z_L, \quad \omega \rightarrow \omega_o + \Delta\omega, \quad g_m \rightarrow g_{mo} + \Delta g \quad (5.56)$$

where $|\Delta\omega| \ll \omega_o$ and $|\Delta g| \ll g_{mo}$

From (5.55) and (5.56), Taylor series expansion:

$$Z_{out}(\omega_o, g_{mo}) + Z_{out}^\omega(\omega_o, g_{mo})\Delta\omega + Z_{out}^g(\omega_o, g_{mo})\Delta g + \dots + Z_{Lo}(\omega_o) + \Delta Z_L = 0 \quad (5.57)$$

Where

$$Z_{out}^\omega(\omega, g_m) = \frac{\partial Z_{out}(\omega, g_m)}{\partial \omega}, \quad Z_{out}^g(\omega, g_m) = \frac{\partial Z_{out}(\omega, g_m)}{\partial g} \quad (5.58)$$

Neglecting higher order partial differential term,

$$Z_{out}(\omega_o, g_{mo}) + Z_{Lo}(\omega_o) = 0 \quad (5.59)$$

$$Z_{out}^\omega(\omega_o, g_{mo})\Delta\omega + Z_{out}^g(\omega_o, g_{mo})\Delta g + \Delta Z_L = 0 \quad (5.60)$$

From (5.60), for a given perturbation in load ΔZ_L , there are two unknown variants $(\Delta\omega, \Delta g)$, the solution of (5.60) can be formulated by applying complex conjugate function (*)

$$Z_{out}^{\omega*}(\omega_o, g_{mo})\Delta\omega + Z_{out}^{g*}(\omega_o, g_{mo})\Delta g + \Delta Z_L^* = 0 \quad (5.61)$$

From (5.60) and (5.61)

$$\begin{bmatrix} \Delta\omega \\ \Delta g \end{bmatrix} = - \begin{bmatrix} Z_{out}^\omega(\omega_o, g_{mo}) & Z_{out}^g(\omega_o, g_{mo}) \\ Z_{out}^{\omega*}(\omega_o, g_{mo}) & Z_{out}^{g*}(\omega_o, g_{mo}) \end{bmatrix}^{-1} \begin{bmatrix} \Delta Z_L \\ \Delta Z_L^* \end{bmatrix} \quad (5.62)$$

$$\begin{bmatrix} \Delta\omega \\ \Delta g \end{bmatrix} = -\frac{1}{J} \begin{bmatrix} Z_{out}^g(\omega_o, g_{mo}) & -Z_{out}^g(\omega_o, g_{mo}) \\ -Z_{out}^{\omega*}(\omega_o, g_{mo}) & Z_{out}^\omega(\omega_o, g_{mo}) \end{bmatrix}^{-1} \begin{bmatrix} \Delta Z_L \\ \Delta Z_L^* \end{bmatrix} \quad (5.63)$$

Where [J] denotes Jacobian determinant [28]

$$J = \begin{vmatrix} Z_{out}^\omega(\omega_o, g_{mo}) & Z_{out}^g(\omega_o, g_{mo}) \\ Z_{out}^{\omega*}(\omega_o, g_{mo}) & Z_{out}^{g*}(\omega_o, g_{mo}) \end{vmatrix} = 2j\gamma \quad (5.64)$$

$$\gamma = Im[Z_{out}^\omega(\omega_o, g_{mo})Z_{out}^{g*}(\omega_o, g_{mo})] \quad (5.65)$$

$$\Delta\omega = -\frac{1}{J} [Z_{out}^g(\omega_o, g_{mo})\Delta Z_L - Z_{out}^g(\omega_o, g_{mo})\Delta Z_L^*] = \frac{1}{\gamma} Im[Z_{out}^g(\omega_o, g_{mo})\Delta Z_L^*] \quad (5.66)$$

$$\Delta\omega = \frac{1}{\gamma} |Z_{out}^g(\omega_o, g_{mo})\Delta Z_L| \sin|(\emptyset - \theta)| \quad (5.67)$$

Where

$$Z_{out}^g(\omega_o, g_{mo}) = |Z_{out}^g(\omega_o, g_{mo})e^{j\emptyset}| \quad (5.68)$$

$$\Delta Z_L = |\Delta Z_L| e^{j\theta} \quad (5.69)$$

Figure 5-15 shows the load impedance locus on a complex plane. From (5.57), frequency shift $\Delta\omega$ depends on the phase of the load deviation ΔZ_L . Revolving θ from zero to 2π as shown on a dashed circumference in Figure 5-15, the frequency shift reaches its maximum, given by [31]

$$|\Delta\omega|_{max} = \left| \left\{ \frac{\Delta Z_L}{\gamma} \right\} Z_{out}^g(\omega_o, g_{mo}) \sin \frac{\pi}{2} \right|_{(\theta-\theta)=\frac{\pi}{2}} \quad (5.70)$$

Normalizing the deviations in Equation (5.70) on both sides by their original values as

$$\left| \frac{2|\Delta\omega|_{max}}{\omega_o} \right|_{DSB} = \frac{1}{Q} \left| \frac{\Delta Z_L}{Z_{Lo}} \right| \quad (5.71)$$

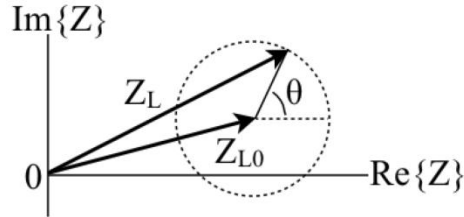


Figure 5-15: Deviated load impedance locus on a complex plane

On the left-hand side of (5.71) frequency deviation is doubled to measure double sideband (upper and lower sideband frequency from the carrier). The coefficient shown in Equation (5.71) can be expressed as $1/Q$ because the frequency deviation ($\Delta\omega$) must be inversely proportional to a certain figure of merit for sustained oscillation condition. From (5.48) and (5.52), the constant Q can be defined as a dimension free positive scalar quantity [32]

$$Q = \frac{\omega_o}{2} \left| \frac{\gamma(\omega_o, g_{mo})}{Z_{Lo} Z_{out}^g(\omega_o, g_{mo})} \right| \quad (5.72)$$

From (5.59) and (5.72)

$$Q = \frac{\omega_o}{2} \left| \frac{\gamma(\omega_o, g_{mo})}{Z_{out}^\omega(\omega_o, g_{mo}) Z_{out}^g(\omega_o, g_{mo})} \right| = \frac{\omega_o}{2} \left| \frac{Im[Z_{out}^\omega(\omega_o, g_{mo}) Z_{out}^g(\omega_o, g_{mo})^*]}{Z_{out}^\omega(\omega_o, g_{mo}) Z_{out}^g(\omega_o, g_{mo})} \right| \quad (5.73)$$

$$Q_{load-pull} = \frac{\omega_o}{2} \left| \frac{Im[Z_{out}^\omega(\omega, g_m) Z_{out}^g(\omega, g_m)^*]}{Z_{out}^\omega(\omega, g_m) Z_{out}^g(\omega, g_m)} \right|_{(\omega=\omega_o, g_m=g_{mo})} \quad (5.74)$$

$$Q_{load-pull} = \frac{\omega_o}{2} \left| \frac{Im[Y_{out}^\omega(\omega, g_m) Y_{out}^g(\omega, g_m)^*]}{Y_{out}^\omega(\omega, g_m) Y_{out}^g(\omega, g_m)} \right|_{(\omega=\omega_o, g_m=g_{mo})} \quad (Y \equiv Z^{-1}) \quad (5.75)$$

Equations (5.52) and (5.75) give insightful view about pushing and pulling characteristics of an oscillator for the optimization of the oscillator design for stable operation against those variations.

5.4.2.5 Active SIBO Circuit Q-Factor (Injection Locking Basis)

Figure 5-16 shows the typical injection-locked oscillator employing 2-port active device: (a) general model, (b) typical Colpitts oscillator, and (c) equivalent representation of (a).

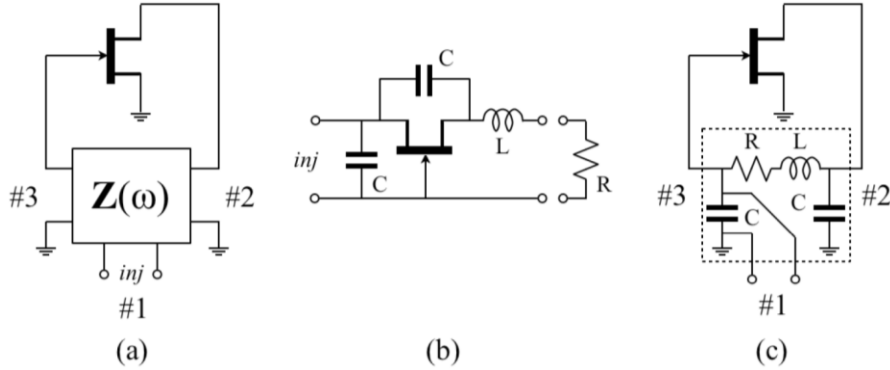


Figure 5-16: Injection-locked oscillator employing 2-port active device: (a) general model, (b) typical Colpitts oscillator, and (c) equivalent representation of (a) [26]

The impedance matrix of Figure 5-17 can be given by [27, 32]

$$Z(\omega) = \begin{bmatrix} Z_{11}(\omega) & Z_{12}(\omega) & Z_{13}(\omega) \\ Z_{21}(\omega) & Z_{22}(\omega) & Z_{23}(\omega) \\ Z_{31}(\omega) & Z_{32}(\omega) & Z_{33}(\omega) \end{bmatrix} = \begin{bmatrix} R_{11}(\omega) & R_{12}(\omega) & R_{13}(\omega) \\ R_{21}(\omega) & R_{22}(\omega) & R_{23}(\omega) \\ X_{31}(\omega) & X_{32}(\omega) & X_{33}(\omega) \end{bmatrix} + \begin{bmatrix} X_{11}(\omega) & X_{12}(\omega) & X_{13}(\omega) \\ X_{21}(\omega) & X_{22}(\omega) & X_{23}(\omega) \\ X_{31}(\omega) & X_{32}(\omega) & X_{33}(\omega) \end{bmatrix} \quad (5.76)$$

Case I (no injected current at port 1), $i_{inj} = i_1(\omega) = 0$

From (5.76)

$$v_3(\omega) = R_{32}(\omega)i_2(\omega) + jX_{32}(\omega)i_2(\omega) = [R_{32}(\omega) + jX_{32}(\omega)]i_2(\omega) \quad (5.77)$$

$$i_2(\omega) = -g_m(\omega)v_3(\omega) \quad (5.78)$$

For stable oscillation to take place at $\omega \rightarrow \omega_o$, neither v_3 nor i_2 should vanish ($v_3 \neq 0$ and $i_2 \neq 0$).

From (5.77) and (5.78)

$$[1 + g_m(\omega)R_{32}(\omega)]_{\omega \rightarrow \omega_o} = 0, \quad [X_{32}(\omega)]_{\omega \rightarrow \omega_o} = 0 \quad (5.79)$$

Where ω_o =free running oscillation frequency

Case II [injection-locked state]: $i_{inj} = i_1(\omega) \neq 0$

$$i_{inj} = i_1(\omega) = I_1 e^{j\theta_1} \quad (\text{Current represented in exponent form}) \quad (5.80)$$

$$i_2(\omega) = -g_m(\omega)v_3(\omega) = I_2 e^{j\theta_2} \quad (\text{Current represented in exponent form}) \quad (5.81)$$

From (5.76)

$$v_3(\omega) = [R_{31}(\omega) + jX_{31}(\omega)]I_1 e^{j\theta_1} + [R_{32}(\omega) + jX_{32}(\omega)]I_2 e^{j\theta_2} \quad (5.82)$$

From (5.80), (5.81), and (5.82)

$$[R_{31}(\omega)\sin\Delta\theta + jX_{31}(\omega)\cos\Delta\theta]I_1 + X_{32}(\omega)I_2 = 0 \quad (5.83)$$

where $\Delta\theta = \theta_1 - \theta_2$ is the phase difference between the currents at two ports.

The injection locked state oscillation frequency ω is slightly offset ($\Delta\omega$) from the free running frequency ω_o , the impedance matrix (8) can be expanded with the help of Taylor series.

$$R_{31}(\omega) \cong R_{31}(\omega_o) + \Delta\omega \frac{d}{d\omega} [R_{31}(\omega)]_{\omega \rightarrow \omega_o} = R_{31}(\omega_o) + \Delta\omega R'_{31}(\omega_o) \quad (5.84)$$

$$X_{31}(\omega) \cong X_{31}(\omega_o) + \Delta\omega \frac{d}{d\omega} [X_{31}(\omega)]_{\omega \rightarrow \omega_o} = X_{31}(\omega_o) + \Delta\omega X'_{31}(\omega_o) \quad (5.85)$$

$$X_{33}(\omega) \cong X_{33}(\omega_o) + \Delta\omega \frac{d}{d\omega} [X_{33}(\omega)]_{\omega \rightarrow \omega_o} = X_{33}(\omega_o) + \Delta\omega X'_{33}(\omega_o) \quad (5.86)$$

$$X_{32}(\omega) \cong X_{32}(\omega_o) + \Delta\omega \frac{d}{d\omega} [X_{32}(\omega)]_{\omega \rightarrow \omega_o} = X_{32}(\omega_o) + \Delta\omega X'_{32}(\omega_o) \quad (5.87)$$

With the help of Taylor series expansion, based on $\omega \rightarrow \omega_o + \Delta\omega$ and free running oscillation condition $[X_{32}(\omega)]_{\omega \rightarrow \omega_o} = 0$; $|\Delta\omega| \ll \omega_o$

From (5.76)-(5.87)

$$\Delta\omega \cong - \left[\frac{R_{31}(\omega_o)\sin\Delta\theta + X_{31}(\omega_o)\cos\Delta\theta}{X'_{32}(\omega_o)} \right] \frac{I_1}{I_2} \quad (5.88)$$

$$\Delta\omega \cong - \left[\frac{\sqrt{R_{31}^2(\omega_o) + X_{31}^2(\omega_o)}}{X'_{32}(\omega_o)} \sin\phi \right] \frac{I_1}{I_2} = - \frac{|Z_{31}(\omega_o)| \sin\phi}{X'_{32}(\omega_o)} \frac{I_1}{I_2} \quad (5.89)$$

where $\phi = \Delta\theta + \tan^{-1} \left[\frac{X_{31}(\omega_o)}{R_{31}(\omega_o)} \right]$, assuming phase difference $\Delta\theta$ is not constrained i.e. $(0 \leq \Delta\theta < 2\pi) \rightarrow 0 \leq |\sin\phi| \leq 1$, from (5.89)

$$0 \leq |\Delta\omega| \leq \left| \frac{Z_{31}(\omega_o)}{X'_{32}(\omega_o)} \right| \frac{I_1}{I_2} \quad (5.90)$$

Eq. (5.90) is identical to Adler's injection-lock range Eq. (13b) ref [31] and Eq. (10.90) ref [33]

$$0 \leq |\Delta\omega| \leq \left[\frac{\omega_0}{2Q} \right] \left[\frac{I_1}{I_2} \right] \quad (5.91)$$

From (5.90) and (5.91)

$$Q = \frac{\omega_0}{2} \left| \frac{X'_{32}(\omega_0)}{Z_{31}(\omega_0)} \right|, \quad \text{where } X'_{32}(\omega_0) = \frac{d}{d\omega} [X_{32}(\omega)]_{\omega \rightarrow \omega_0} \quad (5.92)$$

The circuit shown in Figure 5-16(c), Q-factor can be given by

$$Q = \frac{\omega_0}{2} \left| \frac{X'_{32}(\omega_0)}{Z_{31}(\omega_0)} \right| \quad (5.93)$$

Where

$$Z_{31}(\omega_0) = \left\{ \frac{1}{j\omega C + \frac{1}{R+j\omega L + \frac{1}{j\omega C}}} \right\}, \quad \text{and } X_{32}(\omega) = \frac{1}{\omega C} \left\{ \frac{LC\omega^2 - 2}{\omega^2 C^2 R^2 + (LC\omega^2 - 2)^2} \right\} \quad (5.94)$$

From (5.79), (5.93) and (5.94)

$$X'_{32}(\omega_0) = \frac{d}{d\omega} [X_{32}(\omega)]_{\omega \rightarrow \omega_0} = \frac{d}{d\omega} \left[\frac{1}{\omega C} \left\{ \frac{LC\omega^2 - 2}{\omega^2 C^2 R^2 + (LC\omega^2 - 2)^2} \right\} \right]_{\omega=\omega_0} \quad (5.95)$$

$$Q = \frac{\omega_0}{2} \left| \frac{X'_{32}(\omega_0)}{Z_{31}(\omega_0)} \right| = \frac{\omega_0 L}{R} \left(\frac{L}{L+2CR^2} \right)^{1/2} \quad (5.96)$$

5.5 Resonator Design Criteria for Low Phase Noise Oscillator Applications

The Leeson phase noise equation is given by [34]

$$\xi(f_m) = 10 \log \left\{ \left[1 + \frac{f_0^2}{(2f_m Q_L)^2 (1 - \frac{Q_L}{Q_0})^2} \right] \left(1 + \frac{f_c}{f_m} \right) \frac{FkT}{2P_o} \right\} \quad (5.97)$$

where

$\xi(f_m)$ = ratio of sideband power in a 1Hz bandwidth at f_m to total power in dB

f_m = frequency offset from the carrier

f_0 = center frequency

f_c = flicker frequency

Q_L = loaded Q of the tuned circuit

Q_0 = unloaded Q of the tuned circuit

F = noise factor

$kT = 4.1 \times 10^{-21}$ at 300 K (room temperature)

P_o = average power at oscillator output

From (5.97), phase noise in oscillator is inversely proportional to the square of the resonator loaded Q-factor, indicating that insertion loss of the resonator is linked with figure of merit (FOM) as [31]-[33]

$$[\text{Resonator}]_{\text{FOM}} = 10 \log \left(\frac{I.L}{Q_L^2} \right) \quad (5.98)$$

From (5.98), for low phase noise, designer must minimize the resonator FOM.

At microwave frequencies, resonators can take various shapes and forms [35]-[44]. The shape of microwave structure affects the field distribution and influence the tuning range of the oscillator circuits. Usually, passive lumped LC and planar transmission line resonator networks are used in low cost broadband oscillator circuits.

5.5.1 Passive Lumped LC Resonator

Figure 5-17 shows the typical doubly loaded shunt resonator. Lumped or quasi-lumped resonator will oscillate at $f_o = \frac{1}{2\pi\sqrt{LC}}$.

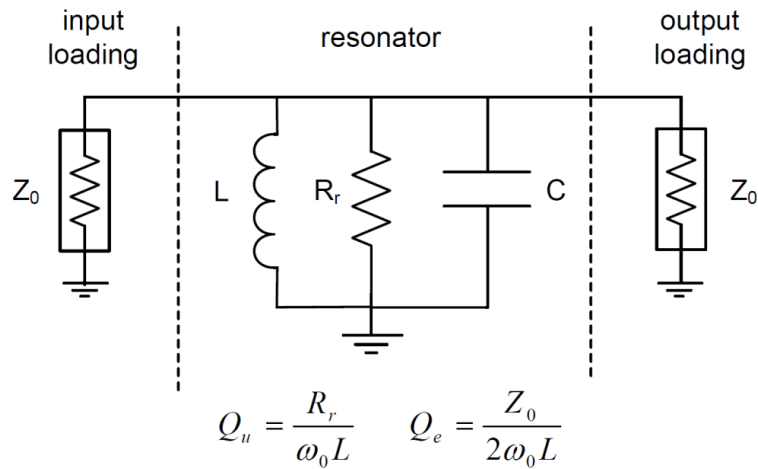


Figure 5-17: A typical doubly loaded shunt resonator [35]

The S_{21} (transmission gain) can be given for doubly loaded shunt resonator (Figure 5-17) is given by [35]

$$S_{21}(\omega) = \frac{2}{\left(\frac{Z_0}{\frac{1}{R_r} + \frac{1}{Z_0} + \frac{1}{Z_0}} \right) + j Z_0 \left(\omega C - \frac{1}{\omega L} \right)} \quad (5.99)$$

$$Q = \frac{\omega_0}{2} \left| \frac{\partial \varphi(\omega)}{\partial \omega} \right|_{\omega=\omega_0} \quad \text{where } (\varphi(\omega)) = \angle S_{21} \quad (5.100)$$

$$I.L = \left| \frac{1}{S_{21}} \right|_{\omega=\omega_0}^2 = \left(1 + \frac{Z_o}{2R_r} \right)^2 = \left(1 + \frac{Q_e}{Q_u} \right)^2 \quad (5.101)$$

From (5.98),

$$[Resonator]_{FOM} = 10 \log \left(\frac{I.L}{Q_L^2} \right) = 10 \log \left[\left(1 + \frac{Q_e}{Q_u} \right)^2 \left(\frac{1}{Q_e} + \frac{1}{Q_u} \right)^2 \right] \quad (5.102)$$

$$\frac{d[Resonator]_{FOM}}{dQ_e} = 0 \Rightarrow (Q_u = Q_e) \Rightarrow Q_{loaded} = \frac{Q_{unloaded}}{2} \quad (5.103)$$

5.5.2 Planar Transmission Line

Various forms of planar transmission lines have been developed. Some examples are strip line, Microstrip line, slot line and coplanar waveguide. The Microstrip line is the most popular type of resonator used for oscillator and filter applications. Figure 5-18 shows the typical structure of a microstrip transmission line. A conducting strip (microstrip line) with a width w and a thickness t is on the top of a dielectric substrate that has a relative dielectric constant ϵ_r and a thickness h and the bottom of the substrate is a ground (conducting) plane.

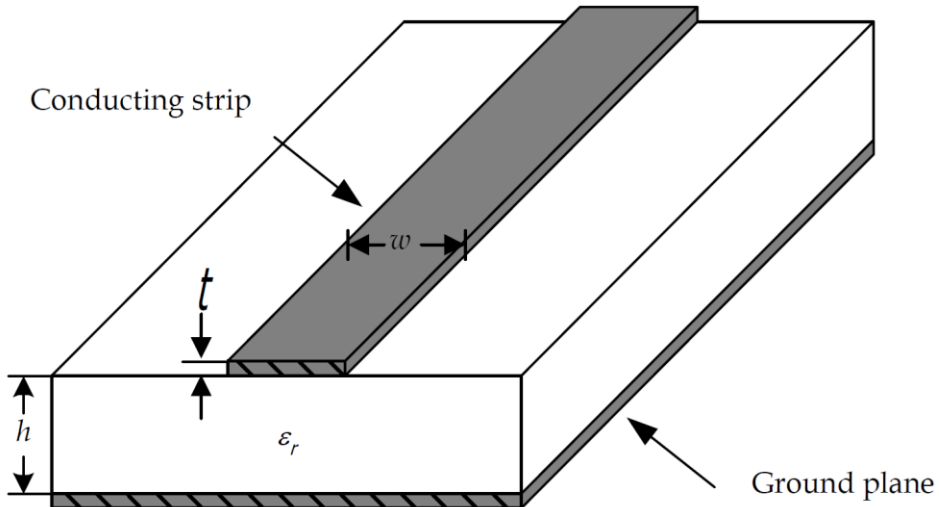


Figure 5-18: A typical structure of Microstrip Line

The fields in the microstrip extend within two media - air above and dielectric below so that the structure is inhomogeneous. Due to this inhomogeneous nature, the microstrip does not support a pure TEM wave. This is because that a pure TEM wave has only transverse components, and its propagation velocity depends only on the material properties, namely the permittivity ϵ and the permeability μ . However, with the presence of the two guided wave media (the dielectric substrate and the air), the waves in a microstrip line will have no vanished longitudinal components of electric and magnetic fields, and their propagation velocities will depend not only on the material properties, but also on the physical dimensions of the microstrip. When the longitudinal components of the fields for the dominant mode of a microstrip line remain very much smaller than the transverse components, they may be neglected. In this case, the dominant mode then behaves like a TEM mode, and the TEM

transmission line theory is applicable for the microstrip line as well. This is called the quasi-TEM approximation and it is valid over most of the operating frequency ranges of microstrip.

5.5.2.1 Effective dielectric constant and characteristic impedance of a microstrip line

The Microstrip transmission line is an inhomogeneous transmission line. The field between the strip and the ground plane are not contained entirely in the substrate but extends within two media, air and dielectric. Hence, the microstrip line cannot support a pure TEM wave. The mode of propagation is quasi-TEM. In the quasi-TEM approximation, a homogeneous dielectric material with an effective dielectric permittivity replaces the inhomogeneous dielectric-air media of microstrip. Transmission characteristics of microstrip lines are described by two parameters, namely the effective dielectric constant ϵ_{re} and characteristic impedance Z_c , which may then be obtained by quasi-static analysis. In quasi-static analysis, the fundamental mode of wave propagation in a microstrip transmission line is quasi TEM; however, for simplification in analysis, it is assumed pure TEM. The above two parameters of microstrips are then determined from the values of two capacitances as follows:

$$\epsilon_{re} = \frac{C_d}{C_a} \quad (5.104)$$

$$Z_c = \frac{1}{c\sqrt{C_d C_a}} \quad (5.105)$$

where C_d is the capacitance per unit length with the dielectric substrate present, C_a is the capacitance per unit length with the dielectric substrate replaced by air, and c is the velocity of electromagnetic waves in free space ($c = 3.0 \times 10^8 \text{ m/s}$). The phase velocity and propagation constant can be expressed as

$$v_p = \frac{\omega}{\beta} = \frac{c}{\sqrt{\epsilon_{re}}} \quad (5.106)$$

$$\beta = k_0 \sqrt{\epsilon_e} \quad (5.107)$$

where c is the velocity of light in free space.

The electrical length θ for a given physical length l of the microstrip is defined by

$$\theta = \beta l \quad (5.108)$$

Therefore, $\theta = \pi/2$ when $l = \lambda_g/4$, and $\theta = \pi$ when $l = \lambda_g/2$. These so-called quarter wavelength and half-wavelength microstrip lines are important for design of microstrip resonators.

For very thin conductors (i.e., $t \rightarrow 0$), the closed-form expressions that provide accuracy better than one percent are given as follows [42, 56]:

For $\frac{w}{h} \leq 1$: effective dielectric constant of a microstrip line is given approximately by

$$\varepsilon_{re} = \frac{\varepsilon_r + 1}{2} + \frac{\varepsilon_r - 1}{2} \left\{ \left(1 + 12 \frac{h}{w} \right)^{-1/2} + 0.04 \left(1 - \frac{w}{h} \right)^2 \right\} \quad (5.109)$$

$$Z_c = \frac{\eta}{2\pi\sqrt{\varepsilon_{re}}} \ln \left(\frac{8h}{w} + \frac{w}{4h} \right) \quad (5.110)$$

where $\eta = 120\pi$ (Ω) is the wave impedance in free space.

For $\left(\frac{w}{h} \geq 1\right)$: effective dielectric constant of a microstrip line is given approximately by

$$\varepsilon_{re} = \frac{\varepsilon_r + 1}{2} + \frac{\varepsilon_r - 1}{2} \left(1 + 12 \frac{h}{w} \right)^{-1/2} \quad (5.111)$$

$$Z_c = \frac{\eta}{\sqrt{\varepsilon_{re}}} \left\{ \frac{w}{h} + 1.393 + 0.6697 \ln \left(\frac{w}{h} + 1.444 \right) \right\}^{-1} \quad (5.112)$$

The effective dielectric constant can be interpreted as the dielectric constant of a homogeneous medium that replaces the air and dielectric regions of the microstrip. Given the dimensions of the microstrip line, the characteristic impedance can be written as

$$Z_c = \begin{cases} \frac{60}{\sqrt{\varepsilon_e}} \ln \left(\frac{8h}{w} + \frac{w}{4h} \right) & \text{for } w/h \leq 1 \\ \frac{120\pi}{\sqrt{\varepsilon_{re}} \left[\frac{w}{h} + 1.393 + 0.6697 \ln \left(\frac{w}{h} + 1.444 \right) \right]} & \text{for } w/h \geq 1 \end{cases} \quad (5.113)$$

For given characteristic impedance Z_c and dielectric constant ε_{re} the w/h ratio can be found as

$$\frac{w}{h} = \begin{cases} \frac{8\exp(A)}{\exp(2A)-2} & \text{for } w/h < 2 \\ \frac{2}{\pi} \left[B - 1 - \ln(2B - 1) + \frac{\varepsilon_{re}-1}{2\varepsilon_{re}} \left[\ln(B-1) + 0.39 - \frac{0.61}{\varepsilon_{re}} \right] \right] & \text{for } w/h > 2 \end{cases} \quad (5.114)$$

Where

$$A = \frac{Z_c}{60} \sqrt{\frac{\varepsilon_{re}+1}{2}} + \frac{\varepsilon_r-1}{\varepsilon_r+1} \left(0.23 + \frac{0.11}{\varepsilon_{re}} \right) \quad (5.115)$$

$$B = \frac{60\pi^2}{Z_c\sqrt{\varepsilon_r}} \quad (5.116)$$

These expressions also provide accuracy better than one percent. If values that are more accurate are needed, an iterative or optimization process can be employed.

In general, there is dispersion in microstrip, its phase velocity is not a constant but depends on frequency. The effective dielectric constant ε_{re} is a function of frequency and can be defined as the frequency dependent effective dielectric constant $\varepsilon_{re}(f)$ [57].

$$\varepsilon_{re}(f) = \varepsilon_r - \frac{\varepsilon_r - \varepsilon_{re}}{1 + (f/f_{50})^m} \quad (5.117)$$

where

$$f_{50} = \frac{f_{TM_0}}{0.75 + (0.75 - 0.332\epsilon_r^{-1.73})w/h} \quad (5.118)$$

$$f_{TM_0} = \frac{c}{2\pi h \sqrt{\epsilon_r - \epsilon_{re}}} \tan^{-1} \frac{\sqrt{\epsilon_r - 1}}{\epsilon_r - \epsilon_{re}} \quad (5.119)$$

$$m = m_0 m_c \leq 2.32 \quad (5.120)$$

$$m_0 = 1 + \frac{1}{1 + \sqrt{w/h}} + 0.32 \left(\frac{1}{1 + \sqrt{w/h}} \right)^3 \quad (5.121)$$

$$m_c = \begin{cases} 1 + \frac{1.4}{1+w/h} \left\{ 0.15 - 0.235 \exp \left(\frac{-0.45f}{f_{50}} \right) \right\} & \text{for } \frac{w}{h} \leq 0.7 \\ 1 & \text{for } \frac{w}{h} \geq 0.7 \end{cases} \quad (5.122)$$

where, c is the velocity of light in free space, and whenever the product $m_0 m_c$ is greater than 2.32 the parameter m is chosen equal to 2.32

The dispersion model shows that the $\epsilon_{re}(f)$ increases with frequency and $\epsilon_{re}(f) \rightarrow \epsilon_r$, as $f \rightarrow \infty$. The accuracy is estimated to be within 0.6% for $0.1 \leq w/h \leq 10$, for $1 \leq \epsilon_r \leq 128$ and for any value of $(\frac{h}{\lambda_0})$.

The effect of dispersion on the characteristic impedance may be estimated by [43]

$$Z_c(f) = Z_c \frac{\epsilon_{re}(f)-1}{\epsilon_{re}-1} \sqrt{\frac{\epsilon_{re}}{\epsilon_{re}(f)}} \quad (5.123)$$

5.5.2.2 Planar Transmission Line Bends

The compact printed resonator is formed by bending the transmission line in closed form such as ring resonator, square loop resonator, hairpin resonator, etc. Right-angle bend and mitered bend of microstrips may be modeled by an equivalent T-network, as shown in Figure 5-19, and its closed-form expressions for evaluation of capacitance and inductance is given by [42]:

$$C = 0.001h \left[(10.35\epsilon_r + 2.5) \left(\frac{w}{h} \right)^2 + (2.6\epsilon_r + 5.64) \left(\frac{w}{h} \right) \right] pF \quad (5.124)$$

$$L = 0.22h \left\{ 1 - 1.35 \exp \left[-0.18 \left(\frac{w}{h} \right)^{1.39} \right] \right\} nH \quad (5.125)$$

For the microstrip mitered bend, and as

$$C = 0.001h \left[(3.93\epsilon_r + 0.62) \left(\frac{w}{h} \right)^2 + (7.6\epsilon_r + 3.8) \left(\frac{w}{h} \right) \right] pF \quad (5.126)$$

$$L = 0.44h \left\{ 1 - 1.062 \exp \left[-0.177 \left(\frac{w}{h} \right)^{0.947} \right] \right\} nH \quad (5.127)$$

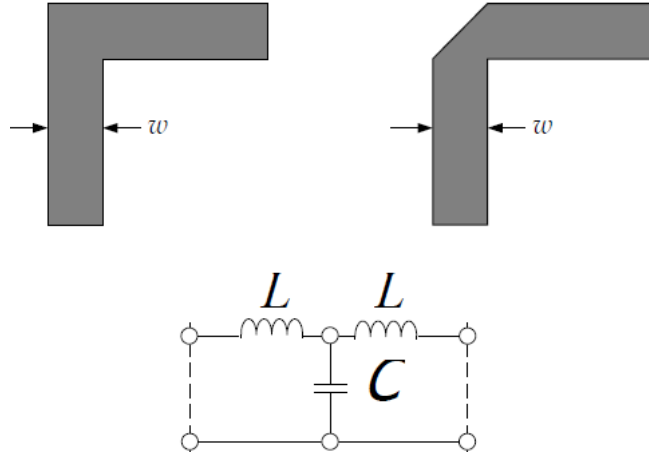


Figure 5-19: Equivalent lumped LC representation of Right-angle bend, mitered bend and model [57]

5.5.3 Planar Transmission Line Resonator

Planar transmission line resonators are formed by using microstrip lines of various wavelengths ($\lambda/4$, $\lambda/2$, λ), where λ is the guided wavelength at the fundamental resonant frequency f_0 . The quarter wavelength resonator $\lambda/4$ long resonates at the fundamental frequency f_0 and at its multiple frequencies of $f = (2n - 1)f_0$ for $n = 2, 3, 4, 5\dots$

The half wavelength resonator $\lambda/2$ long resonates at the fundamental frequency f_0 and at its multiple frequencies of $f = n f_0$ for $n = 2, 3\dots$ etc. This type of resonator can also be shaped into open-loop resonator. The full wavelength resonator, λ long resonates at the fundamental frequency f_0 and at other frequencies of $f = n f_0$ for $n = 2, 3, \dots$ etc. This type of resonator is commonly found in the form of ring or closed loop resonators with a median circumference $2\pi r = \lambda$, where r is the radius of the ring. Because of its symmetrical geometry a resonance can occur in either of 2 orthogonal coordinates. This type of transmission line resonator has a distinct feature; it can support a pair of degenerate modes that have the same resonant frequencies but orthogonal field distributions. This feature can be utilized to design dual mode filters.

5.5.3.1 Microstrip Resonator

A microstrip resonator is any structure that is able to contain at least one oscillating EM field. There are many forms of microstrip resonators; however its large physical size can present a drawback. Hence there is strong interest to miniaturize such resonators particularly for oscillator applications. Miniaturization of microstrip resonators can be achieved by using either high dielectric constant substrates or meander the lines to create a folded microstrip resonator [36].

5.5.3.2 Folded Open Loop Microstrip Resonator

Figure 5-20 shows the typical square open loop resonator, which can be obtained by folding a straight open resonator (as illustrated in Figure 5-20a). Due to the corners and the fringing

capacitance between the open ends, a rigorous calculation of the electromagnetic fields in the square resonator is impractical. However, it is possible to study the main characteristics of the resonant modes of the square open loop resonator by analogy to those of the straight resonator. This qualitative analysis can shed some light on the behavior of the resonator with minimum effort. The conclusions drawn using this approach can then be compared for validation against the actual distribution of the electromagnetic fields obtained with the aid of full wave simulators.

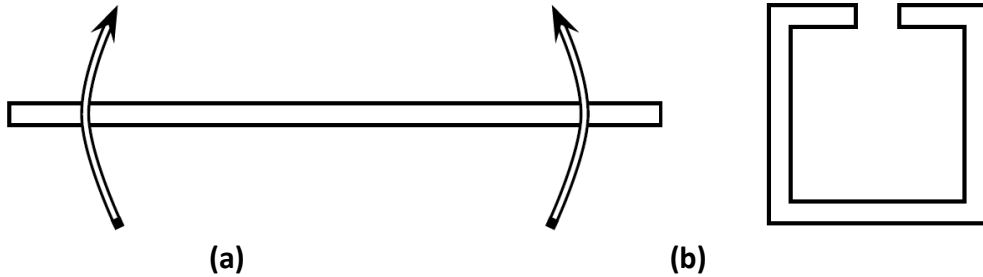


Figure 5-20: The square open loop resonator can be obtained by folding a straight open resonator: (a) straight open resonator, (b) square open loop resonator [36]

The resonant frequency of the straight transmission line (Figure 5-21 (a)) can be obtained by looking at the input admittance from any point within its length. Figure 5-21 (b) shows an equivalent circuit that can be used to calculate this admittance as [37]

$$Y_{in} = jY_0(\tan\theta_1 + \tan\theta_2) = jY_0 \left(\frac{\sin\theta_T}{\cos\theta_1 \cos\theta_2} \right) \quad (5.128)$$

$$[Y_{in}]_{(\theta_1=\theta_2=\frac{\pi}{2})} = \infty \Rightarrow [Z_{in}]_{(\theta_1=\theta_2=\frac{\pi}{2})} = 0 \quad (5.129)$$

where $\theta_T = \theta_1 + \theta_2$, is the total electrical length of the resonator. A standing wave can be maintained in the resonator whenever $Y_{in} = 0$. This yields infinite resonant frequencies at: $\theta_T = n\pi$ or $l = n\frac{\lambda}{2}$

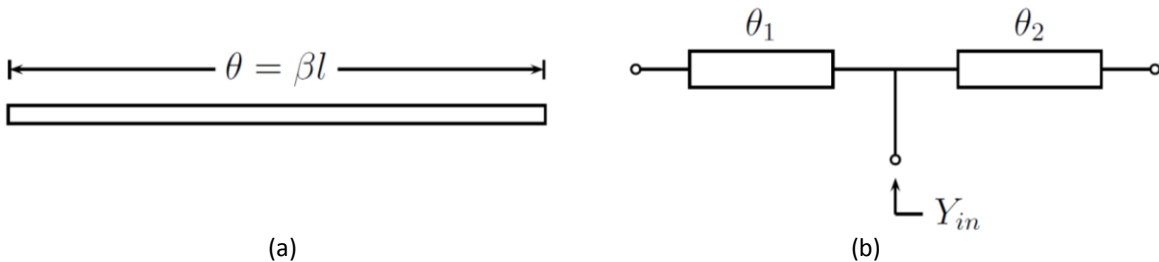


Figure 5-21: Microstrip open resonator (a) Top view of a microstrip straight resonator, (b) Equivalent circuit used to calculate the input admittance from an arbitrary point within the length of the resonator [37]

Figure 5-22 shows the voltage distribution at the first two resonant frequencies ($n=1, 2$). Since the open ends of the resonator force the current to be zero there, the voltage attains a maximum and the modes shown are the only ones allowed at those frequencies. If the loop were closed, this boundary condition would not apply and two orthogonal modes would exist at each frequency [38].

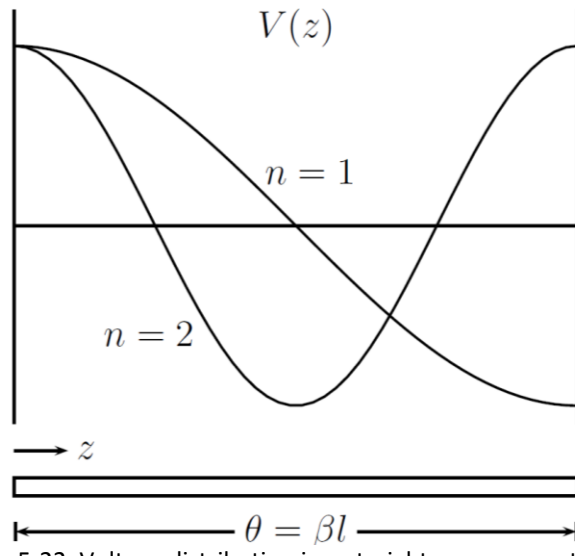


Figure 5-22: Voltage distribution in a straight open resonator [38]

Figure 5-22 shows the positions of the voltage nulls in the mode diagram, at the first resonant frequency there is only one such null at $\theta_1 = \theta_2 = \pi/2$, while at the second resonance there are two of them at $\theta_1 = \pi/2$ and $\theta_2 = 3\pi/2$. From (5.129), location of voltage nulls is important because the resonator cannot be excited there. However, by choosing the feeding point of the resonator it is possible to excite only the odd or even modes of the resonator. As an interesting consequence, the fundamental resonance ($n=1$) or any other odd mode resonance cannot be excited at the center of the resonator. This phenomenon translates to the square open loop resonator as is shown in Figure 5-23.



Figure 5-23: Two ways of exciting only the even modes of the square open loop resonator (a) Excitation of the resonator in a null of the fundamental mode (b) Excitation of the resonator symmetrically with respect to both open ends [38].

The Q_{ex} (external quality factor) of the square open loop resonator obtained by tapping into the resonator depends on the voltage level at the tapping point at resonance. If the tapping point coincides with a voltage null, then no coupling is achieved between the resonator and the external circuit and the resulting quality factor is very large. Similarly, if the voltage at the tapping point is high then the external quality factor will be low. Referring to the voltage distribution of the conventional and the miniaturized resonator; it is possible to predict that in the case of the conventional resonator the external Q will decrease rapidly as the tapping point is moved away from the voltage null at the center of the resonator.

For comparative analysis, Figure 5-24 shows the external quality factor of both conventional and miniaturized resonator with the same resonant frequency (1 GHz) [38]. As illustrated in Figure 5-24, Q_{ex} diminishes relatively fast for unloaded resonator. But in the case of the miniaturized resonator loaded with 1 pF capacitor the change in the Q_{ex} is slower. Therefore, the tapping distance from the null point necessary to obtain a given Q_{ex} is larger in the case of the miniaturized resonator. The tapping point is selected on the side of the miniaturized loaded resonator; this is because the quality factors obtained by tapping closer to the null point produces large values of Q_{ex} that are difficult to estimate accurately.

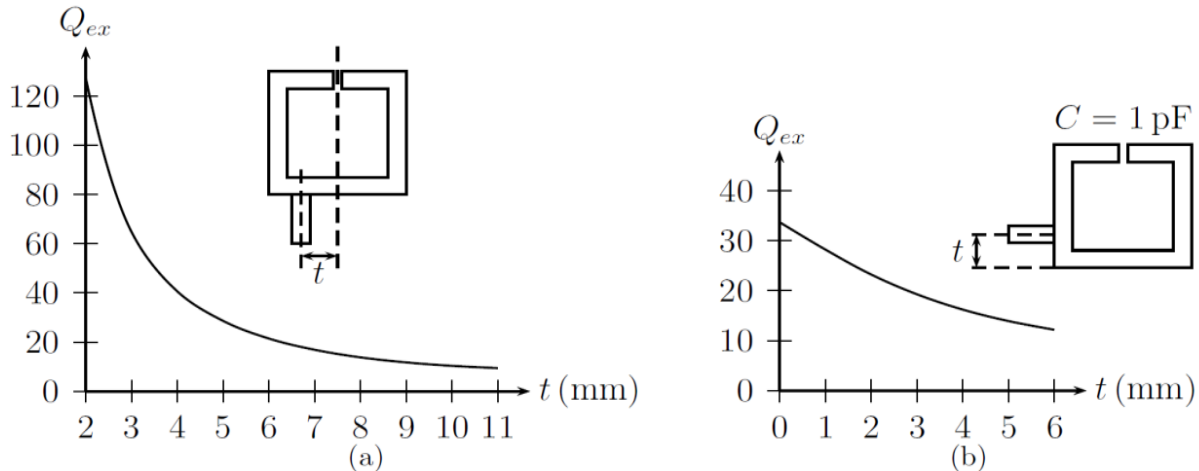


Figure 5-24: External quality factor of an: (a) unloaded resonator, and (b) a resonator loaded with $C = 1\text{ pF}$ [38]

5.5.3.3 Folded Hair-Pin Resonator

Figure 5-25 shows the basic layout of the typical stepped impedance hairpin resonator which consists of the single transmission line l_s and coupled lines with a length of l_c ; Z_s is the characteristic impedance of the single transmission line l_s .

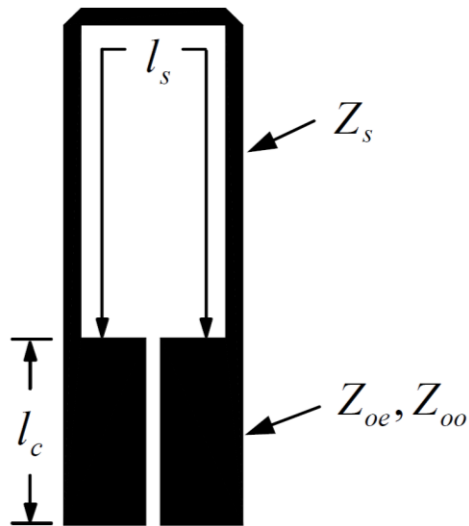


Figure 5-25: A typical layout of the stepped impedance hairpin resonator [39]

As shown in Figure 5-25, Z_{oe} and Z_{oo} are the even-and odd-mode impedance of the symmetric capacitance-load parallel-coupled lines with a length of l_c . The drawback of the stepped impedance Hair-Pin resonator is large size, which can be made smaller by proper selection for the value of Z_s ($Z_s > \sqrt{Z_{oe}Z_{oo}}$) The effect of the loading capacitance shifts the spurious resonant frequencies of the resonator from integer multiples of the fundamental resonant frequency, thereby reducing interferences from high-order harmonics [39]. For the analysis purpose, Figure 5-26 shows the typical configuration of stepped impedance hairpin resonator built from open-end transmission line.

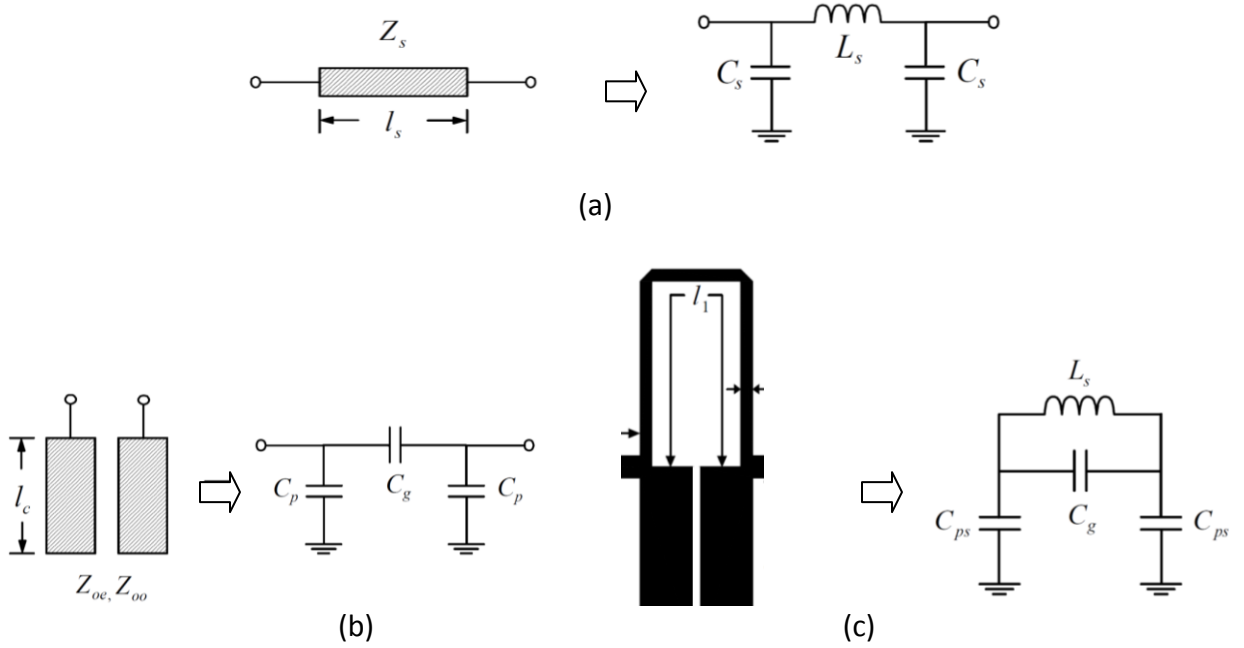


Figure 5-26: Equivalent circuit of (a) single transmission line, (b) symmetric coupled lines, and (c) stepped impedance hairpin resonator [40].

As shown in Figure 5-26 (a), the single transmission line is modeled as an equivalent L-C π -network. Assuming the lossless single transmission line with a length of l_s , the ABCD matrix is given by

$$\begin{bmatrix} A & B \\ C & D \end{bmatrix} = \begin{bmatrix} \cos(\beta_s l_s) & jZ_s \sin(\beta_s l_s) \\ jY_s \sin(\beta_s l_s) & \cos(\beta_s l_s) \end{bmatrix} \quad (5.130)$$

$$\begin{bmatrix} A & B \\ C & D \end{bmatrix} = \begin{bmatrix} 1 + Z_L Y_c & Z_L \\ Y_c (2 + Z_L Y_c) & 1 + Z_L Y_c \end{bmatrix} \quad (5.131)$$

where $Z_L = j\omega L_s$, $Y_c = j\omega C_s$, ω is the angular frequency, L_s and C_s are the equivalent inductance and capacitance of the single transmission line.

From (5.130) with (5.131), the equivalent L_s and C_s can be described by

$$L_s = \frac{Z_s \sin(\beta_s l_s)}{\omega} H \quad (5.132a)$$

$$C_s = \frac{1 - \cos(\beta_s l_s)}{\omega Z_s \sin(\beta_s l_s)} F. \quad (5.132b)$$

In case of the symmetric parallel-coupled lines, the electrical equivalent circuit is capacitive π -network. The ABCD matrix of the lossless parallel-coupled lines is expressed as [41]

$$\begin{bmatrix} A & B \\ C & D \end{bmatrix} = \begin{bmatrix} \frac{Z_{oe}+Z_{oo}}{Z_{oe}-Z_{oo}} & \frac{-j2Z_{oe}Z_{oo}\cot(\beta_c l_c)}{(Z_{oe}-Z_{oo})} \\ \frac{j2}{(Z_{oe}-Z_{oo})\cot(\beta_c l_c)} & \frac{Z_{oe}+Z_{oo}}{Z_{oe}-Z_{oo}} \end{bmatrix} \quad (5.133)$$

$$\begin{bmatrix} A & B \\ C & D \end{bmatrix} = \begin{bmatrix} 1 + Z_g Y_p & Z_g \\ Y_p(2 + Z_g Y_p) & 1 + Z_g Y_p \end{bmatrix} \quad (5.134)$$

where β_c is the phase constant of the coupled lines, $Z_g = 1/j\omega C_g$, $Y_p = j\omega C_p$.

From (5.133) and (5.134), the equivalent capacitances of the π -network can be given by

$$C_g = \left[\frac{(Z_{oe}-Z_{oo})}{2\omega Z_{oe}Z_{oo}\cot(\beta_c l_c)} \right] F, \quad C_p = \left[\frac{1}{\omega Z_{oe}\cot(\beta_c l_c)} \right] F \quad (5.135)$$

The realization of stepped impedance hairpin resonator can be formulated by combining the equivalent circuits of the single transmission line and coupled lines as shown in Figures 5-25 (a) and 5-26 (b), the equivalent circuit of the stepped impedance hairpin resonator in terms of lumped elements L and C is shown in Figure 5-25 (c), where $C_{ps} = (C_p + C_s + \Delta C)$ is the sum of the capacitances of the single transmission line, coupled lines and the junction discontinuity (ΔC) [42] between the single transmission line and the coupled lines.

The widths of the single transmission line and coupled lines resonator can be obtained from selecting the impedances that satisfy the condition $Z_s > \sqrt{Z_{oe}Z_{oo}}$. The lengths of the single transmission line and coupled lines of the filter transformed from (5.132) and (5.135):

$$l_s = \frac{\sin^{-1}(\omega_c L_{st}/Z_s)}{\beta_s} \quad \text{and} \quad l_c = \frac{\tan^{-1}[\omega_c Z_{oe}(C_{pst}-C_s-\Delta C)]}{\beta_c} \quad (5.136)$$

where ω_c is the 3 dB cut-off angular frequency, L_{st} and C_{pst} are the inductance and capacitance chosen from the available L-C tables.

Figure 5-27 shows the typical configuration of hairpin resonator.

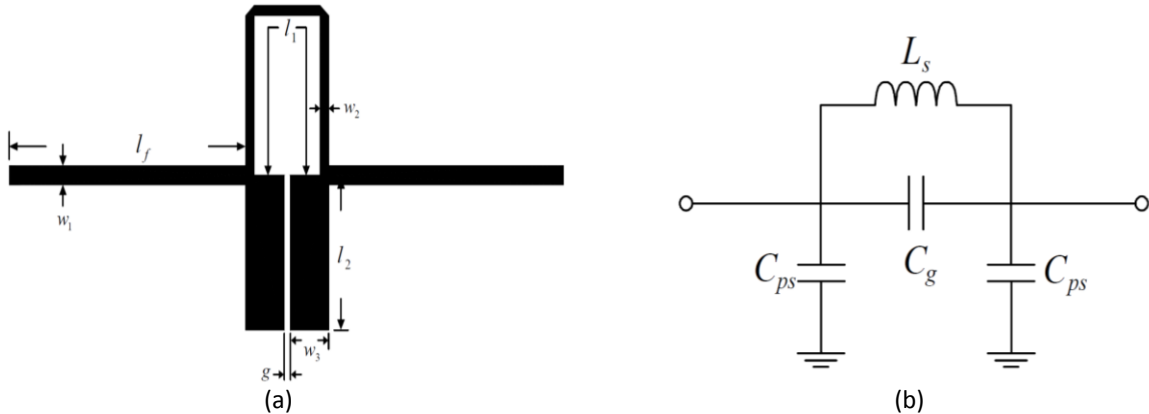


Figure 5-27: A typical low pass filter using one hairpin resonator: (a) layout and (b) equivalent circuit [42]

5.5.3.4 Ring Resonator

A most common closed loop resonator type is the ring resonator, consists of a transmission line of a full wavelength λ long, formed in a circular closed loop, and resonates when the mean circumference of the ring resonator is equal to an integral multiple of a guided wavelength, can be described by

$$2\pi r = n\lambda_g, \text{ for } n = 1, 2, 3, \dots \quad (5.137)$$

$$f = \frac{nc}{2\pi\sqrt{\epsilon_{eff}}} = nf_0 \quad (5.138)$$

$$\lambda_g = \frac{c}{f\sqrt{\epsilon_{eff}}} \quad (5.139)$$

where r is the mean radius of the ring that equals the average of the outer and inner radii, λ_g is the guided wavelength and n is the mode number.

Figure 5-28 shows the typical ring resonator, that consists of feed lines, coupling gaps, and the circular closed loop printed transmission line resonator. As shown in Figure 5-28, power is coupled into and out of the resonator through feed lines and coupling gaps. For the first mode, the maxima of field occur at the coupling gap locations, and nulls occur at 90° from the coupling gap locations, valid only for the weakly coupled case, as it does not account for loading effects from the ports [43].

Coupling is said to be weak or “loosely coupled” if the separation between the feed lines and the resonator is large such that the resonant frequency of the ring is unaffected [44]-[52]. However, if the separation is reduced, the gap capacitance increases, thereby resonator loading will occur and may cause the resonant frequency of the circuit to deviate from the inherent resonant frequencies of the ring.

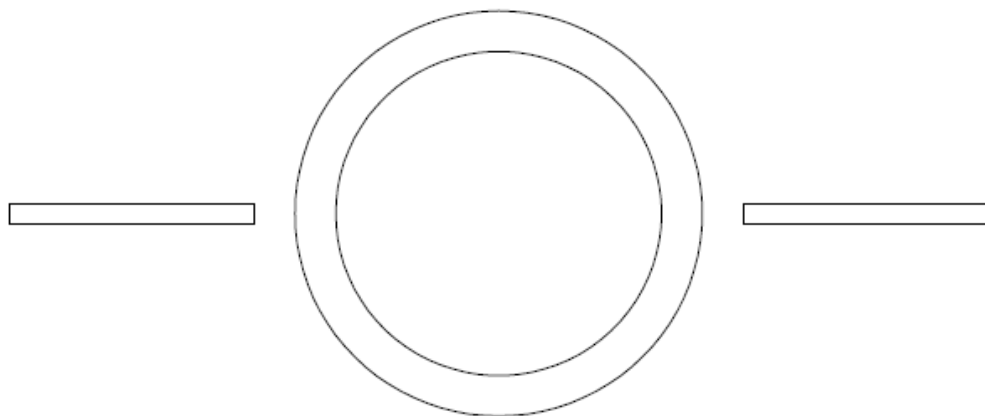


Figure 5-28: A typical ring resonator, consists of feed lines, coupling gaps, and the circular closed loop printed transmission line resonator [43]

The ring resonator can be fed using only one feed line, this configuration is used in dielectric constant, Q-measurements and ring-stabilized oscillations. As shown in Figure 5-29, for the first mode, maximum field occurs at the coupling gap however a minimum occurs at the opposite side 180° from the coupling gap. Thus, when using a single feed, the ring behaves as a half wavelength resonator. Resonance occurs when the ring circumference equals half of the guide wavelength:

$$2\pi r = n \frac{\lambda_g}{2}, \text{ for } n = 1, 2, 3, \dots \quad (5.140)$$

$$f = \frac{nc}{4\pi r \sqrt{\epsilon_{eff}}} \quad (5.141)$$

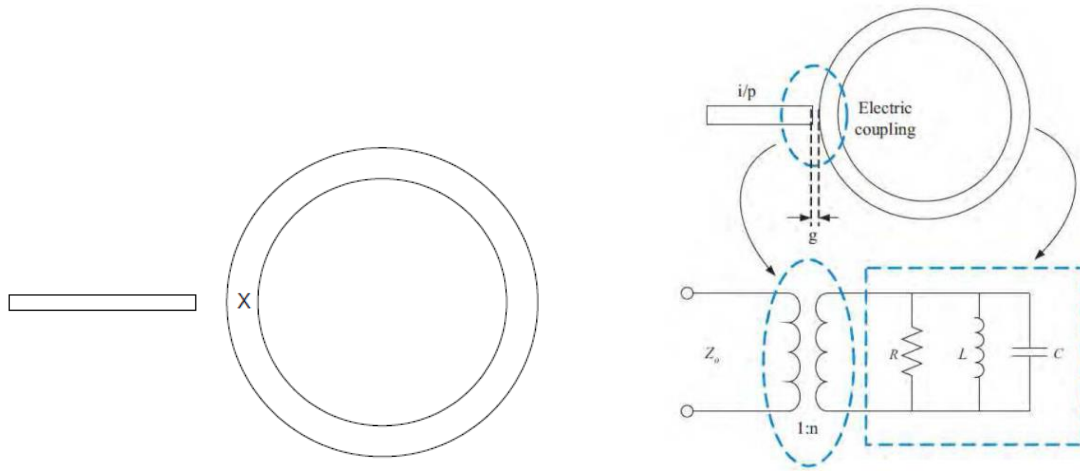


Figure 5-29: A typical ring resonator, consists of single feed lines, coupling gaps, and the circular closed loop printed transmission line resonator [42]

5.5.3.5 Annular Ring Resonator Model

Figure 5-30 shows the 2-port lumped electrical equivalent model of the ring resonator, which can be reduced to a 1-port circuit by terminating one of the ports with arbitrary impedance that corresponds with the feed impedance (usually 50 ohms) [44].

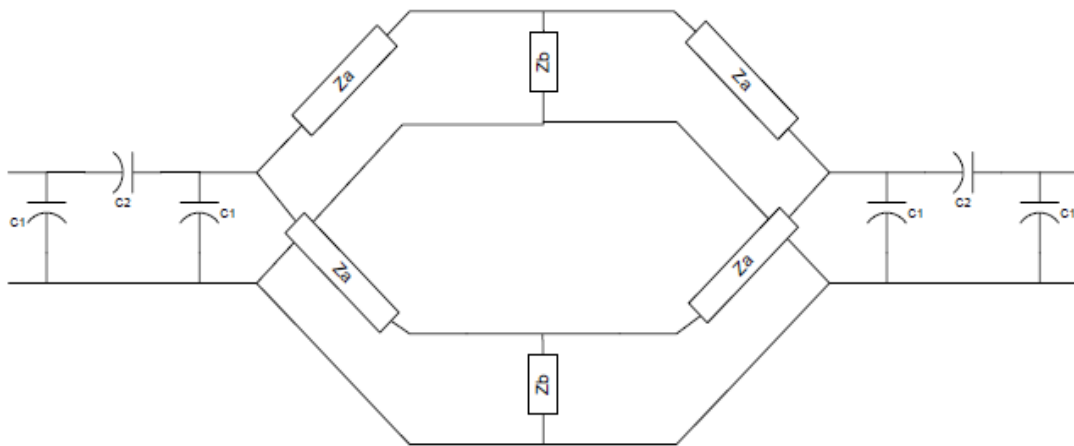


Figure 5-30: Simplified 2-port lumped electrical equivalent model of the ring resonator [43]

The electrical model exhibits symmetry of the circuit, therefore input impedance can be calculated by simplifying parallel and series combinations of the equivalent electrical model as shown in Figure 5-30.

From Figure 5-30, the input impedance is expressed as [44]:

$$R_{in} = \frac{C(C_1+C_2)[(C_1+C_2)-\omega D(C_1^2+2C_1C_2)]}{[(C_1+C_2)-\omega D(C_1^2+2C_1C_2)]^2 + [\omega C(C_1^2+2C_1C_2)]^2} + \frac{[D(C_1+C_2)-\omega^{-1}][\omega C(C_1^2+2C_1C_2)]}{[(C_1+C_2)-\omega D(C_1^2+2C_1C_2)]^2 + [\omega C(C_1^2+2C_1C_2)]^2} \quad (5.142a)$$

$$X_{in} = \frac{[D(C_1+C_2)-\omega^{-1}][(C_1+C_2)-\omega D(C_1^2+2C_1C_2)]}{[(C_1+C_2)-\omega D(C_1^2+2C_1C_2)]^2 + [\omega C(C_1^2+2C_1C_2)]^2} + \frac{[D(C_1+C_2)-\omega C^2(C_1+C_2)(C_1^2+2C_1C_2)]}{[(C_1+C_2)-\omega D(C_1^2+2C_1C_2)]^2 + [\omega C(C_1^2+2C_1C_2)]^2} \quad (5.142b)$$

$$C = \frac{AZ_b^2}{(2A)^2 + (Z_a - 2B - Z_b)^2} \quad (5.143)$$

$$D = \frac{1}{2} \left[(Z_a - Z_b) - \frac{Z_b^2(Z_a - 2B - Z_b)}{(2A)^2 + (Z_a - 2B - Z_b)^2} \right] \quad (5.144)$$

$$A = \frac{RC_2^2}{(C_1+C_2)^2 + [\omega R(C_1^2+2C_1C_2)]^2} \quad (5.145)$$

$$B = \frac{(C_1+C_2)+\omega^2 R^2(C_1^2+2C_1C_2)(C_1+C_2)}{\omega(C_1+C_2)^2 + \omega[\omega R(C_1^2+2C_1C_2)]^2} \quad (5.146)$$

where R is the terminated load, and the input impedance is ($Z_{in} = R_{in} + jX_{in}$), resonance occurs when $X_{in} = 0$

5.5.3.6 Ring Resonator Modes

The ring resonator exhibits different modes depending upon excitation and the perturbation, broadly categorized into regular and forced modes.

(a) Regular Resonant Modes:

The regular resonant mode is realized by applying symmetric input and output feed lines on the annular ring resonator element where resonant wavelengths of the regular mode are determined by $2\pi r = n\lambda g$ [43].

For the simplicity, the annular ring is analyzed as 2 half-wavelength linear resonators connected in parallel, assuming the parallel connection suppresses radiation from open ends resulting a higher Q-factor compared to straight open transmission line resonator shown in Figure 5-21 (a). The resonant condition enforced when standing waves are setup in the annular ring when circumference is integer multiple of guided wavelength.

As shown in Figure 5-31, in the absence of gaps or other discontinuities, maximum field occurs at the position where the feed line excites the resonator. The number of maximum field points increases with the mode order as illustrated in Figure 5-31.

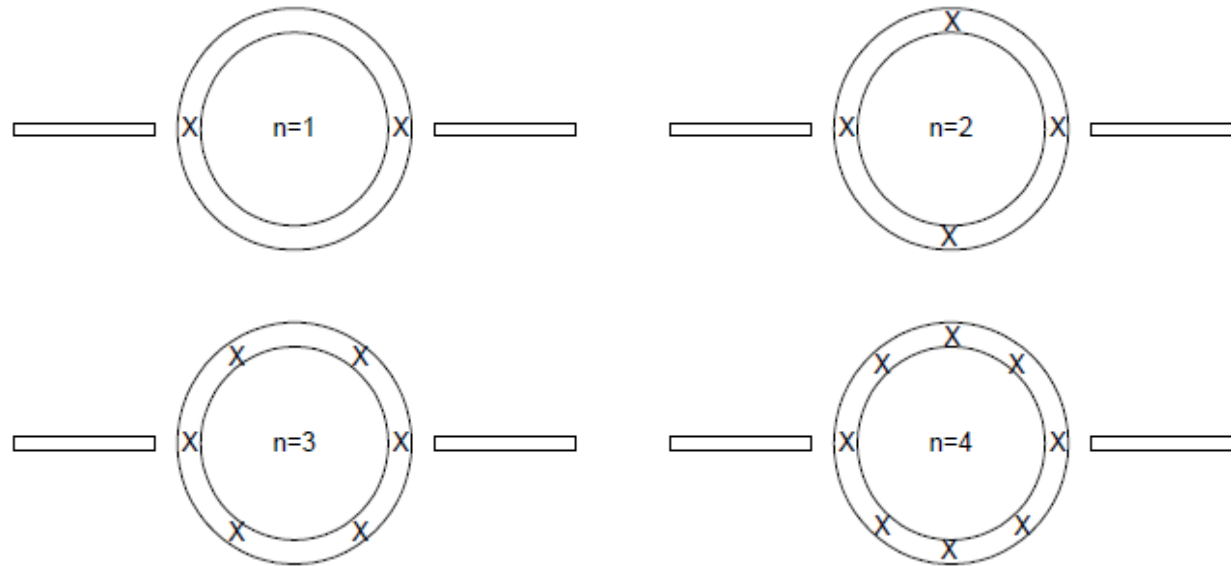


Figure 5-31: Simplified representation of maximum field points on annular ring for different resonant modes [43]

(b) Forced Resonant Modes:

Usually, forced resonant modes are excited by forced boundary conditions on a microstrip annular ring element (ring can be open or shorted to ground). In principle, the boundary condition can either be open as shown in Figure 5-32 or short depending upon the geometry of annular ring. For example, the open boundary condition is realized by cutting slits on the annular ring element, whereas, the shorted boundary condition by inserting vias to ground inside substrate, which forces minima of electric field to occur on both sides of the shorted plane. After analyzing the boundary conditions, the standing wave pattern and maximum field points inside the ring can be determined for the evaluation of the forced resonant modes.

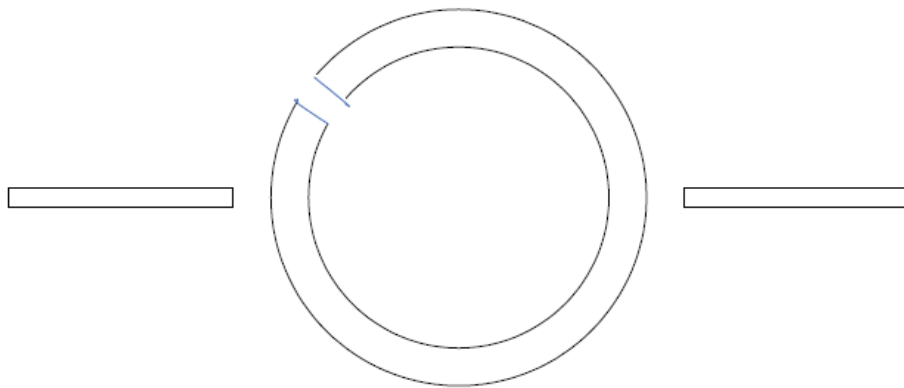


Figure 5-32: Shows a typical open annular ring with slit for satisfying open boundary condition [44]

5.5.4 Active Resonator

A resonator is an important element in oscillator/VCO and its characteristics are based on size, cost, quality factor, manufacturability and integrability. Standard integrated circuits are in planar configurations, therefore, effort is to eliminate discrete and bulky high Q expensive resonators (Ceramic, SAW, Cavity, Dielectric, SLC, BAW, OE, YIG) [53]-[58].

Microstripline/stripline resonator is planar type, formed by disposing a conductive strip onto a circuit board, which is cost-effective and amenable for integration in IC form but at the cost of large size and low Q factor in comparison to the other above discussed resonators. In general, Q factor of the resonator degrades with the increase in frequency because of decrease in skin depth, described by [59]

$$Q = \eta[f]^{-1/2} \quad (5.147)$$

Where Q is the quality factor and η is the constant.

The energy dissipation in the passive resonator and radiation leads to degradation in the quality factor of the resonator tank. To facilitate desired oscillation signal, resonator is loosely coupled and loaded with the external circuit comprised of active devices and peripheral components for compensating the energy losses. Using loose coupling can reduce the loading of the resonator but results in higher attenuation.

In practice, the unloaded Q factor of the resonator ' Q_u ' is finite, and gets degraded after coupling to the external oscillator circuit. Therefore, even an ideal resonator with zero inner losses and $Q_u \rightarrow \infty$ will exhibit finite loaded Q factor ' Q_l '. The unloaded quality factor of the passive resonator can be given by

$$Q_{u(PR)} = \frac{2\pi f_0 E}{W} = \frac{2\pi f_0 C}{G} \quad (5.148)$$

where f_0 , stands for frequency, E is the energy stored in passive resonator (PR), W is energy lost in one oscillation period, C and G correspond to parallel equivalent circuit (capacitance C and conductance G) of the PR respectively.

To overcome the limitation of the Q factor of the passive resonator (PR), active resonator topology has been reported which offers promising alternative for high spectral pure signal sources [60]. The novel AR (active resonator) offers a solution for increasing Q_u and Q_l of the passive resonator (PR) by compensating the inner losses. This can be achieved by means of gain block (active circuit) coupled to the passive resonator (PR) networks.

Figure 5-33 shows the typical example of AR circuit, where PR is coupled to a transmission line. As shown in Figure 5-33, active circuits create negative conductance $-|G_n|$, which adds to the positive conductance of the resonator G , thereby, gives effective conductance of the AR (active resonator) as

$$G_a = -|G_n| + G \quad (5.149)$$

From (5.148), unloaded Q factor ' Q_u ' of the AR is given by

$$Q_{u(PR)} = \frac{2\pi f_0 C}{G_a} \Rightarrow Q_{u(AR)} > Q_{u(CPR)} \quad |G_a| < |G| \quad (5.150)$$

From (5.149) and (5.150), AR can offer high quality factor where PR suffer from losses due to loss resistance and radiations. In practical applications G_a should be greater than zero to prevent the spurious oscillations, still keeping increased loaded Q factor Q_l .

5.5.4.1 Active Resonator Topology

In the AR topology, normally the PR is coupled to the negative resistance generating device network so that in principle AR element is similar to the general oscillator being created. A general oscillator needs both the amplitude and the phase condition to be satisfied for oscillation build up at f_0 . In the case of the AR, the only phase condition for oscillation build up at f_0 is required for stable and sustained oscillations and no amplitude condition is required to compensate the loss of the AR from the active device network.

As depicted in Figure 5-33, active amplifier works in small signal linear regime and just sufficient to compensate partially or 100% losses without creating instability. Design care must be taken so that the oscillations do not build up in AR circuit and growth is restricted. Typically, amplifier's gain will compensate the inner losses of the AR circuits but 100% compensation ($-|G_n| + G = 0$) of W (energy losses) will result in infinite unloaded Q (zero bandwidth). Further loading of the AR (with infinite unloaded Q) with oscillator active circuits for obtaining desired oscillations can increase the bandwidth of the resonator for the application in tunable signal sources with improved phase noise performances. However, AR based on negative resistance approach offers improved Q factors but they have drawbacks: schematic is complex and must have feedback element and the matching networks to produce the negative conductance $-|G_n|$, sensitive to spurious oscillation (if the oscillation start-up condition is satisfied). A normal oscillator requires the amplitude and phase condition to be satisfied for guaranteed and sustained oscillation build up at desired frequency, whereas, for active resonator element, only phase condition is needed to be satisfied.

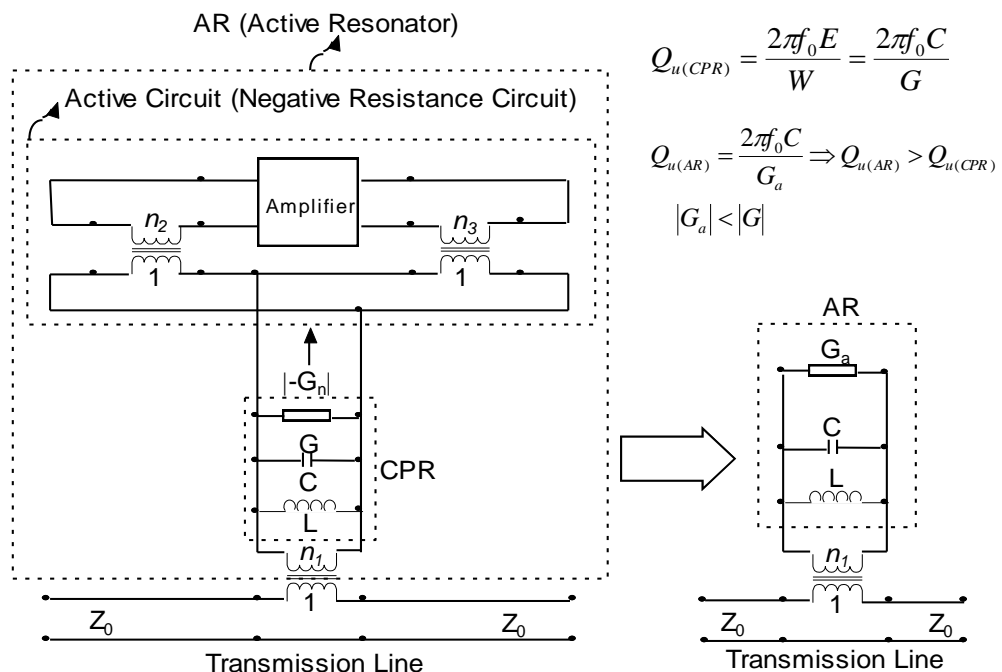


Figure 5-33: Shows a typical AR (active resonator) with feedback arrangement [60]

Hence, oscillation will not build up across the active resonator, and therefore, active resonator module can work in the small signal regime (instead of large signal regime condition required for sustained and guaranteed oscillations), and negative resistance added to the active

resonator circuit will reduce the intrinsic losses of the passive resonators used as active resonators. This approach yields high Q resonator, however, active resonator elements are sensitive to spurious oscillations that may cause generation of unwanted oscillation mode in the event of satisfying start-up oscillation condition.

Printed passive resonators such as hairpin, spiral, ring, and inter-digital resonators are widely used in tunable oscillator circuits. However, printed passive resonators lack the high quality factor due to the dielectric, conductor and radiation losses, therefore limiting factor of the oscillator phase noise performance. One possible approach for compensating these losses is an active resonator topology, thereby improved Q-factor. However, noise contributions from active resonators can be significant if design is not optimized for a given oscillator topology and a resonator figure of merit (FOM). The design philosophy of active resonators is based on active feedback loops or coupling negative resistance devices to passive resonators for compensating the losses. The critical issues are the presence of excess noise added by active devices (transistors), therefore careful design methodology is required for low phase noise oscillator using active resonator networks. Figure 5-34 shows the typical 3.2 GHz VCO (voltage controlled oscillator circuit) using active resonator (AR) network for the comparative analysis of the phase noise performance. As shown in Figure 5-35, the simulated Q factor of AR (active resonator) is three times larger than equivalent PR (passive resonator), the penalty is excess power budget of 60mW. The typical RF output power is +5dBm with 2.1% DC-RF conversion efficiency for a given -210.3 figure of merit (FOM) and 150mW operating DC power consumption (5V, 30mA).

3.2 GHz Active Resonator VCO

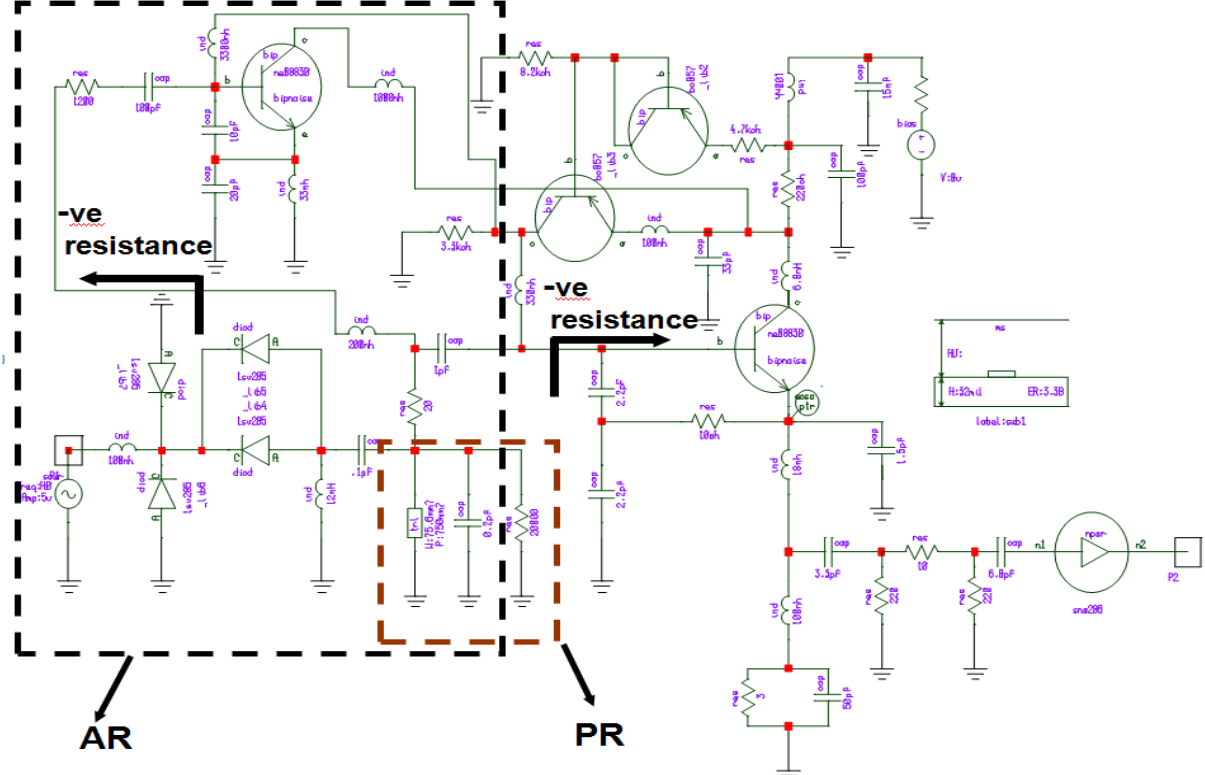


Figure 5-34: shows the typical 3.2GHz VCO using active resonator (oscillator power consumption is 150mW)

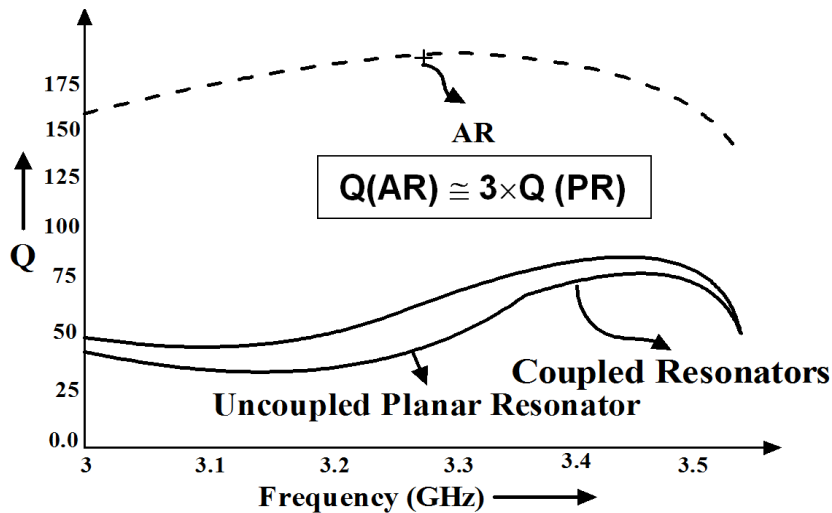


Figure 5-35: shows the typical simulated Q of passive resonator (uncoupled planar resonator and coupled planar resonator) and active resonator (AR) using negative resistance topology (as shown in Figure 5-34)

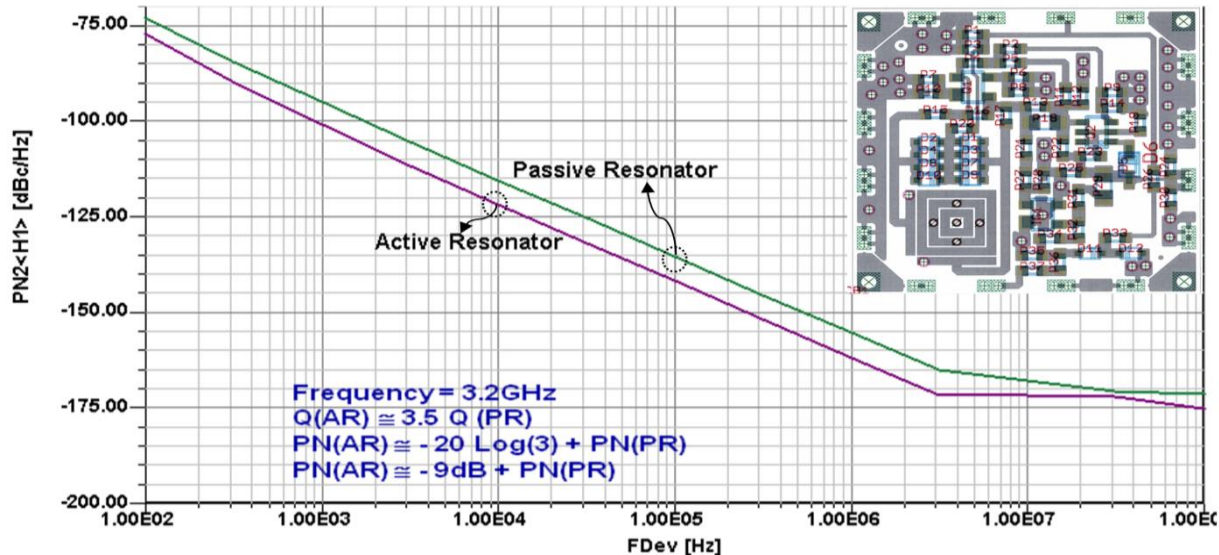


Figure 5-36: shows the typical simulated phase noise plot of 3.2 GHz VCO (voltage controlled oscillator circuit) using active resonator (AR) network (200 MHz tuning) network (FOM=-210.3, $P_o=5\text{dBm}$, DC-RF power conversion efficiency=2.1%)

Figure 5-36 shows the CAD simulated phase noise plot, the improvement in phase noise is 9dB that correlates the 3-times increase in Q -factor as compared to PR network. Different AR (active resonator) technology is described in Appendix B, Appendix C, Appendix B, and Appendix D for giving brief insights about pros and cons with reference to PR (passive resonator) technology. Unfortunately, each development design of VCO using AR technology has its price, since they occupy larger PCB area and extra power budget.

5.6 Conclusion

In this Chapter, an overview of microwave resonator and its characteristics (resonator quality factor, figure-of-merit), resonator design criteria, and oscillator design methodology is discussed.

5.7 References

- [1] G. D. Vendelin, A. M. Pavio and U. L. Rohde, *Microwave Circuit Design Using Linear and Nonlinear Techniques*, New York: John Wiley & Sons, 1990.
- [2] K. L. Kotzebue, 'A Technique for the Design of Microwave Transistor Oscillators', *IEEE Trans. Microwave Theory Tech.*, MTT-32, pp. 719–721, 1984.
- [3] D. Cohn and R. Mitchel, 'Design of Microstrip Transistor Oscillators', *Int. J. Electronics*, 35, pp. 385– 395, 1973.
- [4] G. I. Zysman and A. K. Johnson, 'Coupled Transmission Line Networks in an Inhomogeneous Dielectric Medium', *IEEE Trans. MTT*, 17, pp. 753–759 1969.
- [5] K. C. Gupta, R. Garg and R. Chadha, *Computer-Aided Design of Microwave Circuits*, Dedham: Artech House, 1981.
- [6] H. Howe, *Stripline Circuit Design*, Dedham: Artech House, 1974.
- [7] P. Russer, *Electromagnetics, Microwave Circuit and Antenna Design for Communication Engineering* 2nd Edition, Artech House, Inc. ISBN 1-58053-907-6, 2006
- [8] R. J. Cameron, C. M. Kudsia, and R. R. Mansour, "Microwave Filters for Communication Systems" Fundamentals, Design, and Applications, John Wiley & Sons, Inc, 2007.
- [9] R. M. Foster, "A reactance theorem," *Bell System Tech. J.*, vol. 3, pp. 259-267, 1924.
- [10] R. E. Collin, *Foundation for Microwave Engineering*, McGraw-Hill, New York, 1966.
- [11] D. Pozar, *Microwave Engineering*, 2nd ed., Wiley, New York 1998.
- [12] A. E. Atia and A. E. Williams, Narrow Bandpass waveguide filters, *IEEE Transaction MTT*, Vol. 20, pp. 238-265, 1972.
- [13] A. E. Atia and A. E. Williams, New types of waveguide Bandpass filters for satellite transponders, *COMSAT Tech. Rev.* 1 (1), 21-43 (1971).
- [14] S. J. Fiedziusko, Dual-mode dielectric resonator loaded cavity filter, *IEEE Trans. MTT*, Vol. 30, pp. 1311-1316, 1982.
- [15] D. Kajfez and P. Guilon, *Dielectric Resonators*, Artech House, Norwood, MA, 1986.
- [16] R. R. Mansour, Design of superconductive multiplexes using single-mode and dual-mode filters, *IEEE Trans. MTT*, Vol. 42, pp. 1411-1418, 1994
- [17] V. Walkar and I. C. Hunter, Design of triple mode TE01 resonator transmission filters, *IEEE Microwave Wireless Component Letters*, vol. 12, pp. 215-217, June 2002.
- [18] R. R. Mansour, Microwave superconductivity, *IEEE Trans. MTT*, Vol. 50, pp. 750-759, 1972.
- [19] E. O. Hammerstad and O. Jensen, Accurate models for microstrip computer-aided design, *IEEE-MTT-S Digest*, pp. 407-409, 1980.
- [20] I. Bahl and P. Bhartia, *Microwave Solid State Circuit Design*, 2nd ed., Wiley, New York, April 2003.
- [21] T. Ohira and K. Araki, "Dimensional extension of Kurokawa's stability criterion for general multi-port device oscillators," *IEICE Electronics Express*, vol. 3, pp. 143-148, April 2006.
- [22] T. Ohira and K. Araki, "Oscillator frequency spectrum as viewed from resonant energy storage and complex Q factor," *IEICE Electronics Express*, vol. 3pp. 385-389, Aug. 2006.
- [23] T. Ohira, "Theoretical essence of stable and low phase noise microwave oscillator design (tutorial)," *European Microwave Conf.*, SC2-1, Manchester, Sept. 2006
- [24] T. Ohira and K. Araki, "Active Q factor and equilibrium stability formulation for sinusoidal oscillators" *IEEE Trans. Circuit Systems II*, vol. 54, issue 9, pp. 810-814, Sept. 2007.
- [25] T. Ohira and T. Wuren, "Pseudolinear circuit theory for sinusoidal oscillator performance

- maximization (invited)" IEICE Trans. Electron., vol. E91-C, issue 11, pp. 1726-1737, Nov. 2008.
- [26] T. Ohira, "Extended Adler's injection locked Q factor formula for general one - and two - port active device oscillators" IEICE Electronics Express ELEX, vol. 7, issue 19, pp. 1486-1492, Oct. 2010.
 - [27] T. Ohira, "Dedicated Q factor formulas stemming from oscillation frequency stability against source and load deviations" Toyohashi Univ. Tech. Tutorial Lecture 2012.
 - [28] T. Ohira, "Rigorous Q factor formulation for one- and two-port passive linear networks from an oscillator noise spectrum viewpoint," IEEE Trans. Circuits Systems II, vol. 52, issue 12, pp. 846-850, Dec. 2005.
 - [29] D.B.H. Tellegen, "A general network theorem with applications," Proc. IRE Australia, pp. 265-270, Nov. 1953
 - [30] K. Kurokawa, "Some basic characteristics of broadband negative resistance oscillator circuits," Bell System Technical Journal, pp. 1937-1955, July 1969
 - [31] R. Adler, "A study of locking phenomena in oscillators", Proc. IRE, vol. 34, pp. 351-357, June 1946
 - [32] T. Ohira, "Dedicated Q factor formulas stemming from oscillation frequency stability against source and load deviations" Toyohashi Univ. Tech. Tutorial Lecture 2012.
 - [33] U. L. Rohde, A. K. Poddar, and G. Boeck, "Modern Microwave Oscillators for Wireless Applications: Theory and Optimization", John Wiley & Sons Inc., 2005.
 - [34] D. B. Leeson, "A simple model of feedback oscillator noise spectrum," Proc. IEEE, vol. 54, no. 2, pp. 329–330, Feb. 1966

 - [35] B. Razavi, "A study of phase-noise in CMOS oscillators," IEEE J. Solid-State Circuits, vol. 31, no.3 pp. 331-343, March 1996.
 - [36] Bal S. Virdee, Christos Grassopoulos', "Folded Microstrip Resonator" Microwave symposium Digest, 2003 IEEE MTT-S International, Volume: 3, 8-13 June 2003
 - [37] K. Chang and L.-H. Hsieh, Microwave ring circuits and related structures, Wiley-IEEE, 2004.
 - [38] L. M. Ledezma, " A study on the miniaturization of microstrip square open loop resonators", USF, MS. Thesis 2011,
 - [39] H. Yabuki, M. Sagawa, and M. Makimoto, "Voltage controlled push-push oscillators using miniaturized hairpin resonators", in IEEE MTT-S, Dig., pp. 1175-1178, 1991.
 - [40] L-Hwa Hsieh, "Analysis, Modeling and Simulation of Ring Resonators and their applications to Filters and Oscillators", PhD Dissertation, Texas A&M University, 2004.
 - [41] M. Sagawa, K. Takahashi, and M. Makimoto, "Miniaturized hairpin resonator filters and their application to receiver front-end MIC", IEEE Trans. on MTT, vol. 37, pp. 1991-1997, Dec. 1989
 - [42] B. C. Wadell, Transmission Line Design Handbook, MA: Artech House, pp. 321, 1991.
 - [43] Kai Chang, Microwave Ring Circuits and Antennas, Wiley-Inter science, 1996
 - [44] C.C Yu, Kai Chang, "Transmission-Line Analysis of a Capacitively Coupled Microstrip-Ring Resonator" IEEE Trans MTT, Volume: 45, No 11, pp. 2018- 2024, Nov 1997.
 - [45] K. Hoffmann, and Z. Skvor, "Active resonator", Int. Conf. Trends, Communications, EUROCON'2001, vol. 1, pp. 164-166, July 2001.
 - [46] P. Alinikula, R. Kaunisto, and K. Stadius, " Monolithic active resonators for wireless

- application”, in IEEE MTT-S Dig., vol. 2, pp. 1151-1154, May 1994.
- [47] C. Cenac, B. Jarry, and P. Guillon, “X-band filters with half-wave or ring resonators and variable gain and phase monolithic circuits”, *Microwave Opt. Techno. Lett.*, vol. 11, no. 5, pp. 254-257, Apr. 1996
 - [48] C.-Y. Chang, and T. Itoh, “Microwave active filters based on coupled negative resistance method”, *IEEE Trans. on MTT*, vol.-38, no. 12, pp. 1879-1884, Dec 1990.
 - [49] B. P. Hopf, I. Wolff, and M. Giglielmi, “Coplanar MMIC active bandpass filters using negative resistance circuits”, *IEEE Trans. on MTT*, vol.-42, no. 12, pp. 2598-2602, Dec 1994
 - [50] U. Karacaoglu, and I. D. Robertson”, MMIC Active bandpass filters using varactor-tuned negative resistance elements”, *IEEE Trans. Microwave Theory and Techniques*, vol.-43, no. 12, pp. 2926-2932, Dec 1995
 - [51] Y. Ishikawa, S. Yamashita, and S. Hidaka, “Noise design of active feedback resonator BEF,” *IEEE Trans. Microw. Theory Tech.*, vol. -41, no. 12, pp. 2133- 2138, Dec. 1991
 - [52] H. Ezzedine, L. Billonnet, B. Jarry, and P. Guillon, “Optimization of noise performance for various topologies of planar microwave active filters using noise wave techniques,” *IEEE Trans. Microw. Theory Tech.*, vol. -46, no. 12, pp. 2484-2492, Dec. 1998
 - [53] M. Nick, “New Q-Enhanced Planar Resonators for Low Phase-Noise Radio Frequency Oscillators”, PhD Dissertation, Electrical Engineering, University of Michigan, 2011
 - [54] P. Gardner, and D. K. Paul, “Optimum noise measure configurations for transistor negative resistance amplifiers,” *IEEE Trans. Microw. Theory Tech.*, vol. -45, no. 5, pp. 580-586, May 1997.
 - [55] A. Grebennikov, “RF and microwave transistor oscillator design,” New York: John Wiley & Sons, 2007.
 - [56] H. A. Hauss, and R. B. Adler, “Circuit theory of linear noisy networks,” New York: Wiley, 1959.
 - [57] J.-S Hong and M. J. Lancaster, *Microwave Filter for RF/Microwave Application*. New York: Wiley, 2001.
 - [58] U. L. Rohde, M. Rudolph, “RF/Microwave Circuit Design for Wireless Applications”, Wiley & Sons., ISBN-13: 978-1118431399, Dec., 2012
 - [59] K. Hoffmann and Z. Skvor,” Active resonator”, *EUROCON 2001 proceeding*, IEEE, Vol.1; pp. 164-166, Bratislava, 2001
 - [60] U. L. Rohde and A. K. Poddar, “Active Planar Coupled Resonators Replace Traditional High Q Resonators in Low Phase Noise Oscillators/VCOs, *IEEE RWS 2007*, pp. 39-42, CA, USA, 09-11 January 2007.

Chapter 6

Printed Coupled Slow-Wave Resonator Oscillators

6.1 Introduction

A printed coupled resonator network realized by slow wave dynamics is attractive due to its compact size providing a wide spurious-free band [1]. In addition to this, the physical layout of slow wave resonators enables the implementation of optimum EM (electromagnetic) couplings [2]. Printed resonator based tunable oscillator circuits are large, especially at lower operating frequencies. The physical dimension of conventional printed transmission line resonator can be reduced by incorporating slow wave propagation characteristics, thereby reducing the size of the circuits [3]. Typically, periodic shunt loading of the transmission lines can exhibit a simplified slow wave structure. This periodic shunt loading reduces the phase velocity, thereby increasing the effective electric length of the line [4]. As a result, resonators are not only compact size but due to slow wave effect also exhibit high frequency selectivity, wider stop-band resulting from the dispersion phenomena. In order to facilitate a broad yet precise description of the VCO topology, the layout of the SWR (Slow wave resonator) structure is selected in such a way that it minimizes the effect caused by temperature and mechanical stresses, and supports uniform negative resistance over wide tuning range [5]-[7].

In slow-wave propagation, the electromagnetic wave is transmitted in the guided-wave media with a slower phase velocity, namely, shorter guided wavelength, at a specified operating frequency. This is achieved by modifying electric and magnetic energy storage in the guided-wave media. SWRs are attractive due to several reasons: the slow-wave effect makes them very compact and can support evanescent mode coupling, enabling Q-multiplier effect at resonant frequency, thus providing a low phase noise signal source solution [8]-[9]. Additionally, the geometrical configuration of SWR resonators makes possible the implementation of compact layout and is amenable for RFIC/MMIC realizations [1]-[10]. In conventional transmission lines, the phase velocity v_p is controlled only by the dielectric material and can be expressed as [3]

$$v_p = f \times \lambda = \frac{c_0}{\sqrt{\mu_r \epsilon_{\text{eff}}}} \quad (6.1)$$

where c_0 is the velocity of light, μ_r is the effective relative permeability, and ϵ_{eff} is the effective relative permittivity. From (6.1), increasing the effective relative permittivity of dielectric material at a given operating frequency decelerates the propagation of electromagnetic (EM) waves in a guided medium. The Slow-Wave Effect can be realized by adding periodical shields that decelerate the propagation of electromagnetic (EM) waves in a guided medium. From (6.1), an equivalent inductance L_{eq} , equivalent capacitance C_{eq} , and propagation constant β can be described as [2]:

$$\beta = \omega \sqrt{L_{\text{eq}} C_{\text{eq}}} \Rightarrow V_p = \frac{1}{\sqrt{L_{\text{eq}} C_{\text{eq}}}} \quad (6.2)$$

From (6.2), both distributed inductance (L) and capacitance (C) along the transmission line in the guided medium can be increased for the realization of slow-wave effects owing to increase of the propagation constant β , consequently, reducing the loss of the resonator network [2]. Figure 6.1 shows the simplified topology of a single-coupled slow-wave resonator, which consists of a slow-wave resonator loaded at its near and far ends with series capacitors C_s .

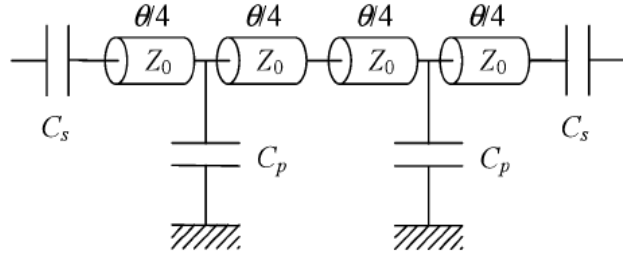


Figure 6-1: A typical topology of a single-coupled slow-wave resonator loaded at the near and far ends with series capacitors C_s [1]

The resonator itself is made up of a transmission line of characteristic impedance Z_0 and electrical length ' θ ', periodically loaded by shunt capacitors C_p . The electrical length θ of the unloaded transmission line is defined at frequency f as [1, 4]

$$\theta = \beta d = \frac{2\pi f \sqrt{\epsilon_{\text{eff}}}}{C} d \Rightarrow \theta|_{f=f_0} = \theta_0 \quad (6.3)$$

where ϵ_{eff} is the effective relative permittivity, d is the physical length of the unloaded line, and C is the free space light velocity. At the center frequency f_0 , the electrical length is θ_0 .

By using $ABCD$ (cascade) matrices, the equivalent characteristic impedance Z_{eq} of a coupled slow-wave resonator can be easily extracted.

As shown in Figure 6.1, the real estate of SWR (slow wave resonator) layout is quite large, therefore not suitable for the application where size is the constraint. For brief insights about the minimization of the size of slow-wave structure, the characteristics of the Lossless transmission and capacitive loaded line (CTL) are discussed.

6.1.1 Lossless Transmission Line

Figure 6-2 shows the typical lossless transmission line circuit, which can be characterized by Z_0 (Characteristic Impedance) and V_p (Phase Velocity) as

$$Z_0 = \sqrt{\frac{L}{C}} \quad (6.4)$$

$$v_p = \frac{1}{\sqrt{\mu\epsilon_e}} = \frac{1}{\sqrt{LC}} \Rightarrow LC = \mu\epsilon_e = k \text{ (Constant depending on medium)} \quad (6.5)$$

where

$$L = \frac{Z_0}{v_p}, \quad C = \frac{1}{v_p Z_0} \quad (6.6)$$

From (6.5), $LC = \mu\epsilon_e$ therefore for a given ϵ_e and μ , it is not possible to reduce V_p by increasing inductance or capacitance per unit length because an increase in inductance L leads to a decrease in capacitance C , ($L \uparrow \equiv C \downarrow$). Hence for a physically smooth transmission line, reduction in phase velocity v_p is only possible by increasing ϵ_r .

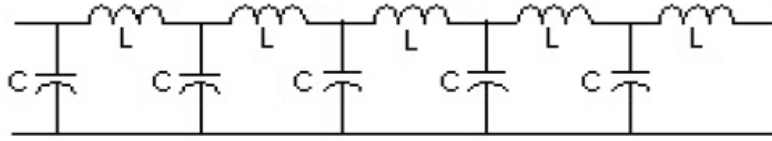


Figure 6-2: A typical lossless transmission line circuit

6.1.2 Capacitive Loaded Transmission Lines (CTL)

By removing the constraint that the line should be physically smooth, an effective increase in the shunt capacitance per unit length C can be obtained without a reduction in inductance L . This can be realized by loading a printed transmission line with shunt capacitance C_p at periodic intervals d . Figure 6-3 shows the typical capacitive loaded transmission (CTL) line circuit formed by loading a printed microstrip line with open stubs that exhibit shunt capacitance at periodic intervals which are shorter than the guide wavelength and causes the periodic structure to exhibit slow wave characteristics [2]-[8].

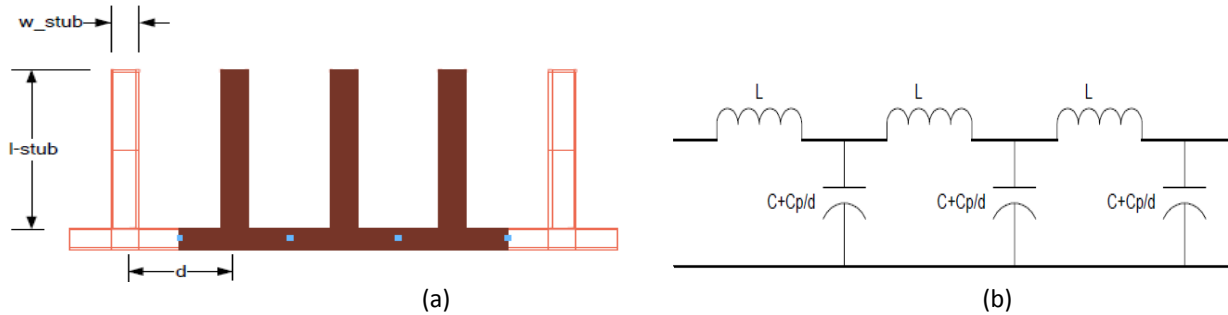


Figure 6-3: A typical capacitive loaded transmission line circuit: (a) printed layout, and (b) lumped equivalent network

The effective characteristic impedance and phase velocity of the CTL circuit shown in Figure 6-3 can be described by [2]-[4]

$$Z_{0CTL} = \left(\frac{L}{C + \frac{C_p}{d}} \right)^{1/2} \quad (6.7)$$

$$Z_{in} = Z_0 \frac{Z_L + jZ_0 \tan(\beta l)}{Z_0 + jZ_L \tan(\beta l)} \Rightarrow Z_\infty(\text{open circuit stub}) = \frac{Z_{stub}}{j \tan[\beta l]} = \frac{1}{j \omega C_p} \quad (6.8)$$

$$v_{pCTL} = \frac{1}{\sqrt{L(C + \frac{C_p}{d})}} = \left[\frac{Z_0}{v_p} \left(\frac{1}{v_p Z_0} + \frac{C_p}{d} \right) \right]^{-1/2} \quad (6.9)$$

where $\frac{C_p}{d}$ = lumped capacitance per unit length, $Z_0 = \sqrt{\frac{L}{C}}$

For an m -section CTL, the equivalent electrical length in angle (\emptyset_{CTL}) and the loaded capacitance of a unit cell C_p can be given by

$$\emptyset_{CTL} = \frac{2\pi m d f_0}{v_{pCTL}} = m d \omega_0 \sqrt{L \left(C + \frac{C_p}{d} \right)} \text{ (rad)} \quad (6.10a)$$

$$C_p = \frac{\emptyset_{CTL}(Z_0^2 - Z_{CTL}^2)}{2\pi m f Z_0^2 Z_{CTL}} \text{ (F)} \quad (6.10b)$$

where f_0 is the operating frequency.

From (6.8)-(6.10), the phase velocity v_{pCTL} can be slowed down either by one or a combination of the following: (i) Increase the characteristic impedance of the unloaded unit cell Z_0 , achieved by reducing the microstrip line width w_{TL} , (b) Reduce the distance between stubs d , and (c) Increase the load capacitance C_p (increasing the stub electrical length $\rightarrow \frac{\pi}{2}$, reducing the stub characteristic impedance $\downarrow Z_{stub}$. This is achieved by increasing the width of the stub $\uparrow w_{stub}$).

Figure 6-4 shows the typical layout of the compact capacitively coupled printed slow wave resonator. As shown in Figure 6-4, capacitive-coupling between two arms of the resonator leads to the slow-wave dynamics. The drawback of a periodically loaded line is dispersion in phase velocity; therefore phase velocity of the capacitively loaded transmission line is frequency dependent, whereas the unloaded transmission line does not exhibit dispersion in the phase velocity [9]-[24].

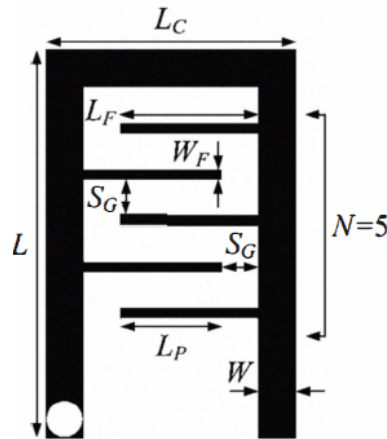


Figure 6-4: A typical slow wave coupled resonator (No. of section, $m=5$) [2]

6.2 Slow Wave Resonator (SWR)

Slow wave resonator (SWR) using stepped impedance hairpin printed transmission line structure can exhibit larger group-delay in compact size, resulting improved Q-factor [3]-[6]. The hairpin resonator introduced initially to reduce the size of the conventional parallel-coupled half-wavelength resonator with subsequent improvements made to reduce its size [3]. Beyond the advantage of the compact size, the spurious frequencies of the stepped impedance hairpin resonator are shifted from the integer multiples of the fundamental resonant frequency due to the effect of the capacitance-load coupled lines, including the low quality factor and high insertion loss [4]. As illustrated in Figure 6-5, the transmission line is periodically loaded with identical open stub elements for the realization of high Q-factor SWR structure. The input impedance Z_{in2} for a lossless line is given by [3]

$$Z_{in2}|_{\tan(\beta l) \rightarrow 0} = \frac{Z_o Z_L}{Z_o} \Rightarrow Z_{in2} \propto Z_L \quad (6.11)$$

where L and C are the inductance and capacitance per unit length of the line, Z_0 and β are the characteristic impedance and phase constant of the open stub, respectively.

From (6.11), for infinitesimal value of $\tan(\beta l)$, the input impedance Z_{in2} is proportional to Z_L , therefore, $Z_{in2} \rightarrow \infty$ or 0 for corresponding $Z_L = \infty$ or 0. Under these cases, the slow-wave

periodic structure loaded by Z_{in2} in Figure 6-5 (b) provides passband ($Z_{in2} \rightarrow \infty$) and stopband ($Z_{in2} \rightarrow 0$) characteristics.

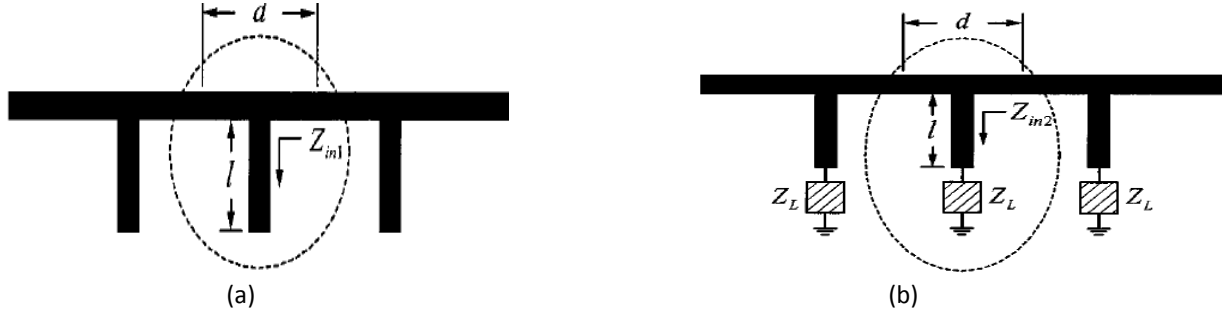


Figure 6-5: A typical slow wave structure: (a) a periodic SW structure, and (b) with loading Z_L at open end [3]

As depicted in Figure 6-5, the layout size is comparatively large and not attractive for VCO applications used in small modern handheld portable and test equipment systems.

Figure 6-6 shows the modified version of SWR, where transmission line is loaded by a square ring resonator with a line-to-ring coupling structure [3]-[8].

As shown in Figure 6-6 (b), Z_{in3} is the input impedance looking into the transmission line I_b toward the ring resonator with the line-to-ring coupling. The input impedance Z_{r1} looks into the line-to-ring coupling structure toward the ring resonator. The input impedance Z_{in3} is given by

$$Z_{in3} = Z_o \frac{Z_{r1} + jZ_o \tan(\beta l_b)}{Z_o + jZ_{r1} \tan(\beta l_b)} \quad (6.12)$$

Where

$$Z_{r1} = \frac{(Z_r + Z_g)Z_p}{(Z_r + Z_g + Z_p)}, \quad Z_g = \frac{1}{j\omega C_g \Delta l}, \quad Z_p = \frac{1}{j\omega C_p \Delta l}, \quad \omega = 2\pi f \quad (6.13)$$

The parallel f_p and series f_s resonances of the slow wave ring resonator as shown in Figure 6-6 can be obtained by setting $|Y_{in3}| = 0$ and $|Z_{in3}| = 0$. The ABCD matrix of the ring circuit (Figure 6-6a) can be described by [9]

$$\begin{bmatrix} A & B \\ C & D \end{bmatrix} = \begin{bmatrix} \cos(\beta l_a) & jZ_o \sin(\beta l_a) \\ jY_o \sin(\beta l_a) & \cos(\beta l_a) \end{bmatrix} \begin{bmatrix} 1 & 0 \\ Y_{in3} & 1 \end{bmatrix} \begin{bmatrix} \cos(\beta l_a) & jZ_o \sin(\beta l_a) \\ jY_o \sin(\beta l_a) & \cos(\beta l_a) \end{bmatrix} =$$

$$\begin{bmatrix} 1 - 2 \sin^2(\beta l_a) + jZ_o Y_{in3} \sin(\beta l_a) \cos(\beta l_a) & -Z_o^2 Y_{in3} \sin^2(\beta l_a) + j2Z_o \sin(\beta l_a) \cos(\beta l_a) \\ Y_{in3} \cos^2(\beta l_a) + j2Y_o \sin(\beta l_a) \cos(\beta l_a) & 1 - 2 \sin^2(\beta l_a) + jZ_o Y_{in3} \sin(\beta l_a) \cos(\beta l_a) \end{bmatrix} \quad (6.14)$$

where $Y_o = 1/Z_o$. Using $Y_{in3}(f_p)$ and $Z_{in3}(f_s)$, the passband and stopband of the ring circuit can be obtained by calculating S_{11} and S_{21} from the ABCD matrix in (6.14).

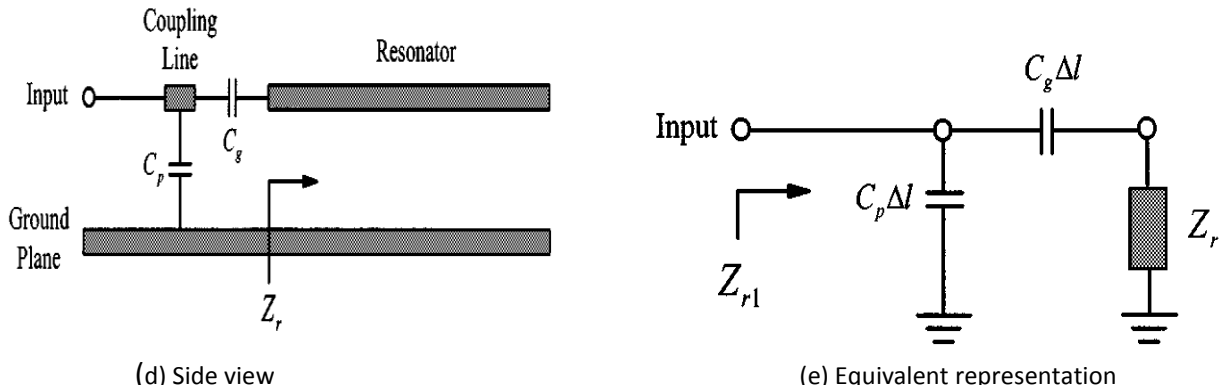
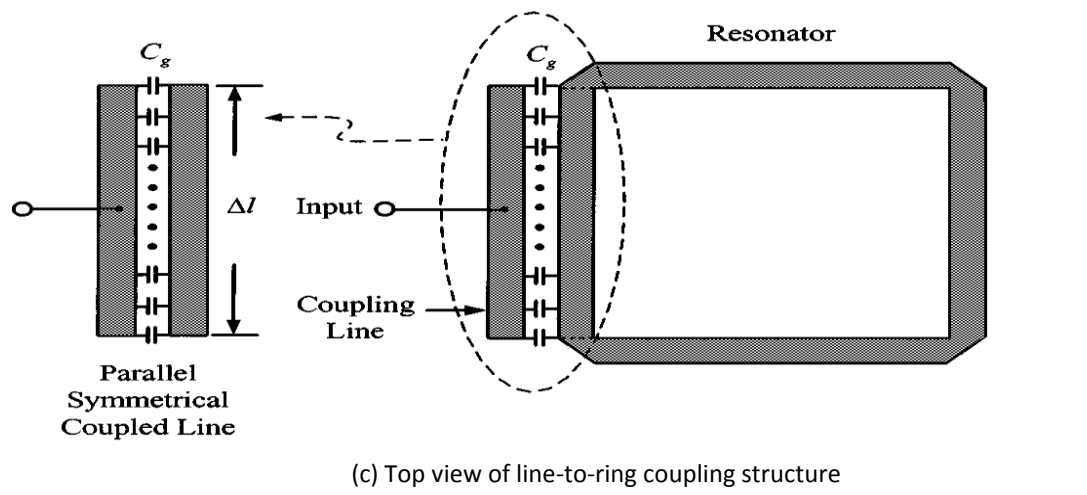
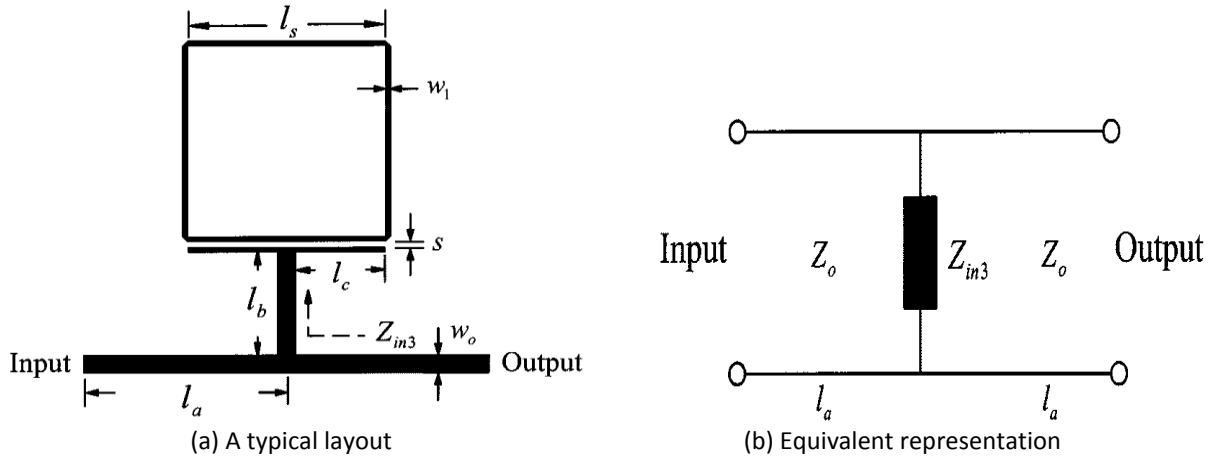


Figure 6-6: A typical slow-wave ring resonator with single edge coupling gap (slower the phase velocity, causing slow-wave effect): (a) printed layout of single edge coupled slow wave ring resonator network, (b) equivalent representation of single edge coupled slow wave ring resonator circuit, (c) top view of line-to-ring coupling structure, (d) side view of line-to-ring coupling structure, and (e) equivalent representation of circuit of line-to-ring coupling structure [3]

6.2.1 Slow Wave Evanescent Mode (SWEM) Propagation

The slow-wave evanescent-mode can represent surface wave propagation in planar printed resonators or the lattice waves in waveguides. In slow-wave propagation, the electromagnetic wave is transmitted in the guided-wave media with a slower phase velocity, namely, shorter guided wavelength, at a specified operating frequency [1]-[8]. This is achieved by modifying electric and magnetic storage energy by incorporating perturbation in the guided-wave media. Slow-wave resonators are attractive due to several reasons: the slow-wave effect makes them very compact and can support evanescent mode coupling for obtaining Q-multiplier effect at resonant condition, thus low phase noise signal source solutions. The wave propagation in SWEM structure can be described well using the Maxwell's equations by partitioning into (a) transmission line (TL) equations in the direction of travel, and (b) orthogonal Transverse Evanescent (TE_V) wave equations [4]-[6]. For the characterization of evanescent-mode propagation, we need four pairs of separate, partially coupled TL and TE_V wave equations for the four fields E, D, B, and H. The four slow-wave evanescent-mode equations for E, D, B, and H all are radial profiles of stored energy. The seven main processes in the formation of evanescent waves are: (i) the spreading function, (ii) the self-coupling function, (iii) (radial) standing wave function, (iv) time variation of phase of stored energy components, (v) Root Sum of the Squares (RSS) combination of the four coupled equations giving dominance to the strongest field in the resonator, (vi) dissipation, radiation or absorption of energy in the resonator, (vii) exchange of energy between inter-coupled evanescent modes in SWEM resonator [4]-[10].

6.2.2 SWEM Resonator Modes and Noise Dynamics

In contrast to lumped LC resonators, which have only one resonant frequency, slow wave resonators (SWRs) can support an infinite number of electromagnetic field configurations or resonant modes [11]-[16]. The resonant modes in SWR structure exist in the form of degenerate modes (i.e., modes having the same resonance frequency with different field distributions). These modes allow the realization of two electric resonators within the same physical resonator (dual-mode resonators) or three electric resonators within the same physical resonator (triple-mode resonators), and n electric resonators within the same physical resonator (n^{th} -mode resonators).

The single-mode resonator possesses two degrees of freedom, namely, the electric and magnetic fields (voltage and current standing waves), each storing a mean thermal energy of $kT/2$ (k: Boltzmann's constant; T: temperature), resulting in improved unloaded quality factor. The multi-mode resonator exhibits 2nd-degrees of freedom, causing neighboring resonant modes which act as spurious modes interfering with the fundamental resonant mode's performances and exhibit higher noise than single-mode resonator oscillator. It is therefore desirable to increase the spurious free window of the multi-mode resonator oscillator in order to improve the stability, phase noise, and mode-jumping problems. An experimental validation supports the convergence of degenerated modes in SWR structure, resulting in improved dynamic loaded Q-factor. It is interesting to note that slow-wave propagation in SWEM structure mode-locking dynamics under large-signal drive-level condition, which is opposite the analysis because of the fact that slow-wave evanescent modes are inter-coupled in phase for a given topology [17]-[26].

The inconsistency of multi-mode oscillator phase noise dynamics calls for a revisit to the phase noise analysis based on physics-based noise modeling in SWEM oscillator circuits. This can be physically understood in time domain: noise perturbation generated at any point $p(x, y, z)$ in SWEM resonator affects the oscillator's phase and timing dynamics only when the respective modes pass through the point $p(x, y, z)$. This notion makes sense as explained above, i.e. noise at any given point $p(x, y, z)$ in SWEM resonator structure has less chance to involve in the phase-noise dynamics for an inter-coupled mode-locked transmission line, leading to lower phase noise than the single-mode resonator oscillator [6]. The Fourier-domain phase noise argument would predict wrong result, i.e. higher phase noise for SWEM oscillator that has a large number of harmonic modes than the single-mode oscillator circuits. Thus, the general phase noise theory is not applicable to the inter-coupled mode-locked resonator oscillator circuits.

It is to note that SWEM design parameters (coupling coefficient, multi-mode sensitivity, and Q factor) can be obtained using full wave EM simulation. It has been found that degenerate modes play important role in improving the Q-factor, therefore, rigorous mathematical treatment is necessary for the minimization of the spurious and jitters in pass-band. The theoretical treatment and experimental validation suggests the possibility of low cost high performance synthesizer using SWEM VCO for low jitter and low phase noise applications.

6.3 Slow-Wave Resonator Oscillator

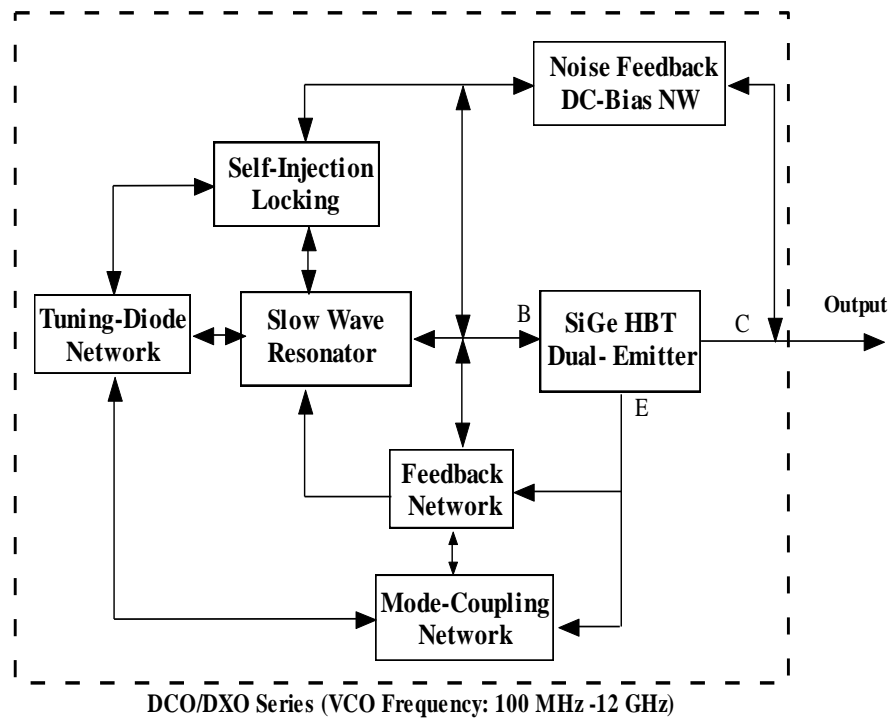
Figures 6.7(a), 6.7 (b), and 6.7 (c) show the typical block diagram and layout of the VCO using mode-coupled SWR, which validate a novel SWR (Slow Wave Resonator) approach, using a SiGe Hetro-junction-bipolar-transistor (HBT) active device fabricated on low loss RF dielectric substrate material with a dielectric constant of 3.38 and thickness of 22 mils printed structure [24].

The SWR structure is modeled using 3-D EM (Electromagnetic) CAD simulator and incorporated into optimized nonlinear oscillator circuit to enable configurable and low phase noise operation over the band. This enables SWR structure to set up optimum standing waves (within the resonator) and the noise impedance transfer function over the tuning range by controlling m_{opt} (by optimizing injection locking) and β_{opt} (by optimizing mode tuning) [17]-[24].

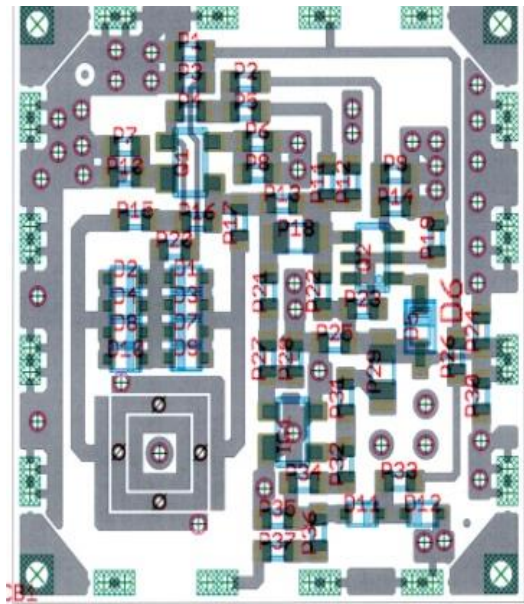
The nonlinear circuit contains the oscillator's active device, with S-parameters. This partitioning of the oscillator into its modeled component parts works quite well, and the combination of the S-parameters and the nonlinear circuit model agrees closely with the measured data in the circuits we already built [25]. The S-parameters used for these transistors are large-signal S-parameters, which improve the optimization cycles using commercial CAD tools such as ADS 2013 (Agilent), AWR, and Ansys (Nexxim) to the limits allowed by physics [26]-[31].

6.3.1 Slow-Wave Resonator Coupling Characteristic and Q-factor

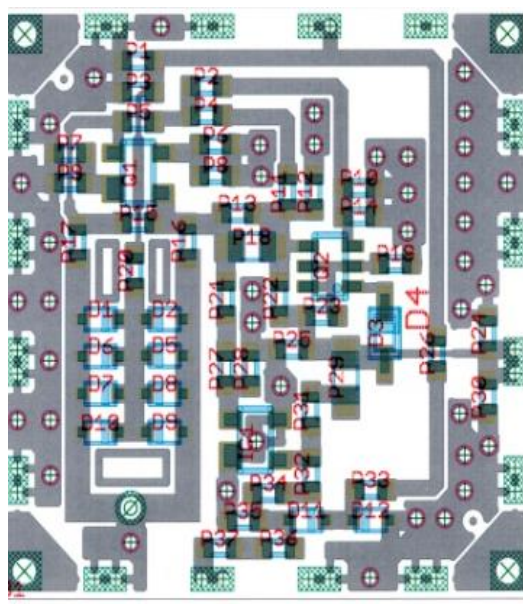
The Q (quality) factor of the printed transmission line resonator can be enhanced by introducing coupling mechanism related to the relative orientation of the neighboring resonators (electric/magnetic/hybrid). Figure (6-8) illustrates the layout of the typical electric, magnetic, hybrid-coupling planar resonator networks, and oscillator circuits for comparative analysis [32]-[37].



(a) A typical block diagram of SWR VCO



(b) Layout of SWR VCO



(c) Layout of mode-coupled SWR VCO

Figure 6-7: (a) A typical Block diagram of SWR VCO, (b) layout of SWR VCO and (c) layout of mode-coupled SWR VCO

As described in Figure (6-8), the coupling dynamics can be characterized by proximity effect through the fringing fields, which exponentially decays outside the region; electric and

magnetic field intensity tends to concentrate near the side having maximum field distribution. The coupling coefficient ' β_j ' depends upon the geometry of the perturbation, given by

$$\beta_j = \left[\left(\frac{\int \epsilon E_a E_b dv}{\sqrt{\int \epsilon E_a^2 dv \int \epsilon E_b^2 dv}} \right)_{electrical-coupling} + \left(\frac{\int \mu H_a H_b dv}{\sqrt{\int \mu H_a^2 dv \int \mu H_b^2 dv}} \right)_{magnetic-coupling} \right] \quad (6.15)$$

where E_a and H_a are, respectively, the electric and magnetic fields produced by the square loop ring resonator, and E_b , H_b are the corresponding fields due to the perturbation ($d \neq 0$) or nearby adjacent resonator (second square loop resonator).

From (6.15), the first term represents the coupling due to the interaction between the electric fields of the resonators and the second term represents the magnetic coupling between the resonators. Depending on the strength of interaction, multi-mode dynamics exist related to electrical, magnetic, and hybrid coupling. The configuration of Figure 6-8a produces an electric coupling since the electric field is maximum near the open ends, maximizing the numerator of the first term of Equation 6.15. As depicted in Figure 6-8c, when the resonators are operating near their first resonant frequency, the pair of resonators interacts mainly through their magnetic field, this is because the magnetic fields is maximum near the center of the resonator opposite to its open ends, maximizing the numerator of the second term of Equation 6.15. The coupling produced by the two configuration (open loop resonator # 1 and open loop resonator #2) as shown in Figure 6-8f are referred as mixed coupling or hybrid coupling because neither the electric fields nor the magnetic fields dominate the interaction between the resonators.

The definition of ' β_j ' given in (6.15) involves complex mathematical analysis and is not suited for practical calculation since it requires the knowledge of the electromagnetic fields everywhere. A useful alternative expression for ' β_j ' can be obtained from a well-known fact in physics when multiple resonators are coupled to each other they resonate together at different distinct frequencies (f_{ee} , f_{em} , f_{eh} , f_{mh}) which are in general different from their original resonant frequency f_0 .

Furthermore, these frequencies are associated with corresponding to their normal modes of oscillation of the coupled system (electric/magnetic/hybrid), and their difference increases as the coupling ' β_j ' (β_e : electric, β_m : magnetic and β_h : hybrid) between the resonators increases [31]-[37].

The main interaction mechanism between resonators is proximity coupling and can be characterized by a coupling coefficient ' β_j ' that depends upon the ratio of coupled energy to stored energy, described by

$$\beta_e \cong \frac{coupled-electrical\ energy}{stored-energy\ of\ uncoupled-resonator} \cong \frac{f_{me}^2 - f_{ee}^2}{f_{me}^2 + f_{ee}^2} \cong \frac{C_{me}}{C} \quad (6.16)$$

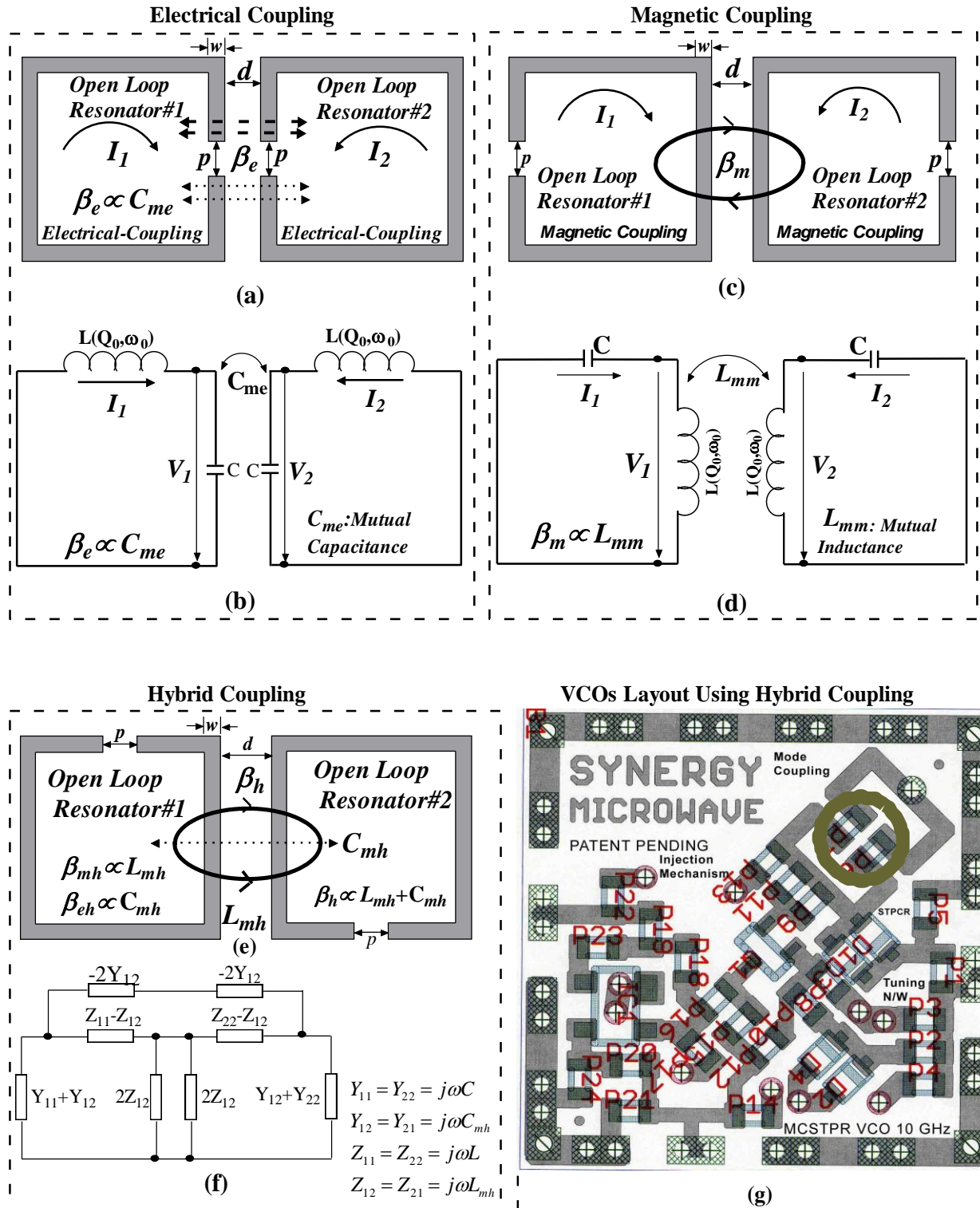


Figure 6-8: A typical simplified structure of open loop microstrip line coupled resonator networks:(a) Electrical coupling, (b) Equivalent lumped model of electrical coupling, (c) Magnetic coupling, (d) Equivalent lumped model of magnetic coupling, (e) Hybrid coupling, (f) Equivalent lumped model of hybrid coupling and (g) Layout of VCO using electric and magnetic coupling.

$$\beta_m \equiv \frac{\text{coupled-magnetic energy}}{\text{stored-energy of uncoupled-resonator}} \equiv \frac{f_{em}^2 - f_{mm}^2}{f_{em}^2 + f_{mm}^2} \equiv \frac{L_{mm}}{L} \quad (6.17)$$

$$\beta_h \equiv \frac{\text{coupled-electro-magnetic energy}}{\text{stored-energy of uncoupled-resonator}} \equiv \frac{f_{eh}^2 - f_{mh}^2}{f_{eh}^2 + f_{mh}^2} \equiv \frac{CL_{mh} + LC_{mh}}{LC + L_{mh}C_{mh}} \quad (6.18)$$

where

$$f_{ee} = \frac{1}{2\pi\sqrt{L(C+C_{me})}}, \quad f_{me} = \frac{1}{2\pi\sqrt{L(C-C_{me})}}, \quad C_{me}: \text{Mutual Capacitance} \quad (6.19)$$

$$f_{em} = \frac{1}{2\pi\sqrt{C(L-L_{mm})}}, \quad f_{mm} = \frac{1}{2\pi\sqrt{C(L+L_{mm})}}, \quad L_{mm}: \text{Mutual Inductance} \quad (6.20)$$

$$f_{eh} = \frac{1}{2\pi\sqrt{(L-L_{mh})(C-C_{mh})}}, \quad f_{mh} = \frac{1}{2\pi\sqrt{(L+L_{mh})(C+C_{mh})}}, \quad L_{mh}: \text{Hybrid Inductance} \quad (6.21)$$

$$f_0 = \frac{1}{2\pi\sqrt{LC}}, \quad f_0: \text{fundamental resonance frequency of uncoupled resonator} \quad (6.22)$$

The time average loaded Q-factor of slow wave resonator: $\overline{Q_{swr}(\omega)}_{\omega \rightarrow \omega_0}$ can be described by

$$\overline{Q_{swr}(\omega)}_{\omega \rightarrow \omega_0} = \left[\frac{\omega}{2(I_{max}-I_{min})} \int_{I_{min}}^{I_{max}} Q_{swr}(\omega, i) di \right]_{\omega \rightarrow \omega_0} \quad (6.23)$$

where I_{min} and I_{max} are the minimum and maximum resonator currents of the SWR network associated with the fundamental modes of the coupled resonator networks, the $Q_{swr}(\omega, i)$ is the instantaneous quality factor at frequency ω and current i provides an effective means to quantify the Q-multiplier effect of SWR when operated in an evanescent-mode coupling condition, especially in printed coupled resonator based oscillator circuits.

From (6.23), the loaded quality factor Q_L of the coupled resonator network is given in terms of unloaded quality factor Q_0 as

$$Q_L(\omega_0) = \frac{\omega_0}{2} \left[\frac{\partial \phi}{\partial \omega} \right] \quad (6.24)$$

$$[Q_L(\omega_0)]_{\text{electrical-coupling}} \equiv 2 \left[\frac{Q_0}{(1+\beta_e)} \right]_{\beta_e \ll 1} \equiv 2Q_0 \quad (6.25)$$

$$[Q_L(\omega_0)]_{\text{magnetical-coupling}} \equiv 2 \left[Q_0 (1 + \beta_m) \right]_{\beta_m \rightarrow 1} \equiv 2Q_0 \quad (6.26)$$

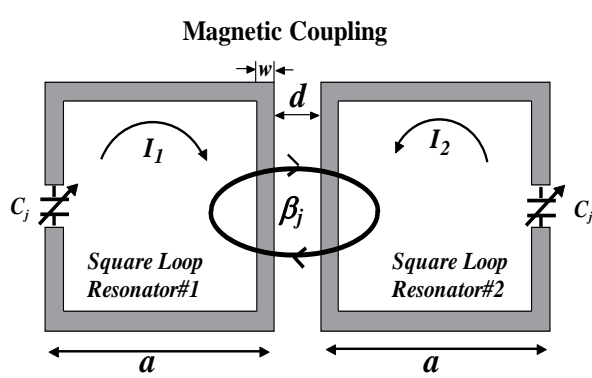
$$[Q_L(\omega_0)]_{\text{hybrid-coupling}} \equiv 2 \left[Q_0 \frac{(1 + \beta_{mh})}{(1 + \beta_{eh})} \right]_{\beta_e \ll 1, \beta_m \rightarrow 1} \equiv 2Q_0 \quad (6.27)$$

where $\frac{\partial\phi}{\partial\omega}$ is the rate of change of the phase, and Q_0 is the unloaded Q-factor of the uncoupled single open loop microstrip line resonator.

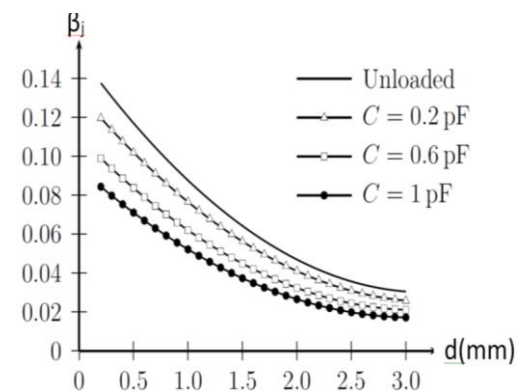
From (6.25)-(6.27), there is trade-off between improving the Q factor and the permissible attenuation required (which is compensated by active device for oscillation build up).

The coupling mechanism described in Figure (6-8) shows improvement in quality factor in comparison to single uncoupled planar resonator but drawback is limited tuning range (less than 1%). By introducing tunable capacitor across the open end of uncoupled planar open loop resonator, dynamic unloaded Q-factor can be improved but limited tuning range (< 25%). This is due to minimization of the radiation losses from the open ends of the resonator because of capacitor loading, causing dielectric polarization in the capacitor since most of the electric field resides inside it [38]-[42]. Therefore, a high Q capacitor could actually increase the unloaded quality factor of the whole resonator. This is analogous to the case of dielectric resonators where the fields are constrained to a small volume dielectric with high permittivity and low loss tangent resulting in a high overall Q [43]-[49]. For wideband tunability (>100% tuning), adjacent coupled open loop resonator network is preferred but at the cost of large real estate area.

In general, the miniaturization of the open loop resonator reduces its capacity to couple to adjacent structures. This is because smaller resonator size represents a smaller volume of electromagnetic interactions between its coupled arms; reason being a smaller size represents a smaller volume of electromagnetic interaction between coupled resonators. The fact that the majority of the electric field that existed in the volume surrounding the open ends of a resonator is now confined to the interior of a capacitor limiting its possibility to interact with a neighboring resonator. It can be seen from the Figure 6-9 that the effect on the magnetic and mixed coupling is less severe than for the electric coupling, where the magnetic coupling coefficient is plotted against the separation between resonators for different loading capacitors [43]-[49].



(a) Capacitive loaded magnetic coupled square loop resonator



(b) plot of magnetic coupling β_j as a function "d"

Figure 6.9: A typical capacitive loaded magnetic coupled square loop resonator characteristics: (a) Printed layout, (b) plot of magnetic coupling ' β_j ' as a function of the distance between resonators for a given capacitive (C_j) loading with resonator physical dimension $w = 2\text{mm}$ and $a = 26\text{mm}$, fabricated using Roger RO4003c substrate with a dielectric constant of 3.55 and a thickness of 60mil) [43]

The microstrip square open loop resonator is one of the most used structures for multi-mode oscillator resonator applications due to its compact size ($a = \lambda/8$). For low phase noise multi-octave band tunability, the loaded quality factor (Q_L) as described in (6.24)-(6.27) can be maximized by either lowering the value of mutual capacitance (C_m) and inductance (L_m) or maximizing the self-capacitance (C) and inductance (L). Therefore the upper limit of the loaded Q -factor is dependent on the coupling ' β_j ' (' β_e : electric, β_m : magnetic and β_h : hybrid) that can be optimized by controlling the width of the transmission line (w), gap of the open line resonator (p), and spacing between the two open line resonators (d) [50]-[55].

For low phase noise tunable oscillator, the coupling coefficient β_j should be dynamically tuned over the operating frequency band. However, dynamic controlling and tuning of the parameters (w , p , a , and d) as shown in Figure 6-8 at high frequency is challenging task. The alternative tuning mechanism is capacitive loading by incorporating tuning diodes [38]-[44]. Figure 6-10 shows the typical tunable square open loop resonator in compact size ($\lambda/8$ by $\lambda/8$) for the applications in oscillator circuits.

As shown in Figure 6-10 (c), the goal is to minimize the real estate area by using meander line into inner part of the resonator. To optimize the geometry of the coupled resonator they are excited with a pair of loosely coupled feed lines to obtain a transmission parameter $S_{21}(w)$ from which the two resonant frequencies f_1 and f_2 can be obtained for a given geometry and values of d between resonators.

The resonator shown in Figure 6-10 (d) offers compact size and exhibits two independent modes (dual-modes), the coupling between them can be optimized by the geometry of the inner structure. This tunable dual mode resonator can then function as two independent tunable resonators providing an immediate size reduction of 50%.

For brief insights about the tuning capability of square open loop resonator (Figure 6-11), a simple equivalent circuit model of the varactor diode loaded resonator as shown in Figures 6-11(a) to 6-11(c) is used to derive its multi-mode tuning dynamics and regime.

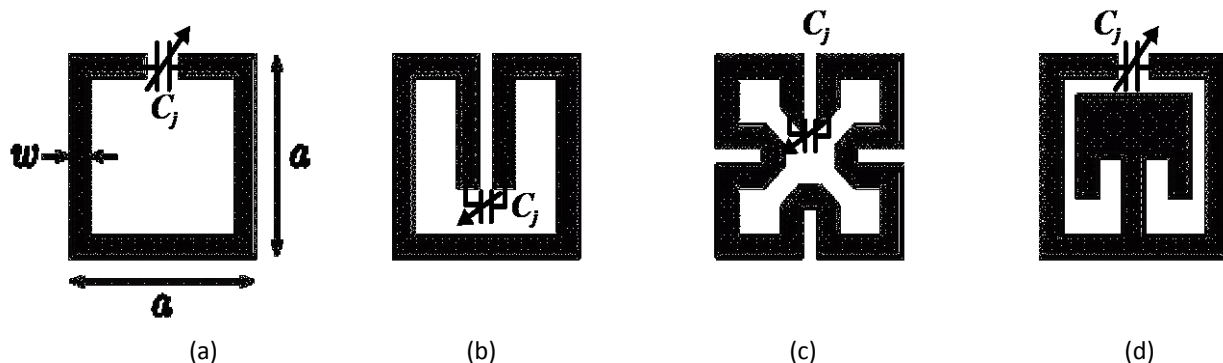


Figure 6-10: A typical layout of tunable square open loop resonator: (a) Conventional square open loop hairpin resonator, (b) Folded arms square open loop resonator, (c) Meander line square open loop resonator, (d) Dual mode square open loop resonator [43]

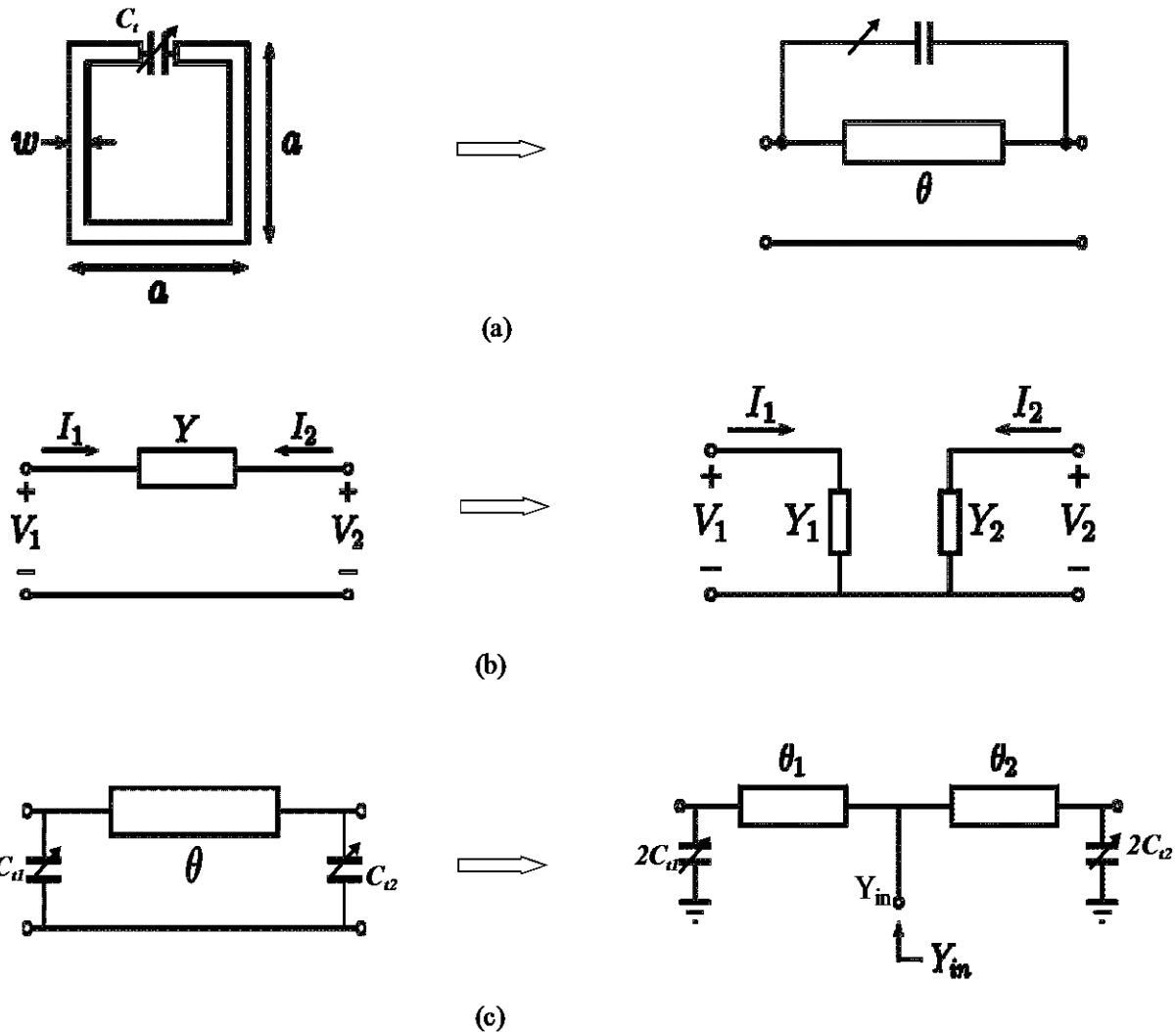


Figure 6-11: A square open loop resonator loaded with a tunable series capacitor: (a) simplified equivalent circuit model for square open loop resonator, (b) Miller-transformed equivalent circuit model, and (c) equivalent circuit of square open loop resonator with two tunable shunt capacitors at open ends [43].

The voltage and current distribution at resonance can be described by using transmission line theory and the shunt equivalent model of Figure 6-11 (c) as:

$$V(\theta) = \left[\cos(\theta) - \frac{\sin(\theta)}{\tan(\theta_T/2)} \right] \quad 0 < \theta < \theta_T \quad (6.28)$$

$$I(\theta) = \frac{j}{Z_0} \left[\frac{\cos(\theta)}{\tan(\theta_T/2)} + \sin(\theta) \right] \quad 0 < \theta < \theta_T \quad (6.29)$$

where $\theta = \beta z$ is the electrical length measured from one open end of the resonator, and θ_T is the total electrical length of the resonator. Figure 6-12 shows the plots of $V(\theta)$ and $I(\theta)$ for loaded and unloaded square open loop resonator network. As shown in Figure 6-12, the current

never goes to zero but remains near its maximum value along the resonator and the voltage varies almost linearly between open ends (Assumptions: these typical plots are just to compare the distribution of the voltages and currents between the loaded and unloaded resonators, but not their amplitudes; they are normalized with respect to their respective maxima and they have either different frequencies or different resonator sizes) [56].

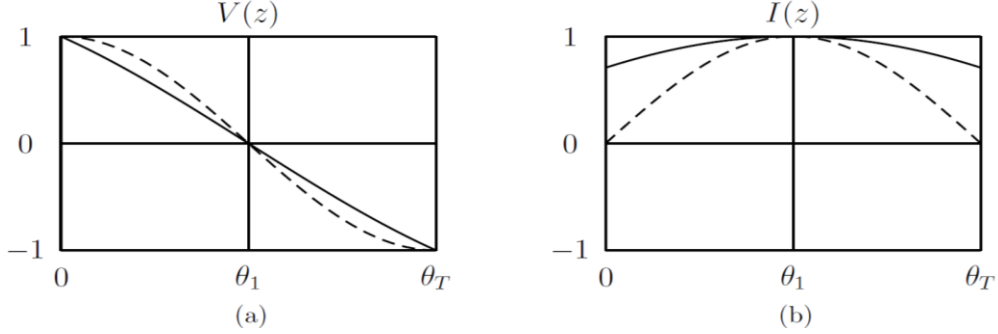


Figure 6-12: Voltage and current distribution at resonance of square loop open resonator (SLOR) shown in Figure 6-10: (a) Voltage distribution in a loaded and unloaded open loop resonator, and (b) current distribution in loaded and unloaded open loop resonator (Dashed lines are for the unloaded case) [43].

Using Miller's theorem, tunable square loop open resonator (SLOR) shown in Figure 6-11a can be equivalently represented as Figure 6-11c, if the following conditions are satisfied:

$$Y_1(\omega) = Y(\omega) \left(1 - \frac{V_2(\omega)}{V_1(\omega)} \right) \rightarrow Y_1(\omega) = Y(\omega)[1 - A(\omega)] \quad (6.30)$$

$$Y_1(\omega \rightarrow \omega_0)|_{A=-1} = 2Y(\omega_0) = j\omega_0 C_{t1} = j2\omega_0 C_t \quad (6.31)$$

$$Y_2(\omega) = Y(\omega) \left(1 - \frac{V_1(\omega)}{V_2(\omega)} \right) \rightarrow Y_2(\omega) = Y(\omega) \left(1 - \frac{1}{A(\omega)} \right) \quad (6.32)$$

$$Y_2(\omega \rightarrow \omega_0)|_{A=-1} = 2Y(\omega_0) = j\omega_0 C_{t2} = j2\omega_0 C_t \quad (6.33)$$

where $A = V_2/V_1$ is the voltage gain from node 1 to node 2, near resonance ($\omega \rightarrow \omega_0$), both voltages (V_1, V_2) are in opposite phase ($V_1 = -V_2$), gain $A = -1$ (odd-mode resonance).

From Figure 6-11 (c), the input admittance can be described by

$$Y_{in}(\omega) = jY_0 \left[\frac{(2\omega C_t + Y_0 \tan \theta_1)}{(Y_0 - 2\omega C_t \tan \theta_1)} + \frac{(2\omega C_t + Y_0 \tan \theta_2)}{(Y_0 - 2\omega C_t \tan \theta_2)} \right] \quad (6.34)$$

From (6.34), at fundamental odd-mode resonance ($V_1 = -V_2$), $Y_{in}(\omega \rightarrow \omega_0) = 0$

$$Y_{in}(\omega \rightarrow \omega_0) = 0 \Rightarrow jY_0 \left[\frac{(2\omega C_t + Y_0 \tan \theta_1)}{(Y_0 - 2\omega C_t \tan \theta_1)} + \frac{(2\omega C_t + Y_0 \tan \theta_2)}{(Y_0 - 2\omega C_t \tan \theta_2)} \right] = 0 \Rightarrow \tan(\theta_1 + \theta_2) = \frac{4Z_0 \omega_0 C_t}{4Z_0^2 \omega_0^2 C_t^2} \quad (6.35)$$

$$\tan(\theta_1 + \theta_2) = \tan(\theta_T)|_{\theta_T=(\theta_1+\theta_2)} = \frac{4Z_0\omega_0C_t}{4Z_0^2\omega_0^2C_t^2} = \frac{1}{Z_0\omega_0C_t} \quad (6.36)$$

$$Y_{in}(\omega \rightarrow \omega_0) = \infty \Rightarrow Z_{in} = 0 \Rightarrow (Y_0 - 2\omega C_t \tan\theta_1) \Rightarrow \tan(\theta_1)|_{(\theta_1=\theta_2)} = \frac{1}{2Z_0\omega_0C_t} \quad (6.37)$$

where $\theta_T = \theta_1 + \theta_2$ is the total length of the resonator.

From (6.36), the electrical length ($\theta_T = \theta_1 + \theta_2$) is calculated for a given resonance frequency ω_0 and loading capacitance C_t . From (6.37), for $\theta_1 = \theta_2$, $Z_{in} = 0$ the center of the resonator is a voltage null at the first resonant frequency. This implies that for $\theta_1 = \theta_2$; Equations (6.36) and (6.37) are equivalent and there will be a voltage null at the center of the resonator whenever the resonance condition exists in square open loop resonator structure.

From (6.30)-(6.37), the resonant condition of the loaded square open loop resonator structure is valid only near an odd mode resonance ($V_1 = -V_2$), where the parameter 'A' of the Miller effect is -1. Away from these voltage conditions ($V_1 = -V_2$) at odd-mode resonant frequencies the voltage relation among the open ends changes, causing change in equivalent admittances Y_1 and Y_2 as shown in Figure 6-11 (b). This leads to difference between the behavior of the series and shunt loaded resonators away from the odd resonant frequencies. The two most important differences are the performance near the even resonant mode and the existence of anti-resonance for the case of series loading [43]-[54].

For even-mode ($V_1 = V_2$), the capacitor (C_{t1} and C_{t2}) as shown in Figure 6-11c is virtually open circuited caused by Miller effect ($A = 1$). Therefore, the series capacitor (C_t) as shown in Figure 6-10a does not have any effect on the behavior of the resonator near even mode resonances; these resonant frequencies are unchanged by the presence of the capacitor.

6.3.2 Loaded Open Loop Printed Resonator Coupling and Mode-Characteristics

Figure 6-13 shows the typical set up used for measurement of the $S_{21}(\omega)$ for deriving the coupling characteristics of the tunable open loop resonator loaded with the varactor diode.

The parameter of interest is the transmission coefficient $S_{21}(\omega)$, where the resonant frequencies are manifested as peaks of maximum transmission between ports. Figure 6-14 shows CAD simulated (Ansoft Designer) plot of the varactor loaded open square loop printed resonator with $\omega = 2\text{mm}$ and $a = 26\text{mm}$, fabricated using Roger RO4003c substrate with a dielectric constant of 3.55 and a thickness of 60mil (1.524 mm) [51]-[55]. As shown in Figure 6-14, the first resonant frequency is shifted down with different values of C , whereas the second resonance frequency remains at same location. Nevertheless, as varactor diode capacitance increases beyond certain value (for example, 1.4 pF), a couple of frequencies where the transmission coefficient S_{21} is zero appears between the first and second resonant frequencies, which is observed in Figure 6-14 for $C = 2\text{pF}$.

As shown in Figure 6-14, the physical size of the resonator ($\omega = 2\text{mm}$ and $a = 26\text{mm}$) is kept constant while C is varied causing a shift in the first resonant frequency. This frequency shift can be capitalized into miniaturization if we let the size of the resonator vary and is minimized while keeping the fundamental resonance fixed.

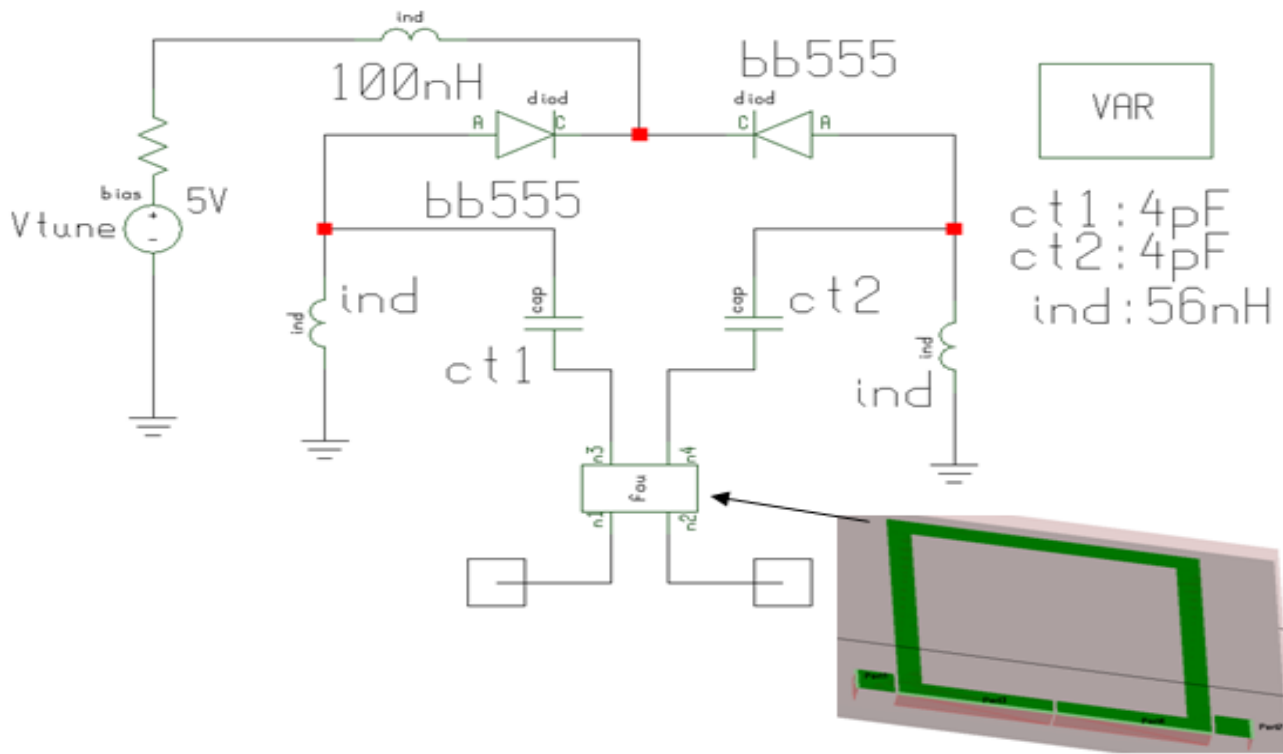


Figure 6-13: A typical setup for carrying out the measurement of the transmission coefficient $S_{21}(\omega)$ for analyzing the coupling characteristics of the varactor loaded tunable open loop resonator [44].

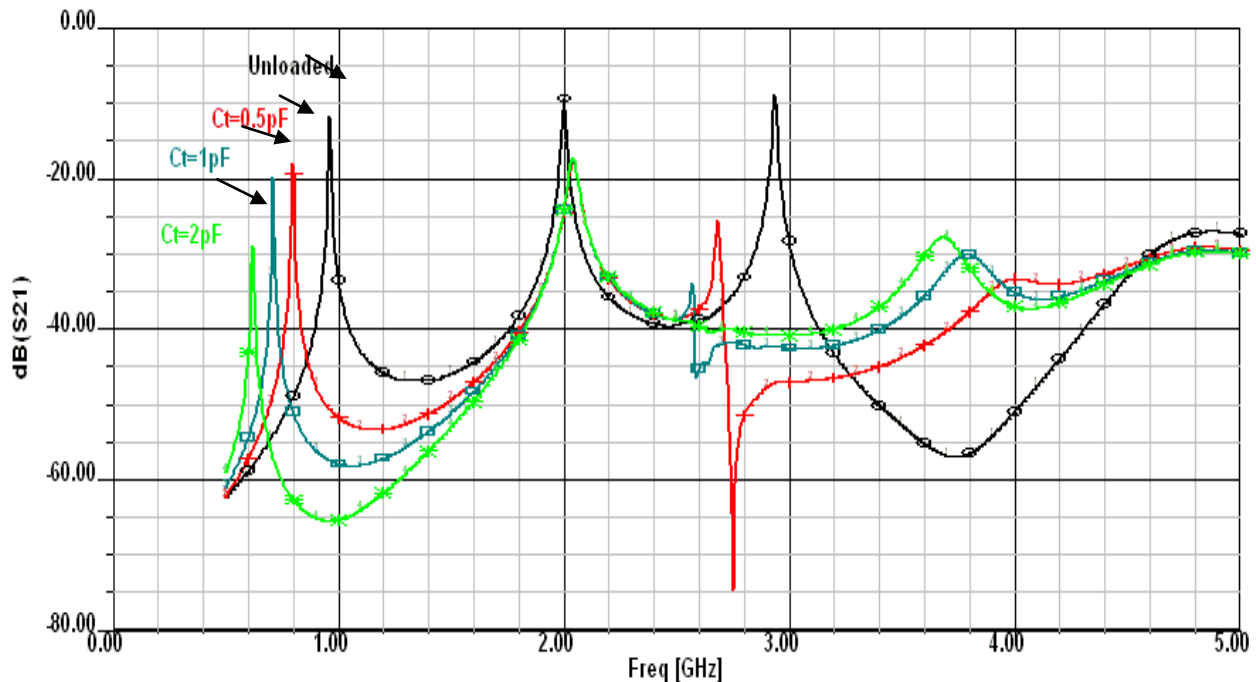


Figure 6-14: A CAD simulated (Ansoft Designer) plot of $S_{21}(\omega)$ of a varactor loaded SOLR for different capacitance values [45].

Table 6.1 describes a summary of the results obtained by fixing the resonant frequency at 1 GHz using the same substrate as before [52]-[56].

As shown in Table 6.1, the ratio of f_1/f_0 increases as the loading increases, when the loading capacitance is 1 pF the last row of Table 6.1 indicates that the area of the miniaturized resonator is 36% that of the conventional resonator (shown in 4th column of Table 6.1).

Table 6.1: Resonator characteristics as a function of loading capacitance

C_t (pF)	a (mm)	A_m (mm^2)	A_m/A_c	f_1/f_0
0	26	676	1	2
0.2	23.2	535.92	0.79	2.23
0.6	19.5	380.25	0.56	2.66
1	17	289	0.427	3.06

where

A_m : Area occupied by the varactor loaded miniaturized resonator

A_c : Area of the conventional (unloaded) resonator

w= width (w =2 mm in all resonators), kept constant for the simplification.

a= length of the SLOR, varying for the miniaturization

f_0 = fundamental frequency is fixed at 1 GHz

f_1 =first spurious frequency

Figure 6-15 shows the plot of area $A(C_t)$ and frequency $\omega(C_t)$ versus capacitive loading provided by the varactor diode in printed square open loop resonator. From (6.37), the total length of the square open loop resonator is $\theta_T = \theta_1 + \theta_2$, for $\theta_1 = \theta_2$:

$$\tan(\theta_1)|_{(\theta_1=\frac{\theta_T}{2})} = \frac{1}{2Z_0\omega_0 C_t} \quad (6.38)$$

$$\theta_1 = \frac{\theta_T}{2} = \omega \left(\frac{l}{2v_p} \right) = \frac{\beta l}{2} = \tan^{-1} \left(\frac{1}{2Z_0\omega C_t} \right) \quad (6.39)$$

$$A (\text{Square Loop Resonator Area}) = \left(\frac{l}{4} \right)^2 = \frac{\theta_T^2}{16\beta^2} = \frac{1}{4\beta^2} \left[\tan^{-1} \left(\frac{1}{2Z_0\omega C_t} \right) \right]^2 \quad (6.40)$$

$$A(C_t) = k_1 \left[\tan^{-1} \left(\frac{1}{p_1 C_t} \right) \right]^2 \Rightarrow A(C_t) \propto \left[\tan^{-1} \left(\frac{1}{p_1 C_t} \right) \right]^2 \quad (6.41)$$

From (6.39)

$$C_t = \frac{k_2}{p_2 \omega \tan(p_2 \omega)} \Rightarrow \omega(C_t) \propto \frac{1}{p_2 C_t \tan(p_2 C_t)} \quad (6.42)$$

Equations (6.41) and (6.42) are trigonometric functions, where 'l' represents the total physical length (perimeter) of the resonator (neglecting the size of the gap where the capacitor is mounted, v_p is the phase velocity, k_1 and p_1 , k_2 and p_2 are constant, and C_t is the capacitive loading provided by varactor diode).

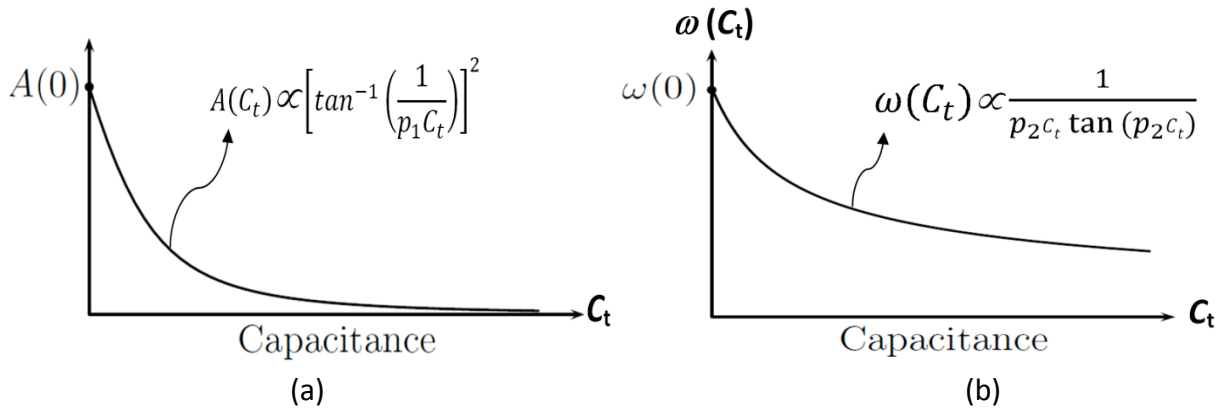


Figure 6-15: Shows the plot of area $A(C_t)$ and frequency (C_t) versus capacitive loading provided by the varactor diode in printed square open loop resonator: (a) relationship between the capacitance value and the resonator's area), and (b) resonant frequency [43]

Since the constants k_1, k_2 and p_1, p_2 have the effect of scaling the x and y axis respectively, any choice of them gives a good representation of the general tendency. A plot of this curve, where for simplicity $k_1=p_1=k_2=p_2=1$, is shown on Figure 6-15.

Both curves shown in Figure 6-15 indicate that there is maximum variability for relatively small values of capacitance. It can be noticed from the Figure 6-15 that as the capacitance increases the rate of change decreases, this leads to following [43]:

- Designs with large capacitance values are more robust (less sensitive to capacitor tolerances).
- For tunable operation, small values of capacitance are better.
- Increasing the capacitance after a certain value does not provide significant advantage.

Based on above, oscillator circuits are designed for the validation purpose.

6.4 Tunable Low Phase Noise Oscillator Circuits

The tunable oscillator circuits using slow wave resonator networks reported in this chapter offers cost-effective alternative of expensive high Q-factor dielectric and YIG resonator oscillators [7].

Figure 6-16 (a) shows the typical simplified schematic of an oscillator comprised of a resonator module and an external circuitry (active device that generates gain for stable oscillation) [29]-[32].

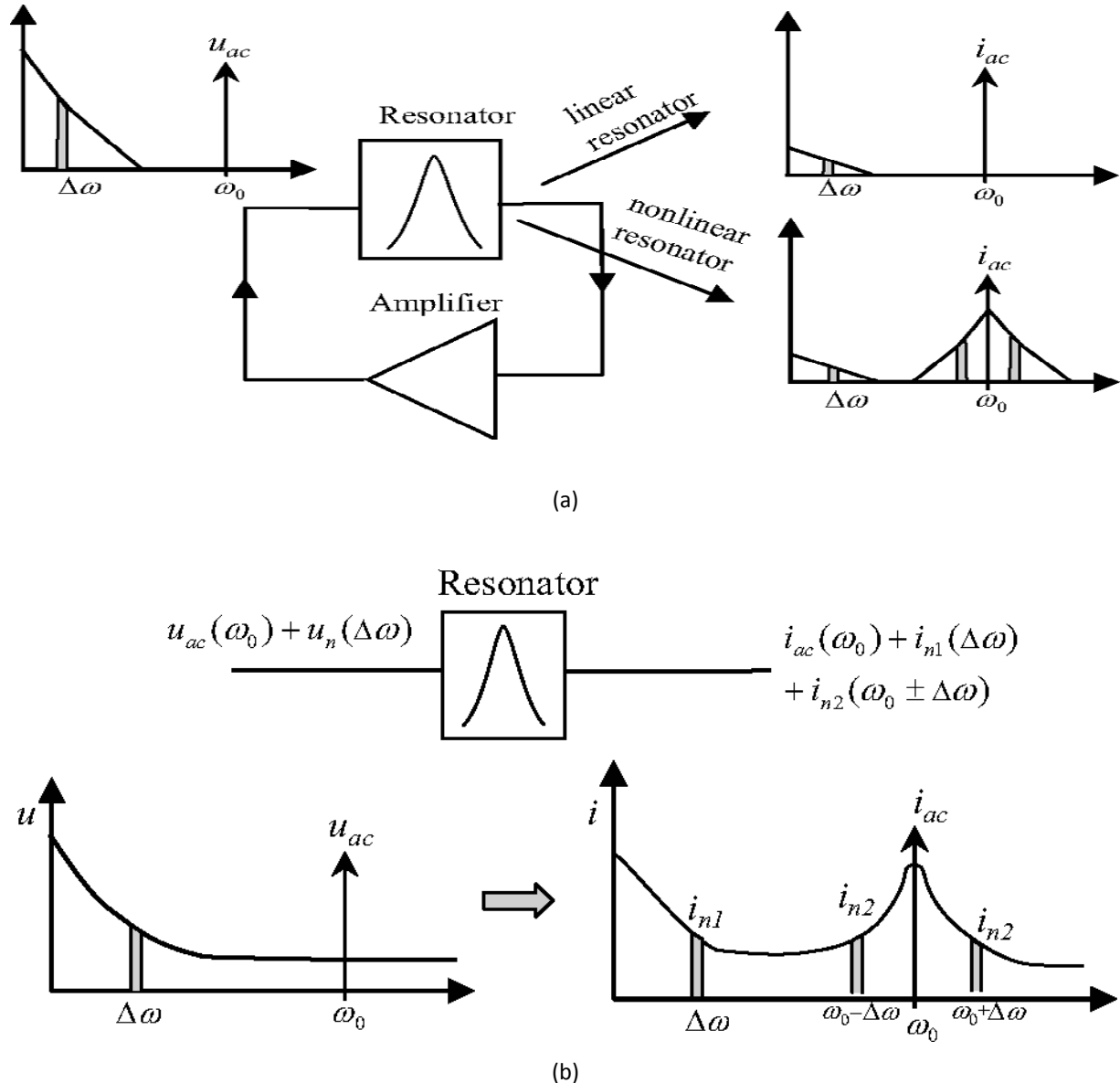


Figure 6-16: A typical noise aliasing phenomena in nonlinear resonator based oscillator circuits: (a) Schematic representation of noise aliasing in oscillator comprises of nonlinear resonator, and (b) Low-frequency noise $u_n(\Delta\omega)$ present at filter input is aliased to carrier side-bands ($\omega_0 \pm \Delta\omega$) due to mixing in nonlinear resonator network [57].

In general, resonator is described as linear model (follows the superposition theorem), ideally high Q-factor resonator used in oscillator would clean the low frequency near-carrier noise. But in reality, the quantum dynamics of Quartz crystal, Ceramic, Dielectric, and MEMS resonator is nonlinear and drive-level dependent [57]. Therefore, nonlinearities associated with these resonators can lead to unwanted aliasing of low-frequency noise to carrier side-bands as shown in Figure 6-16 (b). The aliasing of low frequency noise can be even higher than the thermal noise floor of the expensive high Q-factor piezoelectric Quartz resonators; therefore,

linearization of the resonator is needed for the application in high performance frequency signal sources [53]-[57].

Figure 6-17 shows the layout of 18.87 GHz dielectric resonator oscillator (DRO) in push-push topology for the minimization of unwanted aliasing of low frequency random fluctuation noise [46]. Although DROs in push-push topology (see Appendix-A) minimize aliasing of near-carrier 1/f-noise it is at the cost of size, power and sensitivity to vibration [50]. One way to overcome the unwanted noise aliasing is to use linear passive printed planar resonator but planar resonator lacks with the Q-factor, and are large in size, therefore main limiting factor of the phase noise performances [17]-[21]. This thesis describes the practical examples of low phase noise oscillator circuits using novel slow wave resonator networks that supports reasonably low phase noise for a given conversion efficiency in compact size, and also amenable for integration in the integrated chip (IC) form.

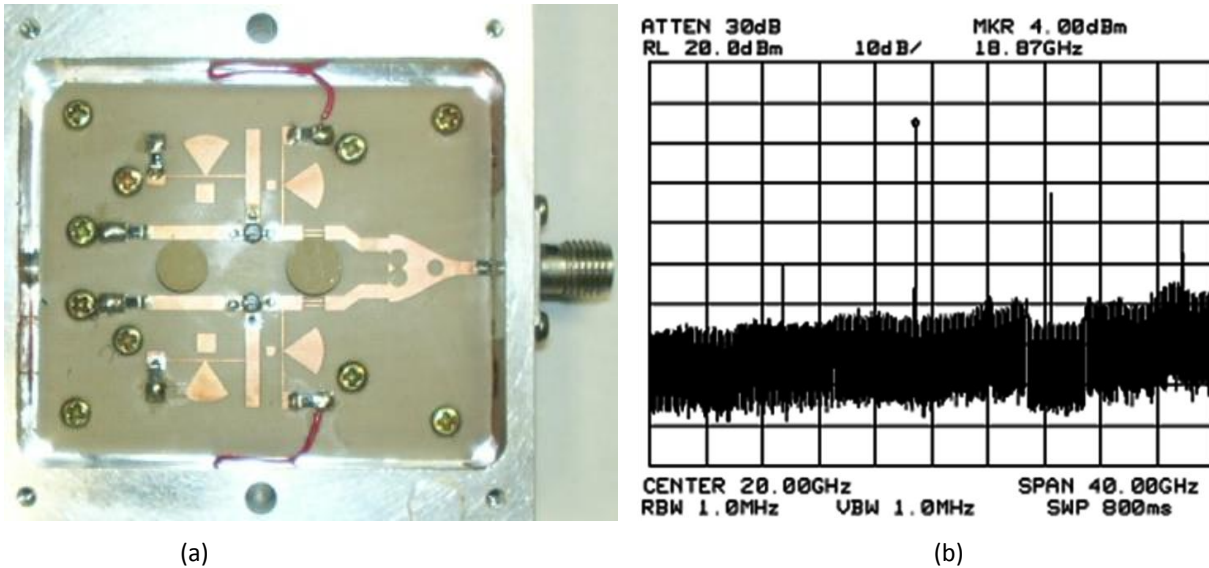


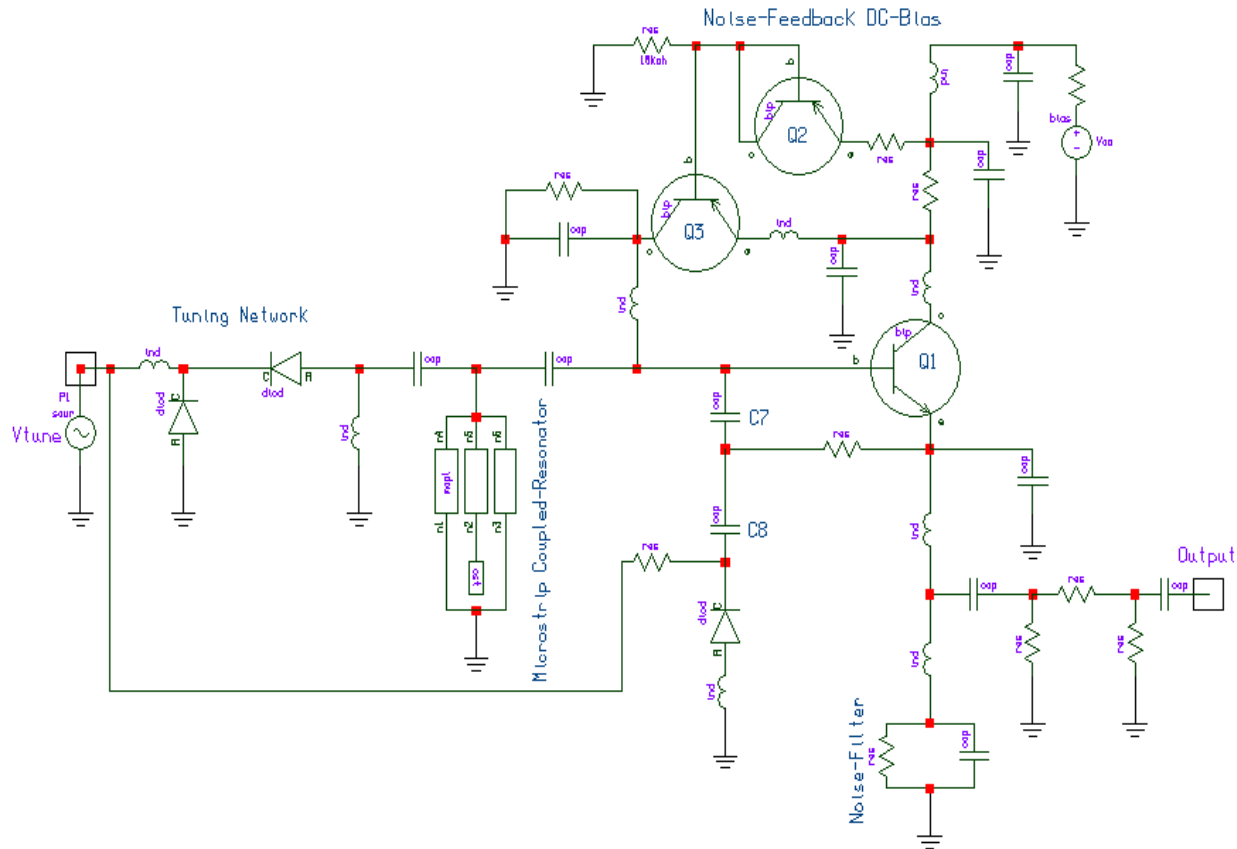
Figure 6-17: (a) shows the layout of 18.87 GHz oscillator using expensive high Q-factor dielectric resonators, (b) measured phase noise plots [46]

6.4.1 Examples: Slow Wave Resonator Based Tunable Oscillator Circuits

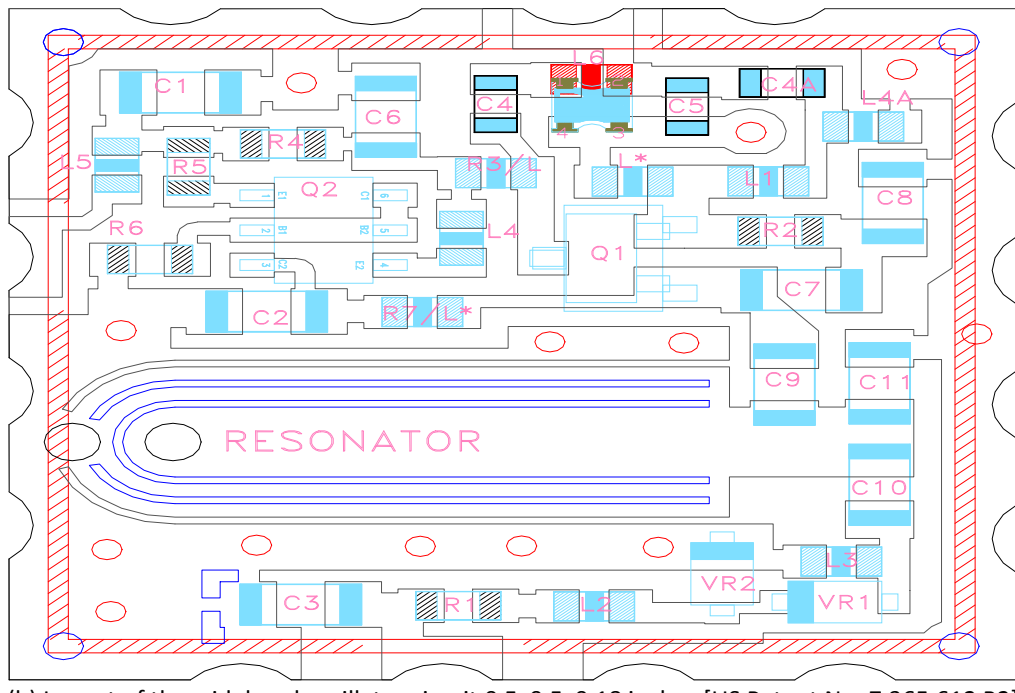
In this section, examples of tunable oscillator circuits using printed coupled resonator network in conjunction with noise minimization techniques are discussed [57]-[74].

6.4.1.1 Tunable (2000-3200 MHz) Oscillator Circuits [US Patent No. 7,365,612 B2]

Figure 6-18 shows a slow wave resonator based tunable (2000-3200 MHz) oscillator (SWRO) circuit illustrating the critical components and layout according to the patent application [65]. As shown in Figure 6-18, the SWRO (slow wave resonator oscillator) circuit includes a noise-feedback DC bias network; noise filter in conjunction with microstripline coupled resonator for improved frequency stability under the allowable temperature fluctuations (-50°C to +95°C) including the fluctuations in the supply voltage (<± 25%).



(a) A typical circuit schematic of tunable oscillator circuit



(b) Layout of the wideband oscillator circuit 0.5x0.5x0.18 inches [US Patent No. 7,365,612 B2]

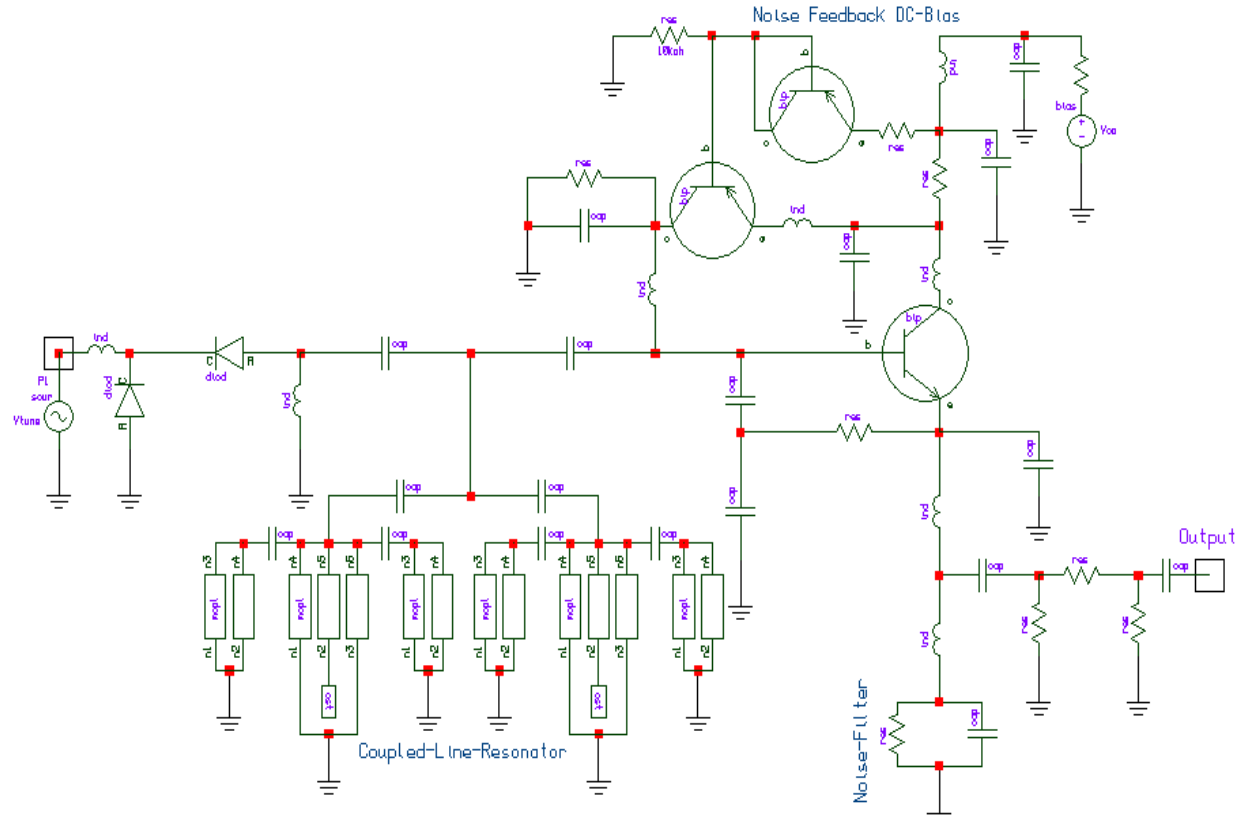
Figure 6-18: (a) Schematic of oscillator (2000-3200MHz), (b) Layout (32 mils, Dielectric constant 3.38) [65]

Other advantages result from the fact that it is not necessary to provide an active current source for the supply voltage. A low supply voltage is possible, and this is a major advantage in mobile communication systems, for instance. In particular, the operating point of the oscillator transistor should be adjusted for a non-overdriven operating mode of the oscillator. The typical phase noise is -95dBc/Hz @ 10 KHz offset for the frequency 2000-3200MHz. The circuit operates at 8 Volt and 25 mA, and gives power output more than 5dBm over the tuning range.

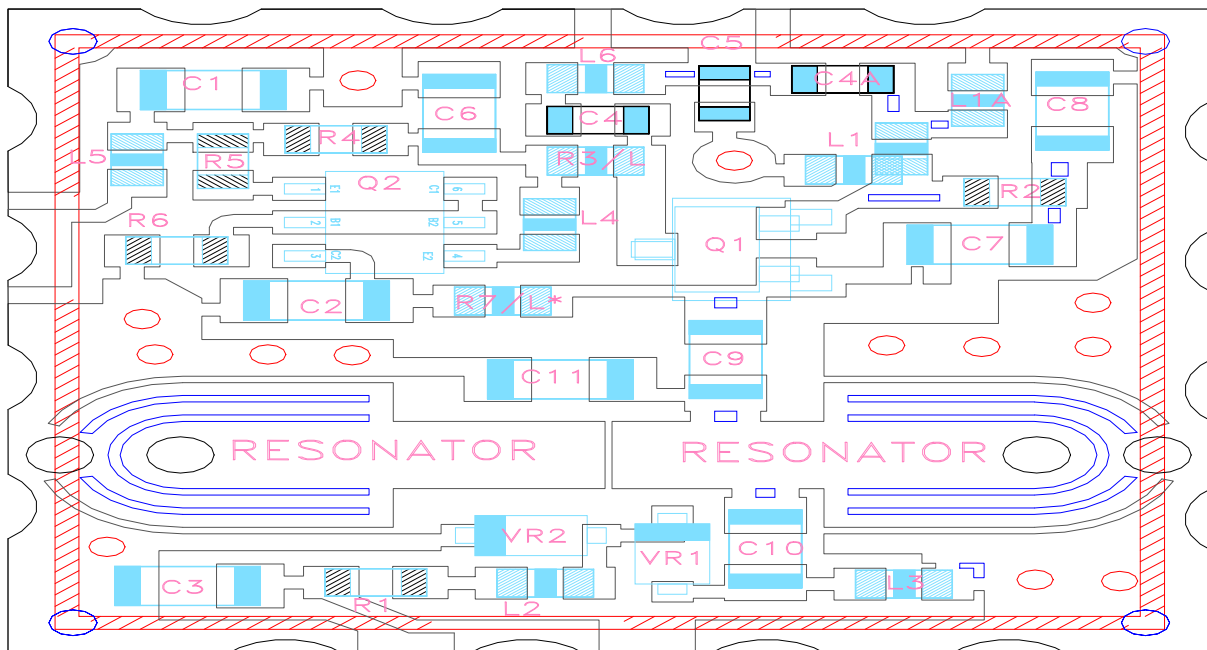
Typically, wideband oscillators undergo compound compromise, i.e. oscillator phase noise, harmonics or tuning sensitivity as a function of control tuning voltage, thereby, resulting poor performance over the band under most of its operating condition. The problem of achieving optimum oscillator performance in terms of phase noise is compounded by the fact that the optimum drive- levels and conduction angle changes with control tuning voltage. These drawbacks are overcome by incorporating the circuitry that adjusts the drive level and conduction angle in response to the changes in the frequency control tuning voltage. The feedback capacitor (C_7 and C_8) as shown in Figure 6-18a is incorporated with tuning diode in order to adaptively optimize the drive level, therefore improved phase noise performance over the band. By doing so, both phase noise performance and the tuning range of an oscillator can be extended, while simultaneously improving the harmonic contents and over the tuning range (2000-3200 MHz), measured phase noise is -105dBc/Hz @ 10 KHz offset for the frequency 2000-3200MHz with 8 Volt and 25 mA, and gives power output more than 3dBm over the tuning range with harmonic rejection better than 20dBc.

Figure 6-19 shows a schematic diagram of the improved version of the SWRO circuit using novel multi-coupled line printed resonators for the improvement of the phase noise performance over the tuning range and associated phase jitter [65]. The resonator structure includes a center strip as an open transmission line in the form of an etched structure with a wavelength, which is shorter than the quarter-wavelength of the desired frequency. The resonator network includes a voltage-controlled variable-capacitance diode, and a resonator terminal connected between the voltage-controlled variable-capacitance diode of the resonator unit and the base of the 3-terminal active device. The resonator is preferably an asymmetric coupled microstripline, and the stages are disposed in a standardized housing in SMD (surface mounted device) technology.

By way of example, the etched structure of the resonator may be provided as a microstrip, or as a coplanar structure or as a slot structure or embedded in a multilayer board, for instance, or in other words may be made by either the monolithic technique or a hybrid technique. This novel approach is associated with reference to a tunable ultra low phase noise and low thermal drift oscillator at 2000-3200MHz employing dynamically tuned microstripline-coupled resonator, which is synchronized to the VCO's tuning port for low phase-hit and better noise performance. It is especially advantageous that in this distributed resonator function; ultra low phase noise performance is achieved without having to use an expensive high Q resonator network with special tuning arrangement to cover wide tuning range. By means of the embodiment as an open strip in center of the coupled-line resonator structure, a distributed resonator function is achieved while maintaining wide tunable range and higher Q factor as shown in the Figure 6-19 (a).



(a) A typical (SWRO) circuit schematic, operating frequency 1900-3200MHz with 240 mW ($V_{cc}=8V$, $I_c=30mA$)



b) Layout of the wideband (SWRO) circuit 0.5x0.5x0.18 inches [US Patent No. 7,365,612 B2]

Figure 6-19: (a) Schematic diagram of the ultra low noise wideband oscillator (2000-3200MHz) using inductively and capacitively coupled microstripline resonator, (b) Layout of oscillator circuit (32 mils substrate, Dielectric constant 3.38)

The novel oscillator circuit layout is shown in Figure 6-19b, stable over operating temperatures of -40°C to $+85^{\circ}\text{C}$, providing sufficient margin for compensating the frequency drift caused due to the change in operating temperature, including the package parasitic and component tolerances.

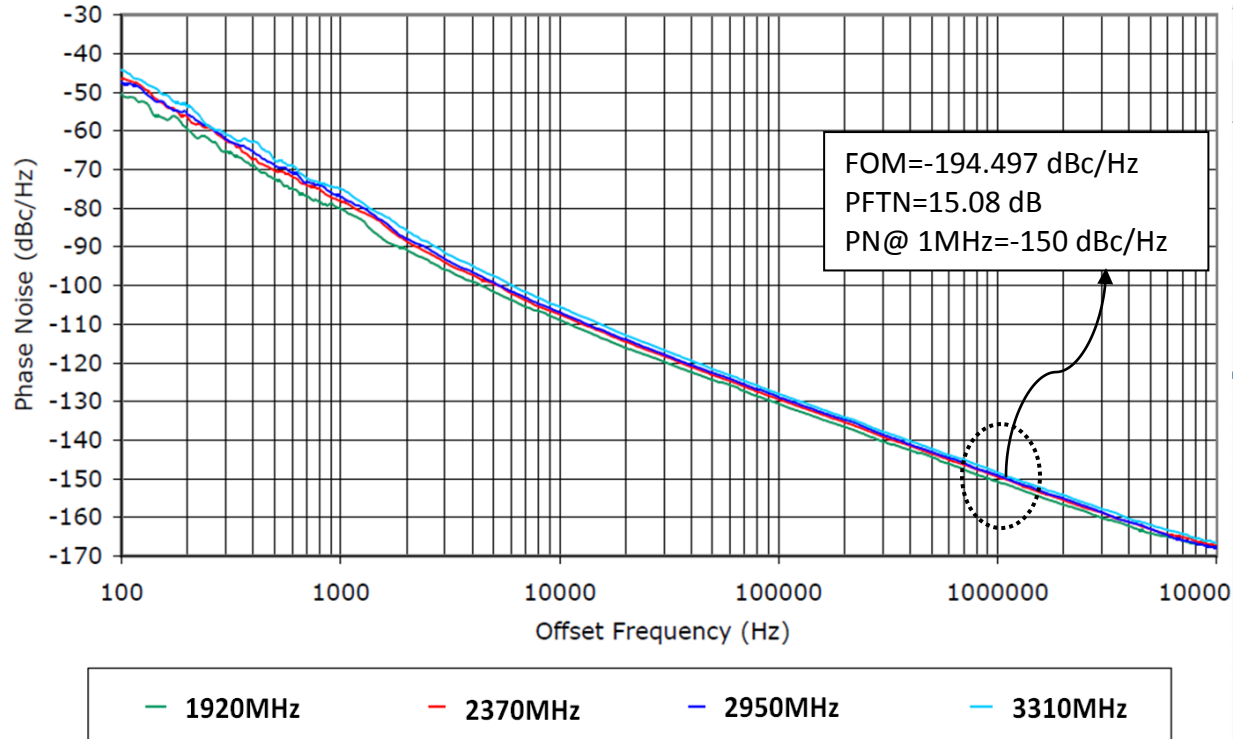


Figure 6-19c: Measured phase noise plot of the oscillator circuits shown in Figure 6-19a, The measured figure of merit (FOM: defined in Ch-1, Eq 1.1) is -194.49 for a given power-frequency tuning notmalized (PFTN: defined in Ch-1, Eq 1.2) 15.08 dB.

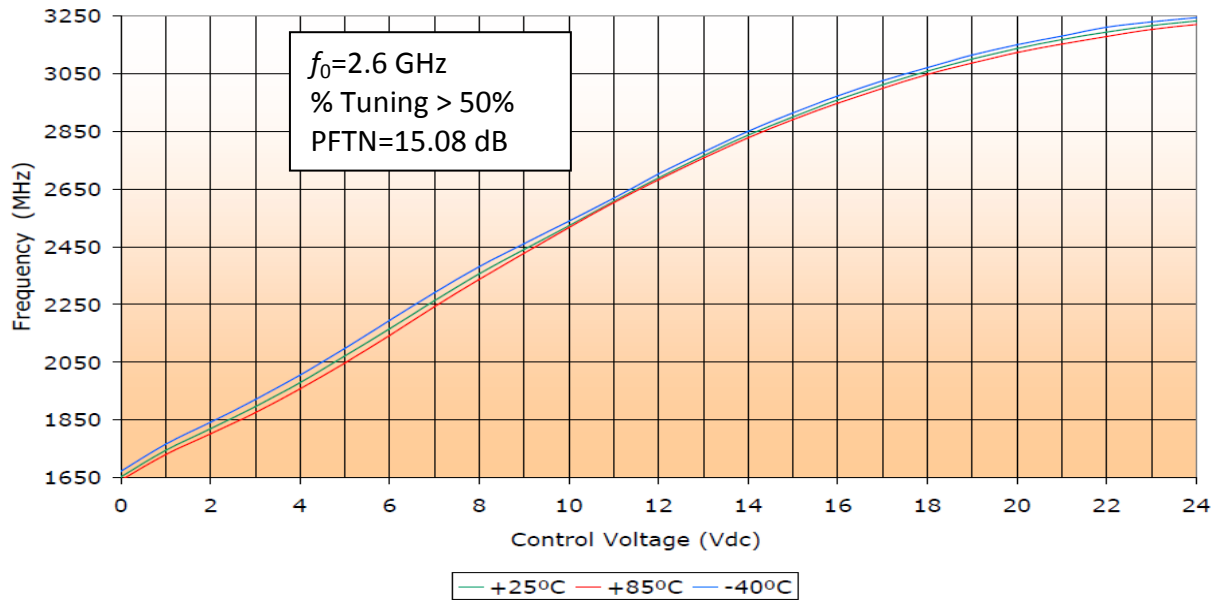


Figure 6-19d: Measured tuning characteristics of the oscillator circuits shown in Figure 6-19a, $f=1650$ MHz @ $Vt=0$ Volt) and upper ($f=3250$ MHz @ $Vt=24$ Volt)

Figure 6-19c shows the phase noise plot, the measured phase noise is better than -105dBc/Hz @10 KHz offset for the operating frequency 1900-3200MHz with 240 mW ($V_{cc}=8\text{V}$, $I_c=30\text{mA}$) power consumption.

The measured RF output power is better than 3dBm with more than 53.1 % tuning ranges (1920MHz-3310 MHz) with sufficient margin at both lower ($f=1650 \text{ MHz} @ V_t=0 \text{ Volt}$) and upper ($f=3250 \text{ MHz} @ V_t=24 \text{ Volt}$), illustrated in Figures 6-19c and 6-19d. The measured figure of merit (FOM: defined in Ch-1, Eq 1.1) is -194.49 dBc/Hz for a given power-frequency tuning normalized (PFTN: defined in Ch-1, Eq 1.2) 15.08 dB .

6.4.1.2 Hybrid-tuned Wideband Circuit (1600-3600 MHz) with Coarse and Fine-tuning

In an oscillator intended for fixed frequency operation, it is relatively easy to select the coupling parameter so that it gives optimum phase noise performance. However, for wideband tunability it is difficult to satisfy optimum coupling factor over the tuning range. The usual approach is to select the spacing between the coupled lines, compromise drive level and conduction angle that permit adequate (rather than optimum) oscillator operation over the desired tuning range. By doing so, however, optimum oscillator performance is achieved at only one frequency, if at all. Further, the use of fixed structure of microstripline necessarily limits the range of possible operating frequencies, sometime preventing certain design criteria from being met.

An alternative approach is to try to design oscillator circuit so that the optimum dimension changes, as a function of frequency, in exactly the same manner and magnitude as the frequency control signal changes as a function of tuning voltage. For the application in fast switching frequency synthesizer, hybrid tuned (facilitates coarse and fine-tuning) wideband oscillator circuit is required. Figure 6-20a shows the typical schematic of the hybrid tuned (coarse/fine) design approach that facilitates coarse and fine-tuning, and maintaining ultra low noise performance over the tuning range (1600-3600 MHz).

Figure 6-20b shows the phase noise plot, the measured phase noise is better than -90dBc/Hz @10KHz offset for the frequency 1600-3600MHz. As shown in Figure 6-20b, the coarse tuning for 1600-3600MHz frequencies is from 0.5 Volt to 16 Volts, and fine-tuning is 1-5 Volt (20-40MHz/Volt). The measured RF output power is better than +4 dBm with more than 75 % tuning rages (1600-3600 MHz)) with sufficient margin at both lower ($f=1350 \text{ MHz} @ V_t=0 \text{ Volt}$) and upper ($f=3850 \text{ MHz} @ V_t=0 \text{ Volt}$) frequencies. Notice that the variation in phase noise is within 1-3dB over operating frequency ranges, and shows state-of-the-art VCOs for a given class of the signal sources.

The measured figure of merit (FOM: defined in Ch-1, Eq 1.1) is -177.27 for a given power-frequency tuning normalized (PFTN: defined in Ch-1, Eq 1.2) 1.027 dB . The novel oscillator circuit shown in Figure 6-20a is stable over operating temperature -40°C to $+85^{\circ}\text{C}$, providing sufficient margin for compensating the frequency drift caused due to the change in operating temperature, including the package parasitics and component tolerances.

Using dynamically tuned resonator network incorporated with the tracking filter at output can use the same circuit for other user defined frequency band. Furthermore, to compensate process and temperature variations, a VCO coarse-tuning (with high gain) would make the circuit more sensitive to coupling from nearby circuits and power supply noise.

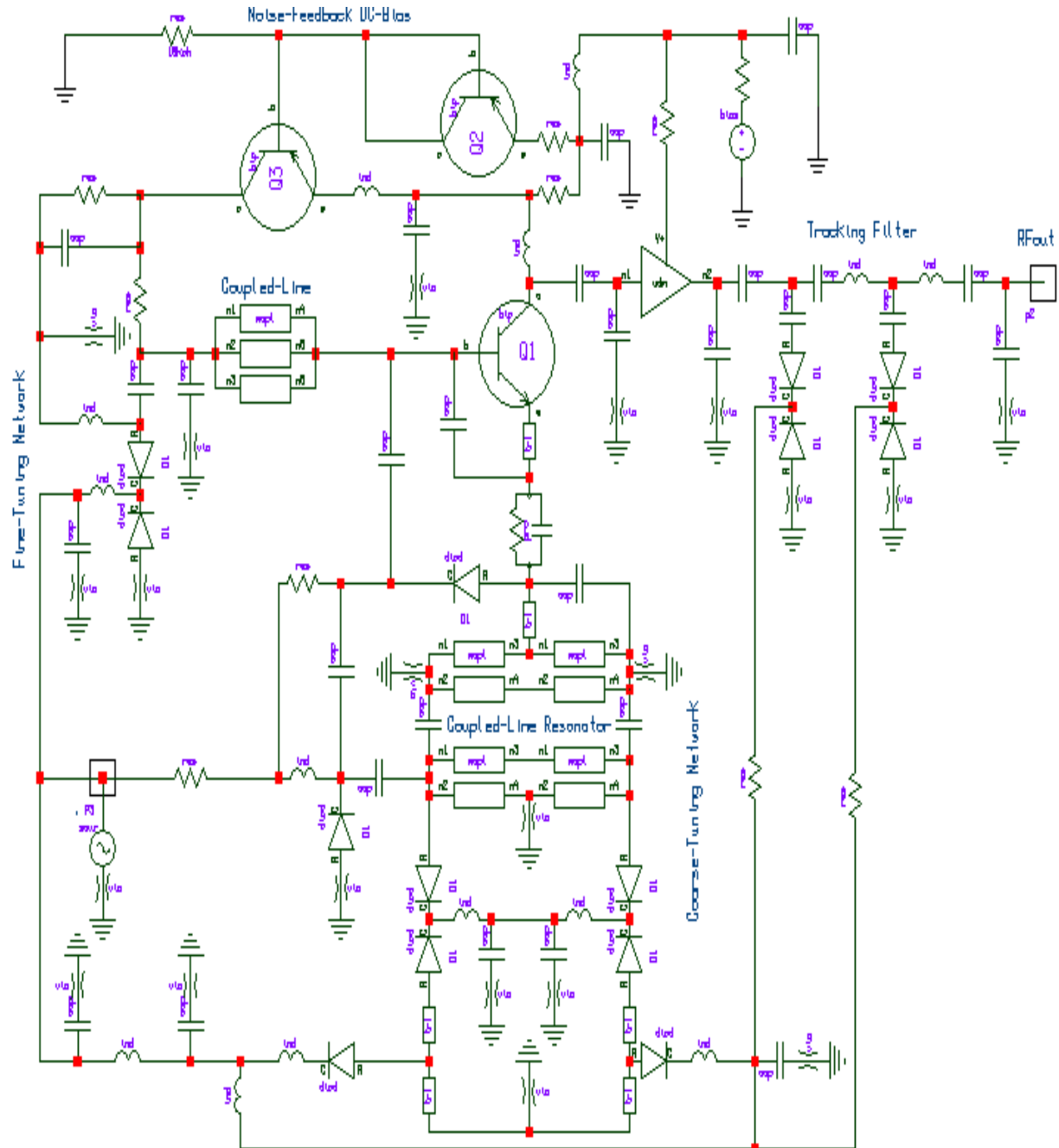


Figure 6-20a: Schematic diagram of hybrid-tuned ultra low noise wideband (1600-3600MHz) (SWRO) with 240 mW ($V_{cc}=10V$, $I_c=40mA$), tuning characteristics: $f=1350$ MHz @ $V_t=0$ Volt $f=3850$ MHz @ $V_t=0$ Volt [65]

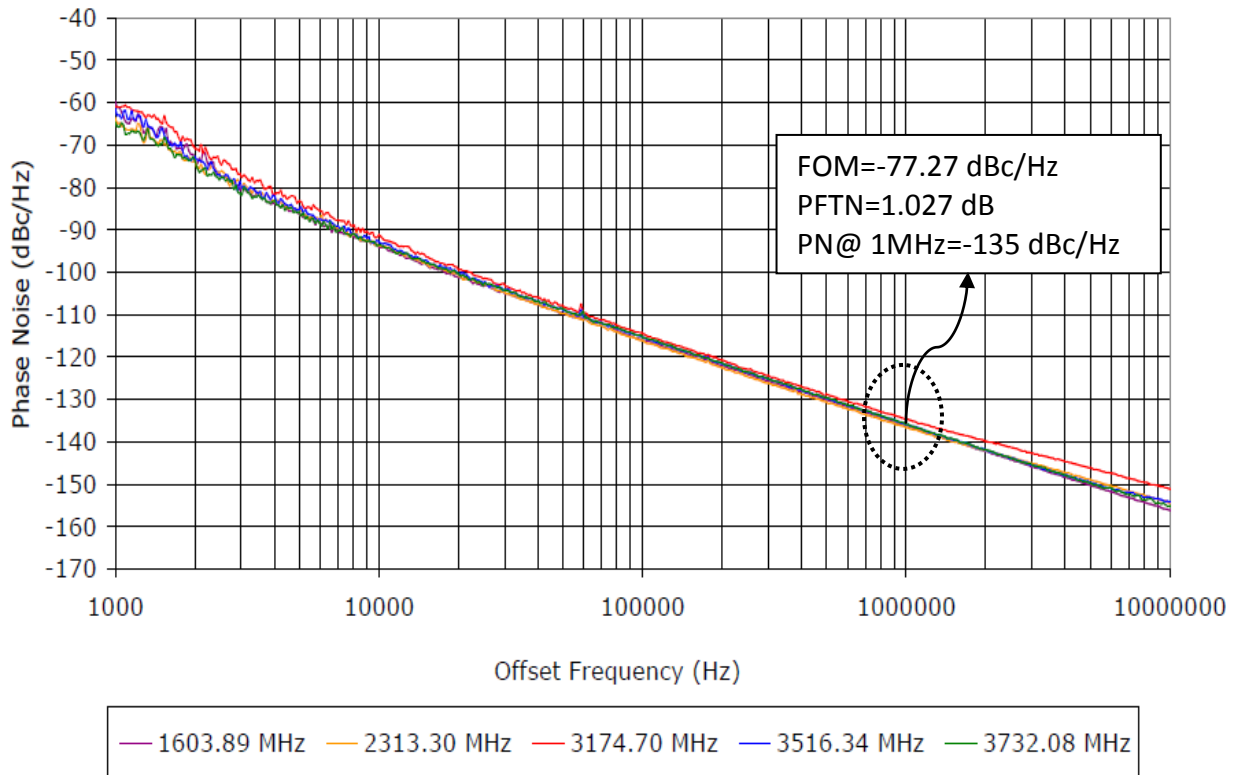


Figure 6-20b: Measured phase noise plot of the oscillator circuits shown in Figure 6-20a, measured figure of merit (FOM: defined in Ch-1, Eq 1.1) is -77.27 dBc/Hz for a given power-frequency tuning normalized (PFTN: defined in Ch-1, Eq 1.2) 1.027 dB .

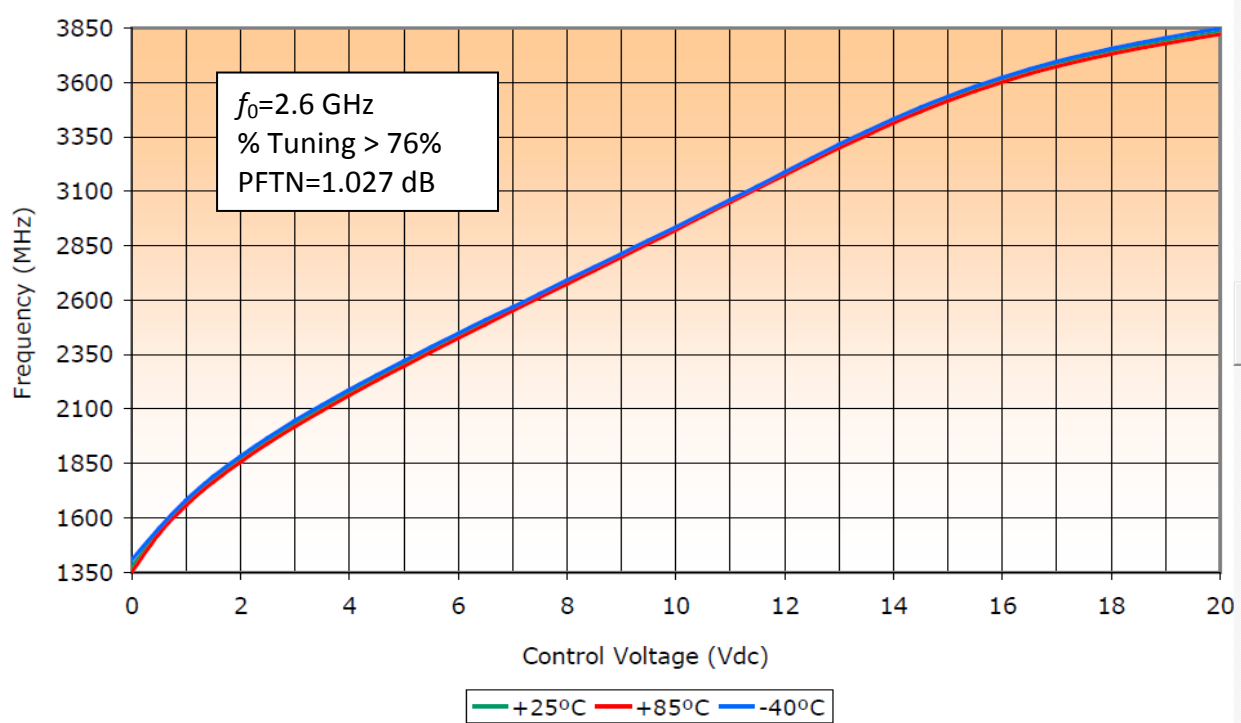


Figure 6-20c: Measured tuning characteristics of the oscillator circuits shown in Figure 6-20a, $f=1350 \text{ MHz}$ @ $V_t=0$ Volt and $f=3850 \text{ MHz}$ @ $V_t=24$ Volt

To overcome this problem, fine-tuning network is incorporated at proper node of the oscillator circuit, which needs less gain to cover temperature and supply variations that minimizes the noise interference. The circuit operates at 12 Volt and 25 mA, and gives power output more than 4 dBm (Figure 6-20d) over the tuning range (1600 MHz -3600 MHz).

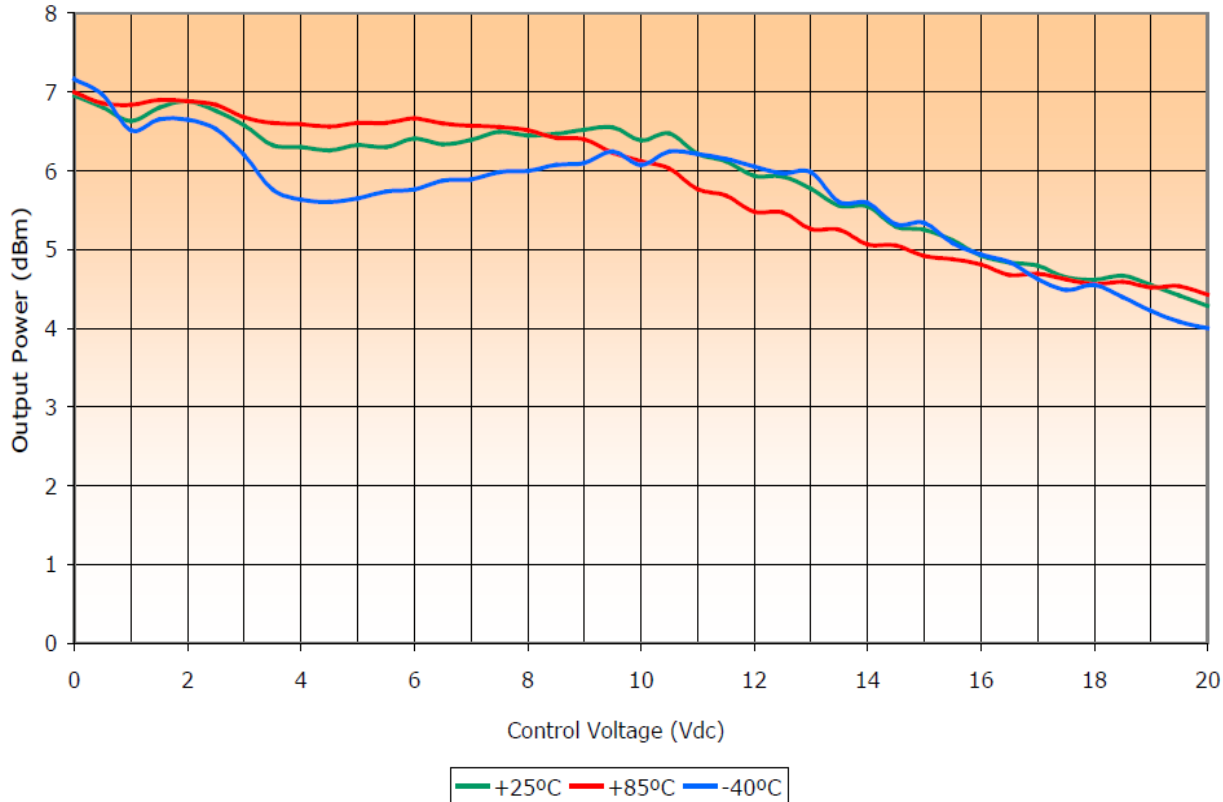


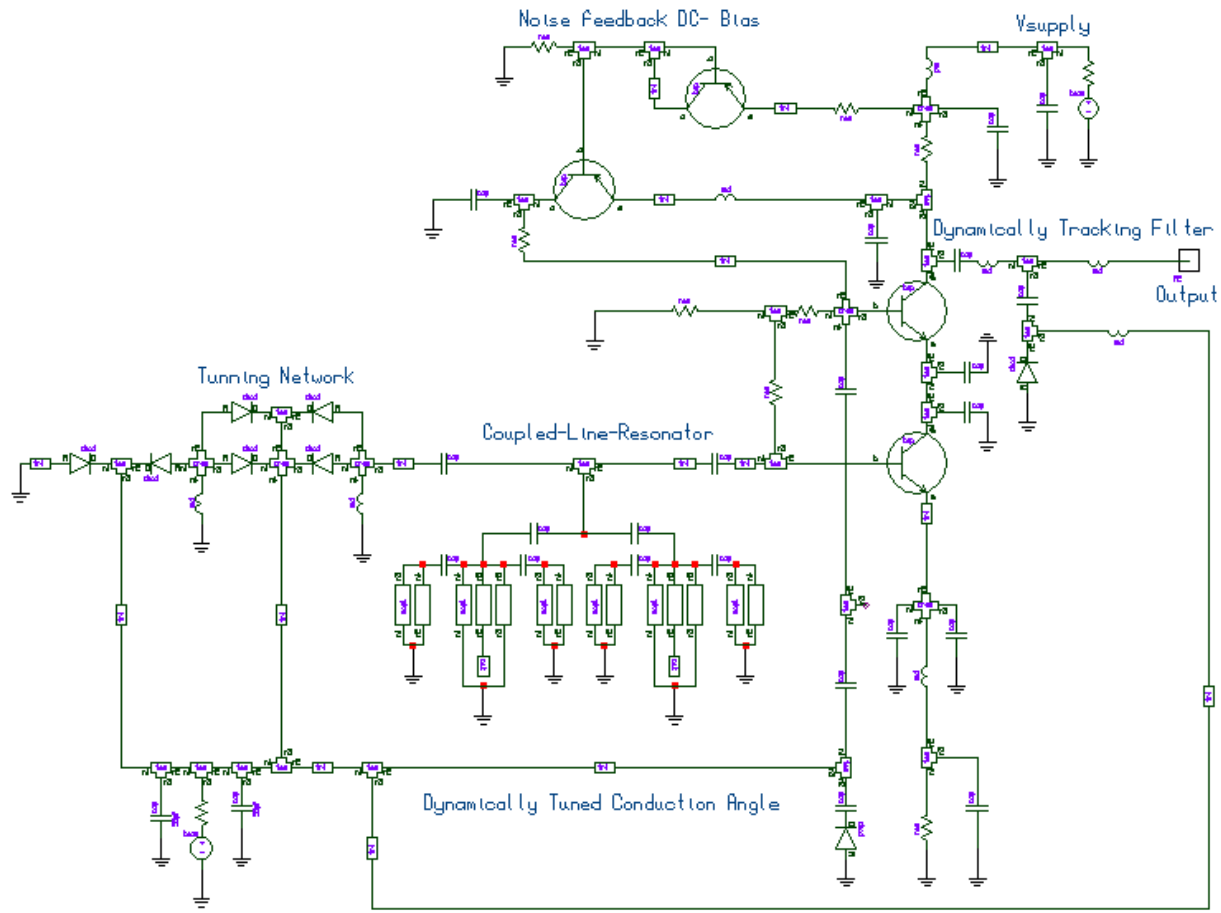
Figure 6-20d: Measured plot of output power of the oscillator circuits shown in Figure 6-20a, The measured RF output power is better than +4 dBm with more than 75 % tuning ranges (1600-3600 MHz) with sufficient margin at both lower ($f=1350$ MHz @ $V_t=0$ Volt) and upper ($f=3850$ MHz @ $V_t=0$ Volt).

6.4.1.3 Power-Efficient Wideband SWRO Circuit (2000-3000 MHz)

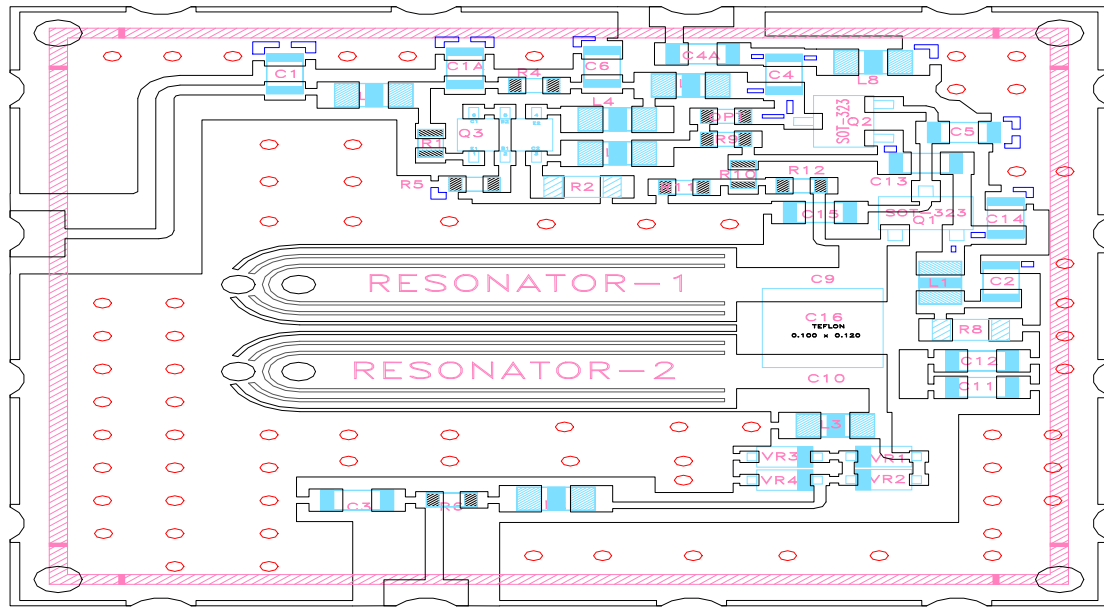
The reported oscillator circuit shown in Figure 6-21 offers the power-efficient (current effective topology), realized by incorporating two, three terminal active devices (bipolar transistors) in cascode configuration so that both the devices share the same bias current. The circuit operates at 10V and 15 mA of current, and gives power output better than -3dBm.

As shown in Figure 6-21, the voltage controlled oscillator, comprising a cascode configuration of the 3-terminal active device is arranged in a common collector and emitter configuration for generating negative resistance under current efficient operation for wideband (2000-3000MHz) signal source applications.

The applications where the phase noise performance at lower offset from the carrier is critical, the reported novel circuit supports ultra low noise performance over the tuning range. Figure 6-21c shows the CAD simulated phase noise plot, typically better than -156 dBc/Hz at 1 MHz offset for 2000-3000 MHz tuning range.



(a) A typical schematic of the cascode (SWRO) circuit (2000-3000 MHz) with 150 mW ($V_{cc}=5V$, $I_c=30mA$) [65]



(b) Layout of the cascode (SWRO) circuit (0.75x0.75x0.18 inches [US Patent No. 7,365,612 B2]

Figure 6-21: A typical power-efficient wideband (SWRO) circuit (a) Schematic of the cascode configuration, and (b) Layout of oscillator circuit (32 mils substrate, Dielectric constant 3.38) [65]

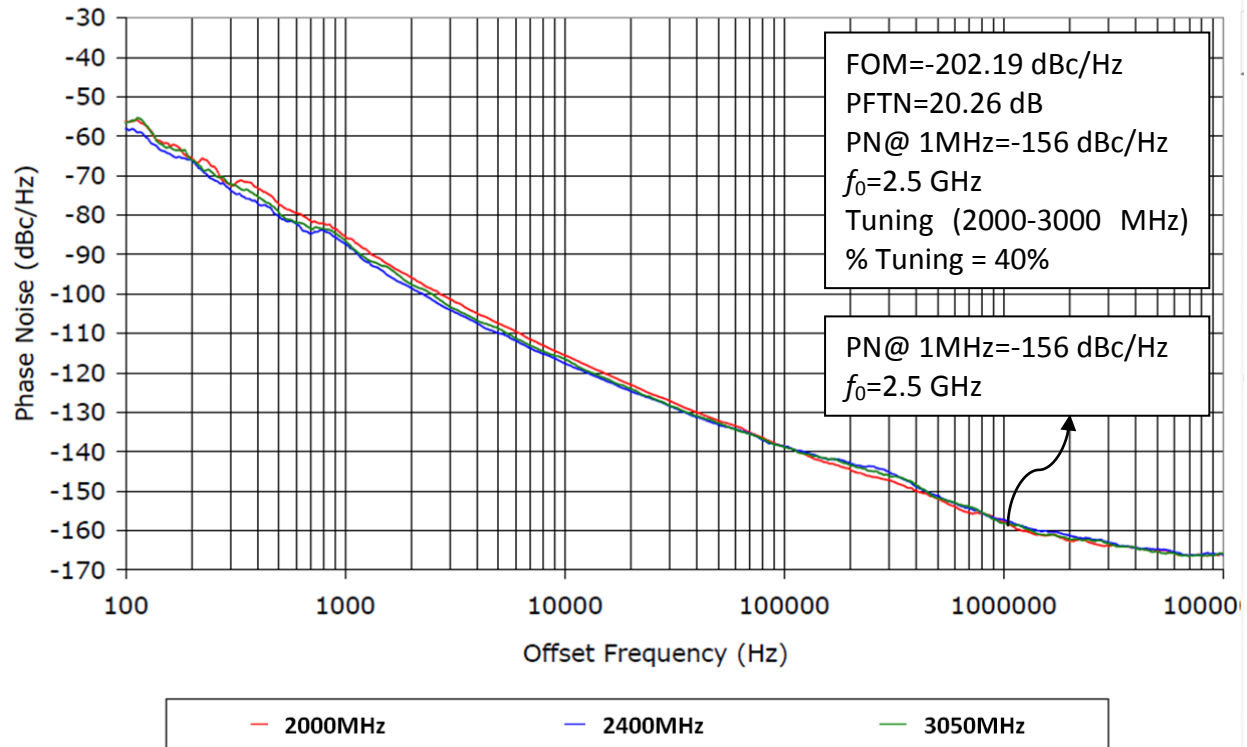


Figure 6-21c: Measured phase noise plot of ultra low noise power efficient wideband (2-3 GHz) (SWRO), measured figure of merit (FOM: defined in Ch-1, Eq 1.1) is -202.19 dBc/Hz for a given power-frequency tuning normalized (PFTN: defined in Ch-1, Eq 1.2) 20.26 dB, with power consumption of 150mW ($V_{cc}=10\text{V}$, $I_c=15\text{mA}$), o/p power is 0dBm .

The proposed oscillator topology (Figure 6-21a) improves the phase noise and thermal drift and also extends the operating frequency of the microstripline based resonator to higher frequency band depending upon the coupling network. The freedom of selection of the frequency, ultra low phase noise, wide tuning range, and stability over temperature will make this technology promising and attractive for next generation integrated high frequency mobile communication system. The novel oscillator circuits shown in Figure 6-21a is stable over operating temperature -40°C to $+85^{\circ}\text{C}$, providing sufficient margin for compensating the frequency drift caused due to the change in operating temperature, including the package parasitic and component tolerances.

6.4.1.4 User-Defined Ultra Low phase Noise Oscillator Circuit [U.S. Patent No. 7,586,381]

The applications where the phase noise performance is most demanding parameter, proposed oscillator topology shown in Figure 6-22 offers user-defined and cost-effective alternative of expensive SAW (surface acoustic wave) and ceramic resonator based oscillators. Ceramic and SAW resonator based oscillators are used as ultra low phase noise oscillators but these high Q resonators are expensive and its availability and performances are limited to the selected frequency and narrow operating temperature range, and these facts make them not suitable for operating in stringent temperature environment and low cost application [7]-[37]. In addition, ceramic resonators are more susceptible to noise interference, and sensitive to phase-hit in PLL applications [30]-[36].

Microstripline resonators are not without flaws, and are susceptible to noise interference, and they exhibit lower quality factor as compared to ceramic resonators. Quality factor of the resonator is the key factor for low phase noise performance but overall oscillator performance is controlled by the time average loaded Q of the oscillator circuit.

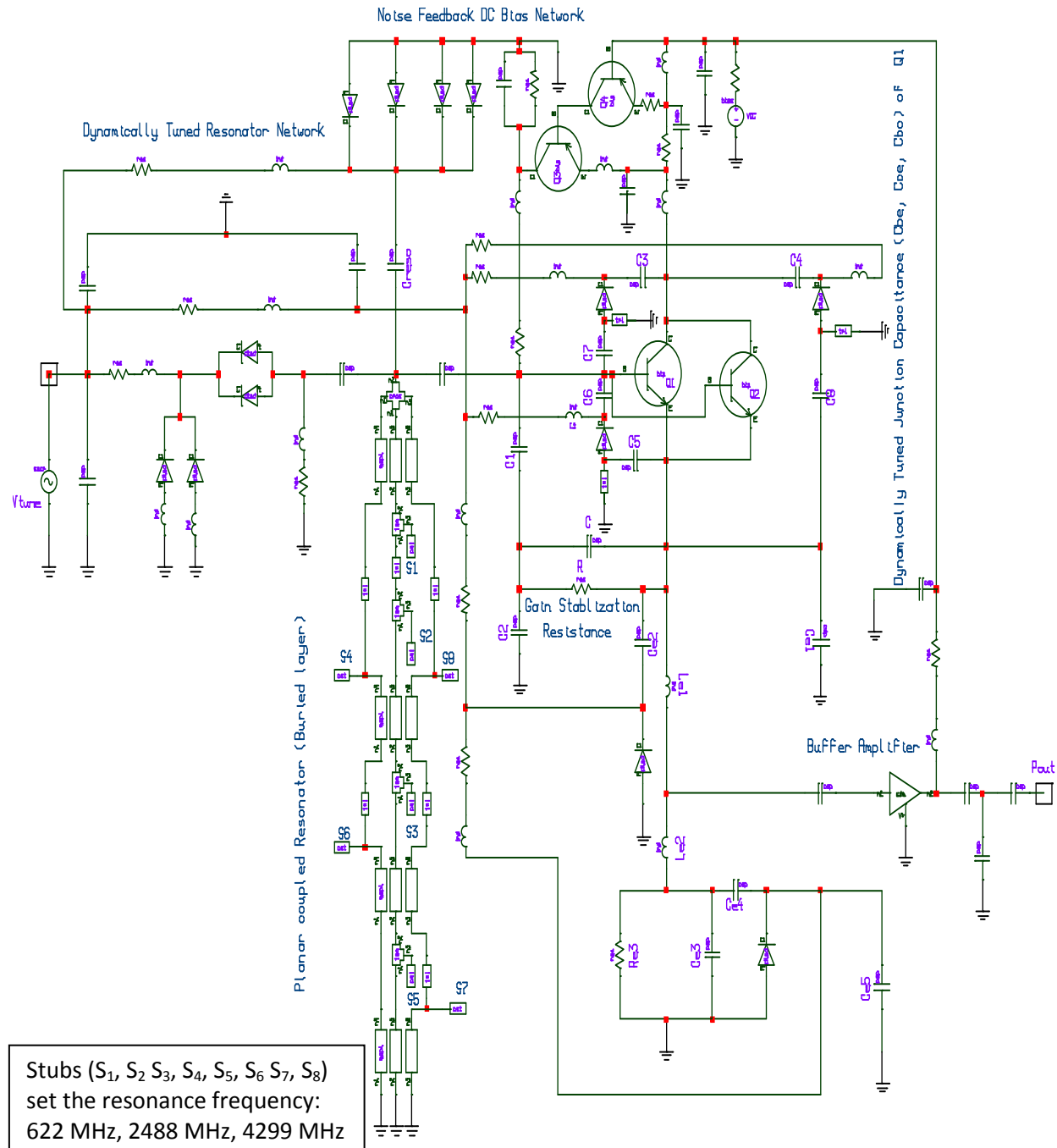


Figure 6-22a illustrates a layout of the oscillator with planar multi-coupled stripline resonator constructed in accordance with the alternative of expensive non-planar SAW and Ceramic resonator based oscillator circuits, with 100 mW ($V_{cc}=5V$, $I_c=20mA$), RF output power is +5 dBm [U.S. Patent No. 7,586,381] [68]

For the most part, these disadvantages have been overcome by means of novel configuration of the compact coupled planar resonator (CCPR) and act like slow wave propagation for improving group delay, thereby improved time average quality factor. The effective Q of the coupled resonator network improves by optimizing the rate of change of the phase over the tuning range by dynamically tuning the coupling parameter.

Figure 6-22b illustrates a layout of the user-defined high spectral purity oscillator with multi-coupled line buried slow wave resonator (SWR) constructed that configures suitable independent transfer function of the resonator by incorporating dynamically tuned junction capacitances (C_{be} , C_{ce} , C_{ce} of Q1), drive level, noise-filtering network across emitter and planar-coupled resonator [68]. They have been fabricated on low-loss 30-mil-thick dielectric material with dielectric constant of 3.38, and tested from 1 to 18 GHz for user-defined frequency sources for reconfigurable synthesizer applications.

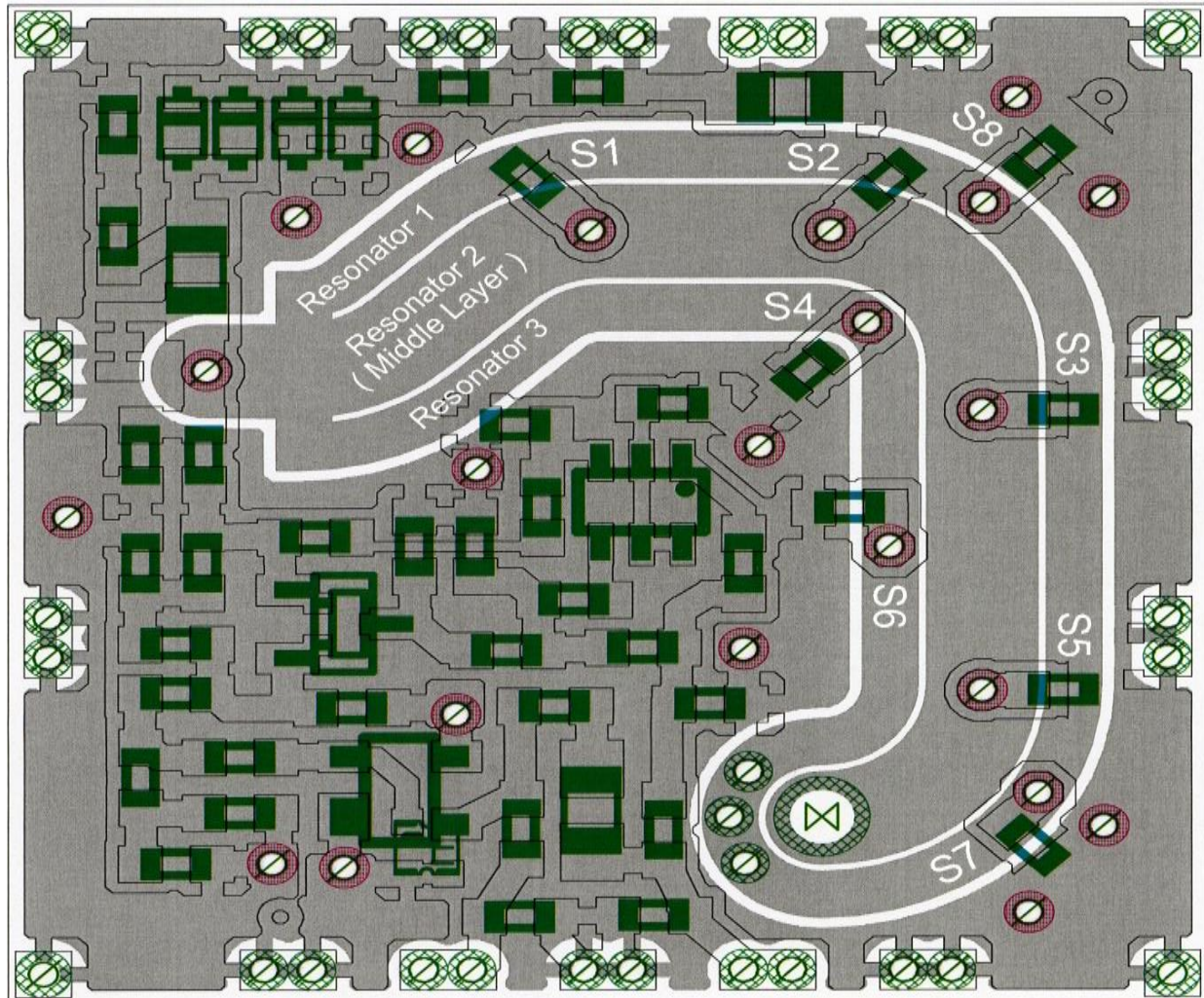


Figure 6-22b: shows a layout of the user defined high spectral purity oscillator with multi-coupled line buried slow wave resonator (SWR) VCO circuit (64 mills substrate, Dielectric constant 3.38) 0.75x0.75x0.18 inches, stubs (S_1 , S_2 , S_3 , S_4 , S_5 , S_6 , S_7 , S_8) sets the desire frequency (622 MHz, 2488 MHz, 4200 MHz) [U.S. Patent No. 7,586,381] [68].

Shown in Figure 6-22b, are printed multi-coupled resonators, positioned parallel to each other, in such a way that adjacent resonators are coupled along the guided length for the given frequencies. The layout shown in 6-22b is 6-layer board, fabricated on 64mil thick ROGER-substrate of dielectric constant 3.38 and loss tangent 2.7×10^4 . The choice of substrate depends on size, higher-order modes, surface wave effects, implementation (couplings, line length, width, spacing, and spacing tolerances), dielectric loss, temperature stability, and power handling (dielectric strength and thermal conductivity). Figure 6-22c depicts the measured phase noise plot of the oscillator circuit shown in the Figure 6-22a for the typical frequency 622 MHz, 1000 MHz, and 2488 MHz; realized by arrangement of stubs-tuning ($S_1, S_2, S_3, S_4, S_5, S_6, S_7, S_8$) as shown in the layout in Figure 6-22b.

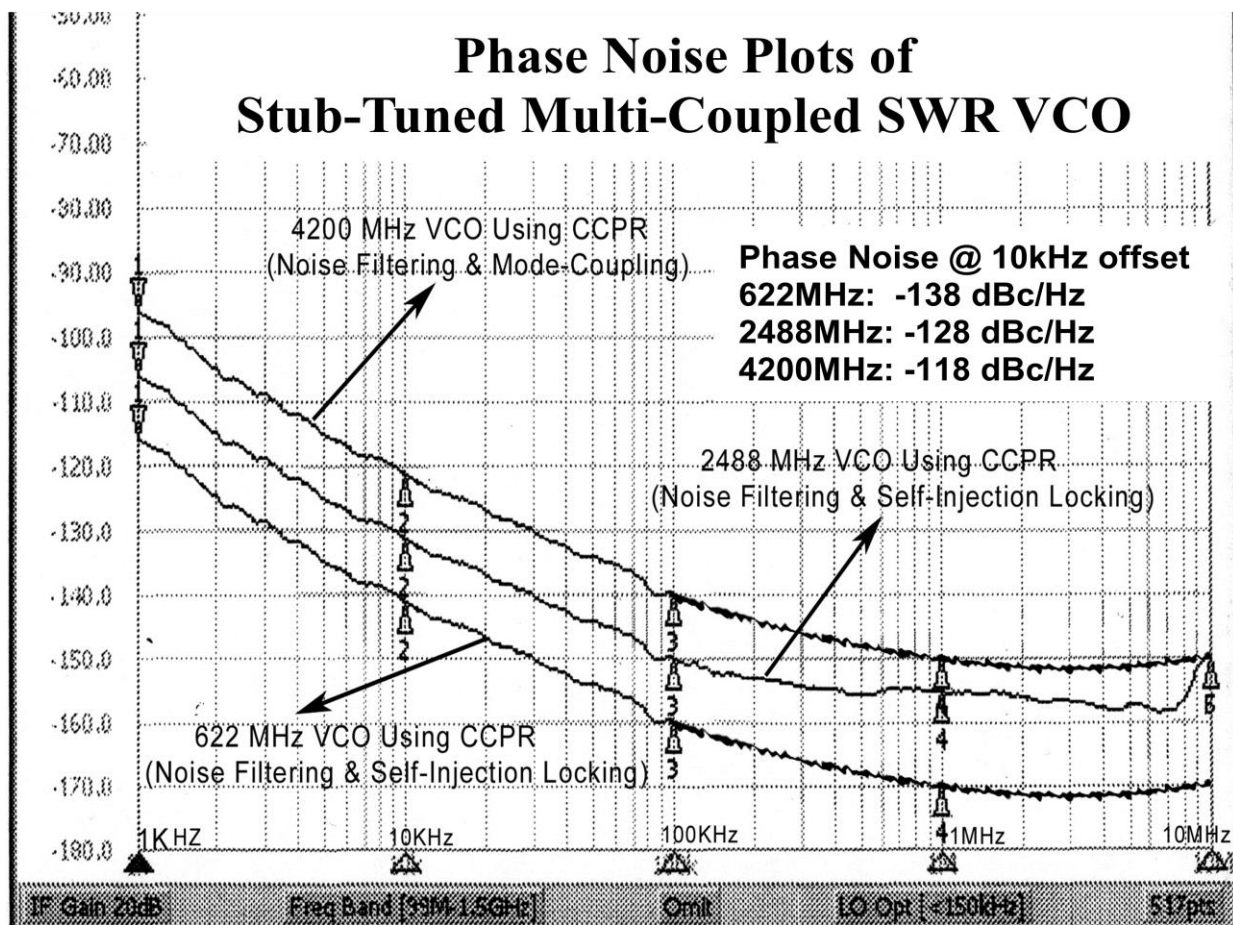


Figure 6-22c: Depicts the measured phase noise plot of the compact coupled planar resonator (CCPR) oscillator circuit shown in the Figure 6-22a for the typical frequency 622 MHz, 2488MHz, and 4200 MHz realized by arrangement of stubs-tuning ($S_1, S_2, S_3, S_4, S_5, S_6, S_7, S_8$) as shown in the layout in Figure 6-22b, measured figure of merit (FOM: defined in Ch-1, Eq 1.1) is -205.876 dBc/Hz for $f_o=622$ MHz, -202.9 dBc/Hz for $f_o=2488$ MHz, -205.46 dBc/Hz for $f_o=4200$ MHz ; with power consumption of 100mW ($V_{cc}=5V$, $I_c=20mA$), RF o/p power is 3.3 dBm

As shown in Figure 6-22c, the typical phase noise @ 10 kHz offset from the carrier, typical values: -138 dBc/Hz (carrier frequency: 622MHz), -128 dBc/Hz (carrier frequency: 2488MHz), and -118 dBc/Hz (carrier frequency: 4200 MHz); and is not limited to these frequencies. The circuit works at 5V, 20mA, and typical output power is 5 dBm, and second harmonic rejection is better than -20 dBc . The measured figure of merit measured figure of merit (FOM: defined in Ch-1, Eq 1.1) is -205.876 dBc/Hz for $f_o=622\text{ MHz}$ with o/p power of $+5\text{ dBm}$, -202.9 dBc/Hz for $f_o=2488\text{ MHz}$ with output power of $+4.2\text{ dBm}$, -205.46 dBc/Hz for $f_o=4200\text{ MHz}$ with output power of $+3.3\text{ dBm}$. The total power consumption of the oscillator circuit shown in Figure 6-33a is 100mW ($V_{cc}=5\text{V}$, $I_c=20\text{mA}$) with stable RF output power better than 3.3 dBm over operating temperature -40 degree C to +85 degree C.

6.4.1.5 Multi-Octave Band SWRO Circuit (U.S. Patent No. 7,605,670) [69]

Modern communication systems are multi-band and multi-mode, therefore requiring an ultra wideband low noise signal source that may allow accessing simultaneously DCS1800, PCS 1900, and WCDMA networks by a single ultra low noise wideband VCO. An ultra low noise, low cost and power efficient VCO is reported that can be tuned over a fairly wide range of frequencies while maintaining the low phase noise over the band.

As a multi-coupled slow-wave (MCSWR) VCO is planar and broadband in nature, it is suited for cost-effective, monolithic-microwave-integrated-circuit (MMIC) fabrication [76]-[83]. With the potential to enable wide operational bandwidths, eliminate discrete resonator (such as a YIG sphere), and produce high-quality-factor planar resonator for low noise VCOs by means of planar fabrication process compatible with existing IC and MMIC processes, the MCSW VCO is a promising technology for present and future broadband communication requirements. The MCSW, for example, is well suited for use in microwave communication systems, test equipment, radar, local multi-point-distribution systems (LMDS), and multi-channel multi-point distribution systems (MMDS).

The multi-coupled distributed resonator design approach demonstrated in this work can satisfy the need for the present demand for wideband VCO, and amenable for integration in chip form. To support a uniform negative resistance over the tuning range, the varactor tuned coupled resonator shown in the Figure 6-23a is connected across the base and collector of the active device, and the loss resistance is compensated by the negative resistance, which dynamically adjusts in response to the change in oscillator frequency over the band by dynamically tuning the phase shift of the negative resistance-generating network to meet the phase shift criteria for the resonance over the operating frequency band of interest. The variable coupling capacitor C_c as shown in Figure 6-23a is designed for the optimum loading of the coupled resonator network across the active device, and dynamically tuned for optimum performance.

The time average Q factor of the resonator has been improved by dynamically optimizing the coupling factor β of the multi-coupled distributed resonator over the desired tuning range. Shown in the Figure 6-23a, is the coupled resonator connected across the base and collector of the three-terminal active device through coupling capacitor, which is electronically tuned by applying the tuning voltage to the tuning network integrated with the coupled resonator. The

values of the coupling capacitor C_c are derived from the input stability circle, and it should be within the input stability circle so that the circuit will oscillate at a particular frequency for the given lowest possible value of the C_c over the band. Figure 6-23b depicts the layout of the Figure 6-23a, points to a planar topology and amenable for integrated circuit solution [69]. The drawback of this topology is mode-jumping; causing drop of oscillation in the desired frequency band, which can be suppressed by incorporating phase-compensating network in conjunction with progressive wave coupled resonator network [75].

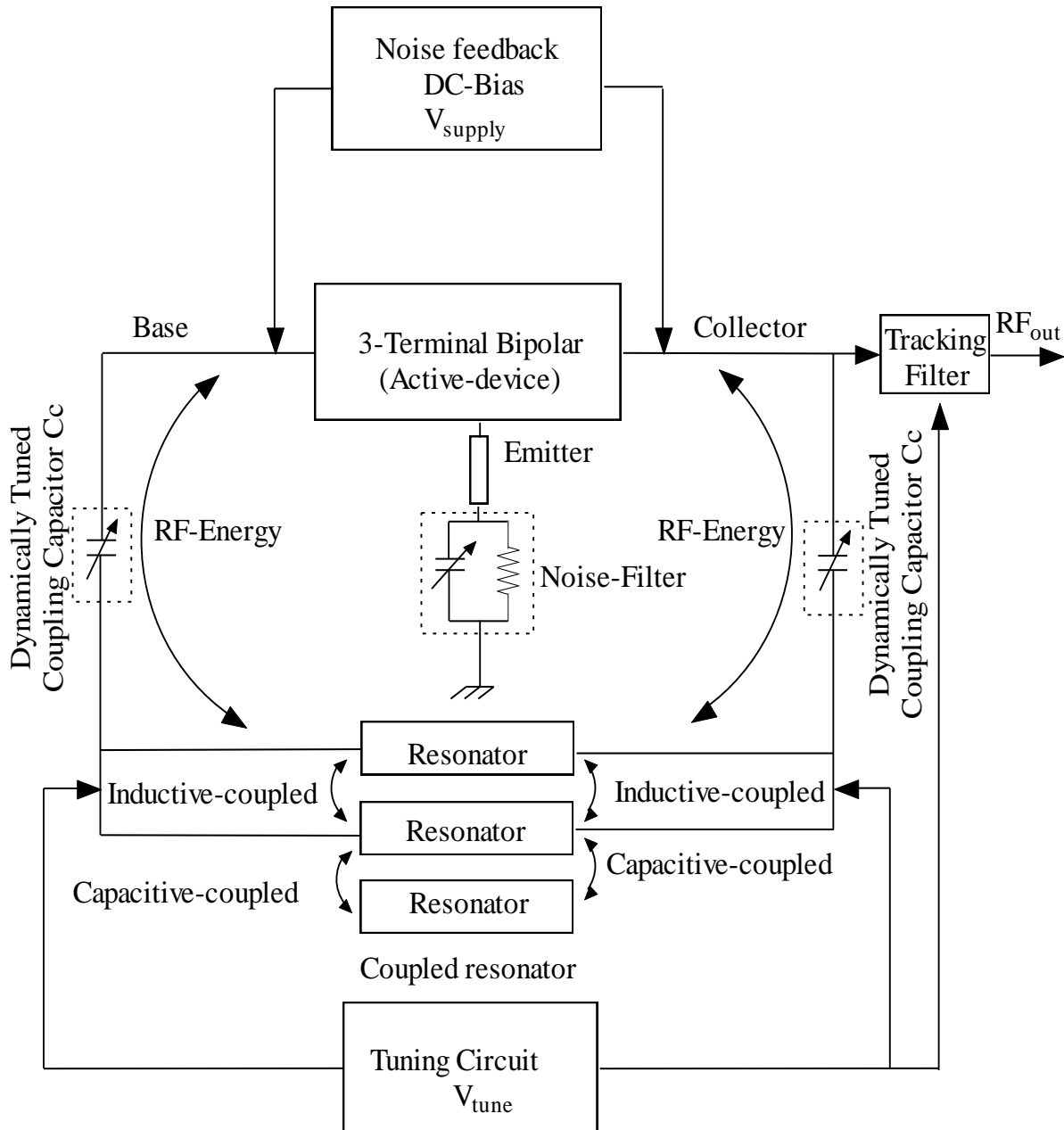


Figure 6-23a: A typical block diagram of the wideband VCO [69]

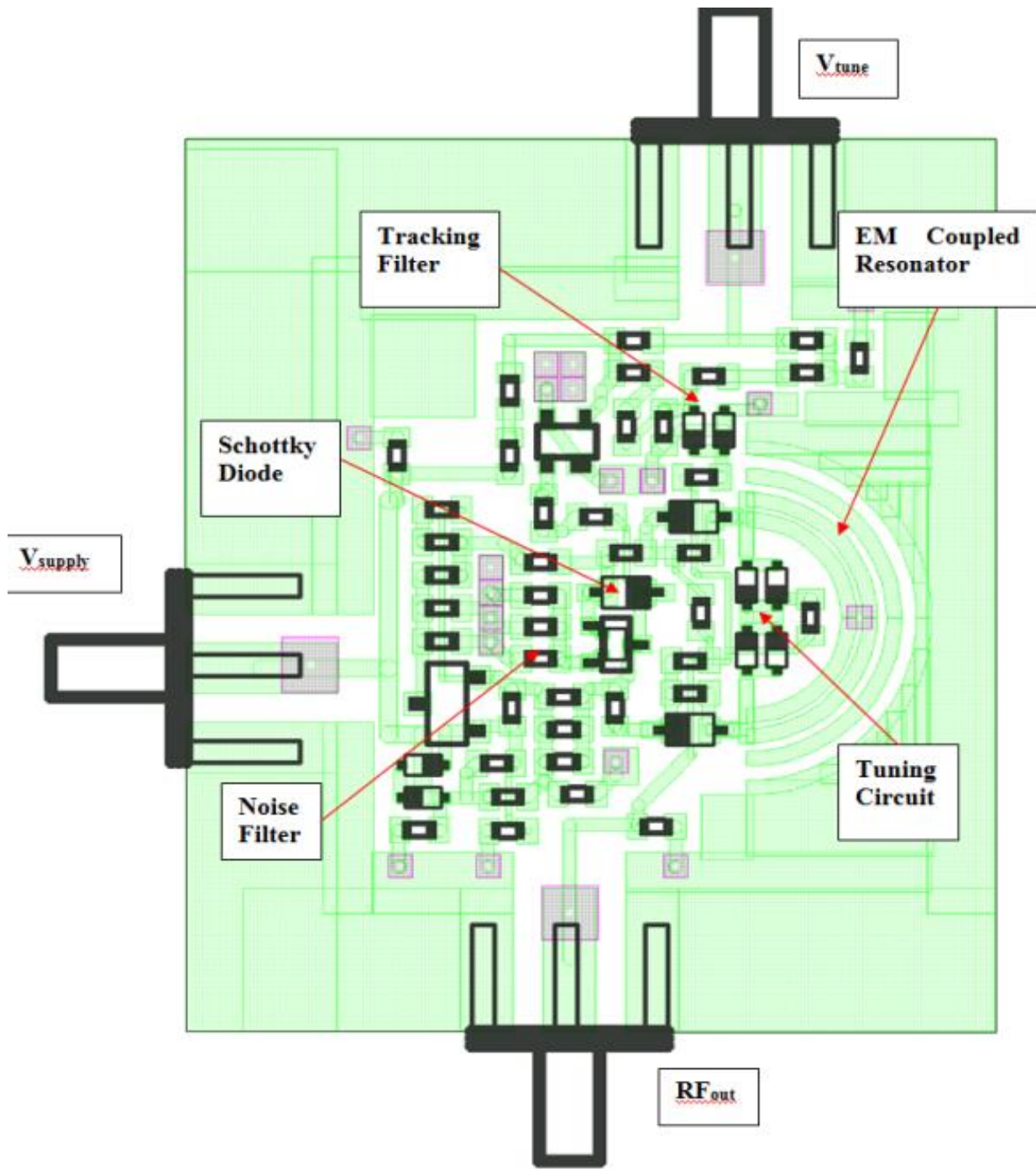


Figure 6-23b: Shows the layout of the oscillator circuit shown in Figure 6-23a, layout is made on 32 mil substrate with Dielectric constant 3.38 in 0.75x0.75x0.18 inches size [U.S. Patent No. 7,586,381] [69]

Figure 6-24a shows a typical block diagram of multi-octave band oscillator circuit using a combination of printed multi-mode, progressive wave, slow-wave coupled resonator for ultra low phase noise and multi-octave band operation [69]. This arrangement can be characterized as a Q-multiplier effect based on evanescent-mode progressive delay that eventually improves the time average loaded Q of the planar resonator over its multi-octave operation.

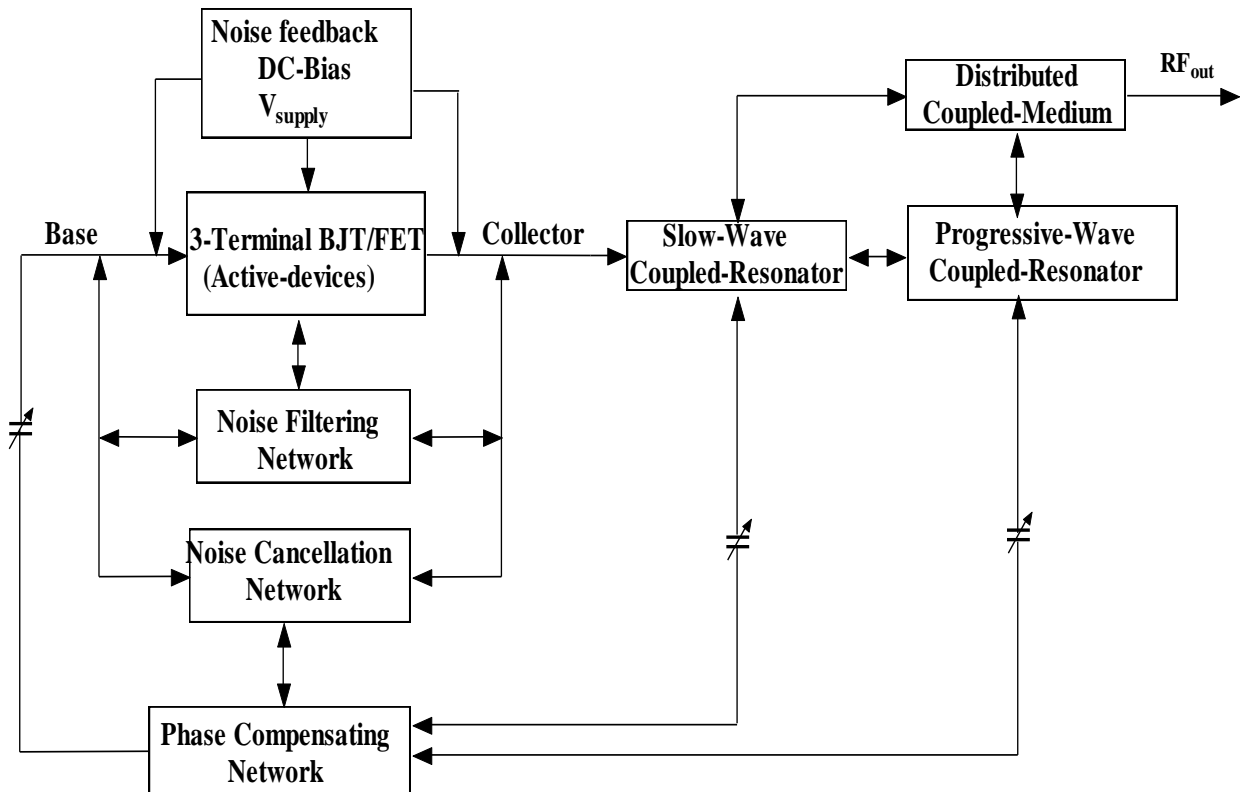


Figure 6-24a: Illustratively depicts a functional block diagram of an oscillator using multi-mode, progressive wave, slow-wave coupled resonator for ultra low phase noise and multi-octave band operation with DC bias of 5V and 40mA.

As shown in Figure 6-24a, the oscillator includes a 3-terminal active device (bipolar transistor NEC 68830), noise filtering network, and a noise cancellation network connected in parallel between the base and collector terminals.

Figure 6-25 shows the transistor (NE 68830) with the package parameters for the optimization of the wideband tuning characteristics. Table 6.2 shows the transistor spice and package parameters of NE68830 from manufacturer (NEC) data sheets.

A noise feedback and DC bias supply (shown in Figure 6-24a) comprises an active feedback network that compensates for change in the DC bias power supply voltage owing to change in the operating temperature of the oscillator or its environment [64]. The active impedance created by the three-terminal device (e.g., a Bipolar or FET transistor) in a MCSWR (multi coupled slow-wave resonator) oscillator circuit exhibits a negative real part with a real magnitude and an imaginary part with an imaginary magnitude. The real magnitude is a function of the imaginary magnitude. The imaginary magnitude is selected such that the real magnitude compensates for the loss of the MCSWR network. The selection of the imaginary magnitude should also coincide with the maximum-slope inflection point of the oscillator's phase characteristics curve, in order to optimize group delay performance.

Figure 6-24b shows the printed circuit board (PCB) layout diagrams of a VCO constructed in accordance with the description shown in block diagram (Figure 6-24a) with an aspect of multi-octave tuning characteristics in which the resonator comprised of multi-mode coupled resonator, progressive wave coupled resonator, and slow-wave coupled resonator network, including the mode-coupling and self-injection locking. Each of these resonators is planar in the form and electromagnetically coupled to each other. As explained above the electromagnetic-coupling between these resonators provide for the wideband tunability and other performance benefits associated with these oscillators. As is also shown, the slow-wave coupled resonator comprises a planar structure having projections that mate with openings (meander lines that support slow wave dynamics).

The unified resonator structure comprised of slow wave and progressive wave resonator network depicted in Figure 6-24b form in combination a single high Q-factor resonator network. The combination of slow-wave resonator and progressive wave resonator enables the advantage of the wideband tunability. The limitation of spurious frequencies of the multi-mode resonator are shifted from the integer multiples of the fundamental resonant frequency, enabling multi-octave band tuning, which otherwise is not possible by using independently either the multi-mode resonator, slow-wave resonator or progressive-wave resonator [76]-[91].

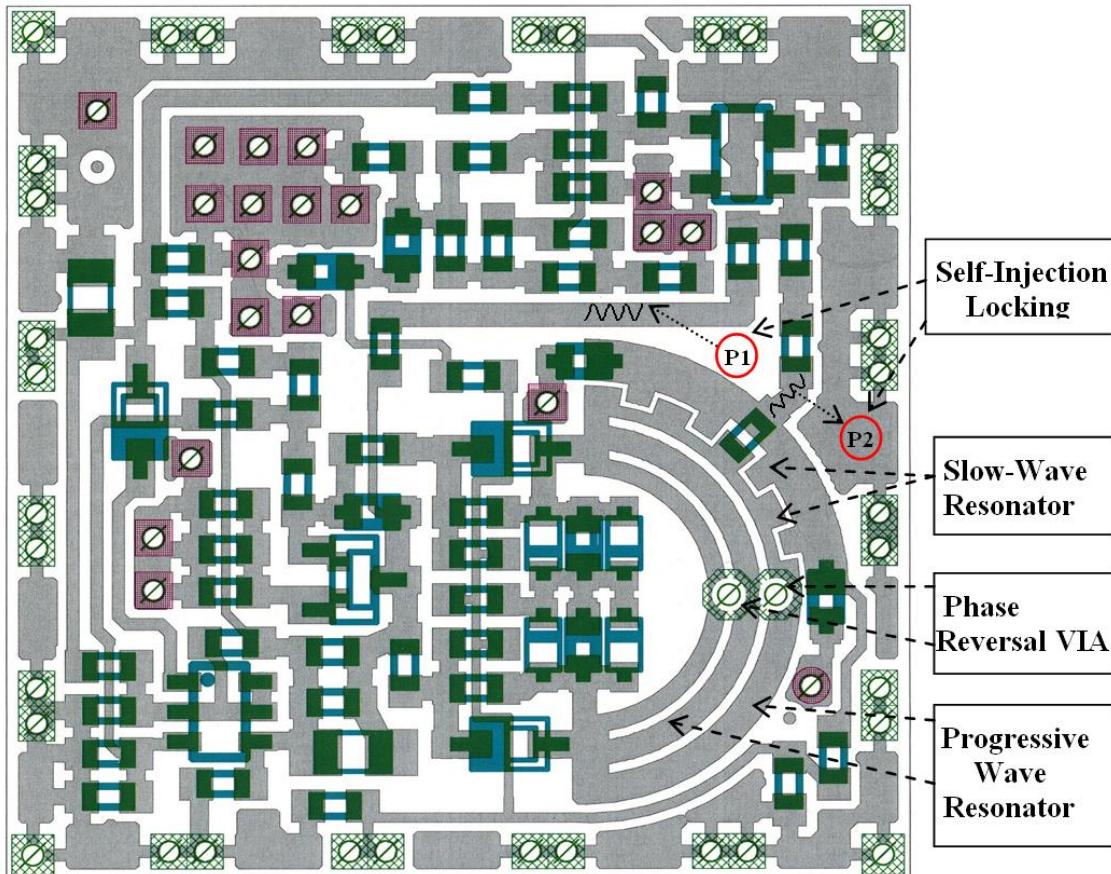


Figure 6-24b: shows the printed layout diagram of an oscillator as per block diagram shown in Figure 6-24a, points to a MMIC technology, layout is made on 32 mils substrate with Dielectric constant 3.38 in 0.75x0.75x0.18 inches.

Table 6.2: Spice parameters (Gummel-Poon Model, Berkley-Spice) [67, pp. 134]

Spice Parameters	Values	Spice Parameters	Value	Packages	NE 68830
IS	3.8E-16	MJC	0.48	C_{CB}	0.24E-12
BF	135.7	XCJC	0.56	C_{CE}	0.27E-12
NF	1	CJS	0	L_B	0.5E-9
VAF	28	VJS	0.75	L_E	0.86E-9
IKF	0.6	MJS	0	C_{CBPKG}	0.08E-12
NE	1.49	TF	11E-12	C_{CEPKG}	0.04E-12
BR	12.3	XTF	0.36	C_{BEPKG}	0.04E-12
NR	1.1	VTF	0.65	L_{BX}	0.2E-9
VAR	3.5	ITF	0.61	L_{CX}	0.1E-9
IKR	0.06	PTF	50	L_{EX}	0.2E-9
ISC	3.5E-16	TR	32E-12		
NC	1.62	EG	1.11		
RE	0.4	XTB	0		
RC	4.2	KF	0		
CJE	0.79E-12	AF	1		
CJC	0.549E-12	VJE	0.71		
XTI	3	RB	6.14		
RBM	3.5	RC	4.2		
IRB	0.001	CJE	0.79E-12		
CJC	0.549E-12	MJE	0.38		
VJC	0.65				

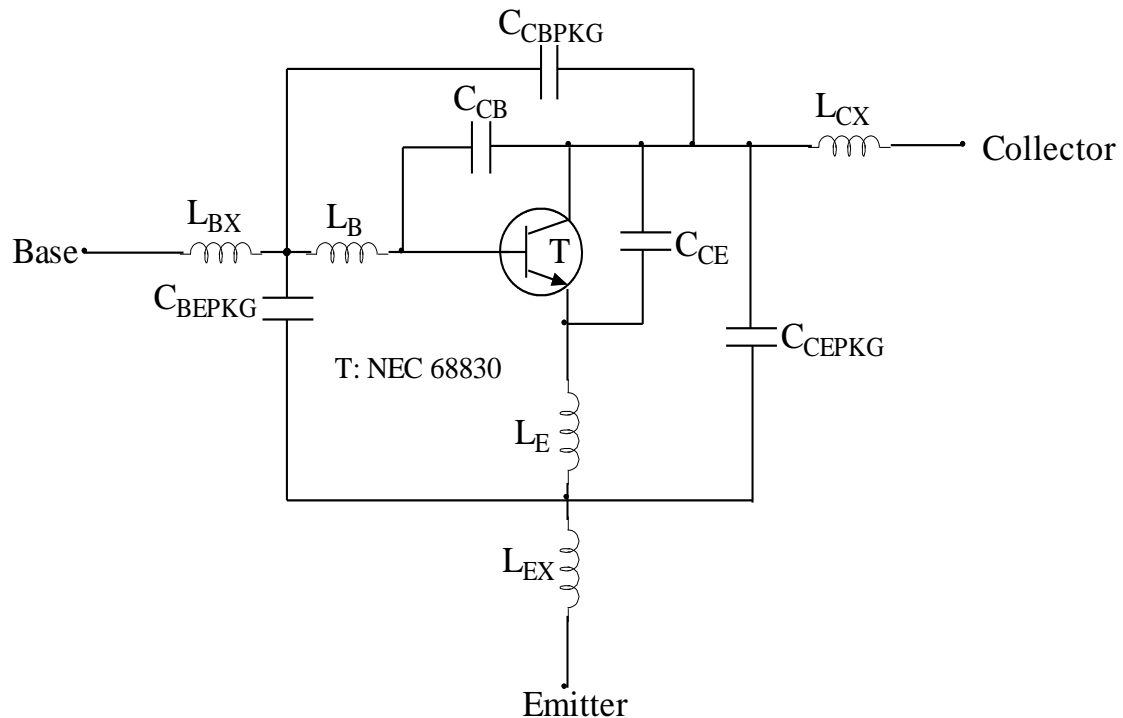


Figure 6-25: shows the transistor NE68830 with package parasitic [67, pp. 133]

The mode-coupling approach also includes a methodology for optimum dynamic coupling; Optimum coupling enhances the dynamic loaded Q, reduces or eliminates phase hits, diminishes susceptibility to microphonics (to an extremely low level), and minimizes phase noise while achieving a broadband linear tuning range.

Figure 6-26a shows the measured phase noise plots of the novel oscillator circuit (Figure 6-24b), the measured phase noise performance is typically better than -129 dBc/Hz @ 100 kHz offset from the carrier frequency over the band (600-2100 MHz). The measured figure of merit (FOM: defined in Ch-1, Eq 1.1) is -187.5 dBc/Hz for a given power-frequency tuning normalized (PFTN: defined in Ch-1, Eq 1.2) 16.02 dB, with power consumption of 200mW ($V_{cc}=5\text{V}$, $I_c=40\text{ mA}$), output power is +3.0 dBm.

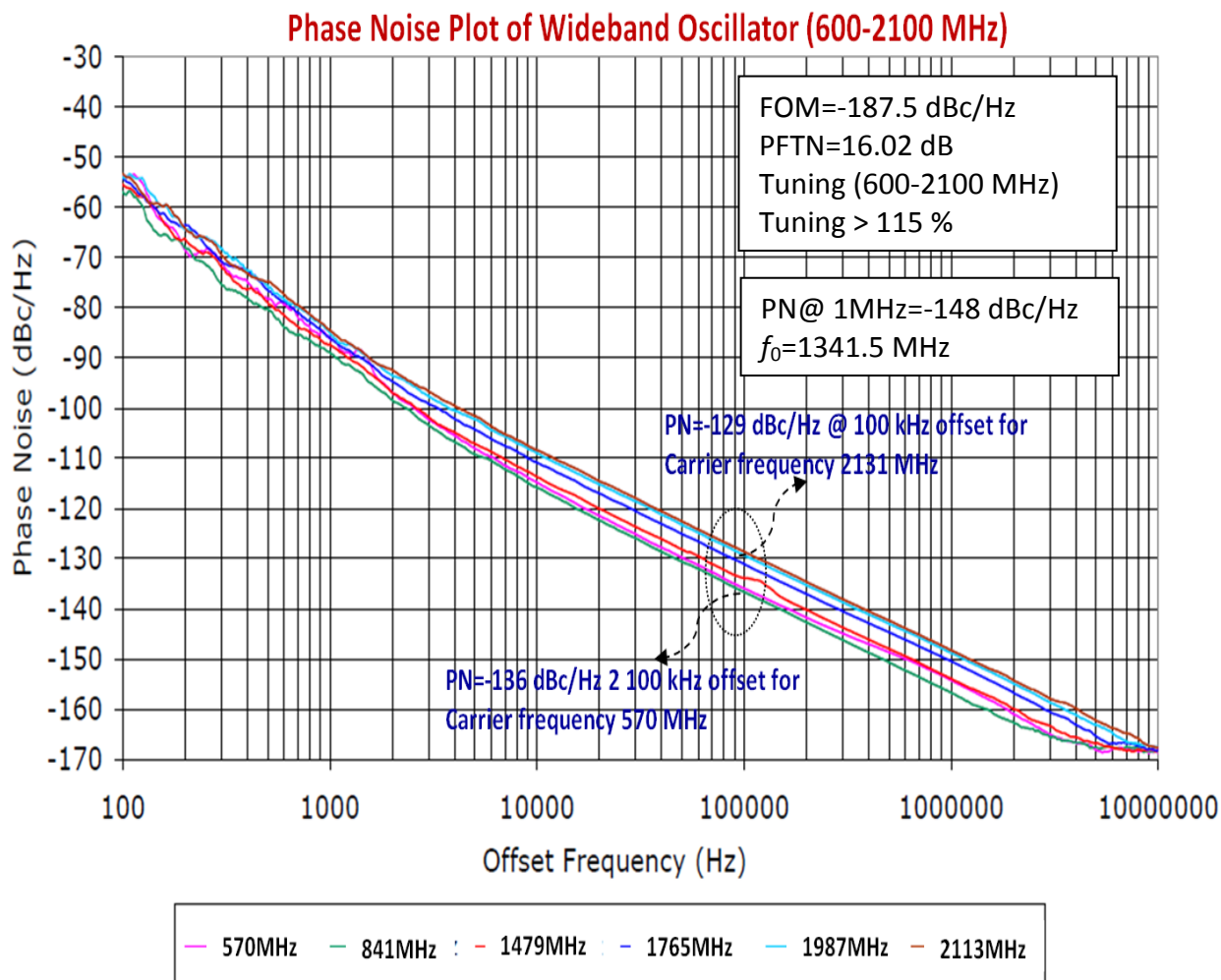


Figure 6-26a shows the measured phase noise plots of this oscillator, the measured phase noise performance is typically better than -129 dBc/Hz @ 100 kHz offset from the carrier frequency over the band (600-2100 MHz), measured figure of merit (FOM: defined in Ch-1, Eq 1.1) is -187.5 dBc/Hz for a given power-frequency tuning normalized (PFTN: defined in Ch-1, Eq 1.2) 16.02 dB, with power consumption of 200mW ($V_{cc}=5\text{V}$, $I_c=40\text{ mA}$), O/P power is +3.0 dBm.

As illustrated in Figure 6-26a, the variation in phase noise over the operating frequency band is typically 10-15dB, this variation is not acceptable in the high performance synthesized signal sources. To overcome the variation in phase noise performance over the desired operating band, novel technique is to incorporate dynamic phase-synchronization mechanism for the suppression of multi-mode dynamics but penalty is external reference source and also require large real estate area.

The innovative approach is to incorporate multi-mode phase injection locking (Fig. 6-24b), (where signal P1 acts like a reference input signal to RF signal P2) that is coupled through a distributed medium for broadband tuning and minimum noise performance. This approach supports multi-octave tuning in a small package, and is comparable with integrated circuit fabrication processing. In addition, the topology allows for a substantial reduction in phase noise by dynamically optimizing the impedance transfer function and coupling factor across a guided distributed medium of the planar multi-coupled network.

As illustrated in Figure 6-24a, a phase compensating network is capacitive coupled between the base terminal and the slow-wave, and progressive-wave coupled resonator for uniform phase noise performance. The slow-wave and progressive coupled resonator network as shown in Figure 6-24a is coupled through hybrid resonance mode causing convergence effect, connected through the phase compensating network which is capacitively coupled between the base terminal and the slow-wave and progressive-wave coupled resonators, optimizes group delay dynamically for uniform and minimum phase-noise performance over the band. As the RF output signal is coupled through a distributed coupled medium, which is coupled across the slow-wave and progressive wave resonator networks, uniform output power and improved higher-order harmonic rejection throughout the operating frequency band can be achieved.

Figure 6-26b shows the measured phase noise plots of this oscillator, the measured phase noise performance is typically -157dBc/Hz at 1 MHz offset from the carrier frequency for multi-octave-band tuning range (500-2500 MHz), the operating DC bias is 5V and 40mA. The typical variation in phase noise over the operating frequency band is typically lower than 3dB with output power varying between 3 dBm to 5.2dBm, which is acceptable limit in the high performance synthesized signal source applications.

The measured figure of merit (FOM: defined in Ch-1, Eq 1.1) is -197.5 dBc/Hz for a given power-frequency tuning normalized (PFTN: defined in Ch-1, Eq 1.2) 26.02 dB, with power consumption of 200mW ($V_{cc}=5V$, $I_c=40\text{ mA}$), output power is +3.2 dBm.

The measured RF output power is better than 3dBm with more than 136 % tuning ranges (500 MHz-2500 MHz) with sufficient margin at both lower ($f=450\text{ MHz}$ @ $V_t=0.2\text{ Volt}$) and upper ($f=2600\text{ MHz}$ @ $V_t=26\text{ Volt}$). The novel oscillator circuit is stable over operating temperatures of -40°C to $+85^{\circ}\text{C}$, and provides sufficient margin for compensating the frequency drift caused due to the change in operating temperature, including the package parasitics and component tolerances.

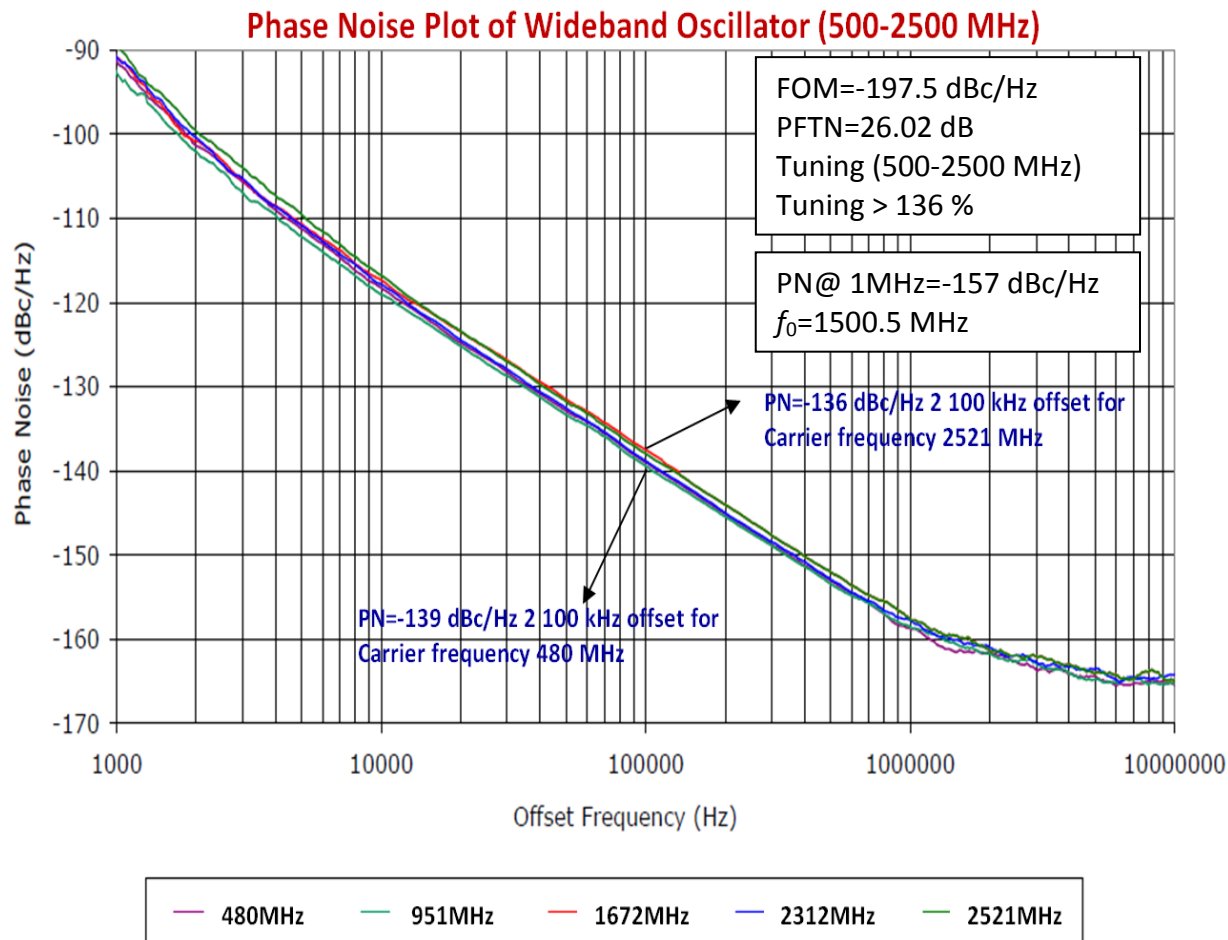


Figure 6-26b shows the measured phase noise plots of this oscillator, the measured phase noise performance is typically better than -136dBc/Hz @ 100 kHz offset from the carrier frequency over the band (500-2500 MHz), measured figure of merit (FOM: defined in Ch-1, Eq 1.1) is -197.5 dBc/Hz for a given power-frequency tuning normalized (PFTN: defined in Ch-1, Eq 1.2) 26.02 dB, with power consumption of 200mW ($V_{cc}=5V$, $I_c=40$ mA), O/P power is +3.2 dBm.

6.4.1.6 High Frequency Push-Push VCO Topology (US Patent No.7, 292,113)

As the frequency band for the wireless communication shifts higher, generation of the power efficient ultra low noise wideband and thermally stable compact signal sources with low cost becomes more and more challenging due to the frequency limitations of the active devices. A high frequency signal can be generated based either on an oscillator operating at a fundamental frequency or on a harmonic oscillator. A typical oscillator operating at the fundamental frequency suffers from a low Q factor, insufficient device gain and higher phase noise at a high frequency of operation. There are two main configurations of the harmonic oscillators: cascade structure, which supports second-harmonic oscillator based on frequency-doubler approach and parallel structure, which supports N^{th} harmonic oscillator (N -push/push-push oscillator topology as an N^{th} harmonic oscillator) based on coupled-oscillator approach. The frequency doubler and other means of up conversion can be a practical and quick solution

to generate high frequency signal from the oscillators operating at lower frequency but it introduces distortions and have poor phase noise performances. This limitation has created interest in microwave community to develop alternative high frequency low cost sources. The push-push topology has several advantages over single-ended versions other than improvement in phase noise. The usable frequency range of the transistors can be extended, and this can be exploited, for instance, using transistors that are larger than usual and have lower $1/f$ noise due to reduced current density. The coupled oscillators N-Push topology improves the phase noise and extends the operating frequency beyond the limitation caused by the cut-off frequency of available active devices, Appendix-A [74]. The novel state-of-the-art topology is based on following:

- Provides constant negative resistance over octave-band
- Novel tuning arrangement for wideband tunability without degrading the loaded- Q of the tuning network over the octave-band.
- Novel coupled-resonator structure, which will support resonance over multi-octave-band
- Optimum size (I_{cmax}/I_{dss}) of the bipolar or FET for low phase noise
- Coupled-oscillator/N-Push approach for improvement in phase noise
- Dynamically tuned phase coupling network

Figure 6-27(a) shows the block diagram illustrating principle modules of the ultra low noise octave-band VCO in the frequency range of 1000-2000MHz/2000-4000MHz. As shown in Figure 6-27a, all the modules are self-explanatory, the oscillator circuit is realized by using dynamically tuned coupled-resonator network, dynamically tuned phase-coupling network and dynamically tuned combiner network for octave-band push-push operation. In push-push topology, two sub-circuits of a symmetrical topology operate in opposite phase at the fundamental frequency, and the output of the two signals are combined through the dynamically-tuned combiner network so that the fundamental cancels out, while the first harmonics interfere constructively, and are available over the tuning range.

The state-of-the-art topology overcomes the limitations of the fixed frequency operation of the push-push oscillator/N-push oscillator by designing a novel tuning and phase controlling network over the desired frequency band (octave-band) [76]-[83]. Figure 6-27b and Figure 6-27c show the schematic and layout of oscillator circuit configured in push-push topology with broadband tuning characteristics (1000-2000MHz/2000-4000MHz). The various modules depicted in the Figure 6-27a are implemented in a way that allows miniaturization, and is amenable for integrated chip design. The structure and application is covered in US Patent No.7, 292,113 and 7,088189. As shown in Figure 6-27a, each sub-circuit is designed at one-half of the desired output frequency (f_0), and thereby the second harmonic ($2f_0$) is constructively combined with the help of the dynamically tuned combiner network. Thus, separation of the two harmonics is accomplished using symmetry, which avoids space-consuming filter elements. The wideband tunability is achieved by incorporating a dynamically tuned phase coupling network so that the 180° phase difference, (mutually locked condition) is maintained over the

tuning range for push-push operation [74]. As shown in the Figure 6-27b, dynamically tuned coupled resonator is connected with the emitter of the transistor (NE68830) to provide a uniform loaded Q over the tuning range. The layout shown in the Figure 6-27c is fabricated on 32 mil thickness Rogers substrate of dielectric constant 3.38 and loss tangent $2.7 \cdot 10^{-4}$, 1.75x1.75x0.18 inches size of the printed circuit board (PCB).

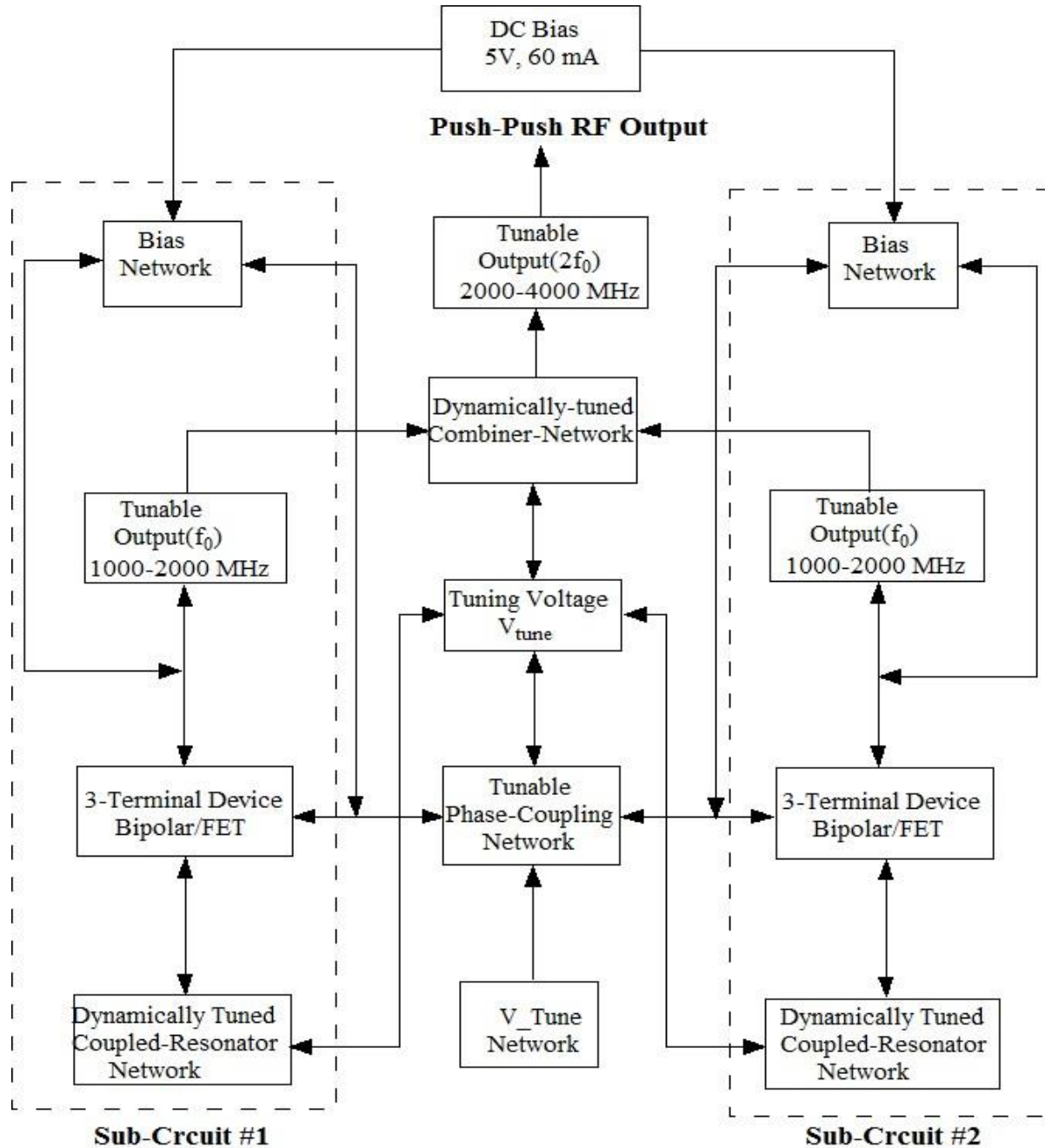


Figure 6-27a: Shows the block diagram illustrating principle modules of the ultra low noise octave-band VCO in the frequency range of 1000-2000MHz/2000-4000MHz (US Patent No.7, 292,113) [60, 74]

Experimental results have shown that a poor mismatch at the fundamental, results in discontinuous tuning due to the non-uniform phase shift over the tuning range. This mismatch in phase-shift between the two sub-circuits is due to possible component tolerances, package parameters, and the phase associated with the path difference over the tuning range. Therefore, oscillator goes out of the locking range. Figure 6-27d shows the compact layout of Figure 6-27c for the minimization of the phase-shift between the two sub-circuits as shown in Figure 6-27a.

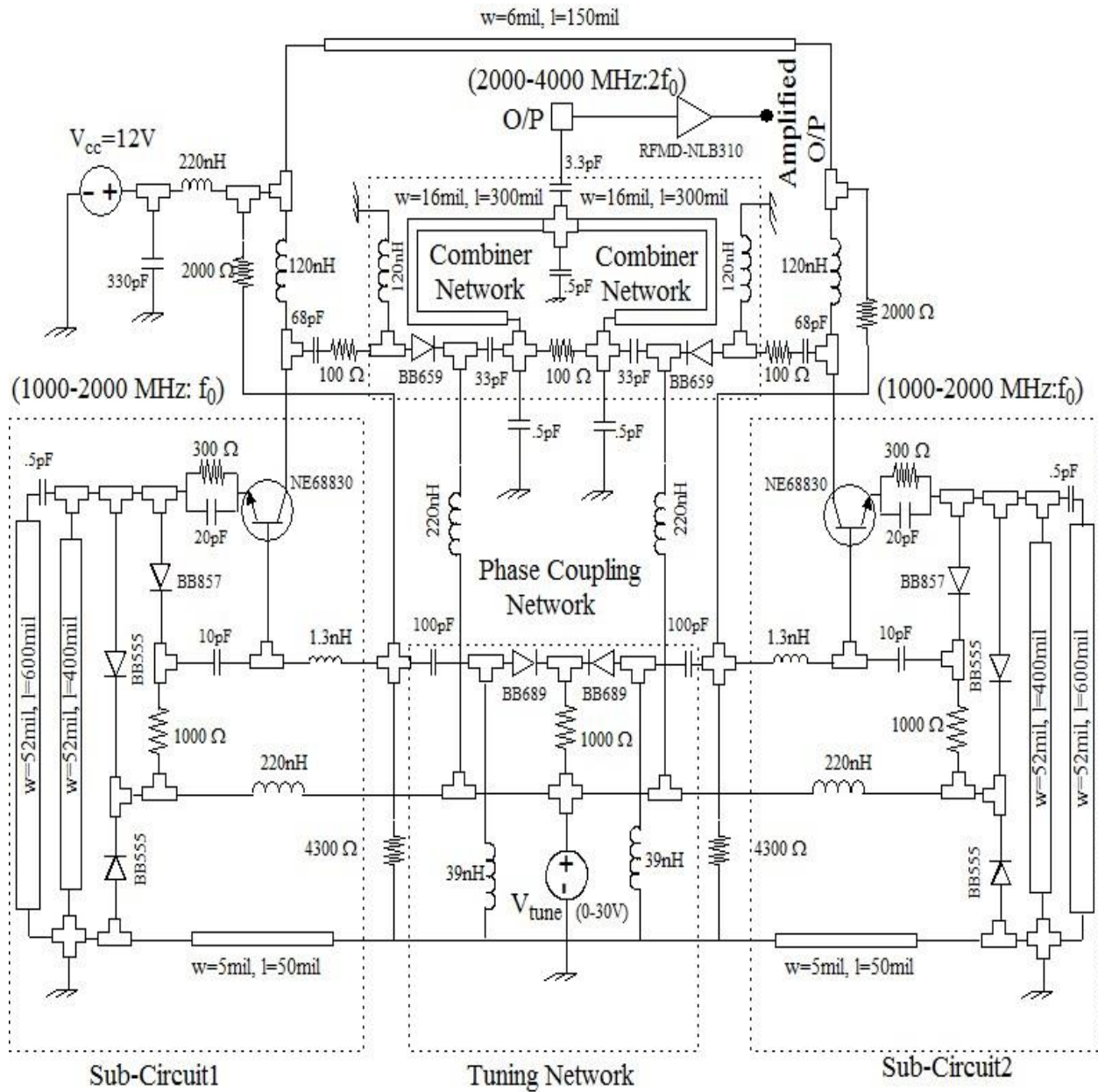


Figure 6-27b: Depicts the schematic diagram of oscillator circuit comprises of printed coupled-resonator network, phase-coupling network and combiner network for octave-band Push-Push operation in accordance with the block diagram shown in Figure 6-27a [60]

The attempt to reduce the size of the PCB is done by combining the resonator of sub-circuit #1 and sub-circuit #2 as in dual horseshoe configuration as shown in Figure 6-27d. This allows 3-times reduction in real state area as compared to the layout shown in Figure 6-27d. An innovative dynamic tuning network integrated with coupled horseshoe microstrip resonator is incorporated to get more than octave band tunability keeping phase noise uniform throughout the band. Figure 6-27d shows the compact layout of integrated structure of the dynamically tuned coupled resonator of both the sub-circuits shown in Figure 6-27c, layout is built using multilayer with 64 mills substrate height and 3.38 dielectric constant of $0.75 \times 0.75 \times 0.18$ inches size of the printed circuit board (PCB).

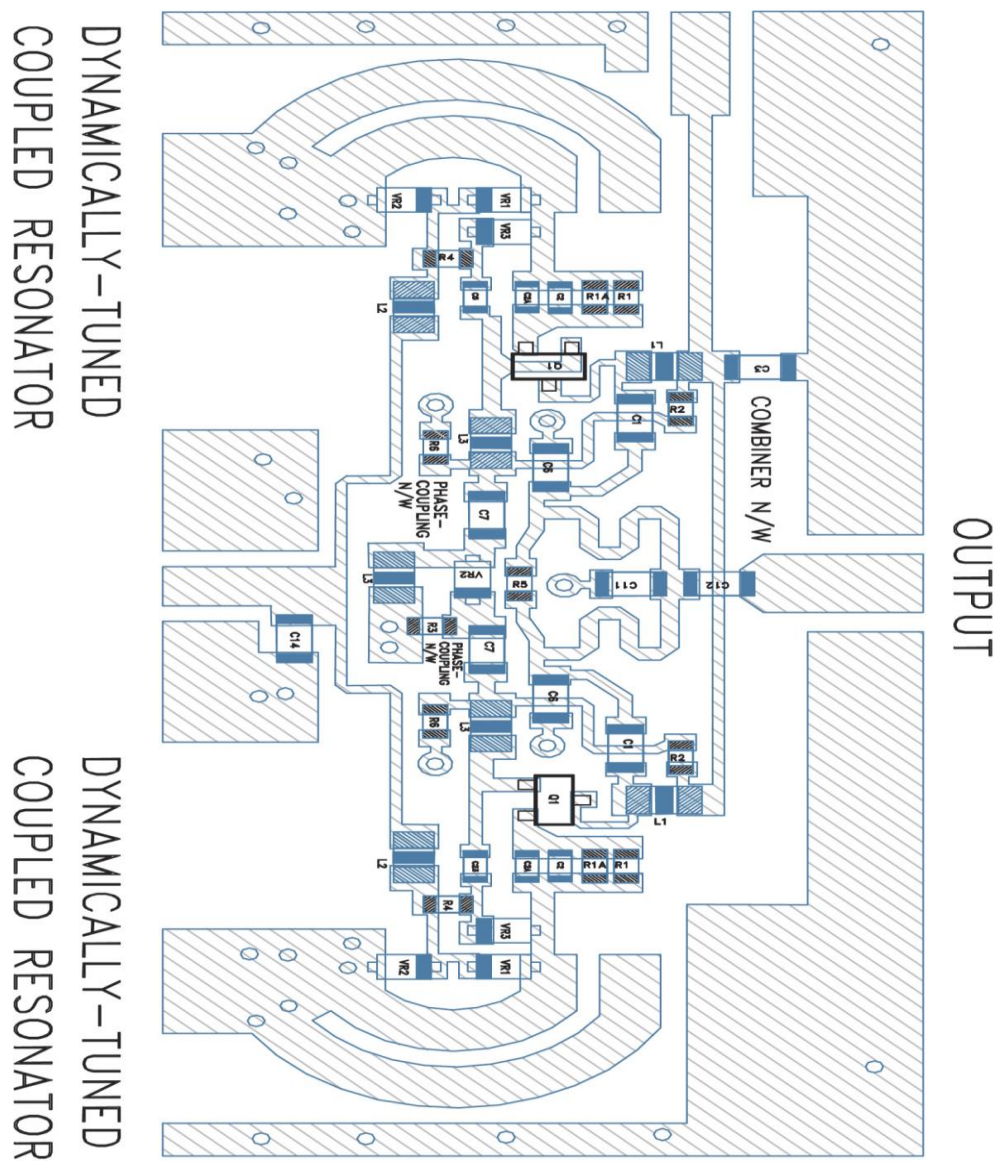


Figure 6-27c: Shows the layout of the schematic of Push-Push oscillator circuit shown in Figure 6-27b (multilayer 32 mils substrate, Dielectric constant 3.38) 1.75x1.75x0.18 inches ROGERS PCB (US Copyright Registration No: Vau-603-982) [60, 74].

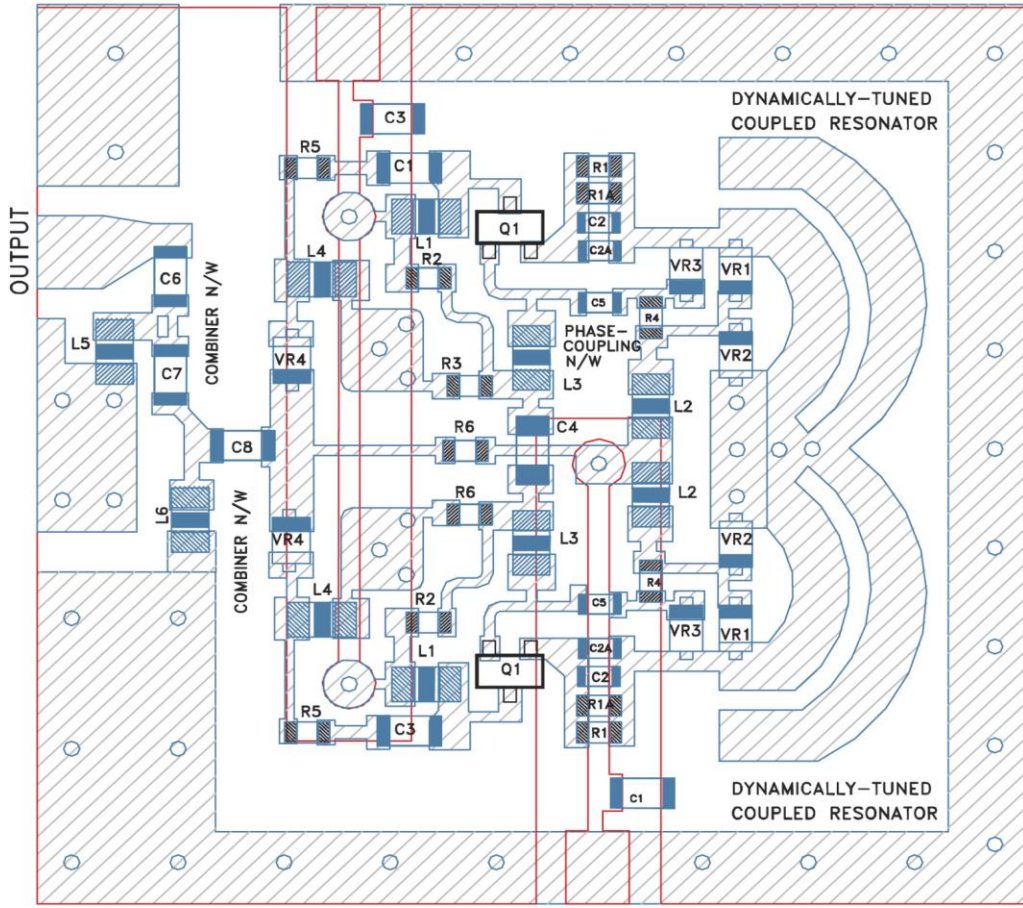


Figure 6-27d : Shows the compact layout of integrated structure (coupled horse-shoe microstrip resonator)of the dynamically tuned coupled resonator of both the sub-circuits shown in Figure 6-27c, layout is built using multilayer with 64 mils substrate and 3.38 dielectric constant of $0.75 \times 0.75 \times 0.18$ inches US Copyright Registration No: Vau-603-982) [60, 74].

Figures 6-27e and 6-27f show the CAD simulated plots of oscillator output signal of sub-circuit #1 and sub-circuit #2 in time domain, and the phase noise plot of push-push oscillator (2000-4000MHz). As shown in Figure 6-27f, the simulated phase noise plot (CAD tool: Serenade 8.71) is typically better than $-109\text{dBc}/\text{Hz}$ @ 100 kHz offset from the carrier frequency over the band (2000-4000 MHz). Referring to Figure 6-27e, RF-collector current of both the sub-circuits is out of phase for the fundamental (undesired frequency of the operation: 1000-2000MHz). Further increase in operating frequency and tuning range is limited by the phase shift and mode locking between two sub-circuits (sub-circuit # 1 and sub-circuit # 2) as shown in Figures 6-27a and 6-27b. The prototype is built by careful selection of active devices but very difficult to tune to RF oscillator output of sub-circuit #1 and sub-circuit #2 in 180° out of phase across the full band (1000-2000MHz/2000-4000MHz) using discrete components.

By optimizing the tuning network, up to 25 % increase in tuning range is obtained but at the cost of increase in level sub-harmonics (due to poor matching), mode-jumping, and degradation in phase noise, which is obvious due to increase in tuning sensitivity [83]. Figure 6-27g shows

the CAD simulated phase noise plots of 3000-6000MHz push-push oscillator circuit. The variation in phase noise performance across the band is typically 10dB.

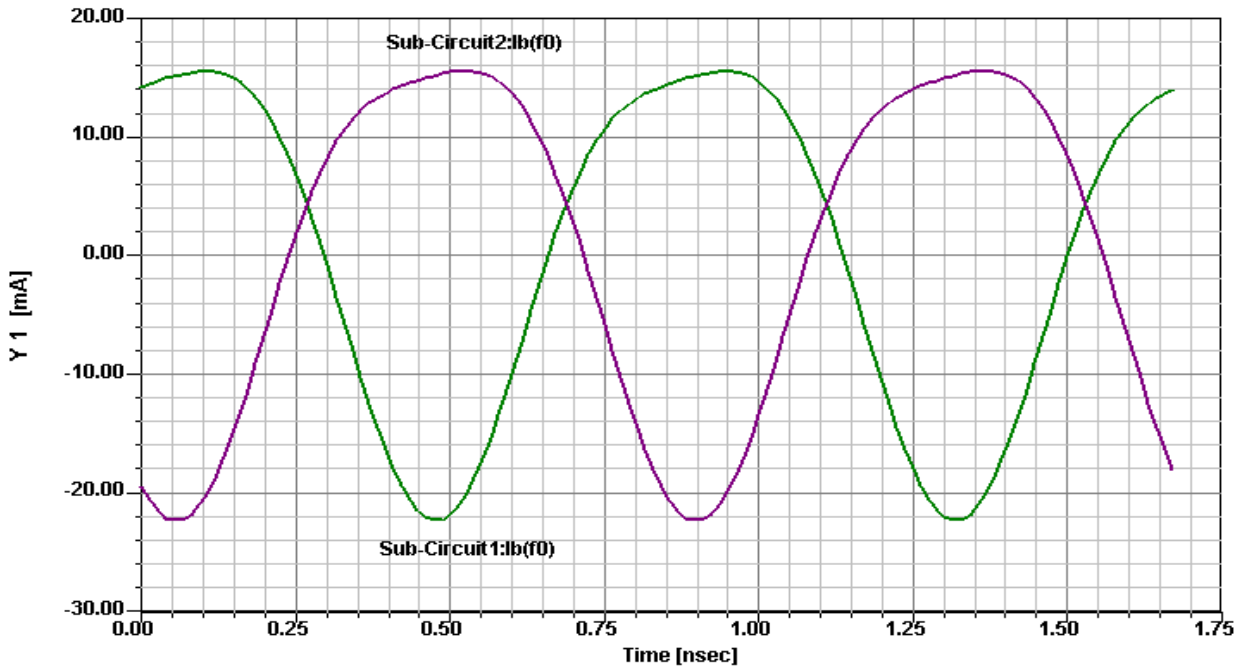


Figure 6-27e: Shows the RF-collector currents Y_1 (mA) of sub-circuit #1 and sub-circuit #2 (Figure 6-27b), the output currents are 180 degree out of phase, the fundamental frequency:1000-2000MHz, push-push operation: 2000-4000MHz

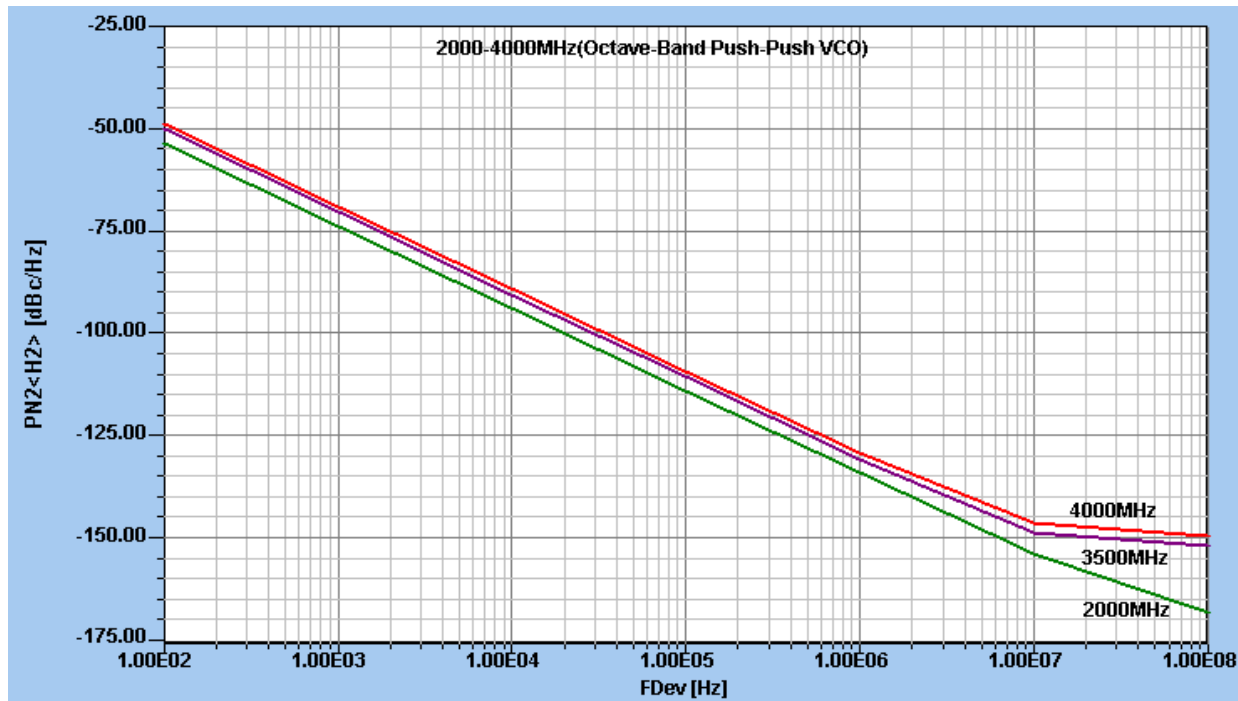


Figure 6-27f: Shows the phase noise plot for octave-band frequency range (2000-4000MHz), configured in push-push topology as shown in Figure 6-27d.

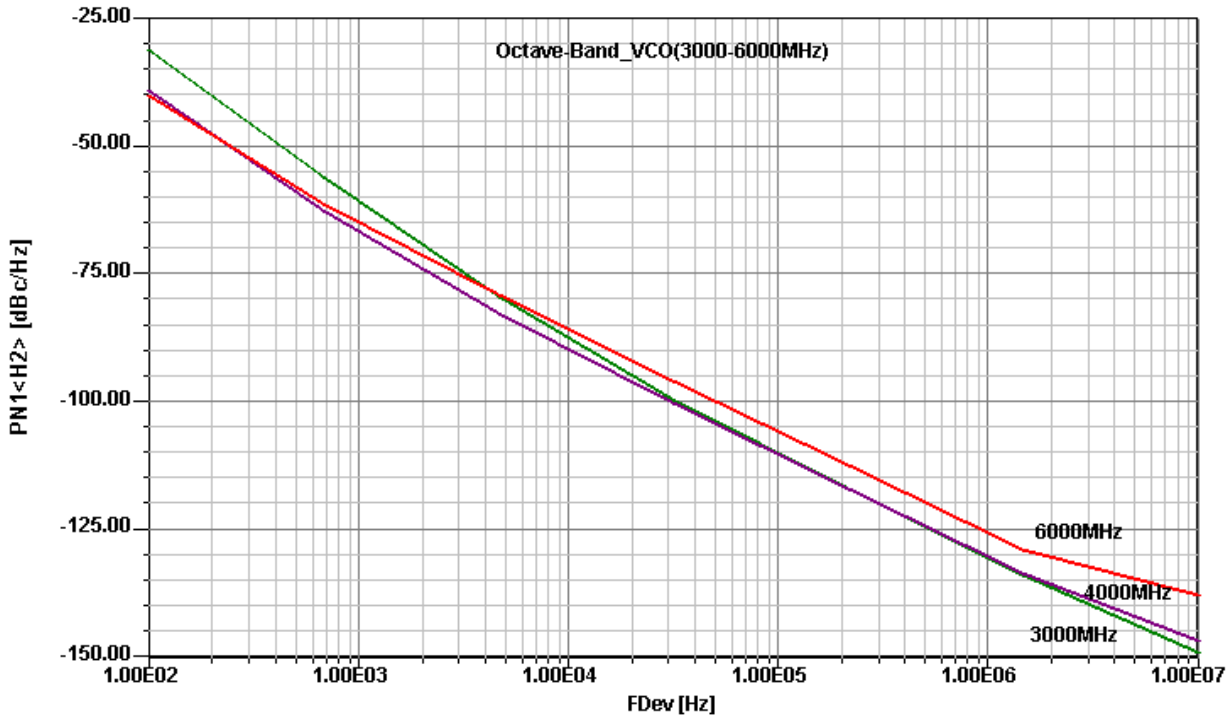


Figure 6-27g: Shows the phase noise plot for 3000-4000MHz, configured in push-push topology as shown in Figure 6-27d.

The layout shown in Figure 6-27d minimizes the phase-shift due to the path difference between the two sub-circuits over the tuning range, but still shows discontinuous tuning at some point over the band due to the package parasitics and component tolerances associated with the discrete components of the circuit. Incorporating a phase detector to overcome the problem of discontinuous tuning allows multi-octave band tuning and improved phase noise performances. The objective is to identify the effects, which limits the wideband tuning range and development of unique topology, which can minimize the phase shift and support the broadband tunability without degrading the phase noise performance. With regard to the state of the art push-push/N-push oscillator, the phase-synchronization techniques using phase detector (PD) provides the general implementation of the wideband dynamically tunable coupled oscillator for the extended frequency range of operation.

6.4.1.7 Multi-Octave Band Push-Push VCO Topology (US Patent No.7, 292,113) [63]

The free running frequencies of the two oscillators in the coupled oscillator system shown in Figures 6-27a-6-27d are not identical because of tolerances in their respective circuit component values. However, a phenomenon known as injection locking takes place , which ensures that the frequencies of the two oscillators are locked to each other. The maximum frequency range over which injection lock can occur is inversely proportional to the external Q of the oscillators. Therefore, in the case of oscillators having low values of external Q, injection locking occurs even with a large discrepancy in their free running frequencies. The circuit principle usually requires a large-signal analysis to verify the odd-mode operation of the sub-circuits and the bias network has to be properly designed with respect to two critical frequencies.

Figure 6-28a shows the typical block diagram illustrating principle modules of the ultra low noise multi-octave-band push-push VCO in the frequency range of 1-5 GHz/5-10 GHz. Figure 6-28b shows the typical schematic diagram in accordance to the block diagram shown in Figure 6-28a. It shows a dynamically tuned coupled-resonator network, dynamically tuned phase-coupling network, dynamically tuned combiner network and dynamically tuned phase detector network for wideband push-push operation, amenable to commercially available MMIC technologies.

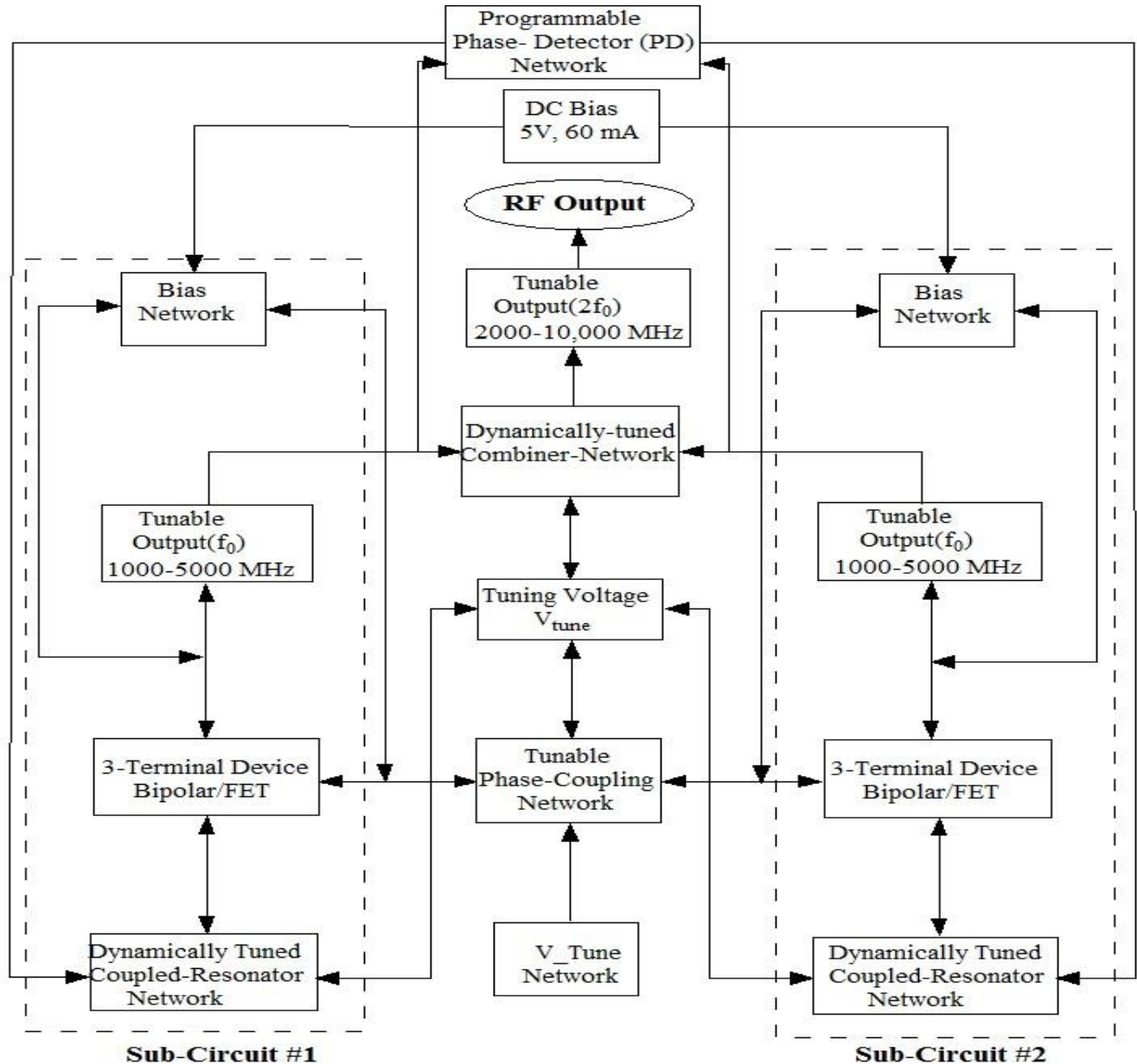


Figure 6-28a: Shows the typical block diagram of multi-octave-band push-push VCO in the frequency range of 1-5 GHz/5-10 GHz (it shows a dynamically tuned coupled-resonator network, dynamically tuned phase-coupling network, dynamic tuned combiner network and dynamically tuned phase detector network), amenable to MMIC technologies [63]

As shown in Figure 6-28a and 6-28b, by incorporating a phase detector network integrated with the tuning diode for compensating the phase error, extended operating frequency range is 1-5GHz/5-10 GHz operation. As shown in Figure 6-28a, the divider may comprise MC10EL32, made by ON Semiconductor, Inc., and the amplifier and balanced mixers may, respectively, comprise OPAMP TL071 from Texas Instruments and mixers available from Synergy Microwave. The phase detector network dynamically compensates for phase errors between each oscillator during wideband operation. The phase detector network detects random fluctuations in the free-running frequency and translates those fluctuations into phase errors.

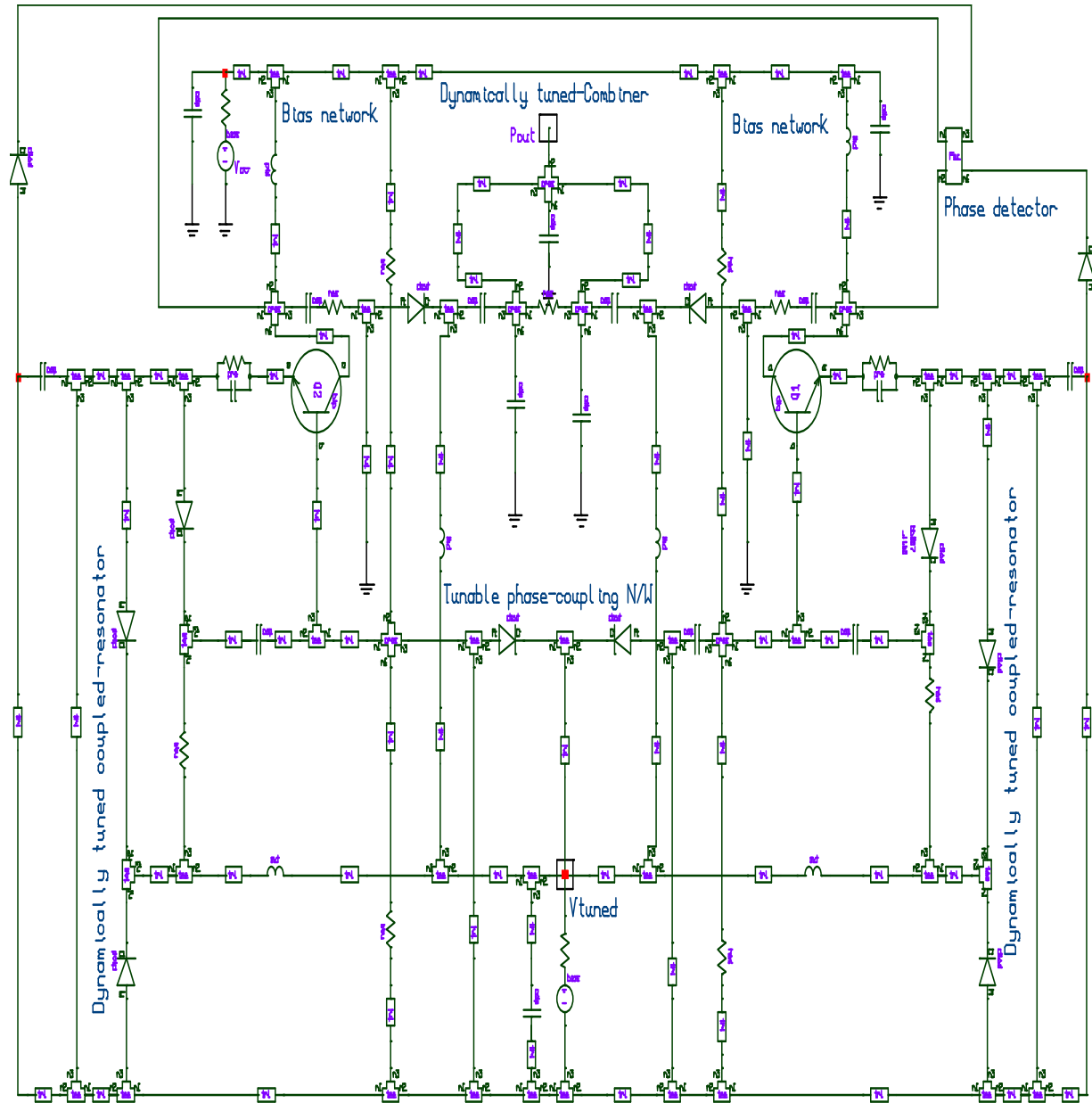


Figure 6-28b: shows the schematic (of the multi-octave push-push VCO (1-5GHz/5-10GHz), DC Bias: 5V, 60mA [63].

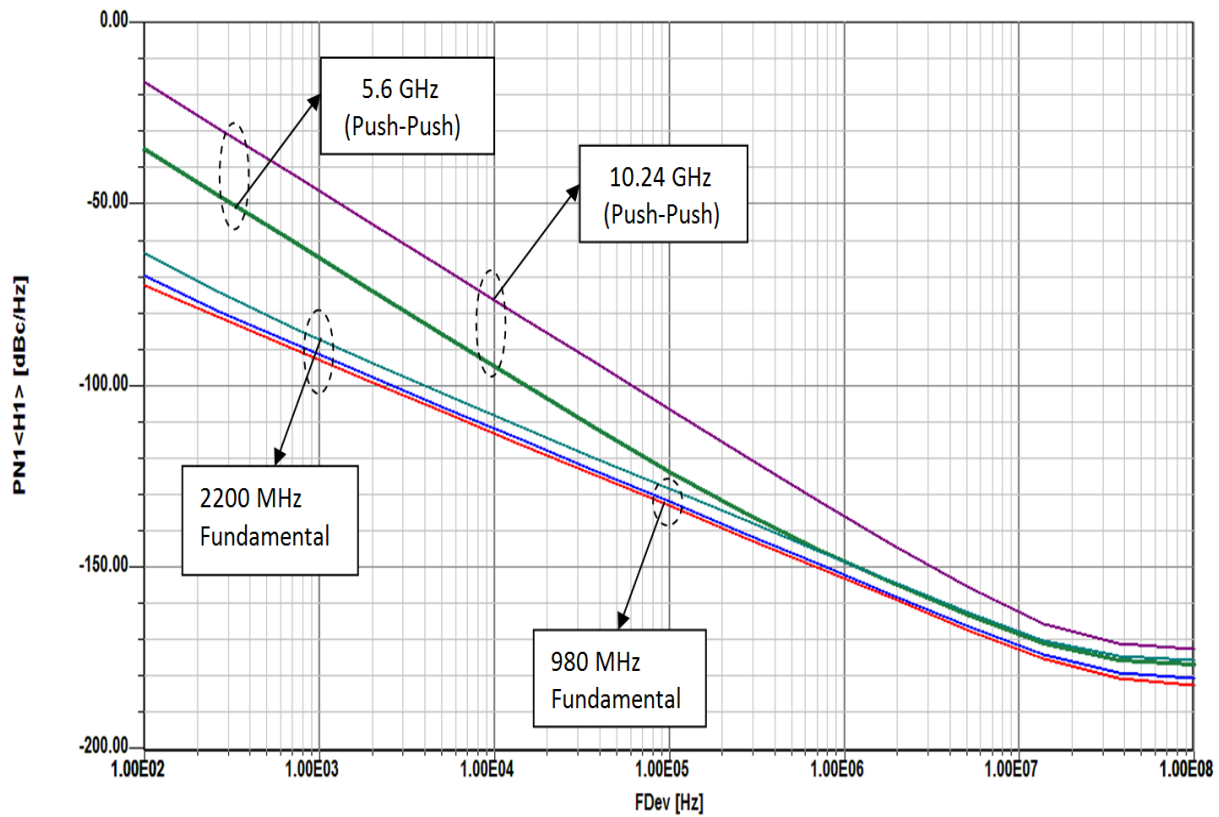


Figure 6-28c: Shows the CAD simulated phase noise plot of multi-octave-band VCO (1-5GHz/5-10GHz), configured in push-push topology as shown in Figure 6-28b.

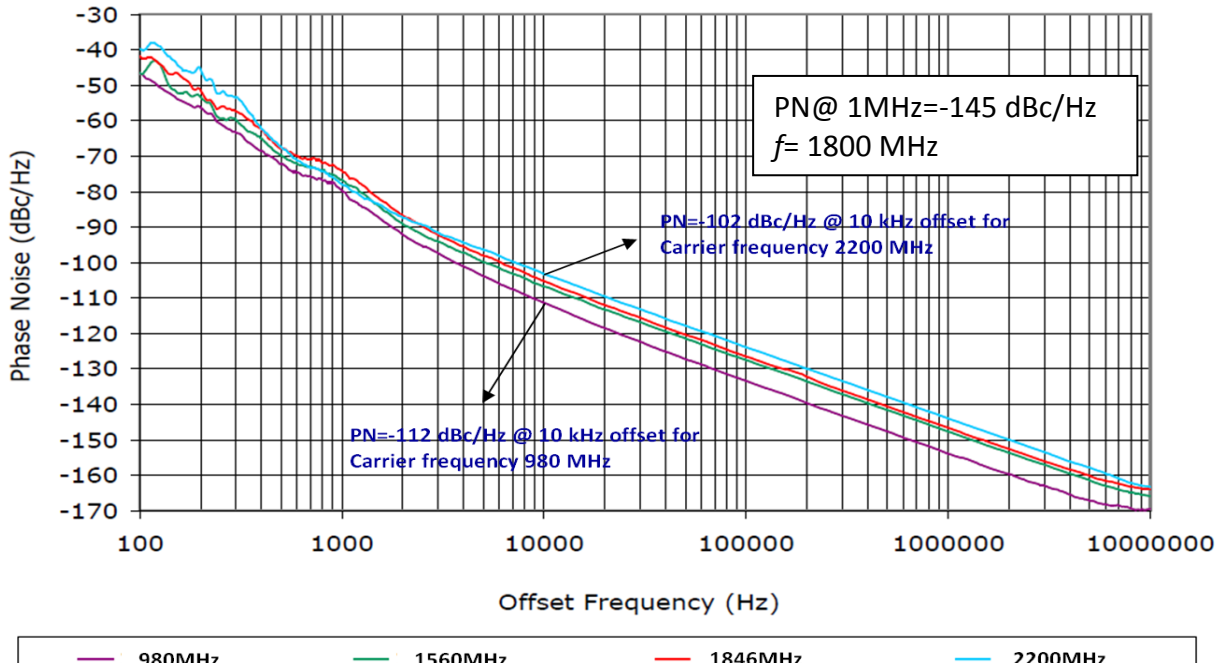


Figure 6-28d: Shows the measured phase noise plot of multi-octave-band VCO (1-5GHz/5-10GHz), configured in push-push topology as shown in Figure 6-28b, with power consumption of 300mW ($V_{cc}=5V$, $I_c=60\text{ mA}$), O/P power is -3.0 dBm.

The phase errors are then fed back to the combiner network and used to control the phase and frequency of the buffered signal during tuning operation. The phase errors are also fed back to the dynamically tuned coupled resonator networks and used to tune the oscillating frequencies of each of the three terminal devices. Figures 6-28c, 6-28d, 6-28e show the CAD simulated and measured phase noise plots of multi-octave-band VCO (1-5GHz/5-10GHz), configured in push-push topology as shown in Figure 6-28a and Figure 6-28b. As shown in Figures 6-28c, 6-28d, 6-28e, the simulated and measured phase noise agree within 3-5 dB for 1-5 GHz operation in push-push configuration, however measured phase noise for 5-10 GHz is 5-8 dB inferior as compared to simulated data. This could be due to component tolerances and phase dispersion across the higher band (5-10 GHz).

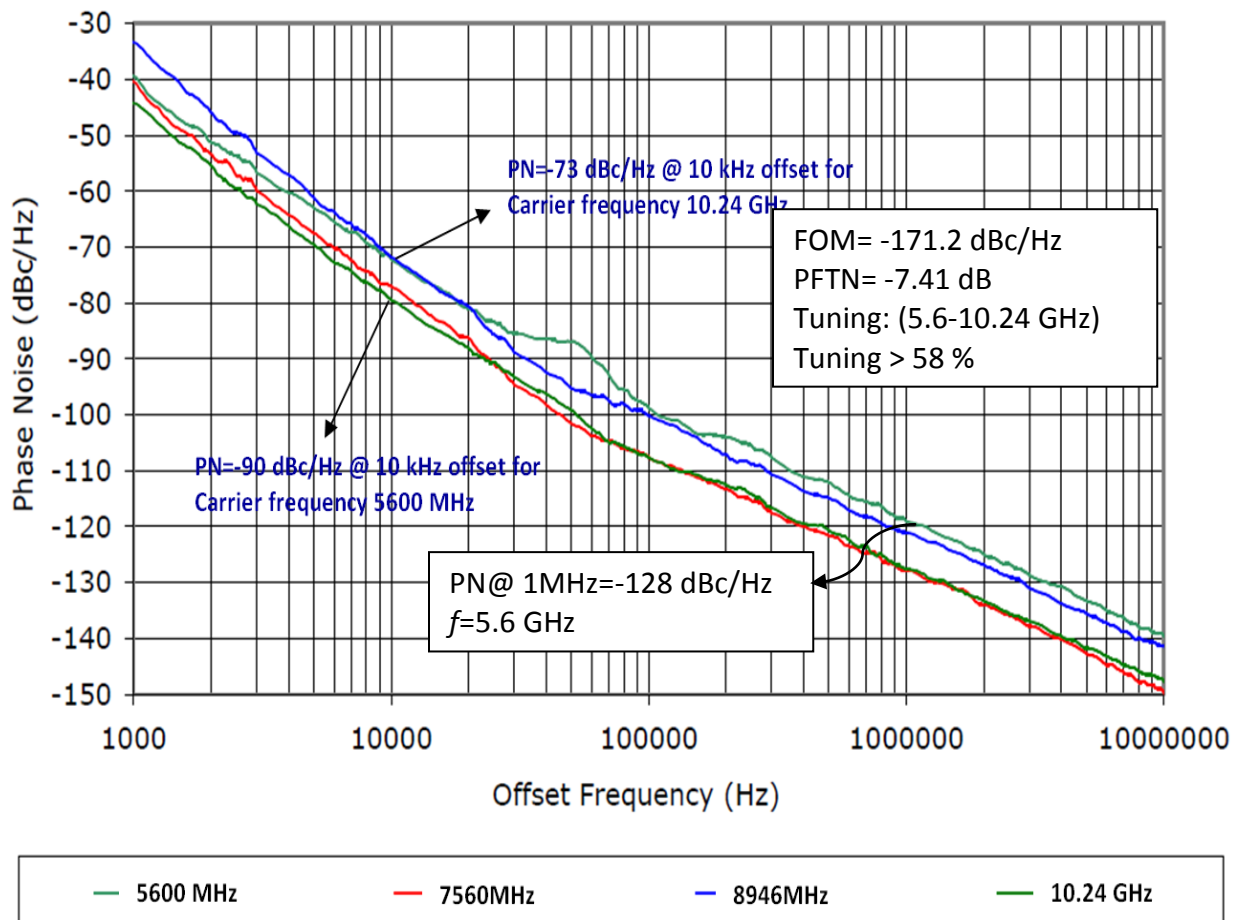
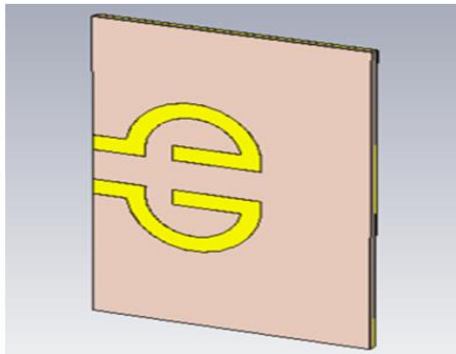


Figure 6-28e: Shows the measured phase noise plot of multi-octave-band VCO (1-5GHz/5-10GHz), configured in push-push topology as shown in Figure 6-28b, measured figure of merit (FOM: defined in Ch-1, Eq 1.1) is -171.2 dBc/Hz for a given power-frequency tuning normalized (PFTN: defined in Ch-1, Eq 1.2) -7.41dB, with power consumption of 300mW ($V_{cc}=5V$, $I_c=60\text{ mA}$), O/P power is -3.0 dBm

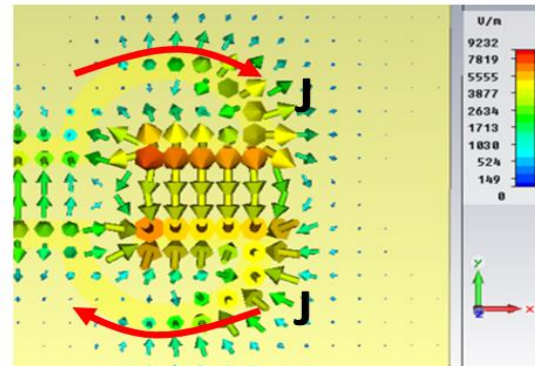
6.4.1.8 Substrate Integrated Waveguide (SIW) Resonator Based Oscillators

For portable communication systems, oscillator's DC-RF conversion efficiency and phase noise play important role. Toward this end, substrate integrated waveguide (SIW) based resonator have drawn attention in microwave communities due to the low radiation losses, high quality

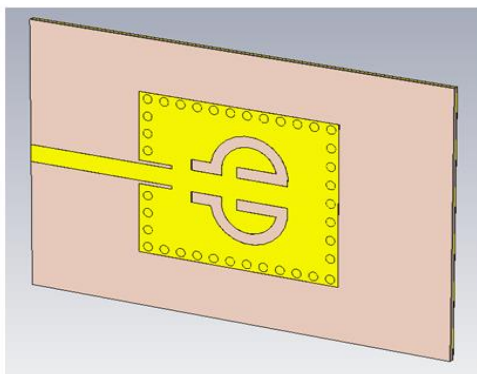
factor, and capability of making waveguide-like structures using planar printed circuit board (PCB) technology [98]. Recent publications on tunable or switchable SIW resonators [[99]-[101] offer tuning or switching mechanism by connecting a varactor/PIN diodes to a floating metal on top of the SIW cavity with jump wires, causing unwanted radiation loss due to the closed-loop slots surrounding the floating metal, and therefore reduces quality (Q) factor . In addition, the jump wires used for DC bias will increase fabrication complexity and may introduce some extra parasitics as well. To overcome these problems, a new type of tunable resonator reported here is based on complementary coupled resonators (CCRs) using SIW technologies [102]-[103]. The proposed complementary coupled resonator is essentially a complementary version of a conventional microstrip coupled line resonator [67, pp. 358]. Incorporated with SIW, the complementary coupled resonators can be excited at its differential mode. In this case, the equivalent magnetic currents on the slots flow in the opposite direction; therefore, radiation loss is minimized and the quality factor of SIW Q resonator improves. To illustrate, Figure 6-29 shows the geometry of a conventional microstrip coupled line resonator and the proposed complementary structure at about 5 GHz. The conventional coupled line resonator shown in Figure 6-29(a) is excited at its differential mode and its electric (E) field is plotted in Figure 6-29(b).



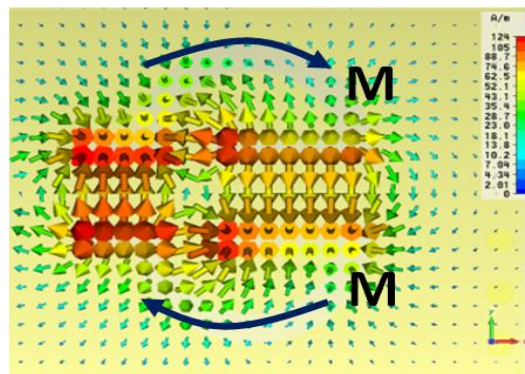
(a) microstrip coupled line resonator



(b) electric field distribution



(c) complementary coupled resonator



(d) magnetic field distribution

Figure 6-29: A typical geometry of coupled planar resonator: (a) A microstrip coupled line resonator, (b) its electric field distribution and electric current flow under differential excitation, (c) a complementary coupled resonator and (d) its magnetic field distribution and equivalent magnetic current flow under the fundamental mode of SIW cavity [102].

Using the principle of duality, the coupling mechanism for the proposed complementary coupled resonator is through magnetic (H) field as shown in Figure 6-29d) and has a similar distribution as E field in the conventional one. Unlike the conventional coupled resonator where the differential mode needs to be excited by a pair of inputs with opposite polarity, the proposed complementary coupled resonator is excited itself at differential mode due to the nature of the fundamental mode in the waveguide. As a result, the equivalent magnetic currents on the slots of the complementary coupled resonator flow in opposite directions at the symmetrically opposite edges on the SIW resonator, and therefore the radiation can be minimized, which in turn generates a high Q factor of the resonator. The calculated unloaded Q factor can be given by [Ch-5, Equation 5.25]

$$Q(\omega_0) = \frac{\omega_0}{2} \left| \frac{Z_{11}(\omega_0)'}{Z_{11}(\omega_0)} \right|_{f_0=5.34\text{GHz}} \approx 287 \quad (6.43)$$

where $Z_{11}(\omega_0)$ and $Z_{11}(\omega_0)'$ signify the impedance and its derivative respectively of the SIW resonator structure at frequency of ω_0 .

Figure 6-30 shows the CAD simulated plots of $[S_{11}]$ of the 1-port CCR (complementary coupled resonator) depicted in Figure 6-29c for the application in Colpitts oscillator configuration where resonator is used as 1-port network. The resonant frequency for this fixed frequency resonator is 5.34 GHz, and the calculated unloaded Q-factor using fractional 3-dB bandwidth from $[S_{11}]$ is 290, which agree closely with the simulated data from (6.43). For giving brief insights about the radiation loss characteristics of this structure (Figure 6-29c), the 3-D EM simulated radiation efficiency is 6.96% and the radiation gain is -4.64 dB, indicating a low radiation loss[103].

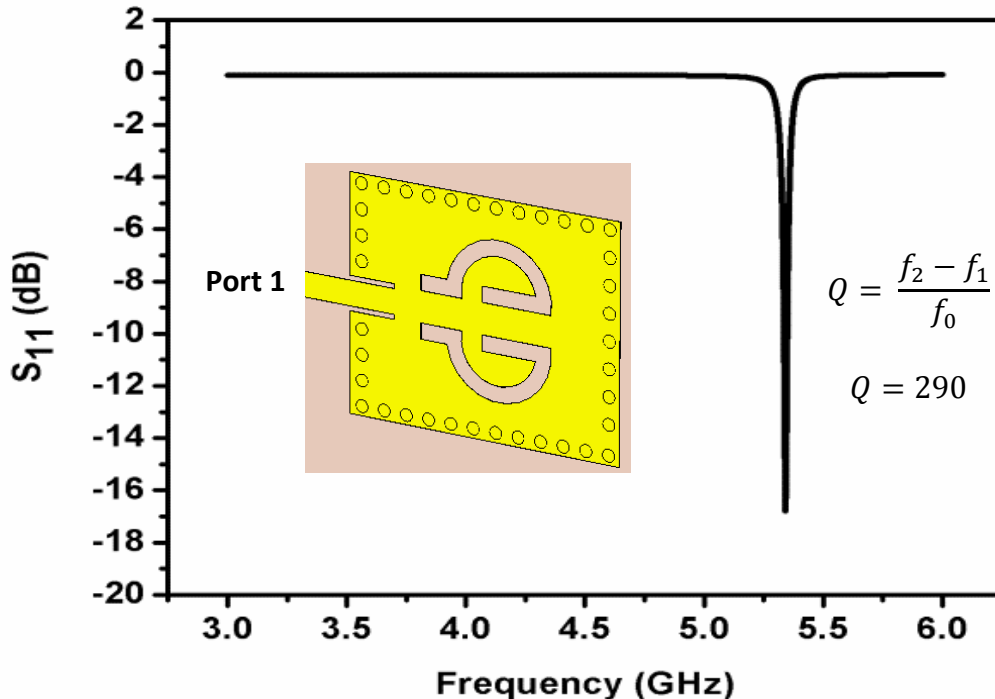


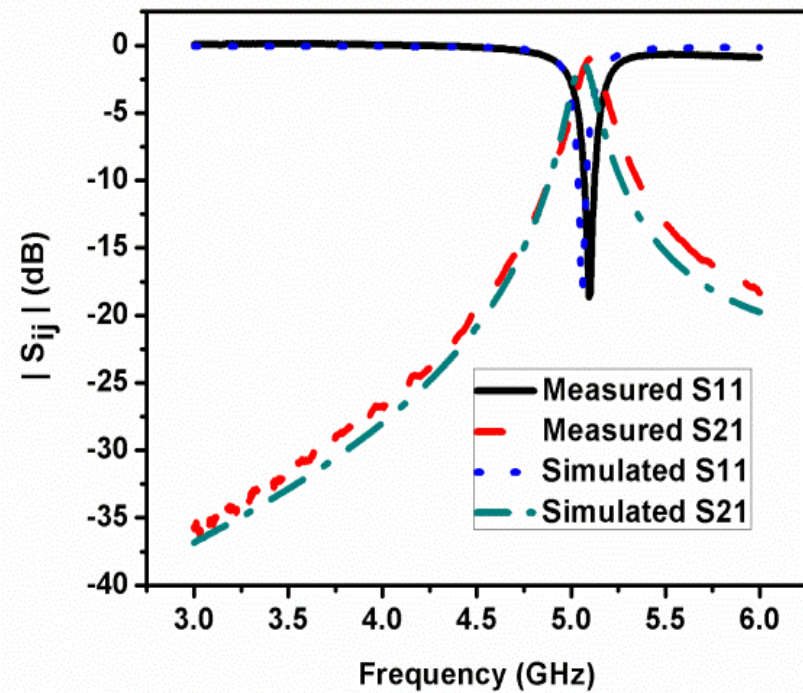
Figure 6-30: CAD simulated $[S_{11}]$ plot of the 1-port CCR depicted in Figure 6-29c [102]

Figure 6-31 shows the typical 2-port complementary coupled resonator for the application in feedback oscillator configuration, using the resonator as a 2-port filtering network. Figure 6-32 shows the CAD simulated and measured plots of $|S_{11}|$, there is a good agreement. The measured insertion loss is less than 1 dB at 5.1 GHz; the unloaded Q of the 2-port resonator can be described by [Ch-5, Equation 5.25]

$$Q(\omega_0) = \frac{\omega_0}{2} \left| \frac{Z_{21}(\omega_0)'}{Z_{21}(\omega_0)} \right|_{f_0=5.1\text{GHz}} \approx 312 \quad (6.44)$$



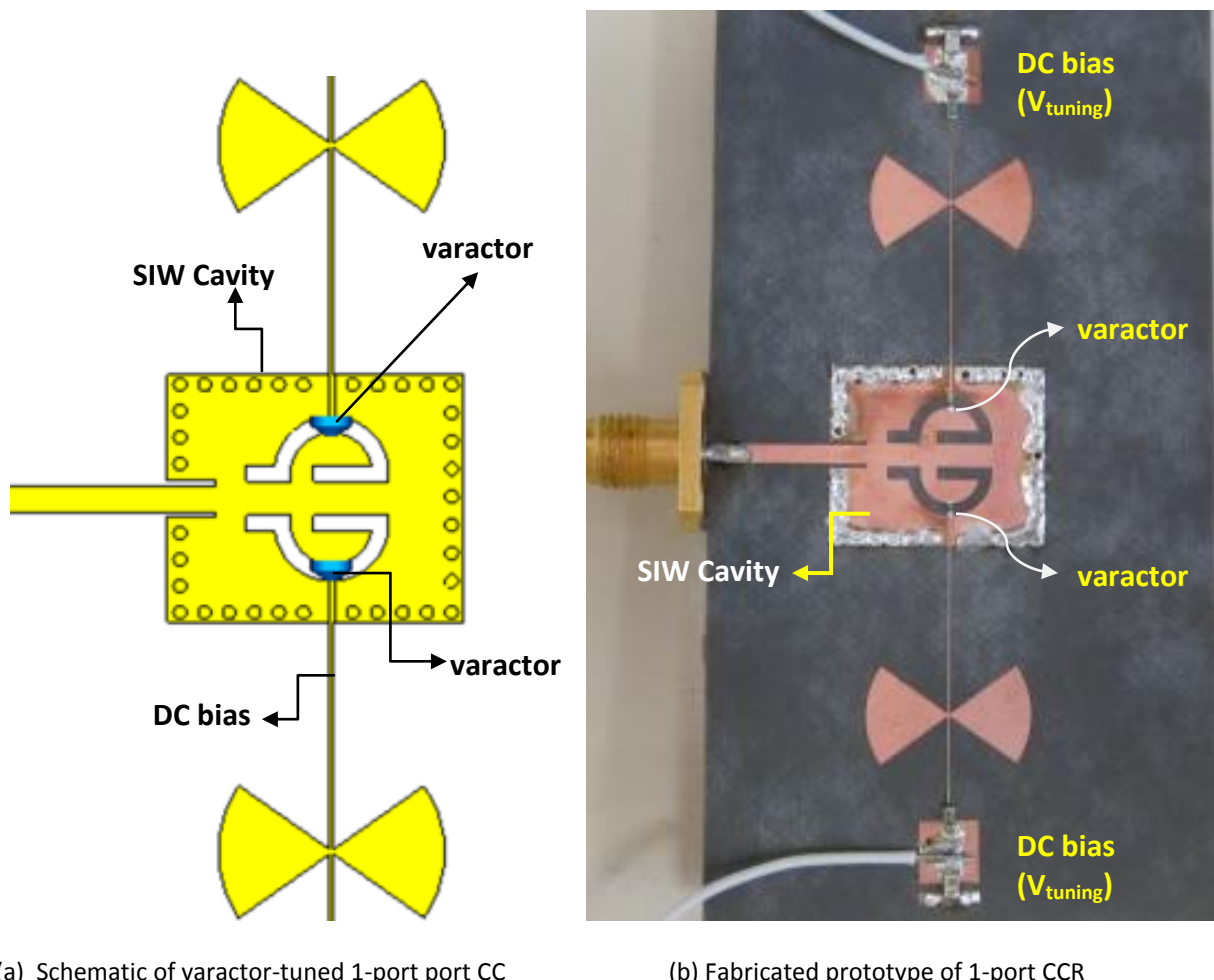
(a) 2-port complementary coupled resonator (CCR) fabricated using RT/Duroid 5880 substrate with a thickness of 0.508 mm and dielectric constant of 2.2 [103]



(b) Fabricated prototype of 2-port CCR

Figure 6-31: Two-port resonator structure (a) Fabricated prototype of 2-port CCR (complementary coupled resonator) and (b) its S-parameters [103].

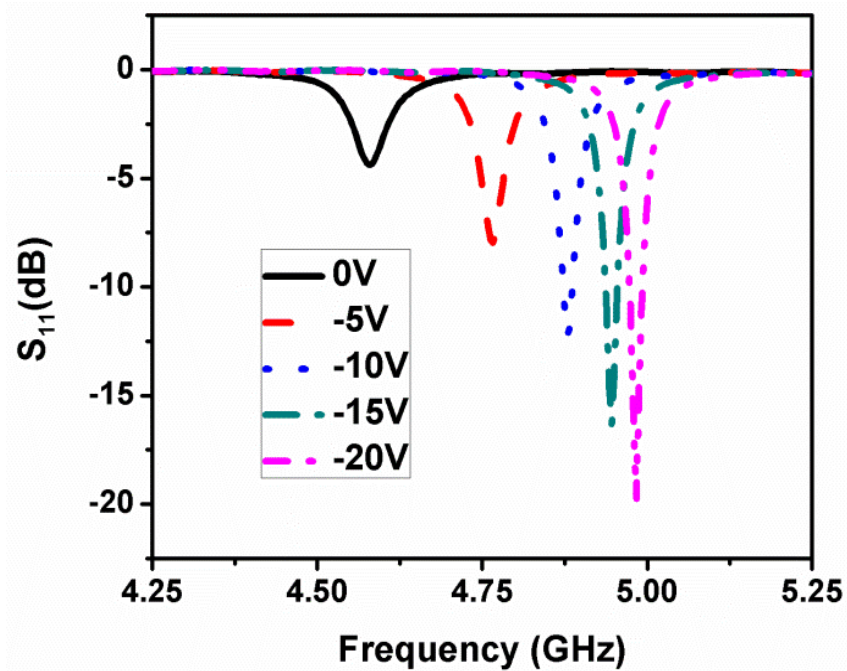
As shown in Figures 6-29 and 6-31, these resonators are not tunable, tuning mechanism is realized by incorporating tuning diodes (varactors) at the location where the E field on the slot is maximum (shown in Figure 6-32) for achieving broadband operation. Figure 6-32 shows the prototype of the 1-port CCTR (complementary coupled tunable resonator tunable resonator) using varactor diodes (MA/COM MA46H120). Figure 6-33 shows the measured S_{11} plots as a function of reverse bias voltages of both varactors from 0V to 20V, indicating the resonant frequency can be tuned from 4.579 GHz to 4.984 GHz, or 8.84% of relative bandwidth. Further, tuning range can be increased by reducing the gap between the DC bias line and SIW cavity, adding a coupling capacitor between the bias line and the resonator, and selecting the hyper-abrupt varactor diodes for broadband filtering and oscillator applications. It can be seen that the measured unloaded Q varies from 50 to 220 (as shown in Figure 6-33 (b)).



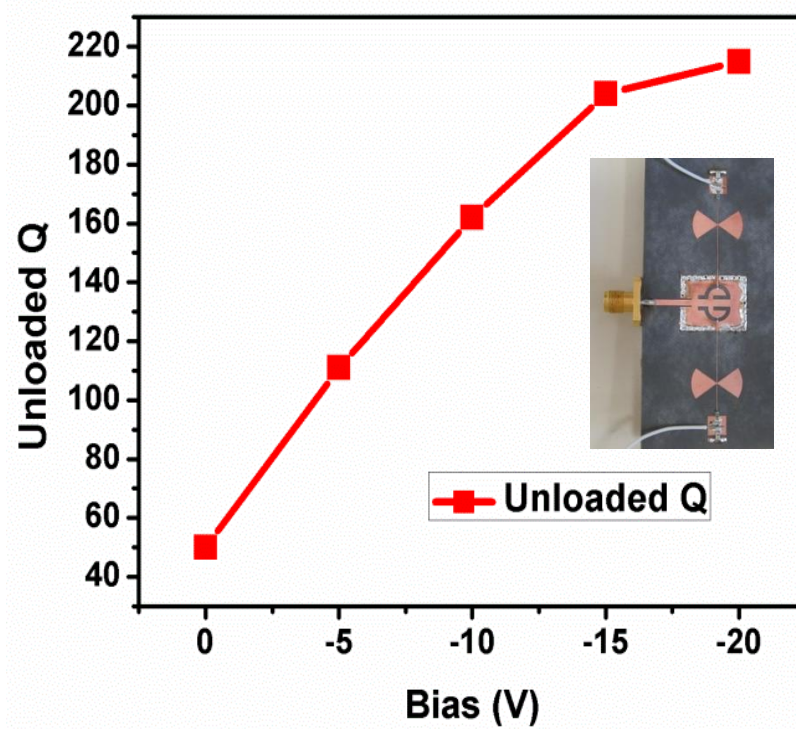
(a) Schematic of varactor-tuned 1-port port CCR

(b) Fabricated prototype of 1-port CCTR

Figure 6-32: Tunable 1-port resonator structure (a) schematic of varactor-tuned 1-port port CCTR (complementary coupled resonator), and (b) prototype of 1-port CCTR fabricated using RT/Duroid 5880 substrate with a thickness of 0.508 mm and dielectric constant of 2.2 [103]



(a) Measured S_{11} plots of tunable 1-port resonator



(b) Measured unloaded Q of the proposed tunable 1-port resonator [103]

Figure 6-33: Measured data (a) measured S_{11} plots of tunable 1-port resonator structure shown in Figure 6-32, and (b) measured unloaded Q of the proposed tunable resonator with various reverse bias voltages.

Figure 6-34 shows the photo of the fabricated prototype of 1-port CCTR (complementary coupled tunable resonator tunable resonator), where adding a coupling capacitor between the bias line and the resonator, increases the tuning range from 8.84% (4.579 GHz to 4.984 GHz) to 66% (2.73GHz to 4.535GHz). Figure 6-35 (a) shows the tuning characteristics of the 1-port CCTR, the resonant frequency varies from 2.73 GHz (marker m16) to 4.535 GHz (marker m15) for change in the bias voltage from 0V to -15V. The increase in tuning range comes at price, Q factor degrades from 10-130 as shown in 6-35 (b), this is due to the additional losses and loading from the coupling capacitors. Multilayer capacitor with lower loss used to improve the resonator quality factor up to some degree. However, there is a design challenge to achieve multi-octave band tuning range without degradation of Q-factor. In this thesis, different approaches discussed toward maximization of both Q-factor and tuning ranges for the application in high performance signal sources. It has been shown that the resonator's loss can be compensated using the negative resistance provided by active devices, thereby enhancing the Q factors (see Ch-5, section 5.5.4.1) [104]-[106].

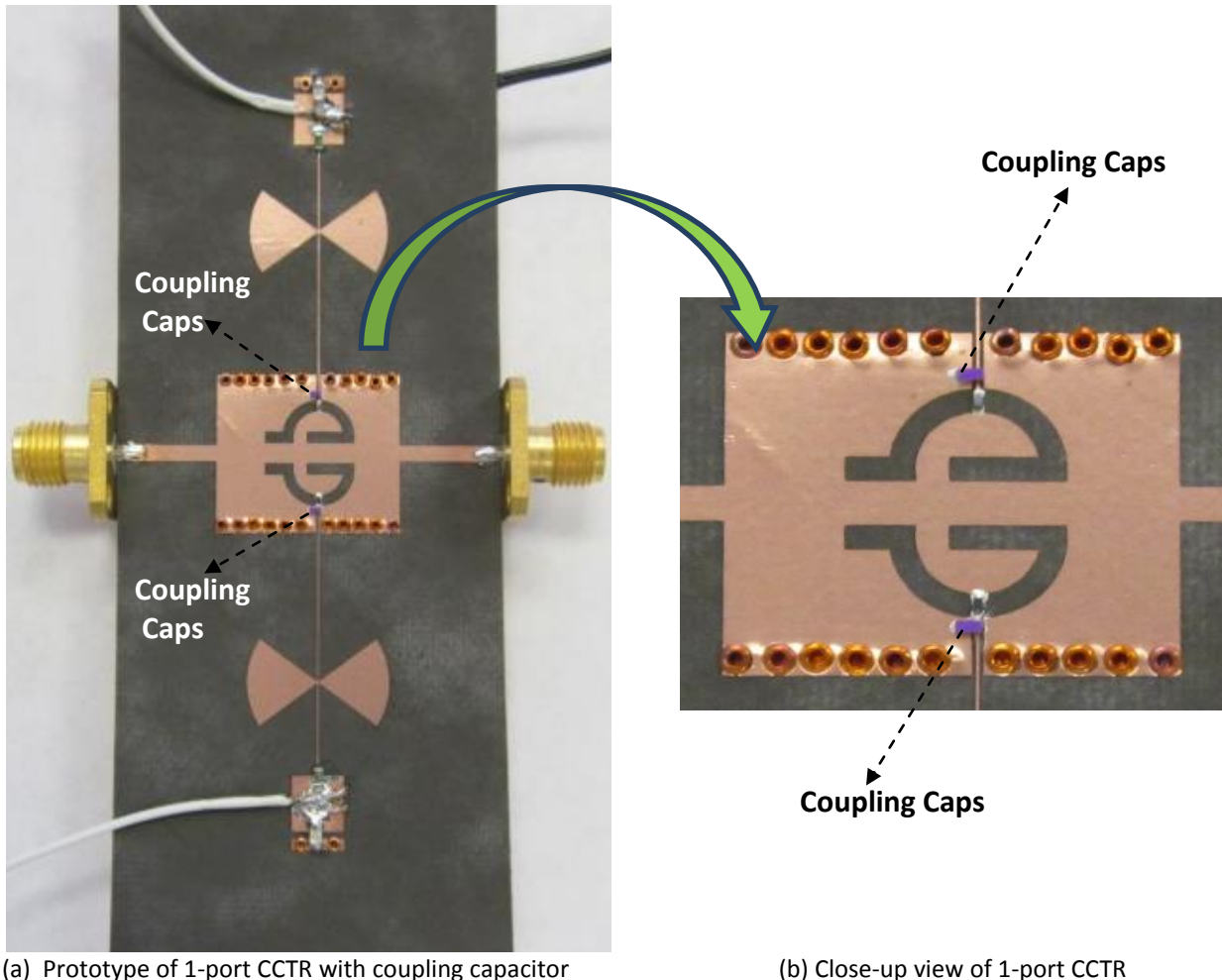
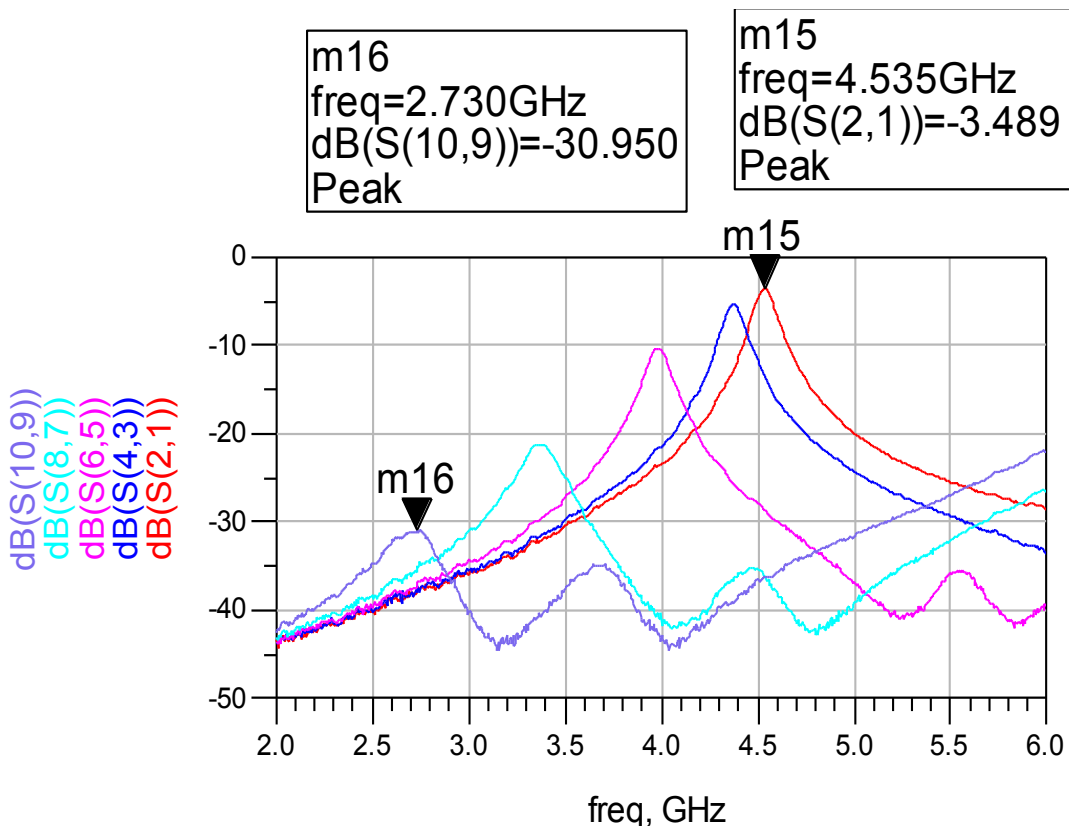
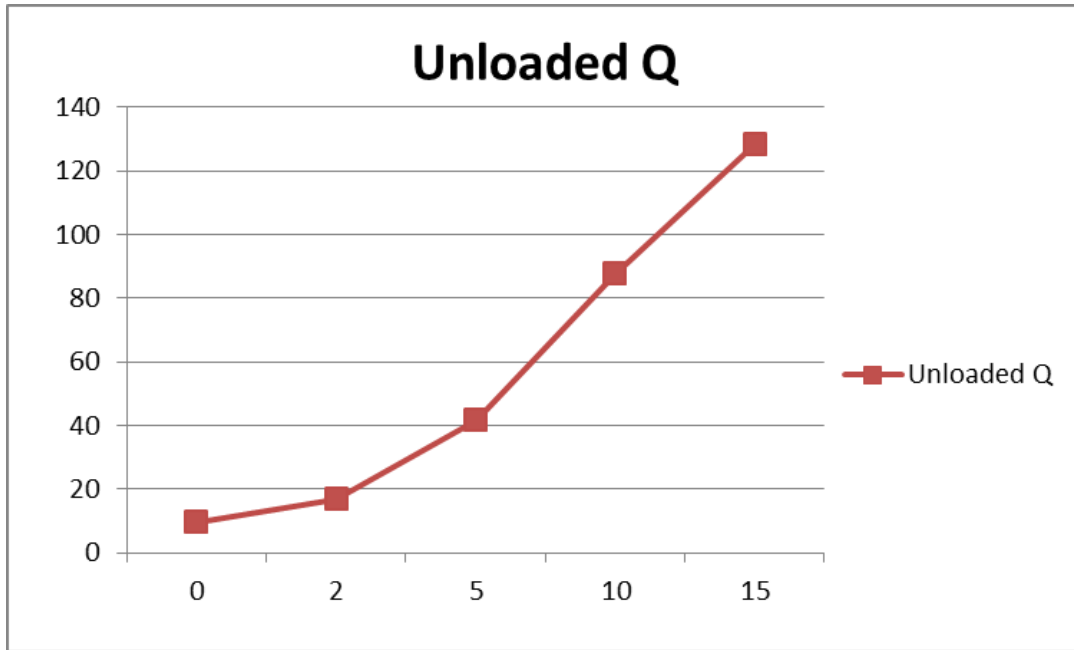


Figure 6-34: Photo of the fabricated prototype of 1-port CCTR (complementary coupled tunable resonator tunable resonator) (a) Shows additional capacitor between the bias line and the resonator, and (b) close-up view [110].



(a) measured S_{21} of the tunable 1-port CCTR with coupling capacitor shown in Figure 6-34



(b) Measured unloaded Q versus reverse bias voltage of 1-port CCTR with coupling capacitor shown in Figure 6-34

Figure 6-35: Measured data: (a) measured S_{21} of the tunable resonator shown in Figure 6-34, and (b) measured unloaded Q versus reverse bias voltage.

In order to optimize the Q of the CCTR shown in Figure 6-34, active device (HJ FET NE3210S01 from NEC), is embedded into the resonator network, powered by DC voltage, for compensating the losses over the desired operating tuning band. The novelty of this design is the compact size with improved Q factor, used for the realization of a low phase noise oscillator operating at X-band for RADAR applications. Figures 6-36 and 6-37 show the simplified schematic representation and layout of the SIW-ACCTR (active substrate wave-guide complementary coupled tunable resonator), fabricated using RT/Duroid 5880 substrate with a thickness of 0.508 mm and dielectric constant of 2.2 [110].

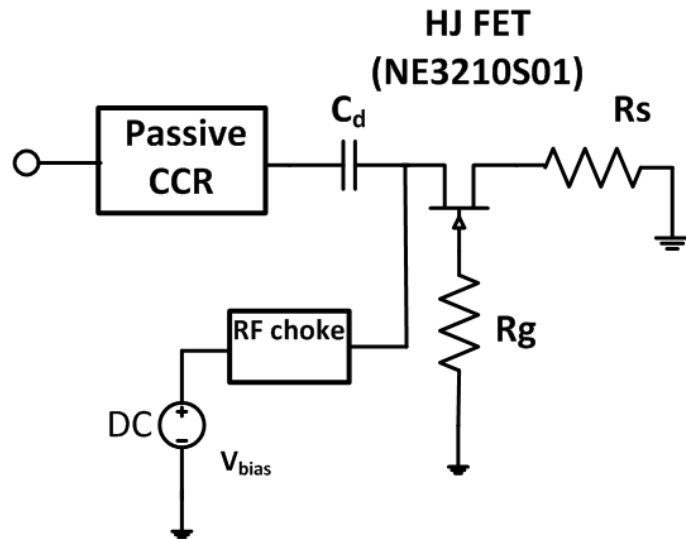


Figure 6-36: A typical schematic of active complementary coupled resonator ($C_d=0.3$ pF, $R_g=50$ ohm, $R_s=127$ ohm)

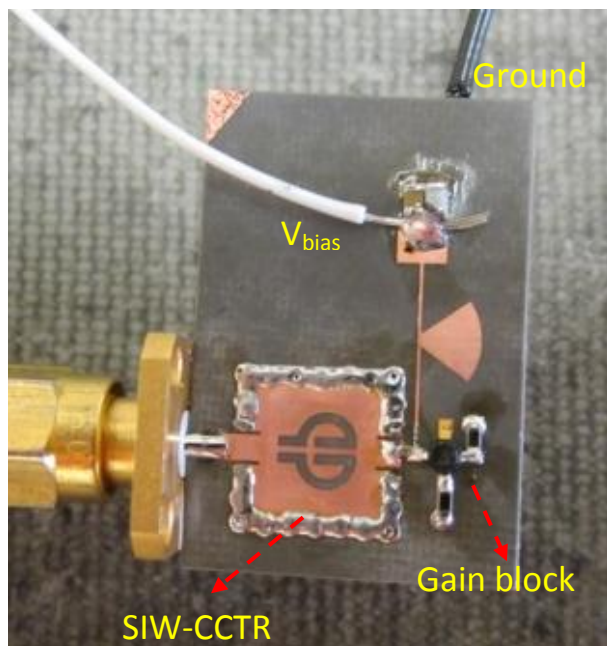


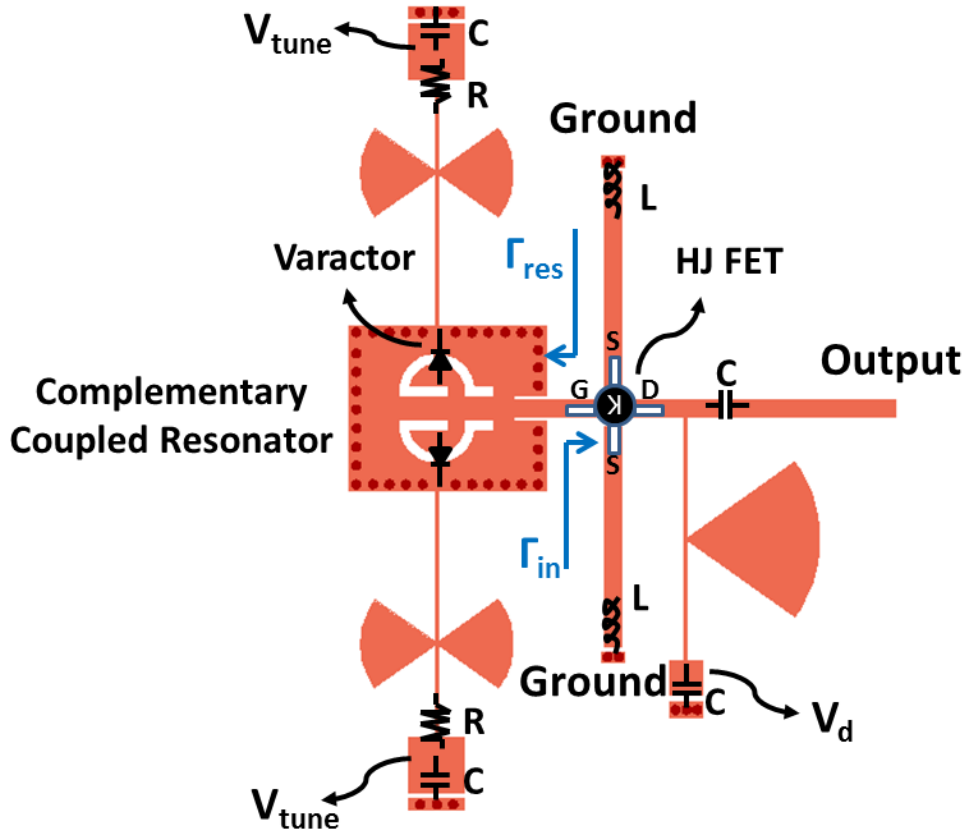
Figure 6-37: The fabricated prototype of SIW-ACCTR (active substrate wave-guide complementary coupled tunable resonator) fabricated using RT/Duroid 5880 substrate with a thickness of 0.508 mm and dielectric constant of 2.2.

Table 6.1 summarizes measured unloaded Q from (6.43), showing that the highest unloaded Q measured is 21172 when the transistor is drain biased at 1.8 V, thereby confirming that the unloaded Q can be maximized by properly optimizing the DC bias operating condition, further enhanced by using active devices [110].

Table 6.1 Measured unloaded Q

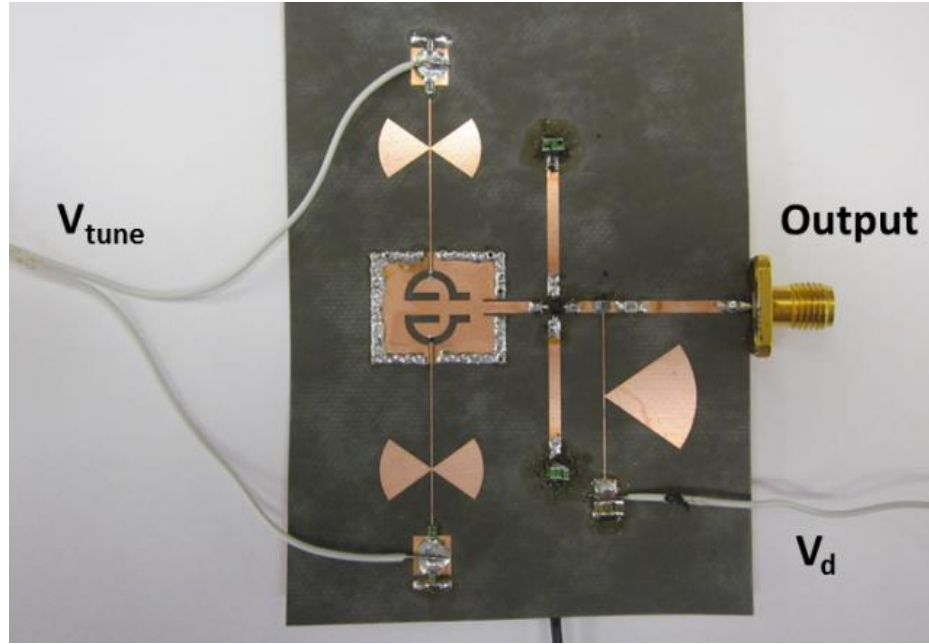
V_{bias}	0V	0.65V	1V	1.2V
Unloaded Q	130.7	95.6	706.3	1913.1
V_{bias}	1.4V	1.6V	1.8V	2.0V
Unloaded Q	3390	7249	21172	6938.5

Figures 6-38 and 6-39 show the layout and photo of the tunable oscillator using SIW-CCTR (substrate wave-guide complementary coupled tunable resonator) network shown in Figure 6-34, fabricated using RT/Duroid 5880 substrate with a thickness of 0.508 mm and dielectric constant of 2.2. As shown in Figure 6-38, NEC's Hetero-Junction FET NE3210S01 is chosen to be used for low power consumption, the transistor is drain-biased at $V_d = 1.5$ V, $I_{ds} = 22$ mA, and both of the varactors are reverse-biased at the same V_{tune} voltage. The gate of the transistor (Hetero-Junction FET NE3210S01) is connected to SIW-CCTR (Figure 6-34) is DC grounded ($V_g = 0V$) through inductive load supported by SIW structure. A DC decoupling capacitor placed on the output path prevents DC leakage.



Figures 6-38: A typical layout of the tunable oscillator using SIW-CCTR (substrate wave-guide complementary coupled tunable resonator) network shown in Figure 6-34 [103]

For stable oscillation, Γ_{in} should be greater than unity [102]. In order to make Γ_{in} greater than unity, two stubs in series with inductors are shorted to ground and connected to the sources of the transistor to increase its instability in the desired frequency band. The lengths of the stubs are also chosen so that $R_{res} = -R_{in}/3$, $X_{res} = -X_{in}$ to fulfill the oscillating conditions [103]. The oscillating frequency and output power after calibrating the cable loss versus the bias voltage are plotted, as shown in Figure 6-40.



Figures 6-39: A photograph of the fabricated tunable oscillator using SIW-CCTR (substrate wave-guide complementary coupled tunable resonator) network shown in Figure 6-34 [103]

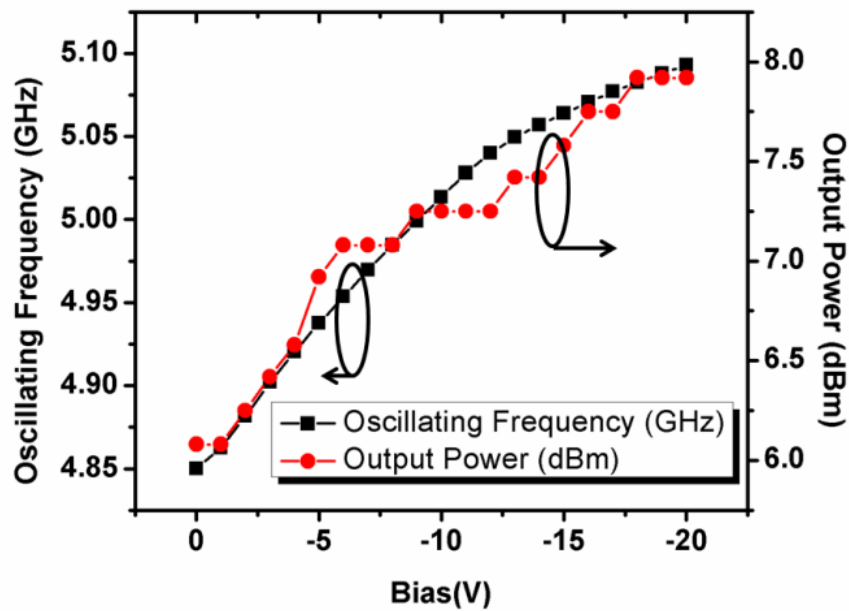


Figure 6-40: Measured performance of the tunable oscillator shown in Figure 6-39 with different bias voltage [103]

As shown in Figure 6-40, the oscillating frequency can be continuously tuned from 4.85 GHz to 5.1 GHz while reverse biased from 0 V to 20 V, which provides a tuning range of 5.15%. In addition, the output power varies from 6-8 dBm in the tuning range. The measured output spectrum of the tunable oscillator at 5.09 GHz is shown in Figure 6-41, measured phase noise is -115.2 dBc/Hz at an offset frequency of 1 MHz. The figure of merit (FOM) is given by (1.1)

$$FOM|_{f_{offset}} = \left[f(f_{offset}) - 20 \log_{10} \left(\frac{f_0}{f_{offset}} \right) + 10 \log_{10} \left(\frac{P_{DC}}{1mW} \right) \right] \quad \left(\frac{dBc}{Hz} \right) \quad (6.45)$$

where $f(f_{offset})$ is the phase-noise at the offset frequency f_{offset} , f_0 is the oscillating frequency, f_{offset} is the frequency offset in MHz, and P_{DC} is the total consumed DC power in milli-watts.

From (6.45)

$$FOM|_{f_{offset}=1MHz} = -174.1 \left(\frac{dBc}{Hz} \right) \quad (6.46)$$

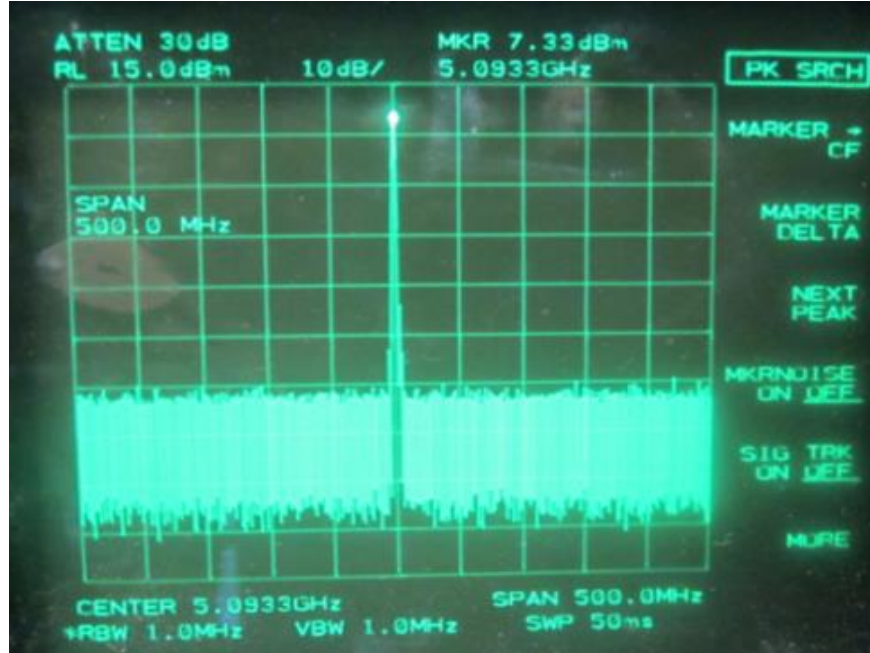


Figure 6-41: Measured output spectrum of the oscillator (Figure 6-39) at 5.09GHz [103]

Figures 6-42 and 6-43 show the layout and photograph of tunable X-band oscillator topology using active resonator as shown in Figure 6-37, fabricated using RT/Duroid 5880 substrate with a thickness of 0.508 mm and dielectric constant of 2.2. As shown in Figure 6-42, NEC's Hetero-Junction FET NE3210S01 is selected for low power consumption and higher DC-RF conversion efficiency, and a shunt stub is added at its source to increase instability at the desired frequency. The DC bias is chosen to be $V_d=2.5$ V and $I_d=6$ mA in the measurement in order to have optimized result for DC-RF conversion efficiency and FOM. It is to note that the entire circuit is biased with one single bias (V_d) enables miniaturization. The oscillator design is based on the negative-resistance method [67]. The length of the stub for the main oscillating transistor is also chosen so that $R_{res} = -R_{in}/3$, $X_{res} = -X_{in}$, to fulfill the starting condition for oscillation, where R_{res} and R_{in} are the real parts of Z_{res} and Z_{in} , respectively, and X_{res} and X_{in} are the imaginary parts of Z_{res} and Z_{in} , respectively.

The required DC biasing is done by adding lumped passive components (resistors) in order to self-bias the two transistors at their appropriate biasing points. Two capacitors are used to decouple the DC components from the transistors.

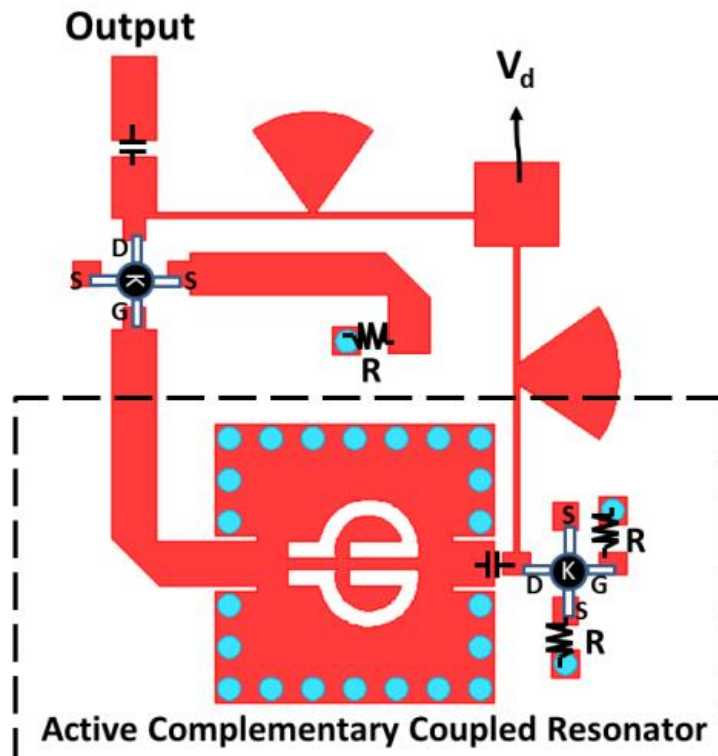


Figure 6-42: A typical layout of tunable X-band oscillator topology using active resonator as shown in Figure 6-37.

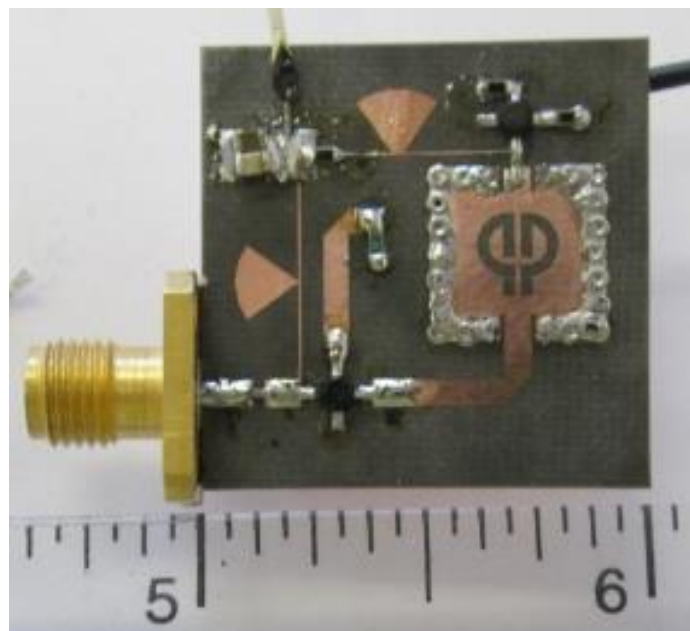
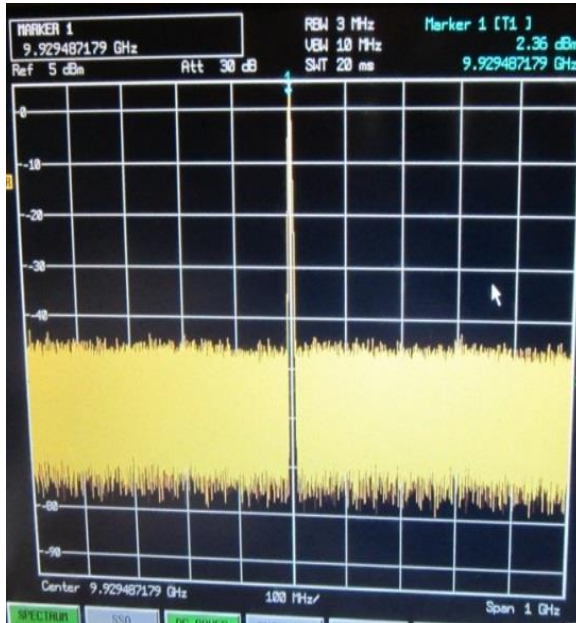
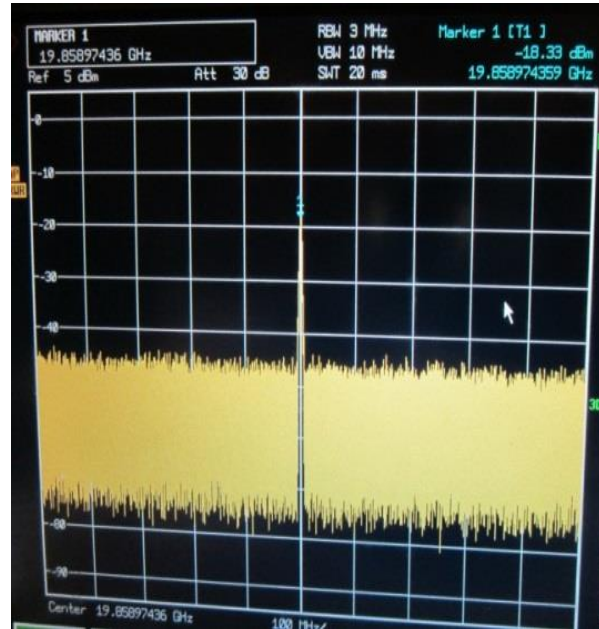


Figure 6-43: Photo of the fabricated tunable X-band oscillator topology (shown in Figure 6-42) fabricated using RT/Duroid 5880 substrate with a thickness of 0.508 mm and dielectric constant of 2.2.

Figure 6-44a shows RF output spectrum of the oscillator circuit depicted in Figure 6-43, the fundamental tone of the designed oscillator is at 9.93 GHz and it has an output power of 2.36 dBm. The second harmonic is -18.33 dBm at 19.86 GHz, as shown in Figure 6-44b



(a) RF output spectrum oscillator shown in Fig 6-43



(b) second harmonic of oscillator shown in Fig 6-43

Figure 6-44: Measured data (a) shows RF output spectrum of the oscillator circuit depicted in Figure 6-43, and (b) shows second harmonic -18.33 dBm at 19.86 GHz of oscillator circuit depicted in Figure 6-43.

The phase noise measurement is carried out by using two different set-ups. The first measurement is done by using R&S FSUP26 Signal Source Analyzer, in which the measured phase noise is -93.96 dBc/Hz and -123.86 dBc/Hz at 100 kHz and 1 MHz offset as shown in Figure 6-45 (a).

The phase noise measurement is repeated on Agilent 5052B Signal Source Analyzer along with E5053A Microwave Down-converter, in which the measured phase noise is -97.65dBc/Hz and -127.01 dBc/Hz at 100 kHz and 1 MHz offset as shown in Figure 6-45 (b), respectively.

Table 6.2 summarizes the measured results of using the two sets of equipments.

Table 6.2

	Oscillating Frequency	Output Power	Phase Noise@ 100 kHz	Phase Noise@ 1MHz	DC Power Consumption	FOM@ 100 kHz	FOM@ 1 MHz
R&S FSUP	9.904GHz	2.02dBm	-93.96dBc/Hz	-123.86dBc/Hz	15mW	-182.2	-192.1
Agilent 5052B	9.883GHz	3.02dBm	-97.65dBc/Hz	-127.01dBc/Hz	15mW	-185.89	-195.25



(a) Measured phase noise plot on R&S FSUP26



(b) Phase noise plot on Agilent 5052B+5053A

Figure 6.45: The phase noise measurement is carried out by using two different set-ups (R&S FSUP and Agilent 5053) (a) measured phase noise plot on R&S FSUP26 Signal Source Analyzer, and (b) measured phase noise plot on Agilent 5052B+5053A.

As shown in Figure 6-45, the close-in phase noise (<100 kHz offset) performance is very poor because of higher 1/f noise for HJ FET device. By incorporating SiGe HBT device in place of HJ FET, the influence of 1/f noise or flicker noise can be reduced [67]. Figure 6-46 (a), and 6-46 (b) show the oscillator circuit schematic using SiGe HBT device, and the measured phase noise plot. It can be seen that measured phase noise plot as depicted in Figure 6-46 (b) shows stable behavior over temperature (-40 degree C to +85 degree C), the novel bias stabilization circuit incorporated in this research work allows optimum phase noise performance over desired operating temperature (-40 degree C to +85 degree C). The oscillator circuit delivers 4.75-dBm O/P power with DC bias of 5V and 12 mA.

As illustrated in Figure 6-46(a), 10 GHz oscillator circuit uses a SiGe Heterojunction-bipolar-transistor (HBT) active device (NEC), fabricated on Rogers substrate material with a dielectric constant of 3.38 and thickness of 32 mil-microstripline medium. The reported paper [8, 10, and 13] by authors use BFP 540 SiGe HBTs from Infineon shows the significant improvement of more than 40 dB in phase noise performance at 10 kHz offset from the carrier frequency 10 GHz but at the cost of the increase in DC power consumption. In this research work, SIW-CCR oscillator topology as shown in Figure 6-39 and 6-43 operating at C-band and X-band, can be easily scaled to a higher frequency such as Ku- and Ka- bands.

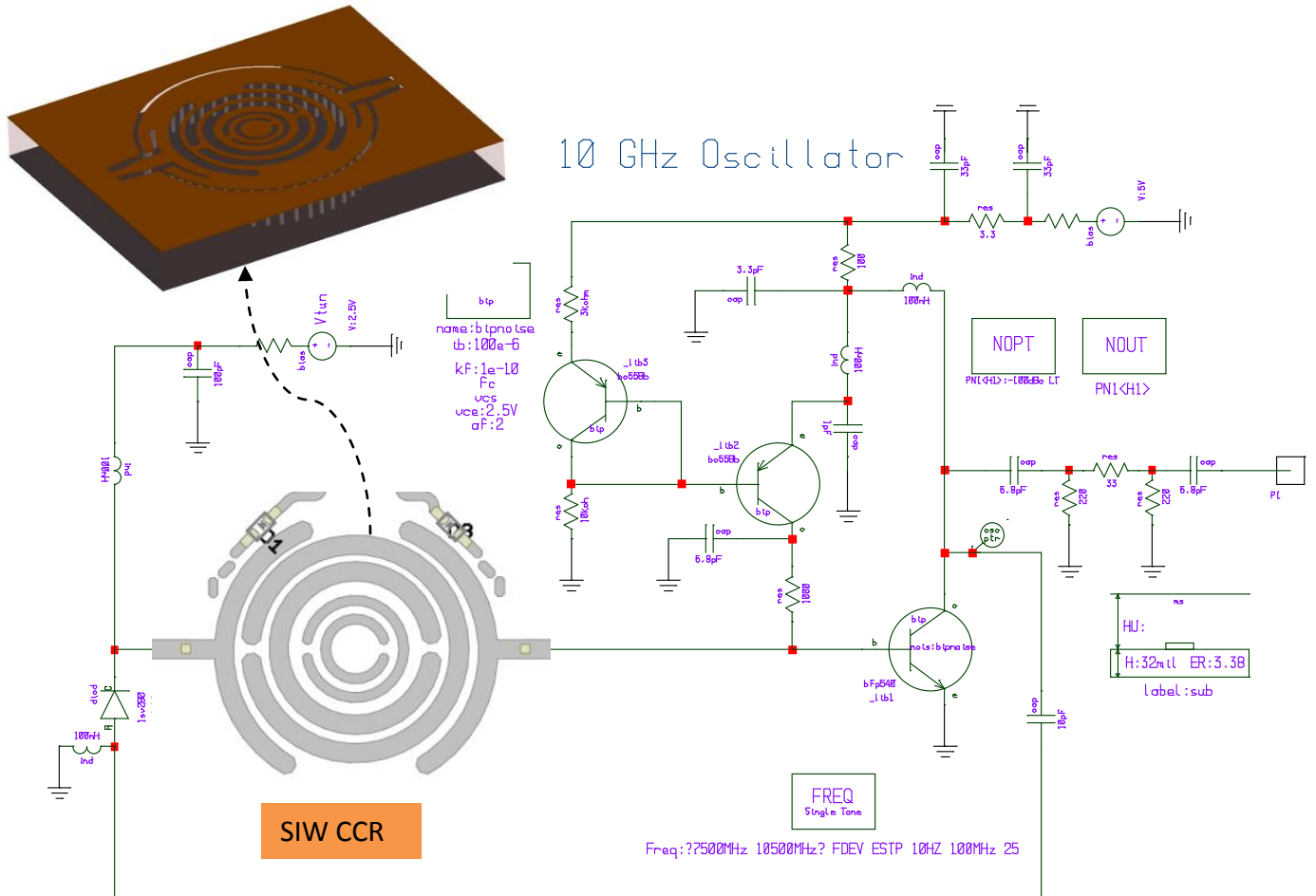


Figure 6-46 (a): A typical circuit schematic of the novel 10 GHz oscillator using printed resonator using 32 mil Roger R4003C, Dielectric constant=3.38 (size of the board 0.5x0.5 inches), with DC bias (5V, 12mA)

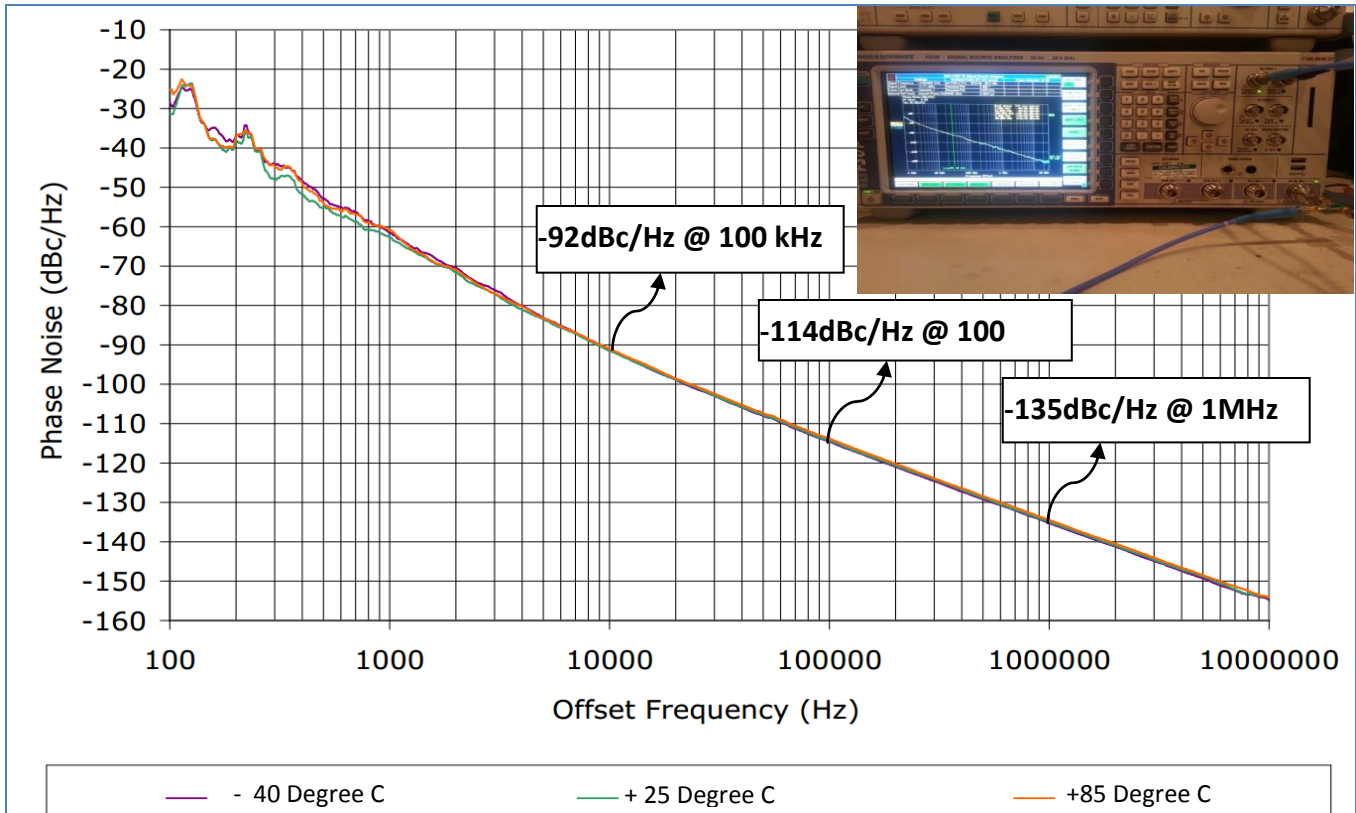


Figure 6-46 (b): Measured phase noise plot of 10 GHz oscillator circuit shown in Figure (6-45 a). It can be seen that phase noise plot shows stable behavior over temperature, the novel bias stabilization circuit helps for optimum phase noise performance over desired operating temperature (-40 degree Celsius to +85 degree Celsius)

Figure 6-47 shows the CAD simulated layout of a Ku-band SIW-CCR with a size of 7.2 mm by 6 mm, whose center frequency is around 16 GHz. CAD Simulated results using HFSS show that the unloaded Q of Ku band CCR is around 350. Similarly, the CCR scaled to Ka-band with a size of 3.6mmx 3mm that has a center frequency around 32 GHz, and the simulated unloaded Q is around 330. In addition to SIW CCRs, Mobius inspired resonators using slow-wave structures discussed in Ch-7 and Ch-8 for the realization of low phase-noise oscillator circuit.

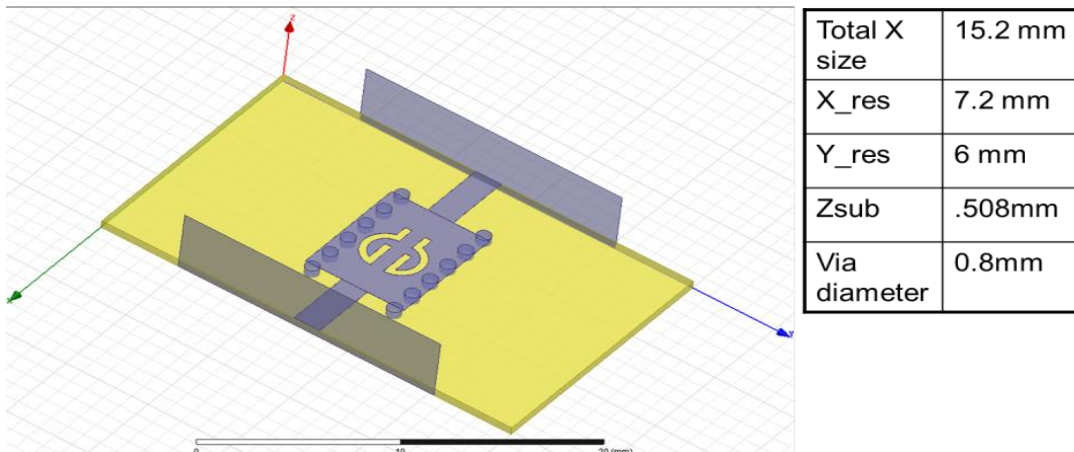


Figure 6-47: A typical CAD schematic of Ku-band SIW-CCR

6.4.1.9 Opto-Electronic Oscillator (OEO) using Metamaterial Resonator

Achieving ultra low phase noise is a great challenge in deep space communication, docking and remote sensing (radar), analog-to-digital convertors (ADC), instrumentation, and timing clocks. In many coherent detection systems, the required phase noise and the associated timing jitters of the stable local oscillators becomes the limiting factor of the overall performance of the system in terms of data bit error rate, achieved spatial and temporal resolution, and effective number of bit resolution. In the past several decades, great efforts made in the development of various techniques for generation of low phase noise oscillators. Opto-electronic oscillator (OEO) stands out among the others for its capability of generating ultra-stable microwave and millimeter-wave oscillations owing to the extremely high Q achieved by utilizing the low loss in optical fibers (Appendix E, F, G, H, and I) [86].

These high Q operation OEOs with their low phase noise performance could be employed as highly stable sources to force oscillate a small size low stability RF oscillator. The standard forced oscillation techniques of injection locking (IL) and phase-locked loop (PLL) are two viable methods for further phase noise reduction by introducing external frequency reference to the oscillator [86]-[89], where the lowest achievable phase noise with these techniques is limited by the phase noise of the external reference source. The concepts of external forced oscillations could not be extended to the already record setting OEO to further stabilize them, but nonetheless self forced oscillation could be provided as a method to further reduce close-in to carrier phase noise of oscillators, as demonstrated by H.C. Chang in [90] (Appendix F). A self-injection locking (SIL) topology proposed by passing the output of oscillator through an electrical delay line or a high Q resonator and feeding it back using a circulator (Appendix G). The experimentally verified modeling demonstrates that the overall oscillator phase noise is inversely proportional to the signal delay time or Q. However, due to the high loss and limited Q in electric circuits, the phase noise improvement is not significant. To bypass the limitation of electrical components, Lee *et al.* [91] employed a 2.4km long optical fiber in the feedback loop of the SIL topology and achieved a phase noise reduction of 27dB at 10kHz offset for a 30GHz oscillator. The concept of forced oscillation could also be extended to Self-phase locked loop (SPLL) demonstrated by Pillet *et al.* [92]. In the proposed structure, the microwave signal generated from the beat note of a dual frequency laser (DFL) sent into a delay-line frequency discriminator (DLFD) whose output used to stabilize the laser frequency for generating a more stable beat note. The analytical modeling provided explanation for this phase noise reduction.

While IL phenomena are easy to implement, the phase noise in the close-in offset frequency range degraded due to frequency offset detuning and limited locking range as explained in [93]. On the other hand, even though PLL has a longer pull-in time that results in a slow response, the high gain loop filter enables the PLL to remove the close-in phase noise significantly, while far away from carrier suffers from a higher noise. Sturzbecher *et al.* [94] demonstrated in externally forced oscillators, a better phase noise characteristics for both close-in and far-away from carrier, and a wider locking range is achieved by combining IL and PLL (ILPLL) [93, 95] ((Appendix H)). However, external reference sources are required in the forced ILPLL topology, which limits the ultimate phase noise performance. The novel approach is to incorporate both SIL and SPLL for noise reduction technique using Push-Push configuration [85]-[86]. Figure 6-48 shows the typical block diagram that describes the novel push-push topology in conjunction

with an evanescent mode metamaterial resonator combiner network. The unique properties of the metamaterial resonator are that it has a negative permittivity and negative permeability, and that it enables amplification of an evanescent mode wave without degeneration. Hence, including a metamaterial evanescent mode resonator can yield a loaded Q-multiplier effect (effectively multiplying the effect of the circuit's Q with regard to the phase noise of the circuit) in the oscillator (or other autonomous circuits). Utilization of the evanescent mode resonator is beneficial, as compared to the use of a multi coupled planar resonator because of higher Q-factor for a given size.

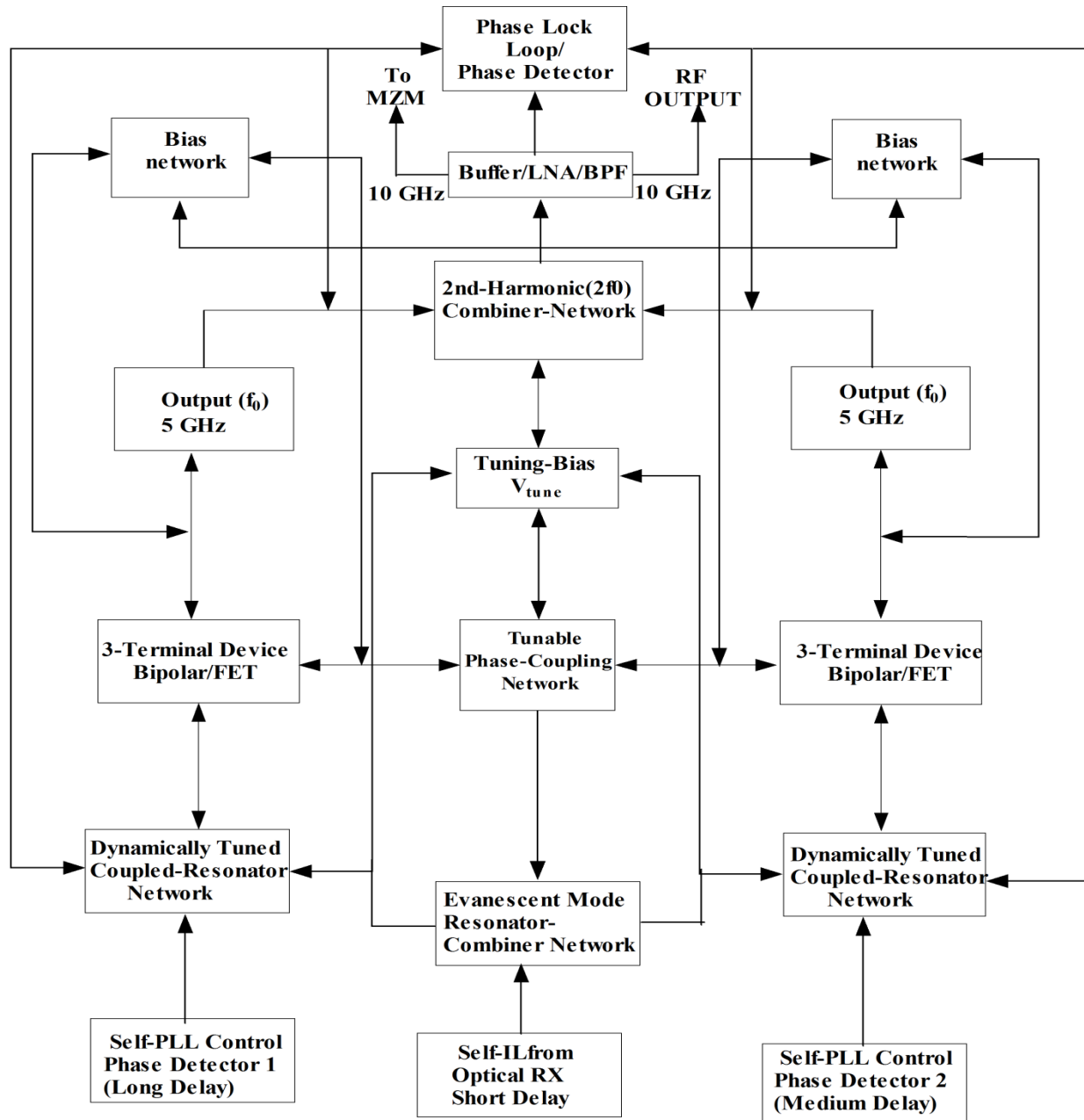


Figure 6-48: Shows the typical block diagram of 10 GHz source: Integrated realization of a highly stable self ILPLL RF Oscillator (US Patent application No.: 61/746, 919; filed on Dec 28, 2012 and US Patent application no. 13/760767; filed on Feb 06, 2013)

The estimation and measurement of the unloaded Q-factor is done by measuring the [S]-parameter using VNA (vector network analyzer). The methods involve circle-fitting procedures applied to multiple data points representing S-parameter responses of the resonator around the resonance. There are two practical methods for Q-factor measurement: (i) Reflection method for reflection mode resonators [107], and (ii) Transmission Mode Quality Factor Technique for transmission mode resonators [108]-[110].

Figure 6-49 depicts the unloaded Q (quality factor) of the evanescent mode resonator and multi coupled planar resonator, plotted against a range of operating frequencies from about 2 GHz to about 16 GHz. The estimation of Q (quality factor) is done by experimental measurement of [S]-parameter using vector network analyzer. As shown in Figure 6-49, the evanescent mode resonator is capable of achieving a quality factor above 1000 at operating frequencies ranging from about 2 GHz to about 15 GHz.

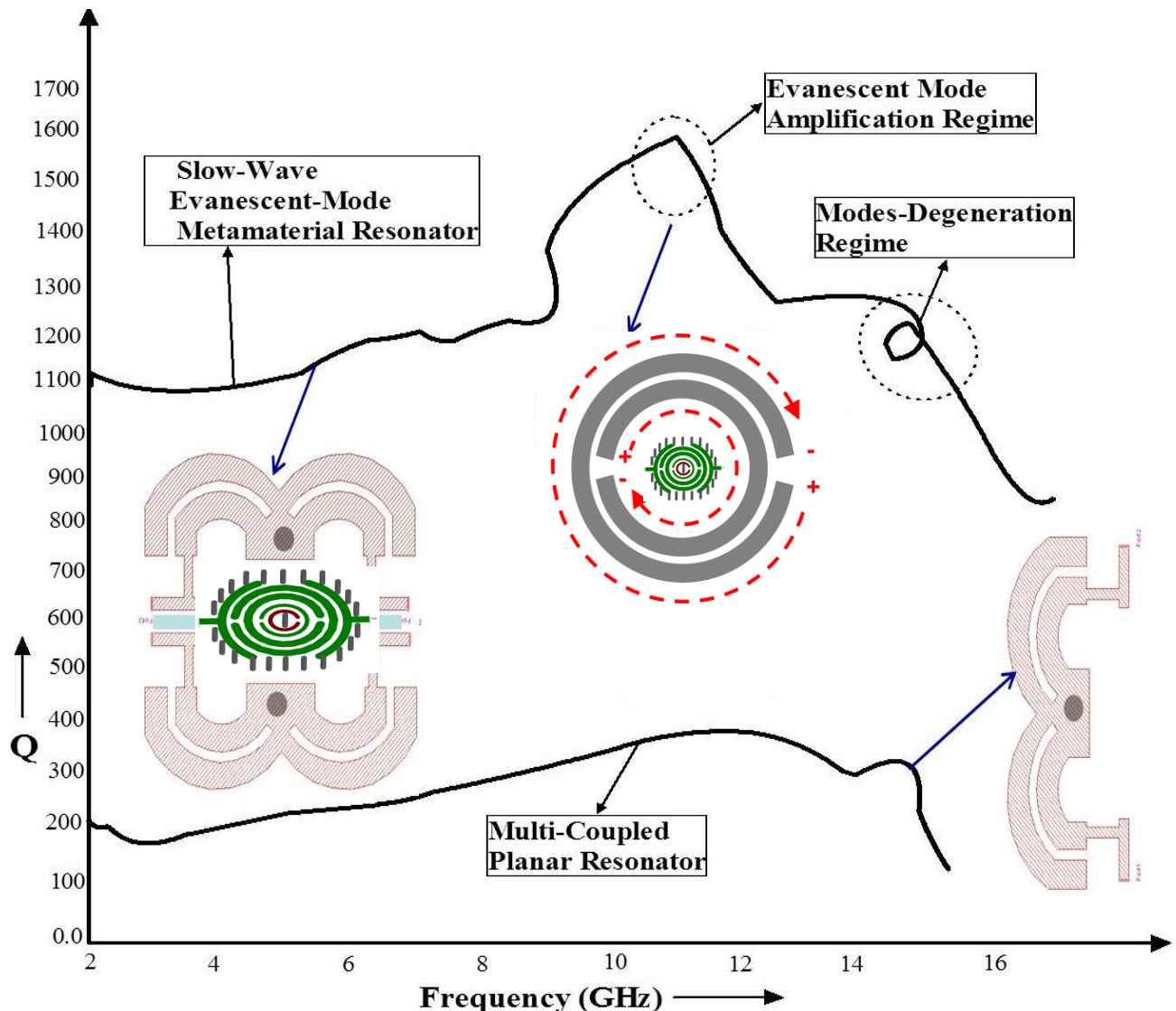


Figure 6-49: Shows the typical measured plot of unloaded quality factor (Q-factor) of novel resonators (Multi-Coupled resonator, Slow-wave evanescent-mode metamaterial resonator, Evanescent-mode amplified resonance regime).

As shown in Figure 6-48, the metamaterial evanescent-mode resonator combiner network coupled (capacitively) to each of the dynamically tuned resonator networks. This acts as an evanescent mode (EM) buffer, storing a portion of the excess radio frequency (RF) energy coupled into the resonator network for a given period of a signal cycle so that the conduction angle of the device can be reduced, thereby reducing the average noise performance for a given period of time. The spectral pure signal generated by locking the optical phase modulation to a free spectral range resonator in conjunction with metamaterial evanescent-mode resonator combiner network.

The oscillator circuit illustrated in block diagram as shown in Figure 6-48 operates in the following manner. The electrical outputs of narrowband RF amplifiers are inputs to the dynamically tuned coupled resonator networks respectively; similarly, the electrical output of narrowband RF amplifier is input to the metamaterial evanescent mode resonator combiner network. These signals provide injection locking (IL) and phase locking loop properties under which the resonance of the VCO is controlled.

The circuit elements comprising of the various modules, e.g., diodes, resistors, capacitors, resonators, etc., are selected so that each of the three terminal devices oscillates at a fundamental frequency, f_0 . As the voltage level of the tuning voltage module is adjusted the fundamental frequency of operation, f_0 , appearing as input signals is tuned over the operating range of the oscillator, e.g., preferably octave-band. These signals are then combined in the combiner network to produce a signal operating at twice the fundamental frequency, $2f_0$, and that is dynamically tuned as the voltage level of the tuning voltage module is adjusted. A portion of the signal from the combiner network is fed to the modulator through electronic circuitry including a buffer, low noise amplifier, and bandpass filter. A portion of the signal may also be output as a tunable output (e.g., a signal operating at the second harmonic of the input signals).

A select portion of the signal from the combiner network and a select portion of a signal from the metamaterial evanescent-mode resonator combiner network is fed back to the tuning network, the portion of the signal is then fed to tunable phase coupling network and used to dynamically tune the phase of the output signals. This makes each of these signals remain in phase during a tuning operation. A portion of the signal also fed to each of the dynamically tuned coupled resonator networks. As the tuning voltage, V_{tune} is adjusted the frequency of the signal f_0 is present at each of the terminals. They are tuned over the operating frequency band through the coupled resonator networks while the phase coupling network keeps the devices operating in an anti-phase mode at the fundamental frequency, f_0 (e.g., push-pull behavior), while the second harmonic, $2f_0$, interferes constructively (e.g., push-push behavior) over the octave band. In addition, the phase detector network operates as described above, dynamically compensates for phase errors during wideband operation.

The microwave carrier at X-band and above, generated by locking the optical phase modulation to a free spectral range resonator, in conjunction with metamaterial evanescent mode resonator combiner network that offers the phase noise performance -160d Bc/Hz @ 10 kHz offset from the carrier, is best to date for the given figure of merit (FOM) and this class of

oscillator topology [84]-[86]. The detailed description of ultra low phase noise sources using optical methods are discussed in Ch-10.

6.5 Conclusion

The oscillator circuits using different resonator networks discussed in this Chapter allow clear understanding about oscillator performance metrics in terms of size, power consumption and frequency tunability [91]-[109]. Different printed resonator technology described in Appendix B, Appendix C, , and Appendix D provides brief insights about pros and cons with respect to cost and implementation issues. The design methodology of OEO technology discussed in Appendix E, Appendix F, Appendix G, Appendix H, and Appendix I. Unfortunately, each development design of VCO using resonator (passive and active) technology has its price in terms of size, cost, efficiency and power budget.

6.6 References

- [1] E. Pistono, M. Robert, L. Duvillaret, J.-M. Duchamp, A. Vilcot, and P. Ferrari, "Compact Fixed and Tune-All Bandpass Filters Based on Coupled Slow-Wave Resonators," *IEEE Trans. on MTT*, Vol. 54, No. 6, June 2006, pp. 2790-2798.
- [2] Wei-Shin Chang, Cheng-Hsien Liang, and Chi-Yang Chang," Compact Microstrip Bandpass Filters Using Miniaturized Slow-Wave Quarter-Wavelength Resonators", Proceedings of Asia-Pacific Microwave Conference 2010, pp. 1958-1961.
- [3] Lung-Hwa Hsieh and Kai Chang, "Slow-Wave Bandpass Filters Using Ring or Stepped-Impedance Hairpin Resonators," *IEEE Transactions on Microwave Theory & Techniques*, Vol. 50, No. 7, pp. 1795-1800, July 2002.
- [4] Hsiu-Ying Cho, et. al., "High-Performance Slow-Wave Transmission Lines With Optimized Slot-Type Floating Shields," *IEEE Trans. on Electron Devices*, Vol. 56, No. 8, August 2009.
- [5] T. Masuda, N. Shiramizu, T. Nakamura, and K. Washio," Characterization and Modeling of Microstrip Transmission Lines with Slow-wave Effect," SMIC in RF Systems, pp.55-158, 2008.
- [6] H. wang et. al., "A 60 GHz Wideband Injection-Locked Frequency Divider with Adaptive-Phase-Enhancing Technique", RFICS, pp. 75-78, 2011.
- [7] A. K. Poddar, S. K. Koul and Bharthi Bhat, "Millimeter Wave Evanescent Mode Gunn Diode Oscillator in Suspended stripline Configuration", IR & MM Wave, 22nd International Conference, pp. 265-266, July 1997.
- [8] A. K. Poddar, U. L. Rohde, " Metamaterial Möbius Strips (MMS): Application in Resonators for Oscillators and Synthesizers", IEEE UFFC Symposia, May 19-22, 2014
- [9] Chung-Tse M. Wu, A. K. Poddar, U. L. Rohde, T. Itoh, " A C-band Tunable Oscillator Based on Complementary Coupled Resonator using Substrate Integrated Waveguide Cavity " EuMW 2014
- [10] A. K. Poddar and U. L. Rohde, "Slow-Wave Evanescent-Mode Coupled Resonator Oscillator", IEEE Frequency Conyrol Symposium, Proceedings, pp. 01-07, May 2012.
- [11] A. K. Poddar and U. L. Rohde, "Adaptive Mode-Coupled Harmonically Tuned High-Q Ultra Low Phase Noise Sources", Microwave Journal, pp. 106-120, Sept 2011.
- [12] U. L. Rohde and A. K. Poddar, "Slow-Wave Structures Slice VCO Phase Noise", Microwave & RF, May 2011.

- [13] A. K. Poddar and U. L. Rohde, "Slow Wave Resonator Based Tunable Oscillators," Proceedings of 2011 Joint Conference of the IEEE International Frequency Control Symposium & European Frequency and Time Forum, pp. 549-558, May 2011.
- [14] U. L. Rohde and A. K. Poddar, "A Digital Frequency Synthesizer Using Adaptive Mode-Coupled Resonator Mechanism for Low Noise and Low Jitter Applications", IEEE (ISCAS), pp. 414-417, Brazil, May 15-18, 2011.
- [15] Wei-Shin Chang and Chi-Yang Chang, "A High Slow-Wave Factor Microstrip Structure With Simple Design Formulas and its Application to Microwave Circuit Design", IEEE Trans. on Microwave Theory and Techniques, Vol. 60, No. 11, pp. 3376-3383, Nov 2012.
- [16] V. K. Gupta, P. P. Kumar, and C. N. Rao, " A Novel Miniaturized, Wideband, High Directivity Microstrip Coupler on FR4", International Conference on Microwave and Photonics (ICMAP), pp. 1-4, 2013.
- [17] U. L. Rohde and A. K. Poddar, "Large-Signal Approach Yields Low-Noise VHF/UHF Oscillators, part 1, pp. 62-76, April 2008.
- [18] U. L. Rohde and A. K. Poddar, "Large-Signal Approach Yields Low-Noise VHF/UHF Oscillators, part 2, pp. 84-96, May 2008.
- [19] U. L. Rohde and A. K. Poddar, "Planar Resonators Arm Tunable Oscillators", Microwave & RF, part 1, pp. 92-96, June 2008
- [20] U. L. Rohde and A. K. Poddar, "Planar Resonators Arm Tunable Oscillators", Microwave & RF, part 2, July 2008.
- [21] U. L. Rohde and A. K. Poddar, "Miniature VCOs Shrink Wideband Synthesizers, Microwave & RF, pp. 87-92, Dec 2008.
- [22] U. L. Rohde and A. K. Poddar, "*STPCR Offers Integrable Alternatives Of DRO*", Microwave Symposium Digest, 2008 IEEE MTT-S, pp. 233-236, Atlanta, USA, 15-20 June 2008.
- [23] U. L. Rohde and A. K. Poddar, "Mode-Coupled Stubs-Tuned Planar Resonator Offers Promising And Integrable Alternatives Of DRO (Dielectric Resonator Oscillator)", IEEE Sarnoff Symposium, pp. 1-7, Princeton, NJ, USA, April 28-30, 2008.
- [24] U. L. Rohde and A. K. Poddar, "Injection-Tuned Coupled Oscillators" IEEE Radio Wireless Symposium 2008, pp. 367-370, Orlando, FL, USA, 22-24 January 2008.
- [25] U. L. Rohde and A. K. Poddar, "*Reconfigurable Concurrent Oscillator (RCO)*" IEEE Radio Wireless Symposium 2008, pp. 371-374, 22-24 January 2008, Orlando, FL, USA.
- [26] U. L. Rohde and A. K. Poddar, "Stubs-Tuned Planar Coupled Resonator Based Spectral Pure Signal Source for Wireless Communication Systems", IEEE/PIMRC 2007, pp. 01-05, Greece, Sept. 03-07, 2007.
- [27] U. L. Rohde and A. K. Poddar, "Reconfigurable Concurrent Oscillator (RCO)", IEEE 18th International Personal, Indoor and Mobile Radio Communications, IEEE/PIMRC 2007, pp. 01-05, Greece, 01-05, Sept. 03-07, 2007.
- [28] U. L. Rohde and A. K. Poddar, "Self-Injection Locked Compact Coupled Planar Resonator Based Cost-Effective Ultra Low Phase Noise VCOs For Wireless Systems", IEEE/ECCTD 2007, pp. 998-1001, Spain, Aug 27-30, 2007.
- [29] U. L. Rohde and A. K. Poddar, "Noise Cancellation and Noise Minimization Techniques for Low Cost Compact Size Configurable RF Oscillators/VCOs", European Conference on Circuit Theory and Design, pp. 986-989, ECCTD 2007 Spain, Aug 27-30, 2007.

- [30] U. L. Rohde and A. K. Poddar, "Concurrent, Reconfigurable and Concurrent Oscillators for Multi-Band Multi-Mode Communication Systems", European Microwave Conference, EUMC 2007, pp. 1050-1053, Munich, October 09-12, 2007.
- [31] U. L. Rohde and A. K. Poddar, "Concurrent, Reconfigurable and Concurrent Oscillators for Multi-Band Multi-Mode Communication Systems", European Conference on Wireless Technology, ECWT 2007, pp. 292-295, Munich, October 08-10, 2007.
- [32] U. L. Rohde and A. K. Poddar, "Low Cost Configurable RF Signal Source For Wireless Applications", European Microwave Conference, EuMiC 2007, pp. 508-511, Munich, October 09-12, 2007.
- [33] U. L. Rohde and A. K. Poddar, "Noise Reduction Techniques For Configurable RF Signal Source", 6th International Conference on Antenna Theory and Techniques, IEEE/ICATT 2007, pp. 163-166, Ukraine, Sept. 17-21, 2007.
- [34] U. L. Rohde and A. K. Poddar, "Minimization of Phase Noise in Scaled Device Coupled Mode Oscillators", 2007 6th International Conference on Antenna Theory and Techniques, IEEE/ICATT 2007, pp. 51-56, Ukraine, Sept. 17-21, 2007.
- [35] U. L. Rohde and A. K. Poddar, "Low Cost Signal Source for Multi-Band Multi-Mode Wireless Systems", 2007 6th International Conference on Antenna Theory and Techniques, IEEE/ICATT 2007, pp. 167-169, Ukraine, Sept. 17-21, 2007.
- [36] Fei Shen, et. al, "A Novel V-Shaped Microstrip Meander-Line Slow-Wave Structure for W-band MMPPM", IEEE Trans. on Plasma Science, Vol. 40, Mo. 2, pp. 463-469, Feb 2012.
- [37] U. L. Rohde and A. K. Poddar, "STPCR VCO Replaces Expensive DRO", IEEE/APMC 2007, pp. 1-4, Dec. 11-14, 2007, Bangkok, Thailand.
- [38] J. -S. Hong and M. J. Lancaster, "Theory and experiment of novel microstrip slow-wave open-loop resonator filters", IEEE Trans. on MTT., vol. 45, pp. 2358-2365, December, 1997.
- [39] M. Sagawa, K. Takahashi, and M. Makimoto, "Miniaturized hairpin resonator filters and their application to receiver front-end MIC", IEEE Trans. Microwave Theory Tech., vol. 37, pp. 1991-1997, December, 1989.
- [40] F. Rouchaud, V. Madrangeas, M. Aubourg, P. Guillon, B. Theron, and M. Maignan, "New classes of microstrip resonators for HTS microwave filters applications", IEEE MTT-S Int. Microwave Symp. Dig., Vol. 2, pp. 1023-1026, June 1998.
- [41] J. T. Kuo, M. J. Maa, and P. H. Lu, "A microstrip elliptic function filter with compact miniaturized hairpin resonators", IEEE Microwave and Guided Wave Lett., vol. 10, pp. 94-95, March, 2000.
- [42] U. L. Rohde and A. K. Poddar, "*STPCR Offers Integrable Alternatives Of DRO*", 2008 IEEE MTT-S, pp. 233-236, 15-20 June 2008 Atlanta, USA.
- [43] R. J. Cameron, C. M. Kudsia, and R. R. Mansour, "Microwave Filters for Communication Systems" Fundamentals, Design, and Applications, 2007 John Wiley & Sons, Inc.
- [44] L. M. Ledezma, "A study on the miniaturization of microstrip square open loop resonators", USF, MS. Thesis 2011.
- [45] J. Hong and M. Lancaster, "Microstrip Filters for RF/Microwave Applications", John Wiley and Sons, 2001.
- [46] F. X. Sinnesbichler, B. Hautz and G. R. Olbrich, "A Si/SiGe HBT dielectric resonator push-push oscillator at 58 GHz", IEEE Microwave and Guided Wave Lett., vol. 10, pp. 145-147, April 2000.

- [47] L. -H. Hsieh and K. Chang, "Slow-wave bandpass filters using ring or stepped impedance hairpin resonators", IEEE Trans. on MTT., vol. 50, pp. 1795 - 1800, July 2002.
- [48] T. .Y. Yun and K. Chang, "Analysis and optimization of a phase shifter controlled by a piezoelectric transducer", IEEE Trans. on MTT, vol. 50, pp. 105-111, January 2002.
- [49] Y. M. Poplavko, Y. V. Prokopenko, V. I. Molchanov, and A. Dogan, "Frequency-tunable microwave dielectric resonator", IEEE Trans. on MTT., vol. 49, pp. 1020-1026, June 2001.
- [50] H. Yabuki, M. Sagawa, and M. Makimoto, "Voltage controlled push-push oscillators using miniaturized hairpin resonators", IEEE MTT-S IMS Symp. Dig., pp. 1175-1178, 1991.
- [51] Jia-Sheng Hong and Michael J. Lancaster" Cross-Coupled Microstrip Hairpin-Resonator Filters", IEEE Trans. Microwave Theory Tech., Vpl. 46, No. 1, Jan 1998
- [52] B. C. Wadell, Transmission Line Design Handbook, MA, Artech House, p. 321, 1991.
- [53] M. Kirschning, R. H. Jansen and N. H. L. Koster, "Measurement and computer aided modeling of microstrip discontinuities by an improved resonator method", IEEE MTT-S Int. Microwave Symp. Dig., pp. 495-497, 1983.
- [54] S. -Y. Lee and C. -M. Tsai "New cross-coupled filter design using improved hairpin resonators", IEEE Trans. Microwave Theory Tech., vol. 48, pp. 2482- 2490, December 2000.
- [55] C. .M. Tsai, S. .Y. Lee, and C. .C. Tsai, "Hairpin filters with tunable transmission zeros", IEEE MTT-S Int. Microwave Symp. Dig., pp. 2175-2178, 2001
- [56] K. C. Gupta, R. Garg, I. Bahl, and P. Bhartia, Microstrip Lines and Slotlines, 2nd Boston: Artech House.
- [57] V. Kaajakari, J . K. Koskinen, and T. Mattila, "Phase noise in capacitively coupled micromechanical oscillators", IEEE Trans. On UFFC, Vol. 52, No. 12, pp. 2322-2331, Dec 2005.
- [58] R. M. Foster, "A reactance theorem," Bell System Tech. J., vol. 3, pp. 259-267, 1924.
- [59] U. L. Rohde, A. K. Poddar," Wideband voltage controlled oscillators employing evanescent mode coupled resonators", US Patent No 7,180, 381 Feb 20, 2007
- [60] U. L. Rohde, A. K. Poddar, "Integrated Low Noise Microwave Wideband Push- Push VCO", US Patent No. 7,088189, Aug 2006.
- [61] U. L. Rohde, A. K. Poddar, "User-Definable Thermal Drift Voltage Controlled Oscillator", US Patent No.7, 265,642 B2, Sept 4, 2007.
- [62] U. L. Rohde, A. K. Poddar, "Low Thermal Drift Tunable Frequency Voltage Controlled Oscillatory", US Patent No.7, 262,670 B2, Aug 28, 2007.
- [63] U. L. Rohde, A. K. Poddar, "Multi-Octave Band Tunable Coupled Resonator Oscillator", US Patent No.7, 292,113, Nov. 6, 2007.
- [64] U. L. Rohde, A. K. Poddar, "Tunable Frequency Low Phase Noise and Low Thermal Drift Oscillator", US Patent No.7196591, March 2007.
- [65] U. L. Rohde, A. K. Poddar, "Low Noise, Hybrid Tuned Wideband Voltage Controlled Oscillator", US Patent No. 7,365,612 B2, April 29, 2008.
- [66] U.L. Rohde, A.K. Poddar, "Tunable Frequency Low Phase Noise and Low Thermal Drift Oscillator", U.S Patent NO. 7, 545, 229, June 09, 2009.
- [67] U.L. Rohde, A.K. Poddar, and G. Boeck, "The Design of Modern Microwave Oscillators for Wireless Applications: Theory and Optimization", Wiley, New York, 2005

- [68] U.L. Rohde, A.K. Poddar, "User-Definable, Low Cost, Low Phase Hit and Spectral Pure Tunable Oscillator", U.S. Patent No. 7,586,381 on September 08, 2009.
- [69] U. L. Rohde, A. K. Poddar, "User-Definable, Low Cost, Low noise, and phase hit insensitive multi-octave-band tunable oscillator", Phase Hit and Spectral Pure Tunable Oscillator, U.S. Patent No. 7,605,670, October 20, 2009.
- [70] M. Rohde, A. K. Poddar, "Visually Inspectable Surface Mount Device Pad", U.S. Patent No. 7612296, Nov 03, 2009,
- [71] U. L. Rohde, A. K. Poddar, "Low Noise and Low Phase Hits Tunable Oscillator", U.S. Patent No. 7,636, 021, Dec. 22, 2009
- [72] U. L. Rohde, A. K. Poddar, "Wideband voltage controlled oscillators employing evanescent mode coupled resonators", Canadian Patent No. 2,563, 174, July 21, 2009.
- [73] U. L. Rohde, A. K. Poddar, "User-Definable Thermal Drift Voltage Controlled Oscillator", Canadian Patent No. 2,548, 317, April 21, 2009.
- [74] U. L. Rohde, A. K. Poddar, "Integrated Low Noise Microwave Wideband Push-Push VCO" Canadian Patent No.:2,548, 311, April 14, 2009.
- [75] U. L. Rohde and A. K. Poddar, "Novel Multi-Coupled Line Resonators Replace Traditional Ceramic Resonators in Oscillators/VCOs", 2006 IEEE International Frequency Control Symposium and Exposition, pp. 432-442, 5-7 June 2006, Florida, USA.
- [76] S. P. Voinigescu, A. Tomkins, E. Dacquay, E. Chevalier, J. Hasch, A. Chantre, B. Sautreuil, "A studyof SiGe HBT Signal Sources in 220-330-GHz Range", IEEE J. of SSC, Issue:99, pp. 1-11, 2013
- [77] T. Tanaka, K. Takata, M. Aikawa, I. Toyoda, "A Ku band Oscillator array using positive feedback type push-push oscillators", IEEE APMC conf. proceedings, pp. 112-114, 2012
- [78] T. Sirburanon, T. Sato, A. Musa, D. Wei, K. Okada, A. Matsuzawa, A 20 GHz push-push voltage-controlled oscillator for a 60 GHz frequency synthesizer", IEEE APMC conference proceedings, pp. 205-207, 2012
- [79] S-Wein Chu, C-Kuang Wang, "An 80 GHz wide Tuning Range Push-Push VCO with gm-boosted full-wave rectification technique in 90 nm CMOS", IEEE Microwave and Wireless Components Letters, vol. 22, Issue 4, pp. 203-205, 2012
- [80] S. Yaoming, C. J. Scheytt, "A low phase noise 61 GHz push-push VCO with divider chain buffer in SiGe BiCMOS for 122 GHz ISM applications", 2012 IEEE RFIC symposium, pp. 79-82, 2012
- [81] Nakamura T. Masuda, K. Washio, H. Kondoh, "A push-push VCO with 13.9 GHz wide tuning range using loop-ground transmission line for full band 60-GHz transreceive", 2102 IEEE Journal of SSC, Vol. 47, issue:6, pp. 1267-1277, 2012
- [82] M. Stuenkel, M. Feng, "A w-BAND TUNABLE Push-Push oscillator with 128X division for frequency synthesis applications", 2013 IEEE MTT-S Digest, pp. 1-3, 2012
- [83] To-Po Wang, "A fully integrated w-band push-push CMOS VCO with phase noise and wide tuning range", 2011 IEEE Trans. on UFFC, vol. 58, Issue: 7, pp. 1307-1319, 2011
- [84] A. K. Poddar, U. L. Rohde, A. S. Daryoush, "Integrated production of self injection locked self phase loop locked Opto-electronic Oscillators", US Patent application no. 13/760767 (filed on Feb 06, 2013).
- [85] A. K. Poddar, U. L. Rohde, A. S. Daryoush, "Self Injection Locked Phase Locked Looped Optoelectronic Oscillator", US Patent application No. 61/746, 919 (filed on Dec 28, 2012).

- [86] Yao, X. Steve, and Lute Maleki. "Optoelectronic oscillator for photonic systems." *Quantum Electronics, IEEE Journal of* 32.7 (1996): 1141-1149.
- [87] Moyer, Harris P., and Afshin S. Daryoush. "A unified analytical model and experimental validations of injection-locking processes." *IEEE Transactions on Microwave Theory and Techniques*, Vol. 48 No. 4 pp. 493-499, 2000.
- [88] C. McNeilage *et al.*, "Review of feedback and feedforward noise reduction techniques," *Proc. IEEE Frequency Control Symp.*, Pasadena, CA, pp. 146 – 155, May 1998.
- [89] A. Suarez *et al.*, "Analysis of Stabilization Circuits for Phase-Noise Reduction in Microwave Oscillators," *IEEE Trans. Microw. Theory Tech.*, vol. 53, No. 9, Sep. 2005
- [90] H. C. Chang, "Phase noise in self-injection locked oscillators – Theory and Experiment," *IEEE Trans. Microw. Theory Tech.*, vol. 51, no. 9, pp. 1994 – 1999, Sep. 2003
- [91] K.H. Lee *et al.*, "A 30GHz self injection locked oscillator having a long Optical delay line for phase noise reduction," *Photonics Tech. Letters*, vol. 19, no. 24, Dec. 2007
- [92] G. Pillet et al, "Dual-frequency laser at 1.5 μ m for optical distribution and generation of high-purity microwave signals," *J. of Lightwave Technology*, vol. 26, no. 15, Aug. 2008
- [93] X.S. Zhou, X. Zhang, A.S. Daryoush, "A new approach for a phase controlled self-oscillating mixer," *IEEE Trans. on MTT*, vol. 45, no. 2, pp. 196-204, Feb. 1997.
- [94] D. Surzbecher *et al.*, "Optically controlled oscillators for millimeter-wave phased-array antennas," *IEEE Trans. Microw. Theory Tech.*, vol. 41, no. 6/7, Jun/Jul 1993
- [95] R. A. York et al, "Analysis of oscillators with external feedback loop for improved locking range and noise reduction," *IEEE Trans. Microw. Theory Tech.*, vol. 47, no. 8, Aug. 1999
- [96] X. Zhang *et al.*, "A theoretical and experimental study of the noise behavior of subharmonically injection locked local oscillators," *IEEE Trans. Microw. Theory Tech.*, vol. 40, no. 5, May 1992.
- [97] R. E. Best, "Phase-locked loops: design, simulation, and applications, 4th ed, McGraw-Hill, New York, pp. 25-26, 1999.
- [98] F. Xu, and K. Wu, Guided-Wave and Leakage Characteristics of Substrate Integrated Waveguide, *IEEE Trans. Microwave Theory & Tech.*, vol. 53, no. 1, pp. 66-73, Jan. 2005.
- [99] Y. Dong and T. Itoh, A dual-band oscillator with reconfigurable cavity-backed complementary split-ring resonator, in *IEEE MTT-S Int. Dig.*, Jun. 1722, 2012, pp. 13.
- [100] F. F. He, K. Wu, W. Hong, L. Han, and X. Chen, A low phase-noise VCO using an electronically tunable substrate integrated waveguide resonator, *IEEE Trans. Microw. Theory Tech.*, vol. 58, no. 12, pp. 34523458, Dec. 2010.
- [101] S. Sirci, J. D. Martinez, M. Taroncher, and V. E. Boria, Varactor loaded continuously tunable SIWresonator for reconfigurable filter design, in *Proc. 41st Eur. Microw. Conf.*, 2011, pp. 436439.
- [102] Chung-Tse Michael Wu, Ajay K. Poddar, Ulrich L. Rohde, and Tatsuo Itoh, "Active Complementary Coupled Resonator for Low Phase Noise X-band Oscillator," *European Frequency and Time Forum 2014*.
- [103] Chung-Tse Michael Wu, Ajay K. Poddar, Ulrich L. Rohde, and Tatsuo Itoh, "A C-band Tunable Oscillator Based on Complementary Coupled Resonator using Substrate Integrated Waveguide Cavity," *European Microwave Conference 2014*.

- [104] Z. Chen, W. Hong, and J. X. Chen. "High-Q planar active resonator based on substrate integrated waveguide technique." *Electronics letters* vol. 48, no. 10, pp. 575-577, May 2012.
- [105] J. Clerk Maxwell, *A Treatise on Electricity and Magnetism*, 3rd ed., vol. 2. Oxford: Clarendon, pp.68–73, 1892.
- [106] M. Nick and A. Mortazawi, "Low phase-noise planar oscillators based on low-noise active resonators", *IEEE Trans. Microw. Theory Tech.*, vol. 58, no. 5, pp. 1133–1139, May 2010.
- [107] K. Leong: "Precise measurements of surface resistance of HTS thin films using a novel method of Q-factor computations for Sapphire Dielectric resonators in the transmission mode", *Ph. D. thesis, James Cook University*, 2000.
- [108] K. Leong and J. Mazierska: "Accurate Measurements of Surface Resistance of HTS Films using a Novel Transmission Mode Q-factor Technique" *Journal of Superconductivity*, vol. 14, No. 1, pp. 93-103, 2001.
- [109] K. Leong et al. J. Mazierska: "Comparing Unloaded Q-Factor of a High-Q Dielectric Resonator Measured Using The Transmission Mode and Reflection Mode Methods Involving S-Parameter Circle Fitting", Electrical and Computer Engineering, James Cook Univ. Townsville. 4811. Australia <http://arxiv.org/ftp/arxiv/papers/1207/1207.5622.pdf>
- [110] Chun-Tse Michael Wu, " Active Integrated Metamaterial-Based Antennas and Microwaves Components" , PhD Thesis June 2014, Department of Electrical Engineering, University of California, Los Angeles.

Chapter 7

Printed Coupled Möbius Resonator Oscillators

7.1 Introduction

Geometrical phenomenon of anholonomy depends on failure of a quantity to recover its original value, when the parameters on which it depends are varied round a closed circuit. Möbius strip provides one of the simplest examples of anholonomy, as the normal to the surface of the strip does not return to its original direction even though the radius vector does. The strip therefore deforms in such a way that its metrical properties are barely changed, some nanostructures have the same elastic properties. A necessary and sufficient condition for a Möbius surface to be developable is that its Gaussian curvature must vanish everywhere. Given a curve with non-vanishing curvature there exists a unique flat ruled surface (the so-called rectifying developable) on which this curve is a geodesic curve (Figure 7-1) is described by [1]

$$\vec{x}(s, t) = \vec{r}(s) + t[\vec{b}(s) + \eta(s)\vec{t}(s)] \quad (7.1)$$

$$\tau(s) = \eta(s)k(s), \quad s = [0, L], t = [-w, w] \quad (7.2)$$

Where \vec{r} is a parameterization of a strip with r as centerline and of length L and width $2w$, where \vec{t} is the unit tangent vector, \vec{b} the unit binormal, k the curvature and τ the torsion of the centerline, the parameterized lines $s = \text{const.}$ are the generators, which make an angle $\beta = \text{arc}[\tan(1/\eta)]$ with the positive tangent direction.

The unique properties of Möbius strips, the shape minimizes the deformation energy, which is entirely due to bending, can be described by

$$V = \frac{1}{2}D \int_0^L \int_{-w}^w k_1^2(s, t) dt ds \quad (7.3)$$

where $D = 2h^3E/[3(1-\nu^2)]$, with $2h$ the thickness of the strip, and E and ν Young's modulus and Poisson's ratio of the material.

In this section, a planar Möbius-coupled resonator is described, and the method for miniaturization can be applied to tunable oscillator circuits and memory devices used for receivers, filters, antenna, and matching networks.

7.2 Planar Möbius strip Resonator

A typical Möbius is a surface with only one side and only one boundary component, the mathematical property of being non-orientable (Figure 7-1). A unified system of differential-algebraic equations that describes models of this type was first published in 2007 together with its numerical solution and many technical applications [1].

The concept of the Möbius strips is based on the fact that a signal coupled to a strip shall not encounter any obstruction when travelling around the loop, the loop shall behave like an infinite transmission line, enabling compact high Q-factor resonators [2]. This characteristic enables many radio and microwave applications including: (i) a compact resonator with the resonance frequency which is half that of identically constructed linear coils [2], (ii) Tesla Coil

for global transmission of electricity without wires [3], and (iii) high temperature superconductors [4] to name a few.

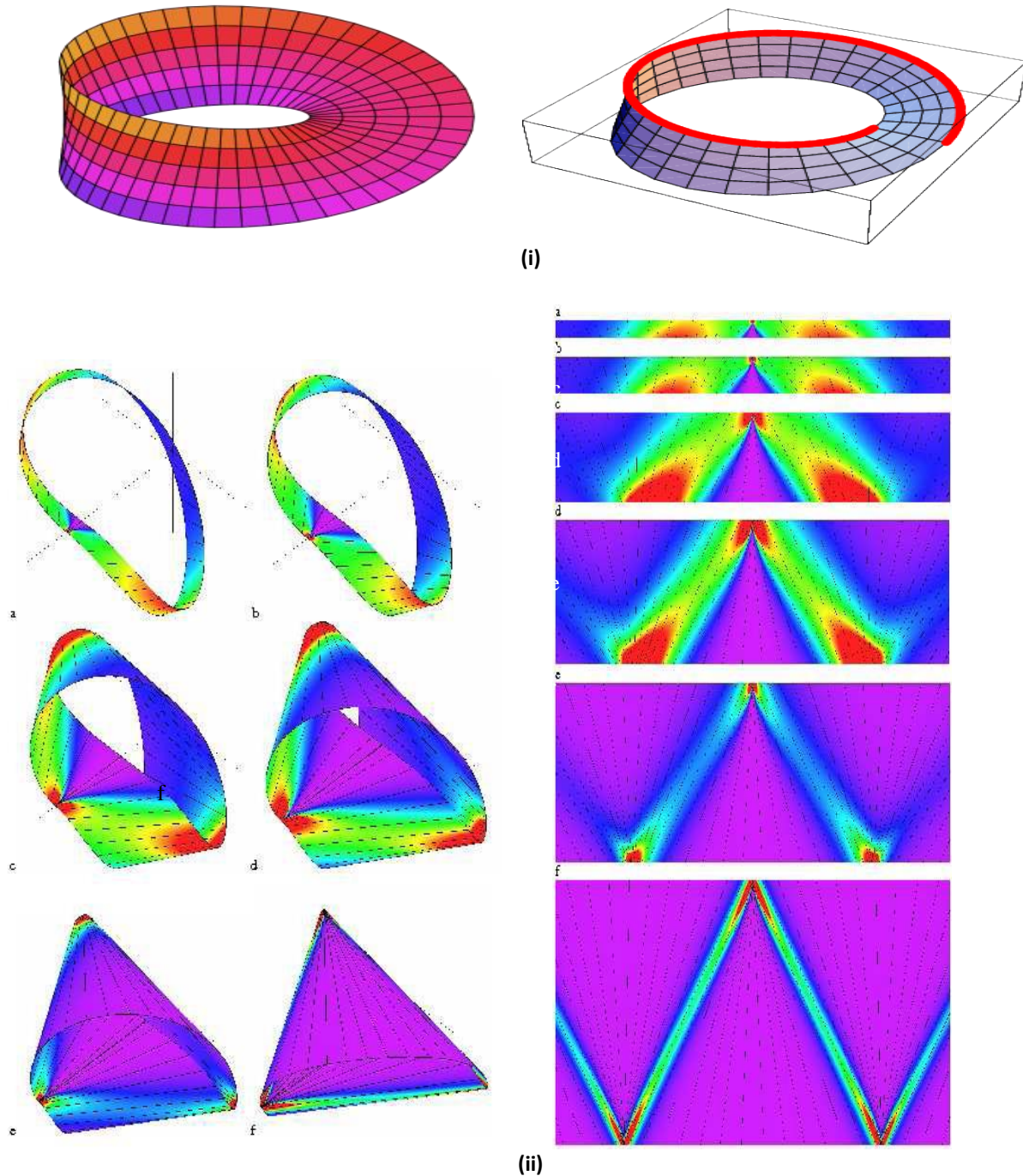


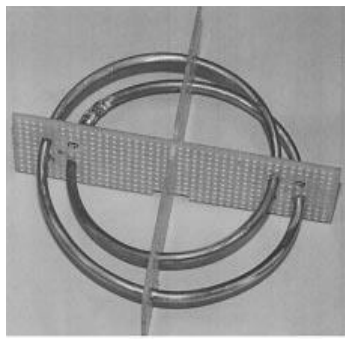
Figure 7-1 (i): A typical Möbius strip, one can move along the length of the strip, return to its starting point having traversed the entire length of the strip without ever crossing an edge, and (ii) Computed Möbius strips (coloring changes according to the local bending energy density, from violet for regions of low bending to red for regions of high bending). The left panel shows their 3D shapes for $w = 0.1$ (a), 0.2 (b), 0.5 (c), 0.8 (d), 1.0 (e) and 1.5 (f), and the right panel the corresponding developments on the plane [1].

Recent publication describes the Möbius strip resonator [2]-[7] but the surface is non planar 3-dimensional structure (Figure 7-2), not suitable for integration and surface mounted device (SMD) technology applications. Printed resonators are a special class of transmission lines of finite extent with well-defined boundary conditions. The particular interest here is a 1-dimensional printed ring resonator that can be equivalently represented by the simple lumped L-C network shown in Figure 7-3. In solving, the electric currents on the resonator can be formulated by a periodic boundary condition of the form described by [8]

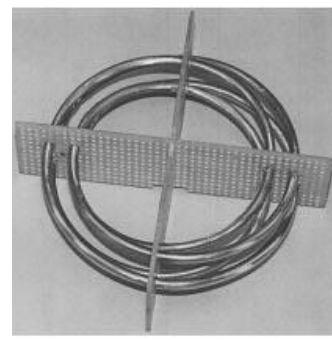
$$I_{j+k} = I_j \quad (7.4)$$

where I_k represents the electric current around the n^{th} closed loop on the periodic ladder structure of k -elements.

The boundary condition of the general form shown in (7.4) governs that I_k is a conserved quantity that gives invariance of solutions under a 2π rotation with a definite handedness.



(a) Dual Mode



(b) Quad-Mode

Figure 7-2 Photograph of the non planar 3-D Möbius wire resonator [3]

From the circuit theory, Kirchhoff's voltage relation for the k^{th} element is given by (assuming that the equivalent low pass ladder network is driven across any equivalent lumped inductor L or capacitor C):

$$\left(\omega^2 - \frac{1}{LC}\right) I_k - \gamma \left(\omega^2 - \frac{1}{2\gamma LC}\right) (I_{k+1} + I_{k-1}) = 0 \quad (7.5)$$

where γ is mutual coupling coefficient (Mutual inductance 'M'=2 γ L) between nearest neighbor elements shown in Figure 7-3, and k is number of element structure.

Equation (7.5) is a 1-dimensional non-dissipative wave equation on the LC network (assuming that the zero resistive loss and electromagnetic wavelength is much larger than the linear dimensions of the network) with a discrete rather than continuous spatial variable [8]. The solution for the ring resonator shown in Figure 7-4 (a) with the periodic boundary condition given in (7.4) can be given in the form

$$I_k = A_1 e^{\left(\frac{i2\pi jp}{k}\right)} + A_2 e^{-\left(\frac{i2\pi jp}{k}\right)} \quad (7.6)$$

where p is an integer specifying the normal mode and k is number of element structure. From (7.5) and (7.6), the dispersion relation for the allowed frequency spectrum can be described by [8]

$$\omega^2 = \left\{ \frac{2\sin^2\left(\frac{p\pi}{k}\right)}{LC\left(1-2\gamma\cos\frac{2p\pi}{k}\right)} \right\} \quad (7.7)$$

where p is an integer specifying the normal mode, γ is mutual coupling coefficient (Mutual inductance ' M' = $2\gamma L$) between nearest neighbor elements shown in Figure 7-3, and k is number of element structure.

From (7.5)-(7.7), for even value of k , there are $k-1$ eigenvalues, including $(k-2)/2$ degenerate doublets and one singlet. A typical ring resonator, whose Eigen function satisfies (7.4), defines a distinct inner and outer surface of the ring, shown in Figure 7-4(a). Figure 7-4(b) shows a topological transformation resulting in a Möbius strip resonator, whose current dynamics can be formulated by applying twisted boundary condition as

$$I_{j+k} = -I_j \quad (7.8)$$

From (7.8), a simple topological transformation on the resonator ring (Figure 7-4) results in a sign reversal of current (I_j) upon a 2π rotation of the solutions, and a 4π rotation is now required for invariance of the Eigen functions [6]-[16]. Note that the eigenfunctions satisfying the condition for twisted boundary are of the same form as (7.5) provided that the mode indices are given half-integral values ($p = 1/2, 3/2, 5/2, \dots, (k-1)/2$) relative to a ring consisting of identical components. The dispersion relation for Möbius ring is same as (7.7), however, the wave-vectors are shifted by

$$\Delta\lambda = -\left(\frac{\pi}{k}\right) \quad (7.9)$$

The two distinct topologies shown in Figures 7-4(a), 7-4(b) can be considered as a complementary pair related by a single transformation.

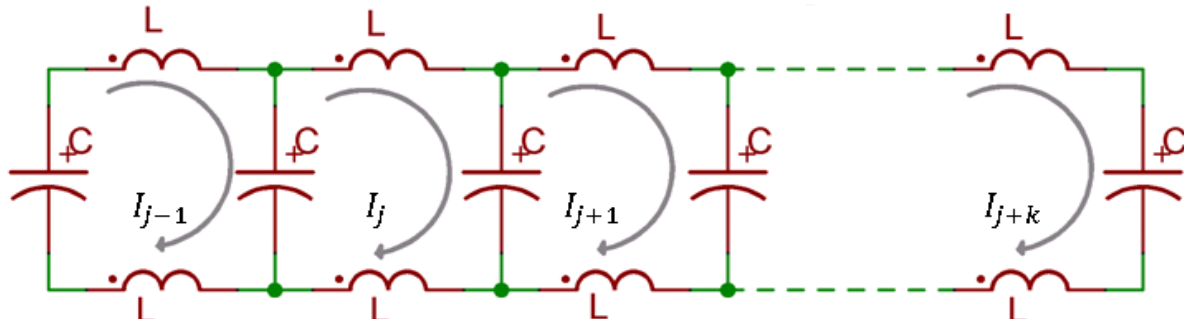
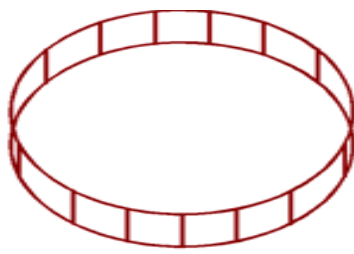
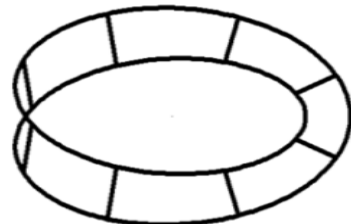


Figure 7-3.: Shows the typical low-pass ladder network consisting of a series of inductances L and capacitances C along the transmission line (Printed resonators are a special class of transmission lines of finite extent with well-defined boundary conditions, the 1-dimensional printed ring resonator can be equivalently represented by the simple lumped L-C network) [8].



(a) Closed loop ring resonator



(b) Möbius strip resonator

Figure 7-4: shows the orientation of typical closed loop resonator: (a)) the ring resonator (b) the Möbius strip resonator (a topological transformation of ring resonator into a Möbius strip resonator) [8]

From (7.4) and (7.8), it is evident that there is no additional structure associated with the Möbius ring resonator, since a second topological half-twist transformation on the Möbius resonator leads back to the boundary condition of (7.4). Their description divides into half-integral and integral normal mode indices. The Eigen functions of the Möbius resonator form an orthogonal basis set; presents an interesting possibility for the design of metamaterial for the application in tunable oscillators, antenna, and filter circuits [6]. The oscillator's loaded Q factor Q_L is described by [15]

$$Q_L = \frac{\omega_0}{2} \left| \frac{d\varphi(\omega)}{d\omega} \right|_{\omega=\omega_0} = \frac{\omega_0}{2} \tau_d; \quad \tau_d = \left| \frac{d\varphi(\omega)}{d\omega} \right|_{\omega=\omega_0} \quad (7.10)$$

$$\tau_d = \left| \frac{d\varphi(\omega)}{d\omega} \right|_{\omega=\omega_0} = \frac{\varphi(\omega_0 + \Delta\omega) - \varphi(\omega_0 - \Delta\omega)}{2\Delta\omega} \quad (7.11)$$

where $\varphi(\omega)$ is the phase of the oscillator's open loop transfer function at a steady state and τ_d is the group delay of the resonator. From (7.10), Q_L is proportional to the group delay; therefore, for low phase noise application, the design goal is to maximize the group delay of Möbius strip resonator by incorporating phase-injection techniques. The eigenfunctions of the Möbius resonator form an orthogonal basis set, therefore all eigenfunctions of the pair are mutually orthogonal; exhibits minimal electromagnetic interactions [8]. This presents an interesting possibility for incorporating phase-injection along the mutually coupled surface of the strips, resulting in higher quality factor for a given size of the printed transmission line resonator [12]. The Möbius strips resonator show an interesting possibility, for example if the arbitrary structure is composed of an array of typical Möbius strips as its basis, complementary strips could in principle be introduced without much disturbance the coupling dynamics for microwave component (sensors, resonators, antenna, and filter) applications [13]-[15].

7.3 MCPR Oscillator: Inexpensive Alternative of DRO

Dielectric resonators (DRs) for example, exhibit a high Q-factor and have been used in high-spectral-purity signal sources at RF and microwave frequencies. However, the DR requires precise machining for fabrication, careful placement of the dielectric puck for optimal coupling, and involves manual mechanical tuning of the DR for desired frequency of operation [7]-[16].

The printed coupled resonator based oscillator can overcome problems associated with DRO, except the poor phase noise performance due to inherent low Q-factor associated with printed transmission line resonator [17]-[29]. The Q (quality) factor of the coupled planar resonator network can be enhanced by introducing slow wave propagation dynamics as discussed in Ch-6, however large physical size and mode-jumping restricts the application especially at lower frequencies. The loaded quality factor Q_L of the coupled resonator network is given in terms of unloaded quality factor Q_0 as [Ch-6, Figure 6-8]:

$$[Q_L(\omega_0)]_{electrical-coupling} \cong 2 \left[\frac{Q_0}{(1 + \beta_e)} \right]_{\beta_e \ll 1} \cong 2Q_0 \quad (7.12)$$

$$[Q_L(\omega_0)]_{magnetical-coupling} \cong 2[Q_0(1 + \beta_m)]_{\beta_m \rightarrow 1} \cong 2Q_0 \quad (7.13)$$

$$[Q_L(\omega_0)]_{\text{hybrid-coupling}} \cong 2 \left[Q_0 \frac{(1 + \beta_{mh})}{(1 + \beta_{eh})} \right]_{\beta_e \ll 1, \beta_{mh} \rightarrow 1} \cong 4Q_0 \quad (7.14)$$

where coupling factor β (β_e for electric field, β_m for magnetic field, and β_h for hybrid field).

From (7.12)-(7.14), hybrid coupling (β_h) shown in Figure 6-8(f) (Chapter-6) acts as a Q-multiplier effect, but this phenomenon holds good for fixed frequency operation only and very difficult to realize broadband Q-multiplier dynamics which is necessary for wideband oscillators. In addition to this, mode jumping caused by undesirable higher order mode generation in hybrid coupling makes this structure not suitable for tunable wideband VCO (voltage-controlled oscillator) applications. The alternative approach is to tune the coupling factor β_j over the desired operating frequency band in conjunction with higher order mode-suppressing network. But broadband mode-suppression is not an easy task in multi-mode resonator structure. A simplified approach is to use injection-locking and phase-synchronization techniques for broadband applications. The Möbius strip resonator topology described in Figure 7-1 can offer promising solution for broadband oscillator circuits in compact size, integratable and inexpensive alternative of expensive DROs [12].

Figure 7-5 shows the typical layout of 10 GHz Möbius resonator based oscillator for building low phase noise signal source for RADAR applications. As shown in Figure 7-5, Möbius strips resonator is formed by connecting the outer and inner strips by via hole for the realization of planar structure. It can be seen that two concentric rings inside the Möbius loop minimize the spurious modes, thereby stable oscillation.

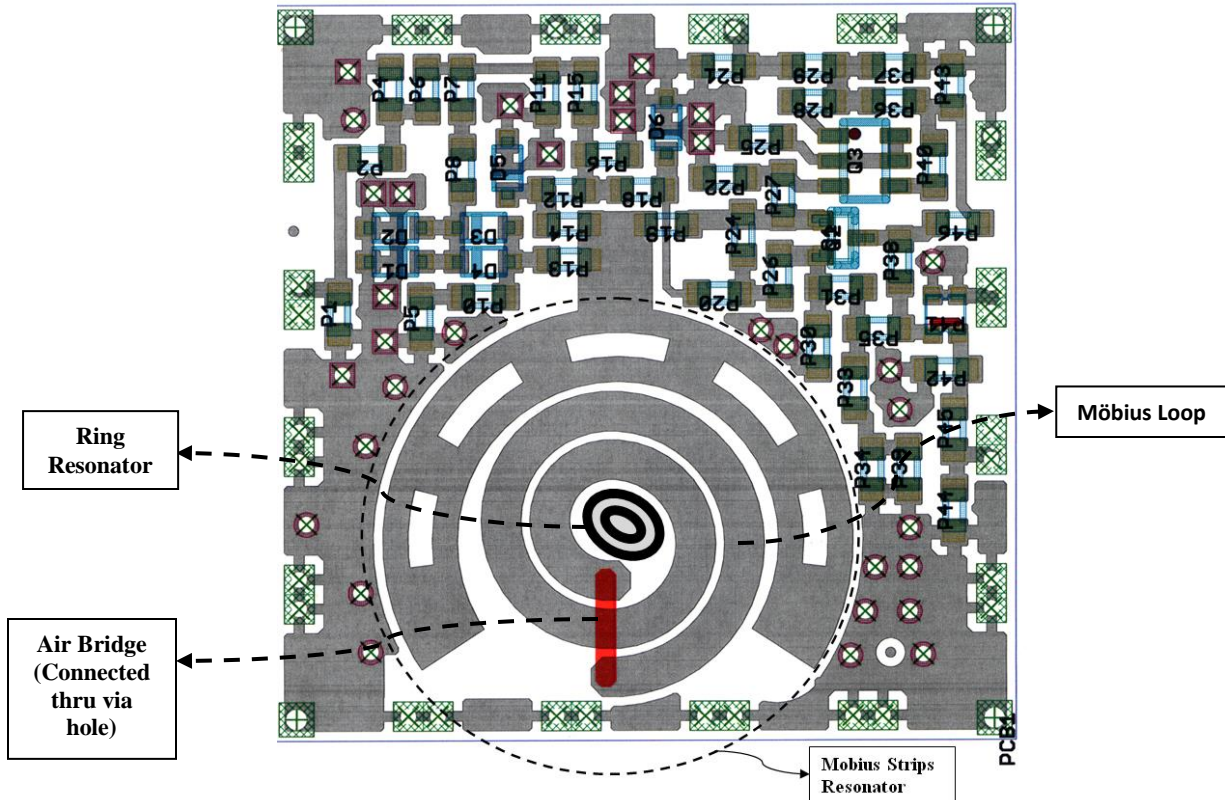


Figure 7-5: Shows the layout of 10 GHz oscillator (depicts the Möbius strips resonator used for high Q-factor resonator (PCB layout is done with 22 mil substrate thickness with 3.38 dielectric constant, 0.5x0.5x0.18 inches)

Figure 7-6 shows the measured plot of unloaded Q-factor of the printed resonator structures (electrical coupled, magnetic coupled, hybrid or mixed coupled, and Möbius coupled) for giving brief insight about the improvement in quality factor in planar domain. As shown in Figure 7-5, the Möbius coupled printed resonator (MCPR) structure and hybrid coupled resonator (Figure 6-8, Ch-6) act like a Q-multiplier, peaking at 8.6 GHz due to the convergence of evanescent-modes. It can be seen in Figure 7-6 that Möbius resonator exhibits the undesired multi-mode resonant characteristics because of non-uniform coupling across the strips (ideally Möbius strip is 3-Dimensional structure (Figure 7-1)), and care must be taken to suppress these spurious modes for low jitter in RADAR applications.

The drawback of this approach is that the multi-mode frequencies and mode-jumping (encircling the resonator characteristics), restricts the broadband operations. To overcome this problem, mode stabilization (injection of higher order modes into the resonant cavity with proper phase shift that improves the stability factor) control circuit is incorporated.

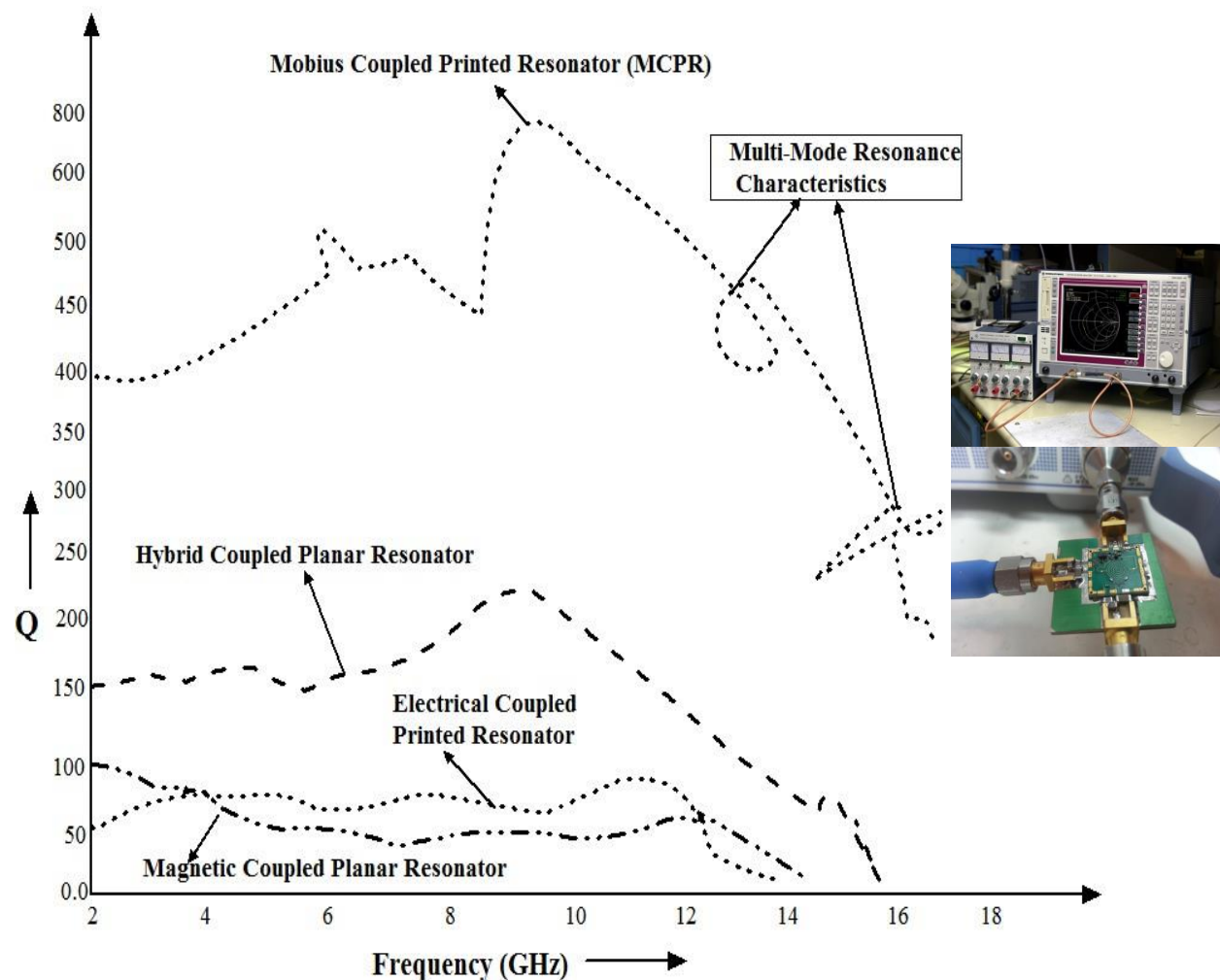


Figure 7-6: Shows the measured plot of unloaded Q-factor of the printed resonator structures (electrical coupled, magnetic coupled, hybrid or mixed coupled, and Möbius coupled) for giving brief insight about the improvement in quality factor in planar domain (PCB layout for these resonators done with 20 mil substrate thickness with 2.22 dielectric constant and PCB size: 0.5x0.5x0.18 inches).

This degrades the Q factor by 10-20% resulting in degradation of phase noise performances by 3-6 dB but overcomes the problem of mode jumping, hence achieving stable operation and inexpensive alternative of 10 GHz DROs (Dielectric resonator oscillator) for X-Band RADAR applications. Figure 7-7 shows the typical block diagram of 10 GHz Möbius coupled resonator VCOs using a SiGe Hetro-junction-Bipolar-transistor (HBT) active device, built on 20mils substrate material with a dielectric constant of 2.2 for the validation of the new approach. Figure 7-8 shows the measured phase noise plot (-110 dBc/Hz @ 10 kHz offset) from the carrier frequency of 10 GHz, offers promising performances for a given size in planar configuration [19]-[22].

As shown in Figure 7-8, the measured figure of merit (FOM: defined in Ch-1, Eq 1.1) is -195.9 dBc/Hz for hybrid coupled resonator, -202.9 dBc/Hz for Möbius coupled resonator, -204.9 dBc/Hz for Mode-locked Möbius coupled resonator network; with power consumption of 160 mW ($V_{cc}=5V$, $I_c=32mA$). The DC-RF conversion efficiency is 1.2% for hybrid coupled resonator, 1.3% for Möbius coupled resonator, 1.7% for Mode-locked Möbius coupled resonator network; with DC power consumption of 160 mW ($V_{cc}=5V$, $I_c=32mA$).

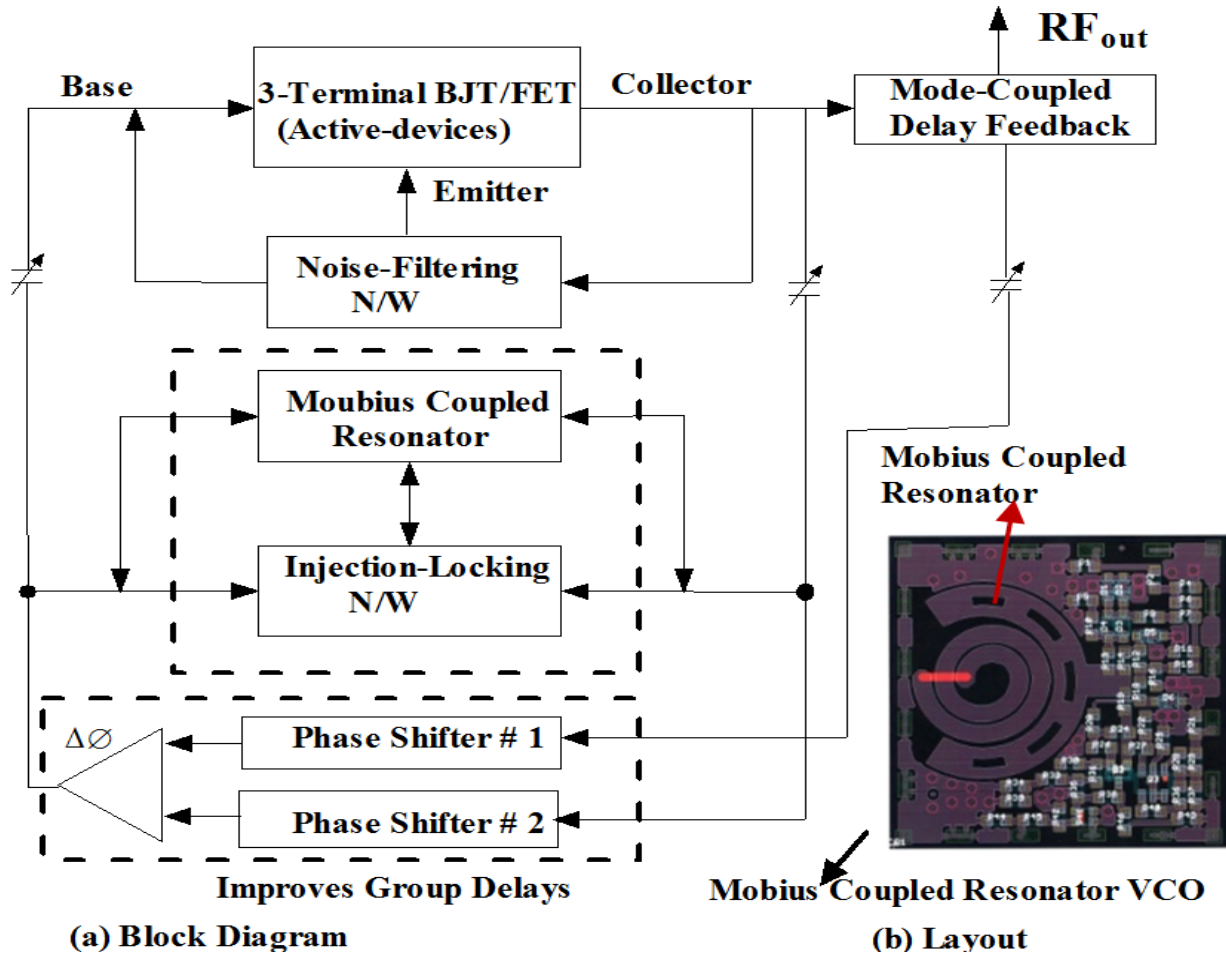


Figure 7-7: Shows the typical block diagram of 10 GHz Möbius coupled resonator VCOs using a SiGe Hetro-junction-Bipolar-transistor (HBT) active device, built on 20mils substrate material with a dielectric constant of 2.2 for the validation of the new approach, PCB size: 0.75x0.75x0.18 inches [15]

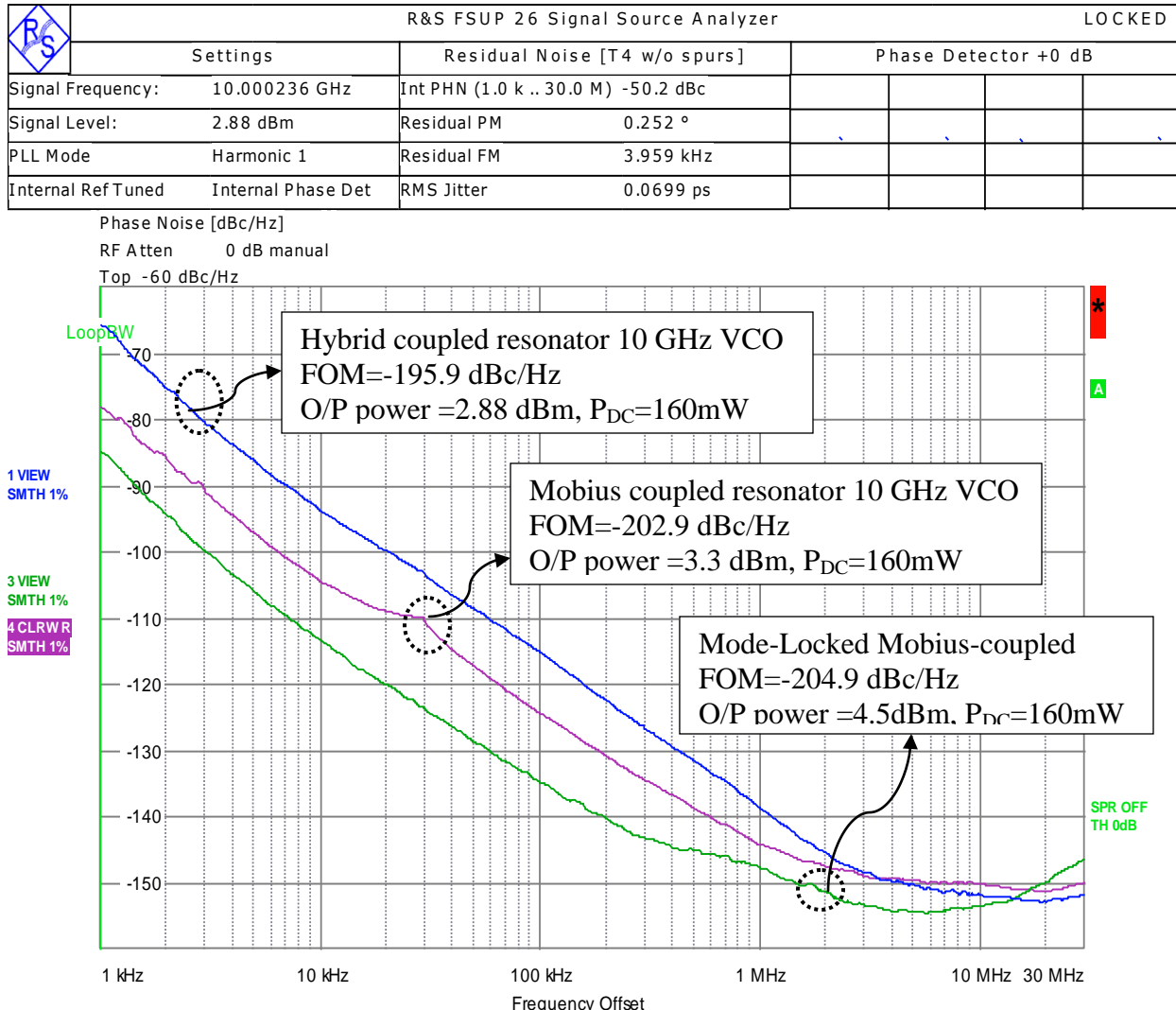


Figure 7-8: Depicts the measured phase noise plot of the 10 GHz oscillator using: Hybrid coupled resonator, Möbius coupled resonator, Mode-locked Möbius coupled resonator network. The measured figure of merit (FOM: defined in Ch-1, Eq. 1.1) is -195.9 dBc/Hz for hybrid coupled resonator, -202.9 dBc/Hz for Möbius coupled resonator, -204.9 dBc/Hz for Mode-locked Möbius coupled resonator network; with power consumption of 160mW (Vcc=5V, Ic=32mA).

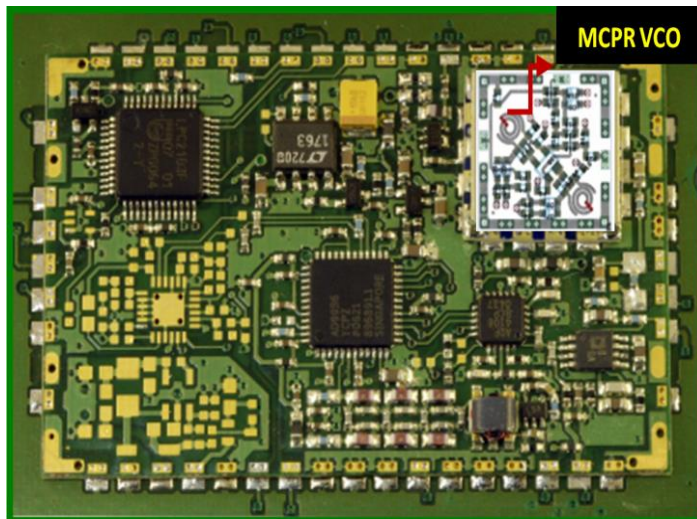
7.3.1 Synthesized Frequency Sources using MCPR (Möbius Coupled Resonator) VCOs

Figure 7-9 (a) shows the layout of 2-8 GHz broadband synthesizer using wideband (2-10 GHz) tunable MCPR VCO (Layout of VCO is shown in Figure 7-9 b), offers a viable cost-effective solution for expensive YIG resonator oscillator with less susceptibility to thermal drift, vibrations, and microphonics.

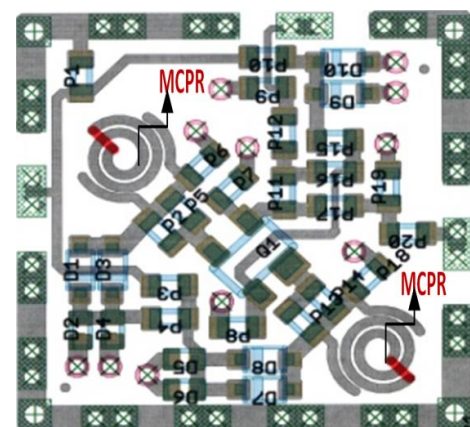
As shown in Figure 7-9(a), the synthesizer circuit draws typically 200 mA current from a 5-V supply, uses multi-band/multi-mode MCPR VCO (operating at 5V, 32mA) resulting in low-cost power-efficient configurable synthesizer. Figure 7-9(b) shows the typical layout of 2-8 GHz wideband MCPR VCO in 0.3x0.3x0.18 inches size, built on 22 mils substrate and dielectric constant of 2.2.

Figure 7-9 (c) shows the typical measured phase noise plot of the mode stabilized synthesizer circuit as illustrated in Figure 7-9(a) using MCPR VCO. The measured phase noise is typically better than -108dBc/Hz @ 10 kHz offset for 2-8 GHz operations.

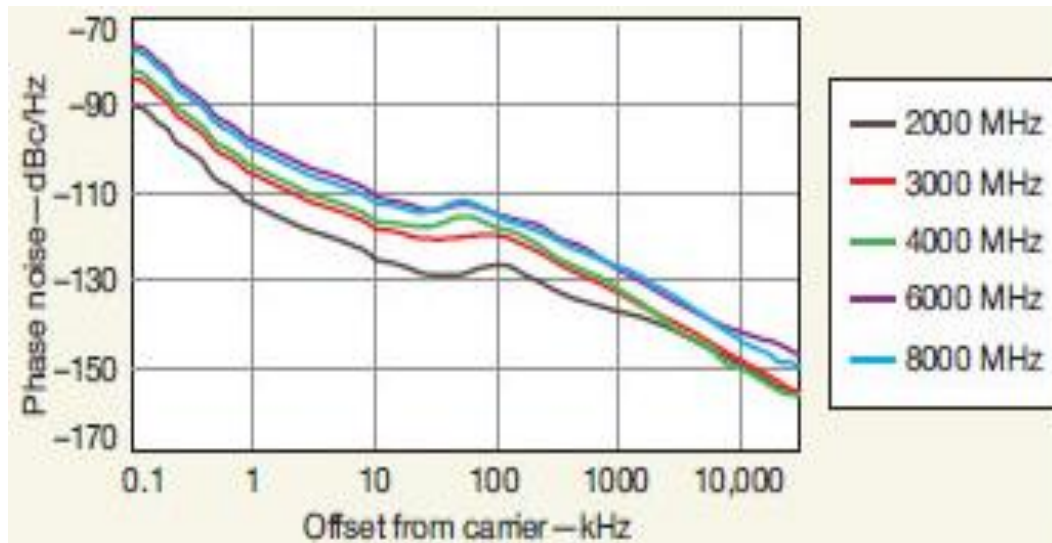
The reported synthesizer module shown in Figure 7-9(a) offers wide bandwidths with excellent performance in terms of phase noise, harmonics (> -20 dBc), settling time (less than 1 millisecond), and sideband spurious content (better than -60 dBc), with low power consumption in compact size (1x1x0.2 inches) built on 22 mils substrate material with a dielectric constant of 2.2 for the validation of the new approach.



(a) Synthesizer Layout (1x1x 0.2 inches) using MCPR VCO



(b) MCPR VCO Layout (0.3x0.3x0.18 inches)



(b) The measured phase noise plot of synthesizer circuit shown in Figure 7-9 (a)
(c)

Figure 7-9: Shows high performance wideband synthesized signal sources for modern communication systems: (a) a typical PCB Layout of 2-8 GHz Configurable Synthesizer Module, (b) a typical layout of Möbius Coupled planar resonator (MCPR) VCO (2-8 GHz), and (c) measured phase noise plot of synthesizer circuit shown in Figure 7-8(a)

The new approach to designing tunable oscillators with Möbius strips resonators yields compact VCOs with excellent phase-noise performance and in configurations that can be readily adapted to modern RF integrated circuit (RFIC) and MMIC semiconductor manufacturing processes. These compact tunable oscillators provide performance levels that are comparable to those of traditional DROs and YIG oscillators, but without the temperature sensitivity, large size, and high cost.

7.4 Möbius Coupled Resonator: Applications

The signal retention characteristics of Möbius coupled strip resonators are useful in radiofrequency and microwave applications, including radio astronomy, medical fields and software driven radios. Conventionally, high Q-factor cavity echo box is used in Radar testing to retain the input signals but this technique has bandwidth limitation [4]. Frequency Memory Loop (FML) technique is used in Military electronics for retention of signals, this is an expensive solution with considerable digital signal processing and invariably noisy and bandwidth limited [11]. The novel Möbius strip configuration (back-to-back coplanar waveguide) reported here shows how the characteristic is non-resonant unlike open or shorted transmission lines, which has ability to store broadband frequencies in compact size.

In this section, a typical back-to-back coplanar waveguide (CPW) in the form of Möbius strip was constructed which resulted in an infinite transmission line capable of retaining a large bandwidth of frequencies that can be useful for real time signal retention device (RTRD) [14]. By providing Möbius twist to CPW, a continuous phase change reported instead of abrupt phase change by using shorting pins between two parallel transmission lines. It is observed that the device retains the injected signal in time domain over a broad band of frequencies. The signal can also be a pulsed signal as in Ultra Wide Band (UWB), or a modulated microwave signal, and can retain transient signals encountered in Radio Astronomy, Medical applications and many more exciting applications.

7.4.1 Möbius Resonator Strips for (Real Time Signal Retention Device) RTRD Applications

To construct a Möbius strip, two back-to-back coplanar waveguides (CPW) with ground plane is used. Figure (7-10) shows the typical cross-section of the transmission line using two back-to-back coplanar waveguides with 50-Ohm impedances. The low loss Taconic TLY5® substrate with thickness of 0.25 mm and dielectric constant of 2.2 is used for fabrication.

As shown in Figure 7-10, the partition ground planes provide the separation between back to back CPW to decouple the top and bottom CPWs.

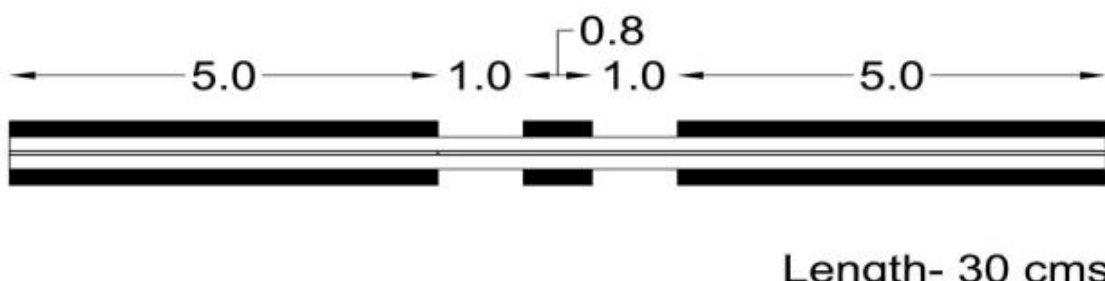


Figure 7-10: A typical cross section view of back-to-back CPW [14]

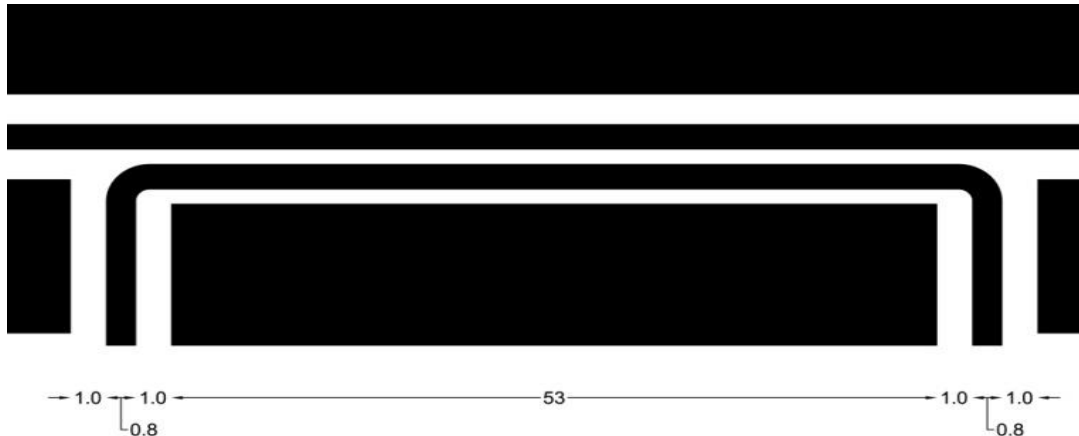


Figure 7-11: A typical layout of the Directional Coupler [14]

These back-to-back CPWs were joined together and then twisted to form a Möbius strip to close the CPWs on itself to obtain the infinite transmission line. To inject signal into the Möbius strip, a directional coupler designed at 4 GHz was incorporated in one of the CPWs. The coupling coefficient of 10 dB was chosen to provide loose coupling to the main loop (Figure 7-11). The length of the loop was chosen as 30 cm, which corresponds approximately to one wavelength at 1000 MHz.

The main function of the partition ground planes is to decouple the top and bottom CPW and it was decided that the continuity of this ground plane is not considered to be important. Experimental verification also confirmed this assumption. No ground plane strapping was used to prevent any unbalanced ground loop current flow. Thus, the Möbius Twist provides a single surface for signal propagation and the central conductor provides a continuous loop along with the ground plane. An edge coupled directional coupler at 4 GHz was designed and incorporated in one of the CPW's, the top layer as shown in Figure 7-10. SMA connectors were used at ports of the directional coupler for coupling and decoupling the signal from the device. The photograph of the finished Möbius device with the 10dB coupler is shown in Figure 7-12.



Figure 7-12: A prototype of CPW Möbius device with SMA connectors [19]

As shown in Figure 7-12, the two CPWs with ground planes are bonded back to back. The top CPW is called CPW-1 and the bottom is called CPW-2. These are then twisted and the ends are brought together manually. The CPW-2 now comes in the same plane as CPW-1. The ground planes and the centre conductors of both CPWs are strap soldered to complete the Möbius configuration. The launching of the signal was done using two SMA connectors soldered to the ports of the coupler.

Agilent Field Fox RF Analyzer N9912 was used to test the proof of concept [17]-[18]. This instrument has a single port S-parameter testing capability (VNA) along with Cable Testing facility; in addition it contains a Spectrum Analyzer up to 6 GHz. The Test setup is as shown in Figure 7-13. First, the return loss was tested from 2 GHz to 6 GHz with one of the ports terminated with 50 ohms. It was observed that the device has a return loss between 6 dB and 20 dB over the frequency range. This indicates that the device is exhibiting broadband behavior and the signal is being coupled to it. In other words the continuous central conductor is getting excited over a broad band of frequencies. Figure 7-14 shows the polar plot of S-parameter (S_{11}) from 2MHz to 6 GHz but useful information lies in the range from 2 to 6 GHz.



Figure 7-13: Shows testing with Agilent Field Fox RF Analyzer N9912 with the device connected. The return loss test shows S_{11} parameter on Smith Chart from 2 MHz to 6 GHz. The display clearly indicates the broad band coupling of signal into the device [19].

Figure 7-15 shows the return loss in rectangular coordinate from 2 GHz to 6 GHz, which is typically 10d B. The Smith Chart display shows the excitation of the signal to the continuous centre conductor of the device over a bandwidth of 4 GHz. In this way the device exhibits an infinite transmission line. The return loss response of more than 10 dB indicates that the energy is efficiently coupled to the device over a bandwidth of 4 GHz.

The Vector Network Analyzer (VNA) was switched to Cable and Antenna Testing Mode to check the delay response in real time. In this way the retention of the signal can be tested. The instrument converts the measured frequency response into time domain response by performing Inverse Fast Fourier Transform (IFFT).

The results are shown in Figure 7-15, the plot is taken from 2 to 6 GHz. As expected, there is a gradual decay of the signal after every transit around the loop.

Agilent Technologies: N9912A

Wed, 22 Feb 2012 9:57:37 AM

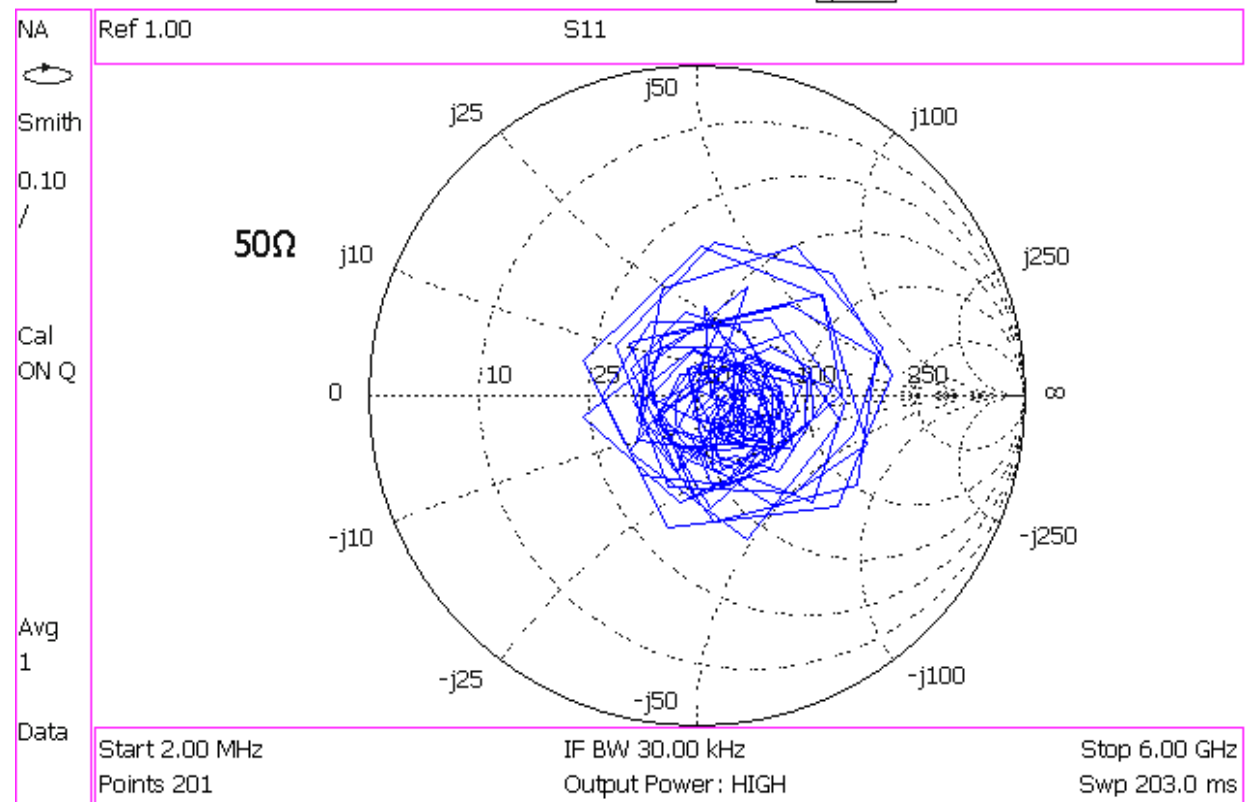


Figure 7-14: The measured S_{11} plot shown on Smith Chart, display from 2 MHz to 6 GHz [19]

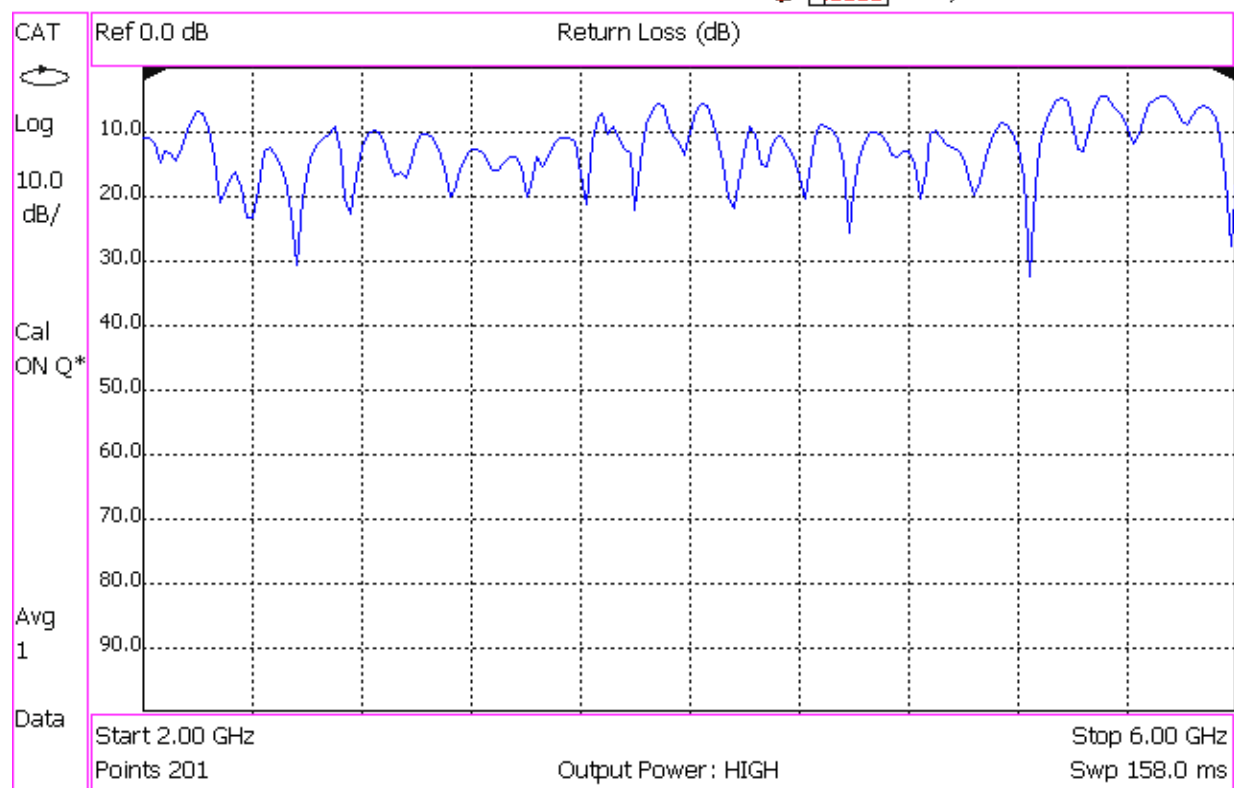


Figure 7-15: The measured return Loss display in rectangular coordinates [19]

Thus testing of the device has confirmed the retention of the signal in real time over broadband of microwave frequencies. The total span time is around 200 milliseconds. The physical length of the loop is 30 cm. The markers as indicated are at 0.72m, 0.89m, 0.98m, 1.05m, 1.13m and 1.46 m. This clearly indicates multiple transit of the signal around the loop. It also shows the broadband retention characteristics since it is derived from the frequency response of the device.

The signal travels twice around the loop before arriving the feeding point, the first signal is at twice the length of the loop which is at 72 cm. The decay of the signal over the time indicates the coupling of the power at the output port along with the losses, considering the radiation losses are minimal. This behavior calls for extensive mathematical modeling of the device. The unusual behavior could be due to the magnetic field coupling between the top and bottom layers. This will result in a distributed mutual inductance between the layers. This characteristic is similar to non-inductive resistor design [9]. The Transmission characteristics S_{21} measured at the output port indicates the coupling of the signal to the load (Figure 7-16).

The frequency response of the device calls for rigorous three-dimensional mathematical modeling and analysis using Maxwell's equations and shall lead to considerable research in the field of signal retention [14].

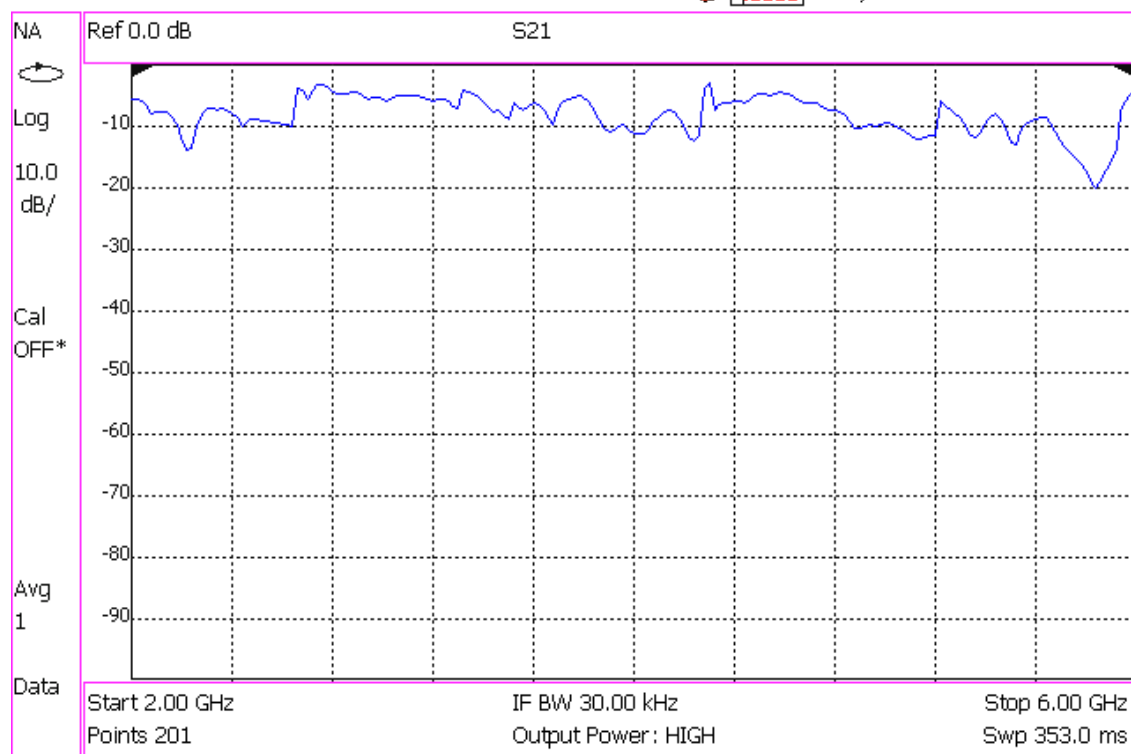


Figure 7-16: The measured transmission Characteristics (S_{21}) of the device [19]

Möbius co-planar structure proposed in Figure 7-12 for signal retention is analog by nature and is an economical solution for signal retention [14]. By providing Möbius twist to CPW as shown in Figure 7-12, a continuous phase change was reported instead of abrupt phase change by using shorting pins between two parallel transmission lines. The true Möbius strip is being created, and can achieve a gradual transition resulting in the wide band behavior of the device. It is observed that the device retains the injected signal in time domain over a broad band of frequencies. The signal can also be a pulsed signal as in Ultra Wide Band (UWB), or a modulated microwave signal. It can retain transient signals encountered in Radio Astronomy, Medical applications and many other such applications. The device is truly an analog device, can improve the performance of Analog to Digital Converter (ADC). One can use a lower speed Digital Signal Processing (DSP) since one has the same signal available for a considerable duration of time in a repetitive manner.

It is also feasible to fabricate the device using rapid proto-typing MEMS applications. This will open out many more exciting millimeter wave applications such as microwave sensors for remote sensing and detection of hidden objects, to find concealed arsenal or explosive and hazardous chemical which is of importance in our world of a growing threat.

7.4.2 Möbius Coupled Resonator Strips: Discussion

- I. GCPW- The transmission line we have used to construct the Möbius strip is CPW with ground plane, so technically the term GCPW can be used. The central partition plane acts more as a separation between top and bottom layer to prevent coupling. The spacing between the central conductor and ground plane on the coplanar side is much smaller than the thickness of the substrate leading to maximum field confinement on the surface.
- II. Higher order modes at interface: There exists a discontinuity in the partition ground planes. This characteristic is taken into account for futuristic study while developing the mathematical model for the infinite strip. Ground looping was avoided to realize the infinite transmission line at the cost of generation of higher order modes.
- III. Abnormal behavior: Unlike any resonant structure the return loss was observed to be around the centre of the Smith Chart (Figure 7-6), which is non resonant behavior from 2MHz to 6 GHz. Based on our observation, any loop was exhibiting resonant nature and the response was touching the outer edge of the Smith Chart, in other words the input impedance moved from short to open.
- IV. The return loss in rectangular coordinates indicates an average of 8-10dB over the frequency sweep from 2 GHz to 6 GHz (Figure 7-6). The future research effort is to improve the return loss for good figure of merit (FOM).
- V. Testing of Loop: A CPW guide with Quadrature coupler was made into a simple loop and tested for performance. The purpose of this was to isolate the effect of the twist. It is found that the loop behaves like a resonant circuit with multiple frequencies and S_{11} touched the 0dBm axis.
- VI. To verify the effect of SRD-performance one more assembly was made with 45 cm length. A quadrature coupler designed at 4 GHz was used for coupling the power. The performance was similar to 30 cm SRD with edge-coupled input.
- VII. Video recording: The Yagi antenna was connected to the spectrum analyzer with and without the Signal retention Device. This is to check whether the device retains pulsed RF waveforms. A cell phone was kept nearby and the filming was done using a digital camera. The uplink from the cell phone is a burst signal. There is a repetitive appearance of the signal on activating the cell phone when the device was connected indicating the retention of burst signal.

7.5 Conclusion

The signal retention device developed here has the ability to store a very broad band of frequencies. It also has the ability to store a transient signal for delayed analysis. This property of the device is extremely useful in many applications including radio astronomy, medical fields and software driven radios, real time retention of signals for signal processing, and Frequency Memory Loop in Electronic Warfare (EW). This device will be less ‘noisy’ compared to digital storage devices, can be very useful in Software Driven Radios (SDR) and help in soft handover from one system to another and other applications.

7.6 References

- [1] Starostin E.L., van der Heijden G.H.M. "The shape of a Möbius strip", Nature Materials 6 (8): 563–7. doi: 10.1038/nmat1929.PMID 17632519, (2007).
- [2] J. M. Pond, "Möbius Dual Mode Resonators and Bandpass Filter", IEEE. Trans. of MTT Vol. 48, No.12, pp 2465-2471, Dec 2000.
- [3] J. M. Pond, S. Liu, and N. Newman, "Bandpass Filters Using Dual-Mode and Quad-Mode Möbius Resonators," IEEE Trans. on MTT, vol. 49, pp.2363-2368, Dec.2001.
- [4] Wilson et al, "High Q Resonant Cavities for Microwave Testing" Bell System Technical Journal, No.5, pp. 1515-1530, doi:10.1364/OPEX.13.001515, (March2005).
- [5] Honkote V., "Capacitive load balancing for Möbius implementation of standing wave oscillator", 5^{2nd} IEEE MWSCAS, pp. 232-235, 2009
- [6] Hoffman, A. J. *et al.* *Nature Mater.* 6, pp. 946–950 (2007).
- [7] J-Francois Gravel and J. S. Wight, "On the Conception and Analysis of a 12-GHz Push-Push Phase Locked DRO" IEEE Trans. on MTT, Vol. 54, No. 1, pp. 153-159, Jan. 2006.
- [8] Ballon, H. U. Voss, ", "Classical Mobius-Ring Resonators Exhibit Fermion-Boson Rotaional Symmetry ", Physical Review Lett. 101, 24;247701, American Physical Society, 2008
- [9] Nikola Tesla, "Coil for electromagnet", US Patent 512340, Jan 9, 1894.
- [10] Enríquez, "A Structural Parameter for High Tc Superconductivity from an Octahedral Möbius Strip in BaCuO :123 type Perovskites", Rev Mex Fis v.48 suppl. 1, p.262, 2002.
- [11] Development in FML and Miniature Millimeter Devices, Watkins Johnson, Tech Note. Vol1, No 2, March, 1974.
- [12] U. L. Rohde and A. K. Poddar, "DRO Drops phase-noise levels", Microwaves RF, pp. 80-84, Feb. 2013
- [13] U. L. Rohde, A. K. Poddar, Anisha Apte, "Phase noise measurement and its limitations", Microwave journal, April 2013.
- [14] A. K. Poddar, U.L. Rohde, D. Sundarajan", Real Time Signal Retention Device using Co-planar Waveguide (CPW) as Möbius strip", 2013 IEEE MTT-S Digest, pp. 1-3, June 2013
- [15] A. K. Poddar, U. L. Rohde, "A Novel Evanescent-Mode Möbius-Coupled Resonator Oscillators", IEEE joint UFFC Symposia with European Frequency and Time Forum (EFTF) and Piezo response Force Microscopy, July 21-25, 2013
- [16] Anritsu Application Note, "Time Domain Reflectometry using Vector Network Analyzers'
- [17] Agilent 'Time Domain Analysis using a Network Analyzer. Appl. Note 1287-12, Jan 6, 2012
- [18] Agilent 'Time Domain Analysis Using a Network Analyzer', Literature Number 5989-5723EN, May 2012
- [19] U. L. Rohde, A. K. Poddar, and D. Sundararajan "Printed Resonators: Möbius Strips Theory and Applications", Microwave journal, pp. 24-54, Nov 2013.
- [20] A. K. Poddar, U. L. Rohde, "The Pursuit for Low Cost and Low Phase Noise Synthesized Signal Sources: Theory & Optimization", IEEE UFFC Symposia, May 19-22, 2014
- [21] A. K. Poddar, U.L. Rohde, T. Itoh", Metamaterial Möbius Strips (MMS): Tunable Oscillator Circuits ", IEEE MTT-S Digest, pp. 1-4, June 2014
- U. L. Rohde, A. K. Poddar, D. Sundararjan "Printed Resonators: Möbius Strips Theory and Applications" ", Microwave journal, pp. 24-54, Nov 2013.

Chapter 8

Printed Coupled Metamaterial Resonator Based Frequency Sources

8.1 Metamaterial

Metamaterials are engineered periodic composites that have negative refractive-index characteristic not available in natural materials [1]. In 1968, Veselago reported artificial composite Left handed material (LHM), which exhibits simultaneously negative values of the electric permittivity ($\epsilon < 0$) and the magnetic permeability ($\mu < 0$), characterized as [2]:

- (i) Simultaneous negative permittivity ($-\epsilon$) and permeability ($-\mu$)
- (ii) Reversal of Snell's Law (negative index of refraction), Reverse Doppler effect, and Reverse Vavilov-Cerenkov effect, Diffraction-limit breaking imaging
- (iii) Electric field, Magnetic field, and wave-vector of electromagnetic wave in a LHM form a left-handed triad
- (iv) LHMs support backward wave propagation: anti-parallel group and phase velocity
- (v) Artificial homogenous structure

The characteristics of the artificial composite metamaterial depend on the properties of the host materials, embedded material, volume of the fraction, operating frequency, and the morphology of the composite material such as the dimensions and shapes of the host structure and the guest structure [3]-[5]. Therefore, when all other variables are known, the important parameter is to control the dynamics of the morphology of the embedded structure that allows control over a change of the properties (permittivity, permeability and the refractive index) in the desired frequency range.

In general, the refractive index of the medium can be characterized by four possible sign combinations in the pair ($\mu\epsilon$), can be described as [6]-[27]:

$$n = \sqrt{(+\epsilon)(+\mu)} = +\sqrt{\mu\epsilon} \rightarrow (\text{DPS-double positive material}) \quad (8.1)$$

$$n = \sqrt{(-\epsilon)(+\mu)} = j\sqrt{\mu\epsilon} \rightarrow (\text{ENG-epsilon negative material}) \quad (8.2)$$

$$n = \sqrt{(-\epsilon)(-\mu)} = -\sqrt{\mu\epsilon} \rightarrow \quad (\text{DNG-double negative material}) \quad (8.3)$$

$$n = \sqrt{(+\epsilon)(-\mu)} = j\sqrt{\mu\epsilon} \rightarrow \quad \text{(MNG-mu negative material)} \quad (8.4)$$

From (8.3), double negative (DNG) material is nomenclatured as metamaterial, which is broadly defined as Left-handed (LH) material with artificial homogeneous structures related to negative refractive index as

$$n = -\sqrt{\mu\epsilon} = -\sqrt{\mu_0\mu_r\epsilon_0\epsilon_r} \quad (8.5)$$

Where ϵ_0 is 8.85×10^{-12} F/m and $\mu_0 = 4\pi \times 10^{-7}$ H/m, n is refractive index of the medium.

From (8.1)-(8.4), there are four possible classes of materials, as illustrated in Figure 8-1 [28]:

(i) DPS ($\epsilon > 0$ and $\mu > 0$)

These are conventional materials, also named as double positive materials (DPS) or right handed materials (RHM) and dielectrics are its examples. The propagation of electromagnetic waves is possible in such materials.

(ii) ENG ($\epsilon < 0$ and $\mu > 0$)

These are epsilon-negative materials (ENG), having characteristic of negative value of permittivity, normally shown by many types of plasma in a particular frequency region. Metals like Gold, Silver etc., demonstrate this negative permittivity in the infrared and visible frequency domains. The propagation of electromagnetic waves is not possible in ENG materials.

(iii) MNG ($\epsilon > 0$ and $\mu < 0$)

These materials are named as mu-negative materials (MNG), having characteristic of negative value of permeability, shown by Gyrotropic materials in certain frequency bands. The propagation of electromagnetic waves is not possible in such materials.

(iv) DNG ($\epsilon < 0$ and $\mu < 0$)

These materials are named as double negative materials (DNG) or Left-handed materials (LHM). These materials do not exist in nature but are physically realizable by making composite structures. The propagation of electromagnetic waves is possible in such material.

From (8.5) the negative refractive index referred to as left-handed (LH) material is characterized as anti-parallel phase and group velocity material that exhibits unusual properties. It can allow an electromagnetic wave to convey energy and group velocity in the opposite direction to its phase velocity, causing strong localization and enhancement of fields, thereby significant enhancement in the slew rate and group velocity of resonator resulting in lower phase noise for oscillator applications [7].

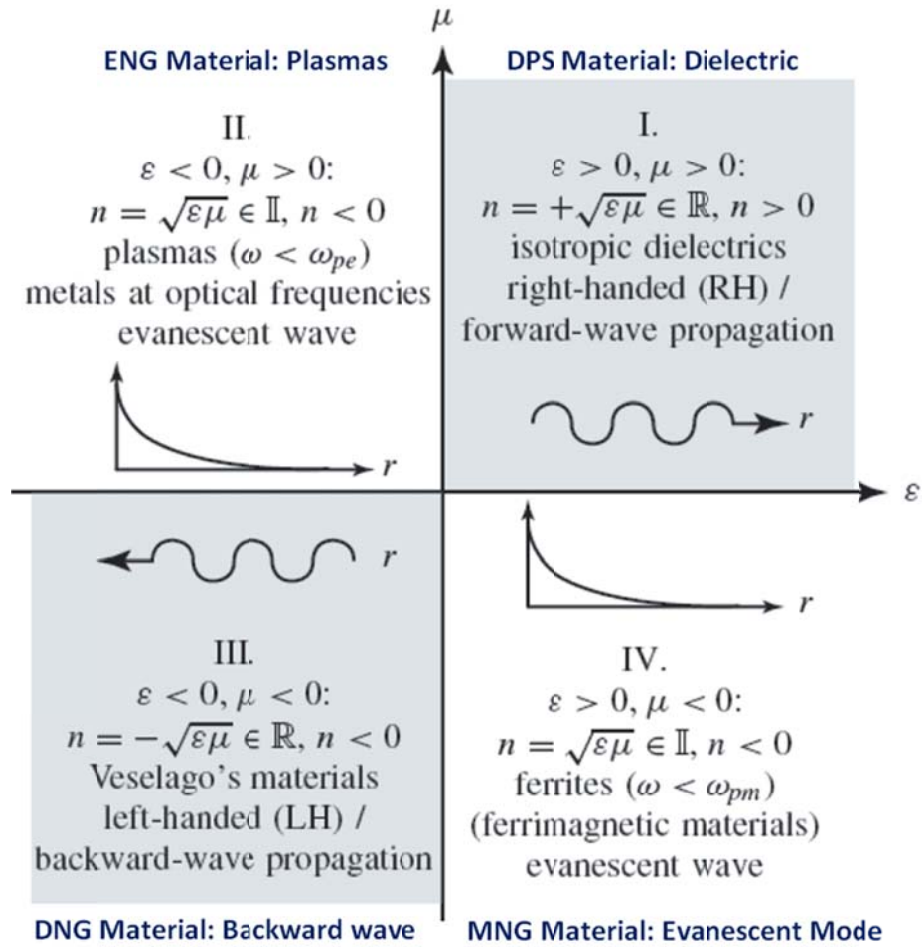


Figure 8-1 Permittivity-Permeability Diagram, R and I represents Real and Imaginary terms; ω_{pe} and ω_{pm} are the electric and magnetic plasma frequencies respectively [28].

These unusual characteristics of metamaterial open new degrees of freedom in resonator design for high frequency oscillator, filter, phase-shifter, antenna and other microwave applications in compact size. The artificial metamaterial components (negative value of permittivity and permeability) have been demonstrated over a large portion of the electromagnetic spectrum, from visible to radiofrequency [12].

The sign (positive or negative values) of permittivity and permeability is not restricted by any physical law, and can be positive or negative. In natural materials, negative permeability can occur during resonant condition [13]. The real part of permeability may take negative values near a resonance of sufficient strength, as for example in ferrites near the ferromagnetic resonance frequency.

For artificial materials, manipulation of a negative permeability response can be realized using electrically small resonant metal inclusions of special shapes, e.g. split rings. Among metamaterial components, a split-ring resonator (SRR) is used for microwave oscillator circuits and planar microwave devices [12]-[14].

8.2 The Electromagnetic Wave Propagation Dynamics of Metamaterial

The Maxwell's equations can be given by

$$\nabla \times \vec{E} = -\frac{\partial \vec{B}}{\partial t} - \vec{M}_s \quad (\text{Faraday's Law}) \quad (8.6)$$

$$\nabla \times \vec{H} = \vec{J} + \frac{\partial \vec{D}}{\partial t} \quad (\text{Ampere's Law}) \quad (8.7)$$

$$\nabla \cdot \vec{D} = \rho_v \quad (\text{Electric Gauss's Law}) \quad (8.8)$$

$$\nabla \cdot \vec{B} = \rho_m \quad (\text{Magnetic Gauss's Law}) \quad (8.9)$$

Where

$$\bar{B} = \mu \bar{H} = \mu_0 \mu_r \bar{H} \quad (8.10)$$

$$\bar{D} = \epsilon \bar{E} = \epsilon_0 \epsilon_r \bar{E} \quad (8.11)$$

$$\epsilon_r = \epsilon' - j\epsilon'' = \epsilon'[1 - jt\tan(\delta_e)], \quad \tan(\delta_e) = \frac{\omega\epsilon' + \sigma_e}{\omega\epsilon'} \quad (8.12)$$

$$\mu_r = \mu' - j\mu'' = \mu'(\delta_m), \quad \tan(\delta_m) = \frac{\omega\mu' + \sigma_m}{\omega\mu'} \quad (8.13)$$

Where \vec{E} (V/m) is the electric field intensity, \vec{H} (A/m) is the magnetic field intensity, \vec{D} (Coulomb/m²) is the electric flux density, \vec{B} (W/m²) is the magnetic flux density, M_s (Volt/m²) is the fictitious magnetic current density, \vec{J} (A/m²) is the electric current density, ρ_v (Coulomb/m³) is the electric charge density, ρ_m (Coulomb/m³) is the magnetic charge density, ϵ_0 is 8.85×10^{-12} (Farad/m), $\mu_0 = 4\pi \times 10^{-7}$ (Henry/m), ϵ_r is the relative permittivity, and μ_r is the relative permeability of the medium.

From (8.6)- (8.7), conventional medium follows right hand rule, which means the electric field intensity vector \vec{E} , magnetic field intensity \vec{H} and Poynting vector \vec{k} inside medium form right handed triplet.

The plane wave propagation along $+z$ direction can be described by Helmholtz Equations [16]:

$$\nabla^2 \vec{E} + k^2 \vec{E} = 0 \quad (\text{Vector wave equation-Helmholtz Equations}) \quad (8.14)$$

$$\frac{d^2 E_x}{dz^2} + k^2 E_x = 0 \quad (\text{Simplified scalar wave equation-Helmholtz Equations}) \quad (8.15)$$

$$\vec{E}(z, t) = \hat{a}_x E_0^+ \cos(\omega t - kz) \quad (\text{Traveling wave E-field solution in time-domain}) \quad (8.16)$$

$$H(z, t) = \hat{a}_y \frac{E_0^+}{\eta} \cos(\omega t - kz) \quad (\text{Traveling wave H-field solution in time-domain}) \quad (8.17)$$

$$\eta = \frac{[E]}{[H]} \quad (\text{Wave impedance}) \quad (8.18)$$

For right-handed material ($\mu, \epsilon > 0$), triad $[\bar{E}, \bar{H}, \bar{k}]$ can be illustrated by [28]

$$\bar{k} \times \bar{E} = +\omega \mu \bar{H} \quad (8.19)$$

$$\bar{k} \times \bar{H} = -\omega \epsilon \bar{E} \quad (8.20)$$

For left-handed material ($\mu, \epsilon < 0$), triad $[\bar{E}, \bar{H}, \bar{k}]$ can be illustrated by [28]

$$\bar{k} \times \bar{E} = -\omega |\mu| \bar{H} \quad (8.21)$$

$$\bar{k} \times \bar{H} = +\omega |\epsilon| \bar{E} \quad (8.22)$$

Assuming the frequency is positive quantity, the phase velocity is given by

$$\bar{v}_p = \frac{\omega}{k} \hat{k}, \text{ where } (\hat{k} = \bar{k}/|\bar{k}|) \quad (8.23)$$

$$LH \text{ Medium: } k < 0 (v_p < 0) \quad (8.24)$$

$$RH \text{ Medium: } k > 0 (v_p > 0) \quad (8.25)$$

$$\bar{k} \times \bar{E} = s\omega |\mu| \bar{H} \quad (8.26)$$

$$\bar{k} \times \bar{H} = -s\omega |\epsilon| \bar{E} \quad (8.27)$$

$$s = \begin{pmatrix} +1, & RH \\ -1, & LH \end{pmatrix}, \quad (\text{where 's' is definition of handedness with respect to } k) \quad (8.28)$$

$$\bar{E}, \bar{H} \approx e^{+j(\omega t + |n|k_0 r)} \quad (8.29)$$

$$U_n = \frac{1}{4} \{ \epsilon |E|^2 + \mu |H|^2 \} \quad (U_n: Energy) \quad (8.30)$$

$$\text{where } k = \frac{\omega}{u_p} \quad (\text{wave number or phase constant}), \quad v_p = \frac{1}{\sqrt{\mu \epsilon}} \quad (\text{Phase velocity}), \quad k = \frac{2\pi}{\lambda}$$

(phase constant in terms of wavelength).

Figure 8-2 (a) illustrates the plane wave propagation characteristics in right-handed and left-handed orthogonal coordinate system. From (8.19)-(8.20), $[\bar{E}, \bar{H}, \bar{k}]$ form a right-handed orthogonal coordinate system for positive values of ϵ and μ , whereas from (8.21)-(8.22), $[\bar{E}, \bar{H}, \bar{k}]$ form a left-handed orthogonal coordinate system for negative values of ϵ and μ [17, 28, and 144].

Figure 8-2 (b) depicts the 2-layer structure (left layer is a DPS material and right layer is a DNG material), the direction of Poynting vector \bar{S} is parallel with the direction of phase velocity or wave vector \bar{k} in DPS material but these two directions are anti-parallel in DNG material (right layer). Figure 8-2 (c) exhibits CAD HFSS simulation illustrating the plane wave propagation dynamics using effective medium [28].

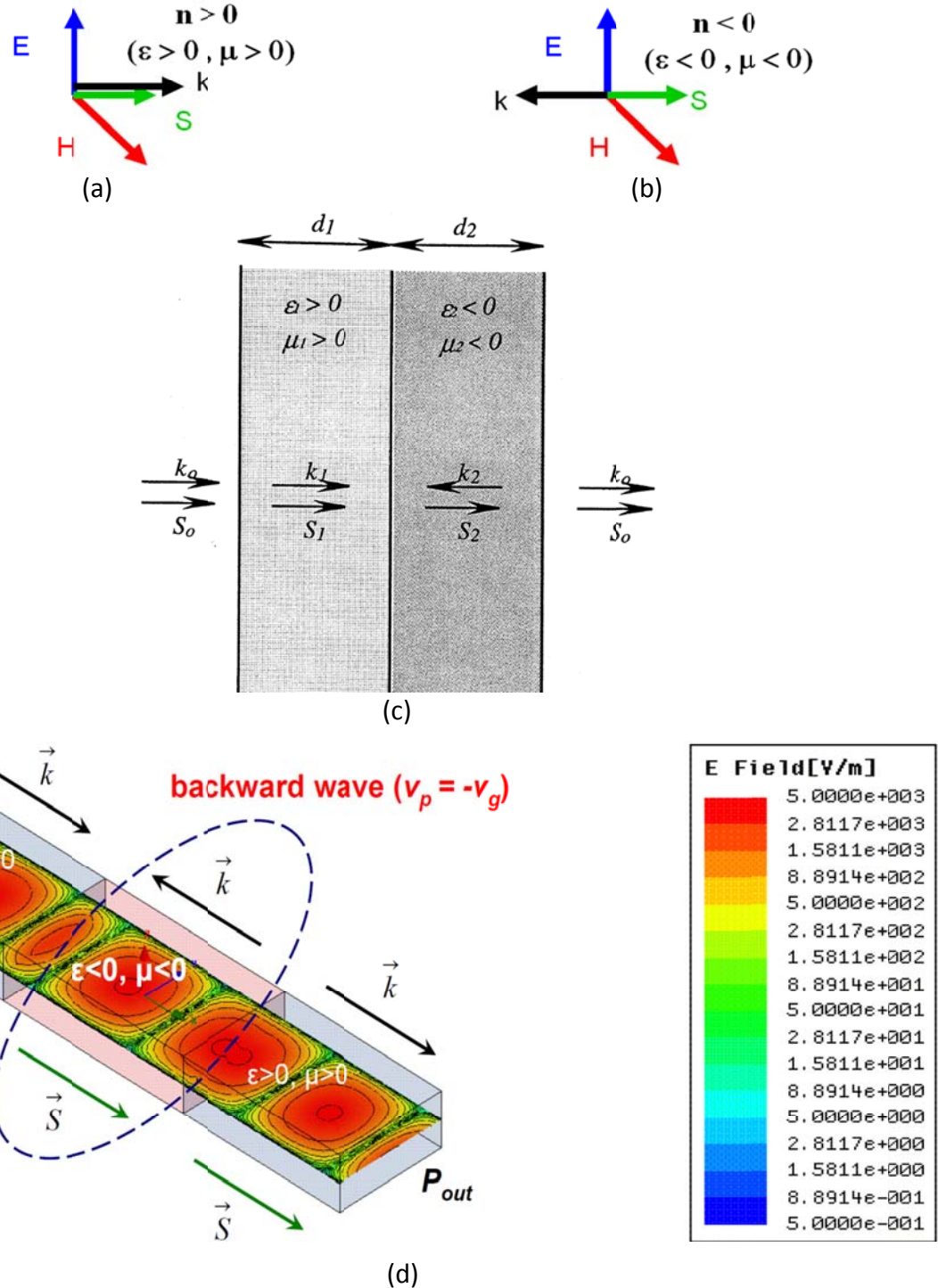


Figure 8-2: (a) Right-handed orthogonal coordinate system for materials with positive ϵ and μ , (b) left-handed orthogonal coordinate system for materials with negative ϵ and μ , (b) depicts the 2-layer structure (left layer is a DPS material and right layer is a DNG material), and (c) CAD HFSS simulation shows the plane wave propagation dynamics using effective medium [28, 144]

From (8.24) in LH (left-handed) medium phase velocity v_p propagates backward to the source in the opposite direction to that of power, related to group velocity v_g (Figure 8-2(c)). The backward propagation implies that the fields have time-space dependence. Backward-wave

media are media in which the energy velocity direction is opposite to the phase velocity direction (or, the scalar product between the corresponding vectors is negative). In particular, this takes place in isotropic materials with negative permittivity and permeability (double negative media). Negative refraction takes place on interfaces between ‘usual’ materials and backward-wave media. Surface waves (waves propagating along a surface but exponentially decaying in the directions orthogonal to the surface) can exist on interfaces between media having material parameters of the opposite sign. The anomalous refraction at the boundary of such media and the fact that for plane wave the direction of the Poynting vector is anti-parallel with the direction of phase velocity, can be advantageous in designing compact high quality factor resonator circuit.

From (8.16) - (8.17), the power flow as shown in Figure 8-2 (c) is given by Poynting theorem as [29]

$$\oint_S (\vec{E} \times \vec{H}) \cdot d\vec{s} = -\frac{\partial}{\partial t} \int \left(\frac{1}{2} \epsilon E^2 + \frac{1}{2} \mu H^2 \right) dv - \int \sigma E^2 dv \quad (8.31)$$

$$\oint_S (\vec{E} \times \vec{H}) \cdot d\vec{s} = \oint_S \vec{S} \cdot d\vec{s} \quad (8.32)$$

where $\vec{S} = (\vec{E} \times \vec{H})$ is the Poynting vector.

From (8.31)-(8.32), the propagation of energy will take place at the direction extracted from Poynting vector. The direction of Poynting vector is same for both LHM and RHM, always calculated as a right-hand-triplet from the electric and magnetic field. From (8.32), average Power density transmitted by a uniform plane wave in z direction is given as [30]-[36]:

$$\vec{S}_{av}(z) = \hat{a}_z \frac{E_0^2}{2|\eta_c|} e^{-2\alpha z} \cos \theta_\eta \quad (\text{Lossy medium}) \quad (8.33)$$

$$\vec{S}_{av}(z) = \hat{a}_z \frac{E_0^2}{2\eta} \quad (\text{Lossless medium}) \quad (8.34)$$

$$\vec{S}_{av} = \frac{1}{2} R_e (\vec{E} \times \vec{H}^*) \quad (\text{Phasor form}) \quad (8.35)$$

The realization of true DNG material (metamaterial) is questionable! In general, it is difficult to build a material or medium simultaneously with negative permittivity and negative permeability for a broad operating frequency ranges from a set of arbitrary passive structure unit cells arranged in predefined order. This may lead to violation of energy conservation principle at the intersecting plane between a RHM (right-handed material) and LHM (left-handed material) media because of the generation of energy. However, an attempt to build the DNG material or medium based on the fact that for a specific orientation and arrangement of the passive structure, the values of permittivity and permeability reduces as the frequency increases till these material or medium initiate demonstrating negative permittivity and permeability at specific narrowband frequencies and lacks the validity for broadband operation. It is however, easy to demonstrate independently MNG (negative permeability) or ENG (negative permittivity) characteristics but achieving negative regime for permittivity and

negative permeability could be challenging task and need complex and active structure to support the evidence of DNG material for broadband operation. For clear understanding, Figure 8-3 exhibits the electromagnetic wave propagation in different media [16].

8.2.1 Backward Wave Propagation Dynamics in Left-Handed Material

A typical material which has both negative permittivity and permeability nomenclatured as left-handed (LH), is where the electric field intensity vector \vec{E} , and the magnetic field intensity \vec{H} vector forms a left-handed triplet (Figure 8-2(b)).

From (8.24), backward wave implies that the phase traveling direction is toward source instead of away from source after electromagnetic wave enters the Metamaterial (Figure 8-3). From (8.32) and (8.35), the energy flowing direction is always away from source irrespective of type of the medium the wave is traveling as shown in Figures 8-2 and 8-3, the main difference is which side of normal face the energy will be flowing to [21]. This intrinsic property of negative phase advance in left-handed material exhibits the properties well suited for perfect lenses or super lenses [25].

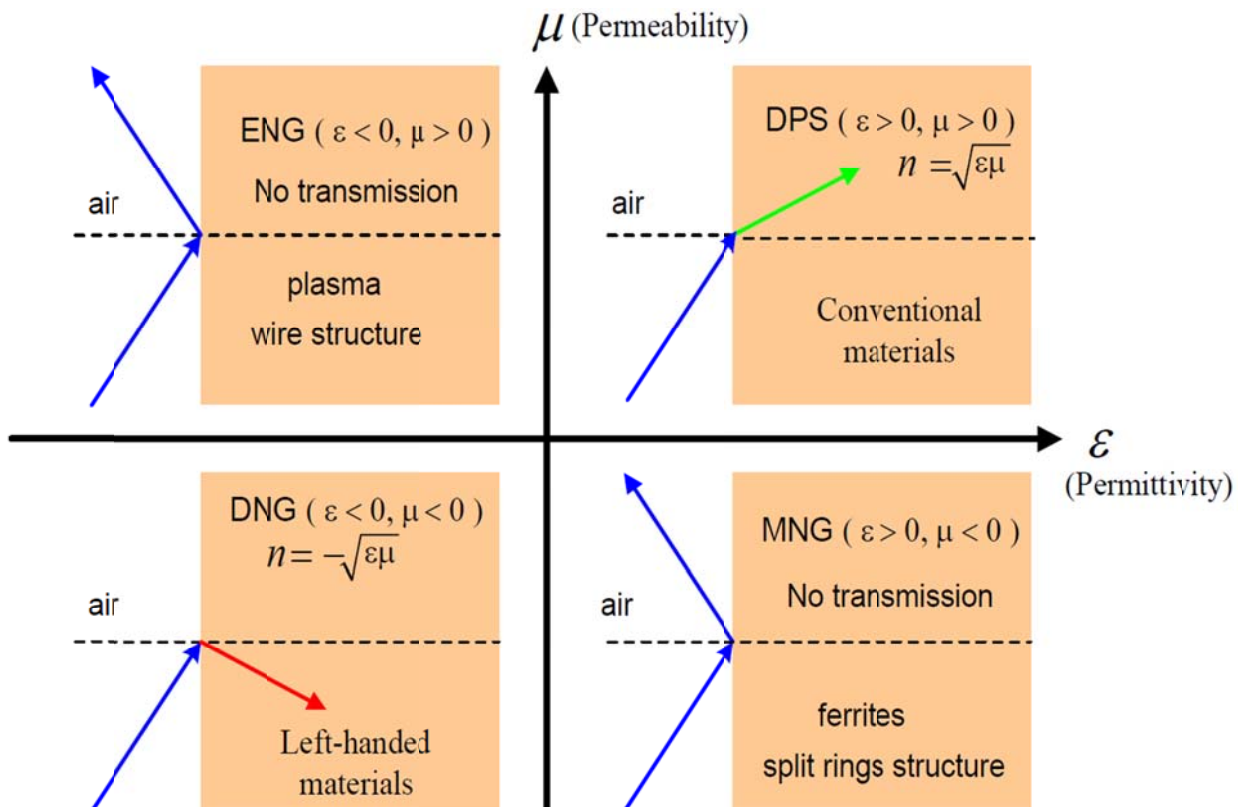


Figure 8-3: shows the electromagnetic wave propagation in different media [16]

If the electromagnetic wave propagation is in the z axis, in order to transmit all the energy through the DNG material slab it is required that we have a propagation constant k'_z [26]:

$$k'_z = -\sqrt{\frac{\omega^2}{c^2} - (k_x^2 + k_y^2)} \quad (8.36)$$

The overall transmission coefficient for the wave entering into DNG slab ($\epsilon=-1$ and $\mu=-1$) as shown in Figure 8-4 is given by [26]

$$T = tt' = e^{-j\left[\sqrt{\frac{\omega^2}{c^2} - (k_x^2 + k_y^2)}\right]d} \quad (8.37)$$

$$T = e^{j(k'_z d)} \quad (8.38)$$

where t and t' are the transmission coefficient of DPS and DNG medium, and d is the distance the wave travels inside the DNG (Metamaterial slab).

The choice of the propagation constant k'_z is made in order to maintain causality and the required phase correction grants the DNG material capability of refocusing the image by canceling the phase of the transmitted wave as it propagates from its source [1]. This is an interesting phenomenon, which can be useful towards improving the phase-dispersion and group delay in resonator for oscillators and filters applications.

8.2.2 Evanescent Wave Propagation Dynamics

Considering the field expression for TE wave propagation in vacuum (medium 1) is

$$\overline{E_1} = e^{j(\bar{z}k_z + \bar{x}k_x - \omega t)} \quad (8.39)$$

$$\text{where } k_z \text{ is a propagation constant, } k_z = j\sqrt{(k_x^2 + k_y^2) - \frac{\omega^2}{c^2}} \text{ with } \frac{\omega^2}{c^2} < (k_x^2 + k_y^2) \quad (8.40)$$

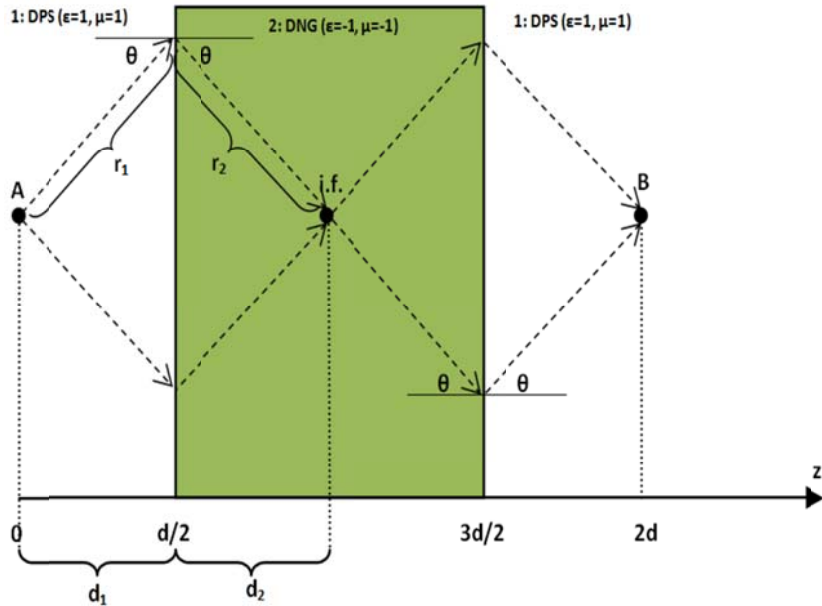


Figure 8-4: shows the wave propagation from free space (DPS) into Metamaterial slab (DNG medium) [26]

In order to maintain the causality the field must decay as it goes away from the interface; the transmitted ($\overline{E_{t2}}$) and reflected field ($\overline{E_{r1}}$) can be described by

$$\overline{E_{t2}} = T e^{j(\bar{z}k'_z + \bar{x}k_x - \omega t)} \quad (8.41)$$

$$\overline{E_{r1}} = Re^{j(-\bar{z}k'_z + \bar{x}k_x - \omega t)} \quad (8.42)$$

$$\text{Where } [k'_z]_{(k_x^2 + k_y^2) > \epsilon_2 \mu_2 \left(\frac{\omega^2}{c^2}\right)} = j \sqrt{(k_x^2 + k_y^2) - \epsilon_2 \mu_2 \frac{\omega^2}{c^2}} \quad (8.43)$$

where ϵ_2 and μ_2 are the permittivity and permeability of the medium 2 (slab) and $\frac{\omega^2}{c^2} < \frac{(k_x^2 + k_y^2)}{\epsilon_2 \mu_2}$. The transmission, T, and reflection coefficients, R, can be derived by matching the electromagnetic wave fields at the interface from medium # 1 and medium #2 [26]:

$$T = \frac{2\mu k_z}{\mu k_z + k'_z} \quad (8.44)$$

$$R = \frac{\mu k_z - k'_z}{\mu k_z + k'_z} \quad (8.45)$$

The transmission, T' , and reflection coefficients, R' , of the transition from slab (inside medium # 2) to medium # 1 is given by

$$T' = \frac{2k'_z}{\mu k_z + k'_z} \quad (8.46)$$

$$R' = \frac{k'_z - \mu k_z}{k'_z + \mu k_z} \quad (8.47)$$

The expression of the wave transmission coefficient (T_e) through both the interfaces can be derived by adding the multiple scattering dynamics, described by

$$T_e = \frac{\overline{E_{transmitted}}}{\overline{E_{incident}}} \quad (8.48a)$$

$$T_e = TT'e^{j(k'_z d)} + TT'R'^2e^{j(3k'_z d)} + TT'R'^3e^{j5(5k'_z d)} + TT'R'^4e^{j7(7k'_z d)} + (\dots) \quad (8.48b)$$

$$T_e = \frac{TT'e^{j(k'_z d)}}{1 - R'^2e^{j(2k'_z d)}} \quad (8.49)$$

For metamaterial (DNG medium), $\epsilon=-1$ and $\mu=-1$

$$[T_e]_{\epsilon \rightarrow -1, \mu \rightarrow -1} = \left[\frac{\left(\frac{2\mu k_z}{\mu k_z + k'_z} \right) \left(\frac{2k'_z}{\mu k_z + k'_z} \right) e^{j(k'_z d)}}{1 - \left(\frac{k'_z - \mu k_z}{k'_z + \mu k_z} \right)^2 e^{j(2k'_z d)}} \right] \quad (8.50)$$

$$[T_e]_{\epsilon \rightarrow -1, \mu \rightarrow -1} = \left[\frac{\left(\frac{-2k_z}{-k_z + k'_z} \right) \left(\frac{2k'_z}{-k_z + k'_z} \right) e^{j(k'_z d)}}{1 - \left(\frac{k'_z + k_z}{k'_z - k_z} \right)^2 e^{j(2k'_z d)}} \right] \cong e^{j(k'_z d)} \quad (8.51)$$

where

$$[k'_z]_{\epsilon \rightarrow -1, \mu \rightarrow -1} = j \left(\sqrt{(k_x^2 + k_y^2) - \epsilon_2 \mu_2 \frac{\omega^2}{c^2}} \right) = j \left(\sqrt{(k_x^2 + k_y^2) - \frac{\omega^2}{c^2}} \right) = k_z \quad (8.52)$$

From (8.51)

$$[T_e]_{\epsilon \rightarrow -1, \mu \rightarrow -1} = e^{j(k'_z d)} = e^{j(k_z d)} \quad (8.53)$$

The overall reflection coefficient can be given by (R_r) as[26]

$$[R_r] = \frac{\overline{E_{reflected}}}{\overline{E_{incident}}} = R \left[1 - \frac{(1-R'^2)e^{j(2k'_z d)}}{1-R'^2 e^{j(2k'_z d)}} \right] = R \left[\frac{1-e^{j(2k'_z d)}}{1-R'^2 e^{j(2k'_z d)}} \right] \quad (8.54)$$

Simplifying the Equations (8.45), (8.47) and (8.54)

$$[R_r]_{\epsilon \rightarrow -1, \mu \rightarrow -1} \rightarrow 0 \quad (8.55)$$

From (8.55), the reflection coefficient R_r is zero in DNG medium. The consequence of having negative index ($\epsilon \rightarrow -\nu e, \mu \rightarrow -\nu e$) refraction result in the wave of the form $e^{(-k_z d)}$ outside the slab (DNG) that couple to waves of the form $e^{(k_z d)}$ inside the slab (DNG). Therefore, even if the waves decay outside the slab, they are amplified on the inside of it, recovering an image on the opposite side of the slab, from the source, and all done by the transmission process [26]. Since the wave decay in amplitude not in phase, as they get further from the source, the DNG slab focus the image by amplifying these waves rather than correcting the phase. Figure 8-5 illustrates the evanescent field variation in DNG slab.

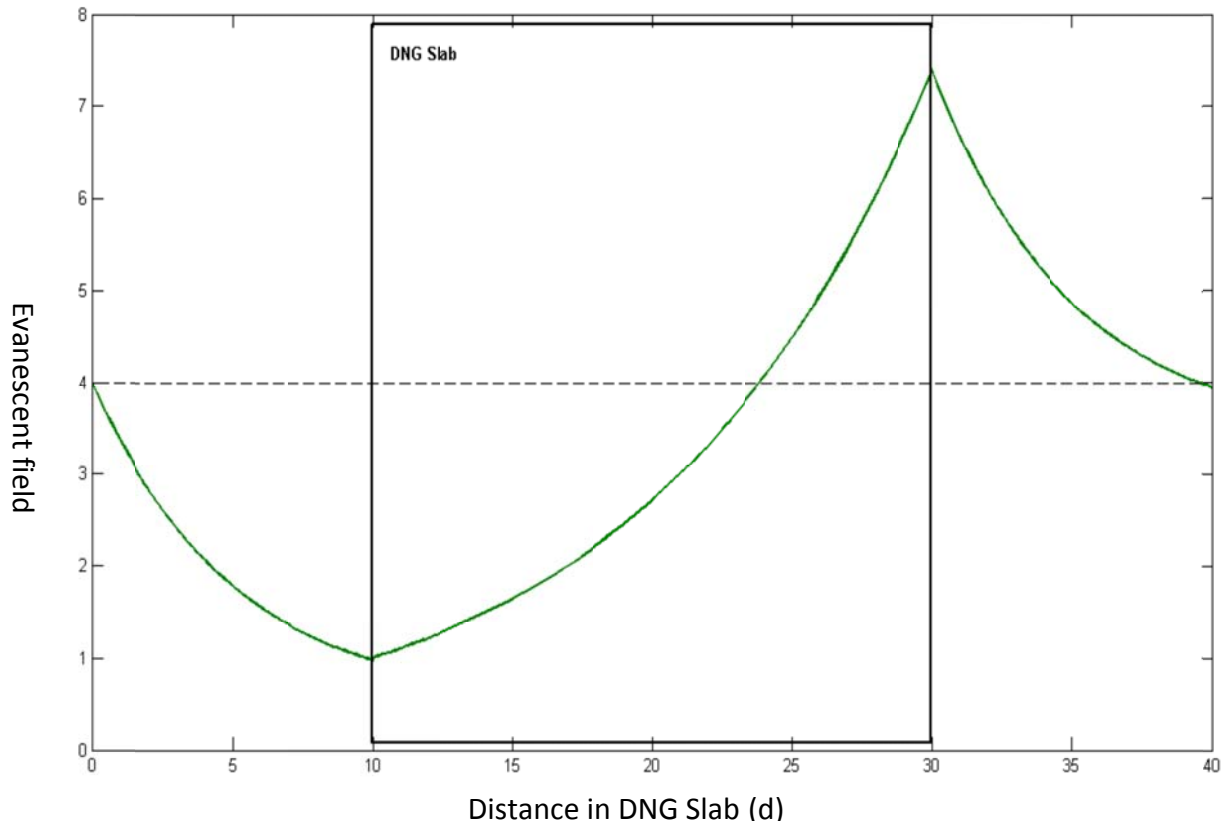


Figure 8-5: Evanescence field variation in Metamaterial slab (DNG), shows amplification of evanescent wave inside the DNG slab [26]

These features can be utilized for improving the Q-factor of the evanescent mode resonator because both the propagating and evanescent waves contribute to improving the group delay.

This phenomenon does not violate energy conservation law because evanescent wave does not transport the energy [27].

8.2.3 Phase Velocity, Group velocity, Energy Density

8.2.3.1 Phase Velocity

From (8.23), the phase velocity of a wave is the rate at which the phase of the wave propagates in space or medium. The phase velocity is given in terms of the wave's frequency ω , wavenumber k , velocity of light c , and refractive index n , given by [28]-[29]

$$v_p = \frac{\omega}{k} = \frac{\omega}{nk_o} \quad (k = \omega\sqrt{\epsilon\mu} = \omega n\sqrt{\epsilon_o\mu_o} = nk_o) \quad (8.56)$$

$$v_p = \frac{c}{n} = \frac{c}{\sqrt{\epsilon\mu}} \quad (8.57)$$

8.2.3.2 Group Velocity

The group velocity is the rate at which the envelope of the waveform is propagating in space or medium, i.e. the rate of variation of the amplitude of the waveform. Assuming the waveform is not distorted significantly during propagation, it is the group velocity, which represents the rate at which information (and energy) is transmitted by the wave. However, if the wave is travelling through an absorptive and strongly dispersive medium, this condition no longer holds. For certain condition, it is possible to reduce the group velocity to zero, stopping the wave, or have negative group velocity, making the wave appear to propagate backwards. In isotropic media, the group velocity is given as [28]

$$v_g(\omega_o) = \frac{d\omega}{dk} = \left(\frac{dk}{d\omega} \right)^{-1} \quad (8.58)$$

Where v_g is the group velocity, ω is the wave's angular frequency, k is the wave number.

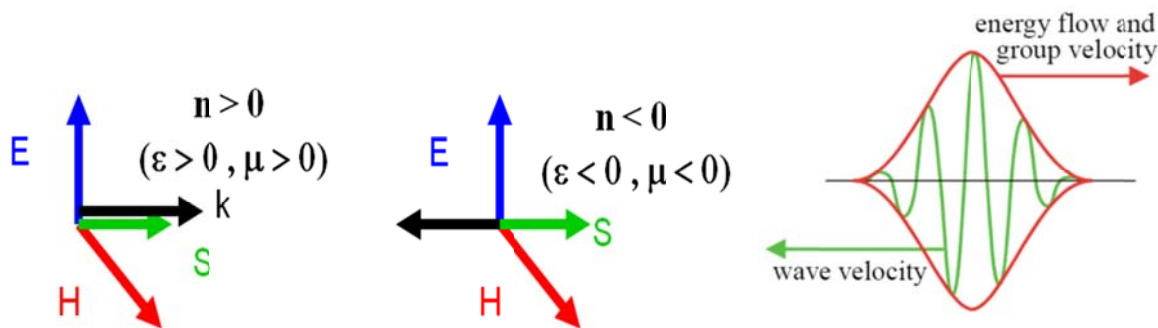


Figure 8-6: shows the typical representation of electromagnetic wave velocity

The function $\omega(k)$, which gives ω as a function of k , is known as the dispersion relation. If ω is directly proportional to k , then the group velocity is exactly equal to the phase velocity.

Otherwise, the envelope of the wave will become distorted as it propagates. Figure 8-6 shows the typical pictorial representation of the electromagnetic wave velocity.

From (8.56) and (8.57) [29],

$$v_g(\omega_0) = v_p + k \frac{d(v_p)}{dk} \quad (8.59)$$

$$v_g(\omega_0) = c \left[\frac{d(n\omega)}{d\omega} \right]^{-1} = \frac{c}{n + \omega_0 \left[\frac{d(n)}{d\omega} \right]}, \quad \text{where } \frac{d(n)}{d\omega} > 0 \quad (8.60)$$

From (8.60), for positive refractive index n , the group velocity is always smaller than the phase velocity and smaller than the speed of light in vacuum.

From (8.60), for negative refractive index material ($n < 0$), the group velocity can take any value because $\frac{d(n)}{d\omega} > 0$ in a low-loss media, including materials with negative refractive index.

8.2.3.3 Energy Density

It is well known that any physical media other than vacuum is dispersive [28]. The expression of energy density U for non-dispersive media can be described by [30]:

$$U = \frac{1}{4} \{ \epsilon |E|^2 + \mu |H|^2 \} \rightarrow U = \frac{1}{4} \left\{ \left[\frac{\partial(\omega\epsilon)}{\partial\omega} \right] |E|^2 + \left[\frac{\partial(\omega\mu)}{\partial\omega} \right] |H|^2 \right\} \quad (8.61)$$

From (8.61), the physical requirement of the existence of the positive energy density is given by

$$\frac{\partial(\omega\epsilon)}{\partial\omega} > 0, \frac{\partial(\omega\mu)}{\partial\omega} > 0 \quad (8.62)$$

From (8.61), for Metamaterial ($\mu, \epsilon < 0$) the energy density results of negative value, which yields nonphysical result. Equation (8.62) is compatible with ($\mu, \epsilon < 0$), provided $\frac{\partial(\omega\epsilon)}{\partial\omega} > \frac{|\epsilon|}{\omega}$ and $\frac{\partial(\omega\mu)}{\partial\omega} > \frac{|\mu|}{\omega}$. Hence, physical left-handed media is highly dispersive (Metamaterial resonator exhibits negative value of ϵ and μ in the highly dispersive regions just above resonances). For Metamaterial, backward-wave propagation implies opposite signs between phase and group velocities [31], can be expressed as [29]

$$\frac{\partial k^2}{\partial\omega} = 2k \left(\frac{\partial(k)}{\partial\omega} \right) = 2 \left(\frac{\omega}{v_p v_g} \right) \quad (8.63)$$

$$\frac{\partial k^2}{\partial\omega} = \omega\epsilon \left(\frac{\partial(\omega\mu)}{\partial\omega} \right) + \omega\mu \left(\frac{\partial(\omega\epsilon)}{\partial\omega} \right) < 0 \quad (8.64)$$

$$v_p v_g < 0 \quad (8.65)$$

Where $v_p = \frac{\omega}{k}$ and $v_g = \frac{d\omega}{dk}$ are the phase and group velocity respectively, and $k = \omega\sqrt{\epsilon\mu}$. Backward wave transmission line can form a non-resonant LHM (left-handed material) [28, 35].

8.3 Realization of Negative Refractive Index material (NRIM) Components

The refractive index is the most fundamental parameter to describe the interaction of electromagnetic radiation with matter. It is a complex $n = (n' + jn'')$ where n' is generally

being considered to be positive. While the condition of $n' < 0$ does not violate any fundamental physical law, materials with negative index exhibit interesting properties. For example, electromagnetic wave when refracted at an interface between positive refractive index material (PRIM) and a negative refractive index material (NRIM), is bent in the “wrong” way with respect to the normal, result in group and phase velocity are antiparallel.

A possible-but not only-approach to achieve a NRIM in a passive medium is to design a material in which the (isotropic) permittivity $\epsilon = (\epsilon' + j\epsilon'')$ and the (isotropic) permeability $\mu = (\mu' + j\mu'')$ obey the inequality [35]-[41]

$$\epsilon'|\mu| + \mu'|\epsilon| < 0 \quad (8.66)$$

This leads to a negative real part of the refractive index $n = (n' + jn'') = \sqrt{\mu\epsilon}$. Equation (8.66) only holds good for passive media and the equality condition is satisfied, if $\epsilon' < 0$ and $\mu' < 0$. But this is not a necessary condition, there may be magnetically active media ($\mu \neq 1$) with a positive real part μ' for which (8.66) is justified and show a negative real part of the refractive index n' . From [100], the incorporating impedance term Z in the general relationship between the refractive index can lead to more general relationship [37]

$$2 \operatorname{Re} \left(\frac{1}{Z} \right) n' = \epsilon' + \mu' \frac{|\epsilon|}{|\mu|} \quad (8.67)$$

$$2n'n'' = \epsilon'\mu'' + \mu'\epsilon'' \quad (8.68)$$

where $Z = \sqrt{\left(\frac{\mu}{\epsilon}\right)}$, the direction of the Poynting vector and wave vectors are governed by the sign of $\operatorname{Re} \left(\frac{1}{Z} \right)$ and n' respectively [101].

Therefore, the sign of $\epsilon' + \mu' \frac{|\epsilon|}{|\mu|}$ should be negative for the NRIM. Equation (8.68) requires $(\epsilon'\mu'' + \mu'\epsilon'')$ being negative for the absorbing effective. medium and positive for a NRIM. The key to the design of the artificial NRIM resonator is to select novel geometric shape so that induced currents form loops with a relatively uniform distribution of the induced current, which produces a strong magnetic moment.

In general, three types of typical geometry are used for the realization NIRM components: (i) split-ring resonators, (ii) coupled wire sets, (iii) and dielectric resonators. Figure 8-7 depicts these resonators, which exhibit negative refractive index property described in (8.66) [38]-[52].

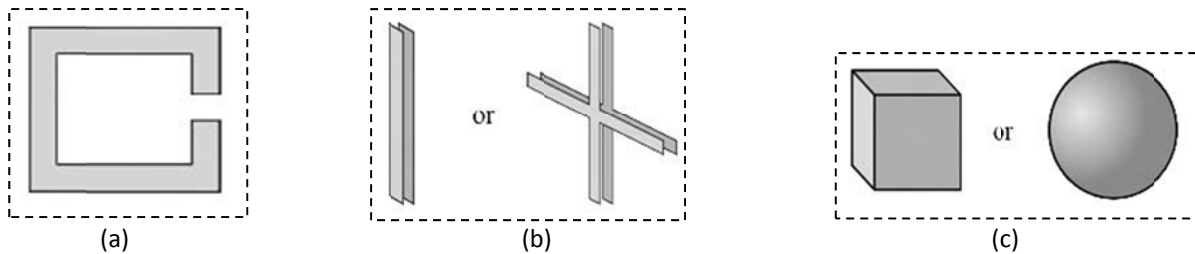


Figure 8-7 illustrates the typical resonator geometries that exhibit negative refractive index property: (a) Split ring resonator, (b) coupled wire sets, and (c) dielectric resonators [53].

8.3.1 Split Ring Resonator (SRR)

As shown in Figure 8-7 (a), Split-ring resonator (SRR) produces a negative permeability just above their resonant frequency, typically these structures are bi-anisotropic exhibiting coupled electric and magnetic effects [52]-[53]. A negative refractive index transmission pass-band occurs at the resonant frequency of the split ring when wires that provide a negative permittivity are aligned with their axis parallel to the plane of the loop [54]-[56]. By incorporating concentric split rings in conjunction with varactor diodes as shown in Figure 8-8, resonant frequency can be switched and tuned for multi-band applications [17, 46, and 57].

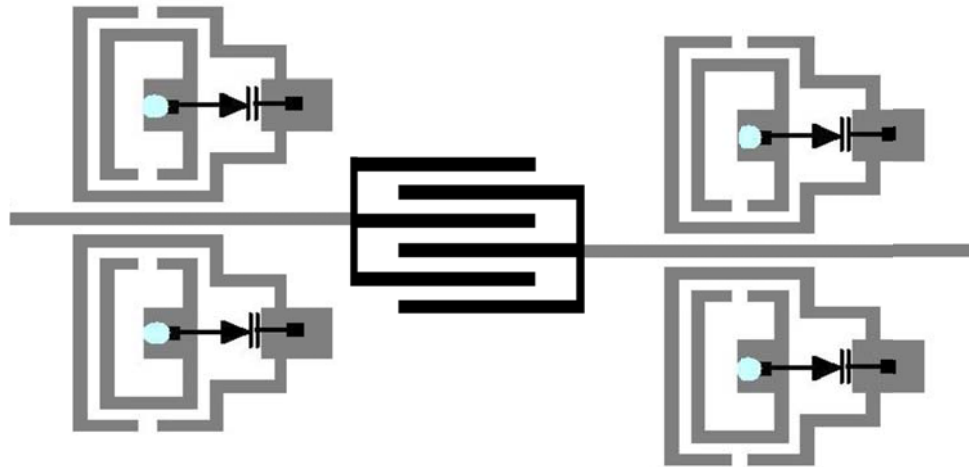


Figure 8-8: shows the typical geometries of metamaterial resonators for switchable band operation.

8.3.2 Coupled Wire Sets NRIM

Figure 8-7 (b) shows a typical coupled wire constructed as negative refractive index material (NRIM) that uses pairs of conducting wire strips, or other shapes, which are spaced apart in the direction of wave propagation at a distance much smaller than the wire's width [53].

As shown in Figure 8-7(b), the electric field interacts with linear elements of the structure leading to negative permittivity, whereas magnetic field interacts with the small gaps between conducting elements, exciting anti-parallel currents in the open loop of the two conducting structures, leading to negative permeability [58]-[86]. While coupled wire structures can be built as a bulk Metamaterial, since the desired properties are achieved face-on, the structure is planar by design. Thus the axis perpendicular to the material face has a different permittivity and permeability than do the axes parallel to the material face. Even though the working angle of the Metamaterial is broad, the refraction angles of different polarizations will eventually decouple because the structure is uni-axial [52].

8.3.3 Dielectric material resonator NRIM

Dielectric material resonator NRIMs (Figure 8-7(c)) uses a non-conductive particle with high permittivity, compared to that of the surrounding material, to create negative permeability [58]. The shape of the inclusions determines the resonant frequencies as well as the level of anisotropy. The resonances are Mie resonances (named after Gustav Mie for his theory of the electromagnetic wave scattering of spheres) for cubes and spheres: the first resonance is magnetic; the second resonance is electric [59]-[72].

8.4 Metamaterial (NRIM) Model

There are different models to describe the Metamaterial behavior (negative permittivity and negative permeability), but the resonator and transmission line models are most common that use the analogy between natural medium and artificial Metamaterial [21].

8.4.1 Resonator Model

Figure 8-9 shows the typical artificial metamaterial resonator model, which consists of dipole shaped thin wire for creating negative permittivity and split ring for negative permeability medium. By adjusting the spacing and dimension of dipole shaped thin wire and split ring, negative permittivity and permeability medium in microwave frequency region can be realized simultaneously, nomenclature as double negative medium (DNG).

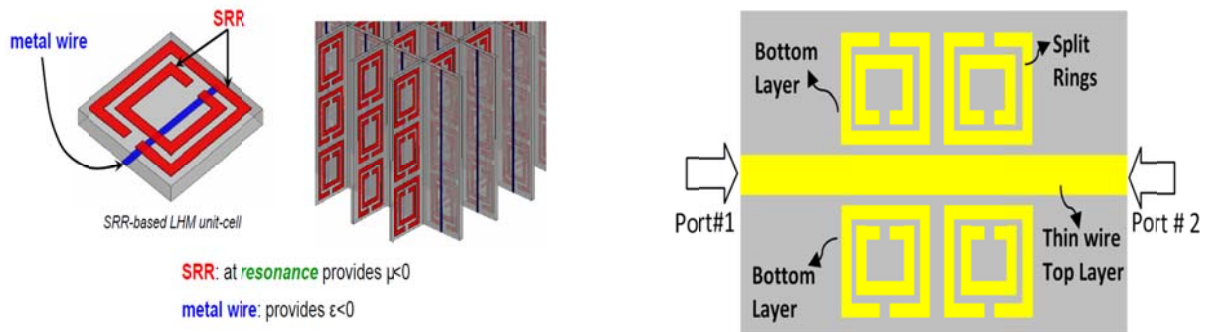


Figure 8-9: shows the typical coupled SRR, exhibits negative permittivity and permeability at resonance [35]

Figure 8-9 shows the 3-dimensional SRR-metal wire which exhibits negative refractive index properties ($\epsilon < 0$ and $\mu < 0$) for the realization of metamaterial resonator, therefore restricts the uses in planar microwave circuit applications [22]. For the application in planar microwave devices, 2-dimensional transmission-line networks can be periodically loaded with series capacitors and shunt inductors for the realization of negative refractive index, such medium makes left-handed material and supports propagating backward waves exhibiting a negative refractive index over a wide bandwidth [23]-[24].

8.4.2 Transmission line model (TLM)

A typical transmission line is a uniform and homogenous structure with invariant cross-section along the direction of propagation, which can transmit signals from zero to very high frequencies [29]. In general, TLM can be classified as Right-handed (printed microstripline). The Left-handed (Metamaterial) material is not available in nature and can be artificially created, nomenclature as CRLH (composite right/left-handed) material. Transmission line model (TLM) assumes Metamaterial as an isotropic and homogeneous medium as contrary to resonator model. A TLM can be represented by distributed series impedance (Z) and shunt admittance (Y) in terms of electric permittivity (ϵ) and magnetic permeability (μ) [22] as

$$Z'(\omega) = \frac{Z(\omega)}{d} = j\omega\mu(\omega) \Rightarrow \mu(\omega) = \frac{Z(\omega)}{j\omega d}; \quad Z' \text{ is impedance per unit length} = Z(\omega)/d \quad (8.69)$$

$$Y'(\omega) = \frac{Y(\omega)}{d} = j\omega\epsilon(\omega) \Rightarrow \epsilon(\omega) = \frac{Y(\omega)}{j\omega d}; \quad Y' \text{ is admittance per unit length} = Y(\omega)/d \quad (8.70)$$

The effective propagation constant $\gamma(\omega)$ of right-handed (normal) material is given by

$$\gamma(\omega) = \sqrt{Z'(\omega)Y'(\omega)} \approx j\beta = j\omega\sqrt{\mu(\omega)\epsilon(\omega)} \quad (8.71)$$

The series inductance and shunt capacitance of right-handed material is given by

$$L = \mu_0 d, \quad L' = \frac{L}{d} = \mu_0, \quad C = \epsilon_0 \epsilon_r d, \quad C' = \frac{C}{d} = \epsilon_0 \epsilon_r \quad (8.72)$$

$$\beta = \omega\sqrt{\mu(\omega)\epsilon(\omega)} = \omega\sqrt{L'C'} \quad (8.73)$$

From (8.69) to (8.73), the effective permittivity is connected with series inductance and permeability is connected with shunt capacitance for right-handed material.

For left-handed material (Metamaterial) that exhibits negative permittivity and permeability, change in polarity is implemented for the realization of negative series impedance for (8.69) and negative admittance for (8.70). There exists a reverse symmetry between right handed medium and left handed medium, hence series inductor and shunt capacitor in right-handed medium is replaced by series capacitor and shunt inductor in the unit cell of the left-handed material (Metamaterial) as shown in Figure 8-10 [21]-[22].

$$Z'(\omega) = \frac{1/j\omega C}{d} = j\omega\mu(\omega) \Rightarrow \mu(\omega) = \frac{\frac{1}{j\omega C}}{\frac{j\omega d}{d}} = -\frac{1}{\omega^2 C'} \quad (8.74)$$

$$Y'(\omega) = \frac{1/j\omega L}{d} = j\omega\epsilon(\omega) \Rightarrow \epsilon(\omega) = \frac{\frac{1}{j\omega L}}{\frac{j\omega d}{d}} = -\frac{1}{\omega^2 L'} \quad (8.75)$$

From (8.74)-(8.75), the left-handed medium distributed series capacitance $C' = C/d$ and shunt inductance $L' = L/d$.

The effective propagation constant $\gamma(\omega)$ of left-handed (Metamaterial) is shown in Figure 8-10 and is given by [97]

$$\gamma(\omega) = \sqrt{Z'(\omega)Y'(\omega)} \approx j\beta = j\omega\sqrt{\mu(\omega)\epsilon(\omega)} = j\omega\sqrt{\left(\frac{1/j\omega C}{d}\right) \times \left(\frac{1/j\omega L}{d}\right)} = \beta = -\frac{1}{\omega\sqrt{L'C'}} \quad (8.76)$$

From (8.76), the phase velocity and group velocity of left-handed material is given by

$$v_p(\omega) = \frac{\omega}{\gamma(\omega)} = -\omega^2\sqrt{L'C'} \quad (8.77)$$

$$v_g(\omega_o) = \frac{d\omega}{d\gamma} = \omega^2\sqrt{L'C'} \quad (8.78)$$

From (8.77) and (8.78), direction of group velocity is opposite of the phase velocity, and group velocity has positive value.

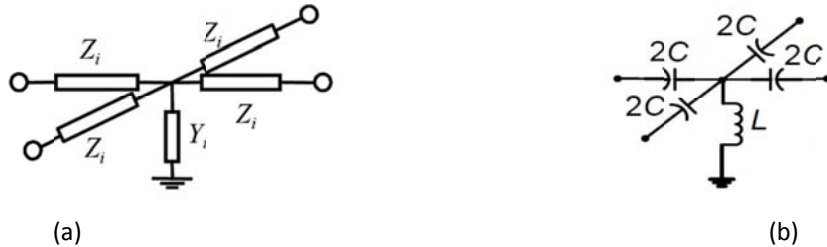


Figure 8-10: Equivalent circuit of the metamaterial unit cell (a) General model, (b) LC model (using shunt inductors for affecting ϵ_r and series capacitors for affecting μ_r) [22]

This implies that phase will propagate backward and the group velocity direction (Poynting Vector) is forward as the direction of energy flowing away from the source. In an isotropic medium for right-handed medium, the phase and group velocity has same direction, therefore no dispersion phenomenon. However, in left-handed medium (LHM) the phase velocity and group velocity are 180 degree out of phase (direction is anti-parallel with group velocity direction), implies medium is dispersive. From (8.77), the negative phase velocity in LHM medium leads to the negative refractive index, which can be given by

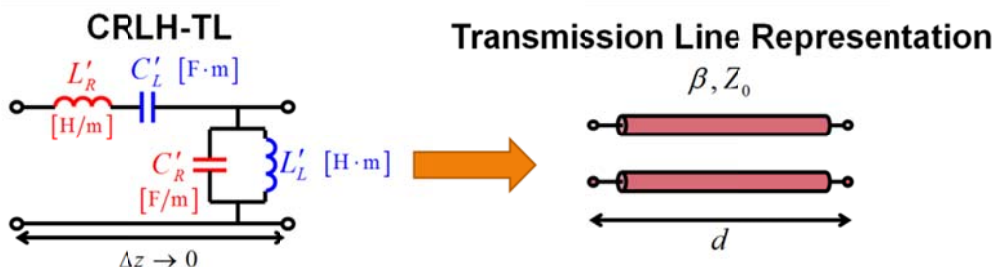
$$n = \frac{c}{v_p(\omega)} = -\frac{\sqrt{\mu(\omega)\epsilon(\omega)}}{\sqrt{\mu_0\epsilon_0}} = -\frac{1}{\omega^2\sqrt{L'C'\mu_0\epsilon_0}} \quad (8.79)$$

$$c = \frac{1}{\sqrt{\mu_0\epsilon_0}} \quad (8.80)$$

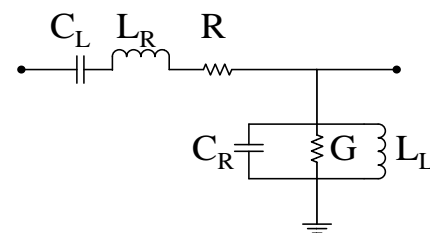
Where c is the velocity of light in free space

8.5 Physical Realization of Metamaterial Component for Oscillator Circuits

Cascaded composite right/left-handed structures (CRLH) with unit dimension much smaller than the guided wavelength behave as Metamaterial, producing simultaneous negative permittivity (ϵ_r) and permeability (μ_r) properties. A CRLH-TL consists of a conventional transmission line (TL), or a right-handed (RH) TL, and its dual consisting of series capacitors (C_L) and shunt inductor (L_L), termed a left-handed (LH) TL as shown in Figure 8-11. CRLH structures may be realized in many different forms such as in Microstrip TL, SIW, and CPW [39]. These types of TLs can be designed to provide a nonlinear phase response with respect to frequency [136]. With proper coupling and termination (either open or short), CRLH resonators can be designed.



(a) Microwave realization of metamaterial (MTM): Lossles Transmission line (CRLH unit-cell)



(b) Equivalent circuit model of lossy ($R>0$) CRLH unit-cell

Figure 8-11: A typical equivalent circuit model of CRLH unit-cell: (a) Lossles ($R=0$) transmission line represenation of CRLH unit cell, and (b) Lossy circuit model of CRLH unit-cell [39]

Comparison between the dispersion relations of the conventional resonators and the CRLH resonator under unbalanced condition is illustrated in Figure 8-12. Note that the spurious (higher order) resonances are not at the harmonic frequencies and the mode spacing may be manipulated. Balanced condition may also be achieved by overlapping the shunt and series resonant frequencies, thereby creating smooth transition from LH to RH regions.

CRLH resonator exhibits a unique resonance $m = 0$, at the frequencies:

$$\omega_{res}^{open} = \omega_{sh} = \frac{1}{\sqrt{L_L C_R}} \quad (8.81)$$

$$\omega_{res}^{short} = \omega_{se} = \frac{1}{\sqrt{L_R C_L}} \quad (8.82)$$

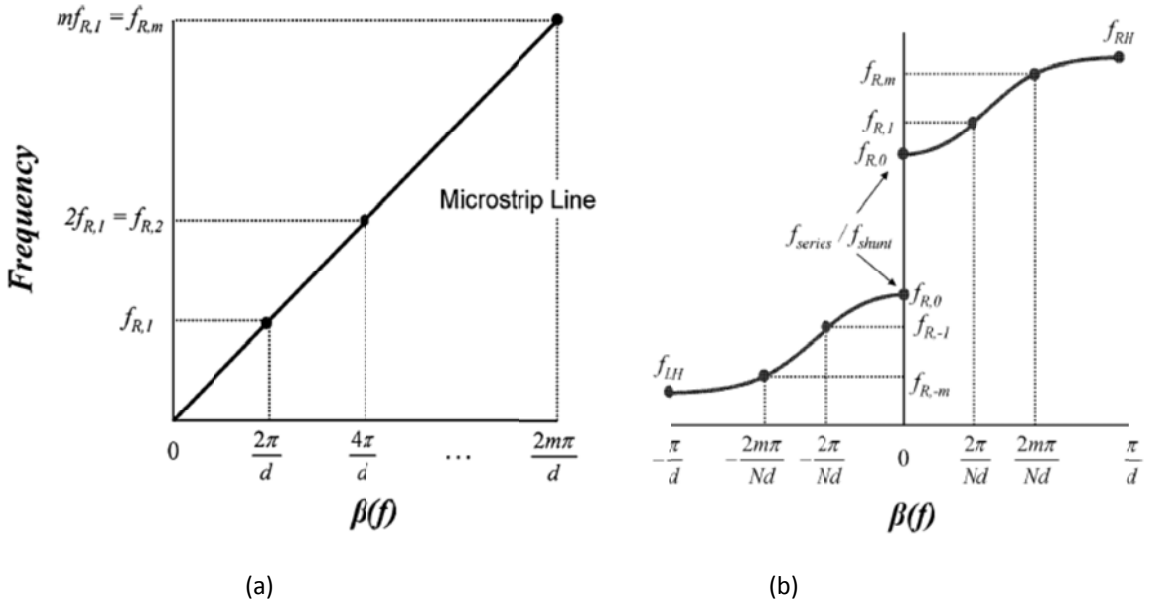


Figure 8-12: Dispersion diagram of a (a) conventional microstrip line and (b) CRLH Transmission Line [39]

The unloaded quality factor Q_o is independent of the physical length of the structure and only depends on one of two present losses, either G or R ,

$$Q_o^{open} = \frac{1}{G} \sqrt{\frac{C_R}{L_L}} \quad (8.83)$$

$$Q_o^{short} = R \sqrt{\frac{C_L}{L_R}} \quad (8.84)$$

For instance, short-circuited format is preferred in order to avoid conductor loss of the shunt inductance L_L . In addition, unlike the conventional resonator, spurious resonances can be engineered to arbitrary frequency away from harmonic frequencies and Q -factor can be improved as compared to the conventional resonators [40].

When aforementioned zeroth order resonators (ZOR) operate under balanced condition, the mode spacing and Q -factor become dependent. The phase slope of the resonant structure can

be manipulated to either increased mode spacing/decreased Q -factor or decreased mode spacing/increased Q -factor. However, under unbalanced condition, the mode spacing and Q -factor become independent and it has been demonstrated where first-order mode can be considerably increased (from $f_{\text{mode}1}/f_{\text{mode}0} = 3.5$ to 5.33), without sacrificing the Q -factor [41]. A high- Q resonator based on unbalanced CRLH resonator was built using lumped components with the first-order resonance occurring at around 5 times $f_{\text{mode}0}$. However, the performance was degraded due to undesired leakage when the resonator is built using distributed technology. To prevent the radiation, proper shielding may be added or lower modes such as $n = -1, -2$, etc. may be used to prevent leakage radiation. If the size is not the constraining factor, higher order modes such as $n = +1, +2$, etc. can be explored.

Figure 8-13 shows the typical CRLH SIW structure, which is a good candidate for oscillator resonators because of high- Q factor. In addition, CRLH substrate integrated waveguide (SIW) structure can support 0th order and negative order resonance and thereby miniaturize the circuit [43].

As shown in Figure 8-14, the one unit-cell CRLH SIW structure and miniaturized CRLH SIW antennas based on negative order resonance. The radiation through the interdigital capacitor creates radiation loss and it is difficult to use this as a guided-wave application, such as a cavity. Shielded CRLH SIW can however eliminate the radiation by enclosing the top side with the metallic shield. The proposed structure has small size when operated in the left-handed frequency region and high quality factor due to the waveguide nature.

Figure 8-14 shows the proposed shielded CRLH SIW unit-cell and the dispersion relation of the structure. Even with the shield, this structure shows CRLH characteristic.

Figure 8-15 shows possible candidates of shielded CRLH SIW resonators. It is noted that the resonators are directly excited by a strip line type feeding structure. However, we could use Microstrip line input using the transition of Microstrip line to strip line.

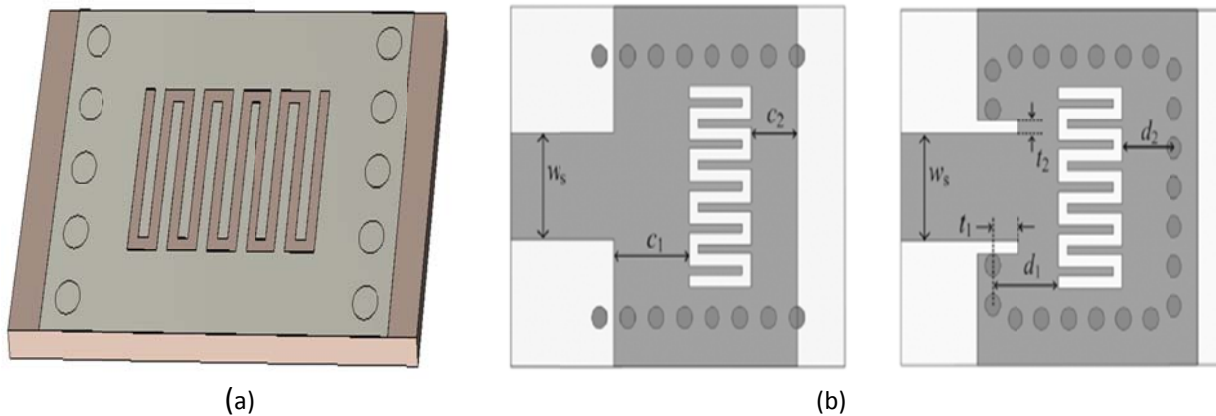


Figure 8-13 (a) The configuration of the CRLH SIW unit-cell and (b) Its applications to resonator antennas [43]

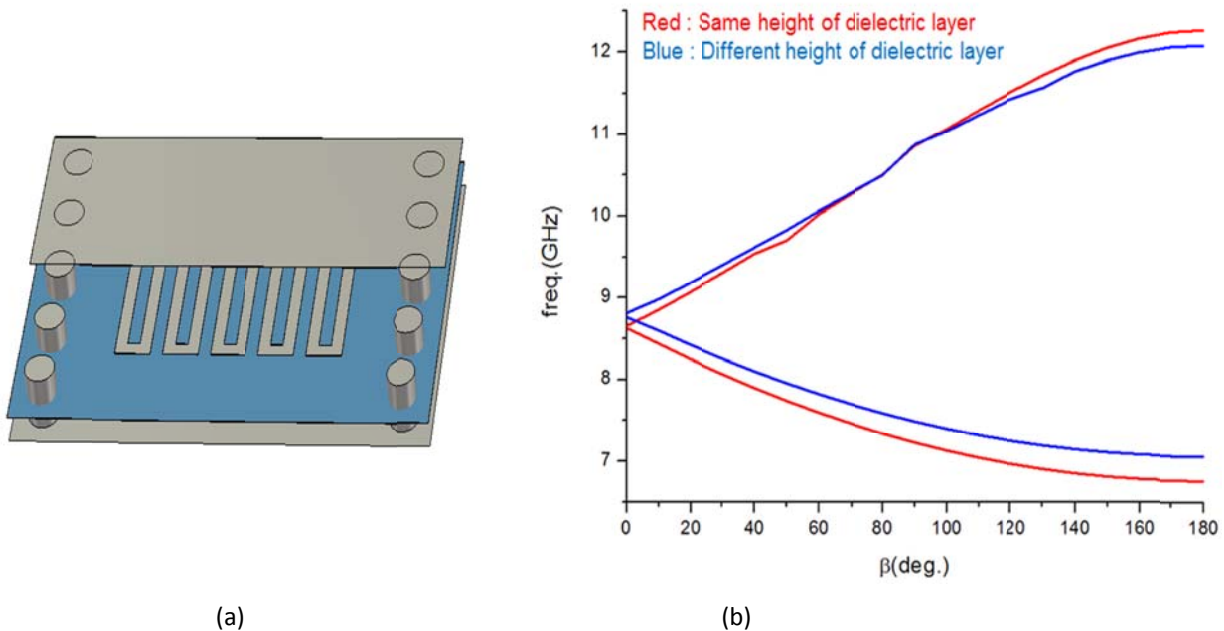


Figure 8-14: (a) The structure and (b) The dispersion relation of the shielded CRLH SIW unit-cell [a preliminary work carried out at UCLA as a joint collaboration research work with Synergy Microwave Corp.]

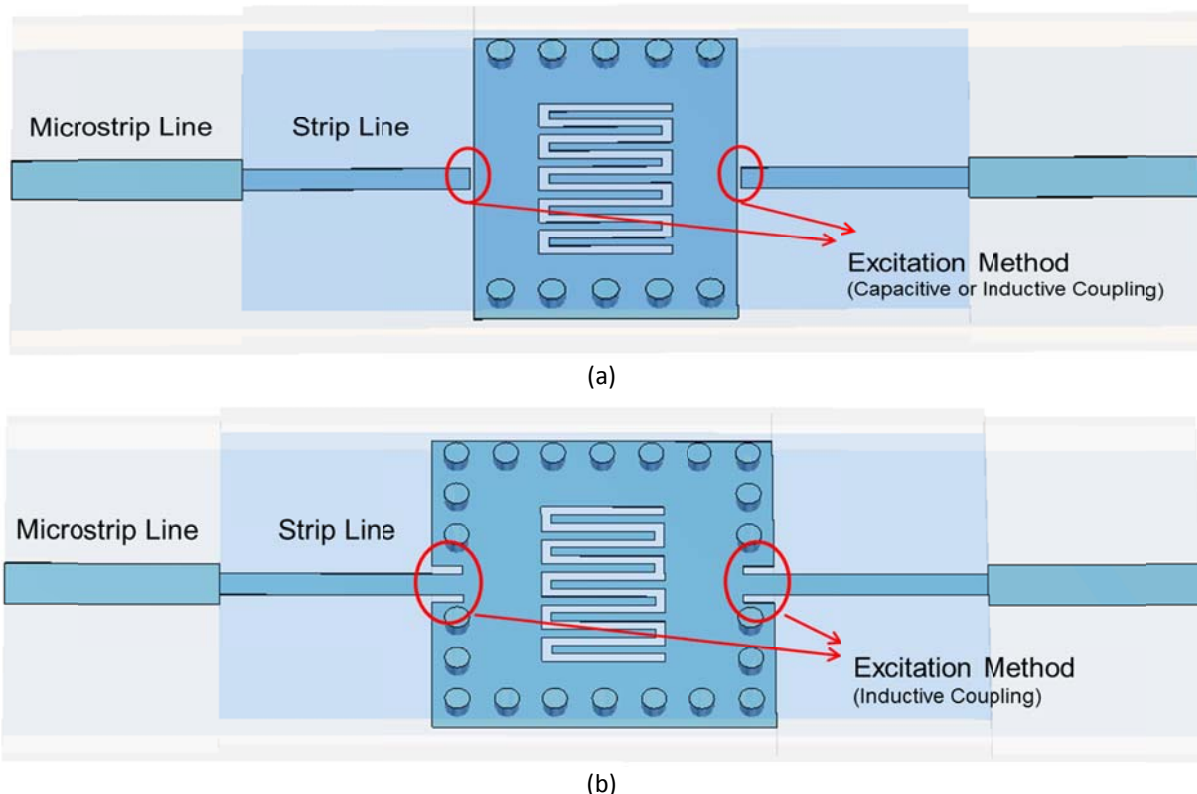


Figure 8-15: Possible resonator structures using the shielded CRLH SIW (a) Open ended and (b) Short ended [a preliminary work carried out at UCLA as a joint collaboration research work with Synergy Microwave Corp.]

Figure 8-16 shows the typical layout of the CRLH CPW resonator for low phase noise oscillator applications. CRLH based ZOR using CPW technology may provide high- Q with spurious resonances far away from the harmonic resonances since this resonator dimension is not proportional to the resonant frequency as the conventional Microstrip resonator. Also, when operated in 0th-order mode, it can also be miniaturized. CRLH based ZOR in CPW technology has been used for miniaturized band pass filter application [44].

Similar concept may be applied in designing resonator for oscillator application. However, as previously mentioned, one major problem with the structure may be the undesired radiation leakage [41]. This may be alleviated by enclosing the structure inside the waveguide shield or using MIM capacitor rather than edge coupled capacitors.

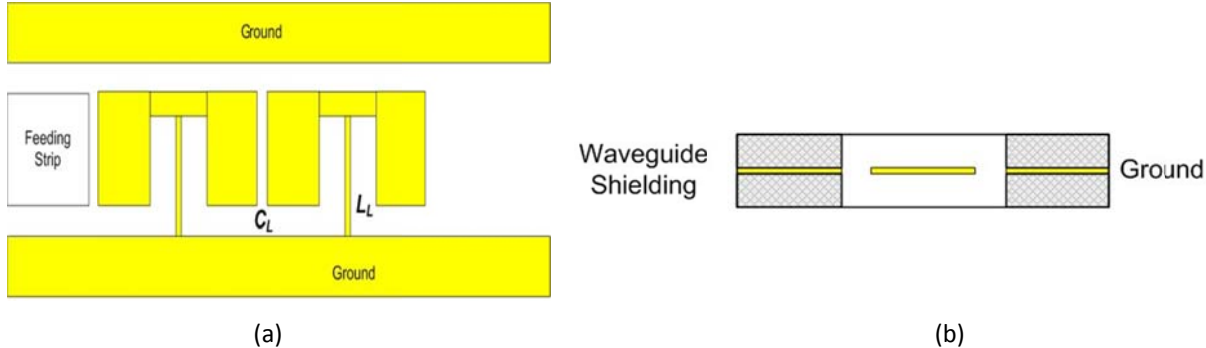


Figure 8-16: Possible resonator structure using the shielded CRLH CPW (a) Top view and (b) Side view [a preliminary work carried out at UCLA as a joint collaboration research work with Synergy Microwave Corp. as a part of this research work]

8.6 CSRR (Complementary Split Ring Resonator) for Oscillator Circuit Applications

Figure 8-17 shows the typical circular Split-ring resonator (SRR) that is one kind of Metamaterial provided effective positive permittivity (ϵ) and negative permeability (μ). As shown in Figure 8-17 (a), SRRs can induce resonating currents in the loop and thus generate equivalent magnetic dipole moments. On the other hand, complementary split-ring resonators (CSRRs), a duality form of SRRs shown in Figure 8-17 (b), behaves as electric dipoles that need an axial electric excitation and are able to exhibit negative permittivity [42].

Typically, waveguide structures are often utilized when it comes to the need of high Q -factor and high power handling capability. When these waveguide structures are loaded with MTMs such as SRRs or CSRRs, they can operate below their original cut-off frequency and thus achieve size reduction. However, main disadvantages in using conventional waveguides are high cost and the difficulty in fabrication. In addition, it is also not easy to load MTMs to the conventional waveguides. Substrate integrated waveguides synthesized in planar form by two rows of metallic via embedded in a dielectric substrate have served as a good candidate in realizing low cost and highly integrated waveguide components, since SIWs can be easily fabricated using printed circuit board (PCB) technology.

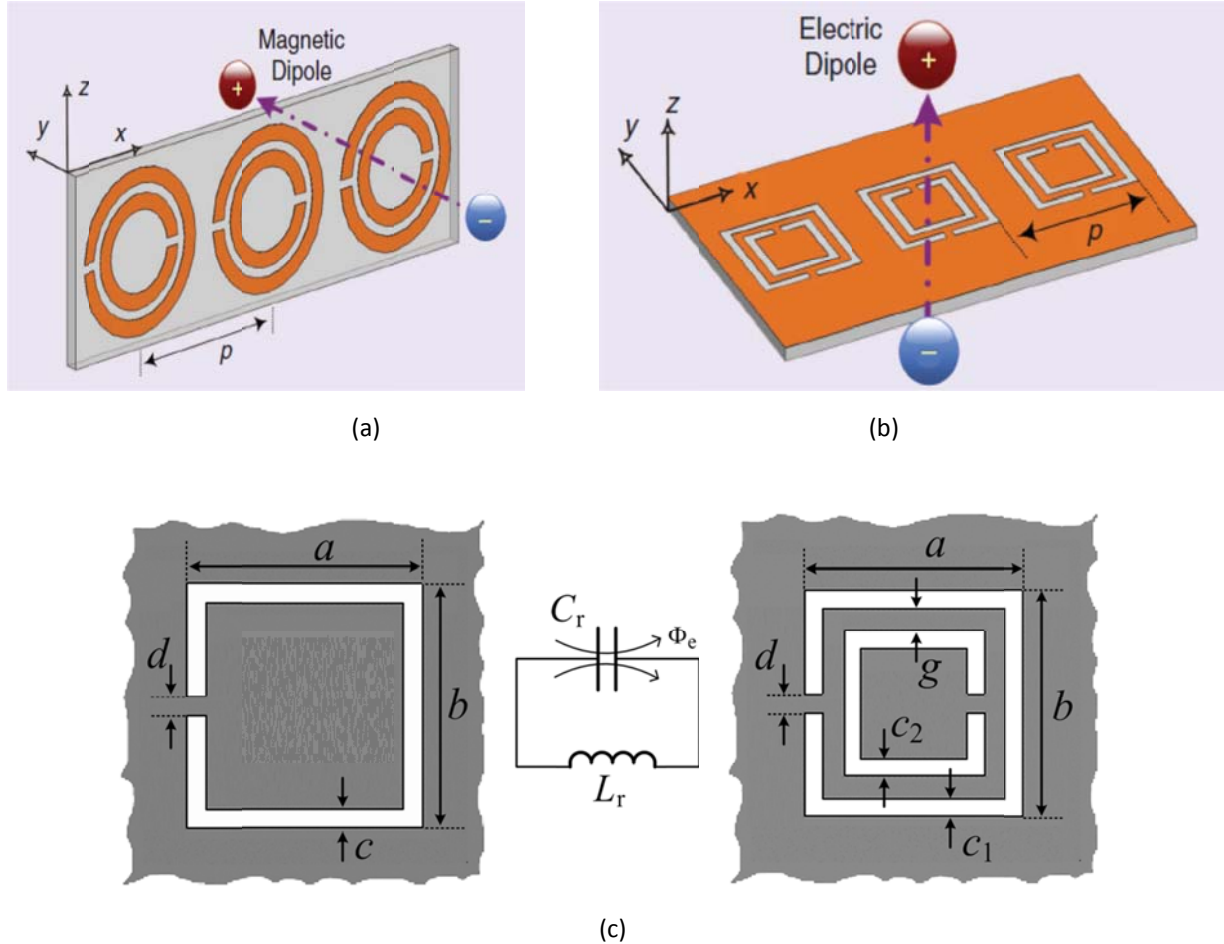


Figure 8-17: (a) SRRs, as equivalent magnetic dipoles (b) CSRRs, as equivalent electric dipoles, and (c) equivalent LC model of CSRR [42]

Moreover, it is very convenient and efficient to create CSRRs on the surface of SIWs, which makes the structures more appealing and competitive (Figure 8-18). Figure 8-19 shows the reconfigurable dual-band oscillator at 2.675 GHz and 3.77 GHz using printed planar CSRR embedded in an SIW cavity [45].

As shown in Figure 8-19, dual band oscillator contains a diode to provide the switching capability of the oscillator. When the diode is on, it behaves as a double ring CSRR that resonates as the lower frequency (2.675 GHz), whereas if the diode is turned off, it becomes a partially single-ring CSRR that resonates at the higher frequency (3.77 GHz). Because the SIW cavity loaded with CSRR can provide high-Q and low loss, the realized oscillator had a low phase noise (~ -120 dBc/Hz @ 1MHz offset). This structure is promising to operate at even higher frequency (> 15 GHz) since the dimension of the SIW can be easily scaled down. With loaded CSRR on the SIW cavity surface, it can create a very narrow band resonance below the waveguide cutoff frequency, and hence an electrically small and high-Q resonator can be realized. Installation of a shielding may be necessary.

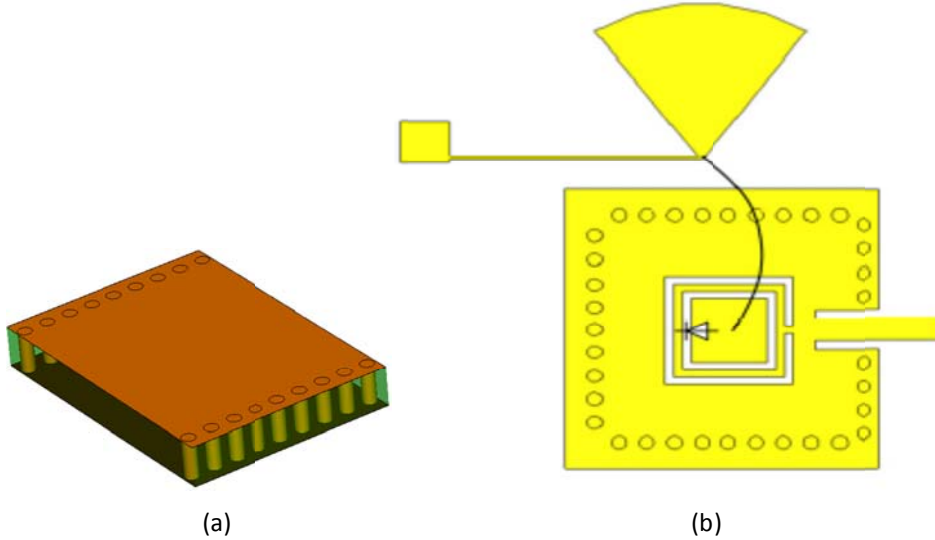


Figure 8-18: (a) a typical SIW cavity, (b) a typical layout of the SIW cavity loaded with CSRR and diode [45]

8.7 Slow Wave Metamaterial Resonator (SWMR)

Conventional Microstrip coupled lines even and odd modes exhibit different phase velocities due to the inhomogeneous dielectric medium [120]-[124]. Signals on a coupled line are the superposition of an even and odd mode and discrepancy between phase velocities of the two modes is undesirable for high quality resonator for low phase noise oscillator applications [121]. Slow wave has been demonstrated in many systems by using very different methods, such as the electromagnetic induced transparency [18] and the coupled resonator structures [19]-[20].

Slow waves on printed cascaded split ring resonators or lattices of resonant elements exhibit interesting characteristics in terms of phase velocity, group velocity, energy velocity, radiation and attenuation characteristics, quality factor, and left-handed material features (negative permittivity and negative permeability) near the resonance condition [104]. Figure 8-20 shows the typical representation of slow wave dynamics in series coupled split ring and nanoparticle resonators that exhibit left-handed and evanescent mode propagation characteristics [37].

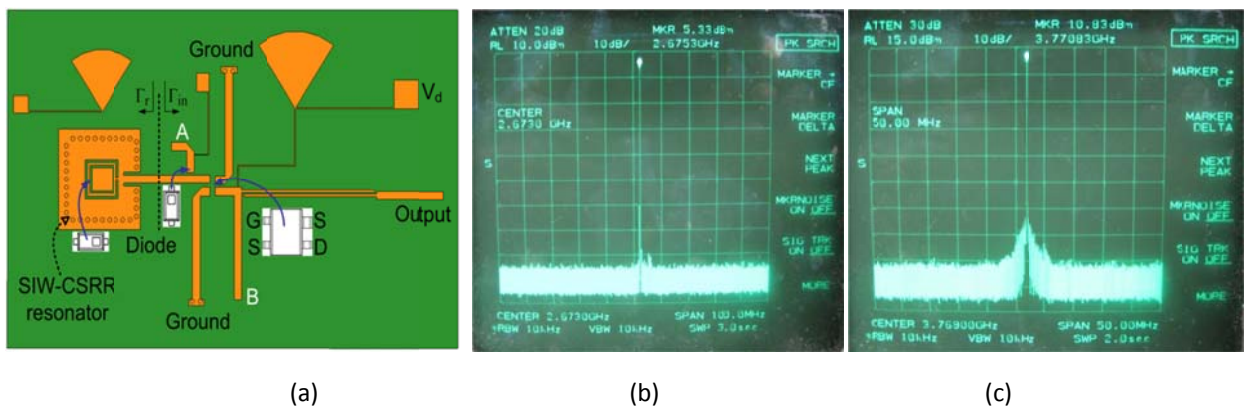
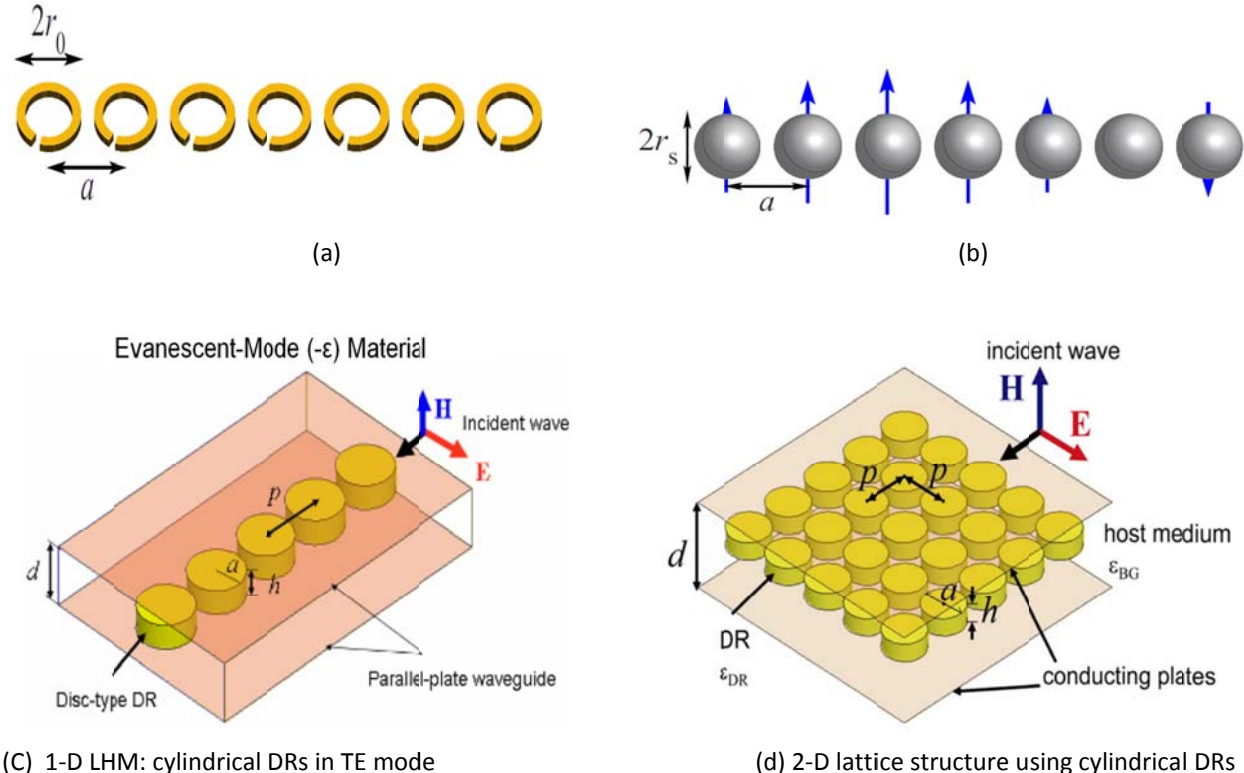


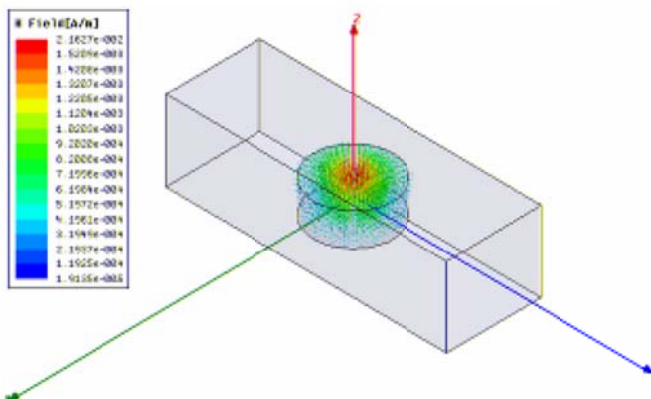
Figure 8-19: (a) A typical layout of Dual-band Oscillator with Complementary Split-Ring Resonator, (b) oscillator output at 2.675 GHz (FOM=171.8), and (c) oscillator output at 3.77 GHz (FOM=169.1) [45].

There is significant interest in slow wave metamaterial resonator (SWMR) for the design of

low phase noise microwave signal sources. Slow-wave Metamaterial coupled line structure improves the group delay and equalization of the phase velocity.



H-field Profile (TE_{010} mode, $-\mu$)



(e) 3-Dimensional negative permeability material

Figure 8-20: A typical representation of slow wave dynamics in (a) series coupled split ring, (b) nanoparticle resonators that exhibit left-handed and evanescent mode propagation characteristics, (c) 2-D LHM: cylindrical DRs in TE mode cutoff parallel plate waveguide ($-\epsilon$) [36], (d) 2-D lattice structure for one dielectric-resonator scheme in the cutoff Waveguide, and (e) 3-Dimensional negative permeability material [37].

The Metamaterial based high-Q resonators provide added advantages such as prevention of unintended generation of harmonic oscillation and structural dimensions that are not dictated by the resonant frequency. Metamaterial with their unique properties in conjunction with slow wave dynamics allow for the design of compact tunable oscillators, filters, phase-shifters and microwave sensors, which otherwise is difficult to achieve using conventional design approaches.

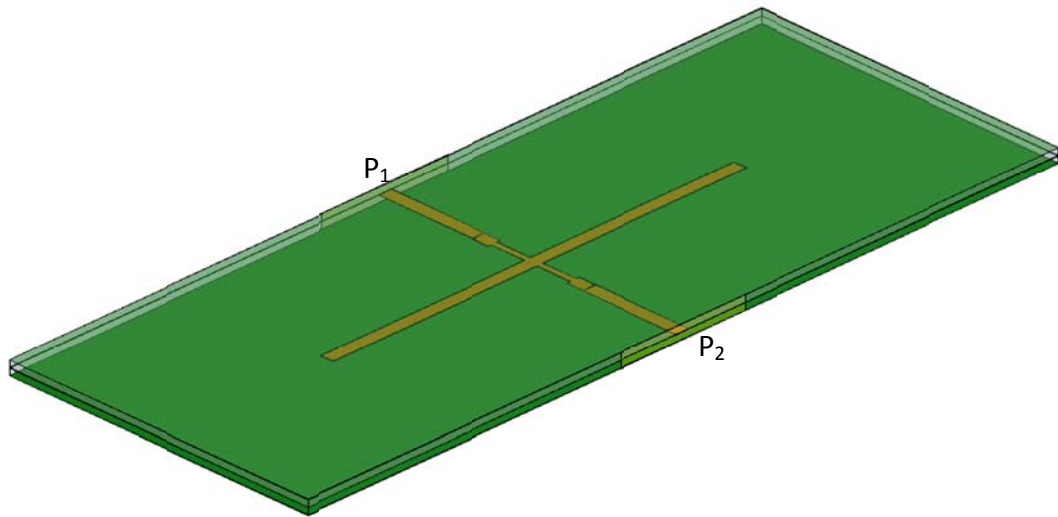
To design integrated oscillator circuits, printed coupled split ring resonator structures enable readily the integration of active devices as an integral part of the resonator. Microstrip based designs are compatible with wafer-level integration and lead to the integration of active device elements as an integral part of the coupled split ring resonators.

Recently, metamaterial coupled-line circuits had been attempted by placing two lines next to each other [32]-[34] with capacitor loadings to enhance coupling. The coupling is capacitive and mostly through the fringing electric fields. The edge coupling between two (coplanar) metamaterial lines is usually weak, particularly on PCB with minimum required line spacing. One would need to enhance the inductive coupling significantly to equalize the phase velocity and to obtain necessary impedance for the odd and even modes.

8.8 Examples: Tunable Oscillators Using Slow Wave Metamaterial Resonator (SWMR)

It has been known that the phase noise of the oscillator depends on the Q-factor of the resonator. But the phase noise of the integrated oscillators is limited by the low Q-factor of the on chip inductors in the conventional LC based resonator tank. In general, Q-factor of the on-chip inductor ranges from 10-20 at X and Ka band. The transmission line slow wave resonators having the metamaterial property exhibit improved Q-factor, enabling lower phase noise characteristics. The main advantages of these structures are high Q-factor, easy fabrication, low radiation loss and sharp selectivity. As a possible candidate, high-Q, non-radiating composite right/left-handed (CRLH) stripline resonator is discussed. CRLH resonators based on Microstrip and co-planar waveguide have previously been researched [40, 41, and 143]. This type of CRLH based resonator provided relatively compact size; however, only moderate Q-factors could be achieved due to undesired leaky-wave radiation loss.

In order to suppress the undesired radiation loss and further increase the Q-factor, CRLH based stripline resonator is preferred. Stripline configuration inherently has good radiation suppression; therefore, loss from radiation may be suppressed. A possible CRLH based resonator is shown in Figure 8-21 (a). The total length is less than $\lambda_g/4$. Therefore, the overall length can be miniaturized in comparison to the conventional $\lambda_g/2$ stripline resonator. To facilitate the fabrication process and avoid the use of vias, we are currently using open stubs. If uses of vias are permitted, the overall dimension can be reduced further by adding vias to the stubs, thereby reducing the stub lengths. The simulated S21 is shown in Figure 8-21 (b). The substrate material used for the realization is RT/Duroid 5880 with $\epsilon_r = 2.2$ and $\tan\delta = 0.0009$. The thicknesses for both substrate and Superstrate are 20 mils. Calculated unloaded-Q is around 300. Therefore, using CRLH based stripline resonator, higher Q-factor can be obtained in a relatively compact form. The Q-factor may be further improved after optimizations. We will also investigate other type of miniaturized/high-Q resonators.



(a) Unit-cell layout

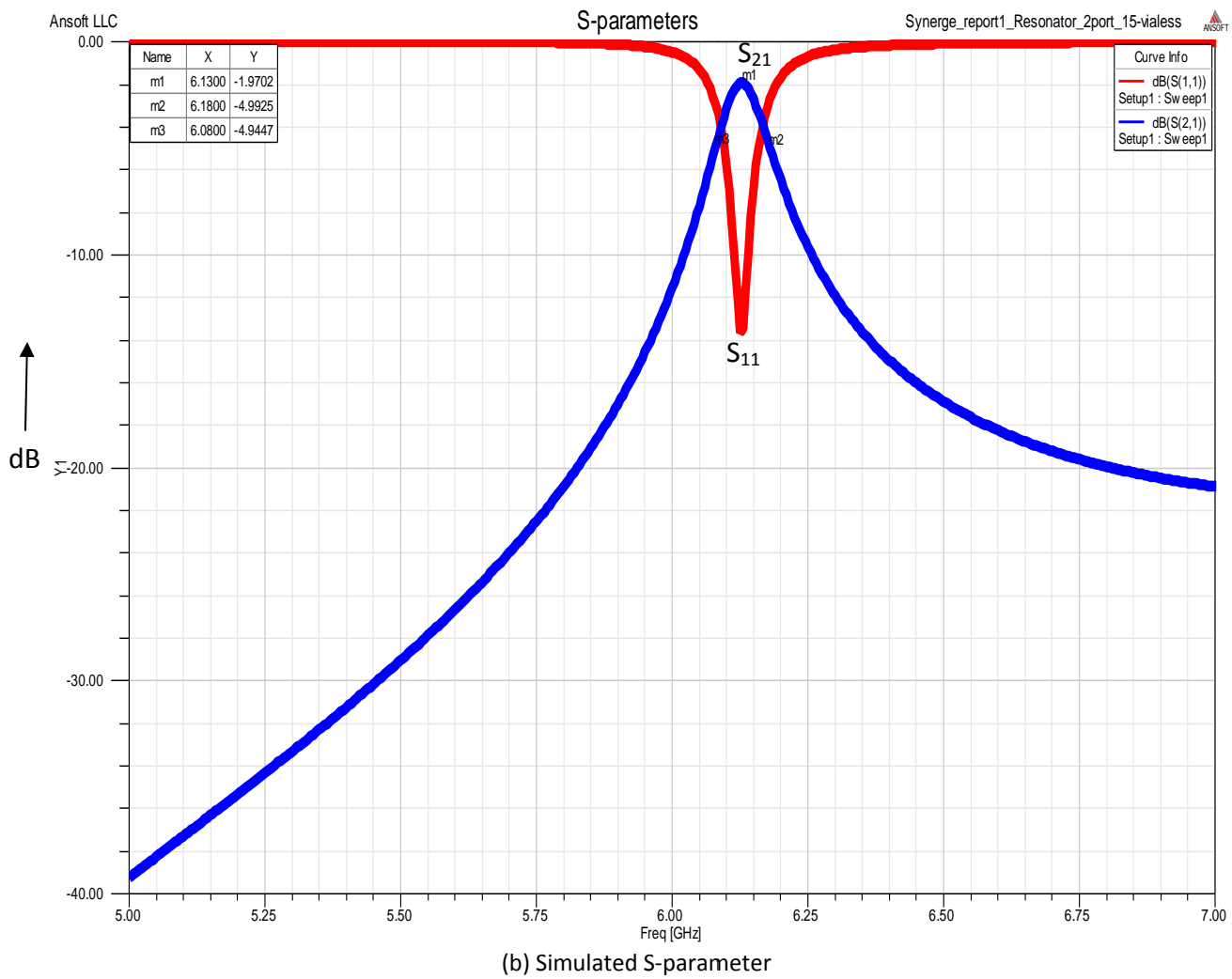
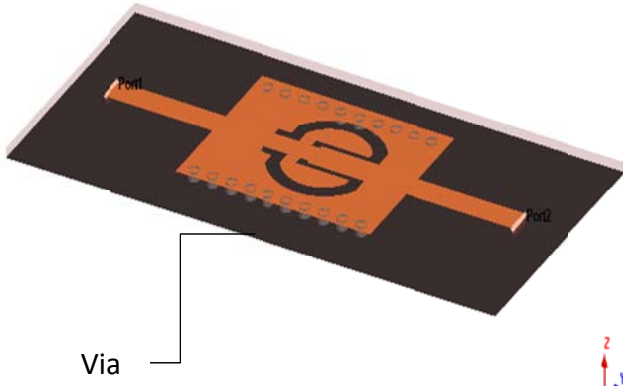
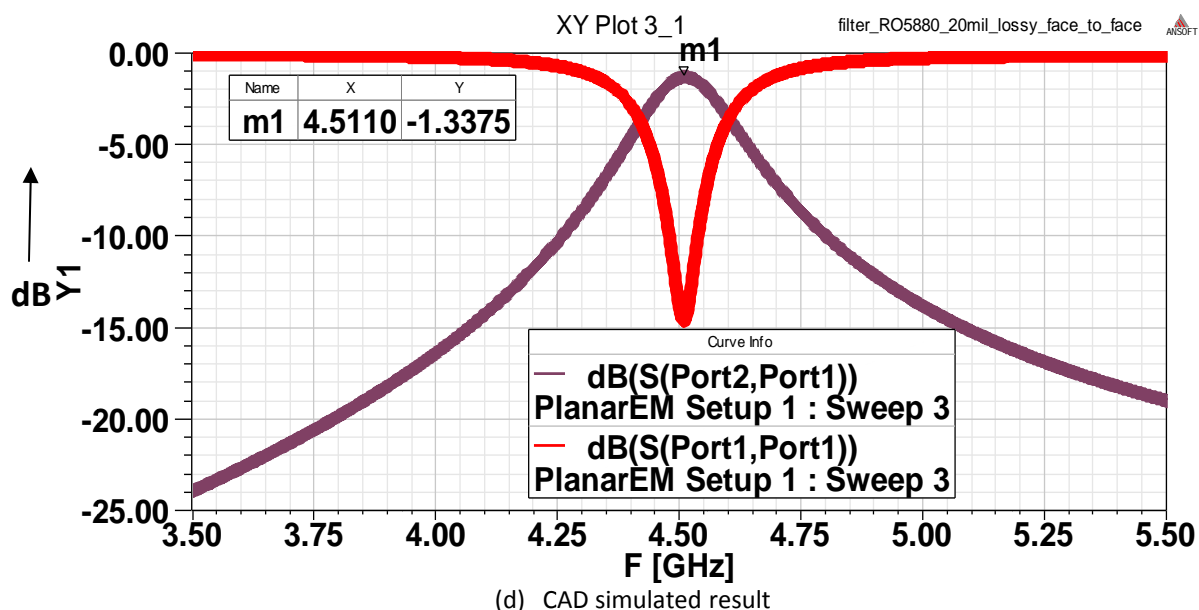


Figure 8-21: CRLH stripline resonator (a) unit-cell layout and (b) CAD simulated S-parameter results [154]

As another candidate, a substrate-integrated waveguide (SIW) loaded with complementary coupled resonator, which is originally depicted in [77, pp. 358] has been studied to form a high-Q resonator. The structure is shown in Figure 8-21 (c) and it consists of two complementary coupled resonators facing each other side-by-side in order to reduce the radiation loss. The simulated S-parameters result is plotted in Figure 8-21 (d), using the same aforementioned substrate (RT/Duroid 5880). The dimension of the resonator itself (excluding the feed lines) is around 18mm by 12mm ($\lambda_g/2$). The simulated results show that, the structure has an insertion loss of 1.34dB at 4.51GHz. The unloaded-Q has also been calculated to be around 180. It is worth mentioning that this SIW loaded with complementary coupled resonator is analogous to the one loaded with complimentary split ring resonators (CSRRs). It can also create a pass band below the original SIW cutoff frequency and hence the size reduction can be achieved.



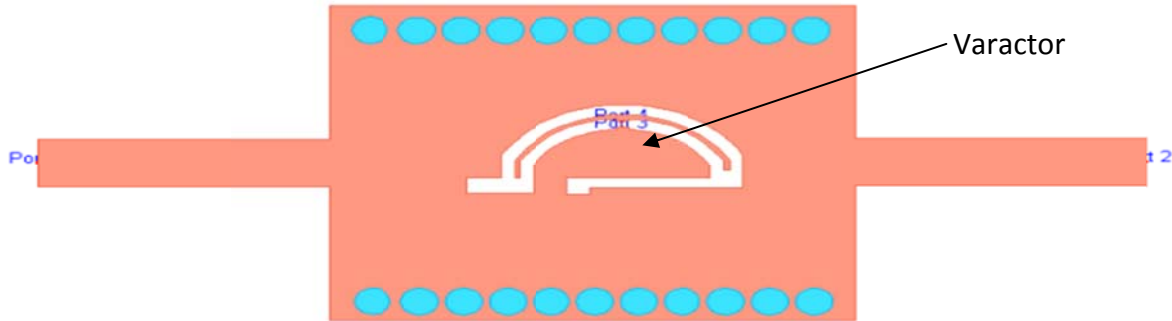
(c) CAD model of SIW loaded with CCR



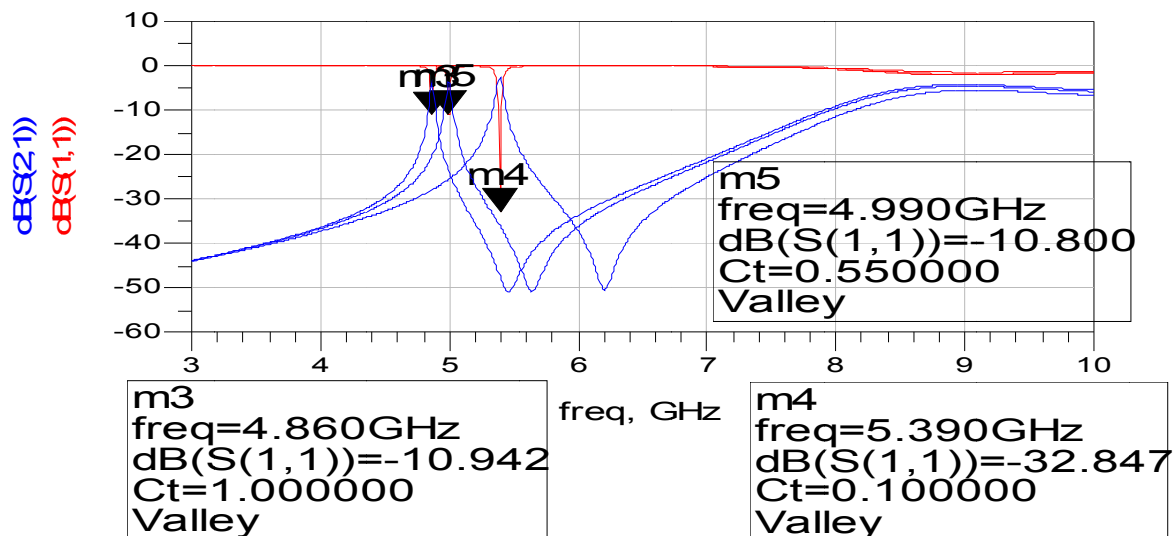
(d) CAD simulated result

Figure 8-21: SIW loaded with complementary coupled resonator: (c) side view, (d) simulated s-parameters (a preliminary work carried out at UCLA as a joint collaboration research work with Synergy) [154]

Furthermore, the tunability of such structure has also been investigated. By inserting a varactor inside the slot of the complementary coupled resonator as shown in Figure 8-21 (e), resonance frequency can be varied; results are plotted in Figure 8-21 (f), with the varactor value changing from 1pF to 0.1pF. As a result, the center frequency of the pass band can be changed from 4.86GHz to 5.39GHz, which is roughly 10% of relative bandwidth.



(e) Top view (a preliminary work carried out at UCLA as a joint collaboration research work with Synergy) [154]



(f) Simulated S-parameter data

Figure 8-21: Complementary coupled resonator equipped with a varactor (e) top view and (f) simulated S-parameter results

8.8.1 Tunable 2-4 GHz oscillator using SWMR

The novel approach is to improve the group-delay and reduce the effective dimension of the resonator by incorporating multiple concentric split-ring resonators without increasing the area occupied by the resonator [149]. They are very attractive to use in the wireless communication systems [46]-[49]. Figure 8-22 (a) shows the typical block diagram of 2-4 GHz VCO using metamaterial slow wave resonator. Figure 8-22 (b) exhibits the phase noise plot of oscillator as shown in Figure 8-22 (a).

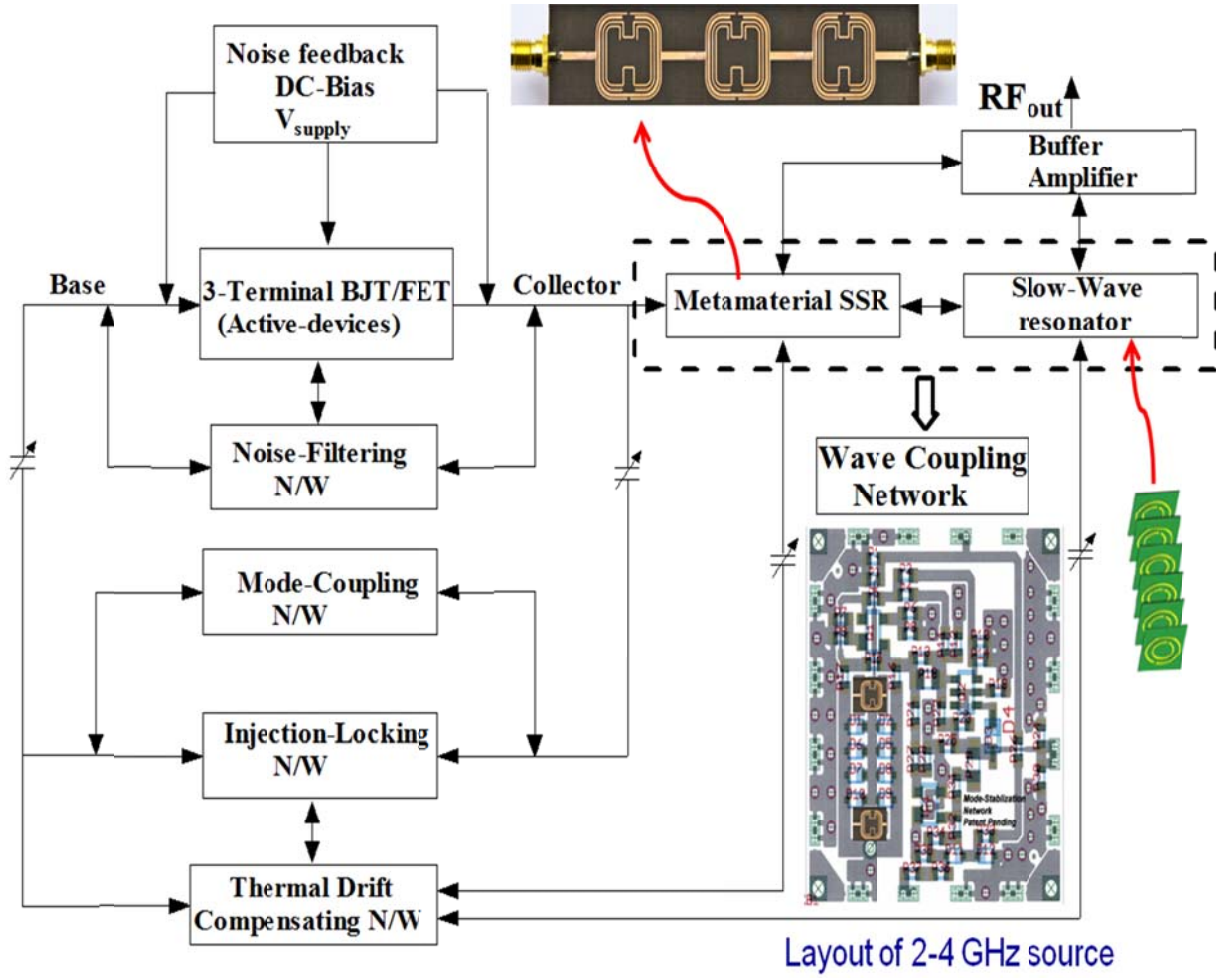


Figure: 8-22 (a): A typical block diagram of Metamaterial slow-wave resonator (SWMR) oscillator, layout of oscillator circuit is realized using 20 mils RT/Duroid 5880 with $\epsilon_r = 2.2$.

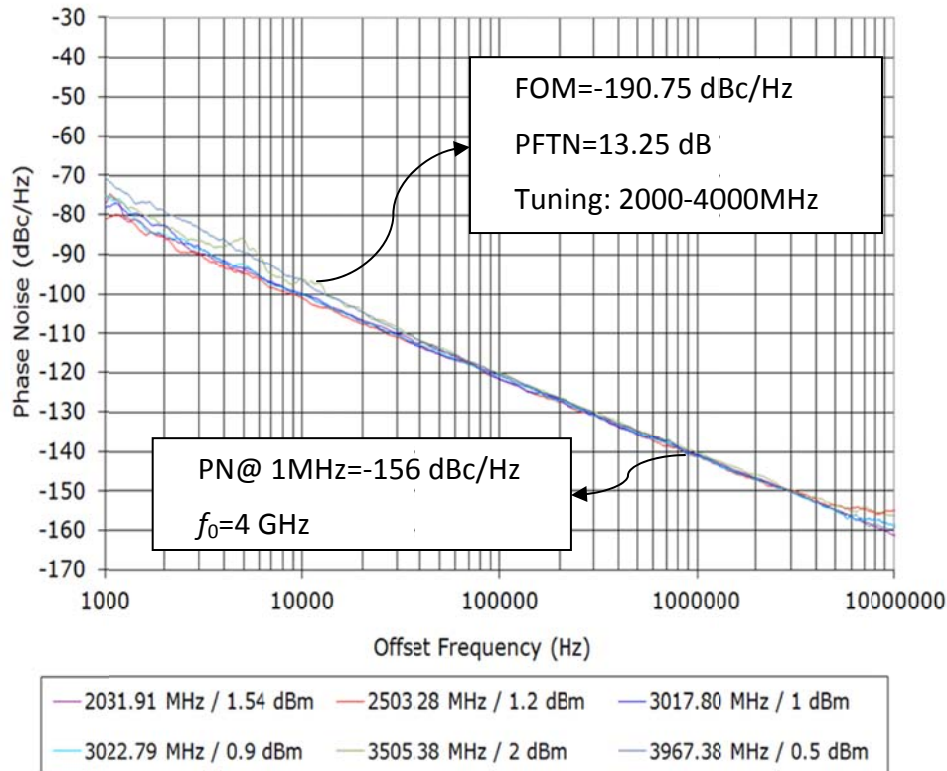
8.8.2 Multi-band Oscillators using Printed Slow Wave Metamaterial Resonator

Efforts to miniaturize wireless communications hardware have led to compact radio designs with tunable oscillators, such as VCOs, to cover a number of different frequency bands. However, tunable oscillators typically exhibit tradeoffs between phase-noise performance and power consumption [106]-[119].

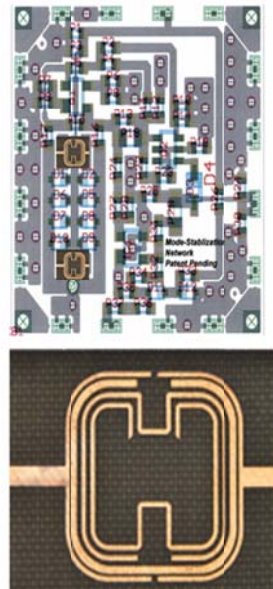
Attempts to develop multiband VCOs with low phase noise often yield large, power-hungry circuits. Numerous techniques take aim at compact source solutions for multiple-band radio designs, including switching among separate VCOs, using intermodal multiple-frequency circuits, or switching among multiple resonators [130]. However, they are inevitably large, or power hungry, or with poor phase noise. For example, switched resonators suffer from the resistive and capacitive parasitic circuit elements associated with the switches. Mode switching has been used to select among multiple oscillation modes of resonant circuits, in ways that the losses and nonlinearities of the switches do not affect the steady state and phase-noise performance of the resonators. However, this approach does not involve concurrent generation

of signals, and is limited in terms of achieving reduced source size, power consumption, and design cycle time.

Measured Phase Noise Plot of 2- 4 GHz source



Layout of 2-4 GHz source



Resonator

Figure 8-22 (b): Measured Phase Noise Plot of 2-4 GHz Metamaterial slow-wave resonator (SWMR) oscillator, measured figure of merit (FOM: defined in Ch-1, Eq. 1.1) is -190.75 dBc/Hz for a given power-frequency tuning normalized (PFTN: defined in Ch-1, Eq 1.2) 20.26 dB, with power consumption of 120mW ($V_{cc}=5V$, $I_c=24mA$), o/p power is typically better than +3dBm.

Traditional band-select sources have incorporated multiple resonators, VCOs, or other tunable oscillators, but any band-selection switch inevitably degrades the performance of this type of multiband source. This new class of oscillator using Metamaterial slow-wave resonator network as shown in Figure 8-23 (a) synchronously generates the signals needed for multiple-band, multimode communications. They provide the performance of separate tunable oscillators with significantly reduced size and power consumption compared to separate oscillators, for use in multiple-band, multimode wireless communications systems.

The VCO circuit showed in Figure 8-23 (a) works without multipliers or switching among resonators and/or oscillators. This is why they reduce the complexity, size, and power consumption compared to other multiple-signal-generation methods along with good phase-noise performance [148]. The CAD simulated phase noise plots (Figure 8-23 (b)) of the prototype source (Figure 8-23 (a)) is typically better than -130dBc/Hz @ 1 MHz from either

carrier range. The measured phase noise plots shown in Figure 8-23 (c) agree with the CAD simulated data within reasonable degree of accuracy (3-5 dB variation). The multiple-band VCOs requires only +5 VDC and 20 mA, and delivers +3 dBm typical output power for Band #1 (2-2.5 GHz), Band #2 (2.5-3 GHz), Band #3 (3-3.5 GHz), and Band #4 (3.5-4 GHz). For multimode, multiple-frequency-band wireless equipment, this one source (Figure 8-23 (a)) may be the match of traditionally many VCOs.

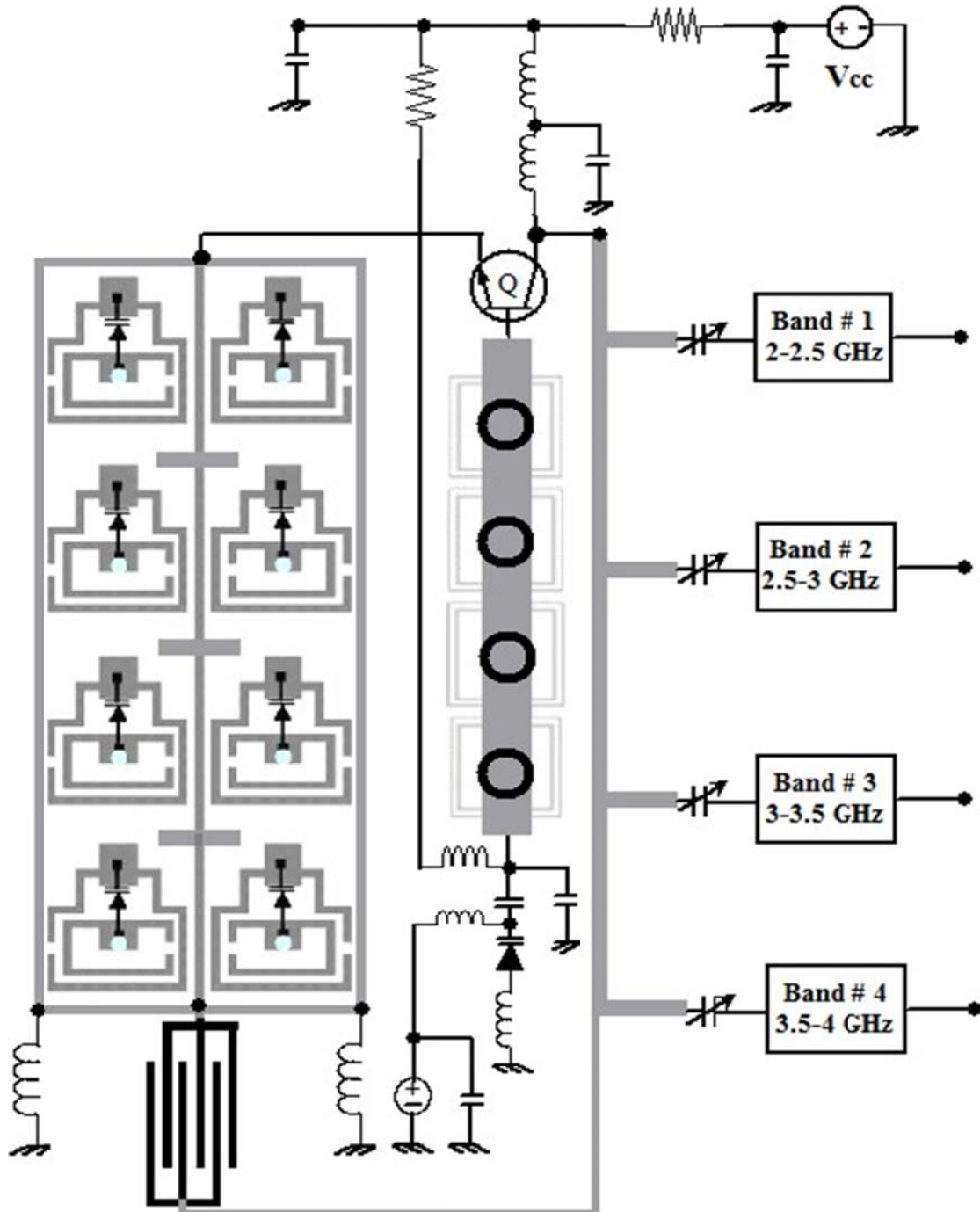


Figure: 8-23 (a): A typical layout of multi-band oscillator using evanescent mode Metamaterial resonator network realized using 20 mils RT/Duroid 5880 with $\epsilon_r = 2.2$

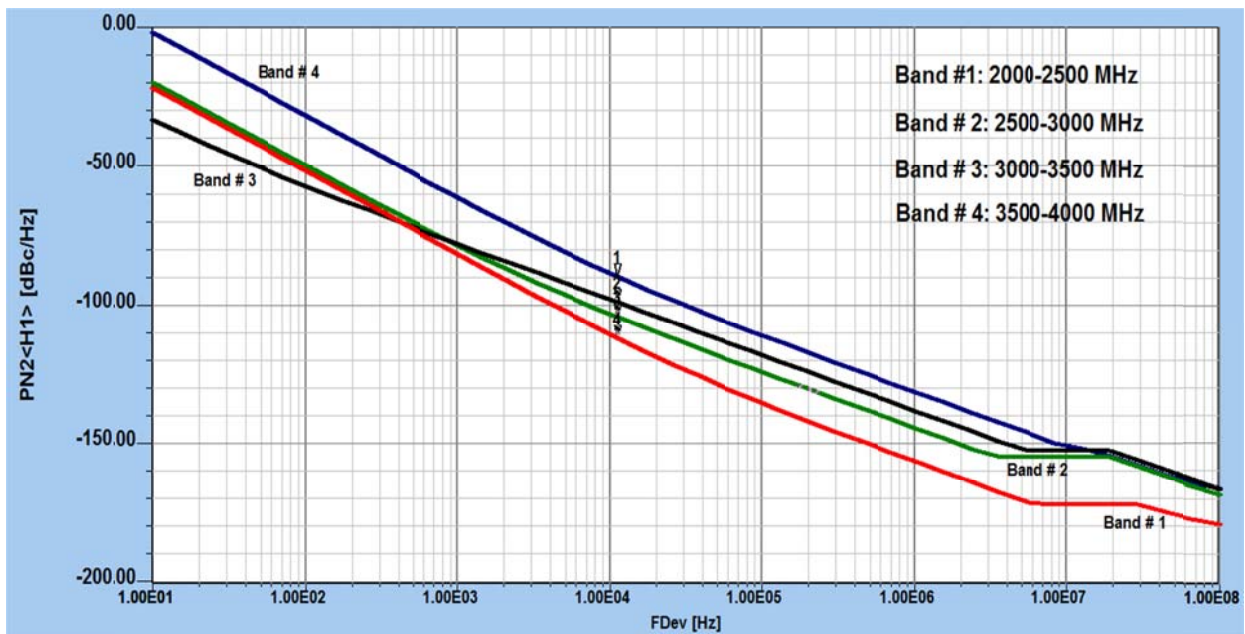


Figure 8-23 (b): CAD simulated Phase Noise Plot of multi-band Metamaterial slow-wave resonator oscillator, predicted phase noise @ 1MHz offset is -130dBc/Hz for Band #1 (2-2.5 GHz), Band #2 (2.5-3 GHz), Band # 3 (3-3.5GHz), and Band # 4 (3.5-4 GHz)

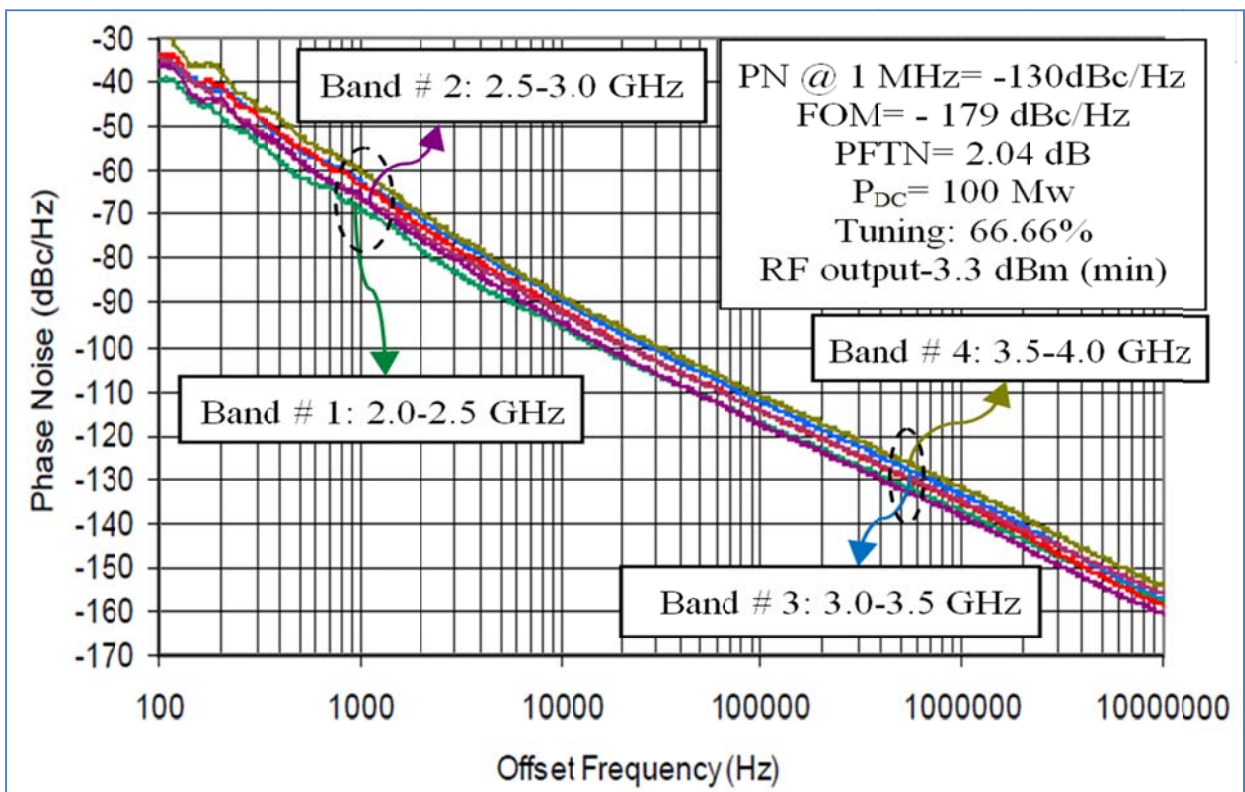


Figure 8-23 (c): Measured Phase Noise Plot of multi-band Metamaterial slow-wave resonator based oscillator circuit, measured figure of merit (FOM: defined in Ch-1, Eq. 1.1) is -179 dBc/Hz for a given power-frequency tuning normalized (PFTN: defined in Ch-1, Eq.1.2) 2.04 dB, with power consumption of 100 mW ($V_{cc}=5V$, $I_c=20mA$), o/p power is typically 3.3dBm.

From Figure 8-23, what kind of communications device can benefit from such a multiple-signal source? WLANs are among the most popular of wireless applications, in home and office environments, operating within different frequency bands, notably within the Industrial-Scientific-Medical (ISM) band from 2.40 to 2.50 GHz and various bands from 5.15 to 5.85 GHz. A WLAN radio capable of operating within both bands might work with switchable VCOs, although a more fully integrated multimode radio design would be based on a single signal source capable of covering both bands, such as an MMSRO (multi-band Metamaterial slow-wave resonator oscillator).

The basic principle of a multimode radio is to process two or more signals of differing frequencies at the same time, using only one transmit/receive signal-processing chain. Figure 8-24 shows a frequency plan for a dual-band, 2.4-GHz/5-GHz WLAN transceiver system. It is based on a single 8-GHz VCO with a divide-by-two divider in a frequency synthesizer to generate a 4-GHz signal. This is followed by divide-by-four divider to reach 1 GHz. These in-phase (I) and quadrature (Q) signals are mixed in a quadrature single-sideband (SSB) mixer to produce the 5-GHz signal which is further divided to obtain the 2.4-GHz signal. This approach requires multiple buffer, divider, and filter stages to produce signals for a dual-band WLAN radio. The multiple signals could also be generated by starting with lower-frequency signals and adding multipliers. But in cases where quadrature frequency converters are used, multiplication is rarely used for the final stage of frequency conversion, given the difficulty of working with differential outputs at higher frequencies.

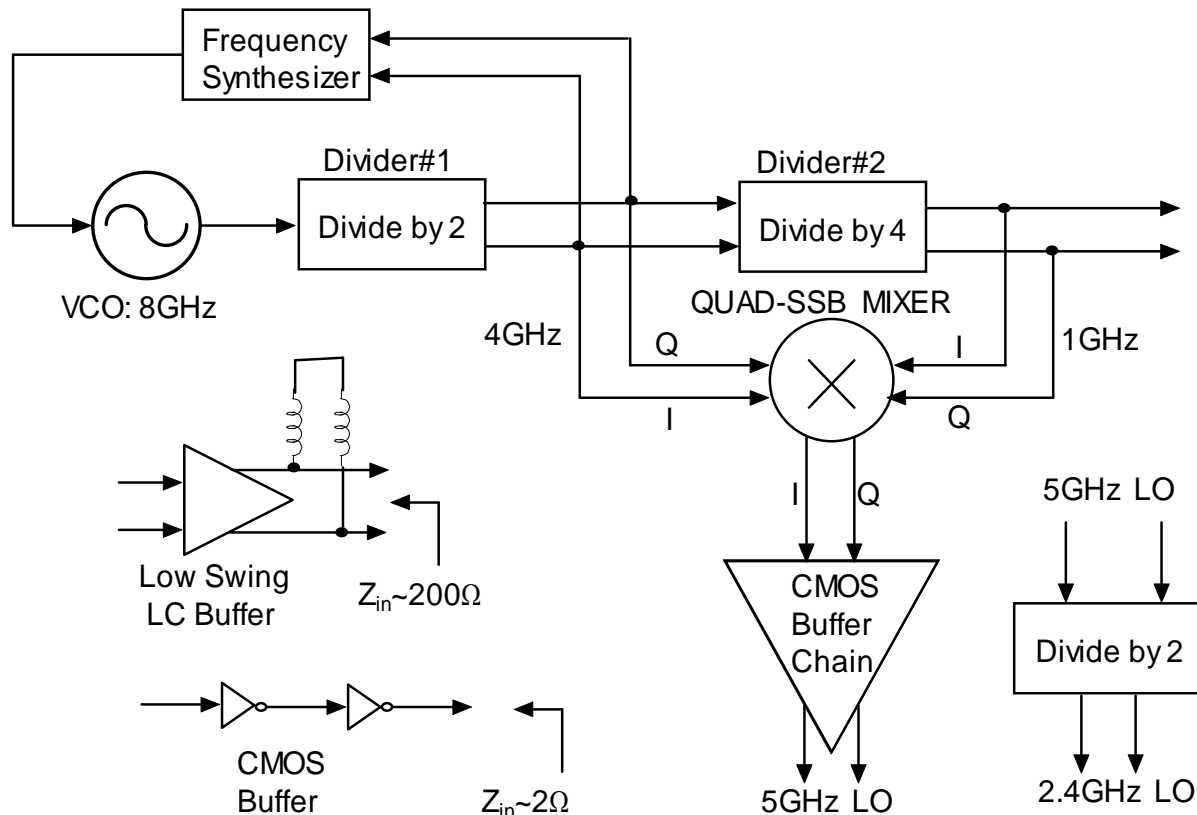


Figure 8-24: Frequency plan for a 2.4/5 GHz WLAN transceivers

Conventional single-output oscillators generate periodic waveforms, essentially a single frequency and its harmonic signal components. Tunable oscillators based on higher-order resonators can provide multiple modes of oscillation and can generate multiple, independent frequencies, individually or simultaneously [75]-[101].

A single-output tunable oscillator is a good starting place to design a multiple-band oscillator. A single-frequency tunable wideband oscillator incorporates a varactor-tuned second-order resonator network to generate a signal at a desired frequency. It employs an active device, such as a bipolar transistor, terminated in a parallel or series inductive-capacitive (LC) resonant-tuned circuit. A parallel LC resonator network exhibits a high parallel resistance (or anti-resonance) while a series LC resonator network provides a low series resistance (or resonance). Such a design will inevitably be limited by the capabilities of the transistor, the electrical contributions of its package, and the large change in capacitance needed to tune the oscillator over a broad frequency range [69]-[89].

A multimode, multiple-frequency oscillator will require more than a simple parallel LC network and an active device. An oscillator circuit that can produce two simultaneous frequencies must be capable of simultaneous negative resistance values at two distinct frequencies, and a higher-order resonator is needed for that purpose. The order of the resonator is dependent upon the number of different frequency signals/bands desired. Whereas a simple second-order resonator network produces one frequency, a fourth-order resonator network can produce two simultaneous frequencies. The trick in designing such an oscillator is learning the values of negative resistance needed to support the multiple separate frequency bands, and this information can be found by performing network analysis. Such analysis contributed to the design of the multimode, multiple-frequency oscillator is unveiled in Figure 8-23 (a). The filters employed in the multimode oscillator are meant to assist with mode leakage, such as when the oscillator circuit oscillates in dual modes. The amount of mode leakage from a given design will depend on the spectral selectivity of the succeeding filter for that portion of the circuit as well as the design requirements for the tunable oscillator.

8.8.3 MCSWMR (Mode-Coupled Slow-Wave Metamaterial Resonator) VCO

It is important to achieve low phase noise in various applications. The phase noise increases a bit error rate in telecommunication links, degrades stability of beam in particle accelerators and decreases sensitivity of radars. DROs represent an interesting solution to improve the stability by reducing the bit error rate because high quality factor of a Dielectric Resonator (DR) allows for achieving an excellent phase noise performance at microwave and millimeter wave frequencies. Dielectric resonators are ceramic materials which have high dielectric permittivity, high quality factor, and high temperature stability, have a much smaller size compared to cavity resonators; therefore, they are frequently employed in the design of frequency stable RF circuits, especially in oscillators.

When high data-rates have to be transferred, as with M-QAM modulation in LTE, LMDS, and fixed frequency point-to-point digital radio and satellite-links, these systems need low phase noise signal sources either free running or phase-locked. RADAR systems and Research Laboratories also require ultra-low noise sources to generate ultra-low noise carrier signals. A wide range of military, industrial, medical, test and measurement markets demand these very

stable frequency sources with enhanced phase noise performance and low thermal drift. A popular solution in the range of 3 to 30 GHz frequency spectrum is the dielectric resonator oscillator (DRO), recognized for its superiority in ultimate noise floor and spectrum purity when compared to other competing solutions such as multiplied lower frequency fundamental sources.

A novel mode-coupled self-injection locked VCO (voltage controlled oscillator) is developed in response to replacing expensive DRO (Dielectric Resonator Oscillator) for reference signal sources for modern communication systems. One of the problems related to the Dielectric Resonator (DR) is fabrication in integrated circuit (IC) form due to its 3-D structure. Mode-coupled slow-wave metamaterial resonator approach described in this thesis offers cost-effective and integrable alternative for DRO circuits. For example, the typical measured phase noise for 10.21 GHz carrier frequency at 10 kHz offset is -109 dBc/Hz with 300 MHz tuning in $0.75 \times 0.75 \times 0.18$ inch circuit board size. The reported topology is not limited to this frequency, and can be extended to other frequency bands (2 GHz to 24 GHz with 500 MHz or more tuning range) by dynamically controlling mode-coupling mechanism. Figures 8-25, 8-26, and 8-27 show the typical block diagram, layout, and measured phase noise plot of the 10.2 GHz VCOs using a SiGe Heterojunction-bipolar-transistor (HBT) active device that was fabricated on Rogers substrate material with a dielectric constant of 2.2 and thickness of 20mils (microstripline/stripline) for the validation of the new approach. The oscillator topology for such applications can use supply voltage between +5 to +10 V and the internal voltage regulation gives high immunity to power supply noise. The supply-current is typically 20 mA and the temperature range is specified from -40°C to $+85^{\circ}\text{C}$.

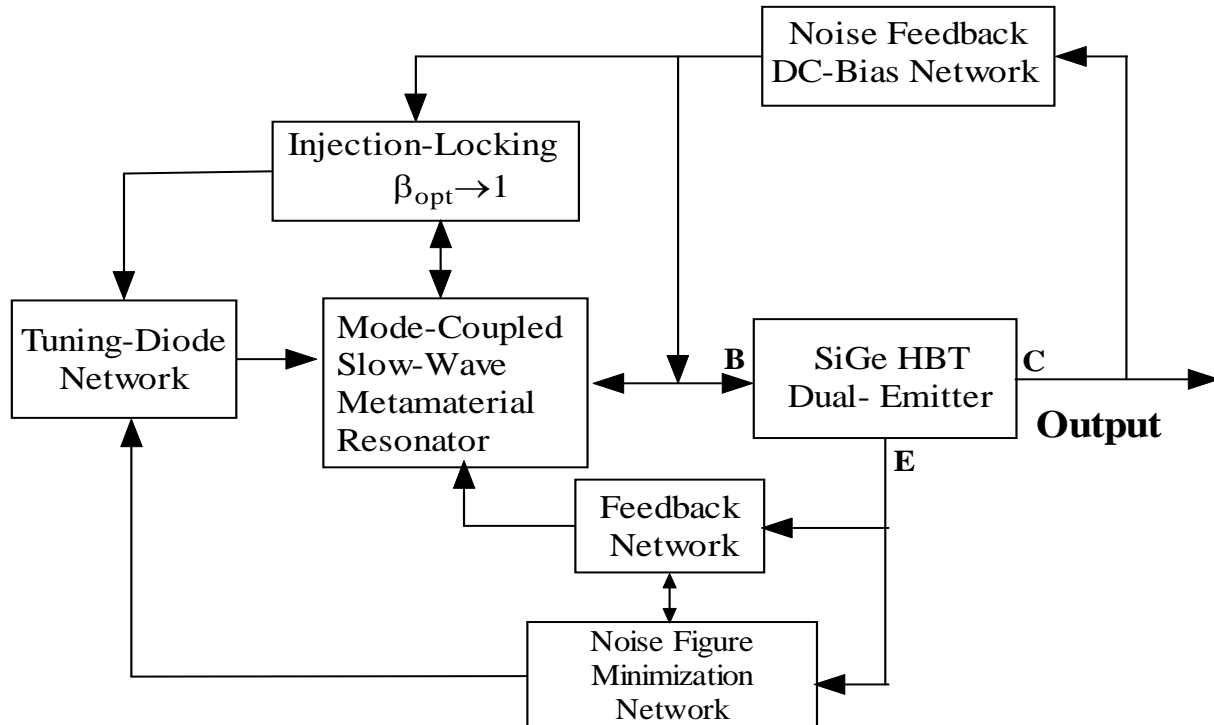


Figure: 8-25: shows block diagram of 10.2GHz MCSWMR (Mode-Coupled Slow-Wave Metamaterial Resonator) VCO

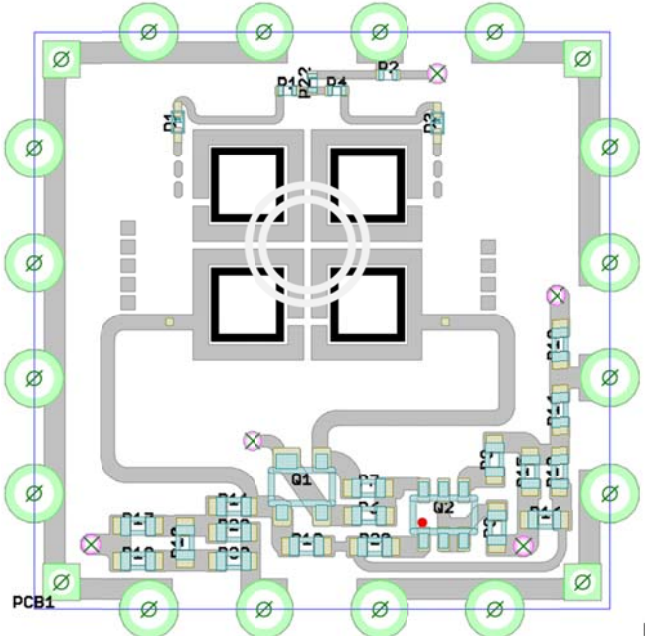


Figure: 8-26: A typical layout of 10.2GHz MCSWMR (Mode-Coupled Slow-Wave Metamaterial Resonator) VCO realized using 20 mils RT/Duroid 5880 with $\epsilon_r = 2.2$, PCB size is 0.75x0.75/0.18 inches

For this particular oscillator circuit layout (Figure 8-26) a DC bias of 10 Volt and 30 mA was provided, the measured output power exceeds +5 dBm. As shown in Figure 8-27 (a), there is hump between 40 kHz and 1 MHz; and dip at 1 MHz offset from the carrier, possibly due to the resonator's multi-mode resonance and mode-jumping phenomena. By incorporating multi-mode-injection-locking, hump can be suppressed and stable oscillation can be guaranteed. Figure 8-27 (b) shows the measured phase noise plots; illustrating the clean signal (without hump in phase noise plot). The measured figure of merit (FOM: defined in Ch-1, Eq. 1.1) is -202.4 dBc/Hz for a given power-frequency tuning normalized (PFTN: defined in Ch-1, Eq. 1.2) -14.1 dB, with power consumption of 300mW ($V_{cc}=10V$, $I_c= 30\text{ mA}$), and output power of +10.05 dBm. The novel oscillator circuit is large in size (0.75x0.75x0.18 inches) but stable over operating temperature of -40°C to $+85^{\circ}\text{C}$, providing sufficient margin for compensating the frequency drift caused due to the change in operating temperature, including the package parasitic and component tolerances. For application requiring compact size VCO, different types of printed resonator using MCSWMR topology is developed and validated for current and later generation signal source applications.

8.8.4 Examples: Compact Size MCSWMR VCOs

Similar to crystal oscillators, DROs (dielectric resonator oscillators) tend to be prone to vibrational noise since the dielectric resonator itself cannot be secured mechanically. Therefore vibrations must effectively be damped by other means before they reach the dielectric resonator. The tiny MCSWMR VCO is designed with rugged construction to minimize vibration noise and microphonic effects to prevent unwanted modulation. Its excellent phase noise performance makes MCSWMR VCOs well suited for low-jitter communication systems, reference oscillators for phase noise measurement, RADAR systems, SDH/SONET, cable TV,

SATCOM systems, aeronautical equipment, digital radios (QAM) and laboratory frequency references. Custom frequencies and packages (hermetic) can be developed on request.

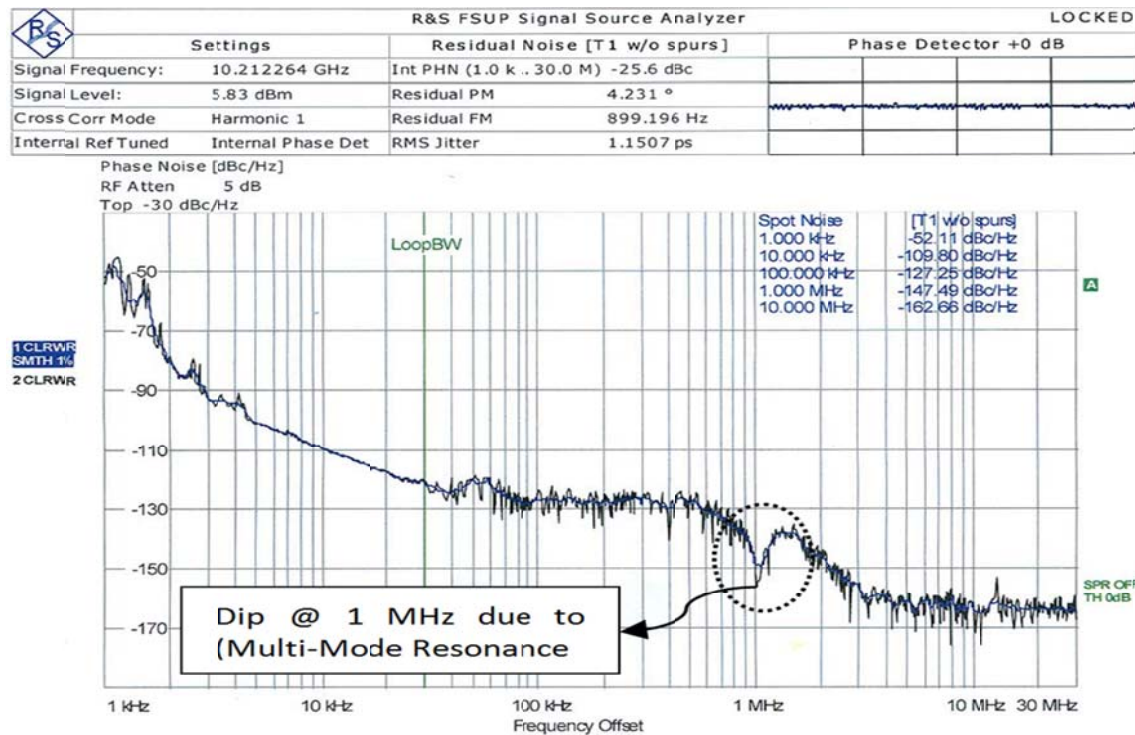


Figure 8-27 (a): Measured Phase Noise Plot of mode-coupled Metamaterial slow-wave resonator oscillator

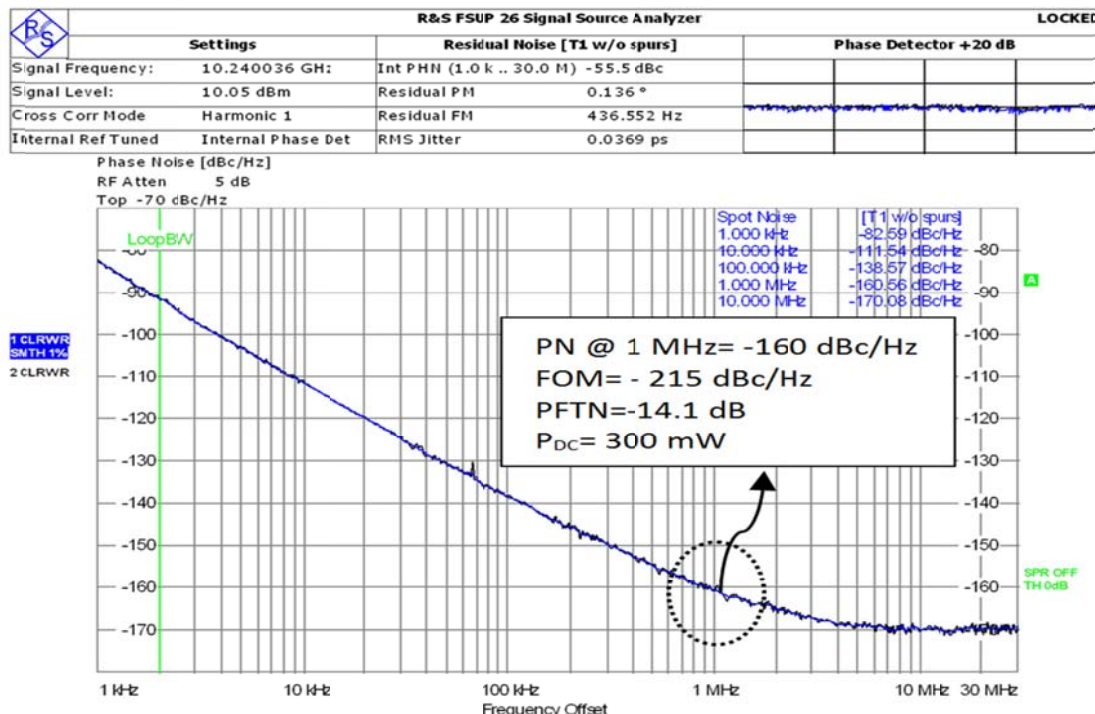
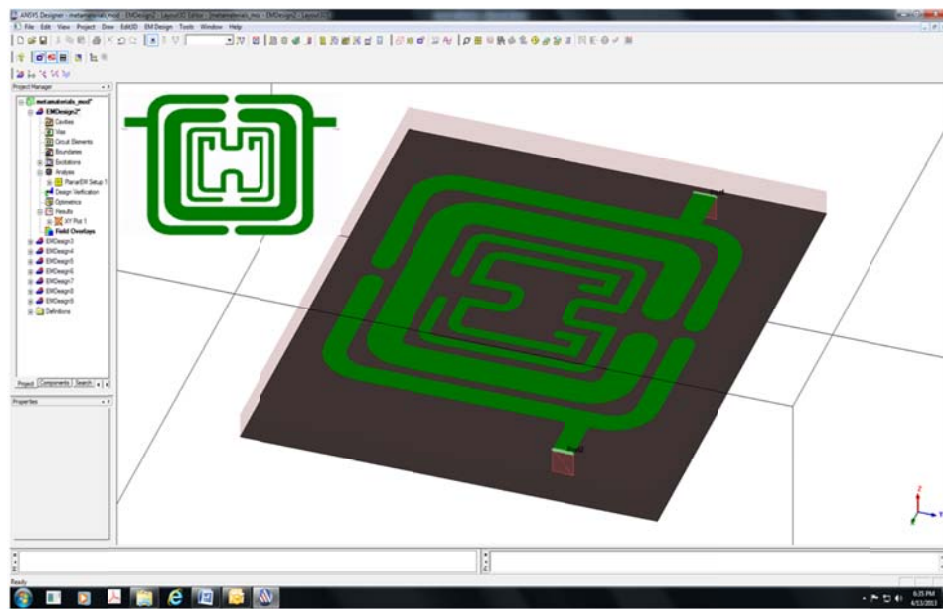
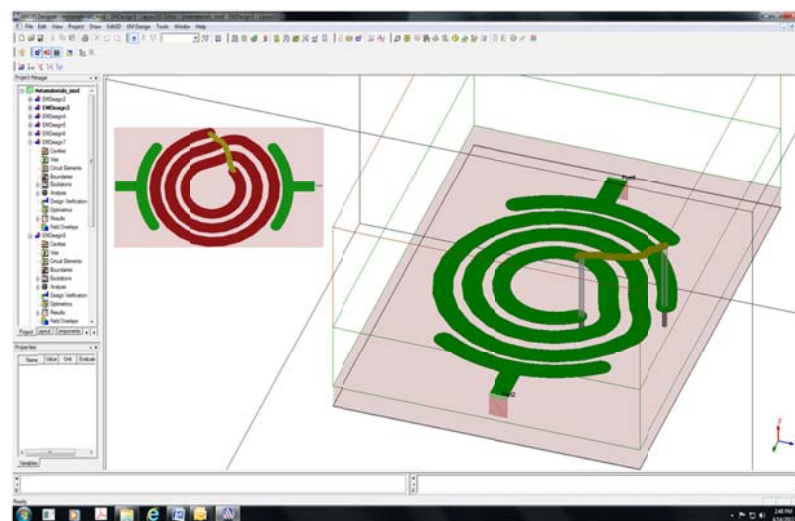


Figure 8-27 (b): Measured Phase Noise Plot of mode-locked 10.2 GHz oscillator (hump/ dip as seen in Figure 8-27 (a) is suppressed)

Figure 8-28 (a) and (b) shows the typical layout of MCSWMR resonator for the realization of MCSWMR VCO in 0.25" x 0.25" x 0.08" inches square package. Figure 8-29 (a) – (f) shows the layout of the various SMD (surface mounted device) version of 0.5" x 0.5" x 0.18" inches square package developed for low cost signal source applications. Figures 8-30 – 8-35 shows the CAD simulated phase noise plots of oscillator circuits using different configuration of planar resonator topologies.



(a) A screen capture shot of HFFS CAD schematic tool of planar slow wave resonator structure



(b) A screen capture shot of HFFS CAD schematic tool of Möbius coupled structure

Figure 8-28: A typical layout of MCSWMR in 0.25x0.25 inches size for the realization of MCSWMR VCO in 0.25" x 0.25" x 0.08" inches package (20 mils RT/Duroid 5880 with $\epsilon_r = 2.2$): (a) slow wave resonator, and (b) Möbius coupled slow-wave resonator

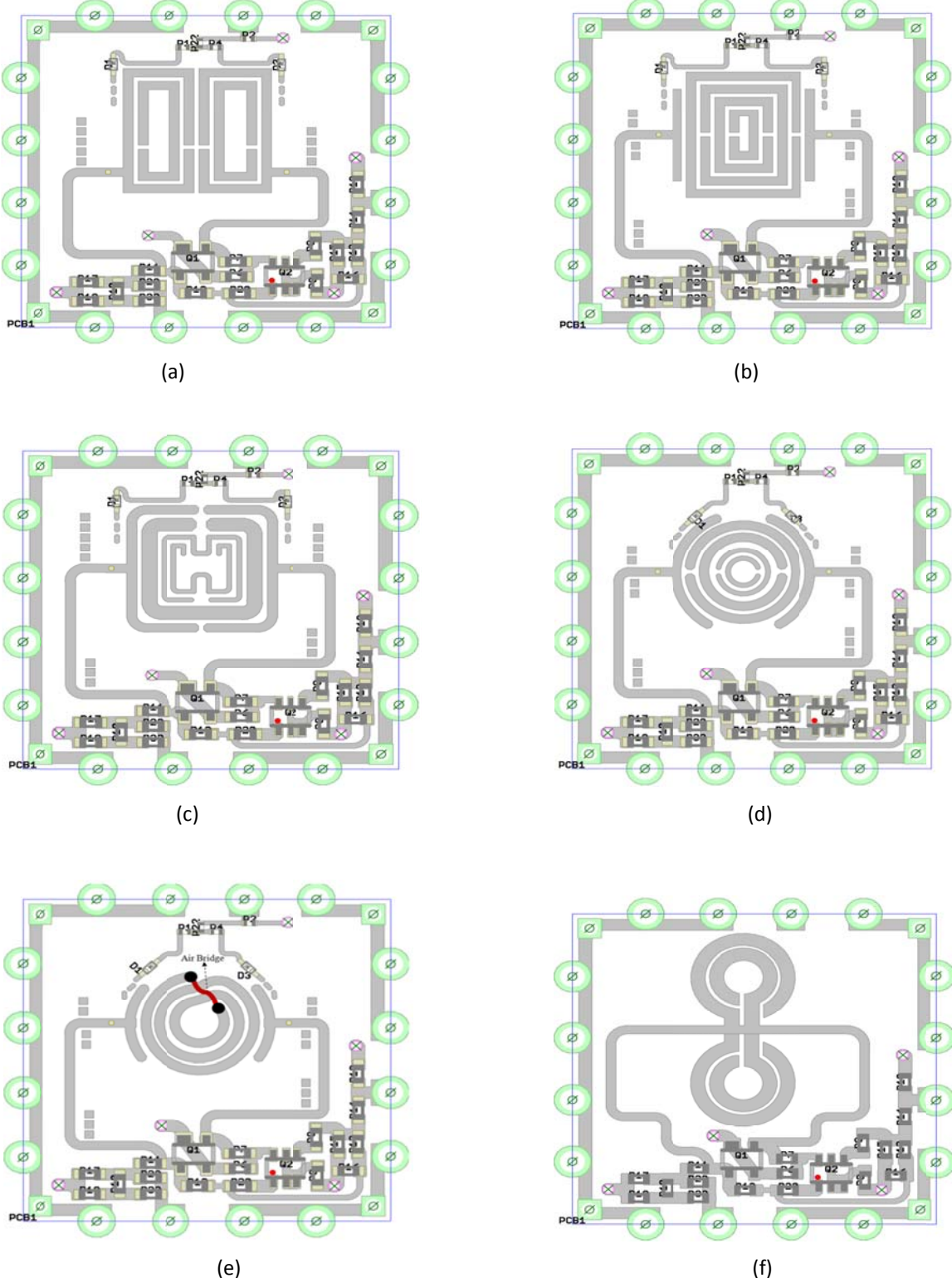


Figure 8-29: A typical layout of the SMD (surface mounted device) version of 0.5" x 0.5" x 0.18" inches square package are developed for low cost signal source applications: (a) 3.2 GHz Oscillator, (b) 4.7 GHz Oscillator, (c) 8.2 GHz Oscillator, (d) 12.2 GHz Oscillator, (e) 14.2 GHz Oscillator, and (f) 18 GHz Oscillator (22mils substrate, 2.22 dielectric constant)

Simulated phase noise plot of Metamaterial Resonator Oscillators shown in Figure 8-29

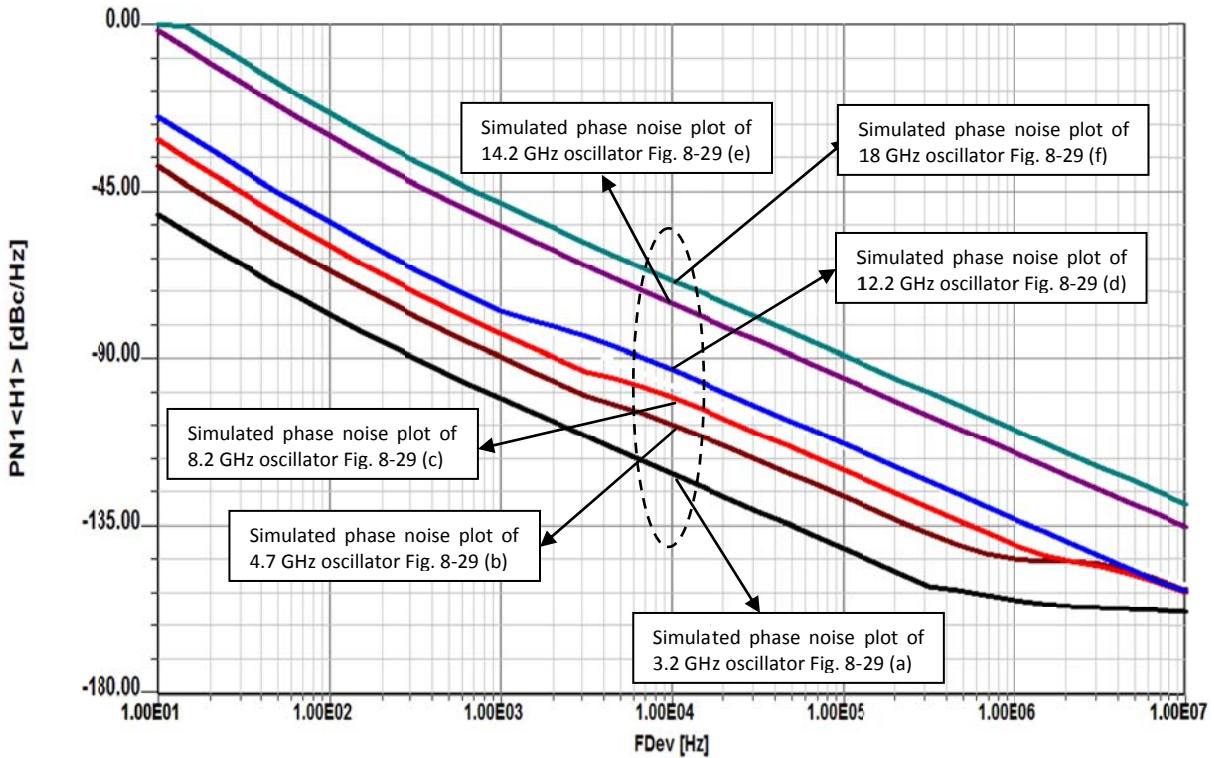


Figure 8-30: CAD simulated phase noise plot of Metamaterial Resonator Oscillator circuits as shown in Figure 8-29

This exercise is done for the basic understanding of the degradation in phase noise performance as operating frequency varies from 3.2 GHz to 18 GHz for given planar resonator topologies, substrate, and real estate area.

8.8.4.1 Example: 3.85 GHz Evanescent-Mode Metamaterial Resonator Oscillator

Figures 8-31 (a), 8-31 (b), 8-31 (c) and 8-31 (d) show the typical 3.8 GHz oscillator circuit schematic using evanescent mode-coupling techniques to improve the performance, CAD simulated phase noise plot, CAD simulated RF output spectrum plot, and the measured phase noise plots. The oscillator layout is fabricated on substrate material with a dielectric constant of 2.2 and thickness of 20 mil (microstripline/stripline) using a SiGe HBT active device, circuit works at DC bias of 5 Volt and 60 mA, measured output power exceeds +5 dBm.

The measured phase noise is typically -120 dBc/Hz @ 10 kHz offset from the carrier frequency of 3.8 GHz, this is very promising result but the main drawback is zero tuning. These drawbacks can be overcome by incorporating Metamaterial based Möbius strips varactor tuned resonator network which is depicted in Figure 8-32. As shown in Figure 8-32, the tuning diodes are incorporated in the resonator structure for improving the tuning characteristics. It can be seen that resonator structure (Figure 8-32) exhibits series and parallel resonance, therefore susceptible for mode-jumping. Care must be taken towards suppressing the higher order modes by phase-injection locking mechanism for reliable and stable operations [145]-[151].

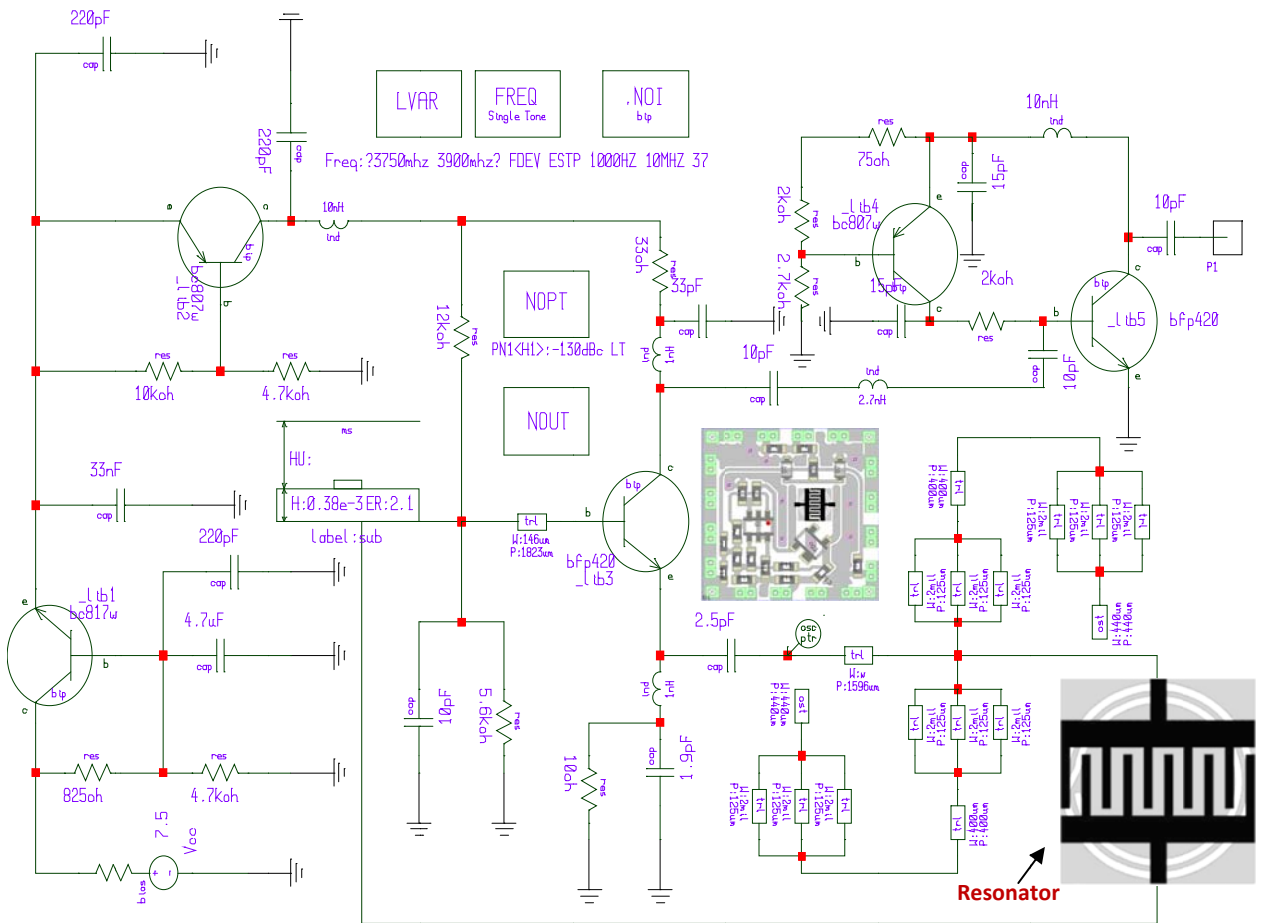


Figure 8-31 (a): A typical oscillator circuit schematic using evanescent mode-coupled metamaterial resonator network (Patent pending, US Patent Application: 61976185) [145]

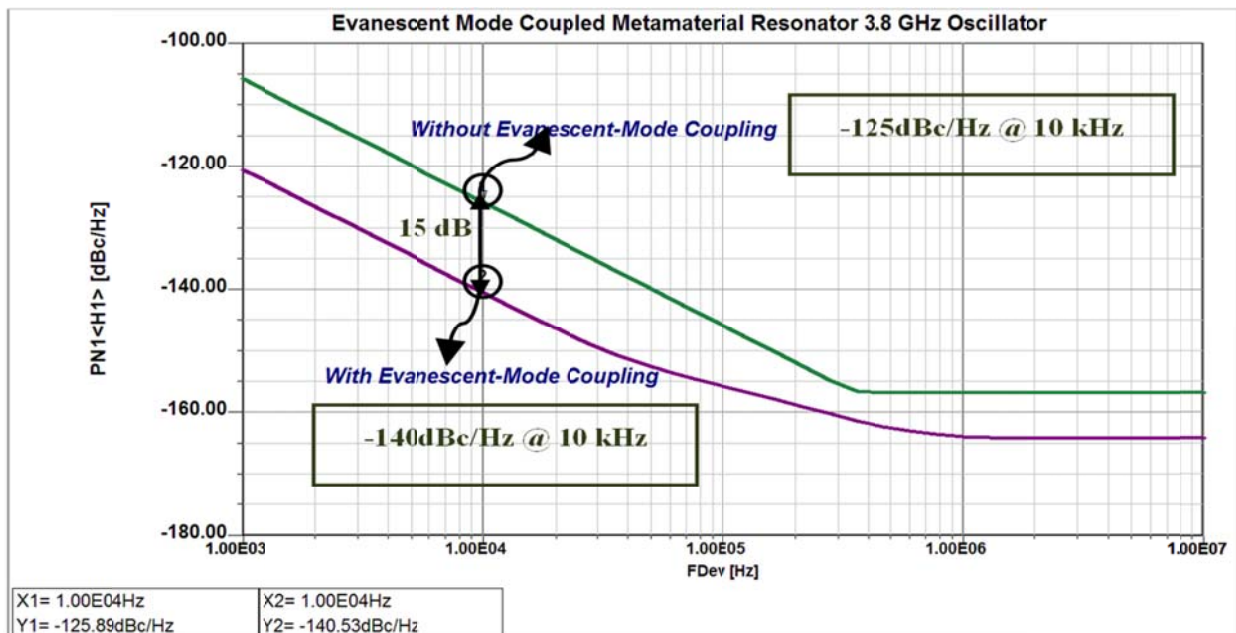


Figure 8-31 (b): CAD simulated phase noise plots of oscillator circuit shown in Figure 8-31 (a), it can be seen that evanescent mode coupling improves the oscillator phase noise by 15 dB

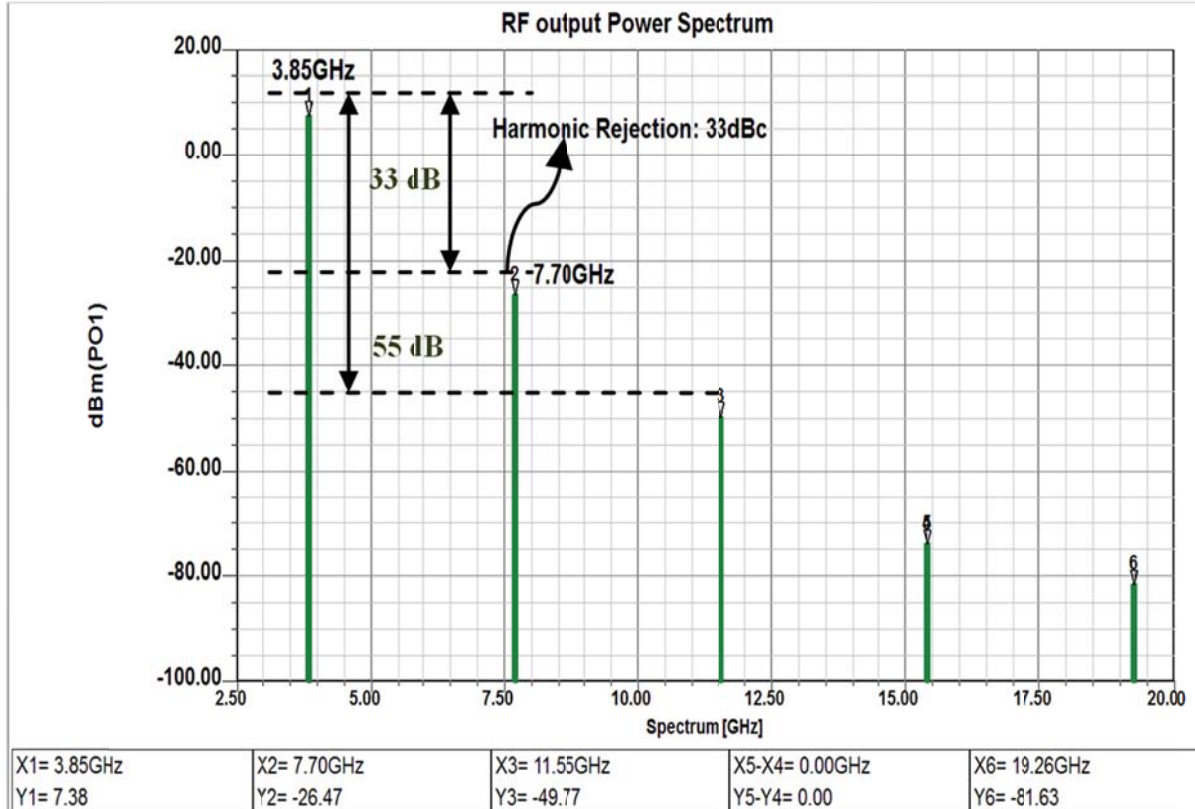


Figure 8-31 (c): CAD simulated RF output of oscillator circuit depicted in Figure 8-31 (a), it can be seen that evanescent mode coupling improves the 2nd and 3rd harmonic rejection level more than 33 dB and 55 dB respectively.

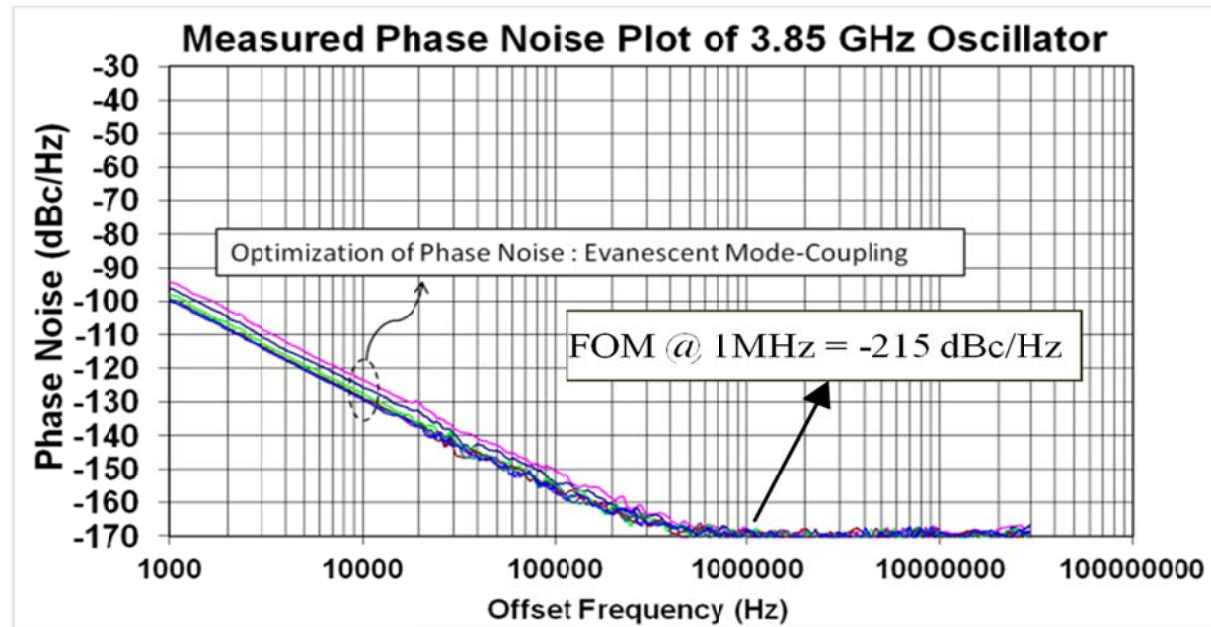


Figure 8-31 (d): The measured phase noise plots of oscillator circuit depicted in Figure 8-31 (a), it can be seen that measured phase noise plots illustrate 5-8 dB improvement depending upon of the level of coupling strength for a given phase-injection and modes.

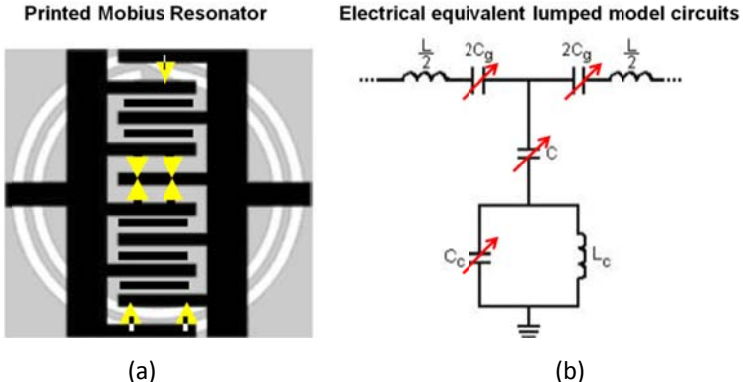


Figure 8-32: A typical tunable Metamaterial based Möbius strips resonator: (a) layout, and (b) electrical equivalent lumped model circuits [145]

8.8.4.2 Example: 7 GHz Evanescent-Mode Phase-Injection Mode (EMPIMC) Oscillator

Figure 8-33 (a) and 8-33 (b) show the typical 7 GHz oscillator circuit schematic of cascaded 3 and 5-resonators for the optimization of differential phase injection locking, thereby improving the phase noise and operating tuning ranges [150]. The design objective was to improve the Q value of the metamaterial resonator by cascading a progressive wave evanescent mode-coupled resonating network (to lower the phase noise without compromising the tuning range [145]-[152]. Figure 8-33 (c) shows the CAD simulated phase noise plots of oscillator circuit illustrated in Figure 8-33 (b), it can be seen that phase-injection-locking improves the oscillator phase noise by 50 dB [147].

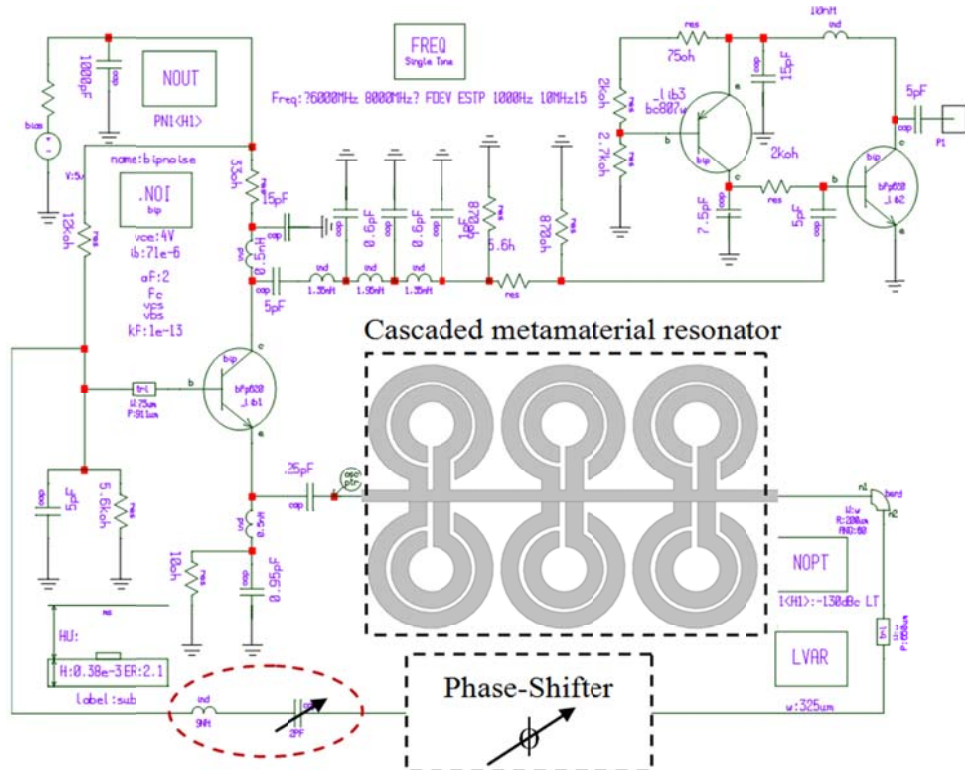
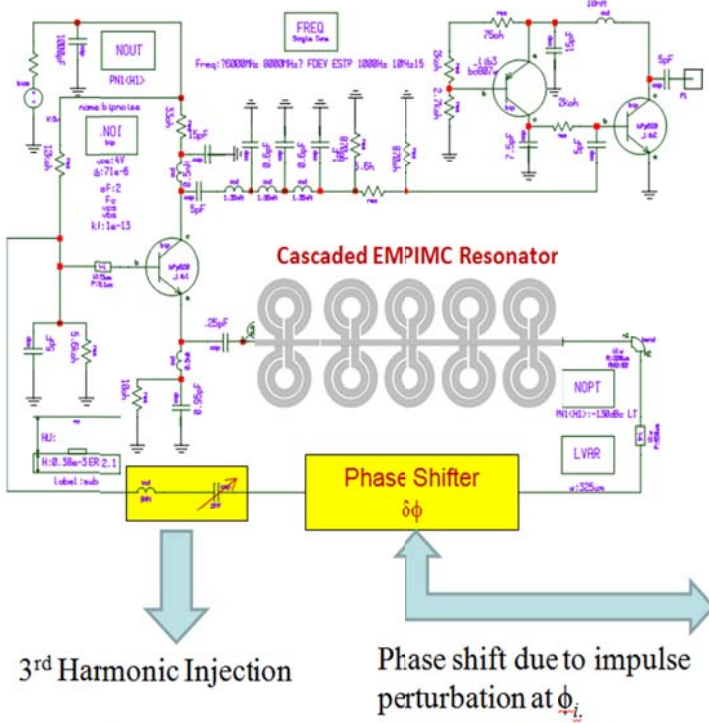
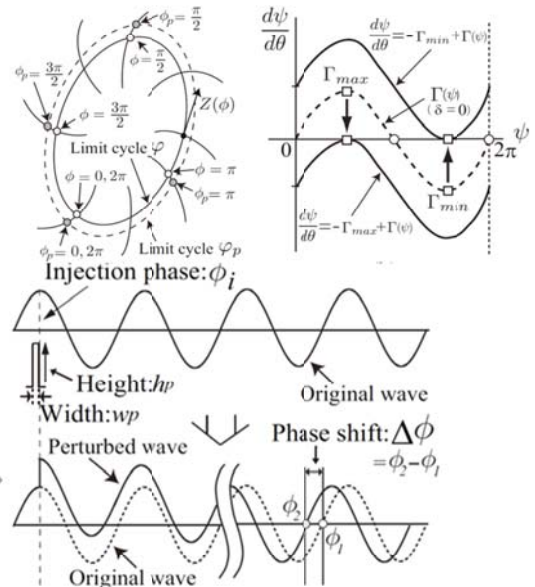


Figure 8-33 (a): A typical 7 GHz oscillator circuit schematic using 3-section cascaded evanescent mode-phase-injection-locked metamaterial resonator (Patent Pending, US Patent Application: 61976185) [145]-[148]



EMPIMC: Evanescence Mode Phase Injection Mode-Coupled



$$Q_L = \frac{\omega_0}{2} \left| \frac{d\phi(\omega)}{d\omega} \right|_{\omega=\omega_0} = \frac{\omega_0}{2} \tau_d; \quad \tau_d = \left| \frac{d\phi(\omega)}{d\omega} \right|_{\omega=\omega_0} \quad \tau_d = \frac{d\phi(\omega)}{d\omega} \Bigg|_{\omega=\omega_0} = \frac{\phi(\omega_0 + \Delta\omega) - \phi(\omega_0 - \Delta\omega)}{2\Delta\omega}$$

where $\phi(\omega)$ is the phase of the oscillator's loop TF at steady state and τ_d is the group delay of the metamaterial Möbius strips resonator

Figure 8-33 (b): A typical 7 GHz oscillator circuit schematic using 5-section cascaded evanescent mode-phase-injection-locked metamaterial resonator (Patent Pending, US Patent Application: 61976185) [146]-[147]

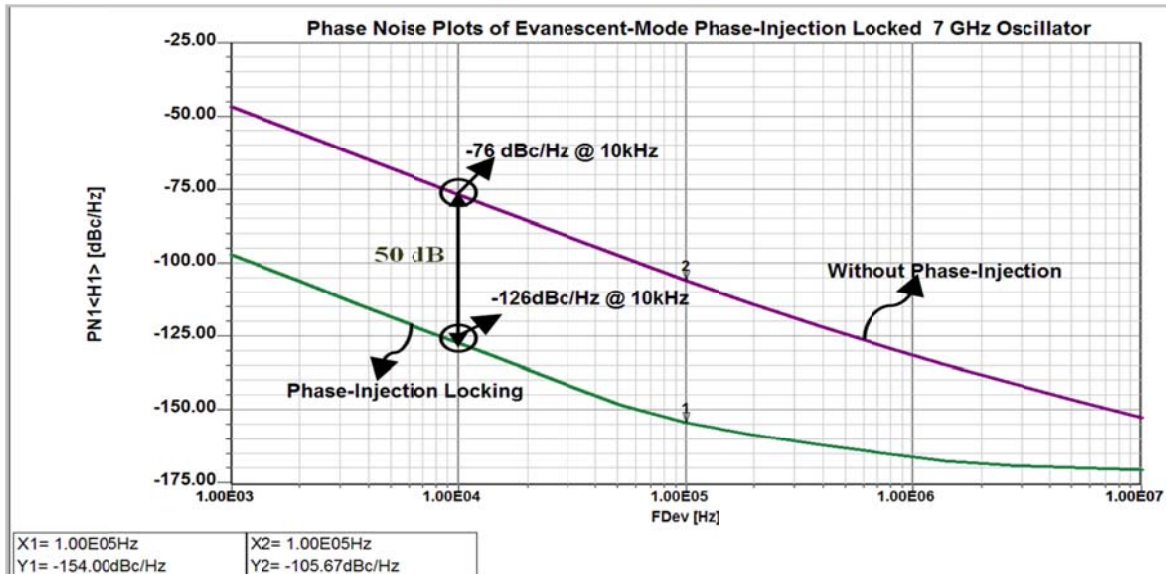


Figure 8-33 (c): CAD simulated phase noise plots; phase-injection-locking improves the oscillator phase noise by 50 dB [147].

As shown in Figure 8-33 (c), phase-injection-locking improves the oscillator phase noise by 50dB. It is to note that cascading improves the Q-factor of resonator; this is due to the fact that

at resonant condition sharp change in permittivity and permeability causing significant increases in group delay, thereby Q-multiplier effect, though care must be taken to avoid or suppress the degeneration modes that limit the application below 20 GHz.

8.8.4.3 Example: Tunable Evanescent-Mode Phase-Injection Mode (EMPIMC) Oscillator

Figure 8-34 shows the typical circuit schematic of tunable progressive injection-locked metamaterial resonator based oscillator topology. Figure 8-35 (a) shows the CAD simulated phase noise plots, it can be seen that phase-injection-locking technique improves the oscillator phase noise by 30 dB. Figure 8-34(b) depicts the measured phase noise plots, it can be seen that phase noise plots illustrate typically 4-6 dB variation over the tuning range from 4.25 GHz to 5.1 GHz for a V_{tune} (0-12 Volt), which otherwise can be more than 10 dB variation in phase noise performance over the tuning range for simple transmission line resonator based oscillator.

Figure 8-35 (c) shows the measure tuning characteristics, the oscillator tunes from 4.25 GHz to 5.1 GHz for a tuning voltage: V_{tune} (0-12 Volt), exhibits typical RF output power better than 3dBm with DC bias of 5V, 80 mA.

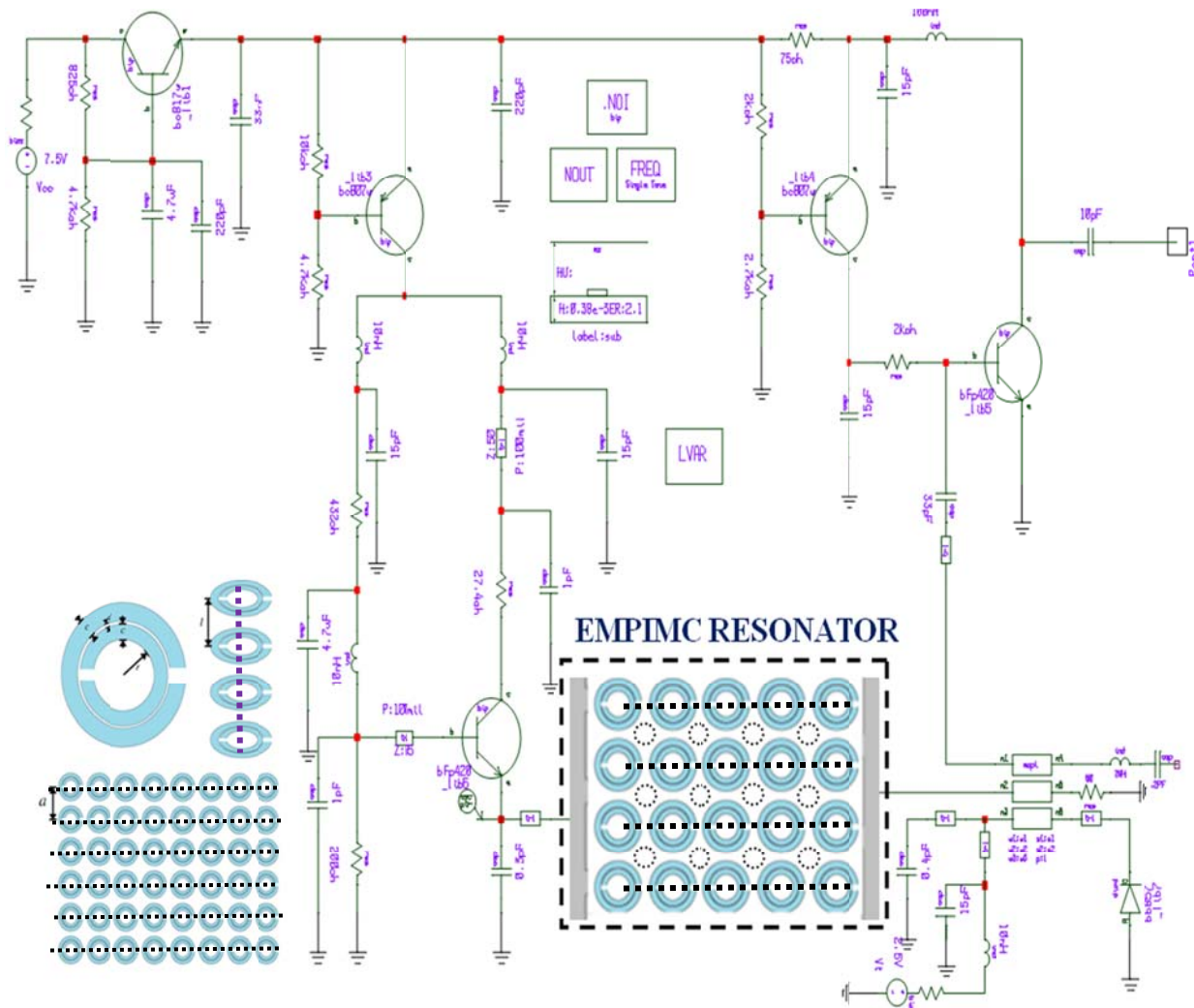


Figure 8-34: A typical tunable oscillator circuit using 2-dimensional cascaded injection-locked metamaterial resonator network (Patent Pending, US Patent Application: 61976185) [147]

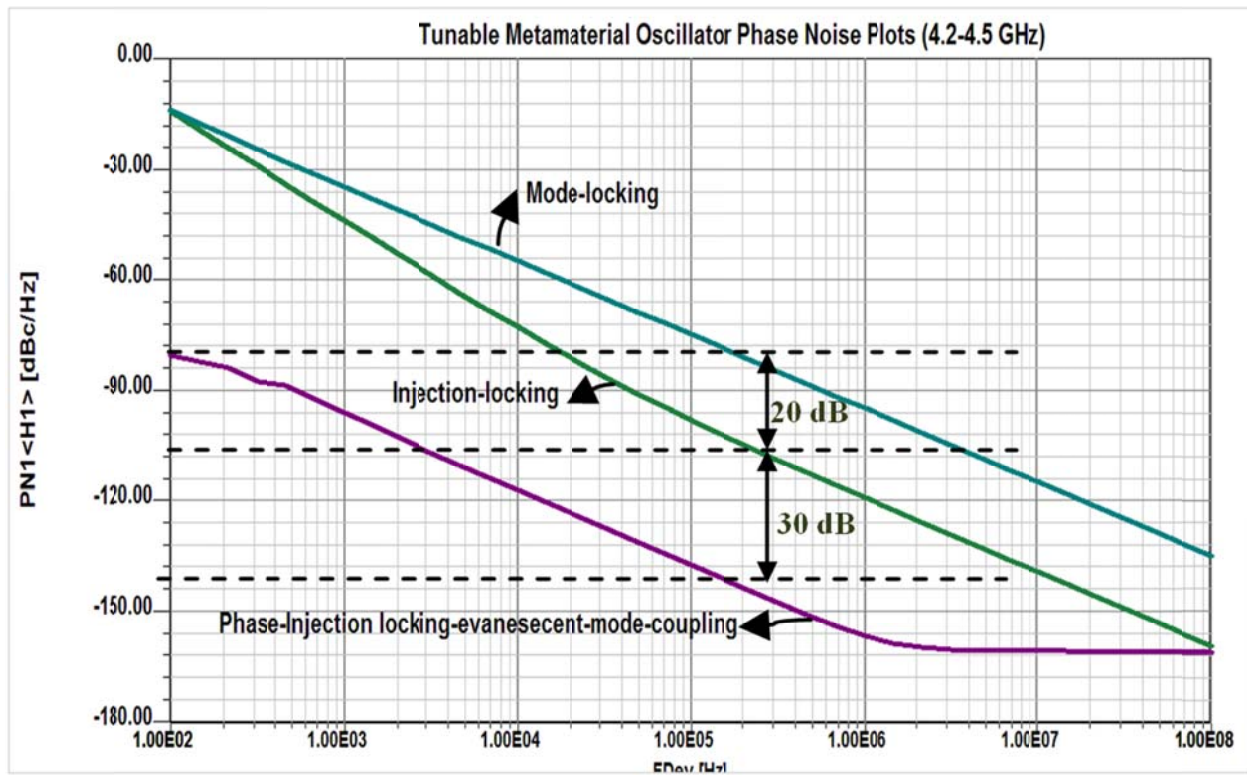


Figure 8-35(a): CAD simulated phase noise plots; phase-injection-locking and evanescent-mode-coupling improves the oscillator phase noise at oscillation frequency 4.5 GHz by 30 dB

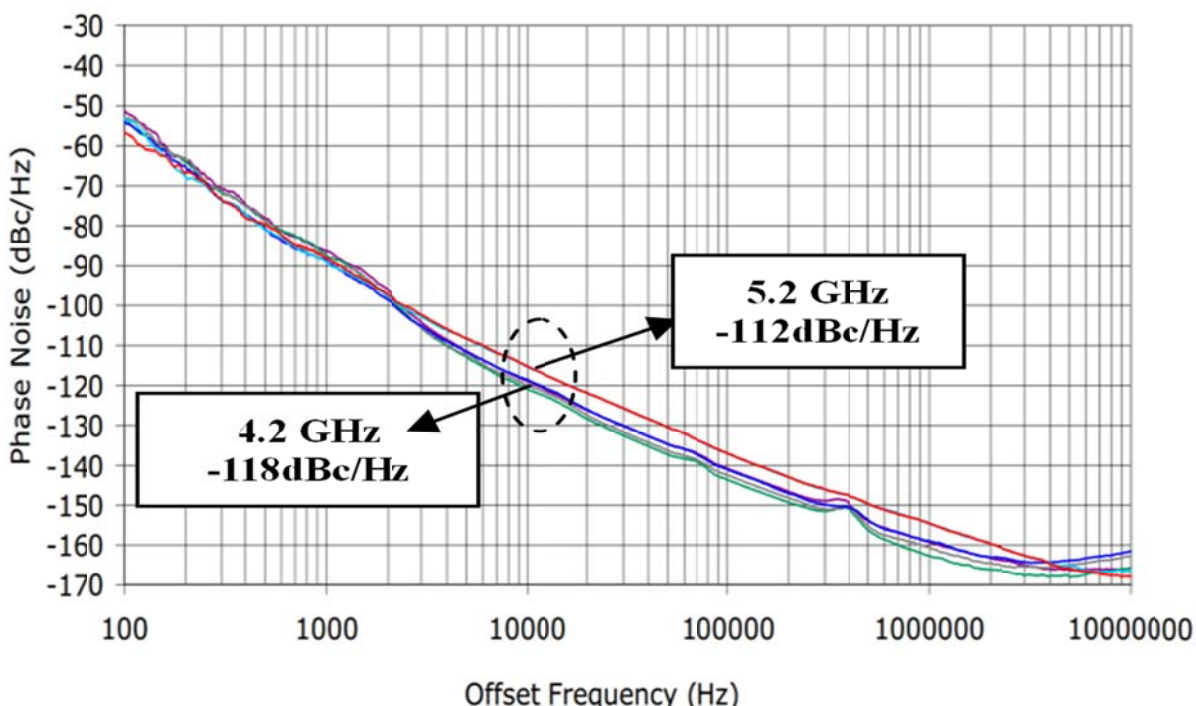


Figure 8-35(b): The measured phase noise plots, it can be seen that phase noise plots illustrate 4-6 dB variation over the tuning range from 4.25 GHz to 5.1 GHz for a V_{tune} (0-12 Volt)

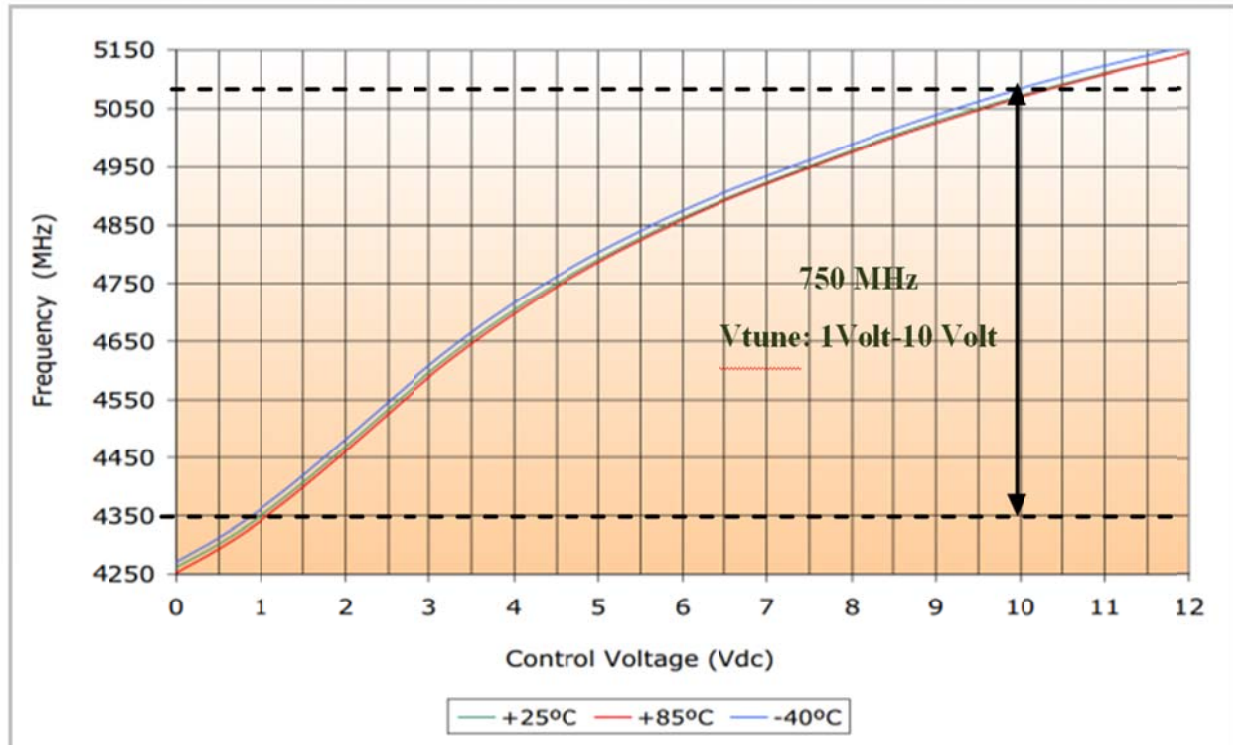


Figure 8-35(c): Measured tuning characteristics of the oscillator circuit shown in Figure 8-34 (a), the oscillator tunes from 4.35 GHz to 5.1 GHz for a V_{tune} (1-10 Volt) with DC power consumption of 5V, 80mA.

8.9 High Performance Frequency Synthesizer Using MCSWMR VCO

Frequency synthesizers are the essential signal sources for many high-frequency systems, from communications to test platforms. Synthesizers come in many forms, from tiny system-on-a-chip (SiC) devices to large rack-mount units [99]-[103]. The number of technologies used to implement them is almost as diverse as their package styles, relying on analog methods, digital techniques, and sometimes a combination of the two approaches [104]-[107]. For many applications, basic frequency synthesizer requirements call for a small unit with excellent spectral purity, but at an affordable price. These simple requirements drove the development of a new line of low-noise sources based on direct-digital synthesis (DDS) at a fraction of the size and cost of currently available commercial sources with comparable performance [142].

Regardless of package style and size, frequency synthesizers can be differentiated by a number of key performance specifications, including frequency tuning range (if not a fixed-frequency synthesizer), output power and output-power flatness across the tuning range, frequency switching speed, phase noise, harmonic levels, spurious levels, power consumption, and a number of other parameters [102]-[128]. Acceptable levels for these parameters are usually set by the application of interest, with something like fast switching speed, for example, being important in a frequency-agile communications system but not as important in other types of communications systems [103]. One of the more common types of synthesizer is a voltage-controlled oscillator (VCO) stabilized by a phase-locked loop (PLL). A conventional PLL-based frequency synthesizer includes a reference phase detector, loop filter, VCO, and VCO frequency divider (Figure 8-36) [104]. Equation (8.85) defines the relationship between the

output frequencies, f_{out} , where N is the value of divider. From (8.35), the minimum output frequency step is f_{ref}/R . Operating the PFD and reference frequency [105]:

$$f_{\text{out}} = N \times \left(\frac{f_{\text{ref}}}{R} \right) \quad (8.85)$$

The phase-frequency detector (PFD) compares the two input signals f_{ref}/R and f_{out}/N and produces an error voltage proportional to the phase difference between them [146]. The loop filter removes the high-frequency noise components from the PFD's output and limits the bandwidth of the error signal. The filtered error voltage is applied to the tuning port of the VCO to stabilize its resulting tuned frequency; the error signal drives the VCO frequency (f_{out}) so that the error voltage at the PFD output is zero when locked [106]. Typically, the VCO frequency divider is implemented as a dual-modulus counter to obtain large continuous division of the VCO output. To vary synthesizer output frequency, f_{out} , N is changed. From (8.85), the minimum output frequency step is f_{ref}/R . Operating the PFD at a lower frequency makes it possible to achieve a smaller step, but also increases R and N and, in increasing N, the PFD noise also increases [107]. A PLL synthesizer's close-in phase noise is estimated by adding the noise of the synthesizer, PN_{SYN} to $20\log N$ (where N is the divider value) and $10 \log(f_{\text{PFD}})$:

$$PN_{\text{TOT}} = PN_{\text{SYN}} + 10\log(f_{\text{PFD}}) + 20\log(N) = PN_{\text{SYN}} + 10\log\left(\frac{f_{\text{REF}}}{R}\right) + 20\log(N) \quad (8.86)$$

$$PN_{\text{PD}}[\text{dBc}/\text{Hz}] = PLL_{\text{FOM}} + 20\log_{10}(f_{\text{VCO}}) - 10\log_{10}(f_{\text{PD}}); \text{ (frequencies are in Hz)} \quad (8.87)$$

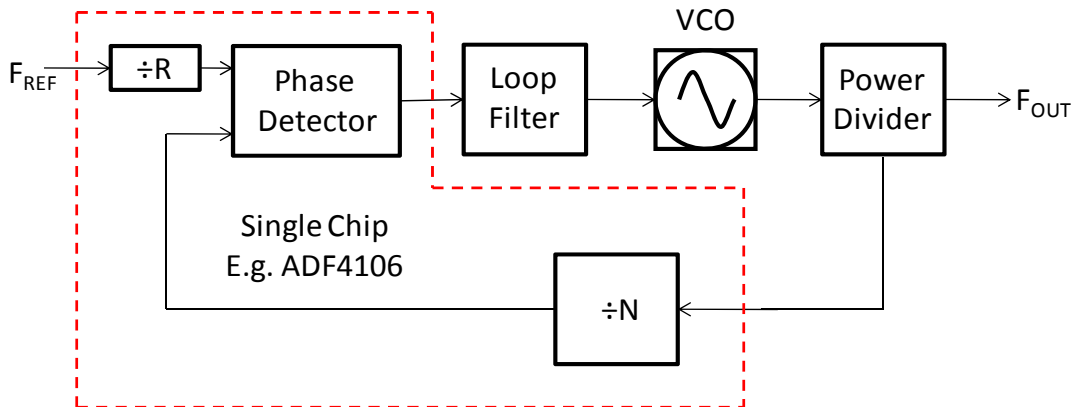


Fig.8-36: This block diagram shows a simplified PLL synthesizer module

These simple equations reveal, PLL synthesizer design is a matter of tradeoffs [108]-[142]. From [103], N should be low to minimize phase noise, but fine frequency resolution results from a PFD that is low in frequency, which leads to an increase in N and degraded noise performance. Loop filters can limit noise, but also prevent fast switching speed. A higher loop filter bandwidth yields faster switching speed, but allows noise to pass. A narrower loop filter cuts the noise level, but with slower switching speed. PLL frequency synthesizers can be implemented with integer or fractional values of N. Figure 8-37 shows the typical phase noise characteristics of integer frequency synthesizer (FSW50120-50, ref.128) that tunes from 500 MHz to 1200 MHz with the step size of 500 kHz, switching time of < 5ms. The typical spurious is -65 dB with 10 MHz reference frequency. To improve the performance of the integer frequency synthesizer, divider "N" can be implemented as a fractional divider instead of integer divider [131].

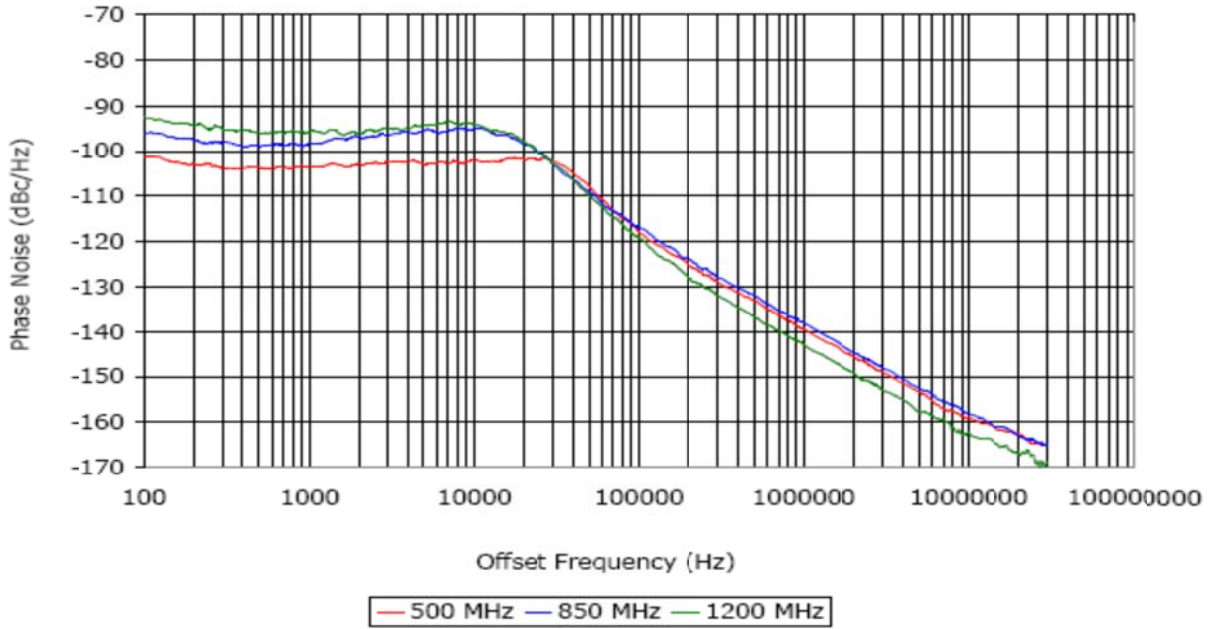


Figure 8-37: This phase-noise plot typifies the performance of an integer-N PLL synthesizer

For example (as shown in Figure 8-38), a commercial fractional-N source (LFSW160290-50, ref [128]), that tunes from 1600 to 2900 MHz in 500-kHz steps and works with a 10-MHz reference might have spurious levels of -60dBc and switching speed of 1ms. When better frequency resolution is needed, a DDS-based multi-loop synthesizer design can be used, such as in Figure 8-39. In this case the DDS clock is fed by a selectable frequency synthesizer, which provides a fixed set of frequencies based on the parallel selection lines. The DDS unit, with its resolution measured in microhertz, provides the fine frequency resolution. As with other frequency synthesizer design, a DDS has tradeoffs, notably poor spectral purity, and high spurious levels.

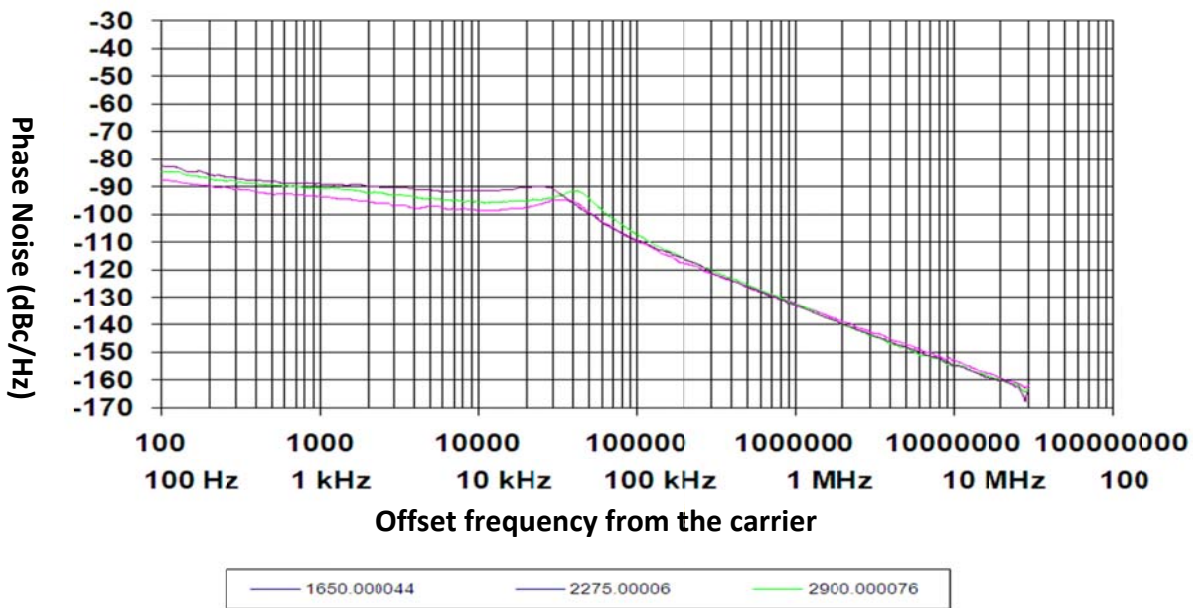


Figure 8-38: This phase-noise plot shows the typical performance of an fractional-N PLL synthesizer.

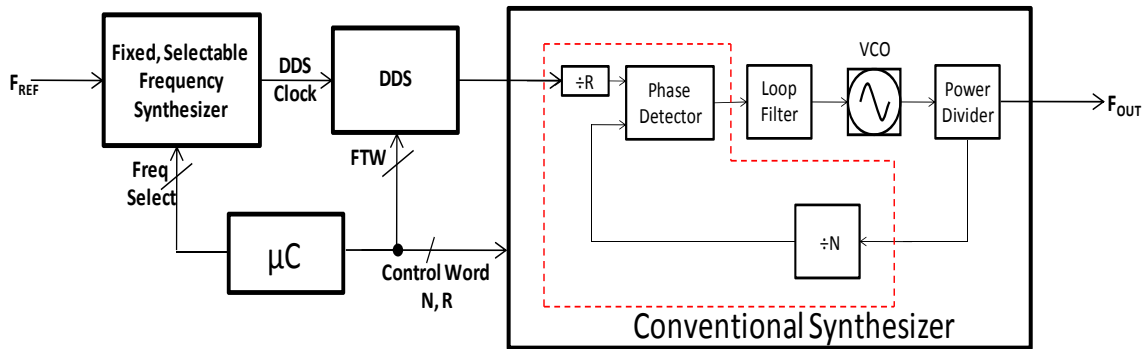


Figure 8-39: This block diagram shows a typical DDS-based dual-loop frequency synthesizer.

DDS spurious signal components that fall within the loop bandwidth are not attenuated by the loop filter. But they can be predicted and moved in frequency by using a different DDS clock frequency. With this approach, the PFD frequency of the output synthesizer can be high, improving phase-noise performance with a 10-MHz reference while still achieving 1-Hz frequency resolution. Such a design has switching speed of better than 1 ms with low phase noise and better than -70dBc spurious performance from 1.1 to 2.5 GHz.

Figure 8-40 shows a typical block diagram for a DDS-based low-noise, fast-switching synthesizer based on a VCSO source. The typical synthesizer generates outputs ranging from 530 to 630 MHz with 1-MHz step size and spurious of -70 dBc or better. Since the analog phase detector has a low noise floor, the synthesizer bandwidth was kept large for faster switching time (about 200 microseconds) with low phase noise performance. With recent developments in frequency synthesizers, the DDS shown in Figure 8-40 can be replaced with a single-chip flying-adder-based synthesizer [106].

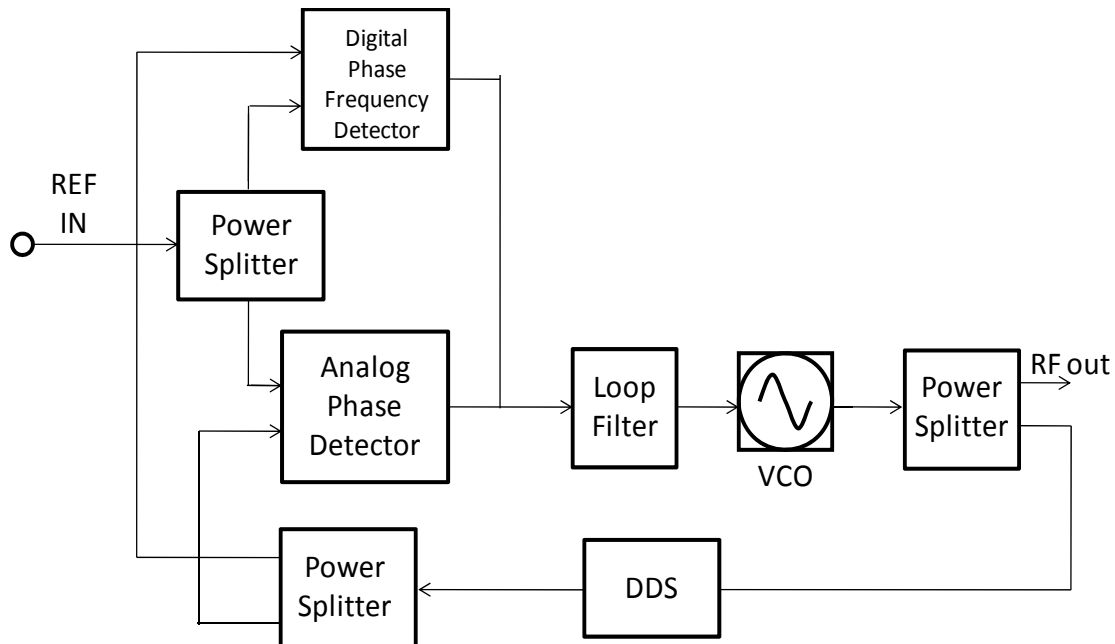


Figure 8-40: This is a block diagram of a typical fast-switching DDS-based frequency synthesizer.

A design challenge of developing a synthesizer was to provide high performance in a compact size (3.25 x 2.25 x 1.25 square in.) and be able to sell for low cost. The first consideration was to use an oscillator with octave tuning range of 4 to 8 GHz, as in ref [2]. Octave tuning allows division by two, and frequencies above 4 GHz could be successively generated. Unfortunately, process, voltage, and temperature variations would make it difficult to guarantee frequency with precision any better than a few MHz. In addition, synchronization techniques, such as locking the oscillator to a stable reference source such as an oven-controlled crystal oscillator (OCXO), would be needed for stabilization. As Figure 8-36 shows, a single-loop PLL can stabilize any frequency to the maximum oscillator's frequency. In this approach, the low-noise crystal oscillator's frequency is multiplied by the PLL to the desired output frequency. Because of frequency multiplication, a 20dB/decade degradation in phase noise is expected. For a 10-MHz crystal oscillator with phase noise of -174 dBc/Hz at 10kHz offset, the phase noise with multiplication at 8 GHz could not be better than -115 dBc/Hz. Taking advantage of PLL behavior, ideally the PLL loop bandwidth would be set to the frequency where the -115 dBc/Hz multiplied noise floor of the crystal intersects the trace of the noise produced by the oscillator, about 400 kHz for a typical scheme [107]. This is rather idealized, since the phase detector and the frequency dividers used in this PLL can degrade the crystal noise floor by about 20 to 30 dB in commercial PLL ICs.

The PLL contribution to the phase noise PN_{PLL} can be summarized as the root-mean-square addition of two components: PN_{PD} , a component determined by the phase detector comparison frequency and $PN_{flicker}$, a flicker component independent of the phase detector comparison frequency given in (8.86) and (8.87):

$$PN_{flicker}[\text{dBc/Hz}] = PLL_{flicker} + 20 \cdot \log_{10}(f_{VCO}) - 10 \cdot \log_{10}(f_{offset}); \text{ (freq. in Hz)} \quad (8.88)$$

In these equations, the PLL_{FOM} and $PLL_{flicker}$ are determined by the PLL design choices, and usually provided by the PLL manufacturer, where f_{VCO} is the output frequency of the oscillator, f_{PD} is the phase detector comparison frequency, and f_{Offset} is the frequency offset from the carrier used when estimating the phase noise. The noise added by the PLL circuit will then be:

$$PN_{PLL}[\text{dBc/Hz}] = 10 \cdot \log_{10} (10^{\frac{PN_{PD}}{10}} + 10^{\frac{PN_{flicker}}{10}}) \quad (8.89)$$

A typical case with $PLL_{FOM} = -220$, $PLL_{flicker} = -250$, $f_{VCO} = 8 \text{ GHz}$, $f_{PD} = 10 \text{ MHz}$, and $f_{Offset} = 10 \text{ kHz}$ will result in $PN_{PD} = -220 + 198 - 70 = -92$; $PN_{flicker} = -250 + 198 - 40 = -92$ and the resulting $PN_{PLL} = -89 \text{ dBc}$. This is 26 dB higher than the -115 dBc/Hz contributed by the crystal oscillator considered above. For this circuit, setting the PLL bandwidth to about 20 kHz will result in the best phase-noise performance for any offset frequency. For an integer PLL, where frequency division is limited to integer numbers, the output frequency could only be set in 10-MHz increments. This is a serious limitation, since many applications require a smaller step size, say 1 Hz to 10 kHz. For an ideal noise floor of -174dBc/Hz, with a 1 kHz comparison frequency at 8 GHz that noise multiplied results in a -36 dBc/Hz PLL noise floor. Even if such noise would be acceptable, the PLL loop bandwidth should be set to about 100 Hz, subjecting the design to high-level microphonic effects. Such a small loop bandwidth will also greatly increase the settling time of the PLL.

Settling time is determined by loop bandwidth and the time needed to charge the loop filter's capacitors with limited charge pump current. A decent design with a 10-kHz loop bandwidth may use a 1-micro Farad capacitor in the loop. With a charge pump current of 5 mA, approximately 5 ms is needed to charge a 1-micro Farad capacitor to 25 V. Again, with a 10-kHz loop bandwidth, the minimum comparison frequency at the phase detector's input would be about 100 kHz limiting the step size to the same 100 kHz. This comparison frequency will ideally result in an 8-GHz output having a loop noise floor of -76dBc/Hz when using a crystal oscillator with -174 dBm/Hz noise floor.

A fractional-N PLL helps overcome some of these limitations, dynamically changing the feedback ratio. As a result, the average divide ratio becomes a fractional number. The major advantage of this technique is that the phase-detector comparison frequency does not change with step size. In the following example, the output frequency is 7999.9 MHz and the reference frequency is 10 MHz. The feedback divider divides 99 times out of 100 by 800 and divides 1 out of 100 times by 799. The average division ratio is 799.9, the output frequency is 7999.9 MHz and the phase detector comparison frequency is 10 MHz. The PLL phase noise is $PN_{PLL} = -89$ dBc/Hz, as calculated above, a major advantage over an integer PLL which ideally would only give -76 dBc/Hz.

The drawback of this technique is the introduction of the fractional spurious product in the spectrum that has a repetition rate determined by the period needed to average the divide ratio, $f_{spur} = 100$ kHz in the simple case presented above. Complex fractional-N PLLs will use higher-order DS modulation techniques to mitigate the spurious amplitude, while adding sub-fractional spurious content to the signal. Generally, a -40 to -60 dBc spurious amplitude is to be expected with this approach, and the PLL loop filter bandwidth must be reduced to attenuate the spurious content to an acceptable level. A PLL bandwidth of 10 kHz will impose a practical limit of about 100 kHz on the step size [101].

Spurs generated by the fractional-N PLL are caused by the inability of digital frequency dividers to position the transitions of the feedback clock with absolute accuracy in time [133]. The time resolution of the transition is equal with the period of the clock provided at the divider's input. A DDS can overcome this limitation by adding a level of analog control to the transition [134]. By generating an analog sinusoidal wave, the position of the zero-crossings of the sine wave can be controlled with high accuracy, resulting in close-to-carrier spurious levels at -100dBc/Hz. It is worth mentioning that the DDS, or any fractional frequency divider, will exhibit a high spurious case when the input frequency of the DDS is close to a rational multiple of the output frequency. This spurious phenomenon is called "integer boundary spur" and is particularly difficult to eliminate. For frequency synthesis purpose, the DDS circuit could be considered as a low-noise frequency divider, and the output frequency of this DDS divider is given by

$$f_{DDS} = \frac{N}{2^k} f_{clk} \quad (8.90)$$

where f_{DDS} is the DDS output frequency, N is a digital number represented with a k-bit resolution and f_{clk} is the frequency of the DDS's input clock. In practice, f_{DDS} is limited to $0.4f_{clk}$, or to about 400-1000MHz when using modern DDS ICs with f_{clk} as large as 1 to 2.5GHz. The resolution of the output frequency is typically set to 32 or 48 bits, allowing a sub-hertz precision

of the output frequency. The availability of low-cost, low-noise VCOs [101]-[128] clears the way for small, low-noise synthesizers. Part of using these sources involves modeling surface-acoustic-wave (SAW) resonators under large-signal drive conditions for better insights about noise dynamics of close-in phase noise, then developing manufacturable methods for producing high-purity and temperature-stable oscillators in chip form. [102].

Figure 8-41 shows a block diagram for a configurable user-defined multi-band low-noise VCO with 2-to-4-GHz/4-to-8-GHz/5-to-10-GHz/6-to-12-GHz tuning range. It is compact ($0.3 \times 0.3 \times 0.08$ in.), operates at 12 mA and 5 V, and exhibits phase noise of typically -135 dBc/Hz offset 1 MHz from the carrier frequency 2GHz [128].

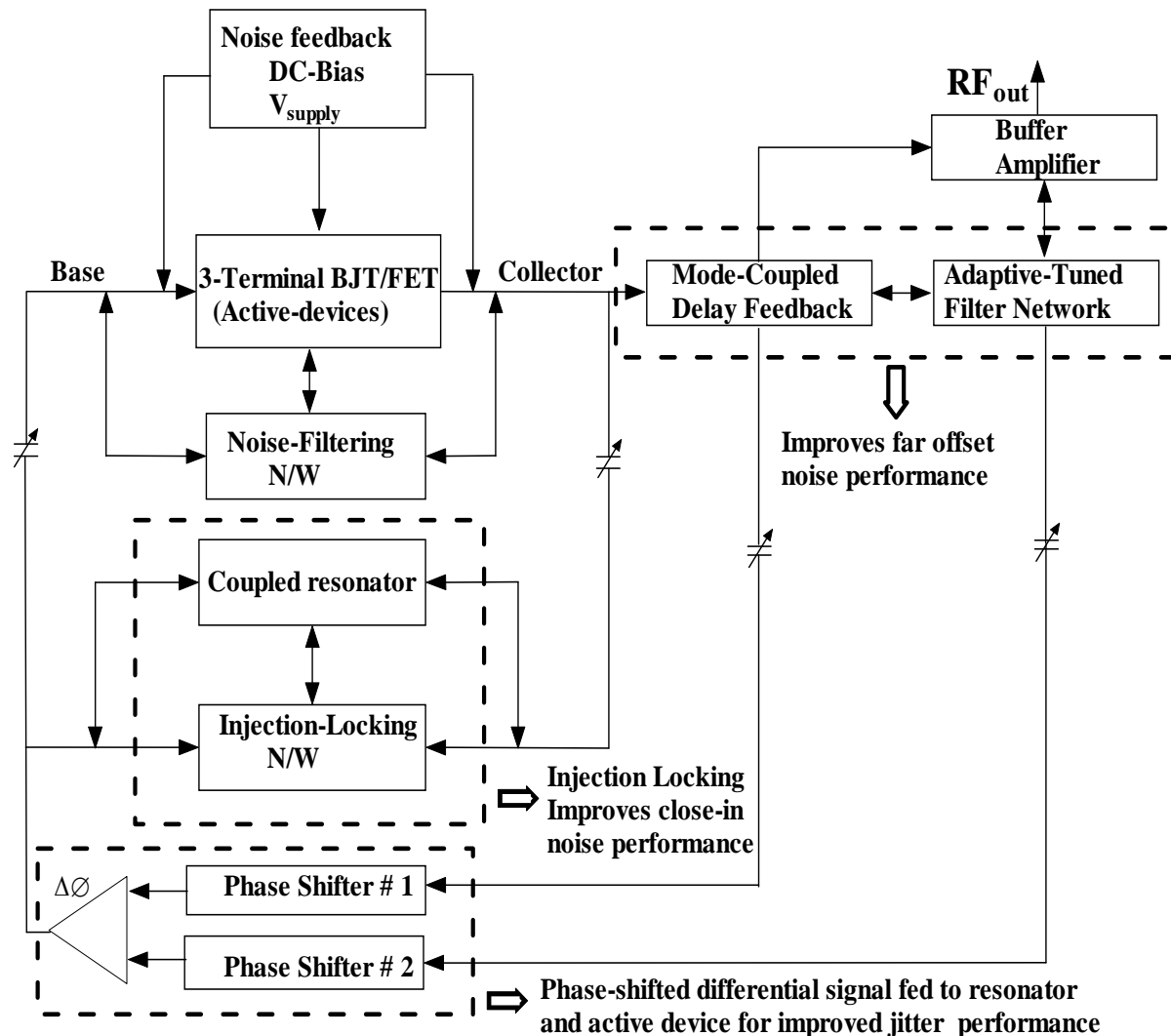


Figure 8-41: A typical block diagram of an ultra low noise wideband VCO using slow-wave resonator oscillator in 0.3×0.3 inches size

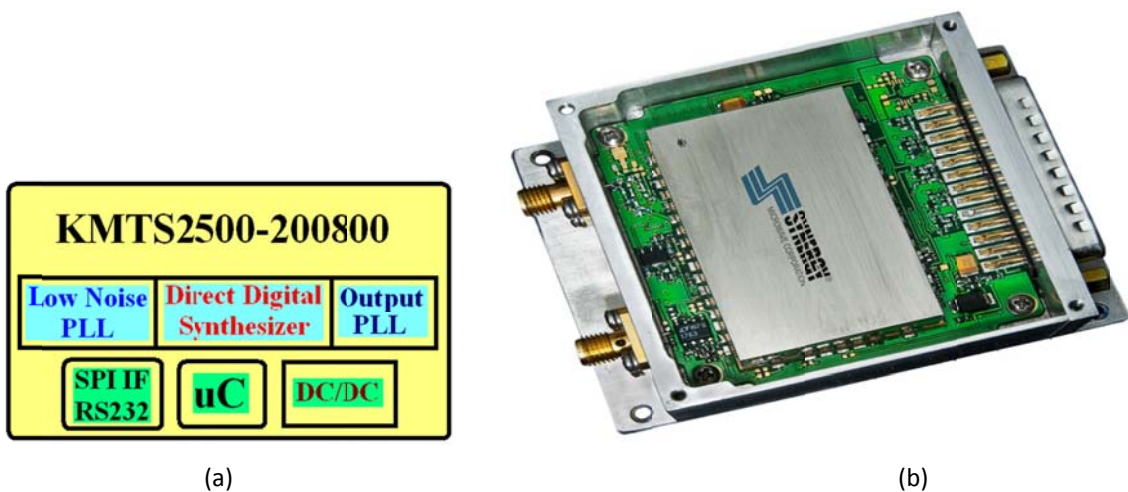


Figure 8-42: shows the prototype model KMTS2500-200800-10 frequency synthesizer module, using DDS technology and slow-wave resonator oscillator: (a) Modular block diagram, and (b) prototype hardware [142].

Figure 8-42 shows prototype version of the DDS-based model KMTS2500-200800 synthesizer using high-performance adaptive dynamic mode-coupled, low-phase-noise VCO using patented techniques [114, 122, and 127]. A low-noise PLL multiplies a reference frequency to the maximum frequency allowed by the DDS circuit. The DDS output signal is then filtered and provided as a reference to a secondary PLL that will multiply the frequency to the desired range. Depending on design choices, the phase-noise performance may be limited by the primary PLL, the DDS circuit, or the secondary PLL. However, the spurious performance is determined by the frequency multiplication and division implemented by the PLL circuits and the DDS.

A particular example will show why the choice of frequencies is important. With this module (Figure 8-42), it is desired to generate 2000.001 MHz using a 10-MHz reference. The low-noise PLL multiplies the 10-MHz clock to 1 GHz, and the DDS uses this signal to produce the 62.50003125 MHz required by the secondary PLL. Strong integer boundary spurious products may be noticed at this point in the DDS output at 500 Hz offset from the ~62.5-MHz carrier. That 500-Hz spurious product will be amplified by 30 dB and would be practically impossible to filter out from the 2.000001-GHz output signal. The KMTS2500-200800-10 [142] employs a proprietary algorithm that selects the best combination of divide ratios, avoiding integer boundary spurious products, as well as other spurious conditions.

The compact synthesizer module of Figure 8-42 (b) can generate 2-to-8-GHz outputs with a typical phase noise of -97 dBc/Hz offset 10 kHz from the carrier, and typical spurious performance of -50 dBc.

Figure 8-43 shows the typical phase-noise performance of the synthesizer for 2 GHz, 4 GHz, 6 GHz, and 8 GHz outputs. The topology can be used at standard and custom frequencies for X and Ka band applications using low noise VCO [128], saving the complexity and the compromised reliability of other reference source solutions. The Table 8-1 offers a summary of these results [153].

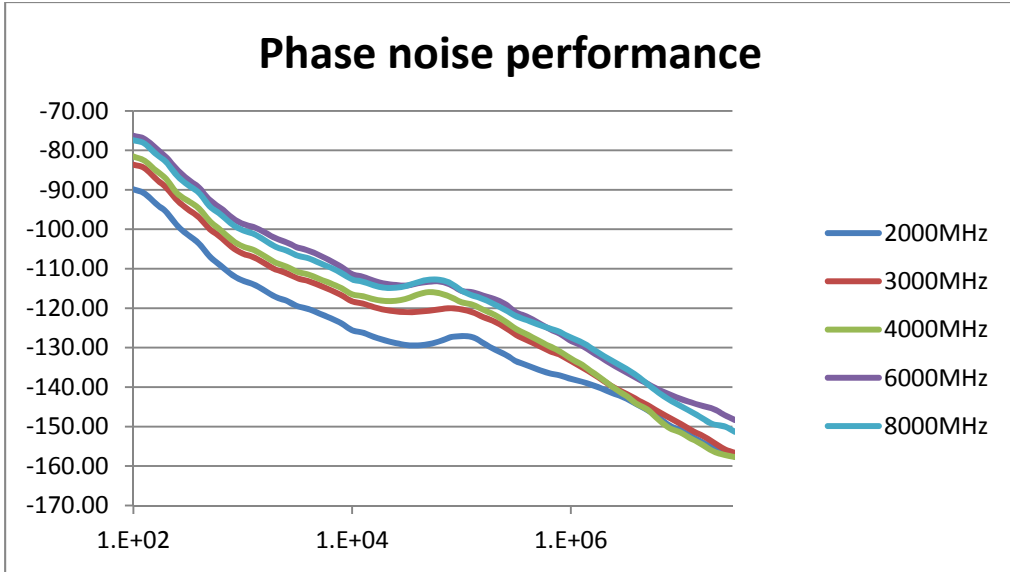


Figure 8-43: These plots show the phase noise of the DDS-based model KMTS2500-200800-10 synthesizer at four different carrier frequencies [142].

Table 8-1: Summary of the phase noise performance of KMTS2500-200800 [153]

PN [dBc/Hz]	KMTS2500-200800 (2000-8000MHz)				
Offset [Hz] ↓	2000MHz	3000MHz	4000MHz	6000MHz	8000MHz
100.00	-89.88	-83.64	-81.56	-76.32	-77.42
1000.00	-111.52	-104.51	-102.73	-97.01	-98.70
10000.00	-123.82	-116.66	-114.90	-109.51	-111.04
100000.00	-127.35	-119.99	-117.16	-114.05	-113.66
1000000.00	-137.05	-133.81	-131.95	-127.50	-126.04
10000000.00	-153.82	-153.78	-151.36	-145.79	-144.16

Figures 8-44, 8-45, 8-46, and 8-47 show the phase noise plot of 10.24 GHz synthesized signal source using novel 10.24 GHz oscillator using printed coupled resonator (slow-wave resonator, slow-wave metamaterial resonator, slow-wave mode-locked Möbius coupled metamaterial resonator, and using 128 MHz OCXO locked Möbius coupled DRO) for the application in modern Radar and communication systems. As shown in Figures 8-47, the measured phase noise @ 10 kHz offset is -139 dBc/Hz for 10.24 GHz carrier, which is best performance to date reported using this technique for a given size, power consumption and figure of merit (FOM).

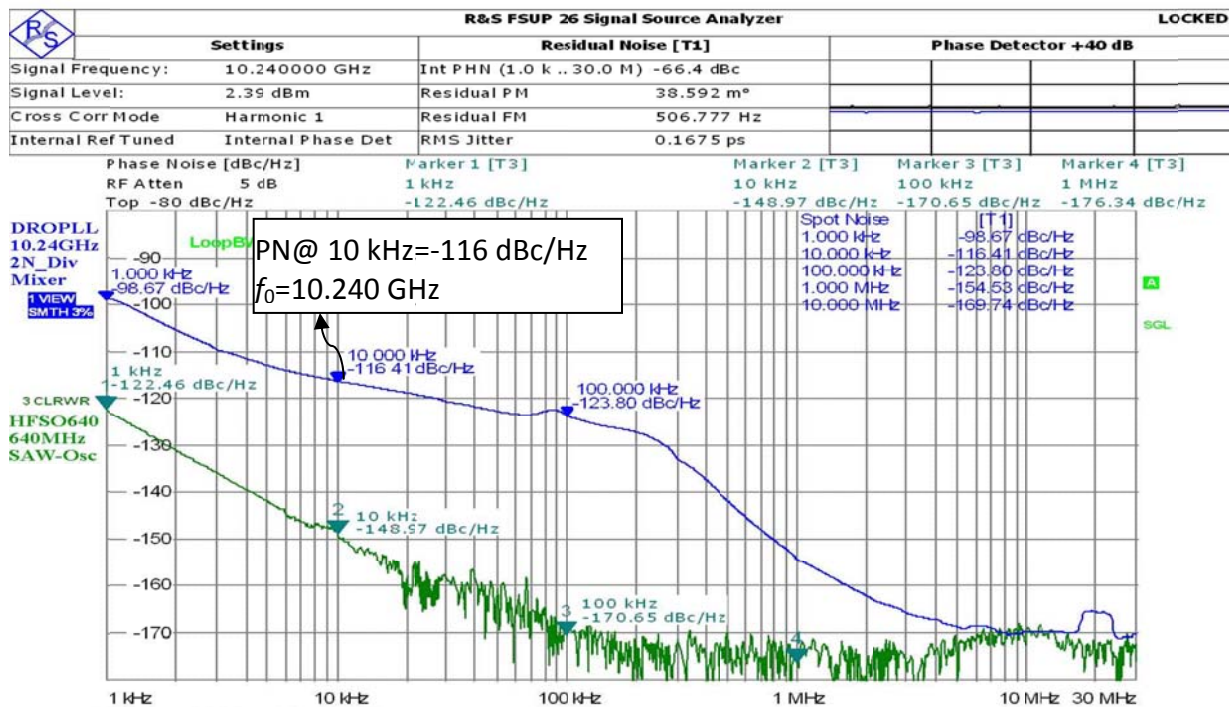


Figure 8-44: Measured phase noise of the 10.24 GHz synthesized signal source using slow-wave resonator

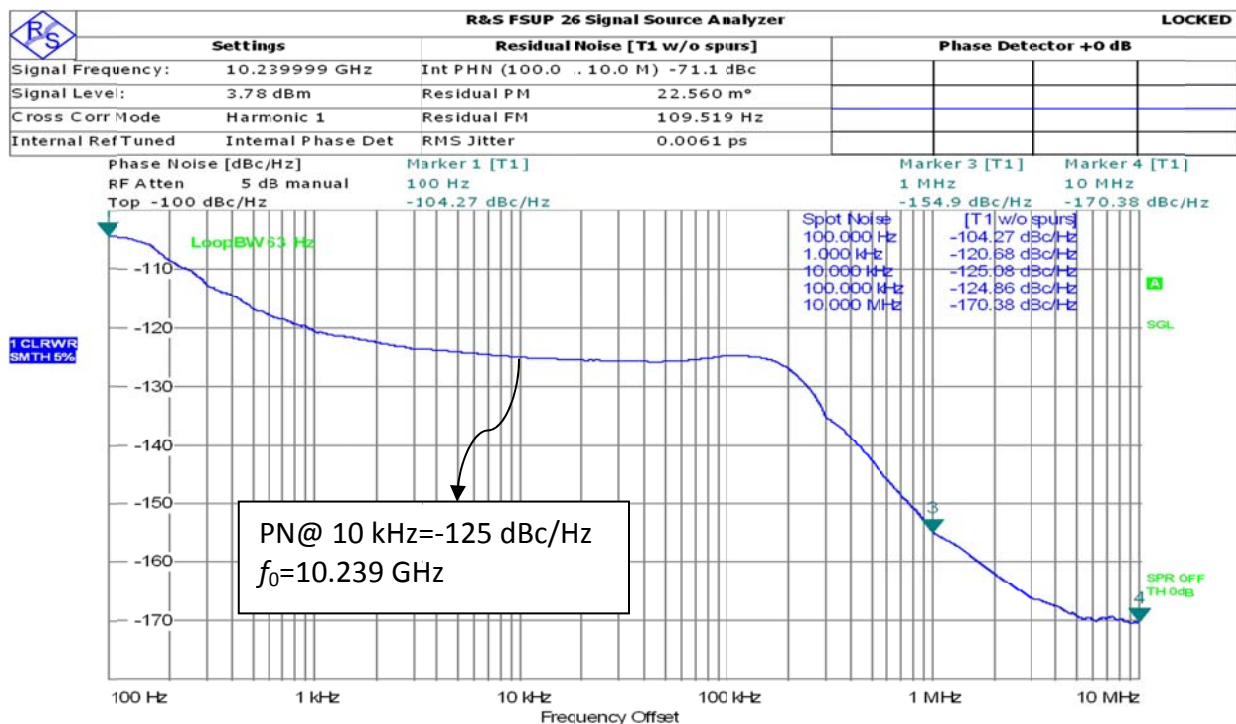


Figure 8-45: Measured phase noise of the 10.24 GHz synthesized signal source using slow-wave metamaterial resonator

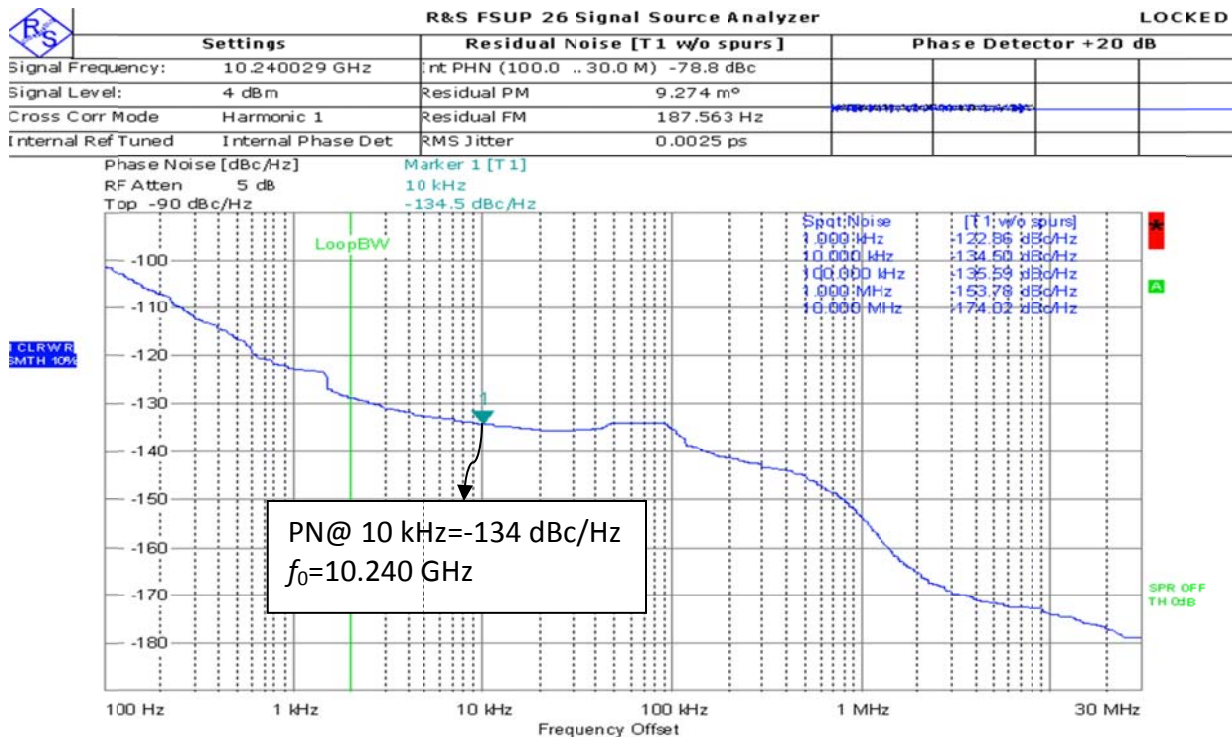
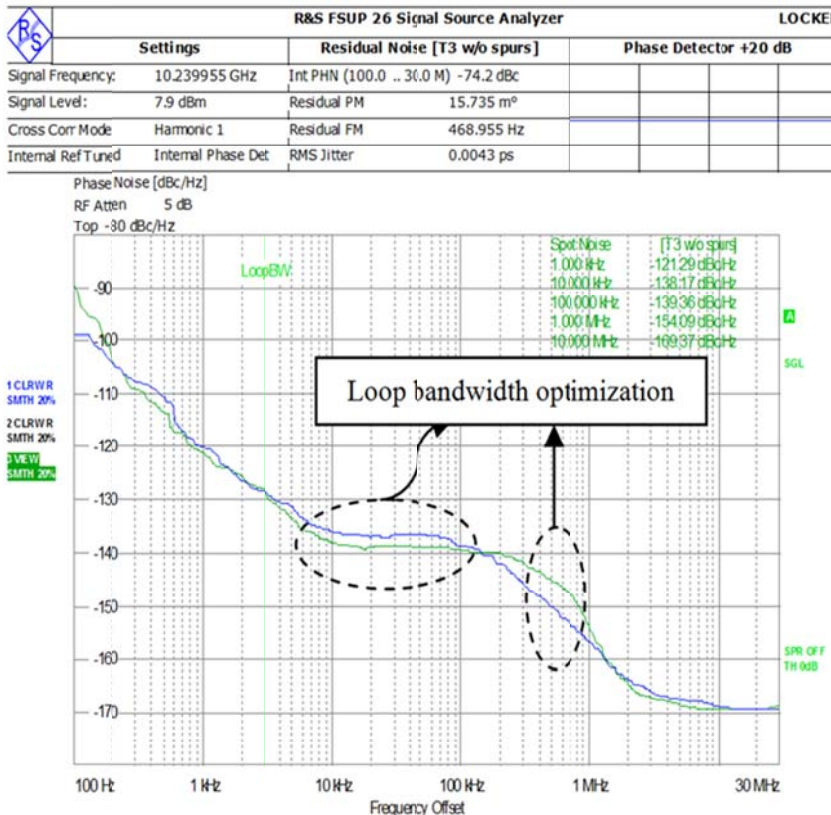


Figure 8-46: Measured phase noise of the 10.24 GHz synthesized signal source using slow-wave mode-locked Möbius coupled metamaterial resonator (uses 500 mW power consumption to produce 12 dBm output power)

The measured phase noise plots and prototype unit as shown in Figure 8-47 is an implementation of novel approach, providing a 10.24 GHz output signal with ultra low phase noise. The design locks a 10.24 GHz Möbius coupled 10.24 GHz VCO to the harmonics of an internal 128 MHz OCXO reference, using a low-noise PLL with double-balanced mixer serving as phase detector [153]. By using frequency multiplication from the reference, the noise performance required from the mixer and loop filter is relaxed by about 40 dB. The design employs low-noise operational amplifiers to achieve low noise levels. The advantages of this topology are: design is simple and small enabling small size packaging, performance over size ratio delivered by the architecture is very high, and architecture uses comparatively low cost components. The synthesizer was characterized with a model FSUP signal source analyzer from Rohde & Schwarz (www.rohde-schwarz.com). The synthesizer and test system were both placed inside a Faraday cage to minimize the effects of outside noise sources. The synthesizer produces typically +10 dBm signal at 10.239 GHz with 5V, 300 mA DC bias. The low-noise internal OCXO determines the synthesizer's performance for offset frequencies between 10 Hz and 1 kHz, with -70 dBc/Hz phase noise at 10 Hz offset, -122 dBc/Hz at 1 kHz offset, -139 dBc/Hz at 10 kHz offset. Above 1 MHz, the noise floor is -169 dBc/Hz. To achieve full-sized performance in miniature packages, this research work describes compact frequency synthesizers that leverage novel Möbius coupled slow-wave mode-coupled resonator (SWMCR) based (VCO) technology for the stability and low noise needed for emerging wideband, high-data-rate wireless communications systems. The hardware realization of phase-injection and mode-injection locked 10.24 GHz synthesizer is a part of futuristic development for the realization of lowest phase noise source for given costs and a class of synthesizer [153].



A typical measured phase noise plot of the 10.24 GHz synthesized signal source (lowest phase noise source reported for a given cost and FOM)



R&S FSUP 50: phase noise measurements

Figure 8-47: Measured phase noise of the 10.24 GHz synthesized signal source using OCXO locked slow-wave mode-locked Mobius coupled metamaterial resonator [153]

8.10 Conclusion

With the development of the MMIC fabrication techniques and the broad application of this artificial material, metamaterial technology is a promising alternative of high frequency planar VCO solutions. The mode-coupled slow-wave Metamaterial resonators' structure based oscillator reported in this chapter has the potential to make a dramatic impact on the design of tunable oscillator using Metamaterial resonator in compact size which otherwise cannot be achieved with conventional printed transmission line resonator. In this chapter, the use of metamaterial resonator structure is proposed for the design of compact high frequency planar VCO solutions.

Metamaterial resonator presents several advantages in comparison with conventional planar resonator, as for example [135]-[154]:

- High Q-factor
- Improved selectivity
- Easy integration in MIC/MMIC technologies
- Small dimensions and weight
- Multi-band characteristics
- Relatively insensitive to EMI and EMC

Figure 8-48 shows the CAD simulated S_{21} plots of metamaterial split-ring, Möbius strips, and Metamaterial Möbius strips resonator; fabricated on substrate material of dielectric constant of 2.2 and thickness of 12 mils [148]. As shown in Figure 8-48, Metamaterial Möbius strips (MMS) exhibits superior S_{21} characteristics resulting in improved Q-factor, suppresses the spurious resonance modes, therefore stable broadband operation as compared to metamaterial split rings and Möbius strips resonator that exhibits undesired second-order modes (marked: Blue trace-Möbius Strips; Green trace-Metamaterial Split-Rings). The typical oscillator layouts using these resonators (metamaterial split rings) shown in Figure 8-29 are sensitive to mode-jumping, causing reliability issues. To overcome mode-jumping issues and tuning problems, mode stabilization (manipulating the phase velocity by introducing *Mode-Suppression Ring* that allows multi-mode-self-injection into the Möbius Strips cavity, improves the stability) technique.

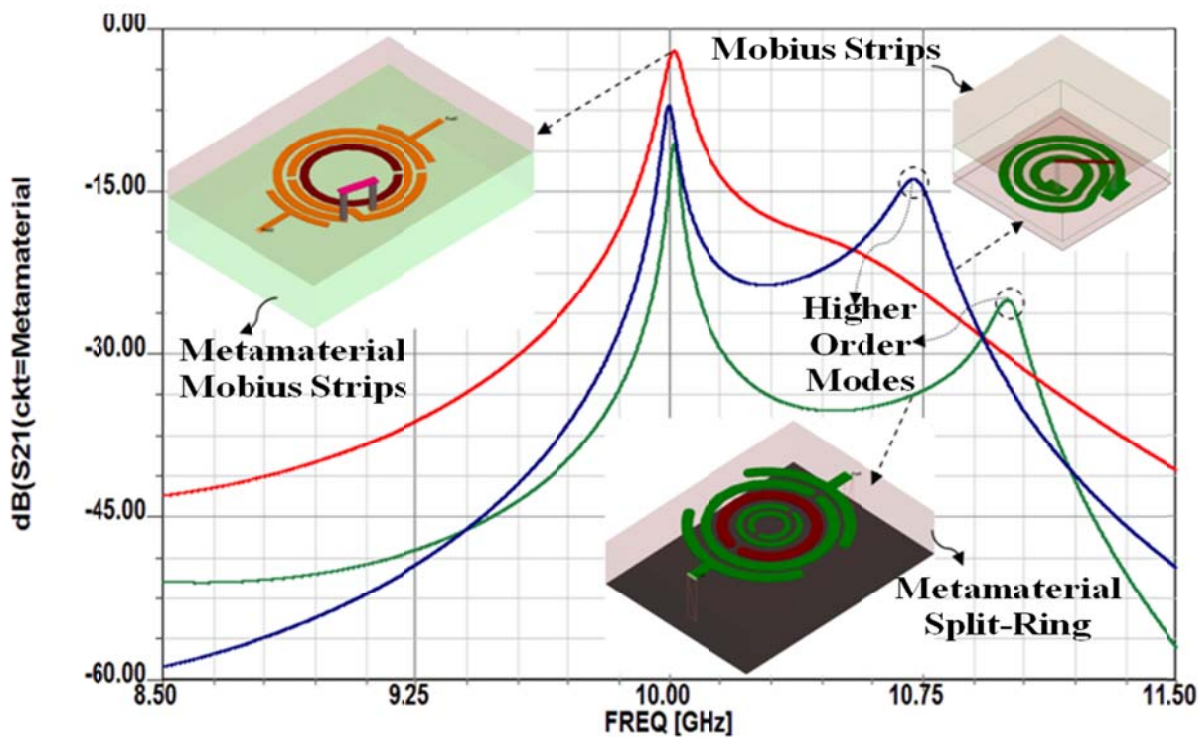


Figure 8-48: CAD simulated S_{21} plots in (dB): (a) Metamaterial split-rings, (b) Möbius strips, and (c) Metamaterial Möbius strips resonator networks [148]

A novel mode-coupled self-injection Metamaterials Möbius Strips resonator based tunable X-band oscillator for RADAR application is developed for high frequency signal sources applications [148]. Figures (8-49), (8-50), and (8-51) show the typical block diagram, layout, and measured phase noise plot of the 10.24 GHz oscillator using a SiGe Hetrojunction-bipolar-transistor (HBT) active device. Figure 8-51 shows the measured phase noise plot, offers superior $FOM = -216 \text{ dBc/Hz} @ 1\text{MHz}$ offset calculated from Eq. 1 given in ref [45]. The O/P power is 11.3 dBm, 500MHz tuning range with 5VDC and 80mA.

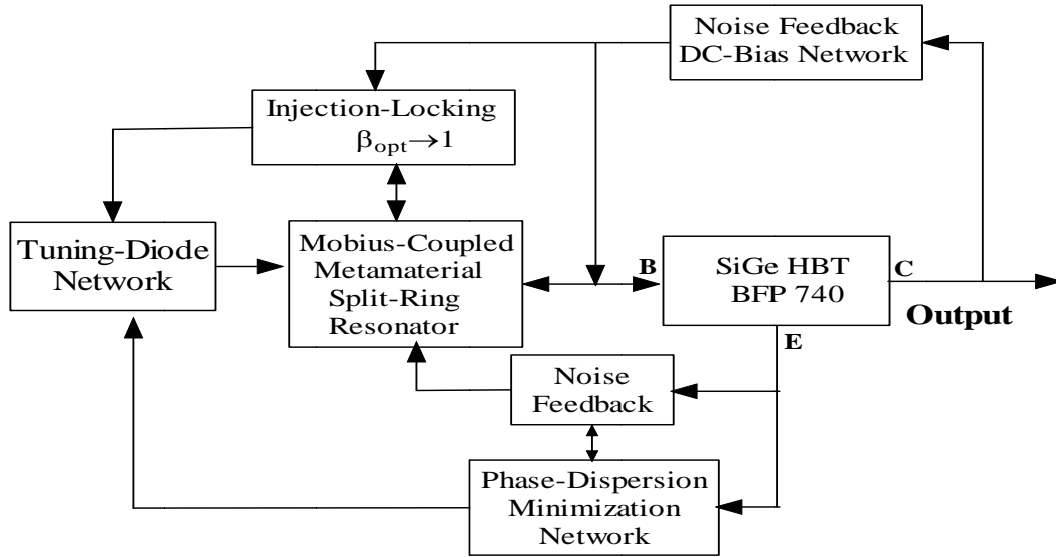


Figure 8-49: A typical block diagram of X-band Metamaterials Möbius Strips Resonator VCO [148]

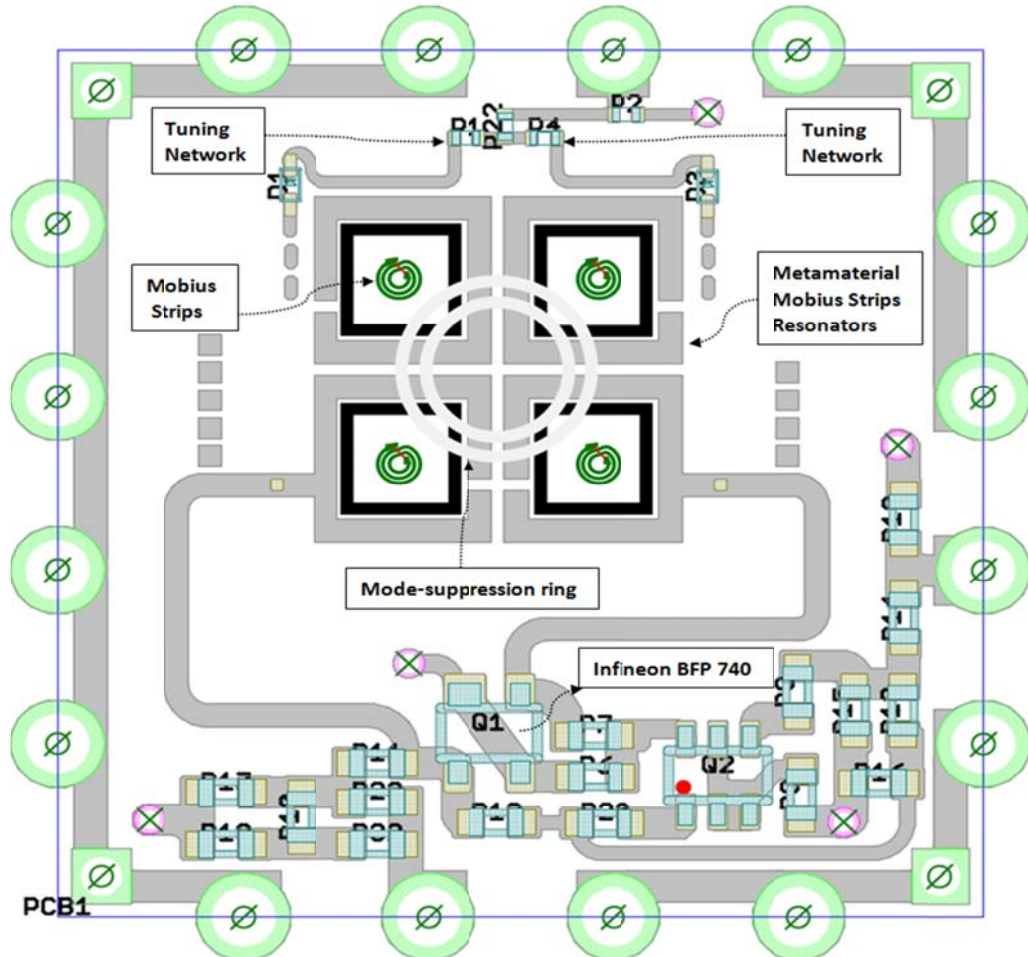


Figure 8-50: A typical layout of 10.24GHz Metamaterial Möbius VCO (0.9x0.9 in) [148]

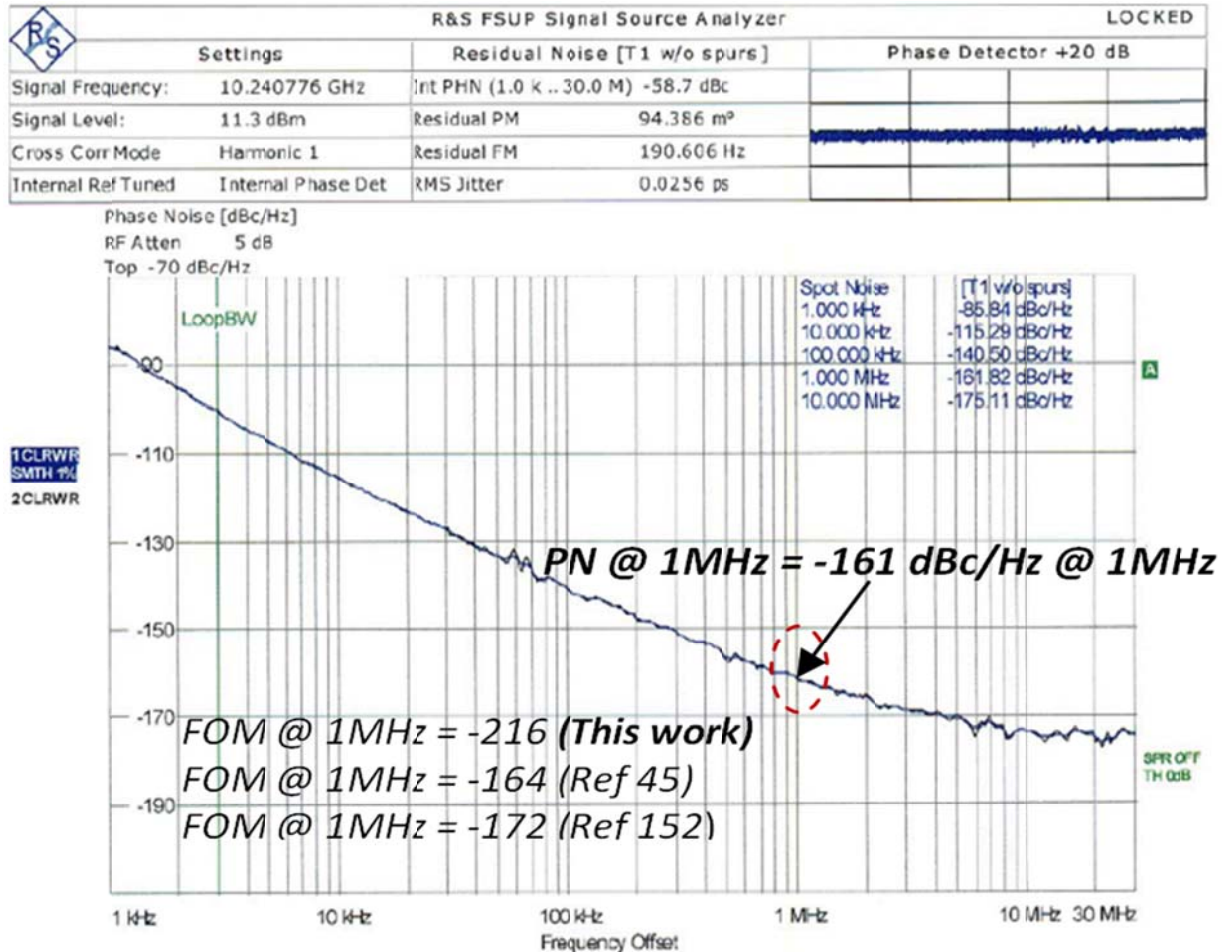


Figure 8-51: Measured phase noise plot of X-band Metamaterial Möbius VCO (oscillator layout is shown in Figure 8-48) [148]

As shown in Figure 8-50, realization of Metamaterial Möbius Strips using discrete components in planar domain is challenging task, therefore future work is in progress to develop integrated MMIC using current technologies.

8.11 References

- [1] Veselago, V.G, "The electrodynamics of substance with simultaneously negative values of ϵ and μ ", *Sov. Phys. Usp.*, 10, 509–514, 1968.
- [2] Pendry, J.B, Holden, A. J., Robbins, D.J., Stewart, W.J., "Magnetism from conductors and enhanced nonlinear phenomena", *IEEE Trans. Microw. Theory Tech.*, 47, 2075–2084, 1999.
- [3] Shelby R. A. Smith D.R., Schultz S., "Experimental verification of a negative index of refraction", *Science* 2001, 292, 77–79, 2001
- [4] Pendry, J.B. "Negative refraction makes a perfect lens." *Phys. Rev. Lett.* 2000, 85, 3966–3969, 2000
- [5] Jacob, Z.; Alekseyev, L.V.; Narimanov, E. "Optical hyperlens: Far-field imaging beyond the diffraction limit", *Opt. Express* 2006, 14, 8247–8256, 2006

- [6] Liu, Z.; Lee, H.; Xiong, Y.; Sun, C.; Zhang, X., "Optical hyperlens magnifying sub-diffraction-limited object", *Science* 2007, 315, 1686–1687, 2007
- [7] Smolyaninov, I.I.; Hung, Y.J.; Davis, C.C., "Magnifying superlens in the visible frequency range", *Science* 2007, 315, 1699–1701, 2007
- [8] Pendry, J.B.; Schurig, D.; Smith, D.R., "Controlling electromagnetic fields", *Science* 2006, 312, 1780–1782, 2006
- [9] Schurig, D.; Mock, J.J.; Justice, B.J.; Cummer, S.A.; Pendry, J.B.; Starr, A.F.; Smith, D.R., "Metamaterial electromagnetic cloak at microwave frequencies", *Science* 2006, 314, 977–980, 2006
- [10] C. W. Chettiar, U.K.; Kildishev, A.V.; Shalaev, V.M, "Optical cloaking with Metamaterials", *Nat. Photonics*, 1, 224–227, 2007.
- [11] Pendry, J.B. , "Metamaterials in the sunshine", *Nat. Mater.*, 5, 599–600, 2006.
- [12] Martin, F.; Falcone, F.; Bonache, J.; Marques, R.; Sorolla, M., "Miniaturized coplanar waveguide stop band filters based on multiple tuned split ring resonators", *IEEE Microw. Wirel. Compon. Lett.* 13, 511–513, 2003.
- [13] Joan, G.G.; Martin, F.; Falcone, F.; Bonache, J.; Baena, J.D.; Gil, I.; Amat, E.; Lopetegi, T.; Laso, A.G.; Iturmendi, A.M.; et al. , "Microwave filters with improved stopband based on sub wavelength resonators", *IEEE Trans. Microw. Theory Tech.*, 53, 1997–2006, 2005
- [14] Bonache, J.; Gil, I.; Joan, G.G.; Martin, F., "Novel microstrip bandpass filters based on complementary split-ring resonators", *IEEE Trans. Microw. Theory Tech.*, 54, 265–271, 2005.
- [15] Nanostructure Metamaterials, Directorate-General for research unit G3-Vlaue-added materials, EUR 24409 EN, 2010
- [16] R. A. Shelby, D. R. Smith, and S. Schultz., "Experimental verification of a negative index of refraction", *Science*, 292(5514):77-79, April 2001.
- [17] Hou-Tong Chen, John F. O'Hara, Antoinette J. Taylor, Richard D. Averitt, "Complementary planar terahertz Metamaterials" Optical Society of America, 2007
- [18] L.V. Hau, Optical information processing in Bose-Einstein condensates, *Nat Photon* 2, 451–453, (2008).
- [19] T. Baba, Slow light in photonic crystals, *Nat Photon* 2 465–473, (2008).
- [20] M. Notomi, E. Kuramochi, and T. Tanabe, "Large-scale arrays of ultrahigh-Q coupled nanocavities", *Nat Photon* 2, 741–747, (2008)
- [21] Xiao Wang, "Simulation of Simultaneously Negative Medium Metamaterials", Master of Science in Electrical Engineering" Falls Church, Virginia, 2009
- [22] George V. Eleftheriades, Omar Siddiqui, and Ashwin K. Iyer, "Transmission Line Models for Negative Refractive Index Media and Associated Implementations Without Excess Resonators", *IEEE MWCL*, Vol. 13, No. 2, Feb. 2003
- [23] A. K. Iyer and G. V. Eleftheriades, "Negative refractive index Metamaterials supporting 2-D waves," in *IEEE MTT-S Symp. Dig.*, vol. 2, Seattle, WA, pp. 1067–1070, June 2–7, 2002.
- [24] A. Grbic and G. V. Eleftheriades, "Experimental verification of backward-wave radiation from a negative refractive index metamaterial," *J. Appl. Phys.*, vol. 92, no. 10, July 2002.
- [25] J. B. Pendry, "Negative Refraction Makes a Perfect Lens", *Physical Review Letters*, Vol. 85, number 18, 30 October 2000

- [26] José Manuel Tapadas Alves, "Metamaterials with Negative Permeability and Permittivity: Analysis and Application", MS thesis, UNIVERSIDADE TÉCNICA DE LISBOA INSTITUTO SUPERIOR TÉCNICO, Oct 2010.
- [27] Mohsin Nawaz, "Low Impedance Wheel Resonators for Low Voltage and Low Power Applications", Dr.-Ing Dissertation, Technischen FakultÄat der UniversitÄat Erlangen-NÄurnberg, 2009
- [28] C. Caloz, T. Itoh "Electromagnetic Metamaterials", IEEE press, Wiley, Hoboken NJ, 2006.
- [29] A. Lai, T. Itoh, "Composite Right/Left-Handed Transmission Line Metamaterials", IEEE Microwave Magazine, pp.34-50, Sept.2004.
- [30] J. Pacheco, T. M. Grzegorczyk, B.-I.Wu, Y. Zhang, and J. A. Kong, "Power propagation in homogeneous isotropic frequency dispersive left-handed media", Phys. Rev. Lett., 89:257401, 2002.
- [31] A. Grbic and G. V. Eleftheriades, "Experimental verification of backward wave radiation from a negative refractive index metamaterial", J. Appl. Phys., 92(10):59305935, 2002.
- [32] L. Li, F. Xu, K. Wu, S. Delprat, 1. Ho, and M, Chaker, "Slow-Wave Line Coupler With Interdigital Capacitor Loading," IEEE Trans. Microwave Theory Tech., vol. 55, no. 11, pp. 2427-2433, November 2007,
- [33] Sun, S. and L. Zhu, "Guided-Wave Characteristics of Periodically Non uniform Coupled Microstrip Lines-Even and Odd Modes," IEEE Trans, Microwave Theory Tech., vol. 53, no. 4, pp. 1221-1227, April 2005.
- [34] Liu, Z. and R.M. Weikle, "A Compact Quadrature Coupler Based on Coupled Artificial Transmission Lines," IEEE Microwave Wireless Component Lett", vol. 15, no. 12, pp. 889-891, December 2005.
- [35] C. Caloz and T. Itoh, Electromagnetic Metamaterials: Transmission Line Theory and Microwave Applications, Wiley and IEEE Press, Hoboken, NJ, 2005.
- [36] T. Ueda, A. Lai, and T. Itoh, "Demonstration of negative refraction in a cutoff parallel-plate waveguide loaded with 2-D square lattice of dielectric resonators," IEEE Trans. Microwave Theory Tech., vol. 55, no. 6, pp. 1280-1287, Jun. 2007.
- [37] M. Zedler, P. Russer, and C. Caloz, "Circuital and experimental demonstration of a 3D isotropic LH metamaterial based on the rotated TLM scheme," IEEE-MTT Int'l Symp., Honolulu, HI, Jun. 2007.
- [38] F. F. He, K. Wu, W. Hong, L. Han, and X. Chen, "A low phase-noise VCO using an electronically tunable substrate integrated waveguide resonator," IEEE Trans. Microw. Theory Tech., vol. 58, no. 12, pp. 3452-3458, Dec. 2010.
- [39] C. Caloz and T. Itoh, "Electromagnetic Metamaterials: Transmission Line Theory and Microwave Applications", New York: Wiley, 2005.
- [40] S. Abielmona, H. V. Nguyen, and C. Caloz, "CRLH zeroth order resonator (ZOR): experimental demonstration of insensitivity to losses and to size," in Proc. Asia-Pacific Microw. Conf., pp. 657-662, Dec. 2006.
- [41] C. A. Allen, K. M. K. H. Leong, and T. Itoh, "Design of microstrip resonators using balanced and unbalanced composite right/left-handed transmission lines," IEEE Trans. Microw. Theory Tech., vol. 54, no. 7, pp. 3104-3112, July 2006.
- [42] J. D. Baena, J. Bonache, F. Martin, R. Marques, F. Falcone, T. Lopetegi, M. A. G. Laso, J. Garcia, I. Gil, and M. Sorolla, "Equivalent circuit models for split ring resonators and

- complementary split ring resonators coupled to planar transmission lines," *IEEE Trans. Microw. Theory Tech.*, vol. 53, no. 4, pp. 1451-1461, Apr. 2005.
- [43] Y. Dong and T. Itoh, "Miniaturized substrate integrated waveguide slot antennas based on negative order resonance," *IEEE Trans. Antennas Propag.*, vol. 58, no. 12, pp. 3856-3864, Dec. 2010.
- [44] C. Li, K. Y. Liu, and F. Li, "Composite right/left-handed coplanar waveguide bandpass filter using capacitively-coupled zeroth-order resonators," *Appl. Phys. A, Mater. Sci. Process.*, vol. 87, no. 2, pp. 317-319, May 2007.
- [45] Y. Dong and T. Itoh, "A dual-band oscillator with reconfigurable cavity-backed complementary split-ring resonator," in *IEEE MTT-S Int. Microw. Symp. Dig.*, Jun. 2012.
- [46] J. Choi, and C. Seo, "Broadband and Low Phase Noise VCO Using Tunable Metamaterial Transmission Line Based on Varactor-Loaded Split-Ring Resonator," Korea-Japan Microwave Conference, pp. 145-148, November 2007.
- [47] S. Im, C. Seo, Jaehoon Kim, Young-wan Kim, Naesoo Kim, "Improvement of microstrip open loop resonator filter using aperture," IEEE MTT-S International, vol.3, pp. 1801-1804, June 2002.
- [48] E. Park and C. Seo, "Low Phase Noise Oscillator Using Microstrip square Open Loop Resonator," IEEE MTT-S International Microwave Symposium, June 2006.
- [49] Young-Taek Lee, Jong-Sik Lim, Jun-Seok Park, Ahn, D.; Sangwook Nam, "A novel phase noise reduction technique In Oscillators using defected ground structure", IEEE Microwave and Wireless Components Letters, vol. 12, Issue: 2, pp.39-41, February 2002.
- [50] D. R. Smith, W. J. Padilla, D. C. Vier, S. C. Nemat-Nasser, and S. Schultz, "Composite Medium with Simultaneously Negative Permeability and Permittivity," Physical Review Letters, vol. 84, no. 18, pp. 4184-4187, May 2000.
- [51] D. R. Smith, P. Rye, D. C. Vier, A. F. Starr, J. J. Mock, and T. Perram, "Design and Measurement of Anisotropic Metamaterials that Exhibit Negative Refraction," IEICE Transactions on Electronics, vol. E87-C, no. 3, pp. 359-370, Mar. 2004.
- [52] R. Marqu'es, F. Medina, and R. Rafii-El-Idrissi, "Role of bi-anisotropy in negative permeability and left-handed metamaterial," Physical Review B, vol. 65, no. 14, p. 144440, Apr. 2002.
- [53] J. Cramer, "Dielectric Resonator Fabrication and Assembly Methods for Terahertz Metamaterials", PhD. Thesis, Univ. of Massachusetts Lowell, 2011
- [54] J. B. Pendry, A. J. Holden, W. J. Stewart, and I. Youngs, "Extremely Low Frequency Plasmons in Metallic Mesostructures," Physical Review Letters, vol. 76, no. 25, pp. 4773-4776, June 1996.
- [55] J. B. Pendry, A. J. Holden, D. J. Robbins, and W. J. Stewart, "Low frequency plasmons in thin-wire structures," Journal of Physics: Condensed Matter, vol. 10, no. 22, pp. 4785-4809, June 1998.
- [56] W. Rotman, "Plasma Simulation by Artificial Dielectrics and Parallel-Plate Media," IRE Transactions on antennas and Propagation, vol. 10, no. 1, pp. 82-95, Jan. 1962
- [57] N. Wiwatcharagoses, K. Y. Park, and P. Chahal, "A New Metamaterial Unit Cell for Compact Microstrip Circuit Designs" Electronic Components and Technology Conference, pp. 169-172, 2011.

- [58] J. Zhou, L. Zhang, G. Tuttle, T. Koschny, and C. M. Soukoulis, "Negative index materials using simple short wire pairs," *Physical Review B*, vol. 73, no. 4, p. 041101(R), Jan. 2006.
- [59] V. P. Drachev, W. Cai, U. Chettiar, H.-K. Yuan, A. K. Sarychev, A. V. Kildishev, G. Klimeck, and V. M. Shalaev, "Experimental verification of an optical negative index material," *Laser Physics Letters*, vol. 3, no. 1, pp. 49–55, Oct. 2006.
- [60] A. V. Kildishev, W. Cai, U. K. Chettiar, H.-K. Yuan, A. K. Sarychev, V. P. Drachev, and V. M. Shalaev, "Negative refractive index in optics of metal-dielectric composites," *Journal of the Optical Society of America B*, vol. 23, no. 3, pp. 423–433, Mar. 2006.
- [61] S. Zhang, W. Fan, N. C. Panoiu, K. J. Malloy, R. M. Osgood, and S. R. J. Brueck, "Experimental Demonstration of Near-Infrared Negative-Index Metamaterials," *Physical Review Letters*, vol. 95, no. 13, p. 137404, Sept. 2005.
- [62] S. Zhang, W. Fan, K. J. Malloy, S. R. J. Brueck, N. C. Panoiu, and R. M. Osgood, "Near-infrared double negative Metamaterials," *Optics Express*, vol. 13, no. 13, pp. 4922–4930, June 2005.
- [63] G. Dolling, C. Enkrich, M. Wegener, C. M. Soukoulis, and S. Linden, "Low-loss negative-index metamaterial at telecommunication wavelengths", *Optics Letters*, vol. 31, no. 12, pp. 1800–1802, June 2006
- [64] G. Dolling, C. Enkrich, M. Wegener, C. M. Soukoulis, and S. Linden, "Simultaneous Negative Phase and Group Velocity of Light in a Metamaterial," *Science*, vol. 312, no. 5775, pp. 892–894, May 2006.
- [65] G. Dolling, M. Wegener, C. M. Soukoulis, and S. Linden, "Negative-index metamaterial at 780 nm wavelength", *Optics Letters*, vol. 32, no. 1, pp. 53–55, Jan. 2007
- [66] J. Valentine, S. Zhang, T. Zentgraf, E. Ulin-Avila, D. A. Genov, G. Bartal, and X. Zhang, "Three-dimensional optical metamaterial with a negative refractive index," *Nature*, vol. 455, no. 7211, pp. 376–379, Sept. 2008.
- [67] Gustav Mie, "Beiträge zur Optik trüber Medien, speziell kolloidaler Metallösungen", *Annalen der Physik*, Vierte Folge, Band 25, 1908, No. 3, p 377-445.
- [68] Gustav Mie, "Contributions on the optics of turbid media, particularly colloidal metal solutions Translation", Sandia Laboratories, Albuquerque, New Mexico, 1978, SAND78-6018. National Translation Center, Chicago, ILL, Translation 79-21946.
- [69] L. Lewin, "The Electrical Constants of a Material Loaded With Spherical Particles," *The Proceedings of the Institution of Electrical Engineers*, vol. 94, pp. 65–68, 1947.
- [70] S. O'Brien and J. B. Pendry, "Photonic band-gap effects and magnetic activity in dielectric composites," *Journal of Physics: Condensed Matter*, vol. 14, no. 15, pp. 4035–4044, Apr. 2002.
- [71] C. L. Holloway, E. F. Kuester, J. Baker-Jarvis, and P. Kabos, "A Double Negative (DNG) Composite Medium Composed of Magneto dielectric Spherical Particles Embedded in a Matrix," *IEEE Transactions on Antennas and Propagation*, vol. 51, no. 10, pp. 2596–2601, Oct. 2003.
- [72] J. Baker-Jarvis, M. D. Janezic, D. Love, T. M. Wallis, C. L. Holloway, and P. Kabos, "Phase Velocity in Resonant Structures," *IEEE Transactions on Magnetics*, vol. 42, no. 10, pp. 3344–3346, Oct. 2006.
- [73] BAENA, J. D., BONACHE, J., MARTÍN, F., MARQUÉS, R., FALCONE, F., LOPETEGI, T., LASO, M. A. G., GARCÍA, J., GIL, I., SOROLLA, M. Equivalent circuit models for split ring

resonators and complementary split rings resonators coupled to planar transmission lines. *IEEE Transactions on Microwave Theory and Techniques*, vol. 53, pp. 1451-1461, 2005.

- [74] G. SISÓ, M. GIL, M. Aranda, J. Bonache, F. Martin," Miniaturization of Planar Microwave Devices by Means of Complementary Spiral Resonators (CSRs): Design of Quadrature Phase Shifters", RADIOENGINEERING, VOL. 18, NO. 2, JUNE 2009
- [75] M. Tiebout, "A CMOS fully integrated 1 GHz and 2 GHz dual band VCO with a voltage controlled inductor," in Proceeding of the IEEE European Solid-State Conference, pp. 799-802, 2002.
- [76] A. Goel and H. Hashrmi, "Frequency Switching in Dual-Resonance Oscillators," IEEE Journal of Solid-State Circuits, Vol. 42, No. 3, March 2007.
- [77] U. L. Rohde, A. K. Poddar, and G. Boeck, "Modern Microwave Oscillators for Wireless Applications: Theory and Optimization", Wiley, New York, 2005.
- [78] A. D. Berny, A. M. Niknejad, and R. G. Meyer, "A 1.8 GHz LC VCO with 1.3 GHz tuning range and digital amplitude calibration," IEEE Journal of Solid-State Circuits, Vol. 40. No. 4, pp. 909-917., 2005
- [79] U. L. Rohde, A. K. Poddar, "Low Noise, Low Power Consumption, Configurable, and Adaptable Ultrawideband VCOs," IEEE International Conference on Ultrawideband (ICUWB), ICUWB Conference proc. pp. 545-550, Sept. 2006.
- [80] A. Bavisi, "Integrated Multi-Mode Oscillators and Filters For Multi-Bnad Radios Using Liquid Crystalline Polymer Based Packaging Technology," Ph.D. thesis, Georgia Institute of Technology, Atlanta, GA, May 2006.
- [81] A. Ravi, B. R. Carlton, G. Banerjee, and K. Soumyanath, "A 1.4-V, 2.4/5.2-GHz, 90-nm CMOS system in a package transceiver for next generation WLAN," in IEEE Symposium On VLSI Technology, Digest of Technical Papers, IEEE, New York, 2005.
- [82] C. Lam and B. Razavi, "A 2.6/5.2 GHz frequency synthesizer in 0.4-{LC MU}m CMOS technology," in IEEE Journal of Solid-State Circuits, Vol. 35, pp. 788-790, May 2000.
- [83] B. Razavi, "RF Microelectronics", Prentice-Hall, Englewood Cliffs, NJ, 2nd edition, 1998.
- [84] M-S Yim and K. K. O., "Switched resonators and their applications in a dual band monolithic CMOS LC tuned VCO," IEEE Transactions on Microwave Theory & Techniques, Vol. 54, No. 1, pp. 74-81, January 2006.
- [85] B. Klepser, M. Punzenberger, T. Ruhlicke, and M. Zannoth, "5 GHz and 2.4 GHz dual-band RF-transceiver for WLAN 802.11a/b/g applications," in IEEE RFIC Symposium Digest Papers, pp. 37-40, 2003.
- [86] K. Araki et al., "Implementation and performance of a multi-band wireless configuration", pp. 207-210, 2004.
- [87] S. Wiggins, Introduction to Applied Nonlinear Dynamics and Chaos, Springer-Verlag, New York, 2nd edition, 1997.
- [88] B. van der Pol, "On oscillation hysteresis in a triode generator with two degree of freedom," Philosophy Magazine, Vol. 43, pp. 700-719, 1922
- [89] J. S. Schaffner, "Simultaneous oscillations in oscillators," IRE Transactions on Circuit Theory, Vol. 1, No. 2, pp. 2-8, June 1954.
- [90] T. Endo and S. Mori, "Mode Analysis of a multimode ladder oscillator," IEEE Transactions on Circuits & Systems, Vol. CAS-23, pp. 100-113, February 1976.

- [91] A. K. Poddar, "A Novel Approach for Designing Integrated Ultra Low Noise Microwave Wideband Voltage Controlled Oscillators," Dr.-Ing. Diss., TU- Berlin, Germany, Dec 2004.
- [92] U. L. Rohde, A. K. Poddar, and R. Rebel, "Integrated Low Noise Microwave Wideband Push-Push VCO," United States Patent No. 7,088189, August 2006.
- [93] I. Bruyland, "Simultaneous oscillations at two frequencies in RLC circuits," Proceedings of the IEEE, Vol. 1, pp. 82-83, January 1968.
- [94] A. K. Poddar, J. K. Bansal, and K. N. Pandey, "Millimeter Wave Evanescent Mode Power Combiner Gunn Oscillator in Suspended Stripline Configuration," Mathematical Methods in Electromagnetic Theory, IEEE/MMET, pp.384-386, June 1998.
- [95] N. Engheta, "Compact cavity resonators using metamaterials with negative permittivity and permeability", in Proc. Int. Conf. Electromagnetics in Advanced Applications (ICEAA), Torino, Italy, Sept. 2001, pp. 739-742.
- [96] U. L. Rohde and A. K. Poddar, "Tunable Frequency, Low Phase Noise and Low Thermal Drift Oscillator," United States Patent No. 7196591, March 2007.
- [97] A. Sanada, and I. Matsuda, "Experimental Verification of Surface Waves of Metamaterials ", IMS 2005, MTT-S Digest, pp. 1737-1740, 2005.
- [98] A. K. Poddar, S. K. Koul, and Bharthi Bhat, "Millimeter Wave Evanescent Mode Gunn Diode Oscillator c Wiley-Interscience, 1997
- [99] Paul P. Sotiriadis, "Exact Spectrum and Time-Domain Output of Flying-Adder Frequency Synthesizers", IEEE Transactions on Ultrasonics, Ferroelectrics, and Frequency Control, vol. 57, no. 9, September 2010.
- [100] U. L. Rohde and A. K. Poddar, "A Digital Frequency Synthesizer Using Adaptive Mode-Coupled Resonator Mechanism for Low Noise and Low Jitter Applications", IEEE International Symposium on Circuits and Systems (ISCAS), pp. 414-417, Brazil, May 15-18, 2011.
- [101] D. Calbaza and Y. Savaria, "A direct digital periodic synthesis circuit," *IEEE J. Solid-State Circuits*, vol. 37, no. 8, pp. 1039-1045, Aug. 2002.
- [102] U. L. Rohde and A. K. Poddar, "A Novel Low Cost High Performance Synthesizer", Proceedings of the IEEE EuMic, pp. 200-203, Oct 2011.
- [103] U. L. Rohde and A. K. Poddar, "A Novel High Frequency Synthesizer Using Adaptive Injection Mode-Coupled VCSO for Low Jitter and Low Noise Applications", Proceedings of 2011 Joint Conference of the IEEE International Frequency Control Symposium & European Frequency and Time Forum, pp. 452-457, May 2011
- [104] U. L. Rohde, A. K. Poddar, and G. Boeck, *Modern Microwave Oscillators for Wireless Applications: Theory and Optimization*, Wiley, NY, 2005.
- [105] W. Egan, "Frequency Synthesis by Phase Lock", John Wiley & Sons Inc., Hoboken, NJ 2000.
- [106] U. L. Rohde and A. K. Poddar, "Wideband voltage controlled oscillators employing evanescent mode coupled resonators," *US Patent No. 7,180,381* Feb 20, 2007 .
- [107] U. L. Rohde, A. K. Poddar, and R. Rebel, "Integrated Low Noise Microwave Wideband Push-Push VCO", *US Patent No. 7,088189*, Aug 2006.
- [108] U. L. Rohde and A. K. Poddar, "User-Definable Thermal Drift Voltage Controlled Oscillator", *US Patent No. 7,265,642 B2*, Sept 4, 2007.

- [109] U. L. Rohde and A. K. Poddar," Low Thermal Drift Tunable Frequency Voltage Controlled Oscillatory", US Patent No.7, 262,670 B2, Aug 28, 2007.
- [110] U. L. Rohde and A. K. Poddar," Tunable Oscillator", US Patent No.7, 292,113, Nov. 6, 2007.
- [111] U. L. Rohde and A. K. Poddar," Tunable Frequency, Low Phase Noise and Low Thermal Drift Oscillator", *US Patent No.7196591*, March 2007.
- [112] U. L. Rohde and A. K. Poddar, "Low Noise, Hybrid Tuned Wideband Voltage Controlled Oscillator", *US Patent No. 7,365,612 B2*, April 29, 2008.
- [113] U. L. Rohde and A. K. Poddar, "Tunable Frequency. Low Phase Noise and Low Thermal Drift Oscillator", U.S Patent NO. 7, 545, 229, June 09, 2009.
- [114] U. L. Rohde and A. K. Poddar, "User-Definable, Low Cost, Low Phase Hit and Spectral Pure Tunable Oscillator", U.S. Patent No. 7,586,381 on September 08, 2009.
- [115] U. L. Rohde and A. K. Poddar, "User-Definable, Low Cost, Low noise, and phase hit insensitive multi-octave-band tunable oscillator, Phase Hit and Spectral Pure Tunable Oscillator", U.S. Patent No. 7,605,670, October 20, 2009.
- [116] U. L. Rohde and A. K. Poddar, "Low Noise and Low Phase Hits Tunable Oscillator", U.S. Patent No. 7,636, 021, Dec. 22, 2009
- [117] U. L. Rohde and A. K. Poddar, "Wideband voltage controlled oscillators employing evanescent mode coupled resonators", Canadian Patent No. 2,563, 174, July 21, 2009.
- [118] U. L. Rohde and A. K. Poddar, "User-Definable Thermal Drift Voltage Controlled Oscillator", Canadian Patent No. 2,548, 317, April 21, 2009.
- [119] U. L. Rohde and A. K. Poddar, Integrated Low Noise Microwave Wideband Push- Push VCO, Canadian Patent No.:2,548, 311, April 14, 2009.
- [120] Low Noise VCOs product datasheet available at <http://www.synergymwave.com/products>
- [121] P. S. (Paul) Khanna, "Microwave Oscillators: The State of The Technology," *Microwave Journal*, pp. 22-42, April 2006.
- [122] A. Chenakin," Building a Microwave Frequency Synthesizer Part-2: Component Selection", *High Frequency Electronics*, pp. 18-26, 2008.
- [123] G. Gonzalez, "*Foundations of Oscillator Circuit*", Ch-IV, Artech House, Inc., London. 2007
- [124] A. Grebennikov, RF and Microwave Transistor Oscillator Design, John Wiley & Sons Ltd., UK, 2007.
- [125] J.K.A. Everard and L. Zhou. "Non Linear Effects in varactor tuned resonators" *IEEE Transactions on Ultrasonics Ferroelectrics and Frequency Control*, Vol. 53, No. 5, pp.853 – 861, May 2006
- [126] T.Ohira and K.Araki, "Active Q factor and equilibrium stability formulation for sinusoidal oscillators", *IEEE Trans.Circuits and Systems Pt II*, vol.54, no.9, pp.810-814, 2009
- [127] J-C. Nallatamby, M. Prigent, M. Camiade, and J.J. Obregon,"Extension of the Leeson formula to phase noise calculation in transistor oscillators with Complex tanks," *IEEE Trans. Microwave Theory Tech.*, vol. 51, issue 3, pp. 690-696, March 2003.
- [128] W. Egan," Frequency Synthesis by Phase Lock", Juhn Wiley & Sons Inc., Hoboken, NJ 2000.

- [129] S. Pamarti and S. Delshadpour, "A spur elimination technique for phase interpolation-based fractional-N PLLs," *IEEE Trans. Circuits Syst. I, Reg. Papers*, vol. 55, no. 6, pp. 1639-1647, Jul. 2008.
- [130] Y. Sun, *et al.*, "Dual-path LC VCO design with partitioned coarsetuning control in 65nm CMOS," to appear in *IEEE MWCL*, Mar. 2010.
- [131] X. Yu *et al.*, "A fractional-N frequency synthesizer with customized noise shaping for WCDMA/HSDPA applications," *IEEE JSSC*, vol. 44, pp. 2193-2201, Aug. 2009.
- [132] T. Wu, P. Hanumolu, K. Mayaram, and U. Moon, "A 4.2 GHz PLL frequency synthesizer with an adaptively tuned coarse loop," in *Proc. IEEE CICC*, pp. 547-550, Sept. 2007.
- [133] A. Chenakin, " Frequency Synthesis: Current SolutionsAnd New Trends", *Microwave Journal*, pp. 256-266, May 2007.
- [134] J. Browne, " Frequency Synthesizers Tune Communication Systems, " *Microwaves & RF*, March 2006.
- [135] Ulrich L. Rohde, Ajay K. Poddar, " Synthesizers Shave Size and Noise", *Microwave & RF*, PP. 132-164, May 2012
- [136] S.-G. Mao, M.-S. Wu, Y.-Z. Chueh, and C. H. Chen, "Modeling of symmetric composite right/left-handed coplanar waveguides with applications to compact bandpass-filters," *IEEE Trans. Microw. Theory Tech.*, vol. 53, no. 11, pp. 3460-3466, Nov. 2005.
- [137] A. K. Poddar, U. L. Rohde, "A Novel Metamaterial Resonator Based Signal Sources for applications in current and later generation radio communication systems", *IEEE BenMAS 2014*, Drexel Univ, Philadelphia
- [138] A. Apte, V. Madhavan, A. Poddar, U. Rohde, T. Itoh, "A Novel Low Phase Noise X-band Oscillator", *IEEE BenMAS 2014*, Drexel Univ, Philadelphia
- [139] Jiangpeng et al, "Metamaterial Extebds Microstrip Antenna", *Microwavws & RF*, PP. 69-73, Dec 2013
- [140] Benmostefa et al, "Metamaterials Form Miniature Bandstop Filters", *Microwavws & RF*, PP. 69-73, 2012
- [141] Katko et al, "Time-varying transistor-based metamaterial for tunability, mixing, and efficient phase conjugation", *Journal of Applied Physics* , Vol 115, Issue 14, pp. 144501 – 144506, , 2014
- [142] Tupin et al, "Near-Zero-Index Metamaterial Lens Combined With AMC Metasurface for High-Directivity Low-Profile Antennas", *IEEE Transactions on AP-S*, Volume: 62 , Issue: 4 , Part: 2 pp. 1928–1936, 2014
- [143] M. Gupta, J. Saxena, "Superdirective patch antenna array using metamaterial", 2014 *IEEE International Conference on Electronics, Computing and Communication Technologies (IEEE CONECCT)*, pp. 1 – 6, 2014
- [144] N. Engheta, " An Idea for thin subwavelength cavity resonators using metamaterials with negative permitivity and permeability", *IEEE Antenna and Wireless Propagation Letters*, Vol. 1, pp. 10-13, 2002.
- [145] A. K. Poddar. U. L. Rohde, "Metamaterial Möbius Strips (MMS): Application in Resonators for Oscillators and Synthesizers", *IEEE UFFC Symposia*, May 19-22, 2014
- [146] A. K. Poddar. U. L. Rohde, "The Pursuit for Low Cost and Low Phase Noise Synthesized Signal Sources: Theory & Optimization", *IEEE UFFC Symposia*, May 19-22, 2014

- [147] A. K. Poddar. U. L. Rohde, "Evanescence-Mode Phase-Injection Mode-Coupled (EMPIMC) Metamaterial Resonator Based Tunable Signal Sources ", IEEE Wamicon , June 06, 2014.
- [148] A. K. Poddar. U. L. Rohde, T. Itoh", Metamaterial Möbius Strips (MMS): Tunable Oscillator Circuits", IEEE MTT-S Digest, pp. 1-4, June 2014
- [149] Chung-Tse M. Wu, A. K. Poddar. U. L. Rohde, T. Itoh, "A C-band Tunable Oscillator Based on Complementary Coupled Resonator using Substrate Integrated Waveguide Cavity " EuMW 2014
- [150] Li Zhang, U A. K. Poddar. U. L. Rohde, and A. S. Daryoush, "*Oscillator Phase Noise Reduction Using Self-Injection Locked and Phase Locked Loop (SILPLL)*", IEEE IFCS, May 2014
- [151] Chung-Tse M. Wu A. K. Poddar. U. L. Rohde, T. Itoh, Active Complementary Coupled Resonator for Low Phase Noise X-band Oscillator ", 2014 European Frequency and Time Forum, Neuchâtel, Switzerland from June 23 – 26, 2014
- [152] W. Fei Shang et. al, "a 96-GHz oscillators by high Q-Differential Transmission Line Loaded with Complementary Split-Ring Resonator in 65-nm CMOS. IEEE Trans. on Circuits and Systems-II, Express Briefs, Vol.60, No.3, pp. 127-131, March 2013
- [153] A. K. Poddar, U. L. Rohde, "The Pursuit for Low Cost and Low Phase Noise Synthesized Signal Sources: Theory & Optimization", IEEE UFFC Symposia, May 19-22, 2014
- [154] Chun-Tse Michael Wu, " Active Integrated Metamaterial-Based Antennas and Microwaves Components" , PhD Thesis June 2014, Department of Electrical Engineering, University of California, Los Angeles.

Chapter 9

High Performance X-band Oscillators

9.1 Introduction

Phase noise can be a limiting factor in modern communications systems, especially those that rely on phase-based modulation. Phase noise can increase the bit error rate (BER) of a telecommunications link, degrade the stability of beams in particle accelerators, and degrade the sensitivity of radar systems [1].

The high quality factor (Q) of a dielectric resonator makes it possible to achieve oscillators with excellent phase-noise performance at microwave and millimeter wave frequencies. Dielectric resonators are fabricated on ceramic materials with high dielectric permittivity, high Q , and high temperature stability. They have much smaller size compared to cavity resonators; therefore, these resonators are frequently employed in the design of frequency stable RF circuits, especially in oscillators [2]-[5]. When high data rates must be transferred as with multiple quadrature amplitude modulation (M-QAM) schemes in Long-Term-Evolution (LTE), local multipoint distribution service (LMDS), and fixed-frequency point-to-point digital radios and satellite-communications (SATCOM) links, such systems rely on free-running or phase-locked signal sources with ultra-low phase noise performance. Such spectrally pure sources are also invaluable for radar systems and in research laboratories [6]-[23].

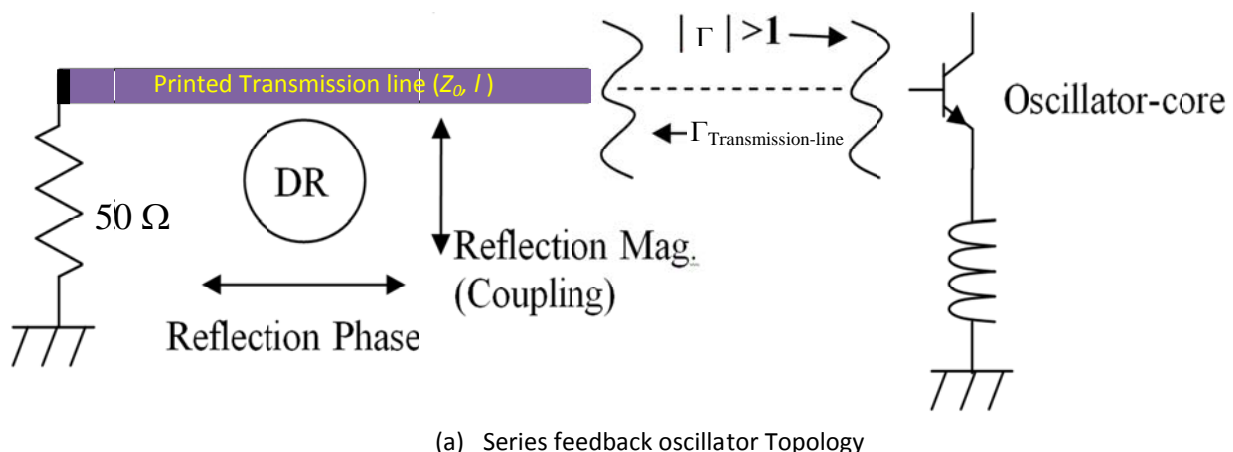
A wide range of military, industrial, medical, and test-and-measurement markets demand stable frequency sources with low phase-noise performance and low thermal drift. Dielectric resonator oscillators (DROs) have provided low-noise solutions in the frequency range from 3 to 40 GHz, with spectral purity that compares favorably to other competing solutions such as multiplied frequency fundamental sources [24]-[29].

9.2 DRO Circuit Topology

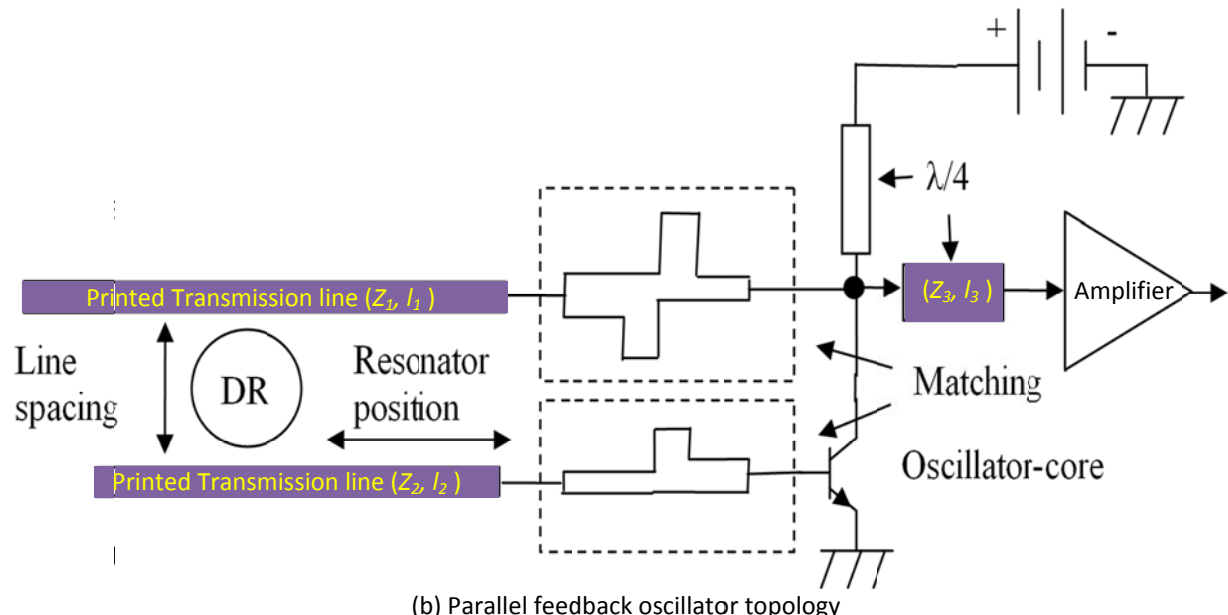
A typical DRO circuit uses high- Q dielectric resonator (DR) and active device in a series/parallel feedback configuration to achieve the negative resistance required for stable oscillations showed in Figure 9-1 [8, 30]. The series feedback DRO (Figure 9-1(a)) is the most common type of DRO mainly because it is easy to handle than the feedback type once the oscillator-core exhibits the required reflection-gain at the resonant frequency [25]. The oscillator core consists of an active device the input port of which does present a reflection coefficient of magnitude >1 to the connected resonator arrangement. The latter is simply formed by the Dielectric Resonator (DR) placed in close proximity to a microstrip line terminated with its characteristic impedance (reaction type resonator) as shown in Figure 9-1(a). Adjustment of phase is done by moving the DR along the line at constant distance and adjustment of reflection magnitude and thus level of oscillation can be done by varying the distance between line and DR [24].

Figure 9-1(b) shows the typical parallel feedback (transmission type) DRO circuit, constructed by a set of two microstrip parallel lines mutually coupled through the interaction with a DR placed between them (transmission type resonator). The transmission lines do not require a

resistive termination. In order to achieve a high Q_L it is rather preferable to use reactive terminations instead i.e. open stubs the lengths of which constitute two additional degrees of freedom. In addition to that matching structures interfacing the oscillator core's in- and output are required to maximize the loaded Q and at the same time establish the necessary round trip phase shift of $2\pi \cdot n$ (integer n) at the target frequency. An appropriate quarter wave transformer between oscillator-core and post-amplifier may be required in order to achieve optimum performance. Since the available layout area is limited in most cases, it is desirable to have fixed positions for the resonator as well as for the core terminals. Therefore a combination of stub matching-elements and meander lines are used to realize arbitrary matching and phase shift while maintaining the mechanical length of the structures [9]-[11].



(a) Series feedback oscillator Topology



(b) Parallel feedback oscillator topology

Figure 9-1 A typical DRO circuit: (a) Series feedback (Reflection type), and (b) parallel feedback (Transmission type)

9.3 Dielectric Resonator (DR)

The DR is typically a piece of a dielectric material (usually manufactured in a circular shape such as a disk or cylinder) with very high (much higher than 1) relative dielectric constant, ϵ_r , that acts like a resonant cavity by means of reflections at the dielectric/air interface. The DR can resonate in a number of modes and frequencies depending on the type of material, dimensions, and the proximity and shapes of enclosures [12].

Figure 9-2 shows a typical DR in a polar coordinate system the magnetic wall at $\rho = a$ used for providing insight into possible resonant conditions for a given physical dimension, such as L , the length of the DR, and a , the radius of the DR [13, 28]. It can be shown that by matching the tangential fields at the resonator (dielectric/air) interface, at $|z| = L/2$ it is possible to derive following expression [14]

$$A \cos\left(\frac{\beta L}{2}\right) = Be^{-\alpha \frac{L}{2}} \quad (9.1)$$

$$-\frac{jA}{Z_d} \sin\left(\frac{\beta L}{2}\right) = \frac{B}{Z_a} e^{-\alpha \frac{L}{2}} \quad (9.2)$$

$$Z_d = \frac{\omega \mu_0}{\beta}, \quad (Z_d : \text{wave impedance within the dielectric}) \quad (9.3)$$

$$Z_a = \frac{j\omega \mu_0}{\alpha}, \quad (Z_a : \text{wave impedance within the air}) \quad (9.4)$$

where α and β are the imaginary and real propagation constants.

From (11.1) and (11.2) [28]

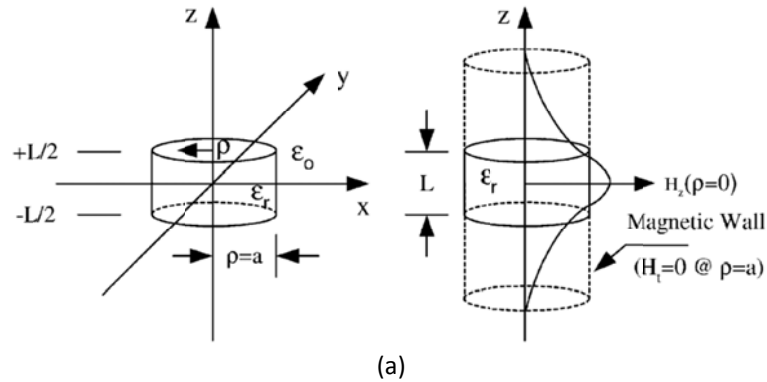
$$-jZ_a \sin\left(\frac{\beta L}{2}\right) = Z_d \cos\left(\frac{\beta L}{2}\right) \Rightarrow \tan\left(\frac{\beta L}{2}\right) = \frac{\alpha}{\beta} \quad (9.5)$$

By solving the transcendental equation (9.5), resonant frequency (f_0), length (L), and radius (a) of the DR is given by [28]

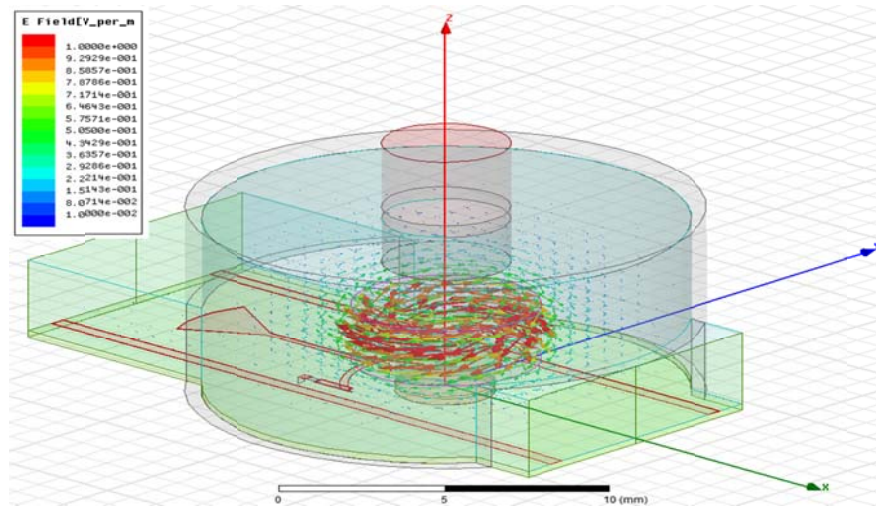
$$\tan\left[\frac{L}{2} \left(\epsilon_r \left(\frac{2\pi f_0}{c} \right)^2 - \left(\frac{2.405}{a} \right)^2 \right)^{0.5}\right] = \left[\frac{\left(\frac{2.405}{a} \right)^2 - \left(\frac{2\pi f_0}{c} \right)^2}{\epsilon_r \left(\frac{2\pi f_0}{c} \right)^2 - \left(\frac{2.405}{a} \right)^2} \right]^{0.5} \quad (9.6)$$

Where L is the length of DR, a radius, ϵ_r is the relative permittivity, and c is the speed of light.

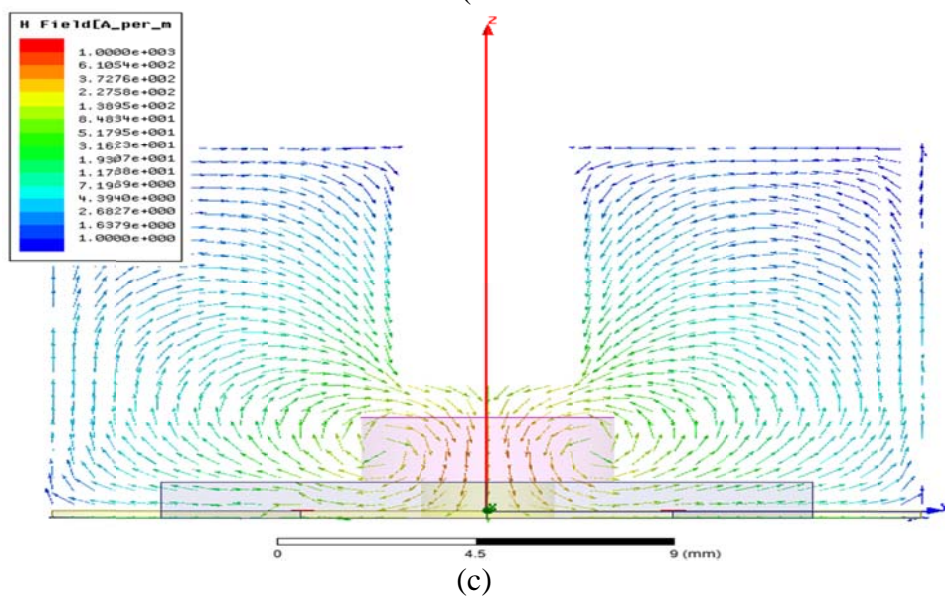
From (9.6), the transcendental equation yields two possible solutions for resonant wavelength, λ but only one of these is valid in yielding a deterministic solution within the dielectric (λ_{er}) and air (λ_{eo}) [2].



(a)



(b)



(c)

Figure 9-2: Shows the typical dielectric disc resonator characteristics : (a) DR TE₀₁₀ mode and H_z field distribution, (b) HFSS CAD simulation, TE₀₁₀ E-Field vector-plot (normalized) generated from an Eigen mode solution of a DR-assembly within a conductive cavity, and (c) H Field vector plot of the TE₀₁₀ resonant mode in YZ-plane (logarithmic scaling) [27]

As shown in Figure 9-2(a), an approximate frequency formula for commonly used $TE_{01\delta}$ mode with about 2% accuracy within the ranges indicated is given by [2]

$$f_{res} = \frac{68}{D \times \sqrt{\epsilon_r}} \left(\frac{D}{2L} + 3.45 \right) (\text{GHz}), \quad 0.5 < \frac{D}{2L} < 2; \quad 30 < \epsilon_r < 50 \quad (9.7)$$

where D denotes the DR diameter and L its length (both in mm).

A closed conductive containment for the DR-assembly leaving openings for the ports only is recommended otherwise the unloaded quality factor (Q_u) would be diminished by radiation loss. Since the proximity of the surrounding matter does alter the boundary conditions to some degree the resonant frequency is shifted upwards in case of metal (conductive) proximity and downwards in case of dielectric proximity for the $TE_{01\delta}$ mode [15].

The determination of the Eigen modes of the complete resonator arrangement (DR and cavity) using CAD tool (3D-EM HFSS from Ansys; www.ansys.com) allows for verification and adjustment of the geometrical parameters of the DR, and tuning elements for a desired resonant frequency while at the same time identification of unwanted modes (modes in the vicinity of the desired one) and also giving estimation for Q_u .

Designing and building low phase noise oscillator circuits based on DRs is not trivial, given the nonlinear nature of the active devices needed for the oscillators as well as the tedious task of placement of the puck and disk resonator [16]. The parallel feedback topology shown in Figure 9-1(b) offers more than six degrees of freedom plus the additional parameters of the matching networks, makes suitable for production.

9.4 Design Methodology of Parallel Feedback 10 GHz DRO Circuit

In this section, design steps are discussed for dielectric resonator oscillators (DROs) that can deliver stable signals at microwave through millimeter-wave frequencies.

With the aid of a unique Möbius coupling mechanism, these fundamental-frequency dielectric-resonator oscillators operate through 10 GHz with extremely low phase noise.

Design Steps:

- (i) Figure 9-3 illustrates the typical layout component with resonator interface and matching structures. The upper matching section between resonator and gain element is split to create a fixed (e.g. 50Ω) impedance level between them to allow arbitrary phase shift to be inserted (meandered if necessary) without changing the outer impedances. Additionally this allows access to an open loop S-parameter simulation and optimization. In order to simplify the process further, the matching process is treated separately and variable reference impedances are used instead at the oscillator-core's input and the resonator-element's output respectively.
- (ii) The lower section is a cascade of a stub-matching element and a 180° meandered transmission line allowing for adjustment of the mechanical length while maintaining the reflection coefficient of the oscillator core's output.

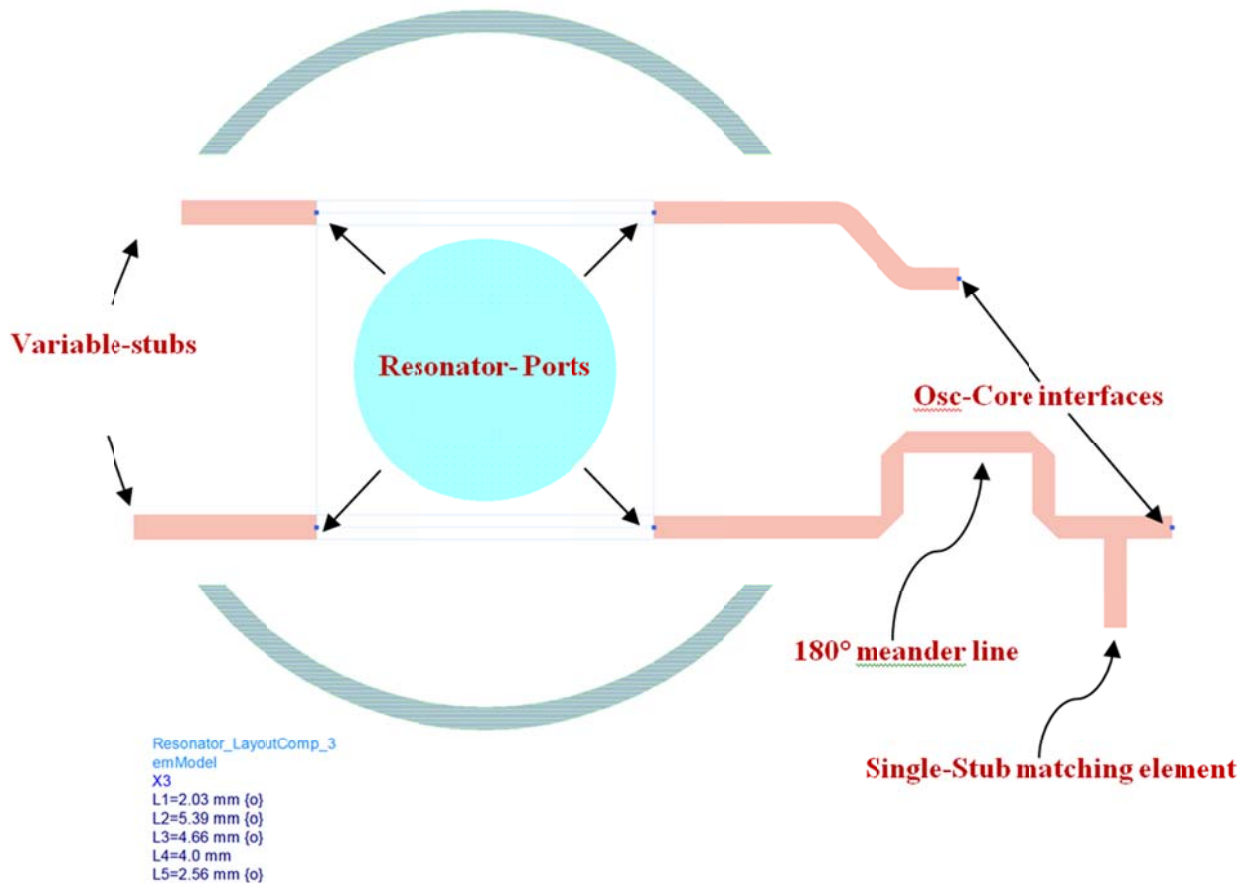


Figure 9-3: A typical layout component with resonator interface and matching structures

- (iii) Using CAD tool (ADS 2013 from Agilent; www.home.agilent.com) a layout-component is created with ports interfacing the resonator and the gain-element. In order to speed up the optimization-process microstrip library elements only are used and a synchronized schematic (i.e. analytical) model created. This allows a coarse optimization to be conducted using the analytical representation and a subsequent fine optimization using EM co-simulation. This may save significant computational effort if the differences between the two representations are rather small which unfortunately is not guaranteed depending on the actual situation and frequency.
- (iv) Figure 9-4 shows the 4-port 3D dielectric disk resonator model with port reference (shown for port 1) de-embedded to the actual interface positions. The resonator's S-parameters are taken from the results of a 4-port model 3D-EM simulation (Figure 9-5). The reference positions of the four ports required to match the corresponding positions in the layout component. The effect of the two tuning varactors has been modeled by voltage dependent lumped boundary conditions at their respective places, the tuning voltage being an additional parameter of the HFSS-model.

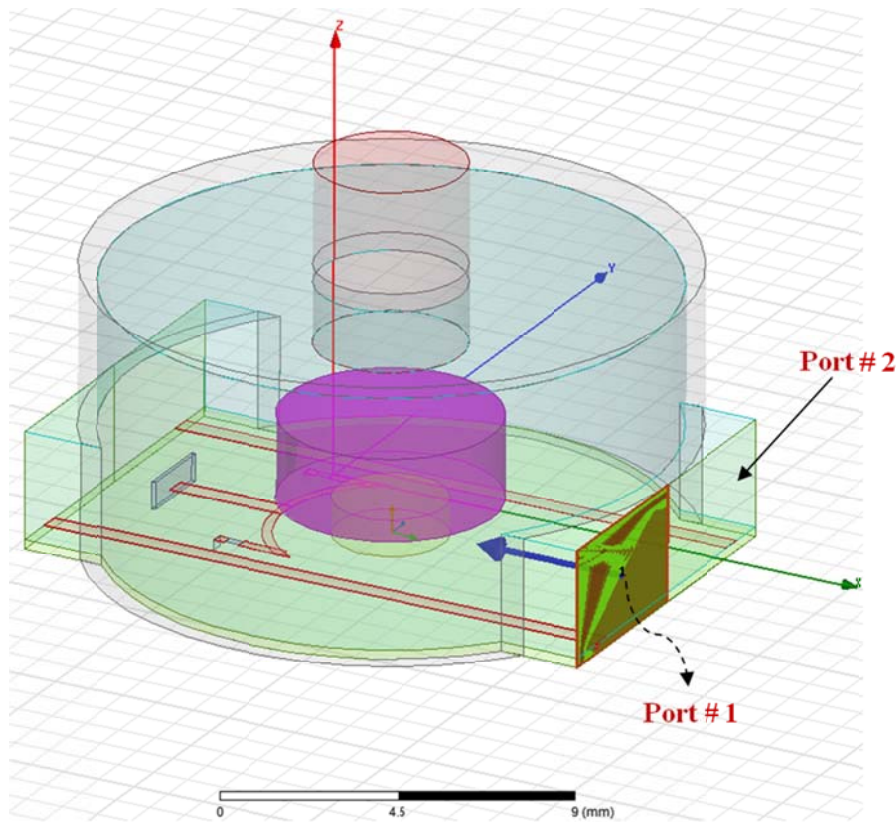


Figure 9-4: 4-port 3D resonator model with port references (shown for port1) de-embedded to the actual interface positions.

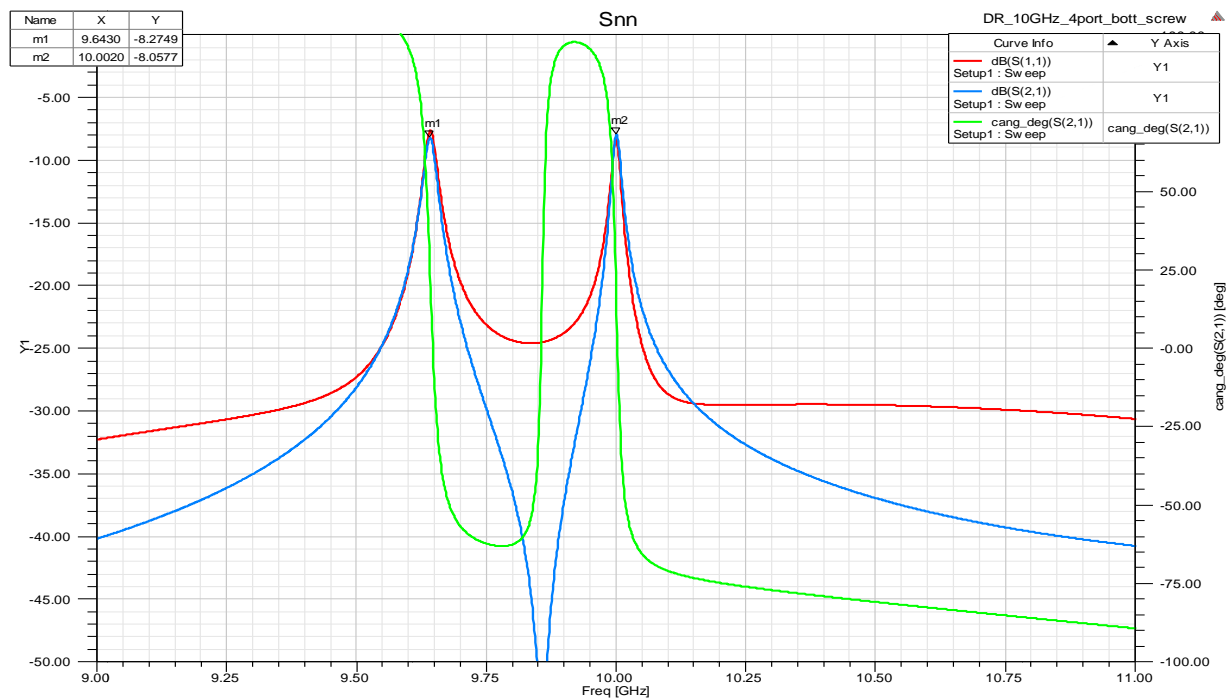


Figure 9-5: S₁₁ magnitude (red) and S₂₁ magnitude (blue) and phase (green) of the 4-port model above for a tuning voltage of 7 V.

- (v) Figure 9-6 shows the typical oscillator core model including bias stabilization circuitry consisting of the layout component for EM co-simulation, models for the gain element, the bias-stabilization transistors and additional lumped components. The oscillator core consists of a BFP740 transistor (from Infineon) in common emitter configuration and a bias-stabilization circuitry. The planar EM co-simulation is utilized in conjunction with substrate and pad scalable lumped component models from Modelithics as well as calibrated internal ports for them.

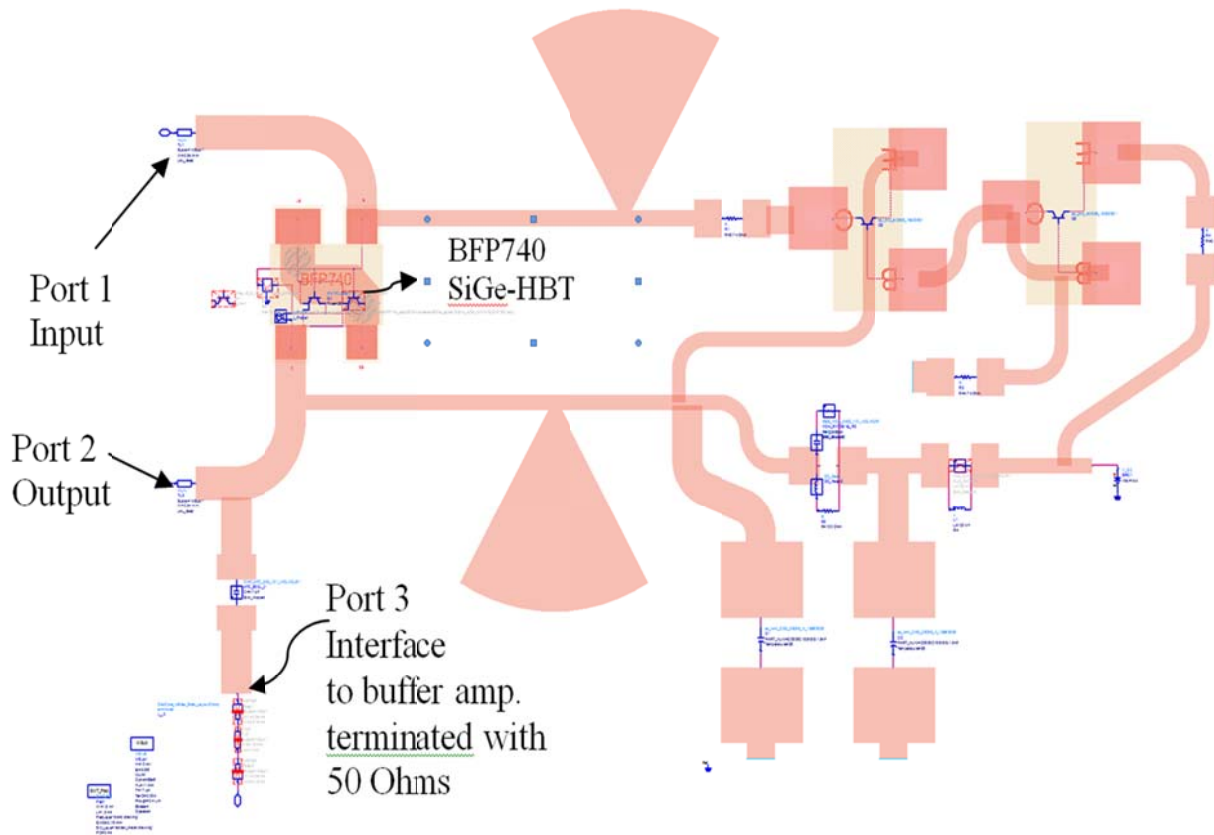


Figure 9-6: Oscillator core model including bias stabilization circuitry consisting of the layout component for EM co-simulation, models for the gain element, the bias-stabilization transistors and additional lumped components.

- (vi) A broadband S-parameter analysis of the oscillator core is recommended in order to identify potential instability issues along with available and associated gain properties. Since the regions of instability are rather small and very close to unity magnitude it is unlikely to encounter instability since lossy matching and phase shifting elements are likely to force the terminations inside the stable region anyway, therefore additional stabilization measure is not necessary. Figures 9-7, 9-8, 9-9, 9-10 show the plots of stability factor, stability circle, gain characteristics of the oscillator core, and noise figure.

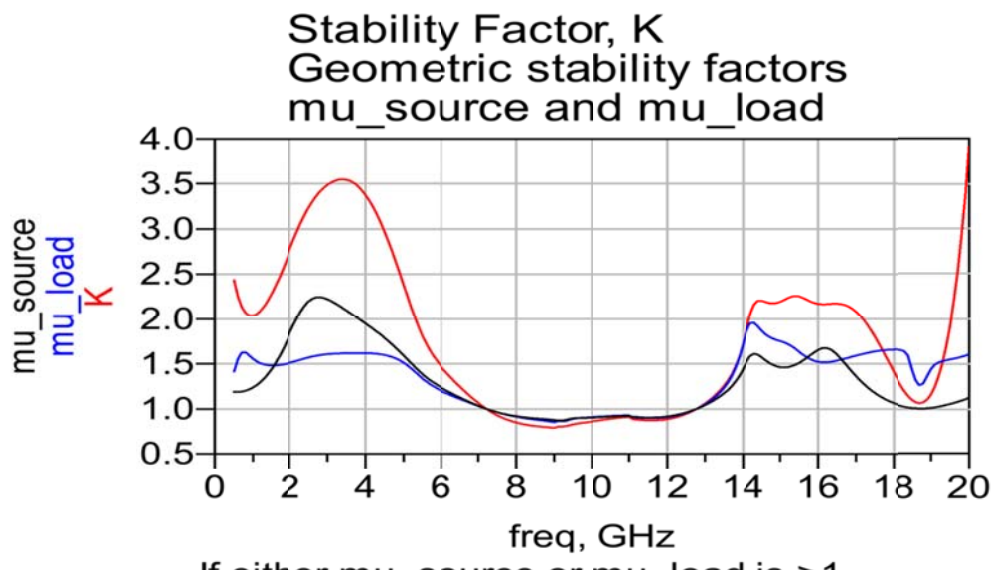


Figure 9-7: Shows the plot of the stability factor "K" versus frequency (unconditional stability is not completely satisfied)

- (vii) The complete setup does allow for an open loop 2-port S-parameter simulation the reference impedances of which being additional variables of the problem. Since the S-parameter data for the resonator does not reflect DC properties ideal DC-blocks must be added if necessary while in reality an open circuit is present at 0 Hz.

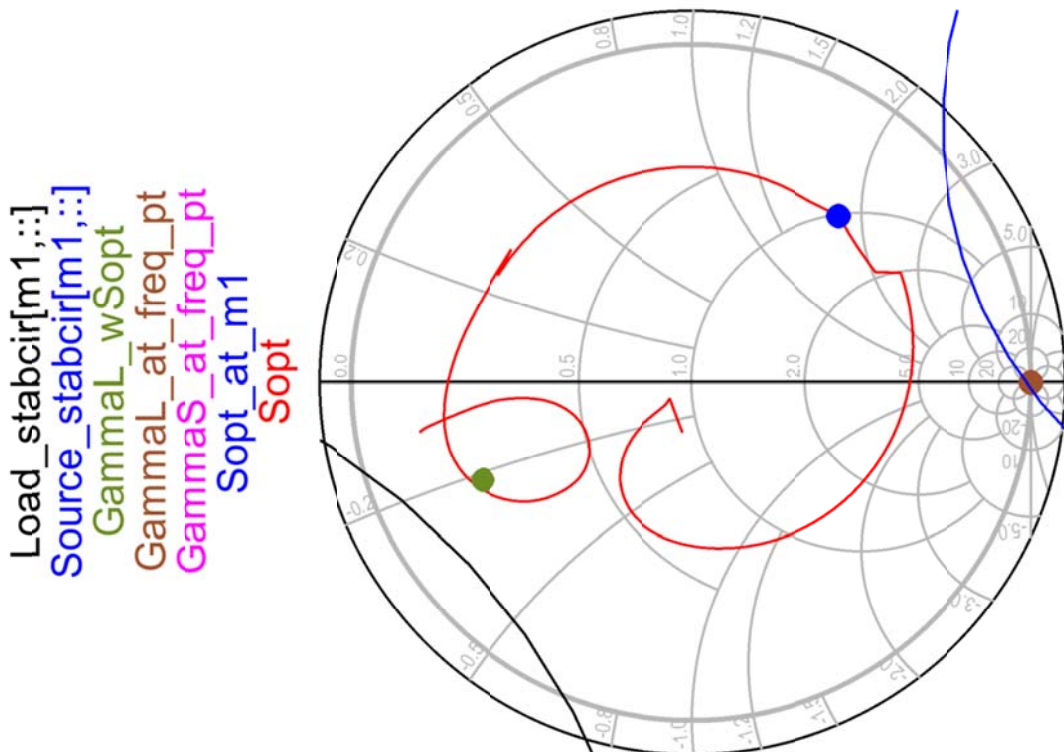


Figure 9-8: Source (blue) and load stability circles (black) at the most critical frequency (9 GHz)

Maximum Available Gain, Associated Power Gain (input matched for NF_{min}, output then conjugately matched), and dB(S₂₁)

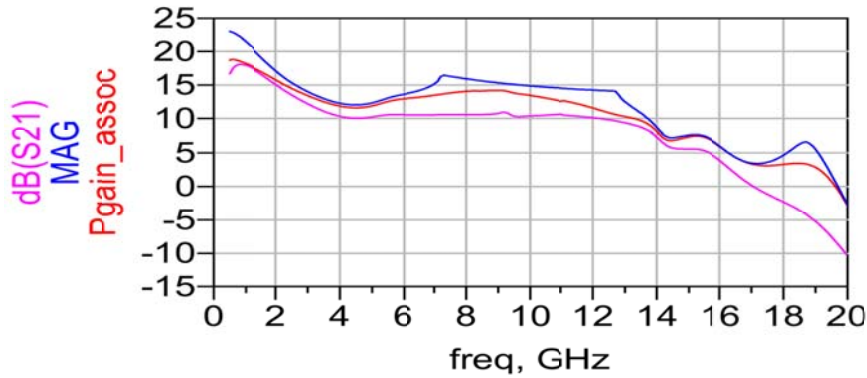


Figure 9-9: A typical gain characteristics of the oscillator core (note that the maximum available gain is invalid within the region of potential instability between 7 GHz and 13 GHz).

Minimum Noise Figure, dB, and Noise Figure with Z₀ Ohm terminations

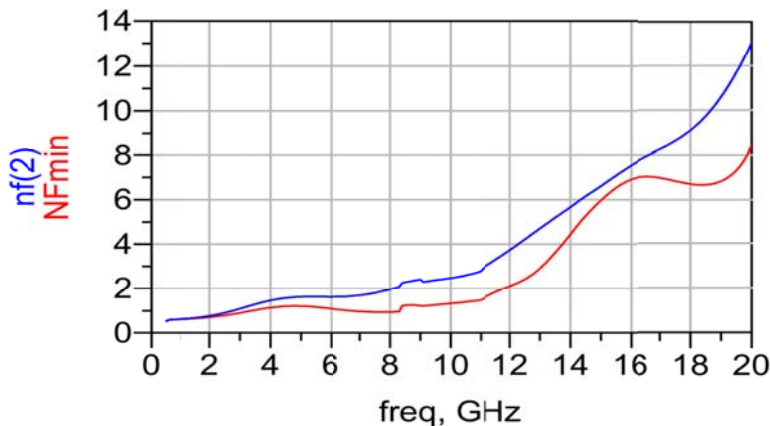


Figure 9-10: A noise figure and minimum noise figure versus frequency

- (viii) Figure 9-11 shows the CAD simulation circuit for (in ADS 2013) open loop (small signal) S-parameter simulation and optimization setup. For the coarse optimization, the random or hybrid optimizer is utilized. There is a set of four main goals: $|S_{11}| < R$, $|S_{22}| < R$, $|S_{21}| > G_{\min}$ and $Q_L \geq 1k$ at or closely around the target frequency f_0 . Appropriate values for the limits are $20 \cdot \log(R) = (-20)$ dB and $20 \cdot \log(G_{\min}) = 6$ dB. Q_L is derived from the frequency of maximum gain and the corresponding 3 dB-bandwidth Δf according to $Q_L = f_0 / \Delta f$. Since the target value for the open loop gain is associated with the coupling coefficient of the resonator a higher gain may increase its value which is still below unity i.e. subcritical. In practice it was not possible to increase it much further without diminishing the other goals. On the other hand a higher gain would increase the overdrive level of the oscillator with severe impact on large signal noise figure and input reflection of the gain element.

- (ix) A phase goal is expendable since arbitrary phase shift may be inserted afterwards. As we will see later, the small signal phase shift is decreased significantly at higher drive levels. A large signal S-parameter simulation will yield an estimation for the additional phase shift necessary in order to arrive at 0° unwrapped phase for 0 dB large signal gain at f_0 . Fine adjustment of the phase noise vs. phase shift will be done at a later stage. Direct optimization vs. phase noise is not recommended at this stage because potential HB convergence problems during the process for certain sets of parameters may cause the optimizer to fail.
- (x) For the fine optimization the gradient optimizer is engaged using the same set of goals but this time invoking the EM view (-model) for the matching layout component instead of the analytical models (Figure 9-11).

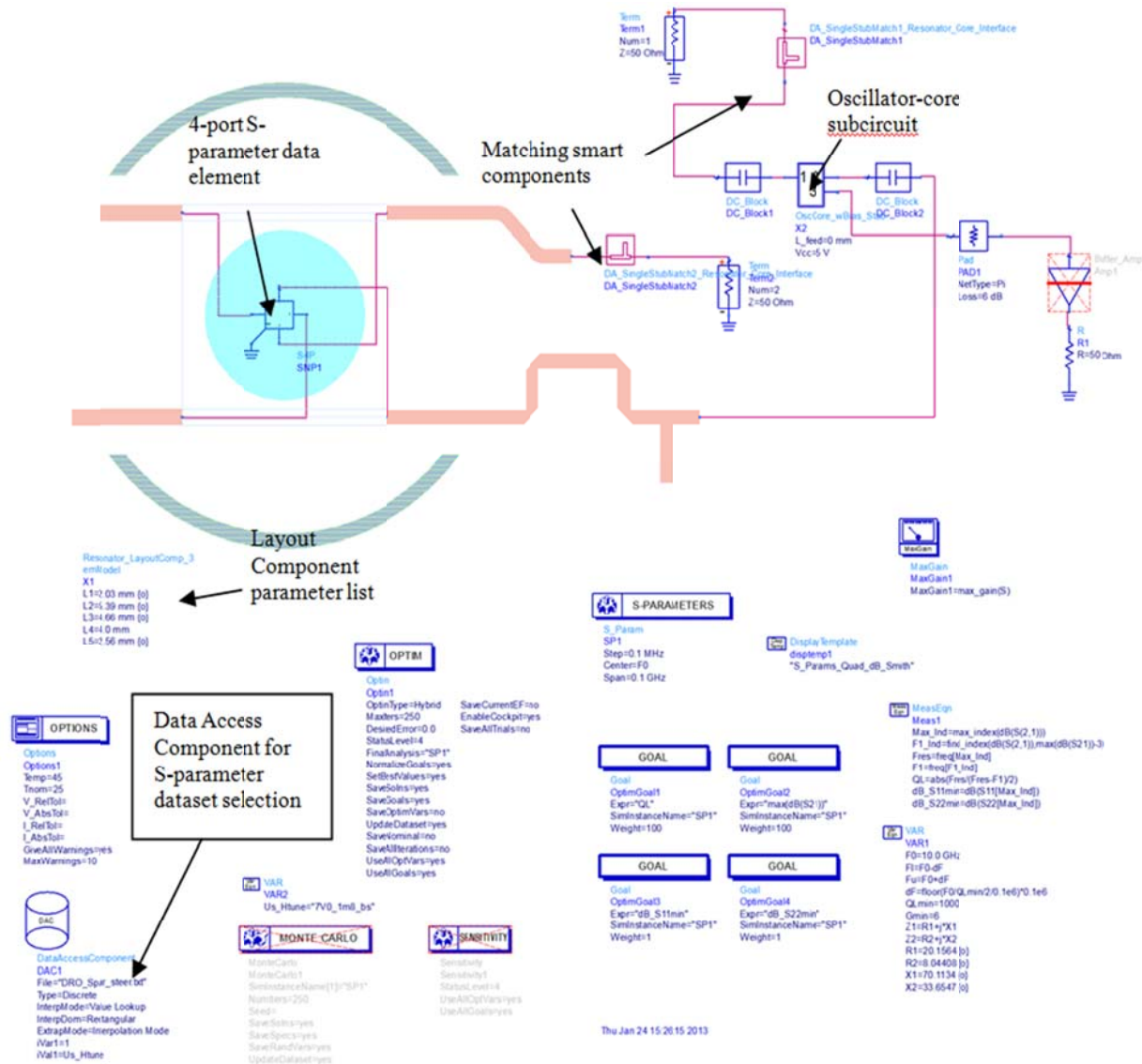


Figure 9-11: CAD simulation setup (ADS 2013) open loop (small signal) S-parameter simulation and optimization setup.

- (xi) When the optimization process is accomplished, the resulting reference impedances then need to be matched to a common (e.g. 50Ω) real impedance. This is accomplished in two steps: First two Single-Stub smart components are inserted to quickly design an electrical (ideal) transmission-line model for each matching element using the ADS-Filter/Matching Design-Guide and then a physical equivalent is created using the ADS-LineCalc or similar tools.
- (xii) Now that the small signal open-loop response and matching are well at their target values, we need to estimate the necessary additional phase shift at large signal excitation and near unity gain at the frequency of maximum gain in the small signal scenario.
- (xiii) Figure 9-12 shows the typical schematic of the parallel transmission line as a part of resonator element. Figure 9-13 shows the CAD simulated open loop S-parameters following coarse optimization using schematic - (blue) and EM-view. As the reflection coefficients and the source impedance for minimum large signal noise figure of the active device do more or less vary with increasing drive level some correction mainly to the matching element at the oscillator core's input may be required in order to establish optimal conditions with respect to minimum phase noise.

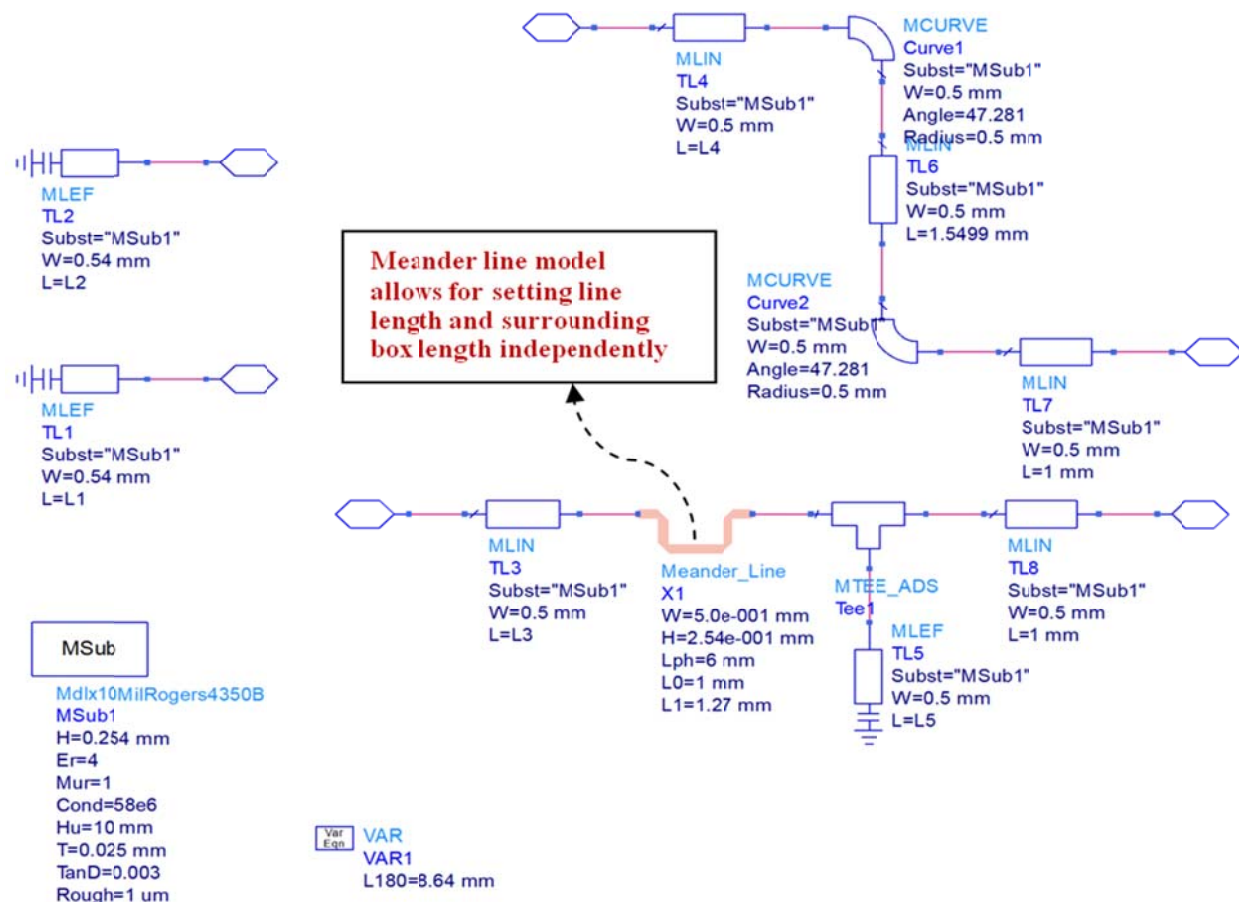


Figure 9-12: A typical schematic view of the resonator layout component

- (xiv) The result obtained in Figure 9-13 indicates an additional phase shift of -116° in this case to be inserted between the two ports to arrive at the required phase shift of 0° . In order to save board space additional meander lines as shown in Figure 9-12 of equivalent electrical length are inserted to establish the required phase shift. The surrounding box length of the meander should be set such, so as to meet the fixed layout positions of the oscillator-core if relevant. Figure 9-14 shows the equivalent physical replacement for the smart matching components as shown in the schematic (Figure 9-11)

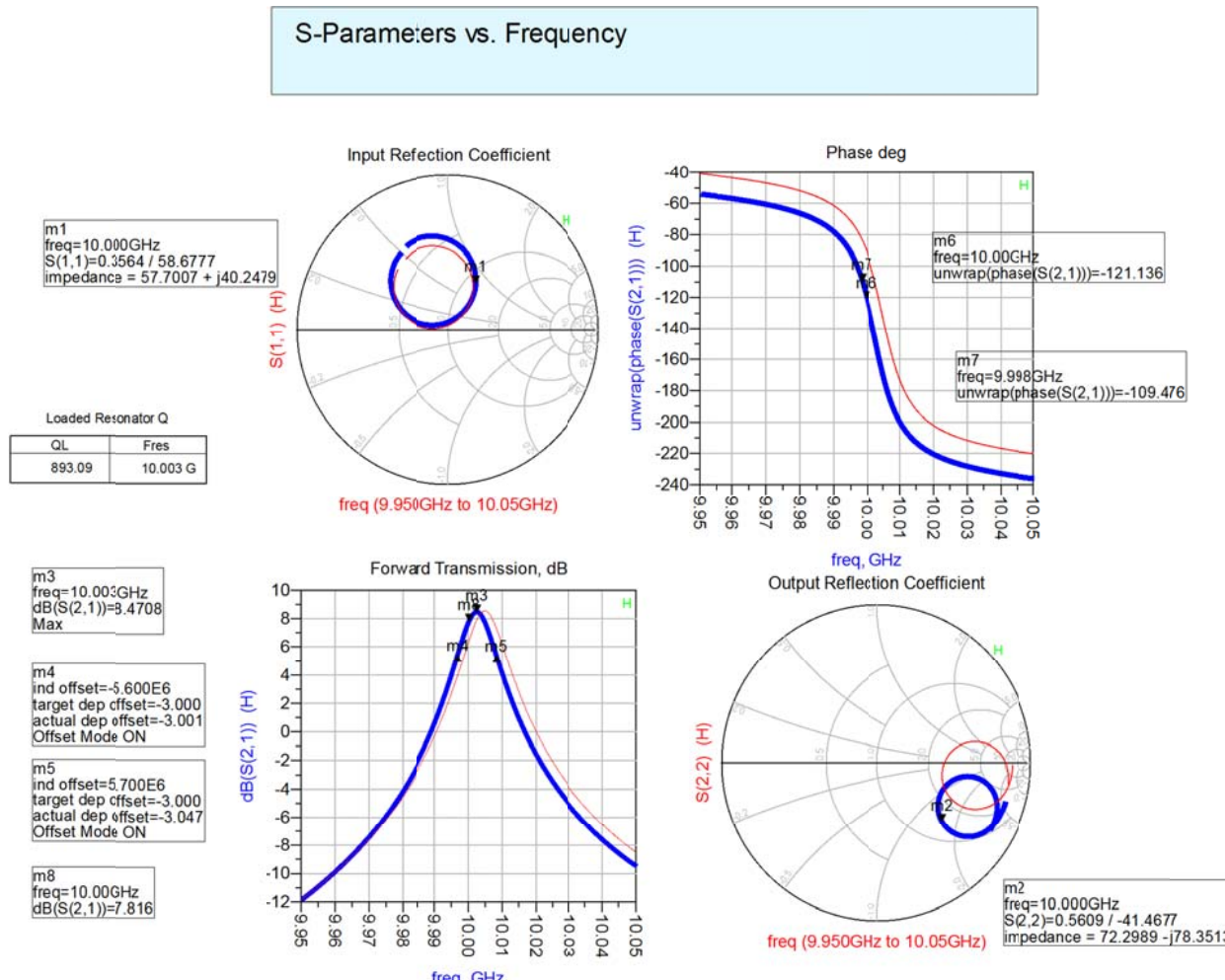


Figure 9-13: simulated open loop S-parameters following coarse optimization using schematic - (blue) and EM-view



Figure 9-14: Shows the equivalent physical replacement for the smart matching components shown in Figure 9-11

Figure 9-15 shows the final optimization result with EM-models for the single-stub matching elements replacing the smart matching components. Note that another 180° meander line has already been added to the lower section to compensate for the physical lengths of the matching elements.

Figure 9-16 shows the CAD simulation setup (ADS 2013) for large-signal open-loop S-parameter simulation.

Figure 9-17 shows the plot of large signal forward transmission at resonance frequency vs. input-power. The marker is set to near unity-gain. The corresponding phase shift is about 116°.

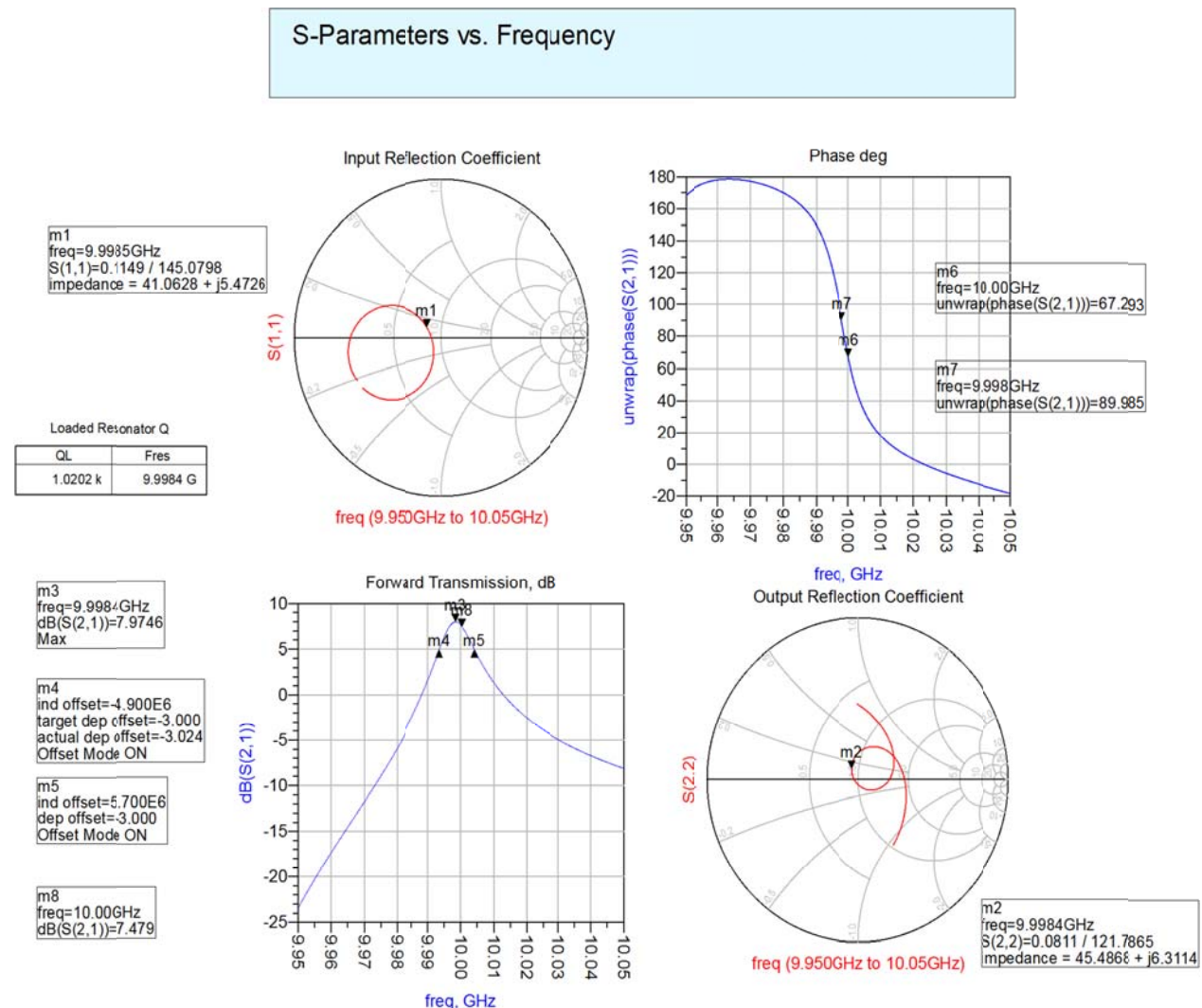


Figure 9-15: shows the final optimization result with EM-models for the single-stub matching elements replacing the smart matching components. Note that another 180° meander line has already been added to the lower section to compensate for the physical lengths of the matching elements

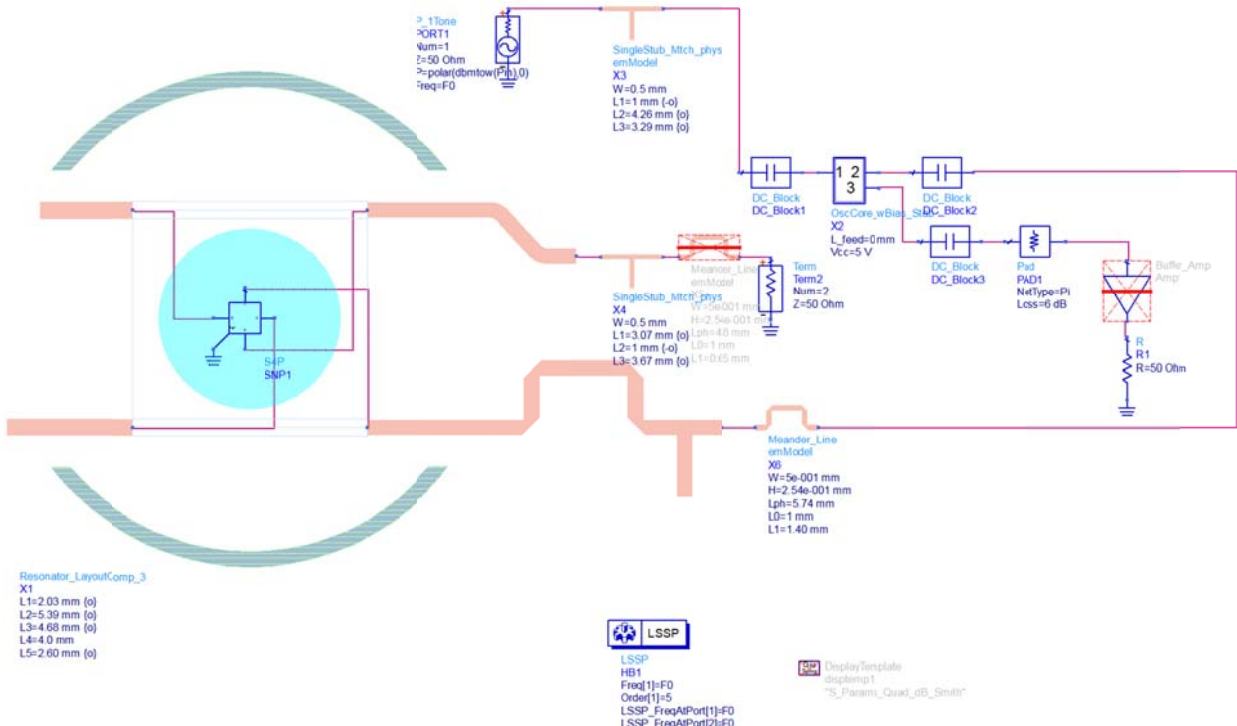


Figure 9-16: shows the CAD simulation setup for large-signal open-loop S-parameter simulation.

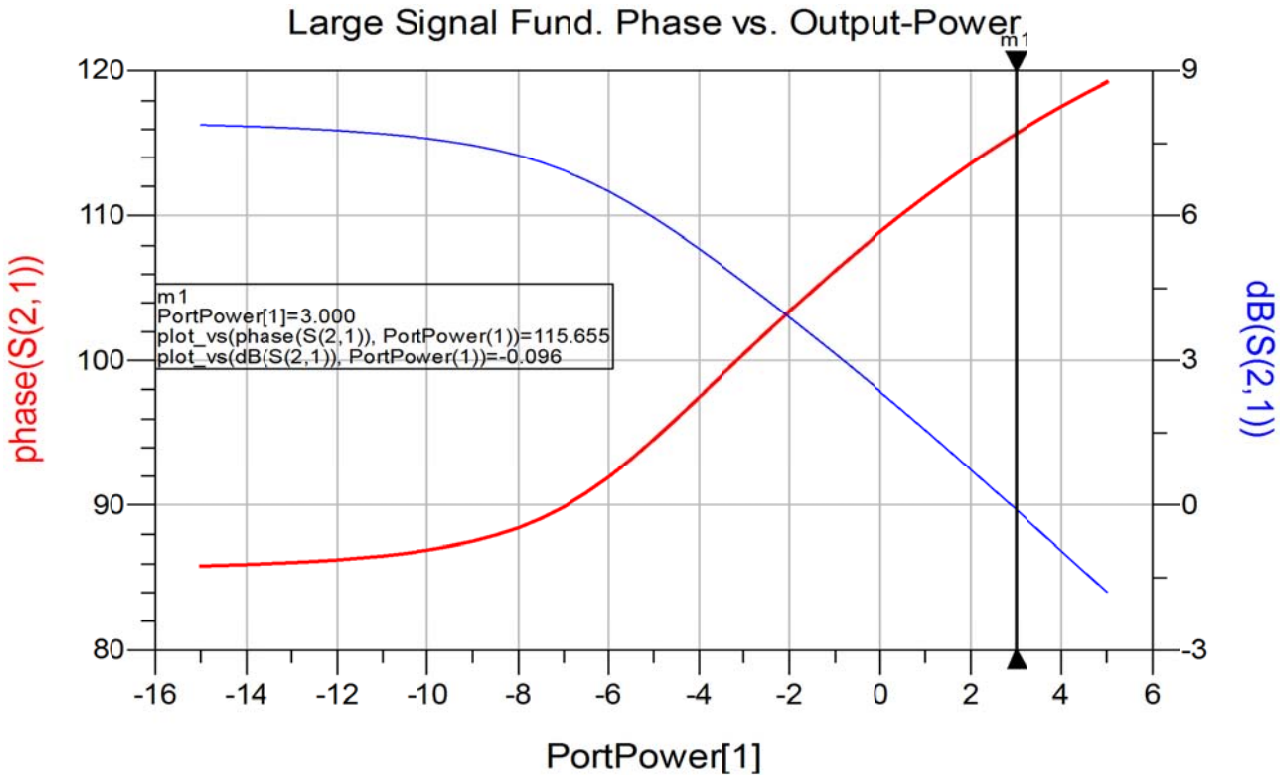


Figure 9-17: shows the plot of large signal forward transmission at resonance frequency vs. input-power. The marker is set to near unity-gain. The corresponding phase shift is about 116°.

Figure 9-18 shows the resonator matching section with delay line added and meander lines adjusted to achieve equal lateral reference positions for the interface ports to the oscillator core. Figure 9-19 shows measured amplitude and phase noise before (blue) and after (red) minor optimization of the input matching component. From the intersection of the 20dB/dec and 0dB/dec tangent a Q_L of approximately 1k can be derived.

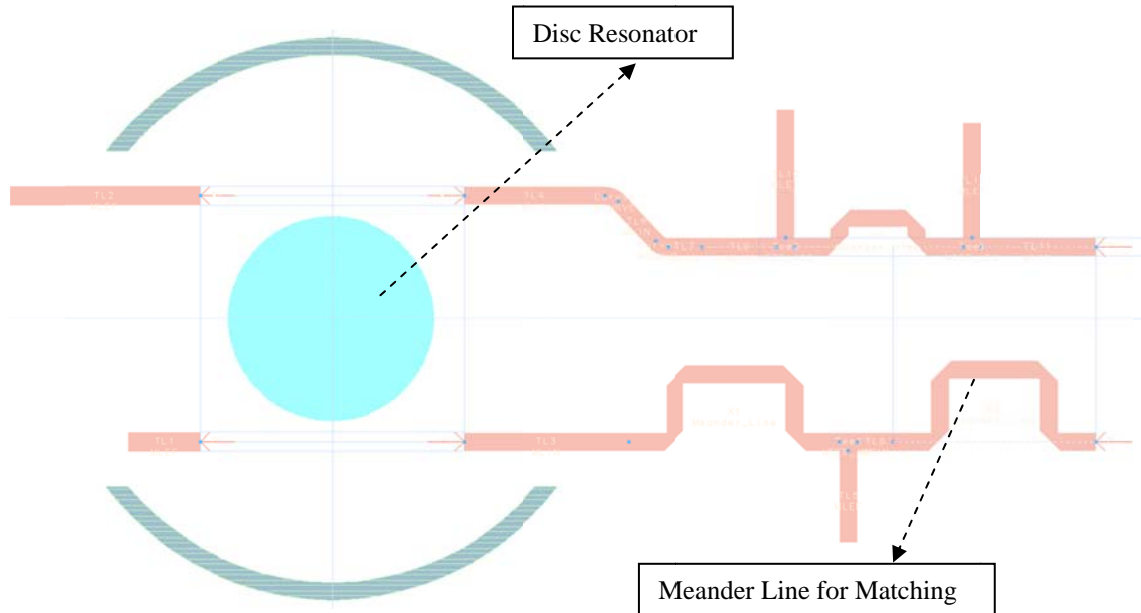


Figure 9-20: shows the plots corresponding to spectral and time-domain waveforms of the voltages at the output of the buffer amplifier (blue) and at the oscillator core output.

FixedFreqOsc

Spectra and waveforms at oscillation frequency = 9.99836 GHz

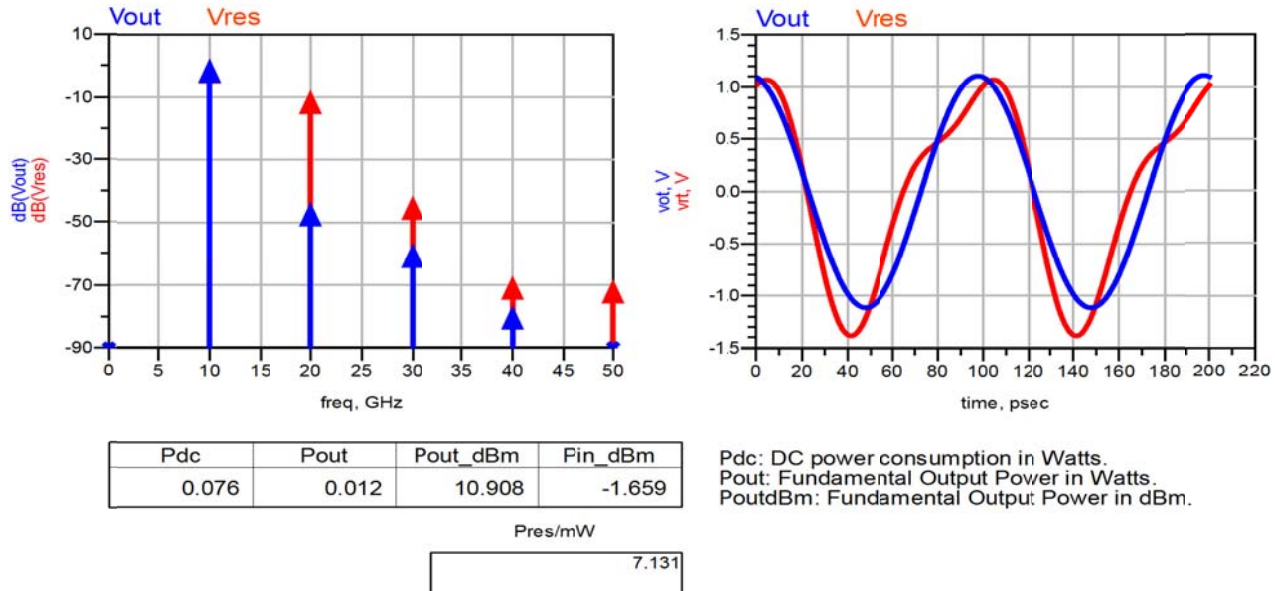


Figure 9-20: shows the plots corresponding to spectral and time-domain waveforms of the voltages at the output of the buffer amplifier (blue) and at the oscillator core output.

Phase-Noise Simulation vs Measured

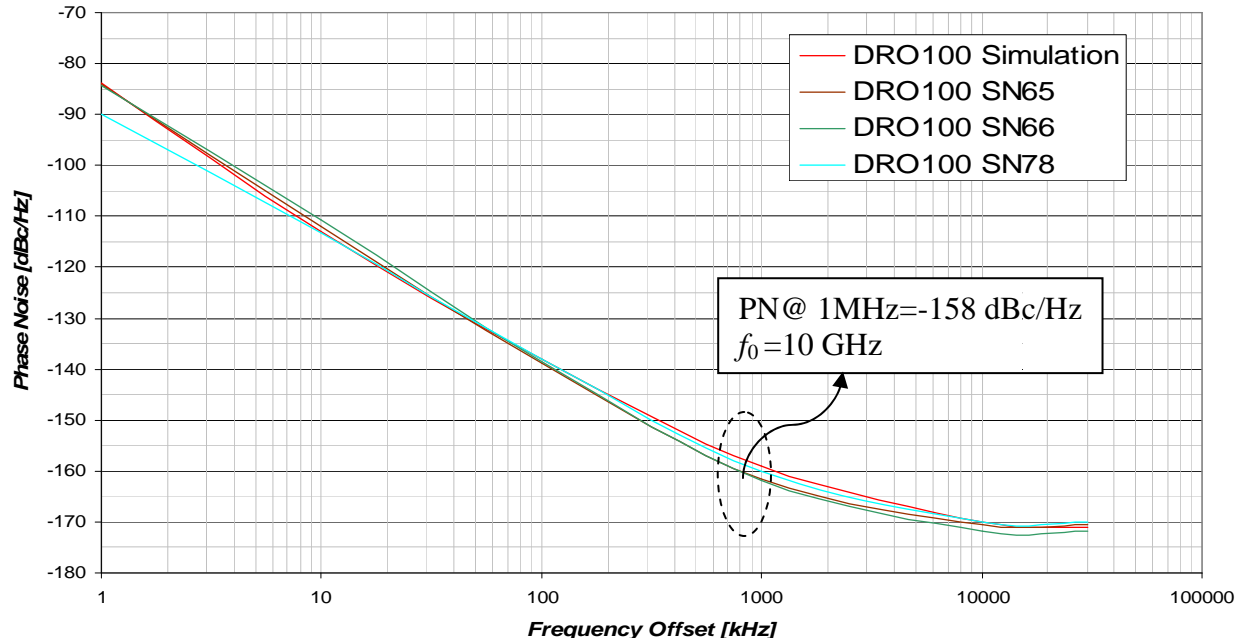


Figure 9-21: shows the CAD simulated and measured phase noise plots (3-prototypes: DRO100 SN65, DRO100 SN66, DRO100 SN78 is built for validation). CAD simulated data (DRO100) matches closely, agree within 2-3 degree of accuracy with measured data of 3-prototypes (DRO100 SN65, DRO100 SN66, DRO100 SN78).

3-prototypes, namely DRO100 SN65, DRO100 SN66 and DRO100 SN78 are built for validation of the novelty of designing low phase noise DRO circuit described above. CAD simulated data (DRO100) matches closely, agree within 2-3 degree of accuracy with measured data of 3-prototypes (DRO100 SN65, DRO100 SN66, DRO100 SN78). The measured phase noise plot is -112 dBc/Hz @ 10 kHz, -137 dBc/Hz @ 100 kHz and <-170 dBc/Hz @ >10 MHz; shows good agreement with the phase noise plots shown in Figure 9-19 and Figure 9-21.

Figures 9-22(a), 9-22(b), 9-22(c) show the Altium (CAD tool) created complete 10 GHz DRO module ready for production, fabricated internal view of the DRO without dielectric resonator (Disc resonator bottom tuning screw is slightly elevated), and resonator cavity and dielectric disc resonator (DR not visible) added.

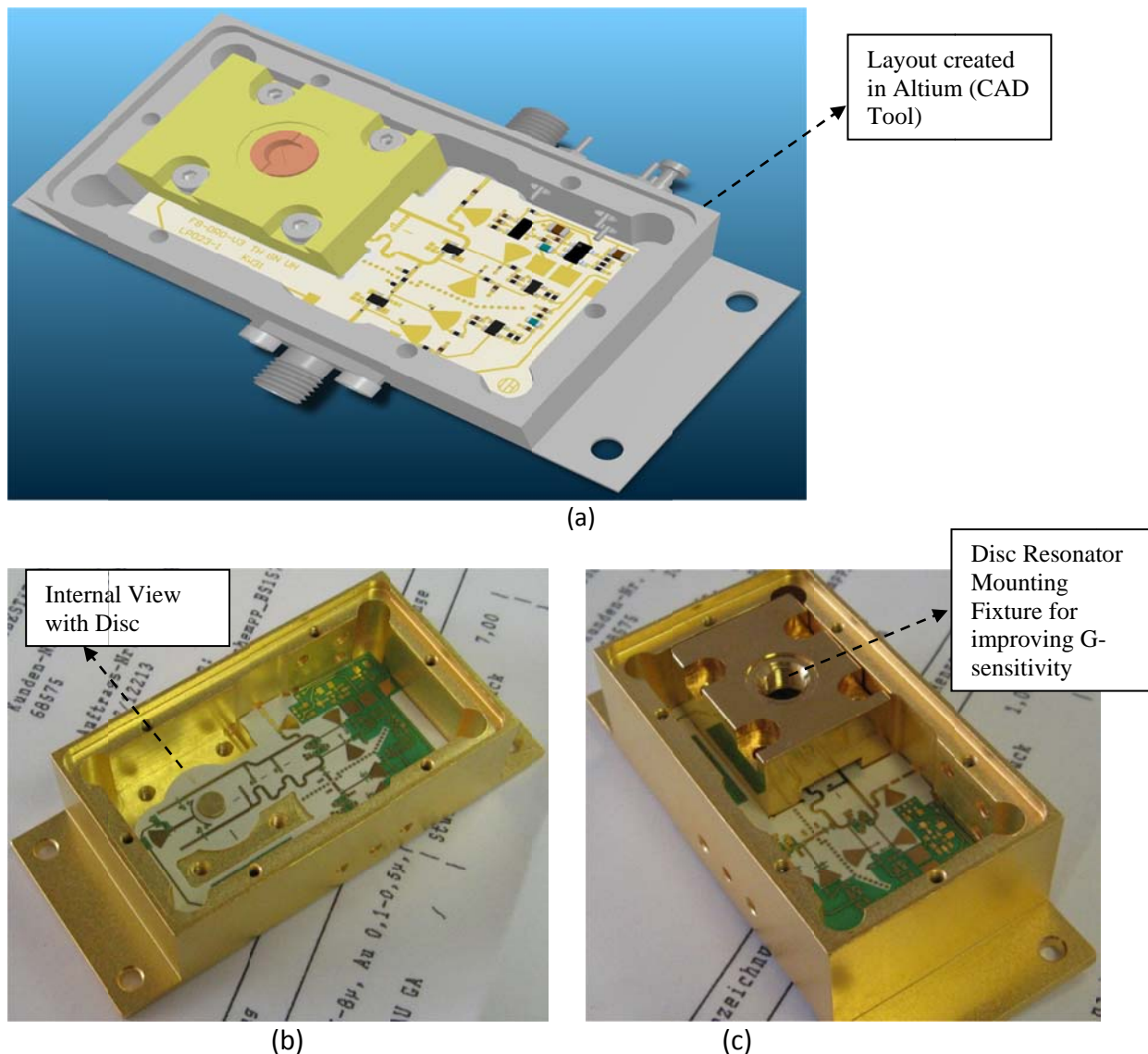


Figure 9-22: (a) CAD internal view of the complete DRO, (b) fabricated internal view of completed 10 GHz DRO internal view of the DRO without dielectric resonator (Disc resonator bottom tuning screw is slightly elevated), and (c) resonator cavity and dielectric disc resonator (DR not visible) added [15]

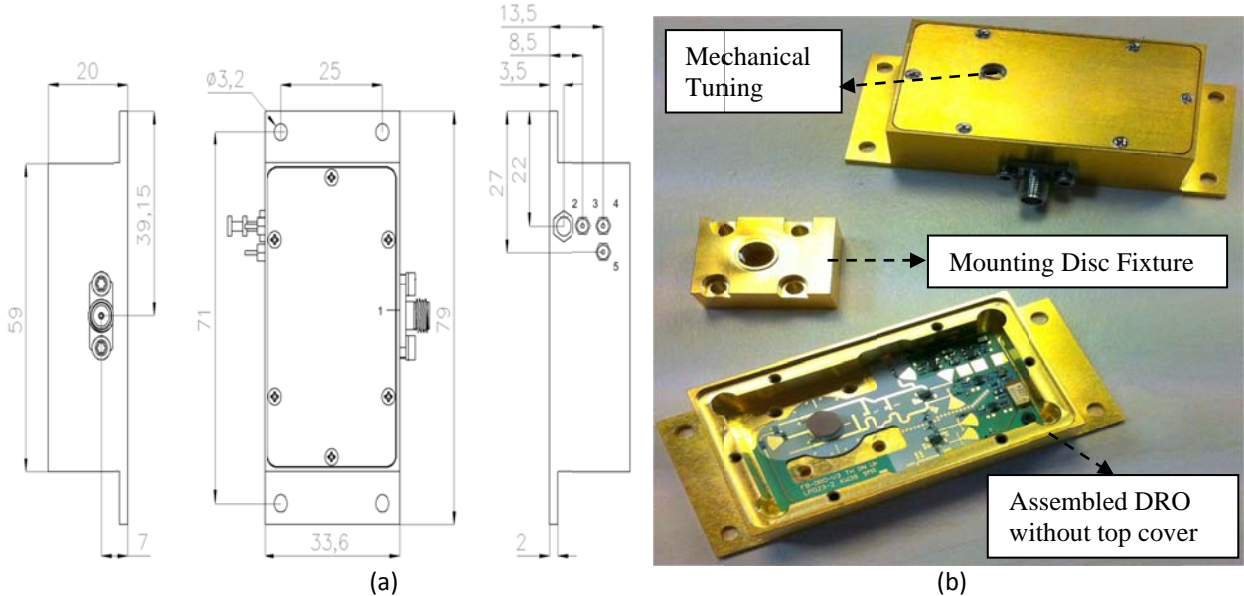


Figure 9-23 shows 10 GHz DRO circuit module: (a) Mechanical drawing of the 10 GHz DRO, and (b) a photograph of a 10 GHz DRO circuit [15]

Figure 9-23 shows the (a) Mechanical drawing of the 10 GHz DRO, and (b) a photograph of a 10 GHz DRO circuit, which is ready for production [15]. The DRO supply voltage can vary between +7 to +10 V and the internal voltage regulation gives high immunity to power supply noise. The supply-current is typically 50 mA and the temperature range is specified from -25°C to +70°C. The output-power exceeds +8dBm. The actual package size is approximately 3.1" × 1.34" × 0.788," including mounting flaps. As shown in Figure 9-23, the large size and high power consumption are main bottleneck and limits the application where size and power consumption is the prime criteria for using these sources. In addition to this, DRO module shown in Figure 9-23 requires precise machining for fabrication, and careful placement of the dielectric puck for optimal resonator coupling. This involves manual tuning of the DR for desired operating frequency [16]. The reported tunable DRO circuit as shown in Figure 9-23 provides performance levels that are comparable to those of traditional connectorized DROs, but large size and expensive.

9.5 Compact surface mounted device (SMD) 10 GHz DRO Circuit

The DRO circuit shown in Figure 9-23 is connectorized version, offers reasonably low phase noise but limited in tuning and poor DC-RF conversion efficiency, including sensitivity to vibration due to mechanical tuning (shown in Figure 9-23(b)). Moreover, the exact placement of the DR disc between two parallel microstriplines shown in Figure 9-22(c) is critical, slight variations can lead to higher harmonics and poor phase noise. In addition to this, the predicted DR resonant frequencies may differ from the measured results due to slight variations in temperature that cause problems during mass production and for integration of circuits. Such problems limit the usefulness of DRO.

The frequency drift is not a straightforward function of temperature changes (due to different thermal expansion coefficients for cavity and dielectric pucks) and not easily corrected. The thermal sensitivity of a DRO can be reduced somewhat by the use of PLL

circuitry and temperature control, although these are not integrable, cost-effective solutions. In short, the new approach to designing DRO circuit with slow-wave-coupled resonators (Ch-6) yields compact VCOs with excellent electrical tuning and phase-noise performance and in configurations that can be readily adapted to SMD (surface mounted device) packages version.

A novel slow-wave mode-coupled self-injection locked VCO (voltage controlled oscillator) is developed in response to replacing expensive DRO (Dielectric Resonator Oscillator) for reference signal sources for modern communication systems [17]-[21]. One of the problems related to the Dielectric Resonator (DR) is fabrication in integrated circuit (IC) form due to 3-D structure. Utilizing slow-wave mode-coupling approach (Ch-6) can offer SMD packaged DRO circuits, which is cost-effective and promising alternative for hybrid circuit (quasi-planar) applications. The reported topology is not limited to this frequency, and can be extended to other frequency bands (2 GHz to 30 GHz with 500 MHz or more tuning range) by dynamically controlling Mobius mode-coupling mechanism.

Figure 9-24 shows a typical block diagram of the DRO circuit used for validating the approach of electrical tuning (varactor-tuned) for improved g-sensitivity and achieving low phase noise performances in compact size with improved DC-RF conversion efficiency. One of the design challenges for DROs circuit is to enable electrical tuning for compensating the frequency drift caused due to change in operating temperature (-40°C to +80 °C) and maintaining low phase noise, while also minimizing the cost of the oscillator by achieving a structure that could be assembled reliably in production. To achieve this consistency in design and manufacturing, computer-aided-engineering (CAE) simulation tools were used, such as ANSYS HFSS from ANSYS (www.ansys.com) and ADS Momentum software from Agilent Technologies (www.agilent.com).

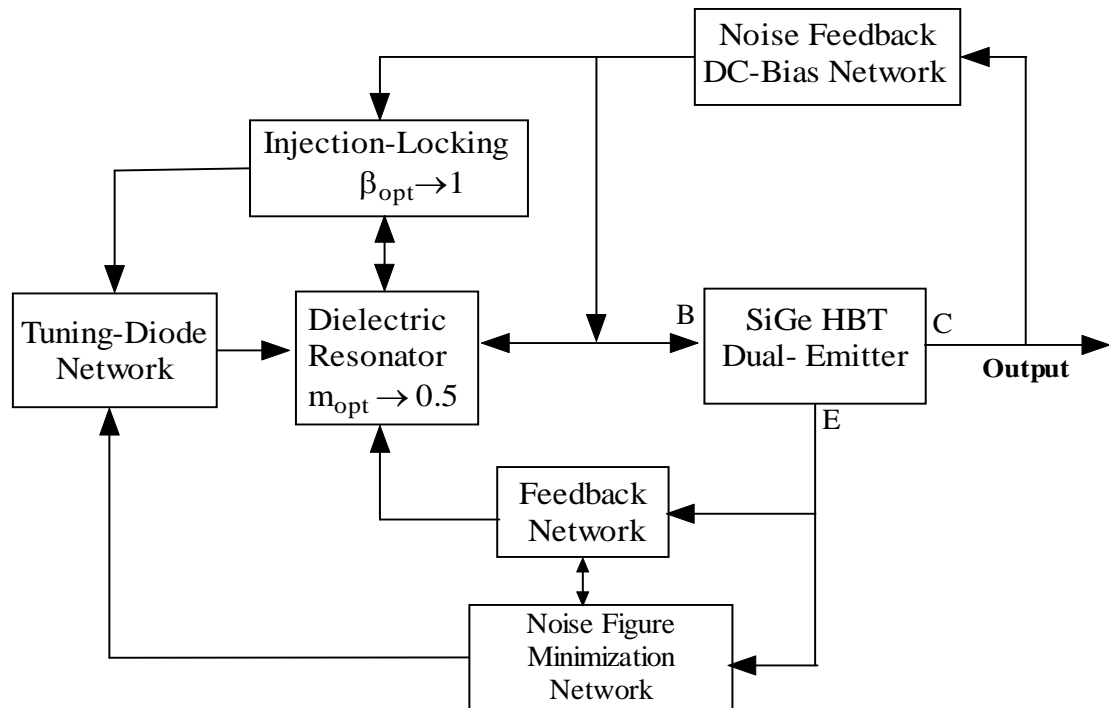


Figure 9-24: A typical block diagram of a SMD version DRO circuit based on self-injection locking [15]

Figure 9-25 shows a three-dimensional (3D) model for the varactor-tuned DRO. The complete DRO design was evaluated and optimized using harmonic-balance circuit simulation along with electromagnetic (EM) co-simulation. This approach allows designers to achieve an optimum dynamic loaded Q-factor for a typical DR coupling arrangement in conjunction with the oscillator core which is one of the preconditions for achieving lowest phase noise. The active device has been selected carefully with respect to noise figure and flicker noise, with optimum bias level conditions.

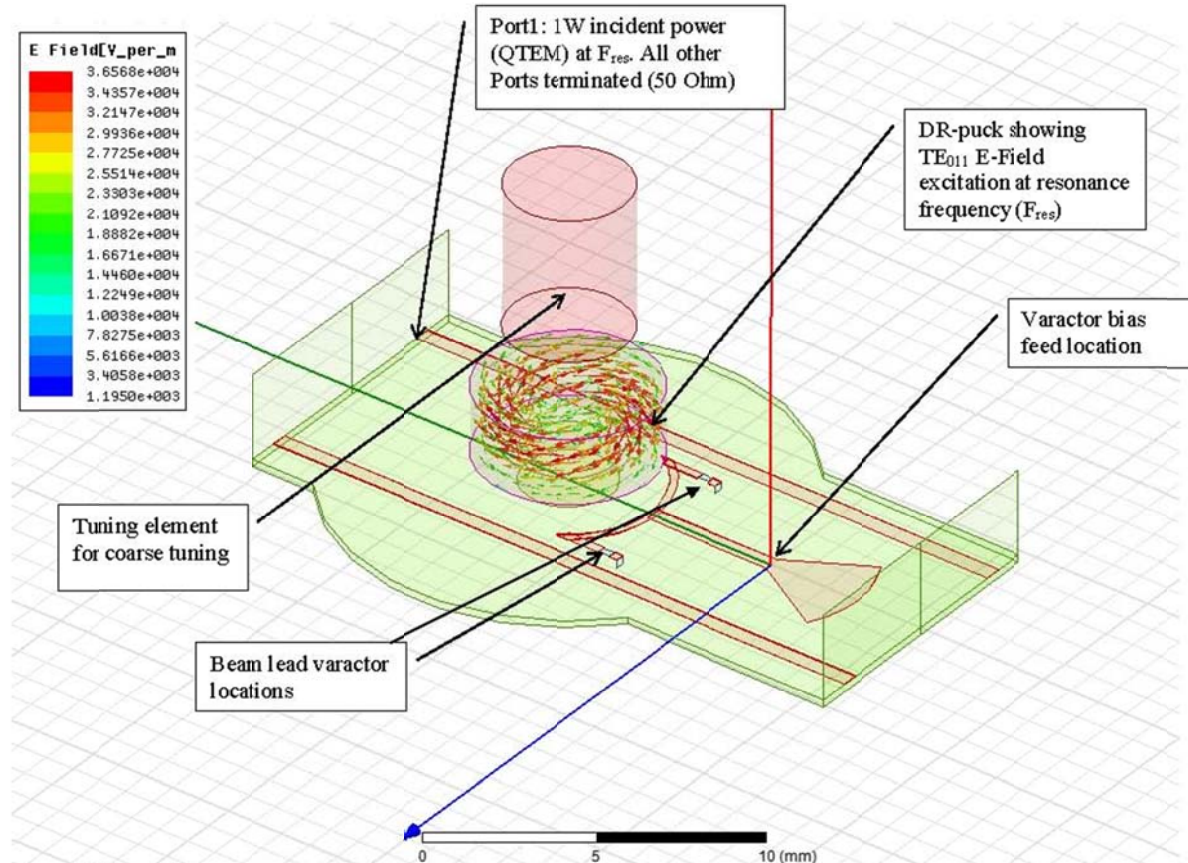


Figure 9-25: A typical 3-D model of varactor tuned Dielectric Resonator for high performance oscillators

The expression of phase noise, can be given by [6]

$$\xi(f_m) = 10 \log \left[\left(1 + \frac{f_0^2}{(2f_m Q_0)^2 m^2 (1-m)^2} \right) \left(1 + \frac{f_c}{f_m} \right) \frac{FkT}{2P_0} + \frac{2kTRK_0^2}{f_m^2} \right] \quad (9.8)$$

where m is the ratio of the loaded and unloaded Q .

The coupling coefficient β can be described as

$$m = \frac{Q_L}{Q_0} \Rightarrow \frac{Q_L}{Q_0} = \frac{1}{1+\beta} \quad (9.9)$$

The dynamic loaded Q can be given by [15]:

$$Q_L = \frac{\omega_0}{2} \left[\frac{\partial \phi}{\partial \omega} \right] \Rightarrow \frac{\partial Q_L}{\partial \omega} = \frac{\omega_0}{2} \left[\frac{\partial^2 \phi}{\partial \omega^2} \right]_{\omega=\omega_0, \phi=\phi_{opt}} \Rightarrow 0 \quad (9.10)$$

For maximum dynamic loaded "Q", $\frac{\partial}{\partial \omega} [Q_L(\omega)]_{\omega=\omega_0} \rightarrow 0$, therefore, minimum phase noise can be found by differentiating (9.8) with respect to m , and equating to zero for minimum value of phase noise as $\frac{\partial}{\partial m} [\ell(f_m)]_{m=m_{opt}} = 0 \Rightarrow (\phi = \phi_{opt})$:

$$\frac{d}{dm} \left[10 \log \left[1 + \frac{f_0^2}{(2f_m Q_0)^2 m^2 (1-m)^2} \right] \left(1 + \frac{f_c}{f_m} \right) \frac{FkT}{2P_0} + \frac{2kTRK_0^2}{f_m^2} \right] = 0 \Rightarrow m_{opt} = 0.5 \quad (9.11)$$

$$m_{opt} \rightarrow 0.5 = \left[\frac{1}{1+\beta} \right]_{\beta=\beta_{opt}} \Rightarrow \beta_{opt} (\phi = \phi_{opt}) \rightarrow 1 \text{ (low phase noise condition)} \quad (9.12)$$

where $\ell(f_m)$, f_m , f_0 , f_c , Q_L , Q_0 , F , k , T , P_0 , R , and K_0 are the ratio of the sideband power in a 1Hz bandwidth at f_m to total power in dB, offset frequency, flicker corner frequency, loaded Q , unloaded Q , noise factor, Boltzmann's constant, temperature in degree Kelvin, average output power, equivalent noise resistance of tuning diode and voltage gain.

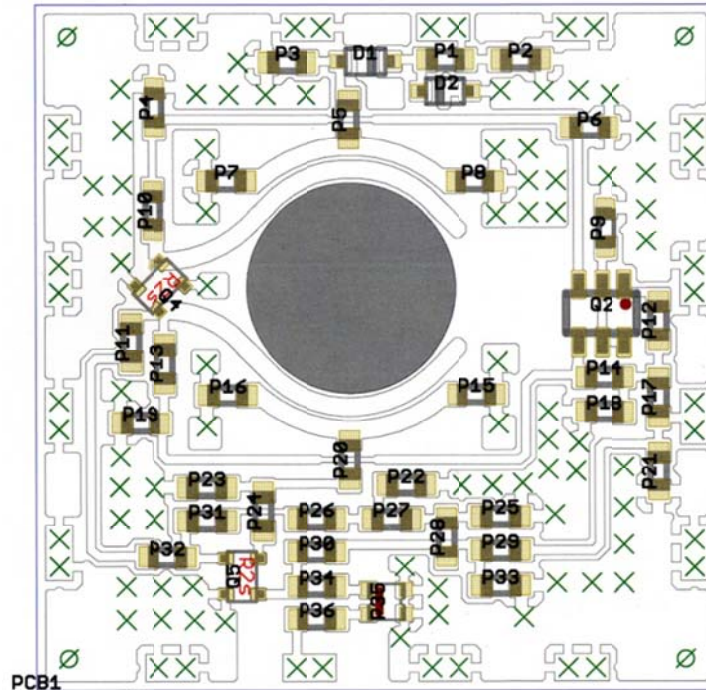


Figure 9-26: shows the typical layout of varactor-tuned compact SMD version 10 GHz DRO in 0.5" x 0.5" square package size with (5V, 30 mA) power consumption

From Equation (9.12), for low phase noise applications, m_{opt} and β_{opt} should be dynamically controlled and must lie in the vicinity of 0.5 ($m_{opt} \approx 0.5$) and 1 ($\beta_{opt} \approx 1$) respectively for the best phase noise performance. Figure 9-26 shows a layout of the 10 GHz DRO circuit (as per block diagram shown in Figure 9-24) used for validating the approach of achieving minimum phase noise performances with 8V, 40mA.

Figure 9-27 illustrates the impact of possible impairments on the phase noise performance. The red trace identifies the measured phase noise performance of DRO for coupling factor $\beta_{opt} (\phi = \phi_{opt}) \rightarrow 1 \Rightarrow m_{opt} \rightarrow 0.5$ (from Equation 9.12). The blue trace corresponds to $m_{opt} \neq 0.5$ with identical oscillator active device core noise properties. The black and magenta traces correspond to identical $\beta_{opt} (\phi = \phi_{opt}) \rightarrow 1 \Rightarrow m_{opt} \rightarrow 0.5$ but significantly higher effective noise figure or flicker corner frequency when the active device is not selected or biased optimally (without noise-feedback DC bias-network as shown in Figure 9-24) [17].

A combination of these impairments together with nonlinear noise effects account for the much higher phase noise performance found in commercially available competing DRO designs [1]-[16]. As shown in Figure 9-27, the phase noise performance of DRO (circuit layout is shown in Figure 9-26) for coupling factor $\beta_{opt} (\phi = \phi_{opt}) \rightarrow 1 \Rightarrow m_{opt} \rightarrow 0.5$ exhibits typical noise floor of -170 dBc/Hz with operating DC bias of 5V, 30mA, and 8.3% DC-RF conversion efficiency, approaching state-of-the-art performance for a given size and power consumption in SMD packaged (0.5" x 0.5" square package size) [15].

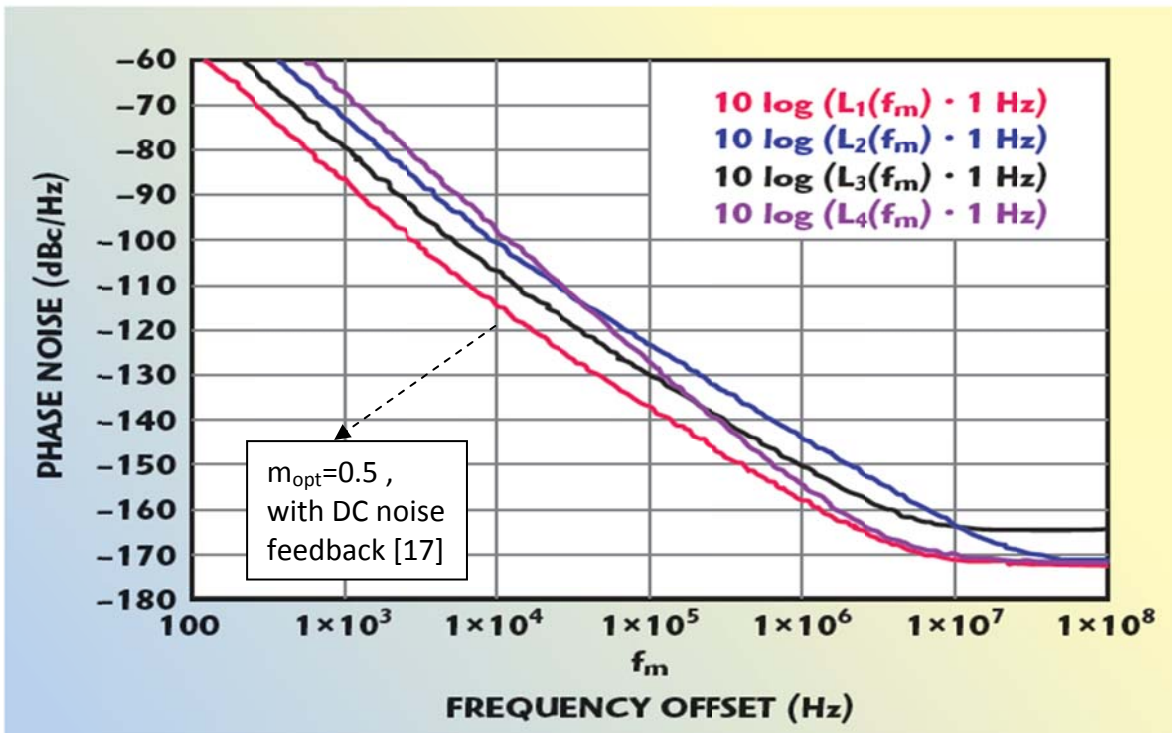


Figure 9-27: Measured phase noise plots of 10 GHz DRO circuit layout shown in Figure 9-26 (The impact of possible impairments on the phase noise performance)

The typical measured phase noise as shown in Figure 9-27 is -112dBc/Hz offset 10 kHz from the carrier with ± 2 MHz electrical tuning for frequency adjustment and injection-locking as shown in block diagram (Figure 9-24). The frequency is set at the fundamental resonance of DR and can be electrically tuned by approximately ± 300 MHz using varactor tuned network (Tuning voltages of 1 to 15 VDC enable variations in the center frequency by ± 200 MHz to compensate for frequency drift in phase-locked systems).

Figure 9-28 shows the typical layout of mode-coupled DRO at 10.24 GHz with 10 MHz tuning range for compensating the frequency drift over the operating temperature (-40°C to $+85^\circ\text{C}$). Figure 9-29 shows the measured phase noise plot @ 10 kHz offset is -109dBc/Hz , validates the tuning capability without much degrading the phase noise performance in SMD packaged version. The oscillator delivers typically +10 dBm output power with 300 mW DC power consumption ($V_{CC}=6\text{Volt}$, $I_C=50\text{ mA}$) in a surface-mount-device (SMD) package measuring 0.750×0.750 inches, where, the layout is made on 22 mils substrate with dielectric constant of 3.38 with dimensions of $0.75 \times 0.75 \times 0.18$ inches.

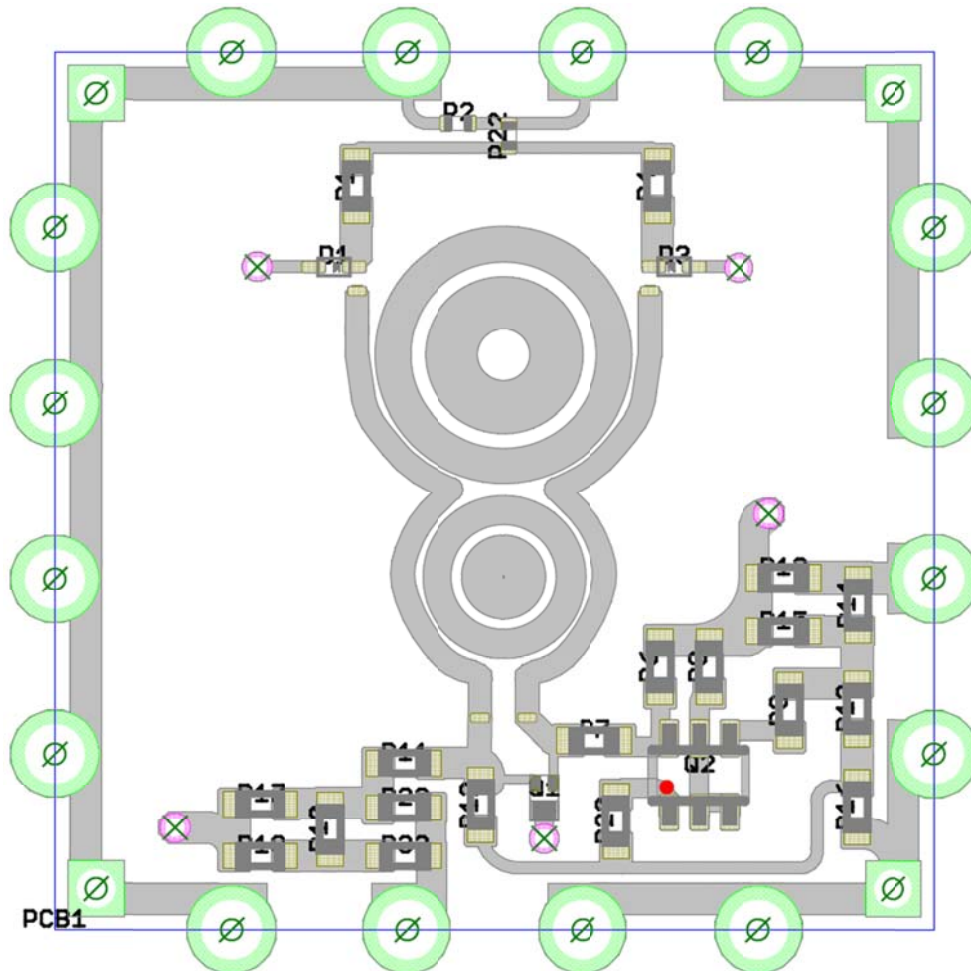


Figure 9-28: shows the typical layout of varactor-tuned compact SMD version 10.24 GHz DRO in $0.75'' \times 0.75''$ square package size with (5V, 40 mA) power consumption, layout is made on 22 mils substrate with Dielectric constant 3.38 in $0.75 \times 0.75 \times 0.18$ inches.

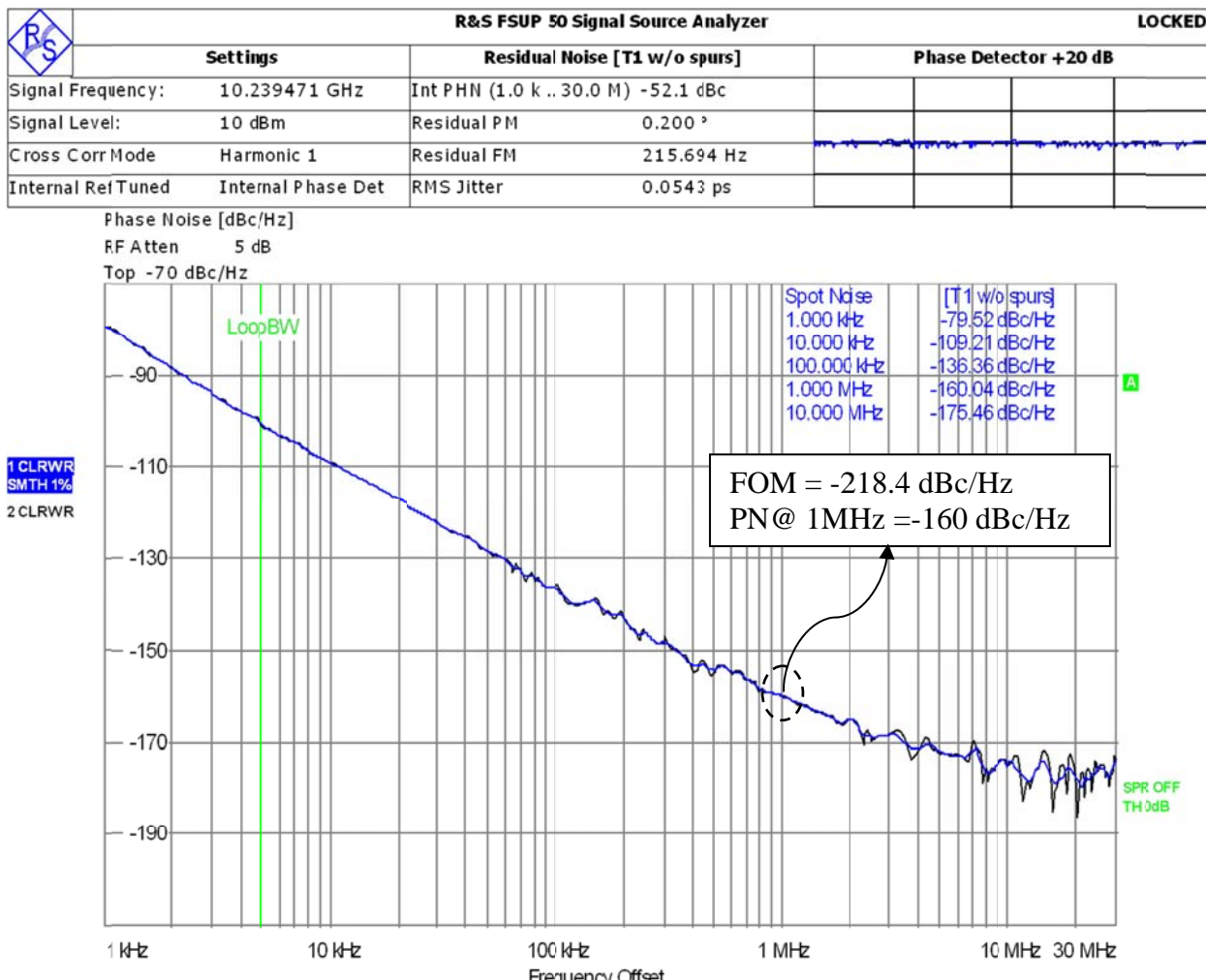


Figure 9-29: Measured phase noise plots of 10.24 GHz DRO circuit

9.6 Conclusion

The step by step procedure of high performance X-band DRO is presented. The reported design methodology of ultra low noise 10 GHz DRO circuit including the Möbius Coupled DRO improves the tuning range without degradation of phase noise performances.

9.7 Reference

- [1] Ulrich L. Rohde, "Microwave and Wireless Synthesizers", Wiley & Sons, pp. 86-90, 1997
- [2] D. Kajfez and P. Guillon, "Dielectric Resonators", Artech House, Dedham, MA, 1986
- [3] Jens Bischoff, Daniel Schwoch, "Entwurf eines ultra-rauscharmen Mikrowellenoszillators mit dielektrischem Resonator im S-Band", Diploma thesis, University of Applied Sciences Bremen, Germany, 2004.

- [4] Ajay Subramanian, "A low Phase Noise K-band Oscillator utilizing an Embedded Dielectric Resonator on Multilayer High Frequency Laminates", Master thesis, University of Central Florida, 2008.
- [5] Olivier Bernard, Robin Croston, "Simulate and Build a Ku-Band DRO", Microwaves &RF, May 2000.
- [6] U. L. Rohde, A. K. Poddar, and G. Boeck, "Modern Microwave Oscillators for Wireless Applications: Theory and Optimization", John Wiley & Sons Inc., 2005.
- [7] Jaechun Lee, Young-Taek Lee, and Sangwook Nam, "A Phase Noise Reduction Technique in Microwave Oscillator Using High-Q Active Filter," IEEE Microwave and Wireless Components Letters, vol. 12 pp. 424-428, November 2002.
- [8] Mahyuddin, N.M, Ain, M.F. Hassan, S.I.S, and Singh, "Modeling of a 10 GHz Dielectric Resonator Oscillator in ADS," IEEE RF and Microwave Conference, pp. 106-110, 2006.
- [9] K. Chow, "On the solution and field pattern of cylindrical dielectric resonators," IEEE Trans. Microw. Theory Tech., vol. MTT-14, no. 9, p. 439, Sep. 1966.
- [10] T. Itoh and R. S. Rudokas, "New method for computing the resonant frequencies of dielectric resonators," IEEE Trans. Microw. Theory Tech., Vol. MTT-25, no. 1, pp. 52–54, Jan. 1977.
- [11] M. W. Pospieszalski, "Cylindrical dielectric resonators and their applications in TEM line microwave circuits," IEEE Trans. Microw. Theory Tech., vol. MTT-27, no. 3, pp. 233–238, Mar. 1979.
- [12] A. M. Pavio and M. A. Smith, "A 20–40 GHz push-push dielectric resonator oscillator," IEEE Trans. Microw. Theory Tech., vol. 33, no. MTT-12, pp. 1346–1349, Dec. 1985.
- [13] F. X. Sinnesbichler, B. Haultz, and G. R. Olbrich, "An SiGe HBT dielectric resonator push-push oscillator at 58 GHz," IEEE Microw. Guided Wave Lett. vol. 10, no. 4, pp. 145–147, Apr. 2000.
- [14] J-F. Gravel and J. S. Wight, "On the conception and analysis of a 12-GHz Push-push phase locked DRO," IEEE Trans. Microw. Theory Tech., vol. 54, no. 1, pp. 153–159, Jan. 2006.
- [15] A. P. S Khanna, "Review of Dielectric Resonator Oscillator Topology", IEEE, Int. Frequency Control Symposium, 1987.
- [16] U. L. Rohde, A. K. Poddar, "Tunable Frequency, Low Phase Noise and Low Thermal Drift Oscillator", US Patent No.7196591, March 2007.
- [17] U. L. Rohde, A. K. Poddar, "Low Noise, Hybrid Tuned Wideband Voltage Controlled Oscillator", US Patent No. 7,365,612 B2, April 29, 2008.
- [18] U. L. Rohde, A. K. Poddar, "Tunable Frequency. Low Phase Noise and Low Thermal Drift Oscillator", U.S Patent NO. 7, 545, 229, June 09, 2009.
- [19] U. L. Rohde, A. K. Poddar, "User-Definable, Low Cost, Low Phase Hit and Spectral Pure Tunable Oscillator", U.S. Patent No. 7,586,381 on September 08, 2009.
- [20] U. L. Rohde, A. K. Poddar, "User-Definable, Low Cost, Low noise, and phase hit insensitive multi-octave-band tunable oscillator", Phase Hit and Spectral Pure Tunable Oscillator, U.S. Patent No. 7,605,670, October 20, 2009
- [21] L. Zhou, R. Chu, Z. Wu, W.-Y. Yin, and J.-F. Mao, "Broad tuning low noise Ku band dielectric resonator oscillators," in Proc. Asia-Pacific Microw. Conf., pp. 1–4, Dec. 2008.

- [22] P. Stockwell, D. Green, C. Mcneilage, and J. H. Searls, " A low phase noise 1.3 GHz dielectric resonator oscillator," in *Proc. IEEE Int. Freq. Control Symp.*, pp. 882–885, May 2006.
- [23] C. Florian, P. A. Traverso, G. Vannini, and F. Filicori, "Design of low phase noise dielectric resonator oscillators with GaInP HBT devices exploiting a non-linear noise model," in *IEEE MTT-s Dig.*, pp. 1525–1528, June 2007,
- [24] U. L. Rohde and A. K. Poddar, "Mode-coupled stubs-tuned planar resonator offers promising and integrable alternatives of DRO," in *Proc. IEEE Freq. Control Symp.*, pp. 296-304, May 2008.
- [25] O. Llopois, G. Cibiel, Y. Kersale, M. Regis, M. Chaubet, and V. Giordano, "Ultra low phase noise sapphire-SiGe HBT oscillator," *IEEE Microw. Wireless Component Letter*, vol. 12, no. 5, pp. 157–159, May 2002.
- [26] K. Hosoya, K. Ohata, M. Funabashi, T. Inoue, and M. Kuzuhara, "V-band HJFET MMIC DROs with low phase noise, high power, and excellent temperature stability," *IEEE Trans. Microwave Theory Tech.*, vol. 51, no. 11, pp. 2250–2258, Nov. 2003.
- [27] U. L. Rohde and A. K. Poddar, "DRO Drops phase-noise levels", *Microwaves & RF*, pp. 80-84, Feb. 2013
- [28] D. M. Pozar," Microwave Resonators." In *Microwave Engineering*, 2nd ed. New York: Wiley, 1998, Ch. 6, sec. 5, pp. 323-327.
- [29] U. L. Rohde and A. K. Poddar, "*STPCR Offers Integrable Alternatives of DRO*", *Microwave Symposium Digest*, 2008 IEEE MTT-S, pp. 233-236, 15-20 June 2008 Atlanta, USA.
- [30] C. V. J. et al., "Design and performance of dielectric resonator oscillators with series feedback", *Electrotechnical Conference Proceedings, Integrating Research, Industry and Education in Energy and Communication Engineering*, pp. 339-342, IEEE MELECON 1989

Chapter 10

High Performance Opto-Electronic Oscillators (OEOs)

10.1 Introduction

The emerging wireless communications standards at higher frequencies, especially above 10 GHz are challenged by the availability of high Q-factor resonator and solid state devices, whose limitation is caused by ohmic and dispersive losses in various active and passive elements in the oscillator [1]-[81]. High spectral purity stable oscillators at high frequencies are required in radar systems as stable local oscillator (STALO) for the up and down conversion [1]. As a result, a lower bit error rate of data can be transmitted over a given communication bandwidth, and could be used as a stable clock for electrical and optical sampling of broadband information in analog to digital converters and a number of other digital processing functions [2]-[3].

Improved stability and spectral purity of oscillators can be achieved by combining electronic oscillators with high Q resonators such as quartz crystals resonators, acoustic resonators, ceramic resonators, dielectric resonators, and printed coupled resonators. Such resonators have low frequency resonant modes; hence, a number of frequency multiplication stages are needed to reach the microwave regime. The drawback of this approach is reduction in output power and degradation of phase and amplitude noise by the factor of $20 \log_{10} (f)$ when operative frequency, f , increases [4]-[7]. The optoelectronic oscillator (OEO) circuit can achieve better phase noise performance at 10 GHz and above as compared to the traditional frequency multiplier and synthesis approaches, such as phase-locked dielectric resonators, YIG, SAW, and quartz crystal oscillators [8]-[12]. A typical OEO uses optical fiber delay line which acts as a fundamental resonator in electronic oscillator circuits in 1 GHz-100 GHz ranges; frequency multiplication stages are not needed for achieving high frequencies (X, Ka, Ku band and above).

The fundamental improvement in phase noise achievable in an OEO is attributable to direct frequency generation from an optical source rather than through electronic multiplication. Typical components of OEO circuits assembled from discrete devices, especially optoelectronic photonic components require a large volume, high power consumption, and require a great deal of real estate and cost. Additionally, due to the assembly of a large number of discrete parts, application of OEO as reference frequency sources are generally subject to vibration and G-sensitivity problems, therefore limit the utility of and possible applications for OEOs in both commercial and military environments [13]-[21]. As a result, there is a need for an optoelectronic oscillator (OEO) system, having design topologies that overcome the above problems and meet the design constraints for implementation of stable ultra-low phase noise frequency synthesizers in a small size, with low power consumption, low phase noise and low cost. The biggest challenge is to develop low cost and reliable integrated photonic components using Silicon CMOS, BiCMOS technology, eliminating the need for bulky and/or discrete microwave components.

In this thesis, a novel high performance, low cost, and integratable OEOs system is developed based on metamaterial evanescent mode-locked resonator dynamics in conjunction with SILPLL

(self injection locked phase locked loop) techniques [US Patent application No.: 61/746, 919; filed on Dec 28, 2012 and US Patent application no. 13/760767; filed on Feb 06, 2013] [22]-[23].

10.2. Opto-Electronic Oscillator (OEO) System

Achieving ultra low phase noise is a great challenge in deep space communication, docking and remote sensing (radar), analog-to-digital convertors (ADC), instrumentation, and timing clocks. In many coherent detection systems, the required phase noise and the associated timing jitters of the stable local oscillators becomes the limiting factor of the overall performance of the system in terms of data bit error rate, achieved spatial and temporal resolution, and effective number of bit resolution. In the past several decades, great efforts have been made in the development of various techniques for generation of low phase noise oscillators. Opto-electronic oscillator (OEO) [8] stands out among the others for its capability of generating ultra-stable microwave and millimeter-wave oscillations owing to the extremely high Q achieved by utilizing the low loss in optical fibers. For example, a 10 GHz OEO is commercially available [25] with phase noise levels of -140 dBc/Hz at 10 kHz offset from carrier.

These high Q operation OEO with their low phase noise performance could be employed as highly stable sources to force-oscillate a small size low stability RF oscillator; the standard forced oscillation techniques of injection locking (IL) and phase-locked loop (PLL) are two viable methods for further phase noise reduction by introducing external frequency reference to the oscillator [26]-[27], where the lowest achievable phase noise of these techniques is limited by the phase noise of the external reference source. The concepts of external forced oscillations could not be extended to the already record setting OEO to further stabilize them, but nonetheless self-forced-oscillation could be provided as a method to further reduce close-in to carrier phase noise of oscillators, as demonstrated in [28].

A self-injection locking (SIL) topology is proposed by passing the output of oscillator through an electrical delay line or a high Q resonator and feeding it back using a circulator. The experimentally verified modeling demonstrates that the overall oscillator phase noise is inversely proportional to the signal delay time or Q. However, due to the high loss and limited Q in electric circuits, the phase noise improvement is not significant. To bypass the limitation of electrical components, Lee *et al* [14] employed a 2.4 km long optical fiber in the feedback loop of the SIL topology and achieved a phase noise reduction of 27 dB at 10 kHz offset for a 30GHz oscillator. The concept of forced oscillation could also be extended to self-phase locked loop (SPLL) demonstrated by Pillet *et al.* [30] in which the microwave signal generated from the beat note of a dual frequency laser (DFL) was sent into a delay line frequency discriminator (DLFD) whose output is used to stabilize the laser frequency for generating a more stable beat note. The analytical modeling provided explanation for this phase noise reduction. While IL (injection locking) phenomena are easy to implement, the phase noise in the close-in offset frequency range is degraded due to frequency offset detuning and limited locking range as explained in [30]. On the other hand, even though PLL has a longer pull-in time that results in a slow response, the high gain loop filter enables the PLL to remove the close-in phase noise significantly, while far away from carrier suffers from a higher noise. Sturzbecher et al. [31] demonstrated in externally forced oscillators, a better phase noise characteristics for both close in and far-away from carrier and a wider locking range is achieved by combining IL and PLL

(ILPLL). However, external reference sources are required in the forced ILPLL topology, which limits the ultimate phase noise performance.

To overcome above problems, the novel approach is to incorporate both SIL and SPLL for close-in and far-offset noise reduction in conjunction with evanescent mode locking for ultra stable low phase noise performance [22]-[23]. Figure 10-1 shows the typical block diagram of OEO system using SILPLL techniques for the realization of stable frequency source for high performance application in modern communication systems.

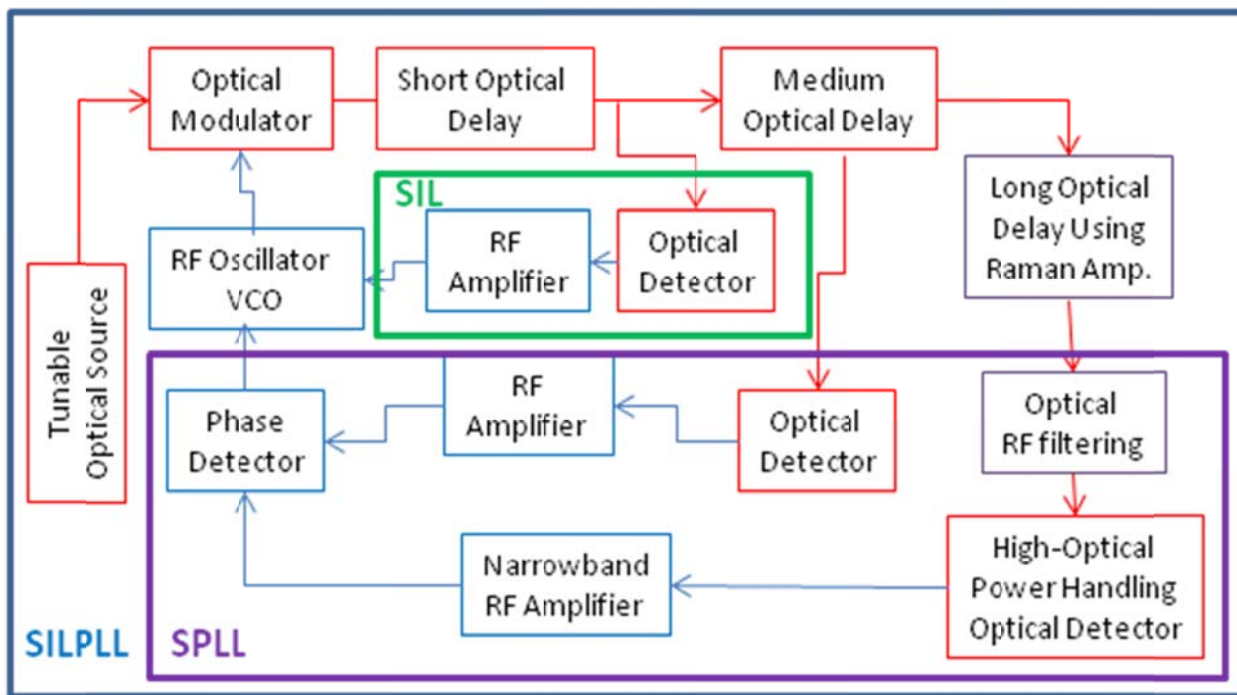


Figure 10-1: shows the typical block diagram of OEO using SILPLL (US Patent applications: 61/746, 919 and. 13/760767) (The color arrangement of various modules in the block diagram exhibits the SIL, SPLL, and SILPLL techniques) [22]-[23]

10.3. OEO Circuit Theories

A typical Opto-Electronic Oscillator (OEO) utilizes the transmission characteristics of a modulator together with a fiber-optic delay line to convert light energy into stable, spectrally pure RF/microwave reference signals. A detailed view of the construction of the oscillator is shown schematically in Figure 10-2 (a). In this configuration, light from a laser is introduced into an E/O modulator, the output of which is passed through a long optical fiber, and detected with a photodetector. After amplifying and filtering, the output of the photodetector is fed back to the electric port of the modulator. This configuration supports self-sustained oscillations at a frequency determined by the fiber delay length, bias setting of the modulator, and the bandpass characteristics of the filter. It also provides RF/microwave outputs in both electrical and optical domain, a feature that would be of considerable advantage for photonics applications [15]-[36].

A regenerative feedback model is used to analyze the spectral properties of the OEO. The conditions for self-sustained oscillations include coherent addition of partial waves each way around the loop and a loop gain exceeding losses for the circulating waves in the loop. The first condition implies that all signals that differ in phase by integer multiples of 2π from the fundamental signal can be sustained. The second condition implies that with adequate light input power, self-sustained oscillations may be obtained without the need for electrical amplifier [16].

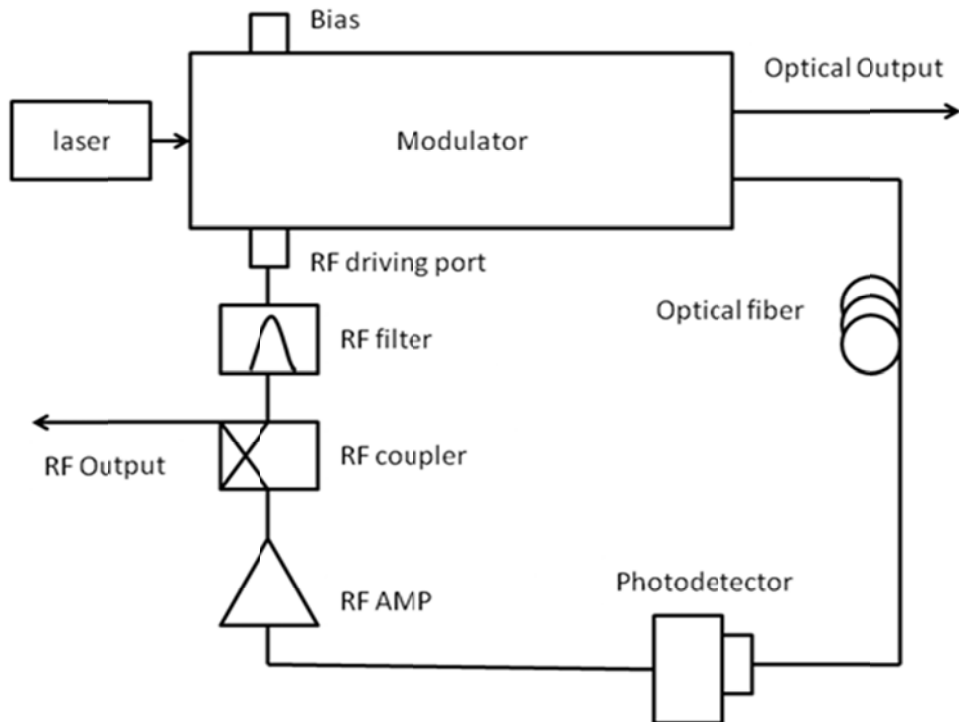


Figure 10-2 (a): A typical schematic of OEO [16, 71]

The phase noise of regenerative feedback model based OEO circuit can be described by

$$S_\phi(f'') = \left(1 + \left(\frac{f_{osc}}{2Qf'}\right)^2\right) S_\theta(f') \quad (10.1)$$

where f'' is the offset frequency; $S_\theta(f'')$ is the input noise to signal ratio; $S_\phi(f'')$ is the output noise spectrum.

The phase noise of an OEO with 16 km long loop (fiber delay) is shown in Figure 10-2b. It can be seen from Figure 10-2 (b) the measured phase noise is -163 dBc/Hz at 6 kHz offset from the carrier frequency of 10 GHz [80]. The superior performance results from the extremely low energy storage loss realized by incorporating long optical fiber. The optical fiber is also virtually free of any frequency-dependent loss, resulting in the same long storage time and high spectral purity signals for both low and high frequency oscillation.

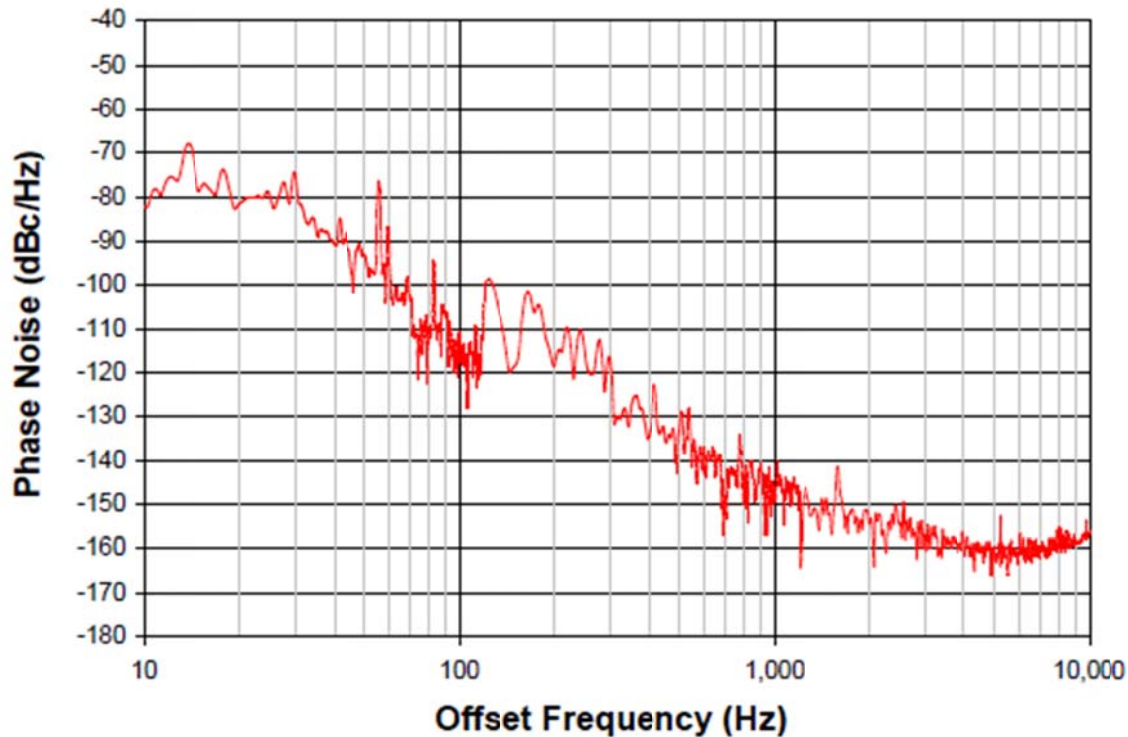


Figure 10-2b: Shows the experimental result of an OEO with 16km loop reported by Eliyahu et al in [80]

10.3.1 Dual-Injection-Locked (DIL) OEO

Even though the OEO has numerous advantages over other oscillator schematics, a difficulty with this configuration is that the long fiber length implies that many oscillation modes can exist in an OEO. In an OEO with a 4km fiber loop (20 μ s time delay), the modes are spaced approximately 50 kHz apart. The mode spacing is too small for the RF filter to eliminate the unwanted modes. Hence, a coupled-OEO approach is proposed to reduce the power level of the unwanted modes. Figure 10-3 shows that dual-injection-locking requires two OEOs [16]. Each of these two OEOs is an independent OEO; one would have a longer loop and act as a master while the other would have shorter loop and follow as slave. The two OEOs shown in Figure 10-3 are injection locked to each other.

The principle of side-mode suppression is shown in Figure 10-4. The modes in the master OEO have small mode spacing while the modes in slave OEO have larger mode spacing. Only those overlapped modes can survive in both master and slave oscillators.

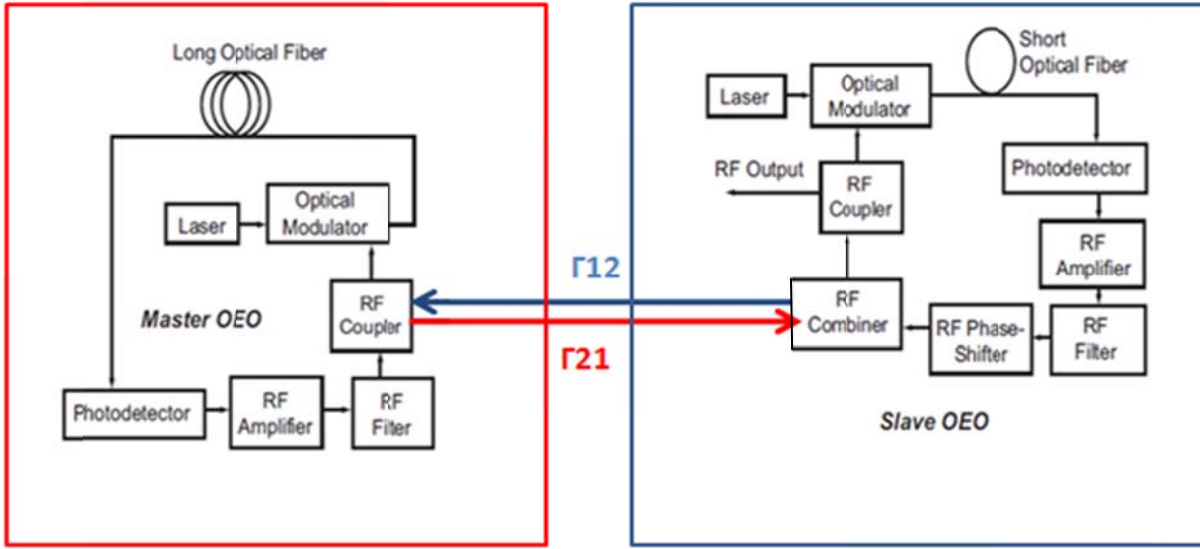


Figure 10-3: Shows the typical Dual-Injection-Locking Schematic Reported by Zhou et al in [16]

For those overlapped modes far away from center frequency, their amplitudes have been cut off by the RF filter.

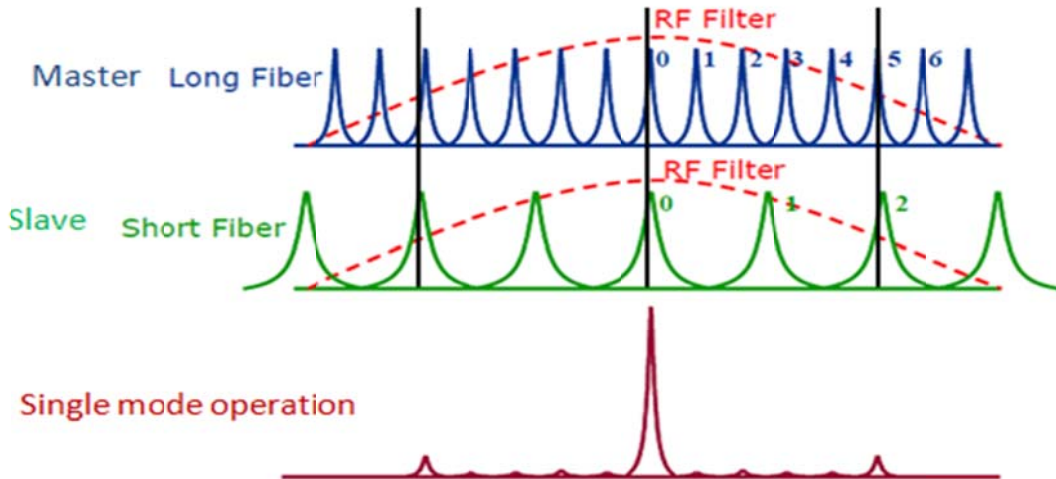


Figure 10-4: shows the principle of Dual Injection Locking for Side-mode Suppression

The phase noise of DIL OEO can be found as [16]

$$P_1(\omega) = \frac{1}{|D(\omega)|^2} \left[|1 - (1 - \Delta_2) \exp(-j\omega\tau_2)|^2 N_1(\omega) + \Gamma_{12}^2 N_2(\omega) \right] \quad (10.2a)$$

$$P_2(\omega) = \frac{1}{|D(\omega)|^2} \left[|1 - (1 - \Delta_1) \exp(-j\omega\tau_1)|^2 N_2(\omega) + \Gamma_{21}^2 N_1(\omega) \right] \quad (10.2b)$$

where $P_1(\omega)$ and $P_2(\omega)$ are power spectrum for master loop and slave loop, respectively.

Using CAD simulation (Matlab), the predicted phase noise can be plotted from Equations (10.1), (10.2a) and (10.2b); shown in Figure 10-5. As shown in Figure 10-5, the first side-mode level is about -100dBc/Hz in both master and slave for DIL OEOs.

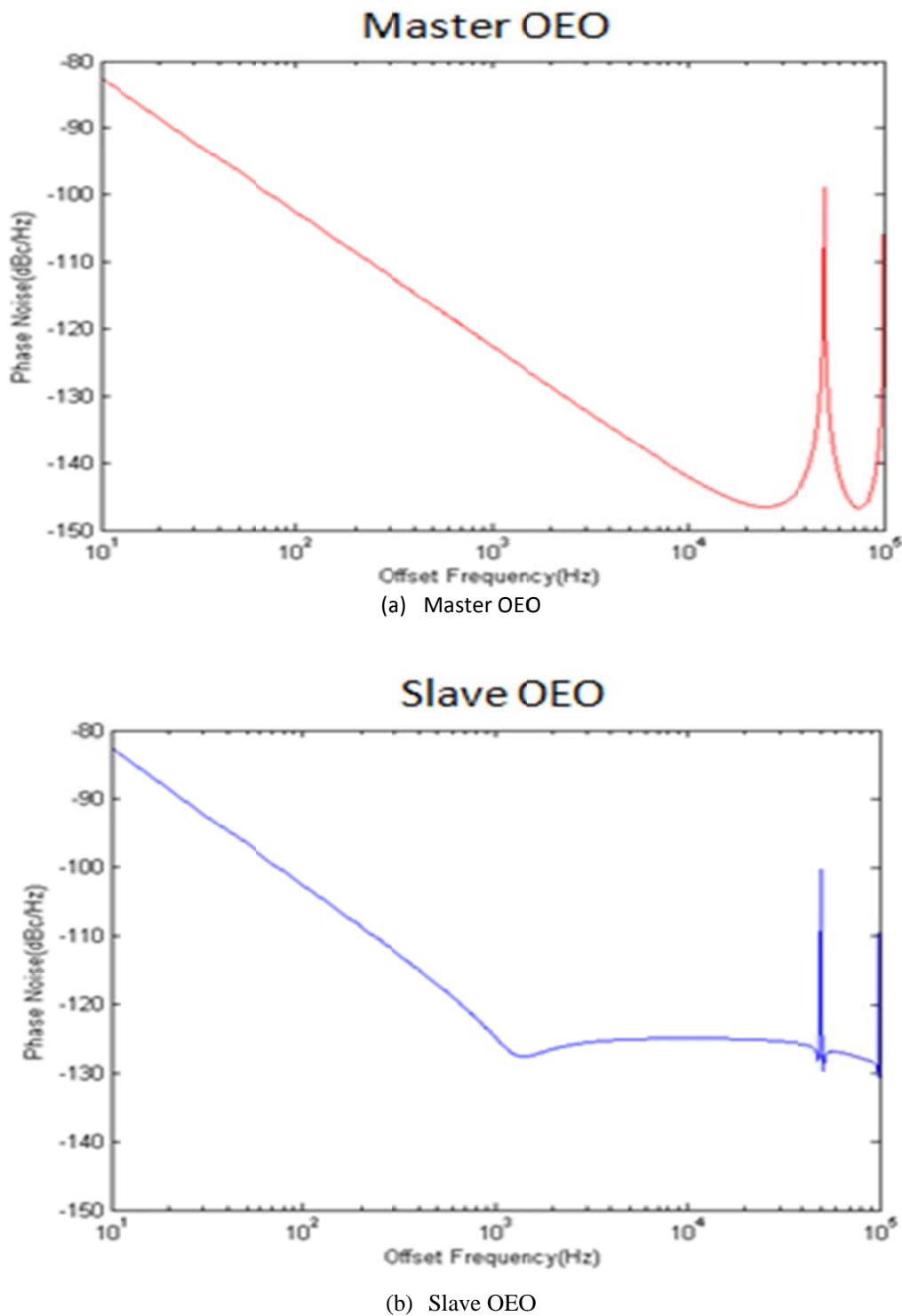


Figure 10-5: Shows the Matlab CAD simulation for DIL OEOs ($\tau_1=20\mu s$, $\tau_2=0.2\mu s$, $\Gamma_{12}^2=-30$ dB, $\Gamma_{21}^2=-20$ dB, $W1=W2=-23$ dBm, $N1=-166$ dBm/Hz, $N2=-170$ dBm/Hz): (a) Master OEO, and (b) Slave OEO

10.3.2 Coupled OEO

In a typical OEO configuration, a long fiber delay line is needed to act as high Q element. However, the long delay causes undesired side-modes and is not appropriate for compact design. To bypass the long delay, a coupled OEO configuration using a fiber ring laser as the high Q element is proposed by Maleki et al [71]. Block diagram of the coupled OEO is shown in Figure 10-6. The fiber ring laser consists of an electro-optic modulator, an EDFA, a piece of dispersion-shifted fiber (DSF) and an optical filter.

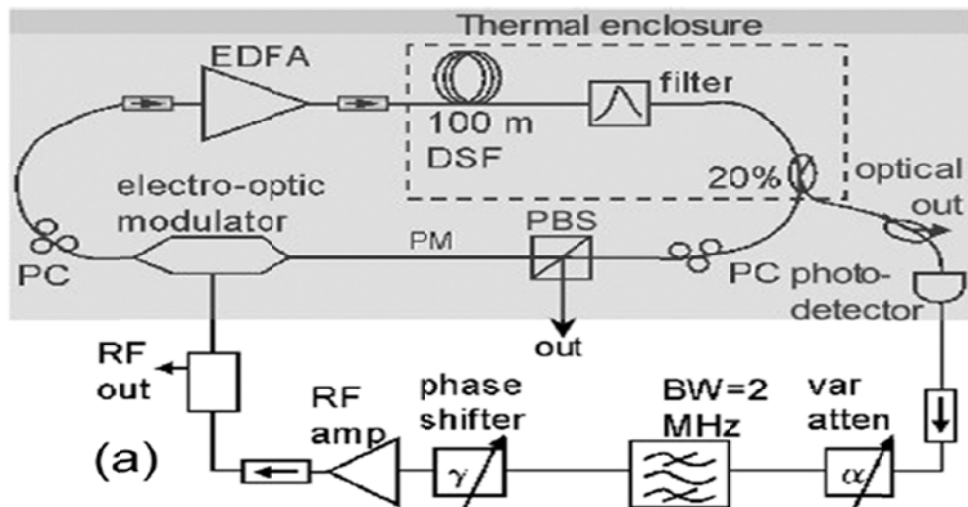


Figure 10-6: A typical schematic of Coupled OEO [71]

To complete the optoelectronic loop, a portion of the light in the fiber ring laser is tapped out and detected by a photo detector. The electrical output is then filtered and amplified and is finally sent back to the electro-optic modulator to provide the modulation frequency. The interaction between the optical modes and electrical modes as explained in Figure 10-7a shows the modes in the fiber ring laser: Δv is the FSR of the ring laser and it is inversely proportional to the length of the ring. Figure 10-7b depicts the beat frequencies of the modes in the fiber ring laser and these beat frequencies are the possible RF output frequencies. The optoelectronic feedback loop is longer than the loop length of the ring laser, resulting in mode spacing smaller than the mode spacing of the ring laser, as shown in Figure 10-7c. The center frequency of the RF bandpass filter is chosen such that it is equal to a beat frequency of a set of modes of the ring laser. Within the passband, many OEO modes are competing to oscillate. The winner is the mode with a frequency that is closest to a beat frequency of the ring laser's modes since only this mode can obtain energy from the laser. This OEO mode is fed back for modulation of the gain of the ring laser and effectively mode locks the ring laser. The mode locking makes the mode spacing of the ring laser equal to the frequency of the oscillating OEO mode, which is multiple of the natural mode spacing of the laser, as shown in Figure 10-7d. Because all the oscillating modes in the mode-locked laser are forced to be in-phase, all the mode beat signals between any two neighboring laser modes will add in phase and generate a strong signal at the frequency of the oscillating OEO mode.

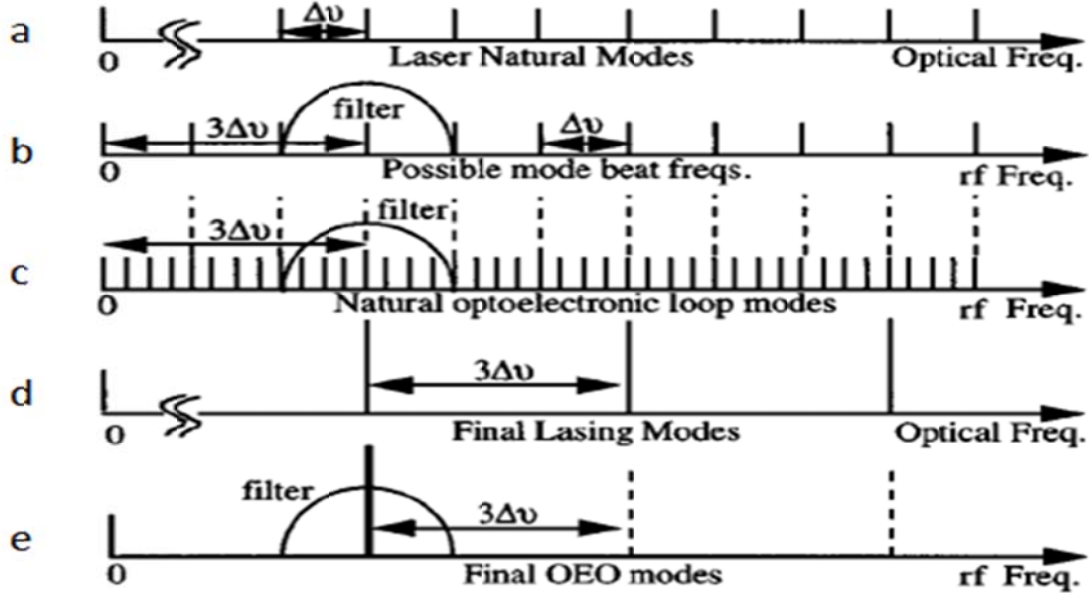


Figure 10-7: Shows the typical Optical and Electrical Modes in Coupled OEO in [74]

This enhanced mode beat signal in turn provides more gain to the oscillating OEO mode and reinforces its oscillation, as shown in Figure 10-7e. The experimental results of the coupled OEO are shown in Figure 10-8. In a 160 meter long loop, 3nm Filter BW results in a shorter pulse width of 2ps and a lower phase noise while 1nm Filter results in a 7ps pulse width and a higher phase noise, as shown in Figure 10-8a. When the filter BW is fixed at 1nm, a 750nm long loop achieved a phase noise of -150dBc/Hz @ 10 kHz offset at oscillation frequency of 9.4GHz.

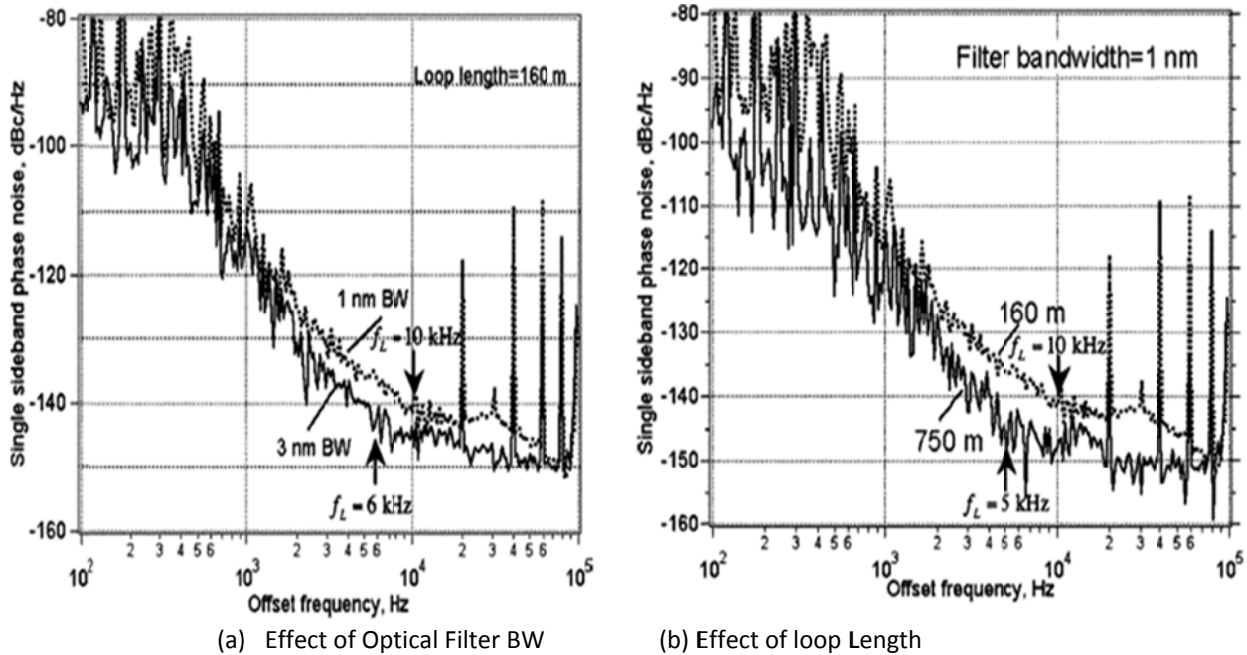


Figure 10-8: Measured Phase noise of Coupled OEO: (a) impact of optical filter BW from 1nm to 3nm bandwidth for a loop length of 160m, and (b) impact of loop length from 160m to 750m using a filter bandwidth of 1nm [74]

10.3.3 Whispering Gallery Mode (WGM) Based OEO

A typical configuration of OEO circuits using Whispering Gallery Mode (WGM) is reported by Langer et al., shown in Figure 10-9 [37]. The main difference is that the fiber delay line is replaced by a WGM resonator, as illustrated in Figure 10-9. The fused silica optical resonator has a diameter about 5mm, yielding a FSR of 10.7GHz. The difference of optical index between fused silica (~ 1.44) and air (~ 1) enables the internal reflection inside the resonator. Tapered fibers are used to couple light into and out of the WGM resonator. Experimental phase noise of WGM OEO is presented in Figure 10-10. The achieved phase noise is -90dBc/Hz at 10 kHz and -110dBc/Hz at 100 kHz when the oscillation frequency is 10.7GHz.

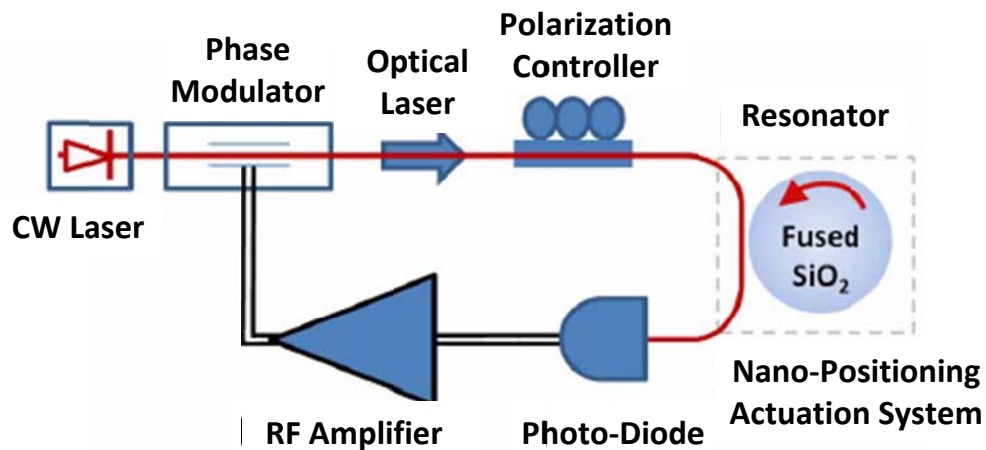


Figure 10-9: A typical schematic of WGM OEO in [37]

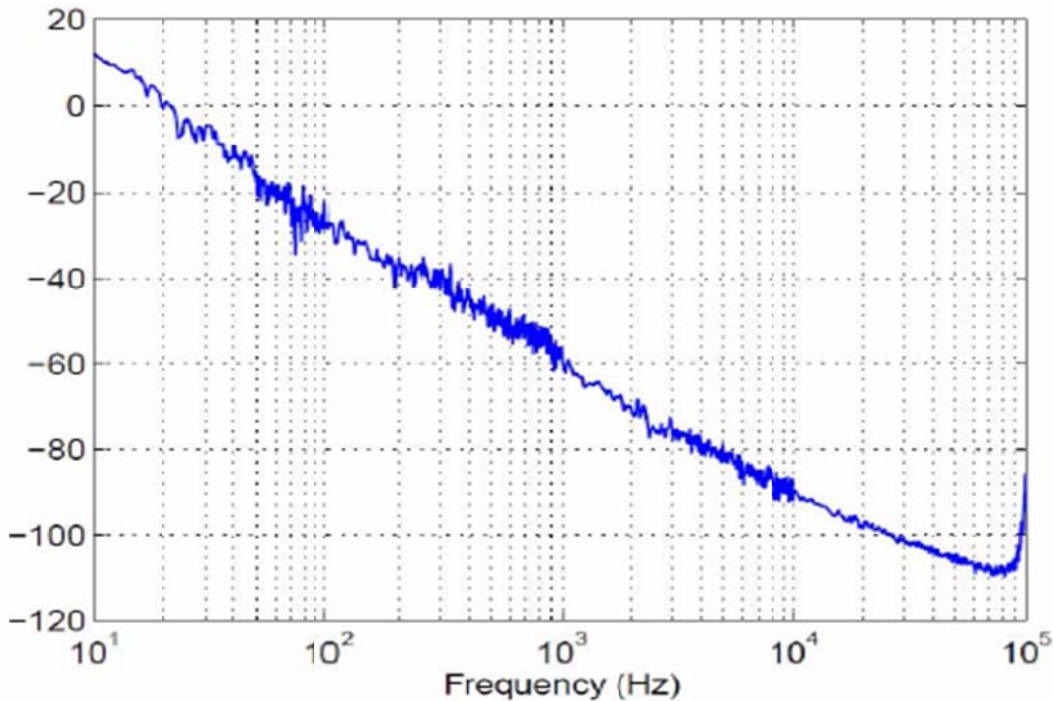


Figure 10-10: Shows the experimental Phase Noise plot of WGM OEO in [38]

As shown in Figure 10-9, the WGM OEO has certain advantages over conventional OEO. First, in the absence of a long fiber delay, the side-modes associated with the long delay no longer exist. In addition to the elimination of the side-modes, the size of the OEO can be greatly reduced since the size of WGM resonator is about millimeters. Finally, the usage of WGM resonator makes it feasible for monolithic fabrication of OEO. However, WGM based resonators suffer from microphonics and high temperature sensitivity.

10.3.4 Optimum Fiber Delay Length (Novel Approach) [22, 23]

The novel approach proposed in this thesis is to build OEO circuit as proposed by Yao and Maleki [16, 37]. However, the reported approach in this thesis identifies an optimum fiber optic delay length to achieve optimum Q factor for a resonator in evanescent mode-locking condition [22, 74, 75, and 76]. A resonator quality factor is directly related to energy stored to power dissipated. For a distributed resonator using TEM line the Q factor is expressed as [74]

$$Q = \frac{\text{Total Phase Stored}}{\text{Total Loss}} = \frac{\pi f_{\text{osc}} \tau}{a^l} \quad (10.3)$$

where $a = 10^{\frac{\alpha}{10}}$, $\tau = \frac{nl}{c}$ and α is the attenuation factor in distributed line.

The advantage of OEO is the associated low attenuation, where α values of 0.3, 0.2, 0.1, 0.05 dB/km are considered to render standard fiber (0.3 and 0.2 dB/Km for Corning SMF-28 fibers) and specialized composite FBG fibers with distributed Raman gain leading to optical attenuation close to 0dB (practically between 0.1 and 0.05dB/km). The optimum Q for each attenuation value is calculated and a plot of the optimum length is depicted in the Figure 10-11. These lengths are to be made using loss levels achieved out of passively temperature compensated composite fiber. Phase noise expression for an oscillator with Q factor at offset frequency of 'f' away from oscillation frequency can be expressed as [40]:

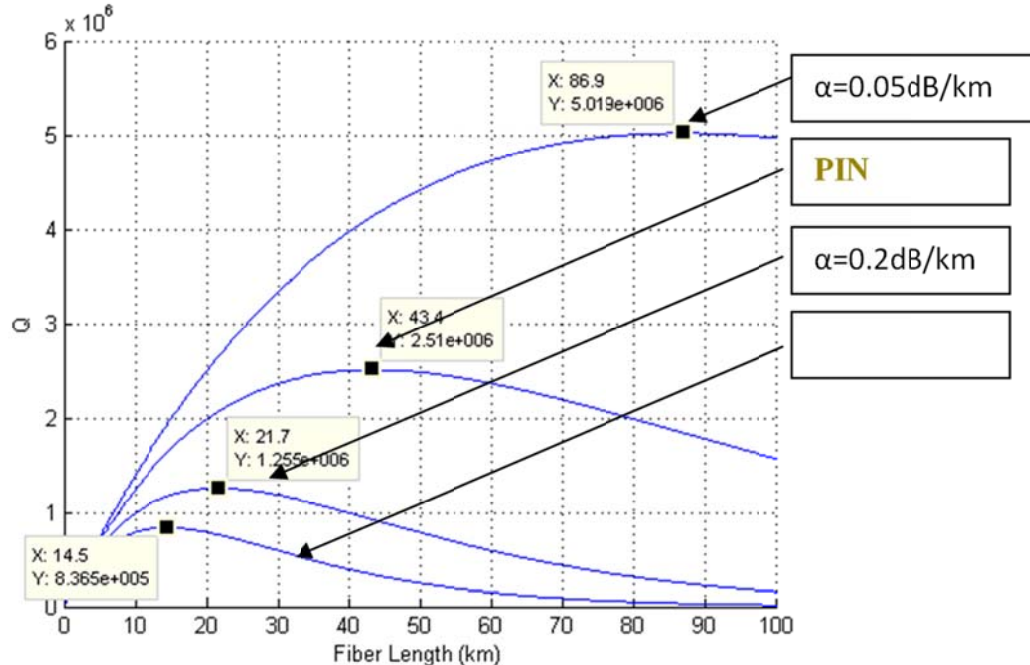


Figure 10-11: shows the plot of Q-factor and optimum length of fiber optic delay line for a 10 GHz oscillator using different fiber attenuations ranging from 0.05dB/km to 1dB/km [22, 23].

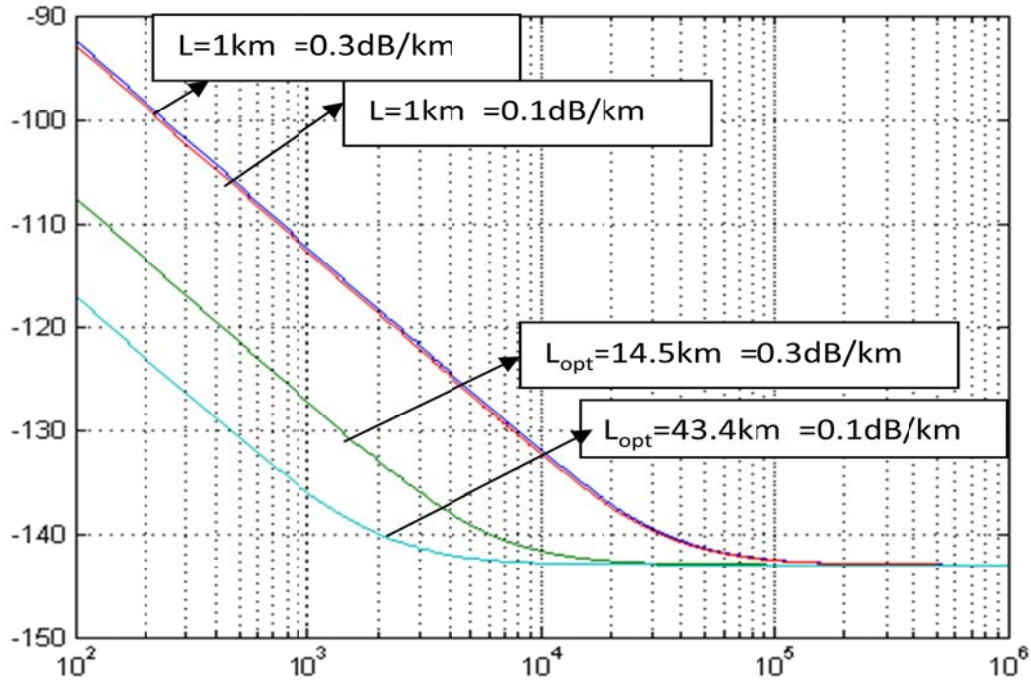


Figure 10-12: Shows the comparison of achieved close-in to carrier phase noise of 10 GHz OEO using optimum and non-optimum lengths for fiber attenuation of 0.1dB/km versus 0.3dB/km

$$\text{Phase Noise} = \left(1 + \left(\frac{f_{osc}}{2Q_f}\right)^2\right) S_\theta \quad (\text{Without noise contribution from active devices}) \quad (10.4)$$

Where $S_\theta = -140 \text{ dBc/Hz}$ is the input noise to signal ratio

Figure 10-12 shows the comparison of phase noise plots for different lengths of the fiber optic delay line for a 10 GHz oscillator.

10.3.5 Forced Frequency Stabilization/Phase Noise Reduction Techniques

The reduction in phase noise and stabilization of OEO circuit can be achieved by incorporating following techniques:

10.3.5.1 Injection Locking (IL)

The phase noise of the injection-locked oscillator is given by

$$n_0(\omega_m) = n_{vco}(\omega_m)S_{vco}(\omega_m) + n_{ref}(\omega_m)S_{ref}(\omega_m) \quad (10.5)$$

Where

$$S_{vco}(\omega_m) = \frac{\left(\frac{\omega}{\Delta\omega}\right)^2}{1+\left(\frac{\omega}{\Delta\omega}\right)^2}, \quad S_{ref}(\omega_m) = \frac{1}{1+\left(\frac{\omega}{\Delta\omega}\right)^2} \quad (10.6)$$

Figure 10-13 shows the spectra of 4.2 GHz oscillator for both free running and injection locked condition [68].

In both PL and IL cases, the close in to carrier phase noise is dominated by the reference source as shown below.

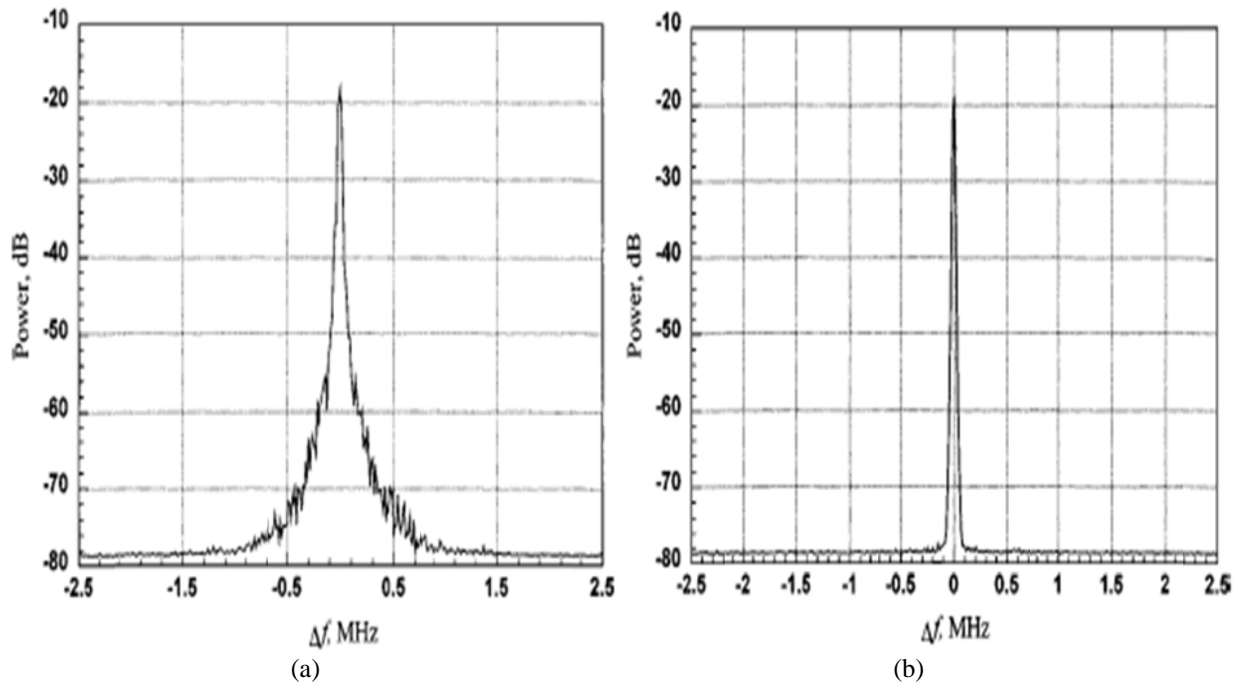


Figure 10-13: Shows the spectra of 4.2 GHz oscillator (a) free running, and (b) injection locked condition [68]

10.3.5.2 Self-Injection Locking (SIL) using Electrical Feedback

Self-injection locking can be used to improve the phase noise of the existing oscillators. Self-injection locking is achieved when the oscillator itself is used for injection locking. The analytical expression for SIL oscillator is given by [13]

$$L_{inj}(f') = \frac{L(f')}{(1 + \sqrt{\kappa} f_{3dB} \tau)^2} \quad (10.7)$$

where $L_{inj}(f')$ is the phase noise of the self injection locked oscillator; $L(f')$ is the phase noise of the free-running oscillator; κ is the injection power with respect to oscillation power; f_{3dB} is the BW of the free-running oscillator; and τ is the feedback delay.

The analytical model indicates that if one increases the self-injection signal strength κ and the loop delay τ while keeping the loop phase to be 0 or 2π , the phase noise of the oscillator at the noise offset frequency near the carrier can be reduced further. However, the longer loop delay τ requires the longer cable delay line, and it will be impractical to use a long electrical cable in the self injection locked oscillator to reduce the phase noise due to the high loss in electrical delay line.

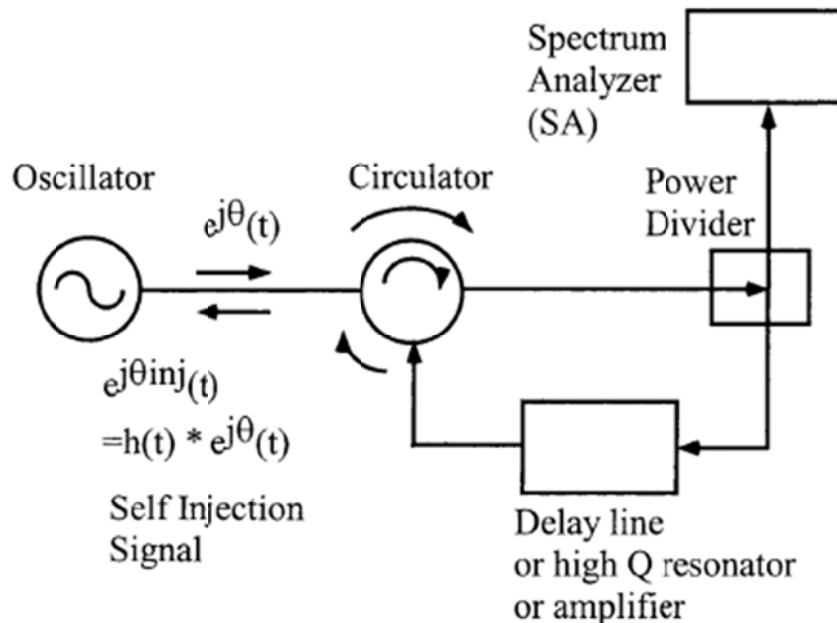


Figure 10-14: Shows the typical block Diagram of Self Injection Locking (SIL) in [13]

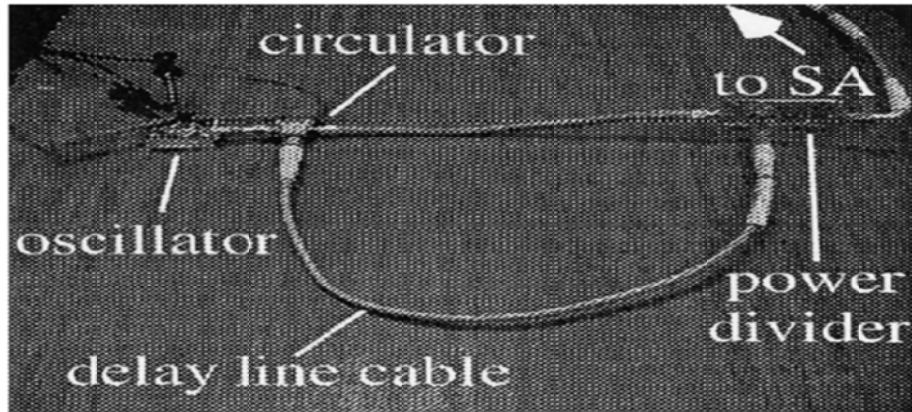
Figure 10-14 shows the typical block diagram of the self-injection locked oscillator [13]. The output of a MESFET oscillator passes through a circulator and is feedback to the oscillator through a delay element for self injection locking.

The experimental result of self-injection locking (SIL) oscillator circuit is shown in Figure 10-15b. A coaxial cable is used to construct the feedback loop, which provides a 15.7ns delay, as shown in the prototype (Figure 10-15a). Different attenuators are also selected to show the behavior of the phase noise under self-injection locking, as shown in Figure 10-15b. Note that the phase noise measurement results show qualitative agreement with the analytical expression. The phase noise departs from its ideal curves within some noise offset frequency ranges, which may be caused by the change of the oscillator output load.

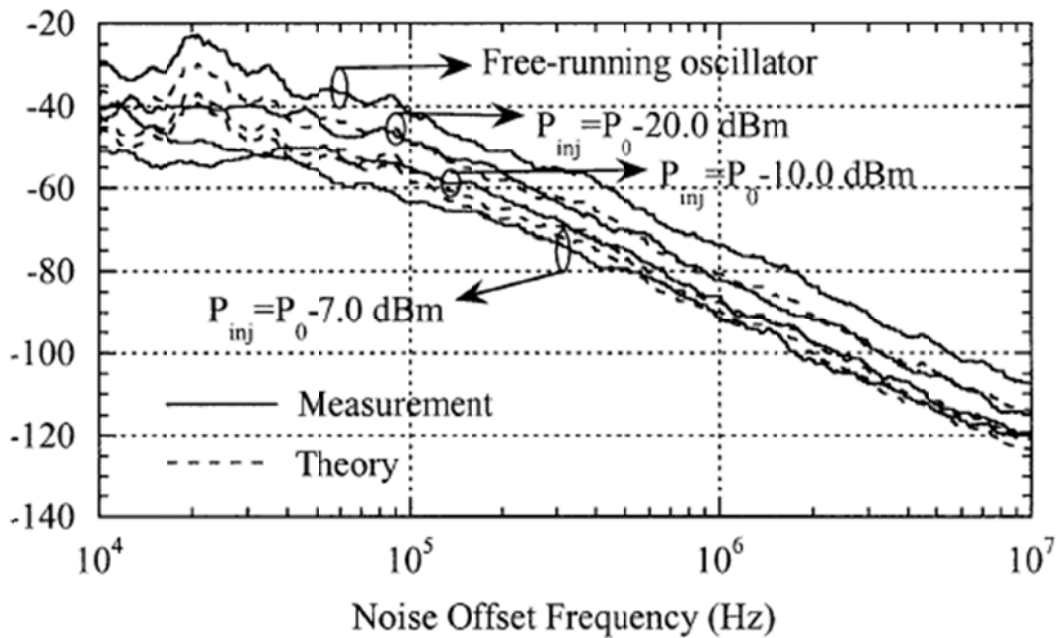
10.3.5.3 Self Injection Locking (SIL) using Optical Feedback

The electrical delay line length is limited by high loss for frequencies beyond several Giga Hertz (up to 100 GHz). Optical fiber delay line, on the other hand, has very low transmission loss and is suitable for building self-injection locked oscillators.

A self-injection locked oscillator using optical feedback is reported by Lee et al [14], as can be seen in Figure 10-16. The electrical loop has sufficient gain to oscillate by itself. A part of output signals from the electrical oscillator, is injected into the oscillator after passing through a long optical delay line and it locks the electrical oscillator, achieving self-injection locking.



(a) Self Injection Locking Experimental Setup [13]



(b) Phase Noise Results of SIL Oscillator under Different Injection Strengths

Figure 10-15: Shows the prototype of SIL oscillator circuit and measured phase noise plots at different injection levels: (a) Self Injection Locking Experimental Setup, and (b) Phase Noise Results of SIL Oscillator under Different Injection Strengths [13]

From (10.7), the phase noise of this oscillator can be expressed for optical feedback case. Measured phase noise of this oscillator is presented in Figure 10-17. A 2.4 km long optical fiber is used in the loop, which will provide 12 μ s delay. The oscillation frequency is at 30GHz. With the help of a long delay, a small injection power ($\kappa=1.6\times10^{-3}$) is already providing a significant phase noise reduction of about 20dB. Further phase noise reduction is also observed with higher injection power ($\kappa=2.5\times10^{-1}$). It is worth mentioning that in the case of $\kappa=2.5\times10^{-1}$, the measured phase noise -119 dBc/Hz at 10kHz offset does not match up with the analytical result -137dBc/Hz obtained from (10.1).

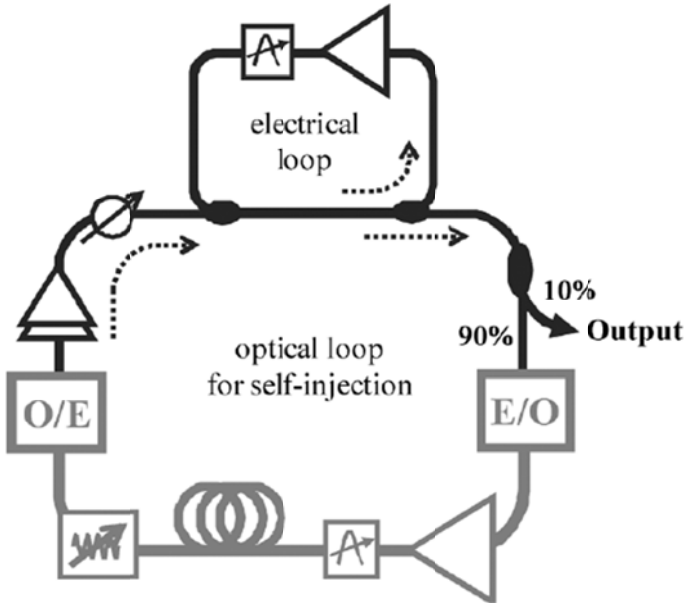


Figure 10-16: Shows the typical schematic of Self Injection Locked Oscillator using Optical Delay in [14]

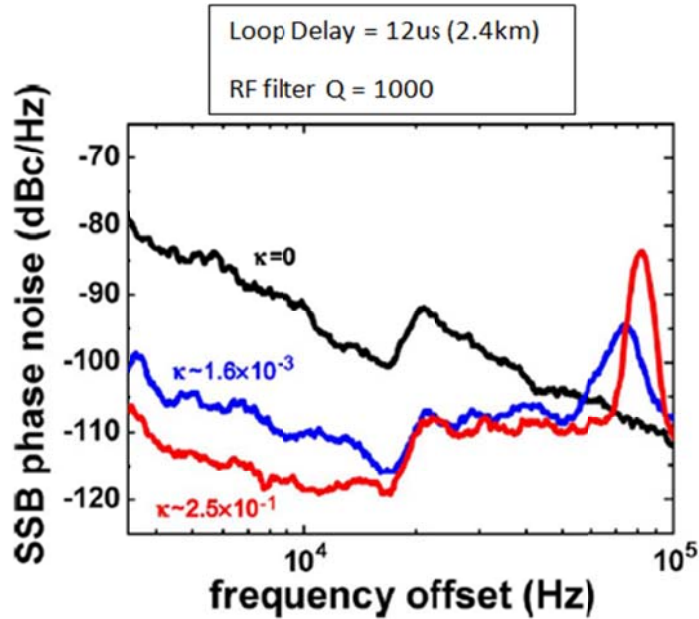


Figure 10-17: Shows the measured phase noise plot of optical feedback SIL (self injection locked) Oscillator under different Injection Power [14]

A possible explanation is that the interaction between electrical oscillation and optoelectronic oscillation may degrade the overall system performance. When there is no power or the power is small in the feedback loop, the side-mode level is low, as can be seen in Figures 10-18a and 10-18b. When the injection power is strong, the circulating power in the optical loop is strong enough to sustain self-oscillation, shown in Figure 10-18c.

This oscillation appears at offset frequencies given by,

$$\Delta f = \frac{1}{\tau} = \frac{c}{nl} \quad (10.8)$$

where τ is the loop delay time; c is the speed of the light; n is the effective refraction index of the fiber; l is the length of the fiber. The interaction between the electrical oscillation and the optical oscillation may have a negative effect on spectral purity and this phenomenon is important research topic.

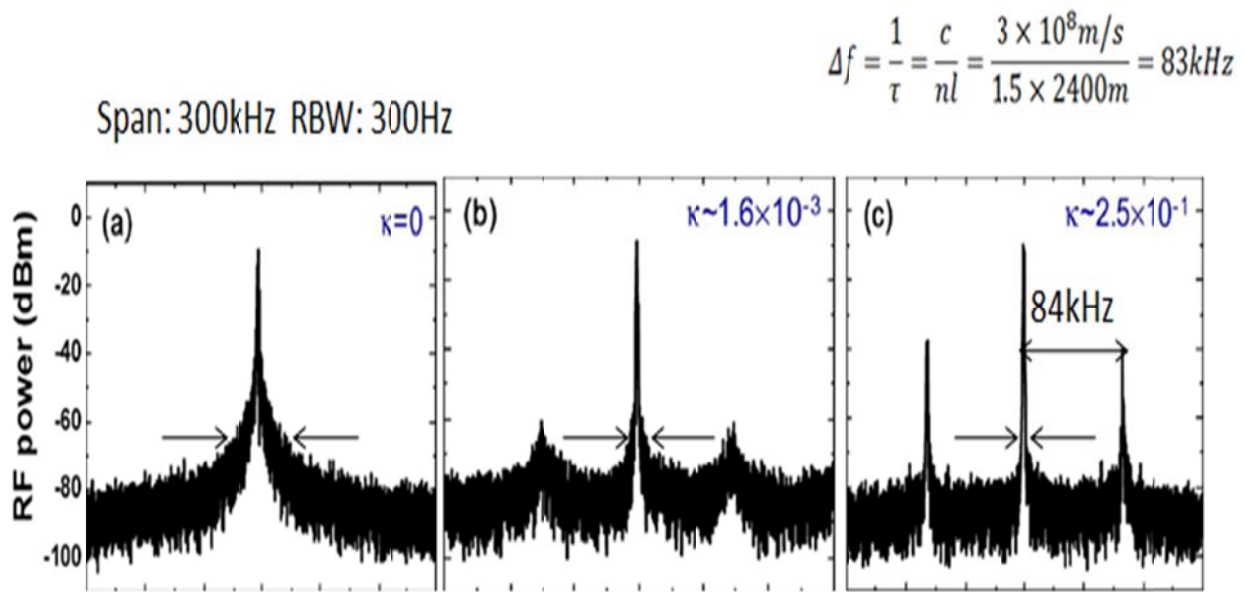


Figure 10-18: Shows the side-modes of SIL Oscillator under Different Injection Power (adopted from [6]) for three different coupling factor, a coupling factor: (a) $\kappa=0$, (b) $\kappa=1.6 \times 10^{-3}$, and (c) $\kappa=2.5 \times 10^{-1}$ [14]

10.3.5.4 Phase Locking (PL)

Figure 10-19 shows the typical block diagram of phase locking technique.

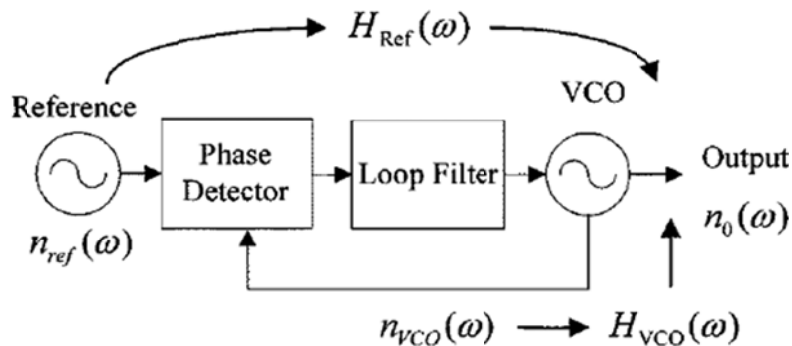


Figure 10-19: Shows the typical block diagram of phase locking technique

The phase noise of the phase-locked oscillator is given by

$$n_0(\omega_m) = n_{vco}(\omega_m)|H_{vco}(\omega_m)|^2 + n_{ref}(\omega_m)|H_{ref}(\omega_m)|^2 \quad (10.9)$$

Where $n_{vco}(\omega_m)$ is the phase noise of the free running oscillator, $H_{vco}(\omega_m)$ is the phase transfer function of the free-running oscillator, $n_{ref}(\omega_m)$ is the phase noise of the reference source, and $H_{ref}(\omega_m)$ is the phase transfer function of the reference source.

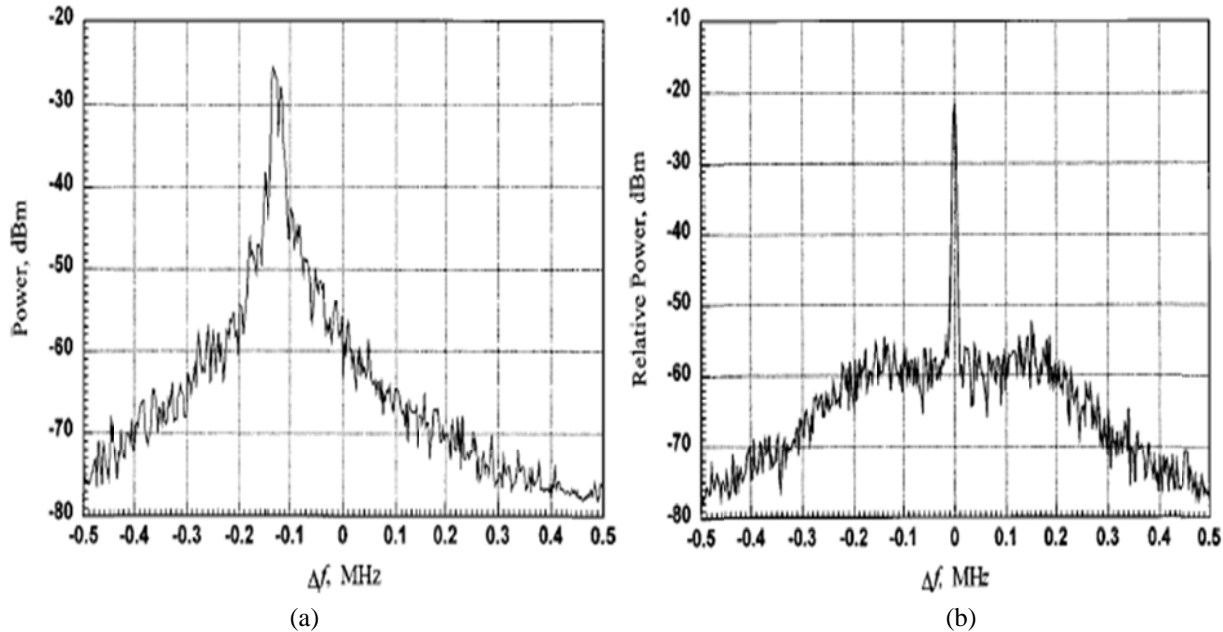


Figure 10-20: Shows the spectra of 4.643 GHz oscillator, spectrum analyzer filter bandwidth 3 kHz: (a) spectra of free running oscillator [68], and (b) phase locked loop oscillator [68]

10.3.5.5 Self-Phase Locked (SPL) Oscillator using Fiber Optic Delay

Self-phase locking is achieved when the oscillator's output itself is used for phase locking avoiding the use of an external reference. The use of a long, stable, fiber optic delay at RF/microwave frequencies provides much greater sensitivity to frequency fluctuations of the electronic oscillator, compared to conventional coaxial delay-line implementations, resulting in improved phase stability. The self-phase locked oscillator configuration is depicted in Figure 10-21a [13, 18].

Phase fluctuations of the voltage-controlled oscillator (VCO) are converted to baseband voltage fluctuations by the fiber optic discriminator. This baseband signal is amplified, filtered, and fed back to the phase control port of the VCO to reduce the phase fluctuations. In the fiber optic discriminator, shown in Figure 10-21b, the RF input signal is split and compared to a delayed version of itself in a phase detector.

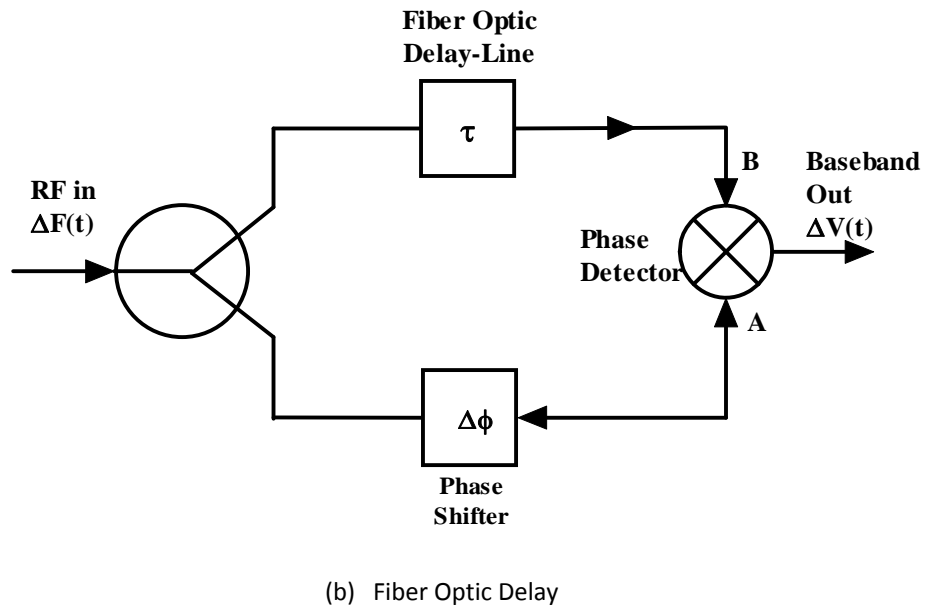
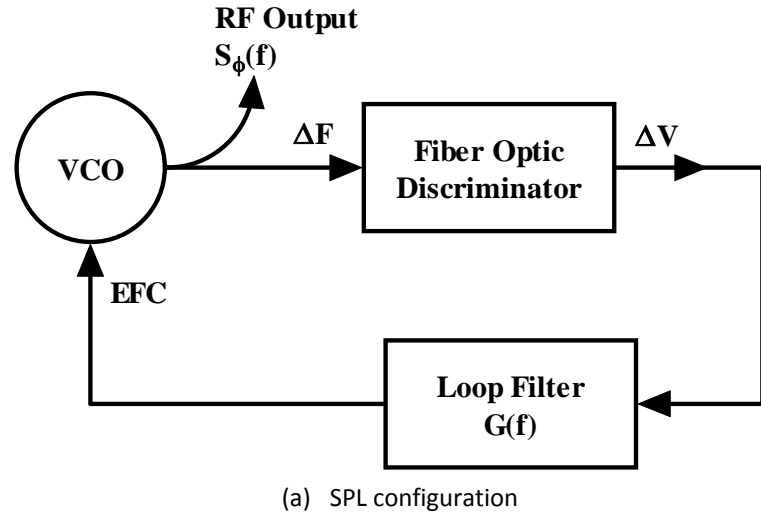


Figure 10-21: Shows the block diagram of (a) SPL configuration, and (b) Fiber Optic Delay Frequency Discriminator Configuration [13, 18]

Analytical modeling of phase noise for SPL oscillator is given by [18],

$$S_\phi(f') = \frac{S_{\phi 0}(f')}{(2\pi\tau f')^2} \quad (10.10)$$

where $S_{\phi 0}(f')$ is the phase noise of the free running VCO; τ is the feedback delay time; f' is the offset frequency. Similar to the self-injection locking case, a long delay is again needed for better phase noise reduction. Measured phase noise is shown in Figure 10-22. A phase noise reduction of about 12dB is achieved (at about 40 kHz offset from a 100 MHz carrier) for a commercially available frequency synthesizer when a 2.2 km long fiber is used in the frequency discriminator. It is noted that we will see secondary peak associated with the long delay.

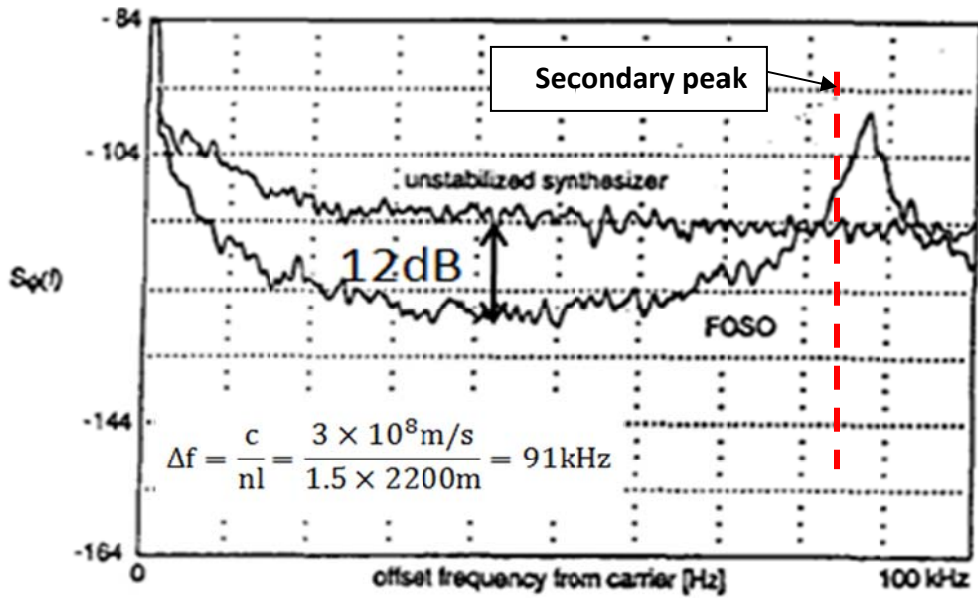


Figure 10-22 Measured Phase Noise of SPL Oscillator [18]

10.3.5.6 Self Phase Locking (SPL) with Multiple Delays

In section 10.3.5.5, it can be seen that SPL (Self Phase Locking) is an effective way to minimize the phase noise of an oscillator. However, the long delay not only brings in the side-mode but also has a limited phase locking range. This is reported experimentally by Huignard et al [19]. In their experiment, a SPL is constructed to stabilize the microwave output from a dual-frequency laser, shown in Figure 10-23.

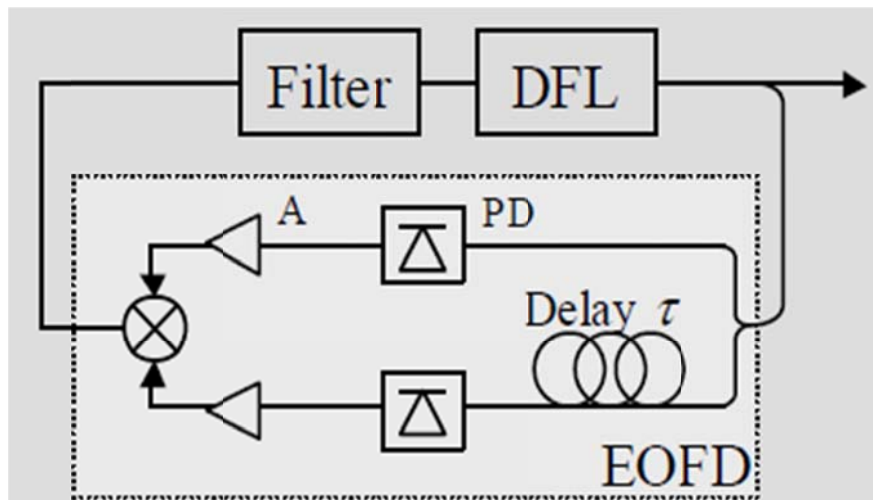


Figure 10-23: Shows the typical block diagram of SPL for Dual Frequency Laser [19]

The DFL has two optical output frequencies that are 12 GHz apart and the beat frequency is the microwave output, depicted in Figure 10-24. The electrical error signal of the FD will control the optical phase of these two modes to eventually stabilize the microwave output.

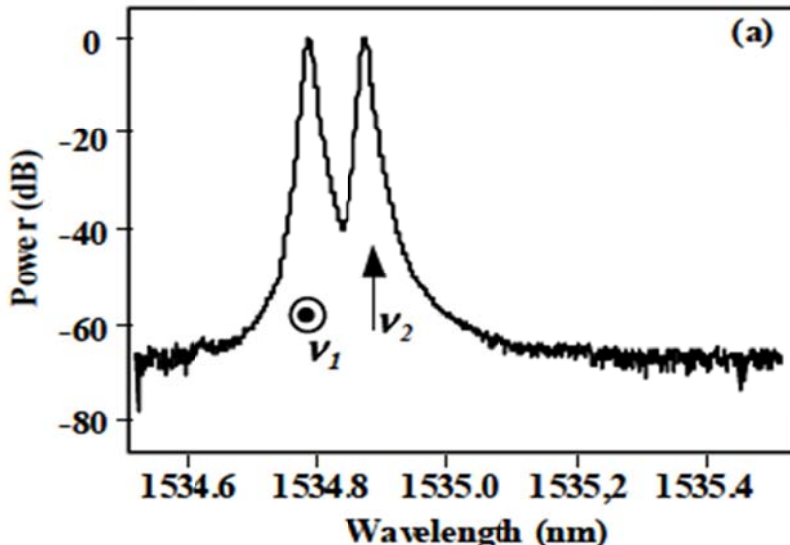


Figure 10-24: shows the Optical Spectrum of Dual Frequency Laser [19]

The measured phase noise of DFL using self-phase locking is shown in Figure 10-25 [48]. When 1km long delay is used in the frequency discriminator, the PLL loop bandwidth is about 4kHz, and the system is out of lock after 4 kHz offset frequency.

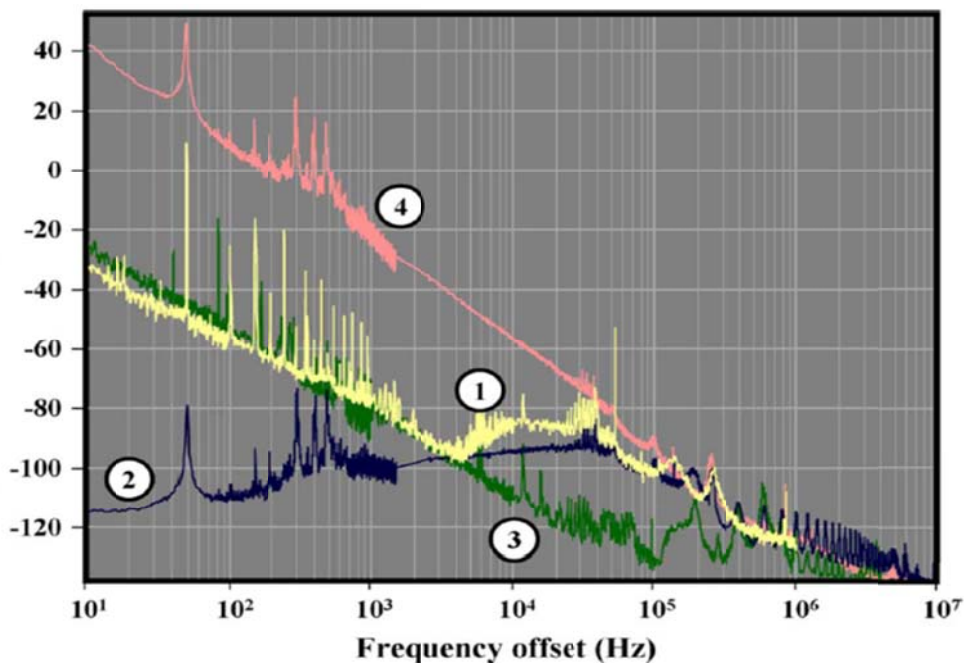


Figure 10-25: Shows the Phase Noise plots of the Microwave Output from the DFL. 1-phase noise of the self phase locked DFL; 2-noise originated from the optics; 3-noise originated from the electronics; 4-phase noise of the free running DFL [19]

To increase the locking range, Huignard et al., have also proposed a SPL structure of multiple frequency discriminators [19]. The configuration of multiple frequency discriminators is depicted in Figure 10-26. Two pieces of optical fiber is inserted into one arm of a standard

frequency discriminator. One has a length of 100m, which provides $0.5\mu\text{s}$ delay while the other is 1km long which provides $5\mu\text{s}$ delay. The overall output of the FD is equivalent to the sum of 2 individual FD with different delays.

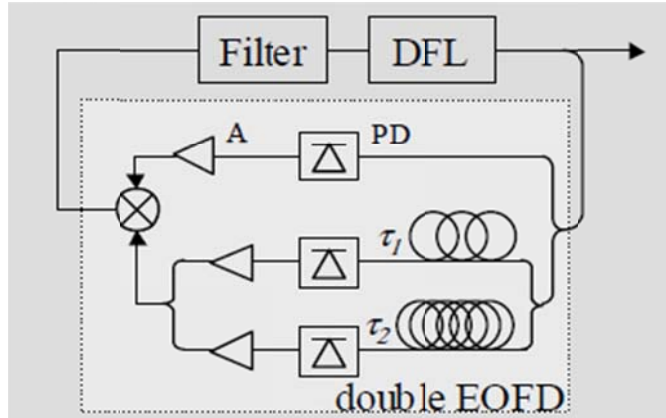


Figure 10-26: Shows the typical configuration of Double Frequency Discriminator ($\tau_1 = 0.5\mu\text{s}$; $\tau_2 = 5\mu\text{s}$) [19]

Experimental result of double frequency discriminator is given in Figure 10-27 as well as the results for single FD with 100m delay and 1km delay. The phase noise of double FD is lower than single FD with 100m delay and the locking range of double FD is better than single FD with 1km delay.

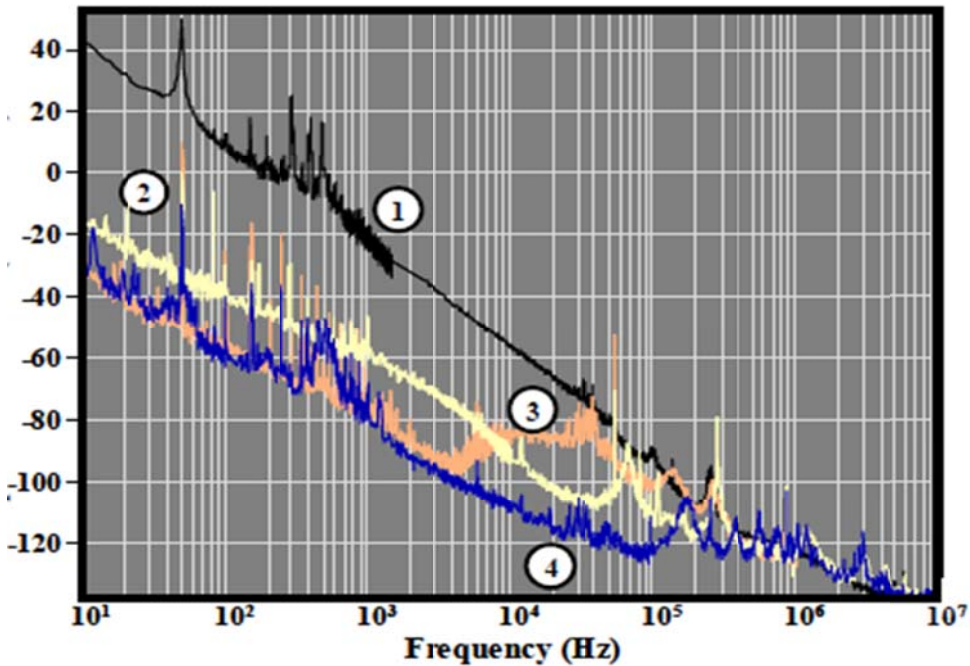


Figure 10-27: Shows the phase noise plots: 1-Free Run; 2-100m alone; 3-1km alone; 4-100m and 1km Combined [19]

10.3.5.7 Multi-Loop OEO Circuits

Figure 10-28 shows the simplified arrangement of 10 GHz multi-loop sapphire loaded cavity oscillator (SLC) for Loop 1=2 km, Loop 2 =10m [69].

As shown in Figure 10-28, in this configuration neither of the loop is oscillating by itself, however the oscillation occurs when the two loops are combined, i.e., $g_1 < 1$, $g_2 < 1$, $g_1 + g_2 > 1$, g is the loop gain.

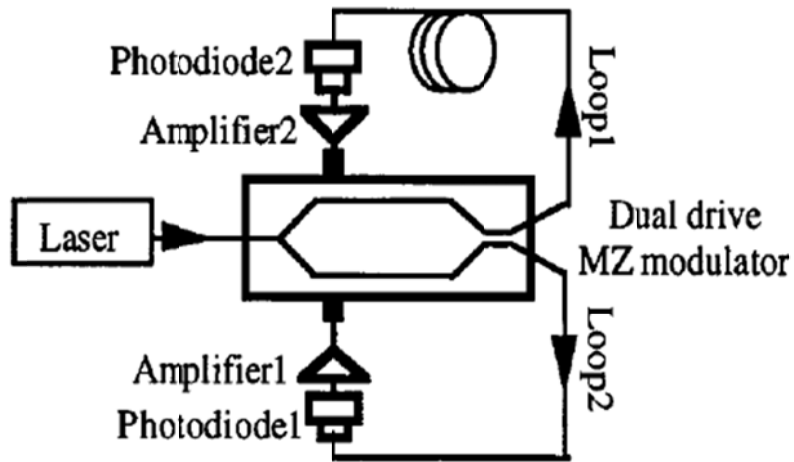


Figure 10-28: Shows the simplified arrangement of 10 GHz multi-loop OEO circuit [69, 75]

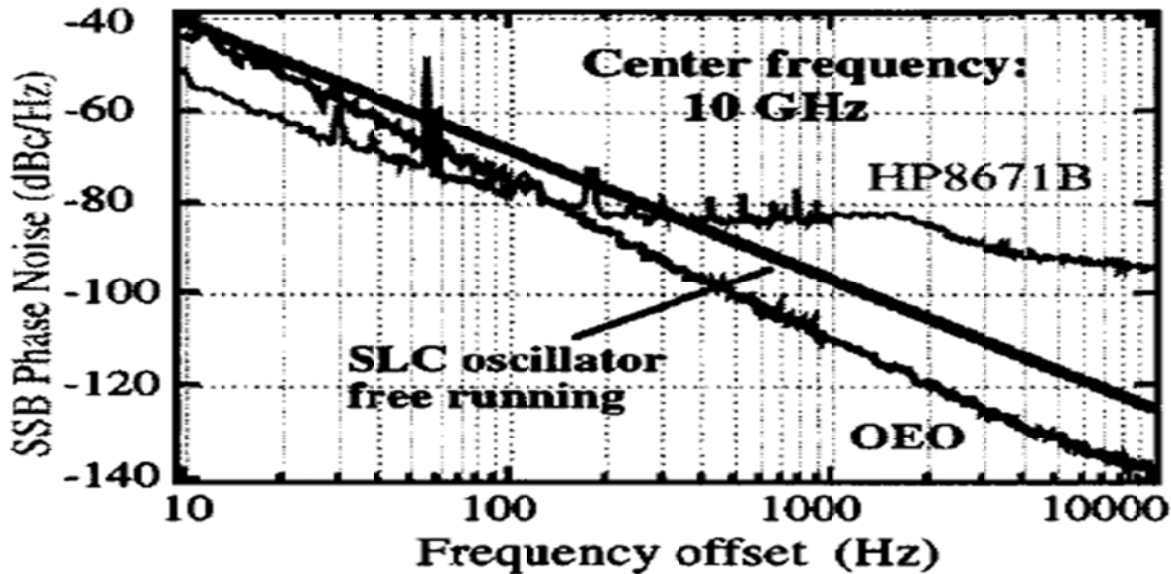
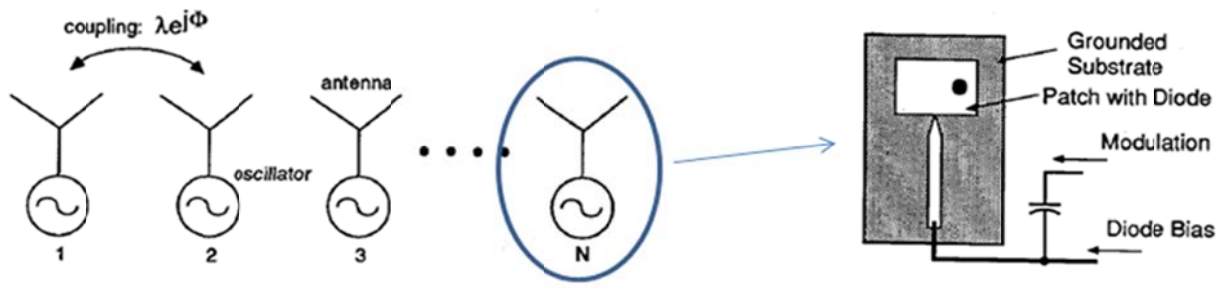


Figure 10-29: Shows the measured phase noise plot of multi-loop sapphire loaded cavity 10 GHz OEO circuit , Loop 1=2 km, Loop 2 =10m [69, 75]

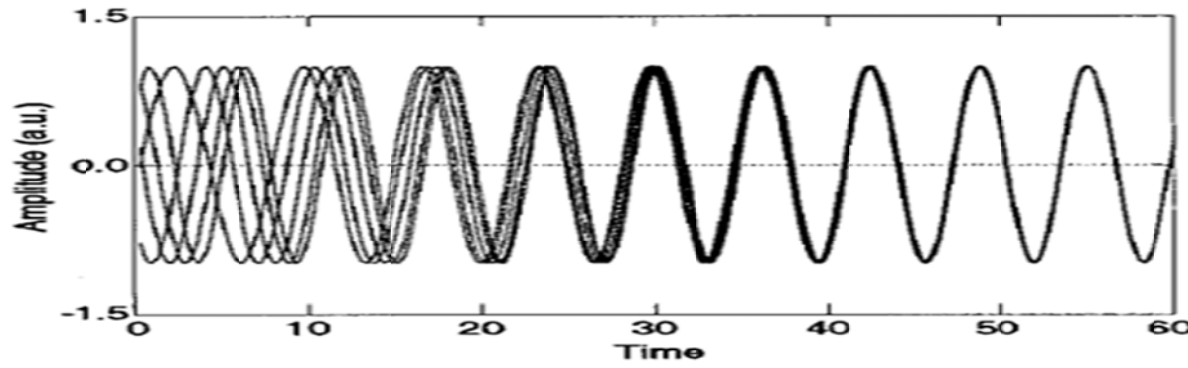
10.3.5.8 Electrical Mode-Locking

Figure 10-30 shows the simplified arrangement of electrical mode locking in coupled oscillator array for frequency and phase synchronization. Figure 10-31 shows the simplified arrangement of electrical mode locking as shown in Figure 10-30, but in this case the frequency and phase are no longer locked to a common frequency and phase, the difference between adjacent oscillators is locked [71].



(a) Mutual coupling between antenna leads to oscillator interaction [70]

(b)



(c) Frequency and phase synchronization

Figure 10-30: shows the arrangement of electrical mode-locking in coupled oscillator array and CAD simulation: (a) each oscillator contains an integrated antenna, and (b) Simulation of 5 identical coupled oscillators, after an initial turn-on transient, the oscillators synchronize to a common frequency and phase [70].

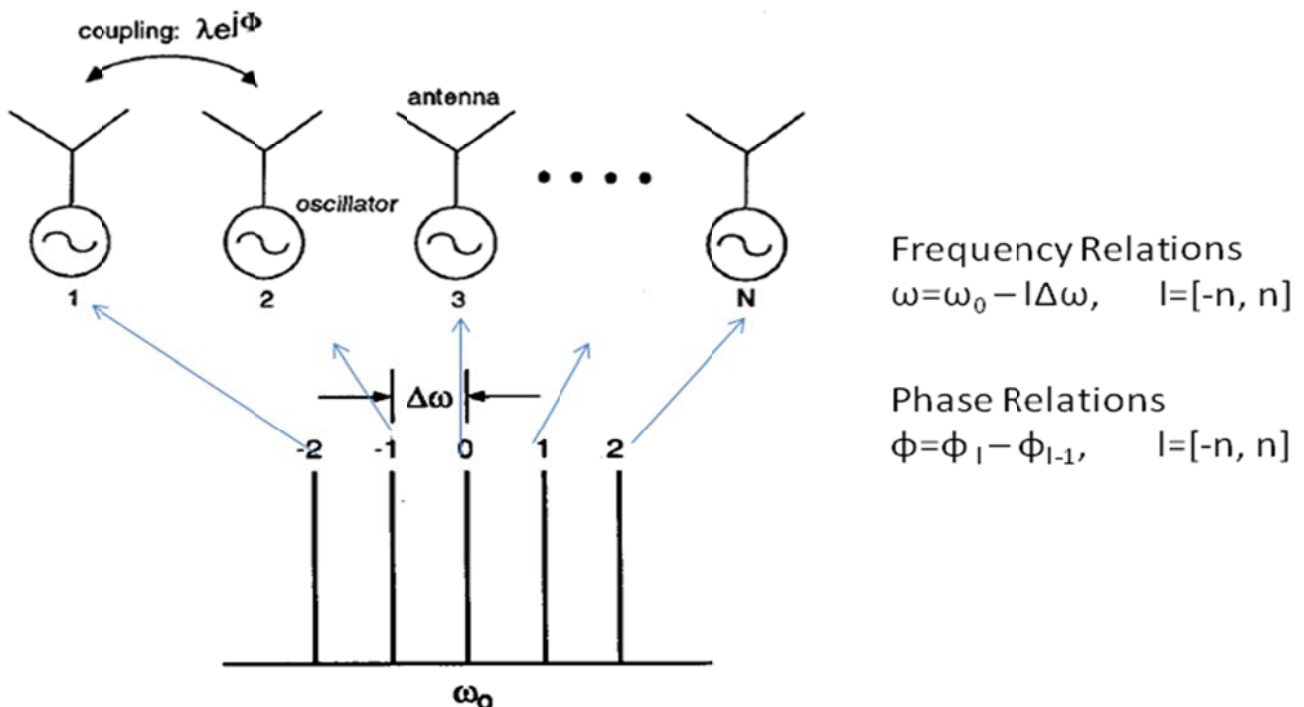


Figure 10-31: Shows the simplified arrangement of electrical mode locking, frequency and phase no longer locked to a common frequency and phase, the difference between adjacent oscillators is locked [71].

10.3.5.9 Optical Mode-Locking

Figure 10-32 shows the simplified arrangement of optical mode locking of coupled optoelectronic oscillators. As shown in Figure 10-33, the mode locking is achieved by modulating the gain in the semiconductor optical amplifier (SOA). The oscillation frequency is limited to 1 GHz because of the slow response of SOA [72].

Figure 10-33 shows the typical arrangement of optical mode locking similar to the Figure 10-55, the difference is that SOA is replaced by M-Z modulator [9]. Since M-Z modulator exhibits comparatively larger bandwidth (BW) as compared to SOA, consequently M-Z ring laser can operate to X-band or higher frequency.

Figure 10-34 shows the experimental phase noise measurement of M-Z modulator based mode-locked coupled OEOs.

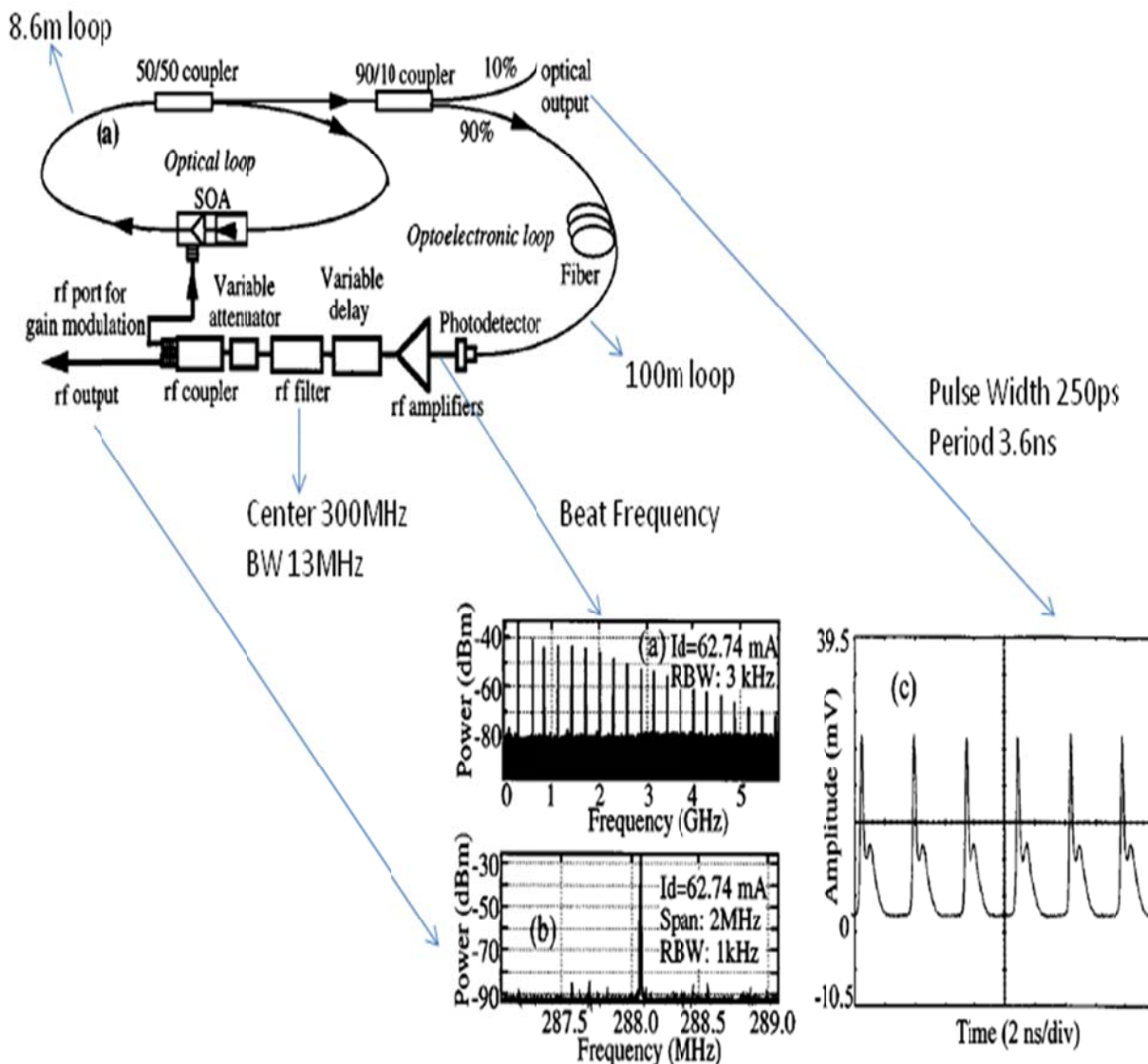


Figure 10-32: Shows the typical arrangement of optical mode locking of coupled optoelectronic oscillators [72]

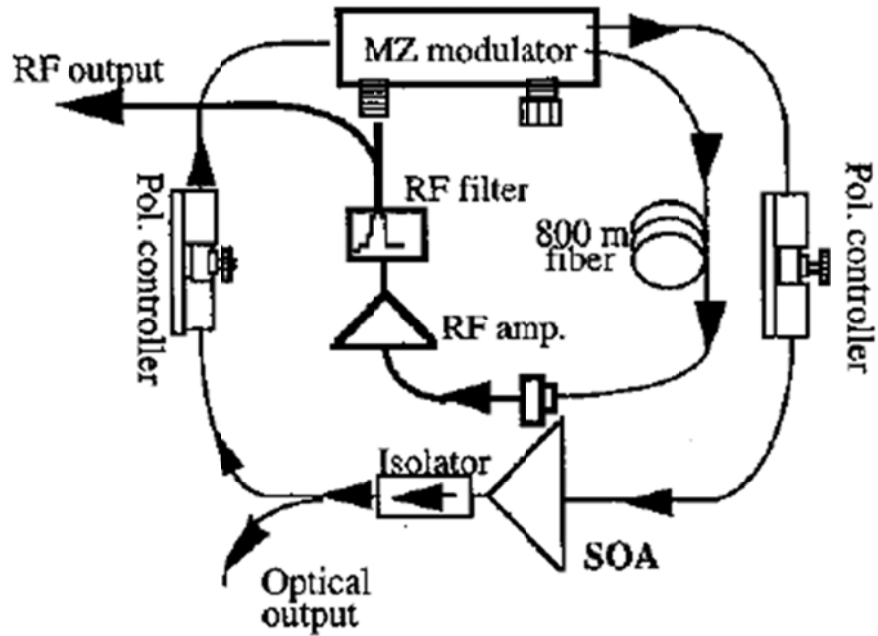


Figure 10-33: Shows the typical arrangement of optical mode-locking similar to the Figure 10-32, the difference is that SOA is replaced by M-Z modulator [9]

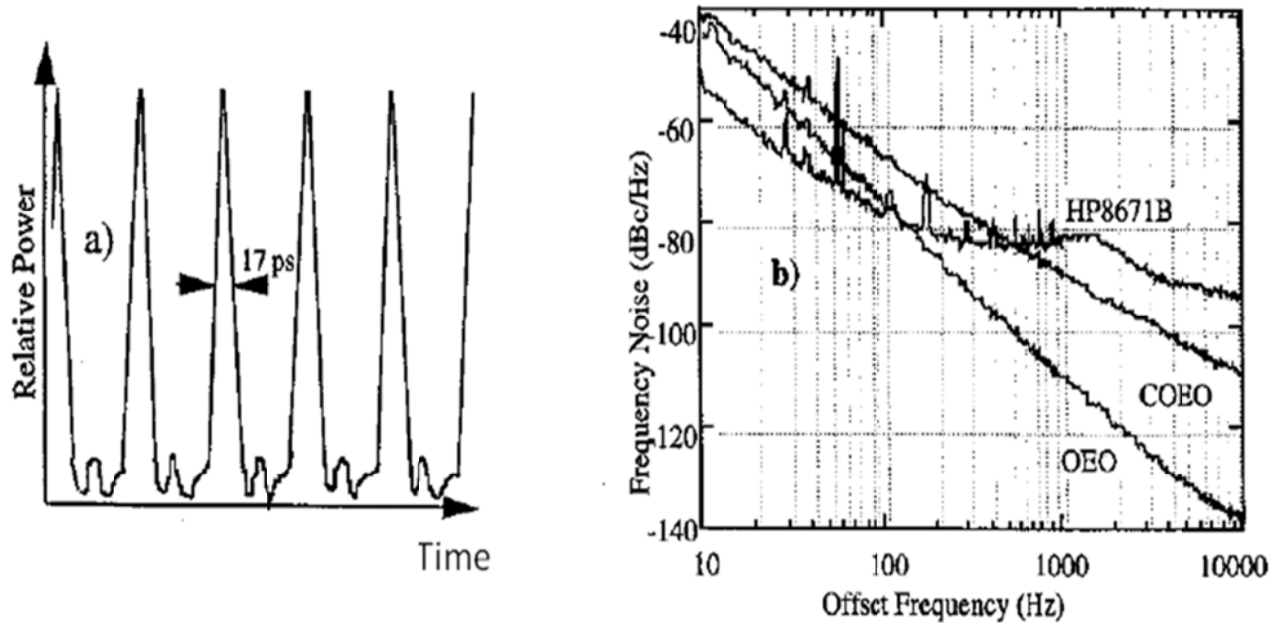


Figure 10-34: Shows the experimental PN measurement of M-Z modulator based mode-locked coupled OEOs [9]

Figure 10-35 shows the typical arrangement of mode-locked COEO (coupled optoelectronic oscillator) for low phase noise requirement. As shown in Figure 10-35, Δv is the ESR of the ring laser, $3\Delta v$ is the RF filter center frequency; the RF filter selects the modulation frequency f_{mod} (also the RF oscillation frequency f_{osc}) to mode lock the ring laser, practically it should be much larger than $3\Delta v$ but here it is just to show that the laser is harmonically locked.

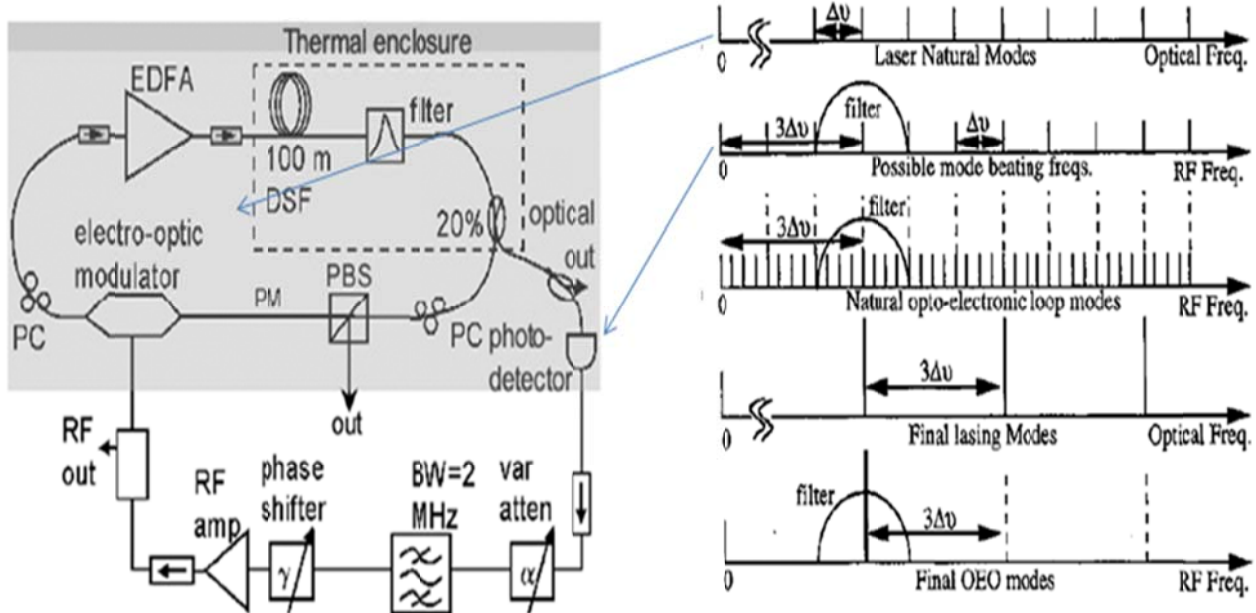
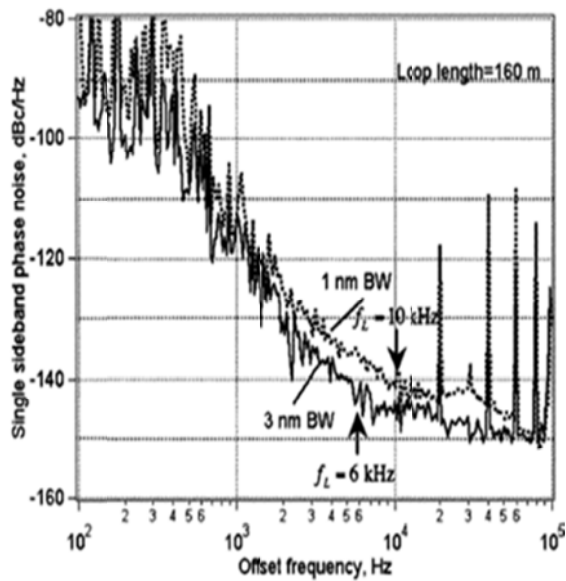


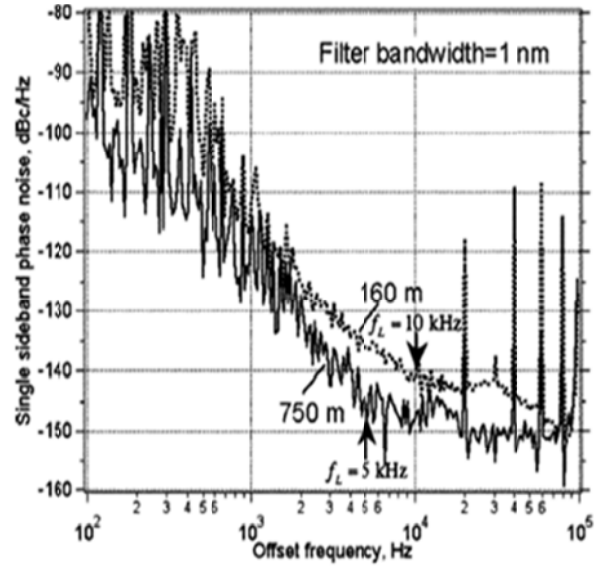
Figure 10-35: Shows the typical arrangement of mode-locked COEO (coupled optoelectronic oscillator) for low phase noise requirement [9]

Figure 10-36 shows the measured phase noise plots and influence of optical filter and loop length on mode-locked COEO (coupled optoelectronic oscillator) shown in Figure 10-35.

Table 10-1 shows the comparative analysis of different optical mode-locking techniques. It can be noticed that shorter pulse results in a lower phase noise.



(a) Effect of Optical Filter BW



(b) Effect of loop length

Figure 10-36: Shows the measured phase noise plots and influence of optical filter and loop length on mode-locked COEO (coupled optoelectronic oscillator): (a) 3nm filter BW results in a shorter pulse width of 2ps and a lower phase noise while 1nm filter results in a 7ps pulse width and a higher phase noise, and (b) loop delay provides lower phase noise, -150dBc/Hz @ 10kHz offset for 10 GHz carrier frequency [9]

Table 10-1: The comparative analysis of different optical mode-locking techniques [9]

	Modulator	Pulse Width	Phase Noise*	Loop Length	Optical Filter BW	Dispersion Compensate
Method 1	SOA	250ps	High	100m	No	No
Method 2	M-Z	17ps	-110	800m	No	No
Method 3	M-Z	7ps	-150	750m	1nm	Yes

* Measured at 10kHz offset at 10GHz; Unit is dBc/Hz

10.3.5.10 ILPLL OEO using self-ILPLL and Optimum Parameter Selection

As demonstrated injection-locking (IL) removes the phase noise in far away offset frequency while phase-locking effectively reduces close-in to carrier phase noise. By combining (Injection Locking (IL) and Phase Locked Loop (PLL), a clean spectrum in a wider range of offset frequency is expected. An Oscillator with ILPLL is reported by Sturzebecher et al [31], its configuration is depicted in Figure 10-37, where an external reference is provided using a fiber optic distribution. The oscillator consists of two transistors with a feedback path. The reference signal, from a laser, is detected by a photo detector and fed to the oscillator through matching network M1 for injection locking. For phase locking, the reference signal is also compared with LO signal to create a low frequency signal to change the varactor diode bias in the feedback loop to provide phase correction.

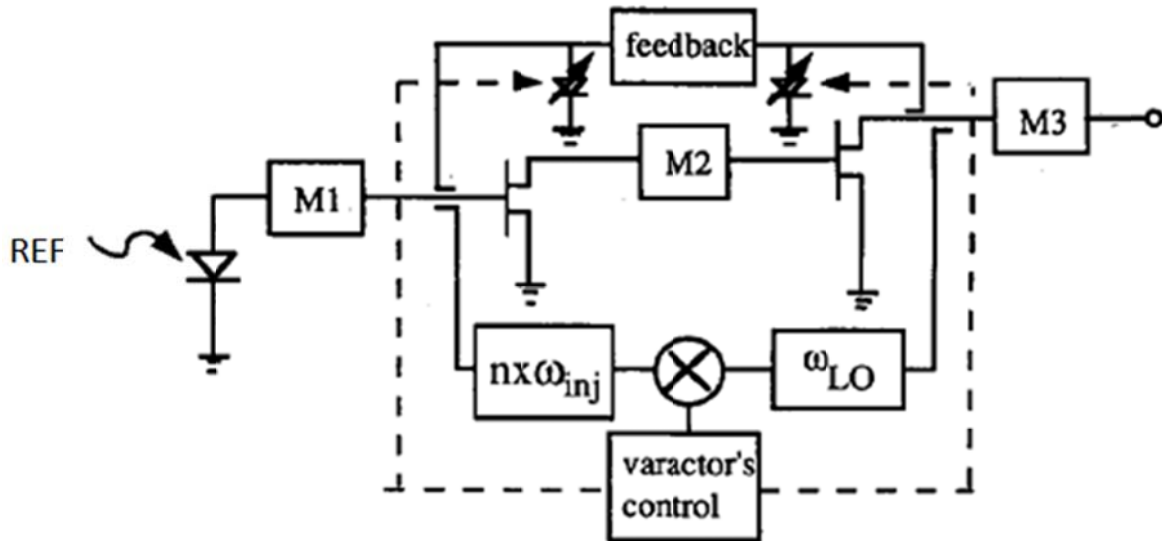


Figure 10-37: Shows the typical configuration of ILPLL Oscillator [31]

The analytical modeling for phase noise of ILPLL oscillator is given below [21, 31]

$$S_{ILPLL}(f') = \frac{S_{ref}(f')\Delta f^2 \cos^2(\phi_{detune}) + f'^2 S_{PLL}(f')}{f'^2 + \Delta f^2 \cos^2(\phi_{detune})} \quad (10.11)$$

where $S_{ref}(f')$ is the phase noise of the reference signal; Δf is the injection locking range. ϕ_{detune} is the phase detuning between the LO signal and the reference signal; f' is the offset frequency; S_{PLL} is the phase noise of the oscillator when it is phase locked to the reference, and is given by [21]

$$S_{PLL}(f') = \frac{f_{n0}^4 S_{ref}(f') + f'^4 S_0(f')}{(f'^2 + f_{n0}^2)^2} \quad (10.12)$$

where f_{n0} is the natural resonant frequency in the phase locked loop.

The Optoelectronic Oscillator (OEO) realization of ILPLL is depicted in Figure 10-38, where a voltage-controlled oscillator (VCO) at f_o is stabilized by using two feedback control mechanisms of self-IL and self-PLL using long fiber delay lines. In this configuration, the phase noise of free running oscillator from a short fiber optic delay (1us for 200m) is to be compared with a phase of longer delay line (50us for 10km). A phase comparison would reduce close-in to carrier phase noise; however, note that side bands of every 20kHz are to be added when a long delay oscillation is considered.

CAD simulation results of the PLL oscillator using (10.12) is shown in Figure 10-39 depicting performance of OEO with 200m delay locked either to a loop of 10km (i.e., Figure 10-39a) or using multiple loops of 200m PLL to 1km and the 1km is locked to a 10km delayed OEO (i.e., Figure 10-39b). The OEO is used with a loop filter bandwidth of $f_{n0}=5\text{MHz}$. A reduced close in to carrier phase noise is seen when 200m OEO is locked to a delay of 10km. Moreover, a higher suppression of side-band modes is observed by consecutive locking of multiple loops of 1km and 10km. CAD simulation results of the self-ILPLL oscillator using (10.11) is shown in Figure 10-40 depicting performance of 10GHz VCO with Q of 100 locked to a loop of 10km. The S_{ref} is the phase noise of the 10km long OEO and S_{PLL} is the phase noise of the electrical oscillator when it is only phase-locked to the 10km long OEO. A $f_{n0}=500\text{kHz}$, locking range of $f_{lock}=10\text{MHz}$, and $\phi_{detune}=45^\circ$ is also considered to represent a frequency drift between free-running VCO and a 10km long (50μs) OEO.

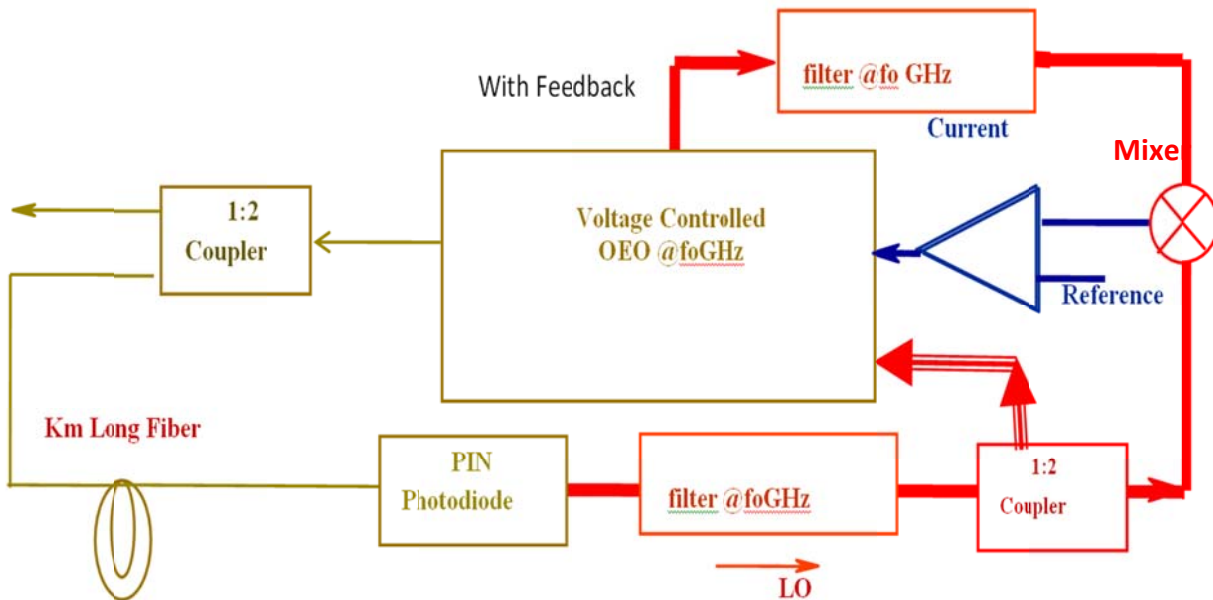
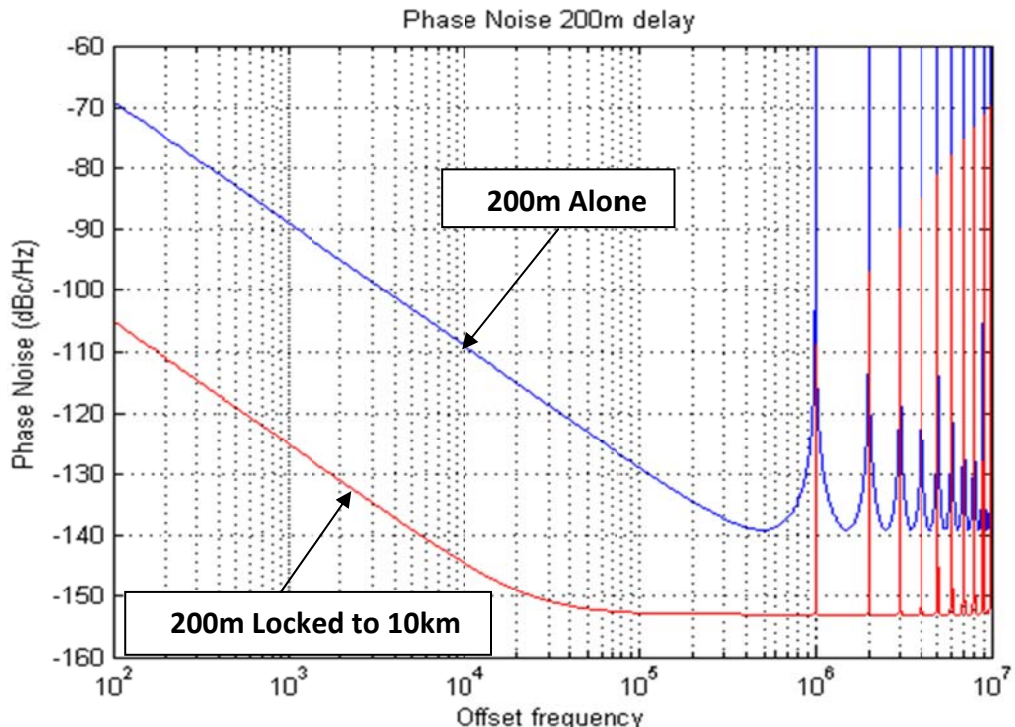
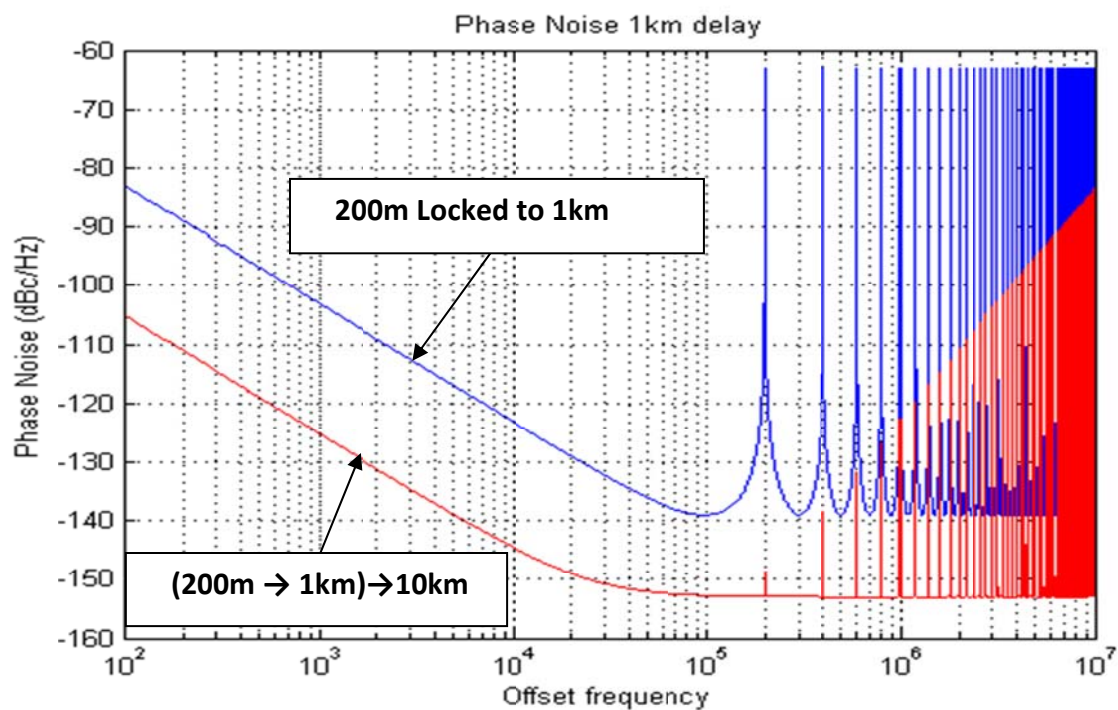


Figure 10-38: Shows the schematic of OEO with self-ILPLL concept when both long delay signals are injected to OEO in addition to phase error correction between short and long delay structures. If only short delay and long delay are injected without phase comparison, then it will be considered as self-IL. When the phase comparison signal is added to the feedback only from either short or long delay signal, a phase locked loop operation is obtained [22].



(a) Locked directly to a 10km long OEO [22]



(b) Locking consecutively to a 1km and then a 10km fiber delay lines [22]

Figure 10-39: Shows the CAD simulated Phase noise plots of Self-PLL Phase Noise of a 200m long OEO as a function of (a) locked directly to a 10km long OEO, and (b) locking consecutively to a 1km and then a 10km fiber delay lines.

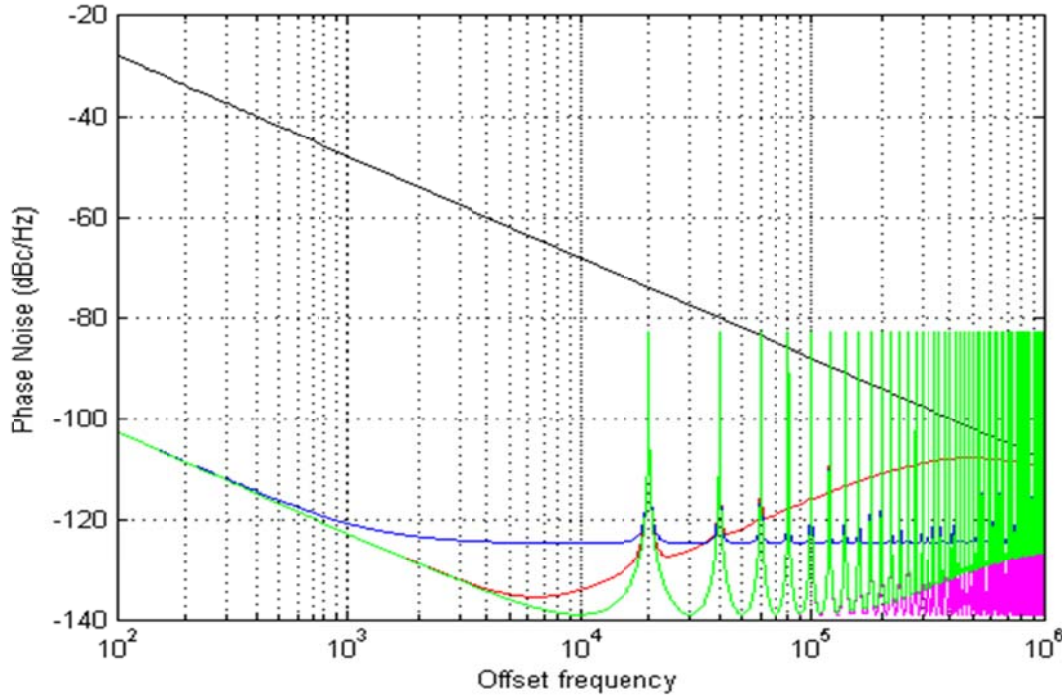


Figure 10-40: Shows the CAD simulated phase noise plots of Self-ILPLL Phase Noise of a VCO locked directly to a 10km long OEO (Black: Free running; Pink: Reference; Red: PLL Only; Blue: IL Only; Green: ILPLL) [22]

The simulation results indicate that small phase detuning, high natural resonant frequency and high injection locking range is preferred to achieve a substantial phase noise reduction. The more details of the impact of these parameters are presented in Figure 10-29.

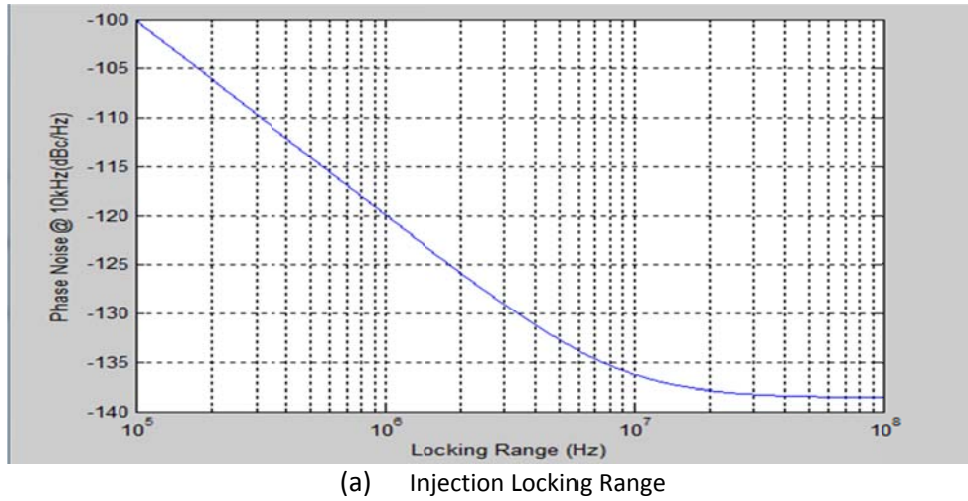
As shown in Figure 10-41a, the performance of ILPLL VCO as locking range is increased for $f_{n0}=20\text{kHz}$ and $\phi_{detune}=45^\circ$, in Figure 10-41b impact of phase detuning is studied as $f_{n0}=20\text{kHz}$ and locking range of $f_{lock}=10\text{MHz}$, and finally in Figure 10-41c the impact of natural resonance frequency as locking range of $f_{lock}=10\text{MHz}$, and $\phi_{detune}=45^\circ$ are considered.

An ILPLL optimum performance is expected for $f_{n0}=50\text{ kHz}$ (i.e., an op-amp gain bandwidth of 200 MHz), locking range of $f_{lock}=20\text{MHz}$ (i.e., a VCO Q factor of under 500), and $\phi_{detune}=5^\circ$ (i.e., a VCO frequency drift of 5000ppm/C) [22].

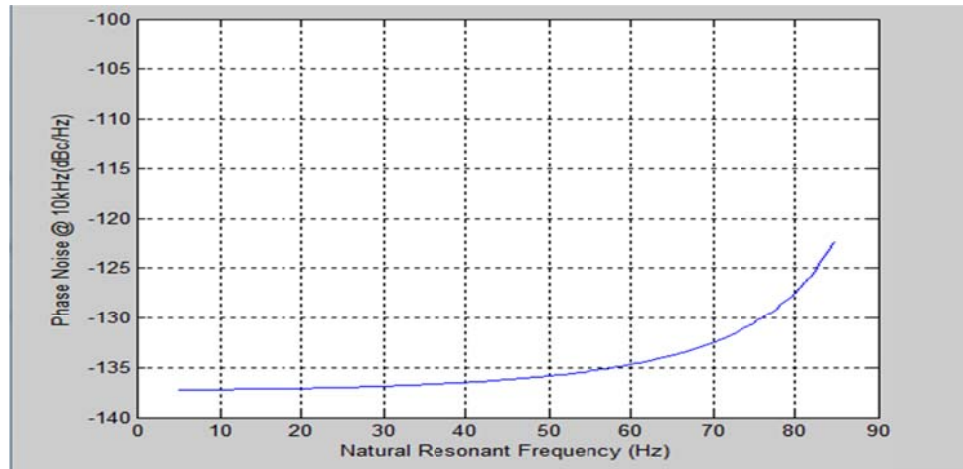
10.3.6 Optical Filtering

10.3.6.1 Optical Filtering using Fabry-Perot Etalon

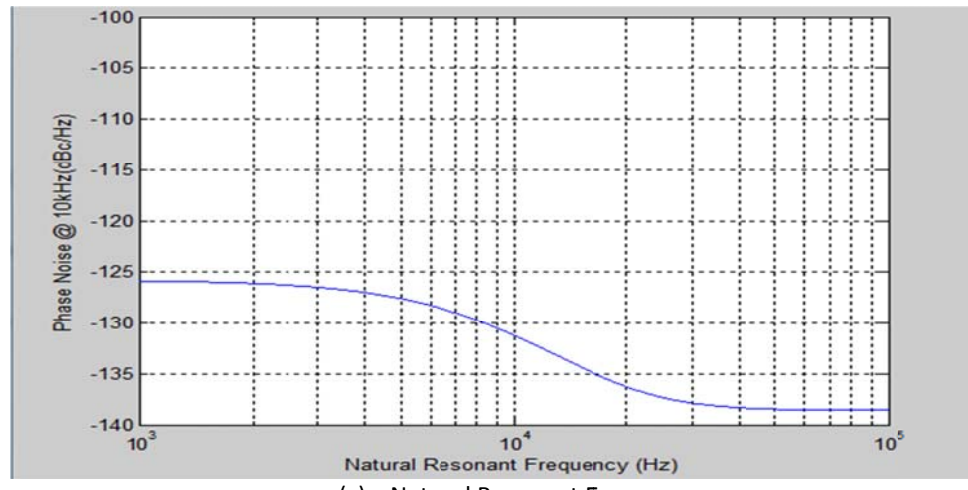
In a typical OEO design, an RF filter is used to provide frequency selectivity. There are some drawbacks with the RF filter. It is costly to make an ultra narrow bandwidth RF filter that is required when the optical delay is long. Another drawback of the RF filter is its temperature dependency. Small fluctuations in temperature result in fluctuations of the resonance frequency, and hence the phase induced by RF filter changes. This phase change affects the total round trip time of the microwave signal, thus changing the oscillation frequency.



(a) Injection Locking Range



(b) Phase Detuning



(c) Natural Resonant Frequency

Figure 10-41: Shows the CAD simulated phase noise plots of ILPLL Phase Noise as a function of: (a) Injection Locking Range, (b) Phase Detuning, and (c) Natural Resonant Frequency [22]

Optical filtering could sufficiently suppress the side-modes associated with long optical delay, thus eliminating the need for electrical filtering. A new optoelectronic design, which uses a high finesse Fabry-Perot Etalon as the frequency selector instead of an RF filter, is reported by Delfyett et al [45].

Figure 10-42 shows the typical schematic of Etalon based OEO. The Etalon has a FSR of 10.28GHz and a finesse of 1000. The total loop length is about 10m. The transmission spectrum of the F-P Etalon is shown in Figure 10-42b. The beat frequency of these transmission peaks becomes the RF output. Figure 10-42c shows the final oscillating frequency.

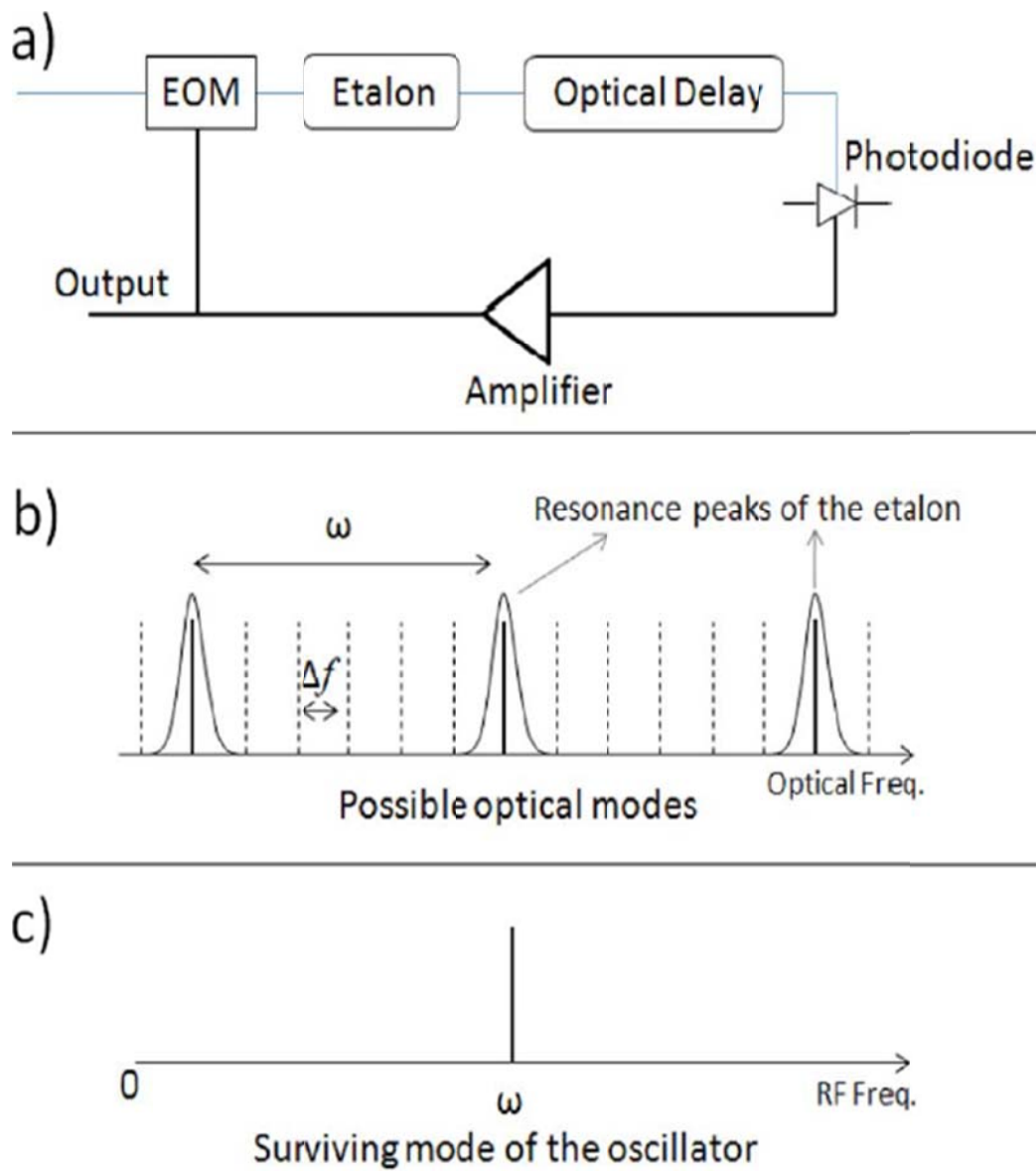


Figure 10-42: Principle of Etalon Based OEO adopted from [45]

Measured phase noise of F-P Etalon based OEO is shown in Figure 10-43, phase noise of a conventional OEO using RF filter is also shown in the same plot for comparison. A 10 dB phase noise reduction is achieved with etalon based OEO.

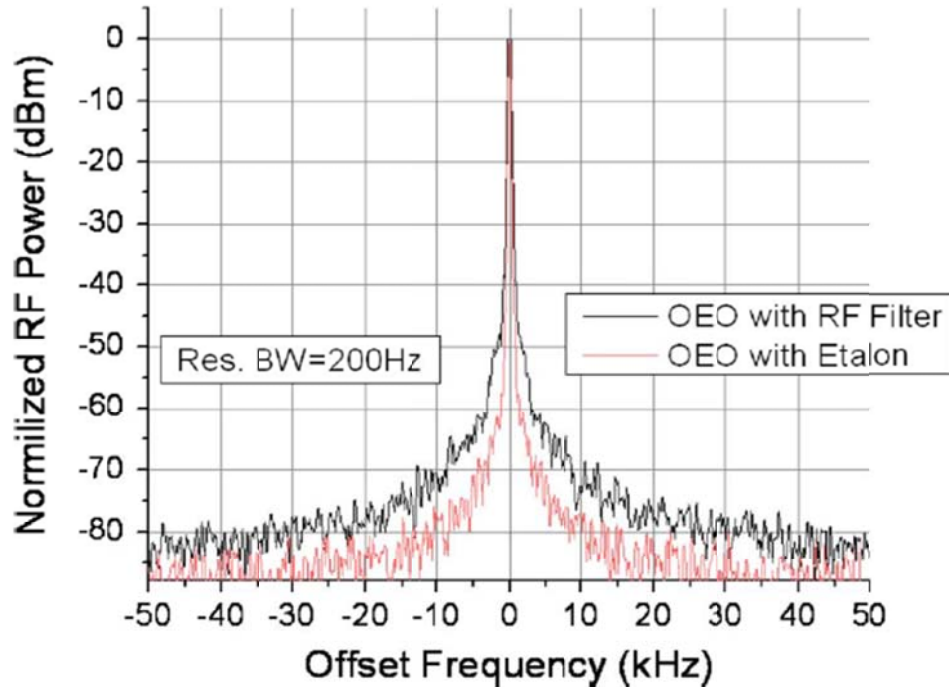


Figure 10-43: Shows the comparison of Phase Noise plots between F-P Etalon based OEO and OEO with RF filter [45]

10.3.6.2 Optical Filtering using Transversal Filter

Optical transversal filter can provide wider tuning range yet still provides very high Q. By incorporating optical transversal filter, a tunable OEO is reported by Li et al [46]. The schematic of the reported OEO is shown in Figure 10-44.

A broadband amplified spontaneous emission (ASE) light source is coupled to a programmable multichannel optical filter, which is employed to slice the broadband spectrum into multiple channels. The spectrum-sliced broadband source is then coupled into a Mach-Zehnder modulator. The modulator is connected to a dispersive element, which can be a high dispersive fiber.

The resonance frequency of the transversal filter is given by [46]

$$f_n = \frac{n}{\Delta\lambda \times \chi} \quad (10.13)$$

where n is the order of the resonance frequency; $\Delta\lambda$ is the optical channel spacing; χ is the dispersion of the optical fiber. From the above expression, frequency tunability of the OEO is achieved by adjusting the optical channel spacing $\Delta\lambda$ and the dispersion χ .

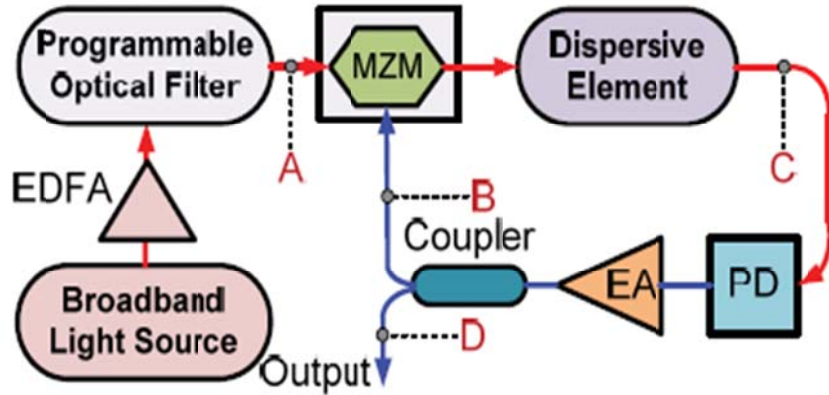


Figure 10-44: Shows the typical schematic of OEO using Optical Transversal Filter adopted from [46]

Experimental demonstration of the tunability of optical transversal filter is shown in Fig. 10-45. In Fig. 10-45a, the fundamental oscillation frequency is 4.1 GHz when $\Delta\lambda=0.4$ nm and $\chi=609$ ps/nmkm. When $\Delta\lambda=0.4$ nm and $\chi=339$ ps/nmkm, the fundamental is 7.3GHz, as can be seen in Fig. 10-45b. The measured oscillation frequency is 9.7 GHz when $\Delta\lambda=0.3$ nm and $\chi=339$ ps/nmkm, as shown in Fig. 10-45c. A tuning range of 5.5 GHz is achieved.

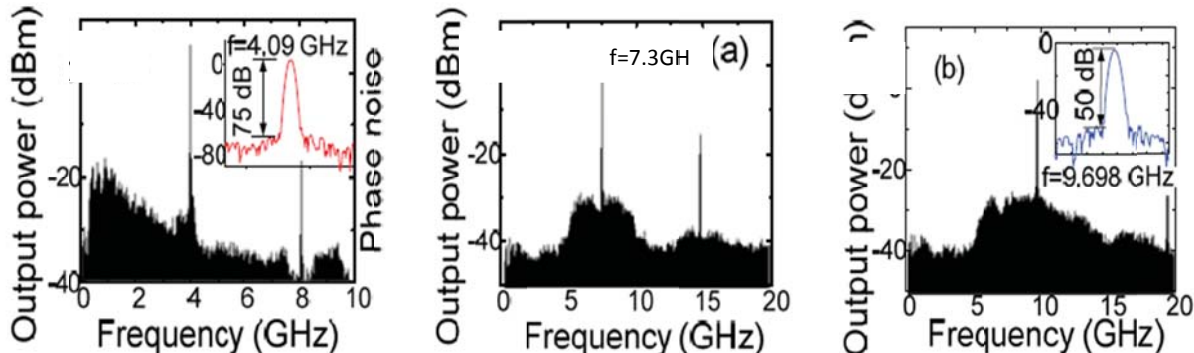


Figure 10-45: Shows the Tunability of Optical Transversal Filter (a) $\Delta\lambda=0.4$ nm, $\chi=609$ ps/nm/km, $f=4.1$ GHz; (b) $\Delta\lambda=0.4$ nm, $\chi=339$ ps/nm/km; $f=7.3$ GHz; (c) $\Delta\lambda=0.3$ nm, $\chi=339$ ps/nm/km; $f=9.7$ GHz [46]

10.3.6.3 Novel OEO using optical “Nested Loop” RF filter

One of major challenges in implementation of OEO is the requirements imposed in narrow band RF filtering of many modes that could be supported within gain bandwidth of the OEO. A narrow band RF filter could be achieved using very high order elliptic filters, where it suffers from excess loss in passband, high group delay sensitivity to passband frequency, and extremely large size due to high order number of resonant tank circuits. To overcome this challenge a number of researchers have moved to all optical filtering using a high quality factor optical resonator; e.g., whispering gallery mode resonators. Our proposed OEO is based on RF filter using a low order cascaded transversal filters, as nested loop narrow band RF filter. Figure 10-46 conceptually depicts the use of this novel optical filter in the OEO, where it has replaced

the electrical based RF filter. System block diagram of a transversal filter is depicted in Figure 10-47a, where delay caused by differential optical length of Δl will lead to narrow band RF filtering as depicted in Figure 10-47b for a $\Delta l=90\text{m}$ using ideal optical couplers with equal amplitude split. Figure 10-47c depicts simulated insertion loss degradation as the amplitude imbalance is observed for the 50% couplers. The simulation results indicate null depth reduction as the optical coupling imbalance is changed from $\kappa=0-1.5\text{dB}$. Practical values of $\kappa=0.6\text{dB}$, which results in null depths of 20dB with 1dB excess loss.

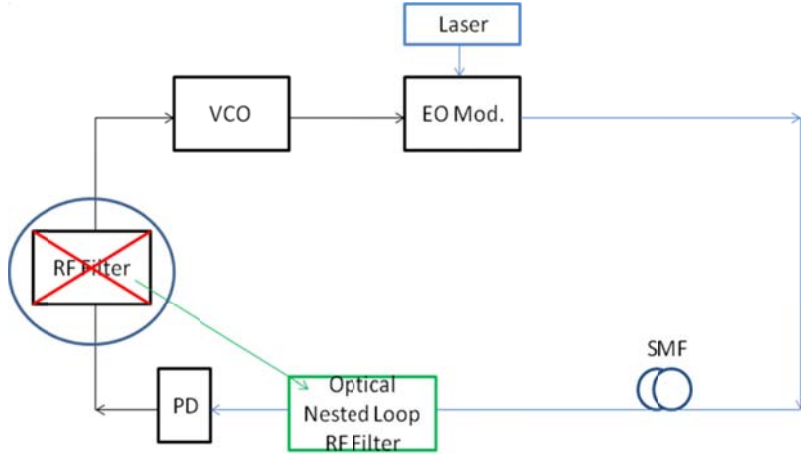
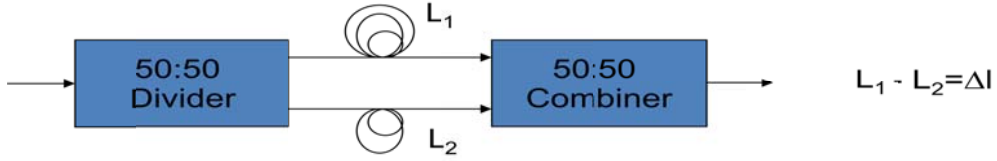


Figure 10-46: shows the typical schematic of a novel design of OEO using narrow band RF filter realized using the concept of optical “Nested Loop” RF filter [22]

Engineering innovations proposed in this thesis to remedy any amplitude imbalance has already been made, as depicted in Figure 10-48 for the 1st order transversal filters [22]. Voltage controlled optical couplers are considered as a readily available solution to overcome amplitude imbalance between two arms of optical couplers, as depicted in Figure 10-48a and 10-48b.

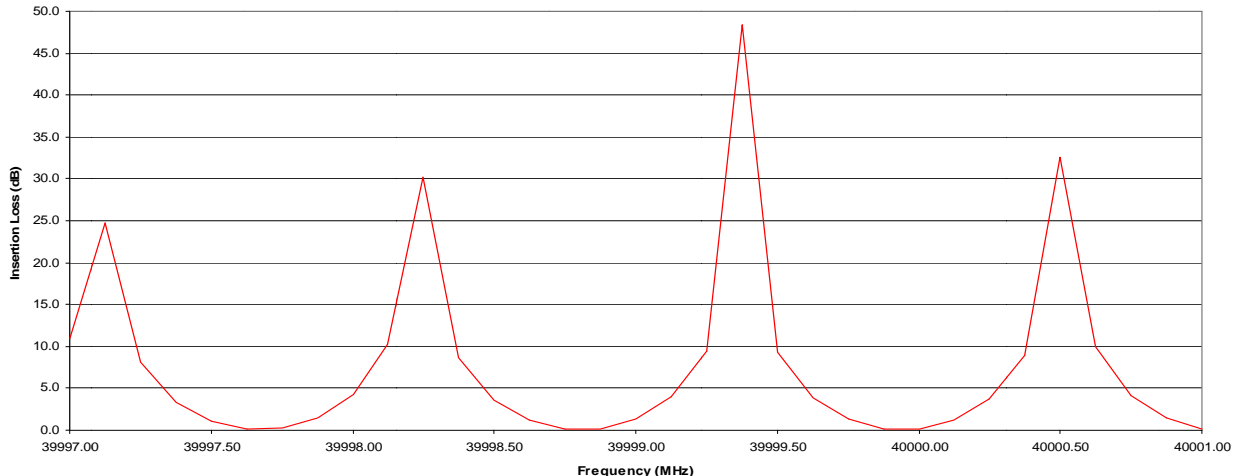
A more elegant approach is use of optical fibers that are polarization-sensitive with fiber core material having bi-refringence characteristics, where two distinct indices of refraction are experienced at two perpendicular polarization states. There are fast (low index of refraction) and slow (high index of refraction) propagating modes.

A delay of $\Delta t = (n_{\text{slow}} - n_{\text{fast}})l/c$ is to be experienced between two propagating modes, where n_{slow} and n_{fast} are the indices of refraction for two states of polarization in Hi-Bi fibers [23]. This time delay is equivalent of differential length of $\Delta l = \Delta t v_g$. The power distribution between two polarization states is controlled using the rotation of linearly polarized input optical signal with respect to the slow/fast axes of fiber.



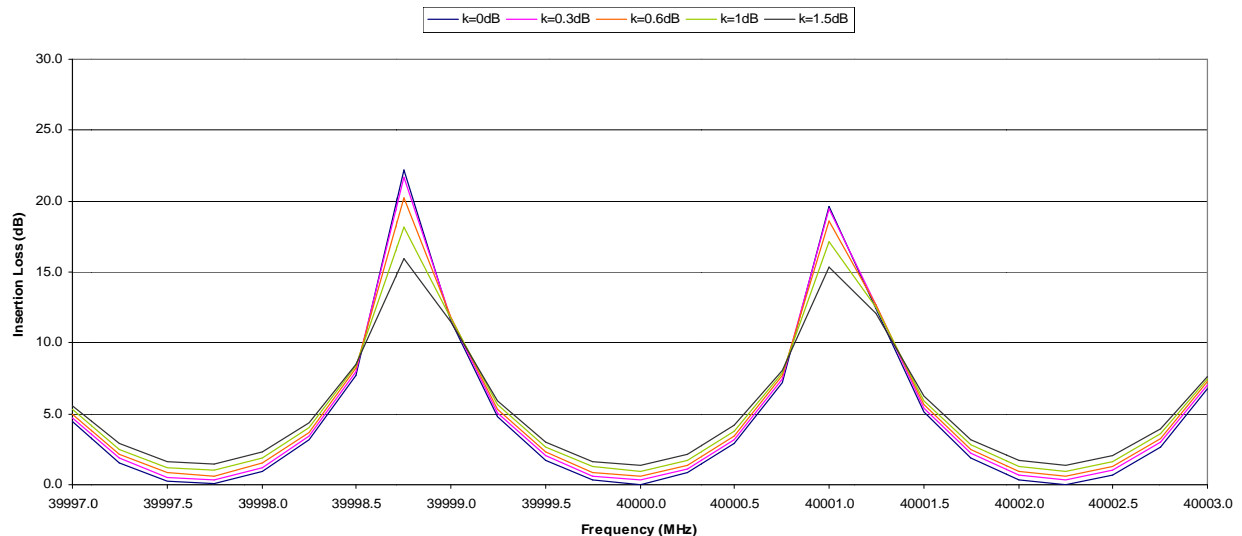
(a) Block diagram of transversal filter implementation

IL of 1st Order Transversal Filter of $\Delta l=90\text{m}$: Zoom-in



(b) Simulated insertion loss as a function of RF frequency zoomed in around 40,000MHz

IL of 1st Order Transversal Filter vs κ : $\Delta l= 90 \text{ m}$



(c) Simulated insertion loss as a function of RF frequency of transversal filter

Figure 10-47: Shows the design and simulation of 1st order transversal filter at $\lambda=1550\text{nm}$: (a) Block diagram of transversal filter implementation using optical couplers and differential delay line length of Δl ; (b) Simulated insertion loss as a function of RF frequency and zoomed in around 40,000MHz for $\Delta l=90\text{m}$; (c) Simulated insertion loss as a function of RF frequency of transversal filter of $\Delta l=90\text{m}$ and zoomed in around 40,000MHz as an amplitude imbalance between two arms of 50% optical couplers are considered ranging from $\kappa=0$ (ideal) and practical values of $\kappa = 0.3-1.5\text{dB}$ [22]

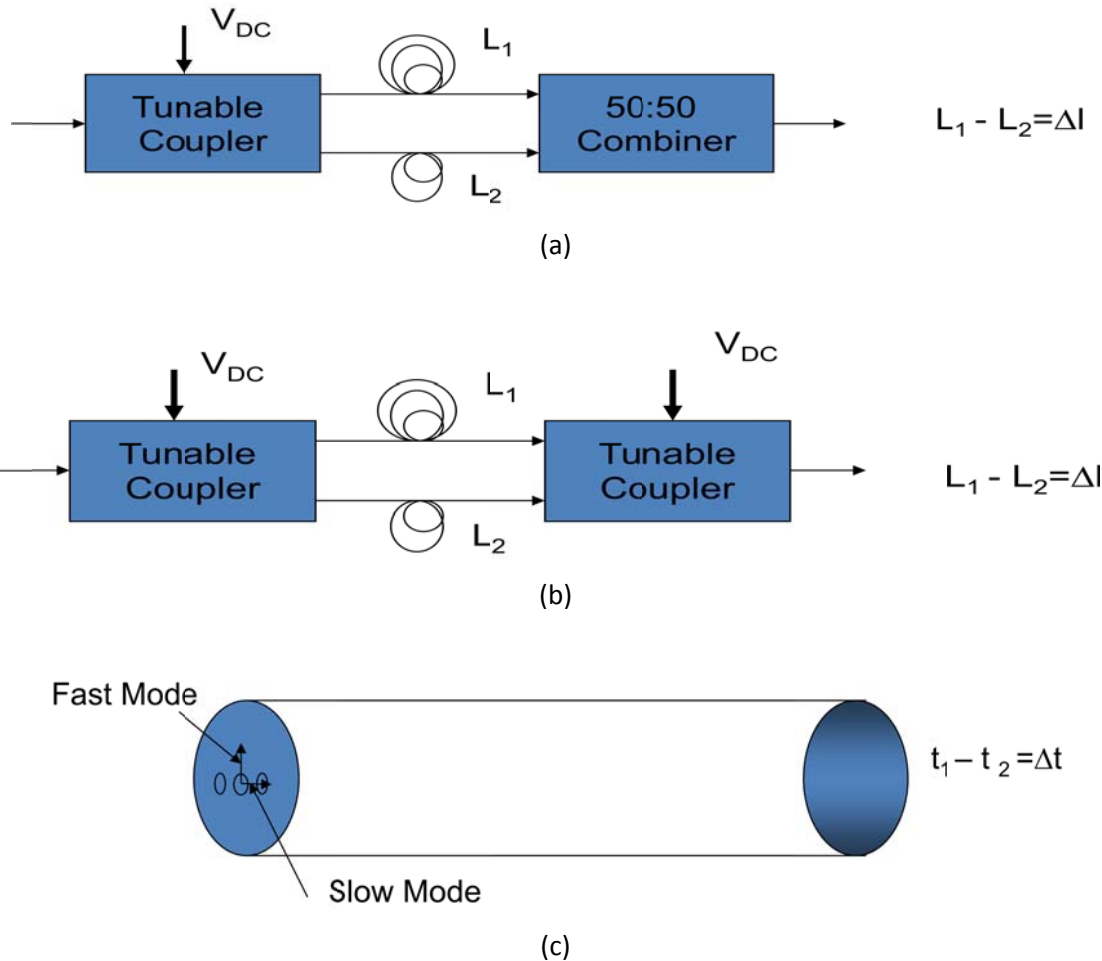
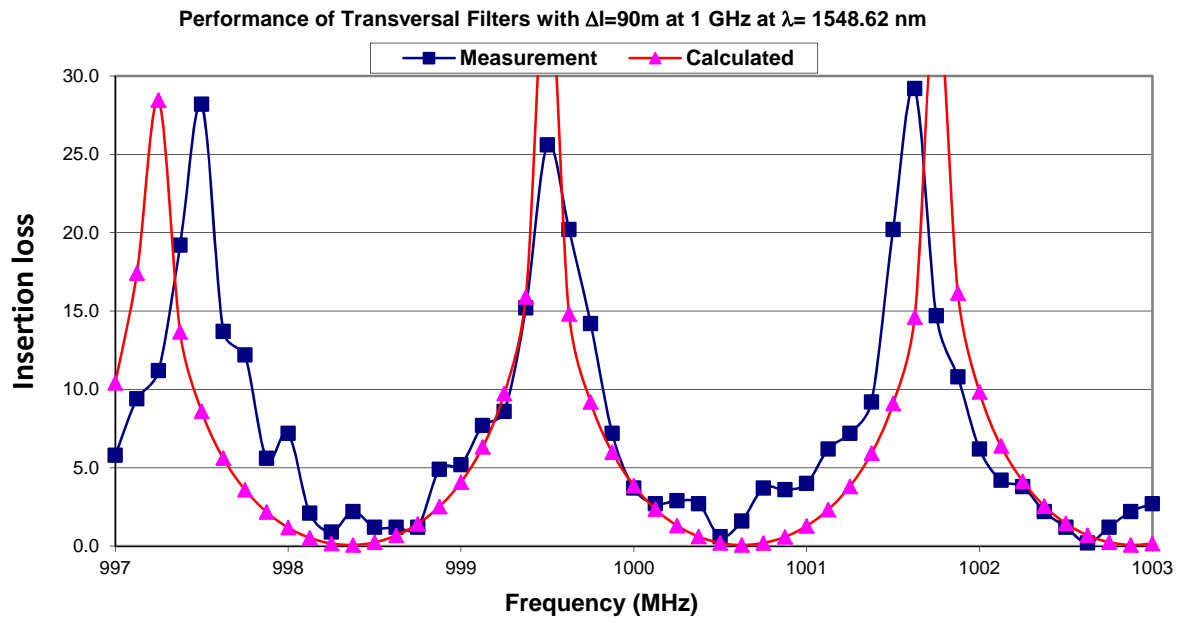


Figure 10-48: Design of 1st order transversal filter with capability to overcome amplitude imbalance between two arms of optical couplers. (a) Block diagram using a variable coupler with control voltage of V_{DC} ; (b) Block diagram using two variable couplers with control voltage of V_{DC} ; (c) Conceptual representation of 1st order transversal filter using specialized Hi-Bi fibers [22].

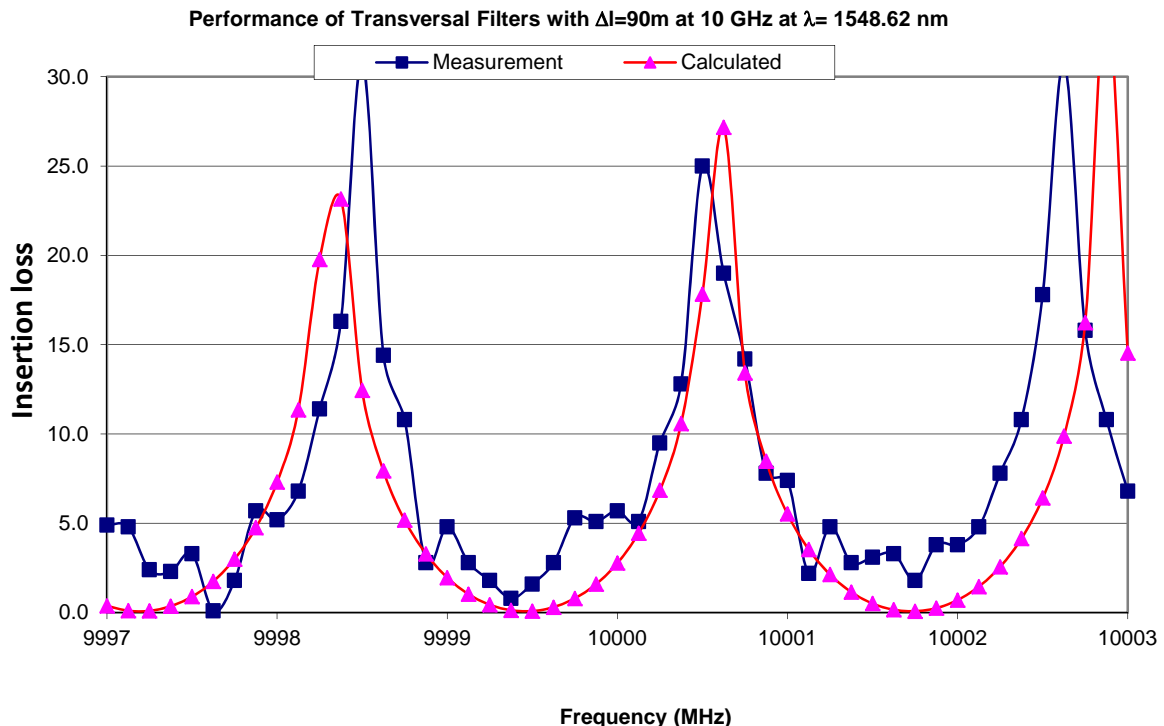
Experimental results of 1st order transversal filter for delay length of $l=90\text{m}$ at source optical wavelength of $\lambda=1548.62\text{nm}$ are depicted in Figure 10-49 for frequencies of 1GHz and 10GHz.

Note that the 1st order transversal filter with a long differential length causes a narrow pass band as the phase variation of zero to 90 degrees are to take place at a much faster rate for longer fiber delay lines. However, there are two concerns that have to be considered: i) the longer length causes multiple pass band as multiples of 180 degrees phase variation is accomplished at a faster rate.; ii) the maximum delay length has to match up with the coherence length (inversely proportional to laser line width) of the optical source used in the OEO. These spurious pass band frequencies are to be rejected by using a higher order nested loop filter.

Optical transversal filters could be combined in parallel and series configuration. Both unequal amplitude and equal amplitude power split couplers are considered. In Figure 10-48 these two topologies are depicted, where fiber length L_i is to be selected appropriately meeting standard filter synthesis procedures.



(a) Operation around 1000MHz



(b) Operation around 10,000MHz

Figure 10-49 : Shows the comparison plots of measured and simulated insertion loss of 1st order transversal filter with $\Delta l = 90m$ operating at $\lambda=1548.62\text{nm}$ as an optical nested loop RF filter (a) Operation around 1000MHz, and (b) Operation around 10,000MHz. Note measured 3dB bandwidth of this filter is less than 1MHz.

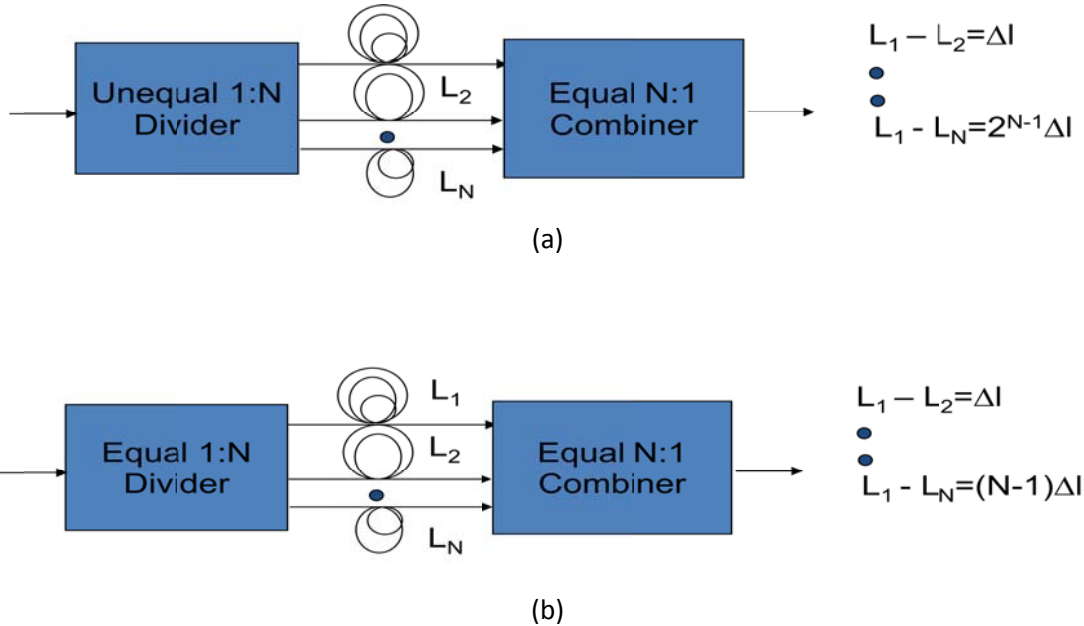


Figure 10-50: Shows the design of higher order transversal filter to form a nested loop RF filter. (a) Unequal optical coupler power split design; (b) equal optical coupler power split design.

The simulated insertion loss results are depicted in Figure 10-49 for both equal and unequal split optical couplers. The length of delay lines for the unequal split are respectively $L_i = 38m$, $78m$, and $152m$ for $i=2, 3$, and 4 as L_1 is selected to be zero. Whereas delay lines for equal power split are respectively $L_i = 75m$, $150m$, and $225m$ for $i=2, 3$, and 4 as $L_1 = 0$ is selected to be zero.

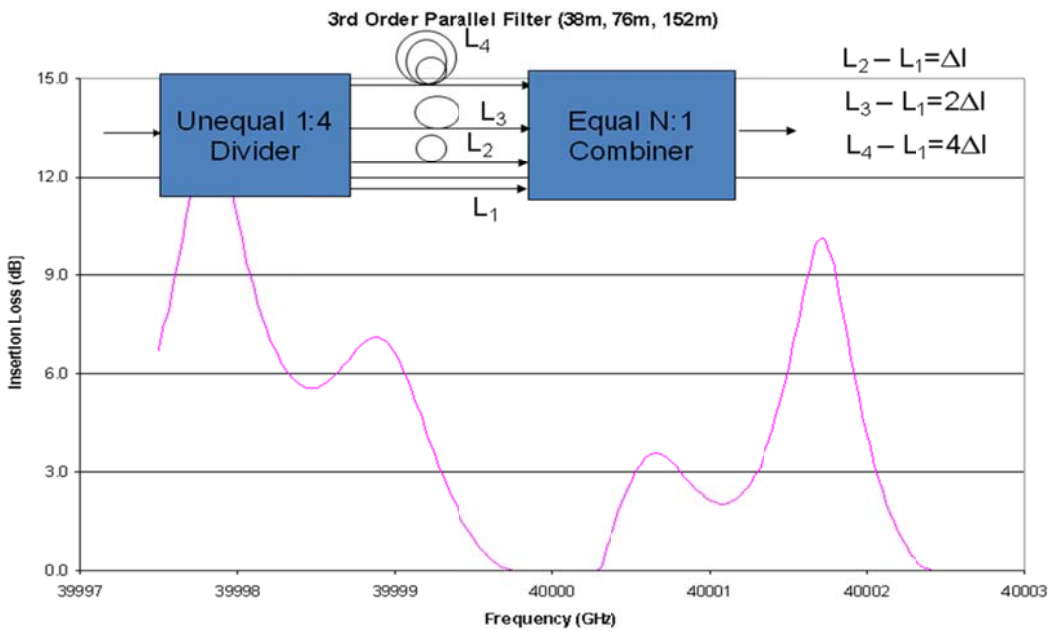
Another option of building higher order nested loops are by series configuration, as depicted in Figure 10-52 with three cascaded 1st order transversal filters with length of $\Delta l = 25m$, $50m$, and $100m$; the depicted insertion loss of this 3rd order optical nested loop RF filter is simulated for optical wavelength of $\lambda=1550nm$. The measured 3dB pass band at RF frequency of $40,000MHz$ is only $1MHz$. Note that in cascaded system rather than requiring 6 optical couplers only 4 optical couplers are required, which are advantageous in space saving [22].

10.3.7 Frequency Tuning using Dispersion of Photonic Band Gap (PBG) Fibers

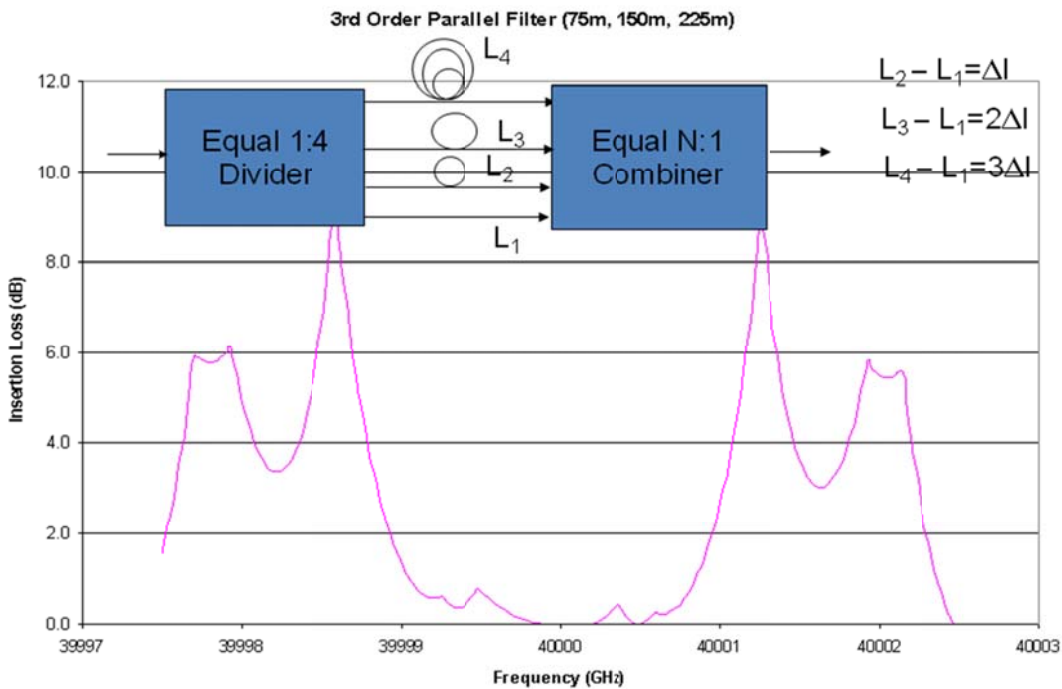
Photonic band gap fiber is a new class of fibers that guide light by the use of photonic band-gaps. It relies on a periodic cladding structure to provide band gaps, i.e., frequency ranges for which light is prohibited from propagating through the cladding structure. PBG fibers feature a cladding comprised of a honeycomb lattice, and a core defect being hollow-filled with air or solid – filled with silica. A PBG fiber employs a new type of wave guiding mechanism and thus exhibits unique properties. Anomalous dispersion is one of the unique properties of PBG fibers.

10.3.7.1 Dispersion of Solid Core Photonic Band Gap Fibers

The structure of a solid core PBG fiber is shown in Figure 10-53. The solid core is assumed circular and has a radius chosen to be equal to the pitch, Λ , as indicated in Figure 10-53. The diameter of the air hole in the cladding is d , also shown in Figure 10-53.



(a) Unequal 1:4 power splitter and combiners



(b) Equal 1:4 power splitter and combiners

Figure 10-51: Shows the CAD simulated insertion loss of 3rd order nested loop filter realized by parallel combination of delay lines at $\lambda=1550\text{nm}$ as a narrowband RF filter at about 40,000MHz. (a) Unequal 1:4 power splitter and combiners, and (b) Equal 1:4 power splitter and combiners. Note measured 3dB bandwidth of this filter is about 2MHz.

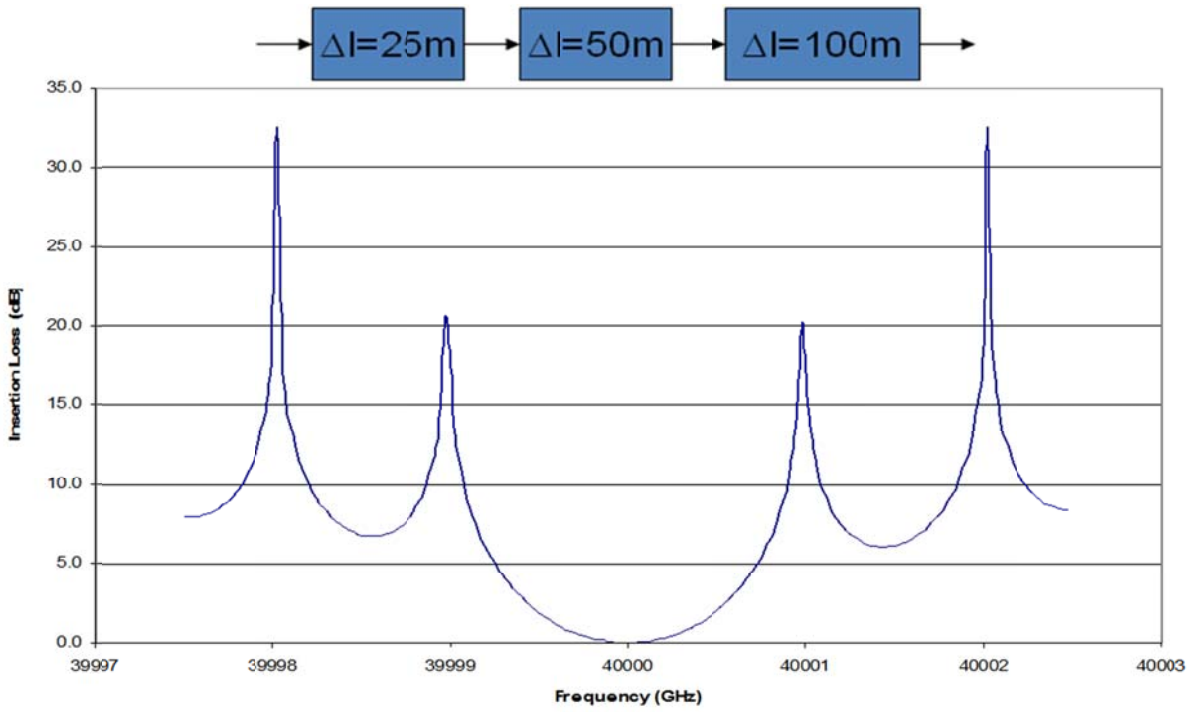


Figure 10-52 Design and simulated insertion loss of 3rd order transversal filter as nested loop RF filter at 40.000GHz. Note 3dB bandwidth is under 1MHz [22]

A specific value of the pitch must be chosen in order to calculate the total dispersion of the fiber. The total dispersion is calculated as the sum of the waveguide dispersion and the material dispersion of pure silica. In Figure 10-54, results are shown for a range of pitch values. The fiber core has a Fluorine doping level of 0.9%, and $d/\Lambda=0.6$. A value of $\Lambda=1.1\mu m$ is seen to give the largest dispersion $D=600ps/km/nm$ for a wavelength of $\lambda=1.55\mu m$. These fiber parameters yield a fiber with a zero dispersion wavelength of 720nm.

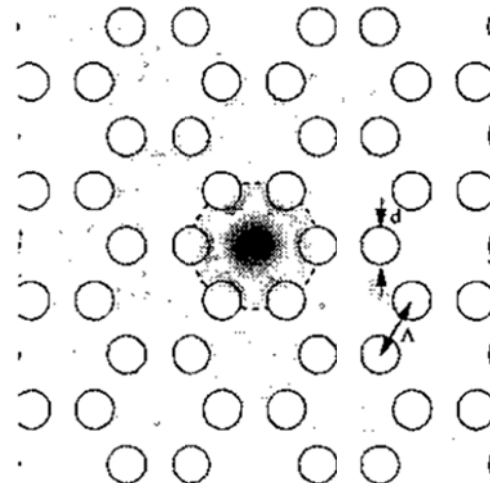


Figure 10-53: Shows the typical structure of Solid Core Photonic Band Gap Fiber adopted from [47]

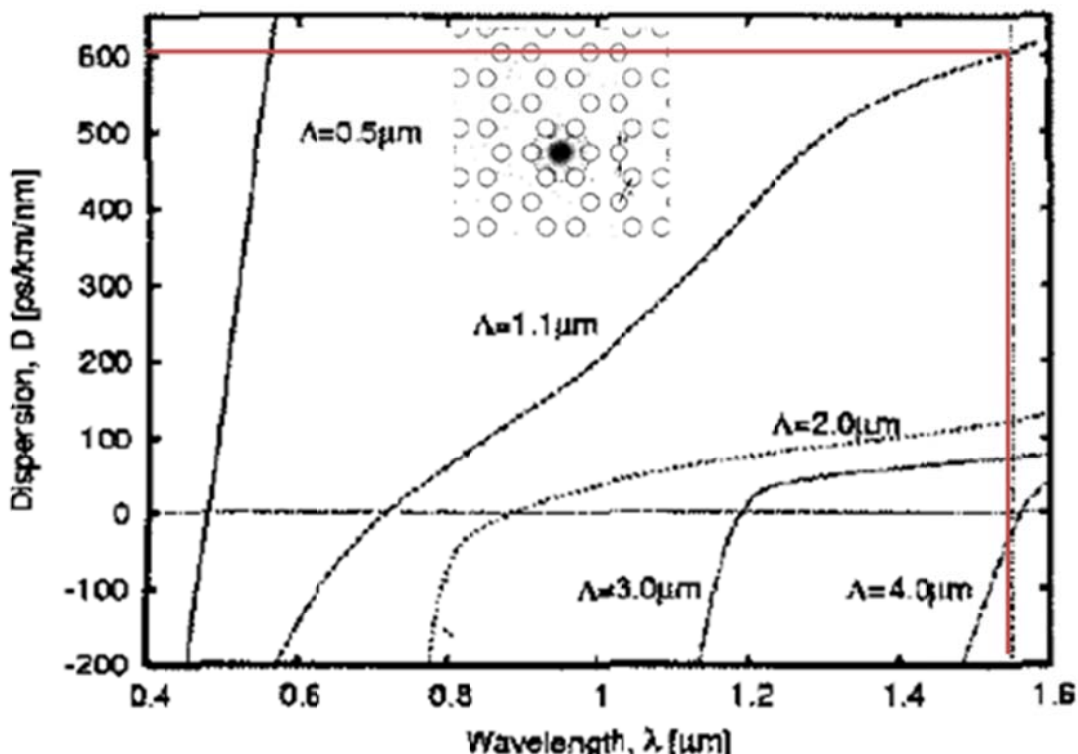


Figure 10-54: The plot of total Dispersion for a Range of Pitch Values when the hole-size is chosen to be $d/\Lambda=0.6$ [47]

10.3.7.2 Dispersion of Hollow Core Photonic Band Gap Fibers

As shown in Figure 10-55(a), a typical 7-cell hollow core PBG fiber is illustrated, where the cladding holes were represented by hexagons with rounded corners described by the relative hole diameter, d/Λ , and the relative diameter of curvature at the corners, d_c/Λ , with Λ being the hole pitch. The corners of the pentagon surrounding the hollow-core are rounded using circles of relative diameter d_p/Λ . The hexagonal core with rounded corners is defined by a thin silica ring of nearly constant thickness t at the boundary of the cladding.

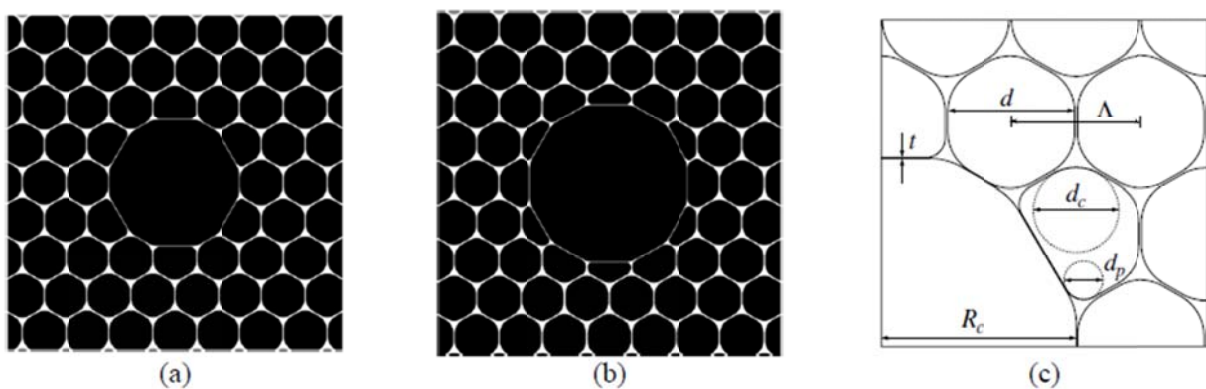


Figure 10-55: (a) All silica HC-PBG fiber with Triangular Lattice Cladding; (b) the Same Structure with the Applied Core Expansion; (c) Fiber Parameters [48]

The dispersion profile of 7-cell HC-PBG fiber with realistic cladding structure can be modified by introducing a two dimensional Gires-Tournois (GT) cavity around the core adopting the one-dimensional PBG structures. In order to introduce the partial reflector layer around the core, the core radius is increased and the thickness of the first air hole layer is decreased, without affecting rest of the structure, as indicated in Figure 10-43(b). The core size is determined by the parameters R_c as shown in Figure 10-55(c), and it is expressed as

$$R_c = (E + 1) \left(1.5\Lambda - \frac{t}{2} \right) \quad (10.14)$$

where E stands for an expansion coefficient.

The dispersion curves for the fundamental air-core mode in HC-PBG fiber with $d/\Lambda=0.98$, $d_c/\Lambda=0.7$, $d_p/\Lambda=0.3$, $\Lambda=2.85\mu m$, and $E=18.7\%$, where the normalized silica ring thickness $T=t/(\Lambda-d)$ is taken as a varying parameter. As depicted in Figure 10-56 by decreasing the silica ring thickness t , the NDS can be decreased, while the corresponding bandwidth becomes narrower.

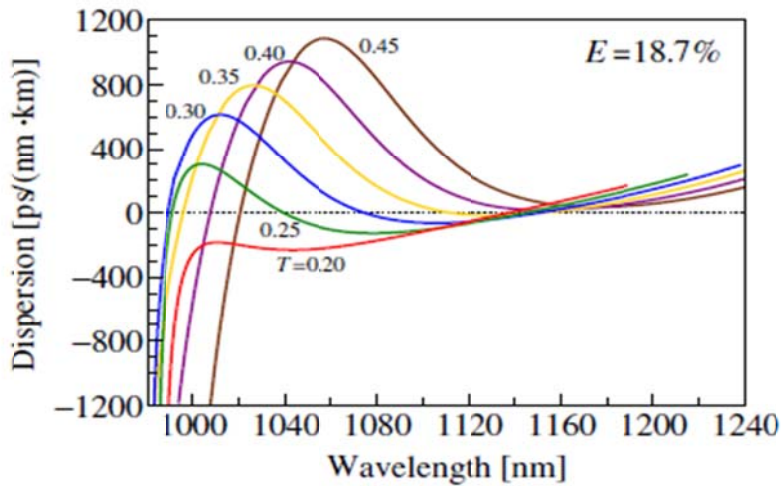


Figure 10-56: Shows the Dispersion curves as a function of the normalized silica ring thickness T with $d/\Lambda=0.98$, $d_c/\Lambda=0.70$, $d_p/\Lambda=0.30$ and $\Lambda=2.85\mu m$ [48]

10.3.8 Raman Amplification in Photonic Crystal Fibers: Approach to Increase the Q-factor of Fiber Delay Line

The Raman properties of photonic crystal fibers (PCFs) with a triangular air hole lattice can be changed by varying the geometrical parameters that characterize the bi-dimensional lattice. The relative hole diameter d/Λ , and the spacing between air holes Λ . By optimizing the air hole diameter d and the lattice pitch Λ of the photonic crystal cladding, it is possible to change the effective index of the cladding and thus the field distribution. Therefore, the effective area and the Raman gain coefficient can be modified. In addition, the presence of a Germanium doped core in a triangular PCF can influence the Raman properties.

The obtained profiles of the Raman effective area and gain coefficient as a function of the pitch Λ are shown in Figure 10-57. PCFs with silica bulk, relative hole diameter $d/\Lambda=0.6, 0.7, 0.8$, and 0.9 and pitch that varies between 0.7 and $2.3\mu m$ have been considered. Fixing the ratio d/Λ is equivalent to considering different PCFs with the same air-filling fraction, the ratio of air to silica in the photonic crystal cross section. The figure shows that for the different PCFs, fixing

the ratio d/Λ , there is an optimal value of Λ that minimizes effective area A_{eff} and maximizes Raman gain coefficient γ_R . This situation, achieved with a very high field tightness, is given when the fiber presents a high refractive index difference between core and cladding and, at the same time, a small core radius.

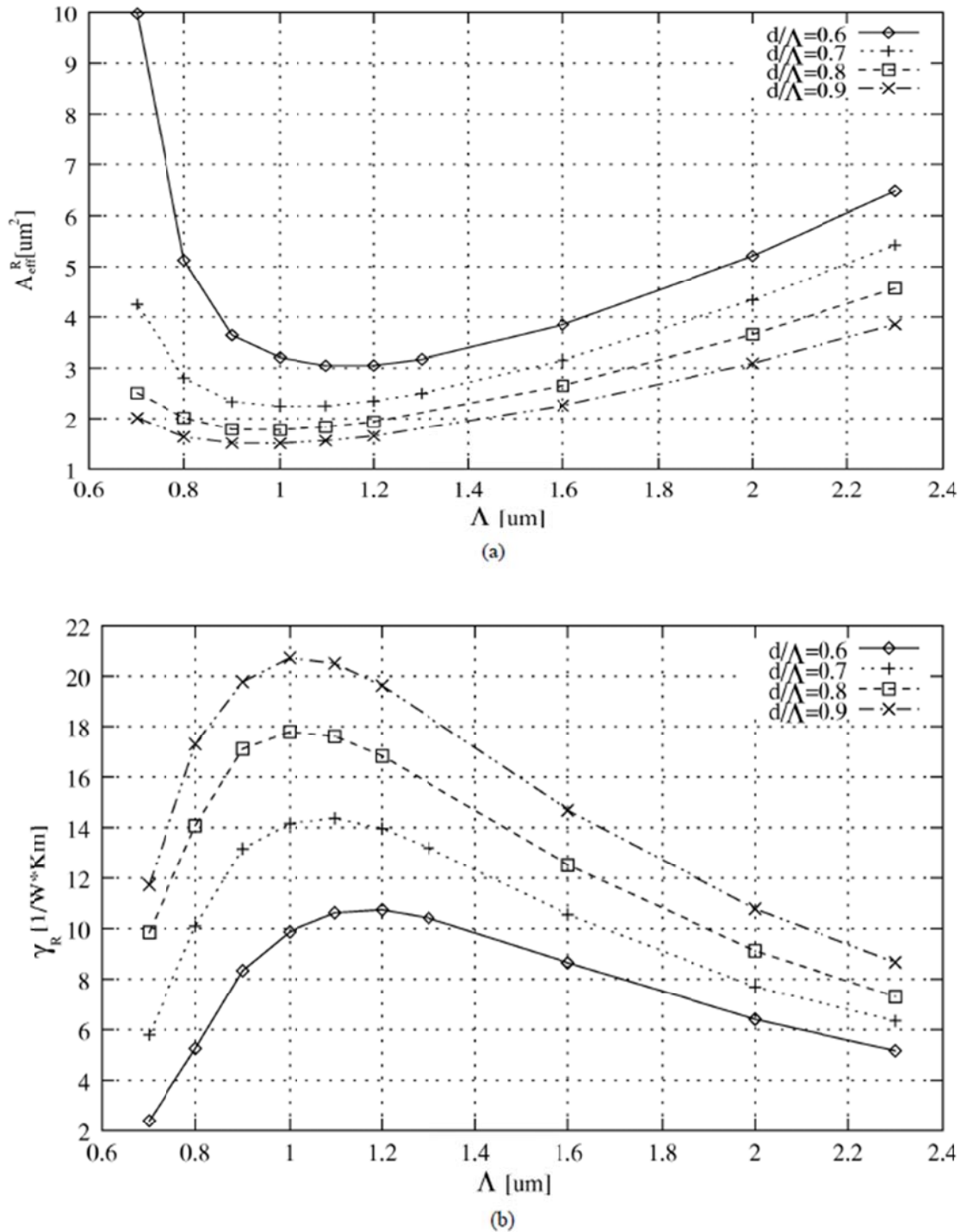


Figure 10-57: (a) Raman Effective Area as a Function of Λ (b) Raman Gain Coefficient as a Function of Λ [49]

Figure 10-58 illustrates the plots of the Raman effective area and gain coefficient as a function of the mean doping radius for the PCFs with $d/\Lambda=0.6, 0.7, 0.8$, and 0.9 . It can be seen that the Raman gain coefficient for each PCF becomes maximum for a well-defined value of the doping radius R_d , the one with Germanium doped area internally tangent to the first ring of air holes.

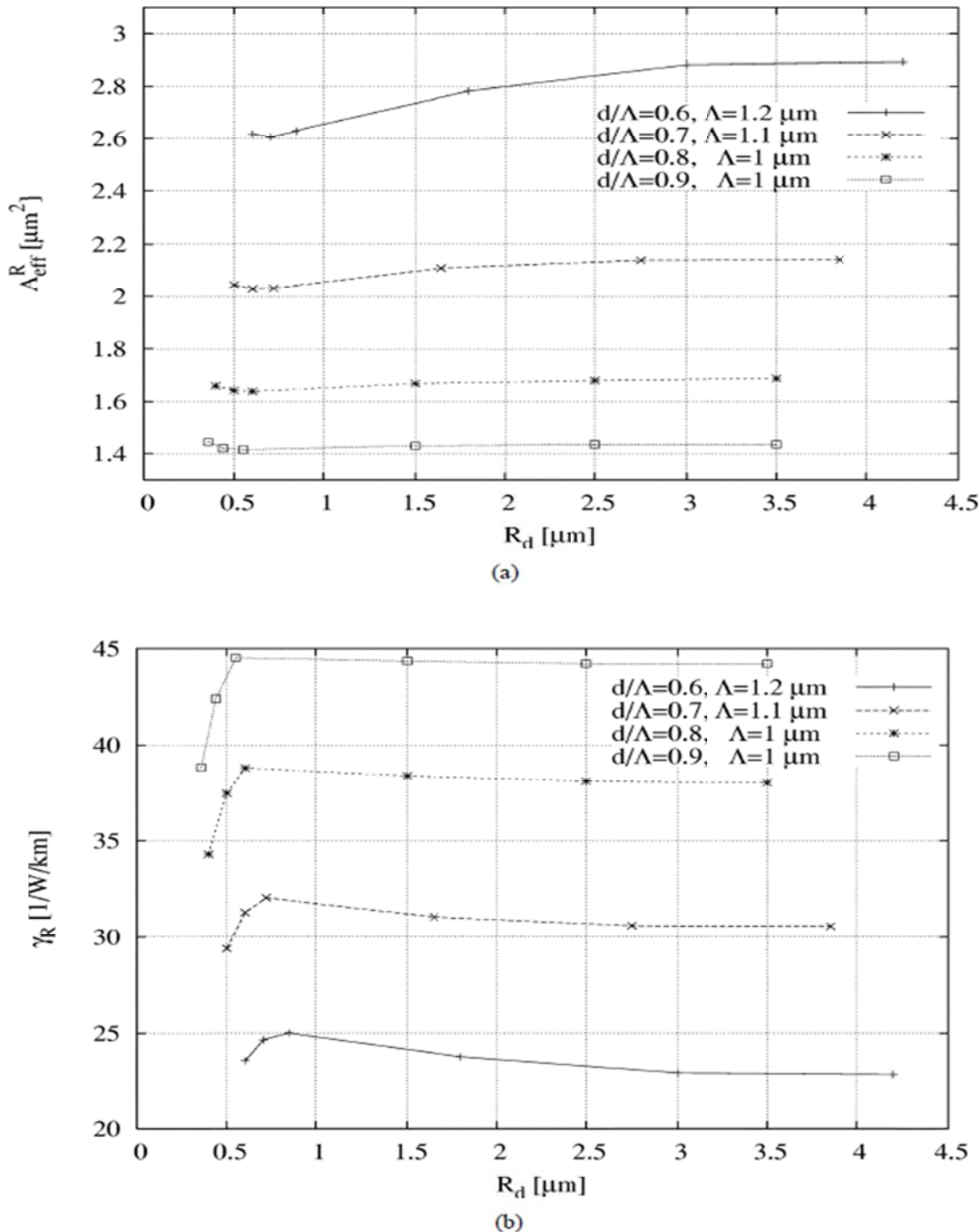


Figure 10-58: (a) Raman effective area as a function of doping radius R_d (b) Raman gain coefficient as a function of doping radius R_d . (Germania doping 20% mol; $d/\Lambda=0.6, 0.7, 0.8, 0.9$ and $\Lambda=1.2, 1.1, 1$, and 1 , respectively; [49])

10.3.9 New Methods in OEO for Temperature Compensation: SMF-28 and HC-PCF to Achieve Passive Temperature Compensation

OEO's are known for their low thermal stability and so temperature compensation techniques for thermal stability become critical. It's shown by Daryoush et al. [51] that the refraction index of composite fiber 'HC-PCF' has negative temperature slope while standard fiber has positive temperature slope. Passive temperature compensation is achieved by combining the 2 fibers at an appropriate length ratio to make the refractive index temperature slope close to zero. The ratio of the HC-PCF to the SMF-28 is chosen to be $l_p = 8l_s$.

The major drawback of composite fiber is that the high loss of HC-PCF degrades the phase noise performance. For quantitative data of the phase noise degradation, the following calculation has been carried out [22]:



Assume $\alpha_p=10\text{dB/km}$ for HC-PCF and $\alpha_s=0.33\text{dB/km}$ for SMF-28

$$Q_{\text{total}} = \frac{\beta_s l_s + \beta_p l_p}{2\alpha_s l_s + 2\alpha_p l_p} \quad (10.15)$$

For $l_p = 8l_s$, $\beta_p = 0.5\beta_s$, $\alpha_p = 30\alpha_s$

$$Q_{\text{total}} = \frac{\beta_s l_s + \beta_p l_p}{2\alpha_s l_s + 2\alpha_p l_p} = \frac{5Q_s}{240} = \frac{Q_s}{48} \quad (10.16)$$

Table 10.2 shows the verification of the reduction of Q-factor and degradation of phase noise performance in composite fiber (SMF-28 and HC-PCF).

Table 10.2 Reduction of the Q and degradation of phase noise in composite fiber [51]

	Phase Noise (dBc/Hz) @ 1kHz	Phase Noise (dBc/Hz) @ 10kHz	Reduction
Experiment Result 30m HC-PCF, $\alpha_p=2\text{dB/m}$ and 1km SMF-28, $\alpha_s=0.33\text{dB/km}$	-58	-78	45 dB
Analytical Result	-57	-77	46 dB

If we take advantage of a Raman amplifier [51], we can lower the attenuation of the HC-PCF. Moreover, as the technology matures, the attenuation of HC-PCF will eventually reach that of a standard SMF-28 fiber or even better. To find out the impact of fiber attenuation on phase

noise, we can use the same equation in the previous section by changing α_p . The reduction is with respect to the Q of SMF-28 with the same total length. Currently the best attenuation from commercially available HC-PCF is about 1dB/km. Table 10.3 shows the verification of the reduction of Q-factor.

Table 10.3 Phase noise: standard fiber and composite fiber [51]

	Phase Noise (dBc/Hz) @ 1kHz	Phase Noise (dBc/Hz) @ 10kHz	Reduction
1km standard fiber	-103	-123	
1km Composite Fiber (HC-PCF : SMF-28 = 8:1) OEO with Different Attenuation			
HC-PCF: $\alpha=1\text{dB/km}^{[2]}$	-89	-109	14dB

(Thorlabs, ESM-12B: $\alpha<1\text{dB/km}$ @ 1550nm measured at bend radius of 16cm; Mode Field Diameter $10\pm1\text{ um}$)

Tables 10-2 and 10-3 show the comparative characteristics of the standard and composite fiber with reference to loss dynamics and reduction of quality factor for a given temperature compensation in OEO application. The dispersion characteristics of the fiber also plays important role, can be incorporated as a tuning feature in synthesized OEO. Figure 10-59 shows the frequency tuning range at 10 GHz as a function of Fiber Dispersion at 1550 nm for 1km Long Fiber.

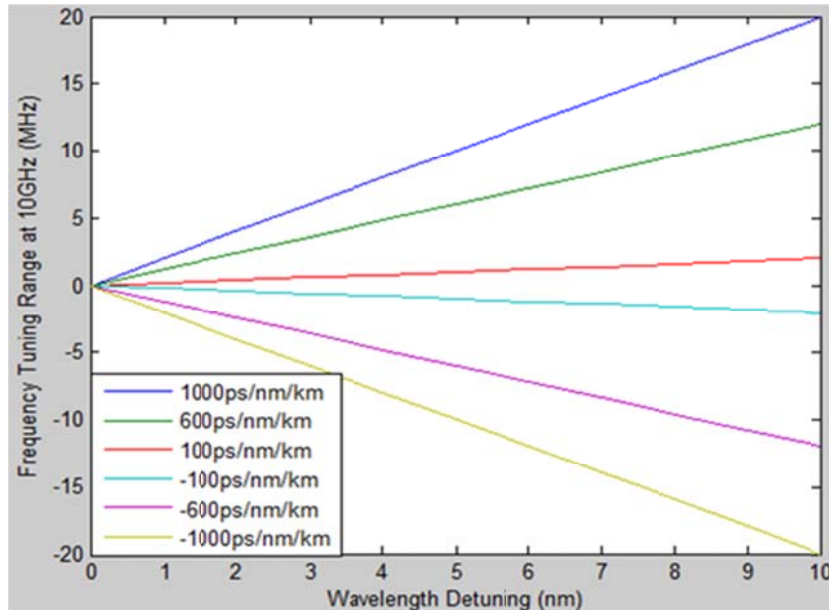


Figure 10-59: Shows the frequency tuning range at 10 GHz as a function of Fiber Dispersion at 1550 nm for 1km Long Fiber $\frac{\Delta f}{f} = \frac{\tau_D}{\tau}$

10.3.10 Composite Fiber with Raman Amplifier

The high loss associated with composite fiber can be compensated by incorporating Raman amplification. Daryoush [51] suggested new approach of compensating for the high loss of HC-

PCF by distributed gain to achieve a very high quality factor long delay line. Figure 10-60 shows the distinct features of Raman amplification. Table 10-4 shows the expected phase noise with various attenuation levels, it can be seen that through Raman amplification, phase noise performance can be improved due to the increase of Q-factor.

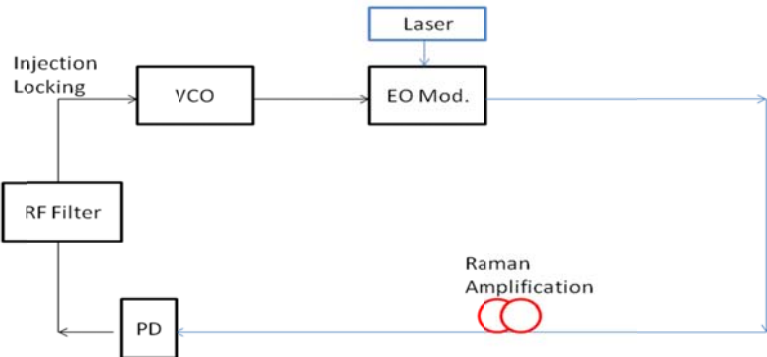


Figure 10-60: Shows the distinct features of Raman amplification [49].

As mentioned above, on taking advantage of Raman amplification (RA) in the HC-PCF section of the composite structure the overall attenuation of the combined structure can be brought down hence increasing the Q factor which in-turn helps improve the phase noise while providing temperature stability through an easy and inexpensive passive technique. Table 10.4 illustrates the simulated achievable effective attenuation, Q-factor and Phase noise before and after Raman Amplification for different lengths of the composite fiber structure. As shown in Table 10-4, low phase noise OEO sources can be realized using Raman amplification techniques in composite fiber structures. The simulated phase noise performance @ 10 kHz offset is -154dBc/Hz for 10 GHz carrier frequency with $\alpha=0.06$ dB/km. Further reduction in noise is possible by incorporating injection and phase locking techniques based on patent applications [54]-[67].

Table 10.4: Effective Q and Phase Noise Comparison between SMF-28 and Composite Fibers before and after Raman Amplifier

10.4 Novel Design Concepts of Passively Temperature Compensated OEOs [22, 23]

The research work undertaken for the part of this thesis is to design and develop ultra low phase noise stable OEO circuit for microwave and millimeter wave applications. Recent publications [1]-[76] discuss the feasibility study and application of OEO in modern communication systems. However, the drawbacks of frequency drift due to change in operating temperature and lack of tunability limits the utility of the current OEO systems available in the market [78]-[79].

10.4.1 Evolution of State-of-the-art SILPLL OEO Circuits for Ultra Low Phase Noise

10.4.1.1 Basic OEO Circuit

The objective of the thesis is to develop low phase noise signal sources for RADAR and test equipment applications. Figure 10-61a shows the basic structure of OEO [36].

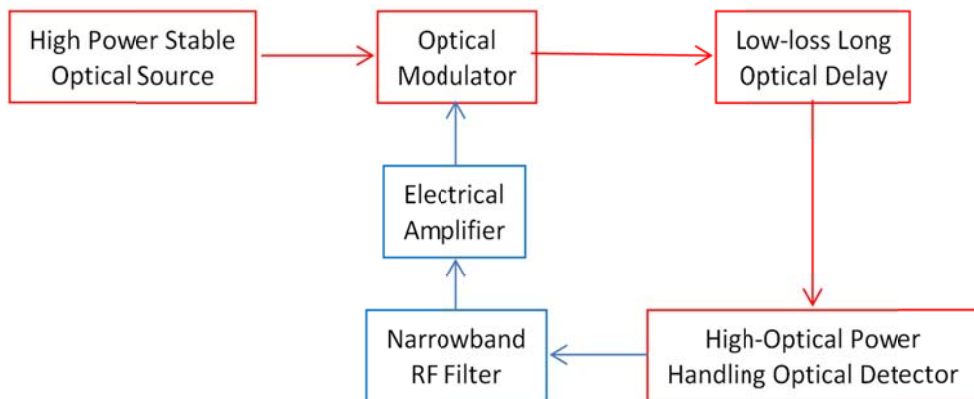


Figure 10-61a: Shows the basic structure of OEO circuit, (the color arrangement shows electrical and optical modules in the block diagram) [36]

10.4.1.2 OEO Circuit with Self-IL (injection-locked)

Figure 10-61b shows the evolution from the basic OEO structure to OEO with self injection locking (electrical and optical domain).

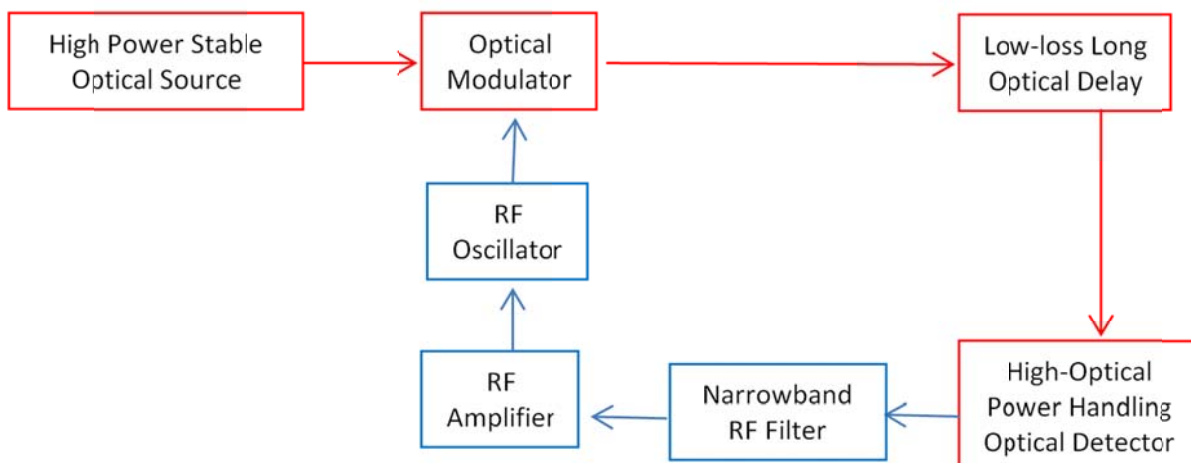


Figure 10-61b: Evolution to basic OEO with self-IL as shown in electrical domain by [9] and in optical domain by [7], the color arrangement shows electrical and optical modules in the block diagram)

10.4.1.3 OEO Circuit with Self-PL (phase-locked)

Figure 10-61c shows the evolution from the basic OEO structure to OEO with self phase locking.

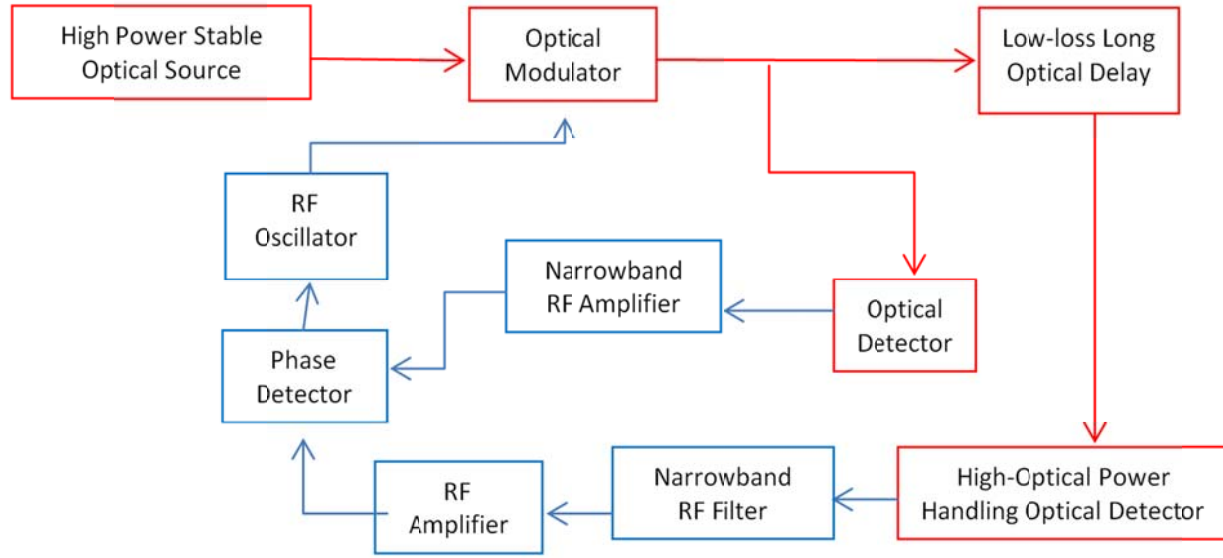


Figure 10-61c: Evolution of basic OEO with self-PLL using single loop by [18] and double optical loops by [19, 20], the color arrangement shows electrical and optical modules in the block diagram)

10.4.1.4 OEO Circuit with SIL-PLL (Self injection locked phase locked loop)

Figure 10-61d shows the evolution from the basic OEO structure to OEO with IL-PLL locking.

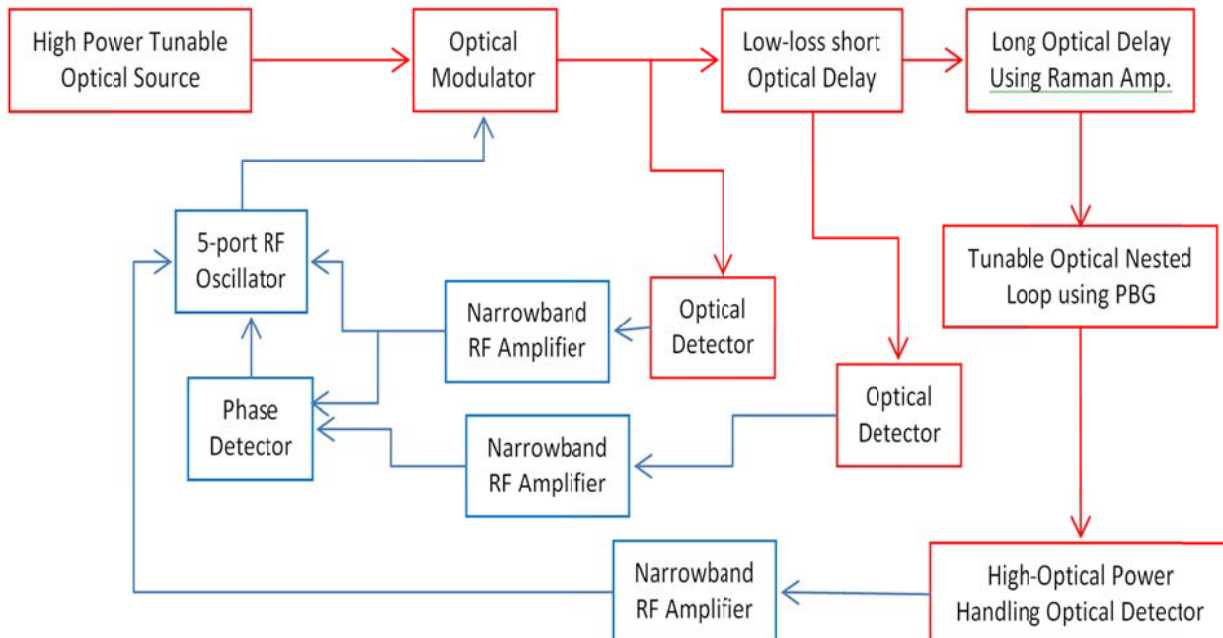


Figure 10-61d: Evolution of basic OEO to ILPLL as an electrical version is demonstrated by [21], the color arrangement shows electrical and optical modules in the block diagram)

10.4.1.5 OEO Circuit with SIL-PLL-Mode-Locking of Optical Modes

Figure 10-61e shows the evolution from the basic OEO structure to OEO with IL-PLL, mode-locking of optical modes [22, 23]

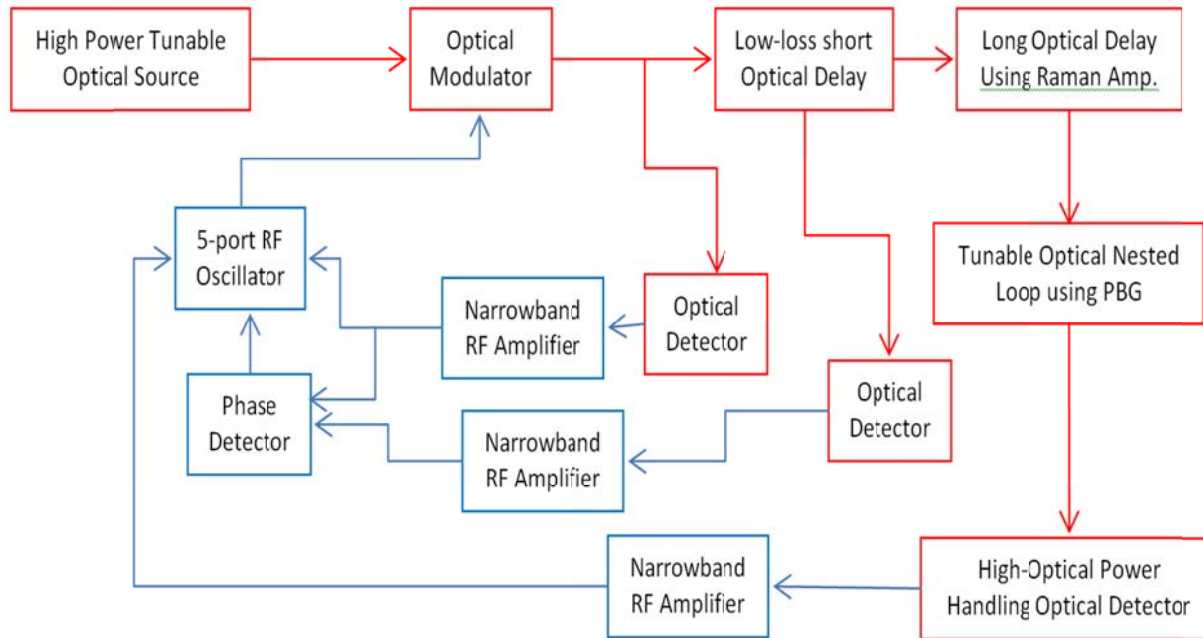


Figure 10-61e: Evolution of basic OEO to include in addition to ILPLL, mode-locking of optical modes, the color arrangement shows electrical and optical modules in the block diagram

10.4.2 Key features added as result of novel design approach for the validation [22]-[23]

Following are the key features added for the realization of novel OEO circuits:

- Use of five port RF oscillator to have ease of self-injection, RF reference for self- phase locking (PLL), RF access for optical modulator, and output in RF domain and frequency control required in self-PLL using low frequency control as VCO port.
- Use of low loss, temperature stable, optimum length of fiber delay based on fiber loss as shown in Figure 10-11 and Figure 10-12
- Use of optical “Nested Loop” as narrowband RF filters in place of narrow band RF filter as shown in Figure 10-51 and Figure 10-52
- Realization of frequency tunable OEO when dispersive PBG optical fibers are combined with tunable optical source as demonstrated in Figure 10-59.
- Compensation of loss using distributed Raman amplifier to compensate and reduce fiber loss in PBG fibers as shown in Figure 10-60 and Table 10-4.
- Inclusion of optical mode-locking by using the phase error comparator to adjust DC bias current of tunable semiconductor laser as optical source for both externally and directly modulated optical links and/or adjusting the DC bias condition on optical modulator in externally modulated optical links (for Mach-Zhender modulator or Electro-absorption modulators).

10.4.3 Realization of Low Phase Noise and Passive Temperature Stable OEO Circuits

Figure 10-62 shows the illustrative block diagram of “passive temperature stable ultra low phase noise optoelectronic oscillator circuits”. As shown in Figure 10-61, the different modules explain their characteristic as follows [22, 23]:

1. Use of self-ILPLL for phase error corrections to a free-running 5 port VCO as the nucleating seed source for OEO using a loop filter bandwidth of few MHz, phase control, efficient self-injection (this component is novelty of design), where
 - (a) Self- injection locking is used for cleaning close-in to carrier phase noise of the VCO at far away from carrier ($\Omega > 1\text{MHz}$) by improving on locking range due to low Q electrical oscillator and higher injected signal using 5 port VCO
 - (b) Self-phase locking is used to improve close-in to carrier phase noise for close to carrier ($\Omega < 1\text{MHz}$) of VCO using a higher natural resonance frequency of loop filter amplifier to the five port VCO using the control port
 - (c) Combining IL and PLL to achieve self-ILPLL topology to reduce close-in to carrier phase noise by optimizing combination of locking range, gain of loop filter amplifier, and fiber delay
 - (d) Ability to maintain phase locking to any phase between -90 to +90 for fundamental frequency and -180 to 180 degrees for 2nd sub-harmonic locking by setting the voltage reference of the operational amplifier in the loop filter amplifier from negative to positive voltage corresponding to a phase detuning close to -85 to +85 degrees, while still maintain a clean close-in to carrier phase noise for a phase detuning of 0 degrees
2. Use of specialized fiber optic delay line providing reduced temperature sensitivity for the optical Fabry Perot resonator and enhanced dispersion characteristics (this component is a significant novelty of the proposed OEO design), which will provide
 - (a) Low-loss and passive temperature compensation using a right combination of standard optical fibers and suffers from as much as -10ppm/C change in index of refraction in silica fibers by +2.5ppm/C of HC-PCF or
 - (b) A reduced temperature sensitivity of -3ppm/C of SC-PBG fibers;
 - (c) Provide distributed optical amplification to actively reduce light attenuation based on principle of Raman amplification using a pump source appropriately selected with respect to the source wavelength based on Stimulated Raman Scattering
 - (d) Changing oscillation frequency of OEO by adjusting phase shift introduced in the optical delay element using high dispersion of PBG fibers to as much as -500ps/nm km from -17 ps/nm km of standard fibers
 - (e) Frequency synthesis of OEO by tuning of the optical source wavelength where the oscillation frequency is being controlled by satisfying Barkhausen oscillation condition in a passively temperature compensated low loss dispersive PBG fibers.

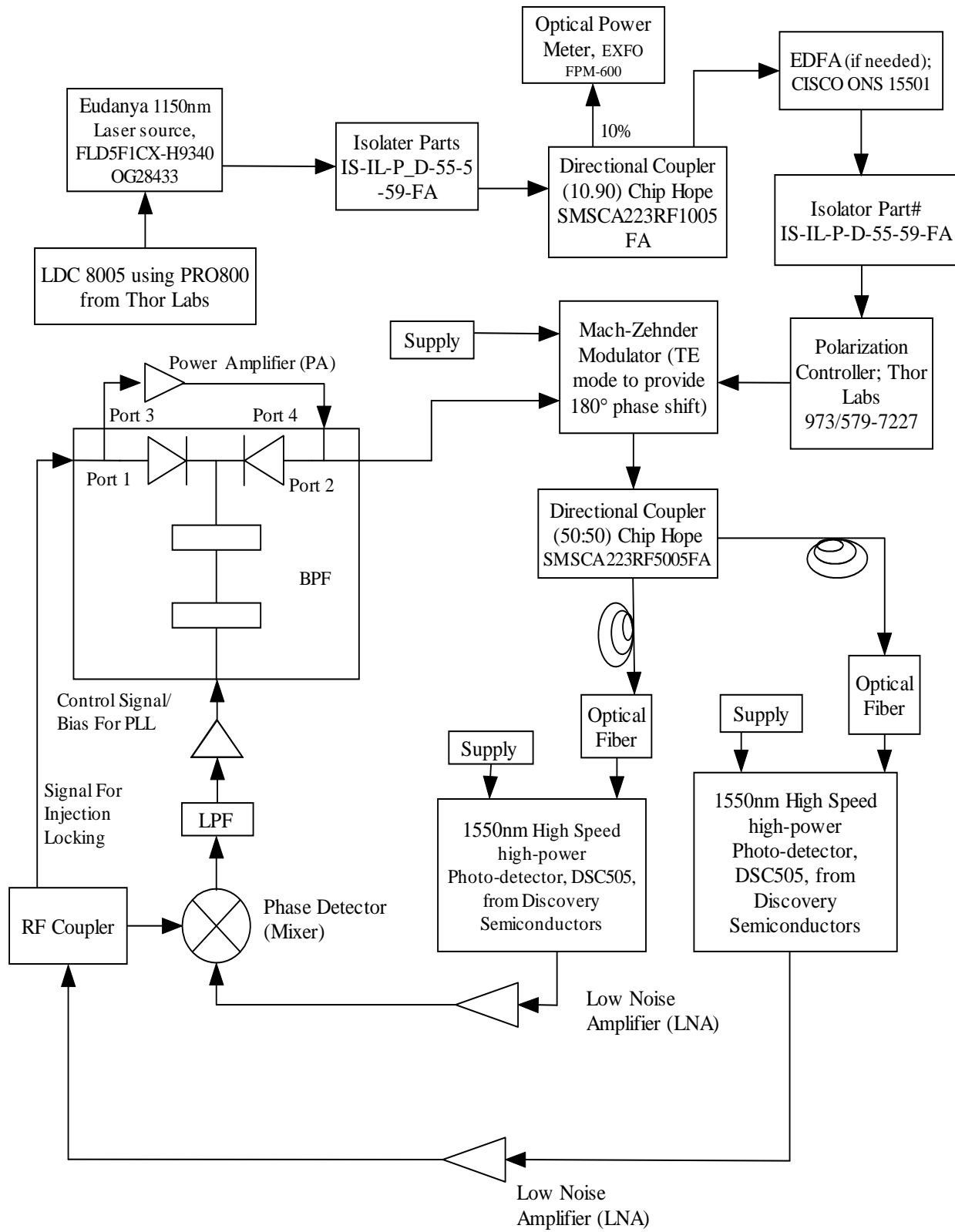


Figure 10-62: Shows the illustrative block diagram of “ultra low phase noise and passive temperature stable optoelectronic oscillator circuits” [22]-[23]

3. Use of multiple loops to perform phase comparison of different references provided through multiple fiber optic delay lines (use of many control feedback loops and phase locking is novelty of this OEO design), where
 - (a) Self-ILPLL made to a reference of 1 us (200m) delay that is fast and minimizes the oscillation frequency of VCO's drift by synchronizing every 1us;
 - (b) Self-ILPLL is being also augmented by delays of 5 μ s (1km) that is minimizing the VCO frequency drift , which in turn is to be augmented by 50 μ s (10km) to make sure that the overall frequency drift is limited to shifts limited within 1 μ s as the VCO oscillation is locked to an equivalent reference of oscillation delay of 50 μ s (10km long fiber delay)
4. Use of temperature compensated nested loop RF filters for the OEO frequency mode selection in a multi-mode system of long delays (every 20kHz for 10km long or 50 μ s delays, every 200kHz for 1km fiber delays, and every MHz for 200m long fiber delays) (this component is novelty of the proposed OEO design), which
 - (a) Adjusts passband frequencies by selecting long fiber optic delay
 - (b) Avoids the need for extremely large size and insertion loss in high order RF metallic filters
 - (c) Achieves a much higher order optical fiber based Nested Loop RF filters for even similar size RF metallic filters
 - (d) Employs Hi-Bi fibers for fully integrated small size structures
 - (e) Maintain higher frequency selectivity using high order parallel or series combination of 1st order transversal optical filters
 - (f) Implement temperature compensated narrow band optical nested loop RF filter by use of PBG fibers
5. Exploring multi-modal locking in the OEO by optical phase locking (this component is novelty of OEO design) using the concepts of mode-locked OEO by establishing optical mode locking of OEO using variable changes to biasing conditions of
 - (a) Mach-Zehnder modulator DC bias in fiber optic links
 - (b) Optical phase delay shift of an integrated optical delay line using EA modulator
 - (c) Change in index of refraction of the directly modulated fiber optic delay element

10.5 Analytical Modeling and CAD simulation

The OEO circuit using longer delay line exhibits higher Q factor but mode spacing is also reduced proportionally. The important challenge is to suppress higher modes generated due to mode spacing is determined by c/nL , where c is the light speed, n is the fiber refractive index, and L is the loop length. For example, a few-km fiber length produces the mode spacing of several tens of kHz [77]; suppression of multi-modes partially or completely is the topic of research towards realization of single-mode oscillation. From [50], the mode spacing is

inversely proportional to the loop length; therefore, designer has to face compromise between the lower phase noise and mode spacing.

Figure 10-63 depicts the equally spaced peaks (or called modes), mode spacing is determined by c/nL , where c is the light speed, n is the fiber refractive index, and L is the loop length. The power-spectral density of each mode is given by [15]

$$S_{RF}(f) = \frac{\delta}{\left[\left(\frac{\delta}{2\tau}\right)^2 + (2\pi)^2(\tau f)^2\right]}, \text{ where } \delta = \frac{\rho_N G_A}{P_{osc}} \quad (10.17)$$

where f is the frequency offset from the oscillation frequency, τ is the loop delay time, γ_N is the total noise density which is sum of the detector noise density including thermal and shot noise and the laser's relative intensity noise density, G_A is the required RF amplifier voltage gain for compensating losses in the delay line and P_{osc} is the oscillator output power.

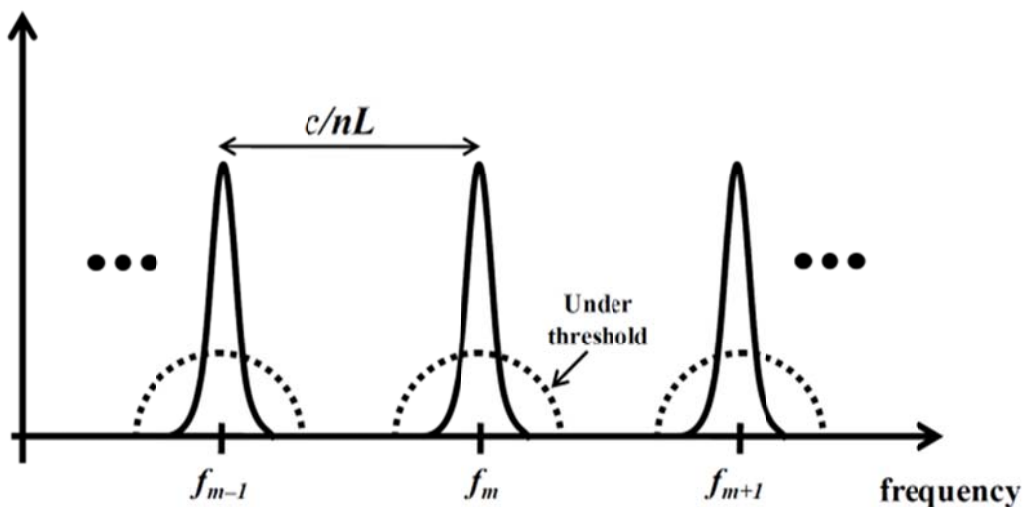


Fig.10-63: shows the multimode oscillation phenomenon OEO

From (10.17), the phase noise of an OEO decreases quadratically with the frequency offset and it is inversely proportional to the square of loop-delay time at given offset frequency. CAD simulated behavior of close-in to carrier phase noise of a 10GHz OEO is depicted in Figure 10-64 for delays of $0.1\mu s$, $1\mu s$, and $10\mu s$ that correspond to fiber delay lengths of 20m, 200m, and 2km respectively as side mode generation is ignored.

For RADAR and space communication applications, the OEO circuit should operate on single mode with low phase-noise signal since the other oscillation modes degrade the system performance by reducing signal-to-noise ratio (SNR). In electrical domain, single-mode oscillation is realized by inserting a high-Q electrical band-pass filter (BPF) to the OEO loop but such high-Q filters are difficult to realize at 40 GHz and above frequencies.

By incorporating high Q-factor evanescent mode WGM (whispering-gallery-mode) resonator disk in OEO circuit, which acts both as a frequency filter (selecting the desired microwave oscillating frequency) and as optical energy storage element, spurious free oscillation can be achieved.

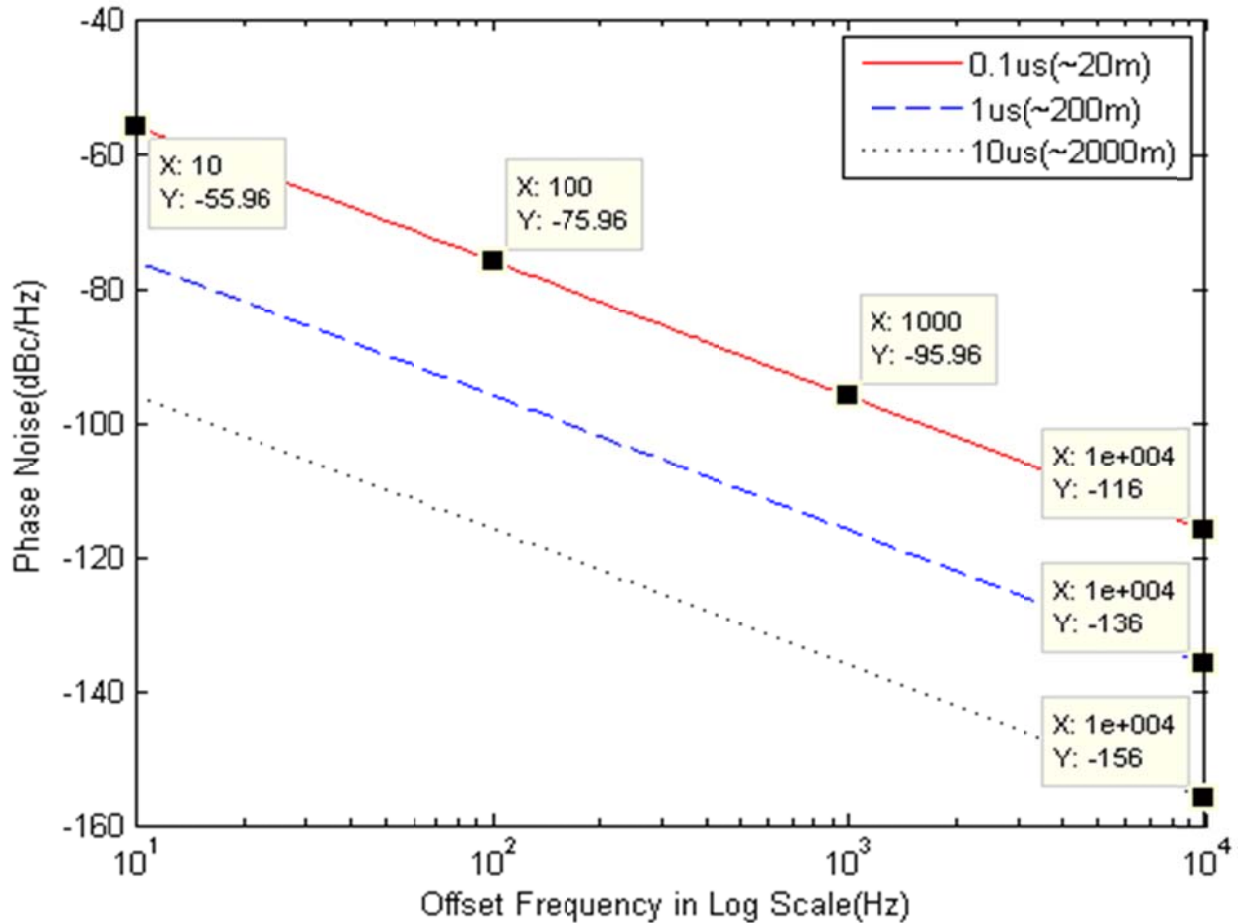


Figure 10-64: CAD simulated phase noise of 10GHz OEO with various fiber delay ($\rho_N=10^{-17}\text{mW/Hz}$, $P_{osc}=10\text{mW}$, $G_A^2=100$).

In this configuration, the oscillating frequency corresponds to the free spectral range of the resonator (between 10 GHz and 12 GHz), and therefore no delay induced spurious peaks are present in the spectrum, in contrast to the case of the classical optoelectronic oscillator where the storage element consists of an optical fiber delay line. However, this approach has limitation of poor temperate stability of WGM.

The possible alternative is to incorporate injection-locking, phase locking, multi-mode-injection-locking for the suppression of higher modes and reducing the noise of an OEO circuit [22]. By combining (Injection Locking (IL) and Phase Locked Loop (PLL), a clean spectrum in a wider range of offset frequency is expected. An electrical oscillator with ILPLL (injection locked phase locked loop) is reported in [24].

Figure 10-65 shows the System block diagram of a SPPLL, where primarily a stabilization loop in which feedback is introduced into a voltage-controlled oscillator (VCO) using a delay line frequency discriminator (DLFD). The DLFD converts frequency fluctuations into baseband voltage fluctuations, which provide an error signal that adjusts the oscillation frequency. The DLFD functions as a phase detector in a standard PLL, however, the transfer response of DLFD is different from a conventional phase detector.

The relationship between the baseband voltage fluctuation ΔV and the frequency fluctuation Δf is given below [29],

$$\Delta V(f) = \left[K_d 2\pi \tau_D \frac{\sin(\pi f \tau_D)}{(\pi f \tau_D)} \right] \Delta f(f) \quad (10.18)$$

where K_d is the mixer conversion efficiency, τ_D is the delay time in the DLFD.

From (10.17), we can see that it is desirable to have a longer delay as it will provide a higher sensitivity. However the transfer response has a $\sin(x)/(x)$ characteristic, which means longer delay results in the singularity to occur much earlier in the offset frequency than a shorter delay.

Phase noise of an oscillator incorporating SPLL with DLFD can be found using standard loop analysis as [30],

$$S_{SPLL}(f) = |H(s)|^2 S_{n1}(f) + |1 - H(s)|^2 S_{n2}(f) \quad (10.19)$$

where $H(s)$ is the loop transfer function given by $H(s)=G/(G+1)$.

Parameter $G=K_0 K_d F(s)$, and K_0 is the VCO tuning efficiency; K_d is the mixer conversion efficiency; $F(s)$ is the loop filter transfer function, n_1 and n_2 are the residual phase noise from the hardware and the phase noise of the VCO, respectively.

By combining a short delay and a long delay, low phase noise spectrum in a wide offset frequency range is expected. Phase noise of the dual DLFD topology is given by [30],

$$S_{SPLL}(f) = \frac{G}{1+G(K_1+K_2)} n_1(f) + \frac{1}{1+G(K_1+K_2)} n_2(f) \quad (10.20)$$

where $K_1=1-\exp(j2\pi f \tau_{d1})$ and $K_2=1-\exp(j2\pi f \tau_{d2})$.

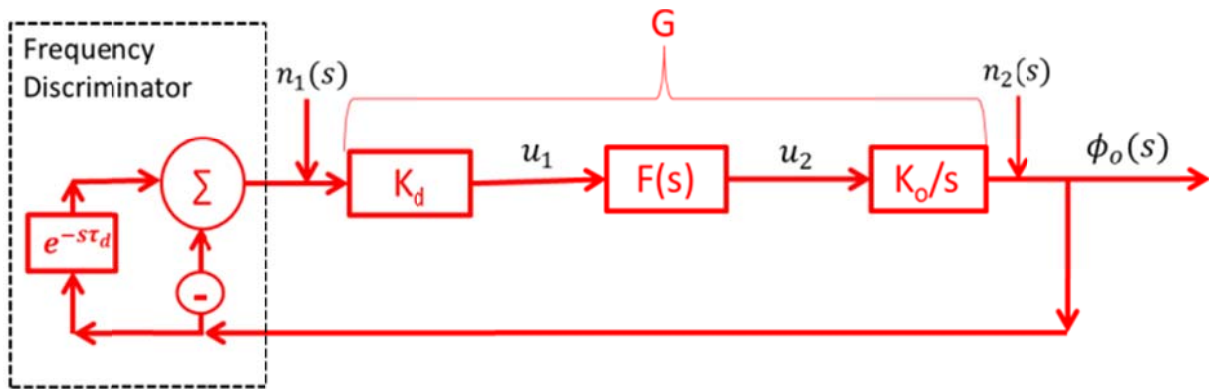


Figure 10-65: shows the typical simplified block diagram of SPLL

Figure 10-66 shows the typical system block diagram of IL. The time domain phase-dynamics of an injection-locked VCO can be found as [25],

$$\frac{d\phi_0(t)}{dt} = \rho \omega_{3dB} \sin[\phi_1(t) - \phi_2(t)] \quad (10.21)$$

$$S\phi_0(s) = \rho \omega_{3dB} [\phi_i(s) - \phi_0(s)] \quad (10.22)$$

where Φ_o is the VCO output phase; Φ_i is the injection signal phase; $\rho = P_{inj}/P_o$ is the injection strength; Q is the quality factor of the VCO resonator; $\omega_{3dB} = \omega_0/2Q$ is half the 3dB bandwidth of the VCO resonator.

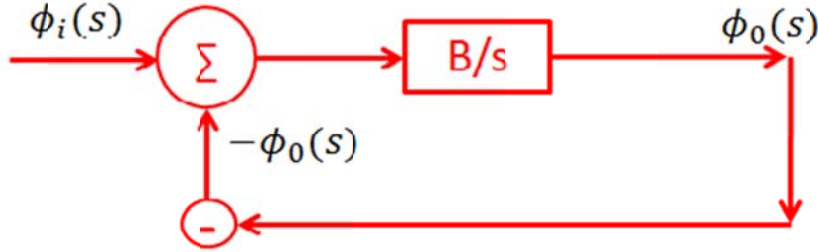


Figure 10-66: shows the Laplace domain representation of IL

From (10.21) and (10.22), the phase transfer function of injection locked VCO can be described by

$$H_B(s) = \frac{\phi_0(s)}{\phi_i(s)} = \frac{B}{1+B} \quad (10.23)$$

where $B = \rho \omega_{3dB}$.

From similarity of $H(s)$ and $H_B(s)$, a first order approximation IL is equivalent type I PLL. A similar phase noise expression is derived for SILPLL as:

$$S_{SILPLL}(f) = |1 - H(s)|^2 S_{n1}(f) + |1 - H(s)|^2 S_{SIL}(f) \quad (10.24)$$

Figure 10-67 shows the CAD simulated phase noise plot of SILPLL VCO. In the simulation setup, a self-injection mechanism is applied to a VCO with dual DLFD SPLL, the short and long delays are 1μs and 10μs respectively. The injection strength is $\rho=0.316$ and the injection delay is 10μs. The green curve represents the phase noise of the VCO incorporating SILPLL. The phase noise of SILPLL reaches the noise floor at around 100 kHz offset while the phase noise of double loop SPLL reaches the noise floor at 100 kHz. For comparison, phase noise of a single SPLL with 10μs delay and a dual SPLL with 1μs and 10μs delay are also provided. The improvement in phase noise for SILPLL is significant. Phase noise of SILPLL VCO is -165 dBc/Hz @ 20 kHz offset from the carrier is predicted.

It can be seen that there is hump & dip after 20 kHz offset from the carrier in Figure 10-67, the reason of degradation in phase noise performance is due to higher order modes prevalent in the fiber delay line. Figure 10-68 illustrates the functional block diagram of the Evanescent-mode-locked IL-PLL OEO circuit for improved phase noise performance at far offset and thermal stability.

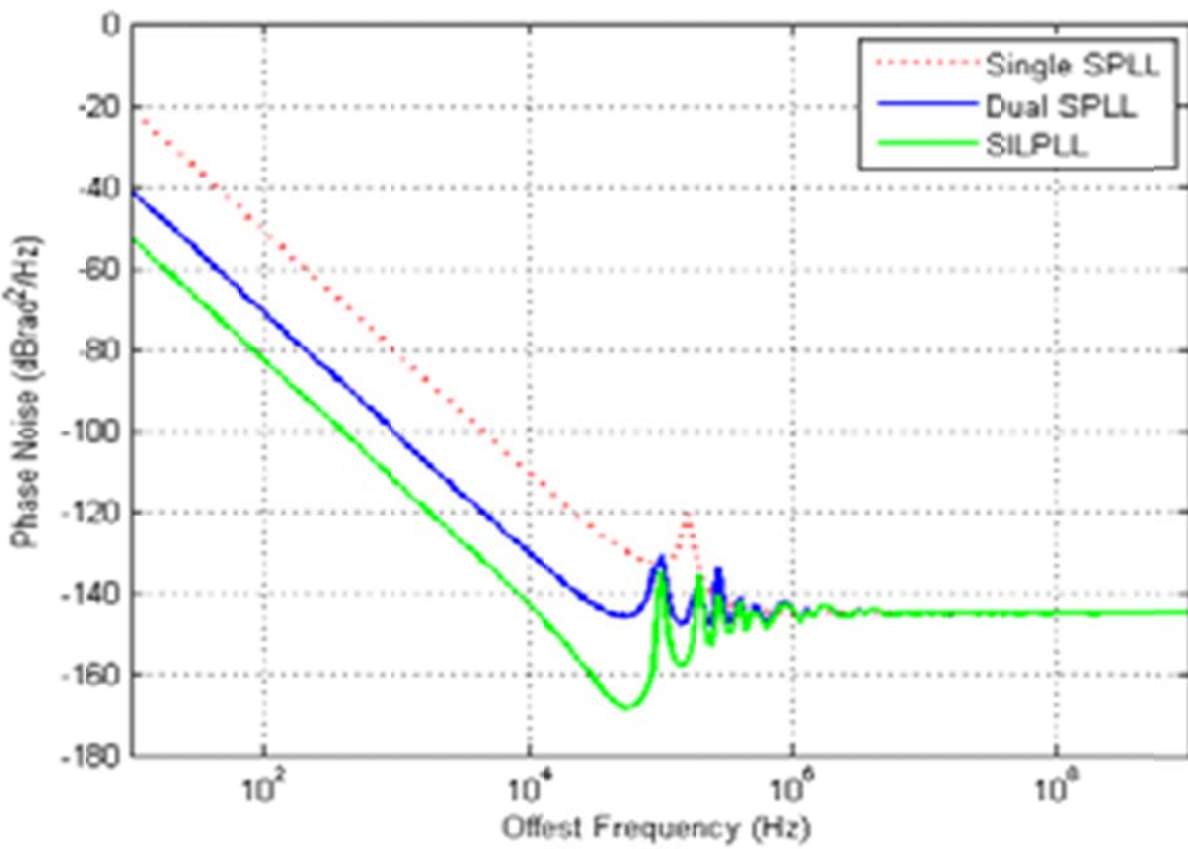


Figure 10-67: Comparison of predicted phase noise of 10 GHz OEO using SPPLL and SILPLL circuit

As shown in Figure 10-68, the phase detector (130) is electrically coupled to the optical source (102) and the modulator (104), significantly reduces the close-in to carrier phase noise using mode-locking of large number of supported modes. The mode-locking technique achieved by coupling the phase detector (130) to either or both the optical source (102) and the modulator (104) include any of mode suppression, mode injection, mode coupling, mode combining, multi-mode injection coupling, evanescent mode coupling [21]-[22]. Mode locking can be beneficial for locking each of the optical modes of the optical source (102) and/or modulator (104) output to a fixed phase and hence significantly reducing the close-in to carrier phase noise.

A typical mode-locking technique uses a delay element (e.g., an optical fiber or electronic cable) to store energy for a sufficient duration using evanescent-mode-coupling and dynamic mode spacing of the optical delay line to achieve a zero or minimum frequency drift. Since the optical fiber may be intrinsically temperature sensitive, causing change in effective length and refractive index over temperature, the oscillator needs a control circuit to regulate the effective fiber length to prevent mode-jumping phenomena and thereby degradation from close-in to carrier phase noise. The active degenerative feedback, in conjunction with the self-injection and mode-locking techniques, produces uniformly fixed mode spacing, thereby reducing frequency drift due to operating temperature changes [21].

Figure 10-69 shows the CAD simulated phase noise plot plotted from 1 kHz to 30 MHz offset from the carrier frequency of 10 GHz, it can be noticed that far offset phase noise plot shown in Figure 10-69 is cleaner as compared to phase noise plots depicted in Figure 10-67. The reported phase noise plot shown in Figure 10-69 is the best performance to date reported for the given figure of merit (FOM) and this class of oscillator topology [22]-[23].

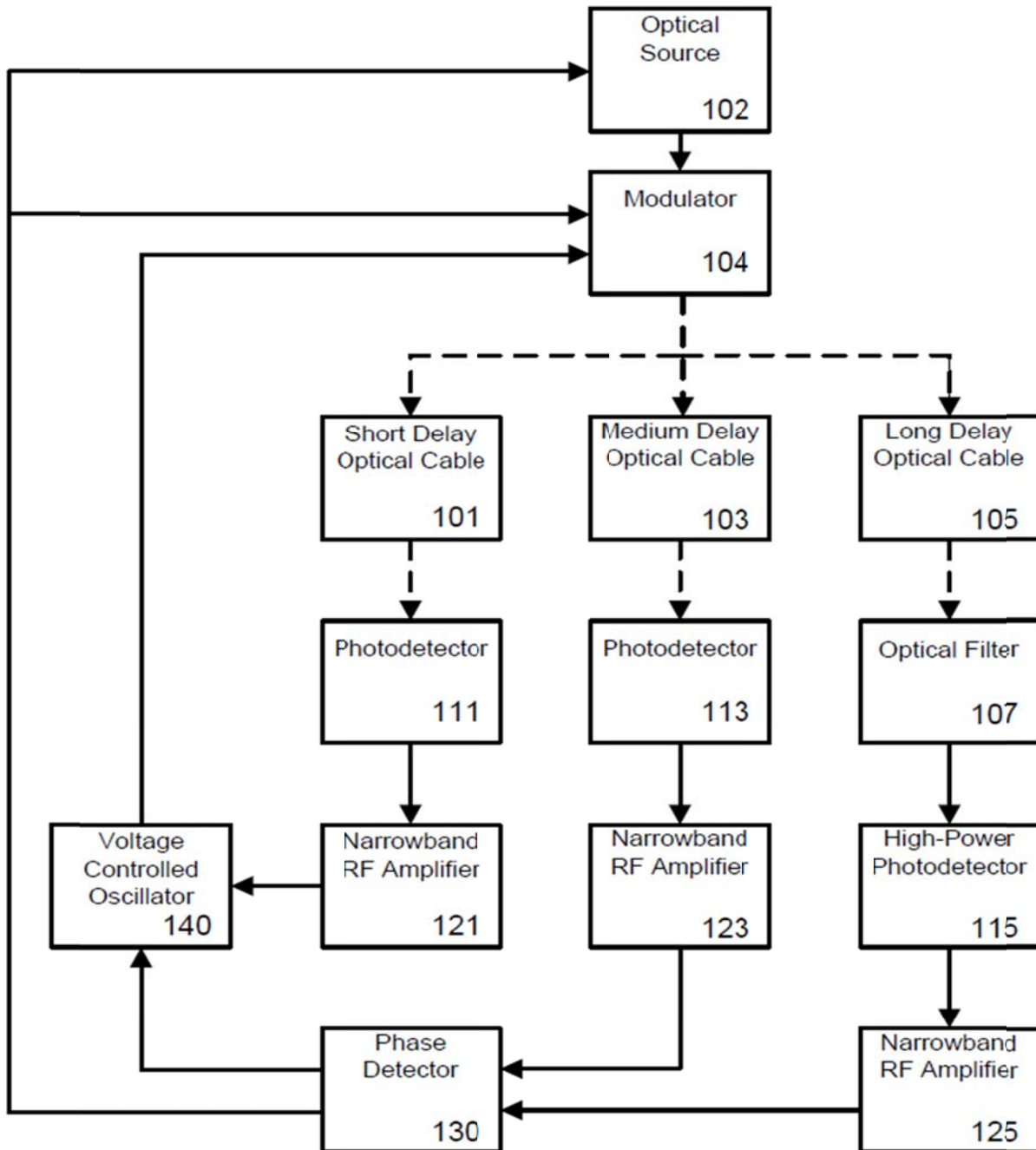


Figure 10-68: show the block diagram of mode-locked OEO circuit using self ILPLL module for stable low phase noise operation (US Patent application No.: 61/746, 919; filed on Dec 28, 2012 and US Patent application no. 13/760767; filed on Feb 06, 2013)

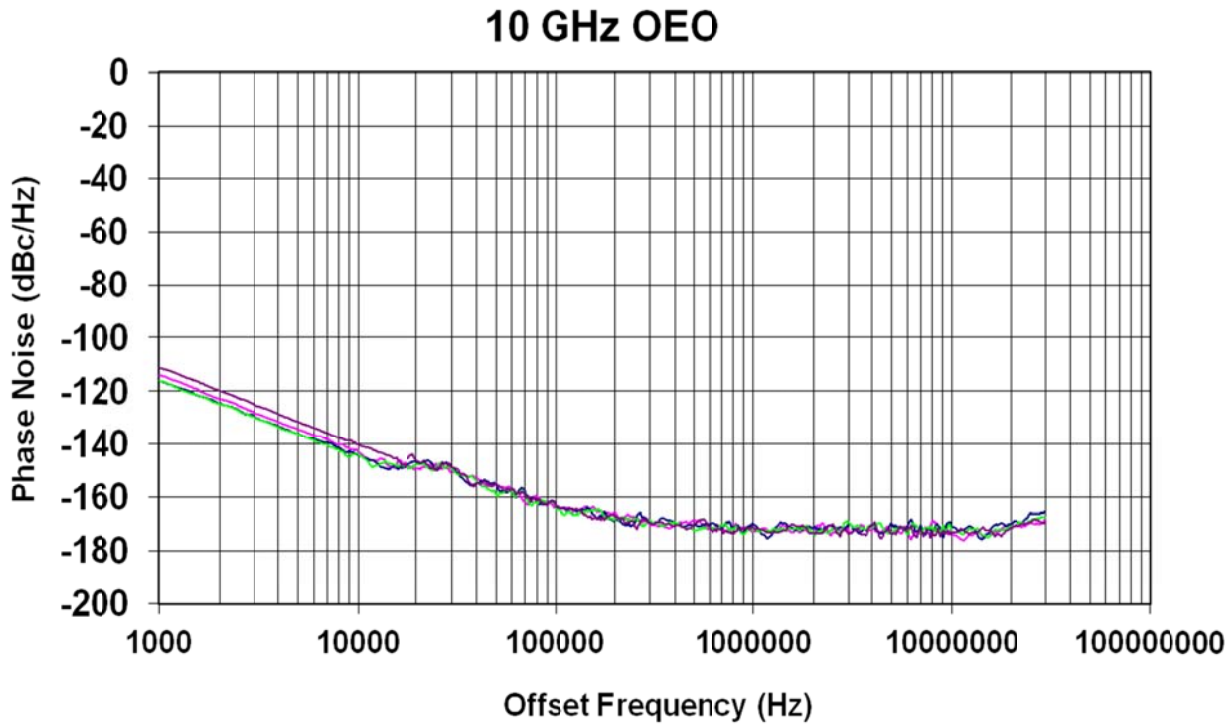


Figure 10-69: shows the CAD simulated phase noise plots of 10 GHz OEO circuit (Fig. 10-68)

10.6. Integrated OEO Solution

In this section, integrated OEO solution is discussed, to demonstrate a dramatic reduction in the size, weight, and power of the OEO, using a platform that monolithically integrates optics and RF electronics and is a successful proof-of-concept of Opto-electronic oscillator integration in silicon [22]. Conventionally, OEO circuit is assembled from discrete devices, thereby sensitive to vibration and shocks that limits its application in high reliability system applications. Moreover, optoelectronic photonic components require a large volume, high power consumption, and require a great deal of real estate and cost. The key to development of integrated photonic components using Silicon CMOS, BiCMOS technology, eliminates the need for bulky and/or discrete microwave components.

Figure 10-70 shows the block diagram of integrated OEO circuit using self ILPLL and Mode-Locking module for vibration and shock insensitive signal source for stable low phase noise operation. As shown in Figure 10-70, the long delay line (105) is coupled to an optical filter (107), such as a tunable nested loop optical filter using photonic bandgap (PBG) fibers. The tunable filter may include a polarization sensitive Hi-Bi fiber, or a multiple arm cascaded filter having two or more optical couplers using bi-conical designs for series power division/combining, or optical waveguides for parallel power division/combining. A typical fiber optic delay line exhibits a large dispersion coefficient to achieve active tuning of the RF oscillator when the optical source wavelength undergoes a shift, the dispersion parameters may be up to about 1000ps/km with an achieved tuning of about 20MHz/km for a 10nm tuning at about 1550nm. Thus, as the optical source wavelength undergoes a shift, the bandpass frequency of the tunable filter is subject to change and the oscillation condition of the oscillator

may be satisfied at a new frequency. The optical tunable nested loop filter is to control the new accepted modes in the RF spectrum. The frequency shift Δf follows the following relationship:

$$\frac{\Delta f}{f} = \frac{\tau_D}{\tau} \quad (10-25)$$

where f is the initial oscillation frequency, τ is the fiber delay time before tuning, and τ_D is the delay time after wavelength tuning in the dispersive fibers. As shown in Figure 10-70, the OEO circuit using self ILPLL module can be fabricated as an integrated device using Si photonics.

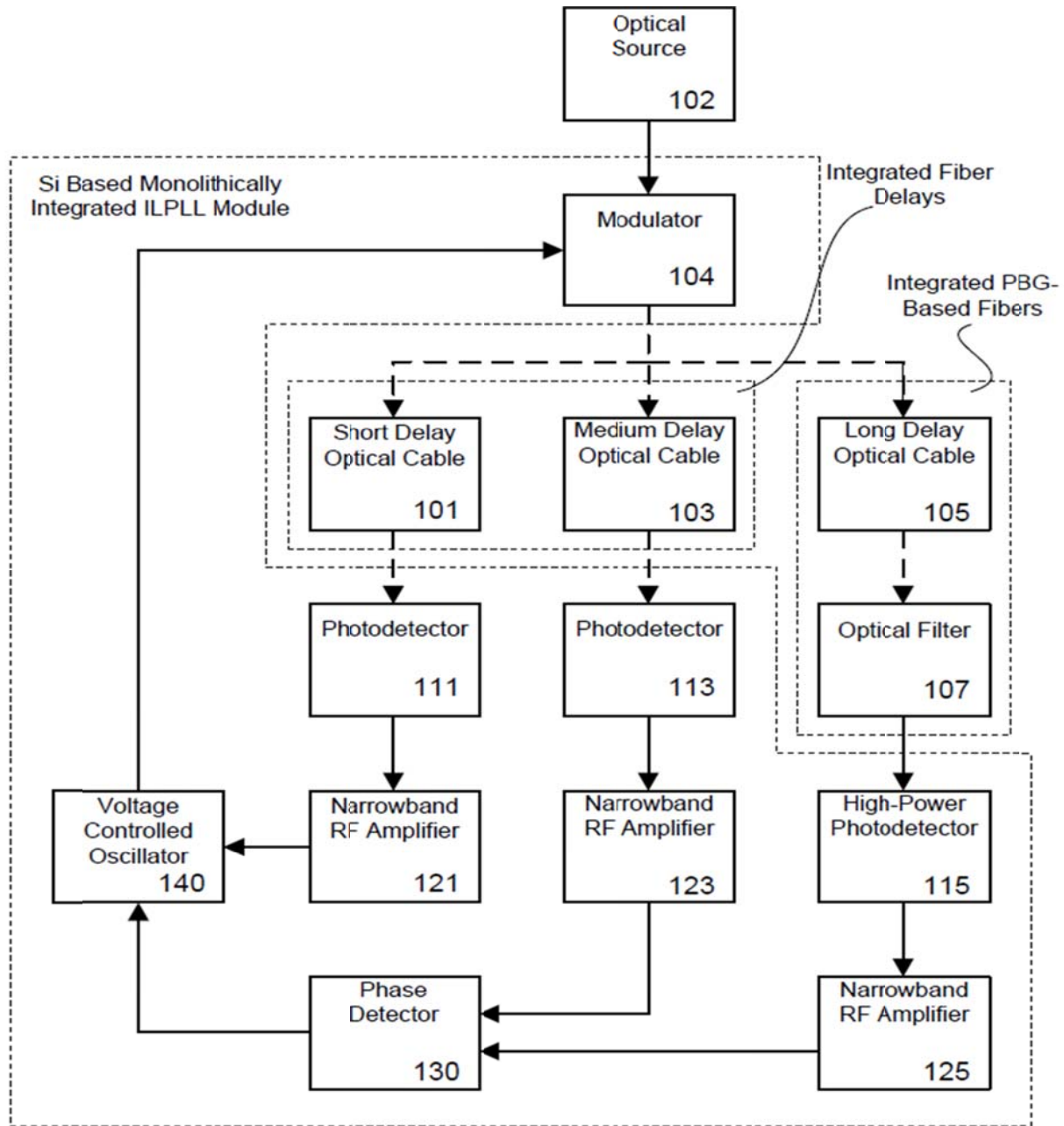


Figure 10-70: shows the block diagram of integrated OEO using self ILPLL module for low phase noise operation (US Patent application No.: 746,919; filed on Dec 28, 2012 and 760767; filed on Feb 06, 2013)

For instance, the fiber optic cables (101), (103) and (105) can be integrated in small form factor mandrels each with a diameter of about 1 inch or less. In some examples, the mandrels could be covered by resin emulsions for mechanical stability. The optical detectors (111), (113), and (115) may be monolithically integrated silicon photodiodes. The amplifiers (121), (123), and (125) may include SiGe HBT devices for degenerative feedback amplification. Like the Si based components described above, the VCO (140) may also be any Si CMOS based voltage controlled oscillator (e.g., a Clapp oscillator, Colpitts oscillator, etc.) The VCO (140) may include a varactor, such as a MOS varactor, Schottky diode, or a reverse biased PN junction diode varactor, or other semiconductor device, which functions as a voltage-controlled capacitor. The effective capacitance of the varactor may vary with changes in the voltage of the processed signal received from RF amplifiers (123) and (125). By adjusting or tuning the effective capacitance of the varactor in the VCO (140), the frequency at which the VCO (140) resonates can be tuned for optimum phase noise performance.

The most critical module for integrated OEO solution shown in Figure 10-70 is Mach Zehnder Modulator (104) and metamaterial resonator based VCO (140).

10.6.1 Mach Zehnder Modulator (MZM)

The MZM may be implemented using a combination of guest and host polymers with strong electro-optic (EO) properties ($r_{33}>500\text{pm/V}$ at wavelength of 1550nm and even stronger 1150pm/V at wavelengths of up to 1060nm). An EO polymer is based on a variety of stable polymers that are spun and poled on Si substrate to achieve desirable EO properties. The MZM may be implemented using nonlinear optical (NLO) chromophores doped polymer systems that exhibit ultrafast (e.g., Pico-second) speeds with large electro optic coefficients (100pm/V or greater) and low optical loss (1.5dB/cm or less). A guest-host system may be formed using a physical mixture of chromophores and an EO polymer host [22]. The EO polymer based MZM may be stabilized using control poling of an electric field between about $10\text{V}/\mu\text{m}$ to about $200\text{V}/\mu\text{m}$, preferably between about $75\text{V}/\mu\text{m}$ to about $150\text{V}/\mu\text{m}$. This may be combined with thermal and optically assisted poling processes at temperatures around 110 degree C. With electrical poling techniques performed at temperatures close to glass melt (i.e., around 110C), polarization dipoles under a nitrogen rich environment can remain polarized as the temperature is reduced. In some examples of disclosure, the control poling may involve lateral electrical poling. In other examples, it may involve transverse electrical poling.

10.6.1.1 Electro Optic Polymer (EO Polymer)

The efficient integration of EO polymer based MZM with Si based voltage controlled oscillator and their associated control circuits are an important aspect of low cost and efficient manufacturing. The use of EO polymers is preferable over the use of Lithium Niobate (LiNbO₃) in the modulator. However, the length of the modulators should be carefully selected in order to achieve a sufficient range of operation frequencies. The maximum operation frequency, f_{\max} , of the modulator is inversely related to its length L [22]:

$$f_{\max} = \frac{2c}{\pi |(n_{\text{eff}} - \sqrt{\epsilon_{\text{eff}}})|L} \quad (10-26)$$

where c is speed of light in free space, n_{eff} is the effective optical index of refraction of the EO material, and ϵ_{eff} is the effective RF permittivity of the EO material.

Because of large difference between the effective index of refraction at optical and RF frequencies for LiNbO₃, the maximum operating frequency of a modulator using such material is relatively limited. In contrast, NLO polymer systems have a relatively small difference between the effective index of refraction at optical and RF frequencies, and thus operate at a relatively greater maximum operating frequency. Furthermore, a pinch-off voltage V_π is required to be applied across one of the arms of the modulator in order to cause a 180 phase shift of the optical wave travelling through that arm (relative to the optical wave travelling through the other arm of the modulator), thereby effectively cutting the modulating signal through wave cancellation effects (i.e., destructive interference or destructive combination in the Mach-Zehnder interferometer). This voltage V_π can be expressed as:

$$V_\pi = \frac{\lambda d}{n^3 r L \Gamma} \quad (10.27)$$

where V_π is the wavelength of the optical wave, n is the index of refraction of the optical waveguide, r is EO coefficient, d is separation between the modulator electrodes, and Γ is the optical confinement factor.

As seen from (10.19), a modulator having a greater EO coefficient (r) requires a lower voltage drop (V_π) to be applied in order to achieve the 180-phase shift. Because EO polymers have an r value of about 735pm/V (as opposed to LiNbO₃ which have an r value of about 30pm/V), the EO polymer based MZM requires a lower V_π . As a result, the EO polymer based modulator of the present disclosure, having a length of about 1 cm (in order to achieve greater maximum operating frequency, as described above) may achieve a 180 degree phase shift at a V_π of as low as 0.5V, as compared to a V_π of 5V obtained in a similarly dimensioned LiNbO₃ MZM. Further performance advantages of an EO polymer MZM, as compared to LiNbO₃, are seen in simulations for modulators having a length of 1 cm. The design of an MZM is integrated with narrowband amplifiers to achieve a closed loop gain of unity. For an optical source power of 12dBm at 1550nm with relative intensity noise (RIN) value of -155dB/Hz, a 30dB amplifier is required for an LiNbO₃ based system, with a system noise floor level of -133 dBm/Hz. By contrast, for an EO polymer based system, a 9 dB amplifier gain is sufficient, with a system noise floor level of -152dBm/Hz. The modulator may be a poled polyimide having high EO coefficients from NLO chromophores, a high degree of chromophores dipole orientation, and a large r of 1250 pm/V at 1.3 μm. By modifying the electronic properties of the cross linking reagents, the temperature window is optimized to achieve hardened materials with optimal properties. The guest-host EO polymers may have a low stabilization temperature since the chromophores are not attached to the polymer matrix and are free to rotate. Guest-host EO polymers are particularly useful in the evaluation of new chromophores because these polymers are easy to prepare and easy to pole.

As discussed above, the modulator (104) is an optical Mach-Zhender modulator (MZM) having an MZM interferometer realized on Si-substrate using Si-Photonic technology, such a modulator is compatible with Si microelectronic steps and is suitable for metal-oxide field effect transistors (MOSFET), particularly for complementary MOSFET (C-MOS) [23]. Figure 10-71 depicts a graphical intensity plot of a Si-photonics based Mach-Zhender modulator that is implemented using Si compatible electro-optic (EO) polymer material [22]. As shown in Figure 10-71, a

transversely poled EO polymer based MZM is simulated in terms of transverse and longitudinal components of optical field in each leg. Intensity values for various positions of the MZM are depicted [23]. The waveguide of the MZM may be a microstrip transmission line which may be monolithically integrated with the oscillator. The operating point of the MZM may be in quadrature or off points to generate a dominant fundamental harmonic or a dominant 2nd harmonic. Figure 10-72 depicts the operation characteristics for the integrated MZM design shown in Figure 10-69, operating at 1550nm with an EO coefficient of typically 735pm/V. Figure 10-70 shows the CAD simulation results , the microstrip line has a simulated single mode quasi-TEM operation of up to about 60 GHz for a substrate with a thickness of about 2m [23].

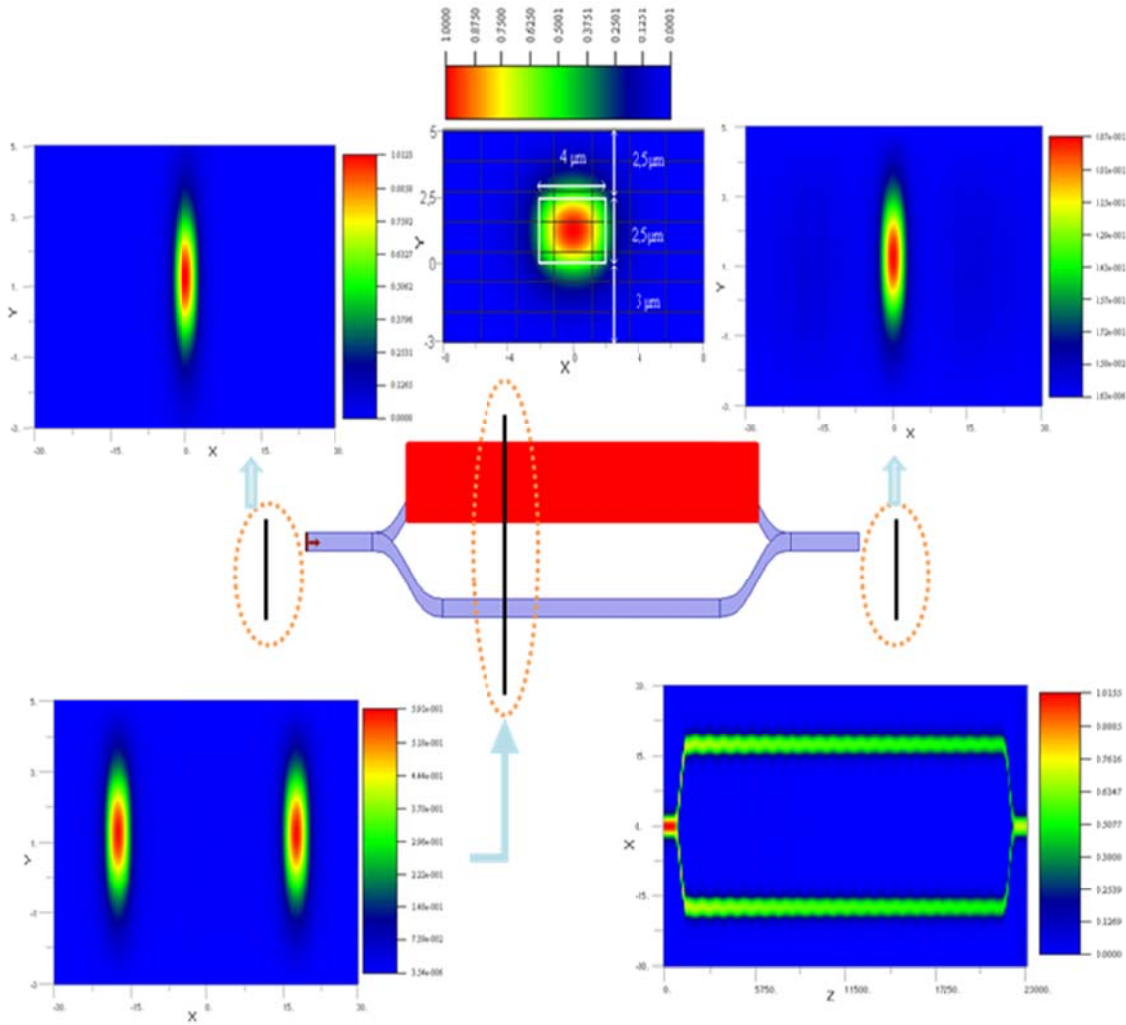


Figure 10-71: shows the performance simulation of an EO polymer based MZM and shows the plot of a Si-photonics based modulator

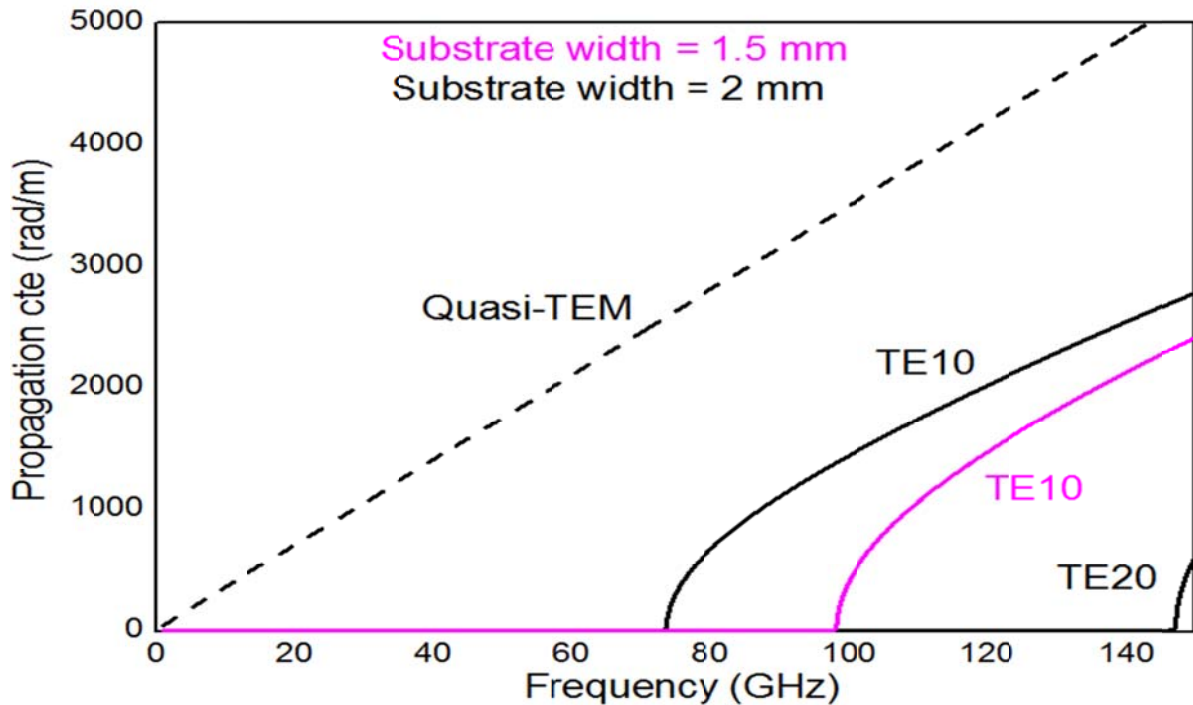


Figure 10-72: Simulated phase propagation constant and single mode operation of the microstrip line for substrate widths of 1.5mm and 2mm in MZM [22].

10.6.1.2 Integrated Tunable OEO Circuits

The tunable OEO circuit module (140) depicted in Figure 10-70 operates in accordance to patented techniques (U.S. Patent No. 7,088,189) [55] based on Push-Push topology [37]-[45]. The significant difference between the oscillator of that disclosure [55] and that of the reported technique (Figure 10-73) incorporates self-ILPLL in conjunction with metamaterial resonator (206) and various delay lines (121, 123, 125), therefore achieves a significantly greater close-in to carrier phase noise reduction [23].

As shown in Figure 10-11, the plot of Q-factor and optimum length of fiber optic delay line as a resonator for a 10 GHz oscillator using different fiber attenuations ranging from 0.05dB/km to 1dB/km [22, 23]. Based on the results [22, 23], it has been found that a fiber optic cable having an attenuation factor of about 0.2 dB/km achieves a maximum Q factor (i.e., energy storage to power dissipation ratio) when the fiber optic cable has a length of about 21.7 km. Accordingly, the optimum length of a fiber optic cable having an attenuation factor of about 0.2dB/km is about 21.7 km. In such an example, a fiber optic cable having a Q factor of about 1.2E6 is obtained. As per block diagram shown in Figure 10-70, utilization of the evanescent mode resonator is beneficial for VCO (140), as compared to the use of a multi coupled planar resonator. The Q-multiplier effect of the evanescent mode resonator with reference to multi coupled planar resonator (Ch-6, Figure 6-30). The evanescent mode metamaterial resonator (Ch-6, Figure 6-30) is capable of achieving a quality factor above 1000 at operating frequencies ranging from about 2 GHz to about 15 GHz. The unique properties of metamaterial resonator is negative permittivity and permeability, enables amplification of evanescent mode wave without degeneration, hence loaded Q-multiplier effect in autonomous circuit such as oscillators.

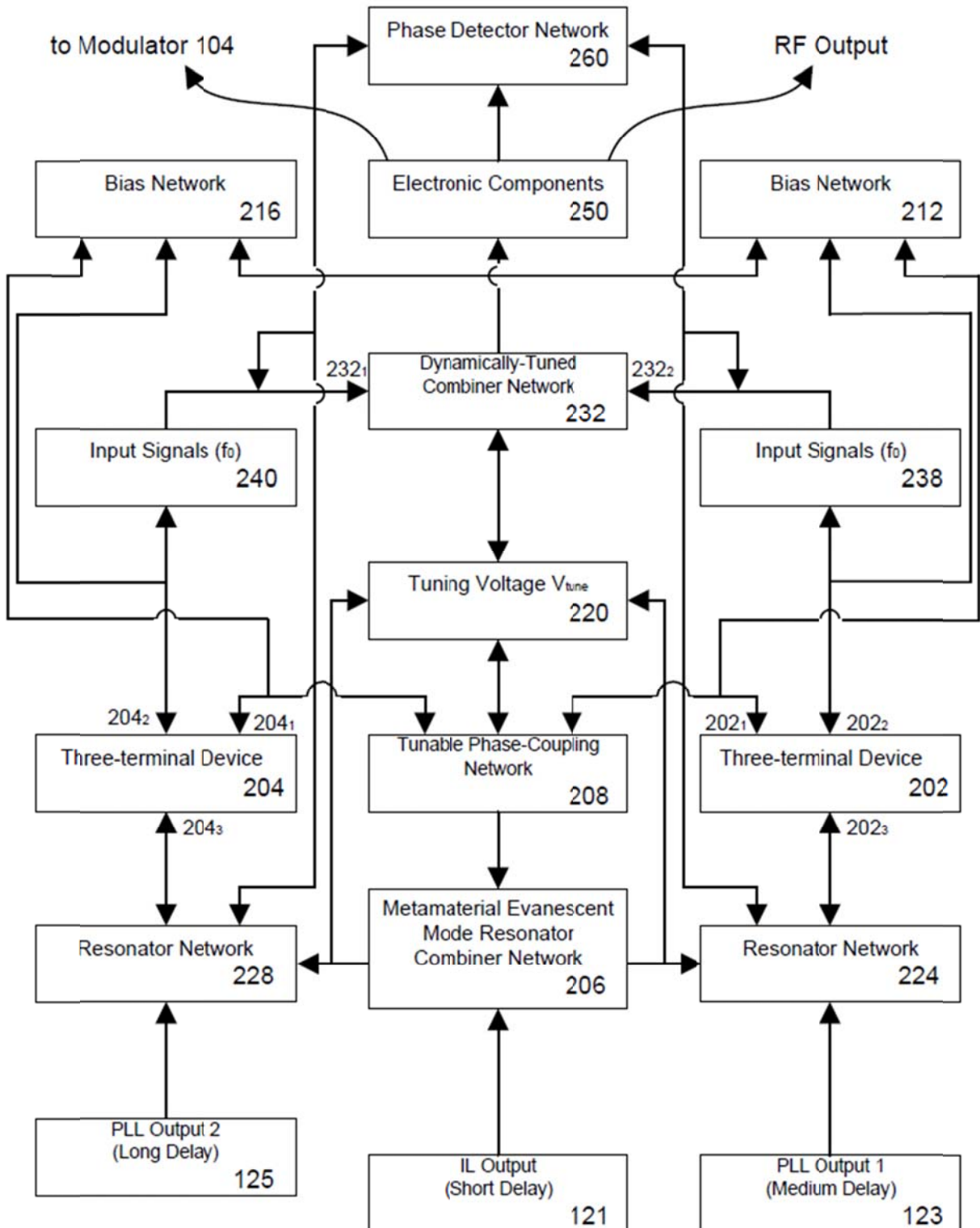


Figure 10-73: Shows the typical block diagram of 10 GHz source: Integrated realization of a highly stable self ILPLL RF Oscillator (US Patent application No.: 61/746, 919; filed on Dec 28, 2012 and US Patent application no. 13/760767; filed on Feb 06, 2013)

As illustrated in Figure 10-73, an evanescent mode resonator combiner network (206), such as a metamaterial resonator is realized using printed micro-stripline resonator in Push-Push oscillator configuration. The evanescent mode resonator combiner network (206) is coupled (capacitively) to each of the dynamically tuned resonator networks (224) and (228). The evanescent mode resonator combiner network (206) acts as an evanescent mode (EM) buffer, storing a portion of the excess radio frequency (RF) energy coupled into the resonator network for a given period of a signal cycle so that the conduction angle of the device can be reduced, thereby reducing the average noise performance for a given period of time. The evanescent mode resonator combiner network (206) is also coupled to the tuning voltage block (220). As such, the tuning circuit (220) can operate as a variable capacitor, thereby improving the loaded Q factor due to the evanescent phenomena of the resonator. The evanescent mode resonator combiner network (206) may be coupled to a tapered optical fiber with a few nanometers position resolution system. The microwave carrier is generated by locking the optical phase modulation to a free spectral range resonator, which occurs in this case in 10 GHz region. Moreover, this carrier is detected by a standard photodiode.

As shown in Figure 10-73, a phase detecting network or phase detector (260) is coupled between resonator networks (224, 228) and combiner network (232). The phase detector network (260) may be realized by using a divider, amplifier and balanced mixers arranged in a conventional manner. The divider may comprise MC10EL32, made by ON Semiconductor, Inc., and the amplifier and balanced mixers may, respectively, comprise OPAMP TL071 from Texas Instruments and mixers available from Synergy Microwave [22]. The phase detector network (260) dynamically compensates for phase errors between each oscillator during wideband operation. The phase detector network (260) detects random fluctuations in the free-running frequency and translates those fluctuations into phase errors. The phase errors are then fed back to the combiner network (232) and used to control the phase and frequency of the buffered signal (250) during tuning operation. The phase errors are also fed back to the dynamically tuned coupled resonator networks (224, 228) and used to tune the oscillating frequencies of the each of the three terminal devices.

The tunable phase coupling network (208) is also coupled to the evanescent mode resonator combiner network (206) to dynamically tune the phase of the resonating wave. A select portion of a signal from the combiner network (232) as well as a select portion of a signal from the evanescent mode combiner resonator network (206), are also fed back to the tuning block (220). A portion of the signal (254) is then fed to tunable phase coupling network (208) and used to dynamically tune the phase of the output signals (238, 240), so that each of these signals remain in phase during a tuning operation. A portion of the signal (254) is also fed to each of the dynamically-tuned coupled resonator networks (224, 228), so that the frequency, f_0 , present at block (238) is at the same frequency as the signal present at block (240). Accordingly, as the tuning voltage, V_{tune} , is adjusted the frequency of the signals, f_0 , present at each of the terminals (202₂ and 204₂) are tuned over the operating frequency band through the coupled resonator networks (224, 228), while the phase coupling network (208) keeps the two devices (202, 204) operating in an anti-phase mode at the fundamental frequency, f_0 (e.g., push-pull behavior), while the second harmonic, $2f_0$, interferes constructively (e.g., push-push

behavior) over the octave band. In addition, the phase detector network (260) operates as described above to dynamically compensate for phase errors during wideband operation.

Figure 10-74 shows the printed circuit board (PCB) realization, readily amenable for monolithic integration of the 10 GHz VCO module (depicted in Figure 10-70), realized as per block diagram shown in Figure 10-71 using CMOS fabrication technology. As shown in Figure 10-72, the design topology is amenable to Si fabrication techniques and can be fabricated by one having ordinary skill in the art with a small form factor as depicted.

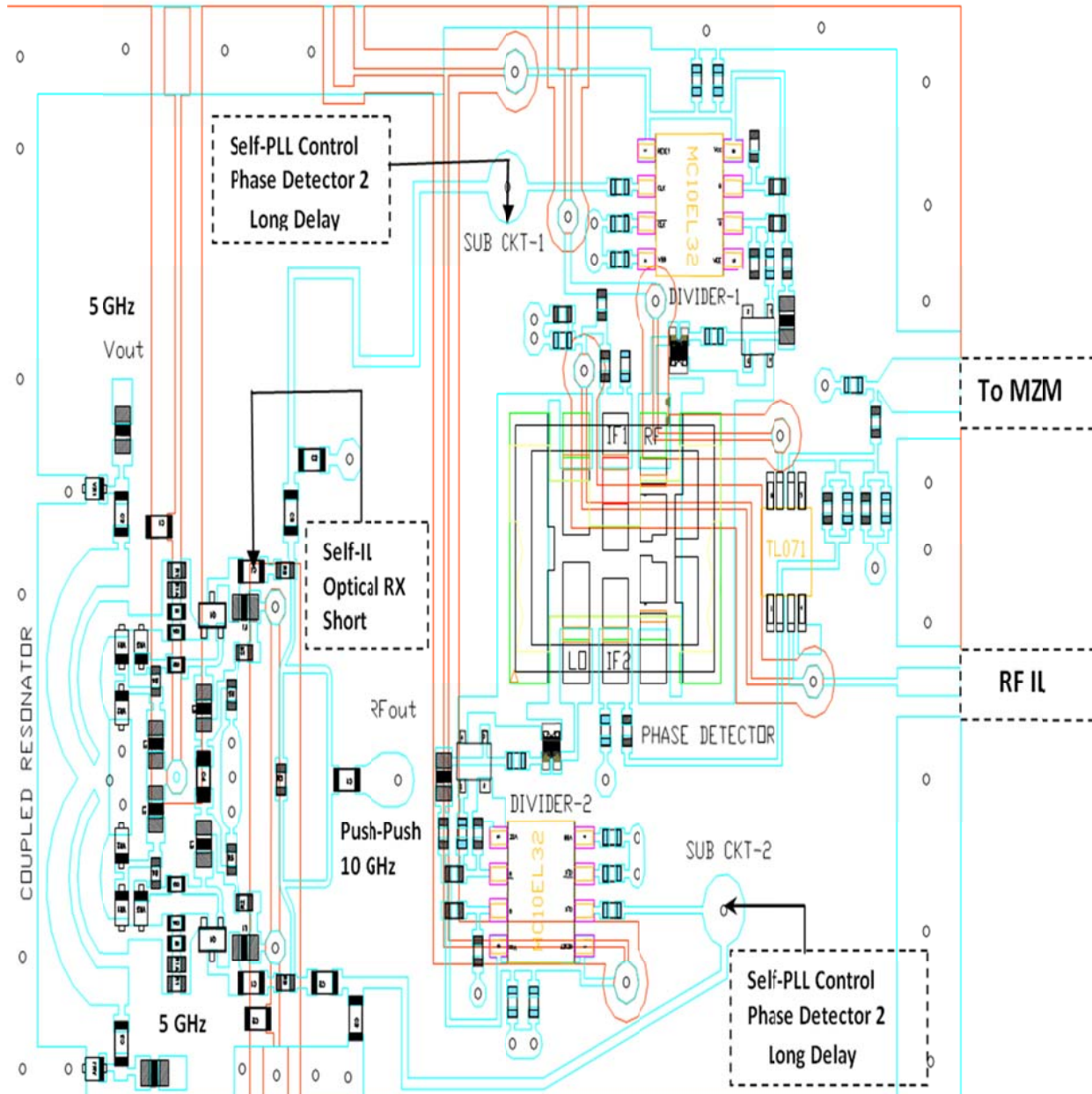


Figure 10-74: shows the layout of stable 10 GHz signal sources as per US patent applications No.: 61/746, 919; filed on Dec 28, 2012 and US Patent application no. 13/760767; filed on Feb 06, 2013.

10.7 Design Challenges, Pros & Cons: Monolithic OEO Circuits

Monolithic integration of the OEO circuit is challenging. For example, while utilization of a long fiber optic delay line can yield significant gains in Q factor, the long delay can also cause very small mode spacing [73]. In order for the multi-mode OEO system to function at a stable frequency, the OEO must be capable of suppressing side modes with a low side modes suppression ratio (SMSR). While use of additional electrical loops can improve SMSR, this can only make the mode spacing greater and the OEO will still be subject to frequency hopping, for example upon startup. While injection locking (e.g., an OEO coupled with a monolithic heterojunction phototransistor (HPT) oscillator, or an electrical oscillator) may mitigate these problems and yield a single mode output, such a design would result in a significant increase in cost.

Addressing the above concerns, a multi-mode injection-locking effect may be incorporated into the OEO system using a Fabry-Pérot laser diode (FP-LD) [22]. Using the laser diode, a single OEO mode may be locked while other mismatched modes are suppressed due to the gain competing and phase-synchronization effect. This ensures that the oscillation frequency and modulation frequency are synchronized in a single-mode operation, and further does not require the addition of any more high speed optoelectronic devices to the OEO system. The laser diode arrangement may lead to an SMSR of 75 dB or better [23].

Tunability of the OEO system as illustrated in Figure 10-70 is also a significant concern. Conventional OEOs generally have densely spaced oscillation modes due to the long length of fiber optic delay lines, and a fixed microwave bandpass filter (MBPF) having a relatively small frequency-tunable range (e.g., in the range of a few MHz) must be used to ensure single-frequency oscillation. The reported technique [22] allows for use of a tunable MBPF implemented in the optical domain which is incorporated in an OEO [23]. One possible technique of frequency tuning may be performed by changing the wavelength of the incident light wave or the longitudinal modes of the FP-LD. Changing the wavelength is possible by changing the operating temperature. However, temperature changes can often deteriorate the quality of a sustained microwave signal. Another possible frequency tuning technique may be performed using a two-port phase modulator (PM) and a linearly chirped fiber Bragg grating. The frequency tuning is realized by tuning the dispersion of the linearly chirped fiber Bragg grating. However, ensuring a large frequency-tunable range requires that the tunable range of the dispersion must be very large, which is hard to realize for practical applications.

A further concern is that the frequency of the generated microwave is usually low, being as that frequency is significantly limited by the bandwidth of the modulator and the central frequency of the MBPF. One could use two optical carriers at two different wavelengths instead of a single optical carrier. In such an arrangement, the MZM modulator may be biased at the quadrature point at one wavelength, to generate a fundamental oscillation, and at the minimum transmission point at the other wavelength, to generate a frequency-doubled operation. However, this arrangement is subject to poor stability due to drift. While a polarization modulator (PolM) may address the bias drifting issues, the frequency-doubling OEOs nonetheless require a fixed MPBF, which again leaves a relatively limited frequency-tunable range for the OEO system.

The above concerns may be addressed using a wideband tunable frequency-doubling OEO incorporating a photonic MBPF based on a PM and a phase shifted fiber Bragg grating (PS-FBG). The key benefits of such an OEO are that: (1) it is capable of generating a frequency-doubled microwave signal while using low-frequency components in the OEO loop, and that (2) it can realize wideband frequency tuning by simply tuning the wavelength of the incident light wave. In addition, no bias control is needed. This simplifies implementation and improves the operation stability. The PM and PS-FBG could be potentially integrated in a photonic integrated circuit chip, which would significantly improve its overall performance.

In an OEO system having a frequency shifter (FS), the oscillating frequency may be tuned by changing the optical pump wavelength. Compared to tunability of an OEO with an MZM, this arrangement may be capable of greater RF power output for a given amplifier gain and laser output. The optical storage element of the OEO system is generally an optical fiber delay line. However, use of this storage element raises certain difficulties in operating the OEO system. For starters, the delay line can be relatively bulky and can make transportability of the OEO difficult. Further, the delay line would need to be temperature-stabilized, which would require a significant amount of energy. Last, the delay line is capable of generating spurious peaks very close to the carrier (few tens of kHz), which can be detrimental in several applications.

In the light of these difficulties, in some examples, the optical fiber delay line may be replaced by an ultra-high Q whispering gallery-mode (WGM) optical resonator. The WGM optical resonator stores energy by trapping laser light, while also defining the oscillation frequency (which is defined by the free spectral range of the resonator). OEOs using WGM technology are generally compact, do not generate delay-induced spurious peaks in the RF spectrum, and are compatible with compact temperature control systems. Thus, use of WGM technology can yield a portable OEO that is capable of producing an ultra-pure microwave signal. This is a highly desirable feature in many applications, such as in aerospace engineering for example. This feature also permits for phase modulation, instead of intensity modulation, of the sustained signal. While intensity modulators are environment sensitive devices (which is not desired when high device stability is required, e.g., for pure tone generation), phase modulation involves a differential phase-to-intensity conversion, which is less sensitive to electro-optic drifts (e.g., slow charge re-distribution). Since the resonator is effectively an imbalanced interferometer, it is clearly useful for differential phase-to-intensity conversion. Like standard differential optical phase modulation techniques, the WGM optical resonator offers superior performances at very high modulation speeds (e.g., >10 Gb/s). Also, configuration of an ultra-high Q WGM optical resonator is compatible with chip integration, and therefore makes for a feasible and transportable source for ultra-pure microwave generation.

As discussed above, the reported OEO system in Figure 10-65 can generate a very high frequency signal (from 5 GHz to 100 GHz). Generally, in order to generate such a high frequency signal, an OEO requires high frequency components (e.g., a 100 GHz photo-detector, a 100GHz intensity modulator, a 100GHz RF amplifier, etc.) which are generally expensive and difficult to implement. The OEO of the present disclosure is in fact capable of producing a high frequency signal using relatively low frequency optical and microwave devices. This aspect of the design can be modeled by a dual loop OEO operating at a low frequency using a directly modulated distributed feedback laser (DFB). By injecting a continuous lightwave into the

directly modulated DFB laser, and properly adjusting the injection power as well as the polarization, the laser diodes are injection locked, thereby generating higher harmonics. The harmonic order can be controlled by varying the frequency difference between the free running DFB laser and the continuous lightwave. Simulated data predicts that a 100 GHz microwave may be produced from an OEO having optical and electrical devices that operate at the frequency no more than 10 GHz [22]-[23].

The advantage of the tunable OEO system illustrated in Figure 10-74 is its superior phase noise performance. The phase noise performance of a tunable OEO is directly related to the fiber length, i.e., increasing the fiber length results in decreasing the phase noise of the OEO. However, an OEO generates multiple resonance frequencies with a mode spacing that is inversely proportional to the fiber length. Thus, increasing the fiber length also results in unwanted modes. Including an extremely narrow pass-band RF filter in the feedback loop of the OEO system can suppress the unwanted modes. Furthermore, the frequency selectivity of the RF filter may be relaxed by use of multi-loop configurations (e.g., additional optical loops, additional electrical loops). However, frequency tuning over a spectral range that is wider than the mode spacing of the longest feedback loop is hard to perform because any change of the frequency is directly related to a change of the loop length. An electrical phase shifter in conjunction with a standard high-pass filter in a dual-loop configuration may be used to make a tunable OEO with an ultra-wide tuning range that overcomes these difficulties.

In summary, the above described OEO system provides for a dramatic reduction in the size, weight, and power of a conventional OEO, using a platform that monolithically integrates optics and RF electronics in silicon (CMOS/BiCMOS/HBTs). Moreover, the disclosed OEO system provides a significant decrease in the RF power consumption of the integrated versus the discrete version of the OEO. While an OEO made of discrete components can include RF amplifiers that use as much as 10-20W, the entire integrated RF chain of the disclosed OEO may use less than 200 mW. Even further, the integrated components are capable of operating from a less than 2V power supply (e.g., a Si device) and do not need matching input and output drivers that discrete components generally require. Additionally, the modulator driver may typically use <1000 mW.

10.8 Conclusion

This research work details integrated optoelectronic oscillators with frequency and phase stability over operating temperature (-40⁰C to +85⁰C), provides an integrated optoelectronic filtering system having higher frequency selectivity in a relatively small size (compared to the larger size of a higher order electrically realized RF filter), reduced temperature sensitivity, and minimized frequency drift.

The reported EMSIPL (evanescent mode self-injection phase-locked) OEO configuration shown in Figure 10-74 is amenable for MMIC in silicon, enabling compact, low noise and low cost solution in which it is possible to synthesize any precise RF frequency by adjusting the optical source wavelength, leading to satisfying stable oscillation conditions for a new RF frequency in highly dispersive photonic bandgap fibers [21].

10.9 Reference

- [1] Yao X. S., Maleki L., "Optoelectronic microwave oscillator," *J. Opt. Soc. Am. B* 13, 1725–1735, 1996
- [2] Howe, D.A., Hati, A., "Low-noise x-band oscillator and amplifier technologies: comparison and status", Frequency Control Symposium and Exposition, 2005. Proceedings of the 2005 IEEE International, Pages: 481 – 487, 2005
- [3] Ilchenko, V.S., "Optical microsphere resonators and laser frequency stabilization" Lasers and Electro-Optics Society Annual Meeting", LEOS '97 10th Annual Meeting, IEEE Conference Proc., Vol. 2, pp 94 – 95, Nov 1997
- [4] Capmany, J., Pastor, D., Ortega, B., Mora, J., Pierro, L., Varasi, M. "Theoretical Model and Experimental Verification of 2×1 Mach-Zehnder EOM With Dispersive Optical Fiber Link Propagation", Quantum Electronics, IEEE J., Vol. 44, Issue 2Page(s):165 – 174, Feb. 2008
- [5] Heismann, F., Ulrich, R "Integrated-optical single-sideband modulator and phase shifter," Quantum Electronics, IEEE Journal of, Volume 18, Issue 4pp 767 – 771, 1982
- [6] Desormiere, B., Maerfeld, C.; Desbois, J., "An integrated optic frequency translator for microwave lightwave systems," LWT, J. of Vol. 8, Issue 4pp. 506 – 513, 1990
- [7] Yang J., Jin-Long Y., Yao-Tian W., Li-Tai Z., En-Ze Y. "An Optical Domain Combined Dual-Loop Optoelectronic Oscillator", Photonics Technology Letters, IEEE Volume 19, Issue 11, , pp 807 – 809, 2007
- [8] X. S. Yao, and L. Maleki, "Optoelectronic Oscillator for Photonic Systems," *IEEE J. of Quant. Elec*, vol. 32, pp. 1141-1149, July, 1996.
- [9] X. S. Yao, L. Davis, and L. Maleki, "Coupled Optoelectronic Oscillators for Generating both RF Signal and Optical Pulses", *IEEE J. of Lightwave Tech.*, vol. 18, pp. 73-78, Jan., 2000.
- [10] B. Analui, D. Guckenberger, D. Kucharski and A. Narasimha, "A Fully Integrated 20-Gb/s Optoelectronic Transceiver Implemented in a Standard 0.13 μ m CMOS SOI Technology," *IEEE J. Solid-State Circuits*, vol. 12, pp. 2945-2955, Dec., 2006.
- [11] D. L. C. Leung, and H. C. Luong, "A Fourth-Order CMOS Bandpass Amplifier with High Linearity and High Image Rejection for GSM Receivers," *Proc. ISCAS*, vol. 2, pp. 589-592, May, 1999.
- [12] W. M. C. Sansen, and R. G. Meyer, "Distortion in Bipolar Transistor Variable-Gain Amplifiers," *IEEE J. Solid-State Circuits*, vol. 8, pp. 275-282, Aug., 1973.
- [13] H. C. Chang, "Phase noise in self-injection locked oscillators – Theory and Experiment," *IEEE Trans. Microw. Theory Tech.*, vol. 51, no. 9, pp. 1994 – 1999, Sep. 2003
- [14] Lee et al., "A 30GHz self injection locked oscillator having a long Optical delay line for phase noise reduction," *Photonics Tech. Letters*, vol. 19, no. 24, Dec. 2007
- [15] Lee et al, "Low-Cost Optoelectronic Self-Injection-Locked Oscillators, Photonics Technology Letters", Vol. 20, No. 13, 2008
- [16] Zhou et al, "An analytical model of the dual-injection-locked Opto-electronic oscillator(DIL-OEO)", Frequency Control Symposium, 2009
- [17] O. Okusaga, W. Zhou, G. Carter, and C. Menyuk, "Investigating the Forward and Backward Injections of Injection-Locked Dual Optoelectronic Oscillators", OFC 2009
- [18] Ronald T. Logan, "Stabilization of oscillator phase using a fiber-optic delay-line", IEEE Frequency Control Symposium 1991.

- [19] Huignard et al, "Self-Stabilization of the Beat note of a 1.5um Dual-Frequency Laser. Applications to optoelectronic microwave oscillators", MWP 2008
- [20] Huignard et al, "Dual-Frequency Laser at 1.5um for Optical Distribution and Generation of High-Purity Microwave Signals, J. of Lightwave Technology", Vol. 26, No. 15, 2008
- [21] Daryoush et al, "Optically Controlled Oscillators for Millimeter-Wave Phased-Array Antennas", MTT VOL. 41, No. 6/7, 1993
- [22] A. K. Poddar, U. L. Rohde, A. S. Daryoush, "Integrated production of self injection locked self phase loop locked Opto-electronic Oscillators", US Patent application no. 13/760767 (filed on Feb 06, 2013).
- [23] A. K. Poddar, U. L. Rohde, A. S. Daryoush, "Self Injection Locked Phase Locked Looped Optoelectronic Oscillator", US Patent application No. 61/746, 919 (filed on Dec 28, 2012).
- [24] D. Surzbecher et al., "Optically controlled oscillators for millimeter-wave phased-array antennas," *IEEE Trans. MTT*, vol. 41, no. 6/7, Jun/Jul 1993
- [25] Moyer, Harris P., and Afshin S. Daryoush. "A unified analytical model and experimental validations of injection-locking processes." *Microwave Theory and Techniques, IEEE Transactions on* 48.4: 493-499, (2000).
- [26] C. McNeilage et al., "Review of feedback and feedforward noise reduction techniques," *Proc. IEEE Frequency Control Symp.*, Pasadena, CA, pp. 146 – 155, May 1998.
- [27] A. Suarez et al., "Analysis of Stabilization Circuits for Phase-Noise Reduction in Microwave Oscillators," *IEEE Trans. Microw. Theory Tech.*, vol. 53, No. 9, Sep. 2005
- [28] H. C. Chang, "Phase noise in self-injection locked oscillators – Theory and Experiment," *IEEE Trans. Microw. Theory Tech.*, vol. 51, no. 9, pp. 1994 – 1999, Sep. 2003
- [29] Pillet et al, "Dual-frequency laser at 1.5 μ m for optical distribution and generation of high-purity microwave signals," *J. of Lightwave Technology*, vol. 26, no. 15, Aug. 2008
- [30] X.S. Zhou, X. Zhang, A.S. Daryoush, "A new approach for a phase controlled self-oscillating mixer," *IEEE Trans. on MTT*, vol. 45, no. 2, pp. 196-204, Feb. 1997.
- [31] D. Surzbecher et al., "Optically controlled oscillators for millimeter-wave phased-array antennas," *IEEE Trans. Microw. Theory Tech.*, vol. 41, no. 6/7, Jun/Jul 1993
- [32] R. A. York et al, "Analysis of oscillators with external feedback loop for improved locking range and noise reduction," *IEEE Trans. Microw. Theory Tech.*, vol. 47, no. 8, Aug. 1999
- [33] X. Zhang et al., "A theoretical and experimental study of the noise behavior of subharmonically injection locked local oscillators," *IEEE Trans. MTT.*, vol. 40, May 1992.
- [34] R. E. Best, "Phase-locked loops: design, simulation, and applications", 4th ed, McGraw-Hill, New York, pp. 25-26, 1999.
- [35] Yao et al, "A Light-Induced Microwave Oscillator", TDA Progress Report, 1995
- [36] To-Po Wang, "A fully integrated w-band push-push CMOS VCO with phase noise and wide tuning range", 2011 *IEEE Trans. on UFFC*, vol. 58, Issue: 7, pp. 1307-1319, 2011
- [37] Larger et al, "Compact optoelectronic microwave oscillators using ultra-high Q whispering gallery mode disk-resonators and phase modulation", *Optics Express*, Vol. 18, No. 21, 2010
- [38] M. Stuenkel, M. Feng, "A W-Band Tunable Push-Push oscillator with 128X division for frequency synthesis applications", 2013 *IEEE MTT-S Digest*, pp, 1-3, 2012
- [39] U. L. Rohde, A. K. Poddar, and George Bock, "*The Design of Modern Microwave Oscillators for Wireless Applications*", John Wiley & Sons, Inc., Hoboken, New Jersey, 2005.

- [40] Nakamura T. Masuda, K. Washio, H. Kondoh, "A push-push VCO with 13.9 GHz wide tuning range using loop-ground transmission line for full band 60-GHz transreceive", 2102 IEEE Journal of SSC, Vol. 47, issue:6, pp. 1267-1277, 2012
- [41] S. Yaoming, C. J. Scheytt, "A low phase noise 61 GHz push-push VCO with divider chain buffer in SiGe BiCMOS for 122 GHz ISM applications", IEEE RFIC symp. pp. 79-82, 2012
- [42] S-Wein Chu, C-Kuang Wang, "An 80 GHz wide Tuning Range Push-Push VCO with gm-boosted full-wave rectification technique in 90 nm CMOS", IEEE Microwave and Wireless Components Letters, vol. 22, Issue 4, pp. 203-205, 2012
- [43] T. Tanaka, K. Takata, M. Aikawa, I. Toyoda, "A Ku band Oscillator array using positive feedback type push-push oscillators", IEEE APMC conf. proceedings, pp. 112-114, 2012
- [44] York et. al, "Coupled-Oscillator Arrays for Millimeter-Wave Power-combining, IEEE MTT-S Digest, 1992
- [45] P. Delfyett et al, "Low Noise Optically Tunable Opto-Electronic Oscillator With Fabry–Perot Etalon", J. of Lightwave Technology, Vol. 28, No. 21, 2010
- [46] Li et al, "Tunable Optoelectronic Oscillator Incorporating a High-Q Spectrum-Sliced Photonic Microwave Transversal Filter", Photonics Technology Lett., Vol. 24, No. 14, 2012
- [47] Hansen et al, "Solid-Core Photonic Band gap Fiber with Large Anomalous Dispersion", OFC 2003
- [48] Saitor et al, "Hollow-Core Photonic Band gap Fibers with Broadband Negative Dispersion Slope", CLEO 2009
- [49] Fuochi et al, "Study of Raman Amplification Properties in Triangular Photonic Crystal Fibers", Journal of Lightwave Technology, Vol. 21, No. 10, 2003
- [50] Donald G. Meyer, US Patent 4,336,505, Jun 22, 1982
- [51] A. Daryoush et al, "*Passively temperature stable opto-electronic oscillators employing photonic crystal fibers*", Proc. of the European Microwave Association Vol. 3, Sept. 2007
- [52] U. L. Rohde, A. K. Poddar, "Wideband voltage controlled oscillators employing evanescent mode coupled resonators", US Patent No 7,180, 381 Feb 20, 2007
- [53] U. L. Rohde, A. K. Poddar, "Integrated Low Noise Microwave Wideband Push- Push VCO", US Patent No. 7,088189, Aug 2006.
- [54] U. L. Rohde, A. K. Poddar, "User-Definable Thermal Drift Voltage Controlled Oscillator", US Patent No.7, 265,642 B2, Sept 4, 2007.
- [55] U. L. Rohde, A. K. Poddar, "Low Thermal Drift Tunable Frequency Voltage Controlled Oscillatory", US Patent No.7, 262,670 B2, Aug 28, 2007.
- [56] U. L. Rohde, A. K. Poddar, "Multi-Octave Band Tunable Coupled Resonator Oscillator", US Patent No.7, 292,113, Nov. 6, 2007.
- [57] U. L. Rohde, A. K. Poddar, "Low Noise, Hybrid Tuned Wideband Voltage Controlled Oscillator", US Patent No. 7,365,612 B2, April 29, 2008.
- [58] U. L. Rohde, A. K. Poddar, Tunable Frequency. Low Phase Noise and Low Thermal Drift Oscillator, U.S Patent NO. 7, 545, 229, June 09, 2009.
- [59] U. L. Rohde, A. K. Poddar, "User-Definable, Low Cost, Low Phase Hit and Spectral Pure Tunable Oscillator, U.S. Patent No. 7,586,381 on September 08, 2009.
- [60] U. L. Rohde, A. K. Poddar, "User-Definable, Low Cost, Low noise, and phase hit insensitive multi-octave-band tunable oscillator", Phase Hit and Spectral Pure Tunable Oscillator, U.S. Patent No. 7,605,670, October 20, 2009.

- [61] U. L. Rohde, A. K. Poddar, "Low Noise and Low Phase Hits Tunable Oscillator", U.S. Patent No. 7,636, 021, Dec. 22, 2009
- [62] U. L. Rohde, A. K. Poddar, "Wideband voltage controlled oscillators employing evanescent mode coupled resonators", Canadian Patent No. 2,563, 174, July 21, 2009.
- [63] U. L. Rohde, A. K. Poddar, "User-Definable Thermal Drift Voltage Controlled Oscillator", Canadian Patent No. 2,548, 317, April 21, 2009.
- [64] U. L. Rohde, A. K. Poddar, "Integrated Low Noise Microwave Wideband Push- Push VCO" Canadian Patent No. 2,548, 311, April 14, 2009.
- [65] Pearson et al, "Frequency Stabilization of Power-Combining Grid Oscillator Arrays", MTT, Vol. 50, No. 5, 2002
- [66] Yao et al, "Multi-loop Optoelectronic Oscillator", IEEE J. of Quantum Electronics, Vol. 36, No. 1, 2000
- [67] M. Rohde, A. K. Poddar, "Visually Inspectable Surface Mount Device Pad", U.S. Patent No. 7612296, Nov 03, 2009,
- [68] York et al, "Mode-Locked Oscillator Arrays", IEEE MGWL, vol. 1 No. 8, 1991.
- [69] Maleki et al, "Dual microwave and optical oscillator", Optics Letters, vol. 22, No. 24, 1997
- [70] S. P. Voinigescu, A. Tomkins, E. Dacquay, E. Chevalier, J. Hasch, A. Chantre, B. Sautreuil, "A study of SiGe HBT Signal Sources in 220-330-GHz Range", IEEE JSSC, pp. 1-11, 2013
- [71] Maleki et al, "An Ultra low phase noise coupled optoelectronic oscillator", Photonics Letters, vol. 19, No. 6, 2007
- [72] S. Yao, "Multi-Loop Opto-Electronic Microwave Oscillator with a wide tuning range", US Patent No. 5, 777, 778, Jan 2000
- [73] Yao et.al, "Integrated opt-electronic oscillators having optical resonators", US patent No. 6,873,631 B2, March 2003
- [74] Li Zhang, A. K. Poddar, U. L. Rohde, and A. S. Daryoush, "Analytical and Experimental Evaluation of SSB Phase Noise Reduction in Self-Injection Locked Oscillators Using Optical Delay Loops", IEEE Photonics Journal, Vol. 5, No. 6, pp. 1-18, DOI: 10.1109/JPHOT.2013.2289958 1943-0655_2013 IEEE, Dec 2013.
- [75] Li Zhang, A. K. Poddar, U. L. Rohde, and A. S. Daryoush, "Oscillator Phase Noise Reduction Using Self-Injection Locked and Phase Locked Loop (SILPLL)", IEEE IFCS 2014
- [76] Li Zhang, A. K. Poddar, U. L. Rohde, and A. S. Daryoush, "Phase Noise Reduction and Spurious Suppression in Oscillators Utilizing Self-Injection Loops", IEEE RWS Jan 2014
- [77] M. Kaba et al, *Improving Thermal Stability of Opto-Electronic Oscillators*, *Microwave Magazine, IEEE Aug. 2006*
- [78] Li Zhang, Ajay K. Poddar, Ulrich L. Rohde, and Afshin Daryoush, "Evanescent-Mode Self-Injection Phase-Locked (EMSIPL) OEO", IEEE IMARC 2013, New Delhi, Dec 13-16, 2013
- [79] L. Zhang, V. Madhavan, R. P. Patel, A. K. Poddar, U. L. Rohde, and A. S. Daryoush, "Ultra Low FM Noise in Passively Temperature Compensated Microwave Opto-electronic Oscillators" IEEE IMARC 2013, New Delhi, Dec 13-16, 2013.
- [80] Eliyahu et al., "Phase noise of a high performance OEO and an ultra low noise floor cross-correlation microwave photonic homodyne system," *Proc. IEEE IFCS*, pp. 19-21, May 2008
- [81] Li Zhang, A. K. Poddar, U. L. Rohde, and A. S. Daryoush, "Optical Feedback Techniques for Phase Noise Reduction in Dielectric Resonator Oscillator", IEEE Photonics Journal, 2014

Chapter 11

Conclusion

11.1 Summary of work

Modern communication systems require two kinds of signal sources: (i) ultra low phase noise fixed frequency reference signal sources, and (ii) low phase noise tunable frequency signal sources. But the common denominator for both sources is identical, which is low cost, low power consumption, and compact size. Intrinsically, high Q-factor resonators (Crystal, SAW-Surface Acoustic Wave, BAW-Bulk Acoustic Wave, Ceramic, Dielectric, MEMS, and Optical Fiber) based oscillator circuit exhibits ultra low phase noise characteristics for fixed frequency or narrow band (< 1%) signal source solutions but at the cost of high power-consumption, vibration sensitive, and significantly expensive. On the other hand, broadband tunable signal sources are realized by using either YIG resonator based or else printed transmission line resonator based tunable oscillator circuits. YIG ($\text{Y}_3\text{Fe}_5\text{O}_{11}$) oscillators are known for low noise broadband signal source but at the cost of size, power and integrability in IC (integrated circuit) form. In addition to this, YIG is sensitive to vibration, lighting, electromagnetic interference (EMI), microphonics, phase hits, and frequency modulation, all of which have a detrimental effect in designing modern communication systems]. Even though, printed resonator based oscillators offer low cost, vibration insensitive and integratable solution, these limit the applications due to poor phase noise and larger real estate area.

During the last decades, design engineers have been improving the phase noise performance of both fixed frequency reference signal sources (using Crystal resonator for low frequency application-100 MHz and below; and Optical fiber delay line resonator for high frequency applications-10 GHz and above) and tunable signal sources (using printed resonator based oscillator circuits) for satisfying the new requirements. This development has taken place in two distinct lines of approach. The first one dealt with the reducing the size and improving the Q-factor of the printed resonator and the second is related with the exploring different novel oscillator topologies (self-injection locking, phase-locking, mode-locking, evanescent-mode coupling, mutual-injection-locking, noise-filtering) for stable and reliable performances.

This research report presents novel techniques to design signal sources using crystal resonator, dielectric resonator, SAW resonator, printed transmission line resonator and optical resonator networks for low cost and high performance applications. The slow-wave evanescent-mode metamaterial and Möbius configuration based resonator topology enables superior performance, can partly or fully meet the criteria of new requirement posed by 4th generation communication systems. A quality-factor enhancement technique based on employing slow-wave resonator is discussed and experimentally verified by designing frequency synthesizer using oscillator employing a slow-wave resonator, slow-wave metamaterial resonator and mode-coupled slow-wave metamaterial resonator oscillators. A procedure is introduced to determine the quality factor of various resonator (passive and active) topologies for low phase-noise oscillators. Active resonators are analyzed and a design procedure is introduced to optimize their performance for low-noise applications. It is shown that, despite

their excess noise, active resonators can be used to design very low phase-noise oscillators, however, at the cost of increased power consumption. In other words, they compromise the DC-to-RF power efficiency for lower phase-noise. This problem can be mitigated by designing MCSWR (mode-coupled slow-wave resonator), which can provide high quality-factors at lower power consumptions and also amenable to integrated circuit design. MCSWR topology not only helps reduce the oscillator's size, but also eases the frequency tunability. An X-band voltage-controlled-oscillator is designed based on the proposed technique. The oscillator achieves a state-of-the-art phase-noise and figure-of merit (FOM) among planar oscillators reported to date. The proposed VCO structure reported in this report occupies a relatively small area making it suitable for integrated circuit fabrication at mm-wave frequencies. The methods discussed in this thesis can be applied to design miniaturized very low phase-noise voltage-controlled-oscillators at microwave and mm-wave frequencies. The slow-wave metamaterial based Möbius resonators have received increasing attention for integrated oscillator design; these resonators present several advantages in comparison with conventional planar resonator, as for example:

- High Q-factor and Improved selectivity
- Easy integration in MIC/MMIC technologies, Small dimensions and weight
- Multi-band characteristics
- Relatively insensitive to EMI and EMC

The intended application is the development of multi-band low phase noise signal source solutions for current and later generation communication systems. With the development of the MMIC fabrication techniques, the future research work is to use the slow-wave metamaterial based Möbius resonators technology for biomedical sensors, imaging, and energy harvesting applications. The following patent applications listed below are the part of the completion of this research work:

1. Metamaterial Resonator Based Oscillators, US Patent applications No. 61976185, April 2014
2. BALUN, US Patent applications No. 61976199, April 2014
3. Integrated production of self injection locked self phase loop locked Opto-electronic Oscillators”, US Patent application no. 13/760767 (Feb 06, 2013).
4. “Self Injection Locked Phase Locked Looped Optoelectronic Oscillator”, US Patent application No. 61/746, 919 (Dec 28, 2012).
5. User-definable, low cost, low phase hit and spectrally pure tunable oscillator, European Patent No. 1 783 893 - January, 9, 2013
6. Wideband Voltage Controlled Oscillator Employing Evanescent Mode, Japanese Patent No. 5102019 - October 5, 2012
7. Passive Reflection Mixer, CA. Patent No. 2524751 - March 1, 2010
8. Tunable Oscillator, CA. Patent No. 2533623 - March 1, 2010
9. Tunable Frequency, Low Phase Noise and Low Thermal Drift Oscillator, CA. Patent No. 2534370 - February 9, 2010
10. Low Noise And Low Phase Hits Tunable Oscillator, US Patent No: 7,636,021 - December 22, 2009

11. Visually Inspectable Surface Mount Device Pad, US Patent No: 7,612,296 - November 3, 2009
12. User-Definable Low Cost, Low Noise, and Phase Hits Insensitive (Multi-Octave-Band Tunable Oscillator), US Patent No: 7,605,670 - October 20, 2009
13. User-Definable Low Cost, Low Phase Hits and Spectrally Pure Tunable Oscillator, US Patent No: 7,586,381 - September 8, 2009
14. User-Definable Low Cost, Low Noise, and Phase Hits Insensitive Multi-Octave-Band Tunable Oscillator, CA. Patent No. 2568244 - September 24, 2009
15. Passive Reflection Mixer, U.S. Patent No. 7,580,693 - August 25, 2009
16. Integrated Low Noise Microwave Wideband Push-Push VCO, CA. Patent No. - 2548311 - August 5, 2009
17. User Definable Thermal Drift Voltage Oscillator, CA. Patent No. 2548317 - August 5, 2009
18. Low Noise, Hybrid Tuned Wideband Voltage Controlled Oscillator, U.S. Patent No. 7,365,612 - April 29, 2008
19. Multi-Octave Band Tunable Coupled - Resonator Oscillator, U.S. Patent No. 7,292,113 - November 6, 2007
20. User-Definable Thermal Drift Voltage Controlled Oscillator , U.S. Patent No. 7,265,642 - September 4, 2007
21. Low Thermal Drift, Tunable Frequency Voltage Controlled Oscillator, U.S. Patent No. 7,262,670 - August 28, 2007
22. Tunable Frequency, Low Phase Noise and Low Thermal Drift Oscillator, U.S. Patent No. 7,196,591 - March 27, 2007
23. Wideband Voltage Controlled Oscillator Employing Evanescent Mode Coupled-Resonators
U.S. Patent No. 7,180,381 - February 20, 2007
24. Oscillator Circuit Configuration, U.S Patent No. 7,102,453 - September 5, 2006
25. Integrated Low Noise Microwave Wideband Push-Push VCO U.S. Patent No. 7,088,189 - August 8, 2006

11.2 Futuristic Work

The slow-wave metamaterial based Möbius resonators have received increasing attention for integrated oscillator design; these resonators can provide high quality-factors while occupying a small area due to small wavelengths at mm-wave frequencies. The Metamaterial Möbius technology discussed in this thesis can open new era in the field of imaging and sensors applications. Following research work as futuristic technology is in under progress:

- Telecom, Biomedical, and Sensors application
- Energy Harvesting, Solar Cells, Go Green Solution
- Subdiffraction Imaging, Superlens
- High Resolution 3-D printers
- Antenna, Invisibility Cloak

Symbols

<u>Symbol</u>	<u>Description</u>
LTV	Linear time variant
$NLTV$	Nonlinear time variant
$LTIV$	Linear time invariant
ATI	Active tunable inductor
AI	Active Inductor
TI or TAI	Tunable inductor or Tunable active inductor
$TAIO$	Tunable Active Inductor Oscillator
$ATIO$	Active tunable inductor oscillator
AIO	Active inductor oscillator
VCO	Voltage controlled oscillator
$G_m/g_m(t)$	Large-signal transconductance
g_m	Small-signal transconductance
$a_n(x)$	Fourier coefficient
$I_n(x)$	Modified Bessel function of order n
$I_e(t)$	Emitter current
$I_c(t)$	Collector current
I_{cob}	Collector reverse current
$V_{n(total)}$	Total noise voltage
V_{sn}	Noise due to source
$V_{n(network)}$	Noise due to network
Y_g	Generator admittance
Y_{opt}	Optimum noise admittance
F_{min}	Minimum achievable noise figure
R_n	Noise resistance
$[C_Y]$	Y-parameter noise correlation matrix
$[C_A]$	ABCD Correlation Matrix
Y_{cor}	Correlation factor
$\overline{i_{bn}^2} = 2qI_b\Delta f$	Mean square value of noise due to base current

$\overline{i_{cn}^2} = 2qI_c\Delta f$	Mean square value of noise due to collector current
$\overline{i_{con}^2} = 2qI_{cob}\Delta f$	Mean square value of noise due to reverse collector current
$\overline{v_{bn}^2} = 4kTR_b\Delta f$	Mean square value of noise voltage due to base resistance
$S(i_{cn}) = 2kTg_m$	Noise power spectral densities due to collector current
$S(i_{bn}) = \frac{2kTg_m}{\beta}$	Noise power spectral densities due to base current
$S(v_{bn}) = 4kTR_b$	Noise power spectral densities due to base resistance
$S(v_{sn}) = 4kTR_s$	Noise power spectral densities due to source resistance
$\overline{i_d^2} = 4kTg_mP\Delta f$	Mean square value of noise due to drain current
$\overline{i_g^2} = \frac{4kT(\omega C_{gs})^2 R}{g_m} \Delta f$	Mean square value of noise due to gate current
$P = \left[\frac{1}{4kTg_m} \right] \overline{i_d^2}/\text{Hz}$	FET noise coefficient
$R = \left[\frac{g_m}{4kT(\omega C_{gs})^2} \right] \overline{i_g^2}/\text{Hz}$	FET noise coefficient
$C = -j \left[\frac{\overline{i_g i_d^*}}{\sqrt{\overline{i_d^2 \overline{i_g^2}}}} \right]$	FET noise coefficient
P	0.67 for JFETs and 1.2 for MESFETs
R	0.2 for JFETs and 0.4 for MESFETs
C	0.4 for JFETs and 0.6-0.9 for MESFETs
Z_s	Complex source impedance
$a = \left[1 + \frac{f^2}{f_b^2} - \alpha_\theta \right] \frac{1}{\alpha_\theta}$	Modified factor
X	Drive-Level
$\left(\frac{kT}{q} \right) x$	Drive-Voltage
$2 \left[\frac{I_1(x)}{I_0(x)} \right]$	Fundamental component of current
$\left[\frac{I_2(x)}{I_1(x)} \right]$	Second harmonic component of current
φ	Conduction angle
n	Transformation factor
n_{opt}	Optimum transformation ratio
R_p	Parallel loss resistance

Q_L	Loaded quality factor
f_0	Center frequency
f_c	Flicker corner frequency
f_m	Frequency offset
P_{sav}	Average power at oscillator output
K_0	Oscillator voltage gain
$F = \frac{\overline{i_L^2}}{\overline{i_{Lo}^2}}$	Noise factor
NF	Noise Figure
$\mathcal{L}(f_m)$	Ratio of sideband power in a 1 Hz bandwidth at f_m
E_B, E_H	Vector of harmonic-balance (HB) errors
E	Vector of real and imaginary parts of all HB errors
X_B, X_H	Vector of state variable (SV) harmonics
J_B, J_H	Vector of forcing terms
$\delta X_B, \delta X_H$	Perturbation of the circuit state
M	Jacobian matrix of the HB errors
$\delta\omega_0(\omega)$	Phasor of the pseudo-sinusoidal components
$N_k(\omega)$	Noise power spectral density
$C_k(\omega)$	Normalized correlation coefficient
$J_p(\omega)$	Side-band noise sources
$U_p(\omega)$	Side-band noise sources
I_k^{SS}	Noise power spectral density
$S_{\Delta\theta}(\omega)$	Power spectral density of the input phase error
θ_d	Peak phase deviation
$e_N(t)$	Noise signal voltage
$R_N(t)$	Time variant negative resistance
k	Boltzmann's constant (1.38E-23 J/K)
kT	4.1×10^{-21} at $300 K_0$ (room temperature)
R	Equivalent noise resistance of tuning diode
G	Compressed power gain of the loop amplifier
$TF(j\omega)$	Closed loop transfer function
$H(j\omega)$	Open loop transfer function
$\langle \delta\varphi_{ck}(\omega) ^2 \rangle$	PM noise at k^{th} harmonic
$\langle \delta\varphi_{mk}(\omega) ^2 \rangle$	PM noise due to contribution of modulation

$\langle \delta A_{ck}(\omega) ^2 \rangle$	AM noise to carrier ratio at k^{th} harmonic
$\langle \delta\varphi_{ck}(\omega) \delta A_k(\omega)^* \rangle$	PM-AM correlation coefficient for the k^{th} harmonic
$\langle J_H(\omega) J_H^\otimes(\omega) \rangle$	Correlation matrix
T_F^\otimes	Conjugate-transpose
T_{Ak}	Row-matrix
T_F	Frequency transfer matrix
$Y_R(k\omega_\theta)$	Trans-admittance matrix
$ I_k^{ss} \exp(j2\varphi_k^{ss})$	k^{th} harmonic of the steady-state current through the load
$C_{k,-k}^*(\omega)$	Correlation coefficient of the upper and lower sidebands
$m(t)$	Modulating signal
K_p	Phase sensitivity
$\beta = \frac{\Delta f}{f_m}$	Modulation index of the modulating signal
SNR	Signal to noise ratio
A_{SSB}	Sideband amplitude of a phase modulation
C_0	Coefficient of Fourier series, 0 th order of the ISF
Δf	Noise bandwidth
$\omega_{1/f}$	1/f noise corner frequency of the device/transistor
q_{max}	Maximum charge on the capacitors in the resonator
$NFT_{inr}(\omega)$	Noise transfer function due to resonator loss resistance
$NFT_{vbn}(\omega)$	Noise transfer function due to transistor base resistance
$NFT_{ibn}(\omega)$	Noise transfer function due to the transistor base current
$NFT_{ifn}(\omega)$	Noise transfer function due to flicker noise
$NFT_{icn}(\omega)$	Noise transfer function due to collector current
K_f	Flicker noise constant
AF	Flicker noise exponent
$\sigma(t)$	Complex envelope of the frequency modulated signal
$\Gamma_{rms}/\Gamma(x)$	Impulse sensitivity function
EMF	Electromotive force
β^+	Large-signal current gain
Y_{11}^+	Large-signal input admittance
Y_{21}^+	Large-signal transconductance
$\Delta A(t)$	Amplitude fluctuation
$\Delta\varphi(t)$	Phase fluctuation

$\Delta\theta$	Steady state phase difference
Y_n	Normalized noise admittance
Y_e	Even mode admittance
Y_o	Odd mode admittance
λ_e	Even mode
λ_o	Odd mode
G_n	In-phase component of noise source
B_n	Quadrature component of noise source
m	Ratio of loaded and unloaded Q
m_{opt}	Optimum value of m for minimum phase noise
Q_0	Unloaded quality factor
β_{ij}	Coupling parameter
α_i	Free-running amplitude of the i^{th} oscillator
$A_i(t)$	Instantaneous amplitude of the i^{th} oscillator
$\varphi_i(t)$	Instantaneous phase of the i^{th} oscillator
ω_i	Free-running frequency of the i^{th} oscillator
MEMS	Micro-electro-mechanical-system
SMD	Surface mounted device
SRF	Self resonance frequency
MSL	Microstripline
$e_{inj}(t)$	Injected signal voltage
$\Delta\omega_{lock}$	Locking bandwidth
ω_{inj}	Injected signal frequency
λ_{ij}	Magnitude of the coupling coefficient
φ_{ij}	Phase of the coupling coefficient
r	Capacitance ratio of the tuning diode
C_{v0}	Capacitance of tuning diode at zero bias voltage
C_{vb}	Capacitance of tuning diode at breakdown bias voltage

P_n	Average power dissipated by the network
μ	Empirical nonlinear parameter
$R_n(t)$	Time variant negative resistance
C_n	Fourier series coefficient
$[\bar{C}]$	Matrix representation of arbitrary coupling topology
c	Coefficient of correlation
θ_n	Phase of the n^{th} harmonic
W_e	Average stored electrical energy
W_m	Average stored magnetic energy
ω_{diff}	Modulation frequency
VNA	Vector network analyzer
VDP	Van der Pol
SWR	Slow-Wave resonator
DR	Dielectric Resonator
MCPR	Möbius coupled printed resonator
RTRD	Real Time Signal Retention Device
IFFT	Inverse Fast Fourier Transform
DPS	Double Positive substrates
ENG	Epsilon Negative Substrate
MNG	Mu Negative Substrate
DNG	Double Negative substrates
NRIM	Negative Refractive Index material
SRR	Split-ring resonator
TLM	Transmission line model
CRLH	composite right/left-handed structures
SWMR	Slow Wave Metamaterial Resonator
SIW	substrate integrated waveguide
CSRR	complimentary split ring resonators
MCSWMR	Mode-Coupled Slow-Wave Metamaterial Resonator

<i>OEO</i>	Opto-Electronic Oscillator
<i>B</i>	Injection locking loop gain
<i>DRO</i>	Dielectric resonator oscillator
<i>DSIL</i>	Dual loop Self-injection locking
<i>DSILPLL</i>	Dual loop Self-injection locked and phase locked loop
<i>DSPLL</i>	Dual loop Self-phase locked loop
<i>f_m</i>	Fourier frequency
<i>f_{osc}</i>	Oscillation frequency
<i>G</i>	Phase locking loop gain
<i>IL</i>	Injection locking
<i>ILPLL</i>	Injection locked phase locked loop
<i>K_d</i>	PLL phase detector gain
<i>K_h</i>	PLL low pass filter gain
<i>K_o</i>	PLL VCO tuning sensitivity
<i>L(fm)</i>	Single sideband phase noise
<i>MMS</i>	Metamaterial Mobius Strip
<i>PLL</i>	Phase locked loop
<i>SIL</i>	Self-injection locking
<i>SILPLL</i>	Self-injection locked and phase locked loop
<i>SLC</i>	Sapphire loaded cavity
<i>SPLL</i>	Self-phase locked loop
<i>S_φ(fm)</i>	Power spectral density of phase
<i>ζ</i>	Damping factor of PLL loop
<i>θ_e</i>	Phase error between input and VCO
<i>θ_i</i>	Phase angle of input signal
<i>θ_o</i>	Phase angle of VCO
<i>τ</i>	Time delay associated with an optic fiber
<i>S_φ(fm)</i>	Power spectral density of phase
<i>θ_i</i>	Phase angle of input signal

θ_o	Phase angle of VCO
θ_e	Phase error between input and VCO
ϕ_i	Instantaneous phase of input signal
ϕ_o	Instantaneous phase of VCO signal
ζ	Damping factor of PLL loop
ω_n	Natural frequency of PLL loop
f_{osc}	Oscillation frequency
f_m	Fourier frequency
τ	Time delay associated with an optic fiber
τ_i	Time delay of the fiber used in self-injection locking
τ_d	Time delay of the fiber used in self-phase locked loop

Appendices

Appendix A

A1 Noise Analysis of the N-Coupled Oscillator

The objective of this section is to find the analytical expression of the phase noise of the N-coupled oscillators relative to a single free running uncoupled oscillator for different coupling configurations. Three types of coupling topology (global, bilateral and unilateral) are described for the noise analysis of the N-coupled oscillator systems. For uncoupled oscillator coupling coefficient $\beta_{ij} \rightarrow 0$, the expression of the coupling dynamics can be characterized as [Ref. 1: pp. 284, Equation 10-191]

$$[\Delta A_i(\omega)]_{uncoupled} = \left[\frac{\mu\omega_i}{2Q\omega} \right] [\alpha_i^2 - 3\dot{A}_i^2] [\Delta A_i(\omega)]_{uncoupled} - \left[\frac{\omega_i}{2Q\omega} \right] \dot{A}_i G_{ni}(\omega) ; i = 1, 2, 3, \dots, N \quad (\text{A.1})$$

$$[\Delta \theta_i(\omega)]_{uncoupled} = - \left[\frac{\omega_i}{2Q\omega} \right] B_{ni}(\omega) ; i = 1, 2, 3, \dots, N \quad (\text{A.2})$$

$$\text{From (A.1), } [\Delta A_i(\omega)]_{uncoupled} = \frac{-\dot{A}_i G_{ni}(\omega)}{\left[\frac{2\omega Q}{\omega_i} \right]^2 + \mu^2 [3\dot{A}_i^2 - \alpha_i^2]} \quad (\text{A.3})$$

The noise spectral density due to the amplitude fluctuation is given by

$$|\Delta A_i(\omega)|_{uncoupled}^2 = \frac{\dot{A}_i^2 |G_{ni}(\omega)|^2}{\left[\frac{2\omega Q}{\omega_i} \right]^2 + \mu^2 [3\dot{A}_i^2 - \alpha_i^2]^2} \quad (\text{A.4})$$

The noise spectral density due to the phase fluctuation for single uncoupled free running oscillator is given from Equation (A.2) as

$$|\Delta \theta_i(\omega)|_{uncoupled}^2 = \frac{|B_{ni}(\omega)|^2}{\left[\frac{2Q\omega}{\omega_i} \right]^2} \quad (\text{A.5})$$

For series tuned free running oscillator, Equations (A.4) and (A.5) can be rewritten as

$$|\Delta A_i(\omega)|_{uncoupled}^2 = \frac{\dot{A}_i^2 |G_{ni}(\omega)|^2 R^2}{4L^2 \omega^2 + (\mu R)^2 [3\dot{A}_i^2 - \alpha_i^2]^2} \approx \frac{2|e|^2}{4L^2 \omega^2 + (\gamma A_0)^2} \quad (\text{A.6})$$

$$|\Delta \theta_i(\omega)|_{uncoupled}^2 = \frac{|B_{ni}(\omega)|^2}{\left[\frac{\omega}{\omega_{3dB}} \right]^2} = \frac{|B_{ni}(\omega)|^2 \omega_i^2}{4\omega^2 Q^2} \approx \frac{2|e|^2}{4\omega^2 L^2 A_0^2} \quad (\text{A.7})$$

where $Q = \frac{\omega L}{R}$, $\gamma A_0 \approx (\mu R)[3\dot{A}_i^2 - \alpha_i^2]$, $|e|^2 \approx \dot{A}_i^2 |G_{ni}(\omega)|^2 R^2$

Equation (A.6) and (A.7) represents the AM and PM noise for the uncoupled free-running series tuned oscillator and this has same form as given in (Ref. 1, Eq. 10-173, Eq. 10-177).

A2 Globally N-Coupled Oscillator Systems

Figure A-1 shows the globally N-coupled oscillator system.

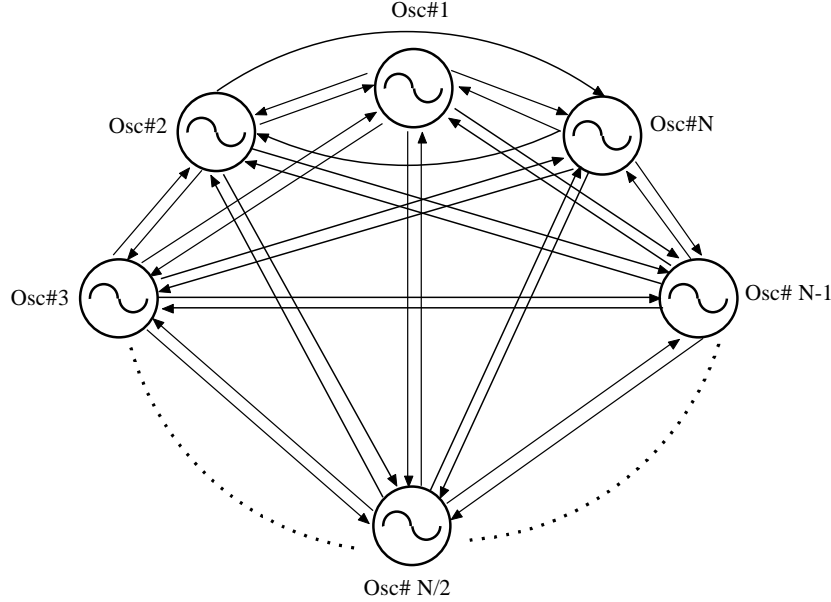


Figure A-1: Globally N-coupled oscillator system

From Equation [Ref.1, pp. 286, Equation 10-194]

$$\left[\frac{2Q\omega}{\omega_i} \right] [\Delta\theta_i(\omega)] = - \sum_{\substack{j=1 \\ j \neq i}}^N \beta_{ij} ([\Delta\theta_i(\omega) - [\Delta\theta_j(\omega)]) \cos[\dot{\theta}_i - \dot{\theta}_j] - B_{ni}(\omega); \quad i = 1, 2, 3..N \quad (\text{A.8})$$

For globally coupled topology, considering coupling coefficient $\beta_{ij} = \beta$ for any i^{th} and j^{th} oscillators and all the oscillators are in phase, Equation (A.8) can be rewritten as

$$\left[\frac{2\omega Q}{\omega_i} \right] [\Delta\theta_i(\omega)] = -\beta \sum_{\substack{j=1 \\ j \neq i}}^N ([\Delta\theta_i(\omega) - [\Delta\theta_j(\omega)]) - B_{ni}(\omega) \quad i = 1, 2, 3..N \quad (\text{A.9})$$

Expanding the series of the Equation (A.9) as

$$\left[\frac{2\omega Q}{\beta \omega_i} \right] [\Delta\theta_i(\omega)] = \{(N-1)[\Delta\theta_i(\omega)]\} + \{[\Delta\theta_1(\omega)] + [\Delta\theta_2(\omega) + ... + [\Delta\theta_N(\omega)]\} - \frac{B_{ni}(\omega)}{\beta} \quad (\text{A.10})$$

$$x[\Delta\theta_i(\omega)] = \left[\{(N-1)[\Delta\theta_i(\omega)]\} + \{[\Delta\theta_1(\omega)] + [\Delta\theta_2(\omega) + ... + [\Delta\theta_N(\omega)]\} - \frac{B_{ni}(\omega)}{\beta} \right] \quad (\text{A.11})$$

Where $x = \frac{2\omega Q}{\beta \omega_i}$, following [138]; from [Ref.1, pp. 286, Equation 10-195] and (A.11), $[\bar{C}]$ for global

coupling can be described as

$$[\bar{C}] = \beta \begin{bmatrix} 1-N-x & 1 & 1 & \dots & 1 \\ 1 & 1-N-x & 1 & \dots & 1 \\ 1 & 1 & 1-N-x & \ddots & \vdots \\ \vdots & \vdots & \ddots & \ddots & 1 \\ 1 & 1 & \dots & 1 & 1-N-x \end{bmatrix} \quad (\text{A.12})$$

From [Ref.1, pp. 286, Equation 10-196]:

$$[\bar{P}] = [\bar{C}]^{-1} = \frac{1}{-x\beta(N+x)} \begin{bmatrix} 1+x & 1 & 1 & \dots & 1 \\ 1 & 1+x & 1 & \dots & 1 \\ 1 & 1 & 1+x & \ddots & \vdots \\ \vdots & \vdots & \ddots & \ddots & 1 \\ 1 & 1 & \dots & \dots & 1+x \end{bmatrix} \quad (\text{A.13})$$

From [Ref.1, pp. 288]:

$$\sum_{j=1}^N p_{ij} = \frac{(N+x)}{-x\beta(N+x)} = \frac{-1}{x\beta} \quad ; \quad \text{For all } i \quad (\text{A.14})$$

From [Ref.1, Equation 10-205], the total output phase noise is given by

$$|\Delta\theta_{total}(\omega)|^2 = \frac{|B_n(\omega)|^2}{N^2} \sum_{j=1}^N \left| \sum_{i=1}^N p_{ij} \right|^2 = \frac{1}{N} \frac{|B_n(\omega)|^2}{\beta^2 x^2} = \frac{1}{N} \frac{|B_n(\omega)|^2}{\left[\frac{2\omega Q}{\omega_i} \right]^2} \quad (\text{A.15})$$

Comparing Equation (A.15) with the single oscillator phase noise Equation (A.5), we find

$$|\Delta\theta_{total}(\omega)|^2 = \frac{1}{N} |\Delta\theta_i(\omega)|_{uncoupled}^2 \quad (\text{A.16})$$

From Equation (A.16) the total PM noise for N globally oscillators is reduced by the factor N of that of a single oscillator.

A3 Bilateral N-Coupled Oscillator Systems

Figure A-2 shows the nearest neighbor bilateral N-coupled oscillator system.

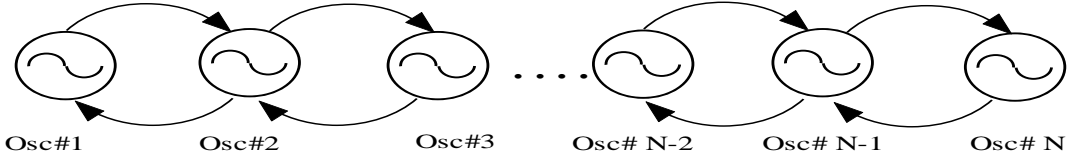


Figure A-2: Nearest neighbor bilateral N-coupled oscillator system

The coupling parameter β_{ij} for the Figure A-2 is defined as [1]

$$\beta_{ij} = \begin{cases} \beta, & |i - j| = 1 \\ 0, & otherwise \end{cases} \quad (\text{A.17})$$

Assuming constant phase progression along the array of the N-coupled oscillator system as [2]

$$\dot{\theta}_i - \dot{\theta}_{i+1} = \Delta\dot{\theta} \quad (\text{A.18})$$

From [Ref.1, pp. 286, Equation 10-195], $[\bar{C}]$ for bilateral coupling can be described as

$$[\bar{C}] = \beta \cos(\Delta\dot{\theta}) \begin{bmatrix} -1-y & 1 & 0 & 0 & \dots & 0 \\ 1 & -2-y & 1 & 0 & \dots & 0 \\ 0 & 1 & -2-y & 1 & \dots & \vdots \\ \vdots & \ddots & \ddots & \ddots & \ddots & 0 \\ 0 & \dots & \ddots & 1 & -2-y & 1 \\ 0 & 0 & \dots & 0 & 1 & -1-y \end{bmatrix}, \text{ where } y = \frac{\omega}{\left[\frac{\beta \omega_i}{2Q} \right] \cos(\Delta\dot{\theta})} \quad (\text{A.19})$$

From [Ref.1, Equation 10-197], $\sum_{j=1}^N p_{ij} = \frac{-1}{\left[\frac{2Q\omega}{\omega_i} \right]}$; For all i (A.20)

From [Ref.1, Equation 10-205], the total output phase noise is given by

$$|\Delta\theta_{total}(\omega)|^2 = \frac{|B_n(\omega)|^2}{N^2} \sum_{j=1}^N \left| \sum_{i=1}^N p_{ij} \right|^2 = \frac{1}{N} \frac{|B_n(\omega)|^2}{\left[\frac{2\omega Q}{\omega_i} \right]^2} (A.21)$$

Comparing Equation (A.22) with the single oscillator phase noise Equation (A.5) we find

$$|\Delta\theta_{total}(\omega)|^2 = \frac{1}{N} |\Delta\theta_i(\omega)|_{uncoupled}^2 (A.22)$$

A4 Unilateral N-Coupled Oscillator Systems

Figure A-3 shows the nearest neighbor unilateral N-coupled oscillator system.

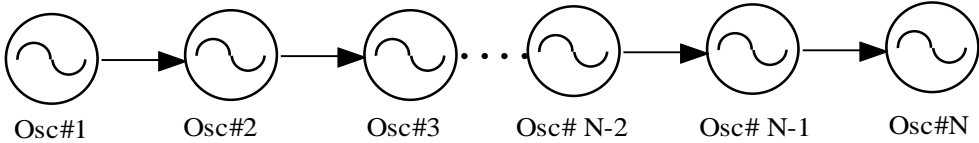


Figure A-3: Nearest neighbor unilateral N-coupled oscillator system

In this topology, each successive oscillator in the array of N-coupled oscillator system is slaved to the previous oscillator and the first oscillator in the array is considered as master oscillator.

The coupling parameter β_{ij} for the Figure A-3 is defined as [1]

$$\beta_{ij} = \begin{cases} \beta, & i - j = +1 \\ 0, & otherwise \end{cases} (A.23)$$

From [2], $[\bar{C}]$ for unilateral coupling

$$[\bar{C}] = \beta \begin{bmatrix} -z & 0 & 0 & \dots & 0 & 0 \\ 1 & -1-z & 0 & \dots & \vdots & \vdots \\ 0 & 1 & -1-z & \dots & \vdots & \vdots \\ \vdots & \ddots & \ddots & \ddots & 0 & \vdots \\ 0 & \dots & \ddots & \ddots & -1-z & 0 \\ 0 & 0 & \dots & 0 & 1 & -1-z \end{bmatrix} (A.24)$$

$$[\bar{P}] = [\bar{C}]^{-1} = \frac{1}{\beta} \begin{bmatrix} -1 & 0 & 0 & \dots & 0 & 0 \\ \frac{-1}{z} & \frac{-1}{(1+z)} & 0 & \dots & 0 & 0 \\ \frac{-1}{z(1+z)} & \frac{-1}{(1+z)^2} & \frac{-1}{(1+z)} & \dots & \vdots & 0 \\ \frac{-1}{z(1+z)^2} & \frac{-1}{(1+z)^3} & \frac{-1}{(1+z)^2} & \ddots & \ddots & \vdots \\ \vdots & \vdots & \vdots & \ddots & 0 & 0 \\ \frac{-1}{z(1+z)^{N-2}} & \frac{-1}{(1+z)^{N-1}} & \frac{-1}{(1+z)^{N-3}} & \ddots & \frac{-1}{(1+z)} & 0 \\ \frac{-1}{z(1+z)^{N-1}} & \frac{-1}{(1+z)^{N-2}} & \frac{-1}{(1+z)^{N-2}} & \dots & \frac{-1}{(1+z)^2} & \frac{-1}{(1+z)} \end{bmatrix} \quad (\text{A.25})$$

Where $z = \frac{2\omega Q}{\beta \omega_i}$

From (A.26), rows and columns of the Equation (A.25) form geometric series; the expression of $\sum_{j=1}^N p_{ij}$ can be calculated analytically. For small value of z , expression of $\sum_{j=1}^N p_{ij}$ can be given as [2]:

$$\sum_{j=1}^N p_{ij} = \begin{cases} \frac{-N}{\beta z}, & i = 1 \\ -\frac{N+1-i}{\beta}, & 2 \leq i \leq N \end{cases} \quad (\text{A.26})$$

From [Ref.1, Equation 10-205], the total output phase noise is approximately given as

$$|\Delta\theta_{total}(\omega)|^2 = \frac{|B_n(\omega)|^2}{N^2} \sum_{j=1}^N \left| \sum_{i=1}^N p_{ij} \right|^2 = \left[1 + z^2 \left(\frac{N}{3} - \frac{1}{2} + \frac{1}{6N} \right) \right] |\Delta\theta_i(\omega)|_{uncoupled}^2 \quad (\text{A.27})$$

$$|\Delta\theta_{total}(\omega)|^2 = \left[1 + \left(\frac{2\omega Q}{\beta \omega_i} \right)^2 \left(\frac{N}{3} - \frac{1}{2} + \frac{1}{6N} \right) \right] |\Delta\theta_i(\omega)|_{uncoupled}^2 \quad (\text{A.28})$$

From Equation (A.29), there is noise degradation with respect to the single uncoupled free running oscillator and the noise of the unilateral coupled oscillator increases quadratically, away from the carrier, and linearly with increasing number of the oscillator of the array of the N -coupled oscillator systems. In general $z \ll 1$ and near the carrier frequency the noise is just that of the first-stage oscillator, thereby the total noise could be significantly reduced by making the first-stage oscillator as a master oscillator having low noise performance.

References:

- [1] U.L. Rohde, A.K. Poddar, G. Boeck, "The Design of Modern Microwave Oscillators for Wireless Applications: Theory and Optimization", John Wiley and Sons, Inc., 2005.
- [2] Heng-Chia Chang, Xudong Cao, Umesh K. Mishra, and R. York, "Phase Noise in Coupled Oscillators: Theory and Experiment," IEEE Trans. MTT, Vol. 45, pp. 604-615, May 1997

Appendix B

B1 Active Resonator using Gain Feedback Loop

Figure B-1 shows the typical active resonator circuit topology using active feedback loop [1, 2].

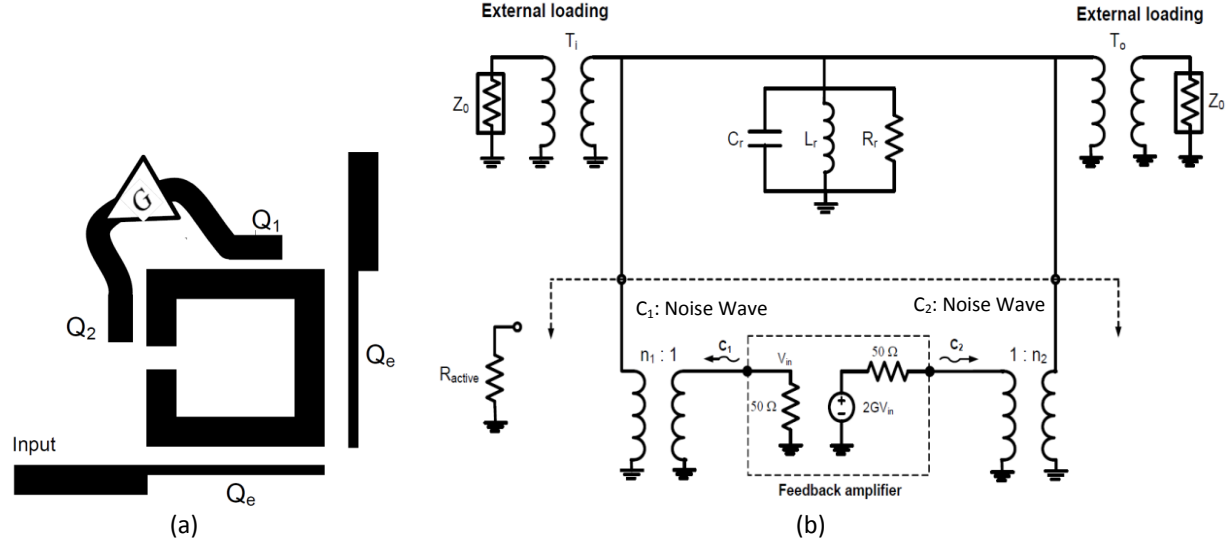


Figure B-1: A typical square open-loop resonator with an active feedback-loop for loss compensation, resonator is doubly loaded through input and output coupled-lines with external quality-factor of Q_e : (a) layout representation, (b) simplified circuit schematic representation, the amplifier is matched to 50Ω at the input and output [1, 2]

As shown in Figure B-1 (a), the external quality factor Q_e , represents the resonator's input and output loadings, external-quality-factors, Q_1 and Q_2 , denote the loading effects due to the gain stage's input and output coupling, and G is the voltage gain of the amplifier. The phase of the active feedback-loop should be an integer multiple of 360° for loss compensation.

Figure B-1 (b) shows the simplified equivalent circuit of the active resonator for the analysis of noise characteristics. As shown in Figure B-1 (b), RLC network models the passive resonator coupled to the amplifier through the transformers with turn ratio n_1 and n_2 . The active resonator's input and output external couplings are represented by the transformers T_i and T_o . For simplification in analysis, the amplifier is bilaterally conjugate matched at its input and output. The resonator is fully loss-compensated when this negative resistance is equal in magnitude to the positive resistance of the passive resonator, R_r . This requirement is fulfilled when the gain of the amplifier is chosen such that [1]

$$G = \frac{\sqrt{n_1 n_2}}{2} \left[\frac{1}{Q_1} + \frac{1}{Q_2} + \frac{1}{Q_3} \right] \quad (\text{B.1})$$

where

$$Q_1 = \frac{50n_1^2}{\omega_0 L_r} \quad (\text{B.2})$$

$$Q_2 = \frac{50n_2^2}{\omega_0 L_r} \quad (\text{B.3})$$

$$Q_u = \frac{R_r}{\omega_0 L_r} \quad (\text{B.4})$$

The active feedback loop shown in Figure B-1 (a) can be represented equivalently as a negative resistance as

$$R_{active} = - \left(\frac{(50n_2^2) \times (50n_1^2)}{\left(2G \frac{n_2}{n_1} - 1 \right) \left(\left(\frac{-50n_2^2}{2G \frac{n_2}{n_1} - 1} \right) + 50n_1^2 \right)} \right) \quad (\text{B.5})$$

The noise sources of the amplifier in the feedback loop generate two noise-waves, C_1 and C_2 (Fig. B-1b), which degrade the doubly loaded resonator's noise figure. It is very important to minimize the effect of the added-noise introduced by the amplifier, especially when the active resonator is intended for low phase-noise oscillator applications. Noise analysis of active resonators has been performed in [1, 2], where it is shown that the contribution of the noise-wave C_1 (shown in Figure B-1) to the noise-figure of the resonator is nullified when the active feedback-loop is designed such that:

$$Q_2 = G^2 Q_1 \Rightarrow \frac{Q_2}{G^2 Q_1} = 1 \quad (\text{B.6})$$

From (B.2)-(B.6), the optimum feedback loop design parameter for a lossless high – Q factor resonator with minimum noise degradation can be given by

$$Q_1 = \frac{(G^2 - 1)}{G^2} Q_u \quad (\text{B.7})$$

$$Q_2 = (G^2 - 1) Q_u \quad (\text{B.8})$$

$$F_{\min} = \left[1 + \left(\frac{2Q_e}{Q_u} \right) + m \left(\frac{2Q_e}{Q_u} \right) \right] = \left[F_{\text{passive-resonator}} + m \left(\frac{2Q_e}{Q_u} \right) \right] \quad (\text{B.9})$$

Where $F_{\text{passive-resonator}}$ is the noise-figure of the passive resonator; m and F_A are the noise-measure and noise-figure of the amplifier, is defined by

$$m = \frac{F_A - 1}{1 - G^{-2}} \quad (\text{B.10})$$

$$F_{\text{passive-resonator}} = 1 + \left(\frac{2Q_e}{Q_u} \right) \quad (\text{B.11})$$

Figure B-2 shows the CAD simulated S_{21} responses of the passive and active resonators with gain feedback for brief insights about the resonator frequency characteristics. Figure B-3 shows the CAD simulated noise-figures of passive and active resonator using different gain feedback-loop parameters ($m = 0.103, 0.425, 0.778$) with $Q_u=200$ and $Q_e=200$, where “m” is the noise-measure of the amplifier used in the active feedback-loop.

As shown in Figure B-3, the noise-figure is measured at the resonant frequency (ω_o) and each marker represents an active resonator designed with different feedback-loop parameters. From (B.6), the minimum noise-figure is achieved when $\frac{Q_2}{G^2 Q_1} = 1$, as also observed in Figure B-3, the noise degradation for active resonator is about 0.5 dB as compared to passive resonator. However, if the design parameter is not optimized ($\frac{Q_2}{G^2 Q_1} \neq 1$), significant noise-figure degradation could occur.

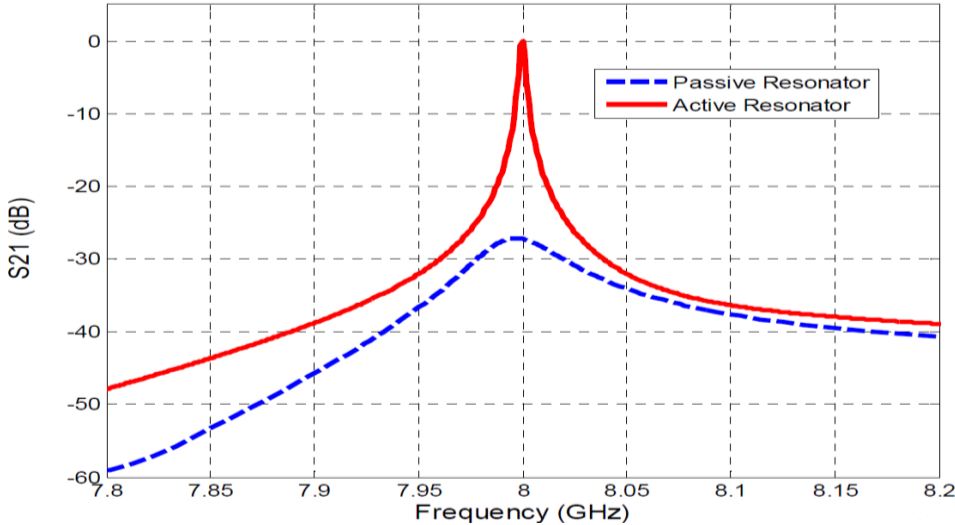


Figure B-2 CAD simulated frequency responses of the passive and active resonators ($Q_u=200$ and $Q_e=200$) [2]

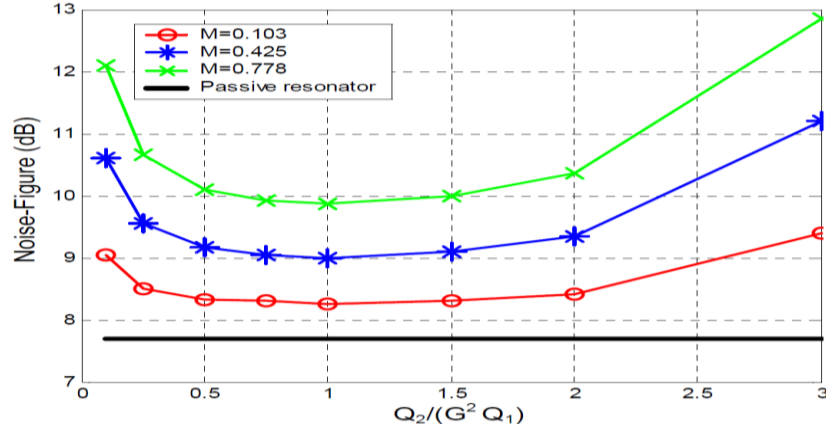


Figure B-3: Simulated noise-figures of passive and active resonator using different gain feedback-loop parameters ($m = 0.103, 0.425, 0.778$), $Q_e=200$ and $Q_o=200$; m : noise-measure of amplifier used in the active feedback-loop [2].

B2. Active Resonator using negative resistance devices

Figure B-4 shows the typical square loop resonator along with a negative-resistance circuitry for its loss compensation. The external quality factor, Q_e , represents the input and output loadings, and Q_r is the resonator's quality factor due to coupling to the negative-resistance device. The square loop active resonators shown in Figure B-4 can be equivalently described by the shunt RLC network which represents the passive resonator coupled to the input and output ports through the transformers with turn ratio n_e . Figure B-5 shows the equivalent electrical circuit representation where the current source I_n models the extra noise introduced by the active device, and the coupling to the negative-resistance device is modeled by the transformer with turn ratio n_r .

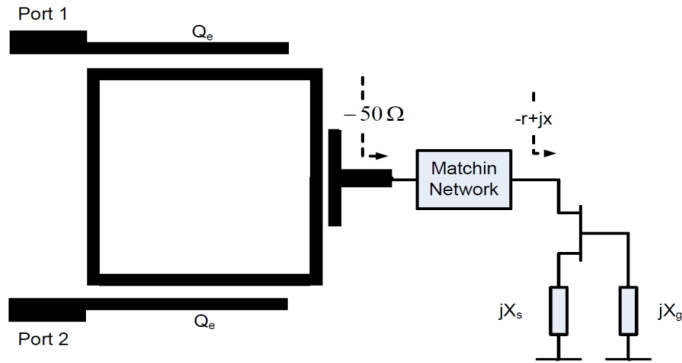


Figure B-4: A printed square loop resonator along with its negative-resistance circuitry for loss compensation [2]

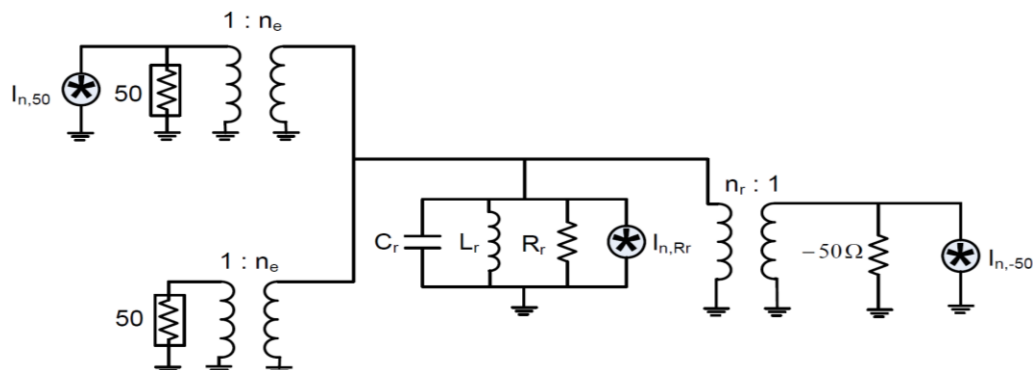


Figure B-5: Shows the simplified circuit representation of active resonators using typical microstrip square loop resonator along with its negative-resistance circuitry for loss compensation [2]

Theoretically, the resonator's losses are fully compensated when the negative resistance presented to the RLC network is equal in magnitude to the positive resistance R_r [3]-[4]

$$R_r = 50n_2^2 \Rightarrow Q_u = Q_{-r} \quad (\text{B.12})$$

$$Q_u = \frac{R_r}{\omega_0 L_r} \quad (\text{B.13})$$

$$Q_e = \frac{50n_e^2}{\omega_0 L_r} \quad (\text{B.14})$$

$$Q_{-r} = \frac{50n_r^2}{\omega_0 L_r} \quad (\text{B.15})$$

From (B.12), the negative-resistance coupling gap as shown in Figure B-4 can be optimized by HFSS or 2.5D EM simulation for the condition: $Q_u = Q_{-r}$. But the drawback of the negative resistance circuit is excess noise generator (noise associated with the active device: transistor), its noise level is determined through the equation for noise-measure defined as [5]

$$m = \frac{P_e}{KT_0 B} \quad (\text{B.16})$$

where K is the Boltzmann's constant, T_0 is the reference temperature and B is the bandwidth used to measure the exchangeable noise power P_e of the active device. For low phase noise oscillator's application, due care must be taken in designing the negative-resistance device considering lowest minimum noise measure "m". As shown in Figure B-4, the optimum X_g and X_s values can be determined for minimum noise-measure is given by

$$m_{min} = \frac{(F_{min}-1)}{\left(1 - \frac{1}{G_a}\right)} \quad (\text{B.17})$$

where F_{min} and G_a are the transistor's minimum noise-figure and associated gain, respectively. The minimum noise-figure of the active resonator can be derived in terms of the circuit and device parameters by analyzing the equivalent circuit as shown in Figure B-5. The output noise contributions are from the input noise ($I_{n,50}$), passive resonator losses (I_{n,R_r}), and the negative-resistance device ($I_{n,-50}$), with the power spectral densities [2] :

$$\overline{I_{n,50}^2} = \frac{4kT_0 B}{50} \quad (\text{B.18})$$

$$\overline{I_{n,R_r}^2} = \frac{4kT_0 B}{R_r} \quad (\text{B.19})$$

$$\overline{I_{n,-50}^2} = \frac{4kT_0 B}{50} m_{min} \quad (\text{B.20})$$

$$\begin{aligned} F_{min}(\text{active-resonator}) &= \left[1 + \left(\frac{2Q_e}{Q_u} \right) + m_{min} \left(\frac{2Q_e}{Q_u} \right) \right] \\ &= \left[F_{\text{passive-resonator}} + m_{min} \left(\frac{2Q_e}{Q_u} \right) \right] \end{aligned} \quad (\text{B.21})$$

$$\text{where } F_{\text{passive-resonator}} = 1 + \left(\frac{2Q_e}{Q_u} \right) \quad (\text{B.22})$$

From (B.21), F_{active} and F_{passive} are the noise-figure of the active and passive resonators, encapsulates the noise effect of the active device on the resonator's noise-figure, indicating that a low noise-measure transistor should be selected for the active resonator design. As shown in Figure B-5, negative-resistance device amplifies RF power in order to compensate for the energy loss within the passive resonator. Assuming the input power at port #1 is P_{in} , the voltage across the LC resonator is given by

$$V_{\text{resonator}} = \sqrt{2\omega_0 L_r Q_e P_{in}} \quad (\text{B.23})$$

Considering the amount of the power added by the negative-resistance device (P_{added}) is equal to the power dissipated by the tank's positive resistance:

$$P_{added} = \frac{V_{resonator}^2}{2R_r} = \left(\frac{2Q_e}{Q_u}\right) P_{in} \quad (\text{B.24})$$

B3. Oscillator Design Methodology Using Active Resonator

As discussed in section B1 and B2, active resonators can be realized either by using active feedback-loops or negative resistance devices to compensate partial or full loss compensation with minimum noise-figure degradations. Theoretically, both loss compensation techniques yield a similar performance in terms of noise-figure and power consumption but designer has to make a choice depending on the implementation constraints for a given figure of merit (FOM).

The important point to note in active resonators, the loaded and external quality-factors are equal because the unloaded quality-factor is infinity due to full loss compensation. From (B.21) to (B.24) [2]:

$$Q_{L,active} = Q_e \quad (\text{B.25})$$

$$F_{passive} = 1 + \frac{2Q_e}{Q_u} \quad (\text{B.26})$$

$$F_{active} = F_{passive} = M \left(\frac{2Q_{L,active}}{Q_u} \right) \quad (\text{B.27})$$

$$\frac{P_{added}}{P_{in}} = \frac{2Q_{L,active}}{Q_u} \quad (\text{B.28})$$

where $F_{passive}$ and F_{active} are the noise-figures of the passive and active resonators, respectively. $Q_{L,active}$, Q_e and Q_u are, respectively, the loaded quality-factor of the active resonator, the external quality-factor, and the unloaded quality-factor of the passive resonator. P_{in} is the power input to the resonator and P_{added} is the power added by the loss compensation network.

From (B.25-B.28), high Q-factors of active resonators enable low phase-noise oscillators provided there is power budget (active resonator consume DC power) and impact of excess noise associated with active resonator is mitigated either by noise filtering and cancellation techniques or optimization of resonator design for minimum noise measure [4]-[9]. In other words, in oscillators using single active resonators as their frequency stabilization elements, DC-to-RF power efficiency is traded for lower phase-noise.

References

- [1] Ezzedine et al, "Optimization of noise performance for various topologies of planar microwave active filters using noise wave techniques," IEEE Trans. Microw. Theory Tech., vol. -46, no. 12, pp. 2484-2492, Dec. 1998
- [2] M. Nick, "New Q-Enhanced Planar Resonators for Low Phase-Noise Radio Frequency Oscillators", PhD Dissertation, Electrical Engineering, University of Michigan, 2011
- [3] P. Gardner, and D. K. Paul, "Optimum noise measure configurations for transistor negative resistance amplifiers," IEEE Trans. Microw. Theory Tech., vol. -45, no. 5, pp. 580-586, May 1997.
- [4] A. Grebennikov, "RF and microwave transistor oscillator design," New York: John Wiley & Sons, 2007.
- [5] H. A. Hauss, and R. B. Adler, "Circuit theory of linear noisy networks," New York: Wiley, 1959.
- [6] J.-S Hong and M. J. Lancaster, Microwave Filter for RF/Microwave Application. New York: Wiley, 2001.
- [7] U. L. Rohde, M. Rudolph, "RF/Microwave Circuit Design for Wireless Applications", Wiley & Sons, Dec., 2012
- [8] K. Hoffmann and Z. Skvor, "Active resonator", EUROCON IEEE Proc. vol. 1; pp. 164-166, Bratislava 2001.
- [9] U. L. Rohde and A. K. Poddar, "Active Planar Coupled Resonators Replace Traditional High Q Resonators in Low Phase Noise Oscillators/VCOs", IEEE RWS 2007, pp. 39-42, 09-11 January 2007, CA, USA.

Appendix C

C1 Planar Resonator Oscillators

Microstrip/stripline/Suspended-Stripline resonators are the most common choice due to their low fabrication cost for planar oscillator designs, can be easily integrated with active circuits such as MMICs and RFICs. Unfortunately, a major drawback of using planar resonators is their large size and low quality-factors, which makes it difficult to design small size low phase-noise oscillators. Various methods have been explored [1]-[14] to improve the Q-factor and achieve miniaturization; these are categorized in two groups: (i) passive planar resonator oscillator, and (ii) active planar resonator oscillator [1].

C2 Oscillators Based on Passive Planar Resonator

Figure C-1 shows the 8 GHz oscillator employing an amplifier gain block to support sufficient loop-gain, and 4-pole elliptical bandpass filter as a frequency stabilization network and a parallel feedback network for phase matching [2]. As shown in Figure C-1, the active device is a packaged SiGe HBT transistor from NEC (NECNESG2030M04) DC biased at $V_{CE}=2V$, $I_C=11mA$. Figures C-2, C-3, and C-4, illustrate the BPF layout, plots of printed BPF characteristics for X-band oscillator, and phase noise plot (simulated and measured) [1]-[4].

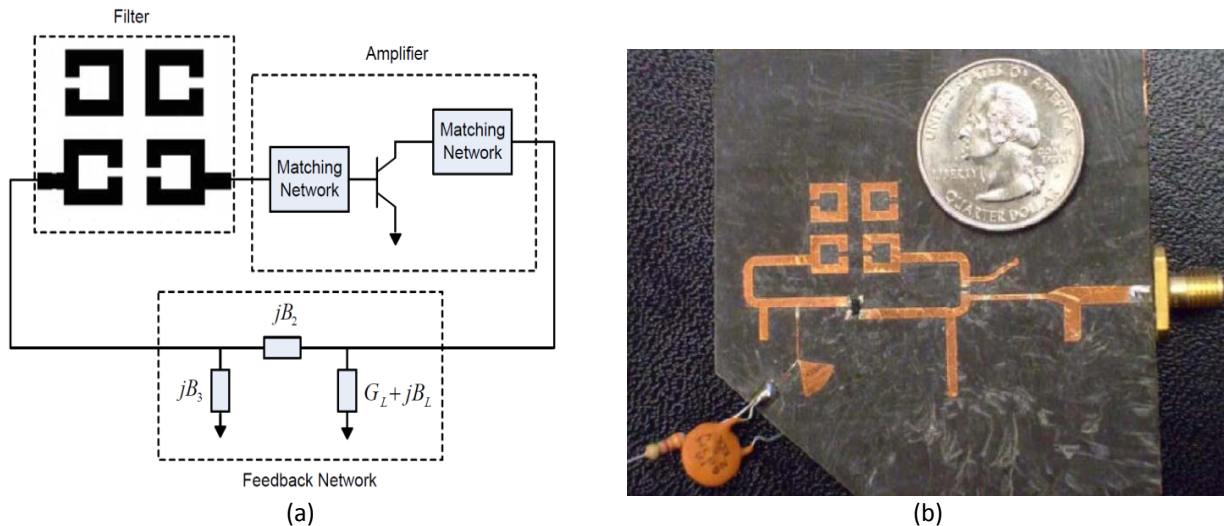


Figure C-1: Shows the typical printed resonator oscillator: (a) Schematic of printed resonator oscillator, and (b) Layout of printed resonator oscillator (Rogers RT/Duroid 5880 substrate) Frequency=8.05 GHz, power output =3.5dBm, DC power consumption=22mW, DC-RF conversion efficiency=10%, oscillator FOM=-207dBc/Hz [1]

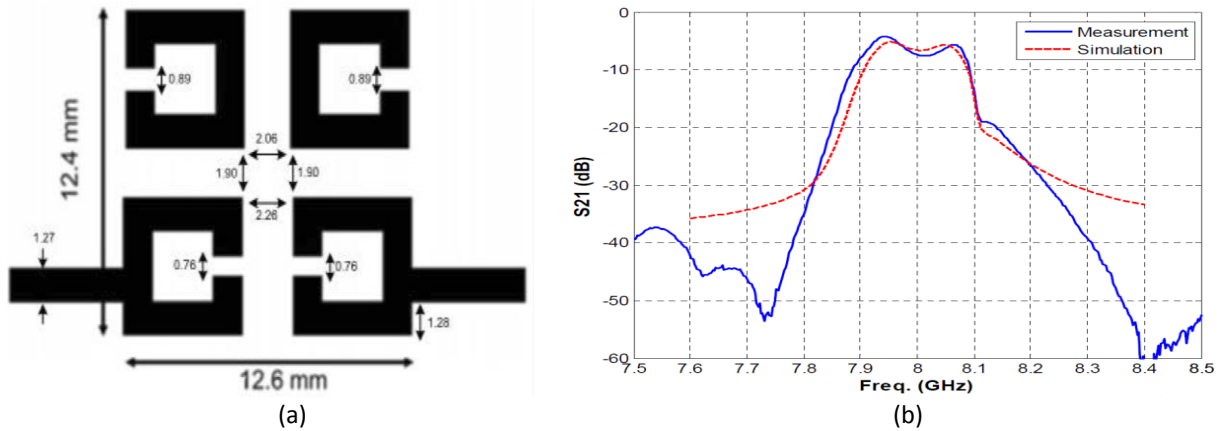


Figure C-2: (a) Layout of printed resonator (Roger 5880 subs.) BPF, (b) Insertion loss of the 4-pole elliptical BPF [1]

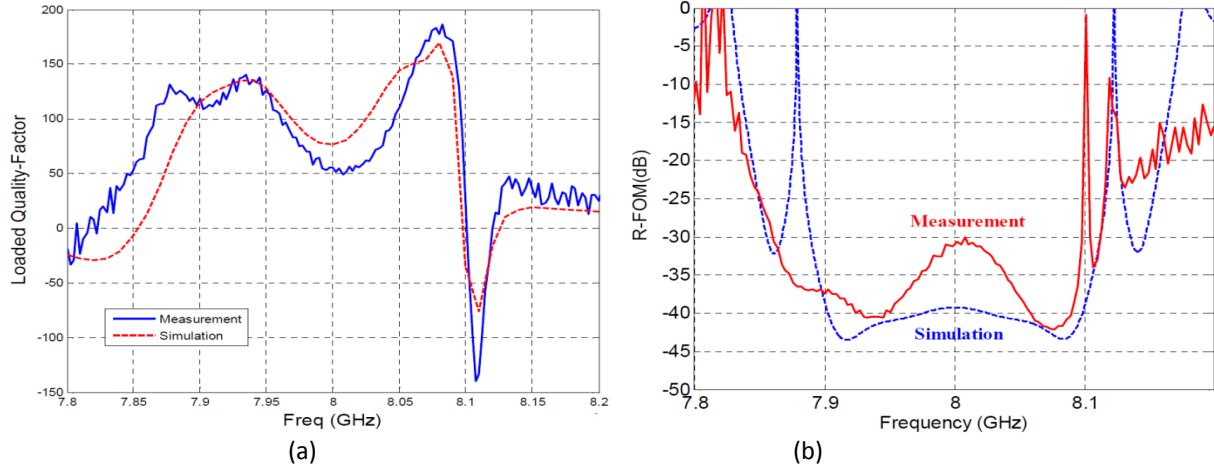


Figure C-3: Shows the simulated and measured (a) quality-factor, and (b) resonator figure of merit of 4-pole BPF [1]

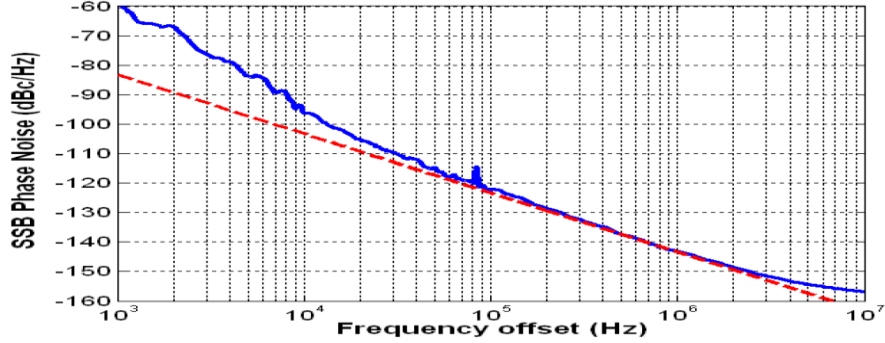


Figure C-4: Simulated (dashed line) and measured (solid line) phase noise plots of oscillator (Figure C-1) [1].

C3 Oscillator Based on Active Planar Resonator

High Q-factor planar active resonator can be realized by incorporating gain block for compensating resonator loss characteristics. Possibly, high Q active resonator can offer solution for low phase noise oscillator but most of the time this is not the case [5]. The resonator's excess noise associated with the gain block increases the noise level in the oscillator's loops which adversely affects its phase-noise. Due care must be taken to minimize the excess noise due to gain block embedded in the active resonator [6]. In addition to this, phase-noise reduction using active resonators comes at the cost of increased power consumption. The FOM of active resonator [FOM]_{AR} is given by [1]

$$[FOM]_{AR} = 10 \log \left(\frac{F_{AR}}{Q_{L-AR}^2} \right) \quad (C.1)$$

$$[FOM]_{AR} = 10 \log \left(\frac{1 + (m+1) \frac{2Q_{L-AR}}{Q_u}}{Q_{L-AR}^2} \right) \quad (C.2)$$

$$\text{where } F_{AR} = \left[1 + \left(\frac{2Q_{L-AR}}{Q_u} \right) + m \left(\frac{2Q_{L-AR}}{Q_u} \right) \right] \quad (C.3)$$

The active device in a resonator's loss compensation network consumes DC power in order to generate RF energy to compensate for the energy dissipation within the passive resonator. The power added by the active device is given by [7]-[9]

$$P_{\text{added}} = \frac{V_{\text{resonator}}^2}{2R_r} = \left(\frac{2Q_e}{Q_u} \right) P_{in} \Rightarrow \frac{P_{\text{added}}}{P_{in}} = \frac{2Q_{L-AR}}{Q_u} \quad (C.4)$$

The power added by the active device given in (C.4) shows the influence of active resonator's loaded quality-factor, increasing the active resonator's loaded quality-factor for lower phase-noise, which directly translates into higher power consumption with a rate of 10dB/decade, shown in Figure C-5 [10].

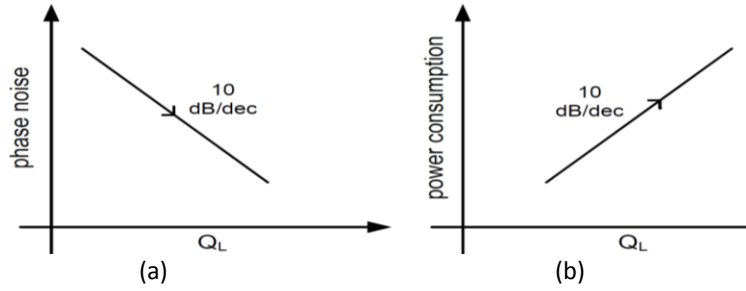


Figure C-5 Shows typical plot of phase noise and power consumption of oscillators versus the loaded quality-factor of the active resonators as their frequency stabilization elements: (a) Phase-noise, and (b) Power consumption.

Figure C-6 shows the typical circuit schematic of the printed active resonator oscillator consisting of an amplifier, the resonator, and a π -feedback-network, where the loaded quality-factor of the active resonator is controlled by adjusting the input/output coupling gaps (g) [1]. Figure C-7 shows the CAD simulated oscillator's phase-noise versus the active resonator's loaded quality-factor.

As shown in Figure C-7 (a), the simulated phase-noise plot monotonically decreases by increasing the resonator's loaded quality-factor (increasing g). The rate of the phase-noise improvement is close to 10dB/decade as predicted in Figure C-5 obtained from theoretical analysis (C.4). It can be seen from Figure C-7(a) that the active resonator with the loaded quality factor of 2000 improves the phase noise performance by 25 dB (-150dBc/Hz @ 1 MHz offset) as compared to oscillator using passive square loop resonator. However, this improvement comes at a price, which is increased power consumption.

As shown in Figure C-7(a), for the quality-factor of 2000, the amplifier in the resonator's loss compensation network should generate 28dBm of RF power (Red), which is about 125 times higher than the oscillator's output power level. Therefore, DC-to-RF power conversion efficiency is less than very poor (< 0.5%), and not suitable for handheld applications. The drawback of poor DC-to-RF power conversion efficiency can be overcome by incorporating Multi-coupled resonator based elliptical filter, which can provide higher loaded quality-factors compared to single resonators because of higher frequency-selectivity due to the presence of close-to-passband transmission zeros [2]-[13].

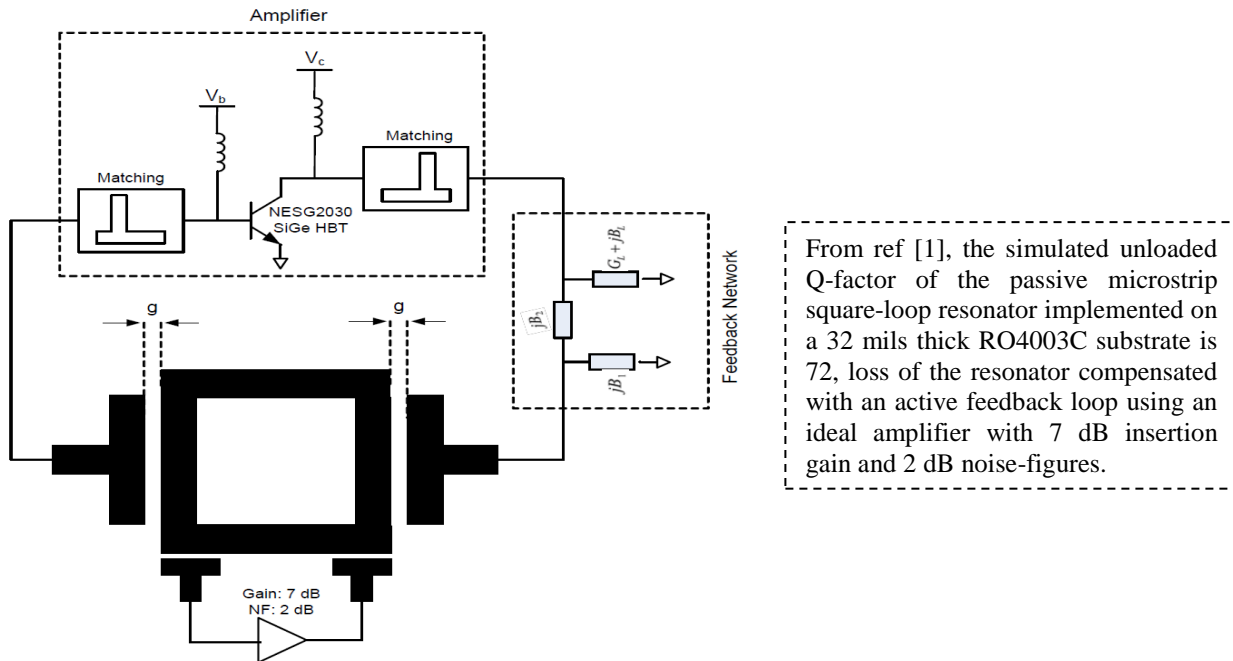
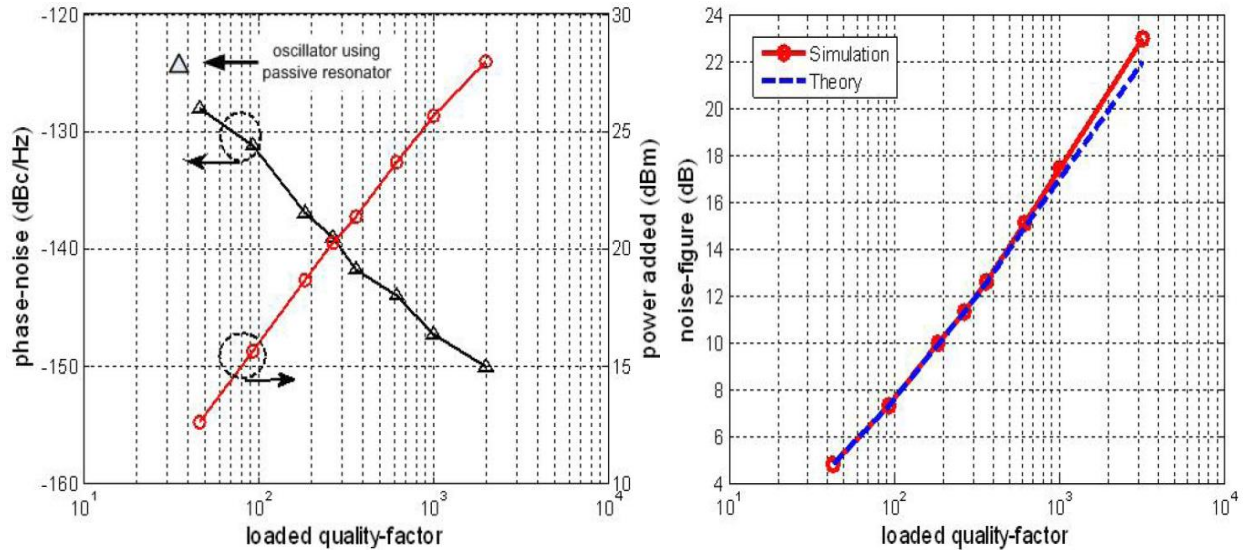


Figure C-6: A typical schematic of an 8 GHz oscillator using a square-loop active resonator with 7dBm output



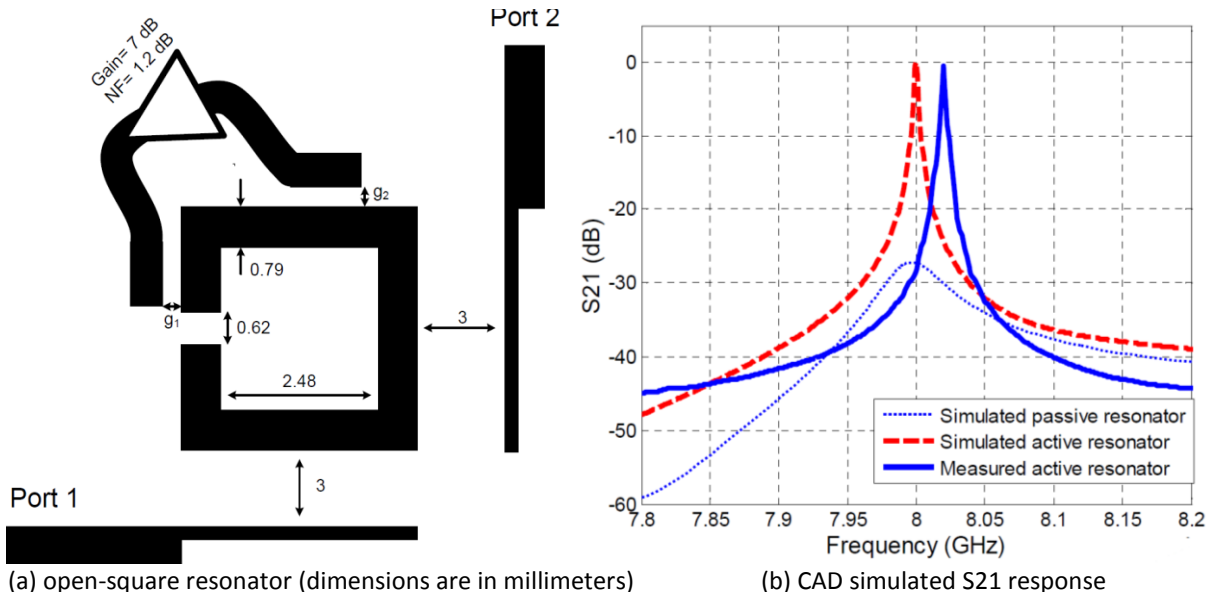
(a) Simulated phase-noise plot (Black) at the resonance frequency 8 GHz, amount of the power added (Red) by the amplifier (P_{added}) in the active resonator's loss compensation network [1]

(b) CAD simulated noise Figure calculated at the square loop resonance frequency of 8GHz [1]

Figure C-7: (a) CAD Simulated oscillator's phase-noise @ 1 MHz offset from the crier frequency 8 GHz versus the loaded quality-factor of its active resonator, and (b) CAD simulated noise-figure [1]

C4 Oscillator Based on Printed Multi-Coupled Active Resonator

Figure C-8 shows the typical open-loop square resonator designed at 8 GHz implemented on a Rogers' RO3035TM substrate with a dielectric constant of 3.55 and a thickness of 0.8 millimeters (32 mils) [1]. The passive resonator's unloaded quality-factor is 180. An ATF-33143 pHEMT transistor from Avago Technologies is selected to implement the amplifier in the feedback loop. The amplifier provides a gain of 7 dB with 1.2 dB noise figure.



(a) open-square resonator (dimensions are in millimeters)

(b) CAD simulated S21 response

Figure C-8: (a) An open-square resonator with an active feedback-loop for loss compensation, (b) Measured and simulated frequency response of the loosely-coupled active resonator compared to a similar passive resonator [1]

The optimum active resonator's feedback-loop design parameters are designed corresponding to Input/output coupling gaps (g_1 and g_2) as depicted in Figure C-8(a). Figure C-8 (b) illustrates the simulated S21 plot of the active resonator shown in Figure C-8(a); it can be seen the unloaded-quality-factor of active resonator is approximately 4000. The measured resonant frequency of the active resonator is slightly shifted to the higher side due to tolerances and parasitics. Figure C-9 shows the typical schematic of the elliptic filter in which the input and output resonators have been cross-coupled to realize the transmission zeros (built on a RO3035TM substrate).

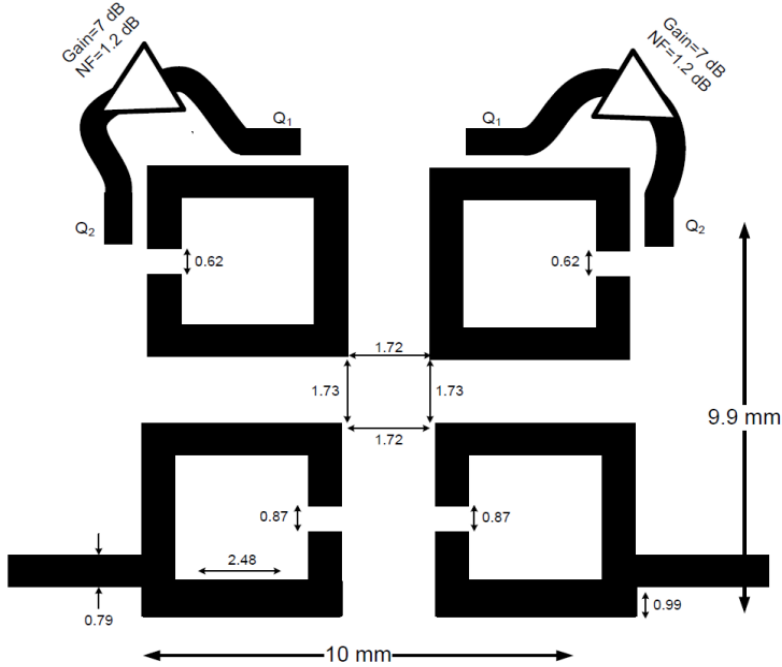
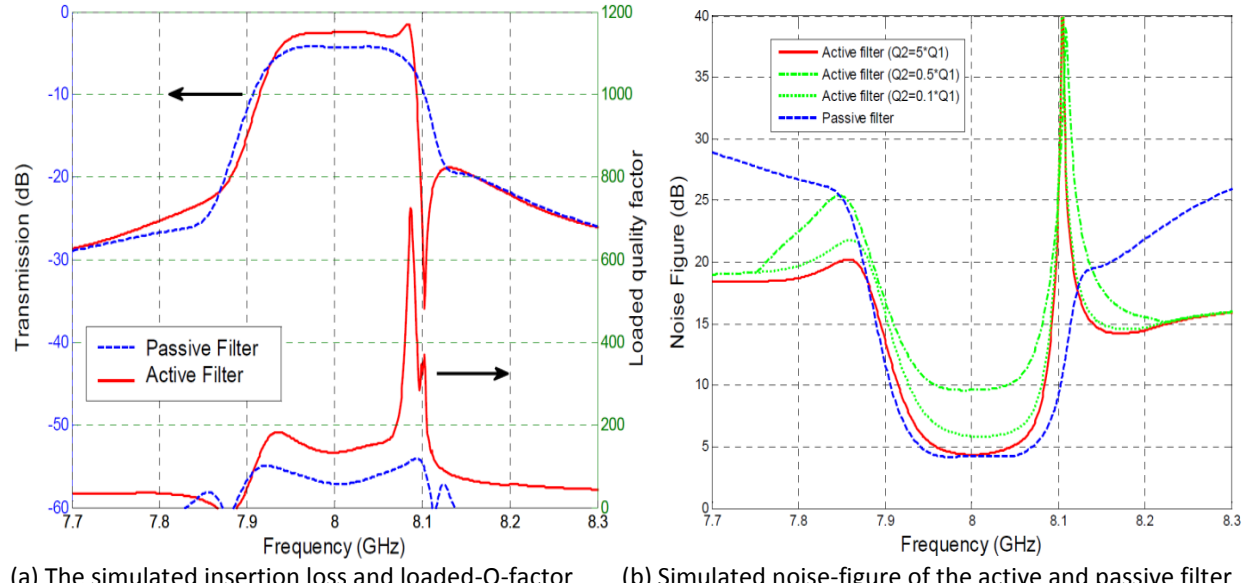


Figure C-9: A typical active four-pole elliptic-response band-pass filter [3]



(a) The simulated insertion loss and loaded-Q-factor (b) Simulated noise-figure of the active and passive filter

Figure C-10: Shows the CAD simulated plots: (a) insertion loss and loaded-quality-factor of the passive and active filter center frequency is 8 GHz with 130 MHz bandwidth, 10 dB return loss and normalized transmission-zero-location of 1.2, and (b) noise-figure of the active and passive filters (Noise-figure simulation results of various other active filters with different feedback-loop parameters Q_1 and Q_2 are also shown for comparison) [2].

As shown in Figure C-9, the gain block (Gain= 7dB, NF=1.2 dB) is not incorporated for compensating the loss at the input and output resonator loop because their loaded quality-factors are limited by primarily the external loadings rather than the internal resonators' losses. Figure C-10 shows the CAD simulated insertion loss and loaded quality-factor of the active filter, exhibits a peak loaded-quality-factor of 720 at the pass-band edge, which is about six times higher than that of the passive filter, suitable for the design of low phase-noise oscillators. As shown in Figure C-10, The 2.2 dB insertion loss of the active filter is due to the uncompensated input and output resonators' losses [2].

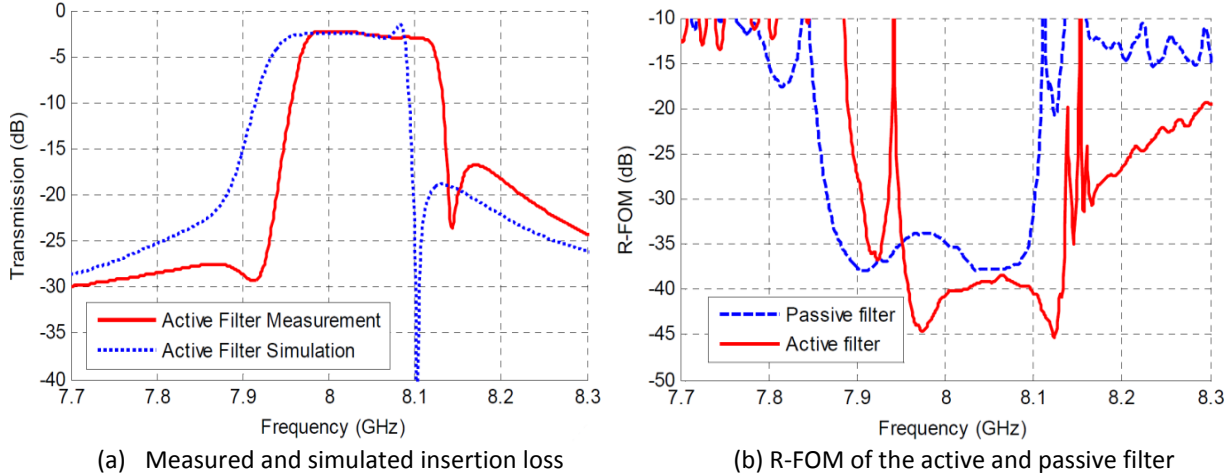


Figure C-11: The frequency performance plot of active filter: (a) Measured and simulated insertion loss of the active filter as shown in Figure C-9 [1, 2], and (b) R-FOM of the active and passive filter (without Q1 and Q2) shown in Figure C-9 (Lower R-FOM values are desired for low phase-noise oscillator applications) [1, 2]

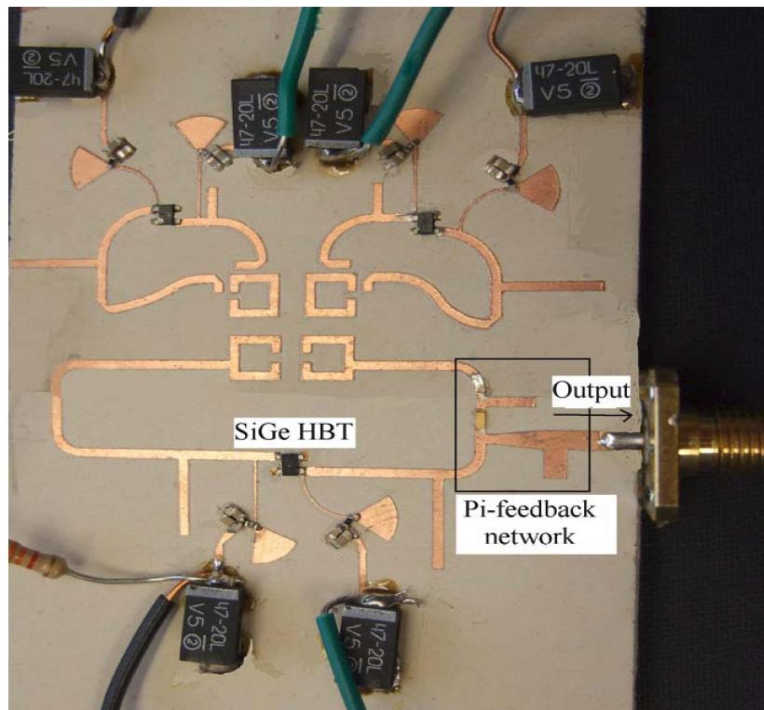


Figure C-12: Shows the layout of 8 GHz oscillator using multi-coupled active filter (transistor is biased at the collector voltage of 2 volts and collector quiescent current of 10 mA, the active device in the oscillator loop is an NESG2030M04 HBT SiGe transistor. The transistors of the active filter are ATF-33143 pHEMT devices; the π -network consists of a series capacitor and two shunt microstrip open stubs) [1, 2].

Figure C-11 shows the measured insertion loss of the active filter, shown in Figure C-9. A slight shift in its center frequency is due to the fabrication tolerances. The resonator FOM of the active filter is calculated based on (C.2) using the measured quality-factor and simulated noise figure of the active filter.

$$[FOM]_{AR} = 10 \log \left(\frac{F_{AR}}{Q_{L-AR}^2} \right) = [FOM]_{AR} = 10 \log \left(\frac{1+(m+1)^2 Q_{L-AR}}{Q_u^2} \right) \quad (C.5)$$

As shown in Figure C-11 (b), the active filter demonstrates up to 8 dB improvement in resonator FOM, compared to a passive filter with similar design parameters. Figure C-12 shows a picture of the fabricated oscillator using amplifier in the oscillator loop employs an NESG2030M04 HBT transistor from NEC with a gain of 8 dB [1, 2].

Figures C-13 (a) and C-13 (b) show the plot of phase noise and output power spectrum, the measured phase-noise at 1 MHz offset from the carrier is about -150 dBc/Hz, compared to an oscillator utilizing a similar passive filter, the oscillator with the active filter provides about 7 dB lower phase-noise at 1 MHz offset from the carrier. As shown in Figure C-13 (b), the oscillator resonance frequency is 7.990 GHz with an output power of 10 dBm. The total DC power consumption for oscillator is 200mW, corresponding to DC-to-RF efficiency of 5%. The core oscillator efficiency, not including the active resonators, is 31%.

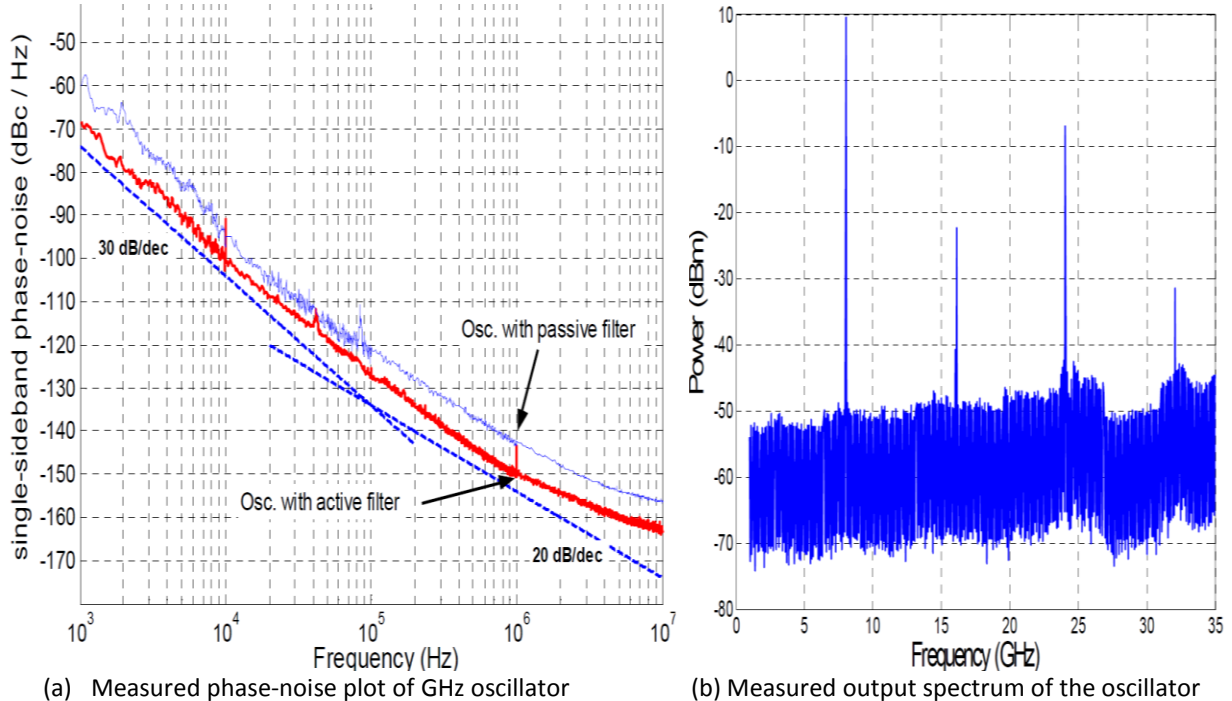


Figure C-13: The measured plots of: (a) phase-noise plot of 8 GHz oscillator using multi-coupled active filter (Figure C-9) at 1 MHz offset from the carrier is about -150dBc/Hz, and (b) Measured output spectrum of the oscillator

C5 Compact Oscillator using Active Printed Resonator

Figure C-14 shows the typical circuit schematic of the compact size dual-mode oscillator using series feedback network. As shown in Figure C-12, the series feedback is realized by connecting the second port of the filter to a reactive termination (jxT) in Figure C-14(a), to boost the filter's instability. The simulated input reflection coefficient of the active filter is shown in Figure C-14 (b) for two cases of matched and reactive terminations. From Figure C-14 (b), it can be seen that the reactive termination causes a strong peak in the input reflection coefficient. The peak frequency depends on the termination

value, jXT , and is set at the filter's pass-band edge for highest frequency selectivity and lowest phase-noise [12]. At the vicinity of the peak reflection coefficient, the reactively-terminated active filter behaves like a high-Q LC resonator having a negative resistance in shunt. The resonator is then connected to the load through the matching network. The matching network is designed based on the well-known device-line theory in order to maximize the oscillation power [10]. Figure C-15 shows the photo of the compact (physical size of the resonator is $7 \times 7 \text{ mm}^2$) prototype oscillator consisting of the high-Q dual-mode active filter, reactive termination, and the external load matching network [1, 13].

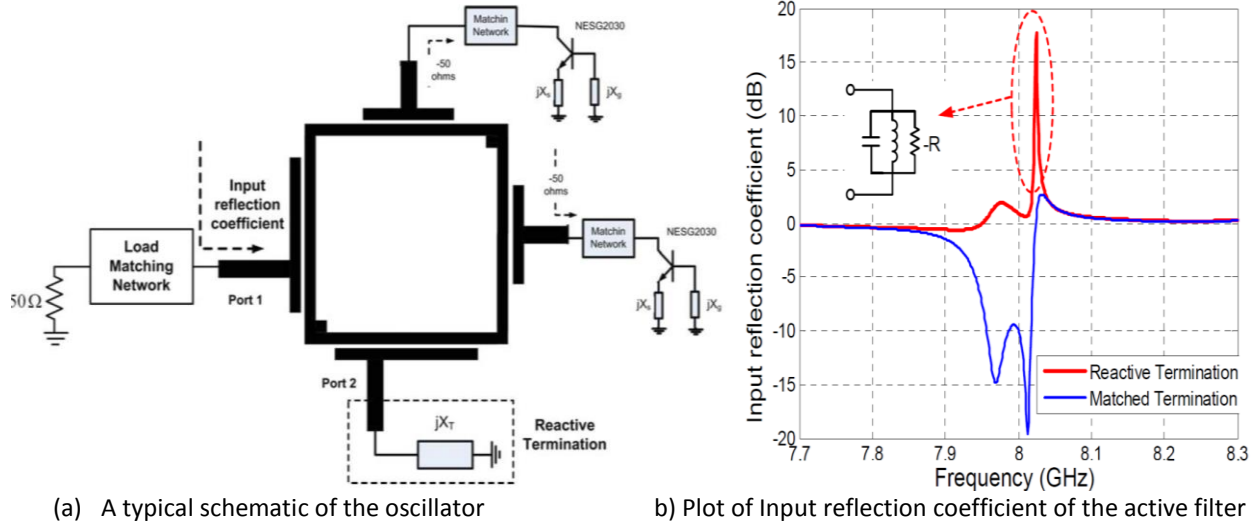


Figure C-14: (a) Dual-mode oscillator (reactive termination XT , and load matching network) consisting of the dual-mode active elliptic filter, and (b) Input reflection coefficient of the active filter (reactive termination causes a strong peak in the input reflection coefficient, at the vicinity of the peak the reactively terminated active filter behaves like a shunt LC resonator having a negative-resistance in shunt)

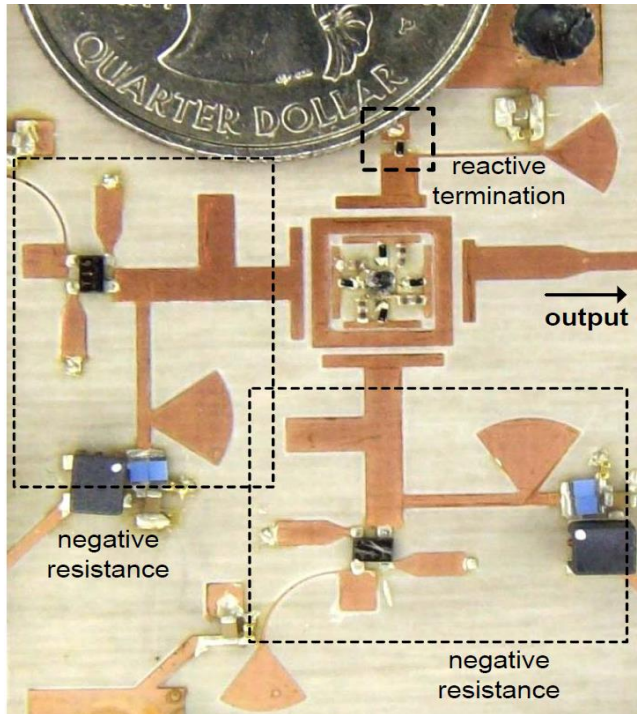


Figure C-15: Photo of tunable oscillator (8.15-8.25GHz) [1, 13]

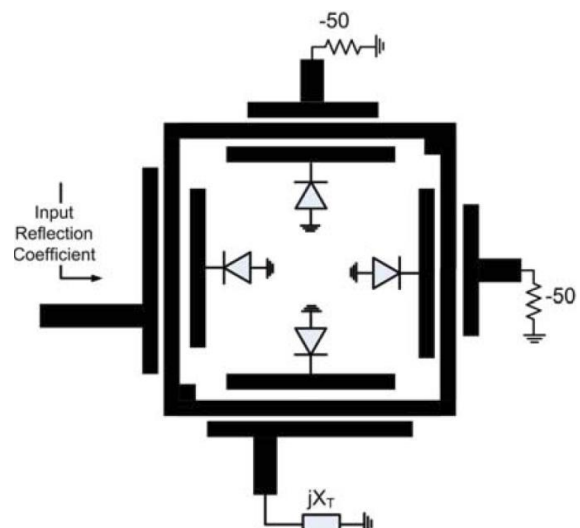


Figure C-16: The schematic shows an arrangement of varactor diodes coupled to the resonator for frequency tuning [1]

As shown in Figure C-15, active device (2-NESG2030M04 SiGe HBT transistors) with 2 dB noise figure and 8 dB associated gain is used to generate the negative-resistance for resonator loss compensation. The tuning diode (hyper-abrupt varactor diodes MA46H120 with capacitance ranges of 0.2-1 pF) is coupled with dual-mode resonator (Figure C-16), for frequency tuning. The measured oscillation frequency range is 8.150-8.255 GHz, with typical 7 dBm output and 12.5 % DC-RF conversion efficiency [13]. Figure C-17 shows the measured phase noise plot, typically better than -149dBc/Hz @ 1 MHz offset from the carrier frequency [14]. As shown in Figure C-17, the flicker phase-noise corner frequency is approximately 90 KHz. The VCO operates at 8.2 GHz with 105 MHz tuning range with 7 dBm output power and 12.5% DC-RF conversion efficiency, FOM is -211.7dBc/Hz [1, 13].

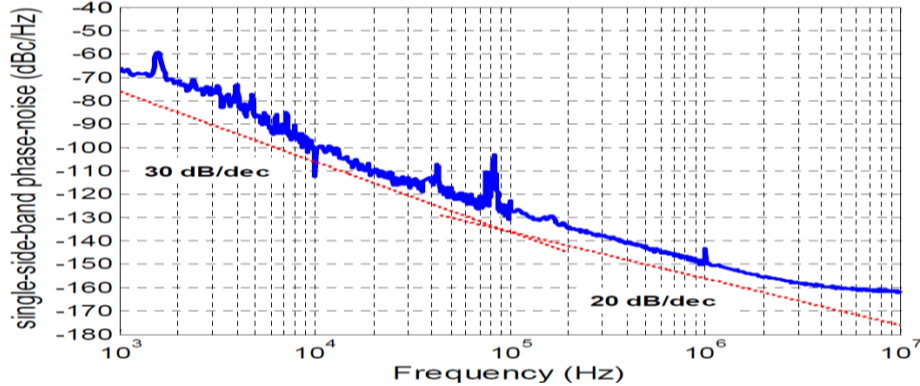


Figure C-17: Shows the measured phase-noise plot of dual mode resonator oscillator (resonant frequency: 8.2GHz)

C6 References

- [1] M. Nick, "New Q-Enhanced Planar Resonators for Low Phase-Noise Radio Frequency Oscillators", PhD Dissertation, Electrical Engineering, University of Michigan, 2011
- [2] C. M. Tsai and H.-M. Lee, "The effect of component Q distribution on microwave filters," *IEEE Trans. Microw. Theory Tech.*, vol. -54, no. 4, pp. 1545-1553, Apr. 2006.
- [3] L. Hsieh, and K. Chang, "High-efficiency piezoelectric-transducer tuned feedback microstrip ring-resonator oscillators operating at high resonant frequencies", *IEEE Trans. MTT*, vol.51, pp. 1141-1145, April 2003.
- [4] L. Dussopt, D. Guillois, and G. M. Rebeiz, "A low phase noise silicon 9 GHz VCO and 18 GHz push-push oscillator," in *IEEE MTT-S Int. Microwave Symp. Dig.*, vol. 2, pp. 695-698, June 2002.
- [5] Y.-T. Lee, J. Lee, and S. Nam, "High-Q active resonators using amplifiers and their applications to low-phase noise free-running and voltage-controlled oscillators", *IEEE Trans. MTT*, vol. 52, pp. 2621-2626, Nov. 2004.
- [6] J. Choi, and A. Mortazawi, "A new X-band low phase-noise multiple-device oscillator based on the extended-resonance technique," *IEEE Trans. Microw. Theory Tech.*, vol. -55, no. 8, pp. 1642-1648, August 2007.
- [7] J. Lee, Y.-T. Lee, and S. Nam, "A phase noise reduction technique in microwave oscillator using high-Q active filter," *IEEE Microw. Wireless Compon. Lett.*, vol. 12, no. 11, pp. 426-428, Nov. 2002.
- [8] J. Choi, M. Nick, and A. Mortazawi, "Low-phase-noise planar oscillators employing elliptic-response bandpass filters" *IEEE Trans. Microw. Theory Tech.*, vol. -57, no. 8, pp. 1959-1965, Aug. 2009
- [9] J. J. Rael, A. A. Abidi, "Physical processes of phase-noise in differential LC oscillators," in *Proc. of Custom Integrated Circuits Conference*, pp. 569-572, May 2000..
- [10] A. Grebennikov, "RF and microwave transistor oscillator design," New York: J. Wiley & Sons, 2007.
- [11] M. Tiebout, "Low-power low-phase-noise differentially tuned quadrature VCO design in standard CMOS," *IEEE J. Solid-State Circuits*, vol. 36, no. 7, pp. 1018-1024, Jul. 2001.
- [12] A. P. S. Khanna, E. Topacio, E. Gane, and D. Elad, "Low jitter silicon bipolar based VCOs for applications in high speed optical communication systems" in *IEEE MTT-S Symp. Dig.*, May 2001, pp. 1567-1570.
- [13] M. Nick, and A. Mortazawi, "Low phase-noise planar resonators based on low noise active resonators" *IEEE Trans. Microw. Theory Tech.*, vol. 55, no. 5, pp. 1133-1139, May 2010.
- [14] A. Victor, and M. B. Steer, "Reflection coefficient shaping of a 5-GHz voltage tuned oscillator for improved tuning", *IEEE Trans. Microw. Theory Tech.*, vol. -55, no. 12, pp. 2488-2494, Dec. 2007.

Appendix D

D1 Multi-Mode Resonator Oscillators

Printed resonator structure can support multi-band multi-mode resonance condition for modern radio architecture. In multi-band multi-mode radio architectures, a number of local oscillator (LO) frequencies are required in order to process the information in various frequency bands. Various methods have been explored to mitigate the mode-jumping and improve the quality factor (Q-factor) and achieve miniaturizations. Since oscillators consume a substantial part of the chip area and battery power, in order to mitigate these issues, the design approach described in here uses a slow-wave resonator. The tunable multi-band multimode injection-locked oscillator can simultaneously generate multiple frequencies, with the user having an option to select the frequency or the combination of frequencies. This eliminates the need for lossy switch to swap the frequency band and thereby improves the throughput. [1-20].

D2 Multi-Mode Resonator Configurations

Figure D-1 shows typical resonator topologies used for multi-mode operation. These topologies possess a pair of degenerate resonant modes whose resonant frequencies split when a perturbation element is strategically introduced. In recent years, multi-mode resonators have been increasingly used in wireless communication systems and other RF applications for their low-loss and compact properties [1]-[7]. Because of their multi-mode resonant characteristics, a multi-mode resonator of a certain order requires half as many resonators when compared to a single mode-resonator for a given Figure of Merit [8].

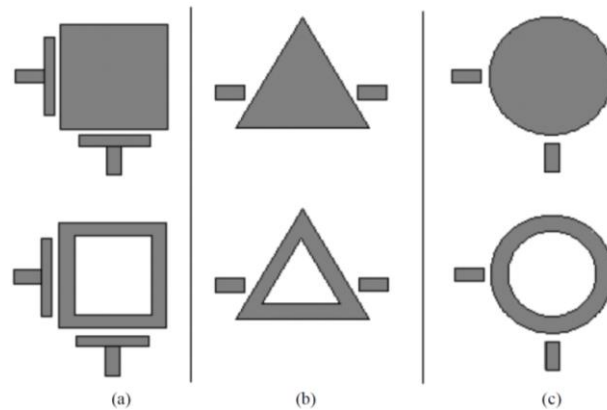


Figure D-1 resonator topologies for dual-mode operation (a) square shape (b) triangular shape (c) circular shape [2].

D3 Frequency Modes of Planar Resonator Networks

A closed circular annular ring and square loop are most common planar resonators for low cost oscillator applications. Figure D-2 shows the typical configurations of the 1-port closed loop square and ring resonators used in oscillator circuits. As shown in Figure D-2, the total length l of any general shaped ring resonator can be divided into l_1 and l_2 sections, whereas in the case of the square ring, each section is considered to be a transmission line associated with coordinates z_1 and z_2 respectively [8].

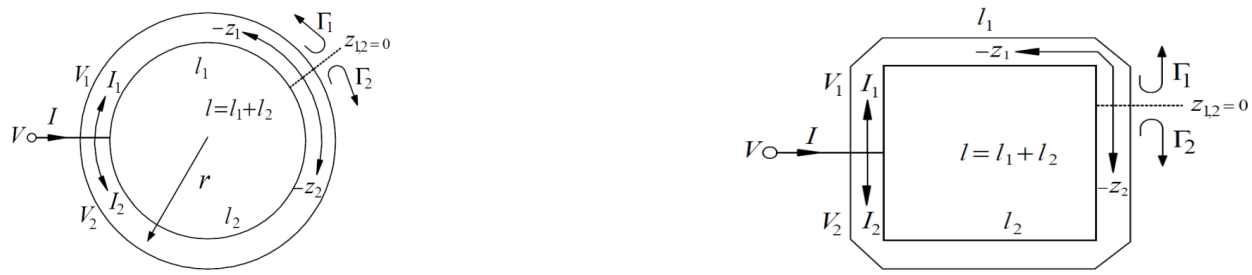


Figure D-2A: (a) A planar closed loop 1-port resonator (a) 1-port annular ring and (b) 1-port square resonator [8].

For a lossless transmission line, the voltages and currents associated with the sections I_1 and I_2 can be described by

$$V_{1,2}(z_{1,2}) = V_o^+ (e^{-j\beta z_{1,2}} + \Gamma_{1,2}(0)e^{j\beta z_{1,2}}) \quad (\text{D.1})$$

$$I_{1,2}(z_{1,2}) = \frac{V_o^+}{Z_o} (e^{-j\beta z_{1,2}} - \Gamma_{1,2}(0)e^{j\beta z_{1,2}}) \quad (\text{D.2})$$

where $V_o^+ e^{-j\beta z_{1,2}}$ is the incident wave propagating in the $+Z_{1,2}$ direction, $V_o^+ \Gamma_{1,2}(0)e^{j\beta z_{1,2}}$ is the reflected wave propagating on the $-Z_{1,2}$ direction, β is the propagation constant, $\Gamma_{1,2}(0)$ is the reflection coefficient at $Z_{1,2} = 0$, Z_o is the characteristic impedance of the ring

From (D.1) and (D.2), resonance occurs when the ring circumference ($I_1 + I_2 = 2\pi r$) is equal to an integral multiple of a guided wavelength, initiating standing wave dynamics on the ring structure. The minimum length of the ring resonator that supports standing wave dynamics can be derived from the location that corresponds to maxima of these standing waves, calculated by letting the derivatives of the voltages and currents equal to zero in (D.1) and (D.2):

$$\frac{\partial V_{1,2}(z_{1,2})}{\partial z_{1,2}} = -j\beta V_o^+ (e^{-j\beta z_{1,2}} - \Gamma_{1,2}(0)e^{j\beta z_{1,2}}) \Rightarrow \left. \frac{\partial V_{1,2}(z_{1,2})}{\partial z_{1,2}} \right|_{z_{1,2}=0} = 0 \rightarrow \Gamma_{1,2}(0) = 1 \quad (\text{D.3})$$

From (D.1)-(D.3), the absolute maximum value of voltage is given by

$$V_{1,2}(z_{1,2}) = 2V_o^+ \cos(\beta z_{1,2}) \Rightarrow |V_{1,2}(z_{1,2})|_{max} = 2V_o^+ (z_{1,2} = m \frac{\lambda_g}{2}, m = 0, -1, -2, -3 \dots) \quad (\text{D.4})$$

$$I_{1,2}(z_{1,2}) = -j \frac{2V_o^+}{Z_o} \sin(\beta z_{1,2}) \Rightarrow I_{1,2}(z_{1,2}) \Big|_{z_{1,2}=m \frac{\lambda_g}{2}} = 0 \quad (I_{1,2} \text{ at location } m \frac{\lambda_g}{2}) \quad (\text{D.5})$$

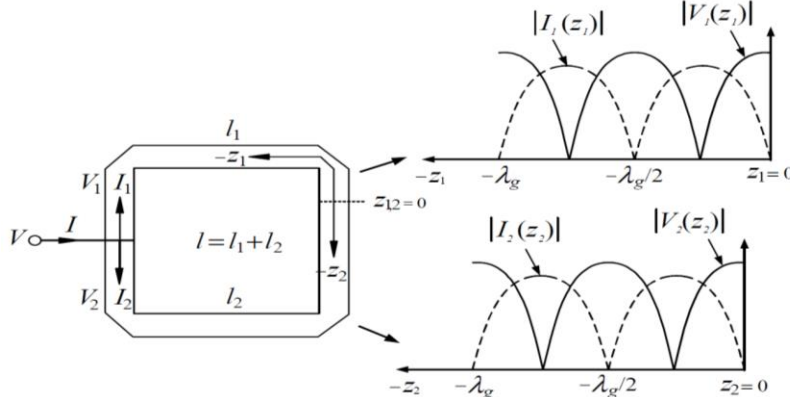


Figure D-2B: A typical representation of standing wave dynamics on section (l_1 and l_2) of the square ring resonator.

Similarly, the absolute values of the maximum currents from (D.2) is given by

$$|I_{1,2}(z_{1,2})|_{max} = \frac{2V_o^+}{Z_o} \text{ for } (z_{1,2} = (2m - 1) \frac{\lambda_g}{4}, m = 0, -1, -2, -3 \dots) \quad (\text{D.6})$$

$$V_{1,2}(z_{1,2}) \Big|_{z_{1,2} = (2m-1)\frac{\lambda_g}{4}} = 0. \quad (\text{D.7})$$

Equations (D.4) and (D.6), show the absolute values of voltage and current standing waves on each section l_1 and l_2 of the square ring resonator and as illustrated in Figure D-2b, standing wave dynamics repeat for multiples of $\lambda_g/2$ on each section of the ring. Therefore, to support standing wave dynamics corresponding to the fundamental mode, the minimum length of each section is equal to $\lambda_g/2$. Whereas, for higher order modes, each section length can be given by

$$I_{1,2} = n \frac{\lambda_g}{2} \text{ (for } n = 1, 2, 3, \dots) \Rightarrow l = l_1 + l_2 = n \lambda_g \quad (\text{n: mode number for square ring}) \quad (\text{D.8})$$

$$l = l_1 + l_2 = n \lambda g = 2\pi r \quad (\text{n: mode number for annular ring}) \quad (\text{D.9})$$

Equations (D.8) and (D.9) are general expressions for frequency modes of any closed loop configuration of microstrip ring resonators [5]-[9]. The multi-mode dynamics is composed of two or more degenerate modes or splitting resonant frequencies, generated by perturbing stubs, notches, or asymmetrical feed lines.

For example, if a ring resonator without perturbations is excited by symmetrical feed lines, only one of the degenerate modes exists, since both modes traveling clockwise and counter-clockwise on the ring resonator are orthogonal to each other without any coupling. However, if the ring resonator is perturbed, two degenerated modes are excited and couple to each other.

Figure D-3 illustrates the dual mode dynamics corresponding to single perturbation at 45° on microstrip square ring resonator designed at fundamental mode of 2 GHz, fabricated on a RT/Duroid 6010.2, $\epsilon_r = 10.2$ substrate with a thickness $h = 25$ mil [8].

As illustrated in Figure D-3, multi-mode dynamics is set up with a perturbing stub at the corner of the square resonator ($\Phi = 45^\circ$) for the value of $n = 1$ and the $n = 2$ modes. For $n = 1$ mode, one of $\lambda g/2$ resonators is perturbed, thus two $\lambda g/2$ resonators fail to balance each other, creating two splitting electrical currents of different resonant frequencies, depicted in Figure D-3 (a) and (b).

For the $n = 2$ mode, as shown in Figure D-3 (c), the perturbing stub is located at the position of zero voltage which is a virtual short circuit. Hence, the perturbation does not disturb the resonator, both $\lambda g/2$ resonators balance each other without frequency splitting.

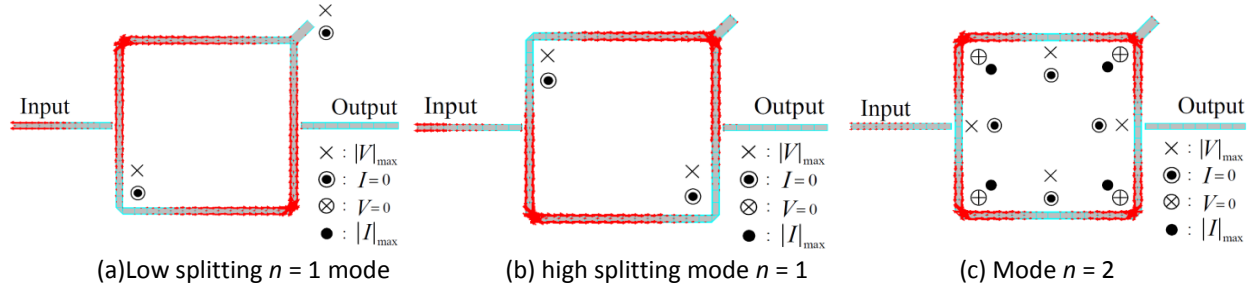


Figure D-3: Shows a typical illustration of electrical currents of the square ring resonator with a perturbation with small stub at $\Phi = 45^\circ$: (a) low splitting resonant frequency of $n = 1$ mode, (b) high splitting resonant frequency of mode $n = 1$, and (c) mode $n = 2$ [8]

Figure D-4 shows the measured S_{21} confirming the splitting frequencies for the $n = 1$ mode around 2 GHz, whereas resonant frequency at the $n = 2$ mode of 4 GHz is not affected by the perturbation.

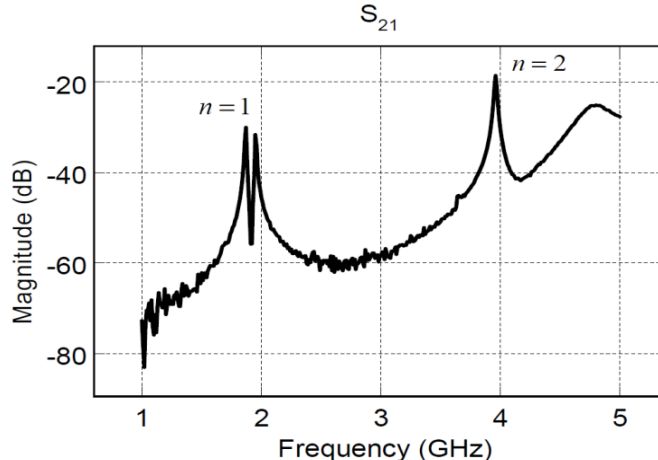


Figure D-4: The measured results for modes $n = 1$ and 2 of the square ring resonator with a perturbed stub at the corner of microstrip square resonator ring ($\Phi = 45^\circ$) [8]

D4 Resonant Properties of Dual-Mode Resonators

Figure D-5 shows the typical configuration and field pattern of perturbed dual-mode square-loop microstripline resonator [6]. As shown in (Figure D-5), two orthogonal resonant modes exist along its vertical and horizontal axes, where the excited resonant mode is associated to TM_{100}^Z mode when Port # 1 is excited, where z is the axis perpendicular to the ground plane [5]. When the excitation port is changed to Port # 2, the field patterns are rotated by 90° for the vertical degenerate mode that corresponds to TM_{010}^Z mode (Figure D-6). Interestingly, the two modes exhibit identical resonant frequencies without the perturbation ($d=0$), however, for a small perturbation ($d\neq 0$), the modes are coupled to each other causing splitting in resonant frequencies as depicted in Figure D-7. The coupling coefficient 'k' depends upon the geometry of the perturbation, and it can be described by

$$k = \left[\frac{\int \epsilon E_a \cdot E_b dv}{\sqrt{\int \epsilon E_a^2 dv \int \epsilon E_b^2 dv}} + \frac{\int \mu H_a \cdot H_b dv}{\sqrt{\int \mu H_a^2 dv \int \mu H_b^2 dv}} \right] \quad (D.10)$$

where E_a and H_a are, respectively, the electric and magnetic fields produced by the square loop ring resonator, and E_b , H_b are the corresponding fields due to the perturbation ($d\neq 0$) or nearby adjacent resonator (second square loop resonator). The definition of 'k' given in (D.10) is not practical for calculation purposes since it requires the knowledge of the electromagnetic fields everywhere on the closed loop. A useful practical alternative expression for 'k' can be obtained from a well-known fact in physics: in presence of small perturbation ($d\neq 0$), the modes are coupled to each other causing splitting in resonant frequencies f_1 and f_2 , different from their original resonant frequency f_0 . These two frequencies f_1 and f_2 are associated with two normal modes of oscillation of the coupled system, and their difference increases as the coupling due to perturbation between stub ($d\neq 0$) and the resonator increases, and can be approximately formulated as [10]-[11]

$$k = \pm \frac{f_2^2 - f_1^2}{f_2^2 + f_1^2} \quad (D.11)$$

where f_1 and f_2 are the lower and upper resonant frequencies.

From (D.11), the sign of 'k' depends on the nature of coupling and geometry of the perturbation. For example, a square small patch perturbation ($d > 0$), exhibits electric coupling with positive k , whereas magnetic coupling with negative k is created through a corner cut ($d < 0$) [12]-[13].

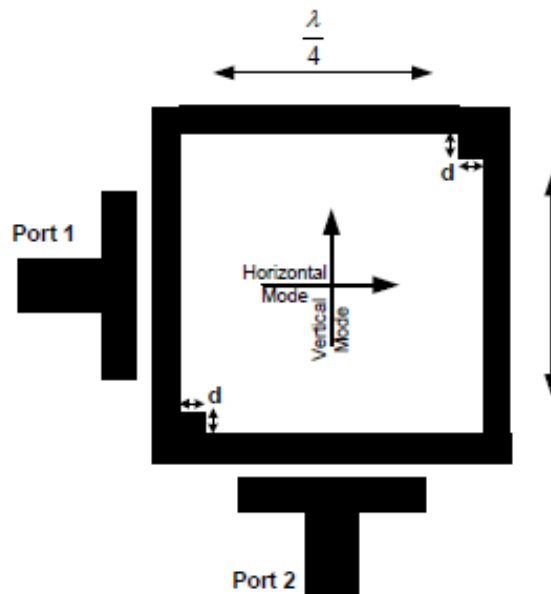


Figure D-5: A typical configuration and field pattern of perturbed dual-mode square-loop microstripline resonator

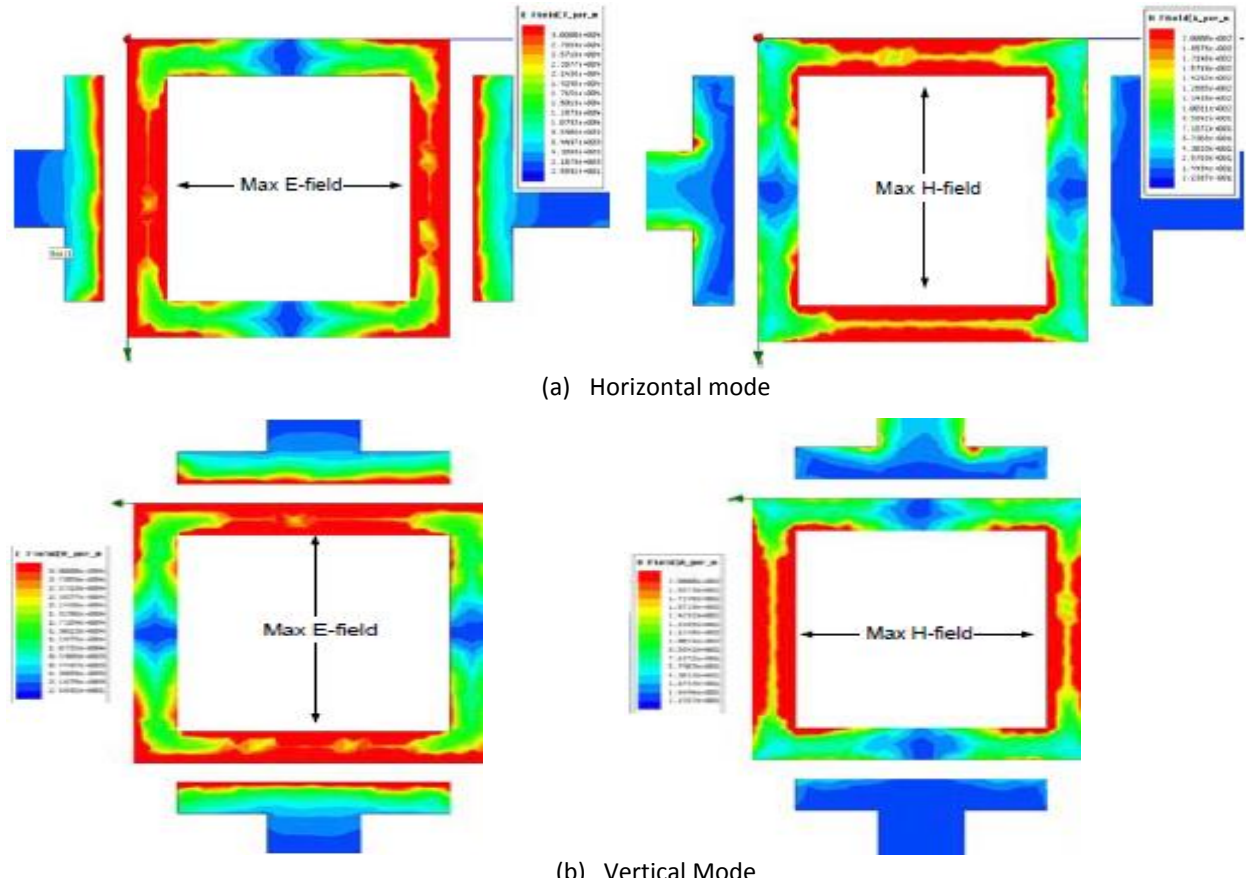


Figure D-6: CAD simulated Field pattern of square loop ring resonator: (a) horizontal mode, the electric and magnetic field patterns indicate that the excited resonant mode is corresponding to TM_{100}^Z mode when port 1 is excited, where z is the axis perpendicular to the ground plane, and (b) Field pattern of vertical mode, When the excitation port is changed to Port # 2, the field patterns are rotated by 90° for the vertical degenerate mode that corresponds to TM_{010}^Z mode [6]

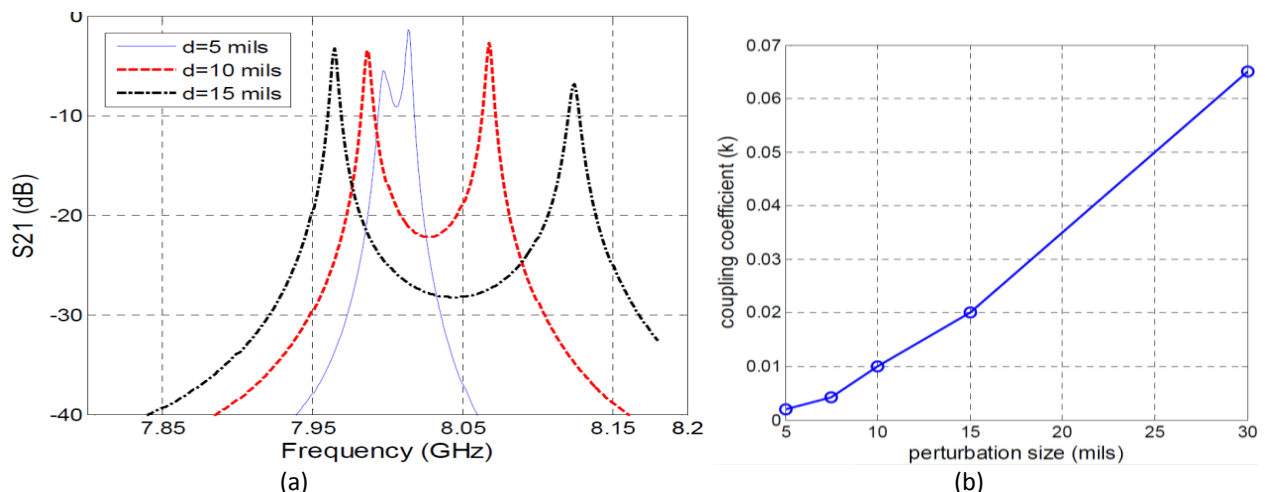


Figure D-7: Shows the CAD simulated plots of perturbed ($d \neq 0$) square loop dual-mode resonator periphery $l = 950$ mils and $w = 32$ mils thick RO4003C substrate at 8 GHz, the modes are coupled to each other and resonant frequency splitting occurs: (a) frequency splitting due to mode-coupling in a square-loop dual-mode resonator shown in Figure D-5), and (b) calculated coupling coefficient ' k ' versus perturbation size d [6]

As shown in Figure D-8, the input/output ports can be coupled to both modes through offset-to-center feeding lines, where external loading effects on the horizontal and vertical modes are represented by the external quality-factors, Q_e^h and Q_e^v [6]. The quality factor of the dual-mode square loop resonator is an important yard stick for designing low phase noise oscillator circuits, Q-factor can be described by [10]

$$Q_e = \frac{f_0}{f_{+90^\circ} - f_{-90^\circ}} \quad (\text{D.12})$$

where f_{+90° and f_{-90° represents the frequencies at which the phase of S_{11} (for horizontal mode) or S_{22} (for vertical mode) shows $+90^\circ$ and -90° difference with respect to the phase at center frequency, f_0 [6]-[10]. For brief insights about the Q-factor, Figure D-8(b) shows the calculated external quality-factor curves versus the feeding line's dimensions.

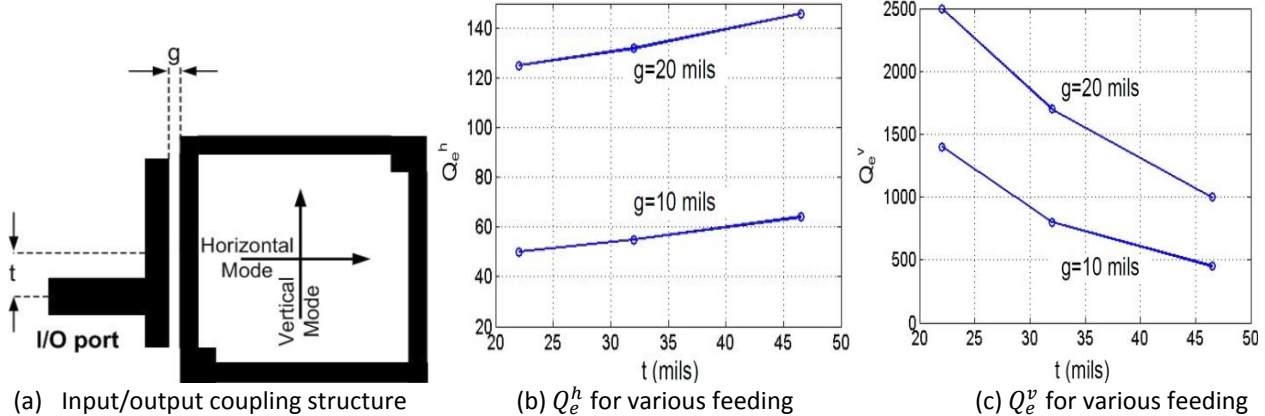


Figure D-8: A typical I/O coupling structure for the dual-mode square-loop resonator with periphery $l = 950$ mils and $w=32$ mils thick RO4003C substrate at 8 GHz (a) I/O port is coupled to both modes through offset to center feeding line, (b) calculated Q_e^h for various feeding line dimensions, and (c) calculated Q_e^v for various feeding line dimensions (Q_e^h and Q_e^v are horizontal and vertical modes external quality-factors due to the loading from I/O line).

D5 Dual Mode Resonators Examples

D5.1 Dual-mode Resonator Using a Single Ring Resonator

The dual-mode consists of two degenerate modes, which are excited by asymmetrical feed lines, added notches, or stubs on the ring resonator (Figure D-9) [14]-[17]. The coupling between the two degenerate modes is used to construct a high Q resonator for dual-mode oscillator applications. As shown in Figure D-9 (a), asymmetrical structure perturbs the field of the ring resonator, excites two degenerate modes, without the tuning stubs, there is no perturbation on the ring resonator and only a single mode is excited.

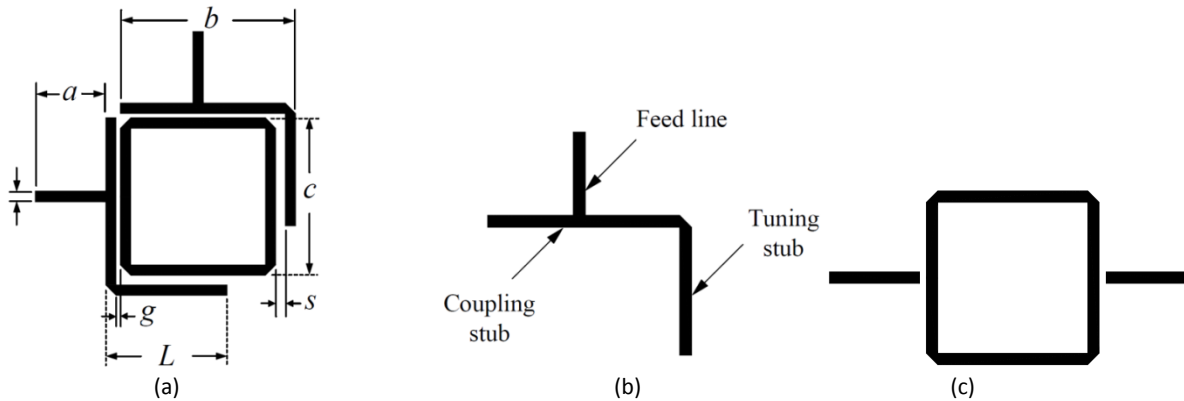


Figure D-9: Dual-mode resonator: (a) layout, (b) L-shape coupling, and (c) square ring resonator for Q measurement

Comparing the dual mode resonator (Figure D-9) with conventional ones (Figure D-8), which use perturbing notches or stubs inside the ring resonator, the conventional filters only provide dual mode characteristics without the benefits of enhanced coupling strength and performance optimization. Table D-1 shows the comparative analysis of 3-cases by varying gap size s with a fixed length $L = 13.5$ mm that generate dual-mode characteristics [8]. The coupling coefficient between two degenerate modes and mid-band insertion loss L_A is given by

$$K = \frac{f_{p2}^2 - f_{p1}^2}{f_{p2}^2 + f_{p1}^2} \quad (\text{D.13})$$

$$L_A = 20 \log \left[\frac{(1+Q_e/Q_u)^2}{2KQ_e} + \frac{KQ_e}{2} \right] \text{ dB} \quad (\text{D.14})$$

where f_{p1} and f_{p2} are the resonant frequencies, L_A is mid-band insertion loss, Q_u and Q_e are unloaded and external Q-factor, and K is coupling coefficient. Figure D-10 (a) shows the square perturbation stub at $\Phi = 45^\circ$ on the ring resonator, where square stub perturbs the fields of the ring resonator in such a way that the resonator can excite a dual mode around the stopband in order to improve the narrow stopband. By increasing (decreasing) the size of the square stub, the distance (stopband bandwidth) between two modes is increased (decreased). The equivalent circuits of the square stub and the filter are displayed in Figure D-10 (b) and (c), respectively. It can be seen in Figure D-10 (b); the geometry at the corner of $\Phi = 45^\circ$ is approximately equal to the square section of width $w_1 + w_p$, subtracting an isometric triangle of height w_1 . Also, the equivalent L-C circuit of this approximation is shown in Figure D-10(c) where $c_{pf} = c_r - c$ and $L_p = \frac{LL_r}{L-L_r}$. The equivalent capacitance and inductance of the right angle bend, C_r and L_r , are given by [18]

$$C_r = 0.001h \left[\left((10.35\epsilon_r + 2.5) \left(\frac{w_1+w_p}{h} \right)^2 + 2.6\epsilon_r + 5.64 \right) \left(\frac{w_1+w_p}{h} \right) \right] \text{ pF} \quad (\text{D.15})$$

$$L_r = 0.22h \left\{ 1 - 1.35 \exp \left[-0.18 \left(\frac{w_1+w_p}{h} \right)^{1.39} \right] \right\} \text{ nH} \quad (\text{D.16})$$

$$C_s = w_p(0.012 + 0.0039\epsilon_r) \text{ pF} \quad (\text{D.17})$$

Figure D-11 shows the typical cascaded multiple ring resonators, exhibit narrower and shaper rejection band than the single ring resonator.

Table D-1: Measured Dual mode Microstrip Line Square Ring Resonator Characteristics [8]

	Case 1: $L = 13.5$ mm $S = 0.3$ mm	Case 2: $L = 13.5$ mm $S = 0.5$ mm	Case 3: $L = 13.5$ mm $S = 0.8$ mm
Resonant Frequency: f_{p1}, f_{p2}	(1.72, 1.855) GHz	(1.7, 1.84) GHz	(1.672, 1.81) GHz
Coupling coefficient: k	0.075	0.078	0.08
External Q: Q_e	6.24	7.9	9.66
Midband Insertion loss IL	2.9dB	1.63dB	1.04dB
3-dB Bandwidth	160 MHz	175 MHz	192.5 MHz
Coupling condition	Undercoupled	Undercoupled	Undercoupled
Substrate	RT/Duroid 6010.2	RT/Duroid 6010.2	RT/Duroid 6010.2
Dielectric Constant : ϵ_r	10.2	10.2	10.2
Width of Line: w	1.191mm	1.191mm	1.191mm
Feed line :a	8 mm	8 mm	8 mm
length of the coupling stub: b	18.839 + s mm	18.839 + s mm	18.839 + s mm
gap size: g	0.2 mm	0.2 mm	0.2 mm
Length: c	17.648 mm	17.648 mm	17.648 mm
Thickness of substrate	50-mil	50-mil	50-mil
Medium	Micro stripline	Micro stripline	Micro stripline

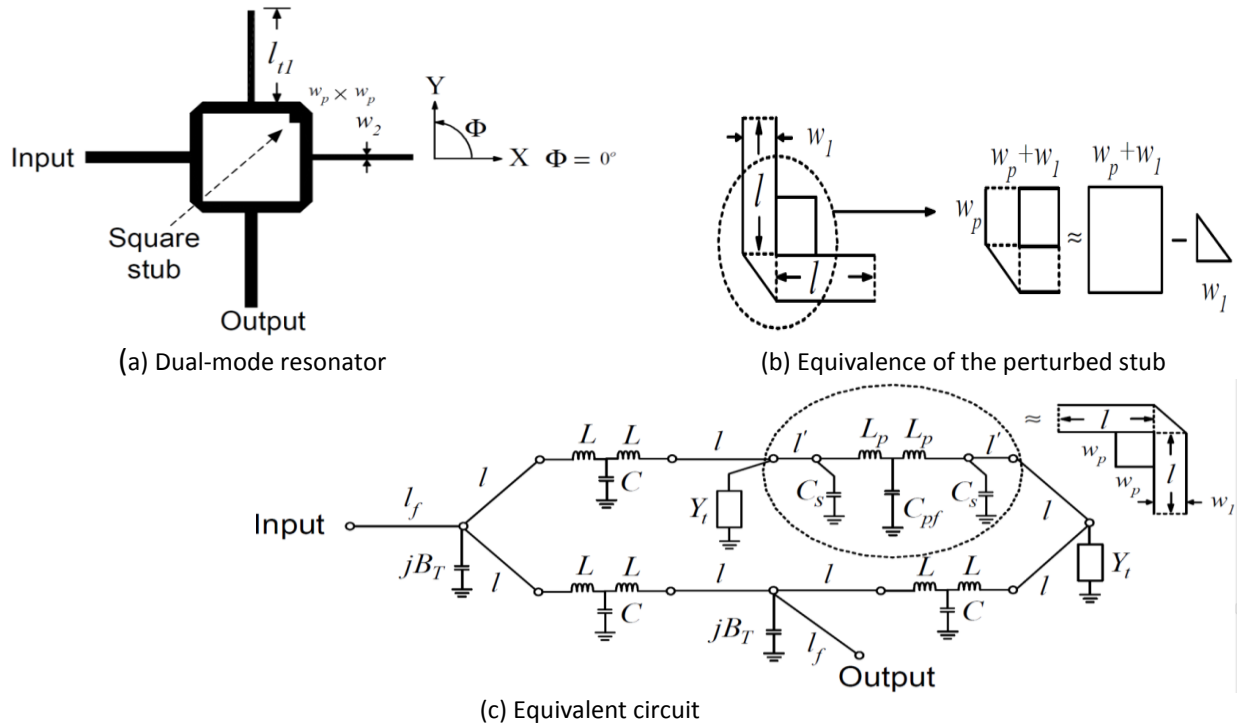


Figure D-10: A typical dual-mode resonator: (a) layout, (b) equivalence of the perturbed stub, (c) equivalent circuit.

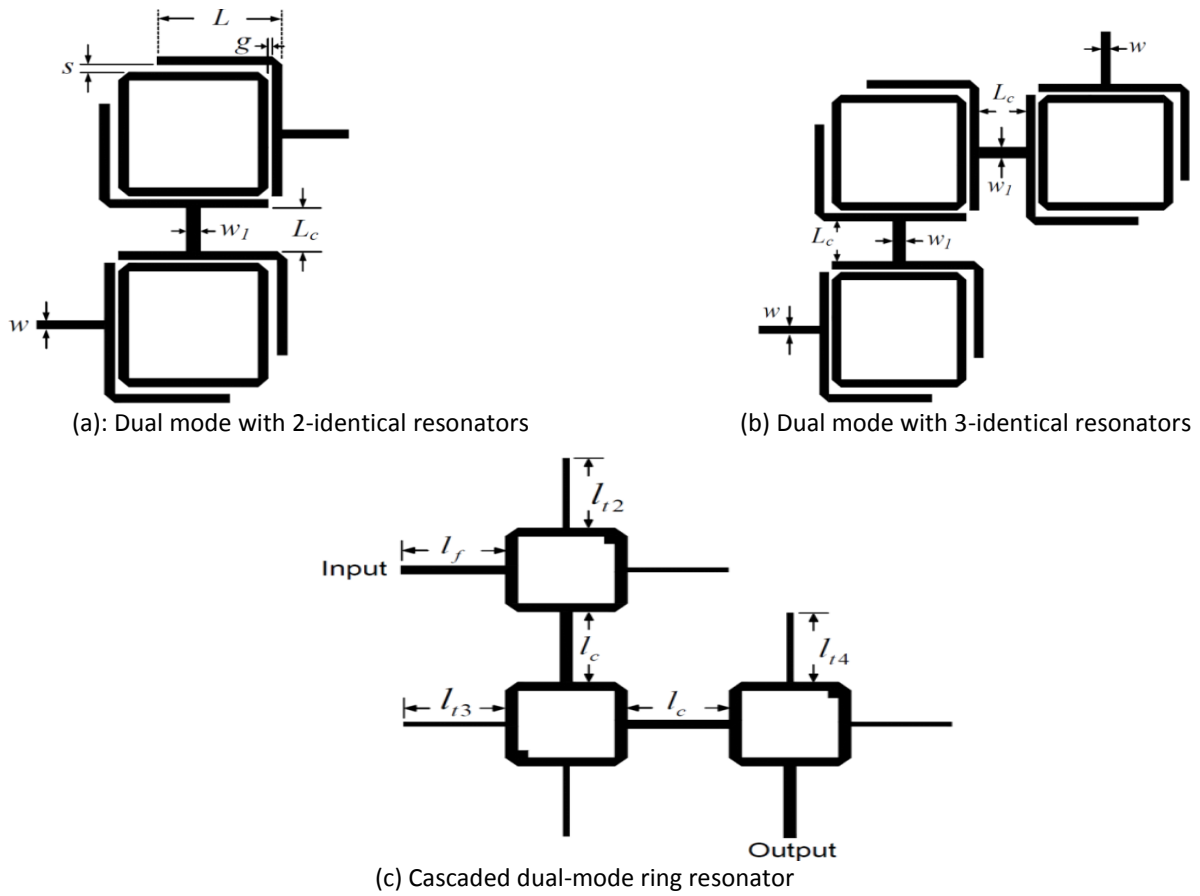


Figure D-11: Shows the dual-mode resonator: (a) with two identical resonators and L-shape coupling arms, (b) 3-identical resonators with L-shape coupling arms, and (c) cascaded configuration of dual-mode ring resonator

D6 Dual-mode Printed Active Resonator

Figure D-12 shows the typical dual-mode miniaturized active resonator, each resonant mode is coupled to a negative-resistance device for loss compensation.

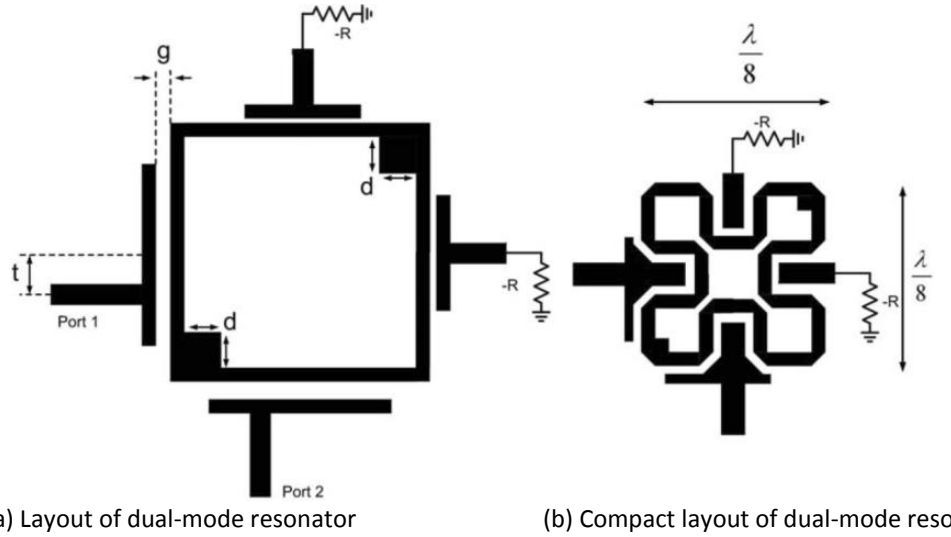


Figure D-12: A typical dual-mode printed active resonator, horizontal and vertical resonant modes are coupled to negative resistances for loss compensation: (a) Layout, and (b) Compact version of the resonator using a meandered-loop resonator [8]

The two lossless resonant modes are coupled to each other by the small patch perturbation at the two inner corners. The input and output ports are coupled to both modes through offset-to-center feeding lines. The resonant modes are loss compensated by coupling to negative-resistance devices realized by using two NESG2030 SiGe HBT transistors, the high-Q and low-noise properties of the dual-mode active filter make it attractive for low phase-noise oscillator designs.

D7 References

- [1] C. Y. Hsu, H. R. Chuang, and C. Y. Chen, "Design of 60-GHz millimeter-wave CMOS RFIC-on-chip bandpass filter," *Proc. of the 37th European Microwave Conference*, pp. 672-675, October 2007.
- [2] J. C. Lugo, and J. Papapolymerou, "Dual-Mode reconfigurable filter with asymmetric transmission zeros and center frequency control," *IEEE Microw. Wireless Compon. Lett.*, vol. 16, no. 6, pp. 499-501, Sept 2006.
- [3] A. Gorur, "Realization of a dual-mode bandpass filter exhibiting either a Chebyshev or elliptic characteristic by changing perturbation's size," *IEEE MWCL*, vol. 14, no. 3, pp. 118-120, March 2004.
- [4] A. Gorur, C. Karpuz, and M. Akpinar "A reduced-size dual-mode bandpass filter with capacitively loaded open-loop arms," *IEEE Microw. Wireless Compon. Lett.*, vol. 13, no. 9, pp. 385-387, Sept 2003.
- [5] J. S. Hong, and M. J. Lancaster, "Microstrip bandpass filter using degenerate modes of a novel meandered loop resonator," *IEEE Microw. Wireless Compon. Lett.* vol. 5, no. 11, pp. 371-372, Nov. 1995.
- [6] M. Nick, "New Q-Enhanced Planar Resonators for Low Phase-Noise Radio Frequency Oscillators", PhD Dissertation, Electrical Engineering, University of Michigan, 2011
- [7] M. Makimoto and S. Yamashita, *Microwave Resonators and Filters for Wireless Communication Theory, Design and Application*, Berlin: Springer, 2001.
- [8] L-Hwa Hsieh, "Analysis, Modeling and Simulation of Ring Resonators and their applications to Filters and Oscillators", PhD Dissertation May 2004, Texas A&M University.
- [9] G. K. Gopalakrishnan and K. Chang, "Bandpass characteristics of split-modes in asymmetric ring resonators", *Electron Letter*, vol. 26, pp. 774-775, June 1990.
- [10] J. Hong, and M. J. Lancaster, "Microstrip filters for RF/microwave applications," Wiley & Sons, 2001.
- [11] S. Park, K. V. Caekenbergh, and G. M. Rebeiz, "A miniature 2.1-ghz low loss microstrip filter with independent electric and magnetic coupling," *IEEE MWCL*, vol. 14, no. 10, pp. 496-498, Oct. 2004.

- [12] A. Gorur, "Description of coupling between degenerate modes of a dual-mode microstrip loop resonator using a novel perturbation arrangement and its dual-mode bandpass filter applications" *IEEE Trans. Microw. Theory Tech.*, vol. 52, no. 2, pp. 671-677, Feb. 2004.
- [13] S. Amari, "Comments on "Description of coupling between degenerate modes of a dual-mode microstrip loop resonator using a novel perturbation arrangement and its dual-mode bandpass filter applications" *IEEE Trans. Microw. Theory Tech.*, vol. 52, no. 9, pp. 2190-2192, Sept. 2004.
- [14] I. Wolff, "Microstrip band pass filter using degenerate modes of a microstrip ring resonator", *Electron Lett.*, vol. 8, pp. 163-164, June 1972.
- [15] Zhu et al "A joint field/circuit model of line-to-ring coupling structures and its application to the design of microstrip dual-mode filters and ring resonator circuits", *IEEE Trans. MTT* vol. 47, pp. 1938- 1948, Oct 1999.
- [16] L. -H Hsieh and K. Chang, .Dual-mode elliptic-function band pass filter using one single patch resonator without coupling gap., *Electron Lett. vol. 36*, pp. 2022 . 2023, November 2000.
- [17] K. Chang, "Microwave Ring Circuits and Antennas", New York: Wiley, 1996.
- [18] M. Kirschning, R. H. Jansen and N. H. L. Koster, "Measurement and compute raided modeling of microstrip discontinuities by an improved resonator method", in *IEEE MTT-S Symp. Dig.*, pp. 495-497, 1983.
- [19] E. Hammerstad, "Computer-aided design for microstrip couplers with accurate discontinuity models", *IEEE MTT-S Int. Microwave Symp. Dig.*, pp.54-56, 1981.
- [20] K. C. Gupta, R. Garg, I. Bahl, and P. Bhartia, *Microstrip Lines and Slotlines*, 2nd Boston: Artech House.

Appendix E

E1. Radio over Fiber (RoF) Link Characterization

Characterization of MZM Link [1]-[4]

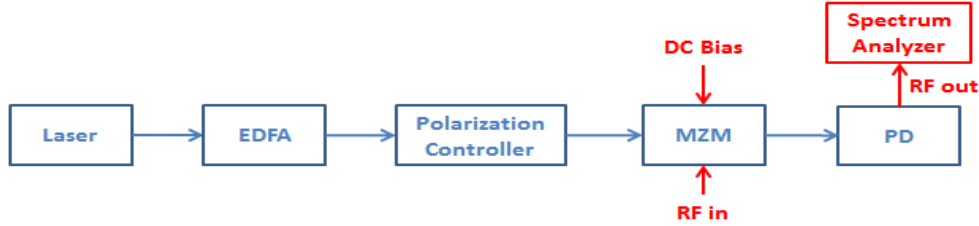


Figure E-1: Experimental Setup for Open Loop Characterization of RoF link using MZM

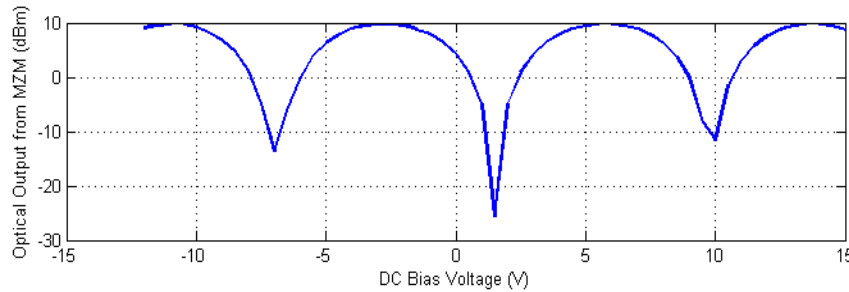


Figure E-2: MZM Output Optical Power as a Function of Bias Voltage

Table E-1 Link Loss of Different MZM Bias Point

	MZM Bias	Link Loss
MZM Link 1	0V	47dB
MZM Link 2	-0.5V	42dB

Characterization of EAM Link

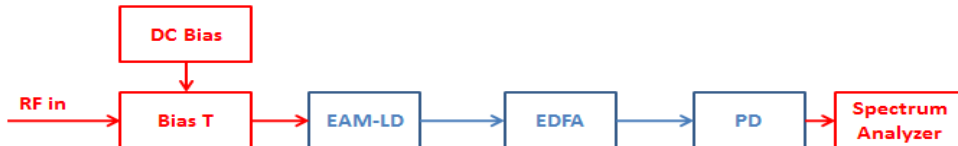


Figure E-3: Experimental Setup for Open Loop Characterization of RoF link

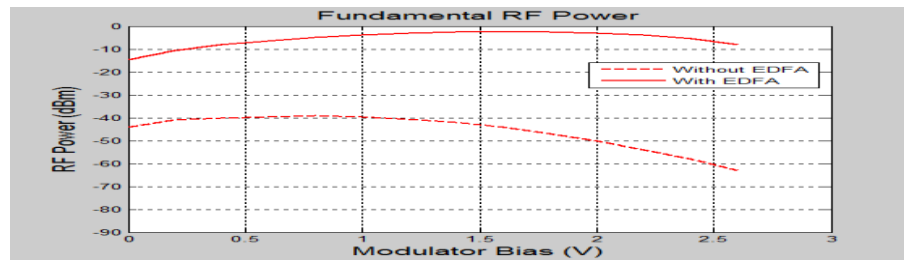


Figure E-4: RF Power vs EAM Bias (Optical Input = 7dBm, RF Driving = 10dBm)

Table E-2 Link Loss of EAM Link w/ and w/o EDFA

	EAM Bias	Link Loss
w/o EDFA	1V	40dB
w/ EDFA	1V	4dB

E2. Noise Estimation of RoF Link

Analysis of MZM Link

Table E-3

Noise Parameters	
RIN = -140dBc	Laser RIN
$I_{photo}=2mA$	DC photo current of the photo detector
$R=50\Omega$	Load resistance of photo detector
$f_c = 1MHz$	Amplifier flicker frequency
$G_A = 10dB$	Amplifier Large Signal Gain

Noise Spectral Density

$$S_N(f_m) = \frac{(N_{RIN} + N_{Shot}) \times G_A}{P_S} \times \left(\frac{f_c}{f_m} + 1 \right) \quad E1-1$$

$$\text{SSB phase noise} \quad L_N(f_m) = 10 \log_{10} S_N(f_m) - 3dB \quad (E1-2)$$

where $N_{RIN} = I_{photo}^2 \times R \times RIN \times G_A = -137dBm/Hz$ and $N_{Shot} = 2e \times I_{photo} \times R \times G_A = -165dBc/Hz$

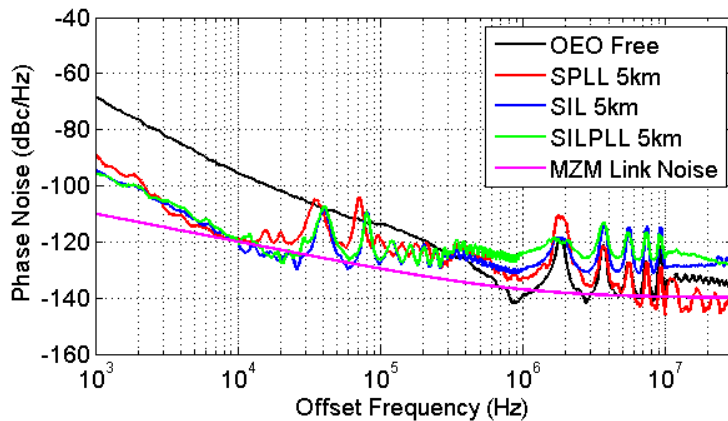


Figure E-5: CAD Simulated noise floor and measured phase noise of different circuit topologies

Analysis of EAM Link

Table E-4

Noise Parameters	
RIN = -120dBc	Laser RIN
$I_{photo}=2mA$	DC photo current of the photo detector
$R=50\Omega$	Load resistance of photo detector
$f_c = 1MHz$	Amplifier flicker frequency
$G_A = 10dB$	Amplifier Large Signal Gain

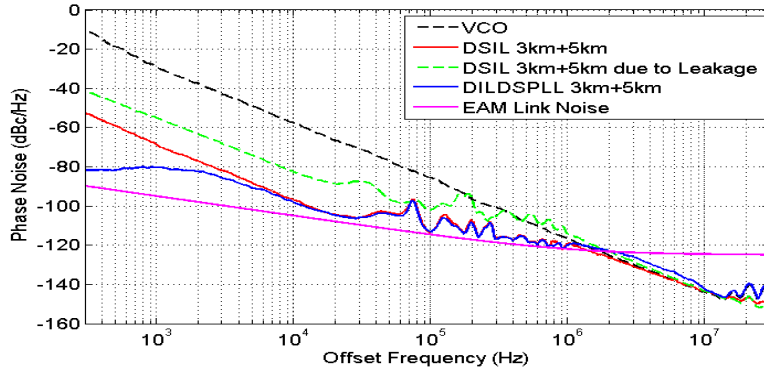


Figure E-6: Simulated noise floor and measured phase noise of different circuit topologies

E3. OEO Characterization

$f=8.8\text{GHz}$, $P_s=5\text{dBm}$

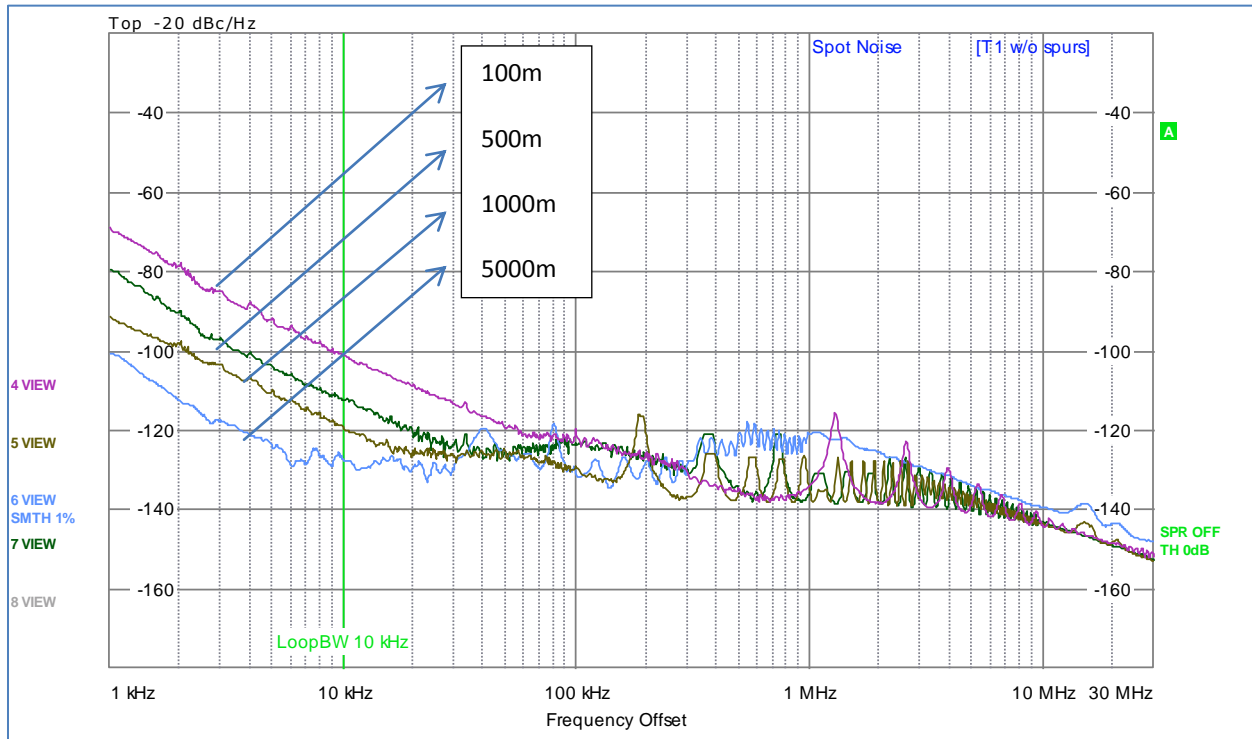


Figure E-7: Plots show the phase noise performance with respect to fiber cable length

Table E-5: Phase Noise for Different Delays

	1kHz	10kHz	100kHz	1MHz	10MHz
100m	-69	-101	-121	-134	-144
500m	-80	-112	-124	-135	-143
1000m	-91	-120	-130	-135	-144
5000m	-101	-127	-131	-121	-140

E4. Loop Filter Characterization

An active low pass filter is constructed using an op-amp. The circuit of the active filter is shown in Figure D1. Different resistors and capacitors are used to achieve different PLL loop bandwidth. The

calculated loop bandwidth is given in Table E-6. Figure E-8 shows the active filter circuit topology. Experiments are performed to verify the PLL loop BW estimation. In the experiment, a DRO (Ch-9, Figure 9-23) is locked to a synthesizer (HP 8340B), and the loop bandwidth is deduced from the measured phase noise of the DRO under locked condition, experiment data is shown in Figures E-8a, E-9, E-10, and E-11.

E5. Comments: OEO Phase Noise and Side-Mode Suppression

The experimental results of a dual self-injection locking (DSIL) and dual self-phase locked loop (DSPLL) employing short and long delays have been considered for side-mode suppression, while maintaining same amount of phase noise reduction provided by the long delay. As an example of DSIL, side-mode suppression of more than 20 dB for fiber delay links of 1 km and 5 km are experimentally achieved compared to a single 5 km long SIL with a phase noise reduction of 40 dB (in reference to free running oscillator) at 10 kHz offset from carrier for both standard OEO and a self-seeded with 3 port oscillator at 10 GHz. For a DSPLL fiber delay lines of 3km and 5km, a side-mode suppression of 29 dB is achieved compared to SPLL of 5km with phase noise reduction of 30 dB (in reference to free running oscillator) at 10kHz offset from carrier.

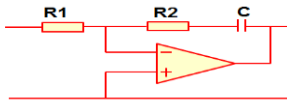


Figure E-8: Active Filter Circuit Topology

Table E-6: Different resistors and capacitors are used to achieve different PLL loop bandwidth

Board	Resistor and Capacitor Values	Loop BW for $K_d=0.1$ and $K_o=200\text{kHz/V}$
1	$R_1=51\Omega$, $R_2=1\text{k}\Omega$, $C=4.7\text{nF}$	about 200kHz
2	$R_1=51\Omega$, $R_2=3.3\text{k}\Omega$, $C=0.27\text{nF}$	about 700kHz
3	$R_1=51\Omega$, $R_2=1000\Omega$, $C=470\text{nF}$	about 20kHz

Circuit 1: $R_1=51\Omega$, $R_2=1\text{k}\Omega$, $C=4.7\text{nF}$

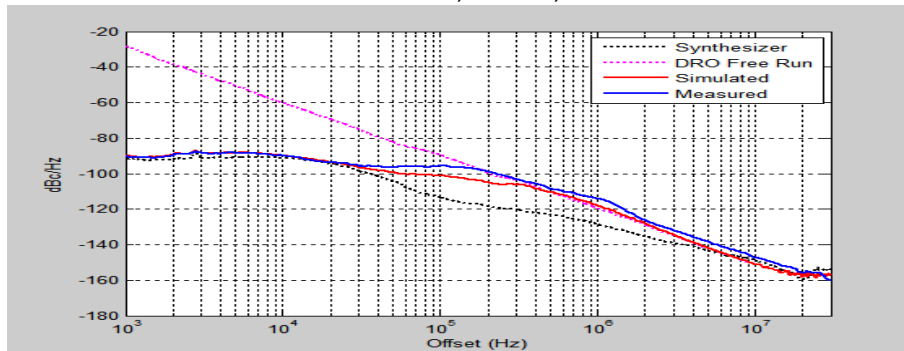


Figure E-8a: Measured phase noise plots of DRO when it is locked to HP8340B. PLL Loop bandwidth about 200kHz

Circuit 2: $R_1=51\Omega$, $R_2=3.3\text{k}\Omega$, $C=0.27\text{nF}$

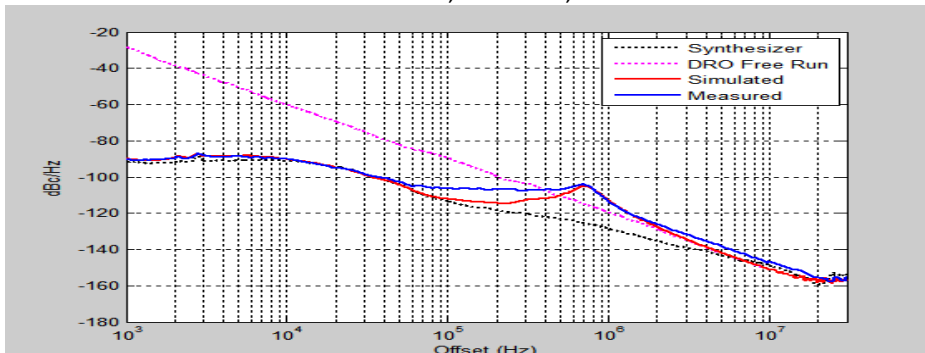


Figure E-9: Figure D.3 Phase noise of DRO when it is locked to HP8340B. PLL Loop bandwidth about 700kHz

Circuit 3: $R_1=51\Omega$, $R_2=100\Omega$, $C=470nF$

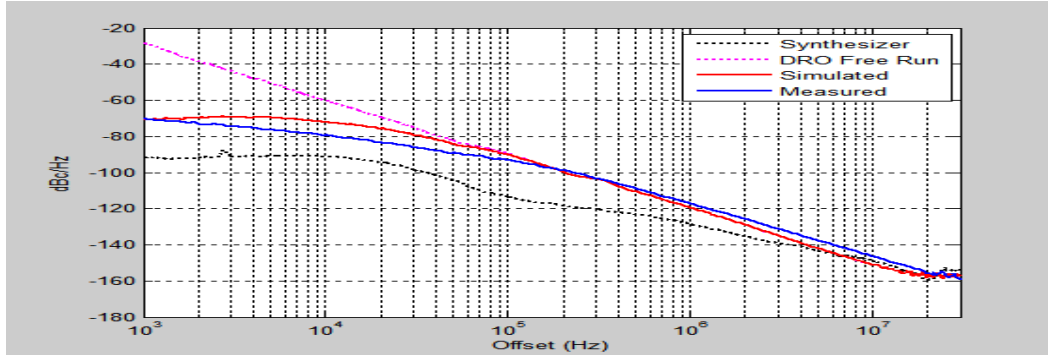


Figure E-10: Figure D.4 Phase noise of DRO when it is locked to HP8340B. PLL Loop bandwidth about 20kHz

For the case of SPPLL, phase locking performances of a 10GHz oscillation signal are experimentally evaluated as various methods of phase locking are compared. The phase locking methods are based on a 5 port bandpass filter as tunable electrical phase shifter, a tunable three port electrical VCO, tunable Mach-Zehnder modulator (MZM) as an optical phase shifter, and a tunable VCO using electro-absorption (EA) modulator. Experimental results that demonstrate the benefit of SILPLL incorporating dual delays have been reported for the first time corroborating analytical predictions. A dual SILPLL (DSILPLL) system with 3 km and 5 km fiber delay has been implemented, and the measured phase noise reduction of 40 dB provided by DSILPLL is the same as DSIL at 10 kHz offset. However, at 1 kHz offset, DSILPLL provides a phase noise reduction of 52 dB which is 11 dB higher than DSIL; at 300Hz offset, DSILPLL provides 70 dB reductions while DSIL provides only 42 dB reduction. Using low flicker noise HBT based amplifier ($f_c=10\text{kHz}$), low V_π MZM and low RIN laser ($\text{RIN}=-160\text{dBc}$) in the SILPLL system; SILPLL based OEO exhibits phase noise of -150 dBc/Hz at 10kHz offset for a 10GHz carrier.

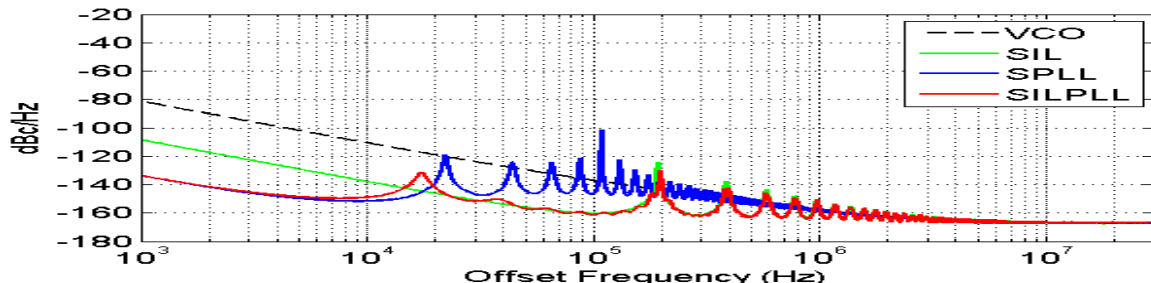


Figure E-11: Phase noise plots for 10 GHz OEO, $f_c=10\text{kHz}$, $\text{NF}=20\text{dB}$, $\text{RIN}=-160\text{dBc}$

In summary, DSILPLL is effective for side-mode suppression and phase noise reduction, where SPPLL using tunable MZM with DSIL of a VCO provides the best performance improvement over other investigated topologies. Due to the advances in low noise electronics and broad bandwidth of the optical components used in the DSILPLL system, the DSILPLL technique has the potential to create highly stable RF oscillators approaching 100GHz.

References

- [1] Li Zhang, Optoelectronic Frequency Stabilization Technique in Forced Oscillators, PhD Thesis, Drexel Univ., 2014.
- [2] J.W. Fisher, L. Zhang, A. Poddar, U.L. Rohde, and A.S. Daryoush, "Phase Noise Performance of Optoelectronic Oscillator Using Optical Transversal Filters", IEEE BenMAS, Drexel, Sept 2014
- [3] A. Poddar, A. Daryoush, and U. Rohde, "Integrated production of self-injection locked self-phase locked Optoelectronic oscillators," US Patent App. 13/60767.
- [4] A. Poddar, A. Daryoush, and U. Rohde, "Self-injection locked phase locked loop optoelectronic oscillator," US Patent App., no. 61/746, 919

Appendix F

F1. Forced Oscillations Using Self-Injection Locking

Frequency stability of local oscillators is paramount in a number of coherent detection systems. Phase noise of oscillators can be reduced by injection locking to an external ultra-low noise source. The lowest phase noise achievable is determined by the noise of the external source in the case of conventional injection locking. However, in many cases we are reaching limits of stability of stable sources to lock free-running oscillators; and ultra-high stability and low noise sources are not readily available at microwave frequencies and beyond for future instrumentation systems. Self-injection locking (SIL) has been developed and demonstrated to be an effective method for phase noise reduction. SIL can be implemented by feeding part of the past oscillator output signal back to itself after passing through a delay line or resonator. It has also been shown that long delay or high quality factor (Q) is crucial for substantial phase noise reduction. Although it is possible to have phase noise reduction using an electrical delay, the improvement is poor because the delay length is limited due to high loss in the electrical delay lines or a limited Q of resonators at microwave frequencies. To overcome the loss due to limitations of electrical delay lines, low loss fiber optic delay lines are proposed for the realization of SIL. However, the side-modes associated with the long optical delay lines become undesirable since they appear as spurious oscillations at offset frequencies very close to carrier frequency and are hard to be removed using standard electrical filtering. Hence, a multi-loop configuration is proposed in Opto-electronic oscillators (OEO) as a side-mode suppression scheme. There are two different topologies reported in multi-loop OEO: (i) oscillation is not established in individual loops since the loop gain is kept to be smaller than unity in each loop, while the combined loop gain of all the loops is equal to or greater than one for joint oscillation [1]-[2], and (ii) the second approach suggests oscillations in each individual loops and the side-mode suppression is achieved using a coupled oscillation scheme [3]. In this thesis, the new approach is to realize oscillation in one loop using positive feedback and just coupling in other loops using negative feedback. Even though dynamic modeling of injection locked oscillator (ILO) is reported in [4]-[9], only conventional injection locking topologies are considered and the focus is on numerical computation of locking range and power spectrum. In this Appendix F, a system level analysis is presented for the phase noise of ILO within locking range, and topologies of both external IL and SIL with delays in μs are described. Experiments are performed to demonstrate the concept of SIL using fiber optic delay lines. This section provides a comprehensive analytical modeling and experimental verification results of self-injection locking of an electrical oscillator in terms of close to carrier phase noise and performance of spurious oscillations using two optical delay loops. In addition to this, analytical modeling and experiment results are reported for self-injection locked OEO using one and two optical delay lines in terms of close in to carrier phase noise and spurious oscillation power levels. Discussions are also provided in terms of physical limitations of SIL technique.

F1. 1 Analysis of IL Phase Noise

In this section, a system level modeling is used as a unified model for phase noise modeling of oscillators with injection scheme. Since the phase dynamics of injection locking process is equivalent to that of first order type I phase-locked loop (PLL), it is intuitive to derive the phase noise expression of ILO using PLL model. This approach is preferred as there is opportunity to extend modeling to PLL and implement a unified modeling of injection locked phase locked loop (ILPLL) oscillators [10]-[12]. As a part of the modeling, let y_i and y_o be the injecting signal and the output signal of the oscillator in the free running case, respectively:

$$y_i = \cos(\omega t + \theta_i(t)) \quad (F.1)$$

$$y_o = \cos(\omega t + \theta_o(t)) \quad (F.2)$$

Defining $\phi_i(t) = \omega t + \theta_i(t)$, $\phi_o(t) = \omega t + \theta_o(t)$, and using (F.1) and (F.2) with the famous Adler's Equation [1], then phase dynamics of IL can be written as

$$d\theta_o(t)/dt = \rho\omega_{3dB}\sin(\theta_i(t) - \theta_o(t)) \quad (\text{F.3})$$

where $\rho = v(P_i/P_o)$ is the injection strength, and $\omega_{3dB} = \omega_o/2Q$ is half the 3dB bandwidth of the oscillator resonator. When the frequency difference between the injecting signal and the free running oscillator is small, the phase difference between them is also small. Thus we can linearize (F.3) to have

$$d\theta_o(t)/dt = B(\theta_i(t) - \theta_o(t)) \quad (\text{F.3})$$

where $B = \rho\omega_{3dB}$. Equation (F.4) is of the same form of the phase dynamics as that of the first order type I PLL. Performing the Laplace transform of the above time domain variable, (F.4) can be expressed in s-domain as

$$s\theta_o(s) = B(\theta_i(s) - \theta_o(s)) \quad (\text{F.4})$$

The transfer function of phase of IL can be found as

$$H_\theta(s) = \theta_o(s)/\theta_i(s) = (B/s)/(1 + B/s) \quad (\text{F.5})$$

The block diagram representing (F.6) is depicted in F-1(a). We can see that IL resembles a negative feedback control loop that contains an integrator. The integrator is usually a voltage-controlled oscillator (VCO), which is suitable for integration of PLL function. The loop behavior in the presence of noise sources is systematically presented in F-1(b), where the major noise contributors in IL are $n_1(s)$ at the injection point that contains injecting signal noise and residual noise of the system, and $n_2(s)$, which is the oscillator phase noise.

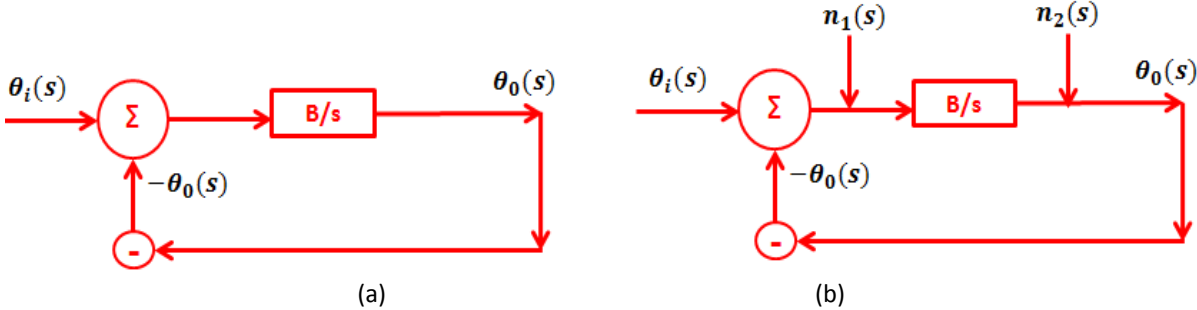


Figure F.1: Conceptual block diagram representation of IL using control theory representation; a) without noise sources present; b) with noise sources of $n_1(s)$ and $n_2(s)$ added in the loop.

Assuming the noises are a small perturbation to the steady oscillation, thus linearity still holds in the IL system. Then we can find the oscillator output due to noise using superposition principle. We first use standard loop analysis to find out the output θ_{o1} due to input noise n_1 only as

$$\theta_{o1} = -(B/s)\theta_{o1} + (B/s)n_1 \quad (\text{F.6})$$

After rearranging (3.7) in terms of θ_{o1} , results in

$$\theta_{o1} = (B/s)/(1 + B/s)n_1 = H_\theta(s)n_1 \quad (\text{F.7})$$

Similarly, the output θ_{o2} due to oscillator phase noise n_2 only is expressed as

$$\theta_{o2} = 1/(1 + B/s)n_2 = (1 - H_\theta(s))n_2 \quad (\text{F.8})$$

Hence the output θ_o due to contributions of both noises is

$$\theta_o = H_\theta(s)n_1 + (1 - H_\theta(s))n_2 \quad (\text{F.9})$$

The power spectral density of the output phase θ_o of offset angular frequency ω_m becomes

$$S_{\theta o}(\omega_m) = |H_\theta(j\omega_m)|^2 S_{n1}(\omega_m) + |1 - H_\theta(j\omega_m)|^2 S_{n2}(\omega_m) \quad (\text{F.10})$$

where $S_{n1}(\omega_m)$ and $S_{n2}(\omega_m)$ are the power spectral densities of n_1 and n_2 respectively.

F1. 2 Analysis of SIL

(a) Derivation of Oscillator Phase Noise with SIL

The conceptual block diagram of SIL using control theory representation is shown in Figure F-2. A portion of the oscillator output signal is delayed by a long delay (τ_d) and is fed back to the oscillator with coupling factor of ρ . The phase of the delayed signal is then compared against that of current signal to generate an error signal for self-injection to the oscillator similar to the one shown in Figure F-1(b).

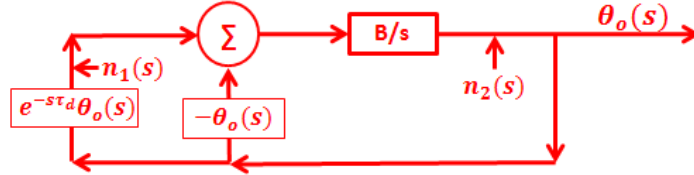


Figure F-2: Conceptual block diagram of SIL using control theory representation with a self-feedback after a delay of τ_d with coupling factor of ρ integrated to system

The phase noise of the SIL can be found by using the same procedure as presented in section F1.1 for external IL. The only difference is that n_1 in this case does not contain the injecting signal noise but only the residual noise of the system. We can first find the output θ_{o1} due to n_1 as

$$\theta_{o1} = -(B/s)\theta_{o1} + \exp(-s\tau_d)(B/s)\theta_{o1} + (B/s)n_1 \quad (\text{F.11a})$$

$$\text{From (F.11a)} \quad \theta_{o1} = \frac{B}{s+B(1-e^{-s\tau_d})} n_1 \quad (\text{F.11b})$$

θ_{o2} (output) due to oscillator phase noise 'n₂' is given by

$$\theta_{o2} = -(B/s)\theta_{o2} + \exp(-s\tau_d)(B/s)\theta_{o2} + n_2 \quad (\text{F.11c})$$

From (F.11c)

$$\theta_{o2} = \frac{s}{s+B(1-e^{-s\tau_d})} n_2 \quad (\text{F.11d})$$

The effective output θ_o is calculated as

$$\theta_o = \theta_{o1} + \theta_{o2} = \frac{B}{s+B(1-e^{-s\tau_d})} n_1 + \frac{s}{s+B(1-e^{-s\tau_d})} n_2 \quad (\text{F.12})$$

The power spectral density of θ_o can be described by

$$S_{sil}(\omega_m) = |H_a(j\omega_m)|^2 S_{n1}(\omega_m) + |H_b(j\omega_m)|^2 S_{n2}(\omega_m) \quad (\text{F.13})$$

where

$$H_a(s) = \frac{B}{s+B(1-e^{-s\tau_d})} \text{ and } H_b(s) = \frac{s}{s+B(1-e^{-s\tau_d})} \quad (\text{F.14})$$

Note that the transfer functions $H(s)$ has resonant peaks that are related to the harmonic of frequencies $s=j\omega$, where $e^{-js\tau_d}=1$. $S_{n1}(\omega_m)$ is the residual noise at offset frequency of f_m :

$$S_{n1}(f_m) = \frac{kTBF}{2P_s} \left(\frac{f_c}{f_m} + 1 \right) \quad (\text{F.15})$$

while $S_{n2}(\omega_m)$ is expressed using Leeson's Equation [13]

$$S_{n2}(f_m) = \frac{kTBF}{2P_s} \left[\frac{1}{f_m^3} \left(\frac{f_0^2 f_c}{4Q_L^2} \right) + \frac{1}{f_m^2} \left(\frac{f_0^2}{4Q_L^2} \right) + \frac{f_c}{f_m} + 1 \right] \quad (\text{F.16})$$

where $k=1.38 \times 10^{-23} \text{ J/K}$ is the Boltzmann constant; $T=290^\circ \text{ K}$ is the room temperature in Kelvin; $B=1 \text{ Hz}$ is the noise bandwidth being considered; F is the system noise figure; P_s is the carrier power level; f_0 is the oscillation frequency; $f_c=1 \text{ MHz}$ is the flicker noise corner frequency; Q_L is the loaded Q of the oscillator resonator. For oscillator phase noise $S_{n2}(\omega_m)$, a roll-off rate of 30dB/decade is expected when $f_m < f_c$ and 20dB/decade for $f_m > f_c$. A higher Q_L provides lower SSB phase noise in the region where $f_m > f_c$. Advantage of opto-electronic oscillators is that Q_L could be enhanced by increasing the fiber delay length.

(b) Simulated Phase Noise of Electrical Oscillator with and without SIL

Single side-band phase noise simulation is provided below for an electrical oscillator with SIL using (F.14). Figure F-3 shows the CAD Simulated SSB phase noise of Opto-electrical oscillators.

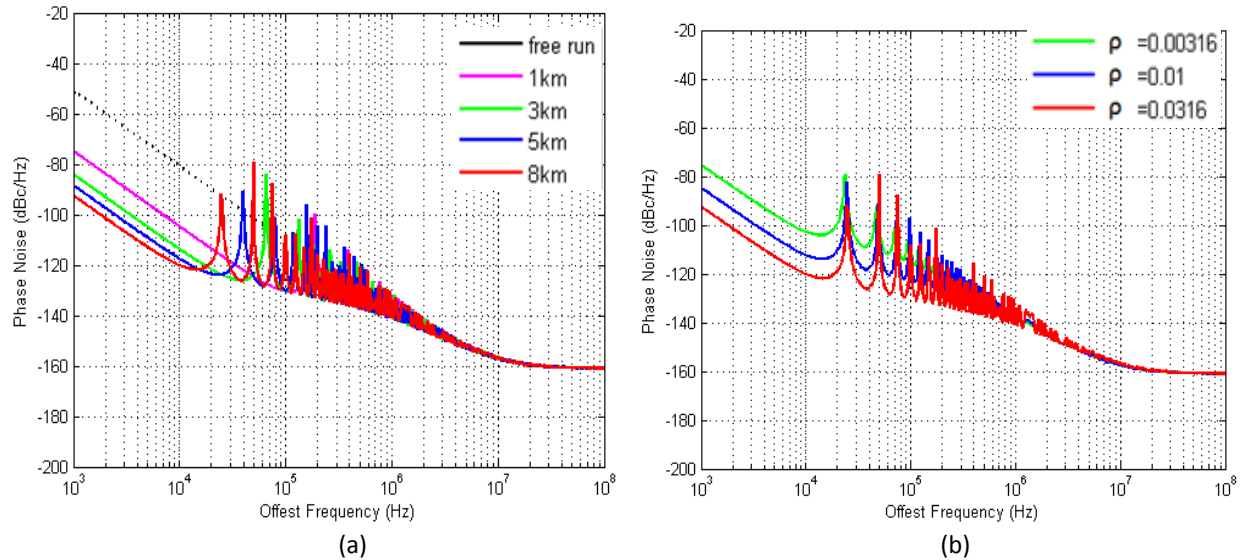


Figure F-3: Simulated SSB phase noise of electrical oscillator; (a) SSB phase noise without (Black: free running electrical oscillator) and with SIL for $\rho=0.0316$ with different delays (Magenta: 1km; Green: 3km; Blue: 5km; Red: 8km). b) Phase noise of 8km long SIL with different injection strengths. (Green: $\rho=0.00316$; Blue: $\rho=0.01$; Red: $\rho=0.0316$.) In all plots the oscillator output power is $P_S=16\text{dBm}$, with fiber optic link NF=60dB, and $P_N=-114\text{dBm}$.

In Figure F-3(a), the black dotted curve shows the SSB phase noise of a free running electrical oscillator (cf. section F.1), whose practical values of loaded quality factor, $Q_L = 500$ and noise figure, $NF=32$ dB are considered, even though dielectric resonator oscillators (DRO) with $Q_L=2000$ and $NF=18$ dB have already been developed, achieving an SSB phase noise of -111 dBc/Hz at 10 kHz offset [2]. The phase noise drops at a rate of 30dB/decade at offset frequencies until flicker corner frequency of about 500 kHz. Other curves in various colors show the phase noise of SIL with various optical delays of 1km to 8 km. From the simulation results, a 1km delay in SIL improves the phase noise by 22 dB at 1 kHz offset and the slope rolls off at a rate of 30dB/decade until corner frequency of 100 kHz. A number of spurious oscillations are also manifested as side-modes of every 200 kHz. When the delay increases to 8 km, the improvement is about 39 dB with a slope of 30dB/decade until corner frequency of 10 kHz and side-modes of every 25 kHz. We can see that long delay is crucial for phase noise reduction. Figure F-3(b) shows the simulation results for 8 km optical delay with various injection strengths. The green, blue and red curves show the phase noise of SIL with $\rho=0.00316$, 0.01 and 0.0316 (i.e., injection ratio of -50dB, -40dB, and -30dB), respectively. The best phase noise is achieved when the injection strength is strongest at a level of -30dB.

(c) Simulated Phase Noise of OEO with and without SIL

An electrical oscillator is replaced by an Opto-electronic (OEO) oscillator with fiber delay line of 1km for achieving high loaded quality factor. By using (F.14), phase noise of OEO with SIL is also simulated. Figure F-4 shows the phase noise of a standard OEO and SIL OEO with various feedback delays when $\rho=0.0316$. (optical link NF=60dB, $P_N=-114\text{dBm}$). The phase noise of this standard OEO is shown in black dashed curve; other colored curves show the phase noise of SIL OEO with different optical delays in the feedback loop. The simulated phase noise is the lowest in the case of 8km delay. Phase noise performance for OEO with 8km SIL delay remains the same under injection strengths of 0.00316, 0.01 and 0.0316. The spikes that appear in Figure F-4 are the poles associated with the transfer functions of different delays, and they may not represent the actual location and level of the spurious signals.

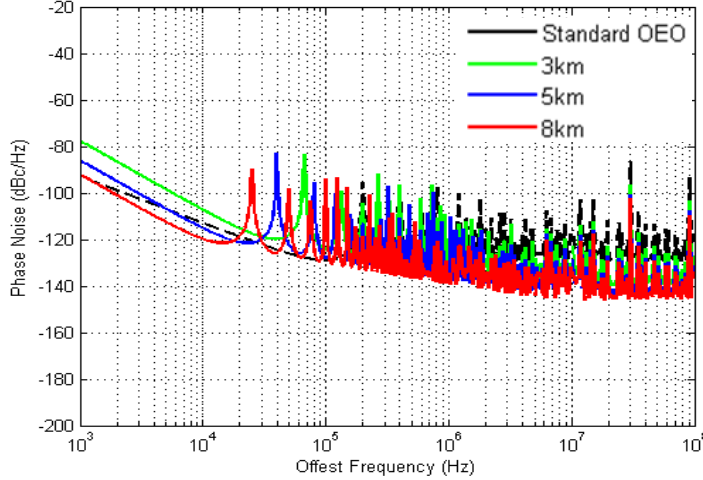


Figure F-4: Simulated phase noise of a standard OEO realized using a 1km long fiber delay without (Black: standard OEO) and with SIL (Green: standard OEO with 3km SIL; Blue: standard OEO with 5km SIL; Red: standard OEO with 8km SIL). The SIL is accomplished for injection ratio of $p=0.0316$ for different fiber delay lengths ($P_S=16\text{dBm}$, fiber).

F1. 3 Analysis of DSIL

From the previous simulations, longer delay is required for better phase noise reduction in SIL configuration. However, the side-modes originated from the spurious oscillation in long delay lines appear as prominent noise sources at offset frequencies very close to the carrier. These side-mode levels are very high because the frequency selectivity of practical RF filtering is not high enough to remove these side-modes. A feasible way to suppress these spurious signals is by implementing two different non-harmonically related delays in the feedback path. Because the two delays have different mode spacing, only those modes that are common to both delays will survive. Other modes are hence being suppressed. This alternative filtering is similar to transversal optical filters reported by others [14]-[16].

(a) Derivation of Oscillator Phase Noise using DSIL

The control theory representation of a dual loop SIL (DSIL) configuration is shown in Figure F-5. In this case, the feedback is split into two separate paths, one passes through a long delay and another passes through a short delay. Phases of two different delayed signals are compared with the current signal separately and error signals are injected to oscillator. When the loop lengths are not harmonically related, then the resultant output becomes the sum of individual loop actions as periodic resonances are suppressed in strength. The system level modeling is employed to derive the phase noise of DSIL. Assumption is made that the two injection loops do not interact with each other, so that the output is a superposition of the actions of individual loops. The residual noise of the system is also going to be the superposition of the noises in each loop (i.e. $n_1=n_{d1}+n_{d2}$). Then, the output θ_{o1} due to noise n_1 is

$$\theta_{o1}(s) = -\left(\frac{B_1}{s}\right)\theta_{o1} + \exp(-sT_{d1})\left(\frac{B_1}{s}\right)\theta_{o1} - \left(\frac{B_2}{s}\right)\theta_{o1} + \exp(-sT_{d2})\left(\frac{B_2}{s}\right)\theta_{o1} + \left(\frac{B_1}{s}\right)n_{d1} + \left(\frac{B_2}{s}\right)n_{d2} \quad (\text{F.17})$$

where $B_1=p_1\omega_{3\text{dB}}$ and $B_2=p_2\omega_{3\text{dB}}$. If equal power split in the loops are assumed, then $B_1=B_2=B$ and (F.17) can be described by

$$\theta_{o1}(s) = \frac{B}{s+B(1-e^{-sT_{d1}})+B(1-e^{-sT_{d2}})} n_1(s) \quad (\text{F.18})$$

Similarly, the output due to VCO phase noise n_2 is found as

$$\theta_{o2}(s) = \frac{s}{s+B(1-e^{-sT_{d1}})+B(1-e^{-sT_{d2}})} n_2(s) \quad (\text{F.19})$$

Adding them together, phase noise for DSIL at offset angular frequency of ω_m is expressed as:

$$S_{DSIL}(\omega_m) = |H_a(s)|^2 S_{n1}(\omega_m) + |H_b(s)|^2 S_{n2}(\omega_m) \quad (\text{F. 20})$$

where $S_{n1}(\omega_m)$ and $S_{n2}(\omega_m)$ are defined as in (F.15) and (F.16), and

$$H_a(s) = \frac{2B}{2s+B(1-e^{-st_{d1}})+B(1-e^{-st_{d2}})}, \quad H_b(s) = \frac{2s}{2s+B(1-e^{-st_{d1}})+B(1-e^{-st_{d2}})} \quad (\text{F.21})$$

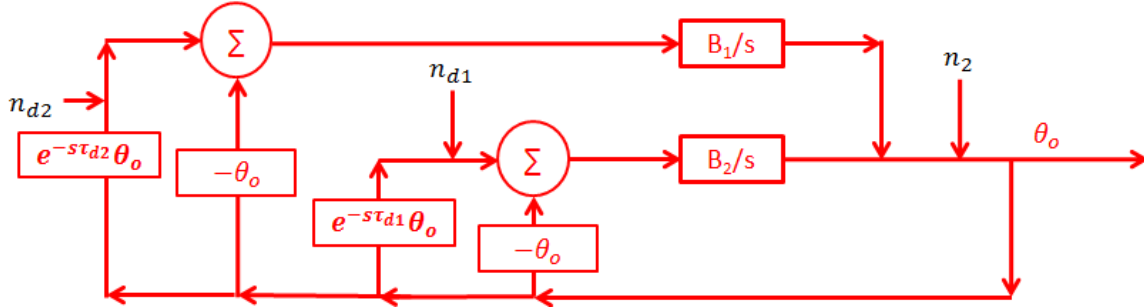


Figure F-5: The block diagram of DSIL using control theory representation. n_{di} for $i=1, 2$ are noise sources associated with each delay line being fed back to injection port of the oscillator and n_2 is output noise power.

(b) Simulated Phase Noise of Electrical Oscillator with DSIL

Figure F-6 illustrates the CAD simulated phase noise of an electrical oscillator using different injection topologies. Simulation using (F.20) for an electrical oscillator with DSIL is depicted in Figure F-6(a). The parameters for the electrical oscillator are kept the same as in the previous simulation. The two delays in the DSIL configuration are 1km and 8km.

By combining two delays, the phase noise is maintained at the same level of 8km SIL while the spurious level is reduced by about 25dB compared to 8km SIL. Phase noise performances for DSIL electrical oscillator with various length combinations are also simulated, and the simulated results are provided in Figure F-6(b). The SSB phase noise level of DSIL is determined by the longer delay in the loop and the spurious level is determined by proper selection of length combinations. The simulated SSB phase noise result is superior for a combination of 5km and 8km delay elements.

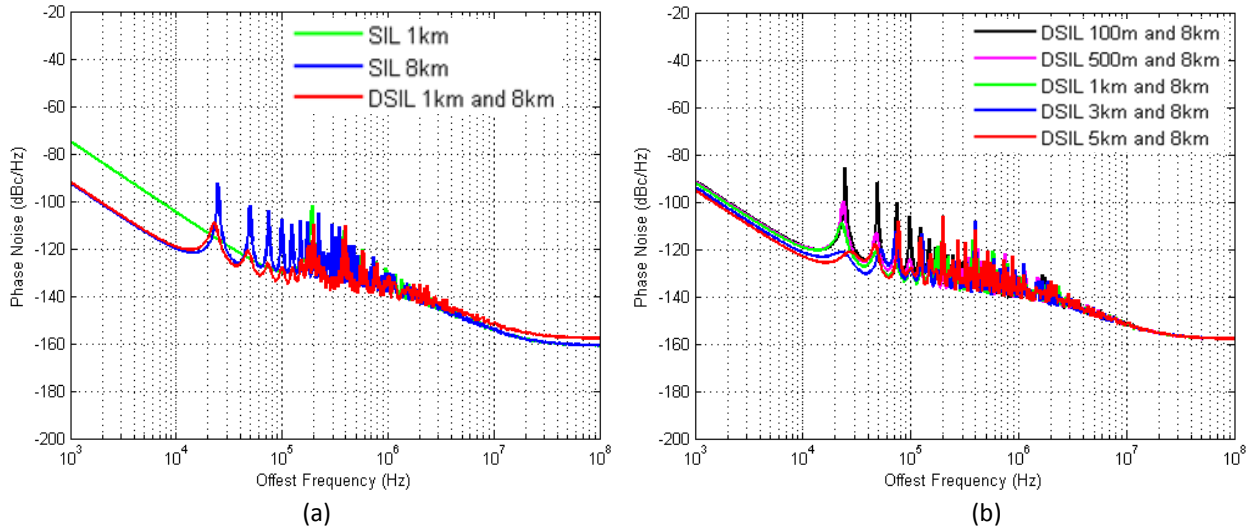


Figure F-6: (a) Comparison of the simulated phase noise of an electrical oscillator using different injection topologies (Red: Dual-SIL 1km and 8km; Green: SIL 1km; Blue: SIL 8km). b) Simulated phase noise of DSIL with various combinations. Black: DSIL 100m and 8km; Magenta: DSIL 500m and 8km; Green: DSIL 1km and 8km; Blue: DSIL 3km and 8km; Red: DSIL 5km and 8km. ($P_s=16\text{dBm}$, fiber optic link NF=60dB, $P_N=-114\text{dBm}$).

(c) Simulated Phase Noise of OEO with DSIL

Simulations for DSIL in a standard OEO are provided in Figure F-7. The combinations of extra delay with a longer delay of 8km provide superior phase noise than the combination with shorter delay of 5km. This result is also intuitively expected.

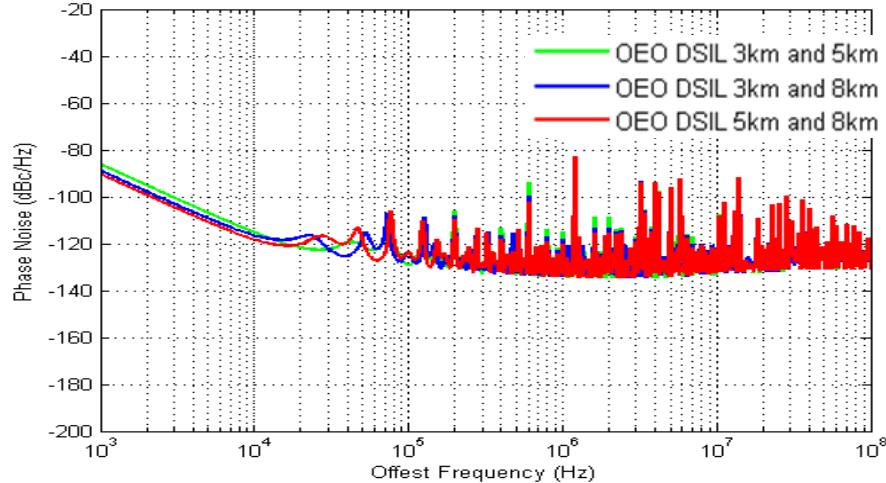


Figure F-7: Simulated phase noise and spurious signal levels of a standard 1km OEO with DSIL, Red: 3km + 5km; Blue: 3km + 8km; Green: 5km + 8km. ($P_s=16\text{dBm}$, fiber optic link NF=60dB, $P_N=-114\text{dBm}$).

F2 Experimental Results of SIL Electrical Cavity Oscillator

F2.1 Electrical Cavity Oscillator Realization

The electrical oscillator consists of a band-pass filter (BPF) constructed using a metallic cylindrical resonant cavity with $Q=2500$ at 10 GHz and a power amplifier (Amp) from B&Z (BZ3-09801050-602422-102020) with small signal gain of 27dB and 1dB compression level of 24dBm. The metallic cylindrical resonant cavity unloaded Q factor of 2500 was estimated from the injection locking of this electrical oscillator. The oscillation power is coupled to spectrum analyzer (R&S FSUP26) for SSB phase noise measurement (cf. Figure F-8). The oscillation frequency is 9.818GHz and the carrier power level is 16dBm. The measured phase noise of this oscillator is shown in the black curve of Figure F-9a. The phase noise of the electrical oscillator is -58dBc/Hz at 1kHz offset and -81 dBc/Hz at 10kHz offset with a roll off rate of about 30dB/decade after 10kHz offset carrier. The flicker corner frequency is estimated to be about 1MHz and the noise figure is approximately 32dB. The loaded Q factor is about $Q_L=500$ based on the measured phase noise. The free running phase noise for this oscillator is poor because of relatively low Q resonator characteristics of this metallic cylindrical resonant cavity.

F2.2 SIL Phase Noise

The block diagram for electrical oscillator with SIL is depicted in Figure F-8. The oscillator is controlled using an Opto-electronic delay line by driving a Mach-Zehnder modulator (MZM) from JDSU (MN21024083) with electrical oscillator signal of 16dBm at 10GHz. The optical input power of 16dBm to the MZM is provided by a DFB laser from Mitsubishi (FU-68PDF-510M67B) whose output is amplified by an EDFA from Nuphoton (NP2000). The modulated optical output of the MZM passes through an optical delay, which is detected by a photodetector from Discovery Semiconductors (DSC50S), and the received RF signal is amplified by a 24dB low noise amplifier from Kuhne Electronic (101A & 101B) and fed back to the oscillator for SIL. The measured NF is 58dB while the calculated NF is 60dB that agrees with the measured data, and these values are used for analytical predictions. The experimental results of the close in to carrier phase noise of the SIL agree well with the analytical modeling predictions. The impact of various delay lengths on the close-in to carrier phase noise was evaluated and the measured phase noise

of the 10GHz electrical oscillator is shown in Figure F-9a. In the experimental setup, the injection strength ρ is kept at 0.0316 for different delays of 1km to 8km. The phase noise for 1km delay improves by 20dB to -101dBc/Hz at 10kHz offset; in the case of 8km delay, the phase noise is -94dBc/Hz at 1kHz offset and -118dBc/Hz at 10kHz offset, corresponding to an improvement of 37dB with respect to the free running case. The diamonds in Figure F-9(a) are the actual spurious levels for the first dominant spurious side-mode associated with the different delays. Note that the diamonds are measured in unit of dBc using super-heterodyning function of R&S FSUP26 while the solid curve are measured in unit of dBc/Hz using PLL function of R&S FSUP26. As the delay becomes longer, the spurious side-mode moves closer to the carrier frequency and the level becomes higher. For 8km delay, the spurious signals are located at offset frequencies of every 25 kHz, and the level is -42dBc for the first side-mode.

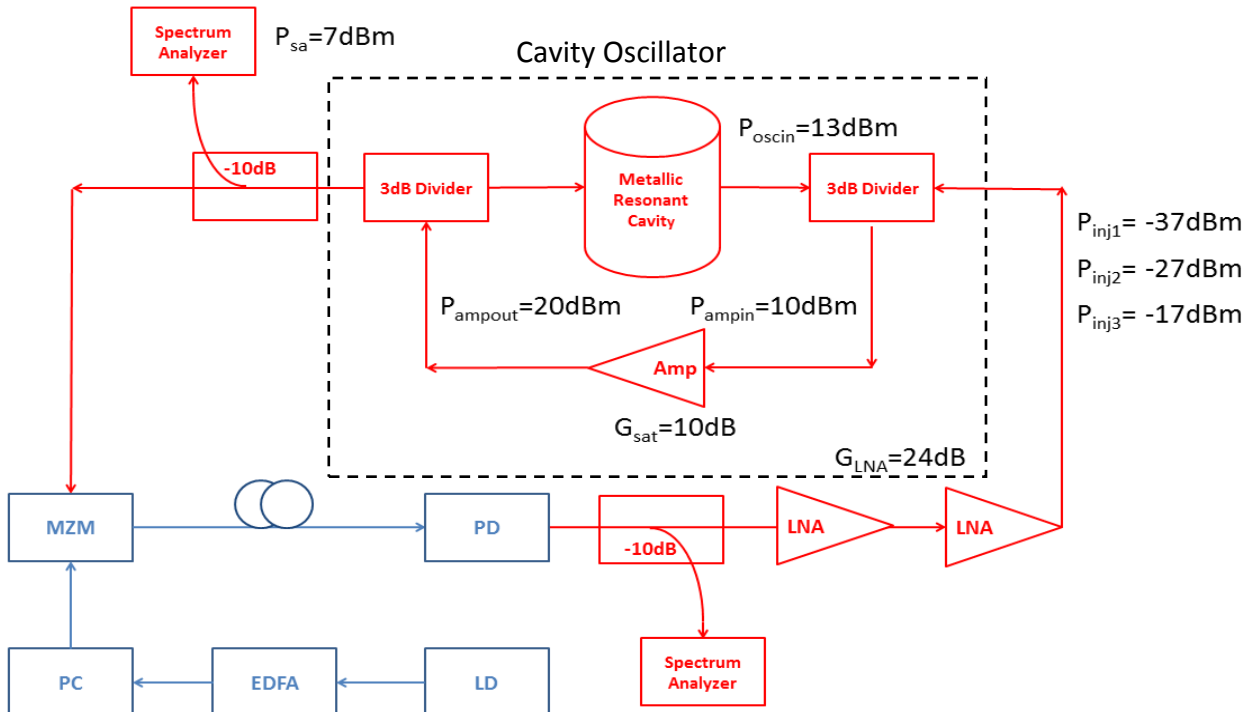


Figure F-8: Block diagram of electrical cavity oscillator with SIL

This spurious level is undesirable for a signal generator and is to be reduced. The effect of different injection strengths is shown in Figure F-9(b). In this case, the delay is fixed at 8km. Three different levels of injection strength with increment of 10dB are considered. The strongest injection strength is -30dB compared to carrier power, we can see that the phase noise under the strongest injection is 20dB lower than the case of weakest injection of -50dB. However, the spurious signal level for weakest injection is 10dB lower than the case of strongest injection.

F2.3 DSIL Phase Noise

The block diagram for the electrical cavity oscillator with DSIL is depicted in Figure F-10. For DSIL, the output of the MZM is split into two paths with different delays using 50% optical coupler from Newport (F-CPL-S12155). The optical signals are detected by two identical optical receivers from Discovery Semiconductor (DSC50S); the received signals of two different delays are then combined and fed back to the oscillator as dual loop SIL after amplification by low noise amplifier of 24dB gain from Kuhne Electronic (101A & 101B). The estimated fiber optic noise figure is 60dB and corresponds to noise power level of -114dBm. Experimental result for electrical oscillator with DSIL is reported for the first time (Figure F-11). Three different optical delay line combinations are used, the phase noise for '3km+8km'

case and '5km+8km' case are practically the same while '1km+8km' case suffers a 5dB degradation at 1kHz offset.

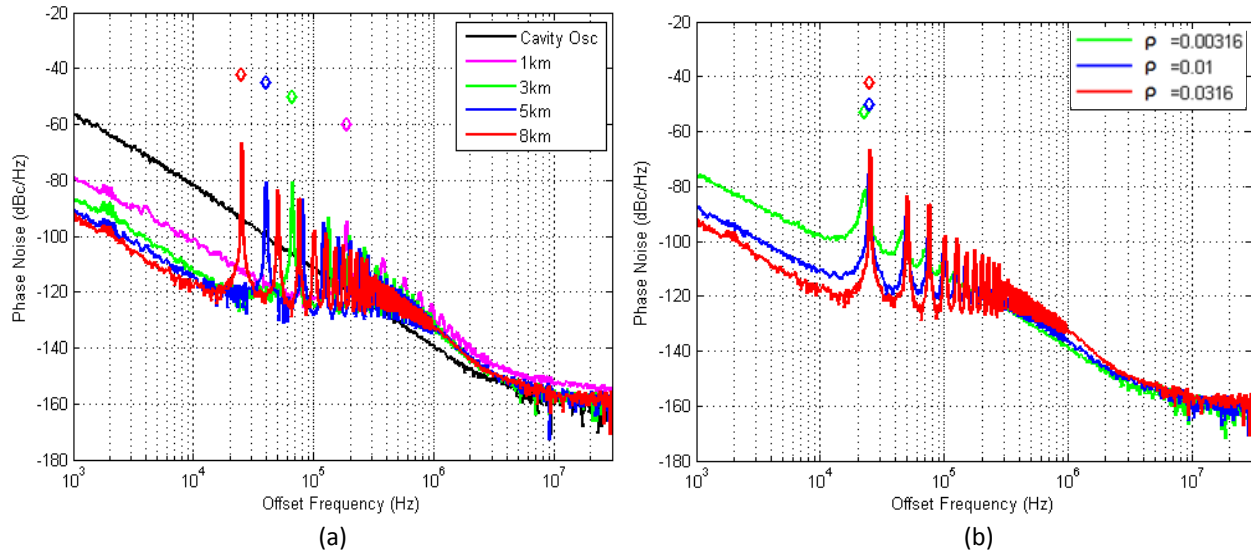


Figure F-9: (a) Measurement of SSB phase noise and spurious signal levels of SIL for $p=0.0316$ with different delays (Magenta: 1km; Green: 3km; Blue: 5km; Red: 8km. Magenta Diamond: 186699Hz, -60dBc; Green Diamond: 66145Hz, -50dBc; Blue Diamond: 40072Hz, -45dBc; Red Diamond: 25147Hz, -42dBc). b) Experimental measurement of SSB phase noise and spurious signal levels of SIL for 8km delay with different injection strengths (Green: $p=0.00316$; Blue: $p=0.01$; Red: $p=0.0316$. Green Diamond: 22576Hz, -53dBc; Blue Diamond: 24733Hz, -50dBc; Red Diamond: 25147Hz, -42dBc). Oscillator characteristics are $P_s=16\text{dBm}$, NF=32dB, optical link NF=60dB for both cases.

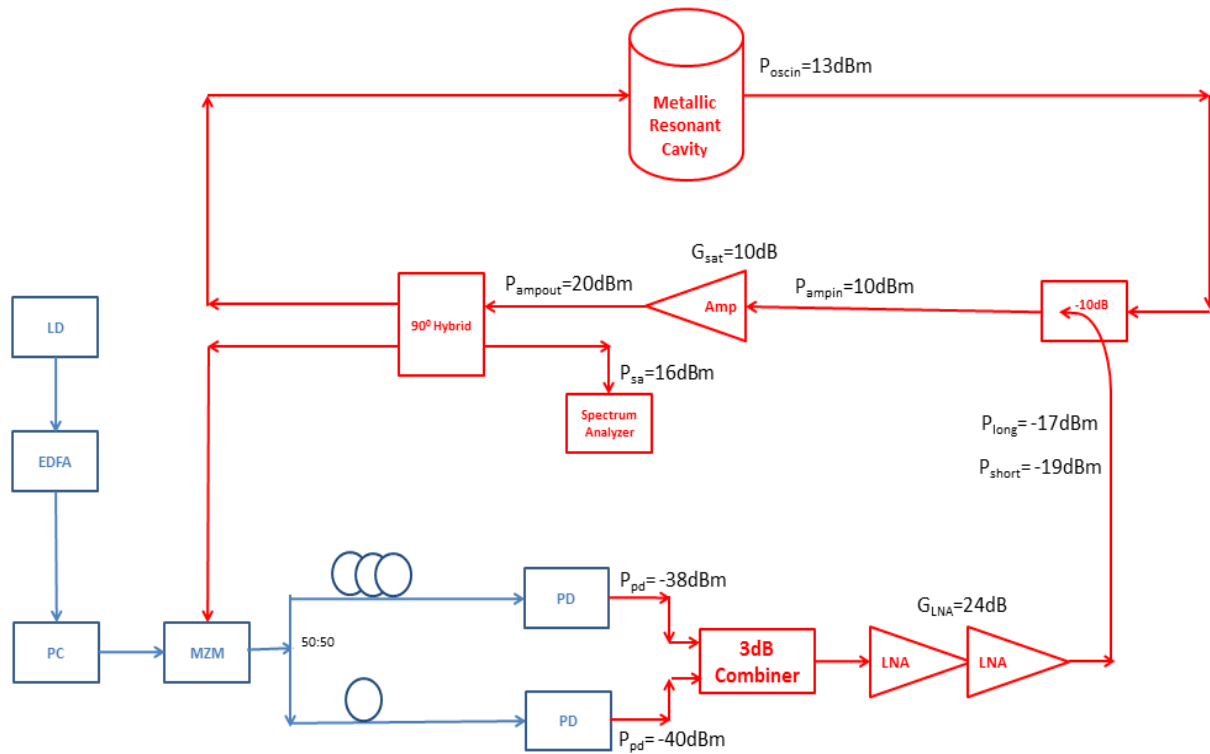


Figure F-10: Block diagram of electrical cavity oscillator with dual loop SIL

One interesting phenomenon for DSIL is that the location and level of the first major spurious mode are all different in three cases. Neither do they appear at 25kHz (mode spacing related to 8km) nor do they appear at 200kHz (mode spacing related to 1km). In fact, they appear at 175kHz, 126kHz and 75kHz offsets respectively. The spurious suppression is significant in DSIL as we can see all the spurious signal moves away from the carrier and the levels are dropped to below -60dBc, which is more than 20dB lower than SIL. Moreover, the spurious signals associated with 8km delay that would have appeared at offset frequencies about 25kHz, 50kHz and 75kHz with high power level are being filtered-out and somewhat suppressed by the shorter loops. The dominant side-modes of 25kHz, 50kHz and 75kHz now appear as humps with a reduced side mode level as seen in the measurement results of Figure F-11. Therefore, a more dominant side mode is observed at 126kHz. However, the mechanism for mode selection in DSIL requires to be explored analytically for optimum delay length in each fiber optic delay lines for dual loop SIL systems.

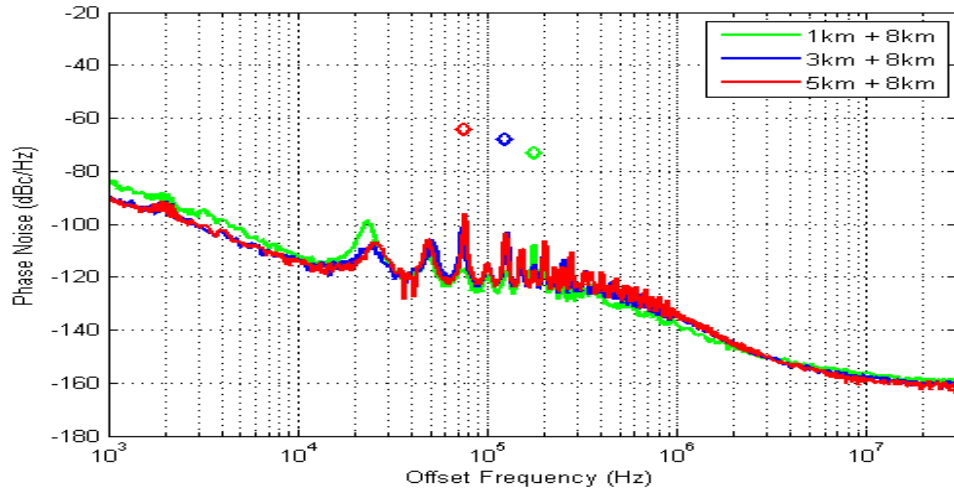


Figure F-11: Experimental measurement of SSB phase noise and spurious signal levels of DSIL with different fiber length combinations (Green: 1km and 8km; Blue: 3km and 8km; Red: 5km and 8km; Green Diamonds: 175447Hz, -73dBc; Blue Diamonds: 125753Hz, -68dBc; Red Diamonds: 75879Hz, -64dBc). Oscillator characteristics are $P_s=16\text{dBm}$, $\text{NF}=32\text{dB}$ and optical link $\text{NF}=60\text{dB}$.

F3 Experimental Results of SIL OEO

The block diagram for standard OEO configuration is depicted in the dashed black box of Figure F-12 where the metallic resonant cavity is employed as a narrowband band-pass filter. Two low noise amplifiers (LNA) and two power amplifiers (Amp) are used to compensate for the RF signal loss in the MZM link. The power amplifiers employed here have very high 1dB compression points to achieve higher oscillator output power while in the current form of the OEO a 1 dB compression is experienced in MZM at a lower power level than the power amplifiers. Hence, the saturation is due to the MZM but not the amplifiers. The fiber optic delay line of 1km long is selected for the OEO and the RF filtering is performed using the metallic cylindrical resonant cavity with unloaded Q of 2500. The measured oscillation is at 10GHz and output power of this standard OEO is 16dBm. Phase noise performance for this standard OEO is shown in the black curve in Figure F-3. The measured phase noise is -83dBc/Hz and -109dBc/Hz at 1kHz and 10kHz offset, respectively. The black diamond shows the actual location of the first spurious signal at 197kHz offset and the level is -40dBc. The measured performance is significantly better than the electrical feedback oscillator presented in section 3.1 and somewhat resembles the performance of electrical oscillator with SIL using a 1km long fiber delay line in Figure F-9.

F3.1 SIL Phase Noise

The block diagram of SIL OEO is depicted in Figure F-12. The output of the MZM is split into two parts; one passes through a 1km delay and another passes through a longer delay and a 10dB optical attenuator. The RF gain is sufficient to compensate for the loss in the 1km loop, but not the second delay; hence, optoelectronic oscillation will take place in the 1km loop and not at the longer delay. Because of the optical attenuator, the longer delay will not get enough gain to oscillate thus it forms a SIL to the OEO. Phase noise for SIL OEO is shown in Figure F-13 for various long delays. Delays of 3km, 5km and 8km are selected, and the lowest phase noise is achieved using an 8km delay as predicted (Figure F-14) at levels of -96dBc/Hz at 1kHz offset (13dB lower than standard OEO) and -118dBc/Hz at 10kHz offset (9dB lower than standard OEO). The spurious level of -69dBc for 8km delay is also the lowest which is 29dB lower than standard OEO.

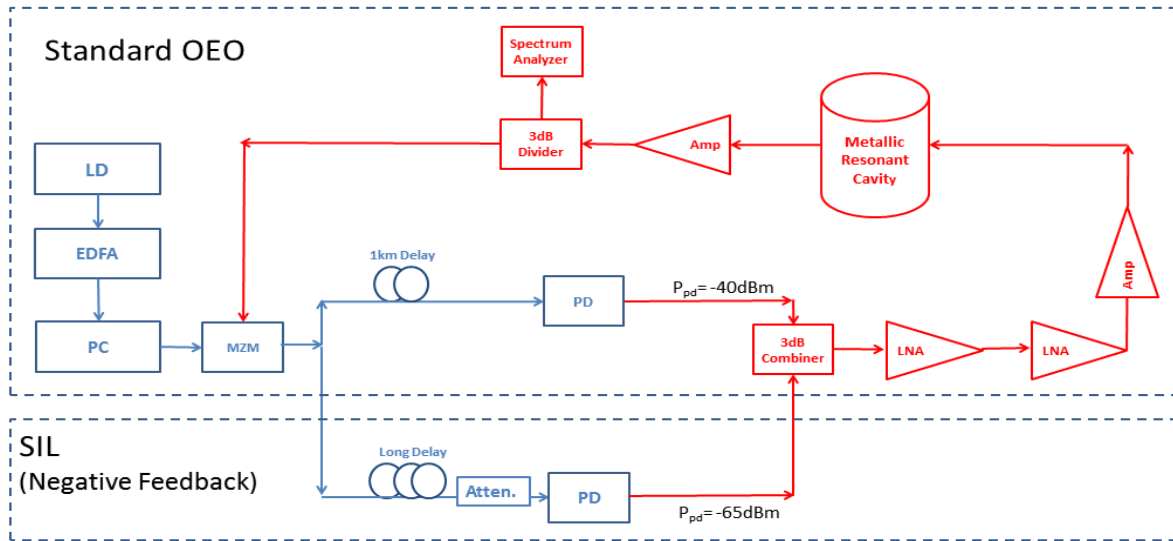


Figure F-12: System block diagram of 1km long standard OEO with SIL using various fiber delay lengths. Optical attenuation provided by block of "Attenuator." assures a negative feedback using the longer delay and the 10dB optical attenuation results in $\rho \approx 0.06$.

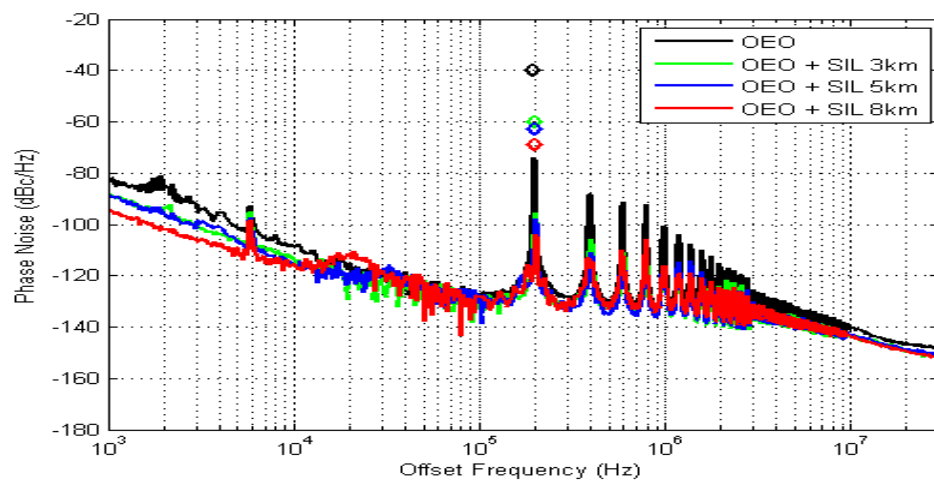


Figure F-13: Experimental measurement results of SSB phase noise of a standard OEO (Black: standard 1km OEO) with various SIL lengths (Green: 3km; Blue: 5km; Red: 8km) and spurious signal levels (Black Diamond: 196627Hz, -40dBc; Green Diamond: 199645Hz, -60dBc; Blue: Diamond: 200485Hz, -63dBc; Red Diamond: 201002Hz, -69dBc). The OEO electrical characteristics are $P_s = 16\text{dBm}$, $P_N = -114\text{dBm}$ and $\text{NF} = 60\text{dB}$.

F3.2 DSIL Phase Noise

The concept of dual loop SIL is employed to reduce the spurious signal levels. Experimental setup for OEO with DSIL is conceptually depicted in Figure F-14. The OEO portion of the setup is the same as in the SIL case. In the feedback path, the optical signal is further split into two branches using 50% optical coupler from Ascentta (CP-S-15-20-22-XX-S-L-10-FA).

The delay lengths in the branches are both selected to be longer than the delay in the standard OEO. The signals from the two branches are combined at the same photodetector using another 50% optical coupler from Ascentta (CP-S-15-20-22-XX-S-L-10-FA). Optical attenuator is omitted since the insertion loss of optical couplers is high enough to prevent optoelectronic oscillation in the feedback path. In order to limit the injection strength, RF signal in the OEO is amplified before combining with the feedback signal. Phase noise for OEO with DSIL is shown in Figure F-15 as different lengths of delay lines are used in DSIL loops. Various length combinations are selected to experimentally evaluation of the phase noise behavior of DSIL OEO and the level of spurious signals. The phase noise for different combinations remains almost the same in close-in offset range but there is a noticeable noise floor variation among the cases. For example, the noise floor for the '5.5km+8km' case is about -108dBc/Hz while it is -122dBc/Hz for the '3.5km+8km' case. The first spurious signal for different length combinations are tabulated in Table F.1. Spurious level of '3.5km+8km' combination is significantly lower than other combinations as the performance is also better in terms of close in to carrier phase noise. In order to understand the behavior of DSIL OEO, the side-mode spacing for different delays are tabulated in Table F.2. It can be seen that 1km, 3km, 5km and 8km long fiber all have common modes at 200kHz while 3.5km and 5.5km long fiber don't have modes at 200kHz, hence the spurious level for these 2 cases are lower than other cases, especially for 3.5km fiber. The phase noise of 5.5km fiber is poor; possible reason is that the modes of 5.5km fiber are too close to those of 8km fiber.

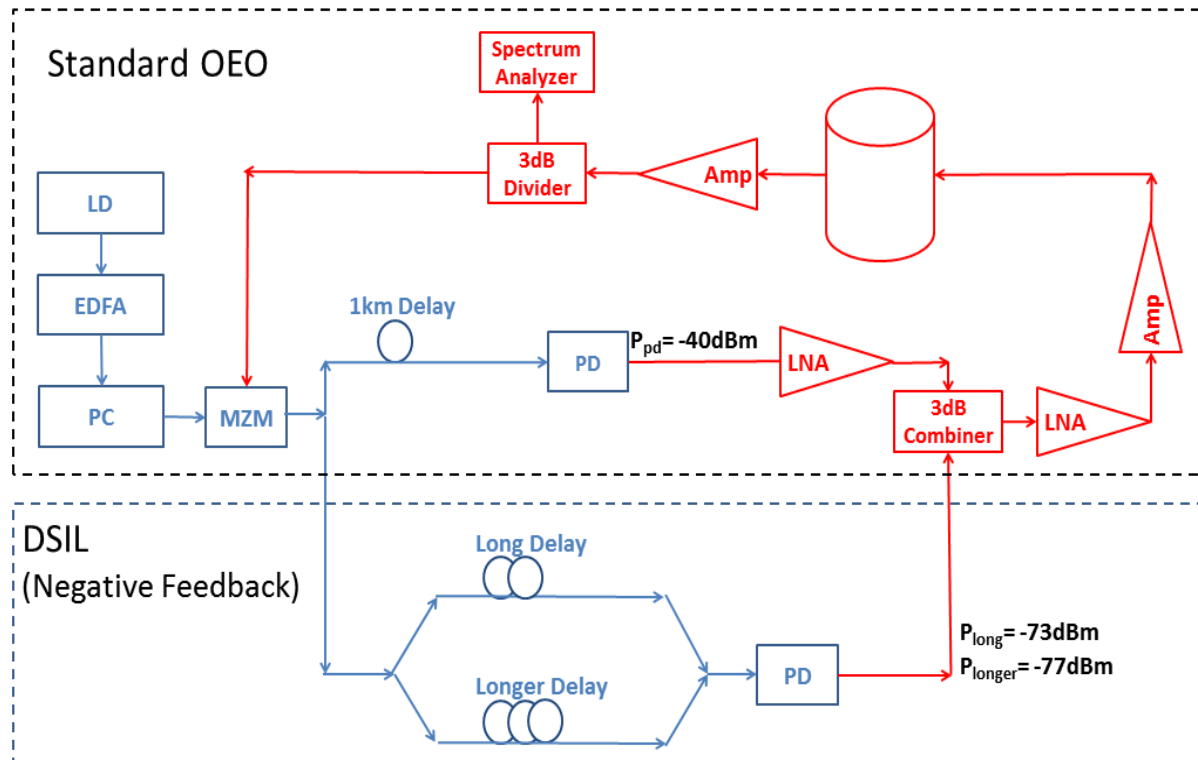


Figure F-14: System block diagram of 1km long standard OEO with DSIL optical delay lines. Optical power levels for short optical delay compared to the longest and longer delay lines are indicated in the figure.

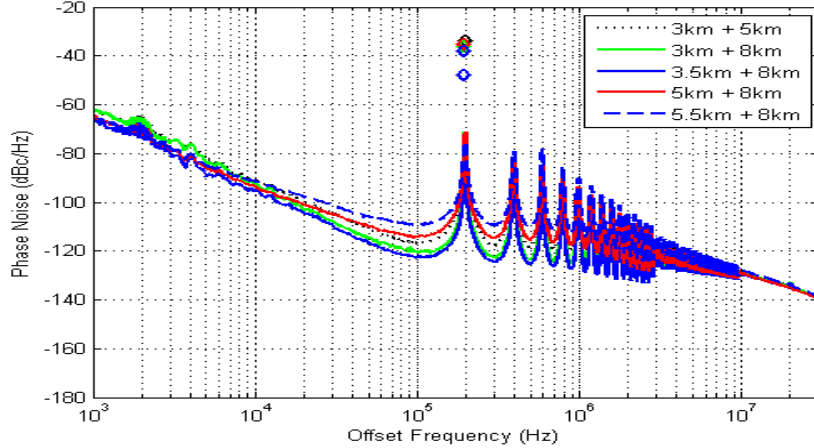


Figure F-15: Results of SSB phase noise of the OEO with various fiber length combinations of DSIL for $P_s=16\text{dBm}$.

Table F.1. Locations and signal levels of the first spurious for different length combinations of DSIL

DSIL Delay Combinations	3km + 5km	3km + 8km	3.5km + 8km	5km + 8km	5.5km + 8km
Spurious Freq. (Hz)	197,658	196,791	196,644	197,147	196,215
Spurious Level (dBc)	-34	-36	-48	-35	-38

Table F.2. Approximate side-mode spacing for different fiber delay lengths

Fiber Length	1km	3km	3.5km	5km	5.5km	8km
Mode Spacing	200kHz	66.7kHz	57.1kHz	40kHz	36.4kHz	25kHz

F4 Conclusion and Discussions

This section provided analytical modeling and experimental measurements of SSB phase noise of forced electrical cavity oscillator and OEO using SIL and DSIL techniques. These results provide insights into understanding of forced oscillation behavior in general and are very attractive in performance for optically realized stable clock signals. These stable clocks will play an important role in many coherent communication and target tracking radar systems. Comparison of SSB close in to carrier phase noise for different electrical cavity oscillator configurations is rendered in Table F.3. The simulated results agree well with the actual measurement results. Moreover, it is clear from Table F.3 that SIL and DSIL are effective for phase noise reduction in electrical oscillator.

Table F.3 Comparison of SSB phase noise for the electrical oscillator with different circuit configurations

Phase Noise Comparison	Simulated (dBc/Hz)		Measured (dBc/Hz)	
Offset-frequency(f_m)	1kHz	10kHz	1kHz	10kHz
Cavity Osc.	-52	-82	-58	-81
SIL 8km	-93	-120	-94	-118
DSIL 5km+8km	-93	-120	-92	-116

Comparison for the spurious levels is provided in Table F.4. The DSIL provided a 22dB reduction in terms of the spurious levels, while it has pushed to the 3rd harmonic at 75kHz. On the other hand, comparison of phase noise performance for OEO with different circuit configurations is rendered in Table F.5. For the case of DSIL case, the simulated results do not agree well with the measured results. Possible reason is that the modes in the two feedback branches interact with each other hence the noise floor becomes much higher.

Table F.4 Measured dominant spurious signals for the electrical oscillator with different circuit configurations

Spurious Comparison	Freq. (Hz)	Level (dBc)
SIL 8km	25147	-42
DSIL 5km+8km	75879	-64

Comparison for spurs of different OEO configuration is given in Table F.6. The higher spurious level in the DSIL case is understandable since DSIL has much higher noise floor. The mode competition between the side-modes of 8km and 5km delays degrades the spectrum purity of forced oscillation for OEO. If so, approaches that mode-lock these spurious frequencies have to be explored, which will reduce the mode-partition noise contributions [17].

Table F.5 Comparisons of phase noise for OEO with different circuit configurations

Phase Noise Comparison	Simulated (dBc/Hz)		Measured (dBc/Hz)	
	1kHz	10kHz	1kHz	10kHz
Standard OEO	-92	-112	-83	-109
SIL 8km	-92	-120	-96	-118
DSIL 5km+8km	-92	-118	-66	-95

Table F.6 Measured Spurious for OEO with different circuit configurations

Spurious Comparison	Freq. (Hz)	Level (dBc)
Standard OEO	1,966,627	-40
SIL 8km	201,002	-69
DSIL 5km+8km	196,644	-48

To improve the overall performance of SIL and DSIL for electrical cavity oscillator or OEO with long fiber optic delay lines, it is important to reduce the overall amplitude noise of the fiber optic delay lines. From the measured data, the noise floor of the optoelectronic system is around -114dBm/Hz, corresponding to a NF of about 60dB, which is typical for an external modulated optical link with the commonly experienced optical power of 10dBm, $V_\pi = 6V$ of Mach-Zehnder modulator (MZM), and RIN of -140dB/Hz. However, the NF could be reduced by increasing the optical power, using a lower V_π MZM, and limiting the optical source laser RIN [18]. Figure F-16 shows the phase noise of SIL OEO with different NF values, where the best performance is observed at a minimum reported noise figure of 4dB [19].

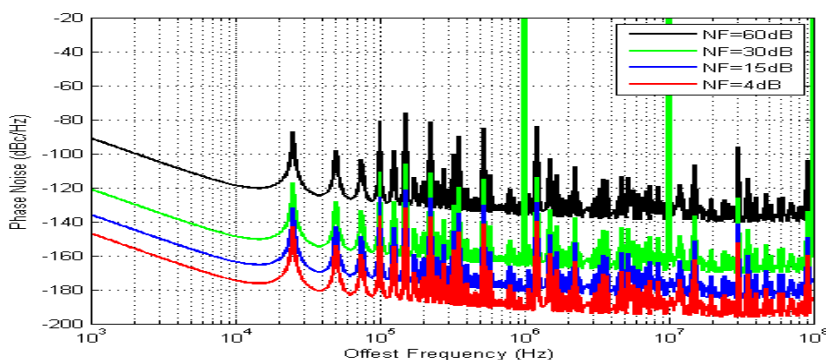


Figure F-16 Simulated SSB phase Noise for injection power ratio of 10dB of SIL OEO 8km with different values of noise figure for fiber optic link delays (Black: NF=60dB; Green: NF=30dB; Blue: NF=15dB; Red: NF=4dB).

It is clear from the figure that phase noise is reduced because of a lower noise floor in the system. On the other hand, the RF link loss of the fiber optic link is about 47dB and to compensate for the excessive loss, more than one stages of amplification are required to maintain operation at appropriate power level. Even though low noise amplifiers are used in the amplification chain, an increase in the overall NF

of the system is experienced. A proper selection of amplifiers will definitely reduce AM-PM conversion of the OEO.

The need for electronic amplifiers can be minimized by using a higher optical power source; a low phase noise is expected [20]. Another mechanism for minimization is phase locking. The phase of the modes associated with the long delay is not locked through injection locking and their frequencies are locked to one another. The mode partition noise becomes a major noise contributor in the coupled mode systems, hence, raising the noise floor and degrading the phase noise performance. By implementing self-phase locked loop (SPLL) combined with SIL low phase noise is expected [11]-[12], [21]-[25].

References

- [1] Eliyahu et al, "Low phase noise and spurious level in multi-loop Opto-electronic oscillators," Proceedings of the 2003 IEEE International Frequency Control Symposium
- [2] Banky et al, "Calculations for the measure of the achievable phase noise reduction by the utilization of optimized multi-loop Opto-electronic oscillators," European Microwave Conference, Oct. 2005
- [3] Levy et al, "Study of dual-loop optoelectronic oscillators," Freq. Control Symp., 20-24 April 2009, Besancon
- [4] R. Adler, "A study of locking phenomenon in oscillators," Proc. IRE, vol. 34, June 1946.
- [5] E. Shumakher et al, "On the noise properties of injection-locked oscillators," IEEE Trans. MTT, vol. 52, no. 5, May 2004
- [6] J. Roychowdhury et al, "Capturing oscillator injection locking via nonlinear phase domain macromodels," IEEE Trans. Microw. Theory Tech., vol. 52, no. 9, Sep. 2004.
- [7] F. Ramirez et al, "Phase noise analysis of injection locked oscillators and analog frequency dividers," IEEE Trans. Microw. Theory Tech., vol. 56, no. 2, Feb. 2008.
- [8] Zhang et al, "A theoretical and experimental study of the noise behavior of sub harmonically injection locked local oscillators," IEEE Trans. Microw. Theory Tech., vol. 40, no. 5, May 1992.
- [9] H. Moyer and A. S. Daryoush, "A unified analytical model and experimental validations of injection-locking processes," IEEE Trans. Microw. Theory Tech., vol. 48, no. 4, Apr 2000
- [10] Sturzbecher et al, Optically Controlled Oscillators for Millimeter-Wave Phased-Array Antennas, MTT VOL. 41, No. 6/7, 1993
- [11] A. Poddar, A. Daryoush, and U. Rohde, "Integrated production of self-injection locked self-phase locked opto-electronic oscillators," US Patent App. 13/60767.
- [12] A. Poddar et al "Self-injection locked phase locked loop optoelectronic oscillator," US Patent no. 61/746, 919
- [13] D. B. Leeson, "A simple model of feedback oscillator noise spectrum," Proc. Of the IEEE, vol. 54, no. 2, Feb 1966
- [14] J. Mora et al, "A single bandpass tunable photonic transversal filter based on a broadband optical source and a Mach-Zehnder interferometer", MWP 2003 proceedings
- [15] You et al, "High-Q optical microwave filtering," Electronics Letters, vol. 35, no. 24, Nov 1999
- [16] Yi et al, "Microwave photonic filter with single bandpass response," Elect. Lett., vol. 45, no. 7, Mar 2009
- [17] M. Mielke et al, "Reduction of mode partition noise in a multi-wavelength semiconductor laser through hybrid mode-locking", Technical Digest of CLEO 2002
- [18] E. Ackerman et al, "Maximum dynamic range operation of a microwave external modulation fiber-optic link," IEEE Trans. Microw. Theory Tech., vol. 41, no. 8, Aug 1993
- [19] C. Cox et al, "Some limits on the performance of an analog optical link," Technical Digest of MWP 1996
- [20] P. S. Devgan et al, "Improvement in the phase noise of a 10GHz optoelectronic oscillator using all-photonic gain," J. of Lightwave Tech., vol. 27, no. 15, Aug 2009
- [21] U. L. Rohde, A. K. Poddar, T. Itoh, and A. Daryoush, "Evanescent-Mode Metamaterial Resonator Based Signal Sources," IEEE IMaRC New Delhi, Dec 14-16, 2013
- [22] Li Zhang, U. L. Rohde, A. K. Poddar, and A. S. Daryoush, "Self-Injection Locked Phase-Locked Loop OEO," IEEE IMaRC New Delhi, Dec 14-16, 2013
- [23] Li Zhang, U. L. Rohde, A. K. Poddar, and A. S. Daryoush, "Ultra Low FM Noise in Passively Temperature Compensated Microwave Opto-electronic Oscillators," IEEE IMaRC New Delhi, Dec 14-16, 2013
- [24] Zhang, Optoelectronic Frequency Stabilization Technique in Forced Oscillators, PhD Thesis, Drexel Univ. 2014.
- [25] J.W. Fisher, L. Zhang, A. Poddar, U.L. Rohde, and A.S. Daryoush, "Phase Noise Performance of Optoelectronic Oscillator Using Optical Transversal Filters", IEEE BenMAS, Drexel, Sept 2014

Appendix G

G1. Forced Oscillations Using Self-Phase Locking

As demonstrated both analytically and experimentally in Appendix F, the forced injection locking could improve the close in to carrier phase noise. The reported results in literature [1]-[2] indicate that forced stability using phase locking also results in improved performance of close in to carrier phase noise. In this section G.1, a comprehensive analytical modeling for various methods of self-phase locking are introduced for both single and multiple self-phase locked loops. Moreover, performance improvements studied in terms of loop filter performance in terms of natural resonance and damping factors of type II phase locking circuits. The experimental evaluation of self-phase locking are presented in section G.2 using a VCO, in section G.3 using a conventional tunable phase shifter, and in section, G.4 for a MZM based optical phase shifting. The performance comparisons of the experimental and analytical results are summarized in section G.5.

G1.1 Phase Noise Analysis of Self-Phase Locking

(a) Conventional PLL

Let us express the input signal y_i and the output signal y_o as

$$y_i(t) = \cos(\omega t + \phi_i(t)) \quad (\text{G.1a})$$

$$y_o(t) = \cos(\omega t + \phi_o(t)) \quad (\text{G.1b})$$

The phase detector output is

$$u_1 = K_d \cos(\phi_i(t) - \phi_o(t)) \quad (\text{G.2})$$

After the filter,

$$u_2 = f(t) * K_d \cos(\phi_i(t) - \phi_o(t)) \quad (\text{G.3})$$

Then the relationship between the VCO output frequency and u_2 becomes

$$\frac{d(\omega t + \phi_o(t))}{dt} = \omega + K_o u_2 \quad (\text{G.4})$$

$$\frac{d\phi_o(t)}{dt} = K_o u_2 = K_o K_d f(t) * \cos(\phi_i(t) - \phi_o(t)) \quad (\text{G.5})$$

Now perform Laplace transform on both sides

$$s\phi_o(s) = K_o K_d F(s)(\phi_i(s) - \phi_o(s)) \quad (\text{G.6})$$

Then we can find the transfer function of the PLL as

$$H(s) = \frac{\phi_o(s)}{\phi_i(s)} = \frac{G}{1+G} \quad (\text{G.7})$$

$$\text{where } G = \frac{K_o K_d F(s)}{s}$$

From the system transfer function, we can represent the PLL system in frequency domain as shown in Figure G-1: Control theory representation of conventional PLL

Assuming that the noise is a small perturbation to the steady state solution, thus the linearity still holds, then we can derive the overall output noise using superposition principle. The first step is to find out the output noise ϕ_{n1} due to the input noise n_1 . Using basic loop analysis, we have

$$\phi_{n1}(s) = -G\phi_{n1}(s) + Gn_1(s) \quad (\text{G.8})$$

$$\phi_{n1}(s) = \frac{G}{1+G}n_1(s) = H(s)n_1(s) \quad (\text{G.9})$$

Then the noise spectrum can be found as

$$S_{\phi_{n1}}(\omega_m) = |H(s)|^2 S_{n_1}(\omega_m) \quad (\text{G.10})$$

Similarly, we can find the output noise ϕ_{n2} due to the VCO noise n_2 as follows

$$\phi_{n2}(s) = -G\phi_{n2}(s) + n_2(s) \quad (\text{G.11})$$

$$\phi_{n2}(s) = \frac{1}{1+G}n_2(s) = (1 - H(s))n_2(s) \quad (\text{G.12})$$

The noise spectrum is

$$S_{\phi_{n2}}(\omega_m) = |1 - H(s)|^2 S_{n_2}(\omega_m) \quad (\text{G.13})$$

The overall output noise spectrum becomes

$$S_{pll}(\omega_m) = |H(s)|^2 S_{n_1}(\omega_m) + |1 - H(s)|^2 S_{n_2}(\omega_m) \quad (\text{G.14})$$

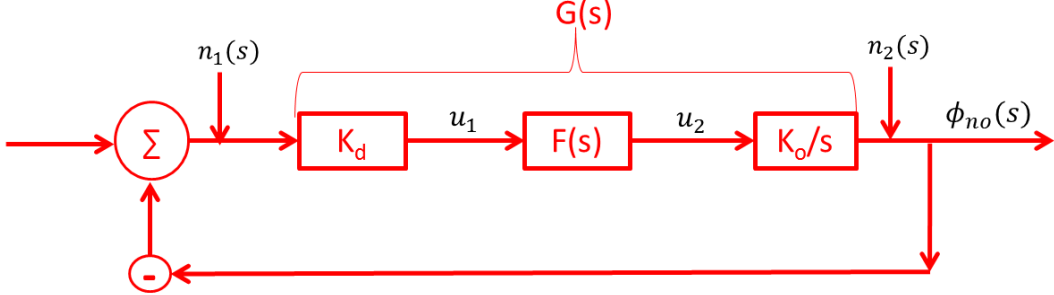


Figure G-1: Control theory representation of conventional PLL

G1.2 SPLL

The control theory representation is shown below in Figure G-2 for SPLL. A portion of the VCO output is being delayed and the phase of the delayed signal is compared against the phase of the current signal. Again, we can use superposition principle to find out the overall noise of the SPLL system. We first find out the output noise ϕ_{n1} due to the input noise n_1 . Using standard loop analysis, the transfer function of output phase ϕ_{n1} is given as

$$\phi_{n1}(s) = -G\phi_{n1}(s) + e^{-s\tau_d}G\phi_{n1}(s) + Gn_1(s) \quad (\text{G.15})$$

From (G.15)

$$\phi_{n1}(s) = \frac{G}{1+G(1-e^{-s\tau_d})}n_1(s) \quad (\text{G.16})$$

Output noise ϕ_{n2} due to VCO noise n_2 can be found in a similar fashion as

$$\phi_{n2}(s) = \frac{1}{1+G(1-e^{-s\tau_d})}n_2(s) \quad (\text{G.17})$$

Then the overall noise ϕ_{no} is given by

$$\phi_{no}(s) = \phi_{n1}(s) + \phi_{n2}(s) = \frac{G}{1+G(1-e^{-s\tau_d})}n_1(s) + \frac{1}{1+G(1-e^{-s\tau_d})}n_2(s) \quad (\text{G.18})$$

Then the noise spectrum becomes

$$S_{pll}(\omega_m) = |H_a(s)|^2 S_{n_1}(\omega_m) + |H_b(s)|^2 S_{n_2}(\omega_m) \quad (\text{G.19})$$

Where $|H_a(s)|^2 = \frac{G}{1+G(1-e^{-s\tau_d})}$, $|H_b(s)|^2 = \frac{1}{1+G(1-e^{-s\tau_d})}$

The CAD simulation results of SPLL OEO using (G.19) is shown below in Figure G-3. The black dashed curve is measured phase noise of an OEO with 100m delay in the free running case. Colored curves represent phase noise of OEO with SPLL for different delays. From the simulation results, phase noise decreases as the delay in SPLL increases. As shown in Figures G-3 and G-4, CAD simulation is performed to investigate the impact of different filter components, where SPLL delay is fixed at 5km while different ‘Mixer Filter’ boards are used. It can be noticed from Figure G-4, board #3 provides best phase noise reduction due to its large filter bandwidth. It should also be noted that when constructing SPLL, loop

stability is of practical concern. A combination of large filter bandwidth and a long fiber delay may result in an unstable loop as the long fiber delay will introduce additional poles (side-modes) in the system.

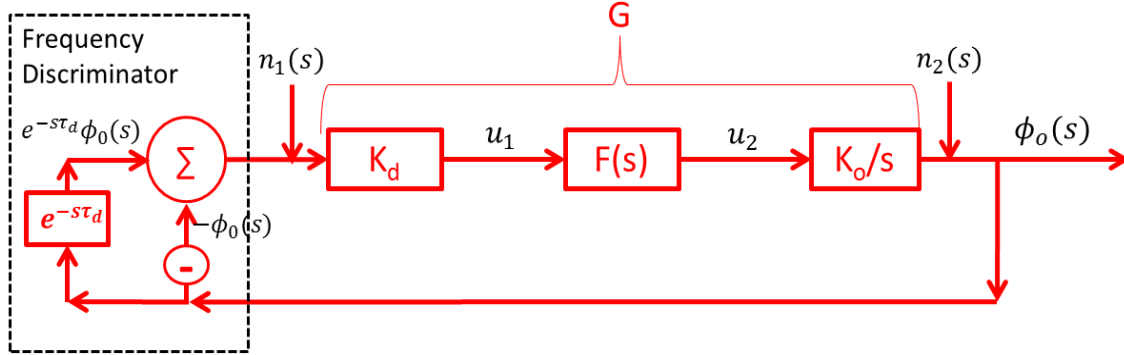


Figure G-2: Control theory representation of SPLL

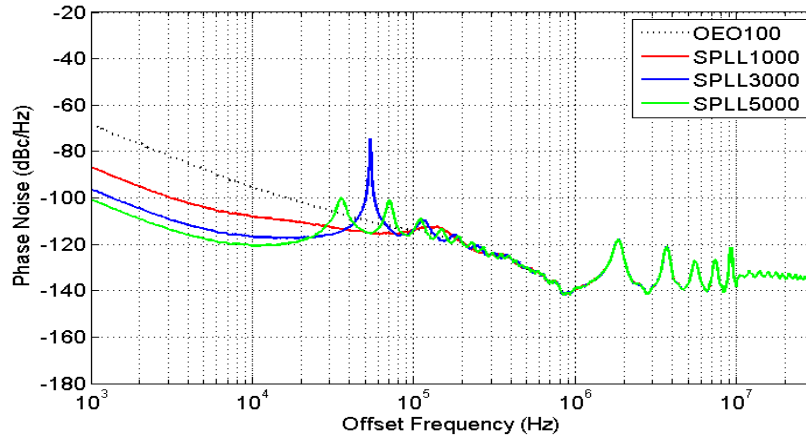


Figure G-3: Simulated phase noise of SPLL with Circuit 1 (medium loop BW) for different delays using RoF Link 2.
 $K_d=0.01\text{V}/\text{rad}$ and $K_o=2\pi\times 200\text{kHz}/\text{V}$

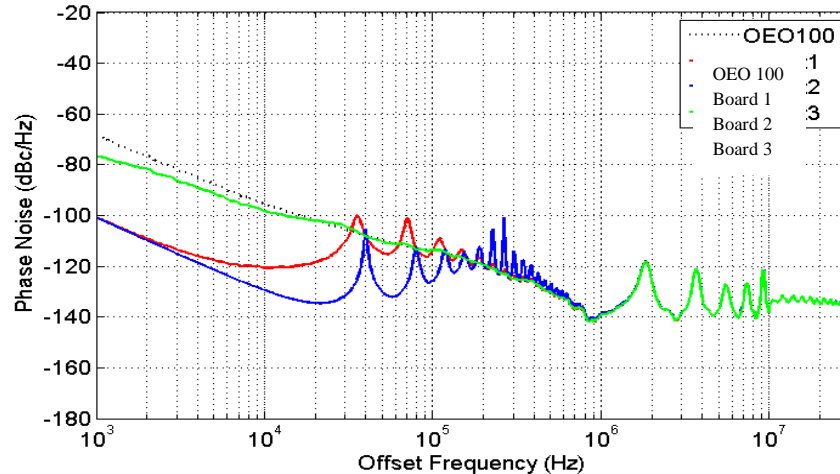


Figure G-4 Simulated phase noise of SPLL with 5km delay for different 'Mixer+LPFA' boards using RoF Link 2.
 $K_d=0.01\text{V}/\text{rad}$ and $K_o=2\pi\times 200\text{kHz}/\text{V}$

G1.3 DSPLL

Control theory representation is shown in Figure G-5 for DSPLL. Phase noise expression of DSPLL can be found using loop analysis in a similar fashion to single loop SPPLL, and is given as

$$S_{\text{DSPLL}}(\omega_m) = |H_c(s)|^2 S_{n_i}(\omega_m) + |H_d(s)|^2 S_{n_o}(\omega_m) \quad (\text{G.20})$$

Where

$$H_c(s) = \frac{G}{1+G(1-e^{-s\tau_{d1}})+G(1-e^{-s\tau_{d2}})}$$

$$H_d(s) = \frac{1}{1+G(1-e^{-s\tau_{d1}})+G(1-e^{-s\tau_{d2}})}$$

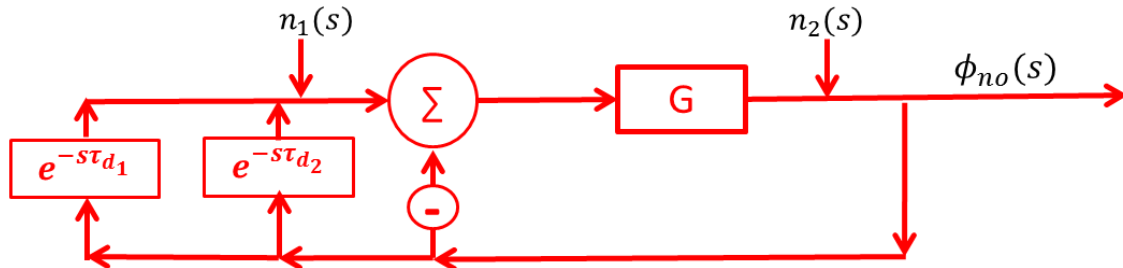


Figure G-5: Control theory representation of DSPLL

Phase noise simulation of DSPLL using (G.20) is shown in Figure G-6. From the simulation results, DSPLL provides similar phase noise reduction compared to SPPLL, but the side-mode level is greatly reduced in DSPLL due to additional loop.

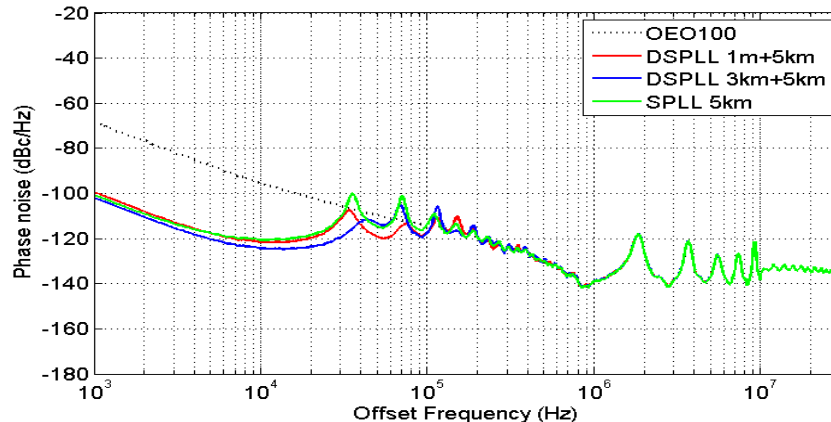


Figure G-6: Simulated phase noise of DSPLL with Circuit 1 (medium loop BW) for different combinations of delays using RoF Link 2.

Impact of different filter components on phase noise is simulated for a length combination of 3km and 5km to identify the optimum filter parameters, simulation results are shown in Figure G-7. Once again, we can see that the best phase noise is provided by board #3. However, in terms of physical implementation, loop stability has to be considered in order for the PLL to function properly.

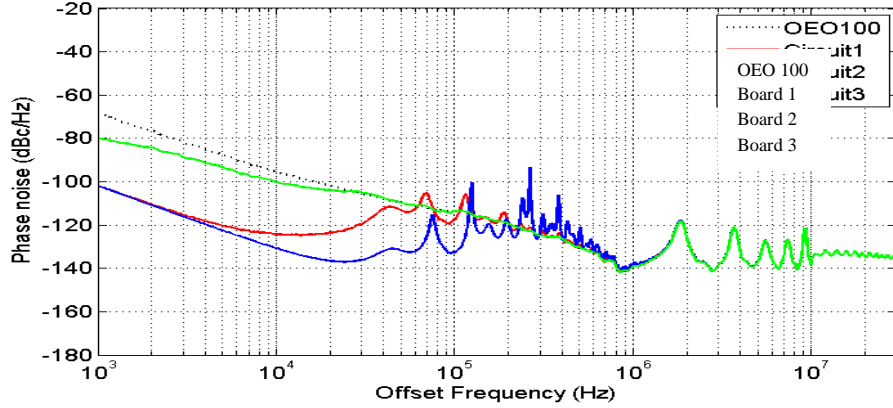


Figure G-7: Phase noise of SPLL with delay combination of 3km and 5km for different circuits using RoF Link 2.

G2 Experimental Results of SPLL VCO

G2.1 VCO Realization

The VCO circuit is shown in Figure G-8. It consists of a tunable filter and an amplifier (Avantek AMT 9634) with small signal gain of 28dB and 1dB compression of 12dBm referred to the output. The tunable filter is constructed using an open circuit microstrip line terminated with two varactor diodes (Aeroflex MGV125-08). The tunability of the filter is achieved by changing the reverse bias voltage of the diodes. The VCO free running frequency is at 8.5GHz with an output power of 0dBm, and the tuning sensitivity is about 200kHz/V at 5V bias voltage. The measured phase noise is shown in the black dashed curve of Figure G-10. The phase noise slope is about 30dB/decade up to 10MHz offset which indicates a flicker noise dominated system. This high flicker noise is usually associated with an FET based amplifier, and flicker noise could be reduced if HBT based amplifier is used.

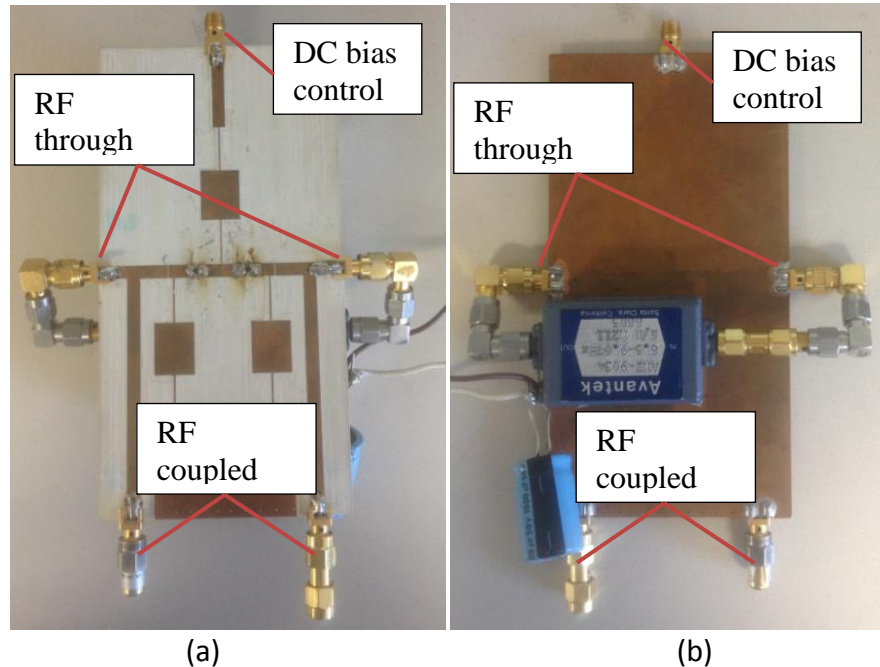


Figure G-8: Picture of the VCO (a) Top view (b) Bottom View

G2.2 SPLL

Experimental setup of SPLL is depicted in Figure G-9. As shown in Figure G-9, the output of the VCO is amplified by amplifier block for and driving the MZM. The modulated optical signal is passed through the

3km fiber delay, and converted to electrical signal by a photodetector. The delayed signal is sent to the RF port of the ‘Mixer+Filter’ board #1 for comparison with the non-delayed signal coupled directly from the VCO output. Measured phase noise of SPLL VCO is shown in blue curve of Figure G-10.

The phase noise of the SPLL VCO is reduced from -26dB of free running case to -71dB at 1kHz offset corresponding to an improvement of 45dB; at 10kHz offset, phase noise is improved by 20dB reaching -78dBc/Hz. Simulation result using (G.19) is also depicted in red curve of Figure G-10. It can be seen that there is excellent agreement between analytical and experimental results. SPLL with 5km delay is attempted to achieve further phase noise reduction, but the long delay introduces strong side-modes that are spaced every 40kHz away from the carrier causing the loop to be unstable, and the PLL fails to acquire a locked state. In the next section, DSPLL has been demonstrated to be effective for side-mode suppression leading to a stable loop operation and eventually a better phase noise reduction.

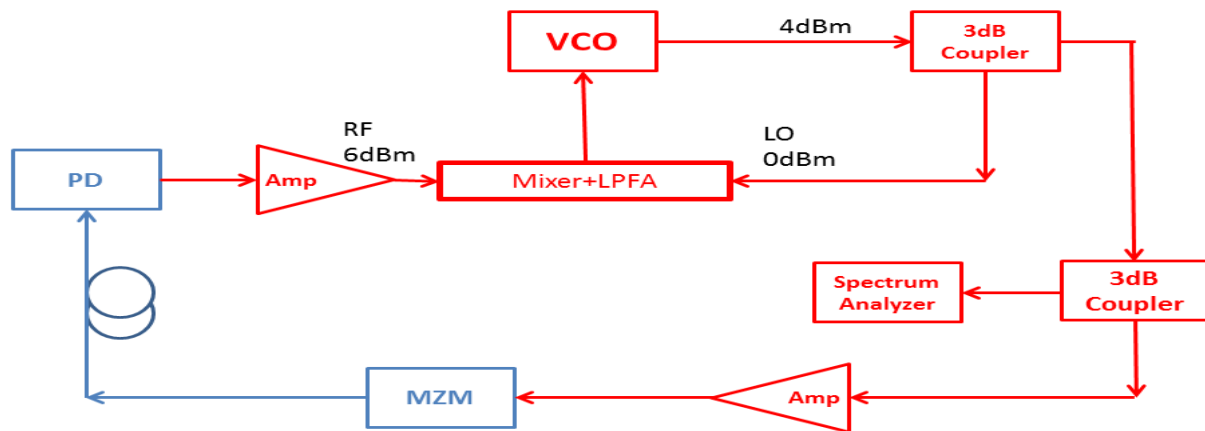


Figure G-9: Experimental Setup of SPLL VCO

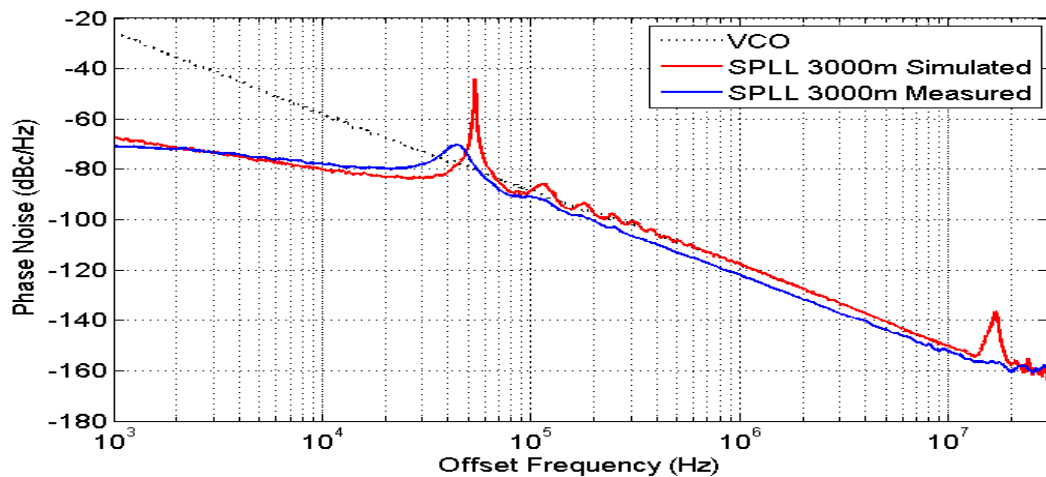


Figure G-10: Phase noise of SPLL with 3km delay and Circuit 1 using RoF Link2. Blue curve is measured phase noise for $K_d=0.01\text{V}/\text{rad}$, $K_o=2\pi\times 1\text{MHz}/\text{V}$; Red curve is simulated phase noise.

G2.3 DSPLL

Experimental setup of DSPLL is depicted in Figure G-11. The circuit diagram of DSPLL is similar to that of SPPLL. The difference is output of the MZM is split into two: one passes through a 5km delay while the other passes through a 3km delay. The two delayed signals are received by two diodes independently, and are combined in a 3dB coupler. The combined signal is amplified and sent to the ‘Mixer+Filter’ board to be compared with a non-delayed signal from the VCO output. Experimental result is shown in blue curve of Figure G-12. The phase noise of the DSPLL VCO is reduced from -26dB of free running case to -91dB at 1kHz offset corresponding to an improvement of 65dB; at 10kHz offset, phase noise is improved by 42dB reaching -100dBc/Hz. Simulation result of DSPLL using (G.20) is also provided in red curve of Figure G-12, and it matches up well with the measurement result. Phase noise comparison between SPPLL with 3km delay and DSPLL with 3km and 5km delay is shown in Figure G-13. We can see that DSPLL provides 20dB more reduction than SPPLL in offset frequencies from 1kHz to 50kHz.

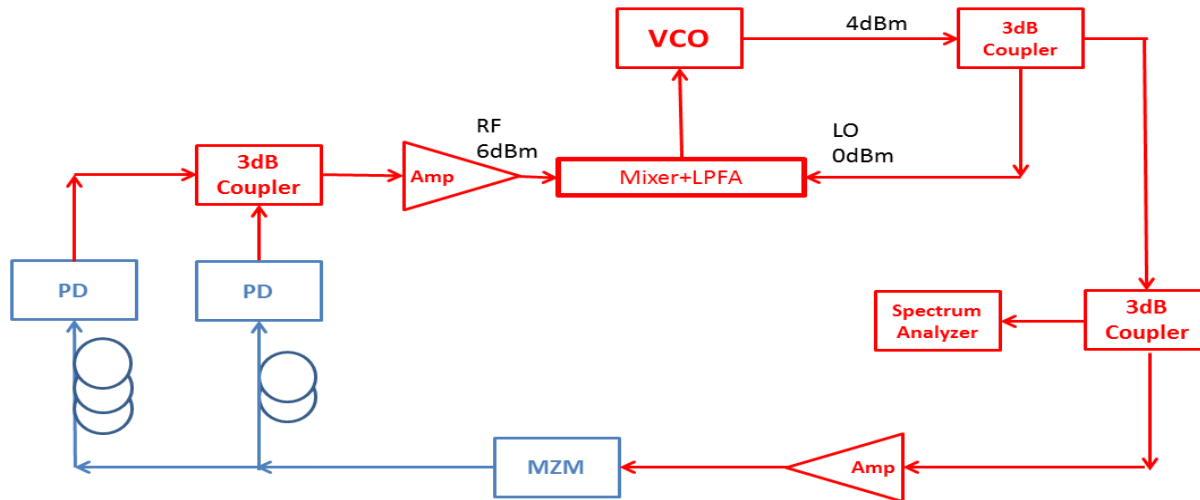


Figure G-11: Experiment Setup of DSPLL for VCO

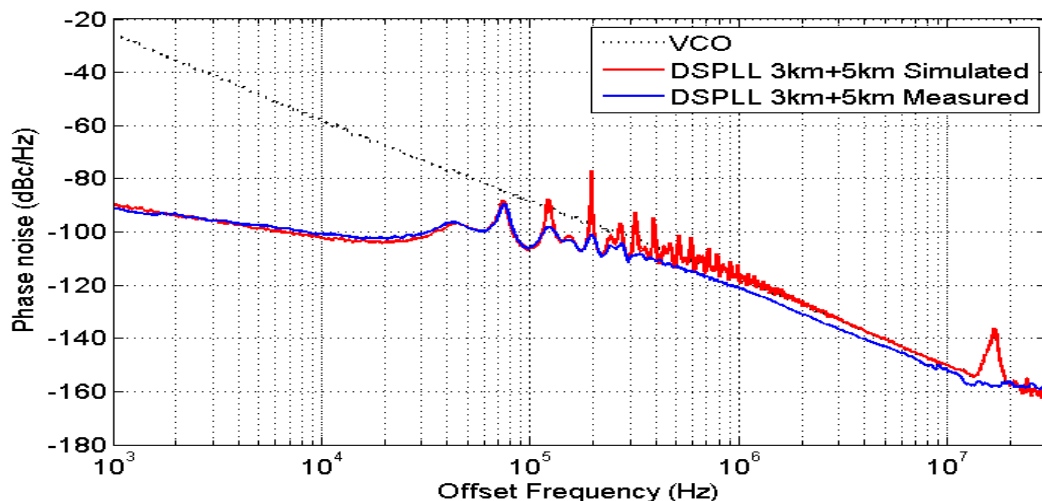


Figure G-12: Phase noise of DSPLL with delay combination of 3km+5km and Circuit 1 using RoF Link2. Blue curve is measured phase noise for $K_d=0.01\text{V}/\text{rad}$, $K_o=2\pi\times 1\text{MHz}/\text{V}$; Red curve is simulated phase noise.

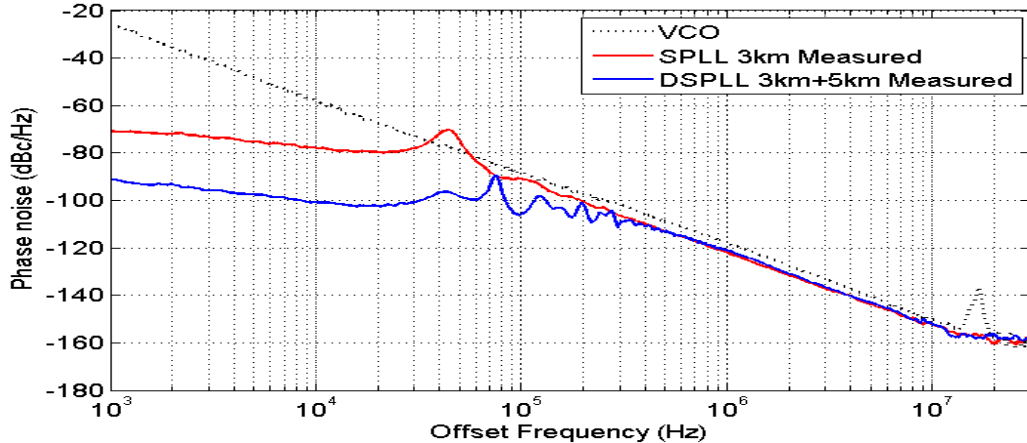


Figure G-13: Phase noise comparison of SPLL and DSPLL

G3 Experimental Results of SPLL OEO based on Tunable BPF

G3.1 OEO realization

The block diagram for standard OEO configuration is depicted in the dashed black box of Figure G-14, where the 5-port BPF is employed as a tunable band-pass filter that determines the OEO oscillation frequency. One low noise amplifiers (Kuhne Electronic 101A) and a power amplifiers (B&Z BZ3-09801050) shown as 'LNA1' and 'PowerAmp1' in Figure G-14 are used to compensate for the RF signal loss in the MZM link. The fiber optic delay line of 100m long is selected for the OEO. The measured oscillation is at 8.5GHz and output power of this standard OEO is 6dBm. Phase noise performance for this standard OEO is shown in the black curve in Figure G-15. The measured phase noise is -53dBc/Hz and -81dBc/Hz at 1kHz and 10kHz offset, respectively.

G3.2 SPLL

Block diagram of SPLL OEO is shown in Figure G-8. In addition to a standard OEO, a portion of the optical power is coupled out and passes through a longer fiber delay of 3km. The delayed signal is amplified by a low noise amplifier (Kuhne Electronic 101A) followed by a power amplifier (Miteq AMF-3D) shown as 'LNA2' and 'PowerAmp2' in Figure G-8 respectively; the delayed signal is then compared with the non-delayed OEO output at the 'Mixer+LPFA' board to generate an error signal to control the bias voltage of the varactor diode for frequency adjustment of the OEO. The measured phase noise of SPLL OEO is provided in Figure G-9. The phase noise of SPLL OEO at 1kHz is -91dBc/Hz, which is 38dB lower than free running OEO; and at 10kHz, -108dBc/Hz is achieved corresponding to a 27dB improvement.

G3.3 Impact of Different 'Mixer+LPFA' Boards on phase noise for a fixed delay

Different 'Mixer+LPFA' boards are used to investigate the impact of PLL loop bandwidth on phase noise for an optical fiber delay of 3km.

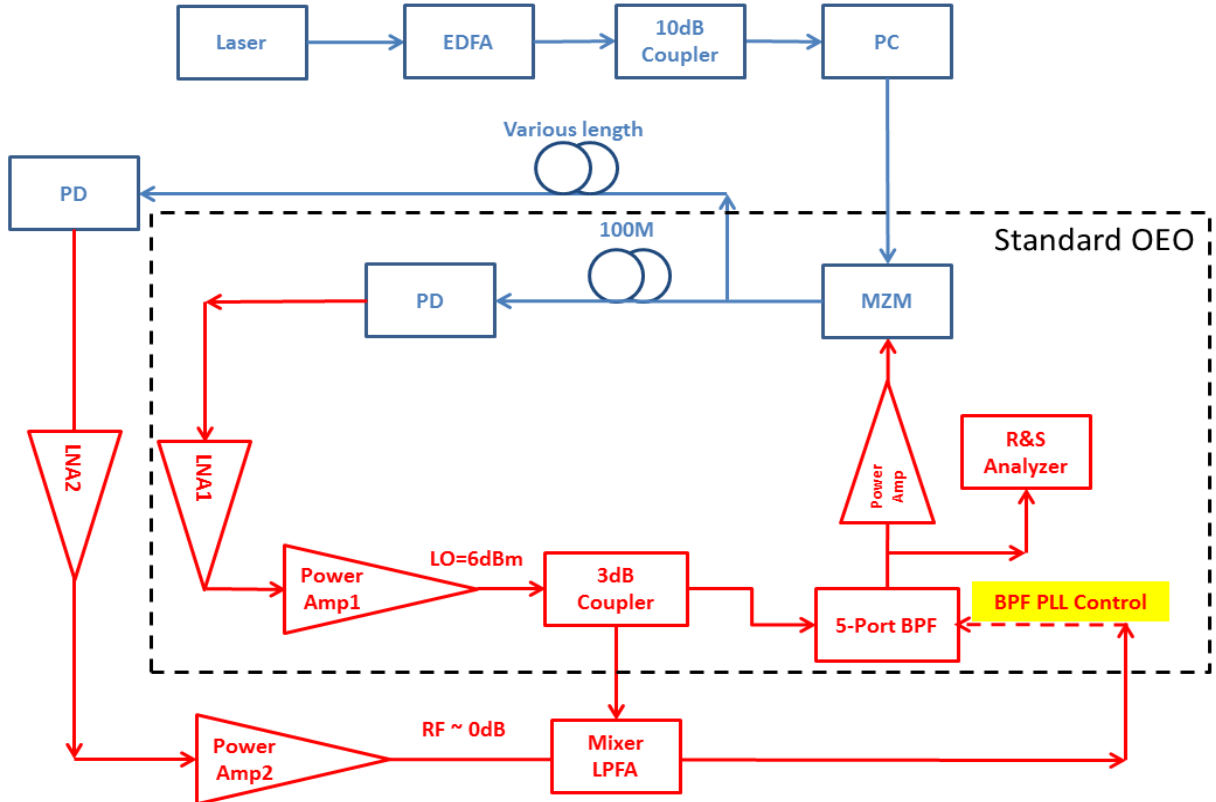


Figure G-14: Experiment Setup of SPPLL OEO based on BPF

Experimental setup is the same as depicted in Figure G-14. From the measurement results, the best phase noise performance is provided by Board #1 with a loop bandwidth of about 100kHz rather than Board #2 with a loop bandwidth of about 1MHz, which contradicts the analytical prediction. Possible reason for the discrepancy is that the 5km delay introduces too many side-modes within the PLL loop bandwidth, and the interaction between the side-modes degrades the performance of SPPLL. Measured phase noise performance is tabulated in Table G.1 for comparison.

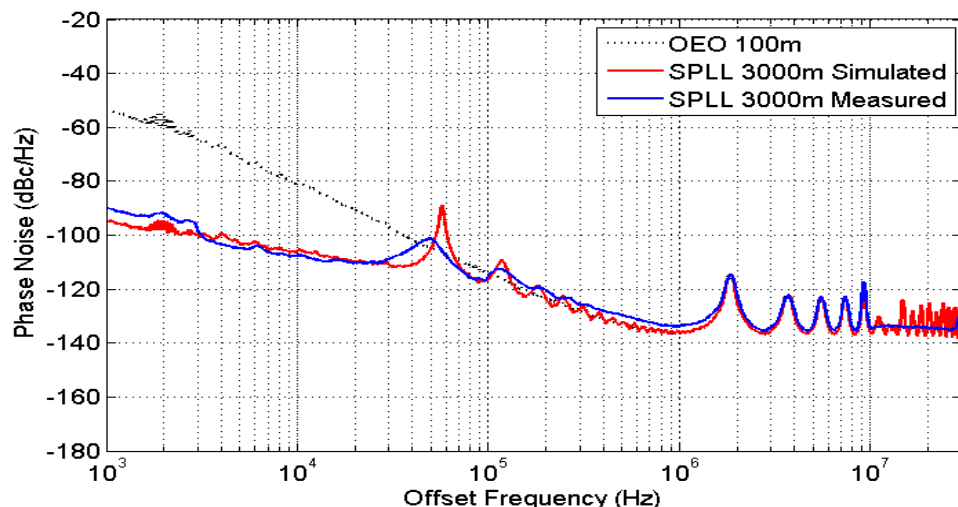


Figure G-15: Comparison of SPPLL phase noise between measured and simulated. RoF Link 2 is used and the loop parameters are $K_d=0.01V/\text{rad}$ and $K_o=2\pi\times 200\text{kHz}/V$.

Table G.1 Comparison of Different Boards for a fixed delay

	1kHz	10kHz
Board 1	-89.2	-105.5
Board 2	-78.9	-95.7
Board 3	-68.1	-96.9

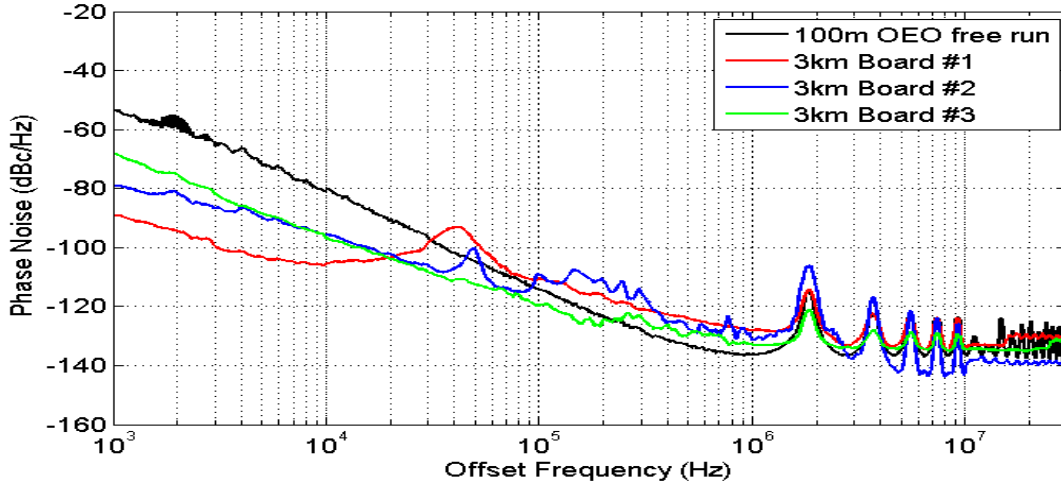


Figure G-16: Measured phase noise of SPLL OEO for 3km delay with different ‘Mixer+LPFA’ Boards. RoF Link 2 is used and the loop parameters are $K_d=0.01\text{V}/\text{rad}$ and $K_o=2\pi\times 200\text{kHz}/\text{V}$.

G4 Experimental Results of SPLL OEO based on MZM

G4.1 Realization of OEO

The block diagram for standard OEO configuration is depicted in the dashed black box of Figure G-11, it is similar to the one depicted in Figure G-11 of section G3. The differences are: (i) power amplifiers with 30dB gain between 8.5 – 9.6GHz from Avantek (AMT 9634) are used in blocks of ‘Amp1’, ‘Amp2’, and ‘Amp3’; and (ii) the error signal is sent to the MZM bias port rather than 5-port BPF bias port to achieve the frequency control of the OEO. The MZM control is advantageous over BPF control since the optical phase deviation introduced by MZM will be increased as the light propagates along the fiber, hence more tuning sensitivity. On the other hand, MZM has much wider bandwidth as opposed to electrical BPF.

The measured oscillation is at 9.6GHz with output power of 6dBm. Phase noise performance for this standard OEO is shown in the black curve in Figure G-12. The measured phase noise is -69dBc/Hz and -96dBc/Hz at 1kHz and 10kHz offset, respectively.

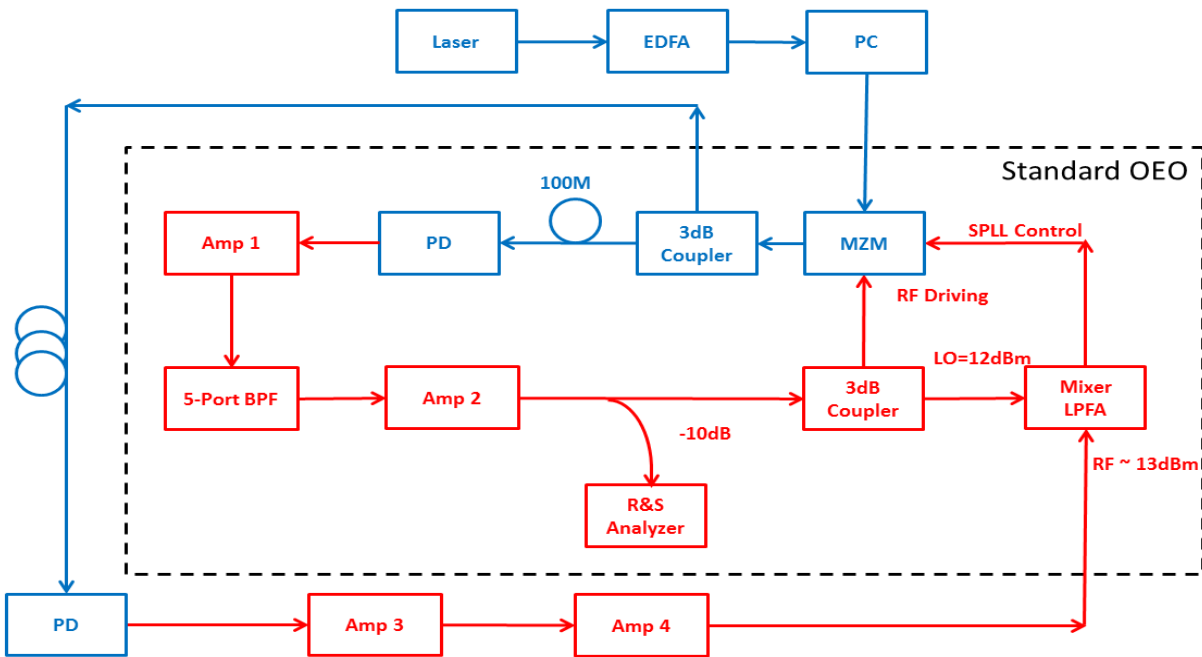


Figure G-11: Experiment setup of SPLL OEO based on MZM

G4.2 SPLL

Experimental phase noise of SPLL OEO with MZM control is shown in Figure G-12. The phase noise reduces as the delay in SPLL increases as expected from the analytical modeling. Best result is obtained using a 5km delay in SPLL, and the noise level is reduced by 20dB reaching -89dBc/Hz at 1kHz offset and by 23dB reaching -119dBc/Hz at 10kHz offset. Note that in section G3 where a BPF control is used for SPLL operation, 5km delay results in an unstable loop operation. In contrast, SPLL is functioning for MZM control with 5km delay and provides improved phase noise reduction. Figure G-13 shows the excellent agreement between simulation (red curve) and measured (blue curve) results of SPLL OEO using MZM control for 5km delay.

G5 Experiment of SPLL VCO using EAM Link

In this section, a DFB laser module integrated with an electro absorption modulator is used in the fiber optic link. The small form factor of the module and the integration of laser and modulator provides avenue of a compact system.

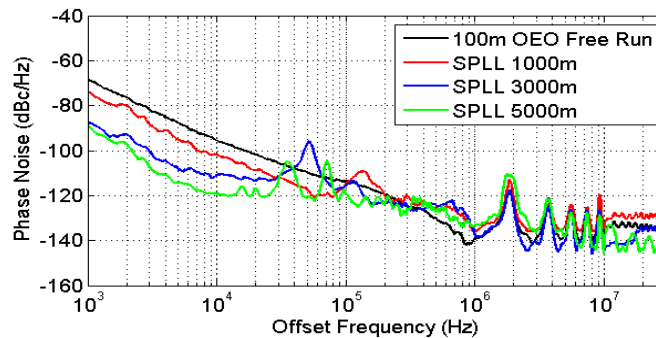


Figure G-12: Measured phase noise of SPLL with Circuit 1 (medium loop BW) for different delays using RoF Link 2. The loop parameters are $K_d=0.01\text{V}/\text{rad}$ and $K_o=2\pi\times200\text{kHz}/\text{V}$. Black curve: phase noise of free running 100m OEO; Red curve: phase noise of SPLL with 1000m delay; Blue curve: phase noise of SPLL with 3000m delay; Green curve: phase noise of SPLL with 5000m delay

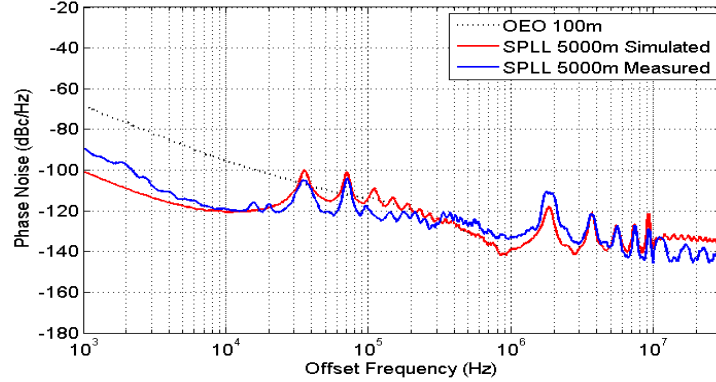


Figure G-13: Comparison of SPPLL phase noise between measured and simulated. RoF Link 2 is used and the loop parameters are $K_d=0.01\text{V}/\text{rad}$ and $K_o=2\pi\times200\text{kHz}/\text{V}$.

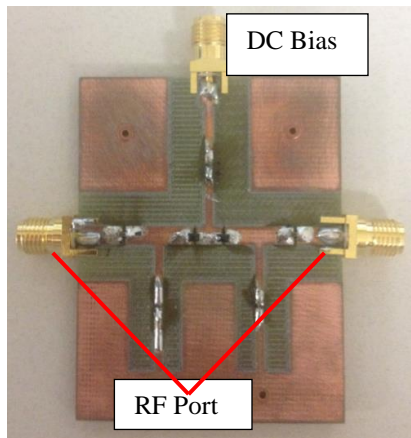


Figure G-14 Tunable BPF based on FR4

G5.1 Realization of VCO using tunable BPF with FR4 substrate

A different tunable BPF is built using FR4 substrate to achieve higher tuning sensitivity, shown in Figure G-14. The measured tuning sensitivity is shown in Figure G-15, maximum sensitivity is 5.5MHz/V at 1V and the sensitivity at 5V is 1MHz/V which is much higher than 200kHz/V of the 5 port BPF based on RT/Duroid. Measured phase noise of SPPLL VCO using EAM link is provided in Figure G-17. Degradation of phase noise performance of 5km SPPLL is most likely due to the side-modes associated with the 5km delay.

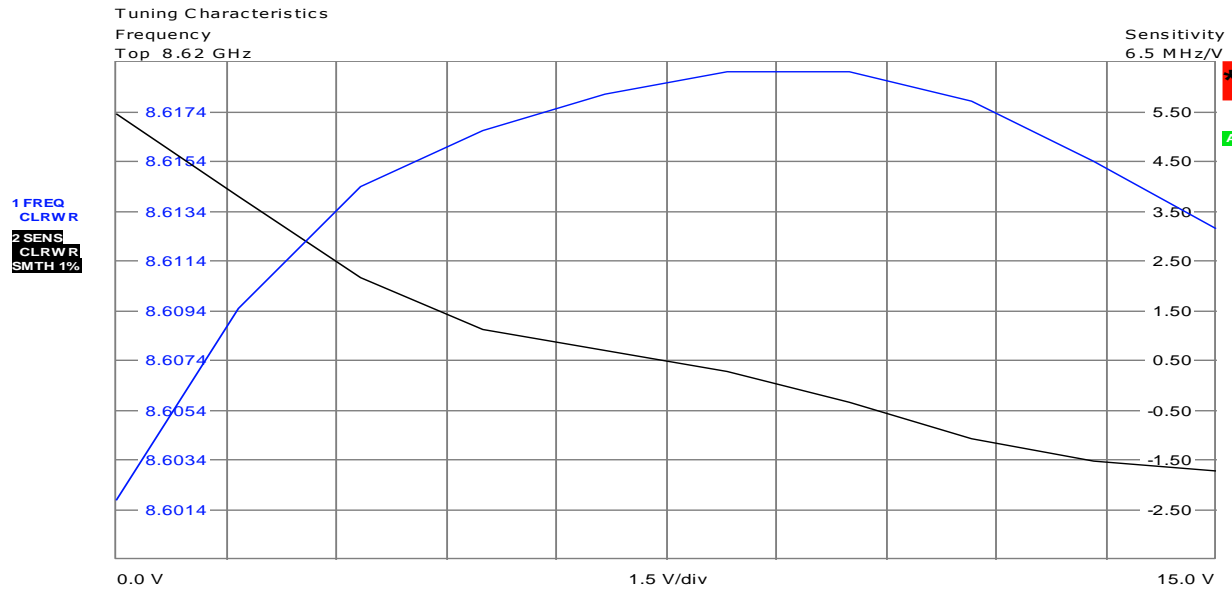


Figure G-15: Tuning sensitivity of VCO using BPF based on FR4.

G5.2 SPPLL VCO using EAM Link

Experimental setup for SPPLL VCO using EAM link is shown in Figure G-16.

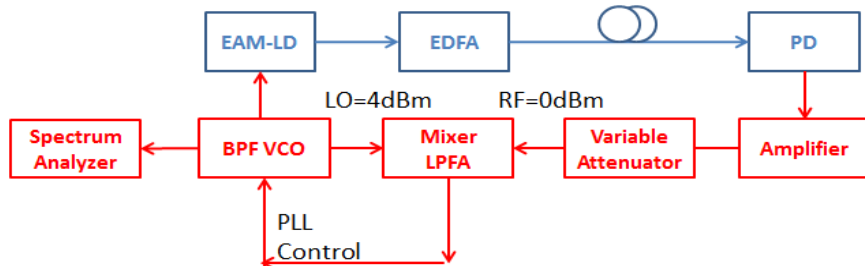


Figure G-16: Experiment setup of SPPLL VCO using EAM Link.

G5.3 DSPLL VCO using EAM Link

Benefit of DSPLL has been experimentally demonstrated where a delay combination of 3km + 5km is used. Mismatch of the pole locations between short and long delay effectively reduces the number and level of the side-modes, helps to stabilize the PLL operation, provides better phase noise reduction.

G6 Summary

This chapter is dedicated to analysis, design, and experimental performance evaluation of self-phase locked loop oscillators using long optical delay lines. Tables G.1, G.2, and G.3 summarizes the experimentally achieved phase noise improvement results at 1kHz and 10kHz offset frequencies using MZM link in comparison to analytically predicted performance. Table G.4 summarizes the experimentally achieved phase noise improvement at 1kHz and 10kHz offset frequencies using EAM link. Measurement results of Table G.1 and Table G.4 indicate that EAM link provide phase noise reduction comparable to that of MZM link, and it is desirable to construct a compact system using EAM link. As demonstrated [8]-[9] for ILPLL oscillators both close-in and far away from carrier phase noise could be reduced by combining IL and PLL function; therefore, one could employ forced self-injection and self-phase locking to build a SILPLL oscillator to improve performance of an oscillator. The merits of the SILPLL techniques are to be investigated in Appendix H.

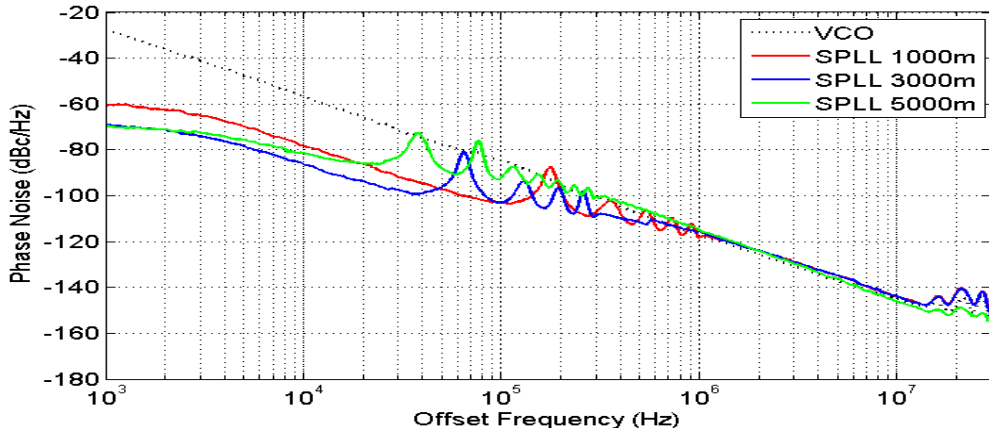


Figure G-17: Phase noise of SPLL with EAM Link and Board #3 for various delays. Black: VCO free run; Red: SPLL 1km; Blue: SPLL 3km; Green: SPLL 5km. $K_d=0.02V/\text{rad}$, $K_o=2\pi\times 1\text{MHz}/\text{V}$

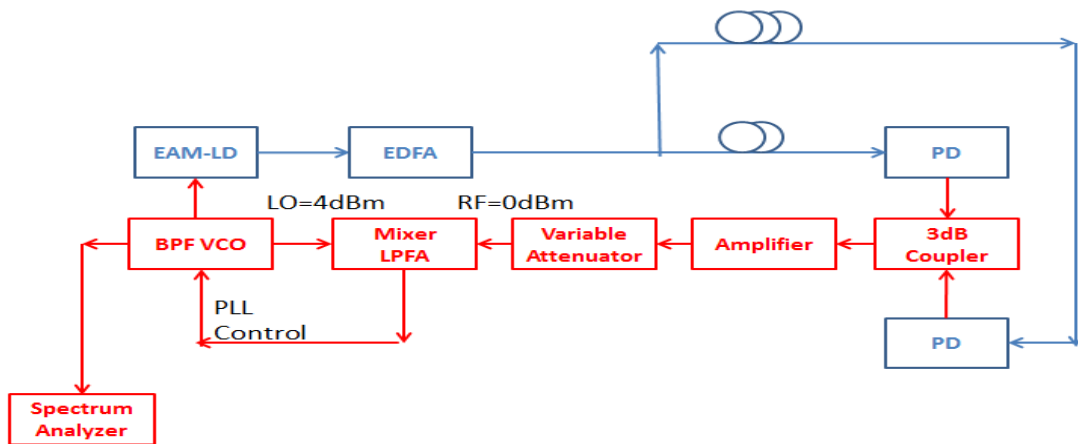


Figure G-18: Experimental setup of DSPLL VCO using EAM Link

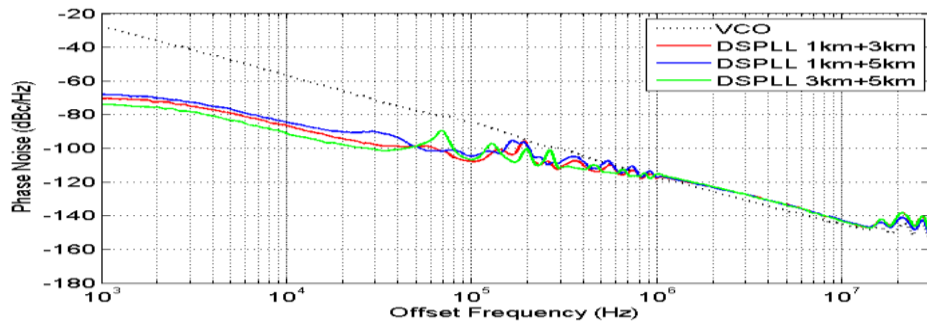


Figure G-19: Phase noise of DSPLL with EAM Link and Board #3 for various delays. Black: VCO free run; Red: DSPLL 1km+3km; Blue: DSPLL 1km+5km; Green: DSPLL 3km+5km. $K_d=0.02V/\text{rad}$, $K_o=2\pi\times 1\text{MHz}/\text{V}$

Table G.1 Comparison of SSB phase noise for VCO with different circuit configurations

Phase Noise Comparison	Measured (dBc/Hz)	
	1kHz	10kHz
VCO w/ 5port VCO	-26	-58
SPLL 3km	-71	-78
DSPLL 3km+5km	-91	-100

Table G.2. Comparison of SSB phase noise for free running OEO and SPLL OEO with BPF Control

Phase Noise Comparison	Measured (dBc/Hz)	
	1kHz	10kHz
OEO 100m	-53	-81
SPLL 3km	-91	-108

Table G.3. Comparison of SSB phase noise for free running OEO using Avantek Amplifiers and SPLL OEO with MZM Control

Phase Noise Comparison	Measured (dBc/Hz)	
	1kHz	10kHz
OEO 100m	-69	-96
SPLL 5km	-89	-119

Table G.4. Comparison of SSB phase noise for free running VCO w/ FR4 BPF and SPLL VCO with MZM Control using MZM Link

Phase Noise Comparison	Measured (dBc/Hz)	
	1kHz	10kHz
VCO w/ FR4 BPF	-29	-58
SPLL 3km	-69	-86
DSPLL 3km+5km	-74	-91

References

- [1] K. Lee et al, "A 30GHz self injection locked oscillator having a long Optical delay line for phase noise reduction," *Photonics Tech. Letters*, vol. 19, no. 24, Dec. 2007
- [2] Ronald T. Logan, Stabilization of oscillator phase using a fiber-optic delay-line, Frequency Control Symposium 1991
- [3] L. Zhang, V. Madhavan, R.P. Patel, A.K. Poddar, U.L. Rohde, A.S. Daryoush, "*Ultra low FM noise in passively temperature compensated microwave Opto-electronic oscillators*," in Proc. 2013 IEEE International Microwave & RF Conf., New Delhi, India, pp. 1-4.
- [4] L. Zhang, A.K. Poddar, U.L. Rohde, A.S. Daryoush, "*Analytical and experimental evaluation of SSB phase noise reduction in self-injection locked oscillators using optical delay loops*," *IEEE Phot. Journ.*, vol. 5, no. 6, Dec. 2013.
- [5] Li Zhang, Optoelectronic Frequency Stabilization Technique in Forced Oscillators, PhD Thesis, Drexel University, 2014.
- [6] Y. Jiang et al., "A selectable multiband bandpass microwave photonic filter," *IEEE Photonics Journal*, vol. 5, no. 3, p. 3, June 2013.
- [7] J. Mora et al., "Photonic microwave tunable single-bandpass filter based on a Mach-Zehnder interferometer," *Journal of Lightwave Tech.*, vol. 24, no. 7, July 2006.
- [8] A. Poddar, A. Daryoush, and U. Rohde, "Integrated production of self injection locked self phase loop locked Opto-electronic Oscillators", US Patent app. 13/760767.
- [9] A. Poddar, A. Daryoush, and U. Rohde, "Self-injection locked phase locked loop optoelectronic oscillator," US Patent App., no. 61/746, 919.
- [10] J.W. Fisher, L. Zhang, A. Poddar, U.L. Rohde, and A.S. Daryoush, "Phase Noise Performance of Optoelectronic Oscillator Using Optical Transversal Filters", IEEE BenMAS, Drexel, Sept 2014

Appendix H

H1 Forced Oscillations Using Self-Injection Locking and Phase Locked Loop (SILPLL)

It has been demonstrated that SIL and SPLL techniques provide excellent phase noise reduction in far-out and close-in offset respectively (Appendix G) [1]-[3]. Combining SIL and SPLL simultaneously, low phase noise level in wider offset range is expected. A control theory based linear model of SILPLL is described to predict the phase noise of SILPLL in locked state, the linear model agrees with experimental data within 5-10% accuracy. The nonlinear model would give correct prediction but convergence problems related with spice and harmonic balance tools can give erroneous result if nonlinearity and mode jumping associated with optical components are not taken care of. Experimental result that demonstrates the benefit of SILPLL over SIL in close in to carrier offset is reported in section H2. Performance of dual loop SILPLL with various delay combinations are reported in section H3, and the performance comparison of the experimental results is summarized in section H4.

H1 Analysis of SILPLL

From Appendix F1 and G1 IL and PLL phase dynamics can be described by

$$\text{IL Phase Dynamics } \frac{d\phi_o(t)}{dt} = B[\phi_i(t) - \phi_o(t)] \quad (\text{H.1a})$$

$$\text{PLL Phase Dynamics } \frac{d\phi_o(t)}{dt} = G[\phi_i(t) - \phi_o(t)] \quad (\text{H.1b})$$

where $B = \rho\omega_{3dB}$ and $G = K_d K_v f(t)$, and K_d is the phase detector sensitivity in V/rad; K_v is the VCO tuning sensitivity in rad/V; $f(t)$ is the impulse response of the loop filter.

Assume linearity still holds when the system is in locked state, the ILPLL phase dynamics can be obtained by adding IL and PLL phase dynamics as

$$\frac{d\phi_o(t)}{dt} = B[\phi_i(t) - \phi_o(t)] + G[\phi_i(t) - \phi_o(t)] \quad (\text{H.2a})$$

The phase dynamics of ILPLL in the presence of noise can be described in a similar fashion in cases of IL and PLL (Appendix F1 and G1)

$$\frac{d[\phi_o(t)+n_o(t)]}{dt} = B[\phi_i(t) + n_i(t) - \phi_o(t)] + G[\phi_i(t) + n_i(t) - \phi_o(t)] \quad (\text{H.2b})$$

From (H.1) and (H.2), the output phase of SILPLL due to noise can be found by converting the above Equations into Laplace domain as

$$\phi_o = \frac{B+G}{s+B(1-e^{-s\tau d_i})+G(1-e^{-s\tau d_p})} n_i - \frac{s}{s+B(1-e^{-s\tau d_i})+G(1-e^{-s\tau d_p})} n_o \quad (\text{H.3})$$

where $\phi_i(t) = e^{-s\tau d_i} \phi_o(t)$ is used for converting time domain into Laplace domain.

From (H.3), the power spectrum for phase of SILPLL becomes

$$S_{\phi_o} = \left| \frac{B+G}{s+B(1-e^{-s\tau d_i})+G(1-e^{-s\tau d_p})} \right|^2 S_{n_i} - \left| \frac{s}{s+B(1-e^{-s\tau d_i})+G(1-e^{-s\tau d_p})} \right|^2 S_{n_o} \quad (\text{H.4})$$

H2 SILPLL OEO using MZM as SPLL control

The technique of SILPLL is applied to a standard OEO for phase noise reduction, and the experimental results have been reported. The block diagram of SILPLL OEO is shown in Figure H-1. A standard OEO with 100m fiber delay is shown within the black dashed box. A portion of the optical signal of the OEO is coupled out and is being delayed by a longer fiber of 5km.

As shown in Figure H-1, the delayed optical signal is converted to electrical signal by a photodetector. It can be seen in Figure H-1 that half of the photodetector output is sent back to the standard OEO directly to form an SIL path (shown in a green curve) and another half is amplified and is sent to the 'Mixer+LPFA' board for comparison against the non-delayed signal to generate an error signal for frequency

adjustment of the OEO by changing the MZM bias voltage. The SPLL portion is shown in purple in Figure H-1.

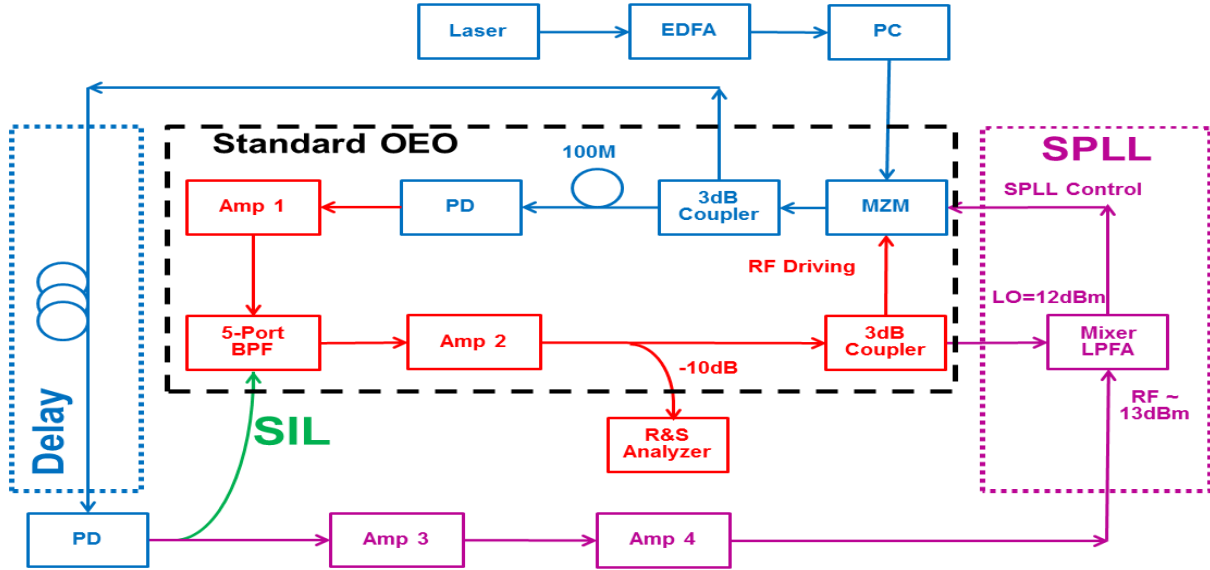


Figure H-1: Block diagram for SILPLL OEO

The measured SILPLL phase noise with 5km delay is shown in blue curve of Figure H-2. The achieved phase noise is -96dBc/Hz at 1 kHz offset and is -120dBc/Hz at 10 kHz offset, which demonstrates a reduction of 27dB and 24dB at 1 kHz and 10 kHz offset, respectively. Simulated phase noise of SILPLL using (H.4) is also provided as red curve in Figure H-2, which agrees well with the measurement. Phase noise of OEO with different frequency stabilization techniques are plotted in Figure H-2, the spot noise at 1 kHz and 10 kHz are also tabulated in Table H.1. From the measured results, the distinction between different technologies are insignificant even though SILPLL is expected to achieve lower phase noise than SIL in the close-in to carrier offset region while maintaining same noise level of SIL in the far-out offsets. A possible reason for the limitation could be due to the high noise level of the system (Appendix E) and PLL operation. The input power at the mixer RF port is limited which results in a low sensitivity (estimated to be 0.01V/rad) of the phase detector function. In addition, the tuning sensitivity of OEO using MZM control is limited to 200 kHz/V at 5V. These parameters result in a PLL loop BW of about 80 kHz, which is not sufficient to provide significant phase noise reduction.

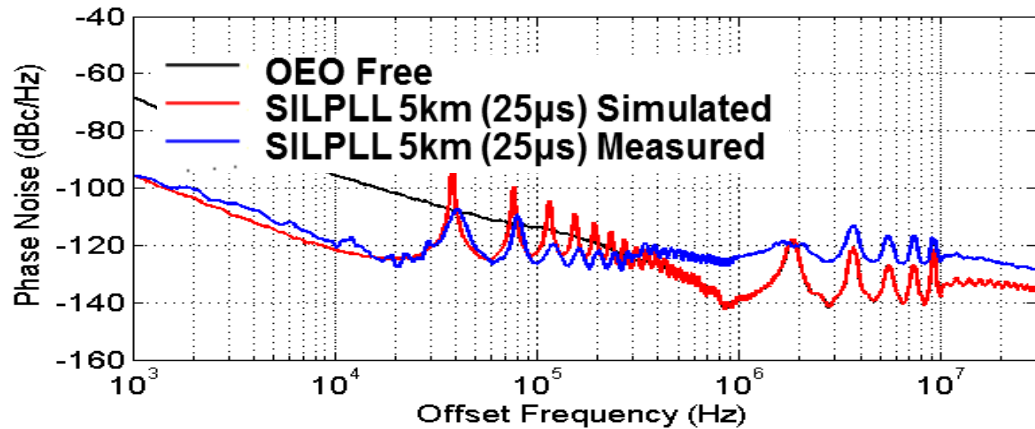


Figure H-2: SILPLL OEO phase noise for 5km delay. Parameters for SPLL portion: $K_d=0.01\text{V}/\text{rad}$, $K_o=2\pi\times 200\text{kHz}/\text{V}$ and Board #1 is used. Red curve is simulated; blue is measured.

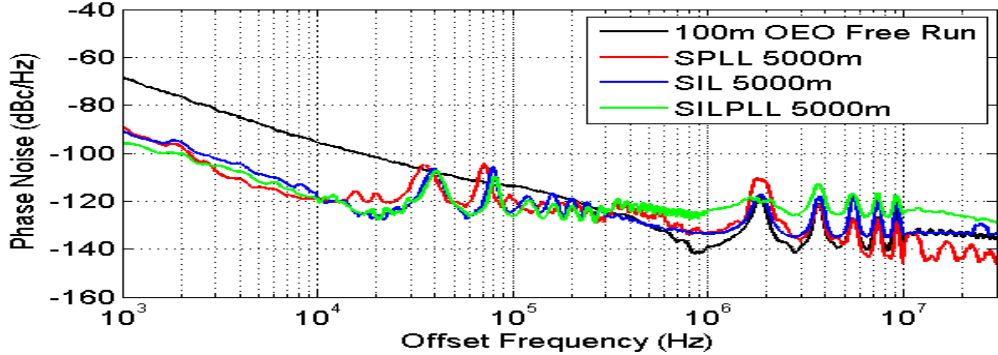


Figure H-3: Comparison for OEO with different frequency stabilization techniques.

Table H.1: Comparison of SSB phase noise for free running OEO and SPLL OEO with BPF Control

	PN at 1kHz	PN at 10kHz
OEO Free-Run	-69dBc/Hz	-96dBc/Hz
SPLL 5km	-89dBc/Hz	-119dBc/Hz
SIL 5km	-91dBc/Hz	-119dBc/Hz
SILPLL 5km	-96dBc/Hz	-120dBc/Hz

H3 SILPLL VCO with EAM Link

In this section, a VCO with higher tuning sensitivity and an EAM link with less loss are used to construct the SILPLL function for achieving higher PLL BW and eventually improving the SILPLL performance.

H3.1 SILPLL VCO

Figure H-4 shows a typical Block diagram of experimental setup of SILPLL VCO using EAM link, where VCO module is identical one used in Appendix G5 with FR4 BPF. The output of the VCO drives an EAM, which is integrated with a DFB laser in a small package. The output of the EAM is amplified by an EDFA whose output passes through a 1km fiber delay, and is received by a photodetector.

The output of the photodetector is sent to ‘Mixer+LPFA’ board #3 with power level of 13dBm after amplification, exhibiting an improved phase detector sensitivity of about 0.1V/rad as opposed to 0.01V/rad in MZM link.

The delayed signal is compared with non-delayed signal for phase comparison, and the generated error signal will control the reverse bias voltage of the varactor diodes on the BPF to adjust the VCO frequency. The tuning sensitivity is increased to 1MHz/V at 5V compared to 200 kHz/V in an OEO.

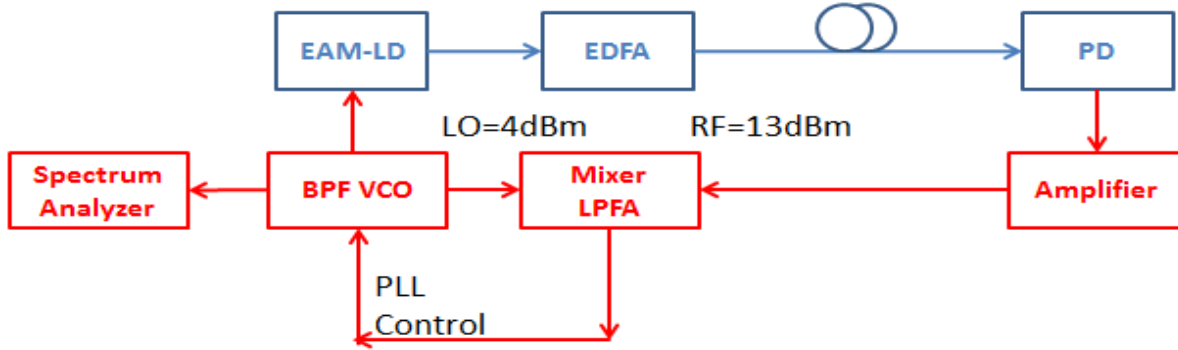


Figure H-4: Block diagram of SILPLL.

It can be noticed that there is not a dedicated path for SIL, but the power at Mixer RF port will leak into the VCO due to finite isolation between RF and LO ports of the mixer. The VCO is very sensitive to

injection locking due to the very low Q BPF, and this power leakage of about -25dBm is strong enough to form a SIL path. The effect of this leakage induced SIL is measured, when the ‘Mixer+Filter’ board is switched off, and the phase noise due to the leakage is shown in green curve of Figure H-5.

Measured phase noise of SILPLL with 1km delay is plotted as blue curve in Figure H-5. As shown in Figure H-5, the measured phase noise is -69 dBc/Hz at 300Hz offset from the carrier; this corresponds to a reduction of 58dB and is -87dBc/Hz at 10 kHz corresponding to a reduction of 29dB. It can be pointed out that when the SPPLL is functioning, the SIL due to power leakage from mixer RF port is also present; the overall phase noise is really due to the combination of SIL and SPPLL. For comparison, phase noise of SIL alone with 1km delay is also provided in red curve of Figure H-5.

Note that SILPLL phase noise is superior to SIL phase noise up to 3 kHz offset, beyond 3 kHz SILPLL phase noise follows SIL phase noise, which is expected, from the analytical modeling. Phase noise of different frequency stabilization techniques for VCO using EAM link are quantitatively tabulated in Table H.2 to show the benefit of SILPLL over SIL.

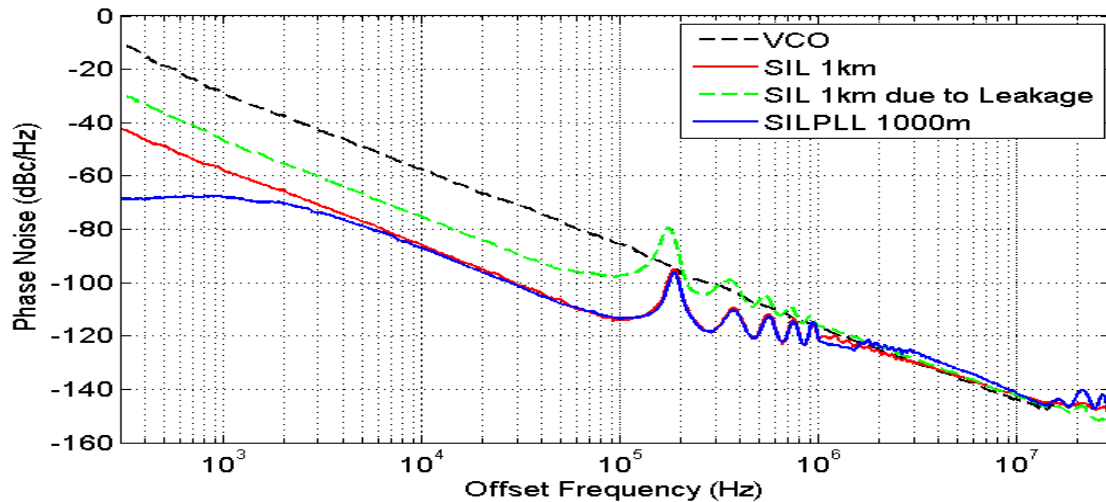


Figure H-5: Experiment Results of VCO with SILPLL. Mixer Board #3 is used, 1km delay, Black: VCO free run; Red: SIL 1km; Blue: SILPLL 1km; $K_d=0.1\text{V}/\text{rad}$, $K_o=2\pi\times1\text{MHz}/\text{V}$

Table H.2: Comparison of different circuit topologies utilizing single fiber delay for VCO with FR4 BPF

	300Hz	1kHz	10kHz
VCO free run	-11	-29	-58
SIL 1km	-42	-58	-86
SILPLL 1km	-69	-68	-87

Fiber delays longer than 1km are also attempted to provide more phase noise reduction. However, the side-modes of the long delay makes the PLL loop to be unstable, and dual loop SILPLL is proposed to reduce the side-mode level of long delay for further phase noise reduction.

H3.2 Dual-Loop SILPLL VCO

The block diagram of dual loop SILPLL is similar to that of single loop SILPLL (Figure H-4). The difference is the output of the EDFA is split into two paths: one with a 5km delay and another with a 3km delay. Signals from the two-delayed path are picked up by two photo detectors independently, and the converted electrical signals are combined in a 90° hybrid. The combined signal is amplified and then is sent to the ‘Mixer+LPFA’ to complete the SPPLL function. Once again, the leakage from mixer RF port will

induce SIL function onto the VCO, and the resulting phase noise is shown in green dashed curve in Figure H-2.

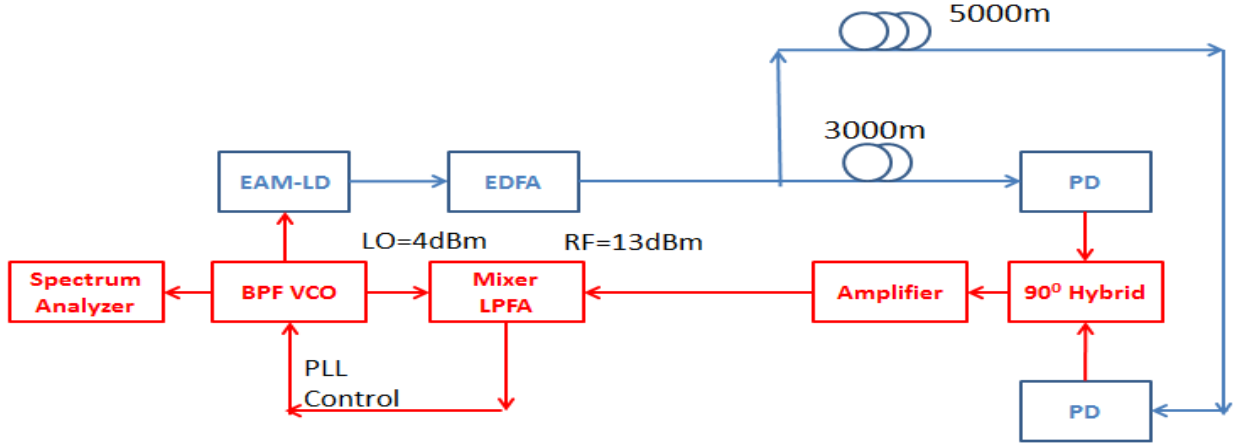


Figure H-6: Block diagram of DSILPLL

Figure H-7 shows the measured phase noise of DSILPLL with various delay combinations. The measured results, combination of 3km and 5km delays yields the best phase noise of -82dBc/Hz at 300Hz offset resulting in a 71dB improvement and -98dBc/Hz at 10 kHz offset resulting in a 40dB improvement. Phase noise performance in the case of 1km and 5km delay is inferior to 3km and 5km delay even though the length of the longer delay is the same.

This could be due to the side-modes of 1km (every 200kHz) and the side-modes of 5km (every 40kHz) are harmonically related therefore the side-modes suppression is not so effective as in the case of 3km and 5km delays, where the side-modes are non-harmonically related. They are spaced every 66.7 kHz for 3km delay and 40 kHz for 5km delay. Phase noise of DSILPLL and DSIL are shown in Figure H-8 for comparison. Same delay combination of 3km and 5km is used for both stabilization techniques. We can see that phase noise of DSILPLL is 29dB lower than that of DSIL, which demonstrates the advantage of DSILPLL over DSIL alone. Spot noise with different circuit topologies are also tabulated in Table H.3 for comparison of different techniques.

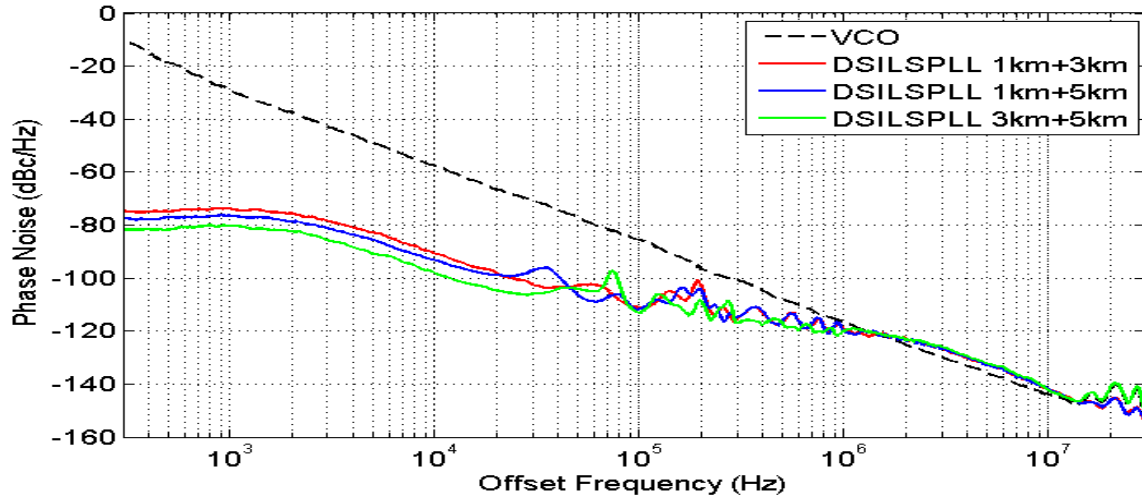


Figure H-7 Phase Noise of DSILPLL VCO. Mixer Board #3 is used, Black: VCO free run; Red: DSILPLL 1km+3km; Blue: DSILPLL 1km+5km; Green: DSILPLL 3km+5km. $K_d=0.1V/\text{rad}$, $K_o=2\pi\times 1\text{MHz}/\text{V}$

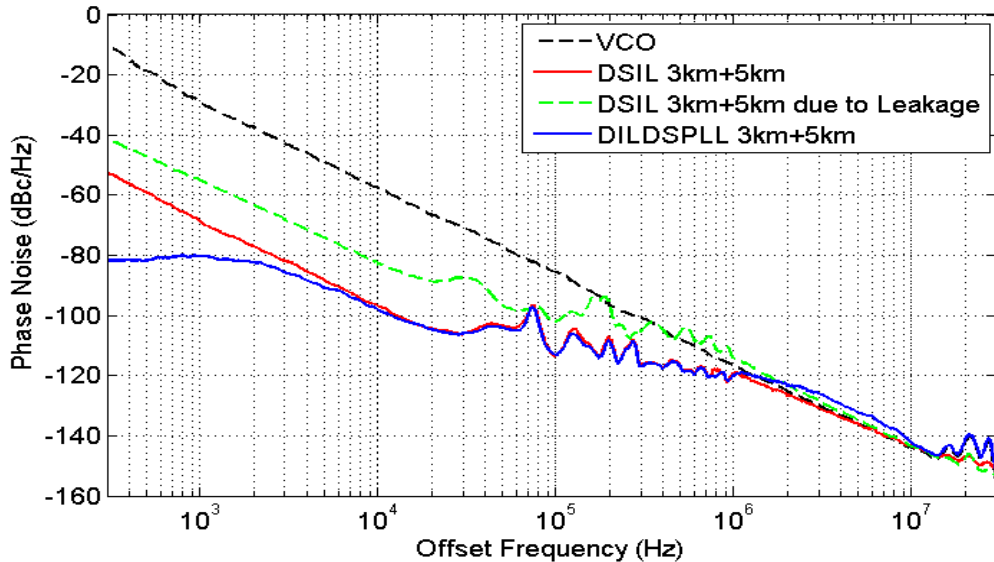


Figure H-8 Phase Noise of DSILPLL VCO. Mixer Board #3 is used, 1km delay, Black: VCO free run; Red: SIL 1km; Blue: SILPLL 1km; $K_d=0.1\text{V}/\text{rad}$, $K_o=2\pi\times 1\text{MHz}/\text{V}$

Table H.3: Comparison of different circuit topologies utilizing single fiber delay for VCO with FR4 BPF

	300Hz	1kHz	10kHz
VCO free run	-11	-29	-58
DSIL 3km+5km	-53	-69	-97
DSILPLL 3km+5km	-82	-80	-98

H4 Summary

This Appendix is dedicated to the analysis and experimental performance evaluation of self-injection locked phase locked loop (SILPLL) oscillators using long optical delay lines. Table H-4 summarizes the reduction of phase noise data experimentally, at 1 kHz and 10 kHz offset frequencies using EAM link.

Table H.4: Comparison of different circuit topologies utilizing single fiber delay for VCO with FR4 BPF

	300Hz	1kHz	10kHz
VCO free run	-11	-29	-58
DSIL 3km+5km	-53	-69	-97
DSILPLL 3km+5km	-82	-80	-98

References

- [1] L. Zhang, V. Madhavan, R.P. Patel, A.K. Poddar, U.L. Rohde, A.S. Daryoush, "Ultra low FM noise in passively temperature compensated microwave Opto-electronic oscillators," in Proc. 2013 IEEE International Microwave & RF Conf., New Delhi, India, pp. 1-4.
- [2] L. Zhang, A.K. Poddar, U.L. Rohde, A.S. Daryoush, "Analytical and experimental evaluation of SSB phase noise reduction in self-injection locked oscillators using optical delay loops," IEEE Phot. Journ., vol. 5, no. 6, Dec. 2013.
- [3] Li Zhang, *Optoelectronic Frequency Stabilization Technique in Forced Oscillators*, PhD Thesis, Drexel University, 2014.

Appendix I

I1 Phase Noise Performance of OEO Circuit Using Optical Transversal Filters

Applications in commercial and military require low-phase noise oscillators [1]. Techniques such as self-injection locking (SIL), self-phase locking (SPLL), and use of a fiber delay have been demonstrated in optoelectronic oscillators (OEO) to improve phase noise over standard oscillators (Appendix F, G, H) [2]. These optical techniques, while demonstrate excellent performance, often have high spurious levels close-in-to-carrier, which could only be removed using narrowband optical filtering such as dual SIL and SPLL [3]. Optical transversal filters, or Mach-Zehnder interferometers (MZI's), are proposed as another alternative to suppress the side-modes present in OEO's. MZI filters RF signals in the optical domain, and have been previously reported in [4]-[5]. The advantage of using optical transversal techniques over equivalent electrical techniques lies in their inherent narrow bandwidth, small size and low loss for very high order, and ease of tunability. Narrowband RF filtering is required for stabilization of optoelectronic oscillators and forced oscillators. An optical transversal filter is proposed to perform narrowband RF filtering in opto-electronic (OEO) oscillators by realizing a Mach-Zehnder interferometer (MZI) at RF frequency of 8.8GHz. This 1st order optical filter is realized utilizing various lengths of SMF-28 fiber and 3dB couplers to perform RF filtering in the optical domain. With proper delay length, arm amplitude balance, and filter implementation, a stable filter with large null depth can be achieved. A tuning of 33 kHz/nm is also achieved using standard fiber dispersion at 1550nm. The phase noise measurements of standard OEO are performed using this transversal filter with excellent results.

I1.1 Optical Filter Analysis and Modeling

The feed-forward 1st order MZI consists of two ideal 3-dB fiber couplers having a delay arm and reference arm as shown in Figure I-1(a). Light is injected into port 1 or 2 and received at port 3 or 4.

The filter transfer function is given at operating RF angular frequency of ω by

$$H(\omega) = |1 + \cos(\omega(\tau_d + \tau_D))|/2 \quad (I.1)$$

where τ_d is due to the fiber delay at source wavelength of λ_0 . For simplicity, (1) assumes 3-dB equal split in the couplers. It is apparent that the filter frequency response is dependent on delay length and optical wavelength tuning. The optical wavelength can be varied to determine the overall tunability of the filter and is specified in units of kHz/nm.

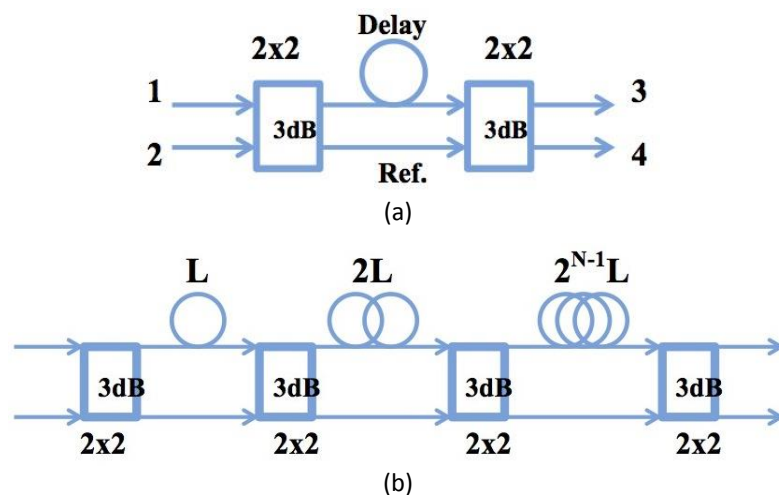


Figure I-1: Optical transversal filter layout showing 3-dB couplers and fiber delays, a) 1st order filter with Delay; b) N^{th} order optical transversal filter with delays of $L, 2L, \dots, 2^{N-1}L$.

This delay is related to index of refraction of fiber core at λ_o by $n(\lambda_o)$, speed of light in free space c , and ΔL the fiber length difference between reference arm and delayed paths as:

$$\tau_d = \Delta L n(\lambda_o) / c \quad (I.2)$$

The term τ_d in (1) is due to fiber dispersion and provides option of narrowband filter tuning by adjusting the optical source wavelength and is represented by

$$\tau_d = D \Delta L (\Delta \lambda) \quad (I.3)$$

where $\Delta \lambda$ is wavelength tuning away from λ_o wavelength of optical source and D is the dispersion parameter in units ps/nm/km.

Simulated results of 1st order filter are depicted in Figure I-2(a) for a 150m long fiber. By cascading a number of 1st order filters, a higher order optical filter can be realized as shown for an N^{th} order optical transversal filter in Figure I-1(b). To achieve a narrowband filtering, delay #2 could be set as twice delay #1.

In the high order transversal filters (Figure I-2a) combinations of fiber delays that are even multiples of one another result in having filter tuned to the same center frequency, while the side-mode that pass in the 1st order are removed as depicted in Figure I-2(b) for lengths of 50m and 100m loops. CAD simulations are also performed for 2nd order transversal filter at source wavelengths of 1534nm and 1565nm to evaluate wavelength tuning of this filter.

Figure I-2(c) illustrates a complete change in passband and stopband in these two wavelengths. Moreover, the simulated results depict filter tuning of 32 kHz/nm for standard fiber dispersion of $D=17\text{ps/nm.km}$. A higher tuning range is expected for dispersive photonic crystal fibers, as reported in [3]. Optical coherence effects are considered when designing an MZI. Upon injection of light into port 1 of the MZI, the light splits and remains coherent for a period defined as the coherence length.

Upon recombination at port 3, if the light remains coherent it will undergo optical interference-this is not desirable as the goal of RF filtering is RF coherence, not optical coherence. To avoid optical coherence, difference in delay between arms 1 and 2 of the MZI should be greater than the coherence length. Assuming a Lorentzian distribution, the laser coherence length is given approximately by

$$L_{coh} = c \tau_{coh} = c / \pi \Delta v \quad (I.4)$$

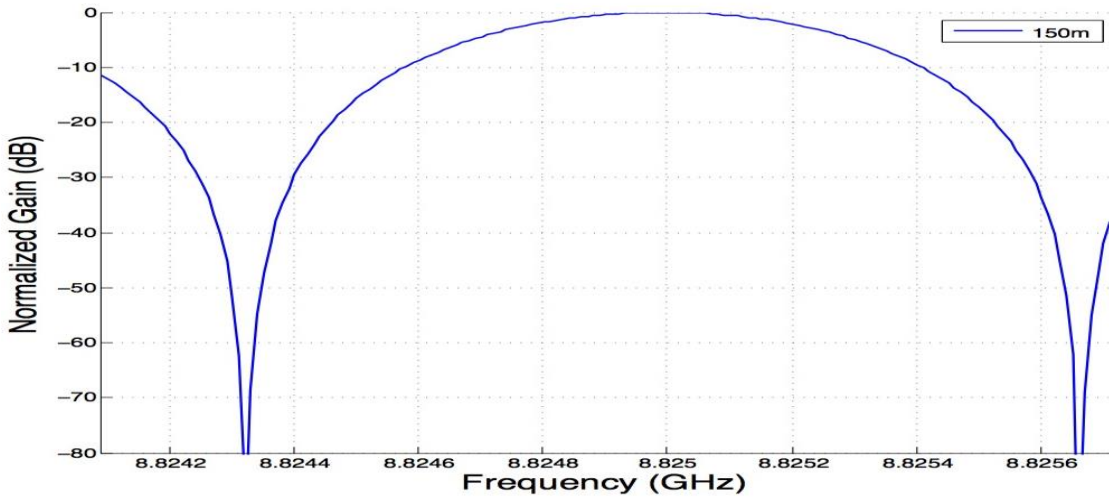
where τ_{coh} is the coherence time, c is the speed of light in a vacuum, and Δv is the laser line width.

The laser selected for experiments is a Eudyna FLD5F10NP C-band DFB laser with an electro-absorption modulator (EAM). The laser line width is approximately 1MHz corresponding to a coherence length of about 95m.

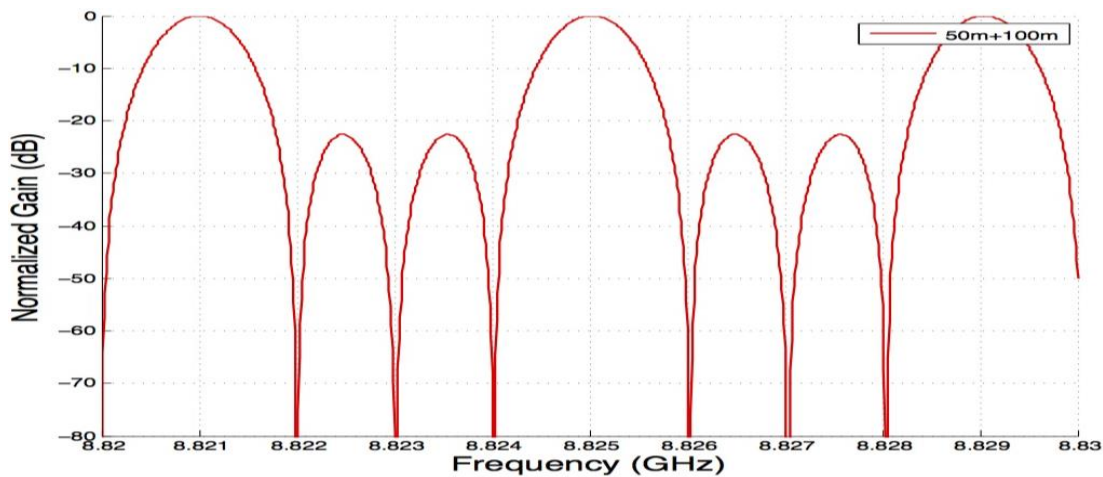
I1.2 Experimental Result

In order to validate the noise suppression performance of the optical transversal filter, the MZI is placed in an Opto-electronic oscillator, as depicted in Figure I-3. Various realization of OEO are reported in [1]-[2], particularly Opto-electronic frequency stabilization of forced oscillators are presented in [3]. The experimental results of Opto-electronic transversal filter are reported for the first time here. The MZI follows the optical delay to provide side-mode suppression, as an alternative to multi loop ILPLL techniques reported in [1]-[3].

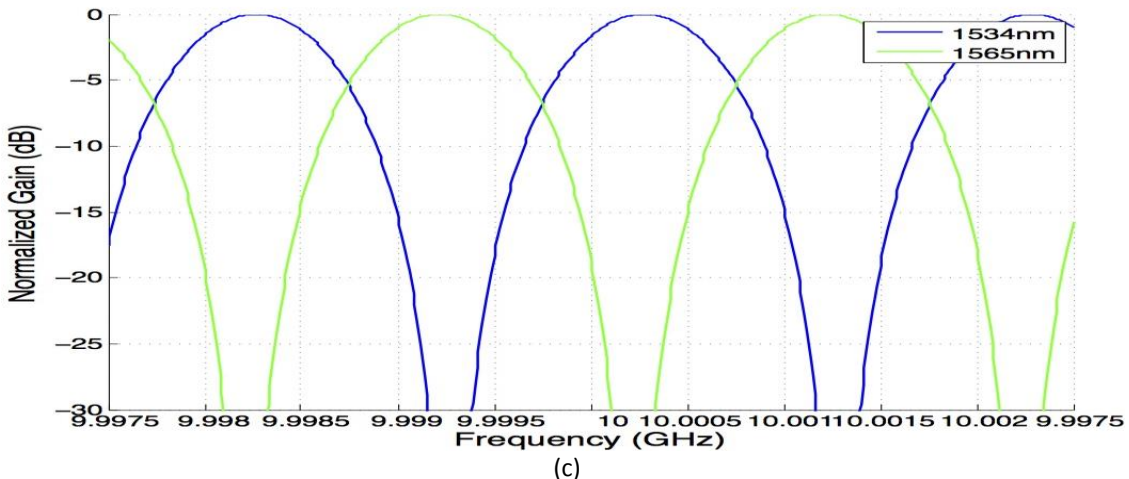
Output ports 3 and 4 are electrically combined after detection by photodiode (PD) using a Wilkinson power combiner (i.e., a 3dB coupler), as opposed to optical combination to avoid higher phase noise generated due to the optical phase fluctuations for optical interference. For differential lengths longer the coherent length of laser diode, the optical phase fluctuations is insignificant for optical MZI.



(a)



(b)



(c)

Figure I-2: Simulated performance of MZI's at source wavelength of 1554nm for a) 1st order of 150m long and b) 2nd order 50m+100m; c) tuning of 2nd order 50m+100m from 1534nm (in blue) to 1565nm (in green).

A 1st order MZI was characterized first. The filter consisted of Corning SMF-28E fiber and Ascentta 2x2 3dB couplers for C-band. A Eudyna FLD5F10NP DFB laser is biased by a Lightwave LDC3900 controller and externally modulated by a Gigatronics GT9000 Microwave Synthesizer.

The operating wavelength is 1554nm as measured with an Anritsu MS9710 optical spectrum analyzer. The MZI output is fed to a Discovery DSC50S PIN photodiode, which produces an RF signal to be amplified by a FET based Avantek 30dB amplifier. The amplified RF signal is monitored using a Rohde & Schwarz FSUP-50 signal source analyzer.

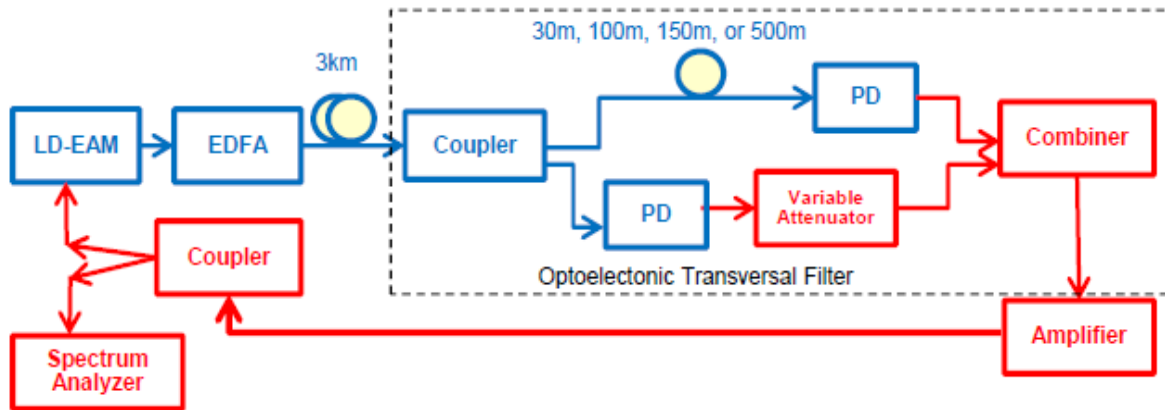


Figure I-3: Experimental set-up of OEO with optoelectronic transversal filter, various lengths of fiber are considered for Opto-electronic transversal filter implementations.

I1.2.1 Transversal Filter Measurement

The filter transfer function is measured for a 150m MZI and results are depicted in Figure I-4, where the max-hold feature of spectrum analyzer is employed, while sweeping frequency of the RF synthesizer in 5 kHz increments. Comparison of simulated and measured results of 1st order transversal filter is summarized in Table I.1.

Measurements were performed using an ID Photonics CoBrite DX4 laser driver module, Corning SMF-28, and Ascentta 3dB 2x2 C-band couplers. The 100m 1st order filter was tested from 1534nm to 1565nm and frequency response is shown in Figure I-5. A tuning of 33 kHz/nm is experimentally measured that is comparable to the simulated performance.

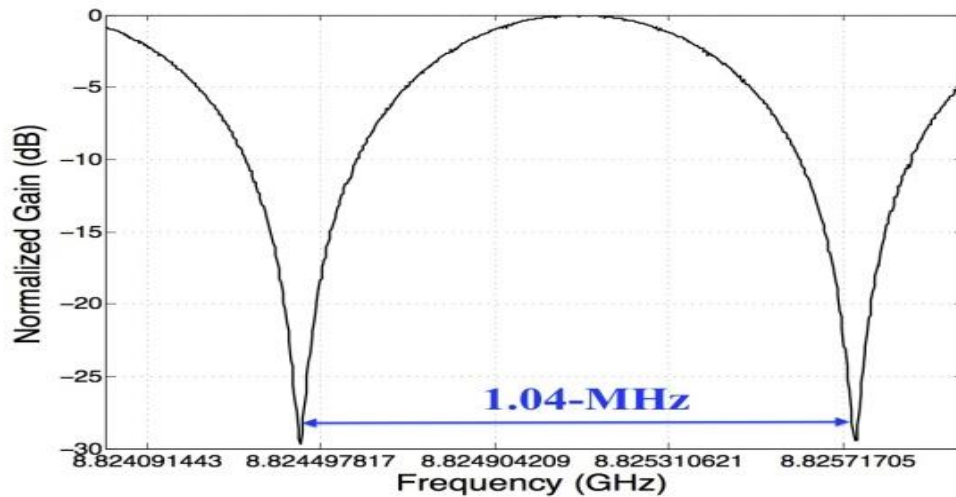


Figure I-4: Transfer function of 1st order MZI with 150m delay, as an optoelectronic transversal filter.

Table I.1: Measured and simulated 1st order transversal filter results

Filter	Full-null bandwidth (MHz) - measured	Max. rejection (dB) - measured	Full-null bandwidth (MHz) - simulated	Max. rejection (dB) - simulated
30-m	5.45	31.3	6.71	inf.
150-m	1.04	29.7	1.34	inf.
500-m	0.41	30.0	0.40	inf.

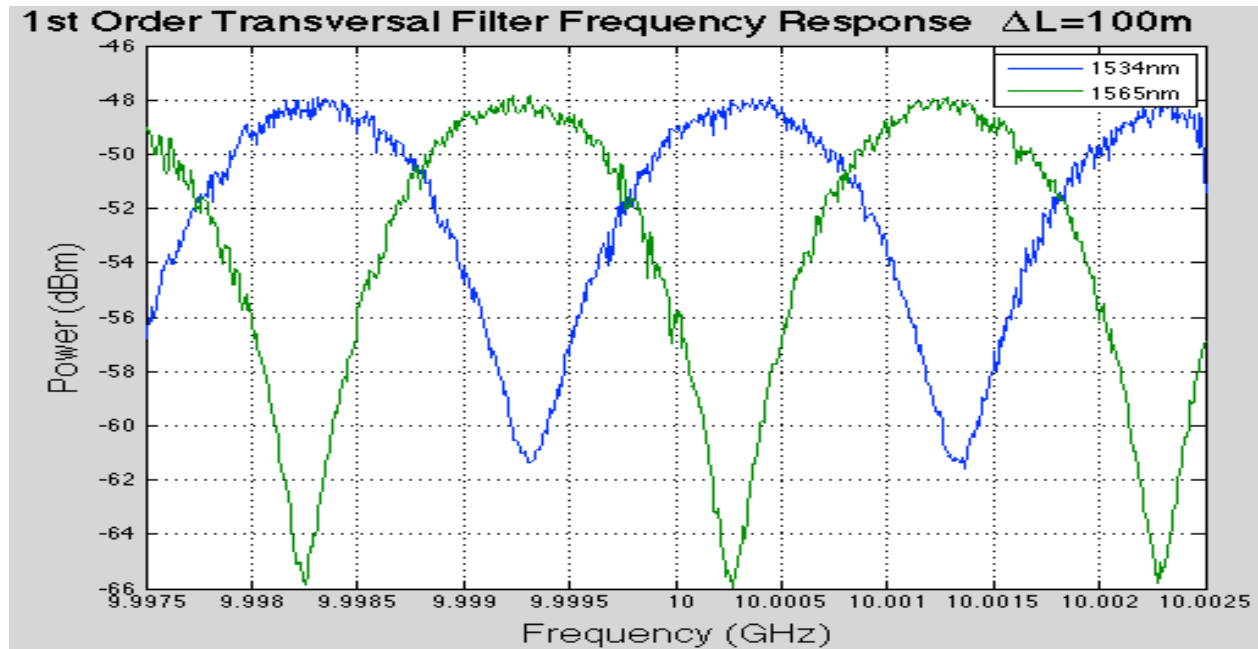


Figure I-5: Experimental results of frequency tuning of a 1st order optical transversal filter using a 100m long fibers at wavelengths of 1534nm (blue) and 1565nm (green). Fluctuations are due to optical phase interference.

I1.2.2 Phase Noise Measurement Using Transversal Filter

Phase noise measurements are performed using the Rohde & Schwarz FSUP-50. A 3km delay is selected for the OEO delay. The 1st order transversal filters with the lengths of 30m, 100m, 150m, and 500m are inserted after the 3km delay; phase noise measurements are shown in Figure I-6.

The experimental results with the filters demonstrate phase noise roll-off slope of -30dB/decade at close in to carrier and phase noise of -125 to -135dBc/Hz at 10 kHz offset. However, the OEO phase noise levels of -145 dBc/Hz and -150 dBc/Hz is intermittently measured at 1 kHz and 10kHz offset carrier respectively, as depicted in Figure I-6.

This intermittent improvement in performance was observed for the cases where a large number of closely packed side-modes exist for the MZI lengths longer than 30m.

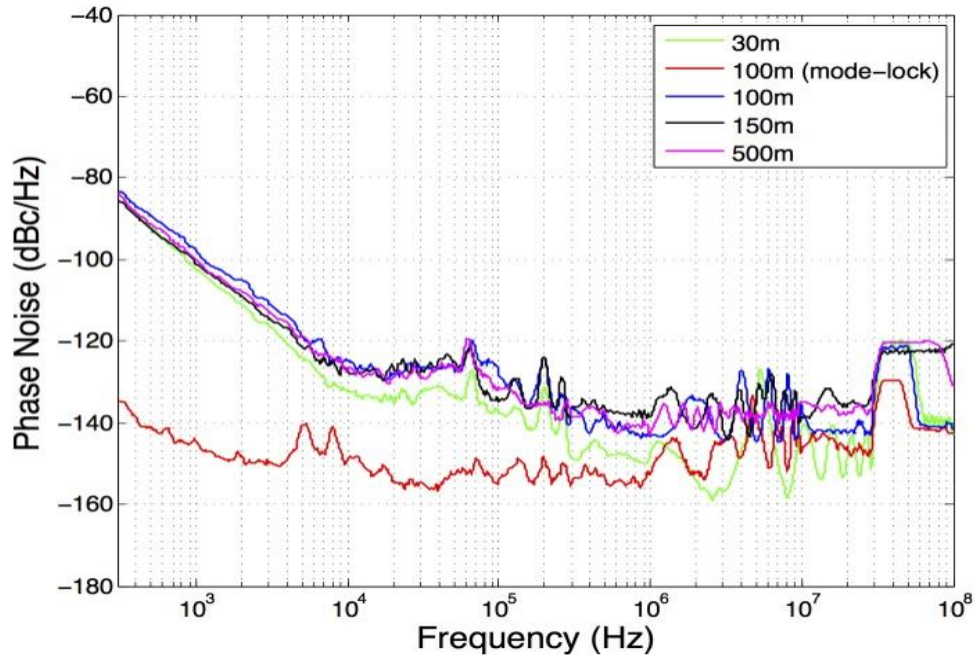


Figure I-6: Measured close-in to carrier phase noise of a 3km OEO using various transversal filter lengths of 30m (green), 100m (blue), 150m (black), 500m (magenta), and 100m during mode-locking (red).

I1.2.3 Summary

Opto-electronic transversal filter is analytically studied and experimentally validated for use as a narrow band filter in OEO. Very low close in to carrier phase noise of better than -100dBc/Hz (and frequently levels of -145dBc/Hz) is observed at 1 kHz offset. This unprecedented low phase noise is attributed to mode locking [6]-[7] of the larger number of modes in the transversal filters.

References

- [1] L. Zhang, V. Madhavan, R.P. Patel, A.K. Poddar, U.L. Rohde, A.S. Daryoush, "Ultra low FM noise in passively temperature compensated microwave Opto-electronic oscillators," in Proc. 2013 IEEE International Microwave & RF Conf., New Delhi, India, pp. 1-4.
- [2] L. Zhang, A.K. Poddar, U.L. Rohde, A.S. Daryoush, "Analytical and experimental evaluation of SSB phase noise reduction in self-injection locked oscillators using optical delay loops," IEEE Phot. Journ., vol. 5, no. 6, Dec. 2013.
- [3] Li Zhang, *Optoelectronic Frequency Stabilization Technique in Forced Oscillators*, PhD Thesis, Drexel University, 2014.
- [4] Y. Jiang et al., "A selectable multiband bandpass microwave photonic filter," IEEE Photonics Journal, vol. 5, no. 3, p. 3, June 2013.
- [5] J. Mora et al., "Photonic microwave tunable single-bandpass filter based on a Mach-Zehnder interferometer," Journ. Lightwave Tech., vol. 24, no. 7, July 2006.
- [6] A. Poddar, A. Daryoush, and U. Rohde, "Integrated production of self injection locked self phase loop locked Opto-electronic Oscillators", US Patent app. 13/760767.
- [7] A. Poddar, A. Daryoush, and U. Rohde, "Self-injection locked phase locked loop optoelectronic oscillator," US Patent App., no. 61/746, 919.
- [8] J.W. Fisher, L. Zhang, A. Poddar, U.L. Rohde, and A.S. Daryoush, "Phase Noise Performance of Optoelectronic Oscillator Using Optical Transversal Filters", IEEE BenMAS, Drexel, Sept 2014